

Journal of

Geophysics

Zeitschrift für

Geophysik

Volume 42 1976/1977

Managing Editors: W. Dieminger, J. Untiedt

Editorial Board

Professor K. M. Creer, University of Edinburgh, Department of Geophysics, James Clerk Maxwell Building, King's Buildings, Mayfield Road, Edinburgh EH9 3JZ, Scotland

Professor W. Dieminger, Max-Planck-Institut für Aeronomie, D-3411 Lindau üb. Northem/Hann., Federal Republic of Germany

Professor K. Fuchs, Geophysikalisches Institut der TU, Hertzstraße 10, Bau 42, D-7500 Karlsruhe, Federal Republic of Germany

Professor C. Kisslinger, Director, Cooperative Institute for Research in Environmental Sciences, University of Colorado, Boulder, Colorado 80302, USA

Professor Th. Krey, Prakla-Seismos GmbH, Postfach 47 67, D-3000 Hannover 1, Federal Republic of Germany

Professor J. Untiedt, Institut für Geophysik der Westfälischen Wilhelms-Universität, Gievenbecker Weg 61, D-4400 Münster/Westf., Federal Republic of Germany

Professor S. Uyeda, Earthquake Research Institute, University of Tokyo, Tokyo 113, Japan

Advisory Board

G. Angenheister, München A.A. Ashour, Cairo W.I. Axford, Lindau/Harz
J. Behrens, Berlin H. Berckhemer, Frankfurt a.M. V. Bucha, Praha
J. Cain, Greenbelt, Md. N. Fukushima, Tokyo B. Haurwitz, Fort Collins, Colo.
I.P. Kosminskaja, Moskwa W. Krauss, Kiel St. Müller, Zürich A. Roche, Strasbourg
O. Rosenbach, Clausthal-Zellerfeld S. Saxov, Aarhus U. Schmucker, Göttingen
H. Soffel, München L. Stegena, Budapest H. Stiller, Potsdam



Springer International

With the acceptance of the manuscript for publication the exclusive copyright for all languages and countries, including the right for photomechanical and any other reproduction, also in microform, is transferred to the Deutsche Geophysikalische Gesellschaft, Hamburg.

The use of registered names, trademarks, etc. in this publication does not imply, even in the absence of a specific statement, that such names are exempt from the relevant protective laws and regulations and therefore free for general use.

Printed in Germany by Univ.-Druckerei H. Stürtz AG, Würzburg

© by the Deutsche Geophysikalische Gesellschaft, Hamburg, 1976/1977



Author Index

- Akasheh, B. 159
Baksi, S.S. 521
Balling, N.P. 237
Bamford, D. 103
Barnstorf, H. 599
Behle, A. 131
Beinroth, H.J. 599
Bird, M.K. 659
Biswas, A. 137
Breyman, U. 391
Čermák, V. 455
Clarke, G.K.C. 373
Closs, H. 547
Dehmel, G. 599
Dieminger, W. 447
Dose, V. 15
Dragert, H. 373
Dresen, L. 111
Drewes, H. 27
Edenhofer, P. 673
Eshghi, I. 159
Esposito, P.B. 673
Faber, S. 103
Fechtig, H. 717
Freystätter, S. 111
Fuchs, K. 175
Fuckner, J. 615
Gammelin, P. 717
Gerharz, R. 163
Giese, R.H. 705
Goldflam, St. 419
Green, G. 615
Grün, E. 717
Guya, N.H. 277
Hanner, M. 699
Hansen, R.T. 673
Hansen, S.F. 673
Hanuš, V. 219
Hartmann, G.K. 447
Hasegawa, A. 271
Heller, F. 47, 475
Hempe, H. 615
Hillebrand, O. 257
Hirschleber, H.B. 419
Horálek, J. 201
Hummervoll, R. 85
Isensee, U. 581
Iwers, B. 615
Jacob, B. 103
Janle, P. 407, 419
Kaminski, W. 103
Keppler, E. 633, 645
Kind, R. 191
Kirsch, E. 1
Kissel, J. 717
Korschunow, A. 89
Kremser, G. 1
Kunow, H. 615
Lammers, E. 591
Lanzerotti, L.J. 271
Leinert, C. 699
Levy, G.S. 659
Link, H. 699
Lüneburg, E. 673
Makris, J. 329
Markert, H. 47
Marsch, E. 561
Martin, W.L. 673
Meyer, B. 561
Miggenrieder, H. 561
Montgomery, M.D. 561
Morelli, C. 171
Mühlhäuser, K.H. 561
Müller, G. 343, 429
Müller, S. 283
Mueller-Mellin, R. 615
Musmann, G. 591
Neubauer, F.M. 591, 599
Nunn, K. 103
Petersen, N. 59, 403
Pilipp, W. 561
Pitz, E. 699
Plésinger, A. 201
Pohl, J. 459
Porsche, H. 551
Prodehl, C. 103
Richter, A.K. 633, 645
Richter, K. 633
Riedler, W. 1
Rietsch, E. 489
Roeser, H.A. 73
Rohde, J. 131
Rohde, M. 727
Rosenbauer, H. 561
Roy, K.K. 521
Rybach, L. 93
Sarma, S.B.S.S. 535, 541
Schäfer, J. 361
Schleusener, A. 27
Schmidt, K.D. 737
Schmocker, U. 15
Schreiber, H. 437
Schult, A. 81
Schulz, K. 175
Schwehm, G. 727
Schwenn, R. 561
Seidel, B.L. 659
Seidl, D. 283
Sele, G. 15
Sharma, M.C. 535, 541
Soffel, H. 351, 459
Soltanian, R. 159
Spitta, P. 507
Steigenberger, N. 47
Stelzried, C.T. 659
Storetvedt, K.M. 59, 403
Thyssen-Bornemisza, S. 169
Töpfer, K.D. 147, 225
Torge, W. 27
Umlauf, G. 633
Vaněk, J. 219
Vees, R. 329
Voges, W. 561
Volland, H. 659
Westphal, M. 399
Wibberenz, G. 615
Wilken, B. 633
Williams, D.J. 633
Witte, M. 615
Zink, S.M. 561
Zygielbaum, A.I. 673

Subject Index

Aegean Sea

Crustal Structure of the Central Aegean Sea and the Islands of Evia and Crete, Greece, Obtained by Refractive Seismic Experiments (Makris, J., Veis, R.) 329

Alps

Die Gesteinsradioaktivität und ihr Einfluß auf das Temperaturfeld in der kontinentalen Kruste. The Radioactivity of Rocks and Its Influence on the Temperature Field in the Continental Crust (Rybach, L.) 93

Fault-Plane Solution of the Earthquake in Northern Italy, 6 May 1976, and Implications for the Tectonics of the Eastern Alps (Müller, G.) 343

Analysis of Data

Note on the Reliability of Subjective Processing of Geomagnetic Pulsation-Records in the Range Pc 2–Pc 5 (Korschunow, A.) 89

Probleme bei der Untersuchung von räumlich und zeitlich veränderlichen Medien, dargestellt am Beispiel der Ionosphäre. Problems in the Investigation of Space and Time Dependent Media Exemplified by the Ionosphere (Dieminger, W., Hartmann, G.K.) 447

The Maximum Entropy Approach to Inverse Problems. Spectral Analysis of Short Data Records and Density Structure of the Earth (Rietsch, E.) 489

Andean South America

Intermediate Aseismicity of the Andean Subduction Zone and Recent Andesitic Volcanism (Hanuš, V., Vaněk, J.) 219

Applied Geophysics

Rayleigh Channel Waves for the In-Seam Seismic Detection of Discontinuities (Dresen, L., Freystätter, S.) 111

Representation and Interpretation of Resistivity Mapping Data in Groundwater Prospecting in Zambia (Töpfer, K.D.) 147

Technique for Simultaneous Observation of Gravity and Vertical Gradient Data (Thyssen-Bornemisza, S.) 169

Computation of Reflection Coefficients for Layered Media (Kind, R.) 191

Magnetotelluric Investigation of a Nearly Circular Salt dome in Northern Germany (Breyman, U.) 391

Model Studies on Redox Logging for Minerals (Roy, K.K., Baksi, S.S.) 521

Atlantic Ocean

Magnetic Anomalies of the African Red Sea Shelf and Their Implications for the Anomalies of Atlantic Continental Margin (Roeser, H.A.) 73

Atmospheric Scattering

Appearance of the Atmospheric Scatter Field during a Solar Eclipse (Gerharz, R.) 163

Auroral Zone Physics

Short-Time Variations of Solar Particle Fluxes during the August 1972 Events (Kremser, G., et al.) 1

Auroral Lyman-Alpha Emission (Dose, V., et al.) 15

Spatial Characteristics of Giant Pulsations (Hillebrand, O.) 257

Balloon-Borne Observations

Short-Time Variations of Solar Particle Fluxes during the August 1972 Events (Kremser, G., et al.) 1

Benioff Zones

Intermediate Aseismicity of the Andean Subduction Zone and Recent Andesitic Volcanism (Hanuš, V., Vaněk, J.) 219

Blue Road Traverse

A Refined Crustal Model and the Isostatic State of the Scandinavian Blue Road Area (Goldflam, St., et al.) 419

Britain

A Lithospheric Seismic Profile in Britain. II. Preliminary Report on the Recording of a Local Earthquake (Kaminski, W., et al.) 103

Canada

- A Detailed Investigation of the Canadian Cordillera Geomagnetic Transition Anomaly (Dragert, H., Clarke, G.K.C.) 373

Conductivity, Anomalies of Electrical

- A Detailed Investigation of the Canadian Cordillera Geomagnetic Transition Anomaly (Dragert, H., Clarke, G.K.C.) 373

Corsica

- Postulated Rotation of Corsica not Confirmed by New Palaeomagnetic Data (Storetvedt, K.M., Petersen, N.) 59
- Comments on: Postulated Rotation of Corsica not Confirmed by New Palaeomagnetic Data by K.M. Storetvedt and N. Petersen, J. Geophys. 42, 59-71, 1976 (Westphal, M.) 399
- Reply (Storetvedt, K.M., Petersen, N.) 403

Cosmic Rays

- Cosmic Ray Measurements on Board Helios 1 from December 1974 to September 1975: Quiet Time Spectra, Radial Gradients, and Solar Events (Kunow, H., et al.) 615
- A Survey on Measurements of Medium Energy Protons and Electrons Obtained with the Particle Spectrometer E8 on Board of Helios (Keppler, E., et al.) 633
- Interaction of Low-Energy (>80 keV) Protons with the January 6 and 8, 1975, Shock Waves: Helios-1 Observations (Richter, A.K., Keppler, E.) 645

Crustal Structure

- The Gravity Field of Northeastern Iceland (Schleusener, A., et al.) 27
- Magnetic Anomalies of the African Red Sea Shelf and Their Implications for the Anomalies of Atlantic Continental Margin (Roeser, H.A.) 73
- Geothermal Models of the Crust and Uppermost Mantle of the Fennoscandian Shield in South Norway and the Danish Embayment (Balling, N.P.) 237
- Crustal Structure of the Central Aegean Sea and the Islands of Evia and Crete, Greece, Obtained by Refractional Seismic Experiments (Makris, J., Veas, R.) 329
- A Refined Crustal Model and the Isostatic State of the Scandinavian Blue Road Area (Goldflam, St., et al.) 419

Czechoslovakia

- Heat Flow of the Bohemian Massif (Čermák, V.) 455

Density Structure

- The Gravity Field of Northeastern Iceland (Schleusener, A., et al.) 27
- The Maximum Entropy Approach to Inverse Problems. Spectral Analysis of Short Data Records and Density Structure of the Earth (Rietsch, E.) 489

Earthquakes

- A Lithospheric Seismic Profile in Britain. II. Preliminary Report on the Recording of a Local Earthquake (Kaminski, W., et al.) 103
- Fault-Plane Solution of the Earthquake in Northern Italy, 6 May 1976, and Implications for the Tectonics of the Eastern Alps (Müller, G.) 343

Fault-Plane Solutions

- Fault-Plane Solution of the Earthquake in Northern Italy. 6 May 1976, and Implications for the Tectonics of the Eastern Alps (Müller, G.) 343

Fennoscandia

- Geothermal Models of the Crust and Uppermost Mantle of the Fennoscandian Shield in South Norway and the Danish Embayment (Balling, N.P.) 237
- A Refined Crustal Model and the Isostatic State of the Scandinavian Blue Road Area (Goldflam, St., et al.) 419

Geodesy

- Modern Standards for Gravity Surveys (Morelli, C.) 171

Geoelectric exploration

- Representation and Interpretation of Resistivity Mapping Data in Groundwater Prospecting in Zambia (Töpfer, K.D.) 147

Geomagnetic Activity

- On the Variation of K_p at Sector Boundaries (Schreiber, H.) 437

Geomagnetic Deep Sounding

- A Detailed Investigation of the Canadian Cordillera Geomagnetic Transition Anomaly (Dragert, H., Clarke, G.K.C.) 373
- Electromagnetic Scale Model Experiments for the Coastline Effect of Geomagnetic Variations (Spitta, P.) 507

Germany

- Magnetotelluric Investigation of a Nearly Circular Salt Dome in Northern Germany (Breyman, U.) 391
- Palaeomagnetic and Rock Magnetic Investigations of Tertiary Volcanics in Northern Bavaria (Pohl, J., Soffel, H.) 459
- Palaeomagnetism of Upper Jurassic Limestones from Southern Germany (Heller, F.) 475

Gravimetry

- Technique for Simultaneous Observation of Gravity and Vertical Gradient Data (Thyssen-Bornemisza, S.) 169
- Modern Standards for Gravity Surveys (Morelli, C.) 171

Gravity Anomalies

- The Gravity Field of Northeastern Iceland (Schleusener, A., et al.) 27
- Technique for Simultaneous Observation of Gravity and Vertical Gradient Data (Thyssen-Bornemisza, S.) 169
- Modern Standards for Gravity Surveys (Morelli, C.) 171
- Provisional Seismicity Map of the Republic of Zambia and Its Preliminary Interpretation (Töpfer, K.D.) 225
- Structure of Lunar Impact Craters from Gravity Models (Janle, P.) 407

Greece

- Crustal Structure of the Central Aegean Sea and the Islands of Evia and Crete, Greece, Obtained by Refractional Seismic Experiments (Makris, J., Veas, R.) 329

Groundwater Exploration

- Representation and Interpretation of Resistivity Mapping Data in Groundwater Prospecting in Zambia (Töpfer, K.D.) 147

Heat Flow, Terrestrial

- Die Gesteinsradioaktivität und ihr Einfluß auf das Temperaturfeld in der kontinentalen Kruste. The Radioactivity of Rocks and Its Influence on the Temperature Field in the Continental Crust (Rybach, L.) 93
- Geothermal Models of the Crust and Uppermost Mantle of the Fennoscandian Shield in South Norway and the Danish Embayment (Balling, N.P.) 237
- Heat Flow of the Bohemian Massif (Čermák, V.) 455

Helios Mission

- General Aspects of the Mission Helios 1 and 2. Introduction to a Special Issue on Initial Scientific Results of the Helios Mission (Porsche, H.) 551
- A Survey on Initial Results of the Helios Plasma Experiment (Rosenbauer, H., et al.) 561
- Plasma Disturbances Caused by the Helios Spacecraft in the Solar Wind (Isensee, U.) 581
- Radial Variation of the Interplanetary Magnetic Field between 0.3 AU and 1.0 AU. Observations by the Helios-1 Spacecraft (Musmann, G., et al.) 591
- Initial Results from the Helios-1 Search-Coil Magnetometer Experiment (Neubauer, F.M., et al.) 599
- Cosmic Ray Measurements on Board Helios-1 from December 1974 to September 1975: Quiet Time Spectra, Radial Gradients, and Solar Events (Kunow, H., et al.) 615
- A Survey on Measurements of Medium Energy Protons and Electrons Obtained with the Particle Spectrometer E8 on Board of Helios (Keppler, E. et al.) 633
- Interaction of Low-Energy (> 80 KeV) Protons with the January 6 and 8, 1975, Shock Waves: Helios-1 Observations (Richter, A.K., Keppler, E.) 645
- Helios-1 Faraday Rotation Experiment: Results and Interpretations of the Solar Occultations in 1975 (Volland, H., et al.) 659
- Time Delay Occultation Data of the Helios Spacecrafts and Preliminary Analysis for Probing the Solar Corona (Edenhofer, P., et al.) 673
- Observations of Zodiacal Light from Helios 1 and 2 (Leinert, C., et al.) 699
- Interpretation of the Optical Properties of Interplanetary Dust (Giese, R.H.) 705
- Micrometeoroid Data from the First Two Orbits of Helios 1 (Grün, E., et al.) 717
- Dynamical Effects on Circumsolar Dust Grains (Schwehm, G., Rohde, M.) 727
- Micrometeoroid Orbits Observable by the Helios Micrometeoroid Detector (E10) (Schmidt, K.D.) 737

Hydrodynamic Waves

- Latitude-Dependent Waves and Impulse-Produced Waves (Lanzerotti, L.J., Hasegawa, A.) 271
- Initial Results from the Helios-1 Search-Coil Magnetometer Experiment (Neubauer, F.M., et al.) 599

Iceland

- The Gravity Field of Northeastern Iceland (Schleusener, A., et al.) 27

Induction Anomalies

- A Detailed Investigation of the Canadian Cordillera Geomagnetic Transition Anomaly (Dragert, H., Clarke, G.K.C.) 373

In Memoriam

- In Memoriam Hermann Reich (Closs, H.) 547

Interplanetary Dust

- Observations of Zodiacal Light from Helios 1 and 2 (Leinert, C., et al.) 699
Interpretation of the Optical Properties of Interplanetary Dust (Giese, R.H.) 705
Dynamical Effects on Circumsolar Dust Grains (Schwehm, G., Rohde, M.) 727

Interplanetary Magnetic Field

- On the Variation of K_p at Sector Boundaries (Schreiber, H.) 437
Radial Variation of the Interplanetary Magnetic Field between 0.3AU and 1.0AU. Observations by the Helios-1 Spacecraft (Musmann, G., et al.) 591
Initial Results from the Helios-1 Search-Coil Magnetometer Experiment (Neubauer, F.M., et al.) 599
Cosmic Ray Measurements on Board Helios 1 from December 1974 to September 1975: Quiet Time Spectra, Radial Gradients, and Solar Events (Kunow, H., et al.) 615
Helios-1 Faraday Rotation Experiment: Results and Interpretations of the Solar Occultations in 1975 (Volland, H., et al.) 659

Inverse Problems

- The Maximum Entropy Approach to Inverse Problems. Spectral Analysis of Short Data Records and Density Structure of the Earth (Rietsch, E.) 489

Ionosphere

- The Diurnal Variation of the Electron Density of the Mid-Latitude Ionospheric D-Region Deduced from VLF-Measurements (Schäfer, J.) 361
Probleme bei der Untersuchung von räumlich und zeitlich veränderlichen Medien, dargestellt am Beispiel der Ionosphäre. Problems in the Investigation of Space and Time Dependent Media Exemplified by the Iono-

sphere (Dieminger, W., Hartmann, G.K.) 447

- Modelling of the Ionosphere and Comparison of the Calculated and Observed Cosmic Radio Noise Absorption over Delhi (Sharma, M.C., Sarma, S.B.S.S.) 535

- Winter Anomaly in VHF Absorption Studies over Delhi (Sarma, S.B.S.S., Sharma, M.C.) 541

Iran

- The Iranian Long Period Array (ILPA) (Akasheh, B., et al.) 159
Study of the Spatial Variation of the Magnetic Field Intensity on North-South Profiles in Iran in Comparison with the IGRF Model of 1970 (Guya, N.H.) 277

Isostasy

- A Refined Crustal Model and the Isostatic State of the Scandinavian Blue Road Area (Goldflam, St., et al.) 419

Italy

- Fault-Plane Solution of the Earthquake in Northern Italy, 6 May 1976, and Implications for the Tectonics of the Eastern Alps (Müller, G.) 343

Jurassic Limestones

- Palaeomagnetism of Upper Jurassic Limestones from Southern Germany (Heller, F.) 475

 K_p

- On the Variation of K_p at Sector Boundaries (Schreiber, H.) 437

Lithosphere

- A Lithospheric Seismic Profile in Britain. II. Preliminary Report on the Recording of a Local Earthquake (Kaminski, W., et al.) 103
Tunneling of Low-Frequency Waves through the Subcrustal Lithosphere (Fuchs, K., Schulz, K.) 175
Intermediate Aseismicity of the Andean Subduction Zone and Recent Andesitic Volcanism (Hanus, V., Vaněk, J.) 219

Lunar Impact Craters

- Structure of Lunar Impact Crater from Gravity Models (Janle, P.) 407

Magnetic Anomalies

Magnetic Anomalies of the African Red Sea Shelf and Their Implications for the Anomalies of Atlantic Continental Margin (Roeser, H.A.) 73

Study of the Spatial Variation of the Magnetic Field Intensity on North-South Profiles in Iran in Comparison with the IGRF Model of 1970 (Guya, N.H.) 277

Magnetotellurics

Magnetotelluric Investigation of a Nearly Circular Salt dome in Northern Germany (Breyman, U.) 391

Maximum Entropy Method

The Maximum Entropy Approach to Inverse Problems. Spectral Analysis of Short Data Records and Density Structure of the Earth (Rietsch, E.) 489

Micrometeorites

Micrometeoroid Data from the First Two Orbits of Helios 1 (Grün, E., et al.) 717

Micrometeoroid Orbits Observable by the Helios Micrometeoroid Detector (E10) (Schmidt, K.D.) 737

Micropulsations, Magnetic

Note on the Reliability of Subjective Processing of Geomagnetic Pulsation-Records in the Range Pc 2-Pc 5 (Korschunow, A.) 89

Spatial Characteristics of Giant Pulsations (Hillebrand, O.) 257

Latitude-Dependent Waves and Impulse-Produced Waves (Lanzerotti, L.J., Hasegawa, A.) 271

Model Electrochemical Experiments

Model Studies on Redox Logging for Minerals (Roy, K.K., Baksi, S.S.) 521

Model Induction Experiments

Electromagnetic Scale Model Experiments for the Coastline Effect of Geomagnetic Variations (Spitta, P.) 507

Model Seismic Experiments

Rayleigh Channel Waves for the In-Seam Seismic Detection of Discontinuities (Dresen, L., Freystätter, S.) 111

Ultrasonic Modelling of a Moving Source (Behle, A., Rohde, J.) 131

Moon

Structure of Lunar Impact Craters from Gravity Models (Janle, P.) 407

Palaeomagnetism

Parabolic Field Dependence of Kinks Occurring in the Logarithmic Time Plots of Viscous Magnetization (Markert, H., et al.) 47

Postulated Rotation of Corsica not Confirmed by New Palaeomagnetic Data (Storetvedt, K.M., Petersen, N.) 59

Further Utilization of the Fluxgate Magnetometer in the Palaeomagnetic Laboratory (Hummervoll, R.) 85

Comments on: Postulated Rotation of Corsica not Confirmed by New Palaeomagnetic Data by K.M. Storetvedt and N. Petersen, J. Geophys. 42, 59-71, 1976 (Westphal, M.) 399

Reply (Storetvedt, K.M., Petersen, N.) 403

Palaeomagnetic and Rock Magnetic Investigations of Tertiary Volcanics in Northern Bavaria (Pohl, J., Soffel, H.) 459

Palaeomagnetism of Upper Jurassic Limestones from Southern Germany (Heller, F.) 475

Radioactivity of Rocks

Die Gesteinsradioaktivität und ihr Einfluß auf das Temperaturfeld in der kontinentalen Kruste. The Radioactivity of Rocks and Its Influence on the Temperature Field in the Continental Crust (Rybach, L.) 93

Redox Logging

Model Studies on Redox Logging for Minerals (Roy, K.K., Baksi, S.S.) 521

Red Sea

Magnetic Anomalies of the African Red Sea Shelf and Their Implications for the Anomalies of Atlantic Continental Margin (Roeser, H.A.) 73

Refraction Seismology

A Lithospheric Seismic Profile in Britain. II. Preliminary Report on the Recording of a Local Earthquake (Kaminski, W., et al.) 103

Crustal Structure of the Central Aegean Sea and the Islands of Evia and Crete, Greece, Obtained by Refractional Seismic Experiments (Makris, J., Veis, R.) 329

Riometer Observations

- Modelling of the Ionosphere and Comparison of the Calculated and Observed Cosmic Radio Noise Absorption over Delhi (Sharma, M.C., Sarma, S.B.S.S.) 535

Rock Magnetism

- Parabolic Field Dependence of Kinks Occurring in the Logarithmic Time Plots of Viscous Magnetization (Markert, H., et al.) 47
- Postulated Rotation of Corsica not Confirmed by New Palaeomagnetic Data (Storetvedt, K.M., Petersen, N.) 59
- Self-Reversal above Room Temperature due to N-Type Magnetization in Basalt (Schult, A.) 81
- Further Utilization of the Fluxgate Magnetometer in the Palaeomagnetic Laboratory (Hummervoll, R.) 85
- Pseudo-Single-Domain Effects and Single-Domain Multidomain Transition in Natural Pyrrhotite Deduced from Domain Structure Observations (Soffel, H.) 351
- Comments on: Postulated Rotation of Corsica not Confirmed by New Palaeomagnetic Data by K.M. Storetvedt and N. Petersen, *J. Geophys.* 42, 59–71, 1976 (Westphal, M.) 399
- Reply (Storetvedt, K.M., Petersen, N.) 403
- Palaeomagnetic and Rock Magnetic Investigations of Tertiary Volcanics in Northern Bavaria (Pohl, J., Soffel, H.) 459
- Palaeomagnetism of Upper Jurassic Limestones from Southern Germany (Heller, F.) 475

Salt Domes

- Magnetotelluric Investigation of a Nearly Circular Salt dome in Northern Germany (Breyman, U.) 391

Scandinavia

- Geothermal Models of the Crust and Uppermost Mantle of the Fennoscandian Shield in South Norway and the Danish Embayment (Balling, N.P.) 237
- A Refined Crustal Model and the Isostatic State of the Scandinavian Blue Road Area (Goldflam, St., et al.) 419

Seismics

- Rayleigh Channel Waves for the In-Seam Seismic Detection of Discontinuities (Dresen, L., Freystätter, S.) 111

Seismic Arrays

- The Iranian Long Period Array (ILPA) (Akasheh, B., et al.) 159

Seismic Channel Waves

- Rayleigh Channel Waves for the In-Seam Seismic Detection of Discontinuities (Dresen, L., Freystätter, S.) 111

Seismic Surface Waves

- Propagation of Love-Type Waves in Heterogeneous Elastic Layers (Biswas, A.) 137
- Seismische Oberflächenwellen. Seismic Surface Waves (Seidl, D., Müller, S.) 283

Seismic Tunnel Waves

- Tunneling of Low-Frequency Waves through the Subcrustal Lithosphere (Fuchs, K., Schulz, K.) 175

Seismicity

- Intermediate Aseismicity of the Andean Subduction Zone and Recent Andesitic Volcanism (Hanus, V., Vaněk, J.) 219
- Provisional Seismicity Map of the Republic of Zambia and Its Preliminary Interpretation (Töpfer, K.D.) 225
- Fault-Plane Solution of the Earthquake in Northern Italy, 6 May 1976, and Implications for the Tectonics of the Eastern Alps (Müller, G.) 343

Seismology

- Ultrasonic Modelling of a Moving Source (Behle, A., Rohde, J.) 131
- The Iranian Long Period Array (ILPA) (Akasheh, B., et al.) 159
- Tunneling of Low-Frequency Waves through the Subcrustal Lithosphere (Fuchs, K., Schulz, K.) 175
- Computation of Reflection Coefficients for Layered Media (Kind, R.) 191
- The Seismic Broadband Recording and Data Processing System FBV/DPS and Its Seismological Applications (Plešinger, A., Horálek, J.) 201
- Fault-Plane Solution of the Earthquake in Northern Italy, 6 May 1976, and Implications for the Tectonics of the Eastern Alps (Müller, G.) 343
- Earth-Flattening Approximation for Body Waves Derived from Geometric Ray Theory-Improvements, Corrections and Range of Applicability (Müller, G.) 429

Seismometry

The Seismic Broadband Recording and Data Processing System FBV/DPS and Its Seismological Applications (Plešinger, A., Horálek, J.) 201

Solar Corona

Helios-1 Faraday Rotation Experiment: Results and Interpretations of the Solar Occultations in 1975 (Volland, H., et al.) 659
Time Delay Occultation Data of the Helios Spacecrafts and Preliminary Analysis for Probing the Solar Corona (Edenhofer, P., et al.) 673

Solar Eclipse

Appearance of the Atmospheric Scatter Field during a Solar Eclipse (Gerharz, R.) 163

Solar Particles

Short-Time Variations of Solar Particle Fluxes during the August 1972 Events (Kremser, G., et al.) 1
Cosmic Ray Measurements on Board Helios 1 from December 1974 to September 1975: Quiet Time Spectra, Radial Gradients, and Solar Events (Kunow, H., et al.) 615
A Survey on Measurements of Medium Energy Protons and Electrons Obtained with the Particle Spectrometer E8 on Board of Helios (Keppler, E., et al.) 633
Interaction of Low-Energy (> 80 keV) Protons with the January 6 and 8, 1975, Shock Waves: Helios-1 Observations (Richter, A.K., Keppler, E.) 645

Solar Wind

On the Variation of K_p at Sector Boundaries (Schreiber, H.) 437
A Survey on Initial Results of the Helios Plasma Experiment (Rosenbauer, H., et al.) 561
Plasma Disturbances Caused by the Helios Spacecraft in the Solar Wind (Isensee, U.) 581
Radial Variation of the Interplanetary Magnetic Field between 0.3AU and 1.0AU. Observations by the Helios-1 Spacecraft (Muschmann, G., et al.) 591
Initial Results from the Helios-1 Search-Coil Magnetometer Experiment (Neubauer, F.M., et al.) 599
A Survey on Measurements of Medium Energy Protons and Electrons Obtained with the Particle Spectrometer E8 on Board of Helios (Keppler, E., et al.) 633

Interaction of Low-Energy (> 80 keV) Protons with the January 6 and 8, 1975, Shock Waves: Helios-1 Observations (Richter, A.K., Keppler, E.) 645

Helios-1 Faraday Rotation Experiment: Results and Interpretations of the Solar Occultations in 1975 (Volland, H., et al.) 659

Spacecraft Influences

Plasma Disturbances Caused by the Helios Spacecraft in the Solar Wind (Isensee, U.) 581

Synthetic Seismograms

Tunneling of Low-Frequency Waves through the Subcrustal Lithosphere (Fuchs, K., Schulz, K.) 175
Computation of Reflection Coefficients for Layered Media (Kind, R.) 191

Temperature, in Earth

Die Gesteinsradioaktivität und ihr Einfluß auf das Temperaturfeld in der kontinentalen Kruste. The Radioactivity of Rocks and Its Influence on the Temperature Field in the Continental Crust (Rybach, L.) 93
Geothermal Models of the Crust and Uppermost Mantle of the Fennoscandian Shield in South Norway and the Danish Embayment (Balling, N.P.) 237

Tertiary Volcanics

Palaeomagnetic and Rock Magnetic Investigations of Tertiary Volcanics in Northern Bavaria (Pohl, J., Soffel, H.) 459

Upper Mantle

Geothermal Models of the Crust and Uppermost Mantle of the Fennoscandian Shield in South Norway and the Danish Embayment (Balling, N.P.) 237

VHF Observations

Winter Anomaly in VHF Absorption Studies over Delhi (Sarma, S.B.S.S., Sharma, M.C.) 541

VLF Observations

The Diurnal Variation of the Electron Density of the Mid-Latitude Ionospheric D-Region Deduced from VLF-Measurements (Schäfer, J.) 361

Wave Theory, Seismic

Earth-Flattening Approximation for Body Waves Derived from Geometric Ray Theory-Improvements, Corrections and Range of Applicability (Müller, G.) 429

Winter Anomaly

Winter Anomaly in VHF Absorption Studies over Delhi (Sarma, S.B.S.S., Sharma, M.C.) 541

Zambia

Representation and Interpretation of Resistiv-

ity Mapping Data in Groundwater Prospecting in Zambia (Töpfer, K.D.) 147
 Provisional Seismicity Map of the Republic of Zambia and Its Preliminary Interpretation (Töpfer, K.D.) 225

Zodiacal Light

Observations of Zodiacal Light from Helios 1 and 2 (Leinert, C., et al.) 699
 Interpretation of the Optical Properties of Interplanetary Dust (Giese, R.H.) 705

Book Reviews 173, 281

Journal of Geophysics

Zeitschrift für Geophysik

1 P 22174 F

Volume 42 · Number 1 · 1976/77

1-673

42 Vol 2148

Contents

Original Investigations

- 1 **G. Kremser, W. Riedler, E. Kirsch:** Short-Time Variations of Solar Particle Fluxes during the August 1972 Events
- 15 **V. Dose, U. Schmocker, G. Sele:** Auroral Lyman-Alpha Emission
- 27 **A. Schleusener, W. Torge, H. Drewes:** The Gravity Field of Northeastern Iceland
- 47 **H. Markert, F. Heller, N. Steigenberger:** Parabolic Field Dependence of Kinks Occurring in the Logarithmic Time Plots of Viscous Magnetization
- 59 **K. M. Storetvedt, N. Petersen:** Postulated Rotation of Corsica not Confirmed by New Palaeomagnetic Data
- 73 **H. A. Roesser:** Magnetic Anomalies of the African Red Sea Shelf and Their Implications for the Anomalies of Atlantic Continental Margin

Short Communications

- 81 **A. Schult:** Self-Reversal above Room Temperature due to N-Type Magnetization in Basalt
- 85 **R. Hummervoll:** Further Utilization of the Fluxgate Magnetometer in the Palaeomagnetic Laboratory
- 89 **A. Korschunow:** Note on the Reliability of Subjective Processing of Geomagnetic Pulsation-Records in the Range Pc 2–Pc 5

Indexed in Current Contents

Niedersächsische Staats- u.
Universitätsbibliothek
Göttingen

21. April 1976



Springer-Verlag
Berlin · Heidelberg · New York

Journal of Geophysics – Zeitschrift für Geophysik

Edited for the Deutsche Geophysikalische Gesellschaft by

W. Dieminger and J. Untiedt

The Journal accepts

Review Articles (invited by the Editors)
Original Papers
Short Communications

Letters to the Editors
Book Reviews

concerned with the entire field of Geophysics and related fields.

Manuscripts may be addressed to any of the Editors. For addresses see last cover page. Manuscripts should conform with the journal's accepted practice as described in the Instructions to Authors.

Members of the Deutsche Geophysikalische Gesellschaft are entitled to purchase the Journal for their own use at a privilege price of DM 70,— payable with the Membership dues. Orders should be sent to the Society's office at the following address: 2 Hamburg 13, Binderstr. 22.

Subscription Information

Volume 42 (6 issues each totalling about 656 pages) will appear in 1976. The publisher reserves the right to issue additional volumes during the calendar year. Information about obtaining back volumes and microform editions available upon request.

North America. Subscription rate: \$80.60, including postage and handling. Subscriptions are entered with prepayment only. Orders should be addressed to: Springer-Verlag New York Inc., 175 Fifth Avenue, New York, N.Y. 10010.

Outside North America. Subscription rate: DM 188,—, plus postage and handling. Orders can either be placed with your book-dealer or sent directly to: Springer-Verlag, Heidelberger Platz 3, D-1000 Berlin 33, W. Germany.

50 offprints of each paper are provided free of charge. Additional copies may be ordered at cost price.

It is a fundamental condition that manuscripts submitted have not been and will not be published elsewhere, either simultaneously or at a later date. With the acceptance of a manuscript for publication, the Gesellschaft acquires the sole copyright for all languages and countries. Unless special permission has been granted, no photographic reproductions, microform or any other reproductions of a similar nature may be made of the journal, of individual contributions contained therein or of extracts therefrom.

The use of registered names, trademarks, etc. in this publication does not imply, even in the absence of a specific statement, that such names are exempt from the relevant protective laws and regulations and therefore free for general use.

Publishing Office

Springer-Verlag, Journal Production Department II
D-6900 Heidelberg 1, Postfach 105 280, Tel. (0 62 21) 4 87-1, Telex 04-61 690

Subscription Offices

Springer-Verlag, D-1000 Berlin 33, Heidelberger Platz 3, Tel. (0 30) 82 20 01, Telex 01-83 319
Springer-Verlag, New York Inc., 175 Fifth Avenue, New York, N.Y. 10010

Responsible for Advertisements:

L. Siegel, D-1000 Berlin 15, Kurfürstendamm 237, Tel. (0 30) 8 82 10 31, Telex 01-85 411

Original Investigations

Short-Time Variations of Solar Particle Fluxes during the August 1972 Events

G. Kremser¹*, W. Riedler² and E. Kirsch³

¹ Space Research Institute of the Austrian Academy of Sciences, Experimental Space Research Group, c/o Technical University Graz, Graz, Austria

² Department of Communications and Wave Propagation, Technical University Graz, Graz, Austria in cooperation with the Kiruna Geophysical Institute, Kiruna, Sweden

³ Max-Planck-Institut für Aeronomie, Katlenburg-Lindau, Federal Republic of Germany

Abstract. Energetic solar particle fluxes were measured with balloon-borne instruments over Kiruna during the August 1972 events. Short-time variations of the particle flux with durations down to a few seconds occurred from 05 to 10 UT on 5 August 1972. Similar variations were observed on simultaneous recordings of cosmic noise absorption. The observations are interpreted as temporal variations of the low-energy (up to some tens of MeV) proton flux. They are discussed in terms of a model, in which drifting protons are intermittently scattered into the loss-cone by a wave-particle interaction process.

Key words: Solar protons – Magnetosphere – Magnetic storm.

1. Introduction

The propagation of energetic solar particles near the earth is largely determined by the geomagnetic field. The different modes of particle entry into the magnetosphere were recently discussed by Morfill (1974) and Gall and Bravo (1974) for protons and by Vampola (1974) for electrons. The understanding of these processes is mainly based on model calculations using the static geomagnetic field configuration.

Investigations on the influence of temporal and spatial field fluctuations during disturbed periods were reported in a number of publications. As a more general result cut-off changes were observed (Barcus, 1969a, b; Bewick *et al.*, 1970; Imhof *et al.*, 1971; Williams and Heuring, 1973). During an isolated substorm strong pitch-angle scattering was found near the boundary of the trapping region (Häusler *et al.*, 1974). A statistical study of the pitch-angle distribution demonstrated its dependence on the substorm phase (Scholer *et al.*, 1974).

We now discuss short-time variations obtained during a strongly disturbed period ($Kp=7-8$). Solar particle data from balloon-borne instruments are used for this purpose. An advantage of this method is that long-term, high time-

* On leave from Max-Planck-Institut für Aeronomie, Katlenburg-Lindau, Germany.

resolution measurements can be performed while the balloon only slowly varies its location. The method provides direct measurements of solar protons with energies above the atmospheric cut-off (about 80–100 MeV) and indirect information on the low energy proton flux by measuring the γ -rays that the protons produce in the atmosphere.

During the solar particle events of August 1972 a total of eight balloons were launched from Kiruna, Sweden ($L = 5.4$) but we shall only refer to balloon KL 3/72, as the short-time variations exclusively occurred within the flight time of this balloon. All balloons carried payloads for measurement of energetic particles and auroral X-rays (Kremser *et al.*, 1974a). Some results were reported earlier, mainly on variations of the energy spectrum (Kremser *et al.*, 1973, 1974b).

2. Instrumentation

The balloon was launched on August 4, 1972, at 17.34 UT. It reached a minimum air pressure level of 4.5 mb and floated at about 5.5 mb during the time of the measurements. From 05 to 10 UT on 5 August 1972 its location changed from a position at 66° N, 15° E to 65° N, 13° E.

The payload contained a scintillation counter with a cylindrical NaI(Tl)-crystal of 2.54 cm diameter and 2.54 cm thickness, and three Geiger-Müller tubes in a telescope configuration. Unfortunately the GM tubes had reached the end of their life (10^6 counts) by the time the event under investigation occurred. A pulse height analysis was performed on the output from the scintillation counter in five channels. The calibration was done in such a way that the five channels correspond to X-ray energy losses of 25, 50, 75, 100 and 200 keV respectively. They are labelled A, B, C, D, E in the Figures. This procedure was applied because the scintillation counter was originally designed for measurements of X-ray photons. It is, however, sensitive to charged particle fluxes, but the species of the particles cannot be separated. As is known from satellite measurements (e.g. Page *et al.*, 1974) protons, electrons and α -particles were emitted from the sun during these events. Inside the atmosphere additional secondary radiations appeared like nuclear γ -rays produced by protons and bremsstrahlung X-rays produced by electrons. The relative importance of these contributions to the count rates of the scintillation counter are discussed below in Section 4.

3. Observations

A summary of observations is given in Fig. 1, containing data from the solar proton monitoring experiment on IMP-5 (Kohl *et al.*, 1973), cosmic noise absorption recordings from Kiruna, and the times of recorded balloon flights. The period of short-time variations occurred on 5 August. It followed a pronounced peak in the particle flux from 03 UT to 05 UT that has been attributed to a cosmic-ray increase caused by an unusual configuration of the interplanetary magnetic field (Venkatesan *et al.*, 1975).

30-second averages of the count rates in the different energy channels of the scintillation counter are shown in Fig. 2 for the time interval 05.00–09.30 UT.

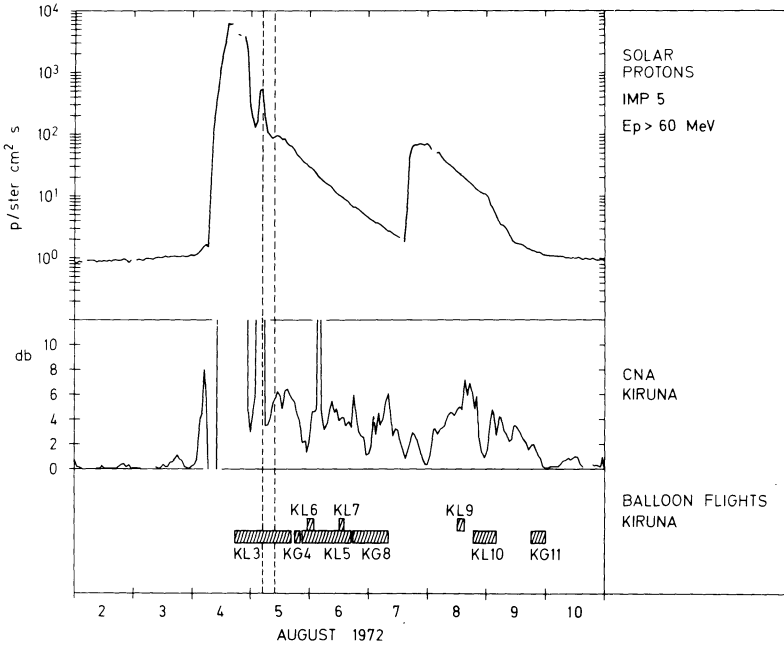


Fig. 1. Development of the August 1972 energetic solar particle events as observed by IMP-5, together with CNA recordings from Kiruna. The time of balloon flights is also shown. The interval of short-time variations is indicated by vertical dashed lines

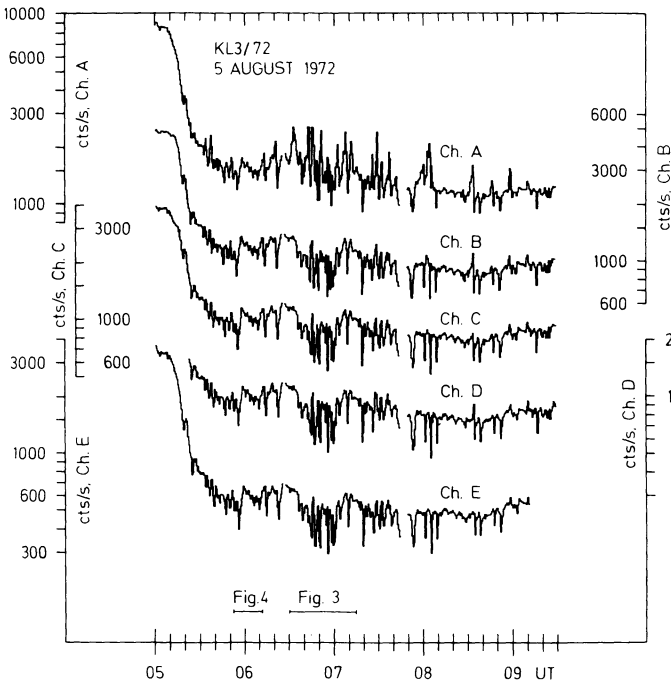


Fig. 2. 30-second averages of the count rates in the different channels of the scintillation counter. The intervals of the high-time resolution data presented in Figs. 3 and 4 are indicated

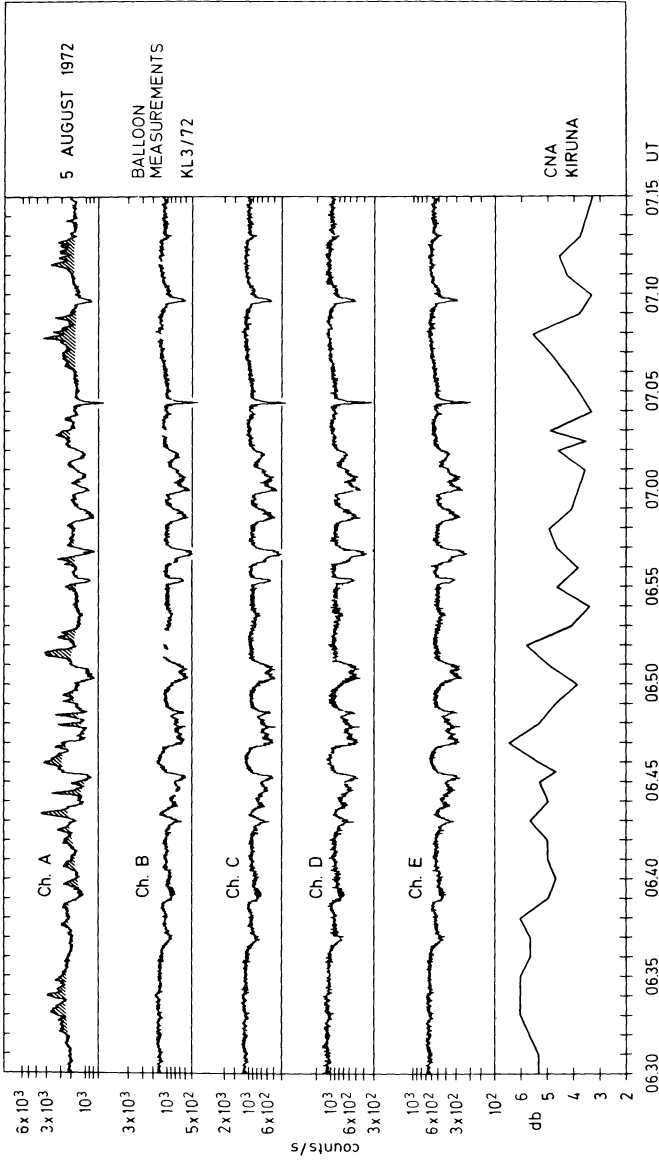


Fig. 3. Example of short-time variations of solar particle fluxes with superimposed auroral X-ray events (hatched area in uppermost curve). The CNA-recording from Kiruna is included for comparison

At the beginning of this interval the count rates decreased due to the end of the above mentioned cosmic ray peak. After 05.30 UT strong temporal variations were recorded in all energy channels. These variations were investigated (Figs. 3 and 4) in more detail by plotting 1-second averages of the count rates obtained during the intervals that are indicated by bars in the lower part of Fig. 2. Cosmic noise absorption recordings have been added. In Fig. 3 the hatched area in channel A indicates variations of the count rates due to auroral X-rays. We attribute these variations to auroral X-rays because they are not to be seen in the higher energy channels. Auroral X-rays have mostly a weak energy spectrum. They can easily be separated from the contributions by solar particles because of their markedly different temporal behaviour. In the present paper these X-rays will not be discussed further.

We are mainly interested in those temporal variations that most clearly appear in channel E. Further examples are shown in Fig. 4 for a period without auroral X-rays. Usually the maxima of these variations were broader than the minima. The minima lasted from some minutes down to a few seconds. They occurred in a rather close sequence or with separations of up to several minutes. The relative amplitudes amount to as much as 50% of the total count rate.

The balloon-borne measurements were performed at a single location. The dimensions of regions, inside which special radiation events occur, often can be determined from riometer recordings of cosmic noise absorption. In Fig. 5 we therefore plotted riometer recordings from several observatories in the European longitude sector. The L -values of these stations range from $L=3.4$ to $L=6.1$. Short-time variations of the cosmic noise absorption were clearly recorded at

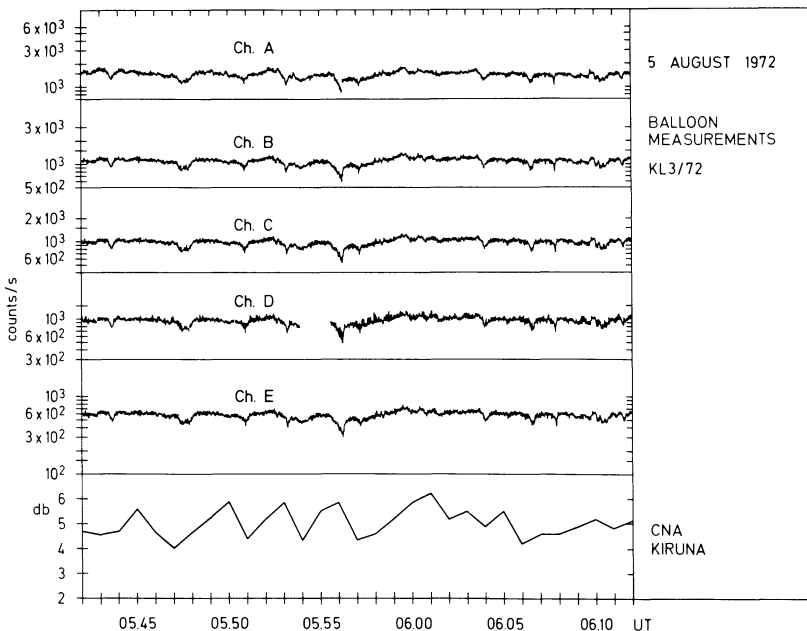


Fig. 4. Example of short-time variations of solar particle fluxes during periods without auroral X-rays. Included are CNA-recordings from Kiruna

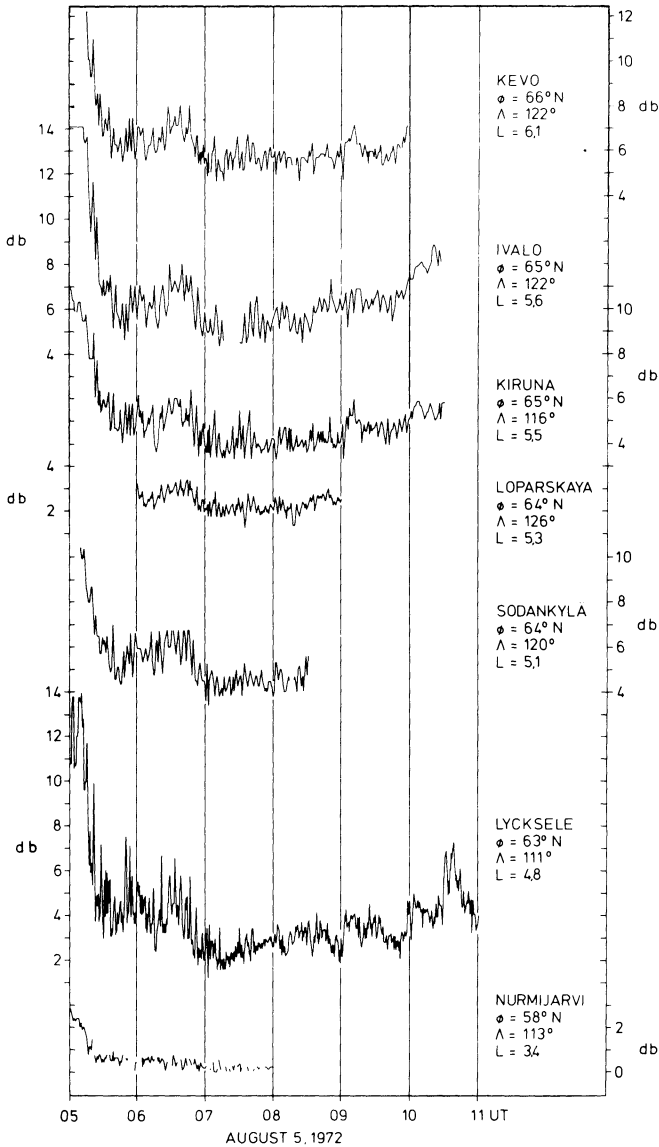


Fig. 5. CNA-recordings from stations in the European longitude sector showing simultaneous variations similar to those measured by balloon-borne instruments. The Loparskaya recording was taken from Brunelli *et al.* (1973)

stations with L values between 6.1 and 4.8. In some cases the absorption varied by more than 2 db in a few minutes. In Nurmijärvi ($L=3.4$) the absorption was too small to permit a clear identification of single peaks. Similar temporal variations also occurred e.g. in Iceland ($L=6.2$) and with very great amplitudes in Thorshavn on the Faeroe-Islands ($L=4.5$). They were not observed in the recordings of the Greenland chain of riometers ($L>7.3$) that reaches far into the polar cap.

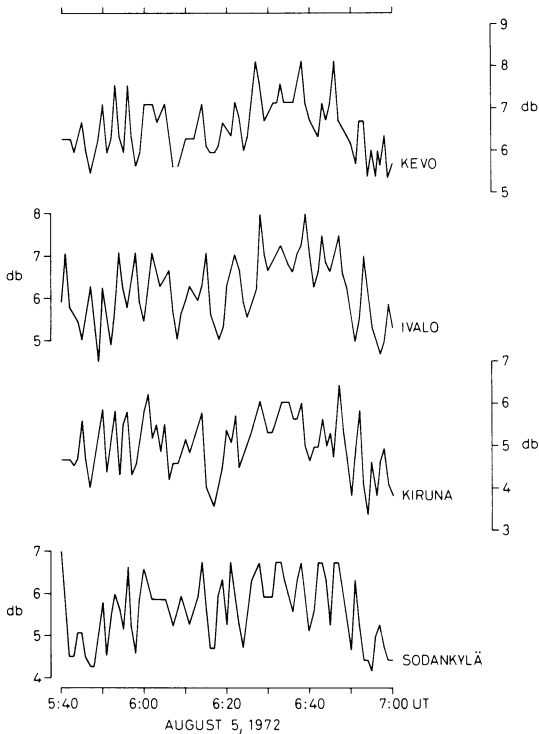


Fig. 6. CNA-recordings from four stations ($L = 5.1 - 6.1$) on an extended time scale (05.40–07.00 UT)

A remarkable feature of the temporal variations of the absorption in the European longitude sector is the strong tendency for these variations to occur simultaneously at different latitudes. This can already be recognized by carefully inspecting Fig. 5 and is demonstrated in more detail in Fig. 6. Here we have plotted on an extended time scale absorption variations recorded at four stations ($L = 5.1 - 6.1$). Obviously many peaks occurred simultaneously at these stations. Some differences can be found in the amplitudes, but these can be due in part to the data reduction procedure. At such high absorption values minor reading errors are transformed in relatively great variations of the absorption.

Comparing now absorption variations to balloon-borne particle measurements (Figs. 3 and 4) we see some similarities between these two recordings but also considerable differences. Before comparing details we have to remember that temporal variations of the kind observed with the balloon-borne instruments are at the limit of the temporal resolution of a riometer. E.g. usual riometers have a characteristic time of about 30 s to record decreases of the absorption. Furthermore, the recorded absorption consists of two different components. One of them is due to the precipitation of auroral electrons and is produced mainly at an altitude of about 90 km. The other component is due to solar protons and is mainly produced at altitudes below about 60 km. Considering these facts the resemblance between CNA and balloon measurements is still close enough to support the assumption that both of them reflect the same kind of temporal variations of the solar particle

flux. An additional argument is the fact that this kind of temporal variations of CNA occurred just in the same time interval, during which the variations of the count rates were observed in the balloon recordings.

4. Discussion

For the interpretation of our balloon measurements we have to consider the following components which may contribute to the count rates of the instrument:

The flux of α -particles: it is usually negligible at balloon altitudes (Pfozter, 1965).

Electrons had direct access to the detector only, if their entry energy was higher than the atmospheric cut-off. For our measurements this amounted to about 10 MeV, and therefore only small electron fluxes could have been present.

The flux of X-rays produced by low energy electrons was probably high enough to be detected by the scintillation counter in spite of the low efficiency of the bremsstrahlung process (see annex).

The atmospheric cut-off for protons corresponded to 80 MeV. The proton flux at energies above 80 MeV was high enough (see e.g. Kohl *et al.*, 1973 or Fig. 1, $E_p > 60$ MeV) to produce a considerable contribution to the count rates.

Another major part of the count rates was due to γ -rays produced by the low energy protons. The efficiency of the corresponding production process was estimated by Bhavsar (1962), Hofmann and Winckler (1963), Keppler (1964), Barcus (1969 a, b). It has been shown that the main contribution to the γ -ray flux stems from protons with energies between 1 MeV and 30 MeV. In our case γ -rays produced by protons with even higher energies may also have been present (see annex).

It follows from these arguments that the main contributions to the count rates of the scintillation counter are expected from solar protons with energies above 80 MeV, γ -rays produced by solar protons with energies up to a few tens of MeV, and X-rays produced by solar electrons with energies up to some hundred keV. It is unlikely that the observed temporal variations reflect changes of the high-energy proton flux, as no variations of this kind were observed outside the magnetosphere and it is very difficult to imagine how these could be produced in the magnetosphere. Furthermore, they can also not have been caused by variations of the solar electron flux, as the small differences observed in the different channels of the scintillation counter cannot be explained by any bremsstrahlung spectrum. We, therefore, conclude that the fast temporal variations occurred in the low energy proton flux.

Similar variations of the solar particle flux were reported previously (Hudson and Anderson, 1969; Domingo and Page, 1972). These observations concerned variations in the polar cap, that occurred with characteristic times between one half and several minutes. In our case cosmic noise recordings indicate that the variations did not occur in the polar cap but were restricted to the auroral zone. Furthermore, the characteristic times reached down to values of a few seconds. These variations therefore may have been of a quite different origin than those observed earlier. Our aim now is to discuss possible processes that could lead to a fast temporal modulation of the low energy solar proton flux in the loss-cone

at auroral latitudes. We must take into account that the magnetosphere was extremely disturbed.

Our measurements were performed at an invariant latitude of about 63° ; the riometer recordings were obtained at invariant latitudes ranging from 62° to 66° . At these latitudes the following mechanism could produce the observed temporal variations:

- a) Variations of the geomagnetic cut-off caused by substorm activity (compare Barcus, 1969 a, b; Bewick *et al.*, 1970).
- b) Radial diffusion of trapped solar protons by violation of the third adiabatic invariant.
- c) Geomagnetic field drift.

Mechanism a) and b) can probably be ruled out in our case as the short time variations seem to have occurred almost simultaneously in a latitude range of several degrees. Cut-off changes caused by substorm activity should have time scales of the order of an hour. A diffusion process should smooth out short-time intensity variations. Both of them cannot produce very fast changes.

We shall therefore discuss mechanism c) in some detail. For this discussion we have to remember that the latitude range in which our observations were made corresponds either to the region of pseudo-trapping (Taylor, 1967; Flindt, 1970; Morfill, 1973) or stable trapping. According to Morfill (1973) the limit of stable trapping can normally be expected at an invariant latitude of 68° , i.e. well poleward of the location of our observations. In our case the magnetosphere was extremely disturbed. Brace *et al.* (1974) found the plasma pause to be located unusually close to the Earth ($L=2$) during this storm. It can therefore be assumed that the stable trapping boundary was located at considerably lower latitudes than usual. But if the effect occurred in the stable trapping region instead of the pseudo-trapping region, some additional continuously operating cross- L diffusion must be assumed in order to transport the protons into this region. Otherwise we have to consider drifting protons and possible processes interacting with them in both cases.

These interaction processes will have to explain how the drifting protons were scattered into the loss-cone. Two possible mechanisms were described in the literature. One of them is related to excessive magnetic field curvature and gradients, by which protons are scattered, when they drift through this region (Morfill, 1973). The other mechanism is due to wave-particle interaction. Häusler *et al.* (1974) mention cyclotron resonance interaction with ELF chorus and/or cyclotron or bounce resonance with geomagnetic micropulsations in the ULF-band. Interaction of trapped or quasi-trapped protons is possible with right hand polarized ELF chorus as well as with left hand polarized ULF micropulsations.

The scattering mechanism by excessive magnetic field curvature and gradients seems unlikely in our case, as the flux variations were observed at L -values as low as 4.5, where extreme deviations from the dipole-like configuration of the magnetic field are difficult to imagine. Furthermore, the scattering region should then have been located on the morning and day side. This possibility can, however, not be ruled out completely due to the unusually strong disturbances of the magnetosphere.

We regard wave-particle interaction as the more likely process to scatter drifting protons into the loss-cone. The short-time variations on August 5 appear

after an increase of the interplanetary magnetic field from 20 to 40 γ and a change of the field direction to a radially outward direction (Venkatesan *et al.*, 1975). This increase and the following decrease of the interplanetary magnetic field could have been the reason of a compression of the geomagnetic field and a stimulation of ULF micropulsations. Gendrin (1972) mentioned also compressional ULF waves as reason for the modulation of trapped and precipitated electron fluxes observed during a rocket flight. Brunelli *et al.* (1973) have reported on the simultaneous occurrence of micropulsations in a period range similar to that of the particle flux variations.

This possible explanation bears some resemblance to the behaviour of drifting magnetospheric electrons. Wilhelm *et al.* (1972) and Wilhelm (1973) explained short-time bursts of precipitated auroral electrons in the morning side by intermittently operating wave-particle interaction on drifting electrons.

Annex

Estimated production rate of γ -rays and X-rays by solar protons and electrons respectively.

A. γ -Ray Flux

γ -rays are produced mainly in the nuclear reactions (p, p'), (p, n), (p, α) on N^{14} and O^{16} . The energy range of the γ -ray lines is 0.51–7.12 MeV. According to Hofmann and Winckler (1963) about 3 ± 1 γ -ray photons are produced per nuclear reaction, and the γ -ray production rate N_γ can be estimated with the aid of the following equation

$$N_\gamma = \int K \times E_p^\rho \times \frac{dN_p}{dE} dE \quad (1)$$

with

$$K = 1.7 \times 10^{-5}, \quad \rho = 3.18 \quad \text{for } E_p < 3 \text{ MeV}$$

and

$$K = 7 \times 10^{-5}, \quad \rho = 1.92 \quad \text{for } E_p > 3 \text{ MeV}.$$

E_p is the proton energy in MeV, dN_p/dE is the differential energy spectrum of the proton flux.

For the time interval 09–10 UT on 5 August 1972 we derive from measurements reported by Yates *et al.* (1973) and Kohl *et al.* (1973)

$$\frac{dN_p}{dE} = 3 \times 10^3 E^{-1.47} \text{ cm}^{-2} \text{ s}^{-1} \text{ sr}^{-1} \text{ MeV}^{-1} \quad \text{for } 1 \text{ MeV} \leq E_p \leq 30 \text{ MeV} \quad (2)$$

and

$$\frac{dN_p}{dE} = 1.2 \times 10^5 E^{-2.57} \text{ cm}^{-2} \text{ s}^{-1} \text{ sr}^{-1} \text{ MeV}^{-1} \quad (3)$$

for $30 \text{ MeV} \leq E_p \leq 80 \text{ MeV}$.

Inserting (2) and (3) in (1) yields

$$N_y = 0.35 \text{ cm}^{-2} \text{ s}^{-1} \text{ sr}^{-1} \quad \text{for } 1 \text{ MeV} \leq E_p \leq 3 \text{ MeV} \quad (4)$$

$$N_y = 19.4 \text{ cm}^{-2} \text{ s}^{-1} \text{ sr}^{-1} \quad \text{for } 3 \text{ MeV} \leq E_p \leq 30 \text{ MeV} \quad (5)$$

$$N_y = 33.4 \text{ cm}^{-2} \text{ s}^{-1} \text{ sr}^{-1} \quad \text{for } 30 \text{ MeV} \leq E_p \leq 80 \text{ MeV}. \quad (6)$$

B. X-Ray Flux

X-rays are produced in the bremsstrahlung process. According to Evans (1955) the X-ray production rate N_x can be estimated with the aid of the following equation

$$N_x = 7 \times 10^{-4} \bar{Z} \times E_e \quad (7)$$

with $\bar{Z} = 7.2$ for air; E_e is the electron energy in MeV.

Measurements reported by Lanzerotti and McLennan (1974) for the time interval 09–10 UT yielded a solar electron flux of

$$10^4 \text{ cm}^{-2} \text{ s}^{-1} \text{ sr}^{-1} \quad \text{for } E_e > 350 \text{ keV}. \quad (8)$$

Using this value we get from (7) the production rate of

$$N_x = 17.6 \text{ cm}^{-2} \text{ s}^{-1} \text{ sr}^{-1}. \quad (9)$$

Acknowledgement. The authors are grateful to Prof. G. Pfozter for supporting the balloon program and for helpful discussions. They acknowledge the advice of Dr. K. Wilhelm in the preparation of the manuscript. Dipl. Phys. K. H. Saeger greatly contributed to the success of the measurements by supervising the payload construction. Dr. H. Specht was engaged in the data reduction. Riometer recordings were kindly provided by Prof. P. Tanskanen, University of Oulu; Civil Ing. J. Taagholt, Ionosphere Laboratory, Lyngby; Cand. real. S. L. Ullaland, University of Bergen. The balloon program was supported financially by the Max-Planck-Gesellschaft, FRG, the Austrian Science Research Council, the Austrian Academy of Sciences and the Swedish Science Research Council.

References

- Barcus, J.R.: Increase in cosmic-ray cut-offs at high latitudes during magnetospheric substorms. *J. Geophys. Res.* **74**, 4694–4700, 1969 a
- Barcus, J.R.: Diurnal variation in low-energy cosmic ray cut-offs. *Planetary Space Sci.* **17**, 1173–1181, 1969 b
- Bewick, A., Haskell, G. P., Hynds, R.J.: Penetration of low-energy solar protons to low geomagnetic latitudes. *J. Geophys. Res.* **75**, 4605–4612, 1970
- Bhavsar, P.D.: Gamma rays from the solar-cosmic-ray-produced nuclear reactions in the Earth's atmosphere and lower limit on the energy of solar protons observed at Minneapolis. *J. Geophys. Res.* **67**, 2627–2637, 1962

- Brace, L. H., Maier, E. J., Hoffman, J. H., Whitteker, J., Shepherd, G. G.: Deformation of the night side plasmasphere and ionosphere during the August 1972 geomagnetic storm. *J. Geophys. Res.* **79**, 5211–5218, 1974
- Brunelli, B. E., Loginov, G. A., Petrova, G. A., Afanasyeva, L. T.: Normal magnetic field, micropulsations and riometer observations at auroral station Murmansk. Rep. UAG-28, Part III, Ed. H. E. Coffey, p. 727–730. Boulder, Colorado: World Data Center A, 1973
- Domingo, V., Page, D. E.: Two-satellite observation of spatial and temporal particle flux variations over the polar caps. *J. Geophys. Res.* **77**, 1971–1975, 1972
- Evans, R. D.: The atomic nucleus. New York: McGraw-Hill 1955
- Flindt, H. R.: Local-time dependence of geomagnetic cut-offs for solar protons, $0.52 \leq Ep \leq 4$ MeV. *J. Geophys. Res.* **75**, 39–49, 1970
- Gall, R., Bravo, S.: On a model of propagation of 5–300 MeV protons in the earth magnetic cavity, the role of neutral and plasma sheets. In: *Correlated interplanetary and magnetospheric observations*. Ed.: D. E. Page, p. 433–447. Dordrecht-Holland: D. Reidel 1974
- Gendrin, R.: Changes in the distribution function of magnetospheric particles associated with gyroresonant interactions. In: *Earth's magnetospheric processes*, Ed.: B. M. McCormac, pp. 311–328. Dordrecht-Holland: D. Reidel 1972
- Häusler, B., Scholer, M., Hovestadt, D.: Variations of the trapped particle population and of cut-off and pitch angle distribution of simultaneously observed magnetospheric solar protons during substorm activity. *J. Geophys. Res.* **79**, 1819–1824, 1974
- Hofmann, D. J., Winckler, J. R.: Simultaneous balloon observations at Fort Churchill and Minneapolis during the solar cosmic ray events of July 1961. *J. Geophys. Res.* **68**, 2067–2098, 1963
- Hudson, P. D., Anderson, H. K.: Nonuniformity of solar protons over the polar caps on March 24, 1966. *J. Geophys. Res.* **74**, 2881–2890, 1969
- Imhof, W. L., Reagan, J. B., Gaines, E. E.: Solar particle cut-offs as observed at low altitudes. *J. Geophys. Res.* **76**, 4276–4290, 1971
- Keppler, E.: Messung von Röntgenstrahlung und solaren Protonen mit Ballongeräten in der Nordlichtzone. *Mitt. Max-Planck-Inst. Aeron.* **15**, 1–50, 1964
- Kohl, J. W., Bostrom, C. O., Williams, D. J.: Particle observations of the August 1972 solar events by Explorer 41 und 43. Rep. UAG-28, Ed. H. E. Coffey, Part II, p. 330. Boulder, Colorado: World Data Center A, 1973
- Kremser, G., Pfozter, G., Kirsch, E., Riedler, W., Specht, H., Zirm, K.: Erste Ergebnisse aus Ballonmessungen während der solaren Protonenereignisse vom 2.–10. August 1972. *Kleinheubacher Berichte* **15**, 405–410, 1973
- Kremser, G., Pfozter, G., Kirsch, E., Specht, H., Riedler, W., Zirm, K.: Temporal variations of solar particle spectra (August 4–7, 1972). In: *Correlated interplanetary and magnetospheric observations*, Ed. D. E. Page, pp. 603–607. Dordrecht-Holland: D. Reidel 1974a
- Kremser, G., Riedler, W., Kirsch, E., Pfozter, G., Saeger, K. H., Slamanig, H., Specht, H., Zirm, K.: Summary of solar particle and auroral-zone X-ray measurements with balloon-borne instruments during the solar particle events of August 1972. *SBARMO-Bulletin* **VI**, 25–65, 1974b
- Lanzerotti, L. J., McLennan, C. G.: Solar particle observations during the August 1972 event. In: *Correlated interplanetary and magnetospheric observations*, Ed.: D. E. Page, pp. 587–596. Dordrecht-Holland: D. Reidle 1974
- Morfill, G.: Nonadiabatic particle motion in the magnetosphere. *J. Geophys. Res.* **78**, 588–596, 1973
- Morfill, G.: Solar particle access into the inner magnetosphere. In: *Correlated interplanetary and magnetospheric observations*, Ed.: D. E. Page, pp. 399–417. Dordrecht-Holland: D. Reidel 1974
- Page, D. E., Domingo, V., Wenzel, K.-P.: MeV electrons, protons and alpha particles observed August 2–12, 1972. In: *Correlated interplanetary and magnetospheric observations*, Ed.: D. E. Page, pp. 573–585. Dordrecht-Holland: D. Reidel 1974
- Pfozter, G.: Balloon measurements of solar protons and auroral X-rays. *Proceedings of a Symposium on high latitude particles and the ionosphere*, Alpbach 1964, Ed.: B. Machlum, pp. 167–204. London: Logos Press 1965
- Scholer, M., Morfill, G., Hovestadt, D.: Statistical analysis of the pitch angle distribution of magnetospheric solar protons during geomagnetic activity. *J. Geophys.* **40**, 37–56, 1974
- Taylor, H. E.: Latitude local-time dependence of low-energy cosmic-ray cut-offs in a realistic geomagnetic field. *J. Geophys. Res.* **72**, 4467–4470, 1967

- Vampola, A. L.: Solar electron access to the magnetosphere. In: Correlated interplanetary and magnetospheric observations, Ed.: D. E. Page, pp. 463–478. Dordrecht-Holland: D. Reidel 1974
- Venkatesan, D., Mathews, T., Lanzerotti, L. J., Fairfield, D. H., Bostrom, C. O.: Cosmic ray intensity variations during 02–07 UT, August 5, 1972. *J. Geophys. Res.* **80**, 1715–1724, 1975
- Wilhelm, K.: The distribution function of energetic electrons measured during a slowly varying ionospheric absorption event. *Space Research XIII*, Eds.: M. J. Rycroft, S. K. Runcorn, pp. 527–533. Berlin: Akademie-Verlag 1973
- Wilhelm, K., Kremser, G., Münch, J., Schnell, M., Legrand, J. P., Petrou, N., Riedler, W.: Measurements of energetic particle fluxes during a slowly varying absorption event by two co-ordinated rocket flights. *Space Research XII*, pp. 1437–1447. Berlin: Akademie-Verlag 1972
- Williams, D. J., Heuring, F. T.: Strong pitch angle diffusion and magnetospheric solar protons. *J. Geophys. Res.* **78**, 37–50, 1973
- Yates, G. K., Katz, L., Sellers, B., Hauser, F. A.: Report UAG-28, Part II, p. 348, 1973. Boulder, Colorado: World Data Center A.

Received September 8, 1975; Revised Version November 24, 1975

Auroral Lyman-Alpha Emission

V. Dose, U. Schmocker and G. Sele

Physikalisches Institut der Universität Würzburg,
D-8700 Würzburg, Röntgenring 8, Federal Republic of Germany

Abstract. We have recently published new measurements on the electronic stopping power of molecular oxygen and nitrogen for protons with energies between 1 KeV and 30 KeV. These results together with known cross sections for excitation of Lyman-Alpha radiation in collisions of H^+ , H^0 and H^- with the atmospheric gases are used to predict auroral Lyman-Alpha emissions. We obtain heights for maximum Lyman-Alpha production which are considerably lower than those obtained using the earlier range data of Cook *et al.* [1953]. Assuming the velocity dependence of the Lyman-Alpha emission cross sections to be similar to the up to now unknown H-Beta cross sections, a comparison of rocket flight data from the experiments of Wax and Bernstein and Miller and Shepherd with the present calculations gives encouraging agreement.

Key words: Lyman-Alpha radiation – Height profiles – Stopping power – Aurora.

I. Introduction

Vegard (1939) was the first to observe hydrogen lines in the auroral spectrum. The discovery of a considerable Doppler-shift of the hydrogen emissions led to the conclusion, that these lines were due to fast protons entering the earth's atmosphere during auroras. Many observations have been made since and a big amount of theoretical work has been done to interpret auroral hydrogen emissions. Comprehensive reviews are given by Chamberlain (1961), Eather (1967), and Omholt (1971).

Reliable calculations, however, are only possible if the necessary laboratory data on the emission of hydrogen lines in collisions of protons, fast hydrogen atoms and negative hydrogen ions with atmospheric gases are available. In addition to emission cross sections, data on charge equilibrated hydrogen beams and on the stopping of hydrogen projectiles in atmospheric gases are needed. A review of the presently available laboratory data has been recently published by Mc Neal

and Birely (1973). We have carried out a few additional measurements on Lyman-Alpha emission in collisions of H^- with nitrogen and oxygen. A complete set of data on production of Lyman-Alpha radiation in collisions of hydrogen projectiles with atmospheric gases is therefore now available. Since data on charge equilibrated hydrogen beams are also well known (Allison and Garcia-Munoz, 1962; Tawara and Russek, 1973) it is possible using a proper atmospheric model and appropriate data on the stopping of protons to apply these results to auroral Lyman-Alpha emission.

Similar calculations with a less complete set of laboratory data have been carried out previously employing the range measurements of Cook *et al.* (1953). Recent measurements on the stopping power of nitrogen and oxygen for protons with energies between 1 KeV and 30 KeV carried out in our laboratory (Dose and Sele, 1975), however, showed that estimates of range for low energy protons obtained from an extrapolation of Cook's data bear a considerable error.

In this paper we report calculations on auroral Lyman-Alpha emission using the new stopping cross sections. The CIRA 72 standard atmosphere is adopted as the atmospheric model. Assuming the velocity dependence of the Lyman-Alpha emission cross sections to be similar to corresponding and up to now unknown H-Beta emission cross sections, a comparison of our calculations with rocket flight observations on H-Beta emission from two different experiments (Wax and Bernstein, 1970; Miller and Shepherd, 1969) yields encouraging agreement.

II. Excitation of Lyman-Alpha Emission

The excitation of Lyman-Alpha emission may be calculated by the equations of statistical equilibrium (Chamberlain, 1954). Take the number density of atmospheric atoms (counting a diatomic molecule as two atoms) to be N_a . Let F_i^∞ be the fraction of hydrogen projectiles in charge state i and Q_{i-2p} the cross section for excitation of the hydrogen in charge state i to the $2p$ state. The volume emission rate of Lyman-Alpha radiation F_{21} per unit incident flux neglecting cascading effects is the given by

$$F_{21} = N_a \{F_1^\infty Q_{1-2p} + F_0^\infty Q_{0-2p} + F_I^\infty Q_{I-2p}\}. \quad (1)$$

The equilibrium fractions are readily obtained in terms of charge changing cross sections as given by Tawara and Russek (1973). Cross sections for excitation of Lyman-Alpha radiation in collisions of H and H^+ with molecular nitrogen and oxygen are available from the review of Mc Neal and Birely (1973) as well as from unpublished work in our own laboratory. Cross sections Q_{I-2p} were recently determined in our laboratory and will be published elsewhere. All emission cross sections were approximated for the present purpose by analytical expressions of the form

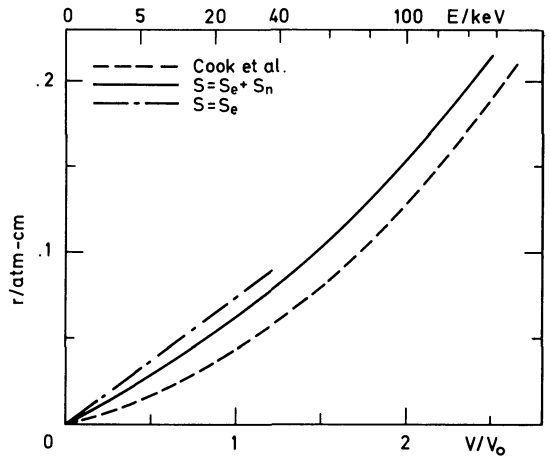
$$Q = \sum_{n=1}^N \frac{a_n v^n}{(b+v)^{n+1}} \quad (2)$$

where v is the projectile velocity in atomic units. The coefficients a_n are given in Table 1.

Table 1. Coefficients for the analytical approximation to Lyman-Alpha emission cross sections as in Eq. (2). The velocity is taken in atomic units. The cross section is in units of 10^{-17} cm² per molecule

	N ₂			O ₂		
	Q_{1-2p}	Q_{0-2p}	$Q_{\bar{1}-2p}$	Q_{1-2p}	Q_{0-2p}	$Q_{\bar{1}-2p}$
b	0.3130	0.4174	1.055	0.3130	0.3130	1.45
a ₁	0.662794	4.09415	247.625	9.36979	-0.67063	397
a ₂	-21.4369	19.0505	-1,217	-3.94790	20.0677	-2,522
a ₃	106.194	-26.4665	2,570	32.6035	-16.8208	6,552
a ₄	-93.8669	44.3644	-1,964	-93.0553	-	-5,896
a ₅	-	-50.2562	-	-37.7109	-	-
a ₆	-	-	-	55.0455	-	-
a ₇	-	-	-	395.936	-	-
a ₈	-	-	-	-393.541	-	-

Fig. 1. Residual range of protons in a standard atmosphere composed of 80% N₂ and 20% O₂. The upper-dash-dotted curve was calculated using the electronic stopping power S_e measured in our laboratory. The solid curve is the atomic stopping power calculated from S_e as before with theoretically calculated contributions S_n from elastic scattering by the nuclei. The lower dashed curve is from the experiment of Cook *et al.* (1953)



The volume emission rate F_{21} is a function of the projectile energy. We calculated F_{21} for a constant density atmosphere. In this case it is more convenient, to take the residual range of the projectiles as the independent variable. The residual range is, in turn, a unique function of the atomic stopping power of the respective gases. The only direct range measurement available is that of Cook *et al.* (1953) for energies $E \geq 7$ KeV in the case of nitrogen and $E \geq 13$ KeV in the case of oxygen. Several measurements have been carried out on the electronic stopping power S_e of oxygen and nitrogen (Jesse and Sadauskis, 1950; Reynolds *et al.*, 1953; Phillips, 1953; Ormrod, 1968; Dose and Sele, 1975) mostly at even higher energies. For the present purpose we take the most recent data from the work of Dose and Sele (1975) for energies between 1 KeV and 30 KeV and the results of Reynolds *et al.* (1953) for $E \geq 30$ KeV. To obtain the atomic stopping power, the nuclear stopping power S_n , which is a small correction at all energies, is calculated from theoretical work of Lindhard *et al.* (1963) and Schiott (1966). Fig 1 shows the resulting residual range of protons in a constant density atmosphere composed of 80%

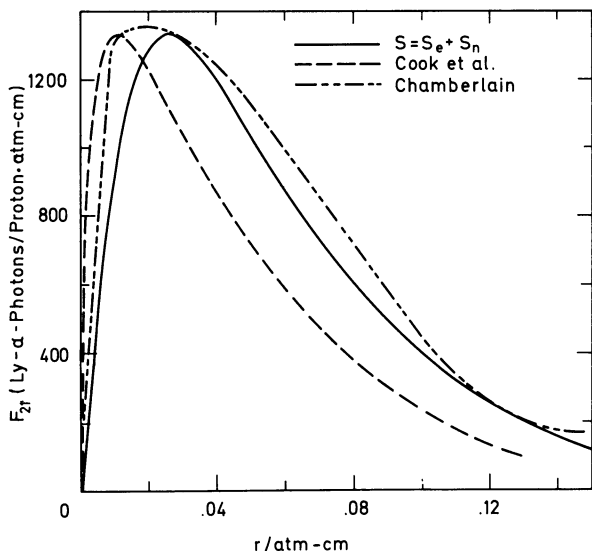


Fig. 2. The emission rate of Lyman-Alpha photons per unit volume per proton as a function of the proton residual range. The upper dash-dotted curve is Chamberlain's estimate (1961) reduced by a factor of four. The lower dashed curve was computed using Cook's range data (1953) while the solid curve is obtained with the range-energy relation of this work

nitrogen and 20% oxygen. The lower dashed curve gives the results of Cook *et al.* (1953) with extrapolation in the low energy region. The upper dashed line is obtained using the electronic stopping power S_e (Dose and Sele, 1975) only, while the solid curve is calculated adding the theoretically computed stopping power S_n to the experimental data on S_e from Dose and Sele (1975) and Reynolds *et al.* (1953). The solid curve is quite accurately given by

$$E = 27.4531 r + 6,611.5 r^2 - 15,863 r^3 \quad (3)$$

with E in KeV and r in atm-cm. Cook's results are approximated by

$$\ln(E/30) = 1.286 \ln(r/0.05). \quad (4)$$

Fig. 2 shows the volume emission rate F_{21} as a function of the proton residual range r . The solid curve is the result of this work using cross sections as given by (2) and Table 1 together with the range energy relation (3). The lower dashed curve is obtained with the range-energy relation (4). The upper dash-dotted curve is an estimate by Chamberlain (1961) which was divided by a factor of four in order to fit into the present picture. F_{21} may be expressed accurately in analytical form by

$$F_{21}(r) = \sum_{n=1}^4 \frac{a_n r^n}{(b+r)^{n+1}} \quad (5)$$

with coefficients as given in Table 2. The calculations displayed in Fig. 2 include contributions due to H^- . The relative importance of H^- , however, remains small everywhere as shown in Fig. 3. This is mainly due to the small fraction of H^- ions in a charge equilibrated hydrogen beam, although the cross sections for production of Lyman-Alpha radiation are larger by roughly a factor of three for H^- impact than those for proton or hydrogen atom impact.

Table 2. Coefficients for the analytical representation of the volume emission rate $F_{21}(r)$ of Lyman-Alpha radiation as a function of residual proton range r . With r in atm-cm F_{21} is given as the number of Lyman-Alpha photons produced per proton and atm-cm

Range-energy relation	(3)	(4)
b	0.0381	0.02
a_1	107.453	261.656
a_2	727.625	-807.032
a_3	-1,299.12	1,443.62
a_4	326.375	-963.375

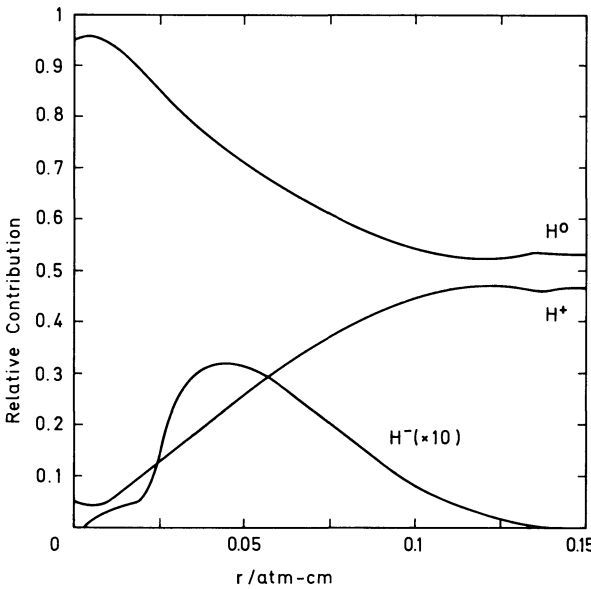


Fig. 3. Relative contribution of the different hydrogen charge states to the production of Lyman-Alpha radiation. The H^- contribution is always smaller than 3% due to the low fraction of H^- ions in a charge equilibrated hydrogen beam

The total number of Lyman-Alpha photons Z_{21} for a proton of given initial energy E_0 is the area under the curves in Fig. 2.

$$Z_{21} = \int_0^{r(E_0)} F_{21}(r') dr' \tag{6}$$

Fig. 4 shows a plot of Z_{21} versus E_0 . The solid curve is obtained using the range energy relation (3) while the dashed curve is obtained with (4). The difference is most pronounced for low initial energies $E \leq 25$ KeV. The upper dash-dotted curve is an estimate used by Clark and Metzger (1969) to correlate auroral Lyman-Alpha emission observations with incident proton flux. Their result is based on an estimate by Eather (1967) of 360 photons per 300 KeV proton. This figure as well as Chamberlain's estimate (1961) of 460 photons per proton appears to be much too high.

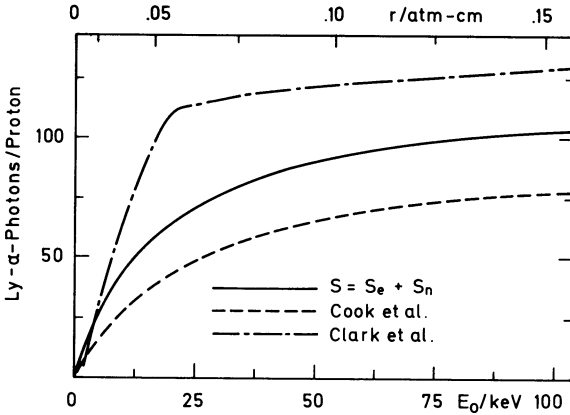


Fig. 4. The total number of Lyman-Alpha photons produced by a proton of given initial energy. The solid curve was computed employing the range-energy relation of this work. The lower dashed curve is obtained with Cook's data and the upper dash-dotted curve is an estimate by Clark and Metzger (1969)

III. Lyman-Alpha Emission in the CIRA 72 Standard Atmosphere

A. Normally Incident Monoenergetic Protons

The results of Section II may be converted to actual atmospheric emissions with the help of an atmospheric model. We have chosen the CIRA 72 standard atmosphere data. The equivalent atmospheric depth ξ in atm-cm is given in terms of actual height h as

$$\xi(h) = \frac{1}{2n_0} \int_h^\infty \{2n(\text{N}_2) + 2n(\text{O}_2) + n(\text{O})\} dh' \quad (7)$$

where n_0 is Loschmidt's number and n is the particle number density as given in CIRA 72. The inverse relation $h(\xi)$ may be conveniently expressed as

$$h = \sum_{k=0}^3 a_k (\ln \xi - \ln \xi_0)^{2k} \quad (8)$$

with h in km and ξ in atm-cm. The constants are

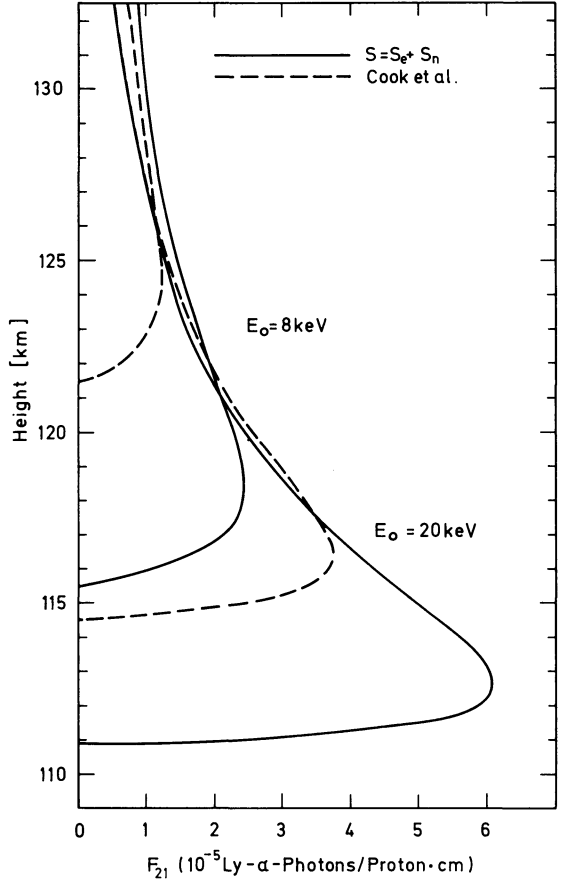
$$\begin{aligned} a_0 &= 99.3828, & a_2 &= 2.36435 \cdot 10^{-2}, \\ a_1 &= 0.726563, & a_3 &= -9.22684 \cdot 10^{-5}, \\ \xi_0 &= 1.5683. \end{aligned}$$

With the help of (8) the volume emission rate F_{21} as a function of height is given by

$$F_{21}(h) = -F_{21}(\xi) \cdot \frac{d\xi}{dh}. \quad (9)$$

Fig. 5 shows examples for initial proton energies of 8 KeV and 20 KeV. Solid curves are obtained with the range-energy relation (3) and dashed curves with (4). The effect is drastic and it is suggestive that recent efforts to obtain agreement between observed and calculated H-Beta emissions (Wax and Bernstein, 1970; Miller and Shepherd, 1969) failed because the stopping power used was too high.

Fig. 5. Height profile of the volume emission rate for production of Lyman-Alpha radiation by normally incident monoenergetic protons of 8 KeV and 20 KeV initial energy in the atmosphere. The CIRA 72 standard atmosphere was used as the atmospheric model. Dashed curves were computed using Cook's range data while solid curves were obtained employing the range-energy relation of this work. A drastic change in the height of peak emission is observed



B. Emission Height Profiles for Given Energy and Pitch Angle Distributions

A convenient and sufficiently flexible pitch angle distribution has been proposed by Chamberlain (1954). If ϑ is the angle against a line normal to the atmosphere then

$$f(\vartheta) = \frac{N+2}{2\pi} \cos^N \vartheta. \tag{10}$$

Let $g(r_0)$ be the energy distribution of the incident protons with the energy E expressed by the initial range r_0 . The number of Lyman-Alpha photons emitted per proton and atm-cm is then given as a function of equivalent depth by (Chamberlain, 1961; Eather, 1967)

$$F_{21}(\xi) = (N+2) \xi^{N+1} \int_{\xi}^{\infty} g(r_0) dr_0 \int_0^{r_0-\xi} \frac{F_{21}(r)}{(r_0-r)^{N+2}} dr \tag{11}$$

where r is the residual range. Actual emission height profiles are again obtained using (9). With the analytic representation of F_{21} given in Section II the inner integration may be carried out analytically. The remaining integration over the

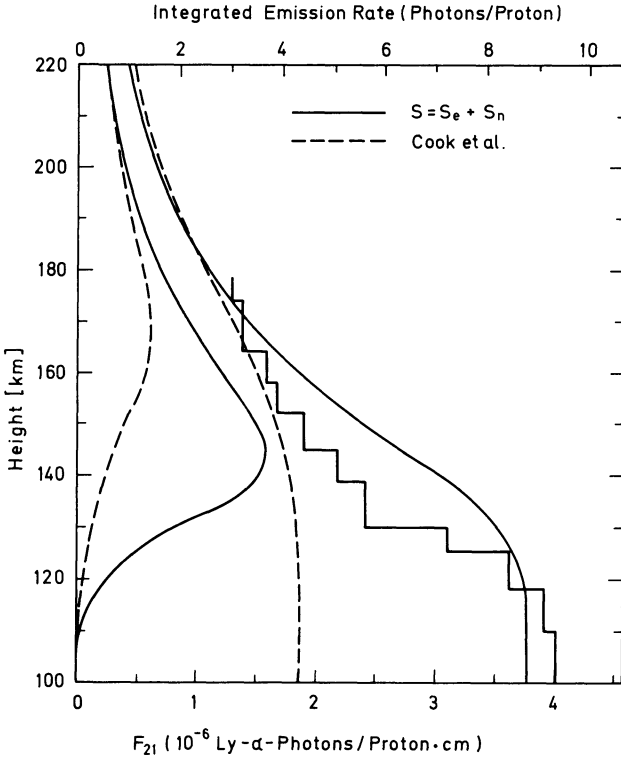
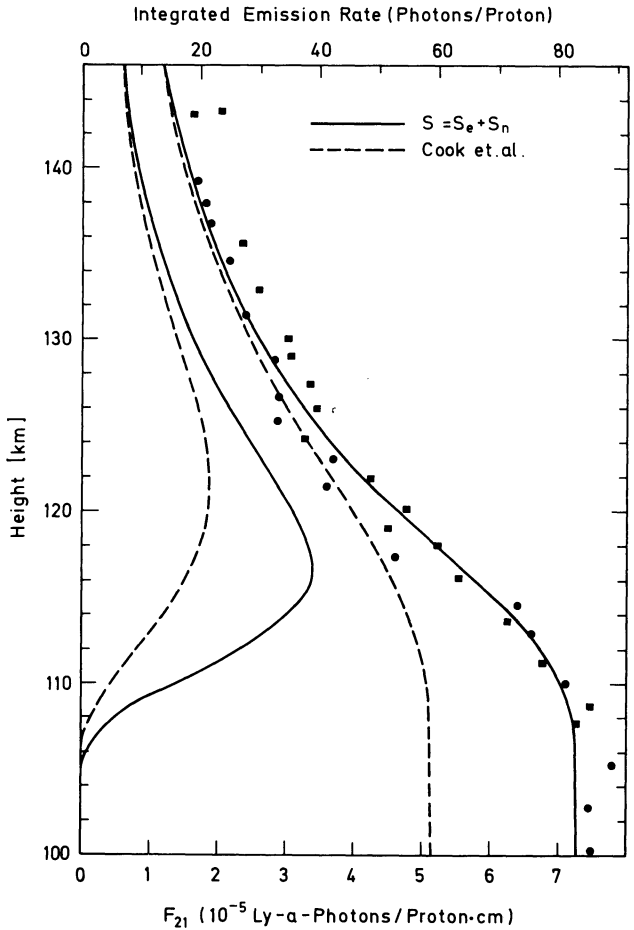


Fig. 6. Height profile and integrated emission rate of Lyman-Alpha radiation produced by protons with an isotropic pitch angle distribution and a power law $E^{-3.2}$ energy spectrum. Solid curves are computed using the range-energy relation of this work and dashed curves are obtained using Cook's range data. The staircase curve is a rocket flight observation of H-Beta radiation from the experiment of Wax and Bernstein (1970)

energy distribution must be done numerically. Of course, there is no unique choice for the energy distribution $g(r_0)$. In fact, strong variations are observed on different occasions (Mc Neal and Birely, 1973). Moreover, since no observations on height profiles for Lyman-Alpha emission have come to our attention, it would appear to be useless to proceed further. However, if we make the reasonable assumption, that cross sections for emission of H-Beta radiation exhibit a velocity dependence similar to Lyman-Alpha excitation cross sections, a comparison to recent rocket flight data is possible. Two rather different sets of observations are available. Wax and Bernstein (1970) measured the integrated emission rate of H-Beta radiation and the particle energy spectrum between 0.5 KeV and 22 KeV during an auroral break up above Fort Churchill. They found that the hydrogen differential energy spectrum fitted very well to a power law E^{-n} with $n=3.2$. We insert this energy distribution in (11), carry out the numerical integration assuming an isotropic pitch angle distribution and arrive at the result shown in Fig. 6.

Rocket observations are displayed by the staircase line. Calculations for both, the integrated emission rate along the line of sight and the volume emission rate as a function of height are shown. Dashed lines are obtained with the conventional range energy relation (4) while solid curves are obtained with the new relation (3). Evidently the latter results are much superior. In particular, the shift in peak emission height from 170 km to 145 km is most remarkable because Wax and

Fig. 7. Height profile and integrated emission rate of Lyman-Alpha radiation produced by protons with an isotropic pitch angle distribution and an energy spectrum corresponding to the auroral conditions in the rocket experiment of Miller and Shepherd (1969). Solid curves are computed using the range energy relation of this work while dashed curves are obtained with Cook's range data. Solid circles and squares are from H-Beta measurements in the rocket flight experiment of Miller and Shepherd (1969)



Bernstein (1970) being unable to get agreement between their observations and calculations, were even prepared to suggest a reduced atmospheric density above Fort Churchill.

The second set of observational data was evaluated from a rocket flight into a quiet evening hydrogen arc at Fort Churchill by Miller and Shepherd (1969). The particle energy spectrum was derived from proton energy measurements for $E \geq 30$ KeV in combination with accepted H-Beta Doppler profile shapes. The derived energy spectrum was approximated by an e -folding energy of 12 KeV with a cut-off at 23 KeV plus "a certain amount" of low energy particles. We have represented the low energy particle component by the constant $\exp\{-23/12\}$ for $10 \text{ KeV} \leq E \leq 23 \text{ KeV}$ and zero for $E \leq 10 \text{ KeV}$. A guess of this kind is suggested by observations of Whalen *et al.* (1971) and Whalen and McDiarmid (1972). Using this energy distribution and an isotropic pitch angle distribution we arrive at the results shown in Fig. 7. Again both, integrated emission rate and height profile are shown. Dashed curves are obtained with range energy relation (4), while solid curves were calculated using (3). The agreement between the latter

results and observations is surprisingly good. In particular, the height of the peak emission rate of 116 ± 2 km as quoted by Miller and Shepherd (1969) is excellently reproduced.

Considering the agreement between our calculations and the two strongly differing sets of observational data the underlying assumption concerning the velocity dependence of the H-Beta production cross sections seems to be well justified.

IV. Conclusions

The present calculations have shown that emission rate profiles and integrated emission rates depend quite sensitively on the range-energy relationship employed. Comparative calculations on Lyman-Alpha emission with a new range-energy relation constructed from recent laboratory measurements of the electronic stopping power S_e of atmospheric gases and theoretically calculated corrections for nuclear contributions S_n and with earlier data from the experiment of Cook *et al.* (1953) suggest that part of the difficulties in interpreting auroral hydrogen emissions can be overcome by using the correct stopping power. In fact, Lyman-Alpha emission cross sections together with our range energy relation reproduce surprisingly well two sets of rocket flight data of H-Beta emission which were taken under rather different auroral conditions. The agreement achieved seems to support the assumption that the velocity dependence of hydrogen emission cross sections is similar for different principal quantum numbers.

References

- Allison, S. K., Garcia-Munoz, M.: Electron capture and loss at high energies. In: Atomic and molecular processes, D.R. Bates, ed.: pp. 722-780. New York-London: Academic Press 1962
- Chamberlain, J.W.: The excitation of hydrogen in aurorae. *Astrophys. J.* **120**, 360-366, 1954
- Chamberlain, J.W.: *Physics of the aurora and airglow*. New York: Academic Press 1961
- Clark, M. A., Metzger, P. H.: Auroral Lyman-alpha observations. *J. Geophys. Res.* **74**, 6257-6265, 1969
- Cook, C.J., Jones, E., Jorgensen, T.: Range-energy relations of 10- to 250-KeV protons and helium ions in various gases. *Phys. Rev.* **91**, 1417-1422, 1953
- Dose, V., Sele, G.: Electronic stopping power of nitrogen and oxygen for low energy protons. *Z. Physik A* **272**, 237-243, 1975
- Eather, R. H.: Auroral proton precipitation and hydrogen emissions. *Rev. Geophys.* **5**, 207-285, 1967
- Jesse, W. P., Sadauskis, J.: The range-energy curves for alpha-particles and protons. *Phys. Rev.* **78**, 1-8, 1950
- Lindhard, J., Scharff, M., Schiott, H.E.: Range concepts and heavy ion ranges (Notes on atomic collisions, II). *Dan. Mat. Fys. Medd.* **33**, No. 14, 1963
- Mc Neal, R. J., Birely, J. H.: Laboratory studies of collisions of energetic H^+ and hydrogen with atmospheric constituents. *Rev. Geophys. and Space Phys.* **11**, 633-692, 1973
- Miller, J. R., Shepherd, G. G.: Rocket measurements of H beta production in a hydrogen aurora. *J. Geophys. Res.* **74**, 4987-4997, 1969
- Omholt, A.: *The optical aurora*. Berlin-Heidelberg-New York: Springer 1971
- Ormrod, J. H.: Low-energy electronic stopping cross sections in nitrogen and argon. *Can. J. Phys.* **46**, 497-502, 1968
- Phillips, J. A.: The energy loss of low energy protons in some gases. *Phys. Rev.* **90**, 532-537, 1953

- Reynolds, H. K., Dunbar, D. N. F., Wenzel, W. A., Whaling, W.: The stopping cross section of gases for protons, 30–600 KeV. *Phys. Rev.* **92**, 742–748, 1953
- Schiott, H. E.: Range-energy relations for low-energy ions. *Dan. Mat. Fys. Medd.* **35**, No. 9, 1966
- Tawara, H., Russek, A.: Charge changing processes in hydrogen beams. *Rev. Mod. Phys.* **45**, 178–229, 1973
- Vegard, L.: Hydrogen showers in the auroral region. *Nature* **144**, 1089–1090, 1939
- Wax, R. L., Bernstein, W.: Rocket-borne measurements of $H\beta$ emissions and energetic hydrogen fluxes during an auroral breakup. *J. Geophys. Res.* **75**, 783–787, 1970
- Whalen, B. A., Miller, J. R., Mc Diarmid, I. B.: Evidence for a solar wind origin of auroral ions from low-energy ion measurements. *J. Geophys. Res.* **76**, 2406–2418, 1971
- Whalen, B. A., Mc Diarmid, I. B.: Further low-energy auroral-ion composition measurements. *J. Geophys. Res.* **77**, 1306–1310, 1972

Received July 24, 1975

The Gravity Field of Northeastern Iceland

A. Schleusener, W. Torge and H. Drewes

Institut für Theoretische Geodäsie der Technischen Universität,
D-3000 Hannover, Nienburgerstr. 6, Federal Republic of Germany

Abstract. From 1964 to 1970, about 1,000 gravity stations have been established in parts of northeastern Iceland. The survey covered the young volcanic zone and the adjoining tertiary plateau basalts mainly in the region between $65^{\circ}5-66^{\circ}$ N and $18^{\circ}-16^{\circ}$ W, with some extensions across the eastern basalt zone. Gravity measurements have been carried out in profiles with LaCoste-Romberg gravity meters (± 0.03 mgal), while heights have been determined by barometric levelling ($\pm 2 \dots 3$ m). Density determinations by rock weighing and by Nettleton-profiles gave mean values between 2.0 g/cm^3 (hyaloclastite rocks) and 2.8 g/cm^3 (tertiary basalt lavas). Bouguer anomalies have been calculated with uniform density 2.6 g/cm^3 and with different density zones ($2.2-2.7 \text{ g/cm}^3$). The accuracy of the anomalies varies between ± 0.5 and ± 4 mgal, depending on the height of the gravity station. The gravity field shows the well-known decrease from north to south ($0.4 \dots 0.5$ mgal/km) and a relative gravity minimum (5 mgal) in the active rift zone. The more irregular gravity behaviour in the central part of the young zone might be due to surface near mass anomalies.

Key words: Gravity anomalies – Rock densities – Icelandic rift zone.

1. Introduction

Iceland and its surroundings are of special interest for the geosciences, as here the central part of the Mid-Atlantic Ridge is rising above sea-level, thus giving the opportunity for detailed geological, geophysical and geodetic investigations at an accreting plate boundary.

A first survey of the gravity field in this region has been carried out in 1938 in northern Iceland as part of a German geological (Bernauer), geodetic (Niemczyk and Emschermann) and geophysical (Ansel and Schleusener) expedition (Niemczyk, 1943). 40 gravity stations have been established at this survey, situated mainly along the line from Akureyri to Grimsstadir (Schleusener, 1943).

A gravity survey of the whole island has been carried out by Einarsson (1954), containing about 900 stations. North of 65°30' latitude, Einarsson occupied about 100 stations between Eyjafjörður and Vopnafjörður.

The investigation of the gravity field in northern Iceland has been taken up again in 1964 (1964–1967: Schleusener; 1970: Schleusener, Torge and Drewes). The aim of these measurements was to give the regional gravity field especially in west-east direction as well as the local gravity field of several small structures and, above all, to detect eventual gravity variations with time by repeated measurements at some monumented stations. This report deals with the result of the regional survey 1964–1970. A short discussion on the gravity field of some local structures and the general regional gravity behaviour has been given by Schleusener and Torge (1972) and by Schleusener (1974). The results of repeated gravity measurements along a west-east profile at 65°40' N latitude have been presented by Schleusener and Torge (1971), the extension of this profile and the description of the survey 1970/71 is given by Schleusener *et al.* (1974).

The gravimetric investigations are part of the research work of German geodetic (*e.g.* Gerke and Pelzer, 1972; Gerke, 1974) and geophysical (geomagnetics: Angenheister *et al.*, 1972; microseismics: Steinwachs (1972)) groups in Iceland. This work is sponsored by the German Research Society (Deutsche Forschungsgemeinschaft).

2. Description of the Survey Area

The regional gravity survey described here, covers mainly the region between 65.5°–66° northern latitude and 18°–16° western longitude. From west to east, the survey stretches over the tertiary plateau basalt zone between Eyjafjörður and the Bárðardalur fault, and the western and central part of the young volcanic zone until the river Jökulsá á Fjöllum (Fig. 1). Some profiles extend to the eastern basalt zone, starting about 20 km east of the river Jökulsá, and end at the eastern coast of Iceland.

The tertiary basalt zone constitutes a rather homogeneous plateau-like formation of basalt lavas with intercalated sedimentary and tuff layers, strongly eroded and interrupted by deep valleys with more or less consolidated sediments. Heights of about 900 m above sea level are reached in this zone. The young volcanic zone may be divided into the flanking intermediate zones, consisting mainly of pleistocene flood basalts, and the still active zone of rifting and volcanism being the central part of this region. Here a variety of pleistocene and postglacial structures is found, as table mountains, shield volcanoes and mainly south-north directed crater rows, fissures and faults. The heterogeneous younger series filling this zone have been designated as palagonite or Móberg formation, consisting of hyaloclastite (palagonite tuff and breccia) rocks, young lava flows and sediments (Thorarinsson *et al.*, 1959; Pálmason and Saemundsson, 1974). The average height of the lowlands of the central zone is about 100...400 m, table mountains and other volcanoes reaching 800 m and more.

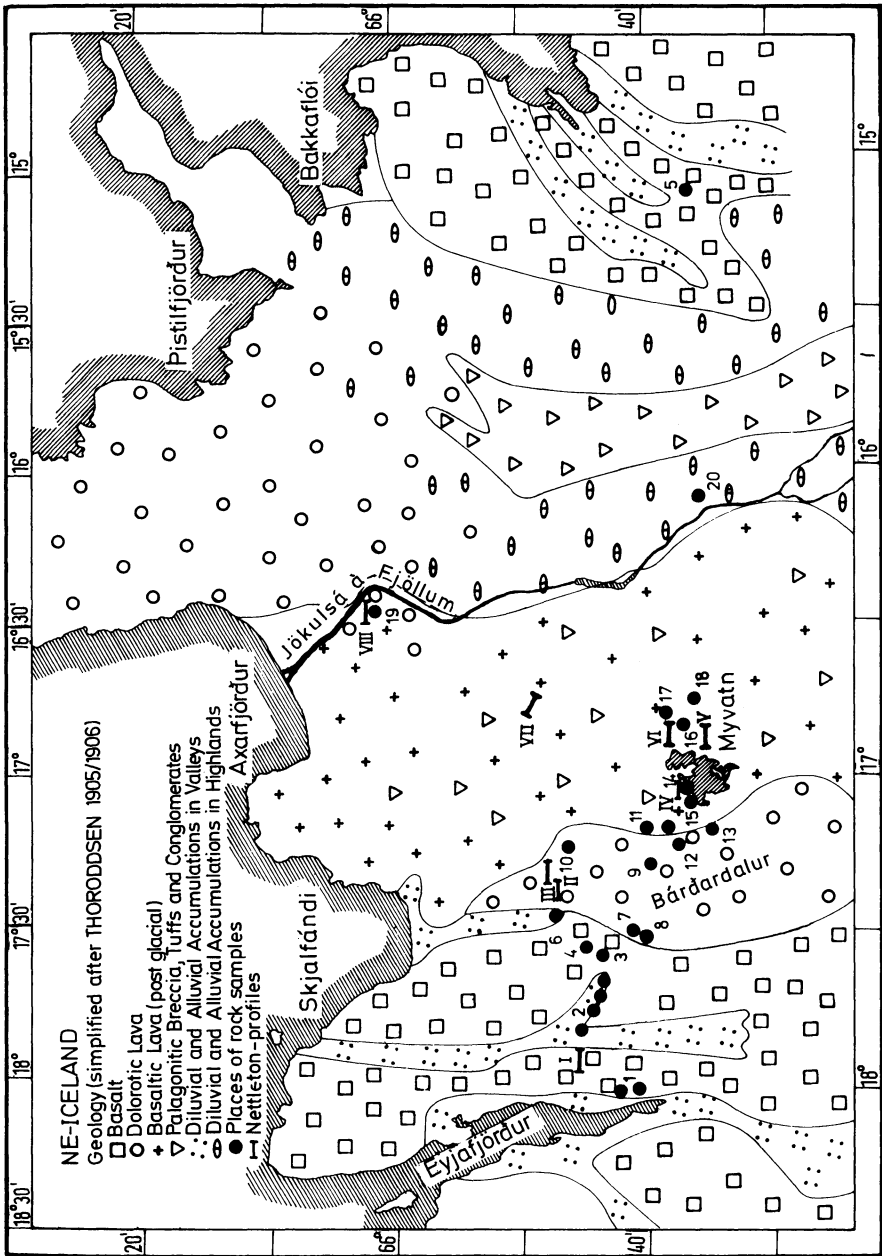


Fig. 1. Geology of the survey region, positions of rock sampling and Nettleton-profiles

3. Measurements and Data Evaluation

3.1. Survey Layout

For economical reasons the gravity stations have been established in profiles mainly along roads and tracks, so that car transport was possible (Fig. 2). The

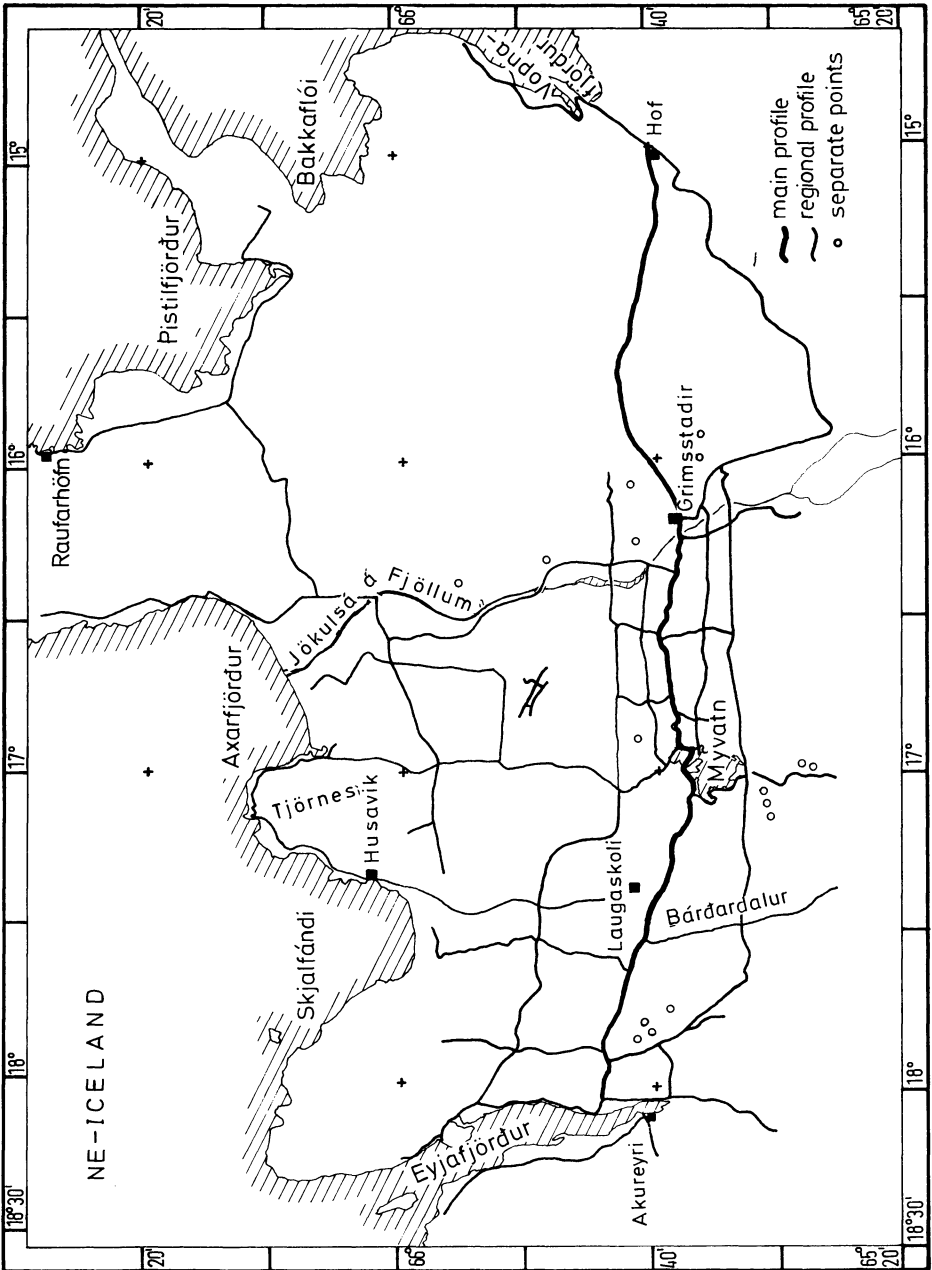


Fig. 2. Gravity profiles

west-east profile following approximately the road from Akureyri to Grimmsstadir, is used for investigations about secular gravity variations (monumented main profile). In order to get a more detailed picture of the gravity field here, four parallel profiles have been observed by foot. East of the river Jökulsá á Fjöllum,

the area is more or less inaccessible by car, so only a few profiles have been measured there in order to obtain an impression of the gravity of the eastern basalt zone.

The average spacing of points on the profiles is about 1 km. Altogether about 1,000 stations have been observed in the measuring periods 1964, 1965, 1967 and 1970.

Gravity, position and height have been determined simultaneously, a survey crew generally consisting of two observers. One observer was responsible for the gravity measurements, the other one for positioning and height determination. If possible the stations have been marked by color, furthermore a point sketch has been prepared. So the station could be found again for connecting surveys.

With the exception of the authors, the following persons participated at the field work and the data evaluation: H. Lehrke, A. Berger, W. Brosche, H. Hahn, B. Köhler, U. Meyer, M. Mimus, H. Mittendorf, B. Stache, H.-J. Voss, H. Zimmermann and the Icelandic and German helpers B. Benediktsson, T. Keil, V. Sauer, H. Tomasson. The Icelandic geologist Thomas Tryggvason † has been a valuable guide to Icelandic geological and geographical conditions and a never tired active aid in difficult field situations, from 1938 to 1965.

3.2. Gravity Measurements

The gravity measurements have been carried out with the LaCoste-Romberg model *G* gravity meters no. 79 and no. 85. Worden gravity meter no. 530 has been used in measuring some Nettleton-profiles for determination of rock density.

The profile measurements always started and ceased at a station of the "main profile", the gravity of these stations being known with $\pm 0.01 \dots 0.02$ mgal accuracy. These loop measurements allowed the detection of gross errors and a drift control. One loop generally contained 15 \dots 25 stations, which could be observed within 8 \dots 10 hrs. At each station, three readings have been made for control, the mean value being introduced as observed quantity.

Evaluation started with the transformation of the mean reading to mgal-scale, using the manufacturers conversion tables. Tidal corrections have been applied from the tables calculated by Goguel (1954) and published annually in "Geophysical Prospecting". Residual loop misclosures were supposed to result from instrumental drift and distributed proportional with time.

Gravity values refer to the Potsdam gravity system, according to the connections measured from 1964 to 1970 between Reykjavik and the continent (Torge, 1971). The gravity value of Reykjavik, University, station no. 21941 A (IAG-SSG5-Catalogue) has been found with

$$g_{\text{Reykjavik}} = 982,279.93 \pm 0.05 \text{ mgal.}$$

This value refers to the conventional Bad Harzburg (station no. 21510 A) value $g = 981,180.40$ mgal. As the IGSN 71 (Morelli *et al.*, 1974) value for Reykjavik

A is

$$g_{\text{Reykjavik}} = 982,264.96 \pm 0.02 \text{ mgal},$$

a correction of -14.97 mgal must be applied to the gravity values of the present survey, if transformation to IGSN 71 is desired.

Accuracy of the gravity values may be estimated from the root mean square errors (r.m.s.e.) of the main profile reference stations and of the observed gravity differences. For the main profile stations, r.m.s.e. of $\pm 0.01 \dots 0.02$ mgal have been found, referring to the station Akureyri being the base station for the survey. The station Akureyri has been connected to Reykjavik with an accuracy of about ± 0.01 mgal (Schleusener *et al.*, 1974). Small gravity differences can be measured with the same order of accuracy (Schleusener and Torge, 1971). So the r.m.s.e. of the stations is about ± 0.03 mgal.

In 1970, 31 field stations established at earlier measuring periods, have been reoccupied. From the differences, a r.m.s.e. of ± 0.07 mgal has been calculated. As this value includes also errors in position and height identification as well as gravity variations caused by local mass shifts, the result is consistent with the value estimated above.

3.3. Positioning

Position of the gravity stations has to be determined for mapping and (geographical latitude) for calculating normal gravity values. Due to economical considerations, positioning was performed by identifying the gravity stations in the topographical maps 1:100,000, published by "Landmaelingar Islands". Identification was carried out in the field, using local structures and distances to identified points, determined by the car kilometre recorder (100 m-reading) or by stepping. The accuracy of the geographical coordinates obtained by this method, has been evaluated in the eastern part of the main profile between Grimsstadir and Hof, where positions were determined by map identification and by tacheometric methods. R.m.s.e. of ± 0.1 in latitude and ± 0.2 in longitude, corresponding to approximately ± 150 m, have been found (Schleusener *et al.*, 1974).

3.4. Height Determination

Due to the high accuracy of gravimeter measurements, the accuracy of gravity anomalies depends mainly on the reduction quantities, especially on the station height. At regional surveys, barometric levelling is the most economical method for height determination, as it is analogue to the gravimetric process. Reading of barometer, thermometer and hygrometer takes about the same time as gravity meter readings. If the horizontal pressure gradient, time variations of pressure and instrumental drift are sufficiently taken into account, height differences at extensive surveys can be determined barometrically with r.m.s.e. of $\pm 2 \dots 5$ m, depending on the difference and on spacing of control points (Bachem *et al.*, 1972).

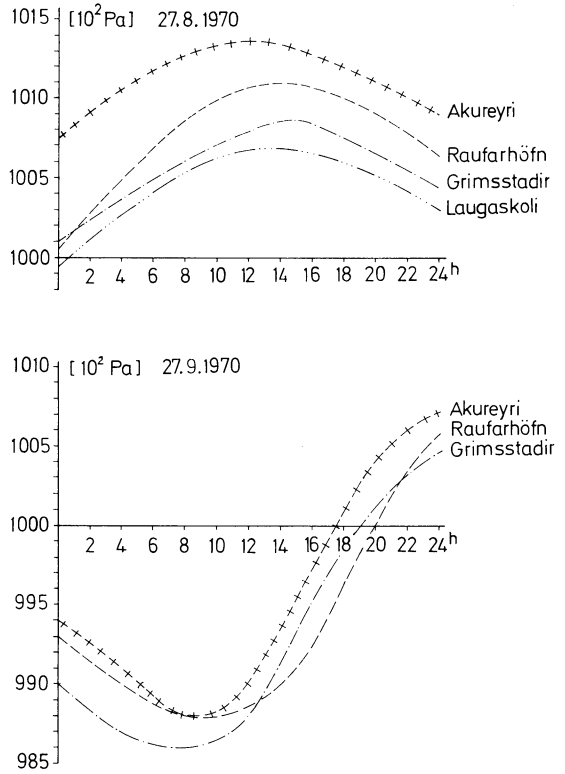


Fig. 3. Time variations of air pressure (example)

In 1965 and 1967, one Thommen and three Paulin altimeters were used for height determination. In 1970, a group of 3 Thommmen altimeters type 3B4 has been operated, in order to control readings and to improve accuracy. Pressure variations with time have been recorded by a Lambrecht microbarograph installed at a central point (Laugaskoli). In addition, pressure records of the meteorological stations at Akureyri, Grimsstadir and Raufarhöfn were available. Similar to the gravity measurements, barometric levelling started and ceased at a reference station with known height.

Absolute heights were available for the bench marks of a high precision geometric levelling between Akureyri and Grimsstadir, carried out by Spickernagel (1966).

Before reading the altimeters at each station, the instruments were kept unclamped for 10 ... 15 min to adapt the local pressure.

At evaluation, at first the instrumental pressure correction determined at the laboratory, has been applied. A correction for time variations of pressure was determined from the pressure registrations of the meteorological stations next to the measured profile, using linear interpolation between the stations. From Fig. 3, showing some extreme pressure changes, we see that pressure behaves similarly at points 50 ... 150 km distant from each other. The different pressure level of the stations results from the different station heights. Finally

a temperature and humidity reduction was applied to the height differences (Möller, 1962). Comparing the sum of the height differences in one loop with the known difference between the control points gave the misclosure, which was distributed proportional with time.

Accuracy of barometric heights depends mainly on the procedure employed for taking into account horizontal pressure gradients, time variations of pressure and instrumental drift. From analysis of more than 300 stations in about 15 profiles, r.m.s.e. of $\pm 1.3 \dots 2.5$ m have been found for height differences of 0 ... 50 m between adjacent points, observed with one altimeter. Averaging the results of three altimeters and regarding the correlation produced by identical meteorological effects, the r.m.s.e. reduces to $\pm 1 \dots 1.5$ m. A comparison of barometric with tacheometric heights in the eastern part of the main profile resulted in a height r.m.s.e. of ± 1.2 m. Finally, repeated altimeter measurements at 21 stations, carried out in 1965 and 1970, gave a r.m.s. difference of ± 4.4 m, this value including identification errors. As a result, the height r.m.s.e. will probably not exceed ± 3 m (one altimeter) resp. ± 2 m (three altimeters).

4. Density Determinations

In order to obtain a smoothed gravity field being free from the irregular influence of the topographic masses, the observed gravity values are reduced by the Bouguer and the terrain reduction. One important error source in the topographic reduction is the uncertainty in estimating the mean density of the topographic masses.

The surface boundaries of the geological formations in the survey area are given in the geological map 1:500,000 by Thoroddsen (1905/06). After checking the existing data about rock densities in Iceland, especially in the northern part, it has been felt necessary to obtain some more information by taking rock samples and observing Nettleton-profiles. The places of observation are distributed over the survey region in order to get values for the different geological formations (Fig. 1).

4.1. Rock Weighing

Rock samples have been taken from 5 places in the tertiary basalt zone and from 15 places in the young volcanic zone. At most places more than one probe has been chosen, especially if larger differences in type occurred. The samples were placed under water for 24 hrs and then weighed in water and in air by means of a spring balance. From the difference of the two weighings, the density of the rock sample was calculated. Altogether 179 samples of weight 0.1 ... 0.5 kg have been measured, the mean results for the different places are given in Table 1. Within one place, density of the samples of one type varied in the range of 0.3 g/cm³ for solid and 0.5 g/cm³ for porous basalt lava, 1.1 g/cm³ for tuffs and 0.4 g/cm³ for tuff breccias. The r.m.s.e. of weighing is estimated to be ± 0.1 g/cm³.

Table 1. Mean densities from rock weighing

No.	Place	Material	Number of samples	Density g/cm ³
<i>Tertiary basalt zone</i>				
1	Vadlaheidi	basalt (solid)	3	2.97
2	Ljósavatndalur	basalt (solid)	6	2.95
		basalt (porous)	3	2.64
		tuff	4	2.31
3	Krossóxel	basalt	1	2.91
		tuff	5	2.14
4	Krossoxel	basalt (solid)	1	2.93
		basalt (porous)	2	2.50
		tuff	7	2.22
5	Urdafell	basalt	11	2.89
		tuff	3	2.63
<i>Young volcanic zone</i>				
6	Kinnarfell	tuff (unconsolid.)	2	1.91
7	Ingjaldistadir	basalt (solid)	2	2.90
		basalt (porous)	2	2.51
		basalt (solid)	2	2.88
8	Godafoss	basalt (solid)	2	2.88
		basalt (porous)	3	2.52
		basalt	1	2.79
9	Reykjadalur	breccia	8	2.21
		basalt (porous)	4	2.66
10	Thorgerdharfjall	basalt (solid)	2	2.95
		tuff	2	2.10
		tuff breccia	3	1.98
11	Laxárdalur	basalt (solid)	5	2.89
		basalt (porous)	2	2.42
12	Laxárdalsheidi	basalt (solid)	2	2.42
		basalt (porous)	5	2.28
13	Hofstadir	basalt (solid)	5	2.28
		basalt (porous)	1	2.86
14	Mývatn	basalt (solid)	1	2.86
		basalt (porous)	10	2.13
		hyaloclastite	8	1.72
15	Vindbelgjarfjall	basalt (solid)	1	2.86
		basalt (porous)	10	2.13
16	Námaskard	hyaloclastite	8	1.72
		basalt	1	2.93
17	Halaskógarfjall	hyaloclastite	5	2.31
		basalt (porous)	13	2.63
		tuff	5	2.12
18	Búrfellsrhaun	hyaloclastite (consolid.)	7	2.47
		basalt (porous)	1	2.42
19	Ásbyrgi	basalt (porous)	33	2.50
20	Tungufjöll	basalt (solid)	1	2.91
		basalt (porous)	1	2.26

As there is a large scattering of the results found at different places, it was decided to apply mean densities for the calculation of the Bouguer anomaly, using as well one common density for the survey area as a few density zones. Taking the simple mean values from Table 1 and calculating the r.m.s.e., we obtain the results given in Table 2.

These results agree sufficiently with the density values found by other authors from rock weighing. In the same area Bernauer (Schleusener, 1943, p. 144/145)

Table 2. Mean densities for rock formation from weighing

Rock formation	Number of places	Density g/cm ³	Range g/cm ³
tertiary basalt lavas	7	2.83 ± 0.07	2.5–3.0
tertiary tuffs	4	2.33 ± 0.11	2.1–2.6
quaternary basalt lavas	19	2.65 ± 0.06	2.1–3.0
hyaloclastite rocks	8	2.10 ± 0.08	1.7–2.5

obtained for

tertiary basalts: density 2.77 g/cm³ (2.3–3.2), $n = 10$
 palagonite tuffs: density 2.20 g/cm³ (2.1–2.5), $n = 8$.

A very detailed study of Hospers (1952) carried out in parts of the main profile, gave for

basalt lava: density 2.84 g/cm³, $n = 48$
 palagonite tuff: density 2.24 g/cm³, $n = 1$
 moraine matrix: density 2.24 g/cm³, $n = 8$
 sandstone: density 2.13 g/cm³, $n = 9$
 unconsolidated sand: density 1.80 g/cm³, $n = 1$.

Einarsson (1954) used variable densities at the calculation of Bouguer anomalies for Iceland, the values varying between 2.0 and 2.9 g/cm³. In the central parts of Iceland mainly the density 2.6 g/m³ has been applied. For basalts he gives the values 2.7 ... 3.0 g/cm³, for tuffs 2.2 g/cm³.

Taking these results into account and regarding, that a precision of 0.01 g/cm³ in density would be unrealistic for a mean value, we may round off the values given in Table 2. Thus we obtain as mean values from rock weighing:

tertiary basalt lavas: density 2.8 ± 0.1 g/cm³
 tertiary tuffs: density 2.3 ± 0.1 g/cm³
 quaternary basalt lavas: density 2.6 ± 0.1 g/cm³
 hyaloclastite rocks: density 2.1 ± 0.1 g/cm³

4.2. Nettleton-Profiles

Nettleton-profiles (Nettleton, 1939) have been observed and calculated at some places with sufficient height differences. Clear results were obtained at 8 places, they are given in Table 3. Some examples are shown in Fig. 4.

Taking simple means, we obtain the following Bouguer densities for different structures from Nettleton-profiles:

basalt mountains (basalts and tuffs):
 tertiary basalt zone: density 2.7 g/cm³
 young volcanic zone: density 2.6 g/cm³,
 tuff volcanoes (hyaloclastite rocks): density 2.0 g/cm³.

Table 3. Density values from Nettleton-profiles

No.	Place	Material	Density g/cm ³
<i>Tertiary basalt zone</i>			
I	Vadlaheidi (basalt mountain)	basalt, tuff	2.7
<i>Young volcanic zone</i>			
II	Múlaheidi (basalt mountain)	basalt, tuff	2.8
III	Thorgerdharfjall (basalt mountain)	basalt, tuff	2.5
IV	Vindbeljarfjall (tuff volcano)	hyaloclastite	1.8
V	Hverfjall (tuff volcano)	hyaloclastite	1.8–2.0 (6 profiles)
VI	Námaskard (tuff volcano)	hyaloclastite	2.05
VII	Hrutafjöll (tuff volcano)	hyaloclastite	2.15
VIII	Ásbyrgi (basalt mountain)	basalt, tuff	2.53 (2 profiles)

4.3. Final Density Assumptions

The results found from rock weighing and from the Nettleton profiles have been compared with the values given by Pálmason (1963, 1971) from *P*-velocities obtained at refraction seismic work in Iceland.

For the near surface rocks (recent lava flows, hyaloclastite tuffs and breccia) of the young volcanic zone (layer o) the density range 2.1 ... 2.5 g/cm³ (mean 2.3 g/cm³) is proposed by Pálmason. For the density of layer 1, consisting of tertiary and quarternary basalt lavas with intercalated sediments and tuffs, a value of 2.6 g/cm³ is given. Layer 2 and 3 do not rise above sea level, so they are of no interest for gravity reduction. The mean values for layer o and layer 1 agree sufficiently with the results found in the survey area.

It was decided to carry out one reduction process with uniform density 2.6 g/cm³, and a second one using three density zones:

tertiary basalt zone: density 2.7 g/cm³
 intermediate zone: density 2.5 g/cm³
 central volcanic zone: density 2.3 g/cm³.

The boundaries of zones have been determined from the geological map 1:600,000 and from Pálmason and Saemundsson (1974). The gravity stations situated in the eroded and sediment filled valleys of the coastal region have been reduced with the lower density 2.2 g/cm³, assuming that the unconsolidated material has a considerable thickness (Fig. 1). This procedure has been performed also by Hospers (1952).

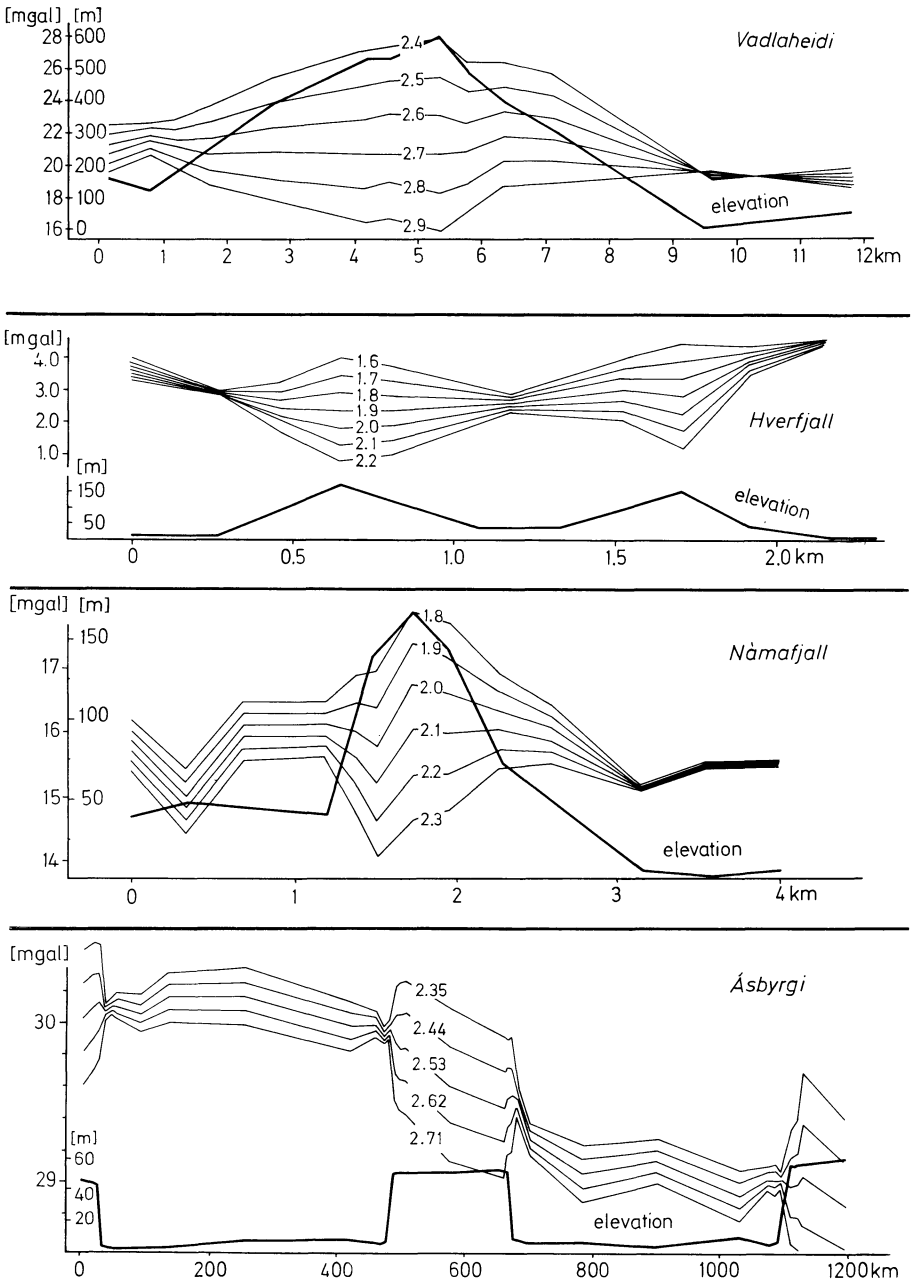


Fig. 4. Nettleton-profiles (examples)

5. Calculation and Accuracy of Bouguer Anomalies

5.1. Reference Systems

The Bouguer anomaly is defined by

$$\Delta g'' = g - \gamma_o + \delta g_F - \delta g_{\text{Top}},$$

where g is the observed gravity, γ_o the normal gravity at sea level, δg_F the free air reduction and δg_{Top} the topographical reduction, taking into account all the masses above sea level. g and γ_o depend on the gravity reference system and on the reference ellipsoid. Reference for the gravity values of the survey is the Potsdam gravity system (see section 3.2). For normal gravity, the international gravity formula of 1930 has been used:

$$\gamma_o = \gamma_a (1 + \beta \sin^2 \phi + \beta_1 \sin^2 2\phi)$$

with

$$\gamma_a = 978,049 \text{ mgal}, \quad \beta = 0.0052884, \quad \beta_1 = -0.0000059,$$

ϕ being the geographical latitude.

5.2. Gravity Reductions

The free air reduction is given by

$$\delta g_F = - \frac{\partial g}{\partial H} H$$

(H =height above sea level). As actual vertical gravity gradients $\partial g/\partial H$ have not been determined, a mean normal vertical gravity gradient of -0.3086 mgal/m has been used. The topographical reduction has been split up—as usual—into the simple Bouguer reduction δg_B and the terrain correction δg_T :

$$\delta g_{\text{Top}} = \delta g_B - \delta g_T.$$

The Bouguer reduction has been calculated from gravitation of an infinite plane slab:

$$\delta g_B = 2\pi G \rho H$$

with $G = 6.67 \cdot 10^{-8} \text{ cm}^3 \text{ g}^{-1} \text{ s}^{-2}$ being the gravitational constant and ρ the Bouguer density. The terrain correction was calculated from planar formulas up to a distance of 50 km, using the templates of concentric circles and radii given by Schleusener (1940). The error produced by this procedure will probably not exceed 0.1 mgal (Drewes, 1974). For the inner zone (0 ... 100 m) a two-dimensional mass distribution was assumed, the effect of gravitation being estimated in the field. Mean heights were estimated from the maps 1:750,000, 1:250,000, 1:100,000, 1:50,000, published by “Landmaelinger Islands”.

From repeated determinations, the r.m.s.e. of the terrain correction is estimated to be ± 0.2 mgal. This estimation contains only the errors of the volume integration, and not the density errors.

5.3. Accuracy of Bouguer Anomalies

The r.m.s.e. of the Bouguer anomalies depends on the errors of the quantities gravity g , geographical latitude ϕ , height H , vertical gravity gradient $\partial g/\partial H$, Bouguer density ρ , and terrain correction δg_T . Introducing the reduction terms into the formula for the Bouguer anomaly $\Delta g''$, differentiating this expression and applying the law of error propagation, gives the m.s.e. of $\Delta g''$:

$$m_{\Delta g''}^2 = m_g^2 + (\gamma_a \beta \sin 2\phi)^2 m_\phi^2 + \left(\frac{\partial g}{\partial H} + 2\pi G\rho \right)^2 m_H^2 + H^2 m_{\partial g/\partial H}^2 + (2\pi GH)^2 m_\rho^2 + m_{\delta g_T}^2.$$

From the Bouguer anomalies calculated with uniform density, we obtain a summed up information about all mass anomalies underneath the observation points. The Bouguer density introduced may be regarded as an errorless reduction quantity. The same is valid for the vertical gravity gradient. The r.m.s.e. of the other quantities mentioned above, has been estimated in the previous sections:

$$m_g = \pm 0.03 \text{ mgal}, \quad m_\phi = \pm 0.1, \quad m_H = \pm 2m, \quad m_{\delta g_T} = \pm 0.2 \text{ mgal}.$$

With these values, we obtain the height independent r.m.s.e. of the Bouguer anomalies

$$m_{\Delta g''} = \pm 0.5 \text{ mgal},$$

the main influence resulting from the height errors.

When we intend to represent mass anomalies underneath a reference level, usually "mean sea level", we have at first to carry out a geological preinterpretation or, at least, to introduce some generalized density assumptions for the formations above sea level. Density and vertical gravity gradient have then to be introduced as quantities with errors. For density we may assume $m_\rho = \pm 0.1 \text{ g} \cdot \text{cm}^{-3}$, while for the gradient no estimate is available in the survey region. From the values given below, we find that the height dependent influence of density errors in the r.m.s.e. of the Bouguer anomaly, surpasses the height independent terms already at heights of about 200 m:

H	0	100	200	500	1,000	m
$m_{\Delta g''}$	± 0.5	± 0.6	± 1.0	± 2.1	± 4.2	mgal

For error analysis between adjacent points, the correlation behaviour of the densities and the vertical gradient must be known, which generally is not available.

From the values given above, we see that for the survey discussed here, a contour interval of 1 mgal for the isoanomalies in the Bouguer maps along

the profiles seems to be reasonable. Using an interval < 1 mgal will produce gravity structures, which are not significant.

6. Description of the Bouguer Anomalies Field

Bouguer gravity anomalies have been mapped in scale 1:250000, the contour interval of the isoanomalies being 1 mgal. Reduced scale maps with 2 mgal-interval (for readability) are given in Figs. 5 and 6. In regions with large profile spacing, interpolation errors will influence the position of the contour lines, and produce errors of the isoanomalies being greater than the point errors. At first, a uniform Bouguer density 2.6 g cm^{-3} has been used, corresponding to the main density value of Einarsson (1954) and representing an average density value in the survey region (see Section 4.3).

The main feature of the gravity field is the well-known gravity decrease to the centre of Iceland, producing a north-south gravity gradient of $-0.4 \dots 0.5$ mgal/km in the survey area. The gravity bowl of $70 \dots 80$ mgal from the coasts to the islands centre found and discussed by Einarsson (1954), is generally explained now by inhomogenities in the density of the upper mantle, only a minor part of the variation being contributed by variations in crustal thickness (Pálmason and Saemundsson, 1974). This regional trend covers and distorts smaller gravity structures in the survey region, thus making their detection and interpretation more difficult.

Passing from west to east, we find relative gravity minima at the Eyjafjörður (a few mgal) and in the tertiary flood basalts southeast of Akureyri (about 5 mgal). East of the Bardardalur, at latitude $65^{\circ}40'$ to $65^{\circ}50'$ N, a west-east inclined gravity plain is to be seen, which stretches approximately to the river Jökulsá á Fjöllum ($22 \dots 16$ mgal). Along the main profile ($65^{\circ}40'$ N) there is a negative structure of about 5 mgal approximately $15 \dots 25$ km east of lake Myvatn, at the central part of the young volcanic zone. To the east, the Bouguer gravity anomalies increase to about 40 mgal at Vopnafjörður. At the southern part of the Tjörnes peninsula, a rather high gravity gradient of about 1.3 mgal/km is found. From the seismic refraction profile across northern Iceland, given by Pálmason (1963, 1967), we may suppose that the relative minimum in the young volcanic zone is produced by the thickening of the light layer 0 (quaternary volcanic rocks) and the corresponding dipping in of layer 1 (upper part of flood basalts). Smaller gravity structures might be due to local near surface mass anomalies, but as the resolution of the survey is of the order of 1 mgal (see section 5.3) they should be regarded with caution.

As the investigations about rock density have shown, regional density differences are probable (see Section 4.3). Therefore another Bouguer anomaly map has been drawn, using the density zones 2.2, 2.3, 2.5, 2.7 g cm^{-3} (Fig. 6). While the regional behaviour of the gravity field does not vary much, local structures are partly changed. For instance, the relative minimum at Eyjafjörður is strongly reduced, whereas the minimum southeast of Akureyri is more pronounced. Altogether, the gravity picture seems to be more quiet now, thus justifying the introduction of density zones, for reducing the influence of mass anomalies above sea level.

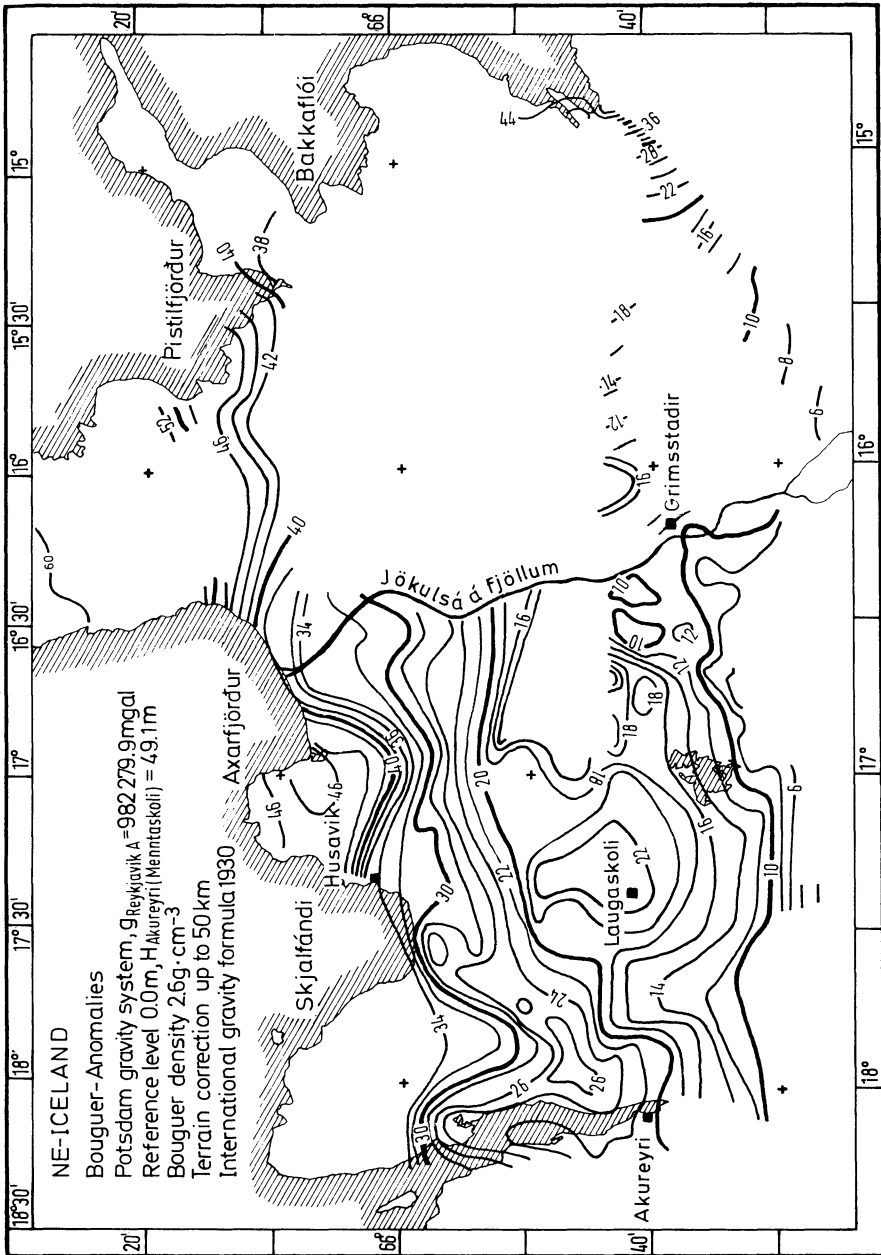


Fig. 5. Bouguer gravity anomalies, uniform density

7. Conclusion

In the present report, the results of a regional gravity survey in northeastern Iceland are given. Special attention has been turned to accuracy investigations of gravity, position and height determination and to evaluation of Bouguer

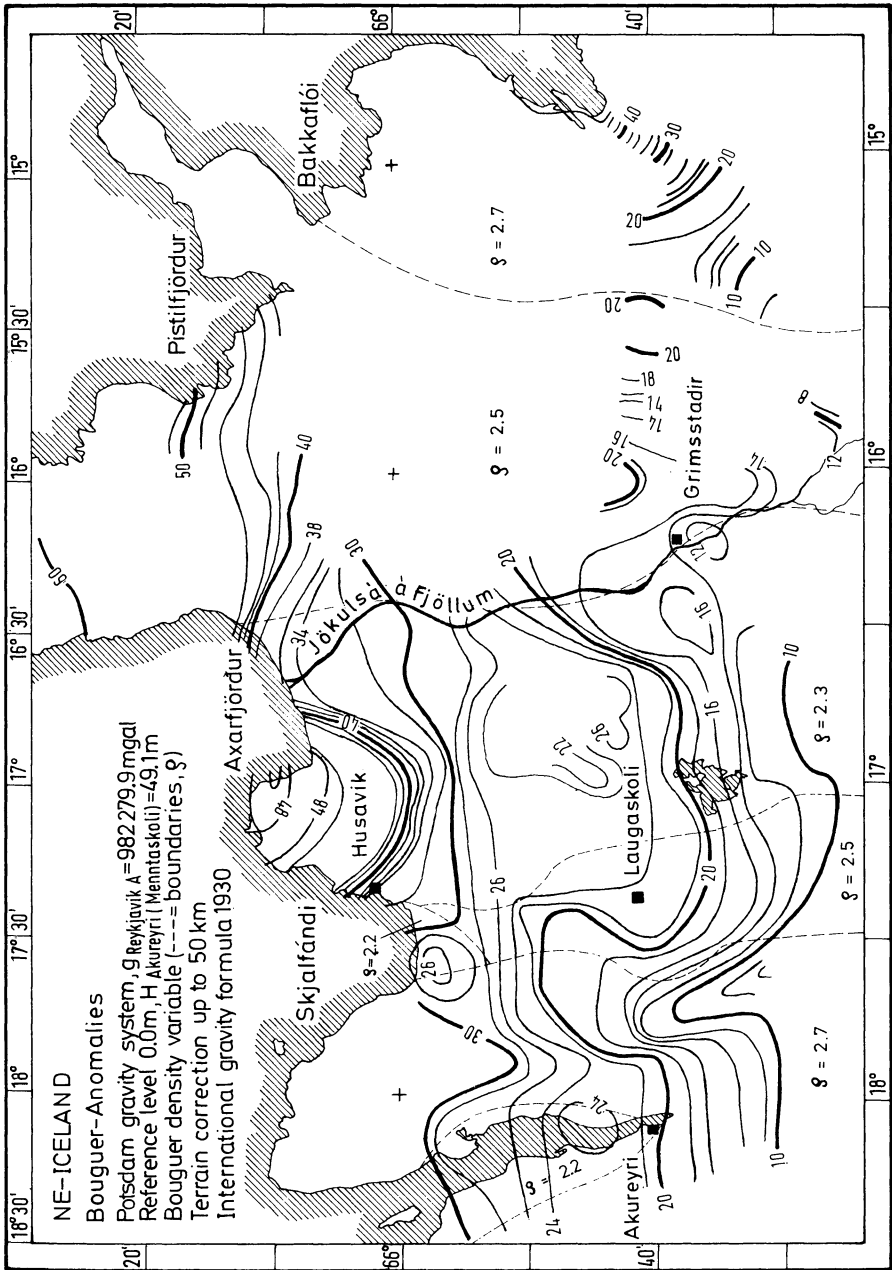


Fig. 6. Bouguer gravity anomalies, density zones

densities. The accuracy of the Bouguer anomalies derived is about $\pm 1 \text{ mgal}$. While rock densities show a rather large scattering, Bouguer densities may be comprehended to density zones. The Bouguer gravity field is characterized by the well-known decrease towards the island's centre, superposed by some smaller

structures of a few mgal amplitude which are partly correlated with the young volcanic zone.

The results of this survey especially give a detailed picture of the gravity field along the western and the central part of the monumented gravity profile Akureyri-Grimsstadir-Hof, established for investigations of gravity variations with time. These results contribute with some details to the gravity map of Iceland, based on a regional gravity survey with about 10 km average point spacing, which started in 1968 by the National Energy Authority, Reykjavik (Pálmason *et al.*, 1973). As one of the seismic refraction profiles measured by Pálmason (1967) crosses the region of the gravity survey, the results may be used for combined investigations about the crustal structure. Finally, regional type calculations in gravimetric geodesy could be supported by the observed data.

Acknowledgments. For valuable assistance the authors especially thank Dr. Gudmundur Pálmason, Reykjavik (National Energy Authority) and Landmaelingar Islands, Reykjavik (Director Águst Bödvasson). Furthermore they want to thank the numerous Icelanders who supported them at the often rather hard field work.

Sincere thanks is due to the Geodetic Institute, Technical University Berlin (Prof. Dr.-Ing. K. Marzahn) for lending the LCR-gravity meter no. 85, and to Prakla-Seismos G.m.b.H., Hannover, for lending a Worden gravity meter and a Landrover. Calculations have been carried out with the CDC 73/76 of the Regional Computing Centre of Lower Saxony.

The authors are very grateful to the German Research Society, (Deutsche Forschungsgemeinschaft), which generously sponsored the investigations.

References

- Angenheister, G., Becker, H., Mohr, P.: Boden-Vermessung des erdmagnetischen Feldes (Δz) in Nord-Island längs Profilen. In: Unternehmen Erdmantel, DFG-Forschungsbericht, Kertz, W., *et al.* (eds.), 113–118. Wiesbaden: Steiner 1972
- Bachem, H.C., Ritter, B., Torge, W.: Barometrische Höhenbestimmung in Äthiopien. Allg. Verm. Nachr. **79**, 176–183, 1972
- Drewes, H.: Zur Berechnung der gravimetrischen topographischen Reduktion. Wiss. Arb. Lehrst. f. Geod., Phot. u. Kart. T.U. Hannover Nr. 56, Hannover 1974
- Einarsson, T.: A survey of gravity in Iceland. Soc. Scient. Islandica XXX, Reykjavik 1954
- Gerke, K.: Crustal movements in the Myvatn—and in the Thingvallavatn-area, both horizontal and vertical. In: Geodynamics of Iceland and the North Atlantic Area. Kristjánsson, L. (ed.), 263–275. Dordrecht-Boston: Reidel 1974
- Gerke, K., Pelzer, H.: Triangulation, Deformationsvierecke, Registrierungen (Island). In: Unternehmen Erdmantel, DFG-Forschungsbericht, Kertz, W., *et al.* (eds.), 102–106. Wiesbaden: Steiner 1972
- Goguel, J.: A universal table for the prediction of the lunarsolar correction in gravimetry (tidal gravity correction). Geophys. Prospecting Suppl. 1954
- Hospers, J.: Reinterpretation of a gravity survey in central northern Iceland. Geologie en Mijnbouw, Nw. Serie 7, 239–247, 1952
- Möller, D.: Beiträge zur barometrischen Höhenmessung. Deutsche Geod. Komm., Reihe C, Nr. 52, München 1962
- Morelli, C., Gantar, C., Honkasalo, T., McConnel, R.K., Szabo, B., Tanner, J.G., Uotila, U., Whalen, C.T.: The International gravity standardization net 1971 (IGSN 71). Assoc. Intern. de Géodésie, Publ. Spec. No. 4, Paris 1974
- Nettleton, L.L.: Determination of density for reduction of gravity observations. Geophysics **4**, 176–183 1939

- Niemczyk, O.: Spalten auf Island. Stuttgart: Wittwer 1943
- Pálmason, G.: Seismic refraction investigation of the basalt lavas in northern and eastern Iceland. *Jökull* **13**, 40–60, 1963
- Pálmason, G.: Upper crustal structure in Iceland. In: Iceland and mid-ocean ridges, *Visindafélag Íslendinga* (Soc. Scient. Islandica) XXXVIII, S. Björnsson (ed.), 67–79. Reykjavik: Leiftur 1967
- Pálmason, G.: Crustal structure of Iceland from explosion seismology. *Visindafélag Íslendinga* (Soc. Scient. Islandica) XL, Reykjavik: Leiftur 1971
- Pálmason, G., Nilsen, T.H., Thorbergsson, G.: Gravity base station network in Iceland 1968–1970. *Jökull* **23**, 70–125, 1973
- Pálmason, G., Saemundsson, K.: Iceland in relation to the Mid-Atlantic Ridge. *Ann. Rev. Earth and Plan. Sci.* **2**, 25–50, 1974
- Schleusener, A.: Nomogramme für Geländeverbesserungen von Gravimetermessungen der angewandten Geophysik. *Beitr. angew. Geophys.* **8**, 415–430, 1940
- Schleusener, A.: Die Gravimetermessungen. In: Niemczyk 124–175, 1943
- Schleusener, A.: Gravity measurements in N-Iceland between Eyjafjord and Vopnafjord. Presented at the NATO Advanced Study institute “Geodynamics of Iceland and the North Atlantic Area”, Reykjavik 1974
- Schleusener, A., Torge, W.: Investigations of secular gravity variations in Iceland. *Z. Geophys.* **37**, 679–701, 1971
- Schleusener, A., Torge, W.: Schweremessungen (Island). In: Unternehmen Erdmantel, DFG-Forschungsbericht, Kertz, W., *et al.* (eds.), 107–113. Wiesbaden: Steiner 1972
- Schleusener, A., Torge, W., Drewes, H.: Präzisionsschweremessungen in Nordostisland 1970/71. *Deutsche Geod. Komm., Reihe B*, Nr. 206, München 1974
- Spickernagel, H.: Höhenmessungen in Nord-Island. *Mitt. aus dem Markschesen*, **73**, 139–152, 1966
- Steinwachs, M.: Seismische Registrierungen (Island). In: Unternehmen Erdmantel, DFG-Forschungsbericht, Kertz, W. *et al.* (eds.), 118–119. Wiesbaden: Steiner 1972
- Thorarinsson, S., Einarsson, T., Kjartansson, G.: On the geology and geomorphology of Iceland. *Geografiska Annaler* **XLI** 135–169, 1959
- Thoroddsen, Th.: Island, Grundriß der Geographie und Geologie. *Petermanns Geogr. Mitt.* **32**, Erg. H. 152/153, 1905/1906
- Torge, W.: Großräumige Schweremessungen mit LaCoste-Romberg-Gravimetern 1964–1970. *Deutsche Geod. Komm., Reihe B*, Nr. 183, München 1971

Received June 26, 1975; Revised Version September 22, 1975

Parabolic Field Dependence of Kinks Occurring in the Logarithmic Time Plots of Viscous Magnetization*

H. Markert¹, F. Heller² and N. Steigenberger³

¹ Fachbereich Physik/Mathematik, Universität Bayreuth, Münzgasse 9, D-8580 Bayreuth
Federal Republic of Germany

² Institut für Geophysik, ETH Hönggerberg, Postfach 266, CH-8049 Zürich, Switzerland

³ Sektion Physik, Universität München, Abt. Prof. Stierstadt, Schellingstr. 4, D-8000 München 40,
Federal Republic of Germany

Abstract. Viscous magnetization of a series of quartz dolerite samples was measured in different constant magnetic fields. Starting from the demagnetized state, each curve of magnetization versus logarithm of time shows a distinct kink in the expected straight line. The kink times depend parabolically on the magnitude of the constant magnetic field in which the viscous magnetization was acquired. An attempt to interpret this result theoretically considers the viscous magnetization in these rocks to be carried essentially by multidomain grains.

Key words: Viscous magnetization — Relaxation mechanism — Magnetization process — Palaeomagnetism — Magnetostriction.

1. Introduction

During an earlier study (Heller and Markert, 1973) experiments on the time dependence of viscous magnetization (VM) were carried out in order to determine the age of the viscous component of natural remanent magnetization. Certain quartz dolerite samples taken from the Roman Wall in northern England showed a strong viscous component aligned more or less parallel to the present earth's field.

The logarithmic time plots of viscous magnetization of these samples measured in different constant magnetic fields, always displayed kinks which occurred at different times depending on the amplitude of the applied field, and which marked a sudden increase of the otherwise strictly linear viscosity rate.

For the dating problem it is essential to know which part of the viscosity slope has to be applied to give the proper viscosity constant for the age calculations. On the other hand the mechanisms causing the VM-kinks are also of general interest as they probably lead to a better understanding of the nature of viscous magnetization in rocks and the processes involved in its generation.

* Contribution Nr. 99, Institut für Geophysik, ETH Zürich.

2. Experimental Procedure, Samples and Results

The experimental device is simple and comprises a field coil, an extremely constant dc-power supply (variation $<10^{-5}$), a fluxgate gradiometer system (to measure the sample's stray field) and a recorder which is switched on automatically at the moment when the applied dc-field reaches its constant value. The measurements usually were done at room temperature. One series of measurements was performed at 6°C by using a water cooled field coil. In this case care was taken to achieve thermal equilibrium between sample and field coil.

The samples were discs of quartz dolerite, 2.5 cm in diameter and varying in thickness from 1 cm to 3 cm. They contain about 5% by volume of titanomagnetite ore grains, the visible size of which ranges from less than $5\ \mu\text{m}$ up to a few millimeters. Electron microprobe analysis showed the titanium content to amount to $x=0.5-0.6$ in the system $(1-x)\text{Fe}_3\text{O}_4 \cdot x\text{FeTiO}_4$, whereas Curie temperatures measured in air are around 550°C (for more details see Heller and Markert, 1973).

All VM-measurements started from the demagnetized state which was achieved by ac-demagnetization in maximum fields between 1 kOe and 3 kOe amplitude. Some representative curves of a great number of experimental results are collected in Fig. 1. It shows two series of logarithmic time plots of viscous magnetization of samples VRW 123 BD and VRW 106 AA at various dc-field amplitudes H_d which were raised step by step. Sample VRW 123 BD was measured at room temperature and sample VRW 106 AA at 6°C using the water cooled coil. All these VM-curves are strictly linear throughout the experimental measuring time (up to 1,200 sec) except at one point where a sudden increase of the viscosity slope is observed causing a distinct kink in the viscosity plot. These kink times depend on the field amplitude and pass through a minimum with increasing dc-field for each sample.

In Fig. 2 the kink times (plotted on a logarithmic scale) of several samples are determined as a function of the respective dc-field. Additionally the bulk coercive force of each sample is marked by an arrow. For each sample the logarithm of the kink times clearly shows an approximately parabolic field dependence. The fields at which the minimum kink times are obtained, appear to agree closely with the respective bulk coercive forces when observing VM at room temperature. At somewhat lower measuring temperatures (sample VRW 106 AA) the kink times seem to increase remarkably and the correlation between bulk coercivity (measured at room temperature) and the field which produces the minimum kink time appears to be less distinct.

3. Fundamental Theory

In 1949 Néel published a logarithmic time law for the representation of viscous magnetization (VM)

$$\Delta J = \chi_{\text{irr}} \cdot S_v \cdot (Q + \ln(t)), \quad (1)$$

where χ_{irr} denotes the irreversible susceptibility, S_v a viscosity factor, $Q = -\ln(t_0)$ a logarithmic time constant, t the time interval considered and ΔJ the viscous

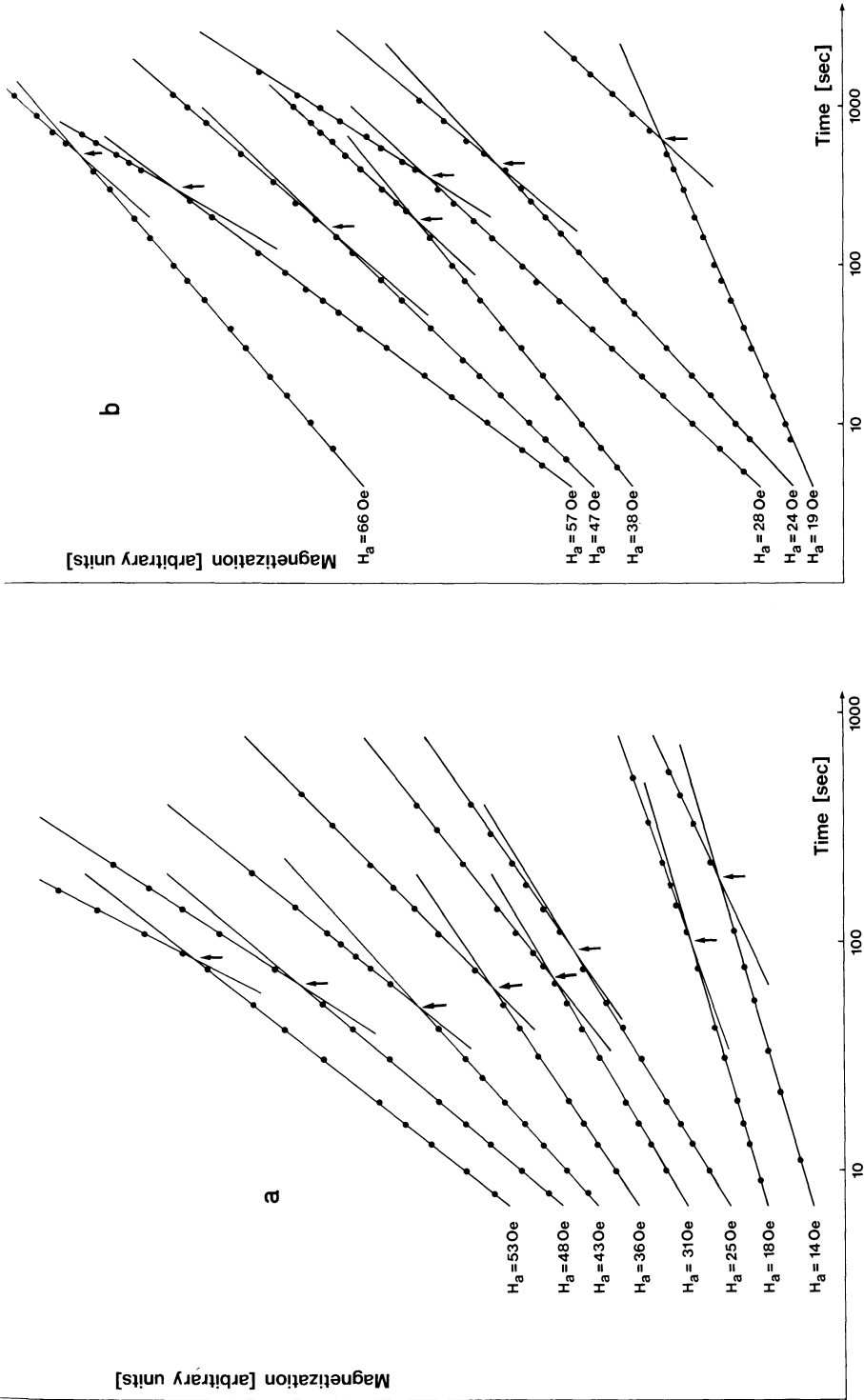


Fig. 1. Two series of logarithmic time plots of viscous magnetization of samples VRW 123BD (a) and VRW 106AA (b). The applied dc-field H_a plays the role of the series parameter. Sample VRW 123BD was measured at room temperature and sample VRW 106AA at 6° C. For better representation of their kinks all successive curves have been shifted along the magnetization axis; therefore the magnetization values of the kinks are arbitrary, whereas the systematic variation of the slopes as well as that of the kink angles is real (although given in relative units)

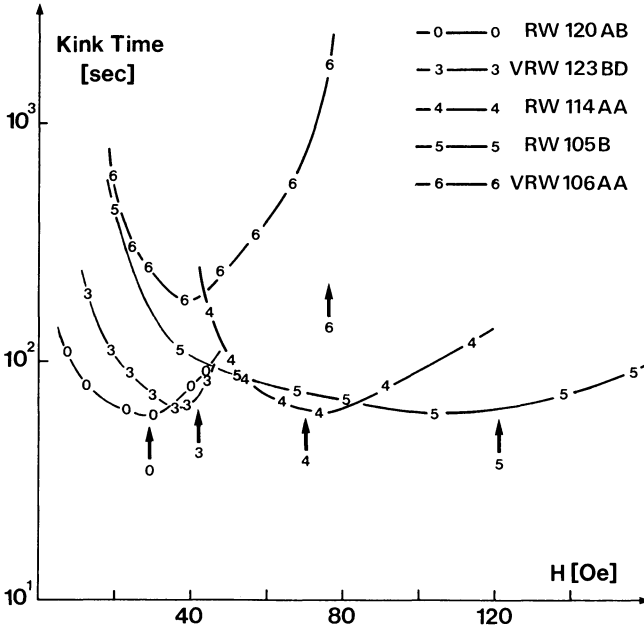


Fig. 2. Parabolic field dependence of the kink times of several samples. All samples plotted have been measured at room temperature except sample VRW 106 AA which has been measured at 6° C. The arrows mark the bulk coercive force of the samples

magnetization caused by thermally activated internal field fluctuations of amplitude

$$H_f = S_v \cdot (Q + \ln(t)). \quad (2)$$

This simple relationship has turned out to be very successful as a quantitative first order approximation of the description of magnetic viscosity phenomena.

Nearly simultaneously a more general formula was proposed by Street and Woolley (1949a):

$$dJ/dt = (\bar{i} \cdot p \cdot k \cdot T/t) \cdot (\exp(-\lambda_0 \cdot t) - \exp(-C \cdot t)). \quad (3)$$

In this expression the symbol \bar{i} represents the average amount contributed to the magnetization in the direction of the applied field by activation of one magnetic domain. The factor p gives the value of the distribution function f of the magnetic domains involved in the magnetization process. f is assumed to be independent of the activation energy E ; k denotes the Boltzmann's constant, T the absolute temperature, C a frequency constant, and λ_0 a frequency defined by

$$\lambda_0 = C \cdot \exp(-E_0/k \cdot T), \quad (4)$$

with E_0 being the upper limit of activation energies.

The general solution of Eq. (3) is of the form illustrated in Fig. 3 by an example of Street and Woolley. Two important approximate solutions within certain time intervals are:

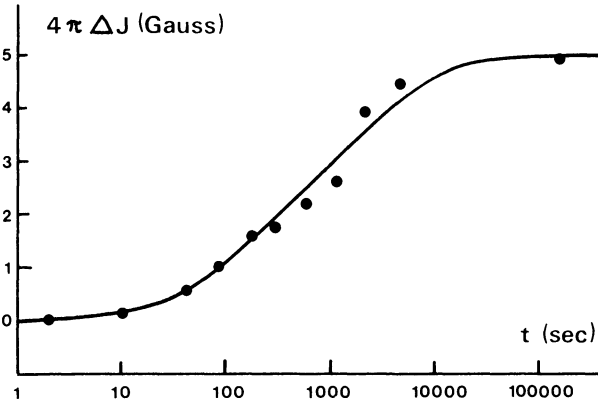


Fig. 3. Magnetic viscosity in Mn-Zn ferrite according to Street and Woolley (1949b). The full line is calculated from Eq. (3), the experimental points are obtained by Snoek (1947)

1. a logarithmic relationship

$$\Delta J = \bar{i} \cdot p \cdot k \cdot T \cdot \ln(t) + \text{const.} \quad (5)$$

which follows from Eq. (3) after integration with respect to t :

$$dJ = (\bar{i} \cdot p \cdot k \cdot T) \cdot \int t^{-1} \cdot \{\exp(-\lambda_0 \cdot t) - \exp(-C \cdot t)\} dt, \quad (5a)$$

if two additional conditions are fulfilled:

$$\int_{t_c}^{\infty} t^{-1} \cdot \exp(-C \cdot t_0) dt \ll \int_{t_c}^{\infty} t^{-1} \cdot \exp(-\lambda_0 \cdot t_0) dt \quad (6a)$$

and

$$\lambda_0 \cdot t_0 \ll 1 \quad (6b)$$

with

$$t_c < t < t_0 \quad (6c)$$

marking the interval of validity of Eq. (5).

2. a linear expression of type

$$\Delta J = \bar{i} \cdot p \cdot k \cdot T \cdot (C \cdot t) + \text{const.}, \quad (7)$$

which yields a good approximation, if

$$\lambda_0 \cdot t \ll C \cdot t \ll 1, \quad (8)$$

and if therefore $\{\exp(-\lambda_0 \cdot t) - \exp(-C \cdot t)\}$ can be estimated to result in

$$\{\exp(-\lambda_0 \cdot t) - \exp(-C \cdot t)\} \approx \{1 - \exp(-C \cdot t)\} \approx C \cdot t \ll 1. \quad (8a)$$

In other words: in its very beginning the theoretical curve of Fig. 3 can be idealized linearly using Eq. (7), whereas the following steeper part may be described

logarithmically in terms of Eq. (5). As actual experiments usually take place within the above limited time interval $t_c < t < t_0$, it does not matter in practice whether to apply Néel's or Street and Woolley's law.

4. Discussion

At first one might try to interpret the above results in terms of Eq. (3) assuming the low-time flexure of its graphic representation (cf. Fig. 1) to be rather sharp and to give the kinks observed in the logarithmic time plots of our measurements. If this were true, according to Eqs. (5) to (8) the logarithmic time plots of VM should obey a linear time law throughout the time range $0 \leq t \ll t_c$. But in our experiments we find a strictly logarithmic time dependence of VM below as well as above the kink times observed. Therefore Eq. (3) does not fit our experimental evidence.

We think that the phenomena observed in our studies can only be described by superposition of more than one independent logarithmic relaxation mechanism. Obviously a second relaxation mechanism is starting with its "logarithmically linear" phase just after a certain expectation time t_c (see Eq. 6c) which may be equivalent to the kink time occurring in the above shown time plots.

a) *Single or Multidomain VM.* Before asking for the nature of these mechanisms and their field dependence, we should find an answer to the question whether single- or multi-domain grains cause the observed after-effects in our samples. We therefore should find experimental criteria which indicate either multidomain or single domain behaviour of their viscous magnetization.

The application of a test which was described by Johnson *et al.* (1975), unfortunately yields ambiguous results, as shown in Fig. 4. This test is used to identify single- or multidomain grains as carriers of remanent magnetization from the stability of IRM and ARM, against alternating demagnetizing fields. The stability trend of ARM produced by different constant fields contradicts the stability comparison between ARM and IRM. For single-domain grains IRM should be less stable than ARM generated in different low constant fields, whereas the ARM stability itself should decrease with increasing dc-field. For multidomain grains the opposite behaviour should hold true. The contradiction shown in Fig. 4 possibly indicates a mixture of single-domain (pseudosingle domain?) and multidomain grains and makes a strong contribution to anhysteretic and isothermal magnetization processes by multidomain particles probable.

Another test which, especially from viscous magnetization processes, may distinguish between single- and multidomain grains, was suggested by Pfrenger (1966). This test might be more helpful to our problem than the previous method, because it is related to the viscosity effects themselves.

Pfrenger has shown theoretically that the viscosity factor of single-domain particles *decreases* with increasing applied constant field. Denoting ϕ as the average angle between the direction of spontaneous magnetization (J_s) of non-interacting grains and the applied field, then $\overline{\cos \phi}$ increases with increasing field and S_v

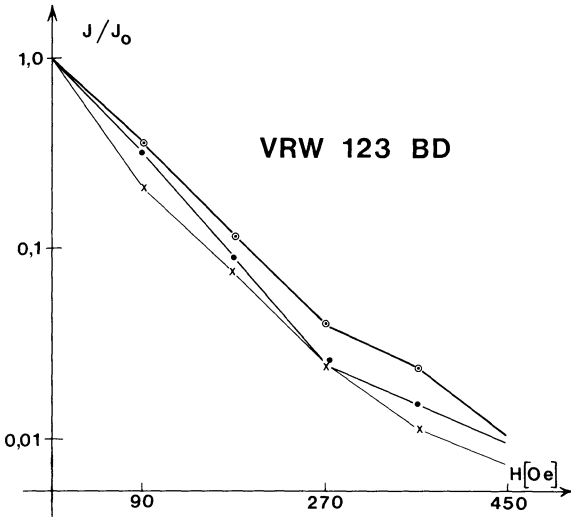


Fig. 4. Test for single domain or multidomain behaviour of sample VRW 123BD using the method described by Johnson *et al.* (1975). ARM given by 0.3 Oe (indicated by dots) respectively 3 Oe (indicated by encircled dots) constant field, shows contradictory stability trend compared to the ARM/IRM stability ratio. IRM is indicated by crosses

decreases according to

$$S_v = \frac{k \cdot T}{J_s \cdot \bar{v} \cdot \cos \phi}, \quad (9)$$

where k denotes Boltzmann's constant, T the absolute temperature, and \bar{v} the average particle volume of the particles participating.

When dealing with multidomain grains, however, S_v will *increase* with increasing applied constant field. At very low fields only displacements of domain walls with favorable orientation (ψ) to the field ($\sin \psi \cong 1$) are expected to cause magnetic aftereffects, whereas with increasing field domain walls whose normals lie close to the field direction ($\sin \psi \cong 0$), are displaced, too. Therefore we get according to Pfrenger

$$S_v = \frac{k \cdot T}{J_s \cdot \sin \psi} \cdot \frac{1}{w}, \quad (10)$$

where w is a factor which mainly depends on the total volume of the wall.

Fig. 5 shows the field dependence of S_v for one of our samples. Both viscosity factors, S_{v_1} denoting the factor before the respective kink is occurring and S_{v_2} the factor after it, increase almost linearly within the error limits with increasing field. Therefore it is suggested according to the theory mentioned above, that the viscous part of magnetization is carried by multidomain grains.

There are other theoretical reasons, too, which oppose an interpretation of our experimental data by assuming single-domain grains as the main carriers of VM. According to Kneller (1966), the relaxation time τ_{H_a} of field dependent

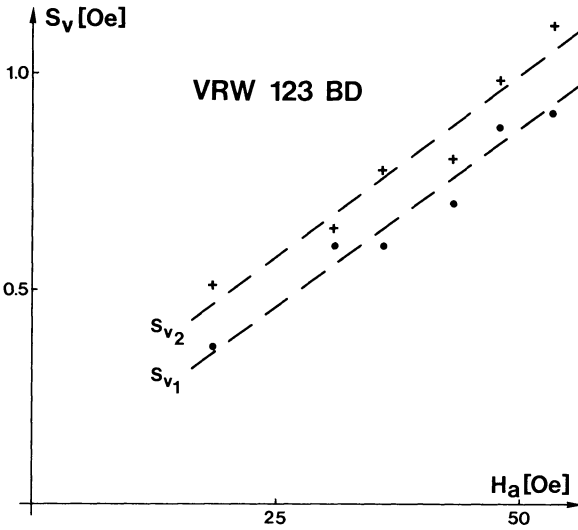


Fig. 5. Field dependence of the viscosity factors S_{v_1} (before kink) and S_{v_2} (after kink). Both factors increase with increasing constant field, thus according to Pfrenger (1966) indicating multidomain particles as carriers of VM

magnetization processes of non-interacting single domain particles can be described by

$$\tau_{H_a}^{-1} = 2 \cdot f_{H_a} \cdot \exp \left\{ -\frac{V \cdot J_s}{2 \cdot kT} \cdot H_k \cdot (1 + H_a^2/H_k^2) \right\} \cdot \cosh \left(\frac{V \cdot J_s}{k \cdot T} \cdot H_a \right), \quad (11)$$

where V is the particle volume, H_k the anisotropy field which equals the coercivity H_c , and H_a the applied constant field. f_{H_a} is a frequency factor depending on both, H_k and H_a . It approaches zero for $H_a = H_k$. In other words: τ_{H_a} is found to have a singularity for $H_a = H_c$. Therefore in rocks which contain mainly single domain grains covering a certain coercivity spectrum range, it is expected that the kink times of logarithmic VM-plots reach a maximum value at a field which is in the range of the bulk coercivity.

Our observations display just the opposite features and are not compatible with single domain carriers. We suppose from this evidence and from the above shown field dependence of S_v that the viscous magnetization of the quartz dolerite samples investigated is carried mainly by multidomain grains.

b) *Multidomain Interpretation.* For the interpretation of the curves given in Figs. 1 and 2, we first would like to confine the discussion to field strengths $H_a < H_c$, with H_c denoting the bulk coercivity. As we have to deal mainly with multidomain grains, it should be possible to understand the occurrence of the kink times and their field dependence in terms of a magnetization theory which has been proposed by Markert (1970). It is shown by this theory that two irreversible relaxation mechanisms may contribute to viscous magnetization and hysteresis losses of single-slip deformed nickel single crystals, and also of magnetite and titanomagnetite multidomain ore grains.

The first mechanism is based on repulsive interaction forces acting between a 180° -domain wall and suitably oriented dislocations. Such a 180° -domain wall, moving towards a hindering dislocation barrier under the influence of an external field, can push and shift the barrier in front of it across a distance d after a certain expectation time t_{e_1} (which corresponds to a first t_c in the sense of Eq. (6c)), until the dislocations will link again with other lattice defects. The coupled motion of such an interacting system represents an irreversible relaxation process which is generated with the assistance of thermal fluctuations.

The second relaxation mechanism is the well known Barkhausen effect which prominently sets in after an expectation time t_{e_2} (which is equivalent to a t_{c_2}) as soon as the sum of the external field H_a and an internal fluctuation field H_i reaches a critical value just high enough to enable even the representative ones among all of the 180° -domain walls to jump over their hindering dislocation barriers, i.e. if $(H_a + H_i)$ just equals the coercivity H_c .

It was intimated by Markert (1970) that t_{e_1} , the expectation time of the first mechanism, is far too small to be actually observed in our experiments. This is in agreement with our results, because otherwise we should find another low-time kink on the logarithmic time plots.

On the other hand t_{e_2} decreases rapidly with increasing H_a . Therefore throughout the range $H_a \leq H_c$ we can explain the decrease of kink time with increasing applied field, by the second mechanism, but this model cannot explain how magnetic dc-fields greater than H_a can cause increasing expectation times of a relaxation process to set in. Thus a third relaxation mechanism has to be introduced, the activation energy of which increases with increasing applied field. We would like to suggest the following mechanism as a third possible process.

In ferrite single crystals, particularly in natural titanomagnetites a great density of point defects such as lattice defects, interstitials and impurity atoms is found. Because of their magnetostrictive lattice deformation the domain walls are among the energetically most favourable places for point defects which therefore show a tendency to diffuse into the domain walls and to damp their mobility. An analogous mechanism is applicable to dislocations. According to our above considerations the domain walls can shift suitable primary dislocations in front of them (first relaxation mechanism). But there are two damping mechanisms for the domain walls: first a direct damping by means of diffusing point defects (after-effect of Richter type) and second an indirect damping caused by point defects which move towards the dislocations lowering their mobility. Among these point defects anisotropic configurations like "dipoles" or pairs of interstitials are of particular interest because of the fact that their interaction with dislocations and domain walls depends on the mutual orientation between dipole axes, dislocations and domain walls.

The dipoles for instance may vary their orientation due to exchanges of places. But the activation energy of these exchange processes increases exponentially with increasing volume magnetostriction, i.e. with increasing magnetic dc-field, if the volume magnetostriction is positive, and with the square of increasing magnetization. Thus exchanges of places causing an additional mobility of dislocations and domain walls can set in after an expectation time t_{e_3} which increases with increasing applied field.

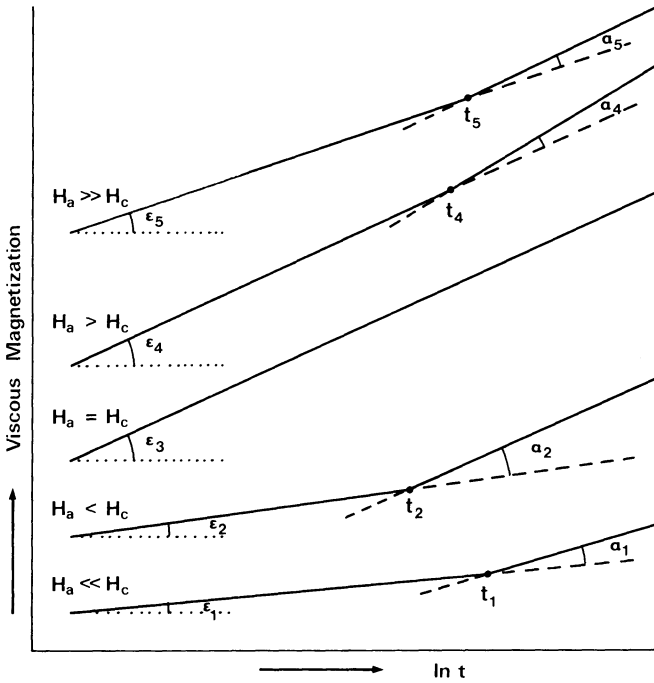


Fig. 6. Schematic diagram of field dependent kink times, kink angles and slopes of the logarithmic time plots of viscous magnetization to be expected due to the model of relaxation mechanisms suggested in points 1 to 3 of the discussion. Angles α_i and ϵ_i are assumed to obey the following rules: $\alpha_1 < \alpha_2$ and $\epsilon_1 < \epsilon_2$ according to point 1, $\epsilon_4 = \epsilon_3 = \alpha_2 + \epsilon_2$ according to points 1 and 2, $\alpha_4 \cong \alpha_5$ and $\epsilon_5 < \epsilon_4$ according to points 1 and 3

If the above interpretation is true, then in an idealized case we should find the following three types of logarithmic time plots of VM which schematically are illustrated in Fig. 6:

1. If the dc-field ranges in the interval $0 < H_a < H_c$, the kinks mark the change from the logarithmic phase of relaxation mechanism one to the superposition of the logarithmic phases of relaxation mechanisms one and two (Barkhausen effect). The slope below the kink in a given time plot of viscous magnetization therefore characterizes the first relaxation process and its viscosity constant. Above the kink the new slope is a measure of the total viscosity constant of both relaxation processes. As the Barkhausen mechanism prominently sets in at about $0.6 \cdot H_c$ and increases to a maximum at $H_a \cong H_c$, the total viscosity after the kink should increase with increasing H_a , whereas at the same time the kink time decreases towards zero.

2. At $H_a = H_c$ the Barkhausen effect and also the total viscosity are passing through a maximum. Both kink times t_{e_1} and t_{e_2} approach zero.

3. For $H_a > H_c$ the Barkhausen effect starts to decrease and the viscosity constant S_v below the kink point also may show a tendency to decrease with

increasing H_a . As only the expectation time but not the intensity of the logarithmic phase of the third relaxation mechanism was shown to depend on the volume magnetostriction, the additional contribution to the viscosity due to the third relaxation process after the kink point should turn out to be more or less constant, i.e. with increasing H_a the kink angle α (Fig. 6) should not change.

c) *Alternative Interpretation.* The interpretation given above fits our data, but we are aware that there are possibly alternative or modifying models which also might be able to explain the parabolic field dependence of the kink times. For instance, we might think of a mixture of single and multidomain grains – perhaps caused by oxidation. Kinks have been observed in those rocks by Creer, Petherbridge and Petersen (1970). These authors, however, did not find straight forward relations between the oxidation state and the development of kinks, and we cannot see how such a mixture would display the kink time characteristics we have observed in our rocks.

d) *Application.* Regarding the age dating problem mentioned in paragraph 1 and relying on the evidence stated by Figs. 1 and 2, it seems to be clear that a dating method like that one used by Heller and Markert (1973) has to use the gradient of the viscosity slope which is observed before the kink point as the appropriate viscosity constant S_v , because of the low magnitude of the earth's magnetic field. From Figs. 1 and 2 it is evident that in very low fields the kinks are expected to happen only after very long expectation times. This is in coincidence with measurements done by Kent and Lowrie (1974) on fine-grained deep sea sediments in a 1 Oe field over as much as 1,000 h. These authors did not find any kinks during their observations concerned with the increase of remanent magnetism with time.

Acknowledgements. We thank Prof. Dr. K.M. Creer for inviting us to work in the Geophysics Department of the University of Newcastle upon Tyne. Our thanks are also due to Prof. Dr. K. Stierstadt (Sektion Physik, University of Munich) for helpful support in experimental device. Valuable criticism by Prof. Dr. W. Lowrie on the manuscript is gratefully acknowledged.

References

- Creer, K.M., Petersen, N., Petherbridge, J.: Partial selfreversal of remanent magnetization and anisotropy of viscous magnetization in basalts. *Geophys. J.* **21**, 471–483, 1970
- Heller, F., Markert, H.: The age of viscous remanent magnetization of Hadrian's Wall (Northern England). *Geophys. J.* **31**, 395–406, 1973
- Johnson, H. P., Lowrie, W., Kent, D. V.: Stability of anhysteretic remanent magnetization in fine and coarse magnetite and maghemite particles. *Geophys. J.* **41**, 1–10, 1975
- Kent, D. V., Lowrie, W.: Origin of magnetic instability in sediment cores from the central North Pacific. *J. Geophys. Res.* **79**, 2987–3000, 1974
- Kneller, E.: Theorie der Magnetisierungskurve kleiner Kristalle. In: *Handbuch der Physik*, **18** (2), 438–544. Berlin-Heidelberg-New York: Springer 1966
- Markert, H.: Über den Ultraschalleinfluß auf den Barkhauseneffekt sowie über die Notwendigkeit und den Entwurf einer neuen Modellvorstellung zum Magnetisierungsablauf in verformtem Nickel – basierend auf der Wechselwirkung der segmentweise gewölbten 180°-Blochwände mit relaxationsartig-irreversibel verschiebbaren Versetzungsanordnungen. *Diss. Nat. Fak. Univ. München*, 1970

- Neel, L.: Théorie du trainage magnétique des ferromagnétiques en grains fins avec applications aux terres cuites. *Ann. Géophys.* **5**, 99–136, 1949
- Pfrenger, E.: Untersuchungen über die thermische magnetische Nachwirkung. Diss. Nat. Fak. Univ. München, 1966
- Snoek, J. L.: *New development in ferromagnetic materials*, p. 55. Amsterdam: Elsevier 1947
- Street, R., Wolley, J. C.: A study of magnetic viscosity. *Proc. Phys. Soc. A* **62**, 562–572, 1949a
- Street, R., Wolley, J. C.: Magnetic viscosity in Mn–Zn ferrite. *Proc. Phys. Soc. A* **62**, 743–745, 1949b

Received September 17, 1975; Revised Version December 5, 1975

Postulated Rotation of Corsica not Confirmed by New Palaeomagnetic Data

K.M. Storetvedt and N. Petersen

Department of Geophysics, University of Bergen, Allégt. 70, N-5014 Bergen, Norway and
Institut für Angewandte Geophysik, Universität München,
Theresienstraße 41, D-8000 München, Federal Republic of Germany

Abstract. Magneto-mineralogical studies of Corsican rhyolitic/andesitic rocks of late Carboniferous-Permian age have revealed an extensive low temperature (weathering) alteration of the primary oxides. In line with this observation analysis of the palaeomagnetic record suggests that at least a substantial part of the “stable” remanence is of chemical origin, probably dating back to the early Tertiary when the West Mediterranean region was subjected to marked uplift and erosion. The relatively stable bulk remanence is composite, constituting both normal and reverse components of magnetization. However, careful demagnetization does not support previous suggestions (based on the same rock formations) of a stable component of magnetization with south-southeasterly declination. Therefore, the idea of a certain anti-clockwise rotation of Corsica, detectable by palaeomagnetic means, does not seem to have a firm basis.

Key words: Palaeomagnetism — Rock magnetism — Possible rotation of Corsica.

1. Introduction

The origin of small ocean basins like those of the West Mediterranean have been a matter of speculation among earth scientists for a long time. Such basins which to a large extent seem to be located between the compressional boundaries of larger crustal blocks may have developed through two entirely different processes: a) by subsidence of previous continental areas (Klemme, 1958; Van Bemmelen, 1969) which subsequently have been turned into a “transitional” type of crust (Menard, 1967) through vertical assimilation by the upper mantle, or b) by crustal separation through the mechanism of sea floor spreading (Vogt *et al.*, 1971; Le Pichon *et al.*, 1971). Theoretically, these mechanisms seem equally plausible and they may both have taken part in the development of at least some of the smaller ocean basins.

Table 1. Rock collection details

Site no.	Sample nos.	Locality	Rock type	Strike and dip	Other remarks
1	1-3	Col de Palmarella	rhyolite dike		
2	4-6	Near Col de Palamarella	rhyolite flow	uncertain	
3	7-10	The rhyolite dikes, site 1	rhyolite dike	The rhyolite dikes are about vertical and there is no information about any post-emplacement tilting	
4	11-14	and 3-8, have been collected along road N 199 from			
5	15-17	Col de Palmarella to			
6	18-20	Cöl de la Croix			
7	21-25				
8	26-30				
9	31-36	Sites 9-12 collected west/southwest of	andesite flow	160°, 30°W	
10	37-40	Osani village		uncertain	
11	41			uncertain	
12	42-44			035°, 27°NW	
13	45-49	On the footpath from Col de la Croix to Tuara	rhyolite dike		
14	50-51	Near Col de Palmarella	rhyolite flow		

As an apparent strong support of a sea floor spreading origin of the Western Mediterranean palaeomagnetic data have suggested anticlockwise rotations of Corsica/Sardinia and of Italy (Nairn and Westphal, 1968; Zijdeveld *et al.*, 1970; Soffel, 1974) in the manner predicted by Carey (1958). It has been noted, however, (Storetvedt, 1970) that many of these results exhibit abnormal smeared distributions in the direction of declination suggesting that there may be something wrong with the fundamentals upon which the rotational estimates have been based. In order to look into this problem some Permo-Carboniferous rocks from NW-Corsica have been re-investigated. The considered rocks which are andesitic/rhyolitic lavas and rhyolitic dikes are those previously studied by Nairn and Westphal (1968) and it is referred to that contribution for a general account of the regional geology. Details of the new rock collection which comprises 51 hand samples, collected by application of standard geological orientation procedures, are given in Table 1.

2. Magnetic Mineralogy

Rhyolites. The original oxide mineralogy generally found in rhyolitic rocks is magnetite (with low Ti content) in coexistence with haemoilmenites (15-50 mol % haematite), but the Corsican rhyolites only occasionally show relics of such phases (in some grains), in general there are no identifiable traces of the supposed primary components. Some grains, for example in sample Co 50 (Fig. 1), show signs of high temperature oxidation by lamellae formation, but this structure is completely overprinted by subsequent disintegration. Microscopic analysis suggests that haematite and goethite (α -FeOOH) constitute the predominant iron oxide mineralogy present, an observation which fits in with the generally reddish colour of these rocks. Rutile may be present as another

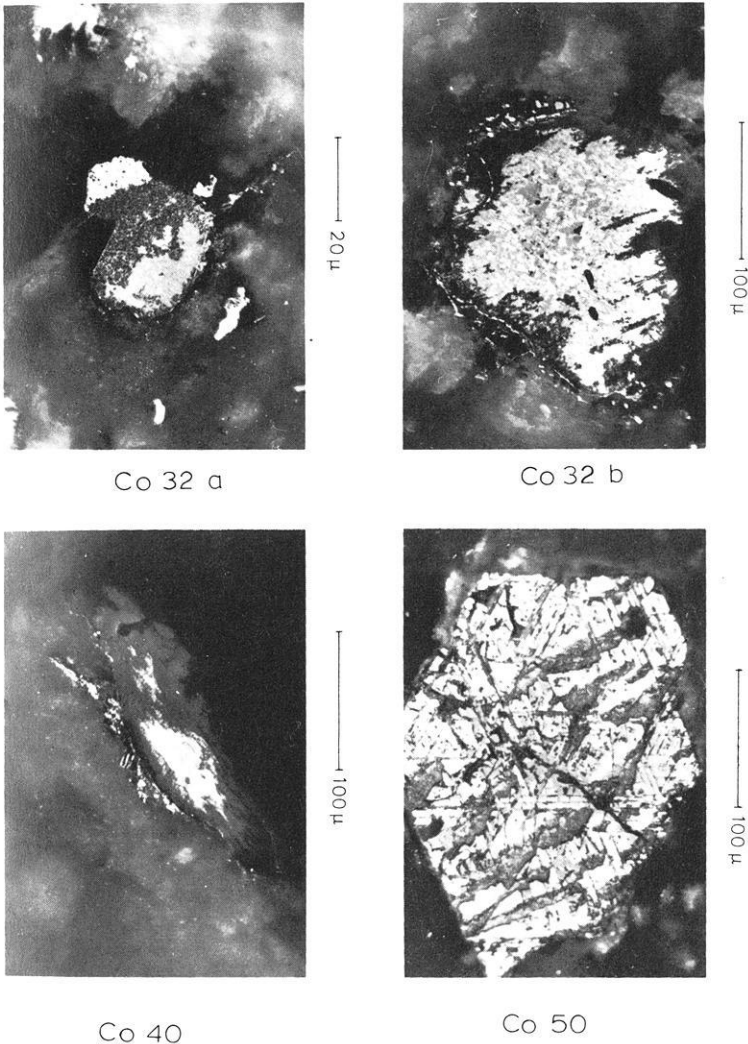


Fig. 1. Microphotographs showing typical examples of mineral disintegration in Corsican volcanics. Co 32: (a) The larger part of the ore grain has been transformed by granulation (dark grey), consisting of a very intimate mixture of presumably haematite, rutile, perovskite and/or sphene. (b) Complete transformation of the titanomagnetite grain into mainly haematite (light grey) and rutil (medium grey). Granulation of the marginal parts of the ore grain (dark grey). Co 40: Almost complete disintegration of an ore grain. Co 50: Original titanomagnetite grain with exsolution lamellae of probably ilmenite (indicating high temperature deuteric oxidation) have been replaced by an assemblage of haematite and rutil (pseudomorphism after magnetite and ilmenite)

alteration product. The microscopic evidence is in part confirmed by measurements of saturation magnetization versus temperature ($J_s - T$). The presence of magnetite (Curie temperature 580 °C) may be suggested in 2 or 3 specimens (cf. Co 50, Fig. 2) but on a whole the high field magnetization decays steadily to zero at temperatures of around 650 °C or more (cf. Co 26, Fig. 2). Another

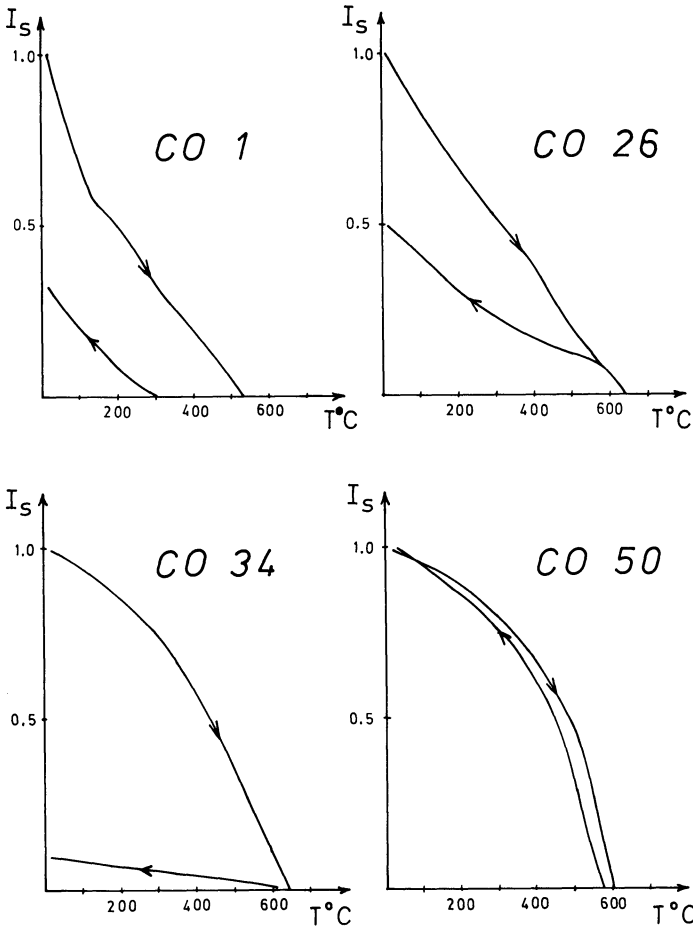


Fig. 2. Representative selection of strong field (4–6 kG) magnetization versus temperature during heating and subsequent cooling

pronounced feature of the J_s-T measurements is the generally strong irreversibility between heating and cooling curves. In general, the magnetization is considerably lower after heating than before heating and in some cases this behaviour is associated with a pronounced lowering of the “Curie point” (cf. Co 1, Fig. 2). Some of these results may be interpreted in terms of a maghaemite/haematite transformation.

Andesites. Similarly as for the rhyolites the primary oxide mineralogy is severely altered—only some small relics of the assumed original phases (titanomagnetite with 30–40 mol% ulvospinel, in coexistence with haemoilmenite) are still present. With very few exceptions the Fe-Ti oxides have been transformed into a mixture of haematite and rutile. In several respects the situation resembles that one encountered in a previous study by the present authors (Storetvedt and Petersen, 1970) involving a practically complete alteration of the magnetite host as well

as the exsolved lamellas (Ti-rich) into haematite and rutile. However, in the present case the disintegration has sometimes proceeded further, producing perowskite and/or sphene. The J_s - T measurements of the andesites are very similar to those of the rhyolites.

On a whole, the original Fe-Ti oxide mineralogy of the Corsican rhyolitic/andesitic rocks undoubtedly has suffered an extensive alteration. Low temperature oxidation probably as a result of weathering and/or moderate reheating, is the dominating form of alteration. Unless these processes took place over a short interval of time or while the geomagnetic field had a constant direction (for example in Kiaman time) these alterations are likely to have imposed a complex build-up of the palaeomagnetic record.

3. The Palaeomagnetic Record

About one hundred specimens were treated by progressive thermal or alternating field analysis, the remanence parameters after each demagnetization step being measured on various astatic magnetometers. In agreement with the previous study (Nairn and Westphal, 1968) the NRM intensity varied widely—from approximately $5 \cdot 10^{-3}$ emu/cm³ to $1 \cdot 10^{-6}$ emu/cm³. No general difference in the total remanence properties between lavas and dikes was found but except for one site (no. 13) the intensity of magnetization of the dikes proved to be less resistant against demagnetization than that of the lavas. The relatively large component of low-stability magnetization in the rhyolite dikes may account for the experimental problems found in the majority of these rocks—the underlying “stable” magnetization in general became unsatisfactorily determined due to scatter in the magnetic parameters at a certain stage of demagnetization. On the other hand, many lava specimens were successfully thermally demagnetized up to temperatures of ≥ 600 °C but stable end points were not reached in any of these rocks. The most important blocking temperature range of the lavas is between 500 °C and 550 °C but in several specimens 20–70 per cent of the natural intensity had its decay at temperatures above 600 °C. This is in line with the high oxidation state of the magnetic minerals—haematite then being a major magnetic constituent—as inferred from microscopy and J_s - T measurements. Some examples of the intensity decay pattern versus temperature are shown in Fig. 3.

As one might suggest on basis of the advanced alteration state of the primary oxides the magnetic remanence shows a fairly complex structure. On a whole the data have led us to an entirely different conclusion than that of the previous authors and it seems absolutely necessary therefore to present a fair amount of directional information. Thus, Figs. 4–7 give the direction data as a function of demagnetization of a total of 36 specimens. Effort has been made to give an adequate presentation of within-sample as well as within-site behaviour. In all the examples given, the associated remanence intensity performs a smooth variation (decay) versus increasing field or temperature. This is one of the necessary requirements if directional changes are to be evaluated in a realistic manner. Also, when the intensities initiate an irregular behaviour (at some

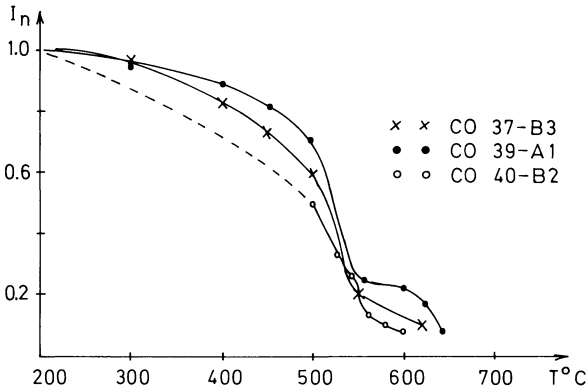


Fig. 3. Decay of remanence intensity during progressive demagnetization of Corsican lavas

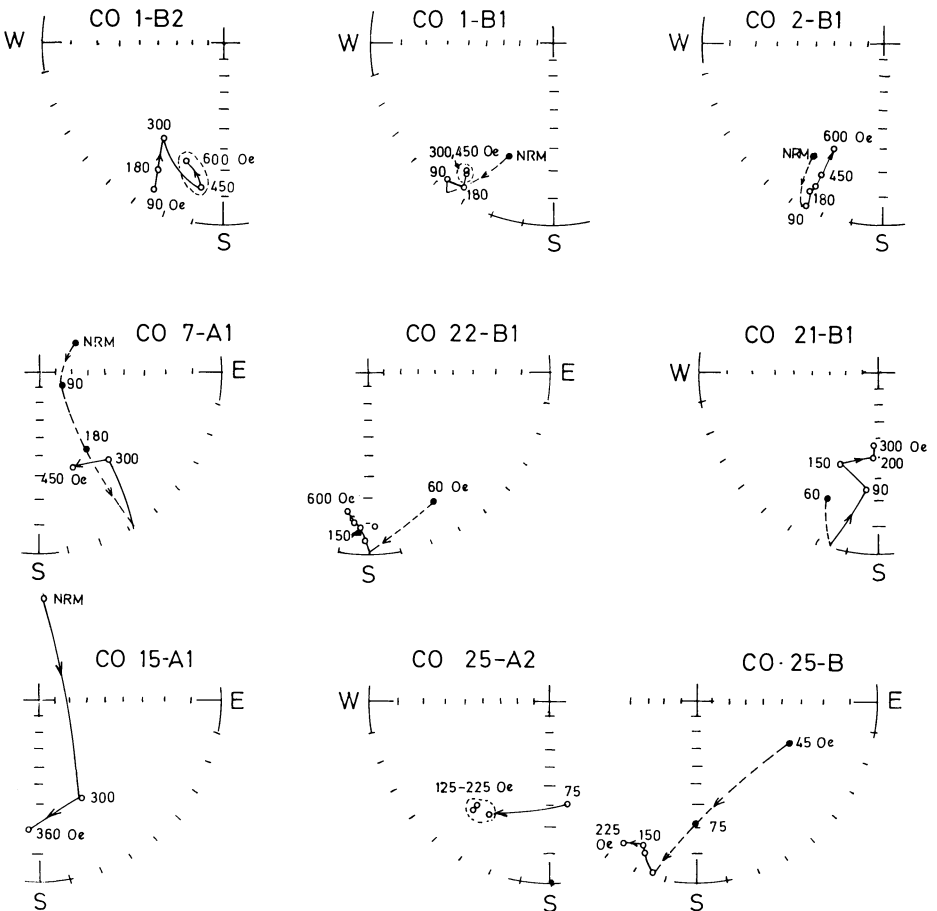


Fig. 4. Stereograms showing directional behaviour as a function of progressive demagnetization. Full circles are downward seeking magnetism while open circles represent upward pointing magnetization vectors. See text for further details

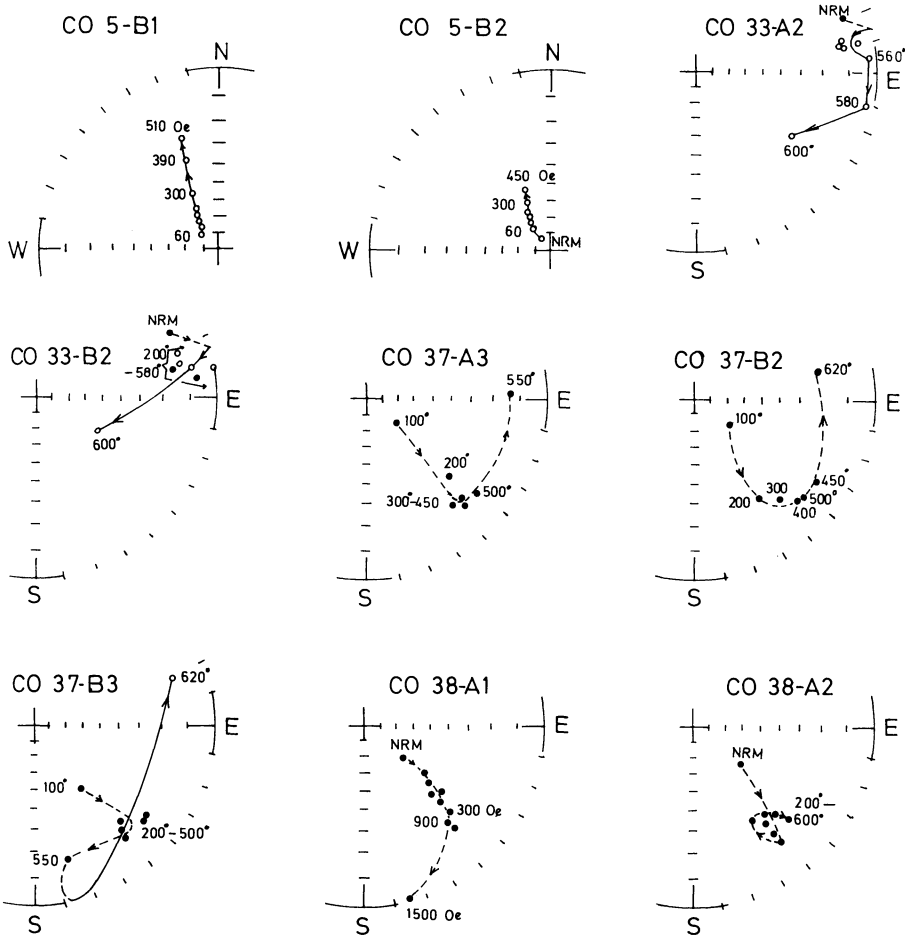


Fig. 5. Text as for Fig. 4

stage of demagnetization) the directional patterns are nearly always erratically disrupted as well. Therefore, the “erratic stage” in the analysis has not been included in the diagrams. Also, directional data associated with intensities below $5 \cdot 10^{-7}$ emu/cm³ have systematically been disregarded.

The south-easterly stable magnetization as previously claimed for Corsican rocks (Ashworth and Nairn, 1965; Nairn and Westphal, 1968) are not verified by the present study. Only one specimen, Co 30-a2, exhibits a satisfactory stable direction in the SE-quadrant (cf. Fig. 5) but the suggested stability to progressive demagnetization in this case neither agrees with that of neighbouring specimens (within the same hand sample) nor with other specimens from the same site. In fact, the general directional behaviour of the specimens of this study consists of gradual movements into or towards the NE and SW quadrants, respectively, suggesting that south-easterly directions may be purely accidental, representing resultant magnetization vectors (consisting of at least a normal and a reversed

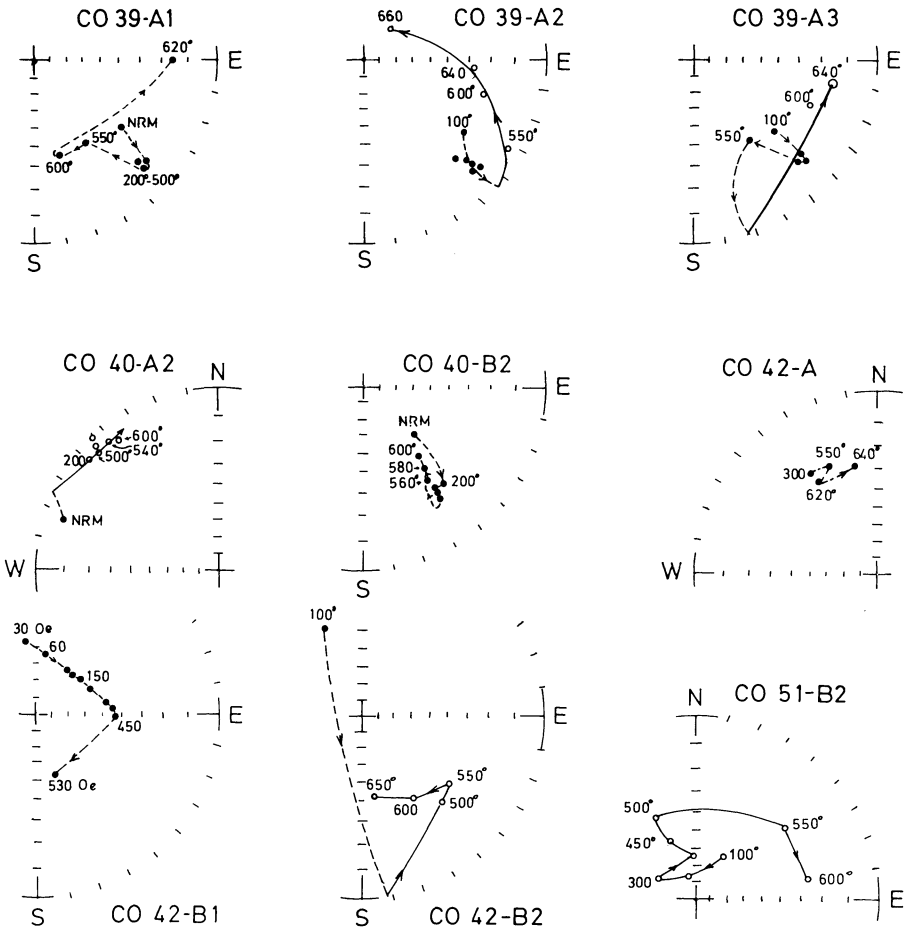


Fig. 6. Text as for Fig. 4

sub-component) having no geophysical reality. The fundamental experimental problems are that the sub-components involved in general tend to have closely similar stability spectra so that terminal directions (for one particular component) are not being achieved at the stage at which disruption of the demagnetization patterns take place. In this context, however, it is obvious that an "end-point" is not by itself a sufficient criterion that a single magnetization component has been isolated and that a field direction marker has been obtained; a composite magnetization may well exhibit high directional stability at strongly discordant and palaeomagnetically irrelevant directions (Storetvedt, 1970; Roy and Park, 1972). Thus, ancient field directions must in general be carefully evaluated through a combination of "stable points" forming one or more clustered groups, together with additional experimental data defining "areas" of directional convergence.

The total directional information from the present rocks suggests that the

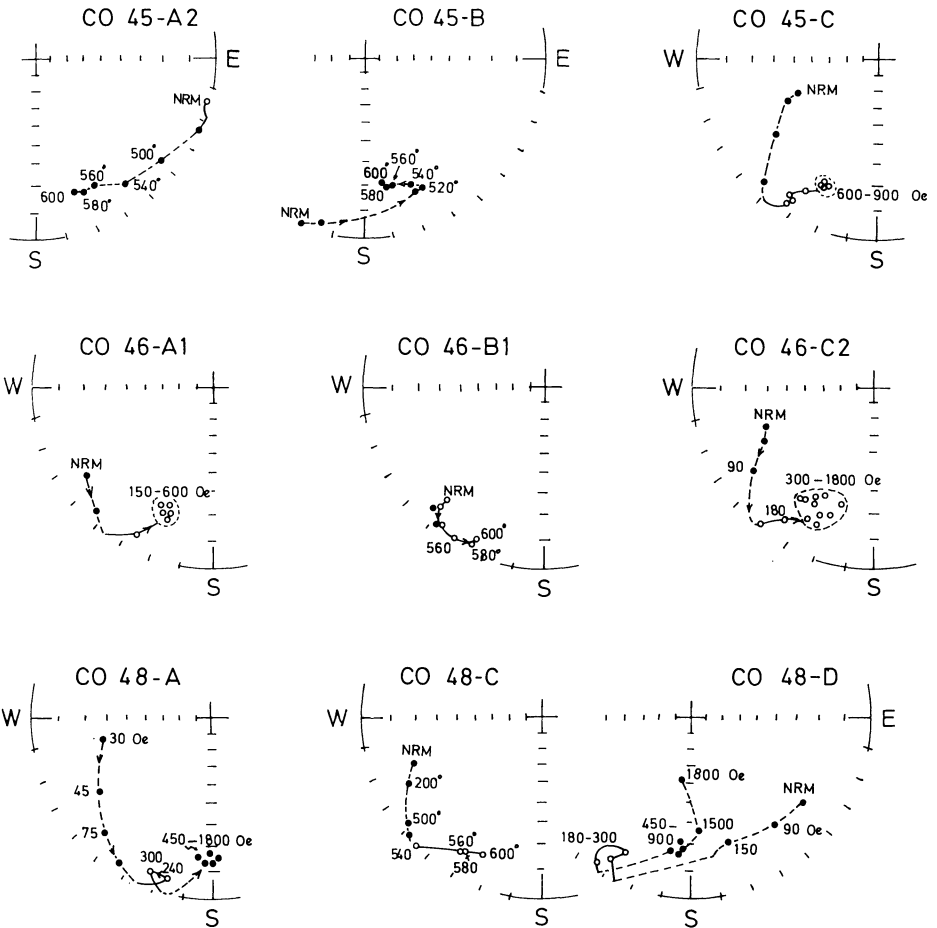


Fig. 7. Text as for Fig. 4

magnetization process (which, based on the extensive low temperature mineral alteration, is most likely chemical in this case) spanned a time interval long enough to cover one or more field inversions. The relative abundance of normal and reversed magnetism varies greatly, resulting in scattered within-sample and within-site distribution of “stable” bulk magnetization, but on a whole the reversed magnetism tends to provide the largest contribution to the resultant. It is important to recognize, however, that specimens from sample Co 50, which had the most strongly developed high temperature oxidation features of the entire collection, possessed a fairly stable northerly directed bulk magnetization ($D \sim 350^\circ$, $J \sim -60^\circ$) in complete disagreement with the relative field for the Kiaman epoch in which these rocks must have acquired their original magnetization.

The only consistent group which can be reasonably inferred from the present study has a direction striking slightly west of south and with a shallow upward

Table 2. Palaeomagnetic data from Permo/Carboniferous dikes, NW. Corsica

Specimen	N	Dec.	Inc.	R	k	α_{95}	Pole
Co 1-B1		214	-10				
Co 1-B2		192	-19				
Co25-A2		212	-18				
Co45-C		203	-18				
Co46-A1		200	-16				
Co46-B1		204	-4				
Co46-C2		204	-17				
All specimens combined	7	201.8	-14.8	6.93	86	6.5	154E, 50N
Eocene volcanics, Lisbon							
(1) tilt-corr. data							158E, 47N
(2) without tilt corr.							160E, 54N
Permian of Europe							~160E, ~42N

inclination. The seven specimens which tend to define this suggested palaeomagnetic direction are all from the rhyolite intrusives. Further details are given in Table 2. Each of these directions represents the mean of two or more demagnetization steps as having been encircled in Figs. 4 and 7. Upon demagnetization other specimens obtained directions in general agreement with the latter group, but as the terminal directions have not been confirmed in these cases the specimens concerned are not included in the paleomagnetic figure. Nevertheless, the latter information gives further support in favour of a geomagnetic reality of the shallow, upward inclined, SSW-striking magnetization. No final normal direction has been achieved.

In site no. 13 (Fig. 7) three or four specimens are showing a certain indication of a reversed direction with a downward dip of around 15–20 degrees (cf. Co 48-A). However, the results from other specimens from the same sample, for example Co 48-D, suggest that these downward pointing directions are probably not true palaeomagnetic field markers.

4. Geophysical Interpretation of the Results

Based on some floral evidence the formations concerned are thought to date back to Westphalian/Stephanian times or in part perhaps to the Permian (cf. Nairn and Westphal, 1968). However, all the observational results of this study seem to establish beyond doubt that the original TRM, if not completely, at least to a major extent, has been replaced by magnetizations of chemical origin. A fundamental question is therefore the timing of these latter components. There is very strong evidence that the geomagnetic field was consistently reversed in late Palaeozoic times: the so-called Kiaman magnetic interval seems to have existed from around 300 Ma B.P. to the end of the Permian, i.e. for about 70 Ma (McElhinny, 1969; Thompson and Mitchell, 1972). Therefore, the relatively strong normal magnetization contribution suggests that a consider-

able mineral alteration (and associated remagnetization) must have occurred in the rocks in post-Permian times. Also, Nairn and Westphal (1968) were puzzled about the relatively strong normal component, which they tentatively suggested might have become imposed sometime in the early Mesozoic, but they seem to have disregarded this important observation in their final interpretation. A question of ultimate importance is in fact to which extent also a major part of the present reversed magnetization post-dates the Permian.

At the latitudes of southern Europe the original (late Palaeozoic) field must have had an approximately zero inclination. It is well known that in tropical environment mineral changes due to surface weathering may penetrate very deeply. Owing to the long time span of the Kiaman interval (reversed) one would suggest therefore that if the considered rocks (first of all the lavas) had been subjected to "surface" conditions throughout the Permian the possibility for further surface alterations of the magnetic oxides should be extremely limited in post-Permian time. For this reason the relatively strong normal magnetization in the lavas suggests that something must have prevented a rapid oxidation of these strata in their earliest history. A clue to this problem may lie in the fact that in the Upper Palaeozoic and throughout the Mesozoic the West Mediterranean formed part of the extensive Tethyan geosyncline—it appears quite likely that Corsica was covered by sediments during an extensive length of time from Permian onwards. A sediment cover may well have provided the postulated slowing down of the oxidation processes first of all in the underlying Permo-Carboniferous lavas. It was not until the end of the Cretaceous or the beginning of the Tertiary that the Alpine folding and upheaval became of importance in the Mediterranean region (Debelmas and Lemoine, 1970). Most likely the area of Corsica participated in this uplift, becoming subsequently the site of extensive erosion and weathering. As a result of the orogenic movement (and erosion) the late Palaeozoic dikes may for the first time in their history have become exposed to surface conditions. In fact, one may suggest that oxidation processes which had been suppressed in the earlier history of the rocks advanced rather quickly during the Lower Tertiary. Because of the excessive alteration of the primary magnetic minerals any remaining Permian magnetization component in the rhyolite dikes, is probably to be associated with hydrothermal alteration during the cooling stage.

With reference to Table 2 there are only 7 specimen directions in this study for which there is reasonable laboratory evidence that palaeomagnetic directions have been obtained. As the chemical processes at ambient temperatures probably encompassed a long time span (compared with the "time constant" of the geomagnetic secular variation) it seems reasonable to suggest that the scatter of the final results is basically due to the difficulty of obtaining completely clean single-component magnetizations rather than being caused by geomagnetic secular variation. Therefore, because of the geomagnetic integration effect most likely following a chemical remanence, it is thought that at least the overall mean direction approximates to that of an ancient axial dipole field relative to Corsica. In Table 2 the estimated palaeomagnetic pole of the considered Corsican rocks is shown in conjunction with the Upper Carboniferous/Permian pole for Europe and with poles for the Lower Tertiary based on recent data from

the Lisbon volcanics (Storetvedt, 1973a). The latter information is referred to Iberia in its pre-drift position in that the rotation and displacement of this continental fragment seem to have occurred as late as early Oligocene (Storetvedt, 1972). The Lisbon data have been given both with and without tectonic correction as the magnetic history of this formation makes it difficult at present to choose adequately between the two alternatives. The relatively low palaeolatitude inferred from the Eocene Lisbon volcanics represents a revision of the early Tertiary geomagnetic dipole axis for Europe originally suggested from a study of the Antrim basalts of Northern Ireland (Løvlie *et al.*, 1972). Recent results from the Faeroe Islands (Løvlie, 1975; Løvlie and Kvingedal, 1975) have given further support for the new early Tertiary pole position. The relative Upper Palaeozoic pole is based on information from minor intrusives from Norway and England (Halvorsen, 1970, 1972; Storetvedt and Gidskehaug, 1969) as the palaeomagnetism of European lavas of Kiaman age seems to have become slightly upset by a certain Mesozoic magnetization overprint (Storetvedt, 1970; Storetvedt and Petersen, 1970). However, the Upper Carboniferous-Permian pole here accepted is very close to the overall late Palaeozoic pole for Europe as well as nearly identical to the one used by Larson and LaFountain (1970).

As one can infer from Table 2 the overall palaeomagnetic pole of the Corsican dikes are in better agreement with the suggested Lower Tertiary pole than with that of the late Palaeozoic. By also taking into account the fact that the considered rocks have a two-polarity magnetization build-up, it seems reasonable to conclude that at least the major component of "stable" remanence was impressed in post-Permian time, probably in connection with the Lower Tertiary uplift of the West Mediterranean domain.

The new evidence casts doubt about the postulated rotation of Corsica. As such a movement would most likely be of Tertiary age the present data may indicate that a rotation detectable by palaeomagnetic methods has not taken place. On the other hand, it is possible that the inferred remagnetization in the early Tertiary has obscured the palaeomagnetic evidence for a rotation which may have occurred either at the time of remagnetization (as a result of the same geodynamic processes causing uplift) or during the Mesozoic. However, based on available information it seems more reasonable to conclude at present that the crust beneath the Ligurian Sea formed through continental subsidence (and subsequent oceanization *in situ*) rather than through crustal separation by sea-floor spreading (Storetvedt, 1973b).

Acknowledgement. Parts of the work described in this paper were carried out in the Department of Geophysics of the University of Bergen, while one of us (N.P.) was invited to give a lecture course there.

The financial support by "L. Meltzers Høyskolefond" is greatly acknowledged.

References

- Ashworth, T.P., Nairn, A.E.M.: An anomalous pole from Corsica. *Palaeogeography, Palaeoclimatol., Palaeoecol.* **1**, 119–125, 1965
- Carey, S.W.: The orocline concept in geotectonics. *Proc. Roy. Soc. (Tasmania)* **89**, 255–288, 1958

- Debelmas, J., Lemoine, M.: The western Alps: Palaeogeography and structure. *Earth Sci. Rev.* **6**, 221–256, 1970
- Halvorsen, E.: Palaeomagnetism and the age of the younger diabases in the Ny-Hellesund area, South Norway. *Norsk Geol. Tidsskr.* **50**, 157–166, 1970
- Halvorsen, E.: On the palaeomagnetism of the Arendal diabases. *Norsk Geol. Tidsskr.* **52**, 217–228, 1972
- Klemme, H.D.: Regional geology of circum-Mediterranean region. *Am. Ass. Petrol. Geol.* **42**, 477–512, 1958
- Larson, E.E., LaFountain, L.: Timing of the breakup of the continents around the Atlantic as determined by palaeomagnetism. *Earth Planet. Sci. Lett.* **8**, 341–351, 1970
- Le Pichon, X., Pautot, G., Auzende, J.-M., Olivet, J.-L.: La Mediterranee occidentale depuis l'Oligocene; schema dévolution. *Earth Planet. Sci. Lett.* **13**, 145–152, 1971
- Løvlie, R.: The oxidation state of some Tertiary rocks from the Faeroe Islands and its implication for palaeomagnetism. *Geophys. J.* **40**, 55–65, 1975
- Løvlie, R., Gidskehaug, A., Storetvedt, K.M.: On the magnetization history of the Northern Irish basalts. *Geophys. J.* **27**, 487–498, 1972
- Løvlie, R., Kvingedal, M.: A palaeomagnetic discordance between a lava sequence and an associated interbasaltic horizon from the Faeroe Islands. *Geophys. J.* **40**, 45–54, 1975
- McElhinny, M.W.: The palaeomagnetism of the Permian of southeast Australia and its significance regarding the problem of inter-continental correlation. *Spec. Publ. geol. Soc. Australia* **2**, 61–67, 1969
- Menard, H.W.: Transitional types of crust under small ocean basins. *J. Geophys. Res.* **72**, 3061–3073, 1967
- Nairn, A.E.M., Westphal, M.: Possible implications of the palaeomagnetic study of late Palaeozoic igneous rocks of northwestern Corsica. *Palaeogeography, Palaeoclimat., Palaeoecol.* **5**, 179–204, 1968
- Roy, J.L., Park, J.K.: Red beds: DRM or CRM? *Earth Planet. Sci. Lett.* **17**, 211–216, 1972
- Soffel, H.: Palaeomagnetism and rock magnetism of the Colli Euganei volcanites and the rotation of Northern Italy between Eocene and Oligocene. *Boll. Geofis. Teor. Appl.* **16**, 333–355, 1974
- Storetvedt, K.M.: On remagnetization problems in palaeomagnetism; further considerations. *Earth Planet. Sci. Lett.* **9**, 407–415, 1970
- Storetvedt, K.M.: Crustal evolution in the Bay of Biscay. *Earth Planet. Sci. Lett.* **21**, 22–28, 1972
- Storetvedt, K.M.: The rotation of Iberia: Cenozoic palaeomagnetism from Portugal. *Tectonophysics* **17**, 23–39, 1973a
- Storetvedt, K.M.: Genesis of West Mediterranean basins. *Earth Planet. Sci. Lett.* **21**, 22–28, 1973b
- Storetvedt, K.M., Gidskehaug, A.: The magnetization of the Great Whin Sill, northern England. *Phys. Earth Planet. Interiors* **2**, 105–114, 1969
- Storetvedt, K.M., Petersen, N.: On chemical magnetization in some Permian lava flows of southern Norway. *Z. Geophys.* **36**, 569–588, 1970
- Thompson, R., Mitchell, J.G.: Palaeomagnetic and radiometric evidence for the age of the lower boundary of the Kiama magnetic interval in South America. *Geophys. J.* **27**, 207–214, 1972
- Van Bemmelen, R.W.: Origin of the western Mediterranean Sea. *Verh. Kon. Ned. Geol. Mijnbouw.* **26**, 13–52, 1969
- Vogt, P.R., Higgs, R.H., Johnson, G.L.: Hypotheses on the origin of the Mediterranean basin: magnetic data. *J. Geophys. Res.* **76**, 3207–3228, 1971
- Zijderveld, J.D.A., Hazeu, G.J.A., Nardin, M., Van der Voo, R.: Shear in the Tethys and the Permian palaeomagnetism in the southern Alps, including new results. *Tectonophysics* **10**, 639–661, 1970

Received September 24, 1975

Magnetic Anomalies of the African Red Sea Shelf and Their Implications for the Anomalies of Atlantic Continental Margin

H.A. Roeser

Bundesanstalt für Geowissenschaften und Rohstoffe
D-3000 Hannover 51, Postfach 510153, Federal Republic of Germany

Abstract: Marine geomagnetic measurements on the African shelf of the Red Sea between 17 and 19° N indicate a sea-floor spreading origin for this area. The spreading rates were somewhat lower than those found by Girdler and Styles for the more southern Red Sea but the crustal ages agree. Model computations require a magnetization much higher than normal for oceanic crust of the same age. Consequently, in the first stage of continental separation, crust with a higher magnetization may be produced. If this is true, it could lead to a better understanding of the slope anomalies which are found at the Atlantic continental margins.

Key words: Red Sea – Atlantic continental margin – Magnetic anomalies – Slope anomaly.

1. Introduction

The Red Sea consists of mildly deformed shelves and marginal zones and a deeper axial trough. A sea-floor spreading origin was soon accepted for the axial trough (Vine, 1966). The nature of the crust under the shelves and marginal zones remained doubtful until the discovery of extremely clear magnetic lineations in the area of the Dahlak Islands on the African shelf of the Red Sea (Girdler and Styles, 1974). So, at least partly, the shelves and marginal zones are created by sea-floor spreading, in accordance with the refraction seismic evidence that much more than the axial trough is underlain by crust with a seismic velocity which is characteristic of oceans (Davies and Tramontini, 1970).

During Valdivia cruise VA 01 in 1971, magnetic measurements were made over the axial trough and some parts of the shelves (Fig. 1). The results of the axial trough survey will be published elsewhere¹. The measurements over the shelves were restricted to fairly small areas by the coral reefs which make navigation hazardous in most parts of the southern Red Sea. The region marked in Fig. 1 by the bold rectangle is the only one where a good coverage is possible. The reason for the absence of coral from only this region is not known. It is possible that the surveyed part of the shelf may be not typical, not only with regard to the present day topography but also with regard to its past history.

¹ Geologisches Jahrbuch, Reihe D, 1975.

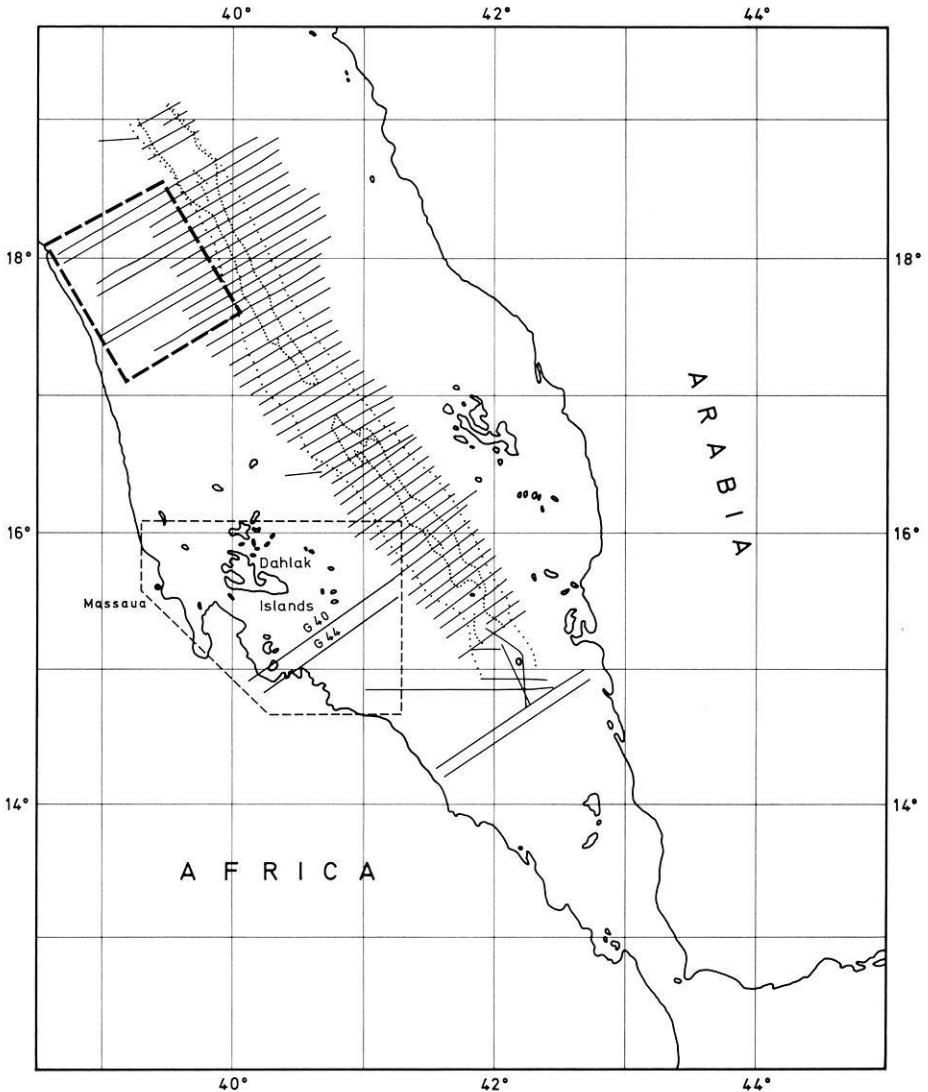
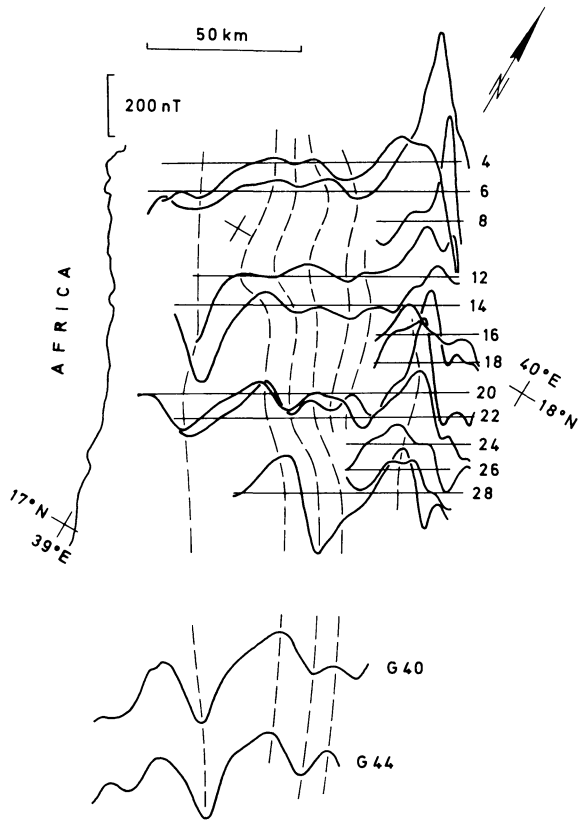


Fig. 1. Magnetic profiles of the Valdivia cruise VA 01 in the southern Red Sea (in 1971). Bold rectangle: area of Fig. 2. The dashed line near Massawa surrounds the area of the Gulf survey interpreted by Girdler and Styles (1974). The profiles G 40 and G 44 are included in Fig. 2. Dotted lines: Edges of the axial trough and the axial rough zone

2. Sea-Floor Spreading Origin of the Crust under the Shelf Profiles

Fig. 2 shows the observed anomalies of the total intensity of the earth's magnetic field for the region of the bold rectangle of Fig. 1, and profiles G 40 and G 44 (latitude 15° to 15°40' N, see Fig. 1) of Girdler and Styles (1974) which are plotted at the proper scale and distance from the Red Sea axis (only shifted

Fig. 2. Magnetic anomalies along the Valdivia profiles on the African shelf. The profiles are slightly straightened. G 40 and G 44: Profiles adapted from Girdler and Styles (1974). These profiles are shifted northwestward along the axis of the Red Sea



along the axis). It is not only possible to identify the anomaly sequence of Girdler and Styles but also is apparent that the distances from the Red Sea axis agree. Hence, the observed anomalies are probably of sea-floor spreading origin, and the crust in this area is of the same age as that under the Dahlak Islands.

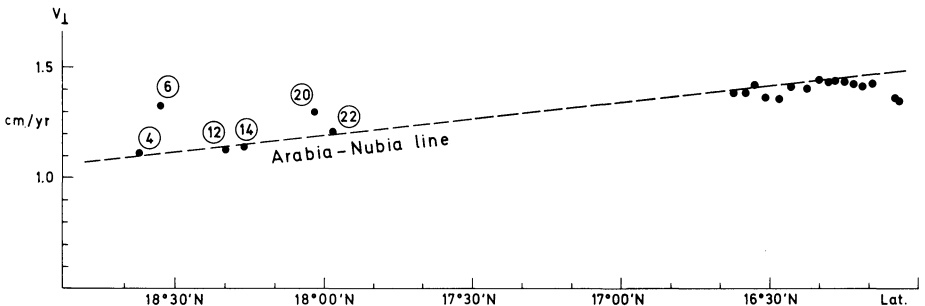


Fig. 3. Spreading for the Valdivia profiles and the northern part of the profiles of Girdler and Styles (1975). The "Arabia-Nubia" line shows the spreading-rates which could be expected for the separation of Arabia and Nubia (Girdler and Styles, 1975). Encircled numbers: Profile numbers of the Valdivia profiles

Spreading rates can be calculated using the anomaly ages determined by Girdler and Styles (1974) (Fig. 4, models). The rates are shown in Fig. 3 together with the "Arabia-Nubia" line of Fig. 8 of Girdler and Styles (1975). The scatter of the spreading rates of the Valdivia profiles is caused by the apparent irregularity of the sea-floor spreading process in this area. All spreading rates are less than those which Girdler and Styles found for the same anomalies between 16° and 16°40' N. Although the pole of rotation for the Arabia-Nubia line is not exactly confirmed, it is clear that the spreading rate at 17° N is significantly smaller than that observed by Girdler and Styles (1975) at 16.5° N.

3. Analysis of the Anomaly Amplitude

Typical oceanic crust consists of a more or less thick layer of sediments ("layer 1") overlying "layer 2" which has a mean thickness of 1.4 km and seismic velocities between 3.4 and 6.0 km/sec. Underneath is "layer 3" which is about 4.7 km thick and has a median velocity of 6.8 km/sec (Fig. 7-8 of Wyllie, 1971). The lower boundary of layer 3 is the Moho discontinuity. Talwani *et al.* (1971) modified this model. They divided layer 2 into an upper part 2A (0.4 km thick) and a lower part 2B and stated that only layer 2A is strongly magnetized whereas layer 2B and layer 3 are magnetized so weakly that they do not contribute significantly to the observed magnetic anomalies.

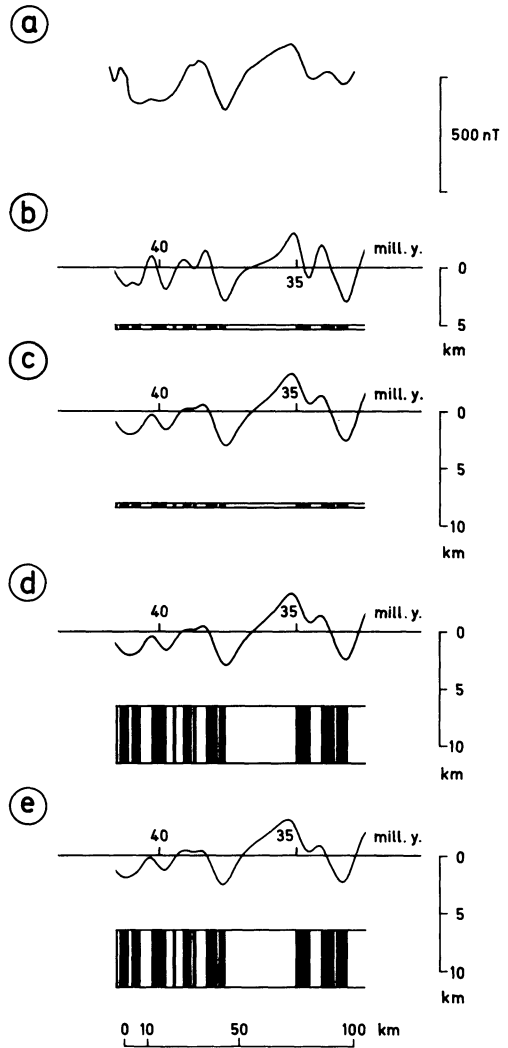
The model computations (Fig. 4) deal with profile G 40 (Fig. 4a) of Girdler and Styles (1975) instead of our profiles which are not regular enough. With one exception, the dip of the remanent magnetization is assumed to be 30° (the dip of the field of a centred dipole directed along the axis of rotation of the earth). The reversal time scale is that of Heirtzler *et al.* (1968).

According to the borehole data which Girdler and Styles (1975) report, the surface of layer 2A lies about 5 km below the survey level. With a magnetization of ± 20 amp/m ("+" and "-" mean parallel and antiparallel, respectively, to the field of a centred dipole) we get the model curve of Fig. 4b whose amplitudes are similar to those of the observed profile. The anomaly character is much different as the peaks of the model curve are too sharp. Fig. 4c matches the anomaly character better; here, the surface of layer 2A is assumed to be 8 km deep and the necessary magnetization is ± 40 amp/m.

This apparent depth discrepancy is encountered in the interpretation of many surveys of *old oceanic crust*. Cox and Blakely (1973) suggested that perhaps not only layer 2A is magnetized but also layer 3. For young oceanic crust the magnetization of layer 2A would dominate, but when the crust gets older the magnetization of this layer would decrease fairly soon whereas the magnetization of layer 3 would be more stable. The result would be that the main sources of the magnetic anomalies would lie much deeper than the surface of layer 2.

Thus the next model (Fig. 4d) assumes a magnetization of ± 3.5 amp/m for rocks at depths between 6.5 and 11 km (the depth range of layer 3). This magnetization value is near the upper limit which is possible for layer 3 (4 amp/m) according to the extensive model calculations for the anomalies of the central trough of the Red Sea (Roeser, 1975). The model matches the amplitude as

Fig. 4. Models for profile G 40 of Girdler and Styles (1975). (a) Observed profile; (b–e) All models use the Heirtzler time scale (Heirtzler *et al.*, 1968), spreading rates are 1.2 cm/year, declination 0°. (b) Layer 2A model: Magnetic layer of thickness 400 m with its surface in 5 km depth; magnetization ± 20 amp/m, dip 30°; (c) Layer 2A model: Magnetic layer of thickness 400 m with its surface in 8 km depth; magnetization ± 40 amp/m, dip 30°; (d) Layer 3 model: Magnetic layer of thickness 5 km with its surface in 6.5 km depth; magnetization ± 3.5 amp/m, dip 30°; (e) Layer 3 model: Magnetic layer of thickness 5 km with its surface in 6.5 km depth; magnetization ± 4 amp/m, dip 15°



well as the character of the observed curve. The curve form is somewhat different. Assuming a smaller dip of the magnetization (15°) would make the model curve more similar to the observed curve (Fig. 4e). There are serious arguments, however, against layer 3 contributing to the magnetic anomalies resulting from sea-floor spreading (Vine and Wilson, 1965; Vine and Moores, 1974; Roeser, 1975).

A difference between the character of an observed curve and that of its computed model exists also for *young oceanic crust* (Matthews and Bath, 1967; Talwani *et al.*, 1971 (Fig. 8); and Roeser, 1975 (Fig. 4)). Generally it is barely noticed because it is overshadowed by other problems. Also, the anomaly scale (cm per nT) is commonly chosen so large that the differences can hardly be seen.

Therefore, it seems more probable (although it cannot be proved) that layer 2A (at 5 km depth) produces the observed anomalies. The magnetization of

20 amp/m necessary for this model (Fig. 4b) is surprisingly high. Talwani *et al.* (1971) calculated 7 to 12 amp/m for oceanic crust 8 to 10 million years old.

Only for the central block of the ridge did they find 30 amp/m. In the Red Sea axial trough, the necessary magnetization for a 0.4 km thick layer at a depth of 2 km is 20 amp/m, for the older parts (4 to 5 million years old) possibly somewhat less. In part, the central block has higher magnetization. These values are in accordance with those of Talwani *et al.* (1971). Thus in the second stage of spreading of the Red Sea floor, the magnetization values are not significantly higher than those of the Reykjanes Ridge, for example.

For the first stage, the model calculations indicate that more magnetic material or material of higher magnetization was produced than the model of Talwani *et al.* (1971) predicts. Furthermore, the magnetic stability must have been high enough to preserve a considerable part of the magnetization for more than about 35 million years.

4. The Magnetic Anomalies of the Continental Slopes of the Atlantic Ocean

The geophysical processes at the beginning of sea-floor spreading are not known. Until now, we have attempted to extrapolate the processes which are observed at the midoceanic ridges to the whole spreading history. However, it is quite clear that this extrapolation must be modified at the very beginning of the sea-floor spreading as it should make a difference whether or not the mantle material comes up in the immediate neighbourhood of continental crust. The Red Sea is at an early stage of sea-floor spreading. Consequently, it is easier to study all those problems which can be investigated at the Atlantic continental margins only with great difficulty because of the great depth to layers 2 and 3. One important problem concerns the nature of the strong magnetic "slope anomalies" of many parts of the Atlantic Ocean continental margins. Even today, 20 years after the discovery of the slope anomaly along the United States Atlantic coast by Keller *et al.* (1954), it is a matter of dispute whether the slope anomaly lies over crust of continental or oceanic origin.

5. The Origin of Slope Anomalies

Seaward, the slope anomalies are often followed by smaller amplitude anomalies or magnetic quiet zones. At least in some cases the low amplitude anomalies are due to magnetic aging and the great depth of the magnetic horizon. This is a possible argument against a sea-floor spreading of the slope anomaly. The data from the Red Sea shed new light on the problem of why the slope anomaly is so much greater than the anomalies immediately seaward of it. In the area of the Dahlak Islands, an extremely clear sea-floor spreading pattern is found. The absence of any disturbance shows that no continental fragments are included in the crust. Real oceanic crust and not a transitional type of crust has been formed. The spreading process lasted only for a few million years. During this

time, crust with a higher than normal magnetization was produced. The amplitudes of the anomalies over the present axial trough are quite normal for young crust produced by sea-floor spreading. This may indicate that crust with normal magnetic properties would have been produced had the former episode of spreading continued. If so, the picture which we observe at the Atlantic continental margins could have been produced, that is, a 50–100 km broad strip with mostly one or two strong anomalies, and smaller amplitude anomalies on the seaward side of the strip.

The symmetry between some parts of the African and the United States coastal anomalies (Roeser *et al.*, 1971) is in agreement with the above concept. Also, the different form of the slope anomalies along the different shelves would be readily explained: As the breakup of Gondwanaland did not start at the same time on the whole length, we must expect different anomaly configurations to have formed.

Of course, it is speculative to draw such far-reaching conclusions from the data of a small area of the Red Sea shelf. However, this speculation is justified by the probability that now and for the next years there will not be much better information on this problem which is of great scientific relevance.

Acknowledgements. The magnetic data were obtained on Valdivia in cooperation with Preussag AG, Hannover. The work was financially supported by the Bundesministerium für Forschung und Technologie.

References

- Allan, T.D.: Magnetic and gravity fields over the Red Sea. *Phil. Trans. Roy. Soc. London Ser. A* **267**, 153–180, 1970
- Cox, A., Blakely, R.J.: Identification of short polarity events from marine magnetic anomalies. Paper presented at the second general scientific assembly of the International Association of Geomagnetism and Aeronomy, Kyoto 1973
- Davies, D., Tramontini, C.: The deep structure of the Red Sea. *Phil. Trans. Roy. Soc. London Ser. A* **267**, 181–189, 1970
- Girdler, R.W., Styles, P.: Two stage Red Sea floor spreading. *Nature* **247** (5435), 7–11, 1974
- Girdler, R.W., Styles, P.: The relevance of magnetic anomalies over the southern Red Sea and Gulf of Aden to Afar. In the press, 1975
- Heirtzler, J.R., Dickson, G.O., Pitman III, W.C., Herron, E., Le Pichon, X.: Marine magnetic anomalies, geomagnetic field reversals, and motions of the ocean floor and continents. *J. Geophys. Res.* **73** (6), 2119–2136, 1968
- Keller, F.J., Meuschke, L., Alldredge, L.R.: Aeromagnetic surveys in the Aleutian, Marshall and Bermuda Islands. *Trans. Am. Geophys. Union* **35** (4), 558–572, 1954
- Matthews, D.H., Bath, J.: Formation of magnetic anomaly pattern of Mid-Atlantic Ridge. *Geophys. J.* **13** (1/3), 349–357, 1967
- Roeser, H.A.: A detailed magnetic survey of the southern Red Sea. *Geol. Jahrb. D*, in the press, 1975
- Roeser, H.A., Hinz, K., Plaumann, S.: Continental margin structure in the Canaries. In: *The Geology of the East Atlantic Continental Margin* (ed. F.M. Delany). *Inst. Geol. Sci. Rpt. No. 70/16*, 27–36, 1971
- Talwani, M., Windisch, C.C., Langseth, M.G., Jr.: Reykjanes Ridge crest: a detailed geophysical study. *J. Geophys. Res.* **76** (2), 473–517, 1971
- Vine, F.J.: Spreading of the ocean floor: New evidence. *Science* **154** (3755), 1405–1415, 1966

- Vine, F.J., Moores, E.M.: A model for the gross structure, petrology, and magnetic properties of oceanic crust. In: Studies in earth and space sciences, 195–205. Geol. Soc. of Am., Boulder, Colorado, 1972
- Vine, F.J., Wilson, J.T.: Magnetic anomalies over a young oceanic ridge off Vancouver Island. *Science* **150** (3695), 485–489, 1965
- Wyllie, P.J.: *The Dynamic Earth: Textbook in Geosciences*, 416 p., New York, London, Sydney, Toronto: John Wiley & Sons, Inc. 1971

Received November 11, 1974; Revised Version August 25, 1975

Short Communications

**Self-Reversal above Room Temperature
due to N-Type Magnetization in Basalt**

A. Schult

Institut für Allgemeine und Angewandte Geophysik,
Theresienstr. 41, D-8000 München 2, Federal Republic of Germany

Key words: Rockmagnetism – Self-reversal – Titanomaghemites.

Self-reversal due to Néel's N-type spontaneous magnetization versus temperature has been reported for some alkali basalts by Schult (1965, 1968), Nishida and Sasajima (1974) and for a basalt from the ocean floor by Sasajima and Nishida (1974). The ferrimagnetic mineral component of these rocks was titanomaghemite. In all cases reported the compensation temperature (temperature at which self-reversal of remanence takes place) was below room temperature. In small parts of a hand specimen obtained from an alkali basalt of Miocene Age (Steinberg at Meensen near Göttingen) also compensation temperatures above room temperature have been observed.

The outer zone of this hand specimen (about 10 cm diameter) appears reddish brown due to weathering, the inner zone is dark grey. From the oriented hand specimen several cylindrical samples were cut, each about 0.5 to 1 cm³. On these samples the direction of the natural (NRM) and characteristic (CARM, after about 150 Oe AF cleaning) remanent magnetization was measured and the temperature dependence of CARM (accuracy about 5%) between –196° C and +100° C (accuracy about 3%). Then the samples (partly) were crushed and the magnetic phase was enriched to about 80 weight % with a hand magnet. On the separated material x-ray powder photographs were taken and the spontaneous magnetization (accuracy 5%) versus temperature was measured between –196° C and the Curie temperature in fields up to 14 KOe. On some basalt samples also the temperature dependence of an artificial thermoremanent magnetization (TRM) was measured. TRM was produced by heating the samples shortly to about 250° C (to above the Curie temperature) by submerging in hot oil and then cooling down to 20° C in a field of about 0.4 Oe.

The direction of NRM and CARM (after AF cleaning with about 150 Oe) at room temperature was reversed with respect to the present Earth's magnetic field for most samples in agreement with other samples from the same locality. Some samples from the outer (weathered) zone of the hand specimen however

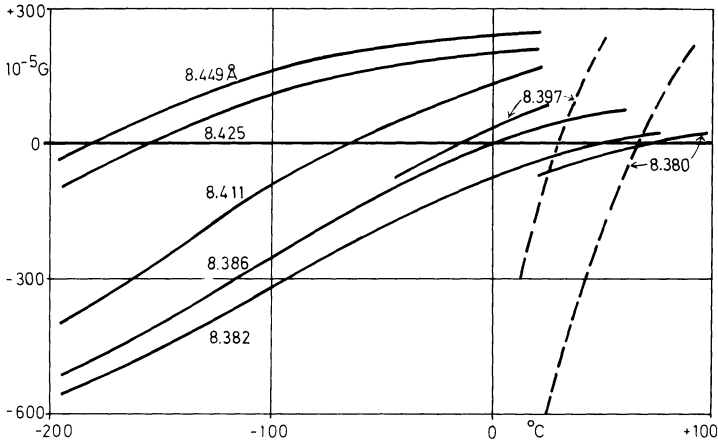


Fig. 1. Temperature dependence of CARM (continuous curves) and TRM (dashed curves) for several basalt samples from the hand specimen from Steinberg at Meensen near Göttingen. The lattice constants of the titanomaghemites in the basalt samples is given as parameter

have normal remanent magnetization with a direction of CARM antiparallel to that of the reversed samples. The temperature dependence of CARM (Fig. 1) shows that all samples undergo self-reversal: Samples with normal remanent magnetization at room temperature show self-reversal above room temperature and samples with reversed remanent magnetization below room temperature. — Also the artificially produced TRM shows self-reversal, sometimes at a temperature a little higher than the CARM (see Fig. 1).

The spontaneous magnetization versus temperature curves ($I_s(T)$) for samples with compensation temperatures T_k below about 0°C are N-type curves similar to those sometimes observed in basaltic rocks (Fig. 2). $I_s(T)$ does not vanish completely but has only a minimum at T_k because the material is not homogeneous. The $I_s(T)$ curves for samples with T_k above room temperature have no minimum but only a small hump below the Curie temperature and seem to approach the Q'-type (Schult, 1971). But these apparent Q'-type curves are "hybrid" N-type curves because the remanence clearly shows self-reversal.

The x-ray powder photographs of the separated material from all samples only shows lines responsible for a cubic spinel phase i.e. titanomaghemites in agreement with microscopic observations. The respective lattice constants are given in Fig. 1 and 2 as parameter. A microprobe analysis on two samples yielded the following compositions (calculated for stoichiometric titanomaghemite) with the respective lattice constants (accuracy 0.002 \AA):



With the aid of the O'Reilly and Readman (1971) diagram an oxidation parameter $z \approx 0.4$ for the first analyzed sample and $z \approx 0.7$ for the second sample was estimated. (This estimation is only tentative because of appreciable Al and Mg content of the titanomaghemites.) The oxidation parameters of the

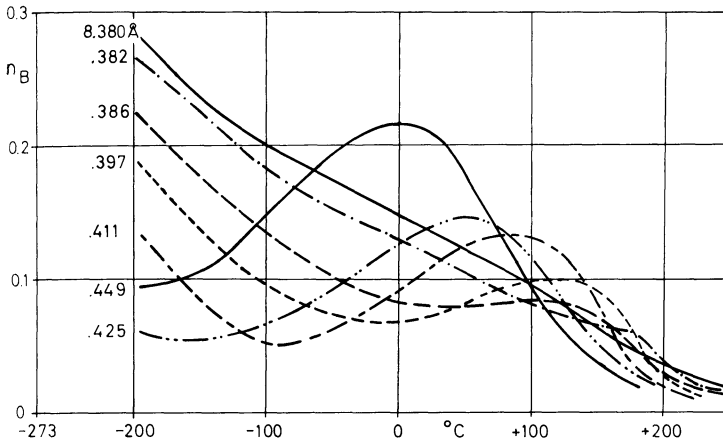


Fig. 2. Temperature dependence of spontaneous magnetization (in Bohr magnetons per formula unit titanomaghemite) measured on separated material from the same samples as in Fig. 1 with their respective lattice constants

other samples are probably between these two extreme values of z , because the two analyzed samples have (nearly) the extreme values in lattice constant and Curie temperature. — In the hand specimen the lattice parameter decreases from the centre to the surface and the Curie temperature increases. It can be assumed therefore that all samples have undergone low temperature oxidation most pronounced near the surface of the hand specimen. From Fig. 2 follows that with decreasing lattice parameter (i.e. increasing oxidation parameter) the spontaneous magnetization at 0°K and the compensation temperature increase. This can be explained by increasing ratio of the sublattice magnetizations at 0°K I_A/I_B (A for tetrahedral, B for octahedral sublattice) with $I_A/I_B > 1$ (Schult, 1971). It may be possible that with further low temperature oxidation the compensation temperature increases further until it equals the Curie temperature thus producing an irreversible self-reversal of remanent magnetization. For this process the Al and Mg content probably is also important. This will be discussed in a more detailed paper.

Acknowledgements. I thank Prof. G. Angenheister, Dr. N. Petersen and Prof. H. Soffel for many stimulating discussions and Prof. G. Angenheister for his support.

References

- Nishida, J., Sasajima, S.: Examination of self-reversal due to N-type magnetization in basalt. *Geophys. J.* **37**, 453–460 (1974)
- O'Reilly, W., Readman, P.W.: The preparation and unmixing of cation deficient titanomagnetites. *Z. Geophys.* **37**, 321–327 (1971)
- Sasajima, S., Nishida, J.: On the self-reversal of TRM in a highly oxidized submarine basalt. *Rock Magnetism and Paleogeophys.* **2**, 5–9 (1974)

- Schult, A.: Über die Umkehr der remanenten Magnetisierung von Titanomagnetiten in Basalten. *Beitr. Mineral. Petrog.* **11**, 196–216 (1965)
- Schult, A.: Self-reversal of magnetization and chemical composition of titanomagnetites in basalts. *Earth Planet. Sci. Lett.* **4**, 57–63 (1968)
- Schult, A.: On the strength of exchange interactions in titanomagnetites and its relation to self-reversal of magnetization. *Z. Geophys.* **37**, 357–365 (1971)

Received October 15, 1975

Further Utilization of the Fluxgate Magnetometer in the Palaeomagnetic Laboratory

R. Hummervoll

Department of Geophysics, University of Bergen, Bergen, Norway

Key words: Fluxgate probes used as detectors – Automatic magnetic balance – Palaeomagnetic laboratory.

The high field magnetic balance is a useful instrument for experimental work in rock magnetism and palaeomagnetism. Several types of balances have been constructed and some of them have been made automatic (Nagata, 1961). The main principle used in such balances is based on that of 'weighing' counterbalancing forces. To detect the deviation from the rest position, application of photo-cells, photo-transistors, condensors or some sort of inductive bridge balances have been used, but another alternative is to apply fluxgate probes which are available in most palaeomagnetic laboratories. The probes, placed centered to an extra magnet mounted on the translation pendulum (cf. Fig. 1), are to be opposed to each other. This is because the field from the strong

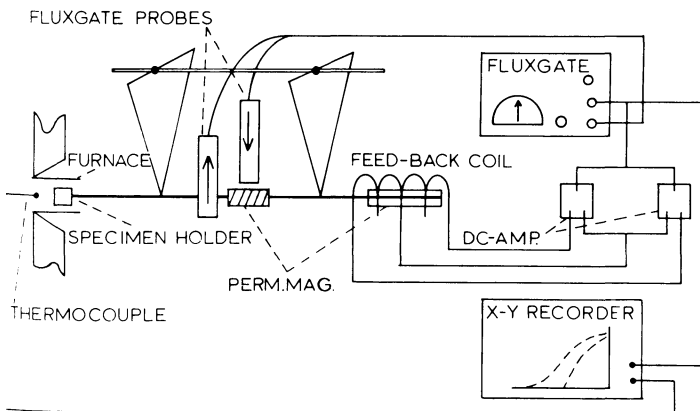


Fig. 1. Schematic diagram of the arrangement of the automatic translation balance with the fluxgate magnetometer as an active element in the feedback loop

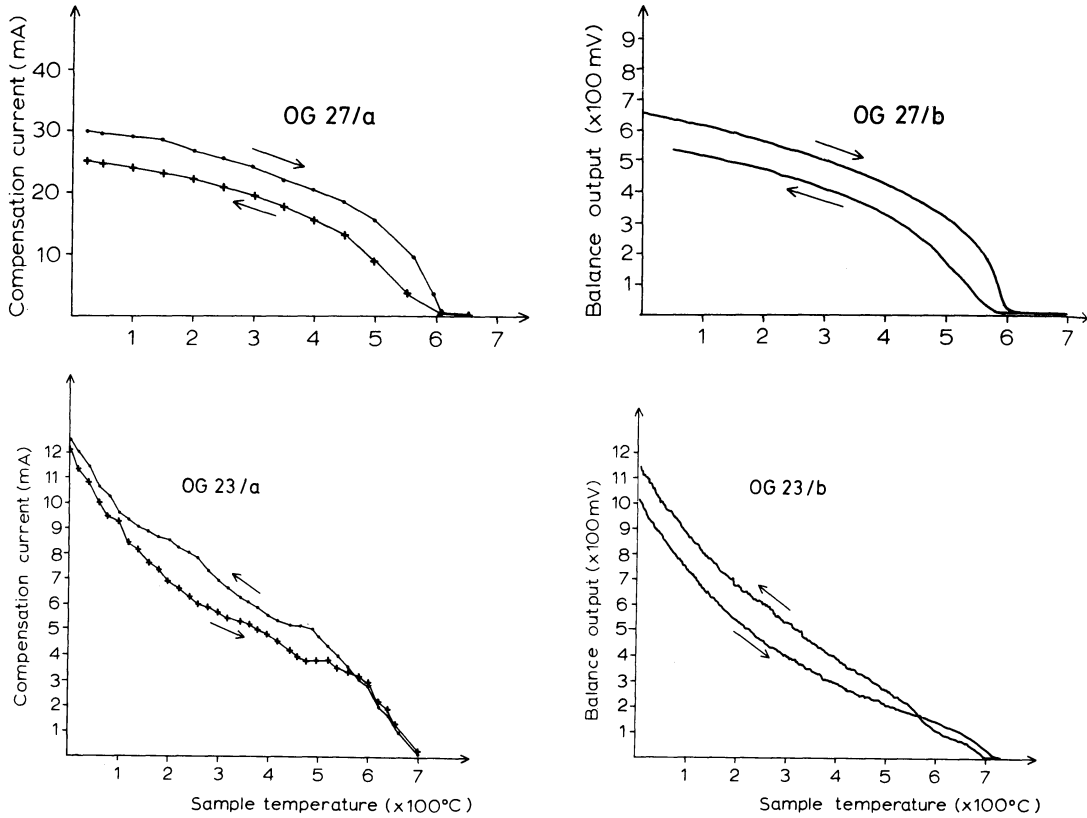


Fig. 2. Two pairs of curves which compares manually obtained results (a) with x-y Chart recordings (b). The initial susceptibility (K_0) for the two materials used (basalt and sediment) are $4.2 \cdot 10^{-3} \text{ emu/cm}^3$ and $3.610^{-7} \text{ emu/cm}^3$ respectively. Applied fields: 3.5 kOe for No. OG27 (basalt) and 6 kOe for No. OG23 (sediment)

electromagnet (which may vary slightly) would otherwise cause a too big influence on the recording system, for example in terms of drift etc. The small extra magnet should be magnetized along the direction of the pendulum as well as being rather short. A short magnet will minimize the effect of the gradient field from the electromagnet at the same time as yielding an optimum field response for the detecting probes (a short magnet has a stronger curvature of its lines of force than a larger magnet).

The arrangement here described may give a very sensitive recording system and a commercial oerstedmeter contains most of the necessary electronics. The only extra equipment needed is two simple dc-amplifiers which act as buffer stages in connection with the feedback arrangement as illustrated in Fig. 1. The feedback coil is centertapped with two halves wound in opposition; this is partly done to counteract the zero current in the two dc-amplifiers and partly to enable the equipment to be applied for complete thermal cycling (heating and subsequent cooling).

The sensitivity of the equipment will, among other things, depend on the position and distance of the probes relative to the permanent magnet as well as of the magnetic moment of the latter. The system here described has been applied at the Department of Geophysics, University of Bergen, for more than two years—in this set-up the minimum detectable movement of the pendulum 0.05 mm is obtained when the sensitivity range of the fluxgate magnetometer (Dr. Förster) is set at 1/20 of maximum value. In practice, it has not been necessary so far to operate on higher sensitivity ranges.

Fig. 2 shows thermal cycling results of two separate specimens having widely different initial susceptibilities. As illustrated in the diagram the specimens having the stronger susceptibility exhibit hardly any difference between manually obtained results and those recorded automatically. On the other hand, the specimens of low magnetic susceptibility (of the order typical for many sediments) exhibit a number of extra inflections on the manually obtained curves, a feature which is non-existent in the automatically recorded results. Thus, it appears that one should be extremely cautious when analysing manually obtained saturation magnetization (J_s) versus temperature curves from specimens having low susceptibilities (of the order of 10^{-7} emu/cm³); the recorded inflections may easily be interpreted in terms of mineralogical properties and changes while they most likely are due to recording/instrumental imperfections.

On a whole, the principle of using the fluxgate magnetometer as a detector and active element in the feedback loop of an automatic translation balance has proved to be a success. The system remains stable for days and the noise caused by external sources is of negligible importance even under workshop conditions. Furthermore, the applications of the fluxgate system concerned simplifies the performance of an automatic balance; the set-up here described may be duplicated with a minimum of technical facilities.

Reference

Nagata, T.: Rock magnetism. Tokyo: Maruzen 1961

Received October 10, 1975

Note on the Reliability of Subjective Processing of Geomagnetic Pulsation-Records in the Range Pc 2–Pc 5

A. Korschunow

Geophysikalisches Observatorium Fürstenfeldbruck
der Ludwig-Maximilians-Universität München,
D-8080 Fürstenfeldbruck, Ludwigshöhe 8, Federal Republic of Germany

Key words: Geomagnetic pulsations – Processing of data.

At the observatory Fürstenfeldbruck (IAGA-code: Fu) an extended statistical evaluation of records of geomagnetic pulsations for the years 1960–1971 (covering the 4,401 days of the sun-rotations: No. 1731–1893) is in progress (Korschunow, 1969; Hollò and Korschunow, 1974). Daily records of GRENET-type variometers are continuously examined with the aid of a glass-scale (subjective method of reading and estimating). Quarter-hourly activity-figures (Schätz-Zahlen) S in grades between 0 and 9 are derived from the records, using components of the geomagnetic field in the horizontal plane: H and D . Thus the photo-optical records are transformed into collections of figures, finally leading to the preparation of punched cards.

Taking into consideration that subjective methods of evaluation often are regarded with suspicion, because of individual errors incorporated into the processing, checks with three independent processors previously had been carried through, leading to promising results. Recently, however, another check was made unvoluntarily: Mistakeably records from five consecutive days were passed two times through routine-work. Thus there had been no planned performance, and a psychologically non-objectionable check had been completed with one and the same processor. A detailed report of the results had been published (Korschunow, 1974). Here one aspect will be demonstrated.

For the days in question (covering a general activity-range between Ap 11 up to Ap 30) the quarter-hourly mean figures of activity S (cf. above) have been derived. In order to simulate the effect of extended processing over a longer set of days, smoothing of the figures S according to the formula $(a+2b+c)/4$ was carried through.

Fig. 1 gives the smoothed curves of daily variation of S in the components H and D , likewise the difference curves ΔH and ΔD (original investigation minus repeated investigation). According to a IAGA-resolution, Berkeley 1963 (published in 1964), the statistical treatment of the Fürstenfeldbruck-records

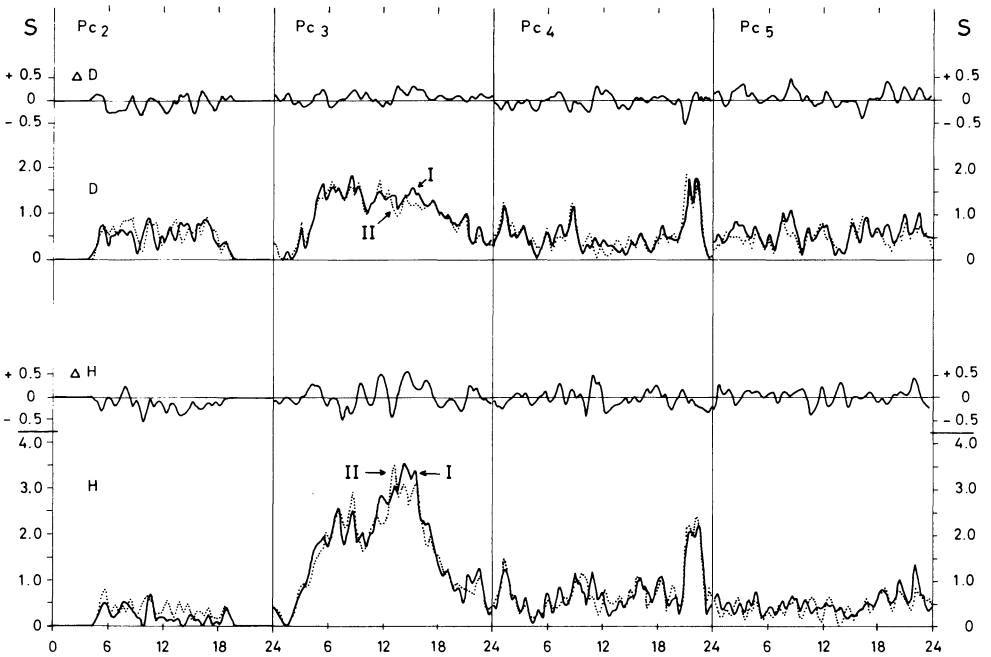


Fig. 1. Smoothed mean daily variation of pulsation activity figures S for the five days Feb. 4-9, 1964. I (full lines) results from first evaluation, II (broken lines) results from second evaluation. ΔD , ΔH differences between the two results. Reference-time: UT or GMT

Table 1. Correlation coefficients between the time-series as resulting from the original, first evaluation and the time-series as resulting from the repeated, second evaluation

	Pc 2	Pc 3	Pc 4	Pc 5
<i>Component H</i>				
Derived from mean daily variation	0,629	0,923	0,776	0,509
Derived from smoothed mean daily variation	0,727	0,949	0,895	0,629
<i>Component D</i>				
Derived from mean daily variation	0,841	0,932	0,822	0,483
Derived from smoothed mean daily variation	0,914	0,943	0,900	0,627

goes on in the four period-ranges of pulsations: Pc 2 5-10 s, Pc 3 10-45 s, Pc 4 45-150 s, and Pc 5 150-450 s, which are denoted correspondingly in Fig. 1.

In Table 1 the effect of smoothing the time-series, leading to better correlation-coefficients, is evident. The good correlation of the ranges Pc 3 and Pc 4, however, is not attained by the ranges Pc 2 and Pc 5. In the case of Pc 2's, being riders on Pc 3's and Pc 4's, obviously there could not be discerned properly the Pc 2's, whenever amplitudes of Pc 3's and Pc 4's had been larger. In the case of Pc 5 (belonging to the longer period-range 150-450 s) the processor seemed to be uncertain in his decision with respect to the borders of the time-base

(quarter-hourly-code!). These two sources of errors are widely known and common in subjective processing.

The results of this check and preliminary results of the statistics in progress (ultimately covering a solar-cycle) of the three consecutive years 1960–1962, not yet being published, demonstrate that sufficient reliability is achieved, provided that one individual processor is permanently taking care of the records. Taking moreover in view that thousands of consecutive days are involved into the complete system of evaluation, rough “quickly-going-schemes”, adopted to extended analogue time-series, seem to be promising. Taking further into consideration that up to now in most observatories daily records are produced by means of galvanometric-photo-optical techniques or with pencil-recorders, such rough schemes of subjective evaluation seem to be the only means to get results out of the abundance of data on the long run.

References

- Hollò, L., Korschunow, A.: A comparison of activity character figures of geomagnetic pulsations at the observatories Fürstenfeldbruck and Nagyckenk. *Acta Geodet., Geophys. et Montanist. Acad. Sci. Hung.* **9**, (1–2), 51–66, 1974
- Korschunow, A.: Erdmagnetische Pulsationen und Erdstrom an der Station Fürstenfeldbruck im Jahre 1968. In: *Veröffentlichungen des Geophysikalischen Observatoriums Fürstenfeldbruck, Serie A, Nr. 11*, 13–30, 1969
- Korschunow, A.: Pulsationen des erdmagnetischen Feldes an der Station Fürstenfeldbruck im Jahre 1973. In: *Veröffentlichungen des Geophysikalischen Observatoriums Fürstenfeldbruck, Serie A, Nr. 16*, 9–16, 1974

Received August 14, 1975; Revised Version November 6, 1975

Original Investigations

Die Gesteinsradioaktivität und ihr Einfluß auf das Temperaturfeld in der kontinentalen Kruste*

L. Rybach

Institut für Geophysik, Eidgenössische Technische Hochschule Zürich, CH-8093 Zürich, Schweiz

The Radioactivity of Rocks and Its Influence on the Temperature Field in the Continental Crust

Abstract. The heat produced in a given rock depends on the amounts of uranium, thorium and potassium present (1 ppm U = 0.718 cal/g y; 1 ppm Th = 0.193 cal/g y; 1% K = 26.2 μ cal/g y). Direct observations as well as inference from seismic data by means of an empirical relationship between compressional wave velocity V_p and heat production A show that A decreases exponentially with depth in continental crust in many regions. For a given surface heat flow, the higher the radioactivity of the surface rocks and the stronger the decrease with depth, the lower are the corresponding crustal temperatures.

The decrease of A with depth in the upper crust is less pronounced in the northern Alpine Foreland than in the Central Alps. Temperature-depth profiles, calculated for steady-state conduction models of these regions indicate that the zone of velocity and density inversion in the upper crust can not be explained by the presence of partially molten material.

Key words: Radioactivity of rocks – Heat flow – Temperature field – Crustal petrology.

1. Einleitung

Die Kenntnis der Temperaturverteilung in der Erdkruste und im Erdmantel ist für zahlreiche Probleme, wie z.B. für die Deutung geodynamischer Vorgänge, für die Beurteilung der Materialeigenschaften in größeren Tiefen und für die Interpretation petrologischer Daten von ausschlaggebender Bedeutung. Direkten Temperaturmessungen ist nur ein sehr beschränkter, oberflächennaher Bereich der Erdkruste zugänglich; in tieferliegenden Bereichen kann das Temperaturfeld nur durch Modellrechnungen erfaßt werden. Solche Modellrechnungen sind u.a.

* Vortrag, gehalten an der 35. Jahrestagung der Deutschen Geophysikalischen Gesellschaft in Stuttgart

Mitteilung Nr. 127 aus dem Institut für Geophysik, Eidgenössische Technische Hochschule, CH-8093 Zürich/Schweiz

Tabelle 1. Radiogene Wärmeproduktion in magmatischen Gesteinen (Mittelwerte). Daten aus Rybach (1973). 1 HGU = 10^{-13} cal/cm³ sec, 1 HFU = 10^{-6} cal/cm² sec

Gestein	ρ (g/cm ³)	A (HGU)	Δq^a (HFU)
Granit/Rhyolit	2,67	5,85	$5,9 \cdot 10^{-2}$
Granodiorit/Dacit	2,72	3,55	$3,6 \cdot 10^{-2}$
Diorit, Quarzdiorit/Andesit	2,82	2,59	$2,6 \cdot 10^{-2}$
Gabbro/Basalt	2,98	0,74	$7,4 \cdot 10^{-3}$
Ultramafit	{ Peridotit	3,23	$2,8 \cdot 10^{-4}$
	{ Dunit	3,28	$4,5 \cdot 10^{-5}$

^a Beitrag einer 1 km mächtigen Schicht zum Oberflächen-Wärmefluß

insbesondere für die sinnvolle Interpretation von magnetotellurischen Messungen unerläßlich.

Für einfache Temperaturabschätzungen genügen eindimensionale Modelle, um die Temperatur als Funktion einer einzigen Raumkoordinate, der Tiefe z , anzugeben. Für solche Modellrechnungen benötigt man im wesentlichen drei Eingangsdaten:

- Oberflächen-Wärmefluß $q(o)$, bestimmbar aus Temperaturgradient dT/dz und Gesteins-Wärmeleitfähigkeit K : $q(o) = K(dT/dz)$,
- vertikale Verteilung der Wärmeleitfähigkeit $K(z)$,
- Verteilung der internen Wärmequellen $A(z)$.

Im folgenden soll auf den Einfluß der internen Wärmequellen auf das Temperaturfeld eingegangen werden und zwar speziell in der kontinentalen Kruste im Alpen- und Voralpen-Bereich.

Als interne Wärmequellen kommen in der Erdkruste und im Erdmantel die natürlichen Radioisotope in Frage, deren Zerfallsenergie sich in unmittelbarer Nähe der zerfallenden Atome in Wärme umwandelt (Hurley und Fairbairn, 1953). Die Wärmeproduktion durch radioaktive Isotope pro Volumeneinheit (A) eines gegebenen Gesteins ist mit dessen Uran-, Thorium- und Kalium-Gehalten direkt proportional:

$$A(\text{HGU}) = 0,317 \rho (0,718 c_U + 0,193 c_{Th} + 0,262 c_K), \quad (1)$$

wo ρ die Dichte des Gesteins (g/cm³), c_U und c_{Th} die Uran- bzw. Thorium-Gehalte des Gesteins (ppm) und c_K den Kalium-Gehalt (%) bedeuten. 1 HGU = 10^{-13} cal/cm³sec. Die Zahlenfaktoren im Klammerausdruck sind die revidierten Konstanten der Wärmeproduktion für U, Th und K (Rybach, 1973). Die Gesteinsradioaktivität, bedingt durch die U-, Th- und K-Gehalte, variiert von Gesteinstyp zu Gesteinstyp über mehrere Größenordnungen. Diese Variation widerspiegelt das geochemische Verhalten der Elemente U, Th und K während der gesteinsbildenden Prozesse (magmatische Differentiation, Sedimentation, Metamorphose). In Tabelle 1 sind charakteristische Mittelwerte für magmatische Gesteine zusammengestellt. Ein eindeutiger Trend ist ersichtlich: die Gesteinsradioaktivität nimmt mit zunehmender Basizität der Gesteine ab, was mit einer Dichte-Zunahme gekoppelt ist. In magmatischen Gesteinen wird also die Gesteinsradioaktivität

Tabelle 2. Radiogene Wärmeproduktion in metamorphen Gesteinen mit granodioritischem Pauschalchemismus. Daten aus Heier und Adams (1965)

Metamorphosegrad	ρ (g/cm ³)	A^a HGU	Δq HFU
Grünschiefer-/Amphibolit-Fazies (niedrig)	2,70	7,54	$7,5 \cdot 10^{-2}$
Amphibolit-Fazies (hoch)	↓	2,83	$2,8 \cdot 10^{-2}$
Granulit-Fazies (niedrig)	↓	1,75	$1,8 \cdot 10^{-2}$
Granulit-Fazies (hoch)	2,90	1,07	$1,1 \cdot 10^{-2}$

^a Berechnet mit $\bar{\rho} = 2,75 \text{ g/cm}^3$

durch den Gesteinschemismus bestimmt. Bei metamorphen Gesteinen ist die Gesteinsradioaktivität, selbst bei isochemischen Gesteinstypen, abhängig vom Metamorphosegrad (Tabelle 2). Sedimentgesteine, welche am Aufbau der Erdkruste prozentual nur wenig beteiligt sind, haben – insbesondere Kalke und Dolomite – sehr niedrige Wärmeproduktion. Näheres über den Zusammenhang Gesteinsradioaktivität-Gesteinschemismus s. in Rybach (1976).

2. Die vertikale Verteilung der Wärmeproduktion in der kontinentalen Kruste

Die Verteilung der radioaktiven Wärmequellen bestimmt auch das Temperaturfeld. Einfache Überschlagsrechnungen zeigen, daß die Wärmeproduktion in der kontinentalen Kruste mit der Tiefe abnehmen muß. Direkte Informationen über die Art der Abnahme sind nur spärlich vorhanden (Lachenbruch und Bunker, 1971; Swanberg, 1972; Rybach, 1973; Hawkesworth, 1974); alle diese Untersuchungen weisen jedoch auf eine Abnahme nach dem Exponentialgesetz hin:

$$A(z) = A(o) \exp(-z/H), \quad (2)$$

wo $A(o)$ die Wärmeproduktion an der Erdoberfläche und H das logarithmische Dekrement bedeuten (bei $z=H$ ist $A(z) = A(o)/e$). H ist ein Maß für die Abnahme: bei großem H -Wert nimmt die Radioaktivität langsam ab und umgekehrt. Der Beitrag einer Gesteinsschicht mit der Mächtigkeit h und mit exponentiell mit der Tiefe abnehmender Wärmeproduktion zum Oberflächenwärmefluß $q(o)$ ist

$$\Delta q = \int_0^h A(z) dz = \int_0^h A(o) \exp(-z/H) dz = HA(o) \{1 - \exp(-h/H)\}. \quad (3)$$

Um den Einfluß von H auf das Temperaturfeld zu demonstrieren, wurden einfache Modellrechnungen durchgeführt gemäß der Formel in Abb. 1. Es wurde dabei mit zwei verschiedenen H - und $A(o)$ -Werten gerechnet, da diese Größen $T(z)$ auf gleiche Weise beeinflussen. Aus der Formel in Abb. 1 folgt nämlich

$$dT/dz = (1/K)q(o) + \{\exp(-z/H) - 1\} HA(o)/K, \quad (4)$$

ferner

$$(dT/dz)_{z \ll H} \approx q(o)/K \quad \text{und} \quad (dT/dz)_{z \gg H} \approx (1/K) \{q(o) - HA(o)\}. \quad (5)$$

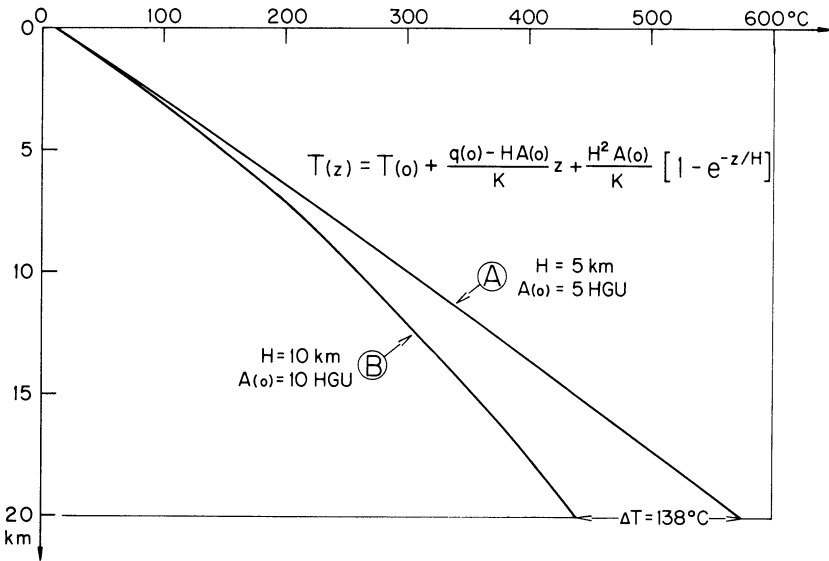


Abb. 1. Einfluß der Gesteinsradioaktivität auf das Temperaturfeld. $A(o)$ ist die radiogene Wärme-
 produktion an der Oberfläche, H das logarithmische Dekrement der exponentiellen Abnahme. Be-
 rechnung gemäß der Formel von Lachenbruch (1968) mit $q(o) = 1,75$ HFU und mit $K = 5,0 \cdot 10^{-3}$ cal/
 cm, sec, $^\circ\text{C}$. Modell (A) mit der niedrigeren, mit der Tiefe rascher abnehmenden Wärmeproduktion
 ergibt die höheren Temperaturen. Gemessene Temperaturwerte in Deutschland (bis max. 7 km Tiefe,
 s. Hürtig und Schlosser, 1973; Haenel, 1975) liegen zwischen den Kurven (A) und (B).

Man sieht daraus, daß in größeren Tiefen der Temperaturanstieg umso größer ist, je *kleiner* H und/oder $A(o)$ sind. Danach spielt H eine dominierende Rolle. Die bisher vorliegenden Untersuchungen (Lachenbruch und Bunker, 1971; Swanberg, 1972; Rybach, 1973; Hawkesworth, 1974) haben gezeigt, daß H in der Größenordnung von einigen Kilometern liegt und daß der H -Wert von Gebiet zu Gebiet variiert. Die geochemischen Vorgänge, welche zu einer Tiefenverteilung der wärmeproduzierenden Radioisotope in der kontinentalen Kruste nach dem Exponentialgesetz geführt haben, sind bei weitem noch nicht klar; es sind nur Lösungsansätze vorhanden (Turcotte und Oxburgh, 1972; Rybach und Labhart, 1973; Albarede, 1975). Es ist also selbst bei genauer Kenntnis der petrologischen Struktur und der geologischen Vergangenheit eines gegebenen Gebietes keine Voraussage des H -wertes möglich, was aber zu Temperaturberechnungen für das betreffende Gebiet unerlässlich wäre.

Im nachstehenden wird eine Methode vorgeschlagen, mit welcher die vertikale Verteilung der radioaktiven Wärmeproduktion, $A(z)$, aus seismischen Daten (Verteilung der Kompressionswellen-Geschwindigkeit, $V_p(z)$) bestimmt werden kann. Gestützt auf die in Rybach (1973) näher beschriebene empirische Beziehung zwischen A und V_p , kann aus einer gegebenen $V_p(z)$ -Struktur (z.B. Profil Eschenlohe-Lago Lagorai, Abb. G 31.2 in Giese, 1968) die entsprechende $A(z)$ -Verteilung bestimmt werden. Wie aus Abb. 2 ersichtlich, ergeben sich bezüglich $A(z)$ regionale Unterschiede zwischen Alpenvorland (Profil Böhmischesbrück-Eschenlohe) und Alpengebiet (Eschenlohe-Lago Lagorai). In der *oberen Kruste* liegt

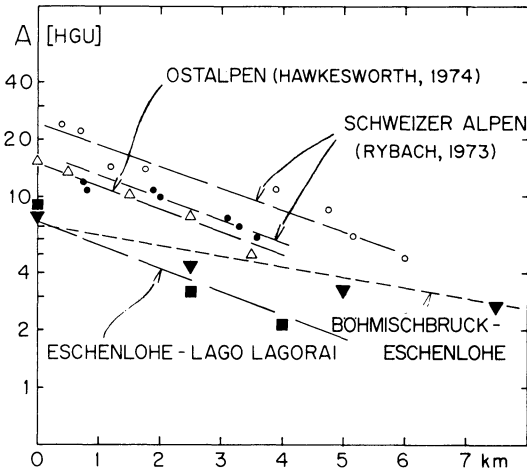


Abb. 2. Exponentielle Abnahme der radiogenen Wärmeproduktion (A) mit der Tiefe ($1 \text{ HGU} = 10^{-13} \text{ cal/cm}^3 \text{ sec}$). Oben: Resultate direkter Bestimmungen (Punkte, kleine Dreiecke). Unten: Wärmeproduktionswerte, aus seismischen Daten ermittelt (s. Text). Die Abnahme erfolgt in den Alpen schneller als im nördlichen Alpenvorland (Profil Böhmschbruck-Eschenlohe)

demnach im Alpen- und Voralpen-Gebiet eine exponentielle Abnahme der Wärmeproduktion mit lokal unterschiedlichem Dekrement H vor.

Was die Wärmeproduktionsverteilung in tieferen Krustenbereichen betrifft, so kann folgendes festgehalten werden: die Zone geringerer seismischer Geschwindigkeiten („Inversionszone“) in der *mittleren Kruste* (etwa im Tiefenbereich zwischen 10 und 20 km, siehe z.B. Giese, 1968; Choudhury *et al.*, 1971; Makris, 1971) zeichnet sich im Bild der Wärmeproduktion nicht ab. Die unserer $A(V_p)$ -Beziehung wesensverwandte NAFE-DRAKE-Beziehung $\rho(V_p)$ ist innerhalb der Inversionszone ebenfalls nicht gültig (Makris, 1971, S. 38). Das Vorhandensein einer Gesteinszone mit sprunghaft erhöhter, der Geschwindigkeitsinversion entsprechender Wärmeproduktion in der mittleren Kruste ist außerdem aus geochemisch-petrologischen Gründen unwahrscheinlich: eine derartige Konzentrationsverteilung der natürlichen Radioisotope kann im p/T -Gefälle der mittleren Kruste nicht bestehen. Für die nachfolgenden Modellrechnungen wurden deshalb in der Inversionszone konstante Werte eingesetzt, die zwischen jenen Werten liegen, welche knapp ober- und unterhalb der Inversionszone mit Hilfe der $A(V_p)$ -Beziehung (Rybach, 1973) ermittelt wurden.

In der *unteren Kruste* nimmt die Wärmeproduktion, entsprechend der V_p -Zunahme, mit der Tiefe ebenfalls ab. Die Abnahme ist, im Gegensatz zur oberen Kruste, weniger stark ausgeprägt. Für Alpenvorland und Alpengebiet wurde, ebenfalls mit Hilfe der $A(V_p)$ -Beziehung, einheitlich $H \approx 15 \text{ km}$ gefunden.

3. Modellrechnungen des Temperaturfeldes für Alpenvorland und Zentralalpen

Für die aus seismischen Daten ermittelten $A(z)$ -Krustenmodelle wurden ein-dimensionale, stationäre Temperaturberechnungen mit einer Schrittweite von

Tabelle 3. Krustenmodelle mit Eingabedaten für Temperaturberechnungen. Schichtmächtigkeiten nach Giese (1968), Harcke (1972) und Makris (1971). 1 TCU = 10^{-3} cal/cm, sec, °C

Alpenvorland $q(o) = 1,75$ HFU				Zentralalpen $q(o) = 2,0$ HFU			
	Mäch- tig- keit (km)	Wärme- leit- fähigkeit (TCU)	Wärme- produktion (HGU) z in km		Mäch- tig- keit (km)	Wärme- leit- fähigkeit (TCU)	Wärme- produktion (HGU) z in km
1. Schicht	10	6,5	$8 \exp(-z/10)$	1. Schicht	4	6,5	$10 \exp(-z/4)$
2. Schicht	12	6,0	2,45 (konstant, s. Text)	2. Schicht	10	6,5	$3,7 \exp[-(z-4)/10]$
3. Schicht	11	5,0	$2 \exp[-(z-22)/15]$	3. Schicht	14	6,0	2,45 (konstant, s. Text)
				4. Schicht	22	5,0	$2 \exp[-(z-28)/15]$
MOHO-Tiefe: 33 km Mantel-Wärmefluß: 0,80 HFU				MOHO-Tiefe: 50 km Mantel-Wärmefluß: 0,93 HFU			

$\Delta z = 2,5$ km durchgeführt. Die Eingabedaten sind in Tabelle 3 gegeben, die Resultate sind in Abb. 3 und 4 dargestellt.

Nördliches Alpenvorland

Für das Alpenvorland (etwa in der Umgebung von Stuttgart) wurde mit einem charakteristischen, mittleren Oberflächen-Wärmefluß $q(o) = 1,75$ HFU (Haenel und Zoth, 1973) gerechnet, für die Oberflächen-Temperatur wurde $T(o) = 10^\circ$ C gesetzt. Die mit den Daten der Tabelle 3 errechnete MOHO-Temperatur beträgt rund 650° C. Eingezeichnet wurden in Abb. 3 die Faziesgrenzen der Metamorphose nach Winkler (1967). Nach neuen petrologischen Erkenntnissen besteht die untere Kruste nicht aus basaltischen bzw. gabbroiden Gesteinen, sondern, entsprechend den dort herrschenden p/T -Bedingungen, aus Metamorphiten (s. z.B. Smithson und Decker, 1974). Die Faziesgrenze Grünschiefer/Amphibolit liegt beispielsweise im nördlichen Alpenvorland in etwa 28 km Tiefe. Teilschmelzen (infolge beginnender Anatexis) sind hier, wie aus Abb. 3 ersichtlich, selbst im untersten Krustenbereich nicht zu erwarten.

Der Mantel-Wärmefluß kann aus Oberflächen-Wärmefluß und $A(z)$ -Modell berechnet werden. Auf diese Weise läßt man die untere Randbedingung des Temperaturfeldes offen. Es wurde damit grundsätzlich anders vorgegangen als Buntebarth (1973), der einen räumlich unveränderlichen Mantel-Wärmefluß annimmt. Verlässliche Daten über den Mantel-Wärmefluß sind jedoch praktisch keine vorhanden. Mit $q(o) = 1,75$ HFU und den in Tabelle 3 angegebenen Wärme-produktionsverhältnissen resultiert für das Alpenvorland ein Mantel-Wärmefluß von 0,80 HFU, in Übereinstimmung mit dem Befund von Haenel (1971).

Zentralalpen

Für den Bereich der Zentralalpen (etwa das Gebiet der Schweizer Zentralmassive) wurde als mittlerer Oberflächen-Wärmefluß $q(o) = 2,0$ HFU eingesetzt, ein mehr oder weniger repräsentativer Mittelwert aus Daten von Clark und Niblett (1956),

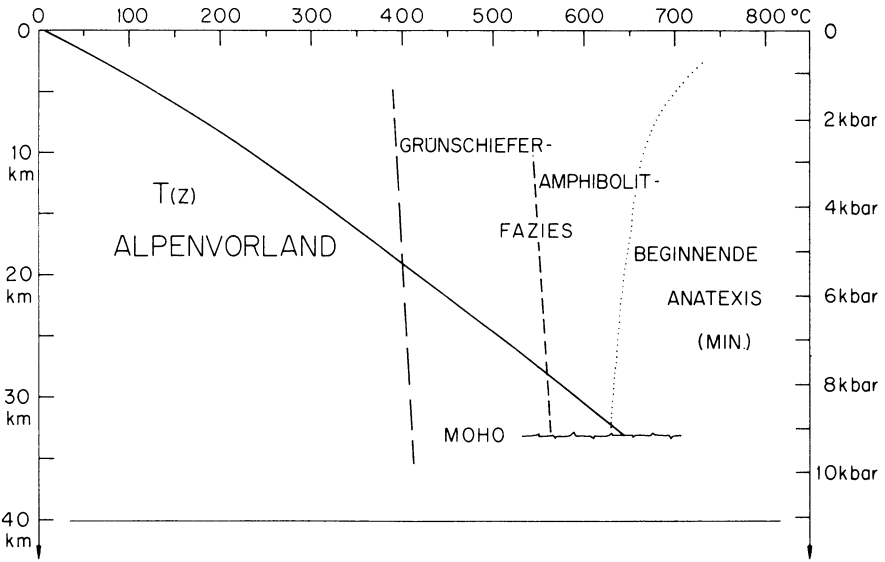


Abb. 3. Temperatur-Tiefenkurve für das nördliche Alpenvorland, berechnet aufgrund der Daten der Tabelle 3. Faziesgrenzen der Metamorphose und Anatexis-Kurve für einen intermediären Gneis in Amphibolit-Fazies nach Winkler (1967)

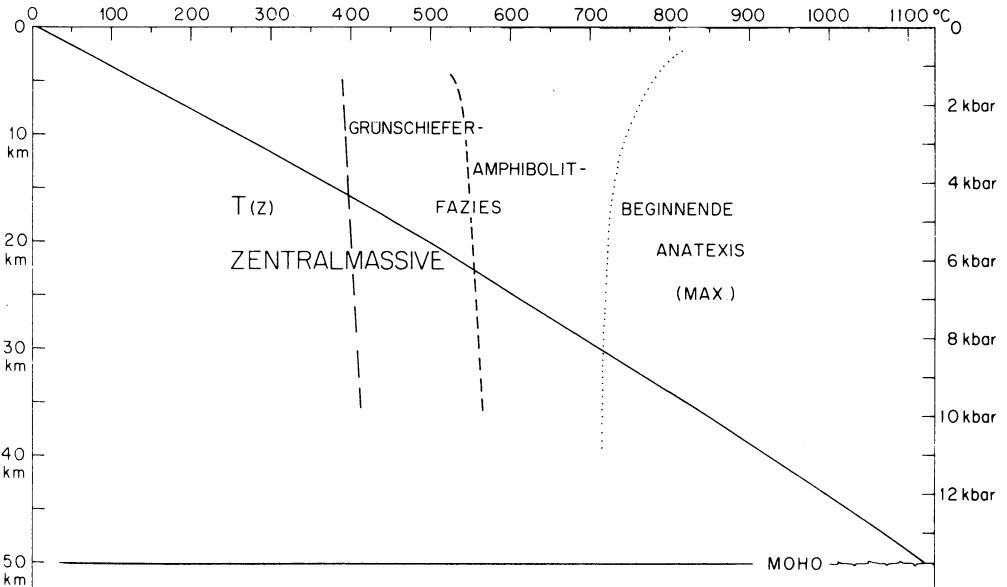


Abb. 4. Temperatur-Tiefenkurve für die Zentralalpen, berechnet aufgrund der Daten der Tabelle 3. Faziesgrenzen der Metamorphose und Anatexis-Kurve für einen intermediären Gneis in Amphibolit-Fazies nach Winkler (1967)

von Herzen *et al.* (1974), Haenel (1974), ferner $T(o) = 5^\circ \text{C}$. Der Mantel-Wärmefluß beträgt hier 0,93 HFU. Die MOHO-Temperatur (Abb. 4) ist wesentlich höher ($\sim 1100^\circ \text{C}$) als im Alpenvorland, dies wegen a) der größeren MOHO-Tiefe, b) des höheren Oberflächen-Wärmeflusses und c) der andersgearteten $A(z)$ -Struktur, insbesondere wegen der rascheren Abnahme der Wärmeproduktion (s. Abb. 1). Wiederum wurden die Faziesgrenzen der Metamorphose in Abb. 4 eingetragen, ferner die Anatexis-Kurve bei $p_{\text{H}_2\text{O}} = p_{\text{tot}}$ für einen Gneis mit intermediärem Plagioklas (Winkler, 1967). In der betreffenden Tiefe sind jedoch basischere Gesteine zu erwarten mit wesentlich höheren Schmelztemperaturen (s. hierzu auch Meissner, 1974; Höhndorf *et al.*, 1975). Auch kann infolge niedrigeren H_2O -Partialdruckes mit einer Erhöhung der Schmelztemperatur gerechnet werden. Anatektische Schmelzen sind, wenn überhaupt, nur an der Basis der Kruste vorhanden.

4. Schlußfolgerungen

Die Gesteinsradioaktivität stellt in der kontinentalen Kruste eine Wärmequelle erster Ordnung dar. Die radiogene Wärmeproduktion in einem gegebenen Gestein hängt im wesentlichen von dessen Gehalten an Uran, Thorium und Kalium ab. Die radiogene Wärmeproduktion ist ein skalarer und isotroper Gesteinsparameter, welcher von der in situ-Temperatur und vom -Druck unabhängig ist.

Die vertikale Verteilung der Wärmeproduktion – wie auch diejenige der Wärmeleitfähigkeit – beeinflusst das Temperaturfeld in entscheidender Weise. Entgegen der weitverbreiteten Meinung, wonach eine mächtige Schicht mit hoher Wärmeproduktion (z.B. Granit-Schicht) zu hohen Temperaturen führt, kann gezeigt werden, daß je geringer die Radioaktivität der Oberflächengesteine ist und je schneller diese mit der Tiefe abnimmt, die Temperatur umso *stärker* ansteigt.

Ein Vergleich der Temperatur-Tiefenverteilung im Voralpen- und Alpengebiet mit Faziesgrenzen der Metamorphose und mit Anatexis-Kurven läßt den Schluß zu, daß die Zone der Geschwindigkeitsinversion in der oberen Kruste durch das Vorhandensein von teilweise geschmolzenem Material nicht erklärt werden kann, da in diesen Tiefen die hierzu notwendige Temperatur noch nicht erreicht ist.

Literatur

- Albarede, F.: The heat flow/heat generation relationship: An interaction model of fluids with cooling intrusions. *Earth Planet. Sci. Lett.* **27**, 73–78, 1975
- Buntebarth, G.: Modellberechnungen zur Temperatur-Tiefen-Verteilung im Bereich der Alpen und des Alpenvorlandes. *Z. Geophys.* **39**, 97–107, 1973
- Choudhury, M., Giese, P., Visintini, G. de: Crustal structure of the Alps: Some general features from explosion seismology. *Boll. Geofis. Teor. Appl.* **13**, 211–240, 1971
- Clark, S.P., Niblett, E.R.: Terrestrial heat flow in the Swiss. *Royal Astron. Soc. Geophys. Supp. Monthly Notices* **7**, 176–195, 1956
- Giese, P.: Versuch einer Gliederung der Erdkruste im nördlichen Alpenvorland, in den Ostalpen und in Teilen der Westalpen mit Hilfe charakteristischer Refraktions-Laufzeit-Kurven sowie eine geologische Deutung. *Geophys. Abh. des Inst. f. Meteorologie und Geophysik der Freien Universität Berlin* **I/2**, 1968

- Haenel, P.: Heat flow measurements and a first heat flow map of Germany. *Z. Geophys.* **37**, 975–992, 1971
- Haenel, R., Zoth, G.: Heat flow measurements in Austria and heat flow maps of Central Europe. *Z. Geophys.* **39**, 425–439, 1973
- Haenel, R.: Heat flow measurements in Northern Italy and heat flow maps of Europe. *Z. Geophys.* **40**, 367–379, 1974
- Hänel, R.: Bericht über flächenhafte Darstellung von Temperaturdaten aus dem Untergrund Deutschlands (Zwischenergebnisse). Bericht Nr. 66728, Niedersächsisches Landesamt für Bodenforschung, Hannover, 1975
- Harcke, H.: Die Struktur der Erdkruste im nördlichen Alpenvorland – eine Synthese aus seismischen und gravimetrischen Daten. Diss. Universität Karlsruhe, 1972
- Hawkesworth, C.J.: Vertical distributions of heat production in the basement of the Eastern Alps. *Nature* **249**, 435–436, 1974
- Heier, K.S., Adams, J.A.S.: Concentration of radioactive elements in deep crustal material. *Geochim. Cosmochim. Acta* **29**, 53–61, 1965
- Herzen, R.P. v., Finckh, P., Hsü, K.J.: Heat-flow measurements in Swiss Lakes. *Z. Geophys.* **40**, 141–172, 1974
- Höhndorf, A., Haenel, R., Giesel, W.: Geothermal models of the Ivrea-Zone. *Z. Geophys.* **41**, 179–187, 1974
- Hurler, P.M., Fairbairn, H.: Radiation damage in zircon: A possible age method. *Bull. Geol. Soc. Am.* **64**, 659–673, 1953
- Hurtig, E., Schlosser, P.: Analyse der Wärmeflußdaten Mitteleuropas. Veröffentlichungen des Zentralinstituts für Physik der Erde Potsdam **14**, 665–699, 1973
- Lachenbruch, A.H.: Preliminary geothermal model of the Sierra Nevada. *J. Geophys. Res.* **73**, 6977–6989, 1968
- Lachenbruch, A.H., Bunker, C.M.: Vertical gradients of heat production in the continental crust 2. Some estimates from borehole data. *J. Geophys. Res.* **76**, 3852–3860, 1971
- Makris, J.: Aufbau der Erdkruste in den Ostalpen aus Schweremessungen und die Ergebnisse der Refraktionsseismik. *Hamburger Geophys. Einzelschriften* **15**. Berlin: De Gruyter & Co. 1971
- Meissner, R.: Viscosity-depth-structure of different tectonic units and possible consequences for the upper part of converging plates. *Z. Geophys.* **40**, 57–73, 1974
- Rybach, L.: Wärmeproduktionsbestimmungen an Gesteinen der Schweizer Alpen. *Beitr. Geol. Schweiz, Geotechn. Ser.* **51**. Bern: Kümmerly & Frei 1973
- Rybach, L., Labhart, T.P.: Regelmäßigkeiten der Radioaktivitätsverteilung in granitischen Gesteinskörpern (Beispiele aus den Schweizer Alpen). *Schweiz. Min. Petr. Mitt.* **53**, 379–384, 1973
- Rybach, L.: Radioactive heat production: A physical property determined by the chemistry of rocks. In: *Proc. NATO Adv. Study Inst. on Petrophysics*. Im Druck 1976
- Smithson, S.B., Becker, E.R.: A continental crustal model and its geothermal implications. *Earth Planet. Sci. Lett.* **22**, 215–225, 1974
- Swanberg, C.A.: Vertical distribution of heat generation in the Idaho Batholith. *J. Geophys. Res.* **77**, 2508–2513, 1972
- Turcotte, D.L., Oxburgh, E.R.: Statistical thermodynamic model for the distribution of crustal heat sources. *Science* **176**, 1021–1022, 1973
- Winkler, H.G.F.: Die Genese der metamorphen Gesteine, 2. Aufl. Berlin-Heidelberg-New York: Springer 1967

Eingegangen am 1. Oktober 1975; revidierte Fassung am 24. November 1975

A Lithospheric Seismic Profile in Britain

II. Preliminary Report on the Recording of a Local Earthquake * **

W. Kaminski¹, D. Bamford^{2,4}, S. Faber¹, B. Jacob³, K. Nunn² and C. Prodehl¹

¹ Geophysikalisches Institut der Universität Karlsruhe,
Hertzstr. 16, D-7500 Karlsruhe 21, Federal Republic of Germany

² Department of Geological Sciences, University of Birmingham,
P.O. Box 363, Birmingham B15 2TT, United Kingdom

³ Institute of Geological Sciences, Seismology Unit, Murchison House,
West Mains Road, Edinburgh EH9, United Kingdom

⁴ Department of Geophysics, University of Edinburgh,

6 South Oswald Road, Edinburgh EH9 2HX, United Kingdom

Abstract. During recording for the 1974 Lithospheric Seismic Profile in Britain (LISPB), a local earthquake (magnitude 3.0) was recorded by 60 mobile stations forming a temporary linear array of about 400 km in length. Observation distances ranged from 80 to 300 km and the data is presented in this paper in the form of reduced travel-time record sections for *P* and *S* waves (vertical components).

Clear phase correlations are visible in the *P*-sections and the general pattern is similar to that observed on LISPB explosion data. Preliminary velocity-depth functions computed for both explosion and earthquake data are presented; as a result of these computations an improved focal depth for the earthquake is established.

The results demonstrate the strong relationship between high-quality earthquake data and high-quality explosion data when both are available in the same area. With a few explosions as control, earthquakes recorded on a closely spaced mobile array could be used to study the fine structure of the lithosphere. At the same time the extensive data then available permits a detailed study of the earthquake itself.

Key words: LISPB – Local earthquake – Velocity-depth functions – Improved focal depth.

1. Introduction

In recent years, explosion seismology—having the advantage of a controlled source—has almost completely replaced the study of near-earthquakes as a method for measuring the velocity-depth structure within the lithosphere. Modern

* Contribution no. 183 within a joint research program of the Geophysical Institutes in Germany sponsored by the Deutsche Forschungsgemeinschaft (German Research Society). Contribution no. 122, Geophysical Institute, University of Karlsruhe

** For part I, see Bamford *et al.*, 1976

explosion seismological data is usually of a very high quality with several explosions fired into closely spaced arrays of mobile recording stations.

Earthquakes, however, do offer the possibility of utilizing inexpensive sources of varying frequencies at a range of depths within the structure of interest, thereby broadening our knowledge of lithospheric structure. Unfortunately because earthquakes are at present essentially unpredictable, there is no area where explosion and earthquake data of comparable high quality have been used for lithospheric studies.

In this note, we describe a very fortunate accident that occurred during a major explosion-seismic experiment in the British Isles when a local earthquake was recorded on a temporary linear array of over sixty magnetic-tape recording stations.

2. Earthquake Studies in the British Isles

Britain is not a seismically active area and destructive earthquakes are very few and far between (for a historical account see Davison (1924)). Though there was an earthquake in the North Sea in 1931 which probably had a magnitude of about $5\frac{1}{2}$ there is little evidence that there have been any earthquakes of magnitude greater than 5 within the land area of Britain (Lilwall, private communication). Because of this there have been few continuously recording stations and most of the ones running at present have been established since 1960 and are concentrated in the North of England and the South of Scotland (e.g. Rookhope, Eskdalemuir (EKA and ESK), Lownet).

Instrumental studies of such earthquakes as have occurred have generally had to make the most of fairly sparse data and a few recent examples include those by Key *et al.*, 1964; Agger and Key, 1965; Cleary, 1967; Browning and Jacob, 1970; Crampin *et al.*, 1972; and Lilwall and Riddle, 1973. The situation has not been improved by the rather approximate knowledge of crustal structure in Britain. Probably the largest recent earthquake was the North of England earthquake in 1970 while the best located were those in the swarm in Glenalmond between 1970 and 1972. Early in 1974 there were earthquakes in both North and South Wales, and while these were not very well located because of the distribution of the national network, they have been the subject of a very extensive macroseismic survey (Browitt and Lilwall, private communication) and may provide the most satisfactory overall investigation of any British earthquakes up to that time.

3. LISP B 1974 and the Kintail Earthquake

During July and August 1974, a combined British-German group carried out a large explosion experiment (LISP B) to study the lithospheric structure of the British Isles. Details of this experiment are given elsewhere (Bamford *et al.*, 1975) but, in summary, sixty mobile stations (recording 3-components of ground-motion on analogue magnetic tape) were deployed at different times on various

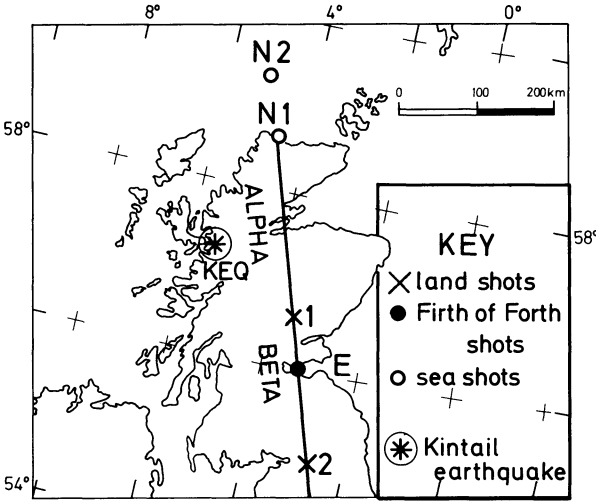


Fig. 1. KEQ location map. The recording stations were set up along lines ALPHA and BETA between shotpoints N1 and 2

Table 1. Data for the Kintail earthquake (KEQ)

Position	57.23°N 05.35°W
Date	6th August 1974
Origin Time	18 h 17 m 36.9 s GMT
Magnitude	$M_b^* = 3.0$ (For a discussion of M_b^* , see Jacob, Willmore, 1972)
Depth	14 km

segments such as ALPHA and BETA shown in Fig. 1. On 6th August 1974, these stations, supplemented by a temporary four-station array in the Grampian Highlands (southern half of segment ALPHA), were positioned at approximately 6–7 km intervals along segments ALPHA and BETA and thus formed a temporary array 400 km long. At about 1820 GMT the stations recorded the seismic waves from an earthquake in the Kintail area of Scotland (Fig. 1). Details of this earthquake (henceforth referred to as KEQ) are given in Table 1; it was one of a swarm of more than 20 events that occurred in the Kintail area during August and September 1974. The study of this group of earthquakes will be reported elsewhere (Crapin, personal communication).

4. KEQ Record Sections

The first-arrival data obtained on the LISP line greatly facilitated the precise location of KEQ and the general study of the group of earthquakes. Fortunately, the gains of our temporary stations had been set for a large shot fired at position N2 (Fig. 1); thus gains increased southwards along ALPHA and BETA

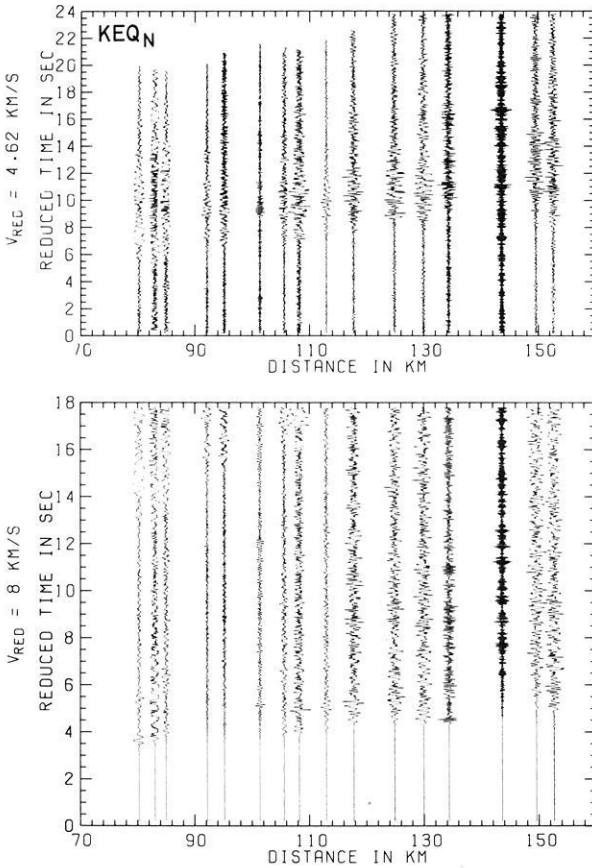


Fig. 2. Record sections of the vertical-component seismograms of the stations north of the point of minimum recording distance (KEQ_N). The upper section shows *S* waves (reduction velocity 4.62 km/s), the lower one *P* waves (reduction velocity 8.0 km/s)

and hence were ideal for recording KEQ out to about 300 km distance. Furthermore, this shock was an intermediate one in the series—the largest one would have completely overloaded our recorders. Therefore, we are able to present the digitized LISP recordings of KEQ in the conventional form for the study of crust and upper mantle structure, that is as record sections with reduced travel-time plotted against distance. In Figs. 2 and 3, we show record sections compiled from the vertical components of ground motion at our stations. The minimum recording distance (80 km) was for stations at about the middle of segment ALPHA; observations north of this point are presented in Fig. 2 (KEQ_N), observations on the rest of ALPHA and on BETA in Fig. 3 (KEQ_S). In both figures, the upper record section shows the *S* waves and the lower one the *P* waves. In an effort to compare the two types of observation, scales have been adjusted in accordance with the nominal *P/S* velocity ratio of $\sqrt{3}$; thus the reduction velocity for *P* waves was 8 km/s and that for *S* waves 4.62 km/s

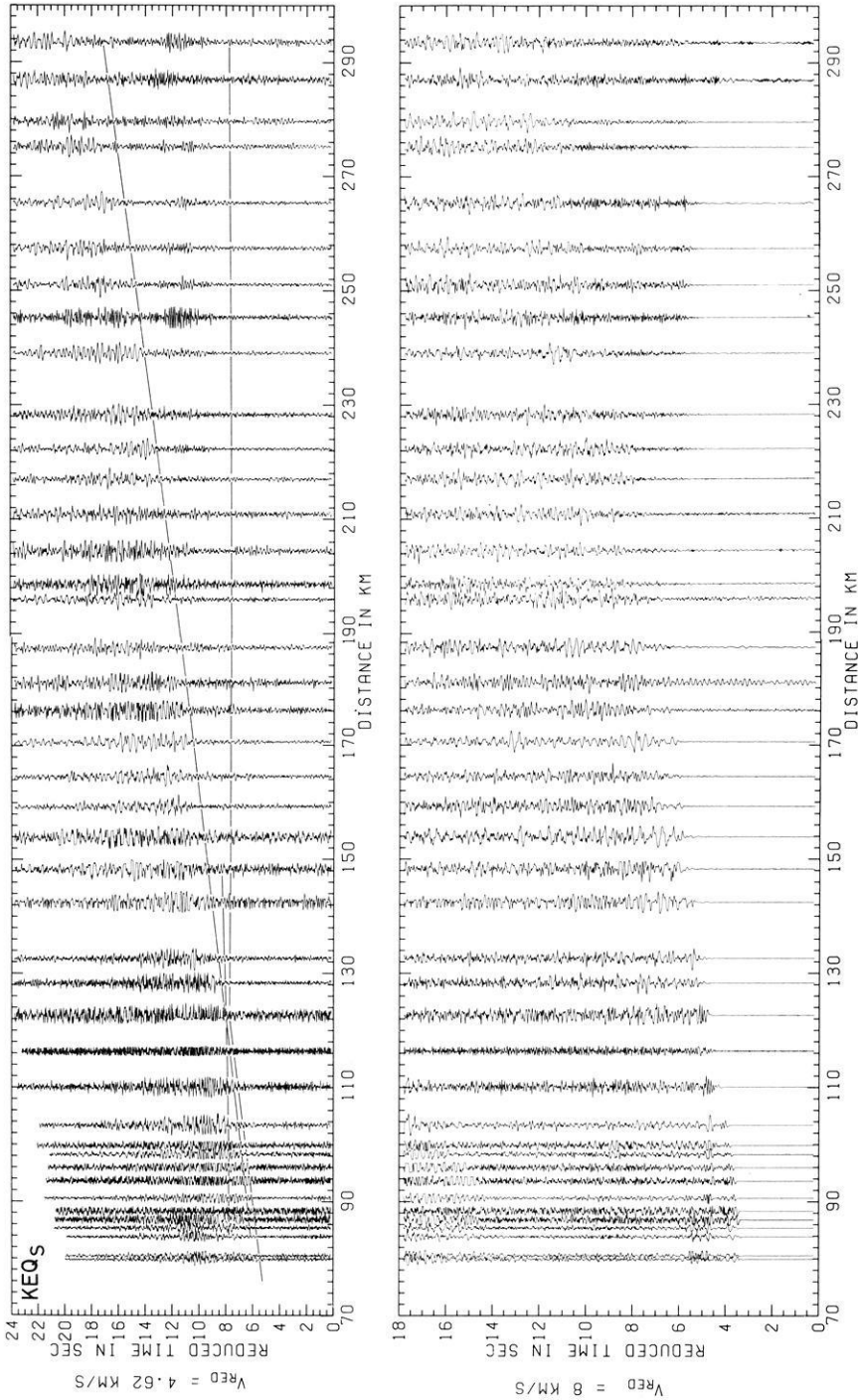


Fig. 3. Record sections of the vertical-component seismograms of the stations south of the point of minimum recording distance (KEQ₃). The upper section shows *P* waves (reduction velocity 4.62 km/s), the lower one *P* waves (reduction velocity 8.0 km/s). *S* travel-time curves drawn as broken lines in the upper section correspond to those for the model in Fig. 4b

whilst the time-scale for S waves was 1.15 cm per second in comparison with 2 cm per second for P .

It is possible to make several phase correlations within these sections. Within the P sections, a direct wave (velocity approximately 6.4 km/s) is a clear first-arrival between 80 and 110 km; beyond 110 km a weak P_n phase (apparent velocity about 8 km/s) is observed as a first-arrival out to 170 km. Especially on KEQ_S (Fig. 3), well developed second-arrivals are seen; a strong $P_M P$ branch is observed at about 4.5 seconds reduced time between 80 and 110 km distance and another strong reflection is observed asymptotic to 6.4 km/s. Several phases can be observed on the S sections with the strongest travelling with a velocity of 3.7 km/s between 90 and 250 km distance.

Elsewhere (Bamford *et al.*, 1976), we have presented the explosion profiles obtained in this area, details of phase correlations and preliminary velocity-depth functions. The correlations on KEQ_S (Fig. 3) are rather similar to those on the explosion profiles and in particular the general pattern is quite similar

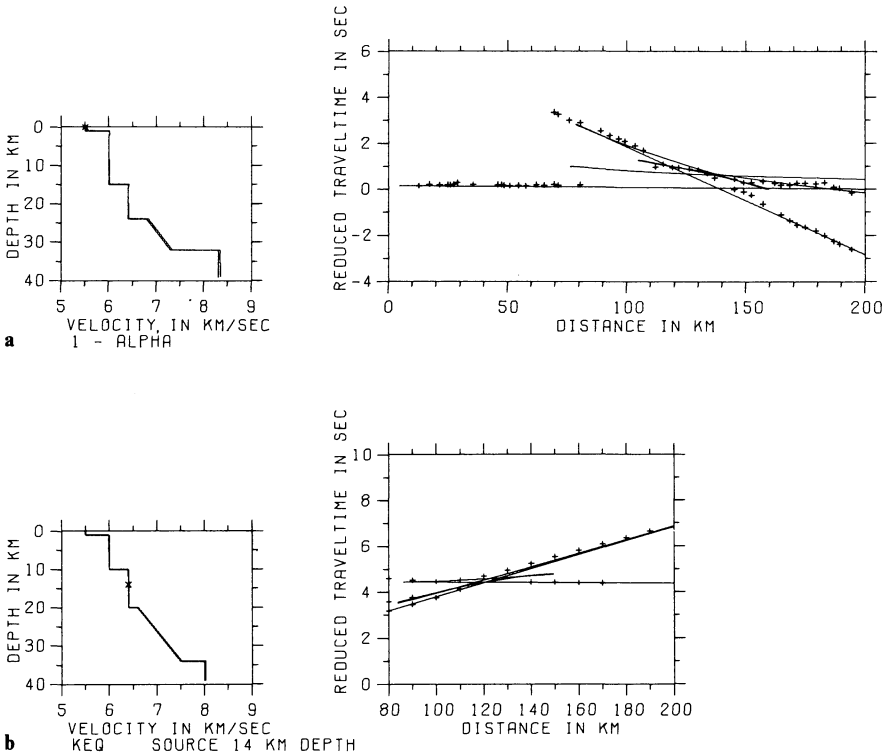


Fig. 4. (a) Velocity-depth function and travel-time diagram of the profile 1-ALPHA (from Bamford *et al.*, 1976). The travel-times are reduced with 6 km/s. In the travel-time diagram, the crosses indicate observed arrivals, the lines are the theoretical travel-time curves based on the model shown on the left side. (b) Velocity-depth function and travel-time diagram of the profile KEQ_S . The travel-times are reduced with 8 km/s. In the travel-time diagram, the crosses indicate observed arrivals, the lines are the theoretical travel-time curves based on the model shown on the left side. In the velocity-depth function, the cross indicates the position of the focus

to that observed on segment ALPHA from shotpoint 1. On geological grounds and on the basis of other seismic data in the area it is reasonable to expect that observations on KEQ_S and 1-ALPHA sample the same or at least rather similar crustal structure. The velocity-depth function presented for 1-ALPHA by Bamford *et al.* (1976) is shown in Fig. 4a. This model is somewhat more complicated than the simple one (with a two-layer crust) that was used for the initial earthquake location (provided by S. Crampin) and which implied a focal depth of less than 10 km. However, a similar velocity-depth function with modifications to the depths and characteristics of some layers, fits the observed KEQ_S travel-times quite well (Fig. 4b), although we must emphasize that this structure is not necessarily unique. In this model, the 6.4 km/s layer remains about 10 km thick, but the gradient zone beneath it is thickened so as to explain the relative separation of P_n and the phase reflected from the bottom of the 6.4 km/s layer. The small separation between this reflection and the P wave refracted at 6.4 km/s indicates that the source should be close to the middle of a 10 km thick layer. Arrivals through the top two layers are not observed and the depth to the 6.0/6.4 interface is controlled simply by requiring P_n arrivals to occur at the correct reduced time (about 6 seconds on the section reduced to 8 km/s). The total effect is to locate the earthquake at a depth of 14 km.

At this stage, no detailed interpretation of S phases has been attempted. However, the relationship between the P -velocity model shown in Fig. 4b and the corresponding S -velocity model can be tested simply by plotting the theoretical travel-times in Fig. 4b on the same scale as the observed P -sections and then overlaying them on the observed S -sections (already plotted according to the $\sqrt{3}$ relationship). These predicted S -travel-time curves are plotted in the upper part of Fig. 3, the observed KEQ_S S -section. They appear to agree quite well with observed phases, and this suggests that the nominal $\sqrt{3}$ ratio is in fact close to the real value.

5. Discussion

By a fortunate accident we have obtained near-earthquake and explosion data of high quality in the same area and thereby have a unique opportunity to broaden our knowledge of lithospheric structure. Clearly a detailed interpretation of the KEQ data should be carried out in conjunction with, and will add significantly to, the evaluation of our explosion data. In this paper we have presented some preliminary results of such a joint interpretation.

Our intention in presenting the KEQ data here is to show the strong relationship between high-quality earthquake data and high-quality explosion data when both are available in the same area. The two sorts of data contain slightly different but compatible information on crust-mantle structure; joint interpretation yields both an improved model of this structure and a much more reliable estimate of the source parameters of the earthquake. Thus, even at a preliminary stage of interpretation, an improved estimate of the focal depth of KEQ has been obtained.

Our conclusions are, we believe, important on both scientific and economic grounds for, as we seek a greater understanding of lithospheric structure and as our ability to locate earthquakes improves, the possibility of using an inexpensive natural source in seismically active areas will become increasingly attractive. With a few explosions as control, earthquakes recorded on a closely spaced mobile array could be used to study the fine structure of the lithosphere.

Furthermore, we note that because of the LISPB data there will be a larger body of instrumental data than for any previous British earthquake allowing a very detailed investigation. Investigation of the other earthquakes in the same series should benefit from the good solution for this one.

Acknowledgements. We are grateful to Stuart Crampin and Graham Neilson, IGS Seismology Unit, Edinburgh, for providing a preliminary location for KEQ.

The LISPB field experiments were supported by the National Environmental Research Council (NERC) and the German Research Society (Deutsche Forschungsgemeinschaft). We are grateful to Max Wyss for his comments on a first draft of this paper. Ingrid Hörnchen typed the manuscript.

References

- Agger, H.E., Key, F.A.: The Glasgow earthquake recorded at the UKAEA seismological array at Eskdalemuir. *Geophys. J.* **9**, 537–539, 1965
- Bamford, D., Faber, S., Jacob, B., Kaminski, W., Nunn, K., Prodehl, C., Fuchs, K., King, R., Willmore, P.: A lithospheric seismic profile in Britain. I. Preliminary results. *Geophys. J.* **44**, 145–160, 1976
- Browning, G.R.J., Jacob, A.W.B.: Preliminary study of the north of England earthquake of August 9, 1970. *Nature* **228**, 835–837, 1970
- Cleary, J.: Array and multi-station analysis of an earthquake in Cornwall: a comparative study. *Geophys. J.* **12**, 437–441, 1967
- Crampin, S., Jacob, A.W.B., Neilson, G.: The Glenalmond earthquake series, February 1970–March 1972. *Nature* **240**, 233–236, 1972
- Davison, C.: A history of British earthquakes, 409 p. London: Cambridge University Press 1924
- Jacob, B., Willmore, P.: Teleseismic P waves from a 10 ton explosion. *Nature* **236**, 305–306, 1972
- Key, F.A., Marshall, P.D., McDowall, A.J.: Two recent British earthquakes recorded at the UK Atomic Energy Authority array at Eskdalemuir. *Nature* **201**, 484–485, 1964
- Lilwall, R.C., Riddle, G.: Earth tremor near Todmorden of March 1972. *Nature* **244**, 113–114, 1973

Received September 15, 1975

Rayleigh Channel Waves for the In-Seam Seismic Detection of Discontinuities

L. Dresen and S. Freystätter

Institut für Geophysik der Ruhr-Universität Bochum, Postfach 21 48,
D-4630 Bochum-Querenburg, Federal Republic of Germany

Abstract. Two-dimensional seismic models are used to reproduce the geological sequence cheek-seam-cheek in deep coal mines. The known reflection method based on Rayleigh channel waves is investigated with respect to discontinuities being composed of a termination of the seam and a fractured zone outside the seam. By means of fractured zones having different reflection coefficients discontinuities are designed representing clay hogs or micro-tectonic faults. Results obtained by investigating amplitudes, frequencies and phase velocities show a strong increase of the rate of amplitude decay with decreasing phase velocity. Furthermore it is demonstrated that the part of the Rayleigh channel wave propagating outside the seam is responsible for the detectability of a discontinuity. Expressing the detectability numerically the ratio E_R of the channel wave's energy inside the seam to its total energy has been used. The value 0.5 for E_R is derived to be a standard value for distinguishing the phase velocity range for which reliable reflection surveys are possible ($E_R > 0.5$) or not ($E_R < 0.5$).

Key words: Detection of discontinuities in deep coal mines – Rayleigh channel waves – Reflection method – Model seismic experiments.

1. Introduction

1.1. The In-Seam Seismic Detection Methods

The increasing mechanisation of coal winning methods and hence the confinement to few intensively exploited coal seams essentially requires the knowledge of the field in front of the operating face. A variety of methods have been examined to predict discontinuities of the coal seam, e.g. microtectonic faults, clay hogs, jamas etc., in front of the operating face. Seismic methods have turned out to be the most promising ones (Baule, 1967). Applying seismic waves in mines for prediction means to use channel waves. As coal has low body wave velocities

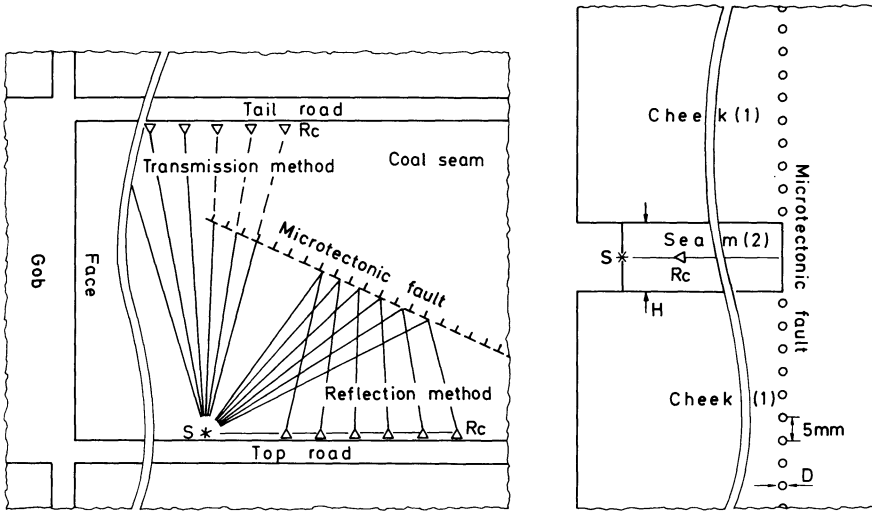


Fig. 1. Experimental set-up in a deep coal mine (left hand side) and on a two-dimensional model (right hand side). S seismic source, R_c Receiver

compared with the cheek—i.e. the rock above and below the seam—channel waves can be generated by a seismic source inserted in the coal. Channel waves propagate along the coal seam and can clearly be recorded at distances as far as 1.5 km from the source (Arnetzl, 1971).

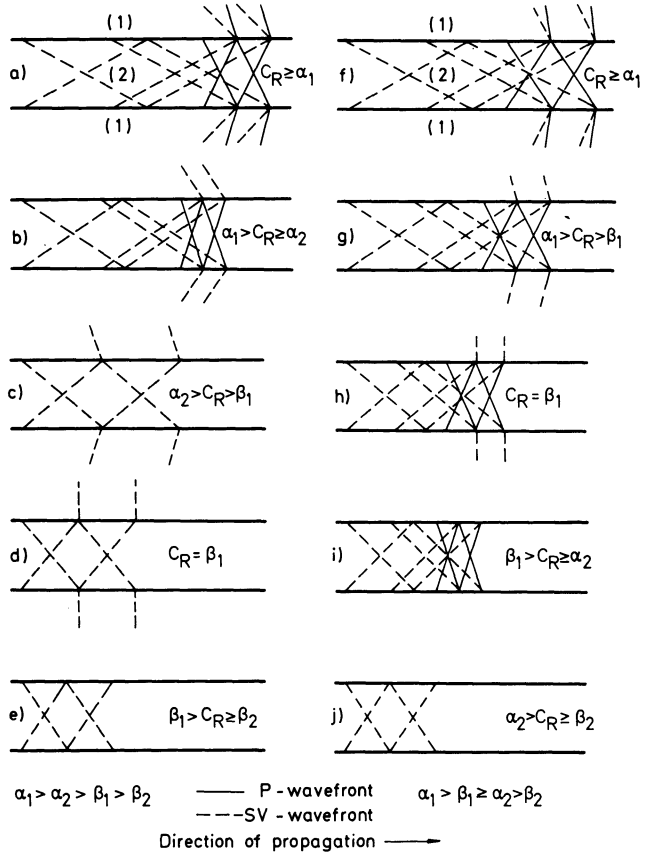
Two methods used for predicting discontinuities are based on channel waves. These methods are to observe channel waves reflected from the discontinuity or to observe the distortion of channel waves being transmitted past the discontinuity (cf. left hand side of Fig. 1). The reflection method has the advantage that it yields not only the presence of a discontinuity but also its location. Therefore this paper will primarily be concerned with the reflection method.

Although the fundamental ideas of the in-seam seismic detection of discontinuities and successful applications have been published (Krey, 1963; Arnetzl, 1971) the method sometimes fails. In these cases of failure it has not been possible to find out whether this failure is due to the properties of channel waves or due to improper field procedures (Brentrup, 1970).

1.2. Properties of the Rayleigh Channel Wave

One of the ways to study the fundamental properties of channel waves is to carry out experiments using seismic models. Two-dimensional seismic models can be used to investigate Rayleigh channel waves and three-dimensional ones to investigate Love and Rayleigh channel waves simultaneously. Because two-dimensional models enable us to record the seismic signal at any distance from the source they are a powerful tool to investigate channel waves in the neighbourhood of a reflecting discontinuity. Thus in this paper the behaviour of the Rayleigh channel wave is described.

Fig. 2. Wave front patterns of the symmetrical Rayleigh channel wave



In nature the P-wave velocity in the coal α_2 may be higher or lower than the SV-wave velocity in the cheek β_1 . Thus two orderings of the body wave velocities are possible:

- i) $\alpha_1 > \alpha_2 > \beta_1 > \beta_2$
- ii) $\alpha_1 > \beta_1 \geq \alpha_2 > \beta_2$,

where α_1 is the P-wave velocity in the cheek and β_2 is the SV-wave velocity in the coal.

Since seam thicknesses in West-Europe are commonly smaller than 2 m the lowest possible – so-called fundamental – mode is of interest. Since furthermore the sequence cheek-seam-cheek modelled by means of two-dimensional seismic techniques (cf. right hand side of Fig. 1) represents a symmetrical low velocity channel the fundamental mode is the first symmetrical mode.

Depending upon the relationship of the phase velocity C_R of the Rayleigh channel wave to each of the body wave velocities there may exist leaking or normal modes. The normal modes are important for the application discussed. The wave front patterns a-c and f-g in Figure 2 represent the leaking mode domain and interference patterns d-e and h-j represent the normal mode domain. According

to the interference patterns d and h we have to expect some portions of the normal mode domain's seismic signal being composed of the channel wave and the critically refracted SV-wave. According to our observations the critically refracted SV-wave can have a predominant influence.

Referring to Figure 2 we find that two situations can exist for normal modes of the Rayleigh channel wave: If $\beta_1 \geq C_R \geq \alpha_2$ PP-, PSV- and SVSV-reflections occur at the roof and the floor (cf. interference patterns h and i). If $\alpha_2 > C_R \geq \beta_2$ the normal mode involves only SVSV-reflections (cf. interference patterns d, e and j). Figure 2 shows that the body wave velocity ordering $\alpha_1 > \alpha_2 > \beta_1 > \beta_2$ yields only the latter type of interference pattern within the normal mode domain whereas the ordering $\alpha_1 > \beta_1 \geq \alpha_2 > \beta_2$ yields both types of interference patterns within the normal mode domain.

1.3. Questions Arising in the Use of Rayleigh Channel Waves for the In-Seam Seismic Detection

For studying the behaviour of the Rayleigh channel wave during its propagation from the source to the discontinuity and from the discontinuity to the receiver the two-dimensional model shown on the right part of Figure 1 is used. This model represents the simplest geometry found in nature namely a seam embedded between two homogeneous, isotropic rock halfspaces. The model contains a discontinuity normal to the stratification. This discontinuity can represent a clay hog as well as a microtectonic fault. Since microtectonic faults have the property that they do not only terminate the seam but are also accompanied by a fractured zone in the cheek being filled with mylonite a single row of holes has been inserted above and below the end of the model seam. Various diameters D of the holes were used. So for $D=0$ mm the model represents a seam terminated by a clay hog whereas for $D>0$ mm microtectonic faults having fractured zones with different elastic properties are investigated.

Concerning the case $D=0$ mm model investigations had been carried out by Freystätter (1974). His results showed that only a portion of the direct Rayleigh channel wave belonging to the normal mode domain is reflected by the discontinuity.

Thus the following question arises:

i) For what range of phase velocities will normal mode waves be reflected by a clay hog or a microtectonic fault?

Freystätter (1974) also showed that even a high value for the absorption of the low velocity coal layer will not seriously effect the shape of the dispersion curve. However we expect a change in the properties of the channel wave along the path of propagation.

This leads to another question:

ii) What sort of change can be expected for the amplitude, phase velocity and frequency of that portion of the direct channel wave which contributes the main energy to the reflected wave?

Answering these questions we have investigated the behaviour of the Rayleigh channel wave along its travel path and at the discontinuity of the seam by means of a number of two-dimensional models.

Some important preliminary measurements concerning materials and modelling the discontinuity are described in Section 2. The results of the model experiments are given in Section 3. Conclusions will follow in Section 4.

2. Details of the Model Seismic Technique and Models Used

2.1. Equipment

The equipment is similar to the one commonly used for the analogue recording model seismograms gained with the ultrasonic transducer technique (e.g. O'Brien and Symes, 1971; Behrens and Waniek, 1972; Dresen, 1972). Due to the possibility of expanding any portion of the seismic signal the set-up used allows a maximum accuracy for analogue recording (Freystätter, 1974). The mean square error produced by the complete set-up amounts to $\pm 2\%$ with respect to phase velocity measurements, $\pm 3\%$ with respect to frequency measurements and $\pm 6\%$ with respect to amplitude measurements.

2.2. Materials

Concerning the cheek in all cases an Aluminium plate has been used as model material (cf. Table 1).

In modelling the case $\alpha_1 > \alpha_2 > \beta_1 > \beta_2$ we found only Pertinax[®] to be a useful material for the seam. As Pertinax is made of several layers of paper coated with phenol resin and the tensile strength of the paper varies with the direction of strain the material is not isotropic. The body wave velocity distribution measured in Pertinax equals the one of an ideal transversely isotropic material (Postma, 1955) within $\pm 2\%$.

In modelling the case $\alpha_1 > \beta_1 \geq \alpha_2 > \beta_2$ we solved the problem of finding a material with a P-wave velocity close to the SV-wave velocity in Aluminium by filling epoxy resin – or its derivative the glue Araldite[®] – with tiny glass balls (Ballotini[®]) which have a diameter of 75 μm to 150 μm . Different rates of filler

Table 1. Parameters of the model materials. The dimension [mm/ μs] used for the models equals the dimension [km/s] used for in-situ measurements

	P-wave velocity α [mm/ μs]	SV-wave velocity β [mm/ μs]	Density ρ [g/cm ³]	Absorption coefficient a_A [dB/ λ]
Aluminium	5.44	3.13	2.7	<0.01
Pertinax	parallel to strike:		1.4	0.65
	4.12	2.18		
	perpendicular to strike:			
	3.3	2.18		
Araldite + Ballotini (1:2)	2.86	1.72	1.63	0.9
Epoxy Resin + Ballotini (1:2)	2.86	1.72	1.63	0.85
Plexiglas	2.33	1.36	1.2	0.7

enable the fabrication of materials with P-wave velocities in the range of approximately 2 mm/ μ s to approximately 3 mm/ μ s. The advantage of this composed material is not only the wide range of body wave velocities but also the non-necessity of an additional bonding layer between the materials for seam and cheek. Besides this we have used the classic model material Plexiglas[®] for the seam.

The combined use of transversely isotropic and isotropic materials does not affect the interpretation by means of dispersion curves calculated according to Anderson (1971). One of the conspicuous properties of the low velocity channel to be investigated is the high absorption contrast between seam and cheek. We may assume the cheek to have an absorption constant between 0.01 and 0.1 dB/ λ whereas the absorption constant of coal has the order of magnitude of 1 dB/ λ . We can generally say that the comparison of the model materials' parameters with the values occurring in nature (Schwaetzer and Desbrandes, 1965; Baule, 1967) show an appreciable correspondence.

2.3. Models

Properties of the models determining the frequency range of the generated Rayleigh channel wave are given in Table 2. I.e. the predominant frequency f_p

Table 2. Parameters of models used. Aluminium has been taken to model the cheek. The dimension [kHz · mm] used for the model measurements equals the dimension [Hz · m] used for in-situ measurements

Materials for the series of models investigated	Code number for the series of models investigated	Pre-dominant frequency of the seismic source f_p [kHz]	Thickness of low-velocity layer (coal seam) H [mm]	Length of low-velocity layer (coal seam) L [mm]	Source-Receiver Distance		Reflector-Receiver Distance	
					x_A [mm]	x_B [mm]	x_C [mm]	x_D [mm]
Aluminium/Pertinax	0312	108	12.6 ± 0.3	785	160	680	105	615
Aluminium/Araldite + Ballotini (1:2)	0506	108	6.2 ± 0.2	770	200	520	50	570
Aluminium/Epoxy Resin + Ballotini (1:2)	0409	108	9.5 ± 0.3	780	200	600	140	580
Aluminium/Araldite + Ballotini (1:2)	0518	108	18.7 ± 0.3	770	240	760	130	610
Aluminium/Plexiglas	0106	108	6.9 ± 0.2	770	240	720	170	570
Aluminium/Plexiglas	0115	108	15.1 ± 0.3	780	280	720	180	580

of the model seismic source and the thickness H of the low velocity layer (coal seam). The length L of the low velocity layer is given too. It follows that the ratio L/H is similar to the situation given in a coal mine.

Furthermore the different investigated series of models have been coded such that the first two figures characterize the material combination and the last two figures characterize the thickness of the seam. Each series of models includes one model containing no fractured zone in the cheek and three models containing a fractured zone with D equals 2 mm, 3 mm and 4 mm.

The source-receiver distances and reflector-receiver distances give the limitations of the range within the records have been evaluated. They will be discussed in paragraph 4.1.

2.4. Experimental Determination of Reflection Coefficients

To get an idea of the influence of the fractured zone on the reflection process of Rayleigh channel waves taking place at the discontinuity of the seam we have experimentally determined the reflection coefficients at different types of reflectors. For this determination we used the amplitudes of the direct and reflected non-dispersive Rayleigh wave propagating normal to the reflector.

The reflection coefficients valid for a single row of holes having a diameter of 2 mm, 3 mm and 4 mm are given in Table 3, line 1 to 3. For comparison the reflection coefficient valid for a thin bonding layer (thickness approximately 0.3 mm) between two Aluminium plates has been measured (cf. Table 3, line 4). According to these results the reflection coefficients valid for fractured zones represented by a row of holes lie in the same order of magnitude as the reflection coefficient valid for the sequence Aluminium/thin bonding layer/Aluminium which is, with respect to its shape, a more typical fractured zone.

Table 3. Reflection coefficients at various reflectors determined by means of the nondispersive Rayleigh wave

	Type of reflector	Reflection coefficients		Remarks
		Component perpendicular to the reflector	Component parallel to the reflector	
1	Aluminium plate containing a single row of holes $D = 2$ mm	0.23 ± 0.03	0.16 ± 0.01	The distances between the holes' centres equal 5 mm
2	Aluminium plate containing a single row of holes $D = 3$ mm	0.50 ± 0.05	0.36 ± 0.01	
3	Aluminium plate containing a single row of holes $D = 4$ mm	0.72 ± 0.08	0.57 ± 0.02	
4	Aluminium/Aluminium Bonding material: Araldite	0.58 ± 0.06	0.40 ± 0.02	The thickness of the bonding layer equals ca. 0.3 mm
5	Plexiglas/Aluminium Bonding material: Araldite	0.42 ± 0.08	0.40 ± 0.04	

However the advantage of the hole-drilling technique is the possibility of producing a set of different fractured zones having reliably reproducible reflection coefficients by means of simply changing the diameter of the holes.

Moreover the reflection coefficient of the materials at the termination of the seam, like e.g. Plexiglas and Aluminium, can be assumed to lie within the range of reflection coefficients valid for the various fractured zones (cf. Table 3, line 5). Hence follows that cases with both relatively low and relatively high influence of the fractured zone are covered by our models. Thus the models correspond with the geological situation in deep coal mines.

3. Model Experiments Concerning Direct and Reflected Rayleigh Channel Waves

3.1. General Remarks

In this part the questions

i) For what range of phase velocities will normal mode waves be reflected by a clay hog or a microtectonic fault?

and

ii) What sort of change can be expected for the amplitude, phase velocity and frequency of that portion of the direct channel wave which contributes the main energy to the reflected wave?

will be answered by means of model experiments. The answer of question ii) will be based on measured values. The answer of question i) however will be based on the mean square errors of these measured values. Therefore we shall firstly discuss question ii) and thereupon question i).

As the features of the reflection process are of main interest the properties of both the direct and the reflected normal mode signal have been investigated. According to the evaluation of analogously recorded signals the oscillation of the direct channel wave with the maximum double amplitude has been evaluated (Fig. 3). Concerning the reflected wave the portion corresponding to the mentioned oscillation of the direct wave with the maximum double amplitude has been evaluated. It should be pointed out that this portion does not always contain the maximum double amplitude of the reflected wave's signal. As an example Figure 3 contains a single seismogram measured for a source-receiver distance of 660 mm (cf. total seismogram section in Fig. 9 b). The signal's portions I, II, III and III_r are labelled "wave groups" and correspond to different parts of the dispersion curve (cf. Freystätter, 1974).

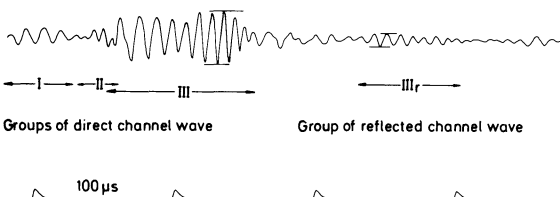


Fig. 3. Seismogram containing several groups of Rayleigh channel waves

The measurements of the direct wave's properties were carried out within the source-receiver distances x_A and x_B and the one's of the reflected wave were carried out within the reflector-receiver distances x_C and x_D (cf. Table 2). These limitations had to be chosen because of the superposition of different wave groups close to the source and close to the receiver.

3.2. Rate of Amplitude Decay

Due to the measurements being carried out on each model of a model series we have derived average values for the rate of amplitude decay between x_A and x_B and x_C and x_D respectively. The decay of the amplitude of both the direct and the reflected wave has been proved to be approximately an exponential one. This has led us to dimension the rate of decay in dB/H thus getting a constant for a given model. Hence follows the equation defining the rate of amplitude decay a of the direct wave:

$$a[\text{dB}/H] = \left| 20 \cdot \frac{\log A(x_B) - \log A(x_A)}{x_B - x_A} \right|$$

where x_A and x_B are expressed in units of H (thickness of the coal seam). A similar equation is valid describing the rate of amplitude decay a_r within the range between the reflector-receiver distances x_C and x_D .

Referring to Table 4 we find the numerical values of a and a_r distinctly differing. For the series of models 0506, 0409, 0518, 0106 and 0115 – representing the body wave velocity ordering $\alpha_1 > \beta_1 \geq \alpha_2 > \beta_2$ – the ratio a_r/a lies between 0.6 and 0.7. I.e. the rate of amplitude decay of the direct wave is clearly higher than the one of the reflected wave.

Concerning the model series 0312 – representing the body wave velocity ordering $\alpha_1 > \alpha_2 > \beta_1 > \beta_2$ – the numerical values of a and a_r distinctly differ too, yet this time the rate of amplitude decay of the direct wave is clearly lower than the one of the reflected wave.

Table 4. Coefficients of the Rayleigh channel wave yielded by means of model seismic measurements

Code number for the series of models investigated	Rate of amplitude decay			Rate of frequency change			Rate of phase velocity change		
	Direct channel wave a [dB/H]	Reflected channel wave a_r [dB/H]	Ratio a_r/a	Direct wave b [dB/H]	Reflected wave b_r [dB/H]	Ratio b_r/b	Direct wave c [dB/H]	Reflected wave c_r [dB/H]	Ratio c_r/c
0312	0.015	0.022	1.5	-0.048	-0.0079	0.2	0.0027	0.0019	0.7
0506	0.085	0.06	0.7	-0.017	-0.0035	0.2	0.0011	0.0027	2.5
0409	0.16	0.089	0.6	-0.025	-0.0059	0.25	0.0024	0.0018	0.8
0518	0.24	0.17	0.7	-0.067	-0.034	0.5	0.0058	0.0097	1.7
0106	0.22	0.13	0.6	-0.022	-0.0078	0.4	0.003	0.0011	0.4
0115	0.33	0.23	0.7	-0.028	-0.021	0.8	0.0081	0.0062	0.8

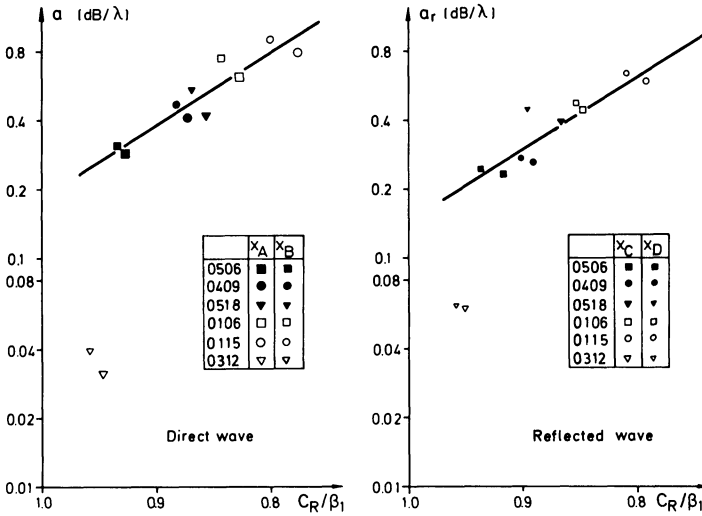


Fig. 4. Amplitude decay of the Rayleigh channel wave

The absolute values of the rate of amplitude decay distinctly differ for the body wave velocity ordering $\alpha_1 > \beta_1 \geq \alpha_2 > \beta_2$ and the ordering $\alpha_1 > \alpha_2 > \beta_1 > \beta_2$.

Because we know from Table 1 that the absorption coefficients of all materials used for modelling the seam lie in the same order of magnitude, the different values for a or a_r , respectively can be explained by the influence of the critically refracted SV-wave (cf. Section 1.2, Fig. 2, pattern d).

For the application of the in-seam seismic detection of discontinuities in deep coal mines it is necessary to get an idea about the rate of amplitude decay depending on the phase velocity C_R of the channel wave or the frequency respectively. This relationship is given in Figure 4 for the measured values of C_R being normalized with β_1 and the values a [dB/λ] or a_r [dB/λ] derived from a [dB/H] or a_r [dB/H] by means of phase velocity and frequency determined for the distances x_A , x_B , x_C and x_D . Figure 4 shows that assuming the body wave velocity ordering $\alpha_1 > \beta_1 \geq \alpha_2 > \beta_2$ (0506, 0409, 0518, 0106 and 0115) and an order of magnitude of 1 [dB/λ] for the absorption coefficient of body waves in the seam material (cf. Table 1) the rate of amplitude decay of the Rayleigh channel wave strongly increases with decreasing phase velocity. According to the discussed ratio a_r/a the absolute values of a and a_r are different yet the curves slopes coincide. This is understandable because the different absolute values are due to the reflection process whereas the discussed curve's slope is a function of the material constants. According to Table 1 these material constants differ for the investigated series of models. Thus the experimentally derived curve provides an evidence to take the numerical value of its slope for estimating the increase of the rate of amplitude decay of several different material combinations. The value for the model series 0312 representing the velocity ordering $\alpha_1 > \alpha_2 > \beta_1 > \beta_2$ which does not fit into the curves of Figure 4 is due to the predominant influence of the critically refracted SV-waves (refer to Section 1.2).

As in these investigations materials with body wave absorption coefficients similar to those existing in nature have been used we may take the graphs given in Figure 4 as a reliable aid for in-situ measurements in deep coal mines. Thus we may assume the numerical values for the rate of amplitude decay of the Rayleigh channel wave to lie in the range of 0.1 to 1 dB/λ where the geometrically caused spread has still to be taken into account.

3.3. Rate of Frequency Change and Rate of Phase Velocity Change

According to the measurements the frequency change and the phase velocity change proved to be approximately exponential ones, too. Thus the rate of frequency change b of the direct wave and b_r of the reflected wave have been derived from the measured signals analogously to a and a_r :

$$b \text{ [dB/H]} = 20 \frac{\log f(x_B) - \log f(x_A)}{x_B - x_A}$$

where f is the predominant frequency of the investigated channel wave portion. x_A and x_B are again expressed in units of H . A similar equation has been used for b_r .

The values of the rate of phase velocity change c of the direct and c_r of the reflected channel wave are gained by means of equations similar to the one for b .

According to Table 4 the numerical values of b , b_r , c and c_r are approximately one and two orders of magnitude smaller than the ones of a and a_r . Thus deter-

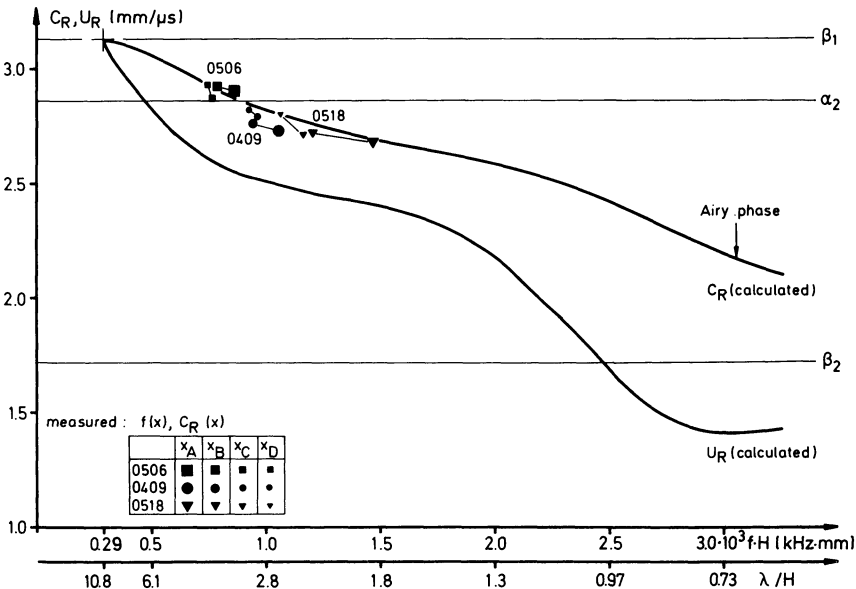


Fig. 5. Comparison between calculated dispersion curves and measured frequency and phase velocity values

mining the absolute values is rather problematic. Only the order of magnitude and the tendency being evident in all measurements is a reliable base for conclusions.

According to this statement the rate of frequency change b or b_r lies between -0.01 dB/H and -0.1 dB/H whereas the rate of phase velocity change c or c_r lies between $+0.001$ dB/H and $+0.01$ dB/H. The negative sign of b and b_r indicates a decreasing frequency with increasing source-receiver distance and reflector-receiver distance respectively. The positive signal of c and c_r indicates an increasing phase velocity with increasing source-receiver and reflector-receiver distance respectively. This means that the properties of the Rayleigh channel wave's portion being of interest for the in-seam seismic detection method changes along the travel path. In other words the point representing the measurements for a certain source-receiver distance "moves" along the dispersion curve from relatively low phase velocities and high frequencies towards higher phase velocities and lower frequencies (Fig. 5). Hence follows that the group velocity changes along the travel path, too. Thus an error has to be taken into account in determining the discontinuity's distance to the operating face.

The order of magnitude of b , b_r , c and c_r and the tendency determined are easily understood in comparing the measured results with the phase velocity dispersion curve. Concerning the model series 0506, 0409 and 0518 this is shown in Figure 5. For comparison the calculated group velocity U_R has been drawn, too.

3.4. Reflection Coefficient and the Reflecting Discontinuity

The measured reflection coefficients R for each series of models are depicted in Figure 6. According to Figure 6 the continually increasing diameter D of the holes in the cheek which represent the fractured zone leads to a series of increasing reflection coefficients for each series of models. How can this be explained?

This can be explained by means of the channel wave's part propagating outside the seam. To support this statement we have calculated the displacement

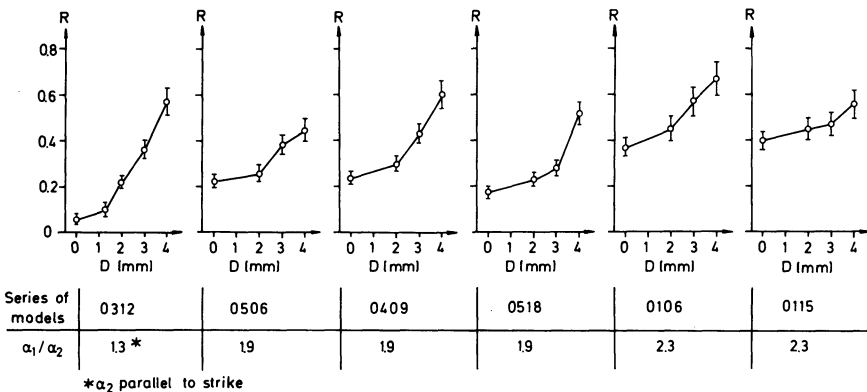


Fig. 6. Reflection coefficient of various discontinuities with respect to the Rayleigh channel wave

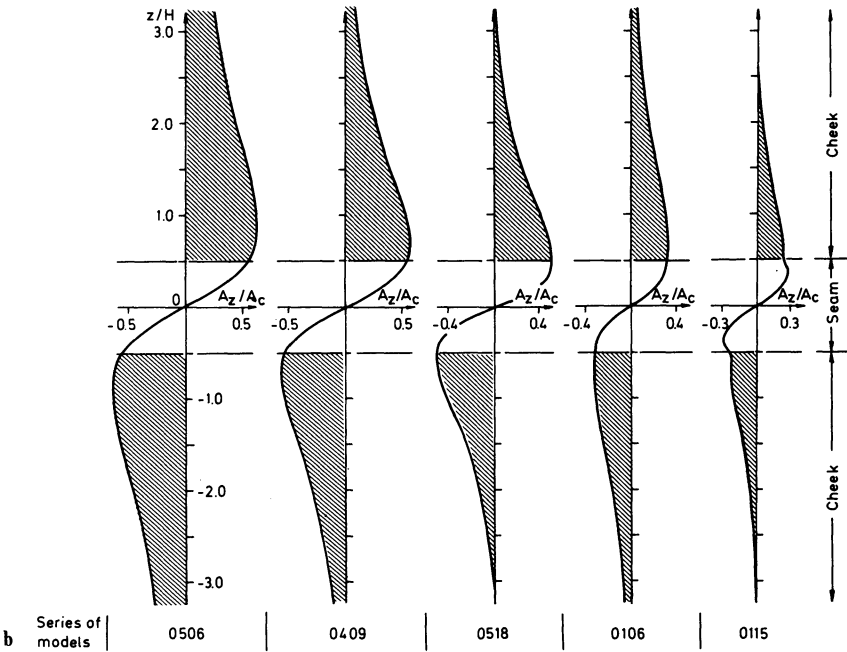
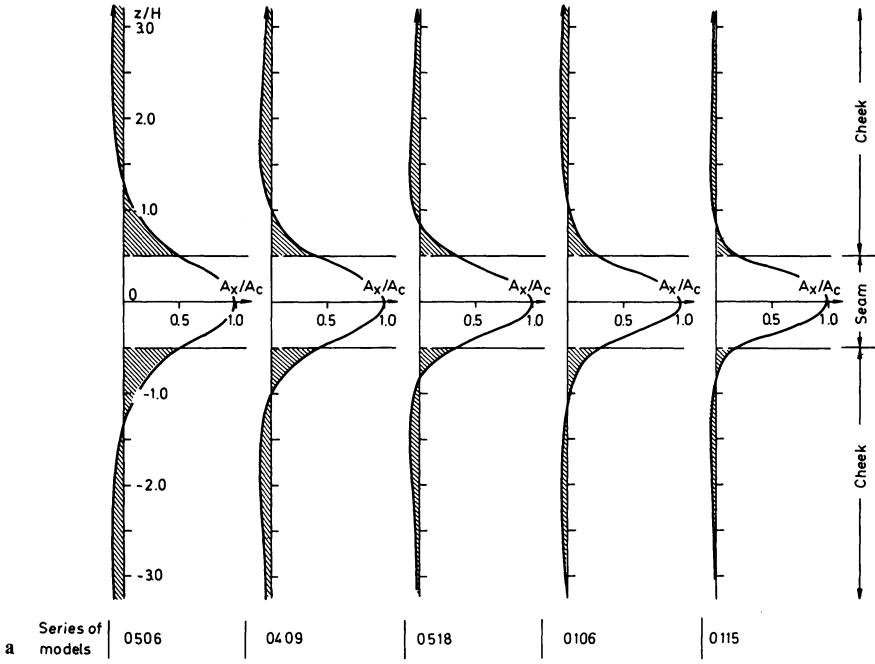


Fig. 7a-b. Amplitude distribution of Rayleigh channel waves along the sequence cheek-seam-cheek

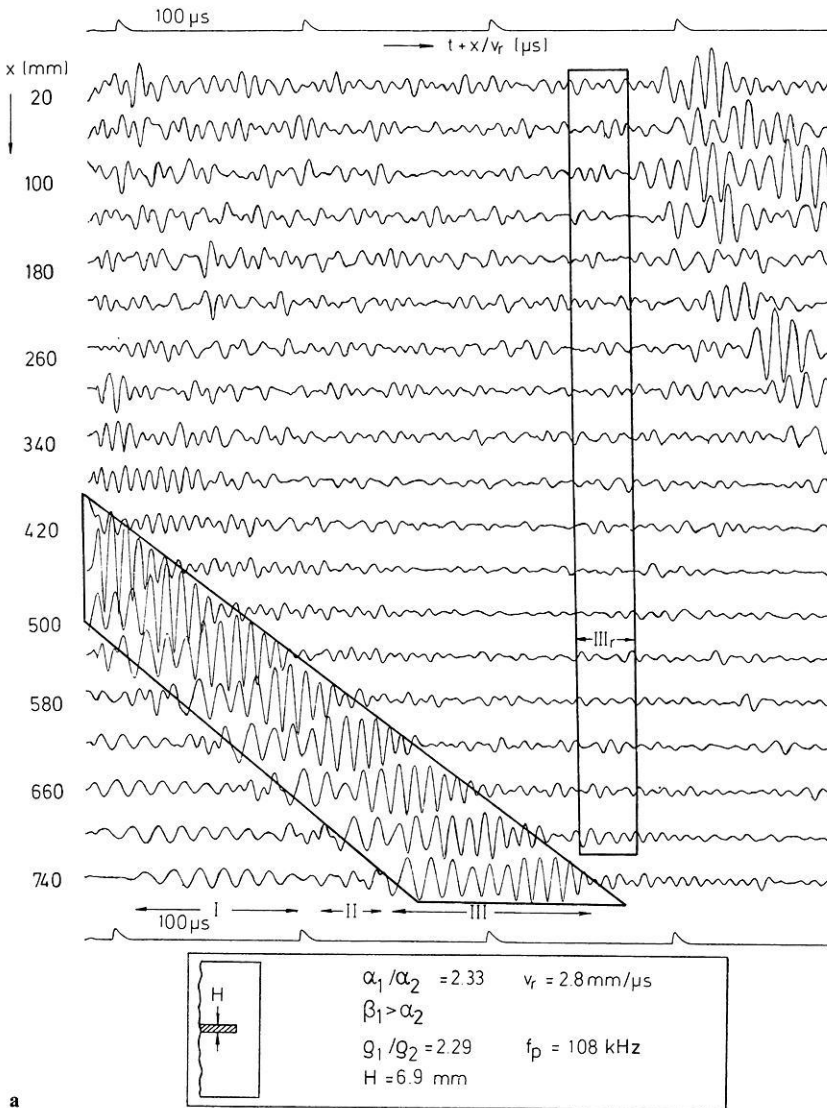


Fig. 8a-b. Seismogram section of the direct (wavegroups I, II, III) and the reflected (wavegroup III_r) Rayleigh channel wave

amplitude distribution (cf. Freystätter, 1974) for the Rayleigh channel wave using the experimentally determined phase velocity and frequency at the reflecting discontinuity. The results for the amplitudes parallel (A_x) and perpendicular (A_z) to the stratification are given in Figure 7a-b. Both amplitudes have been normalized with the maximum amplitude A_c parallel to the stratification in the centre-plane. According to Figure 7a-b the amplitudes of the Rayleigh channel wave outside the seam are not negligible with respect to the reflection process in presence of a fractured zone.

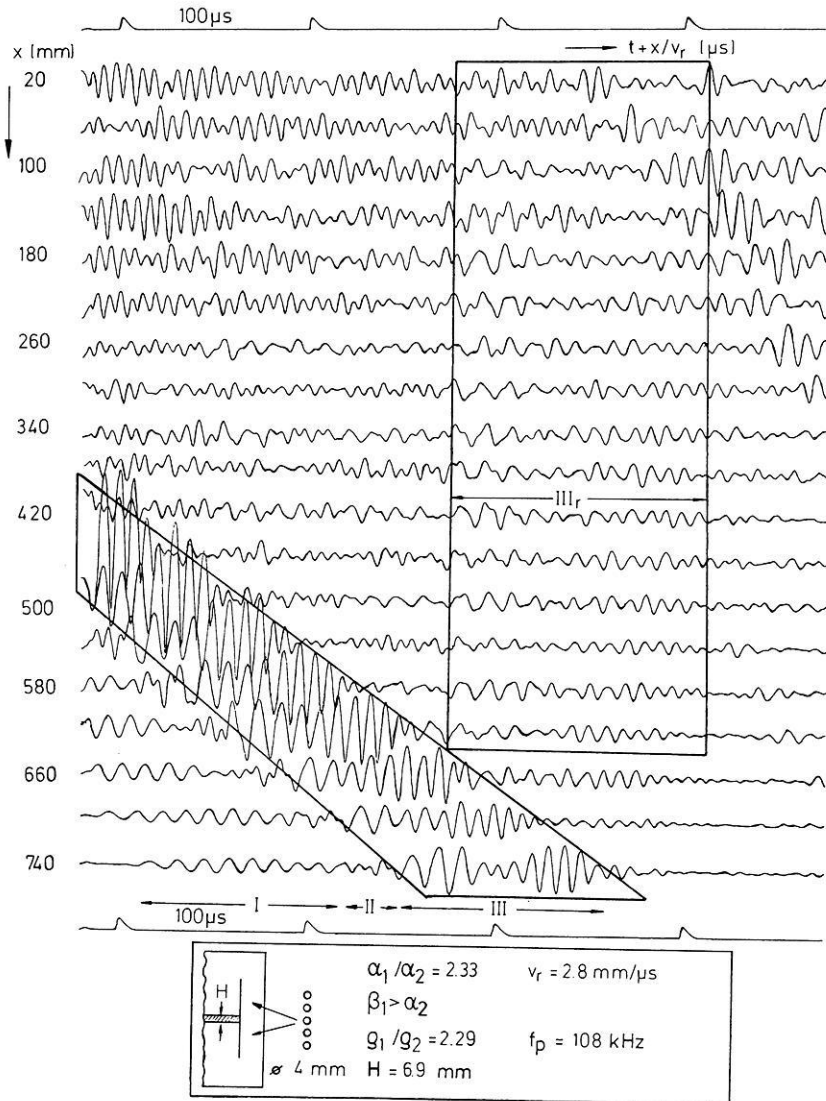


Fig. 8b

Discussing the reflection coefficients for the case $D=0$ mm – i.e. a discontinuity without a fractured zone – we find the trend of increasing reflection coefficients R with increasing P-wave velocity contrast α_1/α_2 (cf. Fig. 6). This is confirmed by distinct steps of R from the model series 0312 to the series 0506, 0409 and 0518 and again from these three series to the series 0106 and 0115.

Discussing the reflection coefficients measured with all series of models for the case $D=4$ mm this distinct stepwise behaviour cannot be observed. According to the results listed in Table 3 we expect the reflection coefficient for a single row

of holes with $D = 4$ mm to be higher than the reflection coefficient for the interface of the material combination with the highest P-wave velocity contrast namely Plexiglas and Aluminium. We thus explain the result found for the case $D = 4$ mm such that the influence of the velocity contrast on the reflection coefficient R has decreased in favour of the influence of the fractured zone.

From these observed results follows that the reflection coefficient for a Rayleigh channel wave at a discontinuity depends on the P-wave velocity contrast and on the existence of a fractured zone in the cheek accompanying the discontinuity. Additionally to this the development of the fractured zone influences the reflection coefficient, too. This means for in-situ measurements that clay hogs will have lower reflection coefficients than microtectonic faults.

3.5. The Detectability of the Reflected Channel Wave

So far only the behaviour of the direct channel wave's portion with the maximum double amplitude and the appropriate reflected channel wave's portion have been discussed. Yet the distinction with which the total reflected wave appears in the seismograms i.e. its detectability has not been quantitatively investigated.

To gain a qualitative impression of the reflected channel wave's shape Figure 8a–b contain seismogram sections for the model series 0106. The models with which the seismograms have been gained only differ in the type of fractured zone due to $D = 0$ mm and $D = 4$ mm. According to Figure 6 this means an increase of the reflection coefficient from $R = 0.37$ for the case $D = 0$ mm to $R = 0.67$ for the case $D = 4$ mm. I.e. approximately a doubling of the reflected channel wave's amplitudes. Moreover comparing the signals of the reflected channel wave in Figure 8a–b we find for $D = 4$ mm the length of the reflected wave's signal distinctly increased which is due to the existence of the fractured zone. Thus its detectability has increased, too.

To estimate the detectability quantitatively the amplitudes' mean square error σ_a of the investigated reflected channel wave's portion has been determined with respect to the amplitude decay curve. Similar quantities for the frequencies (σ_b) and phase velocities (σ_c) have been determined with respect to the frequency change curve and phase velocity change curve respectively. For comparison the mean square errors $\delta_a, \delta_b, \delta_c$ of the appropriate direct wave's portion between the source-receiver distances x_A and x_B have been calculated. From these quantities the integral quantity σ_N was calculated as follows

$$\sigma_N = \pm \frac{1}{3} \left(\left| \frac{\sigma_a}{\delta_a} \right| + \left| \frac{\sigma_b}{\delta_b} \right| + \left| \frac{\sigma_c}{\delta_c} \right| \right).$$

The corresponding parameter δ_N for the direct channel wave equals ± 1 according to

$$\delta_N = \pm \frac{1}{3} \left(\left| \frac{\delta_a}{\delta_a} \right| + \left| \frac{\delta_b}{\delta_b} \right| + \left| \frac{\delta_c}{\delta_c} \right| \right).$$

In Figure 9 the values of σ_N and δ_N are depicted for each model series. The upper hatched area between $|\sigma_N|$ and $|\sigma_N| - |\delta_N|$ represents the values of $|\sigma_N|$ expected

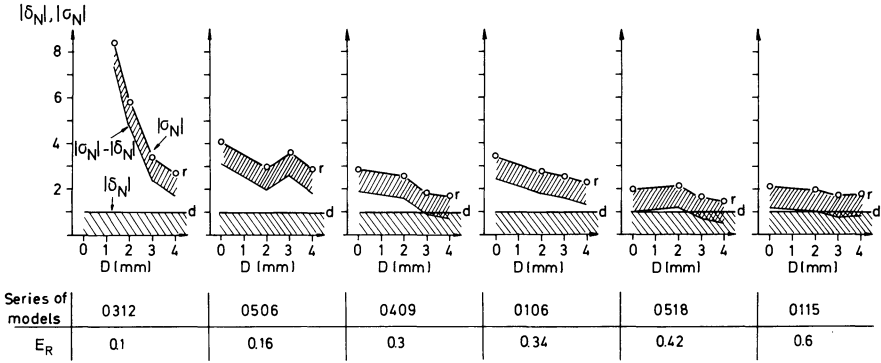


Fig. 9. Detectability σ_N of the reflected Rayleigh channel wave

for a measurement. The lower hatched area represents the values of $|\delta_N|$. It is evident that the fractured zone in the cheek influences the detectability of the reflected channel wave. This means according to the shape of the amplitude curves described in Section 3.4 that the part of the channel wave propagating outside the seam plays an important role for the detectability of the reflected channel wave.

It has to be pointed out, that σ_N is a quantity only for model investigations where the modelled geological situation is known. This means σ_N will only provide a tool for in-situ measurements if we are able to combine its information with a measure which can be calculated for a given field case.

For such a measure the energy ratio E_R was defined:

$$E_R = \frac{\int_{-H/2}^{+H/2} \int_0^T \frac{1}{2} \rho (v_x^2 + v_z^2) dz dt}{\int_{-\infty}^{+\infty} \int_0^T \frac{1}{2} \rho (v_x^2 + v_z^2) dz dt}$$

The numerator expresses the kinetic energy over one period T which is transported inside the seam with the thickness H by the Rayleigh channel wave whereas the denominator expresses the kinetic energy over one period T which is transported inside and outside the seam. The quantity ρ is the density and the quantities v_x and v_z are the particle velocities parallel and perpendicular to the stratification. The integration over the second coordinate y has not been mentioned as the results of both numerator and denominator equal each other. Knowing the parameters of cheek and seam – i.e. elastic moduli, densities and thickness of the layer – and taking the commonly used potentials of a symmetrical channel wave we can calculate the quantity E_R without referring to special in-situ measurements.

The numerical values of E_R calculated for the investigated channel wave's portion are given in Figure 9. Comparing the values for E_R and the behaviour of the $|\sigma_N|$ curve for each model series we find for E_R below 0.42 or 0.6 respectively the distinct tendency of a decreasing $|\sigma_N|$ with increasing D . I.e. the detectability of the reflected wave clearly depends on the distinction of the fractured zone. For E_R equals 0.42 or 0.6 this tendency is very weak and the detectability of both channel waves reflected by clay hogs and channel waves reflected by micro-

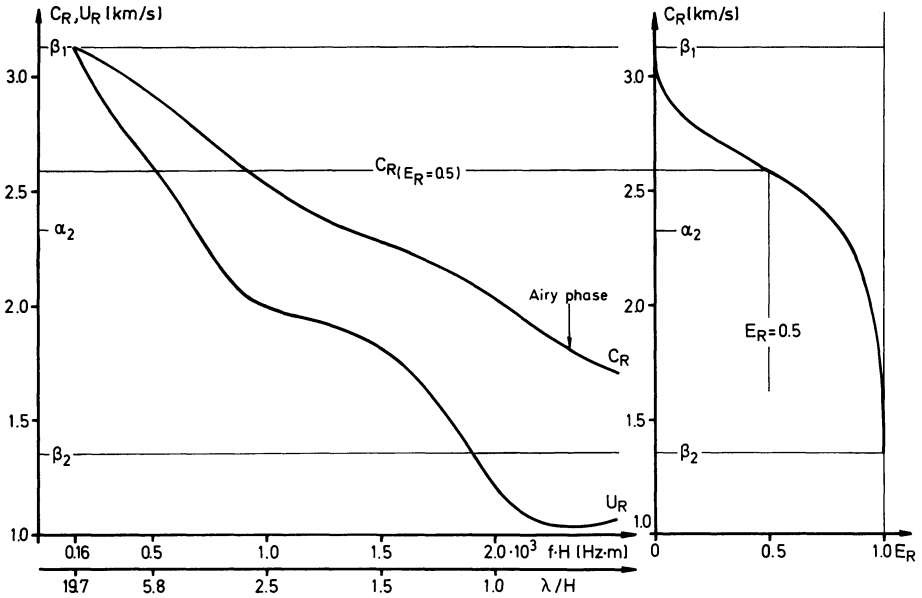


Fig. 10. Example of determining the range of phase velocities useful for the reflection method using Rayleigh channel waves

tectonic faults is similar. Furthermore according to the relatively close neighbourhood of both hatched areas we expect a good detectability for these discontinuities. According to this the value 0.5 for E_R seems to us to be a useful standard value for distinguishing that part of the Rayleigh channel wave being reliable with respect to the reflection method from the impracticable one.

Figure 10 demonstrates for body wave velocity values equal to those of the models 0106 and 0115 how the confinement given by E_R equals 0.5 divides the dispersion curve into two parts. Within the upper one we cannot expect reliable results with respect to the existence or non-existence of discontinuities. Yet within the lower one we may expect to yield results which can reliably be used to determine a discontinuity inside a coal seam.

4. Conclusions

In this paper the principle usefulness of Rayleigh channel waves with respect to the in-seam seismic reflection method has been investigated by means of two-dimensional seismic models. For this purpose the simplest model for a coal seam has been chosen namely a symmetrical low velocity channel. Likewise the simplest type of discontinuity in a coal seam has been chosen too i.e. a complete cut-off normal to the stratification. Furthermore the influence of a fractured zone in the cheek accompanying the discontinuity has been taken into account. Thus models of the two most common discontinuities – namely clay hogs and microtectonic faults – have been investigated. At the beginning of this paper we have formulated two questions the answers of which we will compile in a comprehended form:

Concerning the Rayleigh channel wave reflected by a discontinuity we have found that the part of the channel wave propagating outside the seam plays an important role. To rely on a good detectability of the reflected channel wave it is necessary to choose a phase velocity range where this part outside the seam is so small that the numerical value of the ratio E_R between the channel wave's energy in the seam and the channel wave's total energy will preferably be higher than the standard value 0.5. Thus we recommend, prior to the use of Rayleigh channel waves for a given in-situ case to determine the elastic moduli for coal and cheek. With these values the relevant energy ratio curves can be calculated such that a successful use of the Rayleigh channel wave can be estimated.

Concerning the behaviour of that portion of the Rayleigh channel wave which contributes the main energy to the reflected channel wave we have found that the absorption coefficient rapidly increases with decreasing phase velocity. Frequency and phase velocity changes of the portion mentioned above could be observed too. These changes exactly behave as it is expected according to the shape of the phase velocity dispersion curve. In due course we have to consider a change of the group velocity along the travel path of both the direct and the reflected Rayleigh channel wave. Determining the distances between the reflecting discontinuity and the operating coal face this change of the group velocity has to be taken into account.

Acknowledgement. We are indebted to Dr. R. Schepers for stimulating discussions and critically reading the manuscript. The investigation has been carried out under DFG-contract no. Dr 110/2.

References

- Anderson, D. L.: Elastic wave propagation in layered anisotropic media. *J. Geophys. Res.* **66**, 2953–2963, 1961
- Arnetzl, H.: Seismische Messungen unter Tage. Tagungsbericht der Gesellschaft deutscher Metallhütten- und Bergleute, 8.5. 1971, S. 133–141
- Baule, H.: Vorfelderkundung mit geophysikalischen Mitteln. *Mitt. a.d. Markscheidewesen* **74**, 205–228, 1967
- Behrens, J., Waniek, L.: Modellseismik. *Z. Geophys.* **38**, 1–44, 1972
- Brentrup, F.-K.: Seismische Vorfelderkundung zur Ortung tektonischer Störungen im Steinkohlenbergbau. *Glückauf* **106**, 933–938, 1970
- Dresen, L.: Modellseismische Untersuchungen zum Problem der Ortung oberflächennaher kreiszylindrischer Hohlräume in Festgestein, *Berichte des Institutes für Geophysik der Ruhr-Universität Bochum*, Nr. 1, Bochum 1972
- Freystätter, S.: Modellseismische Untersuchungen zur Anwendung von Flözwellen für die untertägige Vorfelderkundung im Steinkohlenbergbau, *Berichte des Institutes für Geophysik der Ruhr-Universität Bochum*, Nr. 3, Bochum, 1974
- Krey, T.: Channel waves as a tool of applied geophysics in coal mining. *Geophysics* **28**, 701–714, 1963
- O'Brien, P. N. S., Symes, M. P.: Model seismology. *Reports on Progress in Physics* **34**, 697–764, 1971
- Postma, G. W.: Wave propagation in a stratified medium. *Geophysics* **20**, 780–806, 1955
- Schwaetzer, T., Desbrandes, R.: Divergences constatées dans la mesure de la vitesse des ondes acoustiques longitudinales du charbon. *Revue Inst. Française Petrol* **20**, 3–26, 1965

Ultrasonic Modelling of a Moving Source

A. Behle* and J. Rohde

Institut für Geophysik, Universität Hamburg,
Bundesstr. 55, D-2000 Hamburg 13, Federal Republic of Germany

Abstract. An ultrasonic model experiment simulating a finite moving source in a plate is described.

The source consisted of five identical piezoelectric transducers, which were triggered one after another to form a delay-line. The “rupture velocity” was kept constant.

The directivity, as introduced by Ben-Menahem, was computed and a good agreement was found between the observations and theoretical predictions. Some differences result from the fact that a discrete number of single sources have been used instead of a continuous moving source, as required by theory.

Key words: Moving source – Model seismology – Directivity.

Introduction

In order to use seismic model experiments as an aid in the study of earthquake phenomena, it is desirable to simulate the effect of fracture upon the generation of seismic waves. This can be achieved by modelling a moving source. Thereby no restrictions exist in principle with respect to the complexity of the structure employed.

The effect of the moving source upon the spectrum of seismic surface and body waves was investigated by Ben-Menahem (1961, 1962 resp.). He showed that the spectrum is modulated by a function depending on fracture velocity and fracture length. The theoretical method was successfully applied to earthquake data and was also tested by an ultrasonic model experiment (Press et al., 1961). In this experiment the receiver instead of the source was moved, making use of the theorem of reciprocity. For practical purpose, however, it seems more suitable to model a moving source directly. This can be done in a number of different

* To whom offprint requests should be sent

ways. It has been possible for us to model a *P*-wave source which moved unilaterally with constant “fracture velocity”. In the same way Schick and Schneider (1964) used a set of three shearing transducers to study the generation of a head wave, but no quantitative treatment with respect to Ben-Menahem’s formulas was presented.

The source, which will be described in the following chapter, has the advantage of being reproducible. This can hardly be achieved by modelling real fractures as has been done by Mansinha (1964) and Savage and Hasegawa (1965), among others.

The 2-Dimensional Ultrasonic Model

There are several different possibilities of modelling the seismic effect of a propagating fault in a plate model:

- a) One could generate a moving crack, which has the disadvantage of being non-reproducible. This, therefore, was not suitable for our purpose.
- b) A dilational wave in a rod, attached to the plate’s surface, will act as a continuous source of elastic waves in the plate at the area of contact. This has been suggested by Koenig (1974, personal communication). The angle between the rod and the plate will control the propagation velocity of the source, which is equivalent to the fracture velocity v_f . Velocity control is best obtained in the

PULSE - DELAY SYSTEM

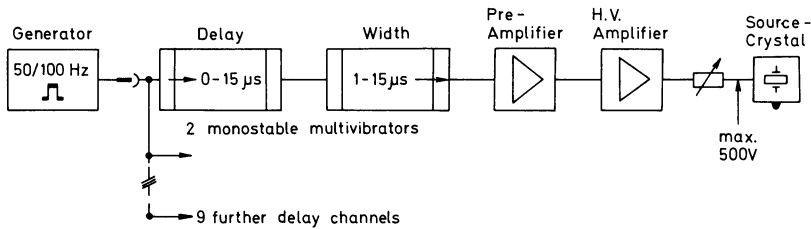


Fig. 1. Schematic diagram of the apparatus used (after Behle et al., 1975)

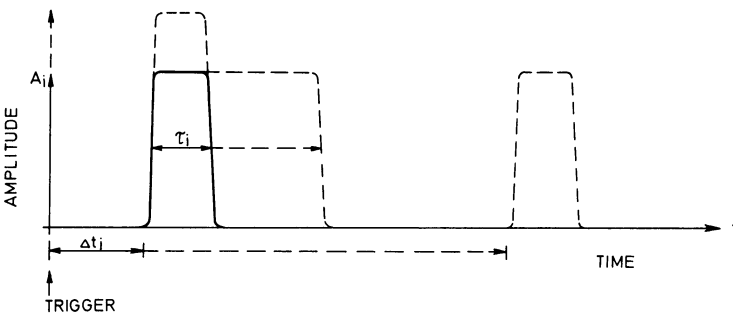


Fig. 2. Schematic representation of the variables of the delaying-system

case of plane wave propagation in the rod. This proved, however, difficult to achieve.

c) A sequence of n sources distributed in the plate and triggered successively with a time-delay $\Delta t_i = (i - 1) \cdot \Delta t$, ($i = 1, \dots, n$) can also be used for the purpose. This method has also been suggested by Press et al. (1961) and represents an experimental approximation to the theoretical concept of Ben Menahem. We have made use of this method with five equivalent sources.

A delaying system has been developed by R. Herber and R. Nortmann¹, which can be used to trigger up to 10 sources (Fig. 1). It has been built in the electronics laboratory of the Institute of Geophysics, University of Hamburg.

Each channel consists of two monostable multivibrators. The first one sets the start at the time Δt_i , whereas the second one controls the duration τ_i of a rectangular voltage pulse of variable amplitude (Fig. 2). The time-settings Δt_i and τ_i can be continuously varied between 0 and 15 μsec and are reproducible with an accuracy of $\pm 0.5 \mu\text{sec}$. The amplitude A_i of the pulse can be chosen between 0 and 500 Volt (see also Behle et al., 1975).

In the experimental setup the delaying system is used to pulse 5 piezo-electric transducers of PZT ceramics (Vernitron Ltd., England) of outer diameter 6.5 mm. We chose tubes with approximately isotropic radiation of mainly P -waves, thus simplifying the experimental conditions. The tubes are put into a homogeneous aluminium plate, centres 7.5 mm apart, forming a line (Fig. 3). The fracture length $L_0 = 30 \text{ mm}$ is defined by the distance between the centres of the outermost tubes. The crystals are triggered to simulate a constant fracture velocity $v_F = 2.9 \text{ mm}/\mu\text{sec}$. This corresponds to approximately half the velocity of the longitudinal plate wave in aluminium.

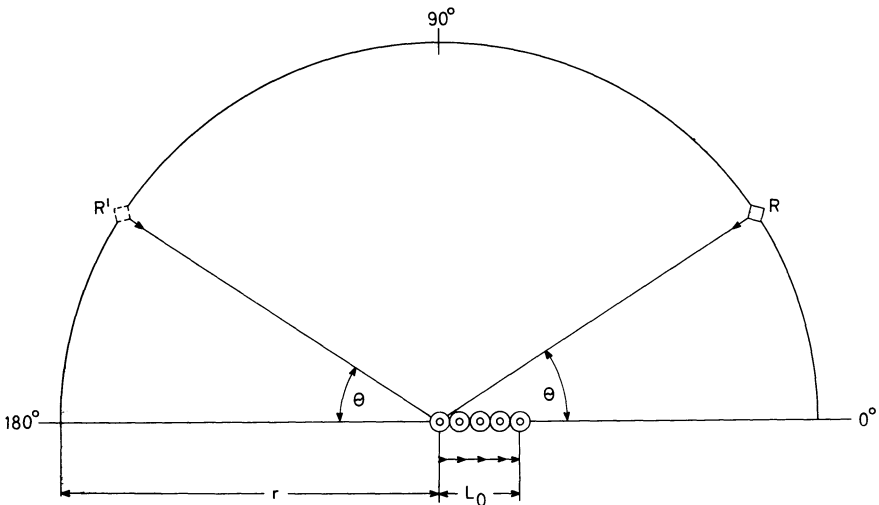


Fig. 3. Corresponding pairs of seismograms were picked up at positions R and R'

¹ R. Herber und R. Nortmann, Institut für Geophysik, Bundesstr. 55, D-2000 Hamburg 13

A multimorph transducer was used to record the radial component of motion. Thus we only consider the longitudinal plate wave P which is analogous to the dilatational wave in the three-dimensional case. If excited individually, the crystals yielded at any point of observation signals identical in shape for all practical purposes. Diffraction at neighbouring crystals has little influence on the results (Rohde, 1975) and shall not be discussed here. Recordings were made at 10° intervals along a half-circle with a radius of $r = 35$ cm around the source (Fig. 3).

The effect of source propagation will be significant only, if the fracture length L_0 is at least of the order of the dominant seismic wave length. The duration t of the fracture should be at least of the order of the dominant signal period T . Both conditions are approximately fulfilled in the experiment, as $L_0 = 30$ mm, $\lambda \approx 36$ mm, $t \approx 10$ μ s, $T \approx 7$ μ s.

Results

Seismograms were recorded on magnetic tape, digitized and processed on the CDC 1700 computer of our Institute. The recording device has been described by Koenig (1969).

The vector directivity D of the P -wave signals was computed according to Ben Menahem's method (1962). For this purpose we used corresponding pairs of observations at R and R' (see Fig. 3) which are symmetrically placed with respect to the source. Figure 4 shows the values of the *directivity function* $|D|$, computed

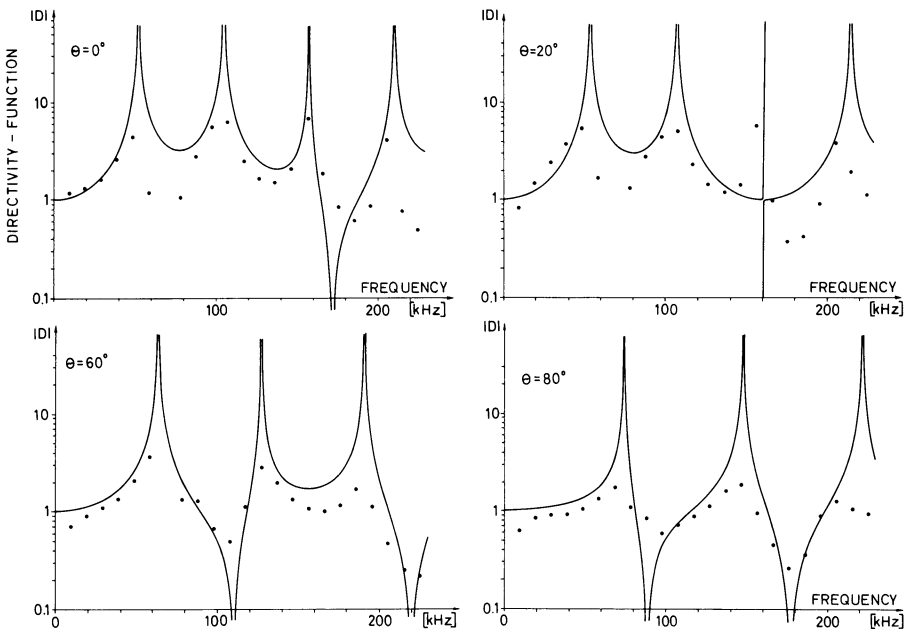


Fig. 4. The experimental (points) and theoretical (solid lines) directivity functions for some angles θ

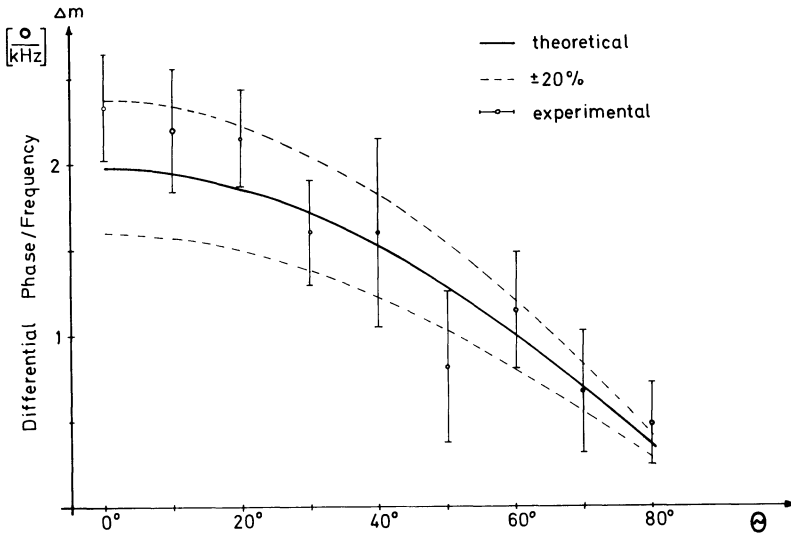


Fig. 5. The slope of the differential phase versus angle θ

from the experimental data for certain angles θ , along with the best possible matching curve obtained from Ben Menahem’s formula.

The parameters of this best fitting curve are: fracture velocity $v_F = 2.9 \text{ mm}/\mu\text{sec}$ and fracture length $L_0 = 37 \text{ mm}$. This best fit fracture length differs from the value of $L_0 = 30 \text{ mm}$ (see Fig. 3) by $+25\% \pm 3\%$. This holds for all values of θ . The value of L_0 happens to be nearly equal, however, to the distance of 37.5 mm between the outer edges of the source. Thus, it would seem natural to define this distance rather than L_0 as the fracture length. That this is not true will be discussed below. The *phase of D*, called the differential phase, with respect to angle θ , should be a straight line through the origin. The slope of this line is proportional to the rupture length L_0 . We have approximated our phase spectra by best line fits and calculated the difference between the average phase slopes of a corresponding pair of observations. This difference is shown as a function of θ in Figure 5. For comparison, the theoretical slope of the phase difference corresponding to the true fault length of 30 mm is plotted. The fracture length computed from the phase slopes differs from the true value of L_0 by $\pm 20\%$ or more.

Discussion

The results can be summarized as follows:

1. The directivity as determined from the experimental data is in significant qualitative agreement with the computed directivity as expected from the theoretical concept of a finite moving source.
2. The deviation of actual fracture parameters from those computed from the experimental data using the formulas of Ben-Menahem (1962) is about 25%.

The reason for this deviation is that the experimental conditions differ from the theoretical assumptions of Ben-Menahem (1962). In the experiment we used a number of single sources whereas theoretically there should be a continuous distribution of sources. This causes the main part of the deviation in the directivity function, as has been shown by Rohde (1975), who also adapted the theory of Ben-Menahem (1962) to the actual conditions of the experiment. He showed that, distributing an increasing number of sources along L_0 , the best fit fracture length L'_0 approaches the value of L_0 . (The above mentioned agreement of $L'_0 = 37$ mm and the distance between the outer edges of the source coincidentally results from the special circular shape of the transducers together with their arrangement.)

Limited frequency resolution and anisotropy of radiation from the transducers are considered to be further sources of error. Besides, another condition which is required by theory, viz. $L_0/r \ll 1$ could not be entirely fulfilled in our experiment.

It is for these reasons that an accuracy of not better than $\pm 3\%$ could be achieved for the parameters L_0 and v_F , calculated from the experimental results.

Conclusions

The above results are an encouraging step towards modelling a more realistic mechanism of earthquake focus. This could be done with the help of shearing transducers, varying the fracture velocity along the fault and proceeding from uni- to bi-lateral fault models.

Acknowledgements. We wish to thank our colleagues Dr. J. Drimmel and Prof. Dr. R. Gutdeutsch, University of Vienna, and Dr. M. Koenig, University of Hamburg, for helpful suggestions regarding the problem.

We are also grateful for the help we received from the technical staff of our institute.

Prof. Dr. S. J. Duda and Dr. T. Lal kindly read the manuscript and gave critical comments.

The Deutsche Forschungsgemeinschaft sponsored this investigation.

References

- Behle, A., Nortman, R., Rohde, J.: Modellseismische Darstellung einer wandernden Quelle. Preliminary report presented at the 35. Jahrestag der Deutschen Geophysikalischen Gesellschaft e.V., Stuttgart, 2.-5. April 1975
- Ben-Menahem, A.: Radiation of seismic surface-waves from finite moving sources. *Bull. Seism. Soc. Am.* **51**, 401-435, 1961
- Ben-Menahem, A.: Radiation of seismic body waves from a finite moving source in the earth. *J. Geophys. Res.* **67**, 345-350, 1962
- Koenig, M.: Digitalisierung modellseismischer Signale. *Z. Geophys.* **35**, 9-15, 1969
- Mansinha, L.: The velocity of shear fracture. *Bull. Seism. Soc. Am.* **54**, 369-376, 1964
- Press, F., Ben-Menahem, A., Toksöz, M. N.: Experimental determination of earthquake fault length and rupture velocity. *J. Geophys. Res.* **66**, 3471-3485, 1961
- Rohde, J.: Modellseismische Darstellung einer bewegten Quelle. Diplomarbeit, Institut für Geophysik, Universität Hamburg, 1975
- Savage, J. C., Hasegawa, H. S.: A two-dimensional model study of the directivity function. *Bull. Seism. Soc. Am.* **55**, 27-45, 1965
- Schick, R., Schneider, G.: Über die Nachbildung eines Erdbebenherdes in der Modellseismik. Veröffentlichungen des Landeserdbebendienstes Baden-Württemberg, Modellseismische Arbeiten 3. Teil, Stuttgart 1964

Propagation of Love-Type Waves in Heterogeneous Elastic Layers

Arabinda Biswas

Department of Mathematics, Indian Institute of Technology, Kharagpur 721302, India

Abstract. The propagation of Love type waves in isotropic non-homogeneous stratum of finite depth has been studied for two different cases: (i) the layer is imbedded by two isotropic homogeneous elastic half spaces; (ii) the layer is in welded contact with another heterogeneous layer of different properties. The existence of such waves has been proved by obtaining the solutions of frequency equations numerically.

Key words: Wave propagation – Love wave – Nonhomogeneous medium.

1. Introduction

Stoneley (1924) investigated the propagation of generalized type of Love waves in the presence of a homogeneous layer imbedded between two half spaces. He proved the existence of such type of waves if the wave length be not very large or the thickness of the sandwiched layer not too thin. He discussed the possibility of Love type wave propagation when the velocity of the distortional wave in the upper medium is less or greater than that in the lower medium. Datta (1963) considered the imbedded layer to be heterogenous to study the propagation of this type of wave for several variations in the modulus of rigidity and density. Sinha (1966) studied a similar problem of propagation of waves in a layer lying between two elastic half-spaces by varying the rigidity and velocity exponentially with depth.

The propagation of elastic waves in two layers in welded contact having two free surfaces was investigated by Jones (1964). He considered the layers to be homogeneous. But Paul (1966) discussed the propagation of SH-waves by taking the layers in welded contact to be heterogeneous for two simple cases. In one case he assumed the rigidity and density to be linear while in the other exponential.

In this paper we consider the problems of propagation of Love type waves in heterogeneous layers for both the cases:

(i) The heterogeneous elastic layer is sandwiched between homogeneous elastic half spaces.

(ii) The medium of propagation of waves consists of two heterogeneous elastic layers in welded contact and having different properties.

The variations in modulus of rigidity μ and density ρ in one of the layers for both the case are taken as

$$\mu = \mu_0(1 - \sin \delta z), \quad \rho = \rho_0(1 - \sin \delta z) \quad (1a)$$

where μ_0, ρ_0 are the constant rigidity and density respectively and δ is a constant. In case (ii) the modulus of rigidity and the density in one of the adjacent layer vary exponentially with depth and those are expressed as

$$\mu = \mu_0 \exp(\gamma z), \quad \rho = \rho_0 \exp(\gamma z). \quad (1b)$$

2. Basic Equations

We assume (u, v, w) to be the displacement components in general at any point (x, y, z) in cartesian coordinate system and the conditions for SH-waves advancing parallel to x -axis as $u = w = \partial/\partial y = 0$. The equations of motion, in the absence of body forces, for the propagation of such type of waves will then reduce to a single equation of the form

$$\rho \frac{\partial^2 v}{\partial t^2} = \frac{\partial p_{xy}}{\partial x} + \frac{\partial p_{yz}}{\partial z}, \quad (2)$$

where

$$p_{xy} = \mu \frac{\partial v}{\partial x}, \quad p_{yz} = \mu \frac{\partial v}{\partial z}. \quad (3)$$

If the rigidity modulus μ and the density ρ are the functions of z only, the Equation (2) will then, after putting the values of p_{xy} and p_{yz} from Equation (3) into it, take the form

$$\rho \frac{\partial^2 v}{\partial t^2} = \mu \nabla^2 v + \frac{d\mu}{dz} \frac{\partial v}{\partial z} \quad (4)$$

where

$$\nabla^2 = \frac{\partial^2}{\partial x^2} + \frac{\partial^2}{\partial z^2}.$$

The above Equation (4) is the standard differential equation to be solved for any problem dealing with the type of heterogeneity considered in this case.

We consider the waves to be plane harmonic, so that the displacement v may be assumed as

$$v = V(z) \exp \{ik(x - ct)\} \quad (5)$$

where k is the wave number and c is the phase velocity of the wave propagated. This assumption transforms the Equation (4) into the form

$$\frac{d^2 V}{dz^2} + \frac{1}{\mu} \frac{d\mu}{dz} \frac{dV}{dz} + k^2 \left(\frac{c^2}{\beta^2} - 1 \right) V = 0 \quad (6)$$

where $\beta = \sqrt{\mu/\rho}$ is the distortional wave velocity.

In order to normalize the Equation (6) we substitute $V(z) = X(z) \mu^{-1/2}$ and therefore, obtain

$$\frac{d^2 X}{dz^2} + \left[\frac{1}{4\mu^2} \left(\frac{d\mu}{dz} \right)^2 - \frac{1}{2\mu} \frac{d^2 \mu}{dz^2} + k^2 \left(\frac{c^2}{\beta^2} - 1 \right) \right] X = 0. \tag{7}$$

The expressions for μ and ρ in Equation (1a) reduce the Equation (7) into the form

$$\frac{d^2 X}{dz^2} + l^2 X = 0 \tag{8}$$

where

$$l = \left\{ \frac{\delta^2}{4} + k^2 \left(\frac{c^2}{\beta^2} - 1 \right) \right\}^{1/2} \tag{9}$$

$$\beta = \sqrt{\mu/\rho} = \sqrt{\mu_0/\rho_0} = \text{constant}. \tag{10}$$

The solution of the Equation (8), in case of layered media can be written as

$$X_1 = E_1 \cos l_1 z + F_1 \sin l_1 z \tag{11}$$

E_1, F_1 being constant, and instead of X and l the notations X_1 and l_1 are used for the layered media.

Now from Equations (5) and (11) and the assumption $V(z) = \mu^{-1/2} X(z)$ we obtain

$$v = \frac{1}{(1 - \sin \delta z)^{1/2}} [B_1 \cos l_1 z + B_2 \sin l_1 z] \exp \{ik(x - ct)\} \tag{12}$$

where $B_1 = \mu_0^{-1/2} E_1, B_2 = \mu_0^{-1/2} F_2$ are constant.

The Equation (7), on application of the Equation (1b) can be reduced to the form

$$\frac{d^2 X}{dz^2} + m^2 X = 0 \tag{13}$$

where

$$m = \left\{ k^2 \left(\frac{c^2}{\beta^2} - 1 \right) - \frac{\gamma^2}{4} \right\}^{1/2} \tag{14}$$

$$\beta = \sqrt{\mu/\rho} = \sqrt{\mu_0/\rho_0} = \text{constant}. \tag{15}$$

Now we write the solution of the Equation (13) as

$$X = E_2 \cos mz + F_2 \sin mz \tag{16}$$

where E_2, F_2 are constant. The displacement component v in this case can then be written as

$$v = \exp \left(-\frac{\gamma}{2} z \right) [C_1 \cos mz + C_2 \sin mz] \exp \{ik(x - ct)\} \tag{17}$$

with $C_1 = \mu_0^{-1/2} E_2, C_2 = \mu_0^{-1/2} F_2$ as integration constants.

The Equation (4) for a homogeneous medium reduces to the differential equation

$$\rho \frac{\partial^2 v}{\partial t^2} = \mu \nabla^2 v \quad (18)$$

and the displacement component v , being the solution of the Equation (18) can be written as

$$v = [D_1 e^{nz} + D_2 e^{-nz}] \exp \{ik(x - ct)\} \quad (19)$$

where $n = k(1 - c^2/\beta^2)^{1/2}$ and D_1, D_2 are constant.

In the case of infinitely extended medium the displacement component can be expressed in more simplified form

$$v = D \exp \{ \pm nz + ik(x - ct) \} \quad (20)$$

where the sign is to be so chosen that the displacement vanishes at infinity.

3. Problem I

Propagation of Waves in a Heterogeneous Layer Sandwiched between Homogeneous Half-Spaces

Solution of the Problem. The aim of this problem is to study the propagation of Love type waves in non-homogeneous stratum of finite depth imbedded between isotropic elastic half-spaces. It has been investigated that Love type wave propagation is possible for $c < \beta_1 < \beta_3$, where c is the phase velocity of the wave propagated, and β_1, β_3 are the distorsional wave velocities in the upper and the lower medium respectively.

The two homogeneous half-spaces $H \leq z \leq \infty$ and $-\infty \leq z \leq 0$ have constant modulus of rigidity and density. The rigidity modulus and the density in the upper medium are denoted by μ_1, ρ_1 and those in the lower medium by μ_3 and ρ_3 respectively. The rigidity modulus μ_2 and the density ρ_2 of the heterogeneous layer $0 \leq z \leq H$ are considered to be functions of z only, and then assumed as in the Equation (1a)

$$\mu_2 = \mu_0(1 - \sin \delta z), \quad \rho_2 = \rho_0(1 - \sin \delta z) \quad (21)$$

so that the velocity $\beta_2 = \sqrt{\mu_2/\rho_2} = \sqrt{\mu_0/\rho_0}$ is constant.

For a plane wave travelling in the direction of x increasing, the displacements v_1, v_2 and v_3 in the upper medium, layer and lower medium respectively are expressed from the Equations (20) and (12), as

$$v_1 = D_1 \exp \{ -s_1 z + ik(x - ct) \} \quad (22)$$

$$v_2 = \frac{1}{(1 - \sin \delta z)^{1/2}} [B_1 \cos s_2 z + B_2 \sin s_2 z] \exp \{ ik(x - ct) \} \quad (23)$$

$$v_3 = D_2 \exp \{ s_3 z + ik(x - ct) \} \quad (24)$$

where

$$s_1 = k(1 - c^2/\beta_1^2)^{1/2} \tag{25}$$

$$s_2 = \left\{ k^2(c^2/\beta_2^2 - 1) + \frac{\delta^2}{4} \right\}^{1/2} \tag{26}$$

$$s_3 = k(1 - c^2/\beta_3^2)^{1/2} \tag{27}$$

$$\beta_1 = \sqrt{\mu_1/\rho_1} = \text{constant}; \quad \beta_2 = \sqrt{\mu_2/\rho_2} = \sqrt{\mu_0/\rho_0} = \text{constant};$$

$$\beta_3 = \sqrt{\mu_3/\rho_3} = \text{constant, and } c < \beta_1 < \beta_3.$$

Boundary Conditions

The boundary conditions are

$$\left. \begin{aligned} \text{(I)} \quad & v_1 = v_2 \\ \text{(II)} \quad & p_{yz} \text{ in the upper medium} = p_{yz} \text{ in the layer,} \\ & \text{or, } \mu_1 \frac{\partial v_1}{\partial z} = \mu_2 \frac{\partial v_2}{\partial z} \end{aligned} \right\} \text{ at } z = H;$$

$$\left. \begin{aligned} \text{(III)} \quad & v_2 = v_3 \\ \text{(IV)} \quad & p_{yz} \text{ in the layer} = p_{yz} \text{ in the lower medium,} \\ & \text{or, } \mu_2 \frac{\partial v_2}{\partial z} = \mu_3 \frac{\partial v_3}{\partial z} \end{aligned} \right\} \text{ at } z = 0.$$

The above boundary conditions along with the Equations (22), (23) and (24) give the following equations

$$\begin{aligned} \text{(i)} \quad & \frac{1}{(1 - \sin \delta H)^{1/2}} [B_1 \cos s_2 H + B_2 \sin s_2 H] - e^{-s_1 H} D_1 = 0 \\ \text{(ii)} \quad & \frac{\mu_0}{(1 - \sin \delta H)^{1/2}} [\{\delta \cos \delta H \cos s_2 H - 2s_2 \sin s_2 H(1 - \sin \delta H)\} B_1 \\ & + \{\delta \cos \delta H \sin s_2 H + 2s_2 \cos s_2 H(1 - \sin \delta H)\} B_2] \\ & + 2\mu_1 s_1 e^{-s_1 H} D_1 = 0 \\ \text{(iii)} \quad & B_1 - D_2 = 0 \\ \text{(iv)} \quad & \mu_0 \delta B_1 + 2\mu_0 s_2 B_2 - 2\mu_3 s_3 D_2 = 0. \end{aligned} \tag{28}$$

Frequency Equation

Eliminating the unknown constants B_1 , B_2 , D_1 and D_2 from the Equations (28), the frequency equation is obtained in the form

$$[(\mu_0 \delta - 2\mu_3 s_3)(2\mu_1 s_1 + \mu_0 \delta \cos \delta H) + 4\mu_0^2 s_2^2(1 - \sin \delta H)] \tan s_2 H$$

$$+ 2\mu_0 s_2(\mu_0 \delta - 2\mu_3 s_3)(1 - \sin \delta H) - 2\mu_0 s_2(2\mu_1 s_1 + \mu_0 \delta \cos \delta H) = 0. \tag{29}$$

We assume $\mu_0 = \mu_3$ and use the following dimensionless parameters

$$\begin{aligned} a &= \delta H, & \xi &= \mu_1/\mu_3, & s &= kH, \\ b_1 &= \beta_2/\beta_1, & b_3 &= \beta_2/\beta_3, & \eta &= c/\beta_2 \end{aligned} \quad (30)$$

so that the frequency Equation (29) takes the form

$$\begin{aligned} [(a - 2s_3 H)(2\xi s_1 H + a \cos a) + 4(s_2 H)^2(1 - \sin a)] \tan s_2 H \\ + 2s_2 H(a - 2s_3 H)(1 - \sin a) - 2s_2 H(2\xi s_1 H + a \cos a) = 0 \end{aligned} \quad (31)$$

and the Equations (25), (26) and (27) also take the forms

$$s_1 H = s(1 - b_1^2 \eta^2)^{1/2} \quad (32)$$

$$s_2 H = \left\{ s^2(\eta^2 - 1) + \frac{a^2}{4} \right\}^{1/2} \quad (33)$$

$$s_3 H = s(1 - b_3^2 \eta^2)^{1/2}. \quad (34)$$

Numerical Solutions

The frequency Equation (29) or (31) may be solved for two different cases

(i) $c < \beta_2$ and (ii) $c > \beta_2$.

We consider the Equation (31) to obtain its numerical solutions for the case $\beta_2 < c < \beta_1 < \beta_3$ and for the following numerical values of the non-dimensional parameters in Equation (30)

$$a = 0.3, \quad \xi = 0.5, \quad b_1^2 = 0.5, \quad b_3^2 = 0.25.$$

The roots in the form c^2/β_2^2 of the frequency Equation (31) for two different values of s are obtained numerically as

$$(i) \quad c^2/\beta_2^2 = 1.4, \quad \text{when } s(=kH) = 2.36693,$$

$$(ii) \quad c^2/\beta_2^2 = 1.2, \quad \text{when } s(=kH) = 4.22820$$

and this proves that Love type waves may propagate under the assumed condition $\beta_2 < c < \beta_1 < \beta_3$.

Similarly the existence of this type of wave may be proved for the condition $c < \beta_2$.

4. Problem II

Propagation of SH-Wave in a Two-Layered Heterogeneous Medium

Solution of the Problem. In this problem we have studied the propagation of SH-wave in a two-layered heterogeneous medium in which the modulus of rigidity and the density are μ_1 and ρ_1 for the first layer, and those for the second layer are μ_2 and ρ_2 respectively. The variations in the rigidity and density of the

layers $H \geq z \geq 0$ and $-H \leq z \leq 0$ are assumed as

$$\begin{aligned} \text{(i)} \quad \mu_1 &= \mu_{10}(1 - \sin \delta z) \\ \rho_1 &= \rho_{10}(1 - \sin \delta z) \end{aligned} \tag{35}$$

$$\begin{aligned} \text{(ii)} \quad \mu_2 &= \mu_{20} \exp(\gamma z) \\ \rho_2 &= \rho_{20} \exp(\gamma z) \end{aligned} \tag{36}$$

so that the distortional wave velocities

$$\begin{aligned} \beta_1 &= \sqrt{\mu_1/\rho_1} = \sqrt{\mu_{10}/\rho_{10}} = \text{constant}, \\ \beta_2 &= \sqrt{\mu_2/\rho_2} = \sqrt{\mu_{20}/\rho_{20}} = \text{constant}. \end{aligned}$$

The existence of *SH*-wave in such a medium has been proved by obtaining the real roots of the frequency equation when the variations are small in each case.

The displacement components v_1 and v_2 , in the first and second layers respectively, with the help of the Equations (12) and (17), are expressed as

$$v_1 = \frac{1}{(1 - \sin \delta z)^{1/2}} [E_1 \cos l_1 z + E_2 \sin l_1 z] \exp \{ik(x - ct)\} \tag{37}$$

$$v_2 = \exp \left(-\frac{\gamma}{2} z \right) [F_1 \cos l_2 z + F_2 \sin l_2 z] \exp \{ik(x - ct)\} \tag{38}$$

where

$$\begin{aligned} l_1 &= \left\{ k^2 \left(\frac{c^2}{\beta_1^2} - 1 \right) + \frac{\delta^2}{4} \right\}^{1/2} \\ l_2 &= \left\{ k^2 \left(\frac{c^2}{\beta_2^2} - 1 \right) - \frac{\gamma^2}{4} \right\}^{1/2}. \end{aligned}$$

Boundary Conditions

The boundary conditions are that the components of stress across the bounding surfaces vanish at the free surfaces $z=H$ and $z=-H$, and the components of displacement and stress across the interface $z=0$ are continuous. Applying these conditions we obtain

$$\begin{aligned} \text{(I)} \quad p_{yz} \text{ in the first layer} &= 0 \text{ or, } \mu_1 \frac{\partial v_1}{\partial z} = 0, \quad \text{at } z = H; \\ \text{(II)} \quad v_1 &= v_2 \\ \text{(III)} \quad p_{yz} \text{ in the first layer} &= p_{yz} \text{ in the second layer} \left. \vphantom{\begin{matrix} \text{(II)} \\ \text{(III)} \end{matrix}} \right\} \text{at } z = 0; \\ &\text{or, } \mu_1 \frac{\partial v_1}{\partial z} = \mu_2 \frac{\partial v_2}{\partial z} \\ \text{(IV)} \quad p_{yz} \text{ in the second layer} &= 0 \text{ or, } \mu_2 \frac{\partial v_2}{\partial z} = 0, \quad \text{at } z = -H. \end{aligned}$$

The above relations along with Equations (35), (36), (37) and (38) give the following equations

$$\begin{aligned}
 & \text{(i)} \quad \{\delta \cos \delta H \cos l_1 H - 2l_1 \sin l_1 H(1 - \sin \delta H)\} E_1 \\
 & \quad + \{\delta \cos \delta H \sin l_1 H + 2l_1 \cos l_1 H(1 - \sin \delta H)\} E_2 = 0 \\
 & \text{(ii)} \quad E_1 - F_1 = 0 \\
 & \text{(iii)} \quad \mu_{10} \delta E_1 + 2\mu_{10} l_1 E_2 + \mu_{20} \gamma F_1 - 2\mu_{20} l_2 F_2 = 0 \\
 & \text{(iv)} \quad (\gamma \cos l_2 H - 2l_2 \sin l_2 H) F_1 - (\gamma \sin l_2 H + 2l_2 \cos l_2 H) F_2 = 0.
 \end{aligned} \tag{39}$$

Frequency Equation

The frequency equation is obtained by eliminating the unknown constants E_1 , E_2 , F_1 and F_2 from the Equations (39) as

$$\begin{aligned}
 & 2l_1 [(1 - \sin \delta H) \{\mu_{10} \delta \gamma + \mu_{20} (4l_1^2 + \gamma^2)\} - \mu_{10} \delta \gamma \cos \delta H] \cot l_1 H \\
 & \quad + 2\mu_{10} l_2 [4l_1^2 (1 - \sin \delta H) + \delta^2 \cos \delta H] \cot l_2 H \\
 & \quad + 4\mu_{10} \delta l_1 l_2 [(1 - \sin \delta H) - \cos \delta H] \cot l_1 H \cot l_2 H \\
 & \quad + [\mu_{10} \gamma \{4l_1^2 (1 - \sin \delta H) + \delta^2 \cos \delta H\} \\
 & \quad + \mu_{20} \delta \cos \delta H (4l_2^2 + \gamma^2)] = 0.
 \end{aligned} \tag{40}$$

We assume δ and γ so small that the terms containing upto first order in δ and γ are to be retained in the Equation (40) and this assumption reduces the frequency equation to the form

$$\mu_{10} l_1 \cot l_2 H + \mu_{20} l_2 \cot l_1 H + \frac{\mu_{10} \gamma l_1^2 + \mu_{20} \delta l_2^2}{2l_1 l_2 (1 - \delta H)} = 0 \tag{41}$$

where l_1 and l_2 in their reduced forms are

$$l_1 = k \left(\frac{c^2}{\beta_1^2} - 1 \right)^{1/2}, \quad l_2 = k \left(\frac{c^2}{\beta_2^2} - 1 \right)^{1/2}.$$

We consider $\beta_1 < c < \beta_2$ and the following dimensionless parameters

$$\begin{aligned}
 \eta_1 &= c/\beta_1, \quad \eta_2 = c/\beta_2, \quad a_1 = \delta H, \quad a_2 = \gamma H, \\
 s &= kH, \quad b = \beta_1/\beta_2 = \eta_2/\eta_1, \quad a = a_2/a_1 = \gamma/\delta.
 \end{aligned} \tag{42}$$

For the condition $\beta_1 < c < \beta_2$, $l_1 = k(c^2/\beta_1^2 - 1)^{1/2}$ is real but $l_2 = k(c^2/\beta_2^2 - 1)^{1/2}$ is imaginary. We introduce the dimensionless parameters from Equation (42) into the Equation (41) and use the condition $\mu_{10} = \mu_{20}$ to obtain the frequency equation in the form

$$\begin{aligned}
 & s(\eta_1^2 - 1)^{1/2} \coth \{s(1 - b^2 \eta_1^2)^{1/2}\} - s(1 - b^2 \eta_1^2)^{1/2} \cot \{s(\eta_1^2 - 1)^{1/2}\} \\
 & \quad - \frac{a_1 \{(1 + a) - (b_2 + a) \eta_1^2\}}{2(1 - a_1)(\eta_1^2 - 1)^{1/2} (1 - b^2 \eta_1^2)^{1/2}} = 0.
 \end{aligned} \tag{43}$$

Numerical Solutions

In order to solve the frequency Equation (43) numerically we assume $a_1 = 0.2$; $b^2 = 0.25, 0.50$; and $a = 1, 2$; and the roots of the Equation (43) in the form of η_1 or η_2 are obtained. The numerical values of η_1^2 and η_2^2 for different values of s are given in tabular forms (Tables 1-4) and it is observed that the phase velocity occurs at a lower $s (= kH)$ with increasing γ .

Table 1. Roots of the frequency equation in the form of η_1^2 and η_2^2 when $b^2 = \beta_1^2/\beta_2^2 = 0.25$, $a_1 = \delta H = 0.2$ and $\gamma = \delta$

$s (= kH)$	2.52751	1.27953	0.82235
$\eta_1^2 (= c^2/\beta_1^2)$	1.20	1.40	1.50
$\eta_2^2 (= c^2/\beta_2^2)$	0.30	0.35	0.375

Table 2. Roots of the frequency equation in the form of η_1^2 and η_2^2 when $b^2 = \beta_1^2/\beta_2^2 = 0.25$, $a_1 = \delta H = 0.2$ and $\gamma = 2\delta$

$s (= kH)$	2.46950	1.15970	0.61275
$\eta_1^2 (= c^2/\beta_1^2)$	1.20	1.40	1.50
$\eta_2^2 (= c^2/\beta_2^2)$	0.30	0.35	0.375

Table 3. Roots of the frequency equation in the form of η_1^2 and η_2^2 when $b^2 = \beta_1^2/\beta_2^2 = 0.50$, $a_1 = \delta H = 0.20$ and $\gamma = \delta$

$s (= kH)$	3.77493	2.07280	0.89681
$\eta_1^2 (= c^2/\beta_1^2)$	1.10	1.20	1.30
$\eta_2^2 (= c^2/\beta_2^2)$	0.55	0.60	0.65

Table 4. Roots of the frequency equation in the form of η_1^2 and η_2^2 when $b^2 = \beta_1^2/\beta_2^2 = 0.50$, $a_1 = \delta H = 0.20$ and $\gamma = 2\delta$

$s (= kH)$	3.713125	1.95320	0.51758
$\eta_1^2 (= c^2/\beta_1^2)$	1.10	1.20	1.30
$\eta_2^2 (= c^2/\beta_2^2)$	0.55	0.60	0.65

References

Datta, S.: Love waves in a non-homogeneous internal stratum lying between two semi-infinite isotropic media. *Geophysics* **XXVIII** (2), 156, 1963
 Datta, S.: On the propagation of Love waves in a non-homogeneous internal stratum of finite depth lying between two semi-infinite isotropic media. *Geofis. pura e appl.* **55**, 31, 1963
 Jones, J. P.: Wave propagation in two-layered medium. *J. Appl. Mech.* **31** (2), 213, 1964
 Paul, M. K.: Propagation of SH-wave in a two layered heterogeneous medium. *Ind. J. Mech. Maths.* **4**, 26, 1966
 Sinha, N. K.: Propagation of Love waves in a non-homogeneous stratum of finite depth sandwiched between two semi-infinite isotropic media. *Pure Appl. Geophys.* **65**, 37, 1966
 Stoneley, R.: Elastic waves at the surface of separation of two solids (transverse waves in an internal stratum). *Proc. Roy. Soc. (London) A* **106**, 424, 1924

Received December 9, 1975

Representation and Interpretation of Resistivity Mapping Data in Groundwater Prospecting in Zambia

K. D. Töpfer

University of Zambia, School of Natural Sciences
P.O. Box 2379, Lusaka, Republic of Zambia, Africa

Abstract. The interpretation of apparent resistivity maps in the field of groundwater exploration in Zambia is discussed. It is proposed to resolve iso-apparent resistivity maps into their regional and residual components to simplify their geological interpretation and therefore the selection of proper drilling sites for production wells. This technique is illustrated by a practical example of an area surveyed north-west of Kabwe, Republic of Zambia.

Key words: Iso-apparent resistivity maps – Regional-residual separation – Groundwater exploration.

1. Introduction

Geoelectrical resistivity measurements are common in the investigation of groundwater resources. Geoelectric sounding methods undoubtedly give the most valuable information on geoelectric underground structures and interpretation in terms of the hydrogeology of an area is often possible.

However geoelectric soundings are not only time consuming but also complicated in many parts of Zambia by recumbent folding which gives repetition of bands, and by iron sulphide mineralization. An economic alternative is to use geoelectric mapping techniques.

2. Difficulties Arising from the Interpretation of Iso-apparent Resistivity Maps

Geoelectric measuring techniques where the electrode array is kept constant and measurements are done most conveniently on a regular grid to cover an area of interest are called “geoelectric mapping techniques”. Results are commonly represented in form of “iso-apparent resistivity maps”.

Their interpretation is generally very difficult because apparent resistivity data not only depend on geoelectric subsurface structures but also on the specific electrode array used. It is the somewhat fictitious nature of the apparent resistivity itself that makes interpretation of apparent resistivity data sometimes ambiguous (Töpfer, 1969).

On the other hand, geoelectric measurements proved to be most efficient to locate groundwater reservoirs or just to site drilling sites within known aquifers (Flathe, 1955; Hallenbach, 1953; Krulc and Mladenovic, 1969; Serres, 1969; Töpfer and Legg, 1974; Flathe and Homilius, 1973; Van Dam and Meulenkamp, 1967).

Large geoelectrically and hydrogeologically unknown areas are most economically surveyed by mapping techniques. Since iso-apparent resistivity maps are difficult to interpret, several electrode spacings have to be applied to decrease at least some of the encountered uncertainties. A few supplementary geoelectric soundings further increase the reliability of geoelectrical interpretation (Kunetz, 1966).

Quantitative interpretation has been tried in the simple case where a sequence of sedimentary rocks of relatively low specific resistivities is underlain by highly resistive basement rocks. If the electrode spacing is selected long enough so that the total longitudinal conductance can be determined (Kunetz, 1966; Keller and Frischknecht, 1966) then the depth to basement rocks can be determined at each individual field station provided that either the depth to basement is known from few boreholes drilled in the area of investigation or the average resistivity becomes known from well-logging techniques. This interpretation procedure however implies that the average resistivity of sedimentary rocks remains constant over the area of investigation – a criterion which is probably never exactly met in nature.

Qualitative interpretation of iso-resistivity maps is more common and in many parts of Zambia this is the only alternative approach.

Main objectives in the field of groundwater exploration in Zambia are to locate zones of contacts between hydrogeologically different rock types, faults, intrusives into host rocks, dykes quartz veins, or to locate zones of fracturing and fissuring in otherwise solid rock (i.e. in limestones) or zones of less weathering (i.e. in schists and phyllites) (Töpfer and Legg, 1974).

3. Alternative Approaches to the Representation of Apparent Resistivity Data

Iso-apparent resistivity maps are often complex in their appearance thus complicating the process of qualitative interpretation. It appears that “smoothing techniques”, – techniques which numerically allow to define resistivity “highs” and “lows” –, and “filtering techniques” which either enhance or reduce certain anomalies, may improve the resolving power of iso-apparent resistivity data and may therefore simplify the process of qualitative interpretation.

These techniques are in common use in the interpretation of gravity and magnetic field data for decades. In gravity and magnetic work these filtering techniques are aimed to separate the field into its regional (REG) and residual (RES) components (Nettleton, 1954). Since residuals are aimed to be interpreted quantitatively

ely, optimal filters have to be applied to maintain magnitude and shape of the anomaly under consideration (Apell, 1974).

Since no quantitative interpretation of apparent resistivity data is attempted, filters must not be necessarily optimal. Thus relatively simple smoothing and filtering techniques may already fulfil the main objectives of this exercise: smoothing of field data, defining analytically resistivity “highs” and “lows”, and defining areas of high gradients. Anomalous zones are thus “enhanced” and either immediately suitable for qualitative interpretation or are selected for further detailed exploration programs, such as resistivity measurements on a reduced grid size, geoelectrical soundings and/or seismic refraction surveys.

The terms REG and RES are maintained in this paper although their meaning is certainly different from that common in gravity and magnetic work.

Four simple smoothing and filtering (averaging) techniques are presented and tested. The mathematics involved is relatively simple and can be done by hand or more conveniently by using small desk – or portable mini-computers with sufficient storage capacity.

The RES_i at the i -th field station is defined as

$$RES_i = \rho_i - REG_i \quad (1)$$

where ρ_i is the apparent resistivity measured at the i -th field station. Residuals are either positive, negative or zero.

3.1. Constant Average Method

The constant average method is certainly the most simple method to define analytically resistivity “highs” and “lows”. The average apparent resistivity of an area is taken to be the mean of all individual measurements, thus

$$REG = \frac{1}{n} \sum_i^n \rho_i \quad (2)$$

where n is the number of field station.

3.2. Moving Average Method

Bhattacharya, Jain and Mallick (1974) introduced a nine point averaging method to smooth apparent resistivity data. Eight points on the periphery and one at the center of a square grid are averaged. It is

$$REG = \frac{1}{9} \left(\sum_1^8 \rho_i + \rho_c \right) \quad (3)$$

where ρ_c is the apparent resistivity as measured at the center of the square grid. The author of this paper defines REG as

$$REG = \frac{1}{8} \sum_1^8 \rho_i \quad (4)$$

and

$$\text{RES} = \rho_c - \text{REG} \quad (5)$$

A similar method has been used in gravity work where four points on the periphery of a circle with radius s (s is the grid length) are averaged and be taken to be the REG at the center of the circle (Nettleton, 1954).

3.3. Least Squares Method

The best fitting REG to the observed data may be determined by least squares methods (Agocs, 1951). The most simple assumption is that a plane of first order is best fitting the observed data:

$$\text{REG} = Ax + By + C \quad (6)$$

where A, B, C are constants and x, y are rectangular coordinates. The constants A, B, C can be determined from the following three independent, linear equations:

$$\begin{aligned} A \Sigma x^2 + B \Sigma xy + C \Sigma x - \Sigma \rho x &= 0 \\ A \Sigma xy + B \Sigma y^2 + C \Sigma y - \Sigma \rho y &= 0 \\ A \Sigma x + B \Sigma y + nC - \Sigma \rho &= 0 \end{aligned} \quad (7)$$

where n is the total number of field stations.

3.4. Moving Least Squares Method

The above outlined least squares method may be applied to eight resistivity values on the periphery and one at the center of a square grid. The mathematical procedure is the same than indicated in Section 3.3. However it must be noted that lines of singularity will necessarily occur where adjacent best fitting planes do intersect.

3.5. Comparison of Proposed Smoothing and Filtering Methods

REG – and therefore RES – values as derived from the proposed smoothing and filtering techniques depend either on the station density (or size of the area of

Table 1. Comparison of proposed smoothing and filtering methods

Method	Dependent on station density	Dependent on grid spacing	Measurements have to be done on an equal grid pattern
Constant average	yes	no	no
Moving average	no	yes	yes
Least square RES	yes	no	no
Moving least square RES	no	yes	yes

investigation) or on the selected grid spacing. Also some methods described require that field measurements are done on a square grid pattern. A summary of these characteristics is given in Table 1.

It is believed that residual resistivity maps as derived from the constant average and least squares methods, as well as regional resistivity maps as derived from the moving average and the moving least squares methods, do represent the broad regional geology of an area at least to a certain degree of accuracy.

Residual resistivity maps as derived from the moving average and the moving least squares methods may help to site production wells within a geological formation.

4. Practical Example

The 4 techniques described above were examined and compared during a groundwater exploration program north-west of Kabwe, Republic of Zambia. All calculations were done by a CompuCorp desk computer, model 425/44. The computing and print-out time for the four methods was 25 s per field station.

4.1. Geological and Geophysical Setting

The existing geological map, which was revised by Kerr (1969), suggests that the investigated area is underlain by metasediments of the Katanga System. The northern and eastern part is mapped to be underlain by schists, phyllites and shales, and the central and south-western parts by dolomites/limestones, both of the Broken Hill Series.

The resistivity contrast between schists and limestones was thought to be sufficiently large, so that these rock types may be located geoelectrically, see Table 2.

Table 2

Rock Type	Location	Spec. resistivity (Ωm)
Weath. schist	Lusaka West	8-100
	NW Dambo (Kabwe)	4-120
Solid schist	Lusaka West	100-900
Weath. chalky limestone	Lusaka West	40-100
Fractured limestone	Lusaka West	140-1,400
	NW Dambo (Kabwe)	250-1,000
	Lusaka West	500-5,000
Solid limestone	Kashitu (Kabwe)	1,500-5,000
	NW Dambo (Kabwe)	1,000-5,000
	Lusaka West	10,000-
Cryst. limestone	Lusaka West	10,000-

Phyllites and schists generally represent poor aquifers because of their poor transmissivity whereas excellent production wells are known to occur in areas underlain by karst-type limestones and dolomites of the Katanga System, (Töpfer and Legg, 1974).

The aim of this exploration program was therefore to first locate the schist/limestone contact more precisely and thereafter to locate suitable drilling sites either close to the contact or within the central part of the limestone body itself.

The area was covered on a 100×100 m grid by 792 field stations. Two electrode arrays were used: the “long array” ($AB = 150$ meters; $MN = 20$ meters) and the “short array” ($AB = 20$ meters; $MN = 5$ meters).

This field procedure was thought to be necessary in order to ascertain whether low apparent resistivities as measured with the long array are either caused by decomposed, fractured limestone at depth or by conductive overburden, i.e. shales and dambo soils (10–60 ohmmeters) and whether high apparent resistivities as measured with the long array are caused by solid, unfractured limestone at depth or by highly resistive laterite cover (1,000–5,000 ohmmeters).

4.2. Representation and Processing of Field Data

It is not possible to deduce the “known” broad geology of this area from the iso-apparent resistivity map (long array), see Figure 1. Anomalies are scattered and complicated and no general trend is readily visible. It is believed that this is mainly caused by irregular sub-karstic surfaces and by lateral changes of resistivities of the overburden (laterites, shales).

Figures 2–5 present alternative maps as derived from the discussed averaging techniques, see Chapter 3.

Generally all derived regional and residual resistivity maps are smooth as compared to the iso-apparent resistivity map of Figure 1.

Residual maps as derived from the constant average method, see Figure 2, and by the least squares method, see Figure 4, and regional maps derived from the moving average method, see Figure 3, and from the moving least squares method, see Figure 5, are of very similar appearance, respectively.

Only zero-residual lines are drawn for sake of clarity in Figures 2 and 4, respectively.

It appears that all derived maps clearly show five zones of similar electric properties. These zones are characterized by negative or positive residuals in Figures 2 and 4 and by smoothed ranges of apparent resistivities in Figures 3 and 5.

Zone *A* occurs in the north-west of the investigated area and is characterized by negative residuals, see Figures 2 and 4, and by relatively low smoothed apparent resistivities (50–100 ohmmeters) see Figures 3 and 5. Zone *A* is interpreted to be underlain by phyllites. This is in agreement with the existing geological map.

Zone *B* is located in the central part of the investigated area. Positive residuals, see Figures 2 and 4, and relatively high smoothed apparent resistivities (101–880 ohmmeters), see Figures 3 and 5, suggest that Zone *B* is underlain by dolomites/limestones of the Katanga System.

This interpretation is supported by the existing geological map.

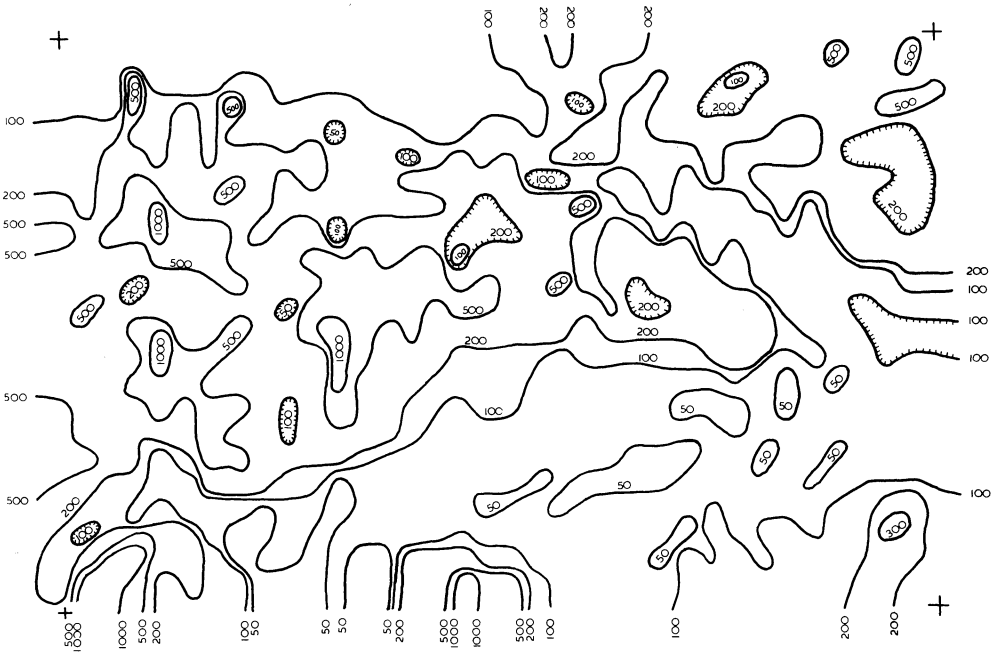


Fig. 1. Iso-apparent resistivity map ($AB = 150$ m, $MN = 20$ m)

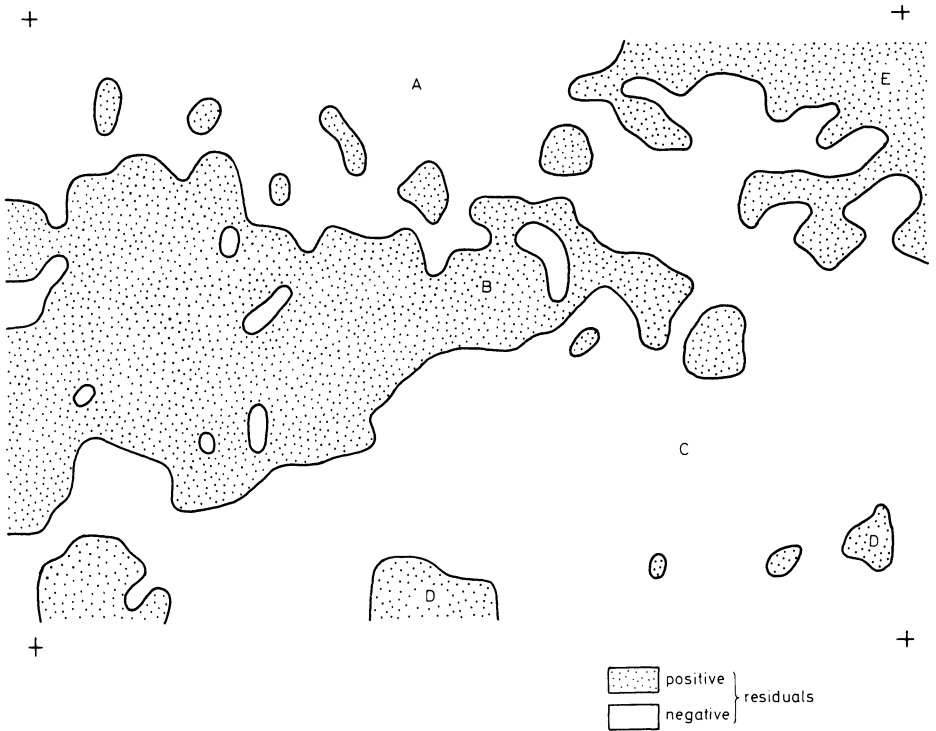


Fig. 2. Residual apparent resistivity map (constant average method)

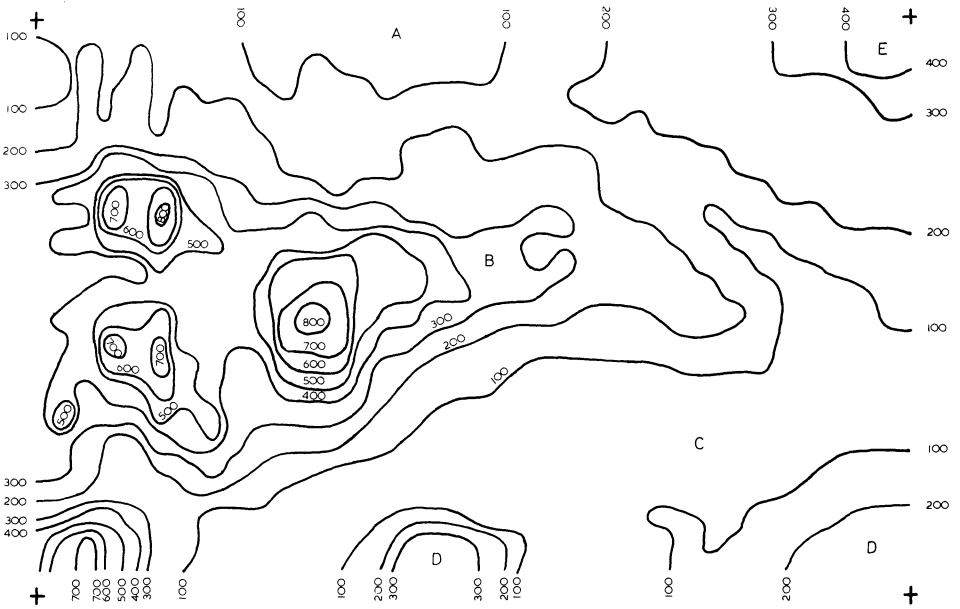


Fig. 3. Regional apparent resistivity map (moving average method)

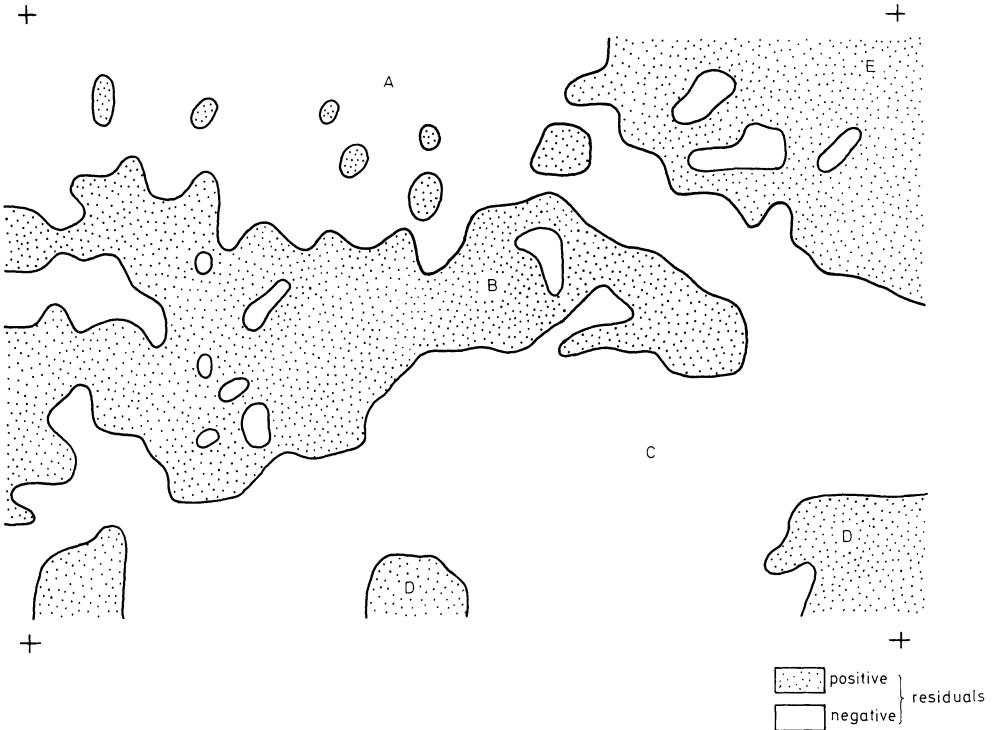


Fig. 4. Residual apparent resistivity map (least squares method)

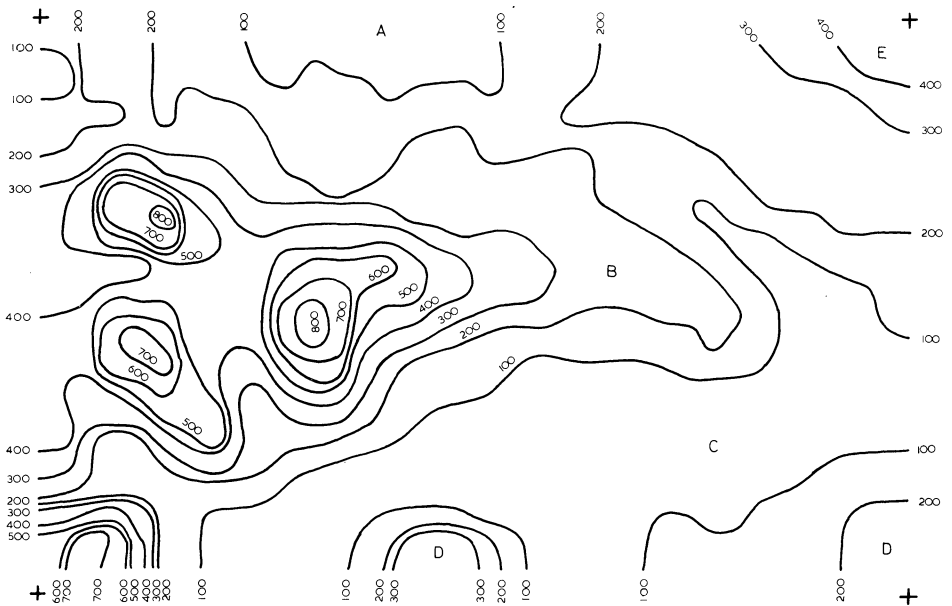


Fig. 5. Regional apparent resistivity map (moving least squares method)

Zone C in the south and south-east reveals negative residuals, see Figures 2 and 4, and low smoothed apparent resistivities (40–100 ohmmeters), see Figures 3 and 5. The existing geological map suggests that this zone is underlain by dolomites/limestones. The uniform low apparent resistivities, which characterize Zone C, however do suggest that this zone is underlain by phyllites. This interpretation is supported by drilling logs of one borehole which has been drilled recently in this zone.

Zone D is apparent as two separated patches in the extreme south of the investigated area. Positive residuals, see Figures 2 and 4, and relatively high smoothed apparent resistivities (101–370 ohmmeters), see Figures 3 and 5, are predominant in this zone. The existing geological map suggests that Zone D is underlain by phyllites. This is in contrast to the relatively high apparent resistivities encountered. It is rather thought that Zone D is underlain by quartzites or by phyllites interbanded with quartzites. This interpretation is supported by a few quartzite outcrops found in the extreme south-east of the investigated area (Mdala, 1975). Zone E, in the north-east, shows positive residuals, see Figures 2 and 4, and moderate smoothed apparent resistivities (200–460 ohmmeters), see Figures 3 and 5. Apparent resistivity values are believed to be too high to represent phyllites, as suggested by the geological map. Resistivity surveys done north and north-east of Zone E would rather suggest that the north-eastern part of Zone E represents a bed of quartzites which apparently separates gneisses and granites of the Basement Complex from meta-sediments of the Katanga System.

Geoelectrical classification of Zones A to E and their geological interpretation is summarized in Table 3.

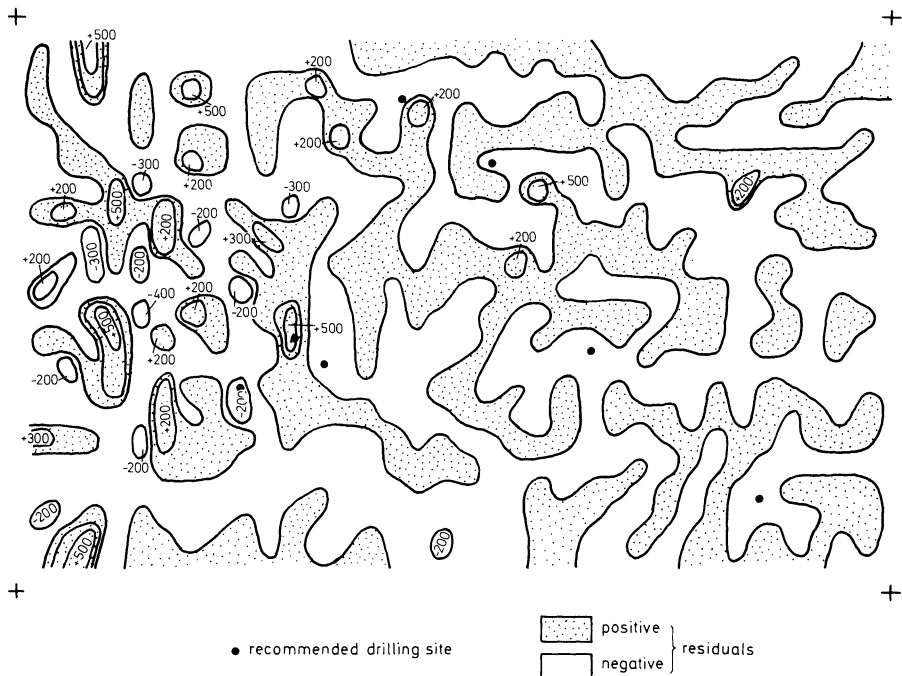
Table 3. Geoelectric Properties

Zone	Geological interpretation	Constant average method (Fig. 2)	Moving average Method (Fig. 3)	Least squares method (Fig. 4)	Moving least squares method (Fig. 5)
A	Phyllite	negative residuals	50–100 Ωm	negative	50–100 Ωm
B	Dolomite	positive residuals	101–815	positive	101–880
C	Phyllite	negative residuals	40–100	negative	45–100
D	Quartzite	positive residuals	101–770	positive	101–815
E	Quartzite	positive residuals	200–460	positive	200–460

4.3. Proposed Hypothetical Geological Model as Derived from this Resistivity Survey and Recommendation of Drilling Sites for Pilot and Possible Production Wells

The qualitative interpretation of apparent resistivity data is based on residual and regional resistivity maps. Their geological interpretation reveals that the investigated area may be underlain by phyllites, dolomites/limestones and by quartzites. This derived geological model, see Figure 7, does not correspond entirely with the existing geological map. Since there are only few outcrops observed in the extreme south of the investigated area, pilot wells become necessary in order to verify the proposed geological model.

It is thought that production wells may be possible only in the central part of the investigated area (Zone B). Drilling sites are recommended either close to the

**Fig. 6.** Residual apparent resistivity map (moving average method)

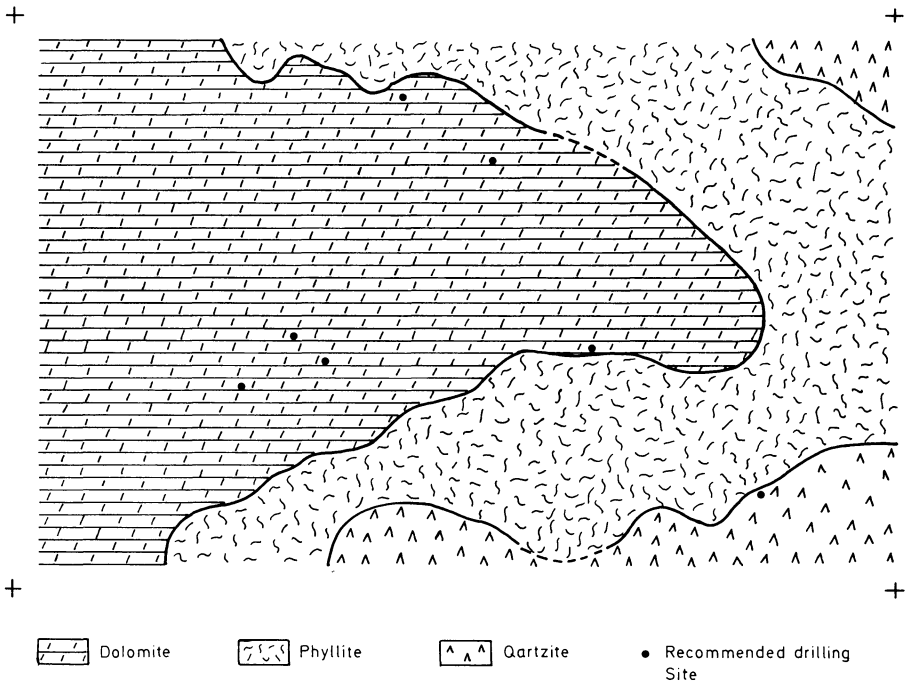


Fig. 7. Interpretation of apparent resistivity data and recommendation of boreholes

interpreted phyllite/limestone contact, or where large negative residuals may indicate cavitation.

A residual resistivity map, as derived from the moving average method, is shown in Figure 6. Large negative residuals and gradients are apparent in the western part of Zone B, whereas small negative and positive residuals are predominant in the remaining parts of the investigated area. Recommended drilling sites for pilot and possible production wells are shown in Figure 7.

5. Discussion of Results and Conclusions

The proposed regional-residual separation apparently does largely improve the resolving power of apparent resistivity data, and does therefore facilitate qualitative interpretation at least in those cases where the isoapparent resistivity map itself appears to be very complicated.

The residual map, as derived either from the constant average method, see Figure 2, or from the least squares method, see Figure 4, are very similar in their appearance. Areas characterized by positive or negative residuals are thought to represent different geological formations. Although the zero iso-residual lines may not necessarily coincide with geological boundaries, they certainly do approximately outline areas of similar geoelectrical properties. The constant

average method is very simple to apply in the field whereas the least squares method makes the use of mini-computers necessary.

The regional resistivity maps of Figures 3 and 5, which were derived from the moving average and the moving least squares methods, respectively, look very similar and represent a smoother image of the iso-apparent resistivity map, shown in Figure 1. This representation of smoothed apparent resistivity data has the advantage that apparent resistivity data can be related to those which were measured elsewhere in similar geological environments. The regional resistivity map as derived from the moving least squares method is extremely smooth, see Figure 5. Its compilation however is only possible by using mini-computers with sufficient storage capacity.

Residual resistivity maps, as derived from the moving average method, see Figure 6, or by the moving least squares method, are thought to represent local anomalies within a geological formation. Large negative residuals, as observed in the western part of Zone B, see Figure 6, may indicate localized fissuring or cavitation in limestones.

References

- Agocs, W.B.: Least squares residual anomaly determination. *Geophysics* **16** (4), 686–696, 1951
- Apell, B.A.N.C.: The quality of some two-dimensional filters in separating regional and local gravity anomalies. *Geophys. Prospecting* **22** (4), 601–609, 1974
- Bhattacharya, B.B., Jain, S.C., Mallick, K.: Geophysical prospecting for barite. *Geophys. Prospecting* **22** (3), 421–429, 1974
- Flathe, H.: Possibilities and limitations in applying geoelectrical methods to hydrogeological problems in the coastal areas of North West Germany. *Geophys. Prospecting* **3** (2), 95–110, 1955
- Flathe, H., Homilius, J.: *Geoelektrik in der Wassererschliessung*. In: Schneider, H. *Die Wassererschliessung*, (Herausg.), 2. Aufl. S. 201–277. Essen: Vulkan 1973
- Hallenbach, F.: Geoelectrical problems of the hydrology of West German areas. *Geophys. Prospecting* **1** (4), 241–249, 1953
- Keller, G.V., Frischknecht, F.C.: *Electrical methods in geophysical prospecting*. New York: Pergamon Press 1966
- Kerr, C.D.: Revised quarter degree sheet 1428 NW quarter. Geological Survey Department, Lusaka, 1969
- Krulc, Z., Mladenovic, L.J.: The application of geoelectrical methods to groundwater exploration of unconsolidated formations in semi-arid areas. *Geoexploration* **7** (2), 83–95, 1969
- Kunetz, G.: *Principles of direct current resistivity prospecting*. *Geoexploration Monographs, Serie 1, Nr. 1*. Berlin: Gebrüder Bornträger, 1966
- Mdala, L.C.: *Geophysical exploration for groundwater in limestone aquifers of the Republic of Zambia*. M. Sc.-thesis, Lusaka, 1975
- Nettleton, L.L.: Regionals, residuals, and structures. *Geophysics* **19** (1), 1–22, 1954
- Serres, Y.F.: Resistivity prospecting in a united nations groundwater project of Western Argentina. *Geophys. Prospecting* **17** (4), 449–467, 1969
- Töpfer, K.D.: Die Ortung von Störkörpern mit dem Schlumberger Messverfahren. *Arch. Meteorol. Geophys. Bioklimatol., Ser. A*, **18**, 191–220, 1969
- Töpfer, K.D.: On the selection of electrode arrays during geoelectrical exploration programs in regard to their filtering characteristics. (in preparation)
- Töpfer, K.D., Legg, C.A.: Geophysical exploration for groundwater in the Lusaka District, Republic of Zambia. *J. Geophysics* **40** (1), 97–112, 1974
- Van Dam, J., Meulenkaamp, J.J.: Some results of the geoelectrical resistivity method in groundwater investigations in the Netherlands. *Geophys. Prospecting* **15** (1), 92–115, 1967

The Iranian Long Period Array (ILPA)

B. Akasheh*, I. Eshghi and R. Soltanian

Institute of Geophysics, Teheran University, Amir-Abad-Bala, Tehran-1', Iran

Abstract. The extended range 7 elements (ER7) seismic array, ILPA, has been installed in Iran. Construction was started in the winter of 1973 as a joint undertaking of the governments of Iran and the United States of America. This array began its operation in January 1976.

Key words: Array – Iranian long period array.

Based on a request from USGS under sponsorship of the Advanced Research Projects Agency (ARPA), the United States Government proposed to Iran, in cooperation with the Institute of Geophysics, University of Tehran in November 1973 the installation of an extended range seismic array on the Iranian Plateau. The purpose of such an array was to provide data for research on seismological detection and identification problems. Field work and instrument installation were performed by Texas Instruments, Geotech, and by the Institute of Geophysics, Tehran University. USGS and Texas Instruments acts as a consultant and technical adviser for ILPA. The purpose of this paper is to inform our colleagues about the capabilities of the array, as well as the research activities which make use of the ILPA data.

ILPA is located southwest of Tehran and comprises 7 three-component wideband borehole seismometers, model 36,000 developed by Geotech. The array is circular in shape with 6 instruments forming the circle and the seventh located in the center of the array. The diameter of the array is about 60 km. The coordinates of the remote sites (Latitude φ , and Longitude λ), the distances between site number 1 in the center of the array and other 6 sites on the circle (Δ_{1-i}) and the azimuth (AZ) with respect to site number 1 and north direction (clockwise direction) are given in Table 1. The coordinates for sites and the elevations have only been estimated from the topographic maps.

The seismometers are in boreholes with depths about 100 m. One borehole seismometer system consists of a cable strain relief, stabilizer, electronics, seismo-

* To whom offprint requests should be sent

Table 1

Site No.	φ Lat	λ Long	Δ_{1-i}	AZ	Elev.
1	35.41 N	50.71 E			1,378km
2	35.66	50.89	32.1 m	28°	1,432
3	35.48	51.00	27.5	74	1,105
4	35.24	50.93	27.5	142	1,396
5	35.21	50.59	24.8	212	1,372
6	35.48	50.43	26.7	284	1,585
7	35.70	50.60	33.6	343	1,287

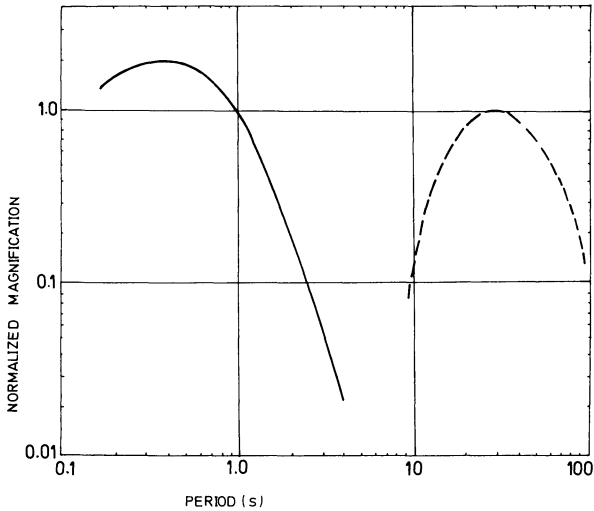


Fig. 1. Normalized response curves for short and long period channels. Short period —, long period - - - -

meter module and a holelock with a length of 3.27 m and 14 cm maximum case diameter. One sensor system consists of three orthogonal by suspended masses of 367 gram each. Each horizontal and vertical component of the seismometer is contained in a separate module having an upper diameter of 8.9 cm and a lower diameter of 6.6 cm and a height of 14.2 cm. The displacement of the mass relative to the frame acceleration is measured by a capacitance bridge transducer, the bridge is excited with a 15,625 Hz sinusoidal voltage. Instruments response curves including long and short period filters are given in Figure 1.

In the Central Recording Station, located in Tehran on the Institute of Geophysic's territory, there are two Texas Instruments model 980A computers and peripheral equipment used for data processing and data recording. There are 21 Long Period (LP) raw data channels, 1 to 21 Short Period (SP) raw data channel, only 5 SP channels are instrumented, 1 to 10 Long Period beams. The processed data will be recorded on Develocorders with a viewing screen to analyze data as it is recorded. The LP Develocorder with 1 to 9 traces will display 4 vertical channel beams, one horizontal transverse beam, one horizontal radial beam and

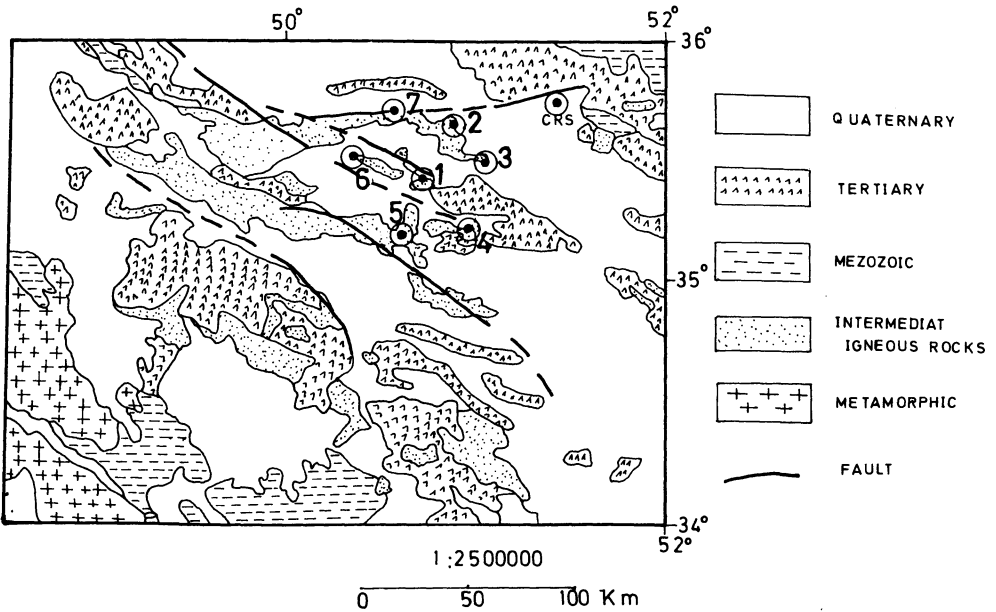


Fig. 2. Geological map of the Iranian Long Period Array

3 components of high gain single site data. The SP Develocorder with 1 to 11 traces records vertical data from 3 sites at high and low gain and the 2 horizontals from one of the 3 sites at high and low gain. There are also drum recorders for data display for 3 components of Long Period and 3 components of Short period on single pen recorders and one drum recorder with 3 pens for test data. The LP data received at the CRS are recorded and stored on magnetic tape for future off-line processing at a computer center and for editing. The data transmission over the satellite is planned for the future, but is temporarily being recorded on an auxiliary tape recorder for special analysis. The beam directions are from 0 to 359°, beam velocities are from 2.5 to 30 km/s and the beam types are vertical, radial and transverse.

More details about instrumentation can be found in references. To show the geology of the Iranian Long Period Array area, a geological map of 1:2,500,000 scale (Fig. 2) has been prepared based on the Iranian Oil Operating Company's geological map.

Most of the mezozoic sediments and metamorphic rocks are present over the south-southwestern parts of the array.

The tertiary rocks are scattered around the array. All of the remote sites are located on the Intermediate Igneous rocks.

There are several faults present within this array, of which a few are close to the remote sites. A brief picture of the geological structures of ILPA siting area is given in Figure 2.

The earth motions (analog signals) from seismometers are converted to gainranged digital signals, multiplexed into the radio carrier and transmitted each

0.05 s to the CRS. The Long Period channels are stored once per second and the Short Period channels are each stored twenty times per second. The transmission system has a capacity of about 1,800 baud of continuous data flow.

The Iranian Long Period Array began the operation in January 1976. The LP data received at CRS are stored on magnetic tape and the LP and SP-data are recorded on film and paper. The tape recorded data are transmitted to the Seismic Data Analysis Center (SDAC), optically recorded data is analyzed at CRS and at the Department of Seismology, Institute of Geophysics. This preliminary analysis is for preparation of a daily seismic bulletin and for the local and regional research; e.g., epicenter determination, magnitude calculation, vertical and lateral velocity anomaly determination, teleseismic residual studies, structural studies under the array, local focal mechanism, short and long period noise studies, etc.

The ILPA project has been sponsored by the United State of American under the overall direction of the Advanced Research Project Agency and technical management of the Albuquerque Seismological Laboratory, U.S. Geological Survey.

The views and conclusions contained in this document are those of the authors and should not be interpreted as necessarily representing the official policies, either expressed or implied, of the Advanced Research Agency or the U.S. Geological Survey.

References

- Teledyne-Geotech: Operation and maintenance manual borehole seismometer system model 3600, part 1 and 2, 28 October 1974
- Teledyne-Geotech: Operation and maintenance manual, short period filter, model 38850, 15 September 1975
- Teledyne-Geotech: Operation and maintenance manual, long period filter model 38840, 15 September 1974
- Texas instruments incorporated: Technical manual, operation and maintenance instructions, ER7 seismic system, 14-08-0001-14031 1 August 1975
- Texas Instruments Incorporated: model 980A computer maintenance manual. System description, Volume 1, Manual 980699-9701, Jan., 1973

Received February 9, 1976

Note Added in Proof. The coordinates for sites and CRS and the elevations have been estimated by the Defence Mapping Agency Topographic Center (DMATC), Department of Geodesy Geodetic Center Division are:

Site No.	Lat	Long	Elev.
1	35°24'58.3" N	50°41'19.5" E	1,346.6 m
2	35 39 46.1	50 53 51.5	1,172.1
3	35 28 34.0	51 01 25.5	1,106.4
4	35 14 19.3	50 54 04.2	1,373.1
5	35 12 46.2	50 34 52.0	1,350.2
6	35 28 25.2	50 25 32.2	1,540.2
7	35 42 10.1	50 36 32.0	1,305.1
CRS	35 45 10.1	51 23 19.6	1,461.7

Appearance of the Atmospheric Scatter Field during a Solar Eclipse

Reinhold Gerharz

USANVL, Bldg. 309, Fort Belvoir, Va. 22060, USA

Abstract. The polarization of the circumsolar scatter field was surveyed during the total solar eclipse of 7 March 1970. Its instantaneous distribution over an area of $50 \times 60 r_{\odot}^2$ was photographically recorded in green light, using a modified Savart filter. This arrangement resolved the unit areal of the polarized component to about $5 r_{\odot}$ and indicated its intensity as being 2.5% of the backscattered light. A distribution asymmetry of about 0.5% was detected.

Key words: Atmospheric scatter field – Solar radiation – Solar eclipse.

Scattered radiation, its content of polarized light, and its angular distribution offers clues to the nature and density of light scattering particles. In the terrestrial atmosphere, investigations of light in the circumsolar near field are much influenced and often impaired by the brightness of the solar aureole. The scattered light is only slightly polarized (Foitzik and Lenz, 1960; Coulson, 1975) and the mapping of the quasi-neutral zone between Babinet and Brewster points becomes difficult to interpret. Its causative variables are: the direct incidence bright solar component, the random density distribution of atmospheric scatterers, and the changes of the terrestrial albedo. Accurate measurements in the zone of the neutral points are usually carried out at low solar altitudes, and by spotwise photoelectric surveys. Ideally, the remnant field of polarization and scatter intensity should be symmetrical around the solar aureole, and the eclipsed sun should render itself most suitable for verifying such symmetry.

Previous polarization surveys were mostly conducted by solar physicists, whose interest remains limited to a region of about 10 solar radii. At this distance, solar atmospheric scattering dominates the field of view (if excellent seeing prevails), and data on the extent, emission and polarization of the corona may be obtained (Newall, 1906; Beckers and Wagner, 1970). Few if any discussions are found in literature on the brightness symmetry and the distribution of polarized light in the solar far field (Dandekar and Turtle, 1971; Shaw,

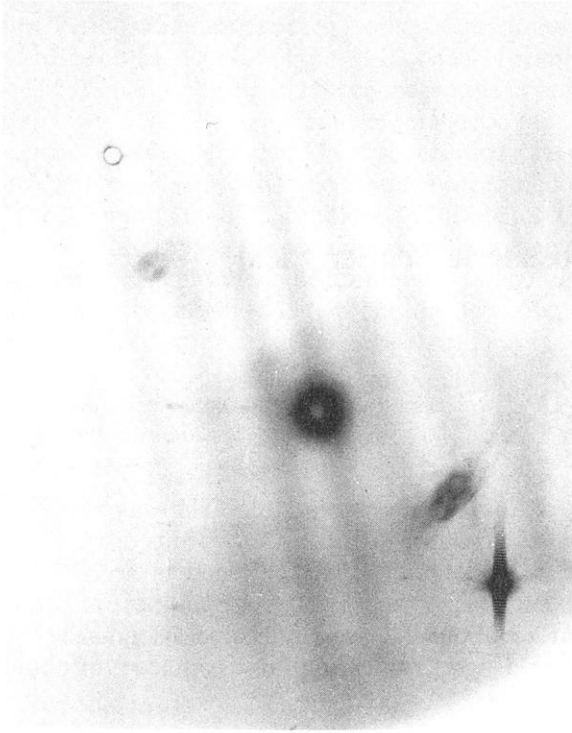


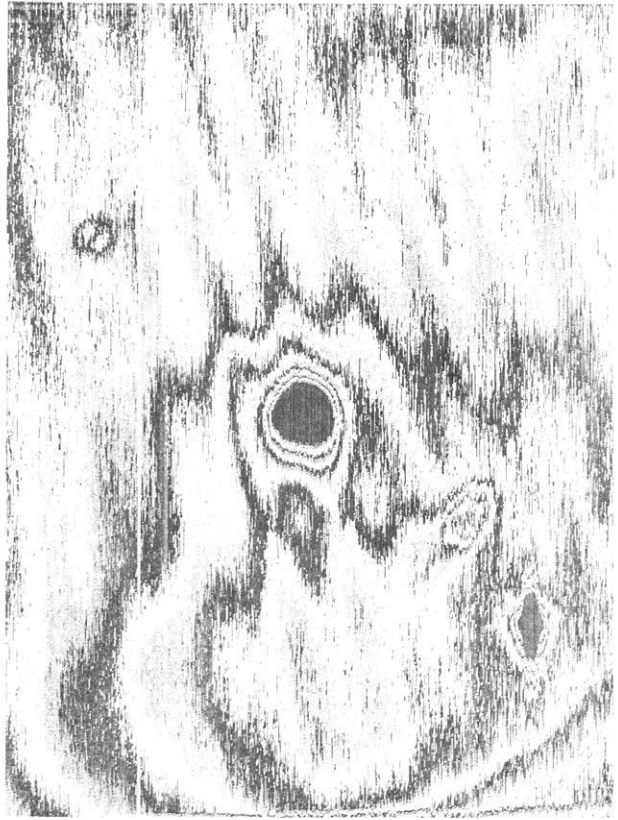
Fig. 1. Positive of the solar far field to $r_{\odot} \approx 50 \times 70$ during the solar eclipse of 7 March 1970. The negative was exposed by filtered light of $\lambda = 540 \mu\text{m}$ through a Savart plate showing extent and orientation of polarized scattering. Measured photographic densities for range 0 to max. 5.27: solar center (overexposed), 1.36; background, 0.12; fringes at $r_{\odot} = 8$: 0.15 to 0.16; derived percentage polarization: 2.5%

1975) which can only be observed with specialized optics (Newall, 1906; Laffineur, 1969; Serkowski, 1973).

The present attempt employed a 30 cm focal length camera with external objective filters that consisted of a modified Savart polariscope and an interference filter for passing monochromatic light at about $\lambda = 535 \pm 5 \mu\text{m}$. The photographic plate was exposed through the filter pack and covered an angular area of about 50×60 solar radii at the sky, or about 12×15 degrees. One of the exposed plates is reproduced as a positive in Figure 1. The image features of the eclipsed sun match those that were photographed by other observers (e.g. Newkirk and Lacey, 1970; or Menzel and Pasachoff, 1970). The original negative shows the same dark bands of interference of low overall contrast, which extend through almost the entire field of view. These fringes originate from the scattered polarized sky radiation that had been intercepted by the filters before entering the camera. The contrast of the interference bands is a measure of the degree of polarization of the light scattered from the sky. Fringes of very high contrast commensurate with 100% polarization, if we discount the small and unavoidable losses by the sensing inefficiency of the Savart plate. Details of the fringe forming mechanism of the Savart filter and of the fringe contrast evaluation are sufficiently described elsewhere (Serkowski, 1973; v. Heel and Strong, 1957; Gerharz, 1975).

The exposed plates were analyzed by a microdensitometer and indicated a maximum component of about 2.5% polarized light in the immediate solar

Fig. 2. Isophotes of the field of Figure 1, showing fringe density asymmetry of 0.5%. The three disturbances in the solar far field were caused by two secondary images and a density calibration mark at the lower right corner



vicinity, starting at $r_{\odot} = 6$. The recorded solar image itself suffers from inferior contrast and resolution because of secondary images from reflections and filter defects. These do not severely restrain the formation and contrast of the fringes and their distribution in the observed area.

Figure 1 was obtained from an exposure in mid-totally of the eclipse of 7 March 1970 in the central path of the umbra at $N35^{\circ} 51.7'$, $W72^{\circ} 2'$ near Williamston, S. Car., USA, when the local solar altitude was 45° at 13.34 UT. Figure 2 reproduces a display of isophotes of the same exposure, ignoring the solar near-field to about 7 solar radii. In this graph, it is very noticeable that a brightness asymmetry of the fringes had developed which follows the direction of the original bands, and which indicates, that contrast and percentage of polarization of the scattering field had slightly increased. This local difference of the fringe contrast amounts to not more than about 0.5% at equal distance from the sun. Such polarization asymmetry should also occur at clear sky without an eclipsed sun (Foitzik and Lenz, 1960), but its cause has not been specifically pointed out in previous reports (see e.g. Shaw, 1975; Fig. 10, p. 392).

During a solar eclipse, polarization asymmetry should be found enhanced, if good seeing prevails, and if the observer positions himself further away from the center of the path of the umbra. A further increase of the polarized com-

ponent may be expected when the scattered light intersects large pockets of cool, moist air that may have formed in the wake of the moving lunar shadow. Moreover, the predominant direction of the plane of polarization is expected to change during totality for any location of the observer, while the eclipse proceeds from 2nd to 3rd contact.

The geometry of these changes is determined by the observer's view through a varying slant range of air in the umbra, before the directly scattered sunlight is encountered. Depending on the observer's site in relation to the center of the umbra, the sources of scattered light may be located at a considerable atmospheric altitude (i.e. the umbral screening height), from where components of scattered sunlight are re-emitted into the umbra at near grazing incidence.

However, the present observer failed to detect such changes of polarization and intensity on account of his limited recording instrumentation. A much more pronounced asymmetry of the polarization field with a value up to 20% was reported by Shaw (1975), who observed when isolated clouds flanked one side of his location. It is not known, if the presence of these clouds might have influenced the polarization field by their tertiary scattering effects.

The large interval between about 10% and 25% of polarized light at $r_{\odot} = 50$, reported by Shaw (1975), contrasts the rather minute and faint signatures of about 0.5% shown in Figure 1, which was obtained in exceptionally clear weather, with no clouds visible at the entire sky, long before and after the center of totality had arrived. It appears questionable that the albedo of the earth may be cited as the principal contributor for this large component of polarization, because Figure 1 was also (like the data by Shaw (1975)) taken in the vicinity of a large body of water (the Atlantic) at one side of the solar azimuth.

Asymmetries of the intensity and the polarization of light curves that were taken through various propagation paths of the terrestrial atmosphere at numerous astronomical events in the past have often been presented implicitly (e.g. by Briggs 1938, de Bary et al., 1961; Gerharz, 1969), but these are still devoid of systematic observations, discussions and analysis from the viewpoint of global physical parameters.

References

- Barry, E. de, Bullrich, K., Lorenz, D.: Messungen der Himmelsstrahlung und deren Polarisationsgrad während der Sonnenfinsternis am 15.2.1961 in Viareggio, Italien, *Geofis. pura e appl.* **48**, 193–198, 1961
- Beckers, J.M., Wagner, W.J.: A photographic polarimeter for solar observations. *Appl. Optics* **9**, 1933, 1970
- Briggs, L.J.: Observed and computed radiation from 1st to 4th contact during a solar eclipse. *Trans. Am. Geophys. Union* **38**, 17–20, 1957
- Coulson, K.L.: Solar and terrestrial radiation, Ch. 7, pp. 191–192 and pp. 200–210. London-New York: Academic Press 1975
- Dandekar, B.S., Turtle, J.P.: Day sky brightness and polarization during the total solar eclipse of 7 March 1970. *Appl. Optics* **10**, 1223, 1971
- Foitzik, L., Lenz, K.: Einfluss des Aerosols auf die Himmelslichtpolarisation. *Optik* **17**, 554, 1960
- Gerharz, R.: Self-polarization in refractive systems. *Optik* **43**, 471–485, 1975

- Gerharz, R.: Photometric brightness asymmetry during a lunar eclipse. Arch. Meteorol. Geophys. Bioklimatol., Ser. A, **18**, 221–226, 1969
- Heel, A.C.S.v., in: Strong, J.: Concepts of classical optics, p. 400ff. London: W.H. Freeman Press 1957
- Laffineur, M., Burnichon, M.L., Koutchmy, S.: Weighted observation of the corona during the total solar eclipse of Sept. 22, 1968. Nature **222**, 461–462, 1969
- Menzel, D.H., Pasachoff, J.H.: The outer corona of the eclipse March 7, 1970. Nature **226**, 1143, 1970
- Newall, H.F.: Polarization phenomena in the solar corona 1905, Aug. 30. Monthly Notices Roy. Astron. Soc. **66**, 475–481, 1906
- Newkirk, G., Lacey, L.: The corona during the March 7, 1970 eclipse. Nature **226**, 1098, 1970
- Serkowski, K.: Polarization techniques. In: Methods of experimental physics, Vol. 2, p. 361. London-New York: Academic Press, 1973
- Shaw, G.E.: Sky brightness and polarization during the 1973 African eclipse. Appl. Optics **14**, 391 and 392 (Fig. 10), 1975

Received August 27, 1975; Revised Version November 21, 1975

Short Communications

Technique for Simultaneous Observation of Gravity and Vertical Gradient Data

S. Thyssen-Bornemisza

Geoscience and Instrumentation, Mayflower Hotel, New York, N. Y. 10023, USA

Key words: Gravimetry – Gradiometry – Vertical gradient – Geophysical prospecting.

The first vertical gravity gradient observations in the field using Δh intervals of 112 to 150 cm were carried out in 1943 (Thyssen-Bornemisza, 1944) and about ten years later a vertical gradient profile was taken in Canada over known geological subsurface structures (Thyssen-Bornemisza and Stackler, 1956). More recently close to one thousand vertical gradients were observed in Texas and New Mexico by Hunt Oil and a brief analysis of some results were presented (Thyssen-Bornemisza and Jacobi, 1971; Thyssen-Bornemisza et al., 1972). Further experimental surveys were taken in Germany and the Alps (Janle et al., 1971) and general assessments are published by Haase (1968), Hammer (1970), Hammer and Anzoleaga (1975), Thyssen-Bornemisza (1957, 1972, 1974) and Trommer (1964).

Purpose of this brief report is to propose a simple technique for simultaneously observing vertical gradients in addition to relative gravity data with the same equipment. Let us consider the equipments used by Janle et al. (1971) or, by Hunt Oil (Thyssen-Bornemisza, 1972), then the lower stage of the up-and-down technique uses a conventional tripod on which the gravity meter is placed. However, the same gravity meter also could be used to observe gravity differences between stations if the instrument is calibrated by a reference point. The upmeasurements to get the vertical gradients then could be carried out in the usual manner. Of course, standard correction of elevation and terrain must be considered to obtain acceptable free-air gravity values, but this could be of value also for the correction of vertical gravity differences. Accordingly, the same equipment would provide gravity and vertical gradient information with only little cost and time. A practical application could be seen in the immediate correction of gravity surveys by vertical gradients presented a few years ago (Thyssen-Bornemisza et al., 1972).

This author believes that experimental evidence to prove the proposed improved technique is not necessary when the standard method in using the up-and-

down technique is employed. Of course, vertical gravity gradiometers (Groten, 1975) could not be used for the suggested simultaneous approach.

Finally, the simultaneously observed gravity and vertical gradient profile is now briefly discussed. As mentioned before, a suitable reference point must be used for calibrating the "down" situation of the gravity meter used for the up-and-down technique. After observing 5 or more profile points a return to the reference point seems to be adequate. Furtheron, for computing the vertical gradient data running averages should be used according to formula

$$\overline{\Delta g/\Delta h} \cong (1/N) \sum_{i=1}^N (\Delta g/\Delta h)_i$$

where N denotes the number of profile stations. This method should reduce possible errors caused by irregular surface density including varying soil humidity (Haase, 1968; Thyssen-Bornemisza and Jacoby, 1971). In general relatively flat terrain and station spacing less than 50 m seems preferable, but with proper corrections vertical gradient measurements are less restricted (Janle et al., 1971).

References

- Groten, E.: A new type of vertical gravity gradiometer. *J. Geophys.* **41**, 321–324, 1975
- Haase, H.-S.: Zur Frage der Messung oder Berechnung vertikaler Schweredifferenzen. Dissertation, Rheinische Friedrich Wilhelm Universität, Bonn 1968
- Hammer, S.: The anomalous vertical gradient of gravity. *Geophysics* **35**, 153–157, 1970
- Hammer, S., Anzoleaga, R.: Exploring for stratigraphic traps with gravity gradients. *Geophysics* **40**, 256–268, 1975
- Janle, P., Makris, J., Menzel, M.: Experimental investigations of the vertical gradient of gravity. *Boll. Geofis. Theor. Appl.* **13**, 254–263, 1971
- Thyssen-Bornemisza, S.: Über die Möglichkeit den vertikalen Schweregradienten mit Gravimetern zu messen. *Beitr. angew. Geophys.* **11**, 36–45, 1944
- Thyssen-Bornemisza, S.: Das zweistufige Gravimeter-Messverfahren. *Erdöl und Kohle* **10**, 8–9, 1957
- Thyssen-Bornemisza, S.: Possible improvement of signal to noise ratio by vertical gravity gradients. *Z. Geophys.* **38**, 1059–1062, 1972
- Thyssen-Bornemisza, S.: An assessment of observed vertical gradients of gravity. *Geophysics* **39**, 114–115, 1974
- Thyssen-Bornemisza, S., Groten, E., Bazhaw, W. O.: Correction of accurate gravity surveys by carefully observed vertical gradients of gravity. *Geophys. Prospecting* **20**, 17–27, 1972
- Thyssen-Bornemisza, S., Jacoby, W. R.: Vertical gradients of gravity for areal density contrast exploration. *Z. Geophys.* **37**, 735–741, 1971
- Thyssen-Bornemisza, S., Stackler, W. F.: Observation of the vertical gradient of gravity in the field. *Geophysics* **21**, 771–779, 1956
- Trommer, R.: Der gravimetrische Vertikalgradient. *Freiburger Forschungshefte C-175 Geophysik*, VEB, Leipzig 1964

Received July 28, 1975

Letters to the Editors

Modern Standards for Gravity Surveys

C. Morelli*

Università degli Studi di Trieste, Istituto di Miniere e Geofisica Applicata,
Viale R. Gessi 4, I-34123 Trieste, Italy

Key words: International gravity standardization – Absolute gravity datum
– Geodetic reference system.

The modern gravity meter is capable of determining differences in gravity between measurement sites with very high accuracy. However, the gravity values established by one survey can be related to those established by another survey only when both are tied to gravity base stations whose gravity values are in a uniform system.

The benefits of adjusting all measured gravity values to a single datum are manifold. The geodesist, for example, must have world-wide coverage of gravity measurements related to a uniform system for computation of the earth's level surface configurations. The geologist and geophysicist benefit by being able to use data from several different surveys for uniform structural interpretations on a local, regional and global scale. Having local gravity surveys which are compatible with compilations over broader areas without systematic errors due to datum shifts is essential for regional-residual separations and interpretations over sedimentary basins and crustal blocks. With today's emphasis on economy in all operations, the ability to trade, buy, and/or use existing data in conjunction with new surveys can lead to important cost savings.

The absolute gravity datum adopted and recommended for all gravity surveys by the International Union of Geodesy and Geophysics is defined by the gravity values at more than 1,800 measurement sites which comprise the International Gravity Standardization 1971 (IGSN71) [1].

In addition to providing an absolute datum for gravity measurements, stations of the IGSN71 are strongly recommended for use in gravimeter calibration.

The readjustment of national gravity networks to IGSN71 datum and scale has been completed in many but not all countries. Therefore, users are cautioned to verify that the base reference values used for any new gravity survey are referred to IGSN71. Verification can be accomplished by contacting the national

* President, International Gravity Commission

agency responsible for gravity standards. In case of doubt, new surveys should be tied directly to IGSN71 stations. Gravity values and site descriptions for all IGSN71 stations, as well as an index map showing their locations, are available on request from the International Gravity Bureau (IGB) [2].

It is very important to recognize that, for calculation of gravity anomalies, the use of IGSN71 for observed gravity must be accompanied by the use of the Geodetic Reference System 1967 [3] for computation of theoretical gravity.

References

1. Morelli, C., Gantar, C., Honkasalo, T., McConnell, R.K., Tanner, I.G., Szabo, B., Uotila, U., Whalen, C.T.: The international gravity standardization net 1971. Int. Ass. of Geodesy, 39th Rue Gay Lussac, 75005 Paris, \$ 10, 194 p.
2. Bureau Gravimétrique International, 9, Quai St. Bernard, Tour 14, Paris (5^e)
3. Int. Ass. of Geodesy, 1971: Geodetic reference system 1967. Publ. Spec. Bull. Géod., 116 p.

Received November 28, 1975

Book Reviews

Physical Volcanology. L. Civetta, P. Gasparini, G. Luongo and A. Rapolla (Eds.). 186 illustrations, 22 tables, 333 pages. *Developments in Solid Earth Geophysics*, 6. ISBN 0-444-41141-0) DM 89.50. Amsterdam-Oxford-New York: Elsevier 1974

The book contains a collection of 14 different articles. It would be too lengthy to give an individual review of each chapter, so only some general impressions of the book are given. The reader who is familiar with volcanological literature will in a first turning over the pages recognize a good few figures which are certainly well-known to him. If he has read the preface before, he possibly will be somewhat disappointed, for he was promised a "collection of fourteen original papers". But the reader was also told in the preface that the book is "certainly not a text book", and now he may begin to wonder for whom the book was written? But notwithstanding this criticism it must be added that for the earth scientist not primarily working in volcanology it might be difficult to get hold of the original publications or it will save him much searching through the journals. So the book may be regarded as a reference book. The following subjects are treated by the authors:

Minakami, T.: Seismology of volcanoes in Japan.

Kubotera, A.: Volcanic tremors at Aso volcano.

Dibble, R.R.: Volcanic seismology and accompanying activity of Ruapehu volcano, New Zealand.

Kinoshita, W.T., Swanson, D.A., Jackson, D.B.: The measurement of crustal deformation related to volcanic activity at Kilauea volcano, Hawaii.

Cassinis, R., Lechi, G.M.: The use of infrared radiometry in geothermal areas.

Keller, G.V., Rapolla, A.: Electrical prospecting methods in volcanic and geothermal environments.

Yokoyama, I.: Geomagnetic and gravity anomalies in volcanic areas.

Clark, H.C.: Remanent magnetism of volcanic rocks.

Sigvaldason, G.E.: Chemical composition of volcanic gases.

Ishikawa, H.: Distribution of rare earths in volcanic rocks.

Machado, F.: The search for magmatic reservoirs.

Gorshkov, G.S.: Island arcs and oceanic ridges: volcanism and geophysical fields.

Ollier, C.D.: Phreatic eruptions and maars.

Minakami, T.: Prediction of volcanic eruptions.

Unfortunately no more than ten pages are devoted to geodynamical models of the origin of volcanism. On the other hand, two chapters deal with chemical composition of volcanic gases and distribution of rare earths in volcanic rocks. Certainly, volcanism can only be studied in a combined effort of all geosciences. But for a book with the title "Physical Volcanology" a comprehensive treatment of the physical aspects of volcanology should be preferred before accepting articles from related fields.

These criticism do not, however, detract from the value which this book has. It is well produced and most of the articles contain up-to-date information. Thus, again referring to the book's preface, one can readily join the editor's opinion "that this book finds its justification in its attempt to fill, at least in part, the lack of books devoted to the geophysical aspects of volcanology".

R. Schick, Stuttgart

Earthquake Prediction and Rock Mechanics. Max Wyss (Ed.). In: Contributions to Current Research in Geophysics. (CCRG), Vol. 1; Special issue of "Pure and Applied Geophysics" (Pageoph), Vol. 113, No. 1/2, 330 pages. Basel-Stuttgart: Birkhäuser 1975

With a volume on "Earthquake Prediction and Rock Mechanics" Birkhäuser Publishing Company starts a new series titled "Contributions to Current Research in Geophysics". To select this topic for the first volume of the series both Pageoph co-editor Max Wyss as well as the publisher were certainly encouraged by the publicity and the rapid development of earthquake research in the U.S., the Soviet Union, Japan and China and the output of the 1974 Penrose Conference on Fracture Mechanics and Earthquake Source Mechanisms, which had the purpose to bring together scientists from rock mechanics and seismology for maximum communication on the present state of art and future trends in both fields. Accordingly most of the original papers presented at this conference by American, Russian and Japanese experts are included in this volume. The 28 papers are written by researchers working in different disciplines in geophysics, and cover (a) laboratory observations related to premonitory earthquake phenomena (dilatancy related changes in elastic wave velocity, magnetisation and electrical resistivity) and frictional sliding characteristics (acoustic emission studies, stable sliding—stick slip transition), (b) theoretical modeling of dilatancy and fracture processes in the earth and fracture mechanics of brittle rock, and (c) in-situ investigations of aseismic fault behaviour, earthquake precursors (tilt, temporal velocity changes, premonitory strain, resistivity changes, deep borehole observations) and in-situ measurements of the crustal stress field by hydraulic fracturing.

Regarding this wide range of topics a formal division of the book into several chapters, introductory review articles to each chapter and an editorial summary would have been of great help for readers not directly acquainted with the field of earthquake research. Nevertheless the collection of papers presents a clear picture on the state of art in this field: Despite a great number of exciting and promising discoveries during the last decade earthquake prediction and the related problems of understanding the earthquake mechanisms or even earthquake control are not yet solved.

F. Rummel, Bochum

Tunneling of Low-Frequency Waves through the Subcrustal Lithosphere*

K. Fuchs** and K. Schulz

Geophysikalisches Institut, Universität Karlsruhe,
Hertzstraße 16, D-7500 Karlsruhe, Federal Republic of Germany

Abstract. Tunnel waves are long period waves which on overcritical incidence have penetrated through thin high-velocity layers. The generation and propagation of these waves are studied by numerical experiments using synthetic seismograms. Tunnel waves may occur as secondary and primary arrivals, on retrograde and prograde branches. Observations from explosion and teleseismic data with low-frequency tunnel waves are presented. – A model of the lower lithosphere with thin high-velocity layers explains not only the occurrence of tunnel waves but also the high-frequency transmission of P_n and S_n waves to teleseismic distances. This model is in accordance with the observation of seismic anisotropy in the upper mantle and suggests refinements of existing petrological models of the lower lithosphere.

Key words: Tunnel waves – Teleseismic P_n , S_n transmission – Thin high-velocity layers in lower lithosphere – Synthetic seismograms – Model of lower lithosphere.

1. Introduction

Within the framework of the plate-tectonic hypothesis the lithosphere is usually regarded as a rigid plate on top of the low-viscosity asthenosphere. While the fine structure of the earth's crust has been revealed by explosion seismic investigations, the subcrustal or lower lithosphere, i.e. the region between the crust-mantle boundary and the asthenosphere, used to be visualized as a rather homogeneous layer in which the velocities of the seismic waves increase only slightly with depth.

Recently there has been increasing evidence that the subcrustal lithosphere possesses a rather complex fine structure with alternating layers of high and low

* Contribution no. 184 within a joint research program of the Geophysical Institutes in Germany sponsored by the Deutsche Forschungsgemeinschaft (German Research Association). Contribution no. 126, Geophysical Institute, University of Karlsruhe

** To whom offprint requests should be sent

velocities (Hirn et al., 1973; Ansorge and Mueller, 1973; Mayer-Rosa and Mueller, 1973; Kind, 1974). In several parts of the globe unexpectedly high velocities up to 9.0 km/s have been observed both in the oceanic and continental lower lithosphere (Hales et al., 1970; Ryaboi, 1966; Kosminskaya et al., 1969, 1972). Kosminskaya et al. (1972) drew attention to the problem which arises in seismology if these high-velocity layers occur in the lower lithosphere. In this case seismic ray theory will not allow rays to penetrate below the lithosphere unless their phase velocity is equal or larger than the high velocities in the subcrustal lithosphere. Therefore ray theory cannot explain the occurrence of the same or of smaller velocities at depths in or beneath the asthenosphere observed by body waves from earthquakes in the crust. Kosminskaya et al. (1972) proposed already a solution to the dilemma: high velocities should occur only in thin layers which are not seen by low-frequency body waves from earthquakes observed on seismic stations. They become visible if observed with high-frequency body waves from explosions.

It is the purpose of this communication to present the results of numerical experiments (Schulz, 1975) with the help of synthetic seismograms computed by the reflectivity method (Fuchs and Müller, 1971) on the low frequency-leakage of waves through thin high-velocity laminas. The main result is a strong low-pass filtering of body-wave signals on non-geometrical ray-paths. This is regarded as dispersion of body waves introduced by the presence of such laminas since multiple path signals with different frequency content arrive at the same location. Then explosion and teleseismic observations are reported which show such a dispersion. This provides new and independent evidence for the presence of thin high-velocity laminas in the lower lithosphere.

2. Numerical Experiments with Tunnel Waves

When a seismic body wave (e.g. P -wave) is incident from a low velocity medium upon the plane boundary of a high velocity medium beyond the critical angle, the wave does not only cause a refracted S wave and overcritically reflected P and S waves but also an inhomogeneous P wave in the lower medium (see. Fig. 1). The amplitude A of this inhomogeneous wave decays exponentially with distance z from the interface:

$$A \sim \exp\left(-\frac{\omega}{c} \sqrt{1 - \frac{c^2}{\alpha_2^2} z}\right)$$

where ω is the angular frequency, c the phase velocity of the wave and α_2 the P -velocity of the lower medium. The amplitude decay increases with increasing frequency and decreasing phase velocity, i.e. with increasing of angle of incidence. If the inhomogeneous wave reaches the boundary to another low-velocity layer with sufficient amplitude, it will produce body waves propagating in the low-velocity medium (Fig. 1 lower part). The P -ray with phase velocity c tunneled into the lower medium with P -velocity α_1 is refracted with the angle of incidence $\gamma_1 = \sin^{-1}(\alpha_1/c)$.

Since the high-frequency parts of the wave decay more rapidly than the low frequencies, the latter will be predominant in the wave penetrating into the lower

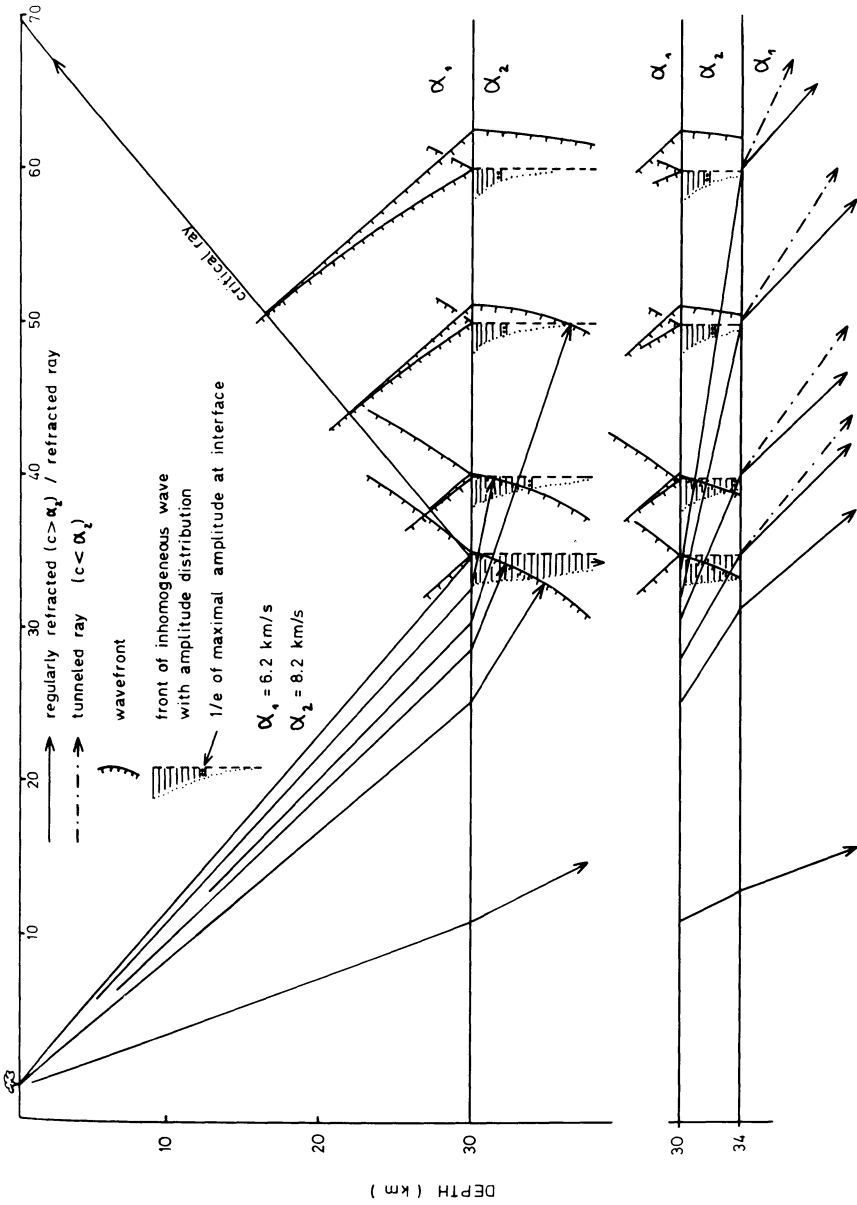


Fig. 1. Generation of a tunnel wave on the overcritical incidence on a thin high-velocity layer. Upper part: The overcritical reflection causes an inhomogeneous wave with amplitudes decaying exponentially with distance from the interface. Lower part: If the lower boundary of the high-velocity layer is reached by the inhomogeneous wave before its amplitudes are too strongly attenuated, a tunnel wave is generated in the lower halfspace. Solid lines: normally refracted rays. Dashed-dotted lines: tunneled rays

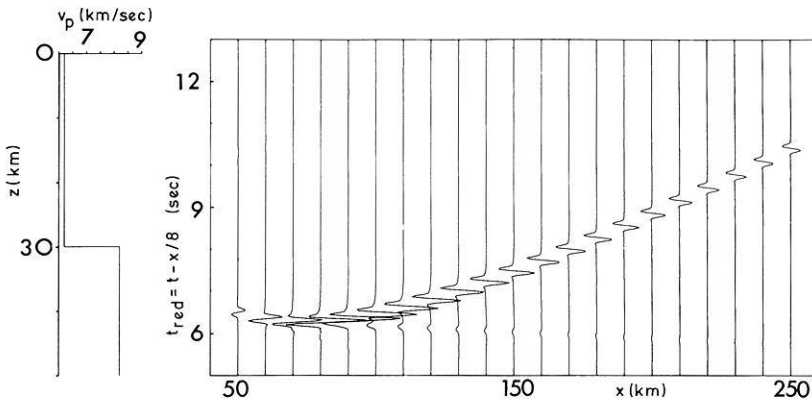


Fig. 2. Synthetic seismogram section of reflection from a first-order discontinuity. Explosion source with signal

$$f(t) = \begin{cases} \sin \frac{20}{3} \pi t - \frac{1}{2} \sin \frac{40}{3} \pi t & \text{for } 0 \leq t < 0.3 \\ 0 & \text{for } t < 0, t > 0.3 \end{cases}$$

S-wave velocity $v_s = v_p/\sqrt{3}$; density $\rho = 0.252 + 0.379 v_p$

medium. In analogy to wave mechanics where a wave particle can penetrate or tunnel through a potential wall we will speak of a tunnel wave. This term has been used before by Richards (1973) for long-period body waves propagating in the lower mantle and leaking into the core, and by Mellman and HelMBERGER (1974) in the same sense as in this paper. The tunneling of low-frequency waves through thin layers has been treated by a number of authors. Brekovskikh (1960) discusses the energy penetrating into a high-velocity medium if a wave is incident from the low velocity halfspace at angles larger than critical (p. 275 and 297). Brekovskikh uses the term "lateral wave". Červený and Kozák (1972) and Červený et al. (1972) studied the occurrence of these waves, termed by them pseudospherical waves in a low-velocity channel with the aid of model seismic experiments using Schlieren-technique. Long-period waves tunneling through thin high-velocity layers have been used with success in seismic refraction experiments of exploration geophysics (Krey, 1957). One of the best examples of tunneled waves may be found in Figure 3 of Krey's paper.

We will now present a series of synthetic seismograms and begin with that for the *P*-reflection from a first-order discontinuity at a depth of 30 km (Fig. 2). The seismograms have been displayed with a reduction velocity of 8.0 km/s. If not stated otherwise the same reduction velocity will be used throughout this paper. The shape of the incident signal with a dominant frequency of 4 Hz is the same as that of the subcritical reflection. The reflection attains the largest amplitudes slightly beyond the critical distance where the head wave propagating in the lower medium separates from the overcritical reflection.

In the following Figures 3–5 a thin layer with thickness $h = 1.25, 0.3$ and 0.1 km, respectively, is placed at a depth of 30 km followed by a low-velocity layer of 10 km thickness with the same mechanical properties as the upper halfspace.

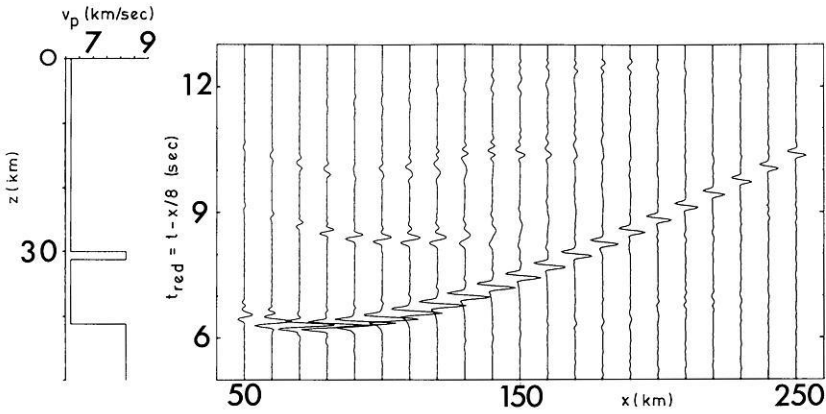


Fig. 3. Synthetic seismogram section of reflection from a thin layer ($h = 1.25$ km) over a low-velocity layer and a high-velocity halfspace. Other parameters as in Figure 2. The first signals following the strong reflection from the top of the thin layer is the undercritical reflection from the base of the low-velocity zone. Later signals are multiple reflections within the channel

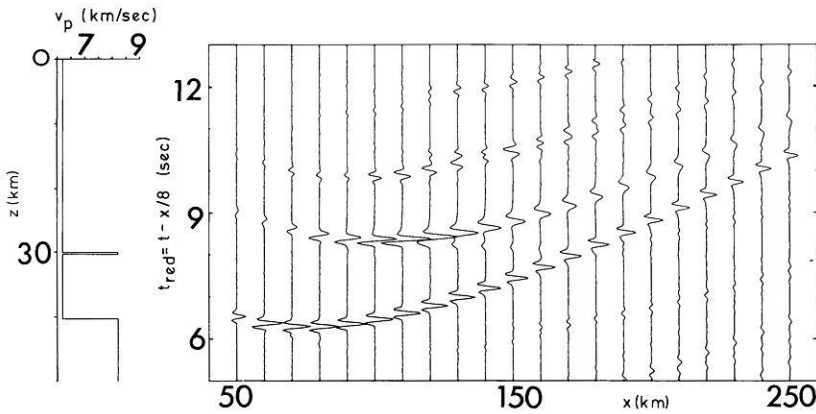


Fig. 4. Thickness of the thin layer $h = 300$ m, otherwise as Figure 3. The reflection from the base of the low-velocity layer beyond 130 km is overcritical and is formed by the wave which is tunneled through the thin layer. The amplitude of the reflection from the top of the thin layer has decreased especially in the neighbourhood of the critical distance

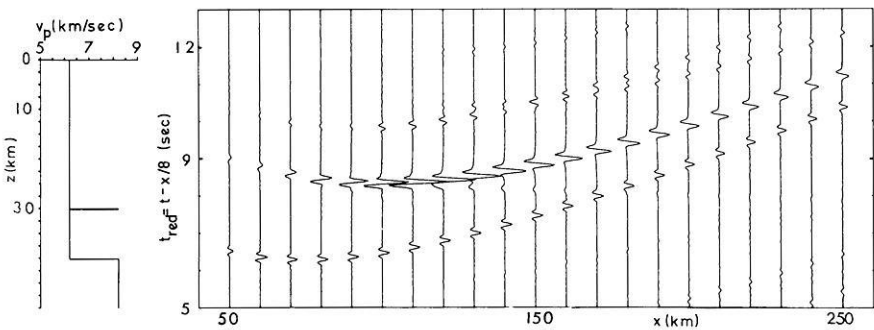


Fig. 5. Thickness of the thin layer $h = 100$ m, otherwise as Figure 3

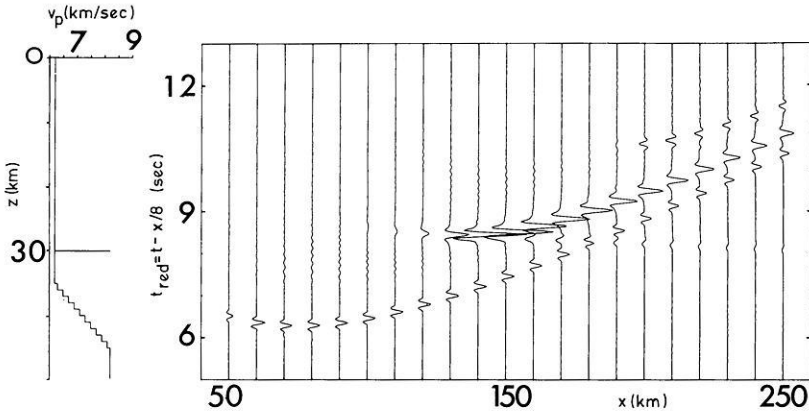


Fig. 6. Base of low-velocity layer is formed by gradient zone which suppresses undercritical reflections. Therefore the signal following the reflection from the top of the thin layer is a pure tunnel wave refracted from the gradient zone

The lower halfspace has the same properties as the thin high-velocity layer. The dominant wave length in the lamina is about 2 km.

In Figure 3 the reflection from the top of the thin lamina is followed by the subcritical reflection from the bottom of the low-velocity layer. Overcritical reflections from this interface are hardly seen since practically no energy with phase velocities less than 8.2 km/s is passed through the high-velocity layer. Only very low frequencies continue the subcritical reflection into the overcritical range. The amplitude distribution of the reflection from the top of the 1.25 km lamina is practically the same as from the first-order discontinuity (see Fig. 2).

In Figure 4 the thickness of the lamina is 0.3 km. In comparison with the previous figure the amplitudes of the overcritical reflections have increased strongly. At the same time the overcritical reflection from the thin layer has decreased, especially near the critical distance. This energy has penetrated the thin layer and appears now as overcritical reflection from the bottom of the low-velocity layer. This tunneling becomes even stronger if the thickness of the lamina is reduced to 0.1 km in Figure 5. The subcritical reflection from the bottom of the low-velocity layer is suppressed if the first-order discontinuity is replaced by a transition zone in Figure 6. The secondary arrival is now a pure tunnel wave reflected overcritically from the transition zone.

The frequency selection introduced by thin laminas becomes especially clear if a broad band signal is incident. In Figure 7 a wavelet with dominant frequencies of 1.6 and 6.5 Hz is used. The lamina has a thickness of 0.3 km as in Figure 4. Only in the subcritical range does the high-frequency component penetrate the high-velocity layer. In the overcritical range the reflection from the bottom of the low-velocity layer becomes abruptly a low-frequency signal. The high frequencies are screened off by the thin high-velocity layer. Such a layer can be regarded as a low pass-filter for tunnel waves and as a high-pass filter for overcritically reflected energy.

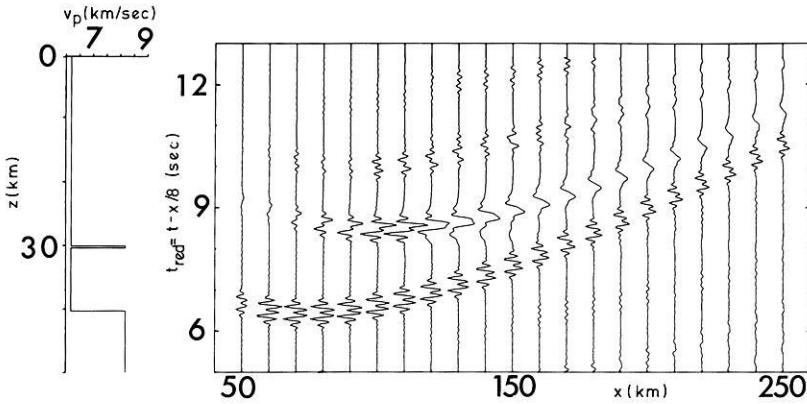


Fig. 7. Reflection of a broad band signal

$$f^*(t) = \begin{cases} \sin \frac{20\pi}{6} t - \frac{1}{2} \sin \frac{40\pi}{6} t + \sin \frac{80\pi}{6} t & \text{for } 0 \leq t < 0.6 \\ 0 & \text{for } t < 0, t > 0.6 \end{cases}$$

from the same model as in Figure 4 ($h = 300$ m). High frequencies are only reflected undercritically but are screened off by the high-velocity layer for overcritical incidence. The tunnel wave can clearly be recognized from its low-frequency spectrum

The observation of high-frequency arrivals separated from low-frequency arrivals on the same seismogram in the P -field closely beyond the critical distance must be taken as strong indication for the presence of thin high velocity lamina. The tunnel waves occur with sufficient amplitudes only if the thickness of the lamina is less than $1/4$ of the dominant wavelength. The velocity in the thin layer is higher or equal to the highest phase velocity of the tunnel wave.

3. Tunnel Waves in Explosion Seismic Observations

In the following figures we present evidence for the presence of tunnel waves in explosion seismic observations. Figure 8 is the record section of the crustal profile Florac 03 along the long-range profile in France (Sapin and Prodehl, 1973). In the distance range around 80 km the $P_M P$ reflection (phase 1) suddenly becomes clearly a low-frequency arrival while earlier phases on the same seismograms remain high-frequency signals. Therefore the low-frequency $P_M P$ -wave cannot be caused by some anomalous behaviour of the near-surface material at the recording stations. The same low-frequency behaviour of $P_M P$ can also be observed at larger distances around 130 and 180 km. In this case also low-frequency $P_M P$ arrivals are clearly preceded by high-frequency signals. This frequency behaviour of the $P_M P$ branch is simulated by the presence of a thin high-velocity lamina overlying the crust mantle boundary in a synthetic record section in Figure 9. The phases 1, 2, and 3 in Figure 8 correspond to the phases C, B, and A, respectively, in Figure 9.

Figure 10a is a collection of similar examples of low-frequency arrivals preceded by high-frequency phases from explosion seismic observations on continents in

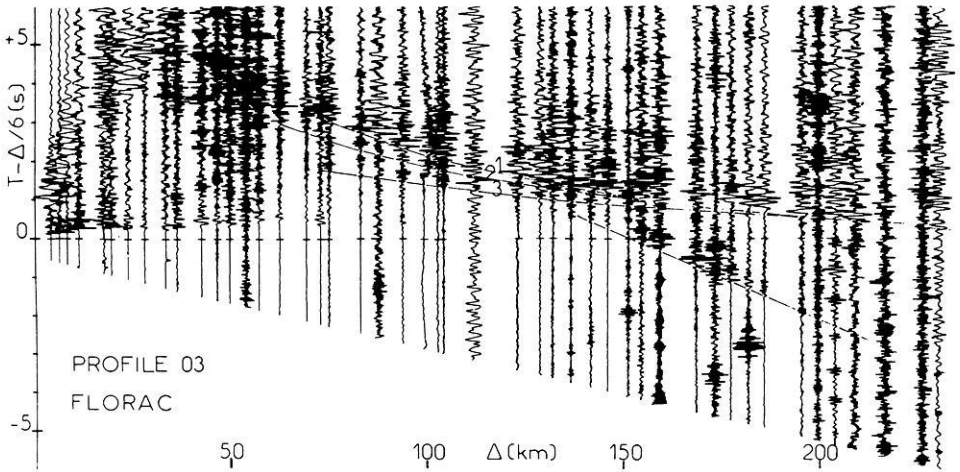


Fig. 8. Observed record section of the crustal profile FLORAC O3 in France (Sapin and Prodehl, 1973). Low frequency $P_M P$ phases can be recognized on seismograms around 80 km and 130 km with earlier high frequency arrival at the same station

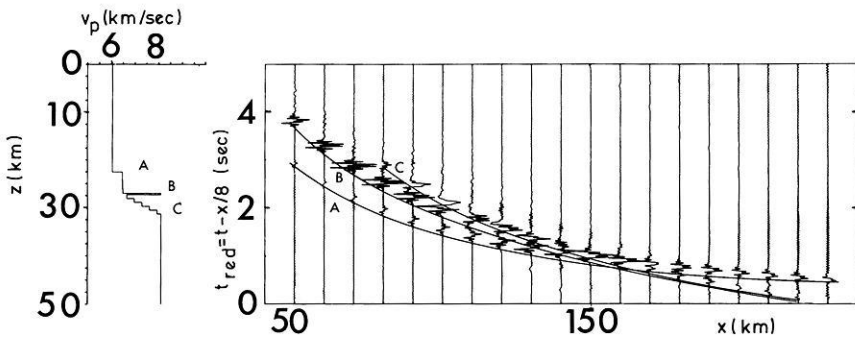


Fig. 9. Synthetic seismogram section for a model of the crust-mantle transition which simulates the observed frequency behaviour

several parts of the world: France, Canada, Portugal, Hungary, USSR. Our most extensive evidence for the presence of low-frequency arrivals in the presence of high-frequency precursors is taken from the LISPB seismic experiment in the British Isles (Bamford et al., 1975). Examples of the phenomena can be found on selected seismograms out to two or three hundred kilometres (Fig. 10b).

4. Tunnel Waves in Teleseismic Observations

In two studies (Walker and Sutton, 1971; Sutton and Walker, 1972) the authors present and interpret their observations of teleseismic P - and S -transmission through the upper mantle of the Pacific. They record events from the circum-

Pacific seismic belt by hydrophones at Midway, Wake and Eniwetok, and by SP-seismometers on Midway, Wake and Marcus. In Figure 11 their observations for events in the part north of 12°N of the Pacific are compiled.

The most striking feature of the hydrophone recordings (crosses in Fig. 11) is the absence of the normal refracted P -phase through the upper mantle which should be observed near the Jeffreys-Bullen travel time curve. Instead the hydrophones which are rather insensitive to 1–2 Hz frequencies receive seismic signals with dominant frequencies between 3–8 Hz lining up with an apparent velocity of 8.28 ± 0.03 km/s out to a distance of about 33° . From thereon the seismic arrivals recorded on the hydrophones follow closely J.-B. travel times. For distances smaller than 33° the hydrophones do not record high-frequency arrivals of normally refracted P -mantle phases with the exception of two deep focus earthquakes with hypocenters below 300 km. This indicates that high-frequency energy is not propagated through the lithosphere and below the asthenosphere unless the ray path is fairly steep in this part of the upper mantle as for deep earthquakes and for arrivals beyond 33° .—On the other hand the 1–2 Hz recordings of the SP-seismometers follow closely the J.-B. travel times.

Sutton and Walker interpret this frequency behaviour of the normally refracted P -wave as being caused by a low Q of the asthenosphere which affects the 3–8 Hz waves. Since the rays emerging beyond 33° plunge more steeply into the asthenosphere than those rays arriving at shorter distances, their total path through the low- Q asthenosphere is shorter. Therefore, high-frequency energy should be less attenuated at large distances.

Synthetic seismograms for a schematical model of the upper mantle with a prograde P -branch through the transition zone are shown in Figure 12. A zone of low $Q=100$ is built into the depth range of 30–40 km. The prograde P -branch refracted through the transition zone shows predominance of low-frequency energy at short distances while high-frequencies start to contribute only at large distances. This is the explanation of the frequency behaviour of teleseismic P -waves as proposed by Walker and Sutton scaled down to smaller depth and shorter distances.

However, the same frequency behaviour of P -transmission through the upper mantle can also be caused by a model of the lower lithosphere with thin high-velocity layers as will be shown in the following figures. The model of the upper mantle in Figure 13 is the same as in Figure 12 except for two differences: in Figure 13 Q is infinite, and a thin layer with thickness 625 m and a P -velocity of 8.2 km/s is introduced at a depth of 30 km. In this figure the wave tunneled through the thin layer forms a low frequency first arrival which is clearly to be recognized in the distance range 120–160 km. For larger distances the high frequencies of normally refracted rays start to appear. If the thickness of the layer or its wave velocities increase the high frequencies are stronger attenuated during tunneling through the thin layer. In Figure 14 its wave velocity is increased extremely to 9 km/s and is now larger than the velocity in the lower halfspace ($v_p=8.5$ km/s). The prograde P -branch is now a tunneled phase. Only beyond 250 km the high frequencies gradually start to contribute.

The frequency-distance behaviour of the refracted P -branch in Figures 12 and 14 is very much alike. A thin high-velocity layer acts as a low-pass filter in

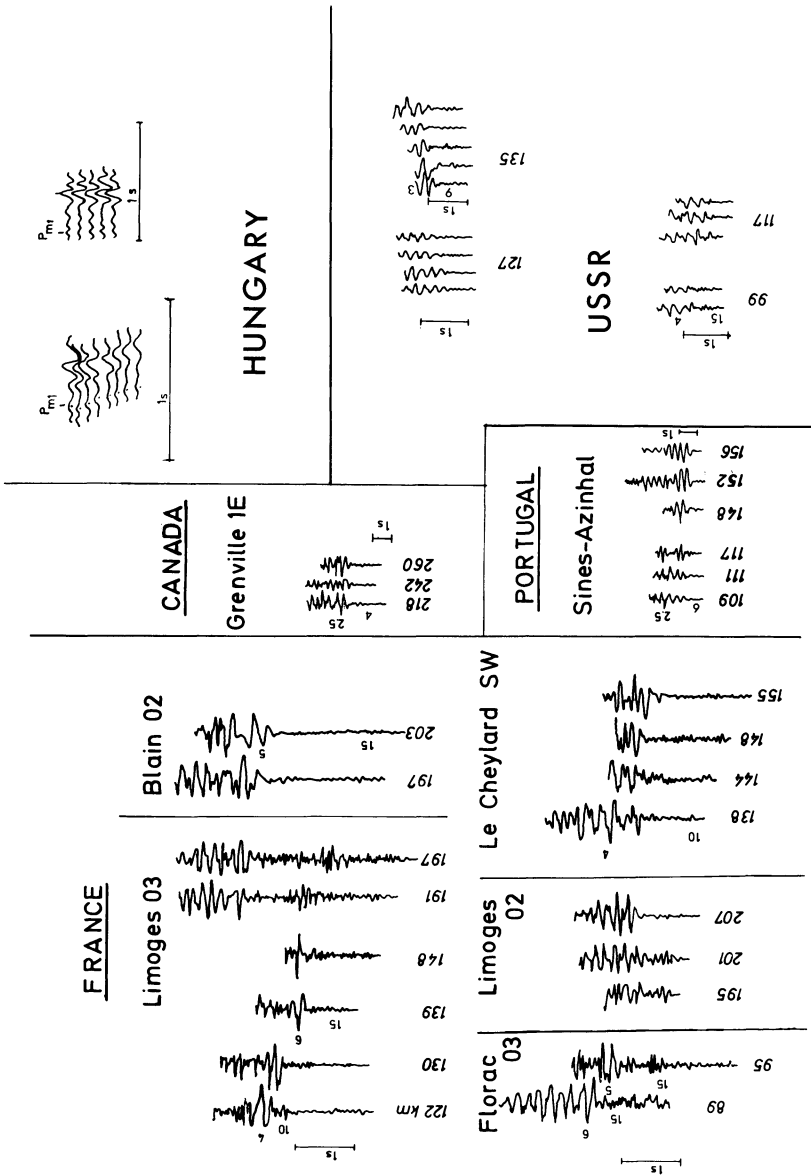


Fig. 10a. Examples of low-frequency $P_M P$ phases following high frequency precursors from various continental parts of the world. Dominant frequencies are indicated at the phases and distances at the beginning of every phase. Seismogram samples are from France (Sapin and Prodehl, 1973); Canada (Berry and Fuchs, 1973); Portugal (Mueller et al., 1973); Hungary (Mituch and Posgay, 1972); U.S.S.R. (Zverev and Tulina, 1971)

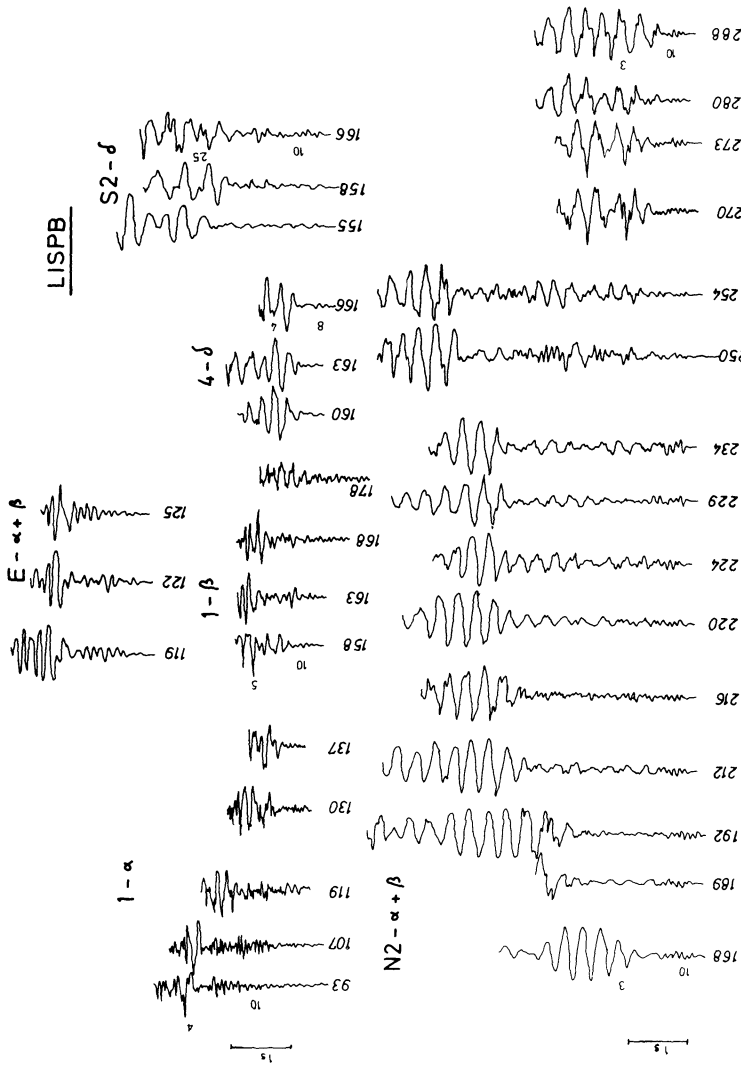


Fig. 10b. Examples of low-frequency $R_M P$ phases following high frequency precursors from the LISPB seismic experiment in Britain (Bamford et al., 1976)

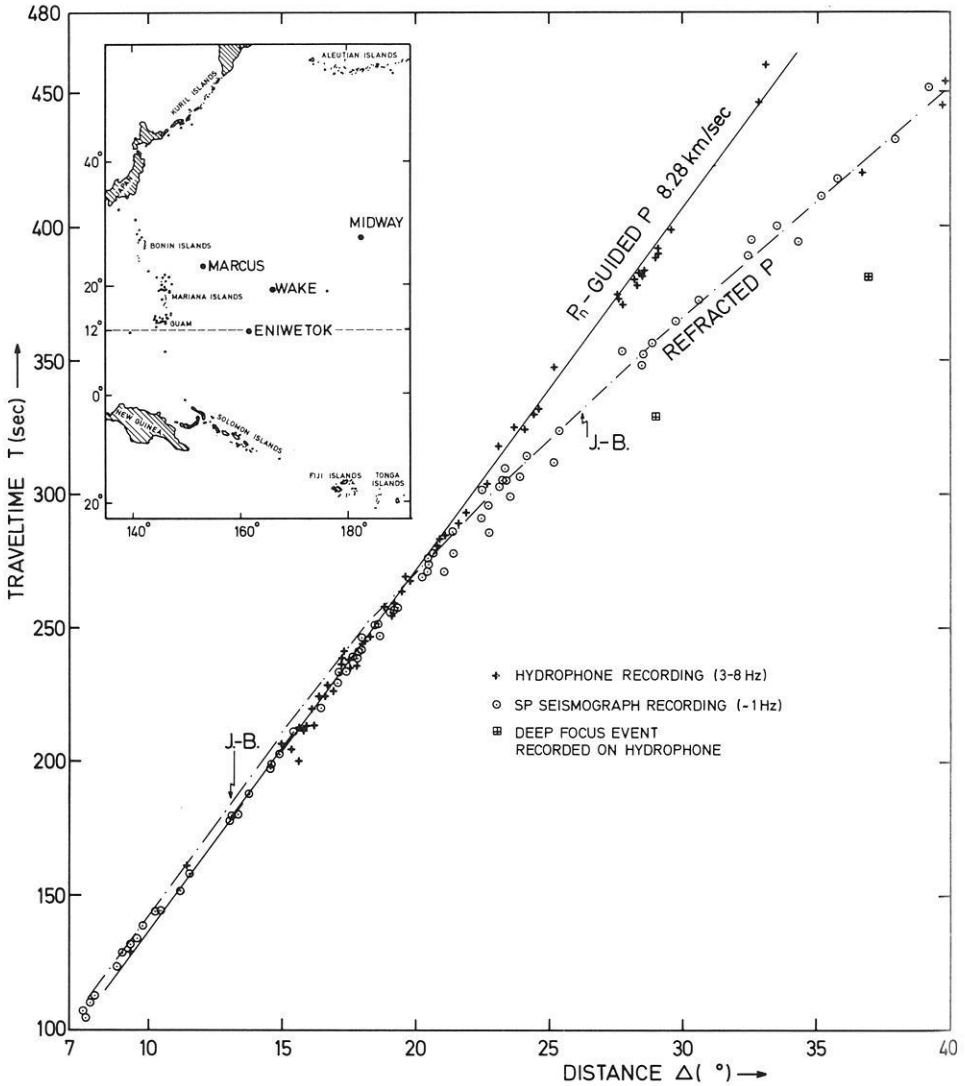


Fig. 11. Time-distance curve for P -waves in the Pacific as reported by Sutton and Walker (1972) and Walker and Sutton (1971). Inlet position map with the recording sites at Marcus, Eniwetok, Wake and Midway

very much the same manner as a low Q zone. Therefore, the presence of thin high-velocity layers in the lower lithosphere is an alternative explanation for the frequency behaviour of P phases refracted through the mantle.

5. A New Model of the Lower Lithosphere

The proposed mechanism of tunneling through high velocity strata in the lower lithosphere does not require that these layers have an infinite extent. A series of

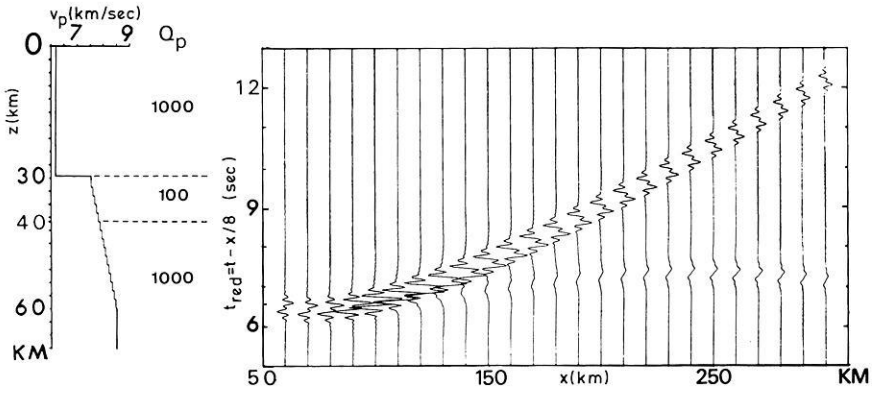


Fig. 12. Synthetic seismogram section for wave field reflected and refracted from a first-order discontinuity over a gradient zone. The first 10 km of the gradient zone possess a low $Q_p = 100$. This low Q zone attenuates high frequencies at short distances on the refracted P -branch. At larger distances high frequencies start to be visible again

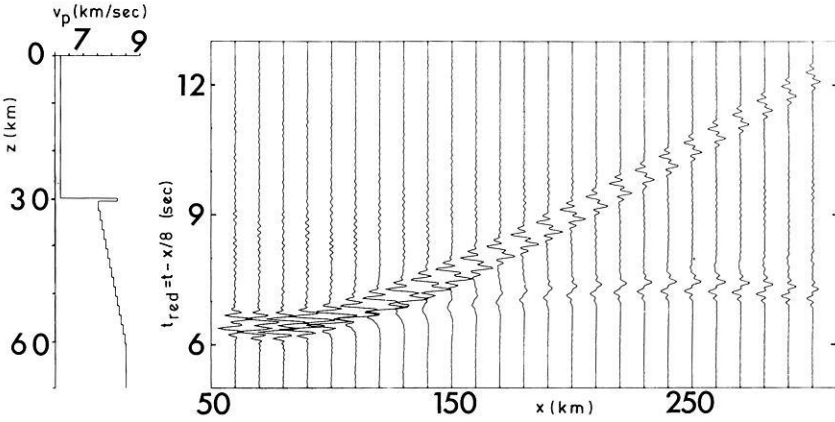


Fig. 13. The same model as in Figure 12, but with $Q_p = \infty$ and a thin high-velocity layer on top of the gradient zone ($h = 625$ m, $v_p = 8.2$ km/s). The low-frequency tunnel wave is now on the prograde branch of refracted P . High frequencies start to arrive on this branch beyond 200 km

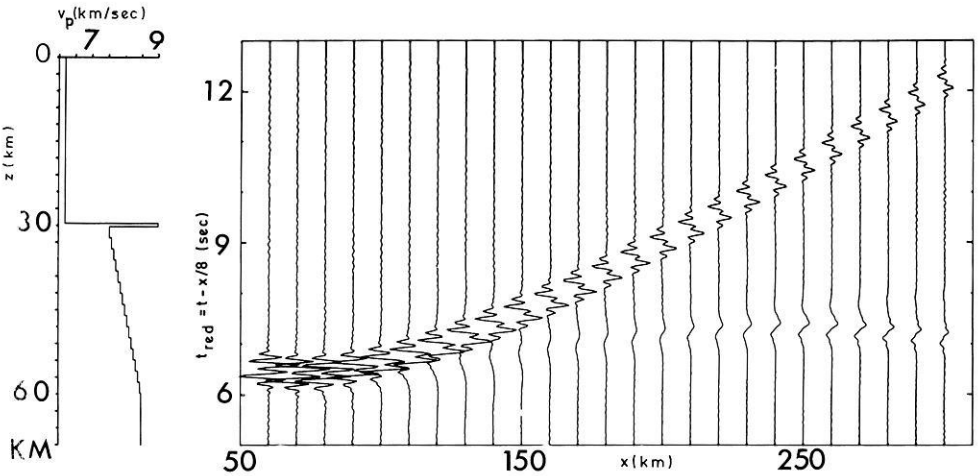


Fig. 14. The same model as in Figure 13, but with $v_p = 9.0$ km/s in the thin layer. High frequencies on the refracted P -branch are strongly suppressed. The wave field is very similar to that in Figure 12

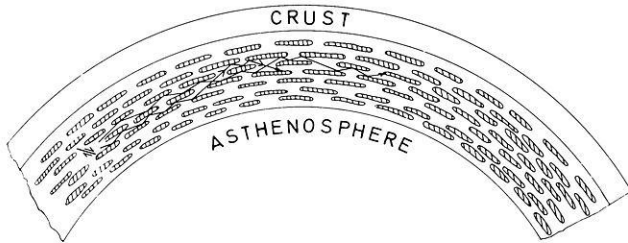


Fig. 15. Schematic seismic model of the lower lithosphere. The model is not to scale. Thin high velocity lenses are imbedded in "normal" upper mantle material. Their lateral extension is estimated to a few tens of kilometres, their thickness to a few hundred metres to a few kilometres. This model does not only explain the generation of tunnel waves it also serves as a possible waveguide for teleseismic transmission of high-frequency P_n -waves

thin parallel lenses of finite horizontal extent would produce a similar effect. A schematic model of the lower lithosphere including such lenses is depicted in Figure 15. The figure is not to scale. The fine structure of the crust and the deeper interior is not indicated. In the lower lithosphere thin high-velocity strata (dashed lenses) are imbedded in material with "normal" velocities, the latter is seen by long-period body and surface waves. Such a structure would also reproduce the high-velocity low-velocity layer alternation observed by Hirn et al. (1973) and Kind (1974). The high-velocity strata should be visualized as extending over only a few tens of kilometres, possibly less. Their thickness is estimated to about 0.5 to 1 km. However, an aggregate of thinner layers concentrated unevenly throughout the lower lithosphere could produce the same result. The high-velocity lenses should be oriented predominantly parallel to each other and more or less horizontally.

Such a model of the lower lithosphere could also explain the teleseismic transmission of high-frequency P_n and S_n waves, to distances of 30° or more (see Fig. 11) (Båth, 1966, 1967; Molnar and Oliver, 1969; Walker and Sutton, 1971; Sutton and Walker, 1972). Teleseismic P_n and S_n transmission is especially effective if the hypocenters are located in the lower lithosphere. In this case P and S waves are overcritically reflected between the high-velocity layers. While the low frequencies tunnel through the thin layers, the high frequencies in the range 2–8 Hz are trapped between the high-velocity layers. Higher frequencies are scattered by inhomogeneities smaller than the high-velocity lenses and leave this part of the upper mantle. Thus the lower lithosphere becomes a wave guide where a high-frequency pass band of P and S waves is propagated by overcritical reflection. S transmission is especially effective since no converted waves can penetrate through the thin layers to leave the wave guide. The frequencies in the pass band are determined by the thickness of the thin layers, their velocity and by the dimensions of scatterers in the wave guide.

Phase velocities of P -waves of up to 8.8–9.0 km/s in thin layers correspond to even higher velocities in the infinite medium (Press et al., 1954). Such high velocities in a depth range of 30–150 km are very likely caused by strongly anisotropic minerals such as olivine with a preferred orientation. Strong seismic anisotropy of the upper mantle with an azimuthal dependence of the seismic velocities is known from the oceans (Raitt et al., 1969) and was recently discovered also in the

continental upper mantle (Bamford, 1973). It is probable that the same mechanism which is generating the preferred orientation of anisotropic minerals is also responsible for the horizontal orientation of the thin high-velocity layers. Creep in regional stress fields can induce such a preferred orientation.

6. Conclusions

Tunnel waves provide new evidence for the presence of high velocities in thin layers within the lower lithosphere. The tunneling of low-frequency waves through thin layers is studied by numerical experiments. Tunnel waves are observed in explosion seismic data and may also be present in teleseismic P observations. The model of a lower lithosphere with thin high-velocity layers serves also as explanation of teleseismic P_n and S_n observations and is related to recent observations of upper mantle anisotropy.

This model requires further verification. It may be tested with a number of experiments. 1. Spectra of teleseismic signals should regularly show a strong decrease in high frequency energy as soon as the rays pass from undercritical to overcritical incidence from the asthenosphere to the base of the lithosphere. 2. Presently only group velocities of P_n and S_n waves are reported. Phase velocities of P_n and S_n waves as measured across large arrays should show similar velocities as measured by phase correlation on closely spaced stations on long-range profiles of explosion seismic experiments. 3. Earthquakes should be observed also with mobile stations to obtain better control on S -wave velocities.

This seismic model of the lower lithosphere provides also new bounds to petrological models. The velocities are definitely larger than admitted by some authors (e.g. Green and Liebermann, 1975) who restrict the velocities in this depth range to not more than 8.25 km/s. The presence of low-velocity zones throughout the lower lithosphere (see e.g. Kind, 1974) raises the question whether the transition from the lithosphere to the asthenosphere is sharp or extends over a considerable part of the lower lithosphere.

It must be concluded that by the explosion seismic investigation of the lower lithosphere new mechanical properties of this part of the upper mantle have been detected which are of considerable importance to geodynamical problems.

Acknowledgements. The authors acknowledge with gratitude the support by the German Research Society (Deutsche Forschungsgemeinschaft). Computations of synthetic seismograms were performed at the Computer Center of Karlsruhe University. Dr. Brian Kennett kindly made available to us his modified version of the reflectivity computer program. Sonja Faber helped with some computations. The authors appreciate also many discussions with their colleagues at the Geophysical Institute Karlsruhe. They are especially indebted to Drs. Bamford (University of Edinburgh), G. Müller, Prodehl for reading and helping to improve the manuscript. Ingrid Hörnchen typed the manuscript. The reviewers' critical comments are gratefully acknowledged.

References

- Anson, J., Mueller, St.: The P -wave structure of the uppermost mantle in Europe based on long-range explosion observations. *Z. Geophys.* **39**, 385–394, 1973
- Bamford, D.: Refraction data in Western Germany—a time-term interpretation. *Z. Geophys.* **39**, 907–928, 1973

- Bamford, D., Faber, S., Jacob, B., Kaminski, W., Nunn, K., Prodehl, C., Fuchs, K., King, R., Willmore, P.: A lithospheric seismic profile in Britain—I. Preliminary results. *Geophys. J.* **44**, 145–160, 1976
- Báth, M.: Propagation of S_n and P_n to teleseismic distances. *Pure Appl. Geophys.* **64**, 19–30, 1966
- Báth, M.: Observation of teleseismic P_n phases. *Pure Appl. Geophys.* **66**, 30–36, 1967
- Berry, M., Fuchs, K.: Crustal structure of the Superior and Grenville Provinces of the northeastern Canadian Shield. *Bull. Seism. Soc. Am.* **63**, 1393–1432, 1973
- Brekhovskikh, L.: *Waves in layered media*. New York: Academic Press 1960
- Červený, C., Kozák, J.: Experimental evidence and investigation of pseudospherical waves. *Z. Geophys.* **38**, 617–626, 1972
- Červený, V., Kozák, J., Pšeučik, I.: Refraction of elastic waves into a medium of lower velocity—pseudospherical waves. *Pure Appl. Geophys.* **92**, 115–132, 1972
- Fuchs, K., Müller, G.: Computation of synthetic seismograms with the reflectivity method and comparison with observations. *Geophys. J.* **23**, 417–433, 1971
- Green, D.H., Liebermann, R.C.: Phase equilibria and physical properties at the low velocity zones. Abstr. of paper presented at the XVI. General Assembly of IUGG, Grenoble, 1975
- Hales, A.L., Helsley, C.E., Nation, J.B.: P travel times for an oceanic path. *J. Geophys. Res.* **75**, 7362–7381, 1970
- Hirn, A., Steinmetz, L., Kind, R., Fuchs, K.: Long range profiles in Western Europe: II. Fine structure of the lower lithosphere in France (Southern Bretagne). *Z. Geophys.* **39**, 363–384, 1973
- Kind, R.: Long-range propagation of seismic energy in the lower lithosphere. *J. Geophys.* **40**, 189–202, 1974
- Kosminskaya, I.P., Belyaevsky, N.A., Volvovsky, I.S.: Explosion seismology in the USSR. In: *The earth's crust and upper mantle*, P.J.Hart, ed. A.G.U. monogr. **13**, 195–208, 1969
- Kosminskaya, I.P., Puzyrev, N.N., Alexeyev, A.S.: Explosion seismology: its past, present and future. In: *The upper mantle*, A.R. Ritsema, ed. *Tectonophysics* **13**, 309–323, 1972
- Krey, Th.: Erweiterte Möglichkeiten für die Refraktionsseismik durch die Verwendung von Geophonen mit niedriger Eigenfrequenz. *Geol. Jahrb.* **74**, 523–530, 1957
- Mayer-Rosa, D., Mueller, St.: The gross velocity-depth distribution of P - and S -waves in the upper mantle of Europe from earthquake observations. *Z. Geophys.* **39**, 395–410, 1973
- Mellman, G.R., Helmberger, D.V.: High-frequency attenuation by a thin high-velocity layer. *Bull. Seism. Soc. Am.* **64**, 1383–1388, 1974
- Mituch, E., Posgay, K.: Hungary. In: *Geophysical Transact. Hungarian Geophys. Institute*. Budapest, P. Müller, ed. pp. 118–129, 1972
- Molnar, P., Oliver, J.: Lateral variations of attenuation in the upper mantle and discontinuities in the lithosphere. *J. Geophys. Res.* **74**, 2648–2682, 1969
- Mueller, S., Prodehl, C., Mendes, A.-S., Moreira, V.S.: Crustal structure in the southwestern part of the Iberian peninsula. *Tectonophysics* **20**, 307–318, 1973
- Press, F., Oliver, J., Ewing, M.: Seismic model study of refractions from a layer of finite thickness. *Geophysics* **19**, 388–401, 1954
- Raitt, R.W., Shor jr., G.G., Francis, T.J., Morris, G.B.: Anisotropy of the Pacific upper mantle. *J. Geophys. Res.* **74**, 3095–3109, 1969
- Richards, P.G.: Calculation of body waves, for caustics and tunneling in core phases. *Geophys. J.* **35**, 243–264, 1973
- Ryaboi, V.Z.: Kinematic and dynamic characteristics of deep waves associated with boundaries in the crust and upper mantle. *Izv. Acad. Sci. USSR, Geophys. Ser., AGU transl.*, **3**, 177–184, 1966
- Sapin, M., Prodehl, C.: Long range profiles in western Europe. I. Crustal structure between the Bretagne and the Central Massif Central. *Ann. Géophys.* **29**, 127–145, 1973
- Schulz, K.: Die Bedeutung von Tunnelwellen in der Explosionsseismik. Diplom-thesis, Universität Karlsruhe, 94 p. 1975
- Sutton, G.H., Walker, D.A.: Oceanic mantle phases recorded on seismographs in the northwestern Pacific at distances between 7° and 40°. *Bull. Seism. Soc. Am.* **62**, 631–655, 1972
- Walker, D.A., Sutton, G.H.: Oceanic mantle phases recorded on hydrophones in the northwestern Pacific at distances between 9° and 40°. *Bull. Seism. Soc. Am.* **61**, 65–78, 1971
- Zverev, S., Tulina, Yu.: Deep seismic sounding of the earth crust in the continental shelf between Sachalin and Hokkaido. *NAUKA, Moscow*, 281 p., 1971

Computation of Reflection Coefficients for Layered Media*

R. Kind

Geophysikalisches Institut, Universität Karlsruhe, Hertzstr. 16, Bau 42, D-7500 Karlsruhe 21,
Federal Republic of Germany

Abstract. A fast computer program of the Thomson-Haskell matrix formalism is presented for the computation of the $P-SV$ reflection coefficients R_{pp} , R_{ps} , R_{ss} and R_{sp} for layered solid media. A matrix formalism and a computer program are also derived for the computation of P reflection coefficients for layered liquid media and of SH reflection coefficients for layered solid media.

Key words: Theoretical seismograms – Thomson-Haskell matrix formalism – Reflection coefficients.

Introduction

The reflectivity method of computing theoretical seismograms (Fuchs and Müller, 1971) is now a more often used tool for the interpretation of data in explosion seismology as well as in earthquake seismology. Although this method has great advantages, it suffers from rather long computer times. This is especially cumbersome if complete seismograms for the whole earth are computed (Müller and Kind, 1976). Therefore increasing the speed of the computations is still a desirable aim. The central part of the reflectivity method is the calculation of plane body waves in a layered medium. This problem is similar to the problem of computing dispersion of surface waves in such a medium. Efficient computer programs for the latter have been published by Schwab and Knopoff (1972). In the present paper a fast program is presented of the Thomson-Haskell matrix formalism for the computation of $P-SV$ reflection coefficients. A computer program for sound wave reflection coefficients for a layered liquid is also presented. Because of the equivalence of sound waves in a liquid and of SH waves in a solid, which was established by Satô (1954), this program can also be used for SH reflection coefficients.

* Contribution No. 136, Geophysical Institute, University of Karlsruhe

Computation of $P-SV$ Reflection Coefficients

We consider monochromatic plane waves propagating in a medium consisting of a number of parallel, solid, homogeneous, isotropic and ideal elastic layers between two halfspaces. A potential vector is defined (see e.g. Dunkin (1965)) for each of the n different media

$$\Phi_i = (\varphi_i^-, \psi_i^-, \varphi_i^+, \psi_i^+), \quad i = 1, n \quad (1)$$

where φ_i^+ , φ_i^- and ψ_i^+ , ψ_i^- are the P wave and SV wave potentials, respectively, corresponding to waves travelling in positive or negative z direction. The application of the boundary conditions yields a relation between the potential vectors of the lower and upper halfspace:

$$\Phi_n = M \Phi_1 \quad (2)$$

where M is the Haskell matrix. It is the product of the matrix of the lower halfspace T_n , the $n-2$ layer matrices G_i , and the matrix of the upper halfspace T_1 :

$$M = T_n \cdot G_{n-1} \dots G_2 \cdot T_1. \quad (3)$$

The elements of all these matrices are given by Fuchs (1968). Equation (2), however, cannot be used directly for numerical computations due to an intrinsic loss-of-precision problem. The delta matrix extension and the reduced delta matrix extension (Pestel and Leckie, 1963; Dunkin, 1965; Watson, 1970) were developed to overcome this problem. The 6×6 delta matrix of the 4×4 Haskell matrix is obtained by computing all possible 2×2 subdeterminants of the 4×4 matrix. The reduced delta matrix extension allows to work with 5×5 matrices instead of the original 6×6 matrices, due to symmetry in the elements.

Červený (1974) has calculated the reflection coefficients from (2) in terms of the elements \hat{M}_{ij} of the delta matrix \hat{M} of the Haskell matrix M :

$$\begin{aligned} R_{pp} &= \hat{M}_{14}/\hat{M}_{11}, & R_{ps} &= -\hat{M}_{12}/\hat{M}_{11} \\ R_{ss} &= -\hat{M}_{13}/\hat{M}_{11}, & R_{sp} &= \hat{M}_{15}/\hat{M}_{11}. \end{aligned} \quad (4)$$

There exists a very important multiplication rule in delta matrix theory: the delta matrix of a product matrix is equal to the product of the delta matrices of the individual factor matrices. Therefore the \hat{M}_{ij} can be computed by multiplication of the delta matrices \hat{T}_n , \hat{G}_i and \hat{T}_1 of T_n , G_i and T_1 (see Eq. (3)). This solves the loss-of-precision problem. Only the first row $\hat{M}_{1,i}$ ($i=1, 5$) of \hat{M} is needed to compute (4). To obtain this row, one has to perform a matrix multiplication of the symbolic form

$$(1 \times 5)_n \cdot (5 \times 5)_{n-1} \cdot \dots \cdot (5 \times 5)_2 \cdot (6 \times 5)_1 \quad (5)$$

where $(1 \times 5)_n$ stands for the first row of the reduced delta matrix \hat{T}_n , the $(5 \times 5)_i$ represent the reduced delta matrices \hat{G}_i , and $(6 \times 5)_1$ represents the required elements of the delta matrix \hat{T}_1 (which is not reduced). The elements of the delta matrices have been given by Fuchs (1968) and Kind and Müller (1975). They will be given in the following, some in a rearranged form, more suitable for computers.

The reduced delta matrix extension (Watson, 1970) uses the equality of the following elements:

$$\begin{aligned} (\hat{T}_n)_{13} &= (\hat{T}_n)_{14}, & (\hat{G}_i)_{13} &= (\hat{G}_i)_{14}, & (\hat{G}_i)_{23} &= (\hat{G}_i)_{14}, & (\hat{G}_i)_{53} &= (\hat{G}_i)_{54}, \\ (\hat{G}_i)_{63} &= (\hat{G}_i)_{64}, & (\hat{G}_i)_{31} &= (\hat{G}_i)_{41}, & (\hat{G}_i)_{32} &= (\hat{G}_i)_{42}, & (\hat{G}_i)_{35} &= (\hat{G}_i)_{45}, \\ (\hat{G}_i)_{36} &= (\hat{G}_i)_{46}, & \text{and } (\hat{G}_i)_{44} &= (\hat{G}_i)_{34} = (\hat{G}_i)_{43} = (\hat{G}_i)_{33} - 1. \end{aligned}$$

From this follows that in the product of the first row of \hat{T}_n and \hat{G}_i the element $(\hat{T}_n)_{14}$ may be omitted if $(\hat{T}_n)_{13}$ is multiplied by 2 and if the 4th row and column of \hat{G}_i is omitted and 0.5 is subtracted from $(\hat{G}_i)_{33}$. The element $(\hat{G}_i)_{33}$ is already replaced by $(\hat{G}_i)_{33} - 0.5$ in (7). The 3rd element of the (1×5) matrix in (5) must be multiplied by 2 in each multiplication step. In the delta matrix \hat{T}_1 only the first, 3rd and 4th columns have equal elements in their 3rd and 4th row, which allows the application of the reduced delta matrix extension only for these columns.

We have in the i -th medium:

$\alpha_i = P$ velocity $\beta_i = S$ velocity $\rho_i =$ density $d_i =$ layer thickness (not defined in the two halfspaces)	$\omega =$ angular frequency $c =$ horizontal phase velocity $k = \omega/c$ wave number $j =$ imaginary unit $\mu_i = \beta_i^2 \rho_i$ $l_i = 2k^2 - \omega^2/\beta_i^2$
$v_i = \begin{cases} \sqrt{c^2/\alpha_i^2 - 1}, & c \geq \alpha_i \\ -j\sqrt{1 - c^2/\alpha_i^2}, & c < \alpha_i \end{cases}$	$v'_i = \begin{cases} \sqrt{c^2/\beta_i^2 - 1} & c \geq \beta_i \\ -j\sqrt{1 - c^2/\beta_i^2}, & c < \beta_i. \end{cases}$

The elements of \hat{T}_n are:

$$\begin{aligned} (\hat{T}_n)_{11} &= -\frac{\beta_n^4 \rho_n}{2\omega^2} (4k^2 v_n v'_n + l_n^2) \\ (\hat{T}_n)_{12} &= j/2 v_n \\ (\hat{T}_n)_{13} &= -\frac{j\beta_n^2}{2\omega c} (l_n + 2v_n v'_n) \\ (\hat{T}_n)_{15} &= -j/2 v'_n \\ (\hat{T}_n)_{16} &= -\frac{1}{2\rho_n \omega^2} (v_n v'_n + k^2) \end{aligned}$$

For the elements of the layer delta matrix \hat{G}_i the following abbreviations are introduced:

$$\begin{aligned} \gamma_i &= -2\beta_i^2/c^2, & W_i &= \sin P_i/v_i, & e_1 &= \cos P_i \cdot \cos Q_i, & r_1 &= c\omega\rho_i, \\ P_i &= k v_i d_i, & Y_i &= \sin Q_i/v'_i, & e_2 &= 1 - e_1, & r_2 &= 1/r_1, \\ Q_i &= k v'_i d_i, & X_i &= \sin P_i v_i, & e_3 &= W_i Y_i, & r_3 &= r_1 \gamma_i, \\ \gamma_2 &= \gamma_i + 1, & Z_i &= \sin Q_i v_i, & e_4 &= X_i Z_i, & r_4 &= r_1 \gamma_2, \\ & & & & e_5 &= W_i \cos Q_i, & f_1 &= e_2 + e_3, \\ & & & & e_6 &= Y_i \cos P_i, & f_2 &= f_1 r_2. \end{aligned} \tag{6}$$

Then, the elements of \hat{G}_i are:

$$\begin{aligned}
 (\hat{G}_i)_{16} &= -r_2(f_2 + (e_2 + e_4)r_2) & (\hat{G}_i)_{15} &= -r_2(e_5 + Z_i \cos P_i) = (\hat{G}_i)_{26} \\
 g_{13} &= -r_3(\hat{G}_i)_{16} + f_2 & g_{23} &= -r_3(\hat{G}_i)_{15} + e_5 \\
 (\hat{G}_i)_{13} &= j g_{13} = (\hat{G}_i)_{36} & (\hat{G}_i)_{23} &= j g_{23} = (\hat{G}_i)_{35} \\
 f_3 &= \gamma_i f_1 + e_3 & (\hat{G}_i)_{21} &= -r_3 g_{23} - r_4 e_5 = (\hat{G}_i)_{65} \\
 f_4 &= r_3 g_{13} + f_3 & (\hat{G}_i)_{12} &= r_2(e_6 + X_i \cos Q_i) = (\hat{G}_i)_{56} \\
 g_{31} &= r_3 f_4 + f_3 r_4 & g_{32} &= -r_3(\hat{G}_i)_{12} - e_6 \\
 (\hat{G}_i)_{31} &= j g_{31} = (\hat{G}_i)_{63} & (\hat{G}_i)_{32} &= j g_{32} = (\hat{G}_i)_{53} \\
 (\hat{G}_i)_{11} &= e_1 - f_4 = (\hat{G}_i)_{66} & (\hat{G}_i)_{51} &= -r_3 g_{32} + r_4 e_6 = (\hat{G}_i)_{62} \\
 (\hat{G}_i)_{33} &= f_4 + 0.5 & (\hat{G}_i)_{22} &= e_1 = (\hat{G}_i)_{55} \\
 (\hat{G}_i)_{61} &= -r_3 g_{31} - r_4(e_3 r_4 + f_3 r_3) & (\hat{G}_i)_{25} &= Z_i W_i \\
 & & (\hat{G}_i)_{52} &= X_i Y_i.
 \end{aligned} \tag{7}$$

The required elements of \hat{T}_1 are:

$$\begin{aligned}
 (\hat{T}_1)_{11} &= -k^2 - v_1 v_1' \\
 (\hat{T}_1)_{21} &= -j \rho_1 v_1' \omega^2 \\
 (\hat{T}_1)_{31} &= -j \mu_1 k(l_1 + 2 v_1 v_1') \\
 (\hat{T}_1)_{51} &= j \rho_1 v_1 \omega^2 \\
 (\hat{T}_1)_{61} &= -\mu_1^2(l_1^2 + 4k^2 v_1' v_1) \\
 (\hat{T}_1)_{12} &= 2k v_1, & (\hat{T}_1)_{15} &= 2k v_1' \\
 (\hat{T}_1)_{22} &= (\hat{T}_1)_{52} = 0, & (\hat{T}_1)_{25} &= (\hat{T}_1)_{55} = 0 \\
 (\hat{T}_1)_{32} &= j 4 \mu_1 k^2 v_1, & (\hat{T}_1)_{35} &= j 2 \mu_1 l_1 v_1' \\
 (\hat{T}_1)_{42} &= j 2 \mu_1 l_1 v_1, & (\hat{T}_1)_{45} &= j 4 \mu_1 k^2 v_1' \\
 (\hat{T}_1)_{62} &= 4 \mu_1^2 l_1 k v_1, & (\hat{T}_1)_{65} &= 4 \mu_1^2 l_1 k v_1' \\
 (\hat{T}_1)_{14} &= k^2 - v_1 v_1' = -(\hat{T}_1)_{13} \\
 (\hat{T}_1)_{24} &= -(\hat{T}_1)_{21}, & (\hat{T}_1)_{23} &= j v_1' \mu_1 (2k^2 - l_1) \\
 (\hat{T}_1)_{34} &= -j k \mu_1 (l_1 - 2 v_1 v_1') = -(\hat{T}_1)_{33} \\
 (\hat{T}_1)_{54} &= (\hat{T}_1)_{51}, & (\hat{T}_1)_{53} &= j v_1 \mu_1 (2k^2 - l_1) \\
 (\hat{T}_1)_{64} &= \mu_1^2(l_1^2 - 4k^2 v_1 v_1') = -(\hat{T}_1)_{63}.
 \end{aligned} \tag{8}$$

The time consuming innermost loop in the computer program contains essentially the construction of the layer matrix \hat{G}_i from (7) and the matrix multiplication (5). Setting up the elements of \hat{G}_i according to (7) requires about three times less operations than in the version of Fuchs (1968). In general the matrix \hat{T}_n is complex. The elements of \hat{G}_i are either real or imaginary. In (5) we have to multiply a (1×5)

complex matrix with a (5×5) real or imaginary matrix, if we do the multiplication from the left to the right. This means 50 multiplications with each step, if the complex multiplication is separated into real and imaginary part. Fuchs (1968) multiplied the (6×6) matrices \hat{G}_i first, which means 216 multiplications with each step. The so far probably fastest program for the layered media problem is due to Schwab and Knopoff (1972). They have in their innermost loop about half as many operations as in the comparable part of the present version. However, their program is real, which is sufficient for Rayleigh wave dispersion computations. For theoretical seismograms, however, the complex version is required. The FORTRAN program for the computation of $P-SV$ reflection coefficients is shown in Appendix 1. A normalization process is contained in the innermost loop of the program in order to avoid overflow problems (see Schwab and Knopoff (1972)). The normalization is not always required in every layer. In some cases a few percent of computer time may be saved by omitting the normalization.

Computation of Reflection Coefficients of Sound Waves in a Liquid and of SH Waves in a Solid

Satō (1954) has established the equivalence of SH waves and sound waves in a liquid. The reflection coefficients in both problems are identical if the following correspondence is used:

$$V_s (= S \text{ velocity in the solid}) \leftrightarrow V_p (= \text{velocity in the liquid})$$

and

$$V_s^2 \cdot \rho_s (\rho_s = \text{density in the solid}) \leftrightarrow 1/\rho_p (\rho_p = \text{density in the liquid}).$$

Therefore, after a density transformation, the same computer program can be used for both problems.

In the following a matrix formalism for a layered liquid medium will be derived, following lecture notes by Gerhard Müller. The potential in the i -th medium is

$$\Phi_i = \exp[j(\omega t - k x)] \cdot [A_i \exp(-jk v_i(z - z_i)) + B_i \exp(jk v_i(z - z_i))]$$

with the same denotations as in the previous section and the depth of the i -th boundary z_i .

At the boundaries $z = z_i$ we have

$$\frac{\partial \Phi_{i+1}}{\partial z} = \frac{\partial \Phi_i}{\partial z} \quad \text{and} \quad \rho_{i+1} \frac{\partial^2 \Phi_{i+1}}{\partial t^2} = \rho_i \frac{\partial^2 \Phi_i}{\partial t^2}.$$

From this follows

$$\begin{pmatrix} A_{i+1} \\ B_{i+1} \end{pmatrix} = m_i \begin{pmatrix} A_i \\ B_i \end{pmatrix}$$

where

$$m_i = \begin{pmatrix} l_i \rho_{i+1} + l_{i+1} \rho_i & (-l_i \rho_{i+1} + l_{i+1} \rho_i) \exp(2j l_i d_i) \\ -l_i \rho_{i+1} + l_{i+1} \rho_i & (-l_i \rho_{i+1} + l_{i+1} \rho_i) \exp(2j l_i d_i) \end{pmatrix} \quad (9)$$

and $d_i = z_{i+1} - z_i$, $d_1 = 0$ and $l_i = k v_i$. The exponential term containing x and t and a factor $\exp(-j l_i d_i) / (2 l_{i+1} \rho_{i+1})$ common to all elements of m_i , have been omitted. Repeated application of the same formalism yields

$$\begin{pmatrix} A_n \\ B_n \end{pmatrix} = m_{n-1} \cdot m_{n-2} \cdots m_2 \cdot m_1 \begin{pmatrix} A_1 \\ B_1 \end{pmatrix} = \begin{pmatrix} M_{11} & M_{12} \\ M_{21} & M_{22} \end{pmatrix} \begin{pmatrix} A_1 \\ B_1 \end{pmatrix}.$$

From this follows the reflection coefficient ($B_n = 0$):

$$R_{pp} = \frac{B_1}{A_1} = -\frac{M_{21}}{M_{22}}. \quad (10)$$

We only need to perform a matrix multiplication of the symbolic form

$$(1 \times 2)_{n-1} \cdot (2 \times 2)_{n-2} \cdots (2 \times 2)_1 \quad (11)$$

in order to obtain M_{21} and M_{22} . This is similar to (5), but a difference is, that in (5) we have one matrix for each medium, whereas we have in (11) one matrix for each boundary. Computer time is saved, if the matrix multiplication is written in the following form

$$\begin{aligned} m_{21}^i &= e_1^i + e_2^i \\ m_{22}^i &= \exp(2j l_i d_i) (e_1^i - e_2^i) \\ e_1^i &= e_1^{i+1} (m_{21}^{i+1} + m_{22}^{i+1}) \\ e_2^i &= e_2^{i+1} (m_{21}^{i+1} - m_{22}^{i+1}) \\ e_1^{i+1} &= l_{i+1} \rho_i \\ e_2^{i+1} &= l_i \rho_{i+1} \end{aligned} \quad (12)$$

for $i = n-1 \dots 1$ and $m_{21}^n = 0$, $m_{22}^n = 1$. Successive application yields: $M_{21} = m_{21}^1$, $M_{22} = m_{22}^1$. A list of the corresponding FORTRAN program is shown in Appendix 2. It should be mentioned, that the two computer programs for a solid medium and for a liquid medium have identical output for R_{pp} for more than five digits, if 0.001 km/s is chosen for the shear velocity in the solid medium. This shows that a mixed model can be approximated with good accuracy if for the liquid layers a small shear velocity such as 0.001 km/s is taken.

Acknowledgements. This research was supported by a grant of the Deutsche Forschungsgemeinschaft. The development of the computer program was done at the computing center of the University of Karlsruhe. I wish to thank Gerhard Müller for discussions and for reading the manuscript and Karl Fuchs for reading the manuscript. The manuscript was typed by Ingrid Hörnchen.

Appendix 1. Computer program for the computation of $P-SV$ reflection coefficients for a layered solid. No provision is made in this program and in the program of Appendix 2 for zero frequency and for phase velocities exactly equal to layer velocities. These cases can easily be avoided.

```

1*      SUBROUTINE RECOP(N,A,B,RHO,D,U,FREQ,RPP,RPS,RSS,RSP)
2*      C
3*      C   COMPUTATION OF P-SV REFLECTION COEFFICIENTS
4*      C
5*      C   N= NUMBER OF DIFFERENT MEDIA, STARTING ON TOP
6*      C   A(I),B(I),RHO(I), (I=1,N)= P-VELOCITY, S-VELOCITY AND DENSITY
7*      C   U(I), (I=2,N-1)= LAYER THICKNESS
8*      C   U= PHASE SLOWNESS, FREQ= FREQUENCY
9*      C   RPP,RPS,RSS,RSP= COMPLEX PP,PS,SS,SP-REFLECTION COEFFICIENTS
10*     DIMENSION A(N),B(N),RHO(N),D(N)
11*     COMPLEX T1,T2,T3,T4,T5,RPP,RPS,RSS,RSP,DET,CN,CNS,T53,T63
12*     A,T11,T21,T31,T51,T61,T12,T15,T32,T45,T42,T35,T62,T65,T13,T23,T33
13*     PI=3.14159265
14*     OMEG=2.*PI*FREQ
15*     C=1./U
16*     RK=OMEG*U
17*     N1=N-1
18*     COM=C*OMEG
19*     U2=U*U
20*     C2=C*C
21*     RK2=RK*RK
22*     OM2=OMEG*OMEG
23*     C   SET MATRIX ELEMENTS OF EQUATION (6)
24*     S=B(N)
25*     P=A(N)
26*     RRO=RHO(N)
27*     S2=S*S
28*     P2=P*P
29*     ARGP=1.-C2/P2
30*     ARG5=1.-C2/S2
31*     IF (ARGP.GE.0.) CN=CMPLX(0.,-RK*SQRT(ARGP))
32*     IF (ARGP.LT.0.) CN=CMPLX(RK*SQRT(-ARGP),0.)
33*     IF (ARG5.LT.0.) CNS=CMPLX(RK*SQRT(-ARG5),0.)
34*     IF (ARG5.GE.0.) CNS=CMPLX(0.,-RK*SQRT(ARG5))
35*     RL=2.*RK2-OM2/S2
36*     RPP=CN*CNS
37*     T1=CMPLX(-S2*S2*RRO/(OM2+OM2),0.)*(CMPLX(4.*RK2,0.)*RPP+
38*     ACMPLX(RL*RL,0.))
39*     T2=CMPLX(0.,0.5)*CN
40*     T3=CMPLX(0.,-S2*U/(2.*OMEG))*(CMPLX(RL,0.)*RPP+RPP)
41*     T4=CMPLX(0.,-0.5)*CNS
42*     T5=CMPLX(-1./(2.*RRO*OM2),0.)*(RPP+CMPLX(RK2,0.))
43*     TR1=REAL(T1)
44*     TI1=AIMAG(T1)
45*     TR2=REAL(T2)
46*     TI2=AIMAG(T2)
47*     TR3=2.*REAL(T3)
48*     TI3=2.*AIMAG(T3)
49*     TR4=REAL(T4)
50*     TI4=AIMAG(T4)
51*     TR5=REAL(T5)
52*     TI5=AIMAG(T5)
53*     IF (N.LT.3) GOTO 2000
54*     C   SET MATRIX ELEMENTS (7)
55*     C   DO MATRIX MULTIPLICATION (5) FROM LEFT TO RIGHT
56*     C   DO NORMALIZATION
57*     DO 1000 J=2,N1
58*     I=N-J+1
59*     S=B(I)
60*     S2=S*S
61*     P=A(I)
62*     P2=P*P
63*     THK=RK*D(I)
64*     ARGP=1.-C2/P2
65*     IF (ARGP.GE.0.) GOTO 190
66*     RA=SQRT(-ARGP)
67*     P=THK*RA
68*     SP=SIN(P)
69*     CP=COS(P)
70*     X=RA*SP
71*     180  ARG5=1.-C2/S2
72*     IF (ARG5.GE.0.) GOTO 200
73*     RB=SQRT(-ARG5)
74*     Q=THK*RB
75*     SQ=SIN(Q)
76*     CQ=COS(Q)
77*     Z=SQ*RB
78*     GOTO 210
79*     190  RA=-SQRT(ARGP)
80*     EP=0.5*EXP(THK*RA)
81*     EM=0.25/EP
82*     SP=EP-EM

```

```

83*      CP=EP+EM
84*      X=-SP*RA
85*      GOTO 180
86*      200  RB=-SQRT(ARGS)
87*      EP=0.5*EXP(THK*RB)
88*      EM=0.25/EP
89*      SQ=EP-EM
90*      CQ=EP+EM
91*      Z=-SQ*RB
92*      210  W=SP/RA
93*      Y=SQ/RB
94*      G1=-2.*S2*U2
95*      G2=G1+1.
96*      E1=CP*CQ
97*      E2=1.-E1
98*      E3=W*Y
99*      E4=X*Z
100*     E5=W*CQ
101*     E6=Y*CP
102*     R1=COM*RH0(I)
103*     R2=1./R1
104*     R3=R1*G1
105*     R4=R1*G2
106*     F1=E2+E3
107*     F2=F1*R2
108*     G16=-R2*(F2+(E2+E4)*R2)
109*     G13=-R3*G16+2
110*     F3=G1*F1+E3
111*     F4=R3*G13+F3
112*     G31=R3*F4+F3*R4
113*     G11=E1-F4
114*     G33=F4+0.5
115*     G61=-R3*G31-R4*(E3*R4+F3*R3)
116*     G15=-R2*(E5+Z*CP)
117*     G23=-R3*G15+E5
118*     G21=-R3*G23-R4*E5
119*     G12=R2*(E6+X*CQ)
120*     G32=-R3*G12-E6
121*     G51=-R3*G32+R4*E6
122*     G22=E1
123*     G25=Z*W
124*     G52=X*Y
125*     TR1=TR1*G11+TR2*G21-TI3*G31+TR4*G51+TR5*G61
126*     TI1=TI1*G11+TI2*G21+TR3*G31+TI4*G51+TI5*G61
127*     TR22=TR1*G12+TR2*G22-TI3*G32+TR4*G52+TR5*G61
128*     TI22=TI1*G12+TI2*G22+TR3*G32+TI4*G52+TI5*G61
129*     TR33=-TI1*G13-TI2*G23+TR3*G33-TI4*G32-TI5*G31
130*     TI33=TR1*G13+TR2*G23+TI3*G33+TR4*G32+TR5*G31
131*     TR44=TR1*G15+TR2*G25-TI3*G23+TR4*G22+TR5*G21
132*     TI44=TI1*G15+TI2*G25+TR3*G23+TI4*G22+TI5*G21
133*     TR5=TR1*G16+TR2*G15-TI3*G13+TR4*G12+TR5*G11
134*     TI5=TI1*G16+TI2*G15+TR3*G13+TI4*G12+TI5*G11
135*     TR1=TR11
136*     TI1=TI11
137*     TR2=TR22
138*     TI2=TI22
139*     TR3=2.*TR33
140*     TI3=2.*TI33
141*     TR4=TR44
142*     TI4=TI44
143*     RMAX=ABS(TR5)
144*     IF(RMAX.LT.ABS(TI5)) RMAX=TI5
145*     IF(RMAX.LT.ABS(TI4)) RMAX=TI4
146*     IF(RMAX.LT.ABS(TI3)) RMAX=TI3
147*     IF(RMAX.LT.ABS(TI2)) RMAX=TI2
148*     IF(RMAX.LT.ABS(TI1)) RMAX=TI1
149*     IF(RMAX.LT.ABS(TR4)) RMAX=TR4
150*     IF(RMAX.LT.ABS(TR3)) RMAX=TR3
151*     IF(RMAX.LT.ABS(TR2)) RMAX=TR2
152*     IF(RMAX.LT.ABS(TR1)) RMAX=TR1
153*     RMAX=1./RMAX
154*     TR1=TR1*RMAX
155*     TR2=TR2*RMAX
156*     TR3=TR3*RMAX
157*     TR4=TR4*RMAX
158*     TR5=TR5*RMAX
159*     TI1=TI1*RMAX
160*     TI2=TI2*RMAX
161*     TI3=TI3*RMAX
162*     TI4=TI4*RMAX
163*     TI5=TI5*RMAX
164*     1000 CONTINUE
165*     2000 CONTINUE
166*     C  SET MATRIX ELEMENTS (8)
167*     P=A(1)
168*     P2=P*P
169*     S=B(1)
170*     S2=S*S
171*     RH0=RH0(1)
172*     AR6S=1.-C2/S2
173*     ARGP=1.-C2/P2

```

```

174*      IF (ARGP.GE.0.) CN=CMPLX(0.,-RK*SQRT(ARGP))
175*      IF (ARGP.LT.0.) CN=CMPLX(RK*SQRT(-ARGP),0.)
176*      IF (ARG5.LT.0.) CNS=CMPLX(RK*SQRT(-ARG5),0.)
177*      IF (ARG5.GE.0.) CNS=CMPLX(0.,-RK*SQRT(ARG5))
178*      RM=RR0*S2
179*      RL=RK2*RK2-OM2/S2
180*      RPP=CN*CNS
181*      RM2=RM*RM
182*      RL2=RL*RL
183*      T11=CMPLX(-RK2,0.)
184*      T13=T11+RPP
185*      T11=T11-RPP
186*      T21=CMPLX(0.,RRO*OM2)
187*      T51=T21*CN
188*      T21=-T21*CNS
189*      T31=CMPLX(0.,-RM*RK*RL)
190*      RSS=CMPLX(0.,2.*RM*RK)*RPP
191*      T33=T31+RSS
192*      T31=T31-RSS
193*      T61=CMPLX(-RM2*RL2,0.)
194*      RSS=CMPLX(4.*RK2*RM2,0.)*RPP
195*      T63=T61+RSS
196*      T61=T61-RSS
197*      T23=CMPLX(0.,RM*(2.*RK2-RL))
198*      T53=T23*CN
199*      T23=T23*CNS
200*      T12=CMPLX(RK+RK,0.)
201*      T15=T12*CNS
202*      T12=T12*CN
203*      T32=CMPLX(0.,4.*RM*RK2)
204*      T45=T32*CNS
205*      T32=T32*CN
206*      T42=CMPLX(0.,2.*RM*RL)
207*      T35=T42*CNS
208*      T42=T42*CN
209*      T62=CMPLX(4.*RM2*RL*RK,0.)
210*      T65=T62*CNS
211*      T62=T62*CN
212*      T1=CMPLX(TR1,T11)
213*      T2=CMPLX(TR2,T12)
214*      T3=CMPLX(TR3,T13)
215*      T4=CMPLX(TR4,T14)
216*      T5=CMPLX(TR5,T15)
217*      C DO LAST PART OF MATRIX MULTIPLICATION (5)
218*      C COMPUTE REFLECTION COEFFICIENTS (4)
219*      DET=T1*T11+T2*T21+T3*T31+T4*T51+T5*T61
220*      DET=CMPLX(1.,0.)/DET
221*      RSS=T1*T13+T2*T23+T3*T33+T4*T53+T5*T63
222*      RSS=-RSS*DET
223*      RPP=-T1*T13-T2*T21-T3*T33+T4*T51-T5*T63
224*      RPP=RPP*DET
225*      T3=T3*CMPLX(0.5,0.)
226*      RPS=T1*T12+T3*T32+T3*T42+T5*T62
227*      RPS=-RPS*DET
228*      RSP=T1*T15+T3*T35+T3*T45+T5*T65
229*      RSP=RSP*DET
230*      RETURN
231*      END

```

Appendix 2. Computer program for the computation of reflection coefficients for a layered liquid and for *SH* reflection coefficients for a layered solid.

```

1*      SUBROUTINE RECOPP(N,A,RHO,U,FREQ,RPP)
2*      C
3*      C COMPUTATION OF REFLECTION COEFFICIENTS FOR A LAYERED LIQUID
4*      C
5*      C N= NUMBER OF DIFFERENT MEDIA, STARTING ON TOP
6*      C A(I),RHO(I),(I=1,N)= VELOCITY AND DENSITY
7*      C U(I),(I=2,N-1)= LAYER THICKNESS
8*      C U= PHASE SLOWNESS, FREQ= FREQUENCY
9*      C RPP= COMPLEX REFLECTION COEFFICIENT
10*     C
11*     C FOR COMPUTATION OF SH REFLECTION COEFFICIENTS REPLACE A BY
12*     C SHEAR VELOCITY B AND RHO BY 1./(B*B*RHO)
13*     C
14*     DIMENSION A(N),RHO(N),D(N)
15*     COMPLEX RPP,NI,NIP,ROI,ROIP,M21,M22,E0,F1,E
16*     U(1)=0.
17*     PI=3.14159265
18*     OMEGA=2.*PI*FREQ
19*     OM2=OMEGA*OMEGA
20*     XK=OMEGA*U
21*     XK2=XK*XK
22*     M22=CMPLX(1.,0.)
23*     M21=CMPLX(0.,0.)

```

```

24* C DO MATRIX MULTIPLICATION (11) FROM LEFT TO RIGHT
25* C USING (12) AND DO NORMALIZATION
26* DO 170 J=1,N
27* I=N-J+1
28* ARG=OM2/(A(I)*A(I))-XK2
29* IF (ARG.GT.0.) NI=CMPLX(SQRT(ARG),0.)
30* IF (ARG.LE.0.) NI=CMPLX(0.,-SQRT(-ARG))
31* R0I=CMPLX(KHO(I),0.)
32* IF (I.EQ.N) GO TO 171
33* E1=NIP*R0I
34* E2=NIP*R0IP
35* E=EXP(NI*CMPLX(U.,2.*D(I)))
36* E1=E1*(M21+M22)
37* E2=E2*(M21-M22)
38* M21=E1+E2
39* M22=E*(E1-E2)
40* RMAX=CABS(M22)
41* RM=CABS(M21)
42* IF (RM.GT.RMAX) RMAX=RM
43* E1=CMPLX(1./RMAX,0.)
44* M22=M22*E1
45* M21=M21*E1
46* 171 NIP=N1
47* R0IP=R0I
48* 170 CONTINUE
49* RPP=-M21/M22
50* RETURN
51* END

```

References

- Červený, V.: Reflection and transmission coefficients for transition layers. *Studia geophys. geodaet.* **18**, 59–68, 1974
- Dunkin, J. W.: Computation of modal solutions in layered media at high frequencies. *Bull. Seism. Soc. Am.* **55** (2), 335–358, 1965
- Fuchs, K.: Das Reflexions- und Transmissionsvermögen eines geschichteten Mediums mit beliebiger Tiefenverteilung der elastischen Moduln und der Dichte für schrägen Einfall ebener Wellen. *Z. Geophys.* **34**, 389–413, 1968
- Fuchs, K., Müller, G.: Computation of synthetic seismograms with the reflectivity method and comparison with observations. *Geophys. J.R.A.S.* **23**, 417–433, 1971
- Kind, R., Müller, G.: Computation of *SV* waves in realistic earth models. *J. Geophys.* **41**, 149–172, 1975
- Müller, G., Kind, R.: Observed and computed seismogram sections for the whole earth. *Geophys. J.R.A.S.* **44**, 699–716, 1976
- Pestel, E., Leckie, F. A.: *Matrix methods in elastomechanics*. New York: McGraw Hill 1963
- Satō, Y.: 2. Study on surface waves *X*. Equivalency of *SH*-waves and sound waves in a liquid. *Bull. Earthquake Res. Inst.* **32**, 7–16, 1954
- Schwab, F. A., Knopoff, L.: Fast surface wave and free mode computations. *Methods in computational physics*, Vol. II, B. A. Bolt, ed. New York: Academic Press 1972
- Watson, T. H.: Fast computation of Rayleigh wave dispersion in a layered halfspace. *Bull. Seism. Soc. Am.* **60**, 161–166, 1970

Received May 28, 1976

The Seismic Broadband Recording and Data Processing System FBV/DPS and Its Seismological Applications

A. Plešinger and J. Horálek

Geofyzikální ústav ČSAV, Boční II/1401, 141 31 Praha 4, ČSSR

Abstract. A brief description of the present state of the feedback-controlled broadband seismograph system FBV installed at the Kašperské Hory (KHC) station and of the appertaining system DPS for processing the recorded broadband information is given. The FBV system provides three-component velocity proportional seismic information in a frequency band which covers nearly the whole standard short-period, intermediate period and long-period interval. Each component is recorded bi-level with an overall dynamic range of 80 db on analogue (FM) magnetic tape. The DPS system allows (i) the recorded data to be selected, reduced and transcribed onto library tapes or loops, (ii) to perform rotation of instrumental axes, determination of the azimuth of seismic events, identification of different wave groups by particle motion analysis, multichannel frequency filtering, plotting of frequency vs. time, rapid and efficient estimate of power spectra by proper analogue devices, and (iii) automatic A/D conversion of the part of the records which has to be treated numerically. The variety of seismological applications of the FBV/DPS complex is demonstrated by investigating teleseismic signals from different aspects. Hitherto the complex has been used for crust and upper mantle structure studies on the basis of body wave spectra and surface wave dispersion, for investigations of the influence of standard class seismographs and band-pass filtering on magnitude estimations, and for the identification of underground explosions.

Key words: Seismic broadband data recording and processing – Instruments and procedures – Seismological applications.

Introduction

A trend towards wide-band seismometry is recently much in evidence in instrumental seismology. The goal of wide-band seismometry is to record all the information, contained in seismic signals, with minimum distortion and in a form which can be evaluated quantitatively (Berckhemer, 1971).

In the last decade a number of papers has been published which deal with the theory of broadband seismographs (Lake, 1964; Sutton and Latham, 1964; Daragan, 1967; Plešinger, 1970), with the problem of the optimum selection of their responses taking into account seismological requirements (Berckhemer, 1971; Aranovitch and Kondorskaya, 1971; Aranovitch et al., 1972; Teupser et al., 1974) and with methods of designing broadband large dynamic range seismograph systems (Plešinger, 1973; Daragan, 1973). The work at several seismological institutions and observatories has presently reached the stage of experimental as well as routine operations of broadband systems with a large dynamic range of the recorded information (Burke et al., 1970; Wielandt 1970 and 1973; Jacoby, 1971; Plešinger, 1971, 1972 and 1973).

This paper gives a brief description of the seismic broadband recording and data processing system FBV/DPS, developed in the Geophysical Institute of the Czechoslovak Academy of Sciences, and outlines some possibilities of its seismological applications.

1. Concept of the FBV/DPS System

In designing the system the general purpose was to create an universal broadband station seismograph system with the largest possible dynamic range and with the possibility of as operative as possible automated processing of the recorded information. A more accurate concept was worked out taking into account the criteria specified by Berckhemer (1971) and Aranovitch and Kondorskaya (1971). The demands made on both parts were the following: (a) recording of 3 components of velocity in the period range from 0.3 to 300 s in a dynamic range of at least 80 db; (b) storing of the data in the most economic form on magnetic tape; (c) the possibility of carrying out procedures such as selection of events, azimuth determination, identification of different wave types, frequency filtering and frequency vs. time analysis immediately from station or library tape; (d) the possibility of rapid automated digitation of selected sections of records or of pre-processed analogue data for further processing on conventional digital computers.

An experimental seismograph, satisfying condition (a), was developed in our Institute already in 1968 (Plešinger, 1971 and 1972). The confrontation of the other demands with economic aspects led to the following concept: (1) establishing the broad-band large dynamic range channels by using conventional long-period seismometers controlled by active frequency-dependent negative feedback, (2) bi-level recording of each component on magnetic tape in analogue frequency modulated form, (3) storing of selected events in the same form, i.e. establishing library tapes by direct transcription, (4) carrying out the required routine procedures by means of economical and effective analogue equipment, (5) analogue-to-digital conversion of selected portions of records or of pre-processed signals in the first stage with single-channel equipment and punch-tape record, in the second stage with multi-channel equipment and magnetic tape record.

2. Description of the FBV/DPS System

The complex of instruments which was gradually established according to the concept outlined above now consists of five sub-systems.

2.1. Broadband Seismometric Channels

This sub-system is installed in the underground rooms of the Kašperské Hory (KHC) station. It is shown schematically in Figure 1. It consists of a set of long-period KIRNOS seismometers (SVK-D, SGK-D), the effective free periods and damping moments of which have been increased to the required values by means of frequency-dependent negative feedback (e.g., the period of the SGK-D from the original value $T_0=24$ s to $T'_0=360$ s and the damping factor from 0.06 to 0.7). Highly sensitive photoelectric amplifiers, the transfer properties of which are also controlled and stabilized by negative feedback, serve as active elements. The internal and external negative feedbacks markedly improve the overall linearity of the seismometric channels and increase their dynamic range to a value in excess of 100 db.

The outputs of the seismometric channels are fed via filters, in which noise components with frequencies $f < 0.001$ Hz and $f > 10$ Hz are suppressed, and via attenuators to voltage-frequency converters. The converters convert each seismic component in two levels with a mutual sensitivity difference of 30 db into the form of frequency-modulated carrier signals which are fed into a long-term magnetic tape recorder. The three components are simultaneously recorded by a standard three-component photorecording device and monitored on the screens of mirror galvanometers.

The system is equipped with a calibration unit which enables all channels to be calibrated by shock tests (impulses of acceleration), release tests (steps of acceleration) or by sinusoidal signals. Figure 2 shows the amplitude-frequency characteristic of the seismometric channels inclusive the magnetic tape recording unit and, for comparison, the magnification curves of the 3 standard class (A, B and C) seismographs.

2.2. Magnetic Tape Recorder

The FM-signals are recorded on magnetic tape by a Racal-Thermionic T8100 Recorder. The necessary additional signals (real time, time code, pilot frequency) are generated in built-in units. The real-time marks are derived from the station time service and used to check and correct the coded time signal, generated by the electronics of the T8100 Recorder. The time code gives the year, month, day and minute of the record each minute between the 0th and 40th second (modified I.R.I.G. standard code).

The speed of the magnetic tape is 3 mm/s. One tape reel has a capacity of 108 h of 12 channel record. The subsidiary information mentioned above is recorded on traces 4, 5 and 6, respectively, and the remaining traces (1–3,

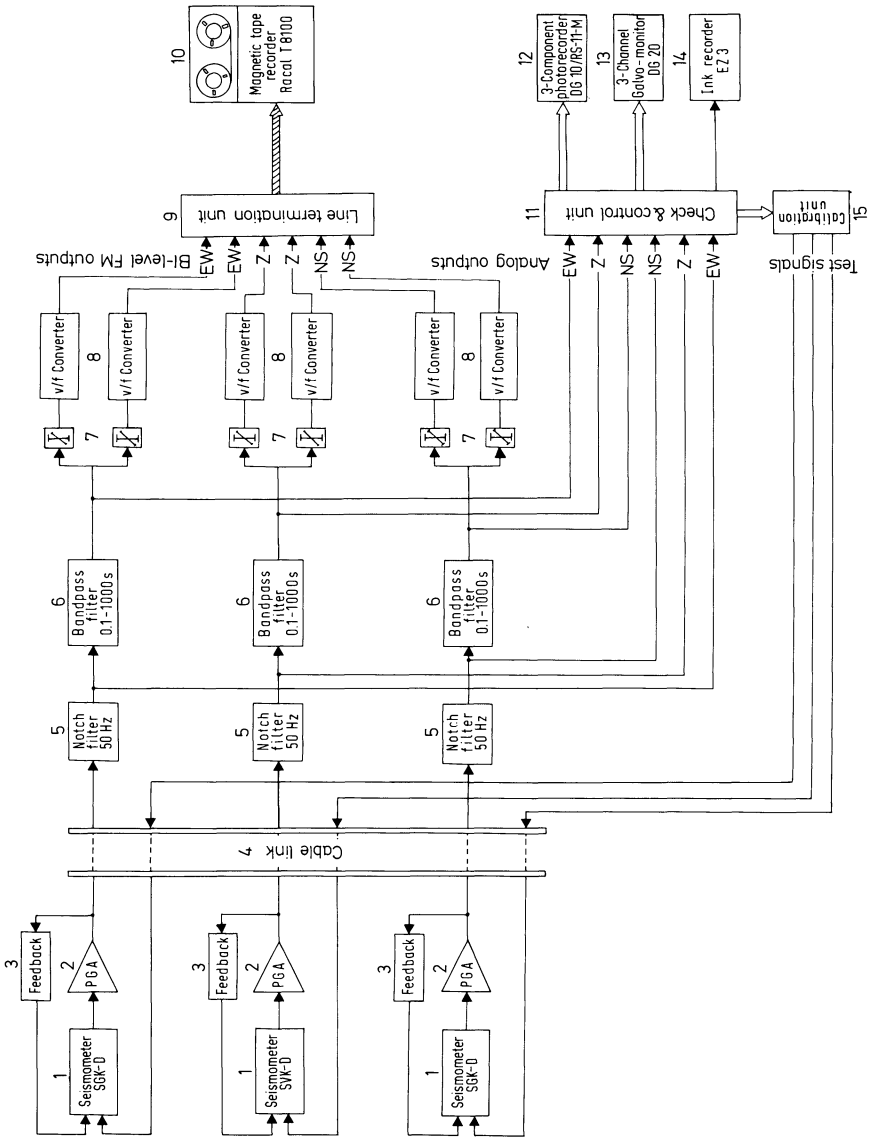


Fig. 1. Structural diagram of the FBV system. The seismometers are installed in the Kristina gallery of the KHC station (gneiss, overburden 30 m, 80 m from opening) under pressure tanks. PGA – photogalvanometric amplifiers EL 022/F 117

7–9, 10–12) carry the seismic information. The whole FBV system is supplied from battery sets and is capable of operating on its own for 4 days.

2.3. Analogue Data Processing

The structural diagram of the subsystem for reproducing, transcribing and analogue processing of the data recorded by the FBV system is shown in Figure 3.

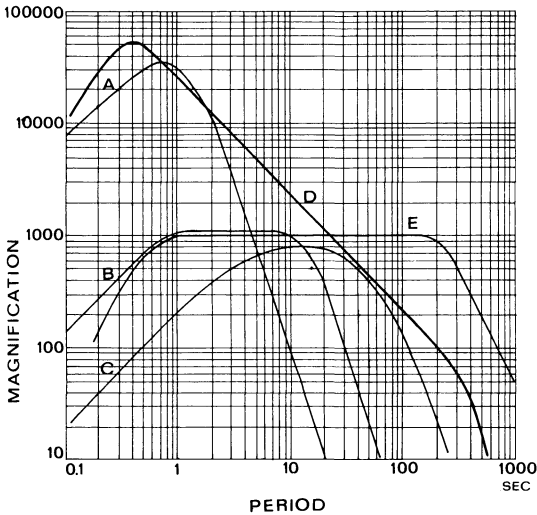


Fig. 2. Response curve for the magnetic-tape record of the FBV system (D) compared with the magnification curves of standard class short-period (A), intermediate band (B) and long-period (C) seismographs. E is the supposed response of the new FBD system (see Conclusion)

The part for reproducing and transcribing the data consists of two tape transports Racal-Thermionic TDR 8(L) the first of which is equipped with demodulation electronics and an additional unit for drop-out elimination, the second with transcription electronics and an additional unit for selecting the type of operation. The first unit is intended for replay from tape only, the second for replay, erasing and recording on tape as well as loop. This set-up, together with the time decoder, performs three fundamental operations: automatic search for seismic events, transcription of selected events onto library tape or a loop, and reproduction of the data from station tape, library tape or loop in analogue form. These operations can be carried out at replay speeds of as much as 256-times the recording speed. Routinely a time transformation to $1/64$ of the real time is used

The set-up for the analogue processing of signals replayed from tape or loop consists of a set of analogue processors (units 5–9 in Fig. 3) and a set of output units for representing the results (units 10–13). The output periphery is formed by a six-channel slow-motion oscilloscope which also allows vectorial representation, an eight-channel heat-pen recorder, an X-Y plotter and a storage oscilloscope. The analogue outputs from the tape replay unit, the inputs and outputs of the analogue processors and the inputs of the output devices are located on a central patch panel which is used to connect the individual units up into the required configuration. Below the functional principles and purposes of the individual analogue processors are explained.

Integrators. In order to obtain the largest possible dynamic range of recorded seismic information the FBV system has a flat-velocity response (see e.g. Lake, 1964). For certain purposes (earthquake mechanism studies, structure investiga-

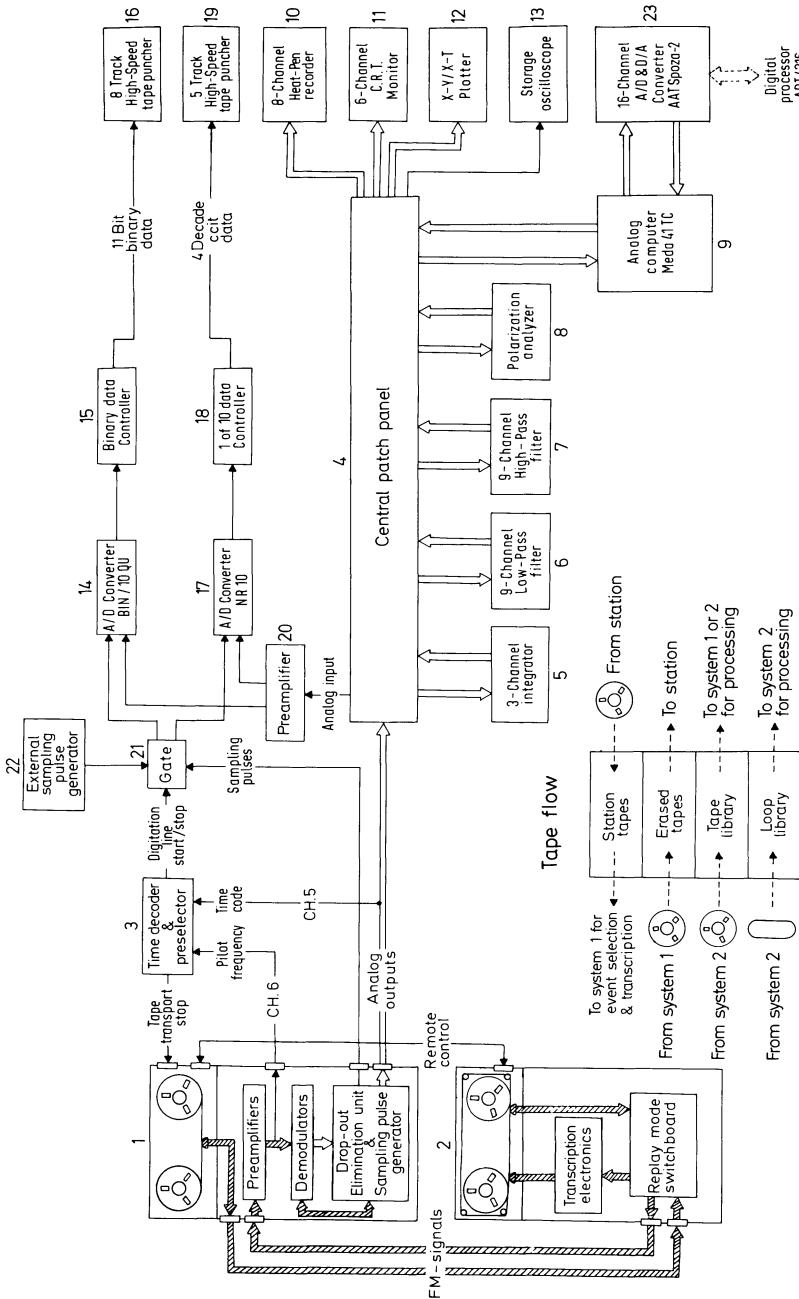


Fig. 3. Structural diagram of the DPS system. 1 - Racal-Thermionic T8100 Replay Unit, 2 - Racal-Thermionic TDR 8(L) Tape Transport equipped with additional electronics

tions on the basis of surface wave dispersion etc.) displacement-proportional information is, however, more convenient. Active integrating filters are used to modify replayed data into this form. The transfer function and frequency response of the filters is given in Figure 4. The filter works as an ideal integrator in the period range of $T < 300$ s (expressed in real time). A derivating circuit

stabilizes the function of the integrator, i.e. eliminates the D.C. component from the input signal and suppresses longperiod noise.

Frequency Filters. The set of frequency filters is composed of nine high-pass and nine low-pass sections with 4th degree Butterworth responses (Fig. 5). The cut-off frequencies can be chosen arbitrarily in the range 0.1–100 Hz and are indicated by a digital panelmeter. Each filter consists of two active filter modules Barr & Stroud EF 40, connected into cascade, and an I.C. buffer amplifier. The individual sections can be used to form various band-pass filters or they can be used independently. They are utilized as anti-aliasing filters, for current frequency filtering and for rough frequency vs. time analyses.

Polarization Analyzer. The polarization analyzer is a single-purpose processor which enables seismic phenomena to be investigated on the basis of particle motion (Sutton and Pomeroy, 1963; Houlston, 1972). The principle of the method can be seen from the simplified diagram of the analyzer in Figure 6. The individual components of the investigated event, reproduced from magnetic tape or loop, are fed to the inputs. With the aid of a pair of coupled sine-cosine potentiometers the longitudinal component $L = NS \cos \Theta + EW \sin \Theta$ (L positive towards the epicentre) and transverse component $T = NS \sin \Theta - EW \cos \Theta$ (T positive to the right of the epicentre direction), Θ being the angle of the azimuth set on the potentiometers, are formed from the NS and EW components. The L and T components can then be multiplied by the vertical component Z . The product $L \times Z$ has the property that it is positive for ground motion of the compression type and negative for ground motion of the SV type. A Rayleigh type surface wave is reflected in the $L \times Z$ product as an alternately positive and negative signal with half the period of the original wave. Thus, the processor separates the following types of ground motion: horizontal transverse, horizontal longitudinal, compressional, vertically polarized transverse, and elliptical longitudinal.

The P -wave azimuth of the investigated event can be determined with the polarization analyzer in the following manner. The wave group P of the given event is first transcribed onto a loop. It is then repeatedly replayed into the polarization analyzer and the potentiometer position is found at which the product $T \times Z$ has its minimum. The potentiometer scale, which is calibrated in degrees, then gives the sought azimuth (the turning of the potentiometer axes simulates the turning of the instrument axes; for P -waves, recorded in the direction of their propagation, $T=0$). The multiplication of component T by Z only has the auxiliary purpose that it facilitates the determination of the minimum of the signal T .

In fact the product $T \times Z$ is never quite zero. This is due to the presence of secondary waves generated at boundaries below the point of observation. The polarization analyzer may, therefore, also be utilized for the study of particle motion with the purpose of separating local effects from teleseismic signals.

Analogue Computer. The analogue computer considerably expands the range of applications of the DPS system. The device is used for simulating responses of standard class seismographs, of inverse, preshaping and other special (integrating and derivating) filters, and as a correction unit in dispersion analyses

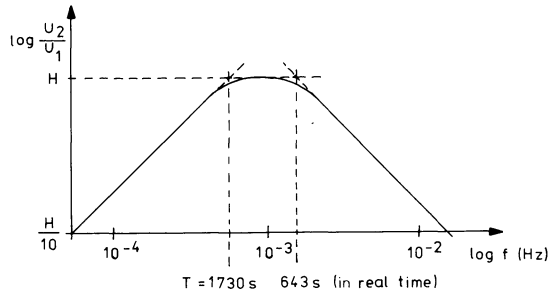
INTEGRATORS

$$\frac{U_2}{U_1} = \frac{H s}{(a_1 s + 1)(a_2 s + 1)}$$

$H_0 = 5, 20 \text{ or } 100, \quad H = 0.88 H_0$

$a_1 = \frac{275}{N}, \quad a_2 = \frac{102}{N}$

$N = 2, 8, 16 \text{ or } 64$



PREAMPLIFIER

$$\frac{U_2}{U_1} = \frac{H}{(a_1 s + 1)(a_2 s^2 + a_1 s + 1)}$$

$H = 1, 2, 4, 8, 16 \text{ or } 32$

$a_1 = \frac{0.0477}{N}, \quad a_2 = \frac{0.00228}{N}$

$N = 2, 8, 16 \text{ or } 64$

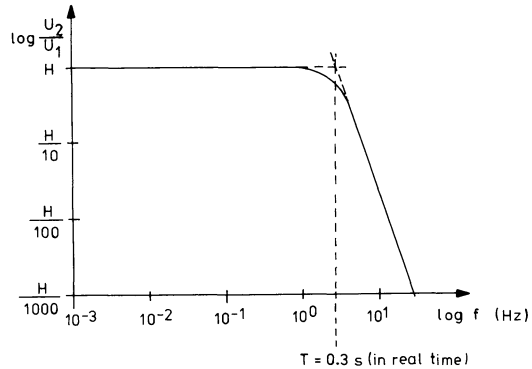


Fig. 4. Transfer functions and frequency responses of the integrators and preamplifier. N is the ratio of replay to record speed. Routine procedures are performed at $N=64$

performed with the aid of narrow band-pass filters. The type of the analogue computer (iteration computer MEDA 41 TC with multichannel A/D and D/A converter unit SPOZA-2; producer AAT Praha) has been selected with a view to a future hybrid processing of the FBV broadband records. For this purpose the completion of the DPS system by an ADT 4316 minicomputer (producer ZPA Praha) is anticipated in near future.

2.4. Analog-to-Digital Converters

In order to be able to process sections of broadband records or analogue pre-processed signals further on commercial digital computers, the DPS system was equipped with two digitizing devices. In Figure 3 the units are numbered 14–19. The analogue signal is fed to the A/D converters via a preamplifier the transfer function and frequency response of which is given in Figure 4. The sampling pulses are derived either from the 100 Hz pilot frequency, recorded on trace 6 of the magnetic tape, or from an external pulse generator. The conversion start-up (beginning of time series) is controlled via decoder 3 by the time code recorded on trace 5 of the magnetic tape.

Fig. 5. Transfer functions and frequency responses of the low-pass and high-pass filter sections. The pass-band gain of all sections is adjusted to 0 db by output buffer amplifiers

LOW-PASS

$$\frac{U_2}{U_1}(s) = - \frac{1}{(s^2 + 1.848s + 1)(s^2 + 0.756s + 1)}$$

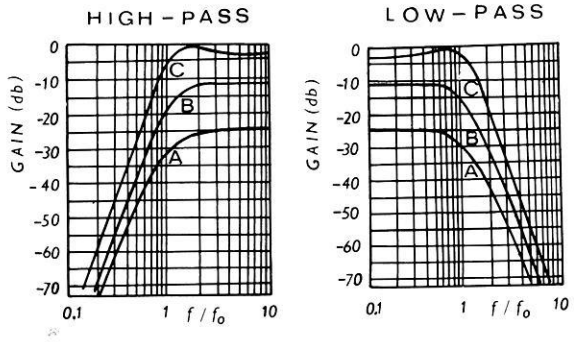
$$s = j \frac{f}{f_0} \quad f_0 = 0.1 \div 100 \text{ Hz}$$

HIGH-PASS

$$\frac{U_2}{U_1}(s) = - \frac{s^4}{(s^2 + 1.848s + 1)(s^2 + 0.756s + 1)}$$

$$s = j \frac{f}{f_0} \quad f_0 = 0.1 \div 100 \text{ Hz}$$

FREQUENCY RESPONSES



A - BESSEL, B - BUTTERWORTH, C - CHEBYSHEFF

The first digitizing line punches the data into a 5-trace punch tape in the C.C.I.T. telex code at a maximum speed of 17 samples/s, the second into an 8-trace punch tape in 11-bit binary code at a maximum speed of 56 samples/s.

The data punched in the telex code can be introduced into computers directly, however, the digitizing process is slow. The second line is faster, but the binary data can only be transcribed onto digital computer tapes by means of a special reading programme. The common disadvantage of both digitizing devices is their low speed and the fact that only a single-channel A/D conversion is possible.

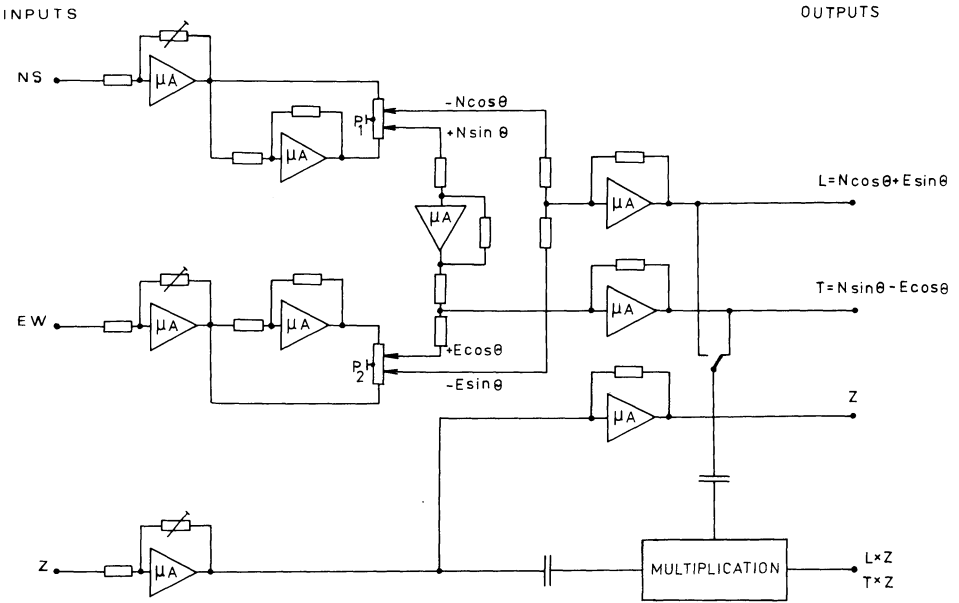


Fig. 6. Simplified wiring of the polarization analyzer. μA —IC operational amplifiers, P_1 and P_2 —coupled sine-cosine potentiometers. The multiplication is performed by a monolithic AD 530 multiplier

2.5. Subsystem for Digital Data Checking and Plotting

For checking and plotting of digital data a special subsystem was developed. It consists of two devices the first of which is intended for checking and D/A conversion of data punched in the C.C.I.T. form and the second has the same function for data punched in the 11-bit binary form.

The data are read from the punch tape at a maximum speed of 1500 characters/s by photoelectric readers, checked for errors in error identifiers and transformed to analogue form. Counters simultaneously generate the time axis for plotting the data on an analogue X-Y plotter. Coincidence circuits stop the reading if a given maximum permissible value is exceeded or if a pre-determined symbol or combination of symbols (e.g. end of data series, error, etc.) occurs. The values of the individual samples are currently given in decadic form on digital displays.

The first device also permits the checking and plotting of two-dimensional (x,y) sequences punched in C.C.I.T. form and of time series punched into 8-trace tape in 7-bit binary code with odd parity. The device can also be used for fast copying of arbitrary 5- to 8-trace punch tapes.

3. Seismological Applications of the FBV/DPS System

In this section we give a few examples of how the analogue processors can be used to investigate teleseismic signals under different aspects.

Figure 7 shows the result of a qualitative investigation of the effect of standard class seismograph responses on the wave image of a distant earthquake

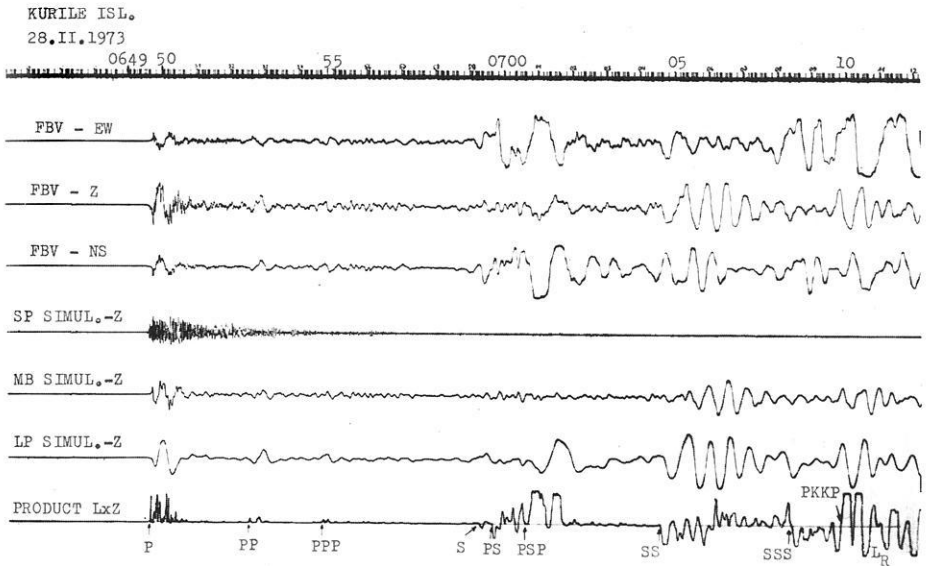


Fig. 7. Simulation of standard class A, B and C seismograms from a broadband FBV recording and result of polarization analysis of the event. The procedures are performed simultaneously with a speed corresponding to 1/64 of the real time

(Kurile Is., 28 FEB. 1973, KHC 06 50 39.7 UT, $D_c = 75.8^\circ$, $m_{ISC} = 6.8$), and the result of the polarization analysis of this event. The first trace carries the record of time, the second to fourth the individual components of the broadband flat-velocity recordings, the fifth, sixth and seventh the filter outputs simulating the outputs of, respectively, a vertical standard class short-period, intermediate period and long-period seismograph. The last trace carries the product $L \times Z$ obtained from the polarization analyzer. It can be seen that the teleseismic signal is recorded relatively most faithfully by the long-period simulation, whereas the short-period record clearly contains also information on local effects. The individual wave groups are distinctly distinguished on the $L \times Z$ record even in sections where waves of different types follow each other closely. The polarization analysis evidently makes it possible to determine more accurately the arrival times of different phases, is capable of separating phases which cannot be distinguished on the direct records and also provides—together with frequency filtering—a certain amount of information on local effects.

Figures 8 and 9 represent examples of the results of an extensive study intended to determine the effect of the recorded frequency band on the determination of the magnitude of earthquakes. In this study a set of band-pass filters with an upper limiting frequency of 2.5 Hz ($T = 0.4$ s) was used and the lower limiting frequencies were set at intervals of one octave over a period range of $T = 2$ to 256 s (expressed in real time). Figure 8 shows the responses of this set of filters to the vertical component of the same event as in Figure 7, and in Figure 9 a detail of the filtered P -wave group is shown. The example proves that recording of the surface waves of the investigated event would require the use of a seismograph with a passband of at least up to $T = 30$ s and that the passband has considerable effect not only on the dynamic character-

istics but also on the kinematic parameters of the recorded signals. In the event investigated the difference between the time of the first onset on the records $F 0.4-2$ s and $F 0.4-256$ s in Figure 9 is 5.3 s.

Figure 10 shows the result of a rough frequency vs. time analysis of the broadband record of another distant earthquake (Alaska, 1 JULY 1973, KHC 13 13 34.6 UT, $D_c=70.7^\circ$, $m_{ISC}=6.5$) by means of a set of one-octave band-pass filters. The uppermost trace carries the record of the broadband signal (vertical ground displacement obtained by integration of the Z-component from the FBV system) and below it the outputs of the individual filters are recorded. This type of processing is used to identify various phases of earthquakes, to separate higher mode surface waves from the basic mode, to investigate the relation between the spectral distribution of an earthquake record and the process in its focus or, respectively, the earthquake magnitude, to construct three-dimensional period vs. time vs. A/T value diagrams etc. Analyses of this type have been also used for investigating the frequency dependence of $(A/T)_{\max}$ data and their relation to earthquake magnitudes. One example of band-pass filtering of FBV broadband records for this purpose is reproduced in Figure 11 (investigated event Japan 17 JUNE 1973, KHC 040702.9 UT, $D_c=77.8^\circ$, $m_{ISC}=6.5$).

In Figure 12 the result of an attempt to estimate the group velocities for surface waves of a distant earthquake (Japan, 8 MAY 1974, KHC 23 45 56.3 UT, $D=85^\circ$, $m_b=6.1$) with the aid of a set of narrow-band filters is represented. The time is plotted at the very top and bottom, the first trace carries the broadband signal and the other traces represent the outputs of the individual filters the resonance periods of which were 14, 19, 25, 33, 45, 60 and 75 s (in real time). The direct presentation of the filter outputs only allows one to observe the spread features of the dispersion curve. Besides, the signals are delayed in time due to the filter phase lags. It is, however, possible to emphasize the maxima of the envelopes of the signals by using squaring devices and a sharp filter with zero phase lag can be established in analogue form using the technique of double filtering in positive and negative time (Sutton and Pomeroy, 1963).

Figure 13 demonstrates the difference between broadband velocity and displacement recordings. The FBV record of the Alaska earthquake of July 1, 1973, was reproduced from the magnetic tape directly (traces 2, 4 and 6) and via integrators (traces 3, 5 and 7). Trace 1 carries the time code, trace 8 the $L \times Z$ signal from the polarization analyzer. It can be seen at first glance that recording the velocity has the advantage that it reflects the short-period and long-period components of the wave image with compatible amplitudes. On the displacement records, on the other hand, the wave image is simpler, short-period components are suppressed (or long-period enhanced) and the amplitude dispersion of the surface waves is smaller. Velocity recording is, therefore, obviously more advantageous for direct interpretation in the classical sense (the amplitudes directly yield the quantity A/T , the onsets of the individual phases can be distinguished better), whereas for earthquake mechanism studies and structure investigations on the basis of surface waves displacement records are more suitable.

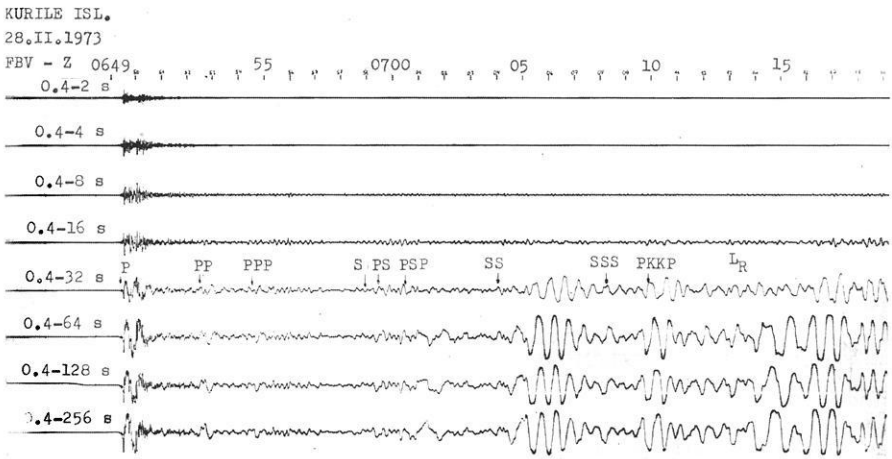


Fig. 8. Example of band-pass filtering with fixed upper and varied lower filter cut-off frequencies

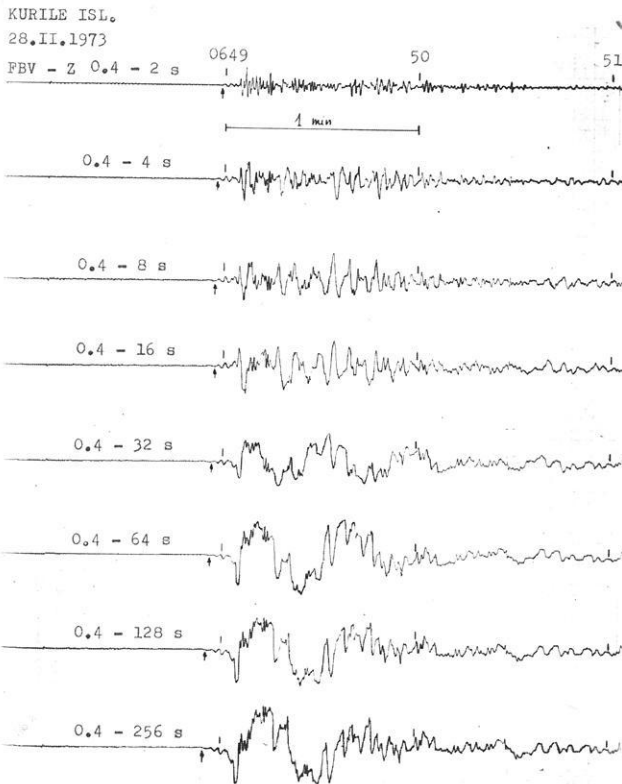


Fig. 9. Detail of the filtered *P*-wave group. The first onsets are denoted by arrows, the vertical dashes are minute marks

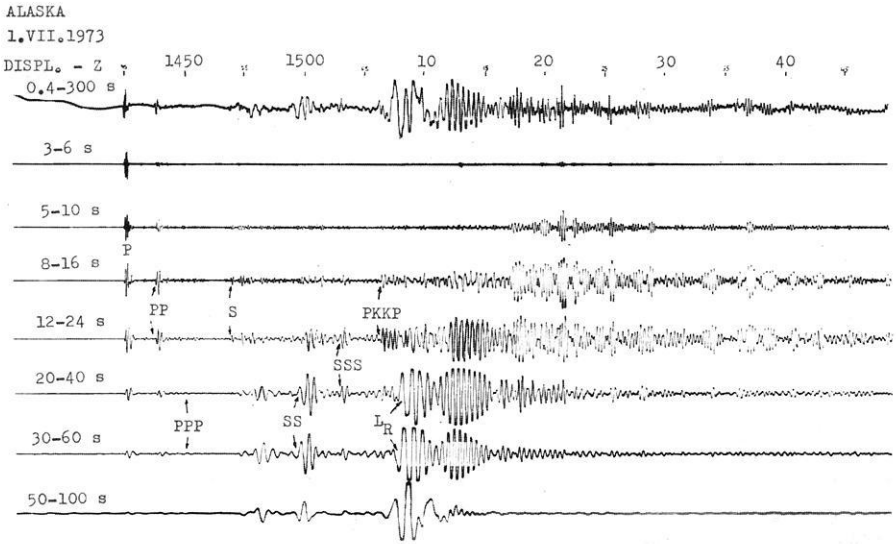


Fig. 10. Rough frequency vs. time analysis by means of a set of filters with pass-bands corresponding in real time to period intervals of 3-6, 5-10, 8-16, 12-24, 20-40, 30-60, and 50-100 s

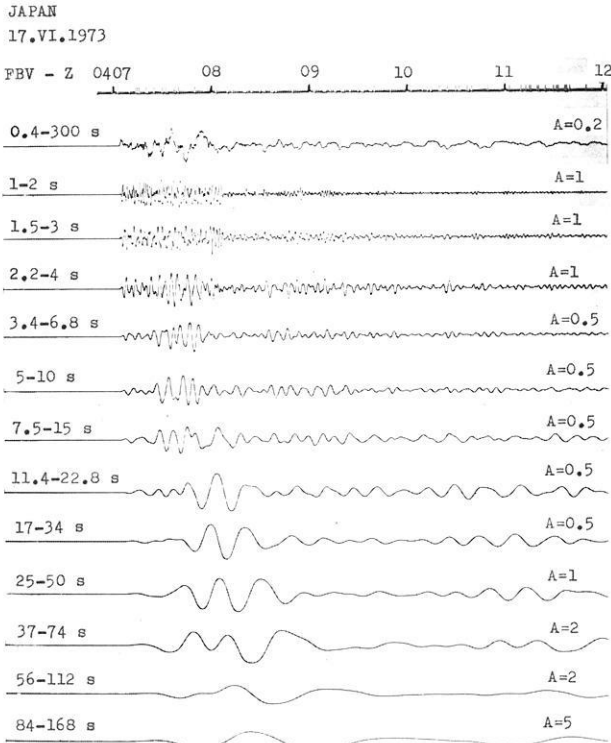


Fig. 11. Example of multichannel one-octave band-pass filtering

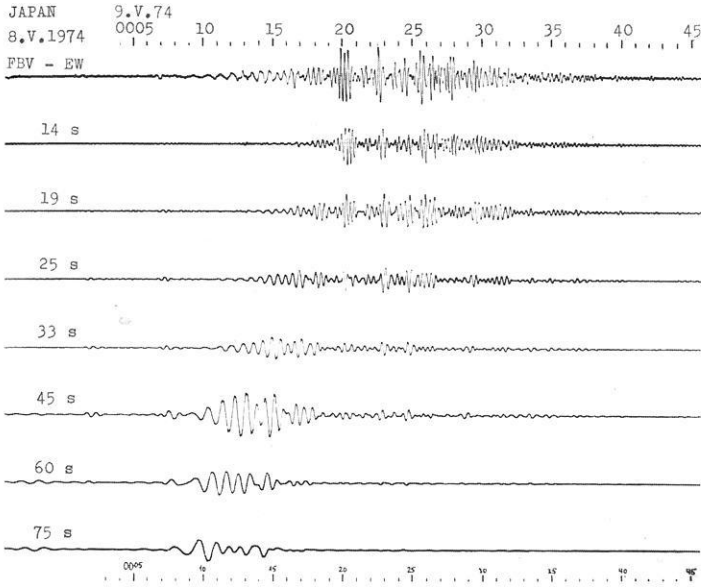


Fig. 12. Estimation of surface wave group-velocities with the aid of a set of selective filters

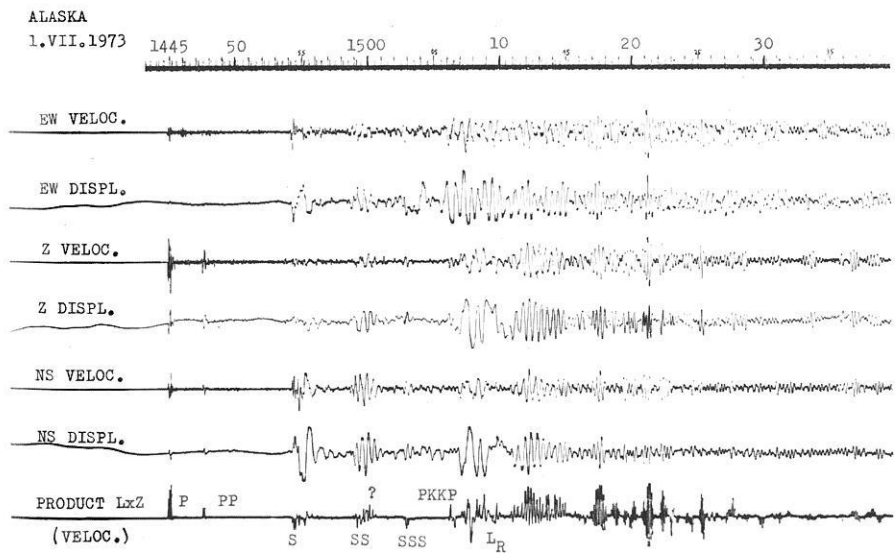


Fig. 13. Comparison of recordings of velocity, displacement, and $L \times Z$ signal

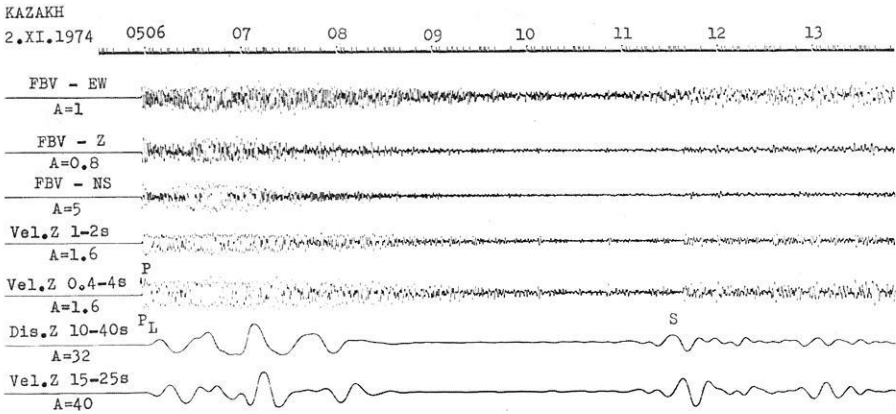


Fig. 14. Example of the application of different frequency filterings (simulations) to the FBV broadband record of an underground nuclear explosion

In Figure 14 the result of applying various filters to the broadband record of an underground explosion (Kazakh, 2 NOV. 1974, KHC 05 05 58.0, $D_c=31^\circ$, $m_b=6.7$) is shown. In the integrated (displacement-proportional) output passed through a 10 to 40 s band-pass filter (trace 7 in Fig. 14) P_L -waves and long-period S -waves are clearly detected. Trace 8 shows for comparison the velocity-proportional (direct FBV) output filtered by a 20 s narrow-band filter which approximately simulates the response curve of high-gain long-period LASA instruments (Molnar et al., 1969).

At present the complex FBV/DPS is used for crust and upper mantle structure investigations, for earthquake mechanism studies, and for studies concerned with the determination of earthquake magnitudes. The results will be published in separate papers.

Conclusion

This informative paper presents a comprehensive review of the present set-up and possibilities of application of the FBV/DPS system. The described devices and methods do not present a final stage of development. Preparatory work is underway for installing a further broadband recording system of the FBV type at the polish seismic station Ksiaz (KSP). Both the KHC and KSP stations are located near the international DSS profile VII which points towards the seismically active region of the Kurile Islands. The installation of a displacement sensing feedback-controlled broadband system (FBD) which is anticipated should record also free oscillations of the Earth is being prepared at the KHC station. The gradual improvement of the DPS system is also anticipated. This concerns in particular the installing of a multichannel subsystem for rapid data digitizing and of an ADT 4316 minicomputer.

Acknowledgements. A number of collaborators, to whom our thanks are due, worked on the development, construction and installation of the FBV/DPS system elements: P. Lang, F. Rubeš, K. Kott, Z. Rameš of the Research Institute of Automation Means, Praha; J. Černohorský of Inova N.C., Praha; P. Brych, S. Čekal and J. Vidiečan of the Aircraft Research Institute, Praha; J. Kübelbeck, J. Sýkora and Z. Nechyba of the mechanical workshop of the Geophysical Institute of the C.S.A.S. and B. Bartizal, J. Máša and J. Soukup of the seismological department of the same institute. We are indebted to D.J. Houlston and P.L. Willmore of the Institute of Geological Sciences, Edinburgh, for their valuable advice concerning Racal-Thermionic instrumentation and the concept of the DPS system.

References

- Aranovitch, Z.I., Borisevitch, E.S., Vorobiev, V.T., Karapetian, B.K., Kevleshvili, P.V., Kirnos, D.P., Nersesov, I.L., Rykov, A.V., Kharin, D.A., Shnirman, G.L., Steinberg, V.V.: Principal directions of development of seismic instrumentation (in Russian). *Izv. Akademii Nauk SSSR, Fizika Zemli* No. 5, 21–27, 1972
- Aranovitch, Z.I., Kondorskaya, N.V.: Methodic bases of the optimization of seismic observations (in Russian). *Izv. Akademii Nauk SSSR, Fizika Zemli* No. 7, 14–30, 1971
- Berckhemer, H.: The concept of wide-band seismometry. *Commun. Obs. Royal de Belgique* 13, Série géophys. No. 101, 214–220, 1971
- Burke, M.D., Kanasevich, E.R., Malinsky, J.D., Montalbetti, J.F.: A wide-band digital seismograph system. *Bull. Seism. Soc. Am.* 60, 1417–1426, 1970
- Daragan, S.K.: On the problem of correcting the frequency response of seismometric channels (in Russian). *Izv. Akademii Nauk SSSR, Ser. geofizicheskaya* No. 3, 61–67, 1967
- Daragan, S.K.: Design of high-precision long-period seismic channels. *Z. Geophys.* 39, 567–572, 173
- Houlston, D.J.: Training course in seismic methods—Advanced analogue processing. Internal IGS Report, Edinburgh 1972
- Jacoby, H.D.: Die Entwicklung eines kleinen Seismometers mit breitbandigem Ausgangssignal. Dissertation, Universität Stuttgart 1971
- Lake, H.R.: Dynamic range of broadband seismographs. VESIAC Report No. 4410-77-X, University of Michigan, 19–35, 1964
- Molnar, P., Savino, J., Sykes, L.R., Liebermann, R.C., Hade, G., Pomeroy, P.W.: Small earthquakes and explosions in Western North America recorded by new high-gain, long-period seismographs. *Nature* 224, 1268–1273, 1969
- Plešinger, A.: Theory of feedback-controlled photoelectric seismographs. *Trav. inst. geoph. acad. sci. tchechosl.* XVIII, 191–227, 1970
- Plešinger, A.: Theory and realization of broadband feedback seismographs. *Commun. Obs. Royal de Belgique* 13, Série géophys. No. 101, 279–284, 1971
- Plešinger, A.: Realisierung von Breitbandseismographen mittels aktiver frequenzabhängiger Gegenkopplungen. *Sammelschrift des Soproner Symposiums der 4. Subkommission KAPG* 1970, 97–117, Budapest 1972
- Plešinger, A.: Synthesis of feedback-controlled broadband modifications of conventional seismograph systems. *Z. Geophys.* 39, 573–595, 1973
- Sutton, G.H., Latham, G.V.: Analysis of a feedback-controlled seismometer. *J. Geophys. Res.* 69, 3865–3882, 1964
- Sutton, G.H., Pomeroy, P.W.: Analog analyses of seismograms recorded on magnetic tape. *J. Geophys. Res.* 68, 2791–2815, 1963
- Teupser, Ch., Berckhemer, H., Kirnos, D.P., Plešinger, A., Souriau, M., Szeidovitz, G.: Broadband seismographs. Preliminary report of the ESC working group on Instrumentation, Jena 1974
- Wielandt, E.: Ein einfacher Entzerrer für Seismometer. *Z. Geophys.* 36, 763–769, 1970
- Wielandt, E.: Noise in electronic seismograph systems. *Z. Geophys.* 39, 597–602, 1973

Intermediate Aseismicity of the Andean Subduction Zone and Recent Andesitic Volcanism

V. Hanuš and J. Vaněk *

Geological Institute, Czechoslovak Academy of Sciences, 16500 Praha 6-Suchbát and
Geophysical Institute, Czechoslovak Academy of Sciences, 141 31 Praha 4-Spořilov,
Boční II, 1401, Czechoslovakia

Abstract. Preliminary investigation of the morphology of the Benioff zone in the Andean South America, based on the distribution of earthquake foci, revealed intermediate aseismic gap in the descending oceanic plate. A close correlation of the occurrence of this intermediate aseismic gap and recent andesitic volcanism in the Cordillera de los Andes was found. This phenomenon may support the hypothesis that the source of andesitic volcanism is the partially melted zone of the oceanic lithospheric plate.

Key words: Seismicity – Andesitic volcanism – Plate tectonics – Andean South America.

The recent volcanism and seismic activity in the Pacific region are generally interpreted as a consequence of the acting global plate tectonics. It seems that andesitic volcanism is spatially bound to the areas characterized by the existence of seismically active Benioff zones. This was confirmed mainly for the island arcs of the western Pacific region (Kuno, 1966; Dickinson, 1968; Hatherton and Dickinson, 1969). No equivalent attention has been paid to the Andean region, although several papers on its seismicity were published (Santô, 1969; James, 1971; Stauder, 1973; Teisseyre et al., 1974).

The accuracy of the earthquake foci determination in the South American region substantially increased after 1966 (Santô, 1969). The ISC data (Regional Catalogue of Earthquakes) for the four years' period 1967–1970, completed by the data of deep shocks from the catalogue of Rothé (1969) for 1953–1965, were used in the present study. The relatively high seismicity of the Andean South America and nearly meridional course of the Peru-Chile trench allowed us to divide the active seismic belt between 0–35°S into 35 parallel sections with a width of 1° of latitude, for which graphs giving the depth distribution of earthquake foci in dependence on longitude were constructed (as an example, two of these sections are given in Fig. 1). According to minor seismicity south

* To whom offprint requests should be sent

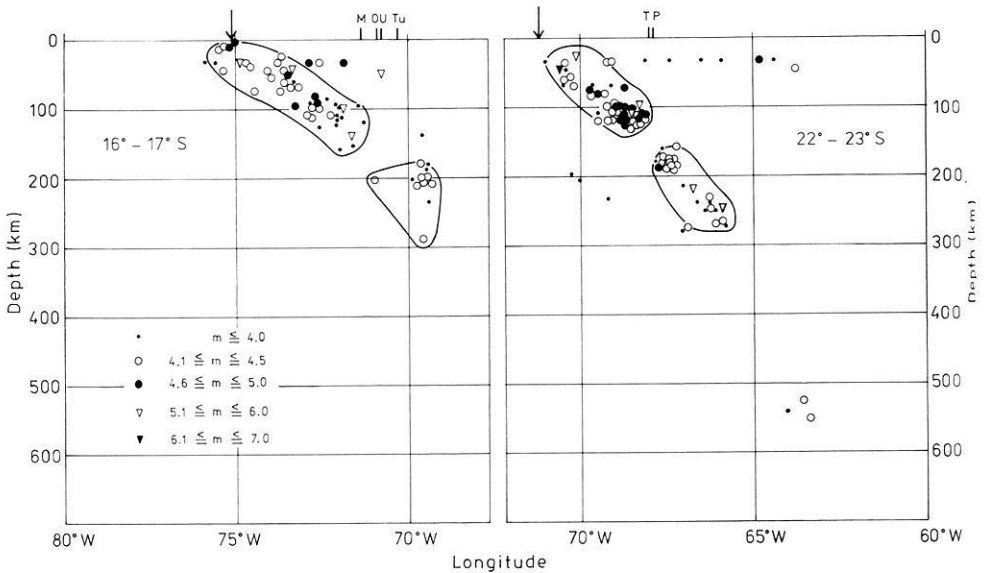


Fig. 1. Two parallel vertical sections of the Benioff zone under the Andes between 16° – 17° S and 22° – 23° S giving the distribution of earthquake foci in dependence on longitude; m-ISC magnitude; volcanoes are denoted by short vertical lines (*MM* Misti, *O* Omate, *U* Ubinas, *Tu* Tutupaca, *T* Tatio, *P* Putana), position of the Peru-Chile trench by arrows

of 35° S only three sections were constructed for the southern part of the Andes. Thus a detailed picture of the morphology of the Benioff zone, characterizing the collision of the Nazca and South American plates, could be obtained for the area limited by 0° – 45° S and 60° – 85° W.

On the basis of the above 38 parallel sections the seismic activity of the Benioff zone could be divided into three zones of shallow, intermediate and deep seismicity¹, separated by a distinct aseismic gap in the laterally variable depths of about 100–200 km, and by an aseismic region between 300 and 500 km. A generalized meridional section of the activity of the Benioff zone (Fig. 2) was constructed so that the shocks with minimum and maximum focal depth in all three zones were taken as their limits at the corresponding interval of latitude. Whereas the zone of shallow seismicity seems to be continuous along the whole section, the zones of intermediate and deep seismicity are interrupted in several places. No foci of intermediate depth have been located between 7° S and 14° S, as well as between 25° S and 27° S, 29° S and 31° S, and south of 40° S. A similar picture was obtained in the recent study by Teisseyre et al. (1974), as well as in papers of Santô (1969) and Stauder (1973), in the last two papers the intermediate aseismic gap appearing as a zone of decreased seismicity. The clear occurrence of this gap in our work is probably caused by more detailed treatment of data and by usage of the revised data after 1966.

¹ Here the meaning of shallow and intermediate seismicity is different from the formal definition of Gutenberg and Richter (1954)

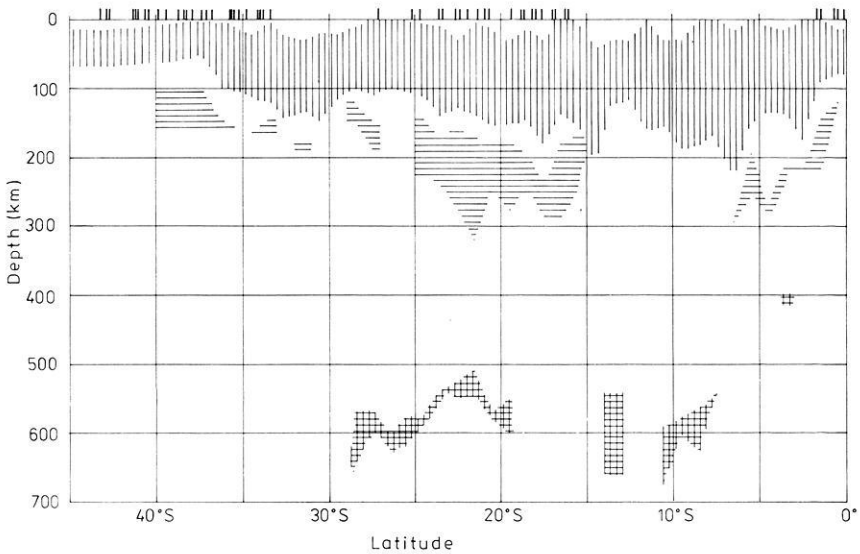


Fig. 2. Meridional section of the Andean seismicity between 0° and 45°S. Zones of shallow, intermediate and deep seismicity are denoted by vertical, horizontal and cross hatching, respectively, volcanoes by short vertical lines

If we correlate the meridional section of seismicity with recently active Andean volcanoes (Gutenberg and Richter, 1954; Gonzales-Ferran, 1972), the positions of which are indicated by short vertical lines in the upper part of Figure 2, a striking spatial relation appears between the occurrence of the intermediate aseismic gap and recent andesitic volcanism in the Cordillera de los Andes. In order to show clearly the above relationship, the surface projection of the intermediate aseismic gap, laterally extending from the westernmost shock with maximum depth of the shallow zone and the easternmost shock with minimum depth of the intermediate zone in parallel sections, and the areal distribution of Andean volcanoes are drawn in Figure 3. The numbers along the contours of the aseismic gap give the depth of the lower boundary of shallow seismicity and that of the upper boundary of intermediate seismicity, respectively.

The picture in Figure 3 confirms the close correlation between the occurrence of the intermediate aseismic gap and the position of active volcanoes. The vertical section of the gap is characterized by a nearly constant thickness of about 40 km between the shallow and intermediate seismicity (Fig. 2). No intermediate aseismic gap of such a shape can be observed between 3°S and 15°S, where also the Benioff zone is poorly defined and the distribution of seismicity is complicated, the earthquake foci being concentrated in two separated branches. The gap and the volcanic line are further interrupted between 25°S and 27°S, as well as between 29°S and 33°S. The intermediate seismicity disappears south of 40°S showing that the Benioff zone is thinning out at the southern margin of the Nazca plate.

The intermediate aseismic gap separating the shallow and intermediate seis-

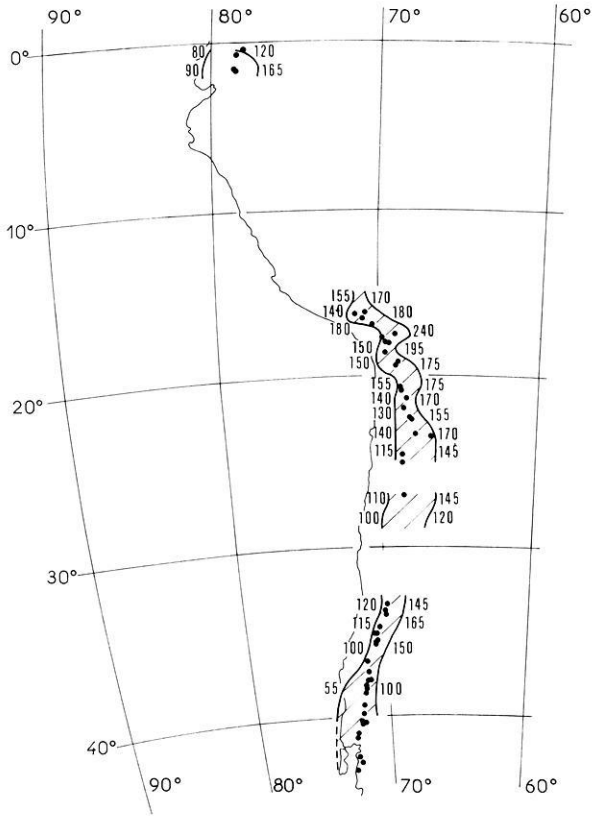


Fig. 3. Surface projection of the intermediate aseismic gap (hatched area) and distribution of active volcanoes (full circles) in the Andean South America. Numbers along contours of the aseismic gap give depth in kilometers

micity of the Andean region, which is spatially related to the occurrence of the recent andesitic volcanoes, indicates possible partial melting of the supposed descending oceanic plate. The partial melting, probably of the whole thickness of the slab (Fig. 1), can be considered as a source of andesitic magma for active volcanoes (Marsh and Carmichael, 1974). At the same time, the decreased viscosity due to the partial melting of the lithospheric material would exclude the accumulation of stress causing the seismic activity. If the above model is correct, the depth of the magma generation of the Andean andesitic volcanism should roughly be in the range between 100 and 200 km (Fig. 3), which is not in contradiction with data estimated in other Pacific regions (Sugimura, 1966a; Dickinson, 1968; Hatherton and Dickinson, 1969). A tendency of seismic activity to decrease in the depths, assumed to be responsible for the occurrence of primary magma, has been already reported for the Japanese island arc (Sugimura, 1966b). An intermediate aseismic gap seems to occur in the Tonga-Kermadec region (Isacks et al., 1968), and, according to our preliminary investigations, in the Benioff zone of Central America. The possible existence of the

partially melted zone in the slab would also modify the model of the Q_p -structure for South America (Sacks and Okada, 1974).

We suppose, similarly as Fyfe and McBirney (1975), that the liberation of water and other volatiles might play an important role in the materialization of most endogeneous processes in the areas of colliding plate margins. Whereas the continuous dehydration in shallower parts of the descending slab may facilitate the plutonic and metallogenic processes in the continental plate, the presence of water in suitable state conditions can cause partial melting in the deeper parts of the slab. Contrary to the latter authors, we assume that the source of andesitic volcanism is the partially melted zone of the oceanic lithospheric plate itself. An open question remains the recent Andean volcanism south of 40°S, which occurs in the region lacking clearly defined Benioff zone and intermediate seismicity. The explanation could be found in the change of the type of volcanism in the southern segment of the Andes (Casertano, 1963).

Similar studies for the region of Central America and for the whole region of the Andean South America on the basis of further seismological data are presently being made.

References

- Casertano, L.: General characteristics of active Andean volcanoes and summary of their activities during recent centuries. *Bull. Seism. Soc. Am.* **53**, 1415–1433, 1963
- Dickinson, W.R.: Circum-Pacific andesite types. *J. Geophys. Res.* **73**, 2261–2269, 1968
- Fyfe, W.S., McBirney, A.R.: Subduction and the structure of andesitic volcanic belts. *Am. J. Sci.* **275-A**, 285–297, 1975
- Gonzalez-Ferran, O.: *Volcanes activos de Chile*. Santiago: Universidad de Chile, 1972
- Gutenberg, B., Richter, C.F.: *Seismicity of the Earth*. Princeton: Princeton University Press 1954
- Hatherton, T., Dickinson, W.R.: The relationship between andesitic volcanism and seismicity in Indonesia, the Lesser Antilles, and other island arcs. *J. Geophys. Res.* **74**, 5301–5310, 1969
- Isacks, B.L., Oliver, J., Sykes, L.R.: Seismology and the new global tectonics. *J. Geophys. Res.* **73**, 5855–5899, 1968
- James, D.E.: Andean crustal and upper mantle structure. *J. Geophys. Res.* **76**, 3246–3271, 1971
- Kuno, H.: Lateral variation of basalt magma across continental margins and island arcs. *Can. Geol. Surv. Paper 66-15*, 317–336, 1966
- Marsh, B.D., Carmichael, I.S.E.: Benioff zone magmatism. *J. Geophys. Res.* **79**, 1196–1206, 1974
- Regional Catalogue of Earthquakes, Vol. 4–7. Edinburgh: Intern. Seismol. Centre, 1967–1970
- Rothé, J.P.: *The seismicity of the Earth 1953–1965*. Paris: UNESCO, 1969
- Sacks, I.S., Okada, H.: A comparison of the anelasticity structure beneath western South America and Japan. *Phys. Earth Planet. Interiors* **9**, 211–219, 1974
- Santó, T.: Characteristics of seismicity in South America. *Bull. Earthquake Res. Inst.* **47**, 635–672, 1969
- Stauder, W.: Mechanism and spatial distribution of Chilean earthquakes with relation to subduction of the oceanic plate. *J. Geophys. Res.* **78**, 5033–5061, 1973
- Sugimura, A.: Composition of primary magmas and seismicity of the earth's mantle in the island arcs (a preliminary note). *Can. Geol. Surv. Paper 66-15*, 337–347, 1966a
- Sugimura, A.: Complementary distribution of epicenters of mantle earthquakes and of loci of volcanoes in island arcs. *Zisin* **19**, 96–106, 1966b
- Teisseyre, R., Wojtczak-Gadomska, B., Vesanen, E., Mäki, M.-L.: Focus distribution in South American deep-earthquake regions and their relation to geodynamic development. *Phys. Earth Planet. Interiors* **9**, 290–305, 1974

Provisional Seismicity Map of the Republic of Zambia and Its Preliminary Interpretation *

K.D. Töpfer**

University of Zambia, School of Natural Sciences, P.O. Box 2379, Lusaka, Republic of Zambia

Abstract. The provisional seismicity map of the Republic of Zambia has been compiled from data made available by Goetz Observatory, Rhodesia, for the period from 1966 to 1972.

Seismicity anomalies have been compared with the Provisional Gravity Map and the Geological Map of Zambia. Seismicity highs are closely associated with negative Bouguer anomalies and the distribution of zones of zero to moderate seismic activity seems to be related to the regional geology of Zambia. It appears that seismicity is not directly related to the geochronological history of Zambia.

Key words: Seismicity – Gravity – Geology.

1. Introduction

Little attention has been paid to seismic events occurring in Southern Africa (Africa south of the Equator) until recently, when the Pan-African Rift system was intensively studied geophysically, (Henning, 1937; Porstendorfer and Kuhn, 1966; Girdler, 1968; Fairhead and Girdler, 1969; Girdler and Sowerbutts, 1970; Chapman and Pollack, in preparation; de Beer et al., in preparation), and when large man-made lakes (i.e. Lake Karika) increased seismic activity in a limited area (Gough and Gough, 1970).

This present paper aims to present seismological data of the Republic of Zambia for the period 1966 and 1972. The Provisional Seismicity Map is compared with the regional geology and the Gravity Map of Zambia.

Possible rifting within Zambia is out of the scope of this present paper, but will be discussed on a more Pan-African scale in a separate paper (Töpfer, in preparation).

* To Prof. Dr. M. Toperczer on the occasion of his 75th birthday

** Address for offprint requests: Lehrkanzel für Geophysik der Universität, Hohe Warte 38, A-1190 Wien, Austria

2. Seismic Network in Southern Africa and Data Collection

Seismological research in Southern Africa has been limited mainly by the inadequate network of observatories, see Figure 1.

A reasonable distribution of seismic observatories exists only in the Republic of South Africa and in Rhodesia (Zimbabwe). Observatories in many other countries have operated only sporadically. The absence of a Southern African Data Center is also regrettable.

Two seismic observatories exist within the Republic of Zambia. LUS is operated by the University of Zambia and BHA is incorporated in the Rhodesian network of observatories.

All data for this present study were taken from available Seismological Bulletins of Goetz Observatory, Bulawayo, Rhodesia, (Archer, 1966–1972) and from Seismological Bulletins of the LUS Observatory, Lusaka, Zambia (Chander, 1971–1974).

Locations of observatories from which data were obtained, are given in Table 1.

The number of listed earthquakes occurring within Zambia apparently decreased from 1966 to 1972, see Figure 2. It is believed that this may be due to administrative changes at Goetz Observatory. Epicenters of earthquakes of magnitudes $mb \geq 2.5$ only were listed from 1971 onwards, whereas all visible events were interpreted in previous years.



Fig. 1. Network of seismic observatories in Southern Africa

Table 1. Locations of seismic observatories

Symb	Location	Country	Lat(S)	Long (E)	Altitude (m)
BHA	Kabwe	Zambia	14 26.8'	28 28.1'	1,206
LUS	Lusaka	Zambia	15 22.8'	28 19.8'	1,259
CLK	Chileka	Malawi	15 40.8'	34 58.6'	781
MTD	Mount Darwin	Rhodesia	16 46.8'	31 35.0'	967
KRR	Karoi	Rhodesia	16 51.1'	29 37.1'	1,380
BUL	Bulawayo	Rhodesia	20 08.6'	28 36.8'	1,341
CHR	Chiredzi	Rhodesia	21 00.8'	31 34.8'	430

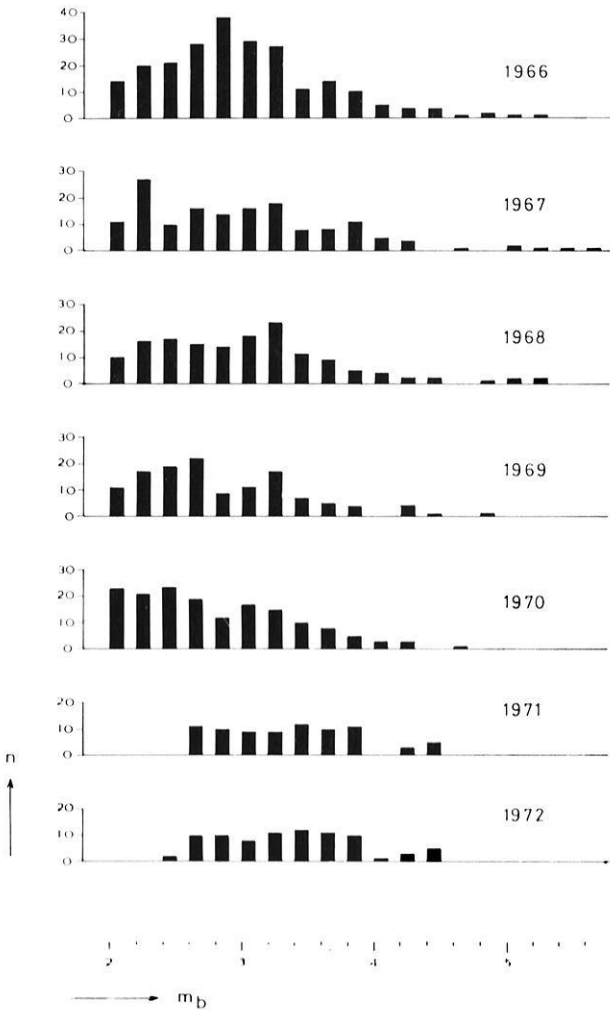


Fig. 2. Yearly distribution of earthquakes with epicenters within Zambia during the period 1966–1972

3. Statistical Analysis of Data

The yearly distribution of the number of events as function of magnitude m_b is represented in Figure 2.

Magnitude estimates given in the Seismological Bulletins of Goetz Observatory are thought to be comparable with Gutenberg and Richter's m_b , although they are based on crustal rather than body waves (Archer, 1969).

Only a few medium intense tremors of magnitudes $m_b \geq 5$ were recorded during the years 1966–1972. The majority of recorded earthquakes have magnitudes between $2 \leq m_b \leq 4$. Many of the reported earthquakes with magnitudes $2 \leq m_b \leq 3.5$ were located around the man-made Lake Kariba, along the mid-Zambesi Valley.

The distribution of earthquakes in magnitude is shown in Figure 3. The distribution appears to be linear for the range $3 \leq m_b \leq 5.7$ and the least-squares fitted line gives

$$\log N = 3.87 - 0.71 m_b \quad (1)$$

obeying the relationship introduced by Gutenberg and Richter (1954)

$$\log N = a - b m_b \quad (2)$$

which has proved to be valid elsewhere on the globe.

The constant b for Zambia is within the range of 0.6–1.2 which is found worldwide, (Schick and Schneider, 1973). Bath and Anderson (1968) used the earthquake catalogue published by Gutenberg and Richter (1954) for earthquakes

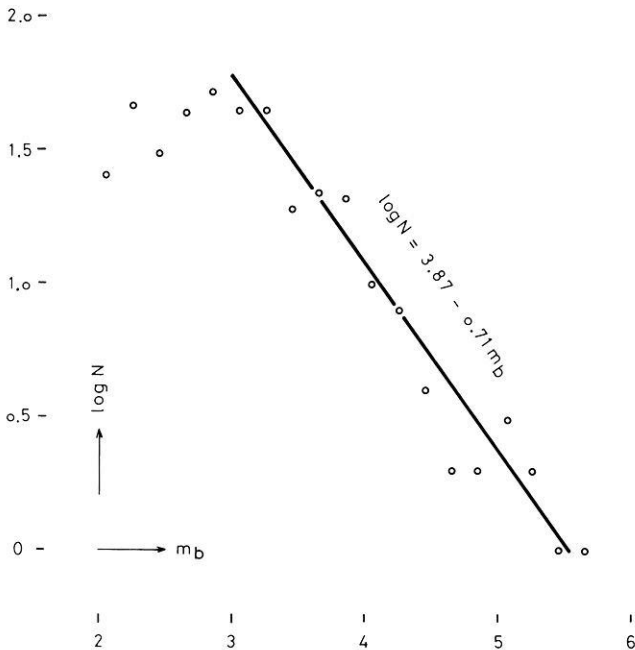


Fig. 3. Distribution of earthquakes in magnitude for the period 1966–1972

of $mb > 5$ during the period 1904–1952 and derived the relationship

$$\log N = 5.25 - 0.71 mb.$$

An analysis of earthquakes of magnitude $mb > 5$ compiled by Sykes and Landisman (1964) for the period 1955–1964 resulted in the relationship $\log N = 4.98 - 0.71 mb$ (Bath and Anderson, 1968).

The constant “ b ” is remarkable constant whereas the intercept “ a ” apparently decreases from 1904 to 1972.

4. Provisional Seismicity Map of the Republic of Zambia¹

The number of earthquakes which occurred within Zambia during the period 1966 to 1972 is contoured in arbitrary intervals of 0, 1, 2–3, 4, 5–9, 10–20 and > 20 , regardless of the magnitude of these tremors, see Figure 4.

Epicenters of earthquakes are related to the center of a $0.5^\circ \times 0.5^\circ$ grid pattern laid over the territory of the Republic of Zambia, applying a moving average technique. This procedure is somewhat unusual in seismological research but is in wide use in the representation of gravity and magnetic data in exploration geophysics.

It results in relative smooth iso-lines and seismicity “highs” and “lows” are readily shown. This applied technique may certainly result in errors of approximately ± 60 km in the location of iso-lines. This estimated error is not considered to be too serious since epicenters of earthquakes as listed by Goetz Observatory are thought to be located to an accuracy in the order of 50 km (Reeves, 1972).

Iso-seismicity lines, representing areas of relatively low or zero seismicity during the period 1966 to 1972, follow approximately a north-easterly trend, see Figure 4. This trend is also observed on the Geological Map (Reeve, 1961) and the Provisional Gravity Map (Masac and Töpfer, 1974), of the Republic of Zambia (see also Chapter 5).

Zones of relatively high seismicity show a north-south trend from latitude 12° S to 18° S and a north-easterly trend from latitude 12° S to 8° S. This trend is not apparent in the geological map and may therefore be related to the Pan-African rift system.

Five major zones of relatively high seismic activity are recognized on the presented seismicity map, see Figure 4. The seismicity high in the area along Lake Kariba in the South of Zambia is related to positive Bouguer anomalies, whereas the remaining zones of relatively high seismic activity are related to large negative Bouguer anomalies.

¹ Seismicity has been defined in this paper as

$$S = \frac{n}{AF \cdot \Delta t}$$

(number of earthquakes per year and unit area of $0.5^\circ \times 0.5^\circ$)

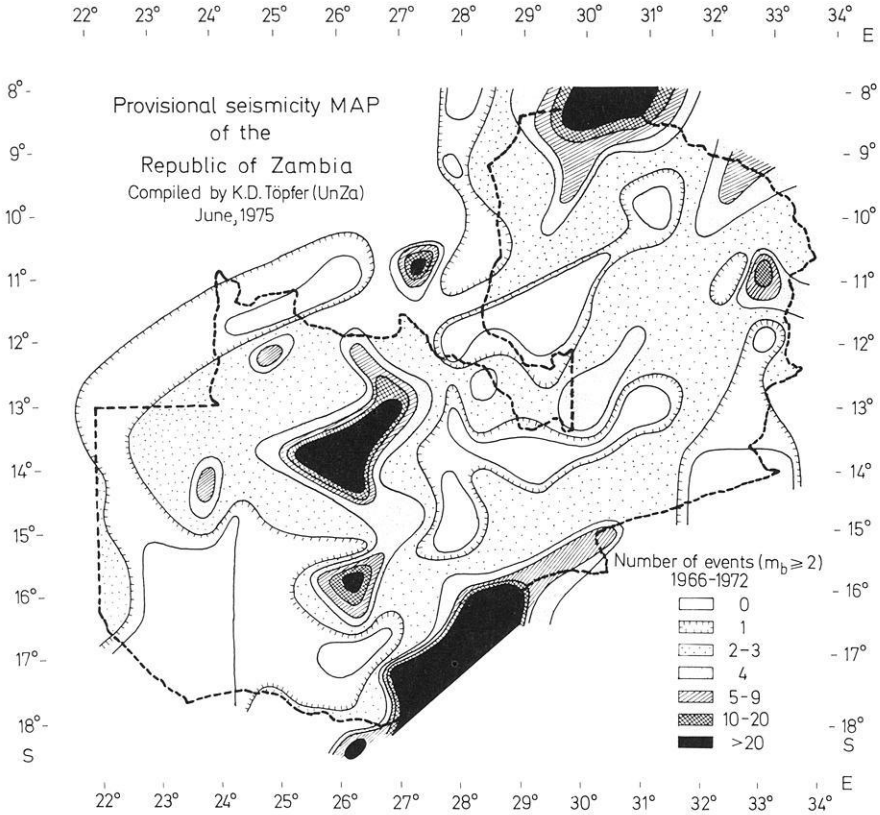


Fig. 4. Provisional seismicity map of Zambia

4.1. Lake Kariba High

All epicenters of this zone of high seismic activity lie in or near the down-faulted rift valley of the mid-Zambezi. A large number of earthquakes were recorded since man-made Lake Kariba was filled in 1963 and it is believed that the lake has re-activated the existing faults formed since late Precambrian times.

Earthquakes of magnitudes $M \geq 5$ and epicenters in Southern Africa were listed for the period 1904 to 1952 by Gutenberg and Richter (1954) and for the period 1955 to 1964 by Sykes and Landisman (1964). No earthquake was reported from the mid-Zambezi Valley until August 1963 when Lake Kariba reached almost its full capacity. Although it seems to be evident that no intensive earthquakes occurred prior to the completion of Lake Kariba, it remains unknown whether this area was inactive or shaken by tremors of relatively small magnitudes.

Gough and Gough (1970) estimated that the elastic strain energy of 5.5×10^{24} ergs is stored in the lithosphere as a result of release of gravitational energy during depression of the rock in a limited volume.

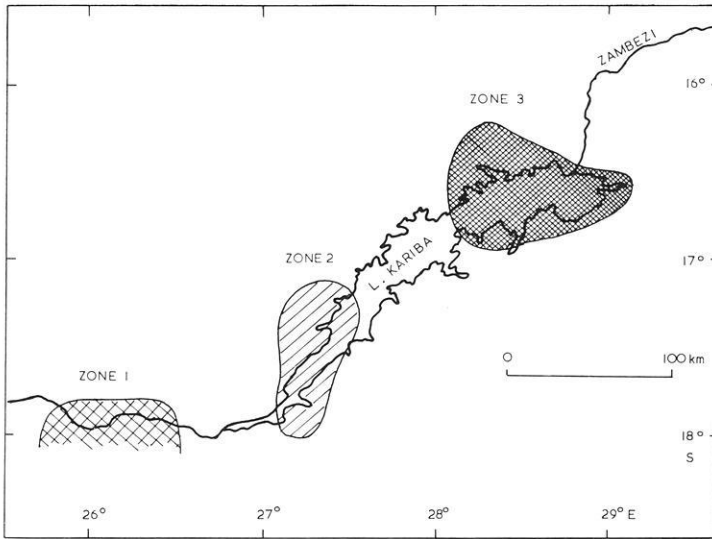


Fig. 5. Seismic energy radiation at Lake Kariba

The elongated seismicity high, which extends from longitude 26° E to 30.5° E, see Figure 4, is resolved into three relatively small zones of high seismic energy radiation, see Figure 5: Zone 1 has an approximate center at 26.3° E/ 18.2° S, Zone 2 at 27.5° E/ 17.3° S and Zone 3 at 28.3° E/ 16.8° S.

Zone 1 occurs approximately 80 km west of the shore line of Lake Kariba and is believed not to be affected by the triggering effect of increasing load. It is more likely that this zone is related to the Pan-African system of rifting.

Zone 2 is associated with the Binga Fault at the south-western shore of Lake Kariba. This zone is believed to have been active before the lake filled (Gough and Gough, 1970).

Zone 3 is located in and near the Sanyti Basin of Lake Kariba, where the water level is highest, and represents the main seismic activity within the lake.

4.2. Namwala and Kasempa Highs

Two seismic active zones occur at Namwala and south of Kasempa, both approximately at longitude 26° E and with centers at latitudes 15.75° S and 14° S, respectively. Both seismicity highs are associated with relatively large negative Bouguer anomalies, see Figure 6.

The gravity low and the seismicity high at the Namwala Anomaly correspond exactly, whereas a displacement of approximately 60 km may be apparent at the Kasempa Anomaly. This displacement may be however fictitious because of the estimated inherent error of ± 60 km in the seismicity map.

The estimated regional gradient of the gravity profile along longitude 26° E is -67 mgal per 1000 km south-north and gradients of -700 mgal and -1500 mgal per 1000 km are evident at Namwala and Kasempa Highs, respectively.

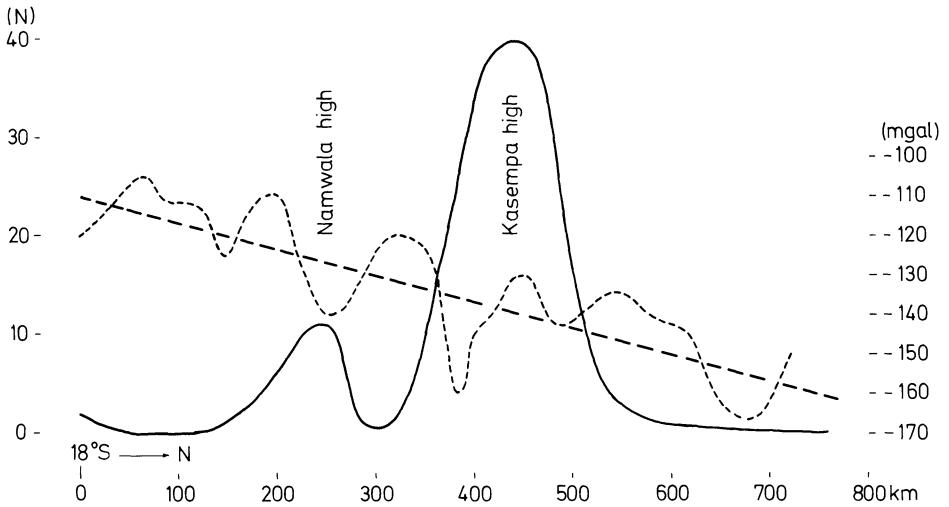


Fig. 6. Seismicity and Bouguer anomaly profiles along longitude 26° E

Although no modelling has yet been attempted to date to interpret the negative anomalies at Namwala and Kasempa, the half-width rule suggests that both gravity anomalies are caused by anomalous mass distributions within the crust.

4.3. Lake Retenue High

Seismic activity at man-made Lake Retenue, some 30 km east of Likasi, Zaire, at approximately 11° S and 27.3° E, is thought to follow the Pan-African system of rifting. No gravity data are available for this region.

4.4. Seismicity Highs in the North-East of Zambia

Three seismicity highs occur in the north and north-east of Zambia and are associated with large negative Bouguer anomalies. They are thought to be related to rifting in Southern Africa (Töpfer, in preparation). It is worth noting that the anomaly at approximately 33° E and 10.8° S is located at the north-eastern edge of the Luangwa Valley, whereas the valley itself shows only moderate seismic activity.

4.5. Seismicity Highs in the North-West of Zambia

The seismicity high at approximate latitude 12° S and longitude 25° E corresponds well with a gravity low (–180 mgals) whereas the seismicity high at 14.25° S and 23.75° E cannot be related to gravity because only few gravity data are available from this region.

5. Comparison of the Seismicity Map with the Geological Map of the Republic of Zambia

Two general trends are visible on the seismicity map of Zambia which may be related to pre-Katanga orogenic episodes which terminated periods of geosynclinal sedimentation: the N to NE Tumbide trend (1,600 m.y.) and the younger NE to ENE Irumide trend (1,000 m.y.) (Vail et al., 1968; Snelling et al., 1972).

The first intense folding of the Katanga System, characterized by the Lufilian Arc (500 m.y.), which is thought to be an extension of the Damara Belt in South-West Africa (Namibia) (van Eden and Binda, 1972), does not find its expression in the seismicity map of Zambia.

Vail (1968) notes that the post-Karoo (Mesozoic) and post-Tertiary Rift Valley fractures tend to follow the ancient orogenic belts, regardless of the age of the belts.

Zones of low and moderate seismic activity apparently resemble geological structures in shape, see Figure 7. This present paper does not attempt to explain this apparent resemblance nor does it go into much detail which would certainly involve the study of the tectonic fault pattern of Zambia. Many large fault systems in Zambia seem to be inactive at present (i.e. Luangwa Valley) so that a tectonic interpretation of the seismicity map becomes difficult.

The western part of Zambia is mainly underlain by rocks of Cretaceous Age (70–130 m.y.) in the far east, of Karroo Age (200–270 m.y.) in the south-west and of Katanga Age (600–950 m.y.) in the north. The boundary between Cretaceous and Karroo, stretching from approximately 14° S along 23° E to 17.5° E (Money, 1972), is comparable to the isoseismicity line of Figure 7 which separates the moderate active zone in the east from the non-active zone in the west.

The large area with no apparent seismic activity, extending approximately from 15° S to 18° S and from 22.5° E to 26° E can be compared to the large area in Western Province which has been mapped to be underlain by Karroo rocks ($\pm 1^\circ$ to the north). The narrow arm of Karroo rocks, which strikes north-westerly into Angola, is also indicated on the seismicity map.

The ENE-striking area of no recorded seismicity, with its center at 17.2° S and 26° E, is underlain mainly by acid igneous rocks believed to be Kibaran in age (1,300 m.y.).

The Namwala High, as discussed in Chapter 4.2, is associated with the Hook Granite Massif of Kibaran Age, whereas the Kasempa High cannot be interpreted on the basis of surface geology.

Areas underlain by rocks of Katanga Age in the Western and North-Western Provinces of Zambia are shown to be zones of moderate seismic activity (2–3 tremors per square grid during the period 1966–1972).

The large seismicity low which strikes NS in the west, from 12.7° S to 15.5° S and ENE from 27.3° E to 31.6° E, cannot be explained on the basis of a single geological unit. The NS-striking western part of the anomaly is underlain by metasediments of Katanga Age, whereas the ENE-striking eastern part follows the Irumide Fold Belt of the Kibaran Orogeny. The small seismicity low with its center at 11° S and 32.3° E also lies in this Fold Belt and may therefore be regarded as an extension of the large seismicity low in the south-east.

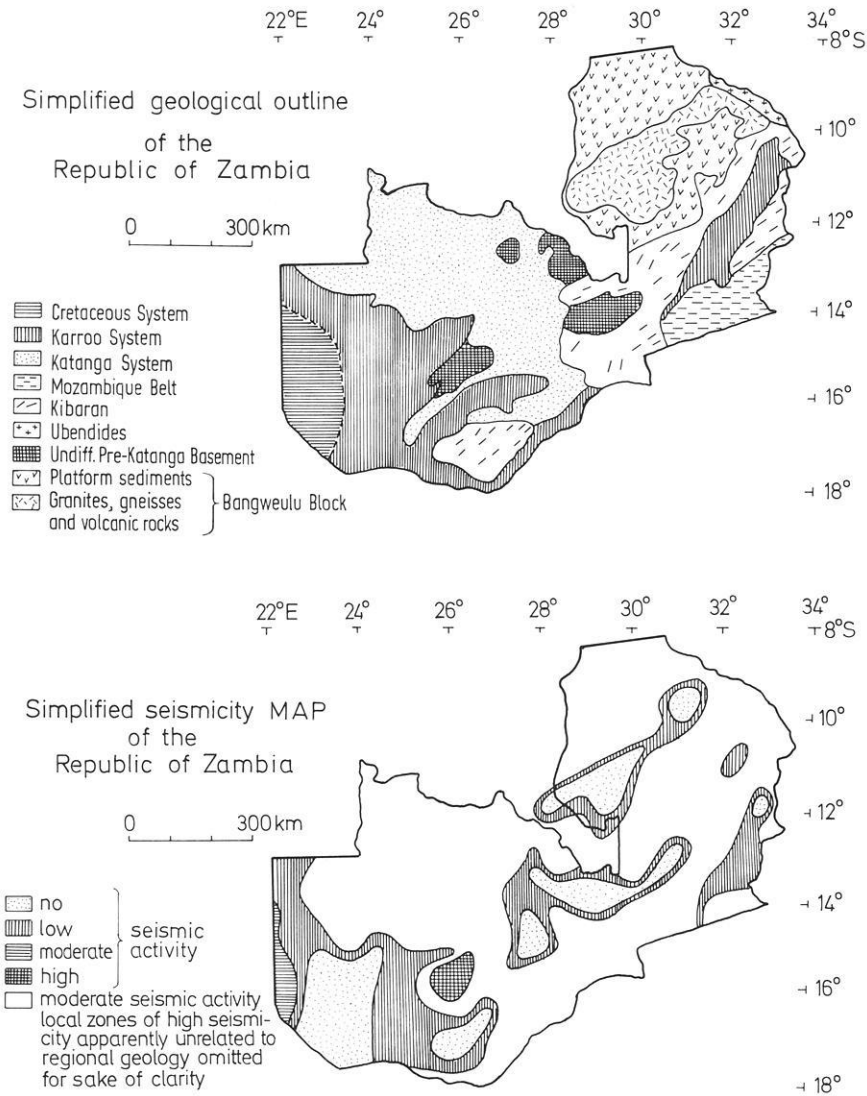


Fig. 7. Simplified seismicity map and geological outline of the Republic of Zambia

The large seismicity low striking approximately NS from 11.5° S to 14.5° S follows the Kibaran Belt in the north and the Mozambique Belt (380–470 m.y.) in the south.

The Luangwa Valley, an erosional valley (Johnson, 1975), which is often mistaken to represent an active rift valley, strikes north-east and is bound by the Irumide Fold Belt in the north and by the same belt and the Mozambique Belt in the south. The large system of faults in the upper Luangwa Valley is seismically inactive and might have been initiated in pre-Karroo times.

The elongated seismicity low, striking NE from 27.5° E and 12° S to 31.6° E and 9.3° S corresponds approximately with granites and gneisses of the Bangweulu Block, whereas the Plateau Series of the Bangweulu Block to the north-west and to the south-east appear to be characterised by moderate seismic activity.

The NS-striking seismicity low along 28° E cannot be explained with available geological data. This low appears to correspond with a large positive Bouguer anomaly.

6. Conclusions

It appears that the general pattern of the presented seismicity map can be partly related to the simplified geological map of Zambia. In general, areas of low to moderate seismicity follow more strictly the geological pattern, whereas areas of high seismicity are more difficult to interpret in terms of the known regional geology. The Kasempa High seems to be unrelated to the known geology of Zambia.

It is also of interest to note that seismicity in Zambia seems to be neither related to the age of orogenic events nor to major cycles of sedimentation.

Seismicity highs may be rather related to the Pan-African system of rifting, stretching from Ethiopia in the north, and probably to Mozambique in the south-east and Namibia in the south-west (Töpfer, in preparation).

References

- Archer, C.B.: A catalogue of earthquakes in the Lake Kariba Area, 1959–1968. Goetz Observatory, Bulawayo, Rhodesia, 1969
- Archer, C.B.: Seismological Bulletin. Goetz Observatory, Bulawayo, Rhodesia, 1966–1972
- Bath, M., Anderson, A.J.: Seismicity of Zambia and surrounding areas with Plans for the Development of a Seismograph Station Network in Zambia. unpublished 1968
- Chander, R.: Seismological Bulletin. University of Zambia, Lusaka, Zambia, 1971–1974
- Chapman, D.S., Pollack, H.N.: Heat flow and incipient rifting in the Central African Plateau. In Preparation
- de Beer, J.H., van Zijl, J.S.V., Huysen, R.M.J., Hugo, P.L.V., Joubert, S.J., Meyer, R.: A magnetometer array in South-West Africa. Botswana and Rhodesia. In Preparation
- Fairhead, J.D., Girdler, R.W.: How far does the rift system extend through Africa. *Nature* **221**, 1018, 1969
- Girdler, R.W.: Drifting and rifting in Africa. *Nature* **217**, 1102, 1968
- Girdler, R.W., Sowerbutts, W.T.C.: Some recent geophysical studies of the rift system in East Africa. *J. Geomagne. Geoelectr.* **22**, 153, 1970
- Gough, D.I., Gough, W.I.: Load-induced earthquakes at Lake Kariba. University of Alberta, Edmonton, Canada, 1970
- Gutenberg, B., Richter, C.F.: Seismicity of the Earth and associated phenomena. Princeton: Princeton University Press 1954
- Henning, E.: Die Ostafrikanische Bruchterappe. *Geol. Rundschau* 2921, 1937
- Johnson, R.L.: Personal communication, 1975
- Masac, O., Töpfer, K.D.: Provisional gravity map of the Republic of Zambia. Geological Survey Department, Lusaka: Govern. Printer 1974
- Money, N.J.: An outline of the geology of Western Zambia. *Records of the Geological Survey, Lusaka* **12**, 103, 1972

- Porstendorfer, G., Kuhn, P.: Geophysikalische Arbeiten auf Sansibar/Tansania. Publikation des Nationalkomitee für Geodäsie und Geophysik der DDR, Berlin, 1966
- Reeve, W. H.: Geological map of Northern Rhodesia. Geological Survey Department, Lusaka, 1961
- Reeves, C. V.: Rifting in the Kalahari. *Nature* **237**, 95, 1972
- Schick, R., Schneider, G.: Physik des Erdkörpers. Stuttgart: Enke 1973
- Snelling, N. J., Johnson, R. L., Drysdall, A. R.: The geochronology of Zambia. Records of the Geological Survey, Lusaka **12**, 19, 1972
- Sykes, L. R., Landisman, M.: The seismicity of East Africa, the Gulf of Aden, and the Arabian and Red Seas. *Bull. Seism. Soc. Am.* **54**, 1964
- Töpfer, K. D.: Rifting in Zambia. In preparation
- Vail, J. R.: The souther extension of the East African rift system and related igneous activity. *Geol. Rundschau* **57**(2), 601, 1968
- Vail, J. R., Snelling, N. J., Rex, D. C.: Pre-Katangan geochronology of Zambia and adjacent parts of Central Africa. *Can. J. Earth Sci.* **5**, 621, 1968
- van Eden, J. G., Binda, P. L.: Scope of stratigraphic and sedimentologic analysis of the Katanga sequence, Zambia. *Geologie en Mijnbouw* **51**(3), 32, 1972

Received December 12, 1975

Geothermal Models of the Crust and Uppermost Mantle of the Fennoscandian Shield in South Norway and the Danish Embayment

N. P. Balling

Laboratory of Geophysics, Aarhus University, Finlandsgade 6–8, 8200 Aarhus N, Denmark

Abstract. A narrow heat flow transition zone between the Fennoscandian Shield and the North Sea Basin has been investigated along a profile from the Precambrian of South Norway to the Danish Embayment in North Jylland. Along this profile the surface heat flow varies from about 42 mW m^{-2} (measured) in South Norway to $60\text{--}70 \text{ mW m}^{-2}$ (estimated) in Denmark. Geothermal, seismic, gravity and other geophysical and geological data have formed the basis for construction of heat production and thermal conductivity models in the depth interval 0–50 km. The related steady-state temperatures and heat flow distributions are calculated by a numerical solution of the heat conduction equation in two dimensions. Three models are presented, a preferred model and two others which yield temperatures assumed to be close to the lowest and highest possible values. The preferred model gives temperatures of about 350°C at the crust-mantle boundary in the Shield and approximately 700°C beneath the Danish Embayment. These differences are associated with considerable variations in the heat flow from the mantle. In the main model variations from $16\text{--}17 \text{ mW m}^{-2}$ in the shield region to about 40 mW m^{-2} in the Danish Embayment have been found. Some geophysical and petrological implications are discussed. In the sedimentary basin partial melting in the lower crust and at shallow depth in the uppermost mantle seems to be likely.

Key words: Geothermal models – Heat flow transition zone – Crust uppermost mantle – Fennoscandian Shield and the Danish Embayment.

1. Introduction

South Scandinavia consists of three main structural-geological units: The southern part of the Paleozoic Caledonian orogenic belt, the southeastern part of the Precambrian Fennoscandian (Baltic) Shield, and the northeastern part of the North Sea Basin (Fig. 1). The shield area is subdivided into two parts by the Permian Oslo Graben. Our present knowledge of geological and crustal physical conditions indicates that the transition zone between the Fennoscandian Shield,

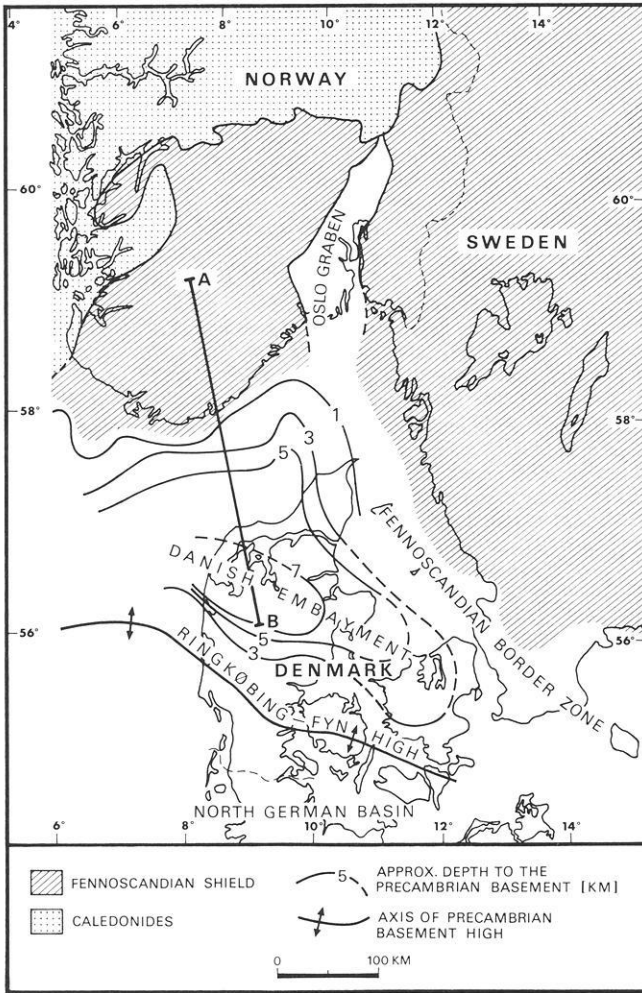


Fig. 1. Main structural-geological units of South Scandinavia and the position of the geothermal profile (AB)

which is a province of low heat flow, and the North Sea Basin where the heat flow in general seems to be considerably higher, also represents a region with great lateral temperature variations in the crust and upper mantle and with great variations in the heat flow from the mantle. To examine this anomaly, general geothermal models are constructed along a profile from the shield region in South Norway to the Danish Embayment (profile AB, Fig. 1). This is the area for which we have the most geophysical and geological information.

Based on heat flow values, thermal parameters for the near-surface rocks, seismic and gravity results, models of the radioactive heat production and of the thermal conductivity distribution for the depth interval 0-50 km are made. The related temperature models are calculated from a numerical solution of the heat

conduction equation

$$A + \nabla \cdot (K \nabla T) = 0 \quad (1)$$

where A is the heat production per unit volume per unit time, K is the thermal conductivity, and T is the temperature. This equation is valid for steady-state conditions in a non-homogeneous but isotropic medium without heat transfer by moving materials.

Heat production and conductivity are functions of the position, while conductivity is also a function of the temperature and the pressure. The variations perpendicular to profile AB are assumed to be so small that the problem can be treated as two-dimensional.

Equation (1) is to be solved with respect to $T = T(x, z)$ using models containing known or assumed thermal conductivity and heat production distribution together with some necessary boundary conditions. Three geothermal models are constructed. What are considered the most probable values of the geothermal parameters are used in model A. In model B and C the parameters are combined in such a way as to yield what is assumed to be close to the lowest and highest possible temperature, respectively. To construct geothermal models, knowledge of the geology, the crustal and uppermost-mantle physics including the measured geothermal parameters of the area, is essential and shall be treated in some details.

2. Geology, Crustal and Uppermost-Mantle Physics

South Norway constitutes a typical Precambrian migmatite area that has undergone a complicated metamorphic, magmatic and structural development (Barth and Dons, 1960; Smithson, 1965; Falkum, 1966, 1972). The area is dominated by high-metamorphic (medium and high grade) granitic gneiss, augen gneiss, banded gneiss and intrusive granites and charnockites. The banded gneiss, which is composed of alternating layers of amphibolite, pyribole, acidic and intermediate gneiss, garnet-cordierite-sillimanite gneiss, quartzite and pyribole-anorthosite, is of special interest as an indicator of the composition of the deeper parts of the crust. The area is considered to be poly-orogenic with the Sveconorwegian orogeny (approx. 1,000 m.y.) as the last one. The main part of the present surface rocks seems to be generated by anatexis and related processes to a large extent. The mean specific density of the main rock units varies from $2.6 \cdot 10^3 \text{ kg m}^{-3}$ for some of the intrusive granites to 2.8 for some banded gneiss formations. The mean density of 658 samples from the above mentioned rock types collected by Professor S. Saxov and the author in connection with a gravity study of the area is $2.68 \cdot 10^3 \text{ kg m}^{-3}$.

The general geological conditions of the sedimentary basin are rather well-known from the many exploration drillings covering the area (Sorgenfrei and Buch, 1964; G. Larsen, 1966; Sorgenfrei, 1969; Rasmussen, 1972, 1974) except for the Skagerrak area and the deepest part of the Danish Embayment. To find the thickness of the sedimentary formations the seismic and magnetic investigations of Sellevoll and Aalstad (1971) and Casten and Hirschleber (1971) together with

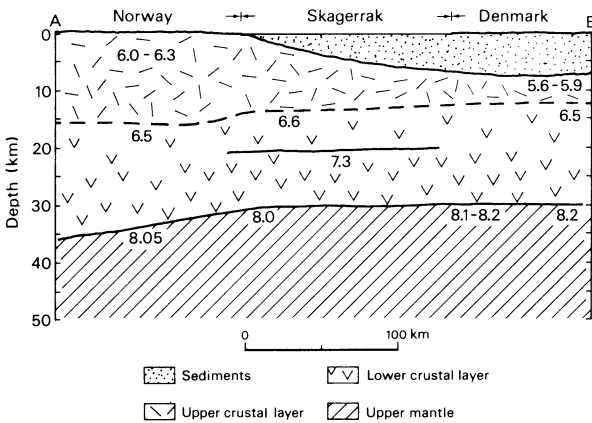


Fig. 2. Crustal structure along profile AB (Fig. 1) from seismic investigations. Results from lines within a distance of ± 50 km are projected on to the profile. The figures indicate P -wave velocities (km s^{-1})

results from drill holes and other geophysical data have been compiled and interpreted (Fig. 1). The total thickness of the Paleozoic, Mesozoic, and Cenozoic sedimentary sequence in the central part of the Danish Embayment is supposed to be 7–9 km. Radiometric dating of some basement cores from Jylland and Fyn indicates a basement age similar to that of the Sveconorwegian orogeny of the shield region (O. Larsen, 1971, 1972).

The general crustal structure of Scandinavia is known from several deep seismic sounding projects (Sellevoll, 1973). Results from the area of profile AB (Hirschleber et al., 1966; Aric, 1968; Weigel et al., 1970; Casten and Hirschleber, 1971; Sellevoll and Warrick, 1971) compiled in Figure 2 show typical continental velocity-depth values. For simplicity the terms 'upper crustal layer' and 'lower crustal layer' are used, although variations within these units are likely both as to physical and petrological conditions. In all investigations the crust-mantle boundary (the Moho) has been found by well-defined depths and P -wave velocities. In the models of South Norway, the crustal thickness is about 32 km in the coast region increasing to about 36 km at the northern part of profile AB. To the south the crustal thickness decreases to 29–32 km below the Skagerrak and North Jylland. The crust seems to be sub-divided by the 6.5–6.6 km s^{-1} refractor – the Conrad 'discontinuity' – which, according to the cited authors, has been observed in the whole area with a well defined velocity but with some uncertainties concerning the depth. For South Norway the depth values in the interpretational models are 14–17 km, and in the Skagerrak and North Jylland 12–14 km. The extremely low values of 8–9 km in the models of Hirschleber et al. (1966) are not realistic, due in part to their use of too low a velocity for the sediments. In the models, the Precambrian basement of North Jylland has a lower velocity than the related rocks at similar pressure close to the surface in South Norway. There are reasons to believe that the basement rocks to the south are more granitic. For both areas there are clear indications of a P_g -velocity increase with depth, which cannot be explained by the effect of pressure alone.

Below the Skagerrak an intermediate velocity of 7.3 km s^{-1} has been observed at a depth of about 20 km. Velocities of about 7 km s^{-1} at that level are also reported at other places in South Scandinavia (Kanestrøm and Haugland, 1971; Gregersen, 1971). Although such intermediate velocities have not been introduced in the models to the north and south along profile AB, it must be assumed that the *P*-wave velocity of the lowest part of the crust is higher than $6.5\text{--}6.6 \text{ km s}^{-1}$. This assumption is based on an analysis of the regional gravity field of South Scandinavia (Balling, in preparation). From these investigations an average density of the upper crustal layer of $2.7\text{--}2.8 \cdot 10^3 \text{ kg m}^{-3}$ increasing to $2.8\text{--}2.9 \cdot 10^3 \text{ kg m}^{-3}$ in the upper part of the lower crust is found. At the base of the crust the density seems to be $2.9\text{--}3.1$ followed by $3.3\text{--}3.4 \cdot 10^3 \text{ kg m}^{-3}$ in the uppermost mantle.

The upper crustal layer is supposed to be dominated by high-metamorphic migmatites similar to those observed at the surface in the Precambrian of South Norway but with an acidity decreasing with depth. Gravity investigation of some of the intrusive granites in South Norway shows a vertical range of the density contrast of 2–5 km, which together with the seismic results support the assumption of this decreasing acidity.

The petrological nature of the lower crust in stable continental areas has been a matter of discussion. The detailed experimental investigations of Green and Ringwood a.o. (see e.g. Green and Ringwood, 1967, 1972) show that it is unrealistic to label the lower crust 'basaltic' or 'gabbroic' as is usual. It is to be assumed in general that gabbro is not stable in the lower crust. Here large amounts of high-density and high-metamorphic elements of the banded-gneiss formations observed in South Norway are presumed to be present.

The geothermal models are constructed on the assumption that the uppermost mantle consists of olivine-peridotite (see e.g. Ringwood, 1969).

Near-surface geothermal conditions of the Precambrian in South Norway have been investigated by Swanberg et al. (1974) and Haenel et al. (1974). Heat flow values are determined at 19 localities, the average being 38.6 mW m^{-2} . Very low values ($20\text{--}25 \text{ mW m}^{-2}$) are found near the centre of the $1,000 \text{ km}^2$ Egersund anorthosite complex with associated low heat production. A large number of heat production values from mainly granites are available (Killeen and Heier, 1974, 1975 a, b). The linear relation between heat flow and heat generation based on only a few localities in the area (Swanberg et al., 1974) is most likely of limited importance. As the vertical extent of the surface formations, with a few exceptions, is less than a few kilometres, and the heat generation varies very much between the different rock units, no linear relation is to be expected, except perhaps, if average values of large geological units are used. The very low heat flow values of $20\text{--}25 \text{ mW m}^{-2}$ are of great importance, as they determine the maximum possible heat flow from the mantle.

In the above-mentioned heat flow values the climatic corrections are supposed to be somewhat under-estimated. A surface value of 42 mW m^{-2} shall be used in the models.

The average geothermal gradient of central parts of the Danish Embayment within a depth of about 5 km is around $27\text{--}30 \text{ }^\circ\text{C km}^{-1}$ (Madsen, 1975). Thermal conductivities of rocks from the southeastern part of the North Sea Sedimentary

Basin have been published by e.g. Majorowicz (1973), Wesierska (1973), and Kappelmeyer and Haenel (1974, p. 55). Taking the temperature dependence into consideration the average conductivity of the sedimentary formations in question is estimated to be 2.2–2.3 W m⁻¹ °C⁻¹. Consequently, the heat flow is estimated to be about 60–70 mW m⁻².

3. Thermal Conductivity Models

The thermal conductivity depends on the material, the temperature, and the pressure. For the majority of materials to be dealt with in the present case in the range of temperatures involved, Clark (1957, 1969) and others have given the total conductivity as

$$K = K_l + K_r \quad (2)$$

where K_l is the lattice (or phonon) component and K_r is the radiative component. K_l is approximately related to the temperature by

$$K_l = (a + bT)^{-1} \quad (3)$$

where a and b are constants.

The investigations of Fukao et al. (1968) and Schatz and Simmons (1972) on olivines show that the contribution of K_r is about 50% at 900–1,300 °C. This is important in estimating the conductivity of the upper mantle. As to crustal rocks at temperatures below 800–900 °C, Equation (3) seems to be an acceptable approximation to the total conductivity, (e.g. Birch and Clark, 1940; Kawada, 1964 and 1966). Here it is appropriate to use

$$K(T) = \frac{K_0}{1 + cT} \quad (4)$$

where $c = a/b$ and K_0 is the conductivity at 0 °C.

The effect of pressure on thermal conductivity has been little studied theoretically and experimentally. Dry metamorphic and magmatic rocks of low porosity exposed to an increase of pressure from 0 to about 1 kb seem to have a conductivity increase of about 10% on an average due to reduction of pore volume (Walsh and Decker, 1966; Hurting and Brugger, 1970). According to Walsh and Decker the effect of water saturation is of the same magnitude, and the saturated samples showed no significant effect due to pressure. At higher pressures the elastic properties of the medium are of importance. A further conductivity increase to the depth interval of 50 km seems to be only a few percent (Bridgman, 1924; Fujisawa et al., 1968) and will be ignored.

The c -value in Equation (4) for the upper crustal rocks of interest is about 0.6–1.3 · 10⁻³ °C⁻¹ with an average value of about 1.0 · 10⁻³ °C⁻¹. For the lower crustal rocks the temperature dependence seems to be somewhat less, with a c -value of about 0.7 · 10⁻³. K_0 -values of 2.8–3.2 W m⁻¹ °C⁻¹ are used for the upper crustal layer, and 2.3–2.6 W m⁻¹ °C⁻¹ for the lower crustal layer. These K_0 -values represent the values of water-saturated samples and therefore, no

pressure correction function is needed. The estimate of these values is based on the geophysical and geological models, conductivity data of rocks in South Norway, data from other areas with rocks of similar composition (e.g. Wenk and Wenk, 1969; Čermák and Jessop, 1971; Smithson and Decker, 1974) together with the values of rock-forming minerals (Horai and Simmons, 1969). In order to approximate the olivine-peridotite model of the upper mantle the conductivity has been calculated for a theoretical composition of 80% olivine ($\text{Fo}_{90}\text{Fa}_{10}$) and 20% enstatite using the experimental data of Schatz and Simmons (1972) on single crystals of olivine and enstatite. The conductivity of this mantle composition has been calculated in the interval between 250 and 1,250 °C. A conductivity-temperature function has been found by fitting a fourth degree least square function to these data:

$$K(T) = a_0 + a_1 T^1 + a_2 T^2 + a_3 T^3 + a_4 T^4$$

with $a_0 = 1.017 \cdot 10^1$ (model A), $a_1 = -2.694 \cdot 10^{-2}$, $a_2 = 4.679 \cdot 10^{-5}$, $a_3 = -3.734 \cdot 10^{-8}$, and $a_4 = 1.115 \cdot 10^{-11}$.

Due to some uncertainties with respect to the composition of the upper mantle and the effect of variable grain size on the conductivity (Fukao, 1969), an interval of variation of $\pm 0.5 \text{ W m}^{-1} \text{ }^\circ\text{C}^{-1}$ in relation to the model A function has been assumed. The thermal conductivity functions are shown in Figure 3.

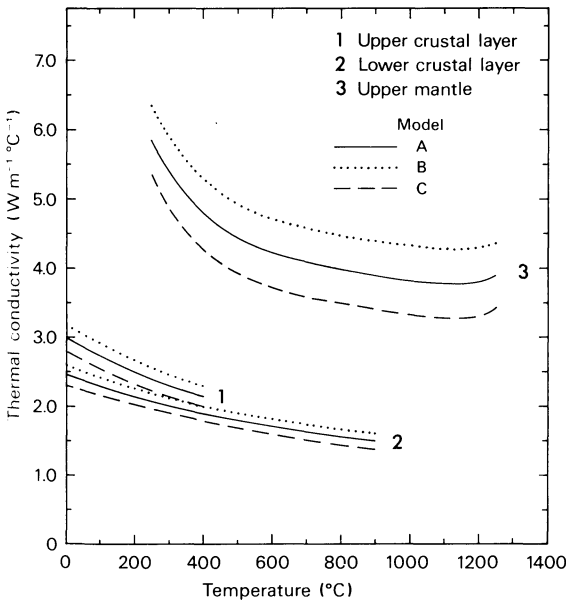


Fig. 3. Assumed thermal conductivity-temperature functions of the main crustal units and the upper mantle. The K_0 -values for the upper crustal layer are 3.0, 3.2, and 2.8, and for the lower crustal layer 2.45, 2.6, and 2.3 $\text{W m}^{-1} \text{ }^\circ\text{C}^{-1}$ in model A, B, and C, respectively. For the upper crustal layer the c -value is 10^{-3} and for the lower crustal layer $0.7 \cdot 10^{-3} \text{ }^\circ\text{C}^{-1}$. The upper mantle functions are described in the text

4. Heat Production Models

The heat production of the surface rocks in the shield area varies strongly from place to place. Very low values of about $0.1 \cdot 10^{-6} \text{ W m}^{-3}$ have been found for anorthosite and amphibolite, and $2.9\text{--}3.3 \cdot 10^{-6} \text{ W m}^{-3}$ for granitic gneiss complexes. Extremely high heat production of up to $6.6 \cdot 10^{-6} \text{ W m}^{-3}$ has been revealed in some of the South Norwegian granites (Killeen and Heier, 1975a, b). Only a few data from the most common migmatites are available, and the average surface values between $1.7\text{--}2.1 \cdot 10^{-6} \text{ W m}^{-3}$ used in the models are thus only preliminary. But no doubt, there is a considerable decrease in heat production with depth speaking of average values of large units. A heat production decrease with increasing metamorphic degree has been found by Heier and Adams (1965) and Lambert and Heier (1967). Theoretical considerations of Lachenbruch (1970) and field observations of Swanberg (1972) also support the idea of a strong concentration of heat producing elements in the upper part of the continental crust. This is in agreement with the assumed geological models.

Besides the values due to authors already cited, a large number of heat generation data published by Čermák (1975), and compilations of a.o. Shaw (1967), Kappelmeyer and Haenel (1974), and Smithson and Decker (1974) have been used as basis for the model constructions. For the sediments average values between 1.1 and $1.5 \cdot 10^{-6} \text{ W m}^{-3}$ are assumed. Below the sediments, values of $2.1\text{--}2.9 \cdot 10^{-6} \text{ W m}^{-3}$ are used for the presumed granitic rocks. Along the whole profile the heat production is assumed to be reduced to $0.5\text{--}0.8 \cdot 10^{-6} \text{ W m}^{-3}$ at the level of the $6.5\text{--}6.6 \text{ km s}^{-1}$ refractor and with a further reduction through the lower crust to $0.15\text{--}0.25 \cdot 10^{-6} \text{ W m}^{-3}$ at the base of the crust. At the upper mantle $0.01 \cdot 10^{-6} \text{ W m}^{-3}$ has been used. Model B contains the highest and model C the lowest heat production values. In model A the mean values have been used. Between these fixed values at the mentioned levels, an exponential decrease with the depth z of the form

$$A(z) = A_0 e^{-\mu z} \quad (5)$$

has been assumed (Figs. 4 and 5).

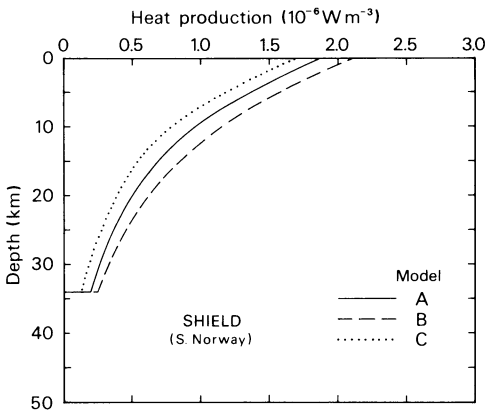


Fig. 4. Assumed heat production models of the Shield (central part)

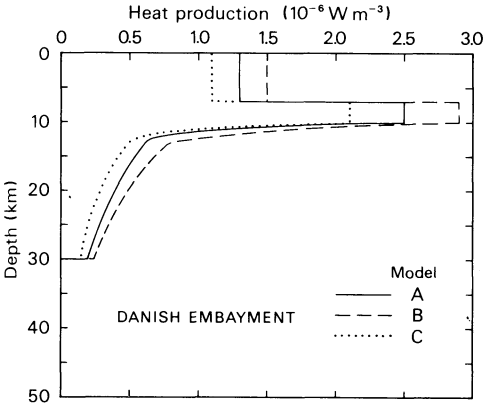


Fig. 5. Assumed heat production models of the Danish Embayment (central part)

5. Solution of the Heat Conduction Equation

We may write Equation (1) as

$$2A + \nabla^2(KT) + K\nabla^2 T - T\nabla^2 K = 0. \quad (6)$$

This is a non-linear differential equation which is to be solved subject to well defined boundary conditions. A modified Gauss-Seidel method in which the temperature dependence on the conductivity is included will be applied to the set of algebraic equations which are obtained from a finite difference approximation to the differential equation. The region for which the differential equation is valid will be divided into a $N \times M$ rectangular mesh. The nodal points of the mesh (i, k) are separated by distances Δx and Δz in the x (horizontal) and z (vertical) directions, respectively. The central difference approximation to Equation (6) using a five-point formula is given by

$$\begin{aligned} & \frac{2A_{i,k} \Delta z^2}{K_{i,k}} + \frac{K_{i-1,k} + K_{i,k}}{r^2 K_{i,k}} T_{i-1,k} + \frac{K_{i+1,k} + K_{i,k}}{r^2 K_{i,k}} T_{i+1,k} \\ & + \frac{K_{i,k-1} + K_{i,k}}{K_{i,k}} T_{i,k-1} + \frac{K_{i,k+1} + K_{i,k}}{K_{i,k}} T_{i,k+1} \\ & - \left[2 + \frac{2}{r^2} + \frac{K_{i-1,k} + K_{i+1,k}}{r^2 K_{i,k}} + \frac{K_{i,k-1} + K_{i,k+1}}{K_{i,k}} \right] T_{i,k} = 0 \end{aligned} \quad (7)$$

where $A_{i,k}$ are predetermined heat production parameters and $r = \Delta x / \Delta z$. This equation is valid for non-boundary points (i, k) . Starting at point $i=1$ and $k=1$, a mixed set of known and estimated values in Equation (7) results in a residual non-zero value on the right hand side of Equation (7), i.e.

$$\begin{aligned} R_{i,k}^0 = & \frac{2A_{i,k} \Delta z^2}{K_{i,k}^*} + \alpha_{i-1,k}^* T_{i-1,k}^0 + \alpha_{i+1,k}^* T_{i+1,k}^0 \\ & + \alpha_{i,k-1}^* T_{i,k-1}^0 + \alpha_{i,k+1}^* T_{i,k+1}^0 - \alpha_{i,k}^* T_{i,k}^0 \end{aligned} \quad (8)$$

where the α 's are the appropriate coefficients of Equation (7). From the foregoing a first order estimate in terms of the original zero order estimates $T_{i,k}^0$ and $\alpha_{i,k}^*$ is written:

$$T_{i,k}^1 = T_{i,k}^0 + R_{i,k}^0 / \alpha_{i,k}^* \tag{9}$$

for all internal points of the mesh. This equation defines an iteration procedure. The K - or α -values are adjusted after say 50 iterations of the $T_{i,k}^j$ to take account of their temperature dependence. The general expression for $T_{i,k}^n$ is:

$$T_{i,k}^n = \frac{1}{\alpha_{i,k}^m} \left[\frac{2A_{i,k} \Delta z^2}{K_{i,k}^m} + \alpha_{i-1,k}^m T_{i-1,k}^n + \alpha_{i+1,k}^m T_{i+1,k}^{n-1} + \alpha_{i,k-1}^m T_{i,k-1}^n + \alpha_{i,k+1}^m T_{i,k+1}^{n-1} \right] \tag{10}$$

where the conductivities have been adjusted m times.

At the boundary a combination of prescribed temperature and prescribed heat flow shall be used.

The starting estimates of the $T_{i,k}$ - and $K_{i,k}$ -values at all nodal points are determined by solving the one-dimensional heat conduction equation:

$$A(z) + \frac{d}{dz} \left(K(T) \frac{dT}{dz} \right) = 0 \tag{11}$$

with different parameters.

Case (a)

$$\begin{aligned} A(z) &= A_0, & K(T) &= K_0 \\ T(z) &= T_0 + \frac{q_0}{K_0} z - \frac{1}{2} \frac{A}{K_0} z^2 \end{aligned} \tag{12}$$

where $T_0 = T(0)$ and $q_0 = K_0 \left(\frac{dT}{dz} \right)_{z=0}$.

Case (b)

$$\begin{aligned} A(z) &= A_0; & K(T) &= \frac{K_0}{1 + cT} \\ T(z) &= \frac{1}{c} \left[(1 + cT_0) \exp \left\{ \frac{c}{K_0} (q_0 z - \frac{1}{2} A_0 z^2) \right\} - 1 \right]. \end{aligned} \tag{13}$$

Case (c)

$$\begin{aligned} A(z) &= A_0 e^{-\mu z}; & K(T) &= \frac{K_0}{1 + cT} \\ T(z) &= \frac{1}{c} \left[(1 + cT_0) \exp \left\{ \frac{c}{K_0} \left(\frac{A_0}{\mu^2} (1 - \exp(-\mu z)) - \frac{A_0}{\mu} z + q_0 z \right) \right\} - 1 \right]. \end{aligned} \tag{14}$$

In order to investigate the accuracy of the described numerical method, with special reference to the influence of variable Δz values, a number of test models have been examined. Results from one of them, a model with variable heat production and variable conductivity of the type c described above will be shown.

The parameters are similar to those of the crustal unit of profile AB:

$$\begin{aligned}
 T_0 &= 10 \text{ }^\circ\text{C}, \\
 q_0 &= 60 \text{ mW m}^{-2}, \\
 A_0 &= 2 \cdot 10^{-6} \text{ W m}^{-3}, \\
 K_0 &= 3 \text{ W m}^{-1} \text{ }^\circ\text{C}^{-1}, \\
 c &= 10^{-3} \text{ }^\circ\text{C}^{-1}, \\
 \mu &= 7 \cdot 10^{-5} \text{ m}^{-1}.
 \end{aligned}$$

Solutions are found for the depth interval 0–40 km. At the upper boundary the temperature is 10 °C. At the side boundaries $K(T)\frac{\partial T}{\partial x}$ is equal to zero, and at the lower boundary $K(T)\frac{\partial T}{\partial z}$ is equal to 33.17 mW m⁻², which defines the boundary conditions. Numerical solutions have been found with the Δz -values of 1, 2.5, 5 and 10 km. With Δz equal to 1 km the deviations between the exact solution given by Equation (14) and the numerical solution are less than 0.1 °C, and even with Δz equal to 10 km the differences are relatively small (Table 1). If poor starting solutions are used (say 10 °C km⁻¹) the computing time increases markedly.

In the solutions for the profile AB of Figures 1 and 2 the mesh size used was $\Delta x=15$ km and $\Delta z=2.5$ km. With these values the seismic boundaries, which are assumed to be also thermal parameter boundaries, are approximated within the accuracy of their determination. The results compiled in Table 1 show that no problems arise due to variations between these boundaries.

The boundary conditions are as follows: The mean annual surface temperature is used at $z=0$ km. In the Skagerrak and South Norway corrections for the effect of water and topography are applied. The profile length is 345 km, which is enough to make the horizontal heat flow below point A and B negligible ($\left(\frac{\partial T}{\partial x}\right)_{1,k} = \left(\frac{\partial T}{\partial x}\right)_{24,k} = 0$). The vertical heat flow across the lower boundary

Table 1. The analytical solution and numerical solutions for the test model

Depth (km)	Analytical solution (°C)	Numerical solutions (°C)			
		Δz			
		1 km	2.5 km	5 km	10 km
0	10	10	10	10	10
5	108.0	107.9	107.8	107.3	
10	201.1	201.0	200.7	199.8	196.2
15	291.2	291.1	290.7	289.4	
20	379.9	379.8	379.3	377.6	371.2
25	468.5	468.5	467.9	465.9	
30	558.4	558.3	557.6	555.3	546.3
35	650.3	650.2	649.4	646.8	
40	745.0	745.0	744.1	741.1	729.6

($z = 50$ km) has been found by "trial and error" starting with the values found by a one-dimensional consideration, with the horizontal heat transfer neglected. This heat flow is determined to produce agreement between the model results and the surface heat flow values observed. For the shield area this is 42 mW m^{-2} , which has been used in all models. For the Danish Embayment 65 mW m^{-2} has been used in model A and 60 and 70 mW m^{-2} in model B and C, respectively. Between the coast regions linear interpolation has been used.

The starting estimates of the temperatures and the conductivities have been found by using Case c (Eq. 14) for the main crustal units and Case a and b (Eqs. 12 and 13) for the upper mantle and the sedimentary region.

After 1,000–1,500 iterations the calculated temperatures at the region of temperature maximum are within $1\text{--}2^\circ\text{C}$ of the asymptotic values.

The computations were carried out at the CDC 6400 at the Aarhus University, Computing Centre. The computation time was about 10 min for each model with the stated accuracy.

6. Computation Results

The models calculated take into account temperature distribution, conductivity distribution, and heat flow distribution. From the model data the average temperatures, vertical geothermal gradients and conductivities for the Shield and the Embayment are calculated (Tables 2 and 3). The Shield values represent average values of the northernmost 90 km of the profile, and the Embayment values are average values of the southernmost 60 km. In these areas the lateral variations

Table 2. Computed temperature distribution and heat flow from the mantle

Depth (km)	Average temperature ($^\circ\text{C}$)					
	Shield			Embayment		
	Model A	Model B	Model C	Model A	Model B	Model C
0	11	11	11	8	8	8
5	78	70	84	148	137	155
10	137	120	152	264	232	292
15	189	162	214	373	313	433
20	242	203	280	489	397	587
25	292	241	346	607	479	749
30	339	275	410	712	549	898
35	376	299	463	765	584	977
40	394	311	492	815	616	1,052
45	412	321	519	866	649	1,129
50	429	332	547	918	682	1,206
Heat flow from the mantle (mW m^{-2})	16–17	11–13	21–22	41	31	51

Table 3. Computed vertical geothermal gradients and thermal conductivity

Unit	$\Delta T/\Delta z$ ($^{\circ}\text{C km}^{-1}$)			$k(T)$ ($\text{W m}^{-1} \text{ }^{\circ}\text{C}^{-1}$)		
	Model A	Model B	Model C	Model A	Model B	Model C
<i>Shield</i>						
Upper crustal layer	10-14	9-13	12-16	2.5-3.0	2.8-3.2	2.3-2.8
Lower crustal layer	9-11	6-10	12-14	1.9-2.1	2.1-2.3	1.8-2.0
Upper mantle	3-4	2-3	5-6	4.7-4.9	5.7-5.9	3.8-4.0
<i>Embayment</i>						
Sedimentary layer ^a	28	26	29	2.25	2.2	2.3
Upper crustal layer	22	17-18	26-27	2.2-2.5	2.4-2.7	2.0-2.3
Lower crustal layer	23-24	16-17	29-34	1.7-1.9	1.9-2.1	1.5-1.8
Upper mantle	10-11	6-7	14-15	3.9-4.1	4.6-4.8	3.3-3.4

^a Average values

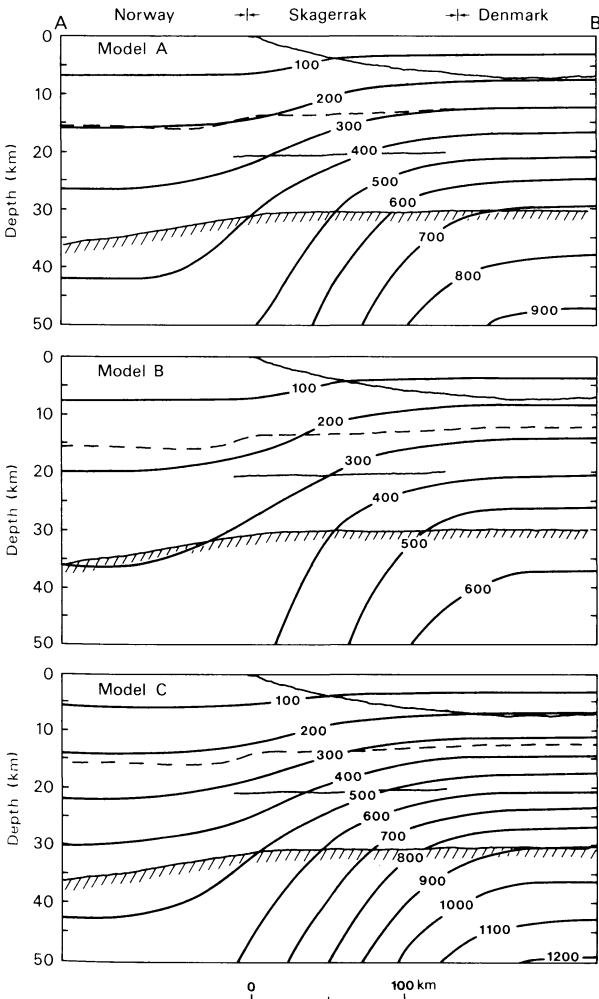


Fig. 6. Isothermal lines ($^{\circ}\text{C}$) of the computed temperature models A, B, and C. The preferred parameters have been used in model A. Models B and C have been constructed to give what is assumed to be close to the lowest and highest possible temperatures, respectively

are very small (Fig. 6). The temperatures in the models of South Norway have been determined within rather narrow limits, whereas the values of North Jylland show a rather large variation as shown in models B and C. It appears that even over a small horizontal distance considerable temperature differences may be discovered. At a depth of 50 km the differences between the temperatures in the models of the Precambrian in South Norway and the Danish Embayment are 350–660 °C (model B and C), with the preferred value approximately 500 °C (model A).

The main reason for the temperature differences in the two areas and the spread between the models is the rather large differences in heat flow, not just at the surface, but through the whole depth interval considered. As the total crustal heat production in the models is almost the same in both areas, the heat flow from the mantle differs considerably with 11–22 mW m⁻² in the shield models, and 31–51 mW m⁻² in the models of the Danish Embayment. The models imply a considerable lateral heat flow in the uppermost mantle from North Jylland into the Skagerrak, the maximum values being between 12 and 15 mW m⁻². Due to this lateral heat transfer the heat flow from the mantle in the southern area is 5–10 % higher than the one-dimensional values. In the coast region of Norway the models show an increase of the surface heat flow of around 10 % due to this phenomenon. None of the models have isothermal lines that follow the seismic boundaries (Fig. 6). At the Moho the model temperatures are 280–470 °C in the shield region and 550–900 °C in the Embayment. The preferred values are approximately 350 °C and 700 °C in the Shield and the Embayment, respectively.

7. Discussion

The computed results show that small changes in the geothermal parameters may produce considerable temperature variations. This applies especially to areas with normal or high surface heat flow. In such areas it is essential that accurate heat flow determinations are available. Use of the model A value (65 mW m⁻²) together with the other model parameters of the models B and C would reduce the differences between these two models by 200–260 °C at a depth of 50 km in the Danish Embayment. Due to the low heat flow in the shield area a small change in this parameter will only cause small variations in the temperature distribution. A change of the average surface value from 42 mW m⁻², used in all models, by ± 3 mW m⁻² will only alter the temperature at a depth of 50 km by about ± 50 °C.

Since there is apparently a high degree of uniformity in seismic velocities and density distribution along the profile, no attempt was made to compute models with variations in the parameters. It should be emphasized that large variations in the heat production distribution in the crust will produce only insignificant temperature variations, provided that the integrated heat production within a given crustal unit is maintained within reasonable limits. As previously mentioned, too few heat production data are available from the migmatites in Southern Norway to construct a definitive model. However, moderate changes from the model parameters used would not change the temperature distribution signi-

ificantly. Recently, Massé (1975) has stated that P^* (Pb) velocities lower than 7.2 km s^{-1} are misinterpretations of retrograde reflections in several refraction studies of the Scandinavian region. The use of possible alternative seismic models to those shown in Figure 2 need not alter the results.

It is obvious that steadily increasing temperature differences with depth between the two regions cannot continue, and at some depth the temperature curves must converge. This can arise due to great differences in heat production and/or large increase in heat transfer, e.g. heat transfer by moving material. This last phenomenon is closely connected to the problem of partial melting (Fig. 7). The lowest possible temperatures of the beginning of anatexis in gneisses are those that produce melting in the system $Q\text{—}Ab\text{—}Or\text{—}H_2O$. It is not possible to make accurate calculations on the effect of anatexis on the temperature depth curves, partly due to lack of experimental data giving information of the thermal conductivity variations in systems with anatexis, partly because this would demand rather exact knowledge of the mineralogical nature of the lower crust. But it is reasonable to assume that the high model C temperatures for the lower crust in the Danish Embayment have to be reduced due to partial melting. From a petrological point of view temperatures above 850°C in the lower crust are not very likely in this area. With the model A temperatures and a water content of only 0.2% the pyrolite solidus is reached at a depth of about 70–80 km in the Danish Embayment. In an upper mantle zone of partial melting the temperature curve is supposed to follow the melting curve. When extrapolating in particular the model A and C curves for the Embayment to greater depths not only melting problems have to be considered. Above about $1,200^\circ\text{C}$ a large thermal conductivity increase due to radiation is expected. Such an increase will also make the temperature curves in the two regions converge more easily.

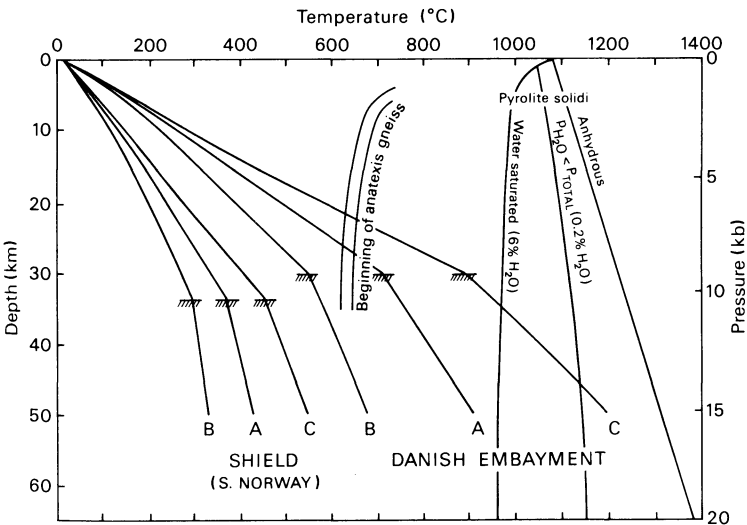


Fig. 7. The average temperature-depth functions of Table 2 in relation to the pyrolite solidi from Green (1973) and the zone of beginning of anatexis from Winkler (1974). The position of the Moho is indicated (TTTTT)

Using the division of metamorphic grade of Winker (1974), the temperature models indicate that the lower crust in the shield region is to be found in the P, T field of very low grade to low grade, while for the Danish Embayment medium to high grade is most likely. Here the preferred temperatures show high grade conditions at the base of the crust. As the lower crust in the shield area has previously had considerably higher temperatures than those to be expected at present, medium and high grade metamorphic rocks are also likely in this region.

In discussing the mineralogical and petrological nature of the crust the investigations on the stability of dry basaltic (gabbroic) rocks are of importance (e.g. Green and Ringwood, 1967, 1972; T.H. Green, 1967; Ito and Kennedy, 1970, 1971). There seems to be a close agreement between the authors as to the experimental data. The experiments which are carried out around 1,100–1,250 °C and with pressures up to 40 kb establish a general pattern of mineralogical variation with increasing pressure from low-pressure pyroxene + plagioclase ± olivine assemblages through pyroxene + plagioclase + garnet ± quartz to plagioclase-free assemblages dominated by garnet + clino-pyroxene. Gabbro transforms under dry conditions via a garnet granulite transition zone with varying width into eclogite. In the present case the main interest is concentrated on the extrapolation of these transitions to lower pressures and temperatures. Here there is some significant disagreement (Green and Ringwood, 1972; Kennedy and Ito, 1972), especially in the extrapolation of the plagioclase-out line. The temperature-depth curves of the lower crust in the Danish Embayment are most likely to be found in the garnet granulite stability field. If the statement of Green and Ringwood (1972, p. 277) “eclogite is the stable mineralogy for dry basaltic rocks along normal geothermal gradients in the continental crust (stable or shield region)” is true, this applies to South Norway. Kennedy and Ito (1972) find garnet granulite to be the stable mineralogy in such regions. This disagreement may be of minor importance in the present discussion. Due to their high density (about $3.5 \cdot 10^3 \text{ kg m}^{-3}$) eclogites cannot be present in large amounts in the crust, and are probably not formed in any significant amount in the continental crust of normal geothermal gradients. This may be due to the presence of some water content. Therefore, it is assumed that rocks of basaltic composition are present as amphibolites also in the main parts of the lower crust in South Scandinavia. If only a very small water content should be present in the lower crust of the Danish Embayment region, garnet granulite is likely to be the stable composition of basaltic rocks. Only under such conditions, and at temperatures higher than those in the calculated models could gabbro have been formed. Before a more detailed discussion of these problems is considered, more information on seismic velocity and the density distribution is necessary. However, in general it is not correct to classify the lower crust “gabbroic” or “basaltic”. Attention should be drawn to the high density amphibolites and/or pyroxene + garnet + plagioclase assemblages.

Most petrophysical properties are temperature dependent. This applies to density, seismic velocity, and especially electric conductivity. There may be conductivity differences of one or two orders of magnitude in the lower crust and upper mantle along the investigated profile, in which case magnetotelluric investigations could give essential information about the geothermal conditions.

A mapping of the depth to the Curie temperature surface, which is of great interest, could be obtained by a magnetic survey.

In great parts of the North Sea area and in particular in areas with thick sedimentary formations the surface heat flow is estimated to be around $60\text{--}70\text{ mW m}^{-2}$ or even somewhat higher. Decreasing values are found in the direction of the shield area and along basement highs as e.g. the Ringkøbing-Fyn high (Fig. 1) (Evans and Coleman, 1974; Madsen, 1975). The same trend has been observed in the southeastern part of the Danish-Polish Trough of which the Danish Embayment constitutes the northwestern part. Here the heat flow is decreasing from the basin area towards the Precambrian Russian Platform (Majorowicz, 1973; Wesierska, 1973).

Deviations from these trends have been found in North West Germany, where low values (47 and 52 mW m^{-2}) are measured at localities in an area with thick sedimentary rocks (Haenel, 1971).

Heat flow values close to those of South Norway have been found also in Finland (Puranen et al., 1968) and in Sweden (Parasnis, 1975). With minor modifications the geothermal models here presented may be valid for the whole transition region between the Fennoscandian Shield and the North Sea Basin.

Considerable temperature variations in the crust and upper mantle and variations in the heat flow from the mantle associated with narrow heat flow transition zones have been found in several cases. The Sierra Nevada-Basin and Range transition in the western United States (Roy et al., 1968, 1972) have been investigated in greater details. Recently Čermák (1975) has investigated in details transitions in Czechoslovakia and adjacent areas. The geothermal models of the Kapuskasing area in the Canadian Shield (Čermák and Jessop, 1971) with temperatures around $400\text{ }^{\circ}\text{C}$ at the base of the crust and a heat flow from the mantle of about 20 mW m^{-2} are close to those of the shield region in South Norway. The Danish Embayment geothermal models show temperatures similar to those calculated for the Alps and the foreland (Buntebarth, 1973).

8. Conclusion

The geothermal model calculations show that the heat flow transition between the Fennoscandian Shield and the North Sea Basin is associated with considerable lateral variation in temperature and in heat flow from the mantle. At the base of the crust variations from $300\text{--}450\text{ }^{\circ}\text{C}$ in the models of South Norway to $700 \pm 150\text{ }^{\circ}\text{C}$ in the Danish Embayment models have been found. The preferred model shows heat flow from the mantle of about 40 mW m^{-2} for the Danish Embayment and $16\text{--}17\text{ mW m}^{-2}$ in the shield area.

Considerable physical differences in the lower crust and upper mantle beneath the Precambrian shield region and the basin region produced by lateral temperature variations must be expected. Magnetotelluric investigations, more heat flow data from the basin area, more heat generation data from common shield rocks and magnetic investigations would increase the knowledge of the geothermal nature of the crust and upper mantle along the transition zone. Crustal and

upper mantle physical and geological investigations in the area of South Scandinavia are of great general interest and would contribute to a better understanding of the composition and formation of the continental crust and upper mantle.

Acknowledgements. The present work was in part carried out at the Institut für Geophysik der Technischen Universität Clausthal. The author wishes to thank Professor O. Rosenbach, Dr. G. Buntebarth, Claussthal, and Professor S. Saxov, Århus, for their cooperation in arranging the stay at the German Institute, and for fruitful discussions.

References

- Aric, K.: Reflexionsseismische Messungen im Skagerrak. *Z. Geophys.* **34**, 223–226, 1968
- Barth, T. F. W., Dons, J. A.: Precambrian of Southern Norway. In: O. Holtedal ed., *Geology of Norway, Norges geol. Unders.* **208**, 6–67, 1960
- Birch, F., Clark, H.: The thermal conductivity of rocks and its dependence upon temperature and composition. *Am. J. Sci.* **238**, 529–558 and 613–635, 1940
- Bridgman, P. W.: Thermal conductivity and compressibility of several rocks under high pressures. *Am. J. Sci. Ser. 5*, **7**, 81–102, 1924
- Buntebarth, G.: Modellberechnungen zur Temperatur-Tiefen-Verteilung im Bereich der Alpen und des Alpenvorlandes. *Z. Geophys.* **39**, 97–107, 1973
- Casten, U., Hirschleber, H.: Seismic measurements in Jutland 1969. *Z. Geophys.* **37**, 47–69, 1971
- Čermák, V.: Temperature-depth profiles in Czechoslovakia and some adjacent areas derived from heat-flow measurements, deep seismic sounding and other geophysical data. *Tectonophysics* **26**, 103–119, 1975
- Čermák, V., Jessop, A. M.: Heat flow, heat generation and crustal temperature in the Kapuskasing area of the Canadian Shield. *Tectonophysics* **11**, 287–303, 1971
- Clark, S. P.: Radiative transfer in the earth's mantle. *Trans. Am. Geophys. Union* **38**, 931–938, 1957
- Clark, S. P.: Heat conductivity in the mantle. In: *The earth's crust and upper mantle*, P. J. Hart, ed. *Am. Geophys. Un. Geophys. Mon.* **13**, 622–626, 1969
- Evans, T. R., Coleman, N. C.: North Sea geothermal gradients. *Nature* **247**, 28–30, 1974
- Falkum, T.: Structural and petrological investigations of the Precambrian metamorphic and igneous charnockite and migmatite complex in the Flekkefjord area, Southern Norway. *Norges geol. Unders.* **242**, 19–25, 1966
- Falkum, T.: On large-scale tectonic structures in the Agder-Rogaland region, Southern Norway. *Norsk geol. Tidsskr.* **52**, 371–376, 1972
- Fujisawa, H., Fujii, N., Mizutani, H., Kanamori, H., Akimoto, S.: Thermal diffusivity of Mg_2SiO_4 , Fe_2SiO_4 , and NaCl at high pressures and temperatures. *J. Geophys. Res.* **73**, 4727–4733, 1968
- Fukao, Y.: On the radiative heat transfer and the thermal conductivity in the upper mantle. *Bull. Earthquake Res. Inst.* **47**, 549–569, 1969
- Fukao, Y., Mizutani, H., Uyeda, S.: Optical absorption spectra at high temperatures and radiative thermal conductivity of olivines. *Phys. Earth Planet. Interiors* **1**, 57–62, 1968
- Green, T. H.: An experimental investigation of sub-solidus assemblages formed at high pressure in high-alumina basalt, kyanite eclogite and grosspyrite compositions. *Contr. Mineral. Petrol.* **16**, 84–114, 1967
- Green, D. H.: Contrasted melting relations in a pyrolite upper mantle under mid-oceanic ridge, stable crust and island arc environments. In: *Experimental petrology and global tectonics*, P. J. Wyllie, ed. *Tectonophysics* **17**, 285–297, 1973
- Green, D. H., Ringwood, A. E.: An experimental investigation of the gabbro to eclogite transformation and its petrological applications. *Geochim. Cosmochim. Acta* **31**, 767–833, 1967
- Green, D. H., Ringwood, A. E.: A comparison of recent experimental data on the gabbro-garnet granulite-eclogite transition. *J. Geol.* **80**, 277–288, 1972
- Gregersen, S.: The Trans-Scandinavian seismic profile of 1969, profile section 4–5. In: *Deep seismic sounding in Northern Europe*, A. Vogel, ed. *Swedish Nat. Sci. Res. Council*, 92–95, 1971.
- Haenel, R.: Heat flow measurements and a first heat flow map of Germany. *Z. Geophys.* **37**, 975–992, 1971

- Haenel, R., Grønlie, G., Heier, K.S.: Terrestrial heat flow determinations from lakes in Southern Norway. *Norsk. geol. Tidsskr.* **54**, 423–428, 1974
- Heier, K.S., Adams, J.A.S.: Concentration of radioactive elements in deep crustal material. *Geochim. Cosmochim. Acta* **29**, 53–61, 1965
- Hirschleber, H., Hjelme, J., Sellevoll, M.A.: A refraction profile through the Northern Jutland. *Geodæt. Inst. Medd. København* **41**, 35, 1966
- Horai, K., Simmons, G.: Thermal conductivity of rock-forming minerals. *Earth Planet. Sci. Lett.* **6**, 359–368, 1969
- Hurtig, E., Brugger, H.: Wärmeleitfähigkeitsmessungen unter einaxialem Druck. *Tectonophysics* **10**, 67–77, 1970
- Ito, K., Kennedy, G.C.: The fine structure of the basalt-eclogite transition. *Mineral. Soc. Am. Spec. Paper* **3**, 77–83, 1970
- Ito, K., Kennedy, G.C.: An experimental study of the basalt-garnet granulite-eclogite transition. In: The structure and physical properties of the Earth's crust, J.G. Haecock, ed. *Am. Geophys. Un. Geophys. Mon.* **14**, 303–314, 1971
- Kanestrøm, R., Haugland, K.: Crustal structure in southeastern Norway from seismic refraction measurements. *Scientific Report No. 5, Seismological Observatory, University of Bergen, Norway*, 72 p., 1971
- Kappelmeyer, O., Haenel, R.: *Geothermics with Special Reference to Application*. *Geoexpl. Monogr. Ser.* **1**, No. 4, 238 p., 1974
- Kawada, K.: Variation of the thermal conductivity of rocks, part 1. *Bull. Earthquake Res. Inst.* **42**, 631–647, 1964
- Kawada, K.: Variation of the thermal conductivity of rocks, part 2. *Bull. Earthquake Res. Inst.* **44**, 1071–1091, 1966
- Kennedy, G.C., Ito, K.: Comments on: "A comparison of recent experimental data on the gabbro-garnet granulite-eclogite transition". *J. Geol.* **80**, 289–292, 1972
- Killeen, P.G., Heier, K.S.: Radioelement variation in the Levang granite-gneiss, Bamble region, South Norway. *Contrib. Mineral. Petrol.* **48**, 171–177, 1974
- Killeen, P.G., Heier, K.S.: A uranium and thorium enriched province of the Fennoscandian shield in Southern Norway. *Geochim. Cosmochim. Acta* **39**, 1515–1524, 1975a
- Killeen, P.G., Heier, K.S.: Radioelement distribution and heat production in Precambrian granitic rocks, Southern Norway. *Skr. Norske Videnskaps-Akad. I. Mat.-Naturv. kl.* **35**, 32 p., 1975b
- Lachenbruch, A.H.: Crustal temperature and heat production: Implications of the linear heat-flow relation. *J. Geophys. Res.* **75**, 3291–3300, 1970
- Lambert, L.B., Heier, K.S.: The vertical distribution of uranium, thorium and potassium in the continental crust. *Geochim. Cosmochim. Acta* **31**, 377–390, 1967
- Larsen, G.: Rhaetic-Jurassic-Lower Cretaceous Sediments in the Danish Embayment. *Danmarks geol. Unders.* **II**, **91**, 1966
- Larsen, O.: K/Ar age determinations from the Precambrian of Denmark. *Danmarks geol. Unders.* **II**, **97**, 37 p., 1971
- Larsen, O.: Kalium/Argon datering af prøver fra danske dybdeboringer. *Dansk geol. Foren. Årsskrift for 1971*, 91–94, 1972
- Madsen, L.: Approximate geothermal gradients in Denmark and the Danish North Sea sector. *Danmarks geol. Unders. Årbog 1974*, 5–16, 1975
- Majorowicz, J.A.: Heat flow data from Poland. *Nat. Phys. Sci.* **241**, 16–17, 1973
- Massé, R.P.: Baltic Shield crustal velocity distribution. *Bull. Seismol. Soc. Am.* **65**, 885–897, 1975
- Parasnis, D.S.: Temperature phenomena and heat flow estimates in two Precambrian ore-bearing areas in North Sweden. *Geophys. J.* **43**, 531–554, 1975
- Puranen, M., Järvinmäki, P., Hämäläinen, U., Lehtinen, S.: Terrestrial heat flow in Finland. *Geoexploration* **6**, 151–162, 1968
- Rasmussen, L.B.: Oversigt over dybdeboringerne på dansk landområde 1965–68. *Dansk geol. Foren., Årsskrift for 1971*, 41–48, 1972
- Rasmussen, L.B.: Some geological results from the first five Danish exploration wells in the North Sea. *Geol. Surv. Denmark III Ser.* **42**, 46 p., 1974
- Ringwood, A.E.: Composition and evolution of the upper mantle. In: The Earth's crust and upper mantle, P.J. Hart, ed. *Am. Geophys. Un. Geophys. Mon.* **13**, 1–17, 1969
- Roy, R.F., Blackwell, D.D., Birch, F.: Heat generation of plutonic rocks and continental heat flow provinces. *Earth Planet. Sci. Lett.* **5**, 1–12, 1968

- Roy, R.F., Blackwell, D.D., Decker, E.R.: Continental heat flow. In: Nature of the solid earth. E. C. Robertson, ed., pp. 506–543. New York: McGraw-Hill 1972
- Schatz, J.F., Simmons, G.: Thermal conductivity of earth materials at high temperatures. *J. Geophys. Res.* **77**, 6966–6983, 1972
- Sellevoll, M.A.: Mohorovičić discontinuity beneath Fenneoscandia and adjacent parts of the Norwegian Sea and the North Sea. In: The structure of the earth's crust, based on seismic data, S. Mueller, ed. *Tectonophysics* **20**, 359–366, 1973
- Sellevoll, M.A., Aalstad, I.: Magnetic measurements and seismic profiling in the Skagerrak. *Marine Geophys. Res.* **1**, 284–302, 1971
- Sellevoll, M.A., Warrick, R.E.: Refraction study of the crustal structure in Southern Norway. *Bull. Seism. Soc. Am.* **61**, 457–471, 1971
- Shaw, D.M.: Uranium, thorium and potassium in the Canadian Precambrian shield and possible mantle compositions. *Geochim. Cosmochim. Acta* **31**, 1111–1113, 1967
- Smithson, S.B.: The nature of the “granitic” layer of the crust in the southern Norwegian Precambrian. *Norsk geol. Tidsskr.* **45**, 113–133, 1965
- Smithson, S.B., Decker, E.R.: A continental crustal model and its geothermal implications. *Earth Planet. Sci. Lett.* **22**, 215–225, 1974
- Sorgenfrei, T.: Geological perspectives in the North Sea area. *Bull. geol. Soc. Denmark* **19**, 160–196, 1969
- Sorgenfrei, T., Buch, A.: Deep tests in Denmark 1935–1959. *Danmarks geol. Unders.* III, **36**, 146 p. 1964
- Swanberg, C.A.: Vertical distribution of heat generation in the Idaho batholith. *J. Geophys. Res.* **77**, 2508–2513, 1972
- Swanberg, C.A., Chessman, M.D., Simmons, G., Smithson, S.B., Grønlie, G., Heier, K.S.: Heat-flow – heat-generation studies in Norway. *Tectonophysics* **23**, 31–48, 1974
- Walsh, J.B., Decker, E.R.: Effect of pressure and saturating fluid on the thermal conductivity of compact rock. *J. Geophys. Res.* **71**, 3053–3061, 1966
- Weigel, W., Hjelme, J., Sellevoll, M.A.: A refraction profile through the Skagerrak from Northern Jutland to Southern Norway. *Geodæt. Inst. Medd. København* **45**, 27 p., 1970
- Wenk, H.-R., Wenk, E.: Physical constants of alpine rocks (density, porosity, specific heat, thermal diffusivity and conductivity). *Schweiz. Min. Petr. Mitt.* **49**, 343–357, 1969
- Wesierska, M.: A study of terrestrial heat flux density in Poland. *Publ. Inst. Geoph. Pol. Ac. Sci.* **60**, 135–144, 1973
- Winkler, H.G.F.: *Petrogenesis of Metamorphic Rocks*, 3rd ed., 320 p. Berlin-Heidelberg-New York: Springer 1974

Received April 6, 1976; Revised Version July 22, 1976

Spatial Characteristics of Giant Pulsations

O. Hillebrand

Institut für Geophysik der Universität Göttingen,
Herzberger Landstraße 180, D-3400 Göttingen, Federal Republic of Germany

Abstract. From records of geomagnetic pulsation measurements along a profile in Northern Scandinavia during 1970 and 1971, all events of giant pulsations (pg) Type A have been selected. Data analysis reveals the spatial characteristics of giant pulsations: in particular the pg region normally has the form of a long ellipse with its major axis roughly parallel to a geomagnetic parallel of latitude; distinct phase differences between similar components at adjacent stations can be seen; the vertical component of the giant pulsations commonly is of the same order of magnitude as the horizontal components, in contrast to other types of pulsations; an opposite sense of rotation in the horizontal vectogram is found between stations north and south of the line of maximum pg amplitudes.

Key words: Giant pulsations — pc4 and pc5 pulsations — Time series analysis — Polarization properties.

1. Introduction

Giant pulsations (pg) have been studied for many years by many authors (e.g. Rolf, 1931; Harang, 1936; Sucksdorff, 1939). Because of their large amplitudes and their regular form, they were one of the first types of geomagnetic pulsations to have been described (Birkeland, 1901). In this paper a definition is used given by Sucksdorff (1939) for the type "A" giant pulsations: their periods of oscillation lie between 80 and 600 s (hence pg belong to the pc4 and pc5 pulsations) according to the classification by Jacobs et al. (1964) and their shape is sinusoidal. Their maximum amplitudes frequently reach values up to 35 nT, normally beginning with small amplitudes and rising to this maximum. The decay of amplitudes after that maximum is much faster in most cases. A pg event can be as short as ten oscillations up to several hours of sinusoidal pulsations. The occurrence of giant pulsations is limited to a narrow range in latitude near the auroral belts.

Initial studies of giant pulsations investigated mainly their diurnal distribution (Rolf, 1931). Harang (1936) studied the diurnal and seasonal distribution of giant pulsations using data from Tromsø. He found a maximum of occurrence in the morning hours at about 04:00 UT and maxima in the seasonal distribution around the equinoxes. Sucksdorff (1939), who used magnetic records from Sodankylä, distinguished two types of giant pulsations: the sinusoidal type "A", as defined above and an irregular type "B" with amplitude maxima at around 03:00 and 10:00 LT and a smaller maximum in the afternoon.

Past studies have investigated the possible dependence of the period of pg oscillations on the degree of disturbance or on the location of the pg event. Ol' (1963) found a connection between the latitude of a pg region and the period of the event. Hirasawa (1970) observed a relationship between the degree of magnetic disturbance and the location of the pg region.

The nonuniform distribution of the existing observatories hampered studies on the spatial distribution of amplitudes of pg events. Specifically, there was a lack of pg observations on north-south profiles with closely-spaced stations. The aim of this project was, therefore, the investigation of the latitude dependence of selected pulsation events recorded by a close-spaced north-south profile near the auroral zone.

2. Instrumentation

At 11 European observatories, geomagnetic pulsations are recorded by induction-type pulsation variometers described by Grenet (1949). In addition to these observatories, the Geophysikalische Institut der Universität Göttingen has employed similar but mobile field instrumentation to obtain measurements in more remote areas.

All these variometers use a bar magnet suspended in the centre of an induction coil. Geomagnetic variations cause the magnet to move and hence a voltage is induced in the coil. (Each instrument system has three variometers recording the magnetic components H, D, and Z respectively). At the observatories, the resultant variometer signals are passed through galvanometers and recorded optically on photo-sensitive paper sheets.

In order to improve the sensitivity Steveling (1973) introduced photo-electric amplifiers consisting of galvanometers and differential photo-resistors.

Three further portable systems were built at Göttingen (Hillebrand, 1974), again utilizing the same variometers. However, for these instruments the output voltages (approximately $10 \mu\text{V/nT}$) are directly amplified by DC amplifiers. The signals are then recorded by slow-speed (15/320 ips) FM tape recorders which allow 10 days continuous recording.

Typical amplitude and phase response curves for these instruments are illustrated in Figure 1. The amplitude response is normalized to the value 1 at a period of 20 s. The resolution at this period is about 0.05 nT when amplifiers are at maximum sensitivity. The amplitude and phase response of all variometers is similar, each amplitude curve differing from the other by a constant calibration factor only.

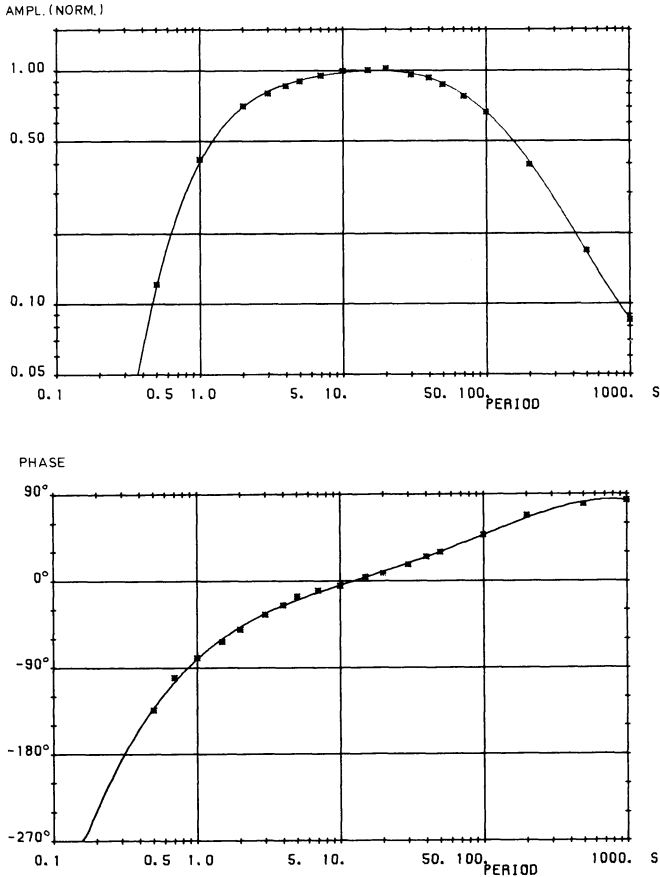


Fig. 1. Amplitude and phase response curves of the pulsation recording equipment

3. Observations in Scandinavia

Studies on the latitude dependence of pc3-4 type pulsations by Voelker (1963) and on the phase reversal of pi2 pulsations between auroral and mid latitudes suggested more finely spaced measurements by mobile field systems in the gap between established observatories in northern Europe. During 6 months in 1970 and 1971 six mobile systems were set up at 16 different sites in northern Scandinavia. Table 1 lists the names, the geographic coordinates, and the geomagnetic latitudes of these sites as well as the observatory stations where similar pulsation instrumentation is used.

The geographic distribution of the stations are shown in Figure 2. At times when the systems covered the entire profile, station spacing was relatively large. However, during some recording periods, station separation was less than 100 km. From the portable systems and from the observatories it was possible to obtain simultaneous data from at most 12 stations.

Table 1. List of observatories (O) and recording sites with tape equipment (T) and film equipment (F) during 1970 and 1971 in Scandinavia

Station	Abbrev.	Type	Geograph. Coordin.		Geomagn. Lat. (centered dipole model)
			Lat.	Long.	
Leirvogur	LI	O	64°10'	338°17'	70.2°
Tromsø	TR	O	69°41'	19° 0'	67.1°
Repparfjord	REP	T	70°22'	24°30'	66.8°
Abisko	ABI	T	68°21'	18°48'	66.0°
Kiruna	KI	O	67°48'	20°24'	65.2°
Ålloluokta	ALL	F	67° 5'	19°30'	64.8°
Porjus	POR	F	66°58'	19°51'	64.6°
Messaure	MES	T	66°39'	20°32'	64.2°
Arjeplog	ARJ	F	66° 0'	17°54'	64.1°
Sodankylä	SO	O	67°23'	26°35'	63.8°
Malä	MAL	F	65°13'	18°50'	63.2°
Lycksele	LYC	T(F)	64°37'	18°44'	62.7°
Åsele	ASE	F	64°11'	17°20'	62.6°
Junsele	JUN	F	63°43'	16°52'	62.3°
Hammarstrand	HAM	T(F)	63° 7'	16°27'	61.8°
Fränsta	FRN	F	62°27'	16° 5'	61.3°
Delsbo	DEL	T(F)	61°48'	16°34'	60.6°
Edsbyn	EDS	F	61°22'	15°49'	60.3°
Svärdsjö	SVJ	F	60°48'	15°53'	59.8°
Garpenberg	GAR	T	60°18'	16°13'	59.3°
Enköping	ENK	O	59°30'	17°17'	58.3°
Wingst	WN	O	53°45'	9° 4'	54.6°

4. Data Collection and Analysis

All data collected at the various stations were examined and categorized. Among numerous pc and pi events observed during the recording periods, 26 events of giant pulsations could be determined. The definition of type "A" giant pulsations by Sucksdorff (1939) was chosen as a base for data selection and only pulsations with a duration of at least ten oscillations were selected. Some of these events were clearly recognizable at as many as 8 stations, whereas others were distinct at only one or two sites. Table 2 lists the time of occurrence of these 26 events as well as the principal period of oscillation, the degree of magnetic disturbance (K_p), and the station at which maximum amplitude in the horizontal plane was recorded.

All components of the events listed, were digitized at 3 s increments using a semiautomatic digitizing table. In order to establish the period and amplitude of the dominant pg pulsations, power density spectral analysis (Blackman and Tukey, 1958) was utilized in which both the autocovariance functions and the power spectra were calculated. Cross-spectral estimates were used to determine phase differences between components at the same location as well as between similar components at different stations. The results of the spectral analyses were then used to draw the polarization ellipses in the H-D, D-Z, and H-Z planes as described by Rankin and Kurtz (1970). These ellipses are used to

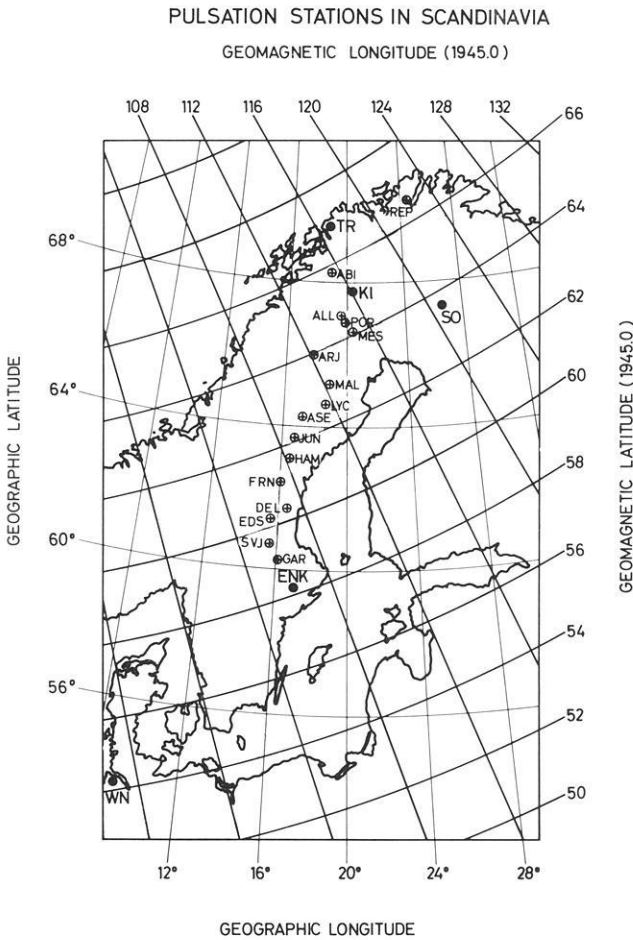


Fig. 2. ⊙ Sites in Scandinavia where the pulsation instruments were set up during 1970 and 1971. ● Observatories in Scandinavia and Northern Germany (WN) with Grenet type pulsation systems whose records were used in data analysis. (Leirvogur (LI) in Iceland is located outside this area)

illustrate the direction of polarization, the rotational sense, as well as the ellipticity and the degree of polarization.

5. Results

An eighteen minute interval of one of the most pronounced events of giant pulsations which occurred during the measurements in Scandinavia is shown in Figure 3. The entire event lasted from about 6:30 to 8:54 UT on June 25, 1971. This event shows the typical sinusoidal oscillations at seven of the eleven recording sites. The pulsations cannot be detected at LI in Iceland which is far away from the other stations. A surprising observation is the attenuation

Table 2. List of giant pulsation events and stations of maximum amplitudes in the horizontal plane

Date	Time (UT)		Principal period (s)	Kp	Station with max. Ampl.	Number of Stations affected
	Start	End				
700810	03:00	05:24	147	2-	TR	5
700811	07:42	08:36	99	2o	TR	3
700811	09:43	11:31	247	2o	SO	1
700812	06:04	06:58	219	2+	TR	3
700812	08:00	11:00	199	2+	SO	4
700813	07:14	08:26	270	2-	MES	3
700816	04:10	04:46	108	1+	TR	4
700822	08:04	08:22	99	1o	LYC	4
700912	03:24	04:00	330	2+	TR	2
710530	03:32	04:26	144	2o	TR	7
710603	10:17	10:53	180	2o	ABI	5
710609	07:47	08:05	219	1-	KI	3
710614	06:50	07:44	114	2-	ABI	7
710618	04:42	05:18	240	2-	SO	8
710625	04:52	05:28	85	3+	KI	6
710625	06:30	08:54	99	4-	SO	7
710627	23:50	00:08	204	1o	REP	3
710628	05:42	06:00	204	1-	REP	3
710708	08:52	09:10	91	2o	REP	2
710718	03:40	04:16	183	2+	ABI	5
710805	06:27	07:21	180	4+	MES	6
710805	10:08	11:02	187	1+	MES	2
710912	09:37	09:55	187	3o	LYC	7
710916	00:27	01:03	103	3-	TR	5
710924	09:31	10:07	225	0o	LYC	3
710929	01:12	01:48	101	3-	TR	4

of pulsation amplitude from ARJ to LYC, which are separated by a distance of approximately 180 km.

During the pg event, the amplitudes of the oscillations rise slowly to a maximum and fall again. The amplitudes of the vertical component are quite large compared to other types of pulsations. Indeed at times the vertical component exceeds the horizontal components. The oscillations of the disturbance seem to be more stable in the D-component than in the H-component: The coherency between H-components of different stations is lower than that of D-components.

The giant pulsations occurring during the time interval illustrated in Figure 3 have a mean period of 99 s. The period varies during the course of the event but is usually the same at different stations and in the three components. The period of this event is initially about 90 s, rises to 99 s during the time of maximum amplitudes, and then returns to its initial value. At the same time coherencies from station to station for this pg approach 1.0, and even records from distant stations often show good coherencies. The phase differences between similar components at different stations can already be seen by visual

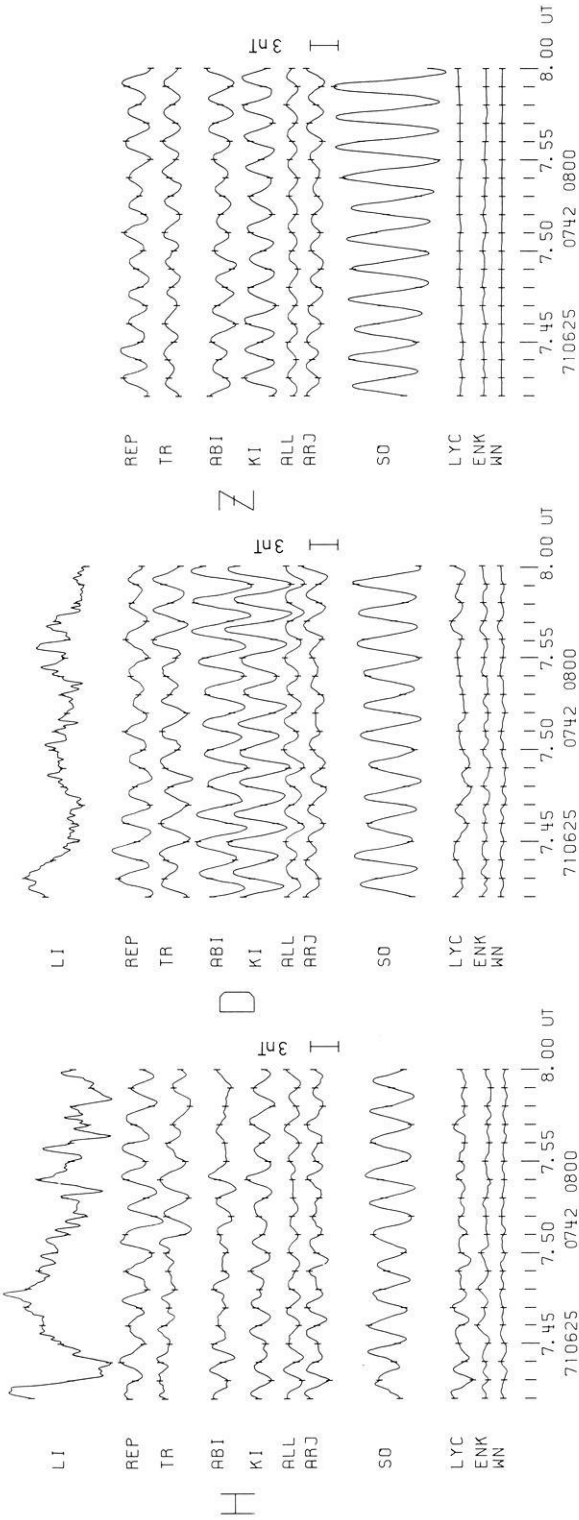


Fig. 3. Example of giant pulsations (pg) on the 25th of June 1971

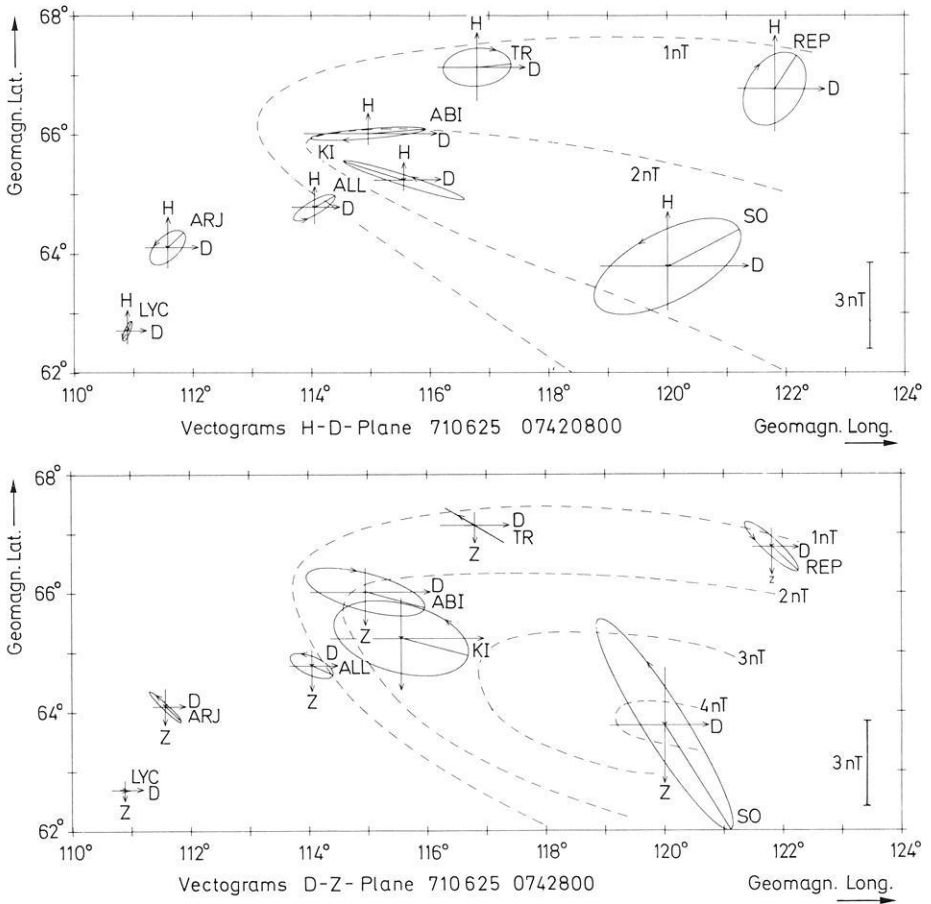


Fig. 4. Polarization ellipses in two planes of the event of giant pulsations on the 25th of June 1971

inspection of the example shown in Figure 3. Even the records of adjacent stations often show distinct phase differences.

With regard to the shape and rotation sense of the polarization ellipse the behaviour of the disturbance vector in the horizontal plane is dependent on the position of the recording site relative to the region where the pg is appearing.

Figure 4 gives an example of the sense of rotation and the shape of the polarization ellipses during an event of giant pulsations. The spatial amplitude distribution of the pg is approximated and marked by dotted lines of equal amplitude. The location of each station is indicated by the position of the centre of the small coordinate system for the polarization ellipses.

From the horizontal vectograms, a relationship between the shape and rotational sense of the polarization ellipses and the position of the observation station relative to the maximum disturbance region is apparent. To the north of this region, oscillations have a clockwise sense of rotation (viewed in the

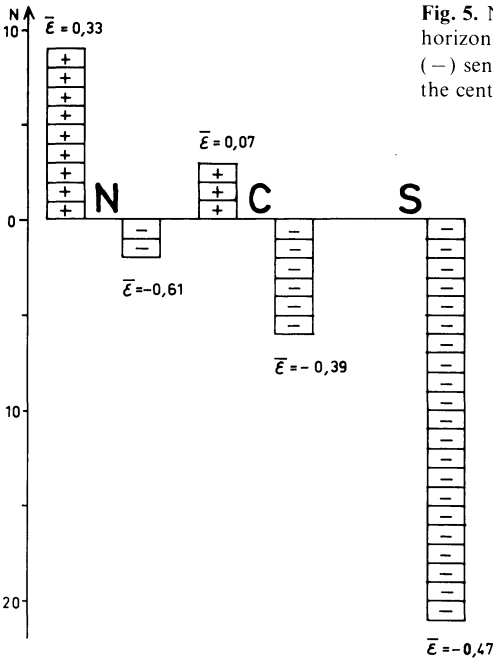


Fig. 5. Number of polarization ellipses in the horizontal plane with clockwise (+) and anticlockwise (-) sense of rotation north (N), south (S) and near the centre (C) of the pg region

horizontal plane in the direction of a fieldline). The opposite sense of rotation is shown at stations to the south of this region. For stations near the line of maximum pg amplitudes, the polarization is almost linear. A similar relationship for the vertical plane vectograms could not be detected.

From the 26 recorded events of giant pulsations nine were selected by criteria which included the number of stations which were affected (at least four), the amplitudes of the oscillations and the coherency of the signal from station to station. The sense of rotation of the polarization ellipse in the horizontal plane for each station was represented by a “+” for clockwise rotation viewed along a line of force, or a “-” for anticlockwise rotation. The stations were then divided into three groups according to their position relative to the region of pg maxima. Group N contains the observations to the north, group S those to the south, and group C those near the centre of the pg region. Furthermore, mean values of the ellipticity were calculated for each group. The results are illustrated in Figure 5. It is clear that an anticlockwise polarization sense is dominant south of the centre of the pg region, whereas to the north clockwise polarization dominates. The relatively small value $\epsilon = 0.07$ of the ellipticity near the centre of the pg region indicates a prevalence of linear polarization.

6. Discussion

When comparing the results of this study with those obtained by other workers, it should be noted that the duration of the period of observation was much

shorter than that examined by Rolf (1931), Harang (1936), and Sucksdorff (1939). The statistical results presented by these authors are based on data recorded over several years. The definition of type "A" giant pulsations and selection criteria should also be kept in mind. Large amplitude pulsations were thus excluded lacking regularity of waveform (for example, those treated by Nagata et al., 1963 or by Ol', 1963). Finally, all giant pulsation events observed during this recording period occurred between midnight and noon. This is in agreement with the statistical investigation of Sucksdorff (1939). His second peak in the occurrence pattern at about 16:00 LT could not be confirmed, possibly due to the relatively limited data.

From this study the shape of the region with simultaneously occurring pg's has the form of a long ellipse with its major axis roughly parallel to a geomagnetic parallel of latitude. A similar elongated pg region has been reported by Veldkamp (1960) who used a network of 24 stations in recording a rare pg event in middle latitudes. Other authors (e.g. Eleman, 1967), who have analyzed data from a network of stations have also described the region of occurrence of a pg as an ellipse extending in the geomagnetic east-west direction.

The analysis of the periods of the giant pulsations in this study yielded results similar to those of Eleman (1967). During a pg event, the period of oscillation often increases until the occurrence of maximum amplitudes and then decreases again. A period range of 85 s to about 5.5 min was observed in this study for different events.

With regard to the polarization of giant pulsation, this study reveals that the sense of rotation in the horizontal plane is opposite at stations north and south of the line of maximum amplitudes. To the north, the disturbance vector rotates clockwise viewed in the direction of a line of force, while to the south, the opposite sense of rotation is dominant. Samson and Rostoker (1972) obtained similar results in their more general analysis of pc4-pc5 pulsations, which did not specially concern giant pulsations. They observed an opposite rotational sense north and south of a demarcation line characterized by linear polarization and maximum amplitudes. Furthermore, the position of this line was found to change latitude during the day and a reversal of the rotational sense in both the north and south region was observed to occur at about 11:00 LT. This latter feature could not be confirmed in this study due to the lack of pg events in the afternoon hours.

The exact location of the line separating the region of opposite polarization is also significant in the study of horizontal vectograms at geomagnetic conjugate stations. Annexstad and Wilson (1968) found a high degree of correlation in the conservation of rotational sense in the direction of the corresponding line of force. Observed exceptions to this rule may be caused by the position of the recording station relative to the centre of the pg region. Assuming that both stations are not completely conjugate points, normally the centre of the pg is situated poleward or equatorward of both stations and a conservation of the rotational sense can be observed. On the contrary when one of the stations is situated poleward and the other equatorward of the pg centre in each hemisphere no conservation of the rotational sense is found as mentioned for several events in the investigation cited above.

It was tried to find a relationship between the latitude of the pg event and the period of oscillation as Ol' (1963) found and a relationship between the degree of disturbance and the location of the pg region as Hirasawa (1970) investigated. Neither of these effects could be confirmed by this study, probably because of the limited number of observed events.

Comparisons of satellite data to ground-based observations do not as yet allow a complete solution to the problem of the generation and propagation mechanism for magnetohydrodynamic waves in the magnetosphere which are observed as giant pulsations at the Earth's surface. Several events of pc4 and pc5 pulsations have been recorded in the magnetosphere and sometimes correlation analysis has been done with ground observations. Some of these magnetic oscillations at the location of the satellite resemble giant pulsations. Cummings et al. (1969) observed elliptical polarized pulsations in the magnetosphere with the disturbance vector orthogonal to the lines of force.

Lanzerotti and Tartaglia (1972) observed compressional waves in the magnetosphere at times when pc5 pulsations occurred on the ground with elliptically polarized oscillations. A characteristic feature of partly compressional waves in the magnetosphere may be the large vertical amplitudes of giant pulsations which are reported by almost all workers.

Pc5 pulsations with regular waveform have also been observed by Barfield et al. (1972) but these events were correlated to geomagnetic storms, and a relation between these oscillations and the occurrence of pg's or normal pc5's has not been described. An explanation of why giant pulsations have not yet been correlated with magnetic oscillations in the magnetosphere may be the very narrow latitude extension of the pg region, requiring that the observatory and the satellite be situated close to the same line of force.

Simultaneous observations of a pc5 storm time event in the magnetosphere and at different ground based stations together with proton density data have been done by Lanzerotti et al. (1975). The ground magnetometer data showed an opposite sense of rotation of the horizontal vector north and south of $L \approx 5$. The authors concluded that an odd mode shear Alfvén wave was excited by a high β drift instability at a gradient region of the hot plasma distribution. These observations are connected to storm times like in the study of Barfield et al. (1972). Consequently those results cannot be completely compared to pg observations on the ground.

Theoretical work on the excitation and propagation of magnetohydrodynamic waves which are observed as giant pulsations on the ground has been done by several authors. Lehnert (1956) considered oscillations in the conductive layers of the ionosphere as a cause of giant pulsations. Kato and Watanabe (1956) concluded that giant pulsations are harmonics of fundamental oscillations of the magnetosphere. The periods of these oscillations should be in the order of 600 s in the latitudes where giant pulsations are usually observed, and much longer in higher latitudes (3,000 s at 70° geomagnetic latitude). Wilson (1966) explains the correlated polarization characteristics of pg events at conjugate points by a model with circularly polarized standing hydromagnetic waves and induced ionospheric currents.

These theoretical investigations have been unable to explain the polarization

characteristics of pg events having an opposite sense of rotation north and south of the amplitude maximum. The theory for pc3 to pc5 by Hasegawa and Chen (1974) explains the polarization characteristics found by Samson and Rostoker (1972). The observed polarization characteristics of giant pulsations are also sufficiently explained by the above theory; i.e., the maximum amplitude and linear polarization at the location of the resonant field line and the opposite rotational sense of the polarization ellipse in the horizontal plane north and south of this region are interpreted. One of the observed characteristics of giant pulsations, the relatively large amplitudes of the vertical component is not explained by this theory.

Acknowledgements. The author acknowledges the cooperative assistance of the Scandinavian observatories and of many individuals during the field work in Scandinavia. This work is part of a project sponsored by the "Deutsche Forschungsgemeinschaft".

References

- Annexstad, J.O., Wilson, C.R.: Characteristics of Pg micropulsations at conjugate points. *J. Geophys. Res.* **73**, 1805–1818, 1968
- Barfield, J.N., McPherron, R.L., Coleman, P.J., Jr., Southwood, D.J.: Storm-associated Pc5 micropulsation events observed at the synchronous equatorial orbit. *J. Geophys. Res.* **77**, 143–158, 1972
- Birkeland, K.: Expédition Norvégienne de 1899–1900 pour l'étude des aurores boréales. Résultats des recherches magnétiques. Videnskabselskabets Skrifter, I. Matematisk-naturvidenskabelig Klasse **1**, 1–80, Christiania: 1901
- Blackman, R.B., Tukey, J.W.: The measurement of power spectra. New York: Dover Publications 1958
- Cummings, W.D., O'Sullivan, R.J., Coleman, P.J., Jr.: Standing Alfvén waves in the magnetosphere. *J. Geophys. Res.* **74**, 778–793, 1969
- Eleman, F.: Studies of giant pulsations, continuous pulsations, and pulsation trains in the geomagnetic field. *Arkiv Geofysik* **5**, 231–282, 1967
- Grenet, G.: Variomètre électromagnétique pour l'enregistrement des variations rapides du champ magnétique terrestre. *Ann. Géophys.* **5**, 188–195, 1949
- Harang, L.: Oscillations and vibrations in the magnetic records at high-latitude stations. *Terr. Magn. Atm. El.* **41**, 329–336, 1936
- Hasegawa, A., Chen, L.: Theory of magnetic pulsations. *Space Sci. Rev.* **16**, 347–359, 1974
- Hillebrand, O.: Registrierung von Riesenpulsationen in Skandinavien und Analyse der Daten. *Diss. Math.-Nat. Fak. Univ. Göttingen*, 1974
- Hirasawa, T.: Long-period geomagnetic pulsations (pc5) with typical sinusoidal waveforms. *Rep. Ionosphere Space Res. Japan* **24**, 66–79, 1970
- Jacobs, J.A., Kato, Y., Matsushita, S., Troitskaya, V.A.: Classification of geomagnetic micropulsations. *J. Geophys. Res.* **69**, 180–181, 1964
- Kato, Y., Watanabe, T.: Further study on the cause of giant pulsations. *Sci. Rep. Tôhoku Univ., Ser. 5, Geophys.* **8**, 1–10, 1956
- Lanzerotti, L.J., Tartaglia, N.A.: Propagation of a magnetospheric compressional wave to the ground. *J. Geophys. Res.* **77**, 1934–1940, 1972
- Lanzerotti, L.J., MacLennan, C.G., Fukunishi, H., Walker, J.K., Williams, D.J.: Latitude and longitude dependence of storm time Pc5 type plasma wave. *J. Geophys. Res.* **80**, 1014–1018, 1975
- Lehnert, B.: Magneto-hydrodynamic waves in the ionosphere and their application to giant pulsations. *Tellus* **8**, 241–251, 1956
- Nagata, T., Kokubun, S., Iijima, T.: Geomagnetically conjugate relationships of giant pulsations at Syowa base, Antarctica and Reykjavik, Iceland. *J. Geophys. Res.* **68**, 4621–4625, 1963

- Ol', A.L.: Long period gigantic geomagnetic field pulsations. *Geomagn. Aeron.* **3**, 90-95, 1963
- Rankin, D., Kurtz, R.: Statistical study of micropulsation polarizations. *J. Geophys. Res.* **75**, 5444-5458, 1970
- Rolf, B.: Giant micropulsations at Abisko. *Terr. Magn. Atm. El.* **36**, 9-14, 1931
- Samson, J.C., Rostoker, G.: Latitude-dependent characteristics of high-latitude Pc4 and Pc5 micropulsations. *J. Geophys. Res.* **77**, 6133-6144, 1972
- Steveling, E.: Erdmagnetische Tiefensondierung mit Variationen und Pulsationen im Einflußbereich der norddeutschen Leitfähigkeitsanomalie. *Diss. Math.-Nat. Fak. Göttingen*, 1973
- Sucksdorff, E.: Giant pulsations recorded at Sodankylä during 1914-1938. *Terr. Magn. Atm. El.* **44**, 157-170, 1939
- Veldkamp, J.: A giant geomagnetic pulsation. *J. Atmospheric Terrest. Phys.* **17**, 320-324, 1960
- Voelker, H.: Zur Breitenabhängigkeit erdmagnetischer Pulsationen. *Mitt. Max-Planck-Inst. Aeron.* **11**, 1-55, 1963
- Wilson, C.R.: Conjugate three-dimensional polarization of high-latitude micropulsations from a hydromagnetic wave-ionospheric current model. *J. Geophys. Res.* **71**, 3233-3249, 1966

Received January 12, 1976; Revised version April 5, 1976

Short Communications

**Latitude-Dependent Waves
and Impulse-Produced Waves**

L.J. Lanzerotti and A. Hasegawa

Bell Laboratories, Murray Hill, New Jersey 07974, USA

Key words: Micropulsations – Hydromagnetic waves.

Recently in this journal there have been two short papers (Kupfer, 1974; Siebert, 1975) discussing the very interesting observations made by Voelker (1962, 1963, 1965) of the latitude dependence of the frequency of certain geomagnetic pulsations as observed on the ground in the European sector. In an earlier discussion of these observations, Siebert (1964) attributed the latitude dependency of the pulsation frequencies to the excitation of the poloidal hydromagnetic wave mode in a “lamellar plasma structure” in the earth’s magnetosphere. In his short paper, Kupfer (1974) pointed out via an idealized model that the hypothesized lamellar plasma structure could probably not maintain such poloidal wave modes. Siebert (1975) commented that indeed, while a poloidal wave mode may not be maintained, nevertheless plasma density gradients with narrow spacings in L -value have been observed in the earth’s magnetosphere by spacecraft (e.g., Chappell et al., 1971; Bewersdorff and Sagalyn, 1972) and that such gradients are undoubtedly important in establishing the conditions for the pulsation characteristics which have been reported by him and by Voelker.

Several years ago Rostoker and Samson (1972) reported the results of a search for such latitude-dependent pulsation events using data from the University of Alberta high latitude magnetometer chain. They reported the observation of two such events in the time period for which they had data. They pointed out that the normal condition in the magnetosphere seems to be that which they had reported earlier (Samson et al., 1971). That is, an individual pulsation event appears to have essentially the same frequency at all latitudes. At subauroral latitudes, however, near $L=4$ and further south, it has become increasingly clear in recent years that a dependence on latitude is indeed seen in the predominant pulsation frequency (e.g., Orr, 1973, 1975; Webb and Orr, 1975; Fukunishi and Lanzerotti, 1974). The changes in pulsation frequency in the region of $L=3$ to $L=4$ have been attributed to the sharp change in the Alfvén velocity V_A in the magnetosphere that comes about because of the plasmapause.

The purpose of this brief communication is to point out that recently developed theory (Chen and Hasegawa, 1974a; Southwood, 1974) appears able to explain dayside latitude-dependent pulsation events. The theory as developed by Chen and Hasegawa (1974a) and by Southwood (1974) envisions surface waves, probably generated at the magnetopause by the solar wind flow, evanescent inward into the magnetosphere. These surface waves can couple to resonant field lines to produce standing shear Alfvén waves where the field line resonant frequency

$$F = [2 \int ds / V_A] \quad (1)$$

is equal to the frequency of the surface wave. The coupling of the surface wave to the resonant field line occurs at a plasma density gradient in the magnetosphere; at the resonance the wave is linearly polarized. On either side of the resonance region the wave is elliptically polarized with an opposite sense of polarization on either side. The sense of polarization depends upon the direction of the azimuthal wave propagation k_x as shown by the expression

$$H/D = ik_x \zeta_y (d\zeta_y/dy)^{-1} = \alpha + i\delta$$

where ζ_y is the plasma displacement in the radially inward (y) direction and α and δ give the orientation of the major axis of the wave ellipse and the sense of wave polarization, respectively (Chen and Hasegawa, 1974; Lanzerotti et al., 1974).

Thus, Voelker's observations (Voelker, 1962, 1963, 1965) can be readily explained if the surface wave source is composed of several discrete frequencies and if the magnetosphere has a series of plasma density gradients at increasing altitudes (perhaps produced by magnetic storm conditions). In this case waves with several different frequencies could be excited at different latitudes (altitudes) in the magnetosphere. The fact that Siebert (1964) reported the events predominantly polarized in the north-south component on the ground would suggest that the coupling conditions for waves at closely spaced density gradients may be somewhat different than for coupling when distinct tilts in the ellipse orientation angles are observed. However, it should be pointed out that recent important work on the propagation of hydromagnetic waves from the magnetosphere through the ionosphere to the ground (Hughes, 1974; Hughes and Southwood, 1976) suggests that there will be a 90° rotation in the major axis of the wave ellipse from the magnetosphere to the ground. Therefore, if these theoretical results are correct, then the predominant north-south orientations observed by Siebert would correspond to essentially purely east-west orientations in the magnetosphere. Such polarizations in the magnetosphere would correspond very closely to the excitation of shear Alfvén waves in what was formerly called the toroidal mode.

In his letter to this journal Siebert (1975) additionally points out that the local time dependence of the latitude-dependent pulsations is similar to that of pulsation single events (PSE) reported by Voelker (1966). That is, the latitude-dependent pulsations tend to be confined to the day side of the magnetosphere, as are the PSE. Such a local time dependence, of course, is entirely consistent with the above discussions of the solar wind/magnetopause origin for the exciting

sources of the latitude-dependent pulsations. It is quite likely, however, that the pulsation single events are not related to the latitude-dependent waves, even though the local time dependences are similar.

A large number of day side, damped hydromagnetic wave events which have properties that are different from those discussed above were studied by Lanzerotti et al. (1973, 1975). They showed that these events seem to be excited at plasma density gradients in the vicinity of the plasmopause. The work of these authors, together with that of Chen and Hasegawa (1974b), would suggest that these damped waves in the Pc 4 frequency band are probably related to the excitation of surface waves at plasma density gradients in the vicinity of the plasmopause or even at the plasmopause itself.

Shown in Figure 1 is the statistical distribution as a function of local time for the PSE (Voelker, 1966) as observed simultaneously at Wingst ($L=2.5$) and at Göttingen ($L=2.3$) and for the damped Pc4 events observed at Durham ($L=3.2$) by Lanzerotti et al. (1975). The PSE are more broadly distributed during the local day than the damped events. Nevertheless, the similarity of these local time distributions, together with the similarities of the reported wave characteristics, strongly suggest that the origins of the two sets of observations are very similar. Voelker (1966) attributes the PSE to the occurrence of sudden commencements (SC) and sudden impulses (SI) in the magnetosphere which he identified from low latitude magnetograms. Lanzerotti et al. (1975) cannot identify their events with tabulations of such SC's and SI's; they attribute this failure to the simple fact that, in general, observatory magnetograms are not sufficiently sensitive to record very small (few γ) changes in magnetospheric conditions. It is amplitude changes of this magnitude that are observed by Lanzerotti et al. (1973, 1975) to accompany the damped oscillations at $L \sim 3.2$. Lanzerotti et al. speculate that more sensitive low latitude ground level magnetometers might indeed show that the damped oscillations are related to small

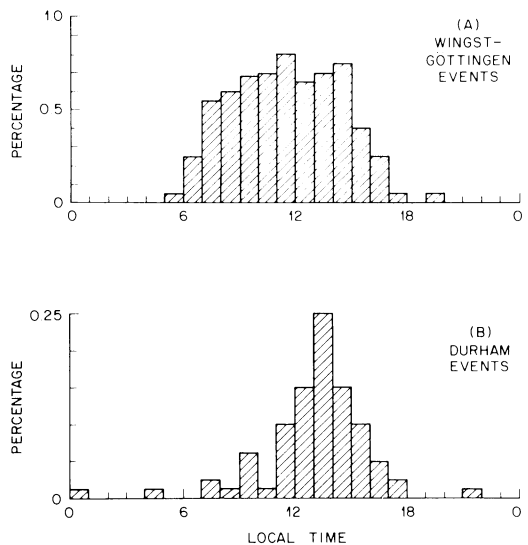


Fig. 1. A Percent PSE events observed simultaneously at Wingst and Göttingen (Voelker, 1966) as a function of local time.

B Percent damped waves observed at Durham as a function of local time

impulsive-like changes in the magnetospheric boundary. They also speculate that these small changes may be the cause of drift echos as seen in energetic particle fluxes by synchronous altitude satellites (e.g. Lanzerotti et al., 1967; Brown, 1968).

Thus, it seems quite likely that the pulsation single events and the lower latitude damped oscillations of Lanzerotti et al. (1975) may be both produced by the same exciting mechanism but with different amplitudes. Fukunishi (1975) has further discussed in more detail the relationships between SC- and SI-excited waves and damped pulsations near $L=4$ and also attributes the multiple-peaked spectra in the SC- and SI-excited waves to differences in the magnitude of the driving force. Both sets of waves, therefore, could be interpreted as damped surface waves excited at plasma density gradients in the magnetosphere (Chen and Hasegawa, 1974b).

In summary, the observations of Voelker (1962, 1963, 1965) and Siebert (1964) would seem to be consistent with the excitation of sheer Alfvén waves at plasma density gradients within the magnetosphere by multi-frequency spectrum surface waves evanescent into the magnetosphere from the magnetopause. These density gradients may well have a lamella nature as postulated originally by Siebert (1964). Secondly, the pulsation single events are probably not directly related to the latitude-dependent pulsation events but rather may well be related to the excitation (at plasma density gradients) of damped surface waves produced by either small sudden changes in the magnetosphere boundary or by larger disturbances such as sudden commencements or sudden impulses. Simultaneous observations between solar wind conditions and hydromagnetic wave conditions inside the magnetosphere are needed to further explore these various possibilities that have been opened by the recent theoretical and experimental developments.

References

- Brown, W.L.: Energetic outer belt electrons at synchronous altitude. In: Earth's particles and fields. B.M. McCormac, ed., p. 33. New York: Reinhold 1968
- Brewersdorff, A.B., Sagalyn, R.C.: Spatial and temporal variations of the thermal plasma between 3,000 and 5,000 kilometer at $L=2$ to 4. *J. Geophys. Res.* **77**, 4734, 1972
- Chappel, C.R., Harris, K.K., Sharp, G.W.: The dayside of the plasmasphere. *J. Geophys. Res.* **76**, 7632, 1971
- Chen, L., Hasegawa, A.: A theory of long period magnetic pulsations, 1. Steady state excitation of field line resonance. *J. Geophys. Res.* **79**, 1024, 1974a
- Chen, L., Hasegawa, A.: A theory of long period magnetic pulsations, 2. Impulse excitation of surface eigenmode. *J. Geophys. Res.* **79**, 1033, 1974b
- Fukunishi, H.: Latitude dependence of power spectra of magnetic pulsations near $L=4$ excited by SSC's and SI's. Submitted to *J. Geophys. Res.* 1975
- Fukunishi, H., Lanzerotti, L.J.: ULF pulsation evidence of plasmopause, 1. Spectral studies of Pc3 and Pc4 pulsations near $L=4$. *J. Geophys. Res.* **79**, 142, 1974
- Hughes, W.J.: The effect of the atmosphere and ionosphere on long-period magnetospheric pulsations. *Planet. Space Sci.* **22**, 1157, 1974
- Hughes, W.J., Southwood, D.J.: The screening of micropulsation signals by the atmosphere and ionosphere. *J. Geophys. Res.* **81**, in press, 1976
- Kupfer, E.: Hydromagnetic waves in a non-uniform plasma. *J. Geophys. Res.* **41**, 123, 1975
- Lanzerotti, L.J., Brown, W.L., Roberts, C.S.: Temporal variations in the electron flux at synchronous altitudes. *J. Geophys. Res.* **72**, 5893, 1967

- Lanzerotti, L.J., Fukunishi, H., Chen, L.: ULF pulsation evidence of the plasmopause. 3. Interpretation of polarization and spectral amplitude studies of Pc3 and Pc4 pulsations near $L=4$. *J. Geophys. Res.* **79**, 4648, 1974
- Lanzerotti, L.J., Fukunishi, H., Hasegawa, A., Chen, L.: Excitation of the plasmopause at ultralow frequencies. *Phys. Rev. Letters* **31**, 624, 1973
- Lanzerotti, L.J., Fukunishi, H., Mellen, D.B.: Excitation of plasma density gradients in the magnetosphere at ultralow frequencies. *J. Geophys. Res.* **80**, 3131, 1975
- Orr, D.: Magnetic pulsations within the magnetosphere: A review. *J. Atmos. Terr. Phys.* **35**, 1, 1971
- Orr, D.: Probing the plasmopause by geomagnetic pulsations. *Ann. Geophys.* **31**, 77, 1975
- Rostoker, G., Samson, J.C.: Pc micropulsations with discrete latitude dependent frequencies. *J. Geophys. Res.* **77**, 6249, 1972
- Samson, J.C., Jacobs, J.A., Rostoker, G.: Latitude-dependent characteristics of long-period geomagnetic micropulsations. *J. Geophys. Res.* **76**, 3675, 1971
- Siebert, M.: Comment on "Hydromagnetic waves in a non-uniform plasma", by E. Kupfer. *J. Geophys.* **41**, 325, 1975
- Siebert, M.: Geomagnetic pulsations with latitude-dependent periods and their relation to the structure of the magnetosphere. *Planet. Space Sci.* **12**, 137, 1964
- Southwood, D.J.: Some features of field line resonance in the magnetosphere. *Planet. Space Sci.* **22**, 483, 1974
- Voelker, H.: Zur Breitenabhängigkeit erdmagnetischer Pulsationen. *Mitteil. Max-Planck-Inst. Aeronomie* **11**, 1, 1963
- Voelker, H.: Breitenabhängigkeit der Perioden erdmagnetischer Pulsationen. *Naturwissenschaften* **49**, 8, 1962
- Voelker, H.: Göttinger Untersuchungen über erdmagnetische Pulsationen and ihre Beziehungen zur Magnetosphäre. *Kleinheubacher Ber.* **10**, 237, 1965
- Voelker, H.: On geomagnetic pulsations accompanying storm sudden commencements and sudden impulses. *Earth Planet. Sci. Lett.* **1**, 383, 1966
- Webb, D., Orr, D.: Spectral studies of geomagnetic pulsations with periods between 20 and 120 seconds, and their relationship to the plasmopause region. *Planet. Space Sci.*, **23**, 1551, 1975

Received February 16, 1976

Study of the Spatial Variation of the Magnetic Field Intensity on North-South Profiles in Iran in Comparison with the IGRF Model of 1970

N.H. Guya

Institute of Geophysics, Tehran University, Tehran, Iran

Key words: Magnetic anomalies – International Geomagnetic Reference Field (IGRF) – Proton magnetometer.

The purpose of this work is to compare the International Geomagnetic Reference Field (IGRF) of 1970 with the data obtained for magnetic elements from the Tehran observatory, as well as the data from two north-south profiles in Iran. Such a comparison, firstly reveals the difference of the IGRF model and the observed data at the observatory, and secondly acts as a guide to determine the accuracy and the cause of spatial irregularities of magnetic elements. An attempt has been made to interpret the existing differences in terms of local magnetic anomalies.

A computer program, originally developed by the U.S. Coast and Geodetic Survey, was modified and adopted for use the IBM computer available in Tehran. Using this program values of the geomagnetic components are derived from spherical harmonic models for given geographic positions and recording intervals, concerning measurements at local sites. The method involved uses models of degree and order up to twelve and the first time derivatives of the coefficients (Hurwitz et al., 1966). A similar method of comparison of field data and the IGRF model was applied by Bleil (1974) for a profile in the Alps.

In Figure 1, the yearly mean values of geomagnetic elements D (declination), I (inclination) and F (total intensity) from the Tehran observatory are compared with the corresponding values, calculated from the IGRF model for the period 1960–1973. The existing differences could be caused by local magnetic anomalies near Tehran or by the occurrence of secular variation which is not adequately included in the IGRF model.

For further studies of this question, the same method of comparison was applied to the data obtained from field observations, measuring the total intensity with a proton magnetometer at intervals of 6–10 km on two profiles (No. 1 and No. 2) both running north and south of the Tehran station from the Caspian

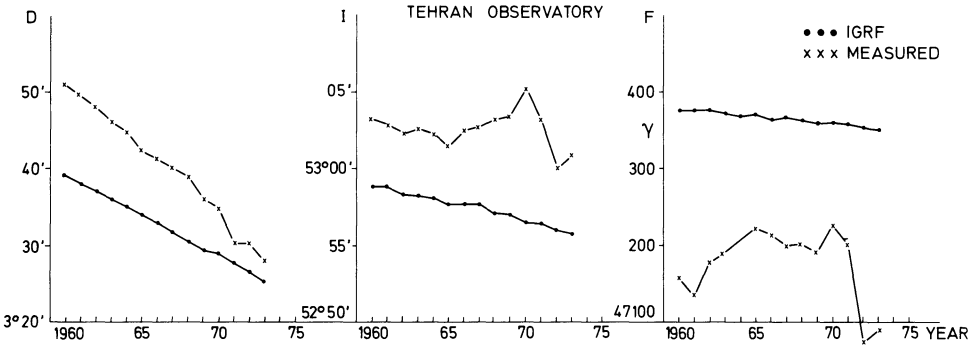


Fig. 1. Comparison between the IGRF model and the yearly mean values of the magnetic elements *D*, *I* and *F*, measured at the Tehran observatory for the period 1960–1973. The occurring differences suggest the presumption of a local magnetic anomaly near Tehran

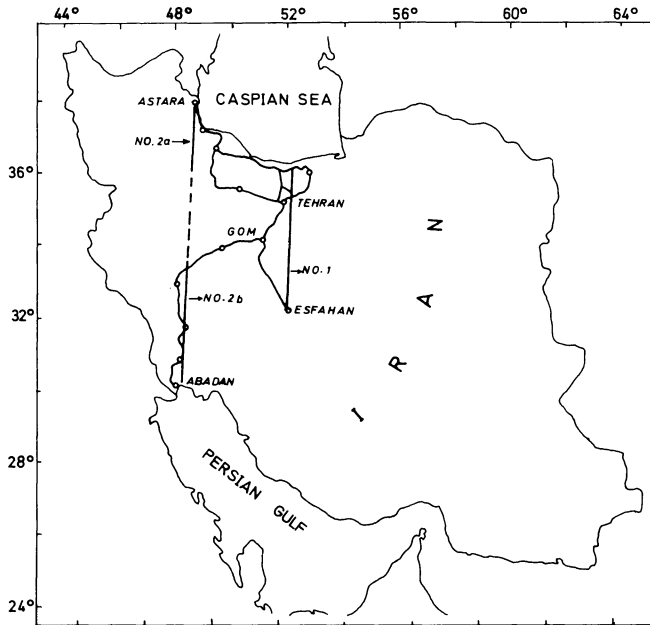


Fig. 2. Geographical map of Iran showing the roads along which the total intensity has been measured. The straight lines are the two north-south profiles to which the data of neighbored sites have been related

Sea to the Persian Gulf (Fig. 2). In the course of this survey a total of 310 points was obtained. Since the field sites are located near big roads by reason of transportation, the profiles represent the general direction to which the data of neighbored single sites or groups of sites is related. The part of profile No. 2, for which the stations are too far, is left out, dividing it into two sections.

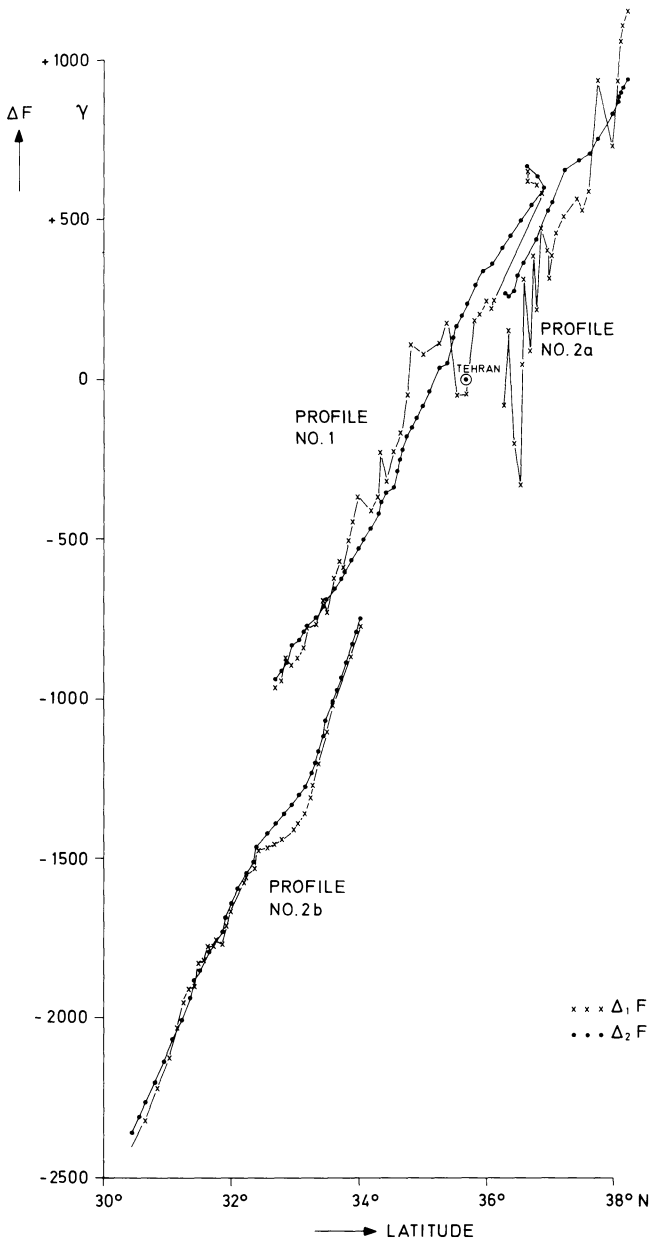


Fig. 3. Difference $\Delta_1 F$ between the total intensity, measured at field sites and at the Tehran observatory and difference $\Delta_2 F$ between the total intensity, evaluated from the IGRF model for field sites and from the monthly mean values of the Tehran observatory as functions of the station's latitude. Notice the prominent anomaly in the surroundings of Tehran

In order to evaluate the magnetic anomaly with respect to the reference field, the following procedure was applied:

$$\Delta_1 F = F(St) - F(TP_1),$$

$$\Delta_2 F = F(RF) - F(TP_2),$$

$$\Delta_3 F = \Delta_1 F - \Delta_2 F.$$

The used symbols have the following meaning:

$F(St)$ = Total intensity at each field site,

$F(TP_1)$ = Total intensity measured at Tehran observatory at the time of field measurement,

$F(RF)$ = Total intensity from the IGRF model for the field sites,

$F(TP_2)$ = The monthly mean value of the total intensity at Tehran observatory with regard to the period of field measurement.

Assuming that secular, daily, and irregular variations show parallel traces at both the field stations and the observatory of Tehran, the influence of these transient variations is eliminated with the above formulae. Hence, $\Delta_3 F$ represents the anomalous magnetic intensities with respect to the IGRF model.

In Figure 3 $\Delta_1 F$ and $\Delta_2 F$ are plotted for the profiles No. 1, 2a and 2b. On profile No. 2b, the curves for $\Delta_1 F$ and $\Delta_2 F$ are very close and no major anomaly can be recognized except between the latitudes 32°40' N and 33°30' N, but larger anomalies can be seen on profiles No. 1 and 2a. We conclude that these anomalies are mainly restricted to the surroundings of Tehran. The anomaly $\Delta_3 F$ itself is to be distinguished from the vertical difference of both the curves.

We hope in the future, with more measurements along some east-west profiles and with the help of geological and tectonic information of the area, to locate these anomalies more accurately and to be able to say more about their nature.

References

- Bleil, U.: Vermessung der Totalintensität und Vertikalintensität längs eines Alpenquerprofiles auf dem nördlichen Abschnitt der Geotraverse 1a, Münchener Universitäts-Schriften, Fakultät für Geowissenschaften, Serie B, Nr. 5, Teil 2, München 1974
- Hurwitz, L., Nelson, J.H., Watson, D.E.: Mathematical model of the geomagnetic field for 1965. J. Geophys. Res. **71**, 2373-2383

Received May 26, 1976

Plate Tectonics and Geomagnetic Reversals. Reading with Introductions by Allan Cox (Editor). 702 S., 360 Abb., 45 Tab. W.H. Freeman and Company, San Francisco, Reading (G.B.) 1973, £8,20 clothbound, £4,30 paperbound.

Dieses Buch enthält vierzig der wichtigsten Originalarbeiten über die Plattentektonik, darunter vier ältere Arbeiten, auf denen dieses Konzept aufbaut. Allein schon für diese in neun Sachabschnitte gegliederte Sammlung der über viele Zeitschriften verstreuten und teilweise schwer zugänglichen Artikel muß man dem Herausgeber Allan Cox dankbar sein; ist doch das Studium der Originalarbeiten durch kein noch so gut geschriebenes Buch über die Plattentektonik ersetzbar. Dies ist auch eines der Argumente, das Cox zur Herausgabe des Buches führte, weil das Erregende des Entdeckungsprozesses durch die Schilderungen der Forscher selbst besser miterlebt werden könne. Doch er verfolgt noch ein weiteres Ziel und geht damit über eine einfache Sammlung hinaus: Wenn wir unsere Wissenschaft darstellen, sagt er dem Sinne nach, dann zielt dies im allgemeinen auf eine Wissenschaft ohne ihre Urheber ab. "The effect is that we inadvertently may leave students with the impression that science is a routine, matter-of-fact business, which it surely isn't". Deshalb hat Cox jedem der neun Abschnitte Einführungen vorangestellt, die eine Kombination darstellen aus einer Einführung in das betreffende Sachgebiet, einer Schilderung der historischen Entwicklung und nicht zuletzt der die Forschung initiiierenden und tragenden Persönlichkeiten, von denen viele Photos, größtenteils Schnappschüsse während der Arbeit, beigefügt sind. Diese auf der wohlthuenden Grundlage einer umfassenden Sachkenntnis und kritischen Beurteilung geschriebenen Einführungen zusammen mit den abgedruckten Originalarbeiten und weiteren Literaturempfehlungen (Reading lists) stellen dem Leser ein ausgezeichnetes Material zur Verfügung für eine gründliche und anregende Beschäftigung mit der Plattentektonik, ihrer historischen Entwicklung und ihrer Tragweite bzw. Weiterentwicklung. Hierfür wenigstens ein Beispiel aus der Einführung zum 2. Abschnitt, wo Cox schreibt, daß Belege für die sogenannte Tiefenstruktur der Kontinente wie etwa die seismische Zone unter der Westküste von Südamerika tatsächlich mehr auf einen *Prozeß* als auf eine Struktur hindeuten würden. Hier ist gewissermaßen die Lösungsmöglichkeit für ein Problem vorweggenommen, das erst kürzlich bezüglich der den Erdmantel durchfurchenden „Kiele“ der Kontinente aufgeworfen wurde.

Das Buch ist in die folgenden Sachabschnitte gegliedert:

I. Paradigm of Plate Tectonics; II. The Beginning: Marine Geology; III. Geometry of Plate Tectonics; IV. Geomagnetic Reversals: The Story on Land; V. Reversals at Sea: The Magnetic Stripes; VI. Earthquakes at the Edges of Plates; VII. Second-Generation Plate Tectonics; VIII. Heat Flow, Gravity, and Driving Mechanism; IX. Plate Tectonics and Geology.

Die Literaturzitate der Originalarbeiten sind am Ende in einem Gesamt-Literaturverzeichnis zusammengestellt, das rd. 1300 Titel umfaßt. Ein Autoren- und Sachregister schließen das Buch ab, an dem alle ihre Freude haben werden, für die Wissenschaft mehr ist als ein „nüchternes Geschäft“.

K. Strobach, Stuttgart

M. Schulz, L.J. Lanzerotti: Particle Diffusion in the Radiation Belts, 215 p. Berlin-Heidelberg-New York: Springer 1974.

The book which is considered in this review gives a rather special account of the field of particle diffusion in the radiation belts. Since both authors are active workers in the field of magnetospheric and particularly radiation belt physics the book is up to date (1974). After some introductory remarks it starts with a presentation of the theoretical framework of particle diffusion using a didactically somewhat novel approach based on Hamiltonian mechanics. The theory is compared with selected observations.

This comparison is by no means complete but relatively well balanced. The final chapter deals with techniques to compare observational data with the appropriate theories.

The book is useful for workers in and newcomers to the field of diffusion in the radiation belts but also in other fields where diffusion by the violation of the adiabatic invariants plays a role. It is valuable not only by giving a logical development of the theory but also as a source book for the various formulas resulting from the theory.

F.M. Neubauer, Braunschweig

Review Article

Seismische Oberflächenwellen*

D. Seidl¹ und S. Müller²

¹ Seismologisches Zentralobservatorium Gräfenberg, Krankenhausstr. 1, D-8520 Erlangen, Bundesrepublik Deutschland

² Institut für Geophysik der Eidgenössischen Technischen Hochschule, ETH-Hönggerberg, Postfach 266, CH-8049 Zürich, Schweiz

Seismic Surface Waves

Abstract. The wide field of seismic surface waves is reviewed emphasising the essential aspects in theory and observation. After a recapitulation of the relevant theory for the propagation of these waves in model structures, such as a layered elastic halfspace and a layered elastic sphere, the effects of anelasticity and heterogeneity are briefly discussed. A presentation of the common methods of observational techniques and data analysis is followed by a short summary of inversion procedures which permit the determination of model parameters from dispersion and absorption measurements. In order to obtain a realistic and meaningful interpretation of the observations, the data must be regionalized for different tectonic provinces. Selected examples are presented for Europe which demonstrate that there must exist pronounced lateral variations in the structure of the crust and upper mantle.

Key words: Seismology – Surface waves – Europe, crust and upper mantle structure.

1. Einleitung

Erdbeben und Explosionen regen seismische Wellen an, die sich sowohl durch das Erdinnere als auch entlang der Erdoberfläche ausbreiten. Zeichnet man den zeitlichen Verlauf derartiger Bewegungsvorgänge mit einem Seismographen auf, so folgen auf die ersten Signaleinsätze mit kleinen Amplituden und sehr kurzen Perioden Wellenzüge mit sehr viel größeren Amplituden und wesentlich längeren Perioden, die das Seismogramm eindeutig beherrschen. Die Vorläuferwellen, die mit einer Kompressions- und einer nachfolgenden Scherungsbeanspruchung des Materials verbunden sind, entstehen gleichzeitig im Erdbebenherd und durch-

* Vom Vorstand der DGG erbetener Übersichtsartikel. Mitteilung Nr. 94 aus dem Institut für Geophysik der Eidgenössischen Technischen Hochschule Zürich

dringen räumlich das Innere der Erde. Anders kommt die Hauptphase der aufgezeichneten Bewegung zustande. Ändern sich die elastischen Moduln und/oder die Dichte eines festen Mediums – wie der Erde – mehr oder weniger abrupt in einer Koordinatenrichtung (wie z. B. mit der Tiefe), so kann ein Teil der ankommenden Raumwellenenergie gezwungen werden, sich entlang der Trenn- oder Grenzfläche auszubreiten. Im allgemeinen Fall werden dabei die Kompressions- und Scherungsraumwellen (*P*- und *S*-Wellen) miteinander in Wechselwirkung treten. Die resultierende Bewegung konzentriert sich im wesentlichen auf die Umgebung der Grenzfläche, beziehungsweise auf die von solchen Flächen abgegrenzten Schichten, und nimmt mit wachsender Entfernung von den begrenzenden Flächen rasch ab. Da die Ausbreitungsgeschwindigkeit dieser Wellen von der Tiefenverteilung der elastischen Moduln und der Dichte bestimmt wird, hängt die Phasengeschwindigkeit entscheidend von der Eintauchtiefe (d.h. von der Wellenlänge) ab. Man spricht in einem solchen Falle von geometrischer Dispersion, zu der in einem Medium mit anelastischen Defekten noch eine materielle Dispersion hinzukommen kann.

Aus der Tatsache, daß zwischen der Laufzeit der dominierenden Wellenzüge eines Seismogramms und der Entfernung vom Erdbebenherd zu den Beobachtungspunkten an der Erdoberfläche ein linearer Zusammenhang besteht, muß man auf eine zweidimensionale Ausbreitung dieser Wellen entlang der Erdoberfläche schließen. Sie sind offensichtlich spezielle geführte Wellen der oben beschriebenen Art, deren Auftreten mit dem Vorhandensein einer freien Oberfläche zusammenhängt. Man bezeichnet sie deshalb zu recht als Oberflächenwellen.

Seismische Oberflächenwellen (Rayleigh- und Love-Wellen), deren Periodenspektrum über 11 Oktaven reicht, spielen eine bedeutsame Rolle in den Bemühungen um eine systematische Erforschung des Erdinnern. Erst nachdem mit dem Bau leistungsfähiger langperiodischer Seismographensysteme sowie mit der Entwicklung neuer Methoden der Analyse, Inversion, Interpretation und Synthese seismischer Daten auf elektronischen Großrechenanlagen die notwendigen experimentellen und theoretischen Grundlagen geschaffen worden waren, konnte man die Lösung vieler, für die Geophysik wichtiger Probleme in Angriff nehmen.

Es zeigte sich, daß für fortschreitende Oberflächenwellen mit Perioden bis zu 50 s ein mehrfach geschichtetes „Sandwich“-Modell mit ebenen Grenzflächen die oberen Bereiche des Erdkörpers hinreichend gut beschreibt. Für die Ausbreitung von Wellen mit längeren Perioden müssen allerdings die Sphärizität und das Schwerfeld der Erde berücksichtigt werden. Bei Perioden über 10 min spricht man wohl besser von „stehenden“ Oberflächenwellen, das heißt von Eigenschwingungen der Erdkugel. Die möglichen Schwingungsformen eines komplizierten Gebildes wie der Erde sind erwartungsgemäß sehr mannigfaltig: Sie umfassen Sphäroidalschwingungen (mit einer Grundperiode von knapp 54 min) und Torsionalschwingungen (mit einer Grundperiode von fast 44 min) sowie deren höhere Moden mit entsprechend kürzeren Perioden.

Von besonderer Bedeutung sind diejenigen höheren Moden („Obertöne“), die in der radialen Verteilung der Partikelbewegungen eine oder mehrere Knotenebenen aufweisen. Sie enthalten aufschlußreiche Informationen über die Feinstruktur des Erdmantels, über die Orientierung von Erdbebenbruchflächen sowie

über die Tiefe, Natur und Dynamik von Erdbebenherden. Eine detaillierte Interpretation der höheren Moden von seismischen Oberflächenwellen wird deshalb Gewißheit bringen über die Existenz von Gradientenzonen und Tiefenbereichen mit erniedrigten Geschwindigkeiten in der Kruste und im obersten Mantel. Verlustbehaftete Moden („leaking modes“) können in diesem Zusammenhang ebenfalls wertvolle Anhaltspunkte liefern.

Aus Platzgründen ist es leider nicht möglich, in dieser Übersicht auf Beobachtungen, die Analyse, Inversion und Interpretation der höheren normalen und der verlustbehafteten Moden von Oberflächenwellen einzugehen. Dasselbe gilt für Anisotropie-Effekte, die zur Deutung der beobachteten Phasengeschwindigkeitsdispersion von Love- und Rayleigh-Wellen in manchen Gegenden der Erde angenommen werden müssen. Nicht berücksichtigt werden konnten hier ferner die faszinierenden Kopplungsphänomene zwischen Rayleigh-Wellen und Schallwellen in der Luft bzw. im Meerwasser. Auf die Bedeutung von seismischen Oberflächenwellen bei der Untersuchung von Vorgängen in Erdbebenherden konnte hier ebenfalls nur kurz hingewiesen werden. Dieser Fragenkomplex sollte an anderer Stelle ausführlicher behandelt werden.

2. Theorie

Elastischer Halbraum

Es ist zweckmäßig, die Lösung des allgemeinen Ausbreitungsproblems seismischer Oberflächenwellen in einem radialsymmetrischen, anelastischen Modell der Erde in drei Schritten vorzunehmen. Die für die Anwendung wichtigen kinematischen und dynamischen Eigenschaften der Rayleigh- und Love-Wellen sollen zunächst am Modell des geschichteten elastischen Halbraums erläutert und zusammengestellt werden. Diese Ergebnisse werden dann durch Berücksichtigung der sphärischen Gestalt und Anelastizität der Erde schrittweise erweitert. Es soll hier versucht werden, die sehr komplizierten theoretischen Zusammenhänge in möglichst übersichtlicher und kompakter Form darzustellen. Einzelheiten der mathematischen Formulierungen können den Originalarbeiten entnommen werden.

Durch das Modell des geschichteten Halbraums läßt sich jede stückweise stetige Parameterfunktion der Tiefenkoordinate x_3 beliebig genau approximieren. Als Schichtparameter werden dabei im elastischen Fall die Geschwindigkeiten der P - und S -Wellen α_i und β_i , die Dichte ρ_i sowie die Schichtmächtigkeit d_i (i =Schichtindex) vorgegeben. Die von Haskell (1964), Ben-Menahem und Harkrider (1964), Harkrider und Anderson (1966), Saito (1967), Harkrider (1964, 1970) sowie Panza et al. (1973) u. a. entwickelte Theorie des Verschiebungsfeldes einer unbewegten Punktquelle in einem geschichteten elastischen Halbraum führt zu folgendem Ergebnis: Der Oberflächenwellenanteil des Fernfeldes läßt sich in einzelne, dem Herd bzw. dem Ausbreitungsmedium zugeordnete Faktoren separieren, nämlich das Herdspektrum S , den Herdgeometriefaktor $H_{R,L}$, die relative Anregungsfunktion $E_{R,L}$ des Ausbreitungsmediums sowie den komplexen Ausbreitungsfaktor einer zweidimensionalen Welle.

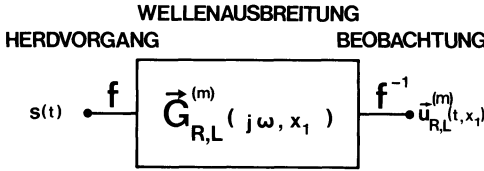


Abb. 1. Blockdiagramm eines linearen Systems, das die Ausbreitung seismischer Oberflächenwellen beschreibt. Die Symbole \mathfrak{F} bzw. \mathfrak{F}^{-1} bedeuten die direkte bzw. inverse Fourier-Transformation

Für die Fourier-Transformierte des Verschiebungsvektors der m -ten Mode der Rayleigh-Welle $\vec{U}_R^{(m)}(j\omega, x_1)$ bzw. Love-Welle $\vec{U}_L^{(m)}(j\omega, x_1)$ gilt an der Oberfläche ($x_3 = 0$) die übersichtliche Darstellung:

$$\begin{aligned}\vec{U}_R^{(m)}(j\omega, x_1) &= \{U_1^{(m)}, 0, U_3^{(m)}\} \\ &= S(j\omega) H_R^{(m)}(\omega, \Theta, h) E_R^{(m)}(\omega) x_1^{-1/2} \\ &\quad \cdot \exp[-jk_R^{(m)}(\omega)x_1] \{1, 0, j/\varepsilon_0^{(m)}(\omega)\}\end{aligned}\quad (2.1)$$

$$\begin{aligned}\vec{U}_L^{(m)}(j\omega, x_1) &= \{0, U_2^{(m)}, 0\} \\ &= S(j\omega) H_L^{(m)}(\omega, \Theta, h) E_L^{(m)}(\omega) x_1^{-1/2} \exp[-jk_L^{(m)}(\omega)x_1] \{0, 1, 0\}.\end{aligned}\quad (2.2)$$

Die Indizes 1, 2, 3, bedeuten die radiale, azimutale und vertikale Komponente des Verschiebungsvektors, x_1 die Epizentralentfernung, Θ das Azimut, h die Herdtiefe und ω die Kreisfrequenz.

In der symbolischen Darstellungsweise der linearen Systemtheorie lassen sich die Gleichungen (2.1) und (2.2) durch ein einfaches Blockdiagramm (Abb. 1) veranschaulichen, das den zeitlichen Verlauf des Verschiebungsvektors der m -ten Rayleigh- bzw. Love-Mode in der Entfernung x_1 als Antwortfunktion eines linearen Systems mit der Übertragungsfunktion $\vec{G}_R^{(m)}(j\omega, x_1)$ bzw. $\vec{G}_L^{(m)}(j\omega, x_1)$ auf einen Herdimpuls $s(t)$ mit dem Spektrum $S(j\omega)$ beschreibt.

Aus den Gleichungen (2.1) und (2.2) folgt für die Übertragungsfunktionen $\vec{G}_R^{(m)}(j\omega, x_1)$ bzw. $\vec{G}_L^{(m)}(j\omega, x_1)$:

$$\begin{aligned}\vec{G}_R^{(m)}(j\omega, x_1) &= H_R^{(m)}(\omega, \Theta, h) E_R^{(m)}(\omega) x_1^{-1/2} \exp[-jk_R^{(m)}(\omega)x_1] \{1, 0, j/\varepsilon_0^{(m)}(\omega)\}\end{aligned}\quad (2.3)$$

$$\begin{aligned}\vec{G}_L^{(m)}(j\omega, x_1) &= H_L^{(m)}(\omega, \Theta, h) E_L^{(m)}(\omega) x_1^{-1/2} \exp[-jk_L^{(m)}(\omega)x_1] \{0, 1, 0\}.\end{aligned}\quad (2.4)$$

Durch Summation über alle Moden (m) und Rücktransformation (\mathfrak{F}^{-1}) in den Zeitbereich folgt für den Verschiebungsvektor \vec{u} in der Epizentralentfernung x_1 :

$$\vec{u}(t, x_1) = \frac{1}{2\pi} \sum_m \int_{-\infty}^{+\infty} S(j\omega) [\vec{G}_R^{(m)}(j\omega, x_1) + \vec{G}_L^{(m)}(j\omega, x_1)] \exp(j\omega t) d\omega.\quad (2.5)$$

Gleichung (2.5) bildet den Ausgangspunkt für die Berechnung synthetischer Seismogramme einer Punktquelle in einem geschichteten elastischen Halbraum. Die relativen Anregungsfunktionen $E_R^{(m)}(\omega)$ und $E_L^{(m)}(\omega)$ in den Gleichungen (2.3) und (2.4) sind Funktionen der Frequenz sowie der Schichtparameter, aber un-

abhängig von Herdtiefe und Herdmechanismus:

$$E_R^{(m)}(\omega) = A_R^{(m)}(\omega) [k_R^{(m)}(\omega)]^{-1/2} \varepsilon_0^{(m)}(\omega) \quad (2.6)$$

$$E_L^{(m)}(\omega) = A_L^{(m)}(\omega) [k_L^{(m)}(\omega)]^{-1/2}. \quad (2.7)$$

$\varepsilon_0^{(m)}(\omega)$ bedeutet die Oberflächenelliptizität der m -ten Rayleigh-Mode, d. h. das Verhältnis der radialen zur vertikalen Halbachse der Schwingungsellipse, die der Verschiebungsvektor nach Gleichung (2.1) durchläuft. Die sog. Amplitudenantwortfunktion $A_R^{(m)}(\omega)$ hat eine für das Ausbreitungsmedium charakteristische Form. Sie läßt sich als Fourier-Transformierte der vertikalen Antwortfunktion der m -ten Rayleigh-Mode deuten, die als Wirkung eines δ -Impulses einer vertikalen Oberflächenpunktkraft beobachtet wird. Entsprechendes gilt für $A_L^{(m)}(\omega)$ und eine horizontale Oberflächenpunktkraft. Dabei ist der Einfluß des komplexen Ausbreitungsfaktors nicht berücksichtigt. Die reellen Ausbreitungsfunktionen $k_R(\omega)$ und $k_L(\omega)$ beschreiben die geometrische (d. h. die durch die Randbedingungen erzwungene) Dispersion der Rayleigh- und Love-Wellen. Aus ihnen lassen sich die Phasengeschwindigkeiten

$$c_{R,L}^{(m)}(\omega) = \omega / k_{R,L}^{(m)}(\omega) \quad (2.8)$$

sowie die Gruppengeschwindigkeiten

$$U_{R,L}^{(m)}(\omega) = 1 / [dk_{R,L}^{(m)}(\omega) / d\omega] \quad (2.9)$$

ableiten.

Für den vom Herdmechanismus abhängigen Geometriefaktor $H_{R,L}$ gilt:

$$H_{R,L}^{(m)}(\omega, \Theta, h) = [k_{R,L}^{(m)}(\omega)]^M \exp[-j(2M+1)\pi/4] \chi_{R,L}(\omega, \Theta, h) \quad (2.10)$$

($M=0$ für Punktkraft, $M=1$ für Krätedipol bzw. Doppeldipol).

Die komplexe Abstrahlcharakteristik $\chi_{R,L}$ hat die Form

$$\chi_{R,L}^{(m)}(\omega, \Theta, h) = d_0 + j(d_1 \sin \Theta + d_2 \cos \Theta) + d_3 \sin 2\Theta + d_4 \cos 2\Theta. \quad (2.11)$$

Die Koeffizienten d_l ($l=0, \dots, 4$; die Indizes R, L und m sind der größeren Übersichtlichkeit wegen weggelassen) sind für ein gegebenes Herdmodell Funktionen der Neigungswinkel der Herdfläche sowie bestimmter Linearkombinationen der Elemente der weiter unten eingeführten Bewegungs-Spannungs-Matrix in der Herdtiefe h . Eine Tabelle der Koeffizienten d_l für die Herdmodelle Punktkraft, Krätedipol und Doppeldipol enthält die Arbeit von Harkrider [1970].

Das Problem, die Ausbreitungsfunktionen k_R und k_L , die Amplitudenantwortfunktionen A_R und A_L sowie die komplexen Abstrahlcharakteristiken χ_R und χ_L für eine bestimmte Rayleigh- oder Love-Mode und für ein vorgegebenes Modell des Herdes und des geschichteten Ausbreitungsmediums theoretisch und numerisch zu berechnen, bildet den Gegenstand einer umfangreichen Literatur. Ausgehend von den klassischen Publikationen von Rayleigh (1885), Lamb (1904) und Love (1911) wurden bis 1950 zahlreiche theoretische Arbeiten über die Ausbreitung von Oberflächenwellen in einfachen Schicht-Modellen veröffentlicht. Ein ausführliches Literaturverzeichnis über diesen Zeitraum enthält die Mono-

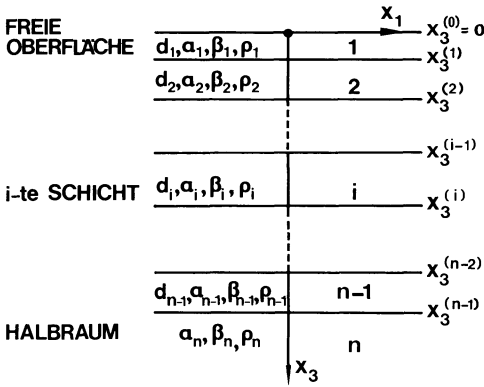


Abb. 2. Orientierung der Koordinatenachsen, Schicht- und Grenzflächenindizierung eines geschichteten elastischen Halbraums. Die Schichtparameter sind: d_i = Schichtmächtigkeit; α_i = P -Geschwindigkeit; β_i = S -Geschwindigkeit; ρ_i = Dichte für die Schicht mit dem Index i ($i = 1, \dots, N$). Die Halbraumparameter sind mit dem Index n bezeichnet

graphie „Elastic Waves in Layered Media“ von Ewing et al. (1957). Eine Behandlung realistischer Mehrschichtmodelle des Erdinnern konnte dagegen erst durch Anwendung der von Thomson (1950) und Haskell (1953) ausgearbeiteten Matrizenmethode sowie durch den Einsatz elektronischer Großrechenanlagen durchgeführt werden.

Die Thomson-Haskellsche Matrizenformulierung liefert eine elegante und für die Programmierung auf EDV-Anlagen geeignete Lösung des Ausbreitungsproblems freier Oberflächenwellen in einem geschichteten elastischen Halbraum. Wegen ihrer Bedeutung sollen die Grundgedanken der Theorie kurz skizziert werden.

Die Matrizenmethode beschreibt den von der x_3 -Koordinate (s. Abb. 2) allein abhängigen Anteil des Verschiebungs-Spannungsfeldes der Rayleigh- bzw. Love-Welle innerhalb der i -ten Schicht durch sog. Bewegungs-Spannungsmatrizen

$$s_{Ri}(x_3) = \{ \dot{U}_1^{(i)}(x_3)/c_R, \dot{U}_3^{(i)}(x_3)/c_R, P_{33}^{(i)}(x_3), P_{13}^{(i)}(x_3) \}^T \tag{2.12}$$

bzw.

$$s_{Li}(x_3) = \{ \dot{U}_2^{(i)}(x_3)/c_L, P_{23}^{(i)}(x_3) \}^T \tag{2.13}$$

T bezeichnet die Matrix-Transponierte. \dot{U}_1, \dot{U}_2 und \dot{U}_3 bedeuten die Fourier-Transformierten der radialen, azimutalen und vertikalen Komponente der Schwinggeschwindigkeit in der Tiefe x_3 , P_{13} und P_{23} bzw. P_{33} die entsprechenden Tangential- bzw. Normalspannungen.

Die Fundamentalbeziehung der Thomson-Haskellschen Methode formuliert nun den Zusammenhang zwischen den Bewegungs-Spannungsmatrizen der Rayleigh- bzw. Love-Welle innerhalb der i -ten Schicht ($i = 1, \dots, n - 1$) an den Stellen $x_3 \leq x_3^{(i)}$ (untere Begrenzungsebene der i -ten Schicht) und $x_3 = x_3^{(i-1)}$ (obere Begrenzungsebene der i -ten Schicht; s. Abb. 2) durch die Matrixgleichungen

$$s_{Ri}(x_3) = a_{Ri} s_{Ri}(x_3^{(i-1)}) \quad x_3^{(i-1)} < x_3 \leq x_3^{(i)} \tag{2.14}$$

bzw.

$$\mathbf{s}_{L_i}(x_3) = \mathbf{a}_{L_i} \mathbf{s}_{L_i}(x_3^{(i-1)}) \quad x_3^{(i-1)} < x_3 \leq x_3^{(i)} \quad (2.15)$$

\mathbf{a}_{R_i} bzw. \mathbf{a}_{L_i} sind (4, 4)- bzw. (2, 2)-Matrizen, deren Elemente komplizierte Funktionen der Schichtparameter, der Frequenz sowie der Wellenzahl bzw. Phasengeschwindigkeit sind.

Aus den Randbedingungen der Stetigkeit des Verschiebungs-Spannungsfeldes für die inneren Grenzflächen folgt:

$$\mathbf{s}_{R_i}(x_3^{(i)}) = \mathbf{s}_{R_{i+1}}(x_3^{(i)}) \quad i = 1, \dots, n-1 \quad (2.16)$$

$$\mathbf{s}_{L_i}(x_3^{(i)}) = \mathbf{s}_{L_{i+1}}(x_3^{(i)}) \quad i = 1, \dots, n-1. \quad (2.17)$$

Aus den Gleichungen (2.14) und (2.15) und den Randbedingungen (2.16) und (2.17) läßt sich ein Zusammenhang zwischen den Bewegungs-Spannungsmatrizen an der freien Oberfläche und an der oberen Begrenzungsebene des Halbraums ableiten:

$$\mathbf{s}_{R_n}(x_3^{(n-1)}) = \mathbf{a}_{R_{n-1}} \dots \mathbf{a}_{R_1} \mathbf{s}_{R_1}(x_3^{(0)}) = \mathbf{p}_R \mathbf{s}_{R_1}(x_3^{(0)}) \quad (2.18)$$

$$\mathbf{s}_{L_n}(x_3^{(n-1)}) = \mathbf{a}_{L_{n-1}} \dots \mathbf{a}_{L_1} \mathbf{s}_{L_1}(x_3^{(0)}) = \mathbf{p}_L \mathbf{s}_{L_1}(x_3^{(0)}). \quad (2.19)$$

In den Gleichungen (2.18) und (2.19) lassen sich die Randbedingungen an der freien Oberfläche (Verschwinden der Normal- und Tangentialspannungen) unmittelbar berücksichtigen. Daneben müssen die Ausstrahlungsbedingungen im Halbraum erfüllt werden. Sie fordern, daß in den Partikularlösungen der Wellengleichungen für den Halbraum, welche durch Superposition ebener P-SV- bzw. SH-Wellen mit positiven und negativen Ausbreitungsgeschwindigkeiten in x_3 -Richtung gebildet werden, die Anteile mit negativen Geschwindigkeiten verschwinden müssen. Die Amplituden der Partikularlösungen mit positiven Geschwindigkeiten werden in den (4, 1)- bzw. (2, 1)-Matrizen \mathbf{c}_{R_n} bzw. \mathbf{c}_{L_n} zusammengefaßt. Der Zusammenhang mit den Bewegungs-Spannungs-Matrizen des Halbraums wird durch die Matrizen $\mathbf{E}_{R_n}^{-1}$ bzw. $\mathbf{E}_{L_n}^{-1}$ formuliert, deren Elemente von den Kenngrößen des Halbraums ($\alpha_n, \beta_n, \rho_n$) abhängen:

$$\mathbf{c}_{R_n} = \mathbf{E}_{R_n}^{-1} \mathbf{p}_R \mathbf{s}_{R_1}(x_3^{(0)}) = \mathbf{J}_R \mathbf{s}_{R_1}(x_3^{(0)}) \quad (2.20)$$

$$\mathbf{c}_{L_n} = \mathbf{E}_{L_n}^{-1} \mathbf{p}_L \mathbf{s}_{L_1}(x_3^{(0)}) = \mathbf{J}_L \mathbf{s}_{L_1}(x_3^{(0)}). \quad (2.21)$$

Die Randbedingungen an der freien Oberfläche (Verschwinden der Normal- und Tangentialspannungen) und die Ausstrahlungsbedingungen im Halbraum (Verschwinden der Partikularlösungen mit negativen Ausbreitungsgeschwindigkeiten in x_3 -Richtung, d.h. keine Energiequellen im Unendlichen) reduzieren die Matrixgleichung (2.20) auf ein homogenes, lineares System von zwei Gleichungen für die Unbekannten $\dot{U}_1(x_3^{(0)})$ und $\dot{U}_3(x_3^{(0)})$. Die Koeffizientenmatrix des Gleichungssystems berechnet sich in einfacher Weise aus den Elementen der Rayleigh-Produktmatrix \mathbf{J}_R . Nullsetzen der zugehörigen Determinante liefert die Dispersionsgleichung

$$F_R(\omega, c) = 0 \quad (2.22)$$

deren reelle Lösungen die Dispersionsfunktionen

$$c_R^{(m)} = c_R^{(m)}(\omega) \quad (2.23)$$

für die Fundamentalmode ($m=0$) und die höheren Moden ($m=1, 2, \dots$) der Rayleigh-Welle ergeben. Durch Lösung des Gleichungssystems läßt sich dann mit Gleichung (2.23) die Oberflächenelliptizität der Rayleigh-Wellen

$$\varepsilon_0^{(m)}(\omega) = \dot{U}_1^{(m)}(x_3^{(0)}) / \dot{U}_3^{(m)}(x_3^{(0)}) \quad (2.24)$$

in Abhängigkeit von der Frequenz berechnen.

Entsprechend vereinfacht sich die Matrixengleichung (2.21) direkt zur Dispersionsgleichung

$$F_L(\omega, c) = 0 \quad (2.25)$$

der Love-Welle. Ihre reellen Lösungen sind die Dispersionsfunktionen

$$c_L^{(m)} = c_L^{(m)}(\omega) \quad (2.26)$$

der einzelnen Love-Moden ($m=1, 2, \dots$).

Die Amplituden-Tiefenfunktionen der Rayleigh- und Love-Wellen lassen sich aus den Gleichungen (2.14) und (2.15) unter Beachtung der Randbedingungen (2.16) und (2.17) und unter Berücksichtigung der Gleichungen (2.23), (2.24) und (2.26) berechnen. Sie beschreiben die für Oberflächen- und Grenzschichtwellen charakteristische Abhängigkeit der Eindringtiefe des Wellenfeldes von der Frequenz bzw. Wellenlänge. Die zweite, für die Anwendung wichtigste Eigenschaft der Rayleigh- und Love-Wellen ist ihre durch die Schichtung des Untergrundes bedingte geometrische Dispersion. Sie läßt sich strahlengeometrisch durch konstruktive Interferenz ebener P-SV- bzw. SH-Wellen deuten, die in dem als Wellenleiter wirkenden Schichtpaket verlustfrei geführt werden [s. z.B. Tolstoy und Usdin, 1953]. Die mit der Dispersion zusammenhängenden Probleme der Wellenausbreitung und Signalverformung werden im Abschnitt 3 ausführlich diskutiert.

Die Thomson-Haskellsche Matrizenmethode führt also die Berechnung der Dispersionsfunktionen und der Amplituden-Tiefenfunktionen auf die Operationen der Matrizenmultiplikation und der numerischen Lösung transzendenter Gleichungen zurück. Dagegen erfordert die exakte Lösung für einen inhomogenen Halbraum mit stückweise stetigen Parameter-Tiefenfunktionen die Lösung eines Systems von Differentialgleichungen (Gilbert und Backus, 1966) und damit im allgemeinen erheblich längere Rechenzeiten. Die ersten, auf dem Matrizen-Algorithmus basierenden EDV-Programme wurden von Dorman et al. (1960) sowie von Press et al. (1961) beschrieben. Um die bei höheren Moden und Frequenzen auftretenden, durch die endliche Wortlänge der Rechanlage bedingten numerischen Instabilitäten zu umgehen, haben Thrower (1965) und Dunkin (1965) sowie Watson (1970) verschiedene Varianten der Matrizenmethode ausgearbeitet (sog. Δ -Matrix- bzw. reduzierte Δ -Matrix-Darstellung; Pestel und Leckie (1963)). Eine weitere, verallgemeinerte Formulierung der Matrizenmethode für geschichtete Medien wurde von Knopoff (1964) entwickelt. Die Programmierung sowie verschiedene Anwendungsbeispiele der Knopoffschen Methode für Rayleigh-Wellen und P-SV-Raumwellen hat Randall (1967) diskutiert.

Die Erstellung von optimalen Dispersionsprogrammen (d. h. Programmen mit minimaler Rechenzeit bei vorgegebener und kontrollierter Genauigkeit) bildet eine wichtige Voraussetzung für die Inversion von Beobachtungsdaten nach der „Hedgehog“- bzw. „Monte Carlo“-Methode (s. Abschnitt 5). Nach Untersuchungen von Schwab und Knopoff (1970) sowie Schwab (1970) liefern die Knopoffsche Theorie und die reduzierte Δ -Matrix-Darstellung (Watson, 1970) die günstigsten Resultate. Danach beträgt die Rechenzeit auf einer Großrechenanlage (z. B. IBM 360/91) pro Phasengeschwindigkeitswert der Rayleigh-Welle bei 5stelliger Genauigkeit für ein 10-Schichtenmodell etwa 10 ms. Das Problem, die Dispersionsfunktionen der Rayleigh- und Love-Wellen für einen geschichteten elastischen Halbraum zu berechnen, kann demnach theoretisch und numerisch als vollständig gelöst angesehen werden.

Harkrider (1964) hat die Matrizenmethode auf die Berechnung der Amplitudenantwortfunktion und der komplexen Abstrahlcharakteristik erweitert und Tabellen zur schnellen Abschätzung der Amplituden- und Phasenspektren von Rayleigh- und Love-Wellen in Abhängigkeit von der Herdtiefe angegeben (Harkrider, 1970).

Die Abstrahlung von Oberflächenwellen durch bewegte Quellen wurde von Ben-Menahem (1961), Haskell (1964, 1966) u. a. untersucht. In diesem Fall ist das Herdspektrum $S(j\omega)$ in den Gleichungen (2.1) und (2.2) für Rayleigh- und Love Wellen verschieden und hängt von der Ausdehnung des Herdes, von der Bruchgeschwindigkeit sowie von der Vorgeschichte des Bruches ab.

Elastische Kugel

Die Dispersionskurven fortschreitender Rayleigh- bzw. Love-Wellen lassen sich als quasi-kontinuierlicher, asymptotischer Grenzwert des Eigenfrequenzspektrums der sphäroidalen bzw. torsionalen Eigenschwingungen (stehende Wellen) der Erde für hohe Frequenzen interpretieren. Zur Berechnung der Dispersion von Oberflächenwellen in einer radialsymmetrisch geschichteten Erde unter Berücksichtigung des Schwerfeldes können grundsätzlich zwei Verfahren angewendet werden:

(a) Lösung des freien Randwertproblems für die Kugel und Umrechnung der Eigenfrequenzen ${}_n\omega_l$ der sphäroidalen (${}_nS_l$) bzw. torsionalen (${}_nT_l$) Eigenschwingungen in die Phasengeschwindigkeiten der Rayleigh- bzw. Love-Wellen mit der Formel von Jeans (1923).

$$c = {}_n\omega_l \cdot a / (l + 1/2) \quad l > 20 \quad (2.27)$$

(a Erdradius, n radiale Ordnungszahl, l breitenabhängige Ordnungszahl).

Von den zahlreichen Publikationen über Eigenschwingungen und sphärische Oberflächenwellen seien die grundlegenden Arbeiten von Alterman et al. (1959, 1961), Bolt und Dorman (1961) sowie von Gilbert und MacDonald (1960) erwähnt. Zusammenfassende Darstellungen haben Bolt (1964) sowie Takeuchi und Saito (1972) veröffentlicht.

(b) Transformation der geschichteten Kugel in einen geschichteten Halbraum („earth-flattening approximation“), Berechnung der Dispersionskurven mit der

Matrizenmethode und Anwendung der Rücktransformation Kugel-Halbraum. Der Hauptvorteil dieses Verfahrens ist neben der geringeren Rechenzeit die Möglichkeit, Phasen- und Gruppengeschwindigkeiten für beliebig vorgegebene Perioden zu berechnen. Nach Vorarbeiten von Alterman et al. (1961), Kovach und Anderson (1962), Anderson und Toksöz (1963) u.a. konnten Biswas und Knopoff (1970) die exakte Transformation einer geschichteten Kugel in einen geschichteten isotropen Halbraum für Love-Wellen ableiten. Kausel und Schwab (1973) haben mit Hilfe der „Biswas-Knopoff“-Transformation die Abstrahlung von Love-Wellen durch eine Punktquelle in einer Kugel berechnet. Eine erste Näherung der entsprechenden Transformation für Rayleigh-Wellen wurde von Schwab und Knopoff (1972) sowie von Biswas (1972) angegeben. Schwab und Knopoff (1972) haben in einem Übersichtsartikel vor allem die numerischen Aspekte der Kugel-Halbraum-Transformation ausführlich dargestellt.

Anelastische Modelle

In den bisher betrachteten Modellen wurden die Raumwellengeschwindigkeiten α und β unter Vernachlässigung der Absorption und der materiellen Dispersion der P - und S -Wellen als reelle, frequenzunabhängige Materialgrößen angesetzt. Die Ausbreitung der Rayleigh- und Love-Wellen erfolgt dann verlustfrei mit einer durch die reelle Funktion $k(\omega)$ charakterisierten rein geometrischen Dispersion. Eine erweiterte, die Absorption einschließende Theorie läßt sich formal durch Einführung einer komplexen Ausbreitungsfunktion

$$k^*(\omega) = k(\omega) - j\kappa(\omega) \quad (2.28)$$

entwickeln. Die reelle Ausbreitungsfunktion $k(\omega)$ enthält die Dispersion, der Absorptionskoeffizient $\kappa(\omega)$ die Absorption. Als zweckmäßiges dimensionsloses Dissipationsmaß hat sich der aus der Elektrotechnik entlehnte spezifische Gütefaktor in der Seismologie eingebürgert. Für fortschreitende Wellen gilt:

$$Q_X^{-1}(\omega) = \frac{2\kappa(\omega)}{k(\omega)} = \frac{q(\omega)}{k(\omega) \cdot s(\omega)} \quad (2.29)$$

q bedeutet die pro Volumen- und Zeiteinheit absorbierte Energie, s den Betrag des Vektors der Energiestromdichte.

In Analogie zu Gleichung (2.28) läßt sich eine durch Dissipation abklingende Eigenschwingung durch eine komplexe Frequenz

$$\omega_n^* = \omega_n - j\gamma_n \quad (2.30)$$

mit der reellen Eigenfrequenz ω_n und der Abklingkonstanten γ_n beschreiben. Für den spezifischen Gütefaktor Q_T gilt dann:

$$Q_T^{-1}(\omega_n) = \frac{2\gamma_n}{\omega_n} = \frac{q_n}{\omega_n \cdot e_n} \quad (2.31)$$

q_n bedeutet wieder die pro Zeit- und Volumeneinheit absorbierte Energie, e_n

die Amplitude der Energiedichte für die Eigenschwingung mit der radialen Ordnungszahl n .

Zwischen den Gütefaktoren Q_X und Q_T besteht eine der Jeansschen Formel in Gleichung (2.27) entsprechende Umrechnungsrelation (Brune, 1962; Knopoff et al., 1964; Seidl, 1971):

$$cQ_X = UQ_T. \quad (2.32)$$

In einem geschichteten anelastischen Halbraum treten als neue Schichtparameter die Gütefaktoren Q_{α_i} und Q_{β_i} der P - und S -Wellen auf. Sie lassen sich in erster Näherung als frequenzunabhängige Größen betrachten. Dieser Näherungsansatz ist allerdings weniger durch eine Extrapolation der bei hohen Frequenzen gewonnenen Labordaten begründet (s. z. B. Knopoff, 1964), sondern vielmehr durch die große Streuung der bis heute vorliegenden experimentellen Q -Daten von Oberflächenwellen gerechtfertigt (s. Abschnitt 6). Ebenso kann man aus der Beobachtung scharfer P - und S -Wellenimpulse in großen Epizentralentfernungen schließen, daß die materielle Dispersion der P - und S -Wellen zu vernachlässigen ist, d. h. daß auch die Schichtparameter α_i und β_i in erster Näherung als frequenzunabhängig anzusetzen sind. Theoretische Betrachtungen auf Grund der Kramers-Kronig-Relationen von Futterman (1962) und Lamb (1962) bestätigen diese Annahme.

Die Berechnung der Phasengeschwindigkeit $c(\omega)$ und des spezifischen Gütefaktors $Q_X(\omega)$ der Rayleigh- bzw. Love-Wellen aus den Schichtparametern $\alpha_i, Q_{\alpha_i}, \beta_i, Q_{\beta_i}, \rho_i, d_i$ ($i=1 \dots N$; N Schichtanzahl) liefert in erster linearer Näherung folgendes Resultat (s. z. B. Yamakawa und Sâto, 1964; Anderson und Archambeau, 1964; Anderson et al., 1965; Seidl, 1971): Die mit der Absorption verknüpfte materielle Dispersion ist um einen Faktor von der Größenordnung 10^{-5} kleiner als die geometrische Dispersion $c(\omega)$ des elastischen Halbraums und kann daher in erster Näherung vernachlässigt werden. Für den spezifischen Gütefaktor folgt dann:

$$Q_X^{-1}(\omega) = \frac{1}{c(\omega)} \sum_{i=1}^N \left[\frac{\alpha_i}{Q_{\alpha_i}} \frac{\partial c(\omega)}{\partial \alpha_i} + \frac{\beta_i}{Q_{\beta_i}} \frac{\partial c(\omega)}{\partial \beta_i} \right]. \quad (2.33)$$

Für Love-Wellen vereinfacht sich Gleichung (2.33), da die partiellen Ableitungen nach den P -Geschwindigkeiten α_i in diesem Fall verschwinden.

Die exakte Berechnung des spezifischen Gütefaktors $Q(\omega)$ und der Dispersionsfunktion $c(\omega)$ von Oberflächenwellen in anelastischen, ebenen und sphärischen Schichtmodellen mit Hilfe der Matrizenmethode wurde erstmals von Schwab und Knopoff (1971, 1972, 1973) durchgeführt. In diesem Fall sind die Dispersionsgleichungen (2.22) und (2.25) komplex. Ihre komplexen Lösungen enthalten die Absorption und die gesamte Dispersion der Rayleigh- und Love-Wellen, die sich aus der mit den Randbedingungen verknüpften geometrischen und der durch die Anelastizität bedingten materiellen Dispersion zusammensetzt. Ihren größten Betrag erreicht die materielle Dispersion für die erste Love-Wellenmode in einem ozeanischen, sphärischen Modell mit etwa 0,003 km/s im Periodenbereich um 25 s. Die Methode von Schwab und Knopoff ist ohne Modifikation auch dann anwendbar, wenn die Phasengeschwindigkeiten und Gütefaktoren der P - und S -Wellen frequenzabhängige Terme enthalten.

Heterogene Strukturen

Mit dem Ansatz lateral homogener anelastischer Schichtmodelle läßt sich die Dispersion und Absorption langperiodischer Rayleigh- und Love-Wellen bei ihrer Ausbreitung durch die Erde in sehr guter Näherung beschreiben. Im kurzperiodischen Spektralbereich beobachtet man zusätzlich sekundäre, an heterogenen Strukturen der Kruste und des oberen Mantels ausgelöste Oberflächenwellen, die mit den hochauflösenden Wellenzahl-Frequenz-Filtern der modernen Arraytechnik (Capon et al., 1967; Capon, 1969) separiert und als Nutzsignale interpretiert werden können. So konnte die von Pilant und Knopoff (1964) zur Erklärung von Schwebungserscheinungen in teleseismischen Oberflächenwellen diskutierte Mehrfachwegausbreitung von Capon (1970, 1971) sowie von Capon und Evernden (1971) mit dem LASA-Array durch strahlengeometrische Rekonstruktion der durchlaufenen Wellenwege unter Anwendung des Snelliusschen Brechungsgesetzes verifiziert werden. Allgemeine Sätze über die Phasen- und Gruppengeschwindigkeiten von Oberflächenwellen in lateral heterogenen Medien haben Knopoff (1969) und Julian (1972) abgeleitet. Die Messung der Phasengeschwindigkeit mit regionalen Stationsnetzen in Gebieten mit ortsabhängiger Dispersion wurde von Knopoff et al. (1967) untersucht.

Bei der theoretischen Behandlung von Schichtmodellen mit geneigten Grenzflächen sowie stetigen oder sprunghaften Übergangszonen lassen sich zwei Klassen von Näherungsverfahren unterscheiden:

(a) Analytische Näherungslösungen für einfache Modelle durch Anwendung der Methode der Greenschen Funktion, der Variationsrechnung u.a.

(b) Numerische Näherungslösungen für komplexe, realistische Modelle durch Anwendung der „Finite Difference“- bzw. der „Finite Element“-Methode.

Es werden in der Regel zweidimensionale Modelle und senkrecht einfallende, monochromatische Wellen behandelt. Die Rechnung liefert Näherungswerte für die ortsabhängige Dispersion sowie für die Reflexions- und Transmissionskoeffizienten der einfallenden Welle und der durch Modenkonzersion entstehenden Sekundärwellen.

Aus der Vielzahl der in der Literatur – vor allem für Love-Wellen – diskutierten analytischen Näherungslösungen soll eine Gruppe herausgegriffen werden, welche die Methode der Greenschen Funktion anwenden. Ausgangspunkt sind die Darstellungstheoreme der Elastodynamik, die den Verschiebungsvektor in einem Beobachtungspunkt als Oberflächenintegral über eine den Punkt umschließende Randfläche (bzw. Randkurve für zweidimensionale Probleme) darstellen. Der Integrand enthält neben der Greenschen Tensorfunktion des Problems das aus Primär- und Sekundärwellen zusammengesetzte Verschiebungsfeld auf der Berandungsfläche. Während die Greensche Funktion im Prinzip beliebig genau approximiert werden kann, muß für das Verschiebungsfeld entlang der Randfläche auf Grund vorwiegend physikalischer Überlegungen ein Näherungsansatz aufgestellt werden.

Hudson und Knopoff (1964) haben mit der Methode der Greenschen Funktion den Reflexionskoeffizienten einer Love-Welle an der keilförmigen Kante eines Zweischichtenmodells in erster Näherung berechnet. Das Problem der Reflexion und Transmission von Rayleigh-Wellen in einem homogenen Keil wurde von

Hudson und Knopoff (1964) sowie von Mal und Knopoff (1966) diskutiert. Um die Amplitudenänderung von Love-Wellen an Kontinentalrändern zu untersuchen, haben Knopoff und Hudson (1964) den Transmissionskoeffizienten von Love-Wellen an einer Sprungstelle der freien Oberfläche eines Zweischichtenmodells abgeleitet. Trotz der extrem stark vereinfachten Übergangszone und des Näherungscharakters der Lösung dürfte das Ergebnis zumindest qualitativ von praktischem Interesse sein. Danach weist der auf die Amplitude an der freien Oberfläche normierte Transmissionskoeffizient bei senkrechtem Einfall eine deutliche Anisotropie des Betrags und der Frequenzabhängigkeit für die Ausbreitungsrichtungen Ozean-Kontinent bzw. Kontinent-Ozean auf. Während der Transmissionskoeffizient im ersten Fall mit zunehmender Frequenz stark abfällt, treten im zweiten Fall nur sehr schwach ausgeprägte Variationen auf. Die tiefrequenten Grenzwerte hängen allein vom richtungsabhängigen Verhältnis der beiden Schichtmächtigkeiten ab [s. auch Knopoff et al., 1970]. Bei Übergangszonen mit stetig geneigten Grenzflächen tritt zusätzlich eine Anisotropie der Dispersion auf [Knopoff und Mal, 1967]. Den Hauptbetrag liefert dabei die Rückwärtsreflexion von der geneigten Grenzfläche, während die Störung der Eigenwerte (geometrische Dispersion) bei kleinen Neigungswinkeln ein Effekt zweiter Ordnung ist. Das wesentlich schwierigere (vektorielle) Problem der Ausbreitung von Rayleigh-Wellen in inhomogenen Übergangsstrukturen konnte bisher nur für den einfachsten Fall eines homogenen Halbraums mit stufenförmiger freier Oberfläche in erster Näherung gelöst werden [Mal und Knopoff, 1965].

Im Gegensatz zu den analytischen Näherungsverfahren lassen sich mit den numerischen Rechentechniken der „Finite Difference“- bzw. „Finite Element“-Methode komplexe, realistische Modelle von heterogenen Übergangsstrukturen behandeln. Zusammenfassende Darstellungen enthalten die Übersichtsartikel von Boore (1972) („Finite Difference“-Methode) sowie von Lysmer und Drake (1972) („Finite Element“-Methode). Im folgenden sollen einige besonders instructive Anwendungsbeispiele dieser numerischen Näherungsverfahren herausgegriffen werden.

Eine Berechnung der Dispersionskurven von Rayleigh-Wellen in einem geschichteten elastischen Halbraum mit Hilfe der „Finite Element“-Methode wurde erstmals von Lysmer (1970) durchgeführt. Heterogene zweidimensionale Schichtmodelle werden in der Regel aus drei Anteilen zusammengesetzt: Zwei geschichteten Halbräumen mit horizontalen Grenzflächen, die durch eine Übergangszone mit geneigten Schichtgrenzen verbunden sind. Die Rechnung liefert Näherungswerte für die Reflexions- und Transmissionskoeffizienten sowie für die Phasengeschwindigkeiten ebener, monochromatischer Oberflächenwellen, die aus einem der beiden Halbräume senkrecht auf die Übergangszone auftreffen. Durch Anwendung der „Finite Element“-Methode konnte Drake (1972) die Phasengeschwindigkeiten und Verschiebungsfelder von Rayleigh- und Love-Wellen ableiten, die sich in einem homogenen elastischen Halbraum sowie in einem Zweischichtenmodell mit einer rampenförmigen Übergangszone der freien Oberfläche bzw. der inneren Schichtgrenze ausbreiten. Boore (1970) hat mit der „Finite Difference“-Methode die Ausbreitung von Love-Wellen in einem einfachen Zweischichtenmodell für die Übergangszone Ozean-Kontinent untersucht und eine ausgeprägte Anisotropie der Phasengeschwindigkeiten und Amplituden

nachgewiesen. Das entsprechende Problem für ein detailliertes Modell dieser Übergangszone sowie für eine unter 45° abtauchende Lithosphärenplatte konnte von Lysmer und Drake (1971) mit der „Finite Element-Methode“ gelöst werden. Ist die Primärwelle die Grundmode der Love-Wellen, so ist in beiden Modellen die reflektierte Energie sehr klein, während ein erheblicher Energieanteil für die transmittierte Welle durch Konversion in höhere Moden übergeht. Im Gegensatz zur Love-Welle wird die Energie der Grundmode der Rayleigh-Welle beim Passieren einer Übergangszone vom Ozean zum Kontinent nur geringfügig durch Reflexion und Konversion abgeschwächt [Drake, 1972]. Als besonders instruktives Anwendungsbeispiel für die Leistungsfähigkeit der „Finite Element“-Methode sei noch eine Arbeit von Drake und Mal (1972) zitiert, in der die Ausbreitung kurzperiodischer Rayleigh- und Love-Wellen entlang einer Nord-Süd-Achse des San Fernando-Tals (Kalifornien) behandelt wird.

3. Beobachtung

In Erdbebenseismogrammen lassen sich zwei Haupttypen von Signalformen der Rayleigh- und Love-Wellen unterscheiden: Quasi-harmonische Schwingungszüge mit zeitlich veränderlicher Momentanfrequenz und impulsförmige, schwach dispergierte Signale. Unter der Annahme eines kurzzeitigen Herdimpulses wird das Seismogrammbild im Fernfeld im wesentlichen von den Dispersionsmerkmalen des durchlaufenen Wellenweges bestimmt. Für eine pauschale Seismogrammauswertung sind dann einige allgemeine Sätze über den Zusammenhang zwischen Signalverformung und Dispersion von großem Nutzen, die am Beispiel einer ebenen Welle kurz diskutiert werden sollen.

Die Verformung, die ein Signal $f_0(t)$ mit dem Spektrum $F_0(j\omega)$ beim Durchlaufen eines verlustfreien, dispergierenden Systems erfährt, kann durch ein Fourier-Integral ähnlich Gleichung (2.5) dargestellt werden:

$$f(t, x_1) = \frac{1}{2\pi} \int_{-\infty}^{+\infty} F_0(j\omega) \exp[j(\omega t - k(\omega)x_1)] d\omega. \quad (3.1)$$

Aus der Ausbreitungsfunktion $k(\omega)$ lassen sich die Dispersionsfunktionen der Phasengeschwindigkeit

$$c(\omega) = \omega/k(\omega) \quad (3.2)$$

und der Gruppengeschwindigkeit

$$U(\omega) = 1/[dk(\omega)/d\omega] = c^2(\omega)/[c(\omega) - \omega c'(\omega)] \quad (3.3)$$

ableiten.

Nimmt die Phasengeschwindigkeit $c(\omega)$ mit zunehmender Frequenz ab ($c'(\omega) < 0$), so spricht man von normaler Dispersion. Dabei ist nach Gleichung (3.3) die Gruppengeschwindigkeit U kleiner als die Phasengeschwindigkeit c . Dieser Fall ist bei seismischen Oberflächenwellen die Regel. Bei anomaler Dispersion ($c'(\omega) > 0$) ist die Gruppengeschwindigkeit U größer als die Phasengeschwindigkeit c . Ein Beispiel ist die anomale Dispersion ozeanischer Rayleigh-Wellen

im Periodenbereich von etwa 30 bis 70 s. In beiden Fällen unterscheidet man noch zwischen den Begriffen der regulären ($U'(\omega) < 0$) und der inversen ($U'(\omega) > 0$) Dispersion.

Eine näherungsweise Auswertung des Integrals in Gleichung (3.1) mit der Methode der stationären Phase liefert folgendes Resultat [s. z. B. Pekeris, 1948; Tolstoy und Clay, 1966; Tolstoy, 1973]:

Der Aufbau des Seismogramms wird im Fernfeld durch die Gruppengeschwindigkeit $U(\omega)$ bestimmt. Aus der Stationaritätsbedingung des Integrals in Gleichung (3.1) folgt:

$$t = x_1 dk(\omega)/d\omega = x_1/U(\omega). \quad (3.4)$$

Den Ästen der Gruppengeschwindigkeitskurve mit regulärer bzw. inverser Dispersion entsprechen amplituden- und frequenzmodulierte Signale, deren Momentanfrequenz sich nach Gleichung (3.4) als Funktion von Ort und Zeit ändert und deren Amplitude infolge der Dispersion proportional zu $x_1^{-1/2}$ abnimmt. Die den Frequenzen mit extremalen Werten der Gruppengeschwindigkeit zugeordneten amplitudenmodulierten Signale werden als AIRY-Phasen bezeichnet. Ihre durch Dispersion bedingte Amplitudenabnahme erfolgt proportional zu $x_1^{-1/3}$. Pekeris (1948) hat die Eigenschaften der AIRY-Phasen theoretisch untersucht und explizite Ausdrücke für ihre Amplitudeneinhüllenden abgeleitet.

Obwohl mit der Methode der stationären Phase eine Reihe wichtiger Aussagen über die Pauschalstruktur eines Wellensignals im Fernfeld gemacht werden kann, ist es nicht möglich, auf diese Weise exakte synthetische Seismogramme zu berechnen. Dieses Problem läßt sich jedoch durch numerische Integration von Gleichung (3.1) mit dem Algorithmus der schnellen Fourier-Transformation (Cooley und Tukey, 1965) für irgendein Eingangssignal $f_0(t)$ und ein beliebiges elastisches oder anelastisches Schichtmodell lösen (Seidl, 1971).

Abbildung 3 zeigt eine Montage synthetischer Seismogramme der Rayleigh-Grundmode für ein elastisches Modell, dessen Gruppengeschwindigkeitskurve $U(\omega)$ den für kontinentale Rayleigh-Wellen typischen Verlauf aufweist.

Anhand der $U(\omega)$ -Kurve läßt sich der Aufbau des Seismogramms im Fernfeld ableiten. Es beginnt mit der weich einsetzenden „umgekehrten AIRY-Phase“ (Pekeris, 1948) des Gruppengeschwindigkeitsmaximums bei $T = 57$ s. Die für einen Einschwingvorgang mit minimaler Gruppenlaufzeit charakteristische Asymmetrie in der Aufeinanderfolge der Maxima und Minima (Müller und Ewing, 1962) ist deutlich zu erkennen. Der Signaleinsatz erfolgt vor dem Zeitpunkt minimaler Gruppenlaufzeit. Diese Erscheinung läßt sich durch die Unschärferelation zwischen der effektiven zeitlichen Dauer eines Signals und seiner effektiven spektralen Bandbreite erklären (Müller und Ewing, 1962). Die AIRY-Phase geht in einen regulär dispergierten Schwingungszug über, dem sich zum Zeitpunkt $t = x_1/U_0$ ein hochfrequentes, invers dispergiertes Signal, die sog. Rg-Phase überlagert. U_0 bedeutet dabei den Wert des relativen Gruppengeschwindigkeitsmaximums für die Periode Null. Das Seismogramm endet mit der AIRY-Phase des Gruppengeschwindigkeitsminimums. Die Amplitudeneinhüllende der AIRY-Phasen zeigt den von der Theorie (Pekeris, 1948) geforderten Verlauf. Der Zeitpunkt des Maximums der Einhüllenden liegt vor bzw. nach der aus den Werten der minimalen bzw. maximalen Gruppengeschwindigkeit berechneten

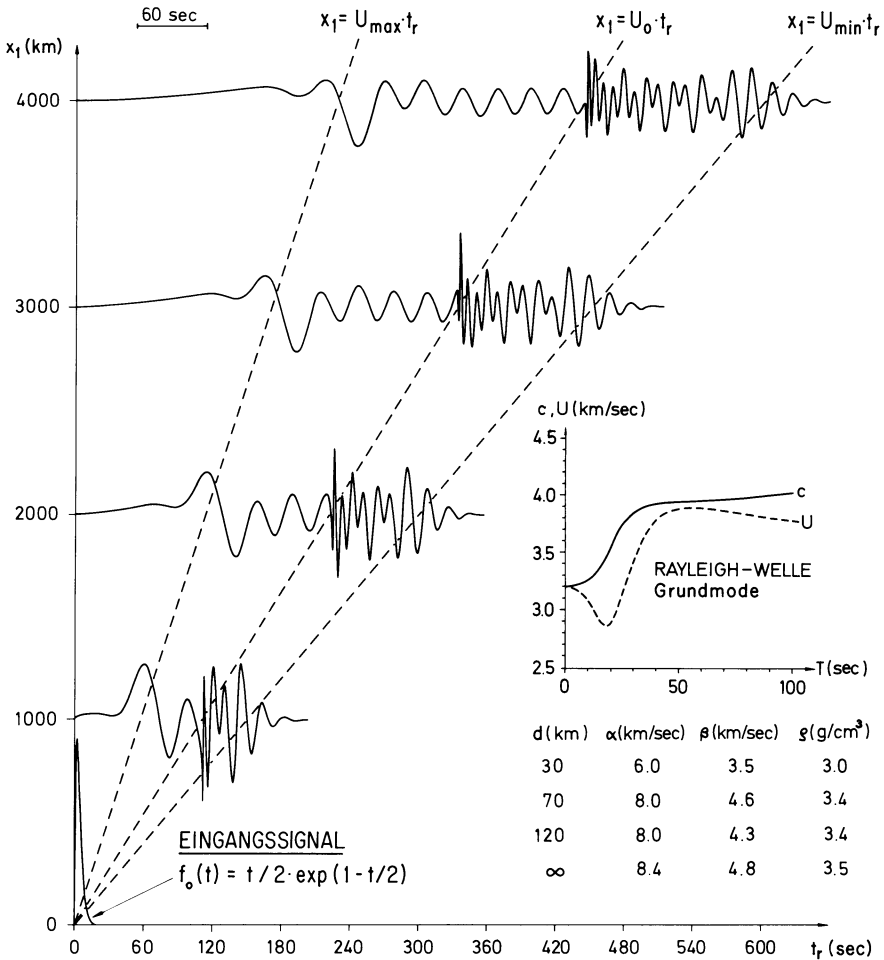


Abb. 3. Montage synthetischer Seismogramme der Rayleigh-Grundmode für ein elastisches Schichtmodell. Reduzierte Zeit: $t_r = t - x_1/V_r$; Reduktionsgeschwindigkeit: $V_r = 5.0$ km/s

theoretischen Gruppenlaufzeit. Tolstoy und Clay (1966) haben Näherungsformeln für die zeitliche Dauer bzw. spektrale Bandbreite von AIRY-Phasen abgeleitet. Eine starke Krümmung der U -Kurve führt zu quasi-harmonischen, eine schwache Krümmung zu impulsförmigen AIRY-Phasen.

Zur phänomenologischen Beschreibung von besonders markanten impulsförmigen Oberflächenwellen werden historisch bedingte Buchstabensymbole verwendet (G, Sa, Ma, Rg, Lg, Li, usw.). Eine ausführliche Zusammenstellung der kinematischen und spektralen Kenndaten dieser Phasen enthält der Übersichtsartikel über Oberflächenwellen von Kovach (1965). Die Zuordnung zu bestimmten Ästen der Gruppengeschwindigkeitskurven der Rayleigh- und Love-Wellen ist bisher nur teilweise gelungen. So entspricht die G-Welle dem breiten Gruppengeschwindigkeitsplateau des ozeanischen Astes der ersten Love Mode (s. z.B.

Oliver, 1962). Die kontinentale Rg-Phase ist dem invers dispergierten kurzperiodischen Ast der Rayleigh-Grundmode zugeordnet. Eine detaillierte Interpretation der kontinentalen Lg-Phase als höhere Love-Wellenmode unter Berücksichtigung von Herdmechanismus, Dispersion und Absorption eines kontinentalen Schichtmodells sowie der Frequenzcharakteristik des aufzeichnenden Seismographensystems wurde von Knopoff et al. (1973) durchgeführt. Die Phasen Ma und Sa leiten sich von den im Periodenbereich zwischen etwa 10 und 30 s invers dispergierten Ästen der ersten höheren Rayleigh-Mode bzw. der zweiten Love-Mode ab, deren Dispersionsmerkmale durch die Struktur des Asthenosphären-Kanals im oberen Erdmantel bestimmt werden.

Die Existenz dieses Kanals begründet auch eine wichtige Einteilung der Oberflächenwellen in sog. „Kanalwellen“ und „Krustenwellen“ (Andrianova et al., 1965; Panza et al., 1972). Ihre Dispersionskurven setzen sich aus den Segmenten der c -Kurven benachbarter Moden mit annähernd gleicher Steigung zusammen. Die diesen Segmenten zugeordneten Amplituden-Tiefenprofile liegen für die „Kanalwellen“ fast ausschließlich innerhalb des Kanals und sind an der Erdoberfläche nicht meßbar. Für die Beobachtung sind daher nur diejenigen Segmente der Phasengeschwindigkeitskurven relevant, die das System der „Krustenwellen“ mit nicht verschwindenden Amplituden an der Erdoberfläche bilden.

Die bisherigen Betrachtungen haben die zentrale Bedeutung der Gruppengeschwindigkeit für den Ausbreitungsvorgang seismischer Oberflächenwellen aufgezeigt. Durch Gleichung (3.4) werden jedem Punkt der (x_1, t) -Ebene in Abbildung 3 im Zeitintervall $x_1/U_{\max} < t < x_1/U_{\min}$ definierte Momentanfrequenzen zugeordnet. Die Kurven konstanter Momentanfrequenz ω sind Geraden mit der Steigung $U(\omega)$. Neben dieser formalen besitzt die Gruppengeschwindigkeit eine sehr anschauliche kinematische bzw. energetische Bedeutung. Nach Macke (1962) bewegt sich der Energieschwerpunkt einer Wellengruppe mit konstanter Geschwindigkeit. Diese Schwerpunktgeschwindigkeit ist gleich der über alle zur Wellengruppe beitragenden Wellenzahlen gemittelten Gruppengeschwindigkeit, wobei als Gewichtsfunktion die Energiedichte im Wellenzahlraum fungiert. Für verlustfrei geführte Wellen ist die Gruppengeschwindigkeit identisch mit der als Quotient Energiestromdichte zu Energiedichte definierten Geschwindigkeit des Energietransports (Biot, 1957).

4. Analyse

Die Grundaufgabe der numerischen Analyse seismischer Oberflächenwellen besteht darin, aus der entlang einer Stationslinie in Wellenausbreitungsrichtung beobachteten Signalverformung die Phasengeschwindigkeit, die Gruppengeschwindigkeit sowie den spezifischen Gütefaktor für jede angeregte Mode als Funktion der Periode zu ermitteln. Da das Wellenazimut im Fernfeld auf Grund durchlaufener heterogener Strukturen in der Regel nicht mit der erforderlichen Genauigkeit aus den Koordinaten des Epizentrums berechnet werden kann, sind zur exakten Richtungs- und Geschwindigkeitsmessung mindestens drei, nicht auf einem Großkreis gelegene Stationen notwendig. Die Dispersionsdaten werden dann derjenigen Stationslinie zugeordnet, die annähernd parallel zur Wellenaus-

breitungsrichtung orientiert ist (Press, 1956; Knopoff et al., 1967). Diese sog. „Zwei-Stationenmethode“ ist das wichtigste Hilfsmittel zur Kartierung von regionalen Dispersionskurven. Daneben lassen sich Phasen- und Gruppengeschwindigkeitsmessungen auch mit einer Station durchführen (s. z.B. Brune et al., 1960; Schneider et al., 1966), und zwar entweder für den Wellenweg Epizentrum-Station oder für den Großkreis durch beide Punkte aus der Beobachtung von Wiederkehrwellen.

Ein Näherungsverfahren der Dispersionsanalyse im Zeitbereich ist die klassische „peak-and-trough“ Methode, deren Anwendungsbereich allerdings auf ungestörte, regulär oder invers dispergierte Wellengruppen beschränkt ist (s. z.B. Savarenski, 1959). Eine Analyse im Frequenzbereich durch Fourier-Transformation (Satô, 1955) ist zwar für beliebig dispergierte Signale anwendbar, setzt aber ebenfalls ungestörte, überlagerungsfreie Seismogramme voraus. Für den Einsatz auf EDV-Anlagen wurden neue Verfahren der numerischen Dispersionsanalyse entwickelt, die sich auch auf die in der Regel sehr komplexen, aus mehreren Teilsignalen (verschiedene Moden, multiple Phasen, kontinentale und ozeanische Anteile) zusammengesetzten Seismogramme energiereicher Fernbeben anwenden lassen. Eine Spektralanalyse im Zeit-Frequenzbereich sowie die Anwendung zeitabhängiger Filter zur Signalseparation sind die entscheidenden Merkmale dieser modernen Programmsysteme.

Eine Analyse seismischer Oberflächenwellen im Zeit-Frequenzbereich wurde erstmals von Ewing et al. (1959) auf analogem Wege mit einem Schallspektrographen und von Iyer (1964) in digitaler Form durch Berechnung von Energie-Konturdiagrammen durchgeführt. Alexander (1963) konnte durch die kombinierte Anwendung eines Bandpaßfilters und eines zeitabhängigen Gruppenlaufzeitfilters einzelne Moden separieren und getrennt analysieren. Das erste kompakte Programmsystem haben Knopoff et al. (1966) veröffentlicht. Ausgehend von diesen grundlegenden Arbeiten wurden neue digitale Auswerteverfahren mit größerer Genauigkeit und erhöhtem Auflösungsvermögen entwickelt: Die „Summen-Differenzen-Methode“ bzw. die „Produkt-Methode“ (Bloch und Hales, 1968), die „Moving-Window-Analyse“ (Landisman et al., 1969), die „Multiple Filtertechnik“ (Dziewonski et al., 1969) sowie die „Residuen-Dispersionsmessung“ (Dziewonski et al., 1972). Eine zusammenfassende Darstellung dieser modernen Rechentechniken enthalten die Übersichtsartikel von Dziewonski et al. (1968) sowie von Dziewonski und Hales (1972).

Im folgenden werden die wichtigsten Verfahren der Dispersionsanalyse für den speziellen Fall einer ebenen Oberflächenwelle diskutiert, die sich in Richtung der positiven x_1 -Achse ausbreitet und in zwei Stationen mit den Koordinaten $x_1^{(i)}$ ($i=1, 2$) von idealen Seismographensystemen verzerrungsfrei aufgezeichnet wird. Der zeitliche Verlauf des Seismogramms in der Station i ($i=1, 2$) sei $f_i(t)$, das zugehörige Spektrum $F_i(j\omega)$. Es wird zunächst vorausgesetzt, daß nur eine einzige Mode angeregt ist. Dann läßt sich das Seismogramm $f_2(t)$ in Analogie zu Gleichung (3.1) durch ein Fourier-Integral

$$f_2(t) = \frac{1}{2\pi} \int_{-\infty}^{+\infty} F_1(j\omega) \exp [j(\omega t - k(\omega) \cdot \Delta x_1)] d\omega \quad (4.1)$$

darstellen. $\Delta x_1 = x_1^{(2)} - x_1^{(1)}$ bedeutet den Abstand der beiden Stationen. Im Frequenzbereich lautet Gleichung (4.1):

$$F_2(j\omega) = F_1(j\omega) \exp[-jk(\omega) \cdot \Delta x_1]. \quad (4.2)$$

Führt man für die Seismogrammspektren die polare Darstellung

$$F_i(j\omega) = A_i(\omega) \exp[-j\varphi_i(\omega)] \quad (4.3)$$

($i = 1, 2$) mit den Amplitudenspektren $A_i(\omega)$ und den Phasenspektren $\varphi_i(\omega)$ ein, so ergibt sich aus Gleichung (4.2) für die gesuchte Dispersionsfunktion der Phasengeschwindigkeit:

$$c(\omega) = \omega/k(\omega) = \omega \cdot \Delta x_1 / [\varphi_2(\omega) - \varphi_1(\omega) + 2N\pi]. \quad (4.4)$$

Die zunächst unbestimmte ganze Phasenzahl N läßt sich aus Näherungswerten der Phasengeschwindigkeit für den langperiodischen Teil des untersuchten Spektralbereichs berechnen.

Neben der Methode der Phasendifferenzen spielt die Kreuzkorrelations-Methode eine wichtige Rolle. Für das Kreuzkorrelogramm der beiden Seismogramme gilt:

$$f_{12}(t) = \int_{-\infty}^{+\infty} f_1(\tau) f_2(\tau + t) d\tau. \quad (4.5)$$

Gleichung (4.5) läßt sich mit dem modifizierten Faltungstheorem der Fourier-Transformation in den Frequenzbereich übersetzen:

$$\mathfrak{F}\{f_{12}(t)\} = F_{12}(j\omega) = F_1^*(j\omega) F_2(j\omega). \quad (4.6)$$

Durch Einsetzen von (4.2) in Gleichung (4.6) folgt:

$$F_{12}(j\omega) = |F_1(j\omega)|^2 \exp[-jk(\omega) \cdot \Delta x_1]. \quad (4.7)$$

Aus Gleichung (4.7) ergibt sich mit dem Phasenspektrum $\varphi_{12}(\omega)$ des Kreuzkorrelogramms für die Dispersionsfunktion der Phasengeschwindigkeit eine zu Gleichung (4.4) analoge Beziehung:

$$c(\omega) = \omega/k(\omega) = \omega \cdot \Delta x_1 / [\varphi_{12}(\omega) + 2N\pi]. \quad (4.8)$$

Innerhalb der Bandbreite des Seismogrammspektrums $F_1(j\omega)$ läßt sich das Kreuzkorrelogramm $f_{12}(t)$ nach Gleichung (4.7) als eine Approximation der Antwortfunktion des Ausbreitungsmediums in Station 2 auf einen δ -förmigen „Herdimpuls“ in Station 1 beschreiben. Da der Abstand der beiden Stationen in der Regel aber wesentlich kleiner ist als ihre Epizentralentfernungen, zeigt das Kreuzkorrelogramm eine entsprechend geringe dispersive Signalverformung als die beiden Seismogramme. Multipliziert man daher die Funktion $f_{12}(t)$ vor Durchführung der harmonischen Analyse mit einem geeigneten Fenster $w(t)$, so läßt sich das Produkt $f_{12} \cdot w$ als echtes Seismogramm mit erhöhtem Signal-Störverhältnis und stabilerem Phasenspektrum interpretieren. Die mit der Kreuzkorrelations-Methode nach Gleichung (4.8) berechneten Phasengeschwindigkeiten weisen daher wesentlich geringere Streuungen auf als die mit der Methode

der Phasendifferenzen nach Gleichung (4.4) ermittelten Werte. Die weiter unten behandelte Gruppengeschwindigkeitsmessung nach der Zwei-Stationenmethode, die Residuen-Dispersionsmessung sowie die Verfahren der Datengeneralisierung (s. z.B. Dziewonski und Landisman, 1970 sowie Dziewonski und Hales, 1972) basieren ebenfalls auf der Kreuzkorrelations-Methode.

Die Verfahren der Dispersionsanalyse im Zeitbereich (peak-and-trough Analyse) bzw. im Frequenzbereich (Methode der Phasendifferenzen bzw. der Kreuzkorrelation) setzen überlagerungsfreie Signale voraus. Sie lassen sich daher auf die in der Regel aus mehreren Anteilen zusammengesetzten Oberflächenwellen energiereicher Fernbeben erst nach Separation einzelner Moden anwenden. Den Ausgangspunkt der Analyse zusammengesetzter Signale bildet die spektrale Zerlegung mit einem multiplen Filter. Man versteht darunter einen Satz von N Bandpaßfiltern mit den Mittelfrequenzen ω_n ($n = 1, \dots, N$). Im folgenden werden Gaußfilter mit der Übertragungsfunktion

$$H_n(\omega) = \exp[-\alpha(\omega - \omega_n)^2/\omega_n^2] \quad (4.9)$$

betrachtet. Der Parameter α legt die spektrale Bandbreite, d.h. die Frequenzauflösung D_ω des Filters fest.

Die Analyse des dispergierten Signals aus Gleichung (3.1) mit einem Gaußfilter nach Gleichung (4.9) liefert das gefilterte Seismogramm $g_n(t)$:

$$g_n(t) = \frac{1}{2\pi} \int_{-\infty}^{+\infty} H_n(\omega) F_0(j\omega) \exp[j(\omega t - k(\omega) x_1)] d\omega. \quad (4.10)$$

Das Fourier-Integral in Gleichung (4.10) läßt sich durch Reihenentwicklung der Funktionen $F_0(j\omega)$ und $k(\omega)$ näherungsweise auswerten. In erster linearer Näherung gilt für die Ausbreitungsfunktion $k(\omega)$ in der Umgebung der Frequenz ω_n :

$$k(\omega) = k(\omega_n) + k'(\omega_n)(\omega - \omega_n). \quad (4.11)$$

Zur Vereinfachung der Rechnung sei angenommen, daß sich das Signalspektrum $F_0(j\omega)$ innerhalb der Bandbreite des Filters durch einen reellen Amplitudenfaktor annähern läßt:

$$F_0(j\omega) = A_0(\omega_n). \quad (4.12)$$

Das Resultat für eine zu Gleichung (4.10) analoge Entwicklung von $F_0(j\omega)$ enthält die Arbeit von Dziewonski und Hales (1972).

Mit den Näherungsansätzen (4.11) und (4.12) ergibt sich für das gefilterte Seismogramm $g_n(t)$ ein amplitudenmoduliertes Signal mit der Frequenz ω_n und der Amplitudeneinhüllenden $a_n(t)$:

$$g_n(t) = a_n(t) \cos[\omega_n t - k(\omega_n) x_1], \quad (4.13)$$

$$a_n(t) = (\pi/\alpha)^{1/2} \omega_n A_0(\omega_n) \exp[-\omega_n^2 [t - \tau_G(\omega_n)]^2 / 4\alpha]. \quad (4.14)$$

Dabei bedeutet $\tau_G(\omega_n)$ das Gruppenlaufzeitspektrum des Seismogramms für die Frequenz ω_n . Mit Gleichung (3.4) erhält man

$$\tau_G(\omega_n) = x_1 \quad k'(\omega_n) = x_1 / U(\omega_n). \quad (4.15)$$

Nach Gleichung (4.14) ist der Zeitpunkt des Maximums der Amplitudeneinhüllenden des gefilterten Seismogramms durch die Gruppenlaufzeit $\tau_G(\omega_n)$ gegeben. Die Breite der Einhüllenden, d.h. die Zeitauflösung D_t des Filterprozesses ist wiederum durch den Parameter α aus Gleichung (4.9) festgelegt. Die Zeitauflösung D_t und die Frequenzauflösung D_ω sind durch die Unschärferelation der Fourier-Transformation miteinander verknüpft (s. z.B. Fischer, 1969):

$$D_t \cdot D_\omega \geq 1. \quad (4.16)$$

Das Gleichheitszeichen gilt nur für Gaußfilter, d.h. diese Filter liefern unter allen nicht bandbegrenzten Filterfunktionen die höchste, durch $(D_t \cdot D_\omega)^{-1}$ gemessene Zeit-Frequenzauflösung.

Zur Berechnung der Amplitudeneinhüllenden des gefilterten Signals ist es zweckmäßig, das zu $g_n(t)$ analytische Signal $z_n(t)$ einzuführen (s. z.B. Fischer, 1969). Es sei $g_n(t)$ die inverse Fourier-Transformierte von $G_n(j\omega)$:

$$g_n(t) = \mathfrak{F}^{-1} \{G_n(j\omega)\}. \quad (4.17)$$

Dann gilt für das zu $g_n(t)$ orthogonale Signal $q_n(t)$:

$$q_n(t) = \mathfrak{F}^{-1} \{G_n(j\omega) \exp [j\pi/2]\}. \quad (4.18)$$

Aus den zueinander orthogonalen Funktionen $g_n(t)$ und $q_n(t)$ läßt sich das dem reellen Signal $g_n(t)$ zugeordnete analytische Signal $z_n(t)$ bilden:

$$z_n(t) = a_n(t) \exp [j\varphi_n(t)] = g_n(t) + jq_n(t). \quad (4.19)$$

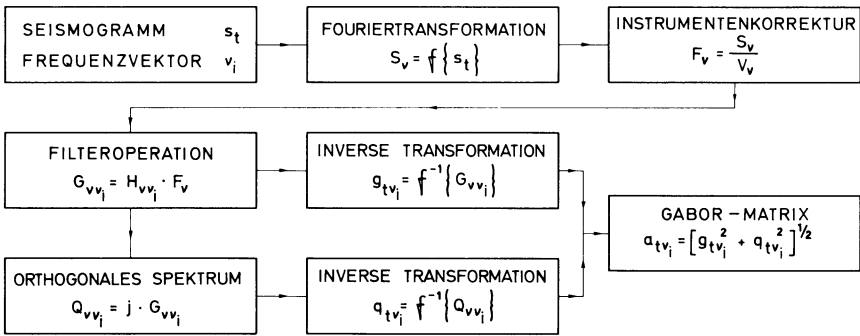
Für die Momentanwerte der Amplitude und Phase folgt dann aus Gleichung (4.19) (Goodman, 1960):

$$a_n(t) = [g_n^2(t) + q_n^2(t)]^{1/2}, \quad (4.20)$$

$$\varphi_n(t) = \tan^{-1} [q_n(t)/g_n(t)]. \quad (4.21)$$

Durch Variation der Mittelfrequenz ω_n des Bandpaßfilters läßt sich nach Gleichung (4.20) das Amplitudenspektrum des Seismogramms im Zeit-Frequenzbereich konstruieren. Seine diskrete Darstellung wird als Gabor-Matrix bezeichnet. Abbildung 4 zeigt ein schematisches Blockdiagramm zur praktischen Berechnung der Gabor-Matrix eines digitalisierten Seismogramms s_i für eine Folge von Frequenzen ν_i unter Berücksichtigung der komplexen Frequenzcharakteristik V_ν des Seismographensystems. Die Operationen der direkten bzw. inversen Fourier-Transformation lassen sich mit dem Algorithmus der schnellen Fourier-Transformation (Cooley und Tukey, 1965) sehr einfach durchführen. Als Beispiel zeigt Abbildung 4 weiter die Antwort eines digitalen Bandpaßfilters ($\nu_0 = 0.071$ Hz) für ein synthetisches Seismogramm, das sich aus der Grundmode aus Abbildung 3 ($x_1 = 4000$ km) und der ersten höheren Mode zusammensetzt. Die Amplitudeneinhüllende wurde mit Gleichung (4.20) berechnet. Die Pfeile markieren die theoretischen Gruppenlaufzeiten für die Frequenz ν_0 .

Die multiple Filtertechnik nach Abbildung 4 läßt sich bei der Analyse seismischer Oberflächenwellen in mehreren Varianten anwenden:



SYNTHETISCHES SEISMOGRAMM (GRUNDMODE + ERSTE HÖHERE MODE)

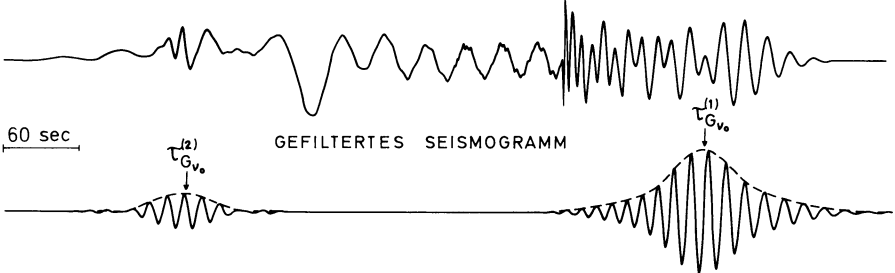


Abb. 4. Blockdiagramm der multiplen Filtertechnik zur Berechnung der Gabor-Matrix eines Seismogramms. Als Beispiel ist die Analyse eines synthetischen Seismogramms wiedergegeben

a) Messung der Gruppengeschwindigkeit nach der Ein- bzw. Zwei-Stationenmethode

Für das Seismogrammspektrum $F_1(j\omega)$ in der Epizentralentfernung x_1 läßt sich unter Vernachlässigung des Phasenspektrums des „Herdimpulses“ $F_0(j\omega)$ als Spezialfall von Gleichung (4.2) formal schreiben:

$$F_1(j\omega) = |F_0(j\omega)| \exp[-jk(\omega) x_1]. \tag{4.22}$$

Sind also das Epizentrum und die Herdzeit eines Bebens bekannt, so lassen sich mit einem multiplen Filter nach den Gleichungen (4.10) und (4.15) aus einem einzigen Seismogramm die mittleren Gruppengeschwindigkeiten entlang des Wellenweges Epizentrum-Station für alle angeregten Moden bestimmen.

Als praktisches Beispiel zeigt Abbildung 5 die Gabor-Matrix der Rayleigh-Wellen eines Bebens in Südostalaska (Datum: 3. 7. 1973; Herdzeit $t_0 = 16$ h 59 m 35.1 s; Epizentrum: $\varphi = 58^\circ$ N, $\lambda = 138^\circ$ W), aufgezeichnet von einem langperiodischen Seismographensystem in Zürich (Epizentralentfernung $x_1 = 8002$ km). Der analysierte Seismogrammausschnitt ist in einem der Gruppengeschwindigkeitskala entsprechenden verzerrten Zeitmaßstab wiedergegeben, um die Zuordnung von Seismogramm und Gabor-Matrix zu erleichtern. Das Matrixelement in einer Spalte bei der Periode T_n und einer Zeile bei der Gruppengeschwindigkeit U_i bedeutet den Wert der Amplitudeneinhüllenden des mit einem Gaußfilter (Mittelfrequenz $\omega_n = 2\pi T_n^{-1}$) analysierten Seismogramms zum Zeitpunkt $t_i = t_0 + x_1/U_i$.

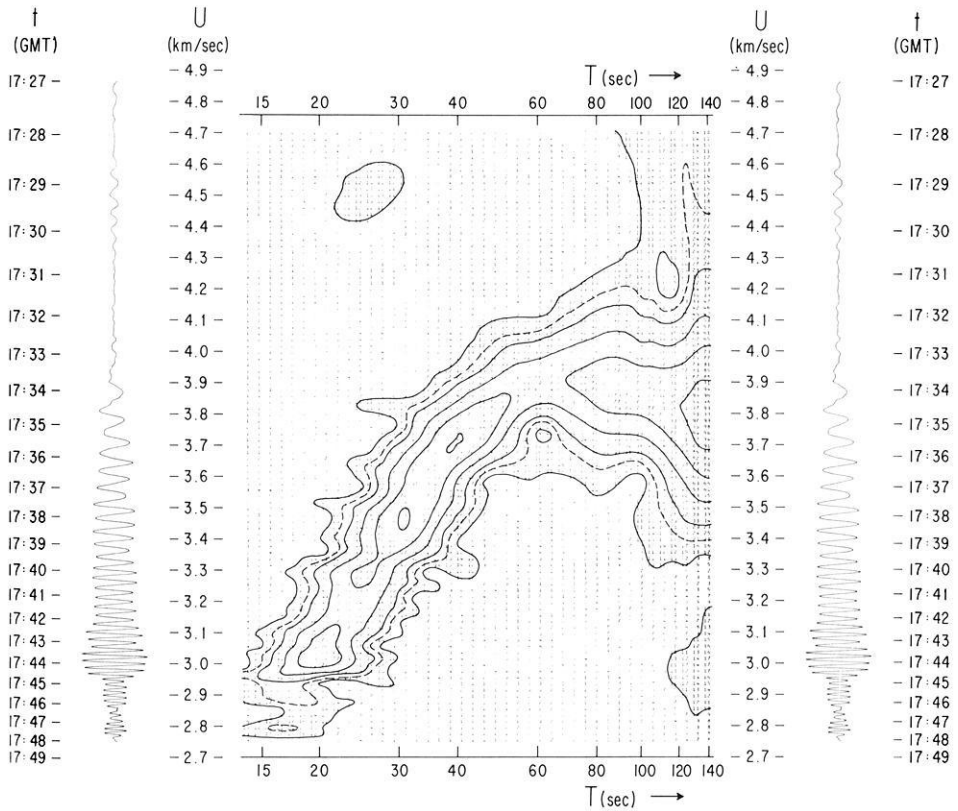


Abb. 5. Gabor-Matrix der Rayleigh-Wellen eines Bebens in Südostalaska (Datum: 3.7.1973; $t_0 = 16:59:35.1$; $\varphi = 58.0^\circ N$, $\lambda = 138.0^\circ W$; $m_b = 5.9$), aufgezeichnet von einem langperiodischen Seismographensystem in Zürich (Schweiz)

Die Konturen sind Höhenlinien konstanter Amplitude. Die (nicht eingezeichneten) Verbindungslinien der Spaltenmaxima liefern die Gruppengeschwindigkeitskurven für die im Seismogramm enthaltenen Moden. Abbildung 5 zeigt die Grundmode im Periodenbereich von 20–140 s sowie Andeutungen der ersten höheren Mode für Perioden um 25 s.

Wäre die Zeit-Frequenzauflösung des multiplen Filters unendlich hoch, so würden alle, nicht auf Gruppengeschwindigkeitskurven gelegenen Matrixelemente verschwinden. Wegen der endlichen Auflösung nach Gleichung (4.16) erscheinen die Dispersionskurven als Funktionsstreifen, die sich in bestimmten Bereichen der Matrix überlagern können. Um solche Interferenzeffekte zwischen regulär und invers dispergierten Ästen einer Mode sowie zwischen verschiedenen Moden beurteilen zu können, haben Dziewonski et al. (1969) ein Diagnoseverfahren in Form einer die Interferenz charakterisierenden Kennzahlen-Matrix entwickelt, das außerdem zur Bestimmung eines optimalen Wertes für den Filterparameter α in Gleichung (4.9) angewendet werden kann.

Bei der Gruppengeschwindigkeitsmessung nach der Zwei-Stationenmethode

wird das Kreuzkorrelogramm zweier, von einem in Wellenausbreitungsrichtung gelegenen Stationspaar aufgezeichneter Seismogramme mit einem multiplen Filter analysiert. Aus der Gabor-Matrix des Kreuzkorrelogramms lassen sich nach Gleichung (4.7) die mittleren Gruppengeschwindigkeiten entlang der Verbindungslinie der beiden Stationen ableiten. Die Zwei-Stationenmethode läßt sich immer dann anwenden, wenn das Epizentrum annähernd auf dem Großkreis durch beide Stationen liegt und die Wellenfront bei ihrer Ausbreitung bis zur ersten Station keine starken Drehungen durch laterale Strukturen erfahren hat. Im übrigen gelten die bei der Ein-Stationenmethode gemachten Überlegungen.

b) Residuen-Dispersionsmessung

Die multiple Filtertechnik stellt ein Näherungsverfahren dar, dessen Güte davon abhängt, mit welcher Genauigkeit die Reihenentwicklungen in den Gleichungen (4.11) und (4.12) das Phasen- und Amplitudenspektrum des Seismogramms innerhalb der Bandbreite des Filters approximieren. Numerische Experimente mit synthetischen Seismogrammen zeigen (Dziewonski et al., 1972), daß die aus Gleichung (4.14) abgeleiteten Gruppenlaufzeiten einen systematischen, zur Bandbreite annähernd proportionalen Fehler aufweisen. Bei gegebener Bandbreite ist der Fehler umso kleiner, je flacher die Dispersionsfunktion verläuft. So ist zum Beispiel das mit einem multiplen Filter bestimmte Gruppenlaufzeitspektrum der nur schwach dispergierten impulsförmigen G -Welle gegen Änderungen der Bandbreite weitgehend unempfindlich. Da bei der praktischen Seismogrammanalyse die Bandbreite nicht beliebig auf Kosten der Zeitauflösung verringert werden kann, ist eine Erhöhung der Meßgenauigkeit nur durch eine Abflachung der Dispersionsfunktion zu erreichen. Diese Abflachung läßt sich realisieren, indem man das beobachtete Seismogramm durch Kreuzkorrelation mit einem synthetischen Referenzseismogramm in ein impulsförmiges, schwach dispergiertes Signal transformiert. Der Grundgedanke des Verfahrens soll am Beispiel der Ein-Stationenmethode nach Gleichung (4.22) kurz erläutert werden.

Es sei $\hat{k}(\omega)$ eine Näherung der gesuchten Dispersionsfunktion $k(\omega)$. $\hat{k}(\omega)$ läßt sich entweder aus einem plausiblen Schichtmodell berechnen oder durch Seismogrammanalyse mit einem multiplen Filter bestimmen. Für das Spektrum $\hat{F}_1(j\omega)$ des synthetischen Antwortseismogramms auf einen δ -förmigen „Herdimpuls“ gilt analog zu Gleichung (4.22):

$$\hat{F}_1(j\omega) = \exp[-j\hat{k}(\omega)x_1]. \quad (4.23)$$

Das Spektrum $\hat{F}_{11}(j\omega)$ des Kreuzkorrelogramms zwischen dem beobachteten und dem synthetischen Seismogramm hat dann nach Gleichung (4.6) die Form:

$$\begin{aligned} \hat{F}_{11}(j\omega) &= F_1^*(j\omega) \hat{F}_1(j\omega) = |F_0(j\omega)| \exp[-j(\hat{k}(\omega) - k(\omega))x_1] \\ &= |F_0(j\omega)| \exp[-j\bar{k}(\omega)x_1]. \end{aligned} \quad (4.24)$$

Wenn $\hat{k}(\omega)$ eine gute Näherung von $k(\omega)$ darstellt, dann wird der durch die endliche Krümmung der Dispersionsfunktion nach Gleichung (4.11) bedingte Fehler

wegen $\bar{k}''(\omega) \ll k''(\omega)$ für $\bar{k}(\omega)$ wesentlich geringer ausfallen als für $k(\omega)$. Für den verbesserten Schätzwert $\hat{k}_1(\omega)$ der gesuchten Dispersionsfunktion gilt dann $\hat{k}_1(\omega) = \hat{k}(\omega) + \bar{k}(\omega)$. Durch mehrfache Wiederholung des Rechenganges läßt sich die Genauigkeit schrittweise erhöhen. Einzelheiten über den Einfluß des frequenzabhängigen Amplitudenspektrums des Seismogramms auf die Bestimmung des Phasenlaufzeitspektrums sowie praktische Anwendungsbeispiele der Residuen-Dispersionsmessung können der Arbeit von Dziewonski et al. (1972) entnommen werden.

c) Analyse von 3-Komponenten Registrierungen

Durch Anwendung der multiplen Filtertechnik auf die Seismogramme einer 3-Komponenten Station läßt sich die komplexe Amplitude des Verschiebungsvektors in Abhängigkeit von der Gruppenlaufzeit und der Periode rekonstruieren. Ein Vergleich der beobachteten Partikelbewegung mit theoretischen, für vorgegebene Schichtmodelle berechneten Schwingungsformen liefert wichtige Hinweise zur Identifizierung und Trennung von verschiedenen Moden der Rayleigh- und Love-Wellen. Aus der Orientierung der horizontalen Schwingungsellipse relativ zur Großkreisrichtung Epizentrum-Station lassen sich Rückschlüsse auf laterale Refraktionen entlang des durchlaufenen Wellenweges ziehen. Anwendungsbeispiele für synthetische und praktische Seismogramme sind zum Beispiel in den Arbeiten von Dziewonski et al. (1968) und Landisman et al. (1969) enthalten.

d) „Moving-Window“ Analyse

Die „Moving-Window“ Analyse kann als Gegenstück zur multiplen Filtertechnik im Zeitbereich charakterisiert werden. Das Matrixelement $a(t_i, T_n)$ wird als Betrag der Fourier-Transformierten des mit einem Zeitfenster $w(t - t_i, T_n)$ multiplizierten Seismogramms $f(t)$ für die Periode T_n gebildet:

$$a(t_i, T_n) = |\mathfrak{F}\{f(t) \cdot w(t - t_i, T_n)\}|_{T=T_n}. \quad (4.25)$$

Durch eine variable, zur Periode T_n proportionale Länge des Zeitfensters läßt sich eine für alle Perioden konstante relative Frequenzauflösung erzielen. Eine eingehende Beschreibung der „Moving-Window“ Analyse enthalten die Arbeiten von Dziewonski et al. (1968) sowie von Landisman et al. (1969).

Die spektrale Zerlegung eines Seismogramms mit der multiplen Filtertechnik bzw. der „Moving-Window“ Analyse bildet den Ausgangspunkt für den Entwurf von zeitabhängigen Filtern, mit denen sich die definierten Bereichen der Zeit-Frequenzebene zugeordneten Seismogrammanteile abtrennen lassen. Die Separation einzelner Moden sowie die Erhöhung des Signal-Störverhältnisses durch Unterdrückung störender (z.B. durch Mehrfachwegausbreitung erzeugter multipler) Wellengruppen sind die wichtigsten Anwendungsbereiche dieser Filter. Zeitabhängige Filter lassen sich im Zeit- und Frequenzbereich realisieren. Im Zeitbereich wird das Seismogramm mit der Gewichtsfunktion eines Bandpaß-

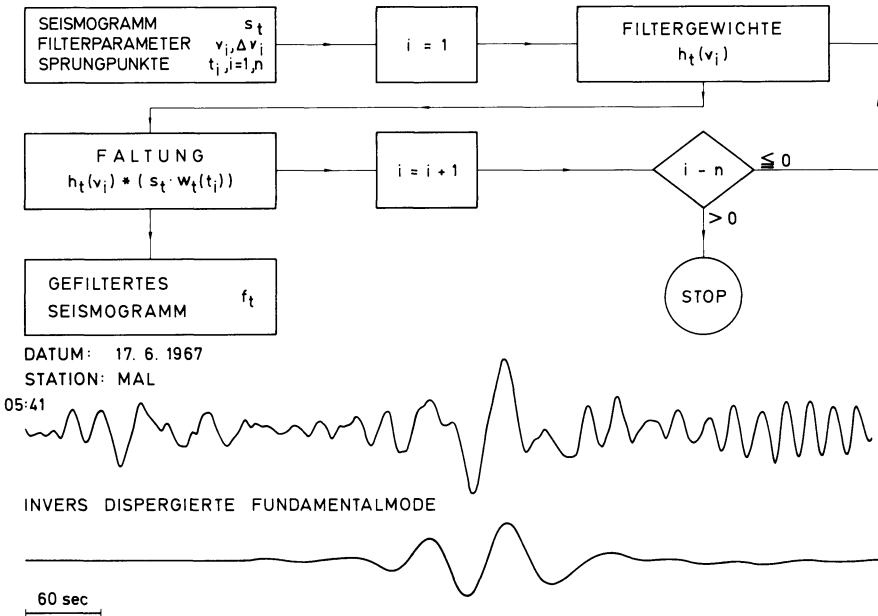


Abb. 6. Blockdiagramm eines zeitabhängigen Filters zur Signalseparation. Als Beispiel ist die Analyse eines aus mehreren Teilsignalen zusammengesetzten Erdbebenseismogramms wiedergegeben (Datum: 17. 6. 1967; Epizentrum: Südliche Sandwich-Inseln; Station: Malaga)

filters gefaltet, dessen Durchlaßfrequenz sich entsprechend dem Gruppenlaufzeitpektrum des abzutrennenden Signals zeitlich ändert. Abbildung 6 zeigt in einem Blockdiagramm die einfachste Realisierung eines solchen Filters. Durch die Sprungpunkte t_i auf der Zeitachse und die Filterparameter v_i (Durchlaßfrequenz) sowie Δv_i (Bandbreite) wird der Durchlaßbereich des Filters in der Zeit-Frequenzebene aus rechteckigen Teilbereichen zusammengesetzt. Durch Multiplikation mit einer Folge von Zeitfenstern $w_t(t_i)$ wird das Seismogramm s_t in einzelne Segmente zerlegt, die mit den Gewichtsfunktionen $h_t(v_i)$ der zugeordneten Bandpaßfilter gefaltet werden. Im unteren Teil von Abbildung 6 ist als Beispiel die Analyse des Seismogramms eines Bebens bei den Südlichen Sandwich-Inseln wiedergegeben, aufgezeichnet von dem langperiodischen vertikalen Seismographensystem der WWSS-Station Malaga. Der Seismogrammausschnitt zeigt neben Signalanteilen der ersten höheren Rayleigh-Mode regulär und invers dispersierte Wellengruppen der Grundmode sowie den Beginn des Wellenzuges der ozeanischen Rayleigh-Wellen. Die gefilterte Spur umfaßt den Seismogrammanteil, der dem invers dispersierten Ast der Gruppengeschwindigkeitskurve langperiodischer Rayleigh-Wellen mit Perioden oberhalb 60 s (s. z.B. Oliver, 1962) zugeordnet ist. Im Frequenzbereich läßt sich die Filteroperation am einfachsten durchführen, indem man die mit einem frequenzabhängigen Gruppenlaufzeitfilter multiplizierten harmonischen Teilwellen des Seismogramms unter Anwendung der schnellen Fourier-Transformation superponiert. Eine ausführliche Diskussion zeitabhängiger Filter im Zeit- und Frequenzbereich enthalten

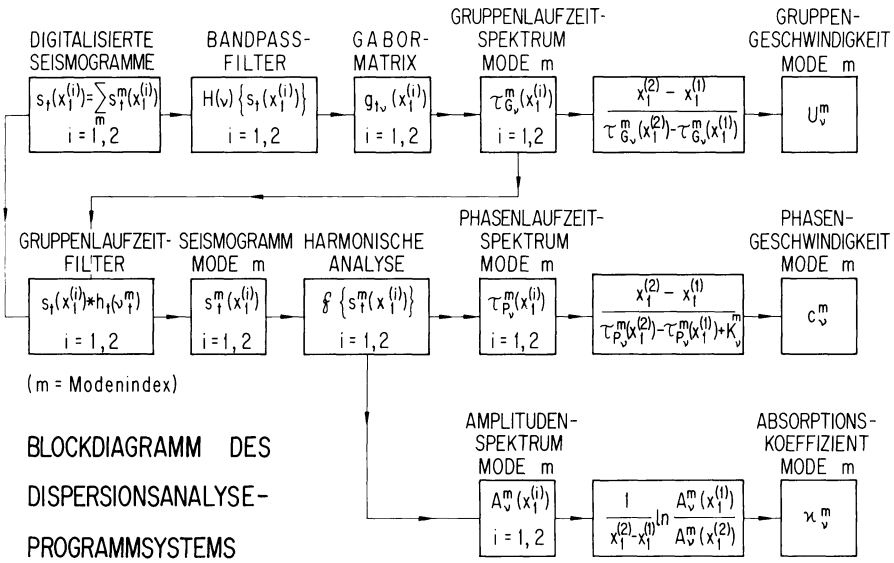


Abb. 7. Schematisches Blockdiagramm zur numerischen Analyse der Dispersion und Absorption von seismischen Oberflächenwellen

die Arbeiten von Landisman et al. (1969) sowie von Dziewonski und Hales (1972). Die durch die Anwendung zeitabhängiger Filter verursachten Verzerrungen des Amplituden- und Phasenspektrums, die vor allem bei Amplitudenuntersuchungen (z.B. Absorptionsmessungen) beachtet werden müssen, werden im Übersichtsartikel von Dziewonski und Hales (1972) diskutiert.

Die Spektralanalyse im Zeit-Frequenzbereich mit den verschiedenen Varianten der multiplen Filtertechnik, die Signalseparation mit zeitabhängigen Filtern sowie die Messung der Phasen- und Gruppengeschwindigkeit mit der Phasendifferenzen- bzw. Kreuzkorrelations-Methode bilden die Grundoperationen der Analyse seismischer Oberflächenwellen. Sie lassen sich je nach Aufgabenstellung und Seismogrammtyp in verschiedenen Kombinationen zu einem Gesamtprogramm zusammenstellen. Praktische Hinweise zur Datenvorbehandlung, eine Zusammenstellung der wichtigsten Fehlerquellen sowie eine ausführliche Anleitung zur Anwendung der Schnellen Fouriertransformation enthält der bereits mehrfach zitierte Artikel von Dziewonski und Hales (1972).

Abbildung 7 zeigt das schematische Blockdiagramm eines in der Praxis bewährten, relativ einfachen Programmsystems zur Messung der Gruppengeschwindigkeit U , der Phasengeschwindigkeit c sowie des Absorptionskoeffizienten κ nach der Zwei-Stationenmethode (s. Abschnitt 6). Die Gruppengeschwindigkeit wird nicht aus der Gabor-Matrix des Kreuzkorrelogramms der gefilterten Seismogramme, sondern direkt aus den Gruppenlaufzeiten der Gabor-Matrizen der zusammengesetzten Seismogramme bestimmt. Die Phasengeschwindigkeit wird aus den Phasenspektren der gefilterten Seismogramme nach der Methode der Phasendifferenzen berechnet. Die Verzerrungen der Phasenspektren durch die Seismographensysteme können am einfachsten korrigiert werden, indem man von den

Phasen- und Gruppenlaufzeitspektren die entsprechenden instrumentellen Größen subtrahiert. Der Absorptionskoeffizient läßt sich mit der Zwei-Stationenmethode in der Regel nur größenordnungsmäßig abschätzen, da die Absolutvergrößerung langperiodischer Seismographensysteme mit den üblichen Routineeichverfahren nicht mit der erforderlichen Genauigkeit ermittelt werden kann. Genauere Absorptionsmessungen können mit der Ein-Stationenmethode durch Beobachtung langperiodischer Wiederkehrwellen durchgeführt werden (s. z.B. Dziewonski und Hales, 1972 sowie Abschnitt 6).

5. Inversion

Das Grundproblem jeder geophysikalischen Inversion besteht in der Ableitung von Modellparametern aus Beobachtungsdaten. Im Fall seismischer Oberflächenwellen werden die Phasen- und Gruppengeschwindigkeiten in Abhängigkeit von der Periode gemessen. Die gesuchten Modellparameter sind die Raumwellengeschwindigkeiten und die Dichte als Funktionen der Tiefe (s. Abb. 2). Da eine eindeutige Lösung dieses Inversionsproblems nicht existiert (s. z.B. Knopoff, 1961, 1962; Gerver und Kazhdan, 1972; Gerver, 1972), muß die Vielzahl aller Modelle ermittelt werden, die mit der endlichen Menge der fehlerbehafteten Beobachtungsdaten verträglich ist.

Durch Anwendung einiger Faustformeln läßt sich in der Regel relativ schnell ein plausibles Näherungsmodell ableiten, das dann durch Iteration schrittweise verbessert werden kann. Zunächst zeigt eine Berechnung der partiellen Ableitungen der Phasengeschwindigkeiten nach den Schichtparametern, daß Änderungen der S -Geschwindigkeiten den größten Einfluß auf die Dispersionskurven ausüben. Da die Eindringtiefe der Oberflächenwellen von ihrer Wellenlänge abhängt, lassen sich verschiedenen Periodenintervallen bestimmte Tiefenbereiche zuordnen. Nach Knopoff und Schlue (1972) gelten für die Eindringtiefen $x_3^{(R)}$ und $x_3^{(L)}$ der Grundmode von Rayleigh- bzw. Love-Wellen mit den Wellenlängen λ_R bzw. λ_L die Faustformeln:

$$x_3^{(R)} \approx 0,4 \cdot \lambda_R = 0,4 \cdot c_R \cdot T, \quad (5.1)$$

$$x_3^{(L)} \approx 0,25 \cdot \lambda_L = 0,25 \cdot c_L \cdot T. \quad (5.2)$$

Um die theoretischen Dispersionskurven von Schichtmodellen an die experimentellen Daten anzupassen, sind demnach die S -Geschwindigkeiten im Tiefenbereich um $x_3^{(R)}$ bzw. $x_3^{(L)}$ zu variieren.

Mit der Zwei-Stationenmethode (s. Abschnitt 4) wird für Rayleigh-Wellen in der Regel der Periodenbereich von etwa 20 bis 200 s erfaßt. Nach Gleichung (5.1) entspricht dies dem Tiefenbereich zwischen der Krusten-Mantelgrenze und der ausgedehnten Übergangzone vom oberen zum unteren Erdmantel. Die dominierende Struktur in diesem Tiefenintervall ist eine Zone verminderter S -Geschwindigkeit, die sich je nach Ausprägung in einer mehr oder weniger deutlichen Abflachung der Phasengeschwindigkeitsdispersionskurven bemerkbar macht. Für die mittlere Phasengeschwindigkeit \bar{c} gilt dann näherungsweise eine als „Entkopplungseffekt“ bezeichnete Relation (Knopoff et al., 1966; Seidl, 1971).

$$\bar{c} \approx c_{RC} \approx 0,92 \cdot \beta_C \quad (5.3)$$

wobei β_C die mittlere S -Geschwindigkeit im Asthenosphären-Kanal und c_{RC} die zugehörige Rayleigh-Halbraumgeschwindigkeit bedeuten. Mit der Faustformel (5.3) läßt sich also der Schichtparameter β_C aus dem Beobachtungswert \bar{c} näherungsweise abschätzen.

Nach den bisherigen Überlegungen wird der Inversionsprozeß wesentlich dadurch erleichtert, daß sich die $4N$ Parameter eines N -Schichtenmodells in aktive (variable) und passive (konstante) Kenngrößen unterteilen lassen. Wenn die passiven Parameter (P -Geschwindigkeiten und Dichten) näherungsweise bekannt sind, läßt sich die Inversion durch alleinige Variation der aktiven Parameter (S -Geschwindigkeiten) durchführen.

Die schrittweise Verbesserung eines plausiblen Anfangsmodells nach der Methode der kleinsten Quadrate wurde erstmals von Dorman und Ewing (1962) praktisch durchgeführt. Es seien $\hat{c}(T_i)$ ($i=1, \dots, L$) die experimentellen Dispersionsdaten, p_k ($k=1, \dots, M$) die gesuchten aktiven Parameter und $c(T_i, p_k)$ die theoretischen Phasengeschwindigkeiten.

Dann lautet die Minimalisierungsbedingung:

$$\sum_{i=1}^L [c(T_i, p_k) - \hat{c}(T_i)]^2 = \varepsilon(p_k) = \text{MIN}. \quad (5.4)$$

Für das System der linearisierten Fehlergleichungen gilt dann:

$$\sum_{k=1}^M [\partial c(T_i, p_k) / \partial p_k]_{p_{k0}} \cdot \Delta p_k = \hat{c}(T_i) - c(T_i, p_k) \quad i = 1, \dots, L > M. \quad (5.5)$$

Die p_{k0} ($k = 1, \dots, M$) sind die Werte der aktiven Parameter für das Anfangsmodell. Das lineare Gleichungssystem (5.5) lautet in Matrixschreibweise:

$$\mathbf{P} \cdot \mathbf{D} = \mathbf{C}. \quad (5.6)$$

Die Elemente der (L, M) -Matrix \mathbf{P} sind die partiellen Ableitungen

$$[\partial c(T_i, p_k) / \partial p_k]_{p_{k0}}.$$

Die $(M, 1)$ -Matrix \mathbf{D} enthält die gesuchten Korrekturen Δp_k der aktiven Parameter p_k , die $(L, 1)$ -Residuenmatrix \mathbf{C} die Abweichungen der theoretischen von den experimentellen Phasengeschwindigkeiten. Das überbestimmte Gleichungssystem (5.6) läßt sich formal durch linksseitige Multiplikation mit der transponierten Matrix \mathbf{P}^T auf die Form der Normalgleichungen bringen (Gauß-Transformation):

$$(\mathbf{P}^T \cdot \mathbf{P}) \cdot \mathbf{D} = \mathbf{P}^T \cdot \mathbf{C}. \quad (5.7)$$

Führt man die (M, M) -Matrix $\mathbf{N} = \mathbf{P}^T \cdot \mathbf{P}$ sowie die $(M, 1)$ -Matrix $\mathbf{B} = \mathbf{P}^T \cdot \mathbf{C}$ ein, so lautet Gleichung (5.7):

$$\mathbf{N} \cdot \mathbf{D} = \mathbf{B}. \quad (5.8)$$

Die Lösungs-Matrix \mathbf{D} enthält die gesuchten Korrekturen Δp_k . Damit lassen sich verbesserte Werte der aktiven Parameter

$$p_{k1} = p_{k0} + \Delta p_k \quad (5.9)$$

gewinnen. Die Standardabweichung m_{c1} der Residuen für das verbesserte Modell beträgt:

$$m_{c1} = [\varepsilon(p_{k1}) / (L - M)]^{1/2}. \quad (5.10)$$

Die Standardabweichungen der aktiven Parameter m_{pk1} lassen sich aus den Diagonalelementen der inversen Matrix \mathbf{N}^{-1} berechnen:

$$m_{pk1} = m_{c1} [(\mathbf{N}^{-1})_{kk}]^{1/2}. \quad (5.11)$$

Der Index 1 bezeichnet den ersten Iterationsschritt. Der Prozeß wird solange wiederholt, bis eine durch die endliche Meßgenauigkeit gegebene Schranke erreicht ist.

Obwohl die Inversion nach der Methode der kleinsten Quadrate ein brauchbares praktisches Verfahren darstellt und der häufig angewandten, mehr oder weniger willkürlichen „trial und error“-Iteration in jedem Fall vorzuziehen ist, stellt sie doch nur eine Teillösung des allgemeinen Inversionsproblems dar. Eine kritische Lösung dieses Problems verlangt, die Gesamtheit aller mit den Beobachtungsdaten verträglichen Modelle zu finden, die durch die Beobachtungsfehler bedingte Genauigkeit und Tiefenauflösung der Modellparameter abzuschätzen sowie die Möglichkeiten einer Parameterseparation (d.h. einer simultanen Bestimmung verschiedener Schichtparameter, wie z. B. der S -Geschwindigkeit und der Dichte) zu untersuchen. Weiter sollen die miteinander zu vergleichenden Modelle so beschaffen sein, daß zwar die gesamte in den Beobachtungsdaten enthaltene Information ausgenutzt, eine Überinterpretation der experimentellen Daten aber vermieden wird.

Qualitativ läßt sich der Zusammenhang zwischen Meßgenauigkeit und Parameterrauflösung mit Hilfe von synthetischen Seismogrammen sehr anschaulich darstellen. Die Abbildungen 8 und 9 zeigen die Ergebnisse einiger numerischer Experimente, aus denen sich der Abstand benachbarter Modelle abschätzen läßt, die hinsichtlich der Verformung eines gegebenen Erdbebensignals unter Zugrundelegung einer bestimmten Ablesegenauigkeit als äquivalent anzusehen sind (Seidl, 1971). Die ausgezogenen synthetischen Seismogramme bedeuten das Antwortsignal eines einfachen anelastischen Modells auf das gefilterte Erdbebensignal aus Abbildung 6 in einer Entfernung von 2000 km. Abbildung 8 zeigt die Änderung der Signalform, die einer Erhöhung der S -Geschwindigkeit β_c im Asthenosphären-Kanal um 0.1 km/s entspricht. Danach dürfte die Auflösung für β_c in diesem Fall etwa 0.05 km/s betragen. In Abbildung 9 ist der Einfluß eines Doppelkanals mit variabler mittlerer S -Geschwindigkeit veranschaulicht. Eine Berücksichtigung von Schichtmodellen mit Doppel-Kanal beim Inversionsprozeß würde demnach in diesem speziellen Fall eine Überinterpretation der Beobachtungsdaten bedeuten.

Von den zahlreichen Publikationen, die sich mit der numerischen Lösung des oben formulierten, allgemeinen Inversionsproblems seismischer Oberflächen-

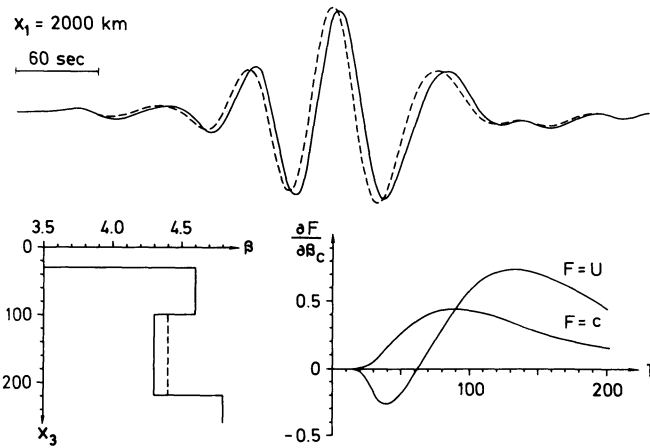


Abb. 8. Zusammenhang zwischen Änderungen der Verformung eines Erdbebensignals und der Variation von Schichtparametern, aufgezeigt am Beispiel der S-Geschwindigkeit des Asthenosphärenkanals

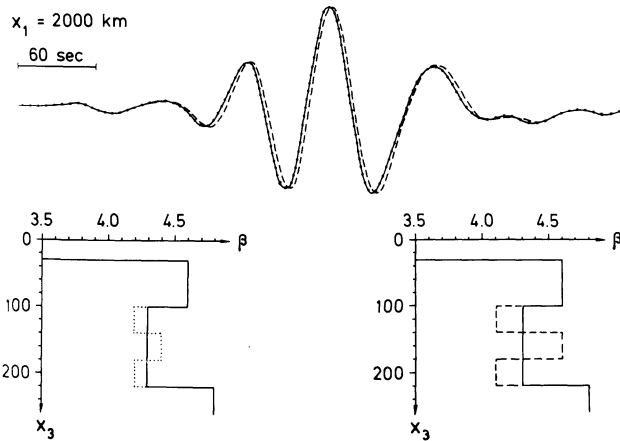


Abb. 9. Änderung der Verformung des Erdbebensignals aus Abbildung 8 durch Einführung eines Doppelkanals in der Asthenosphäre, dessen mittlere S-Geschwindigkeit variiert

wellen und Eigenschwingungen beschäftigen, soll im folgenden eine kleine Auswahl zitiert werden. Backus und Gilbert (1967, 1968) sowie Gilbert und Backus (1968) haben die Auflösung des Inversionsprozesses unter Vernachlässigung von Beobachtungsfehlern untersucht. Der Einfluß der endlichen Meßgenauigkeit wurde u. a. von Der et al. (1970), Backus und Gilbert (1970) sowie von Der und Landisman (1972) diskutiert. Wiggins (1972) hat eine Matrizenmethode zur Lösung des allgemeinen linearen Inversionsproblems entwickelt. Die wichtigsten Ergebnisse dieser Untersuchungen sollen kurz zusammengefaßt werden.

(a) Die Vieldeutigkeit des Inversionsproblems läßt sich quantitativ in Form einer Reziprozitätsrelation zwischen Genauigkeit, Tiefenauflösung und Separation von Modellparametern formulieren und graphisch durch sog. „trade-off“-Flächen bzw. Kurven veranschaulichen. Um unter den unendlich vielen Lösungsmodellen ein „bestes“ auszuwählen, müssen zusätzliche Nebenbedingungen vorgegeben werden.

(b) Die Dispersionsdaten der Phasengeschwindigkeit für die Rayleigh-Grundmode enthalten mehr Information über die Tiefenfunktion der *S*-Geschwindigkeit als entsprechende Daten für die Love-Welle. Eine zusätzliche Messung der Gruppengeschwindigkeit erhöht die Genauigkeit, liefert aber keine neue Information (s. auch Pilant und Knopoff, 1970).

(c) Die Inversion von kombinierten Dispersionsdaten verschiedener Moden der Rayleigh- und Love-Wellen erhöht nicht nur die Genauigkeit und Auflösung, sondern ermöglicht auch eine Separation von *S*-Geschwindigkeit und Dichte.

Neben den bisher beschriebenen iterativen Inversionsverfahren sind drei weitere Lösungswege von praktischem Interesse: Die Monte Carlo-Methode, die „Hedgehog“-Methode und die „Edgehog“-Methode. Die Monte Carlo-Methode (s. z.B. Press, 1968, 1970, 1972) erzeugt mit Hilfe von Zufallszahlen eine große Anzahl von statistischen Kombination der aktiven Schichtparameter innerhalb vorgegebener Schranken, die dann auf ihre Verträglichkeit mit den Beobachtungsdaten überprüft werden. Die „Hedgehog“-Methode (Keilis-Borok und Yanovskaya, 1967) läßt sich als systematisches Suchprogramm innerhalb eines Punktgitters im multidimensionalen Raum der aktiven Parameter charakterisieren. Ein praktisches Beispiel enthält die Arbeit von Knopoff und Schlue (1972). Die von Jackson (1973) entwickelte „Edgehog“-Methode sucht dagegen die mit den Beobachtungsdaten verträglichen Randlösungen innerhalb des Parameterraums auf.

6. Interpretation

Dispersionsmessungen

Eine erste Zusammenfassung weltweit gemessener Phasen- und Gruppengeschwindigkeiten seismischer Oberflächenwellen wurde von Oliver (1962) vorgenommen. Die summarischen Dispersionsdiagramme umfassen einen Frequenzbereich von etwa elf Oktaven und lassen zwei Merkmale der mittleren Grobstruktur des Systems Erdkruste—oberer Erdmantel erkennen: Eine deutliche Unterteilung in kontinentale und ozeanische Regionen sowie die Existenz lateraler Inhomogenitäten, die sich in einer zunehmenden Auffächerung der Dispersionskurven zu kurzen Perioden hin ($T < 300$ s) bemerkbar macht. Eine weitergehende Klassifizierung von Dispersionsdaten nach strukturellen Merkmalen haben Brune (1969) und Dorman (1969) durchgeführt. Ausgehend von der Beobachtung, daß die durch die Analyse von Wiederkehrwellen entlang verschiedener Großkreise gemessenen mittleren Phasen- und Gruppengeschwindigkeiten der Oberflächenwellen signifikante Unterschiede aufweisen, haben Toksöz und Ben-Menahem (1963), Toksöz und Anderson (1966), Kanamori (1970), Dzie-

wonski und Landisman (1970) sowie Dziewonski (1970) u.a. die Methode der Großkreis-Segmentierung entwickelt. Unter der Voraussetzung, daß die Erde in drei elementare Strukturen (Ozeane, stabile und tektonisch aktive Regionen) unterteilt werden kann, lassen sich aus den Großkreisdaten repräsentative („pure-path“) Standard-Dispersionskurven der drei Strukturtypen ableiten. Eine Inversion dieser Dispersionsdaten (s. z.B. Dziewonski, 1971) zeigt deutliche regionale Variationen im Aufbau des oberen Erdmantels. Der Hauptvorteil der Methode der Großkreis-Segmentierung ist der große Umfang des auswertbaren Datenmaterials, ein Nachteil ist die relativ geringe Auflösung in wenige Strukturtypen.

Das wichtigste Beobachtungsverfahren zur systematischen Kartierung regionaler Dispersionsdaten ist die erstmals von Brune und Dorman (1963) angewandte Zwei-Stationenmethode (s. Abschnitt 4). Die in zahlreichen Gebieten der Erde durchgeführten Beobachtungen beschränken sich fast ausschließlich auf die Untersuchung von Rayleigh-Wellen, da Love-Wellen sehr häufig durch Interferenzeffekte gestört sind und eine Separation verschiedener Moden wegen der eng benachbarten Dispersionskurven schwierig ist. Eine zusammenfassende Interpretation weltweit gemessener Phasengeschwindigkeiten für die Grundmode der Rayleigh-Wellen zeigt, daß im Periodenbereich von etwa 20 bis 150 s mindestens fünf verschiedene geologische Strukturtypen unterschieden werden müssen (Knopoff, 1972): Präkambrische Schilde, seismisch stabile Kontinentalmassen, Ozeane, Rift-Strukturen und alpidische Zonen. Die höchsten Phasengeschwindigkeiten (typische Werte: 4.1 bis 4.2 km/s für Perioden von 60–80 s) werden im Bereich der alten Schilde beobachtet. Sie zeigen hohe mittlere *S*-Geschwindigkeiten in der Lithosphäre sowie einen nur schwach ausgeprägten Asthenosphären-Kanal an. Die Inversion der Dispersionskurven für die seismisch stabilen Kontinentalmassen (typische Phasengeschwindigkeiten: 4.0 bis 4.1 km/s im Periodenbereich von 60–80 s) liefert Modelle mit einem ausgeprägten Asthenosphären-Kanal und einem scharfen Geschwindigkeitskontrast zu einer etwa 100 km mächtigen Lithosphäre. Für die Ozeane liegen bisher nur spärliche Ergebnisse vor. Charakteristisch ist der extrem flache Verlauf der Dispersionskurven für Perioden zwischen 20 und 70 s sowie sehr niedrige Phasengeschwindigkeiten um 3.9 km/s im Periodenbereich um 70 s, entsprechend einer dünnen Lithosphäre mit einem scharfen Kontrast zu einem stark ausgeprägten Asthenosphären-Kanal. Die Dispersionskurven von Rift-Strukturen zeigen einen ähnlichen Verlauf wie die der Schilde, aber mit etwa 0.3 km/s geringeren Geschwindigkeiten. Sie deuten auf niedrige *S*-Geschwindigkeiten in geringen Tiefen mit einem nur sehr schwach ausgeprägten bzw. nicht existenten Kanal hin. Ein Beispiel einer alpidischen Zone wird weiter unten behandelt. Neben der Methode der Großkreis-Segmentierung und der Zwei-Stationenmethode läßt sich gelegentlich auch die sog. Ein-Stationenmethode anwenden, die vor allem für Messungen entlang ozeanischer Wellenwege von Bedeutung ist. Voraussetzung ist, daß die Herdzeit, das Epizentrum sowie das Phasenspektrum des Herdimpulses hinreichend genau bekannt sind und der Wellenweg Epizentrum-Beobachtungsstation relativ zur Wellenlänge annähernd homogen ist. Da die letzte Bedingung in der Regel kleine Epizentralentfernungen voraussetzt, lassen sich beide Forderungen im allgemeinen nicht gleichzeitig erfüllen; denn die zur Bestimmung des Phasenspek-

trums erforderlichen herdmmechanischen Elemente (Knopoff und Schwab, 1968) können nur für starke, weltweit zu beobachtende Beben ermittelt werden, welche die Aufzeichnungssysteme herdnaher Stationen in den meisten Fällen übersteuern. Einen Ausweg liefert die Hypothese, daß starke und schwache Beben innerhalb eines bestimmten Herdgebietes annähernd gleiche Herdmmechanismen haben. Mit dieser Annahme konnten Knopoff et al. (1969) sowie Knopoff et al. (1970) die Ein-Stationenmethode für einige pazifische Profile erfolgreich anwenden. Weidner (1974) hat mit der Ein-Stationenmethode die Phasengeschwindigkeiten von Rayleigh-Wellen für zahlreiche Wellenwege im nördlichen Atlantik abgeleitet und einen ersten Versuch einer Regionalisierung ozeanischer Dispersionsdaten unternommen.

Nach dem kurzen allgemeinen Überblick über die Möglichkeiten der Regionalisierung von Dispersionsdaten und Strukturelementen der Kruste und des oberen Mantels sollen einige spezielle Untersuchungen aus Europa diskutiert werden. Abbildung 10 zeigt eine Karte der regionalen Stationsnetze in den Alpen, im Alpenvorland und im Riftsystem um den Rheingraben, in denen systematische Phasengeschwindigkeitsmessungen an Rayleigh-Wellen durchgeführt wurden. Das Meßprogramm begann mit einer Untersuchung von Berckhemer et al. (1961) im Stationsnetz Stuttgart – Tübingen – Meßstetten – Ravensburg des Landes erdbebendienstes Baden-Württemberg, das mit Nahbeben seismographen übereinstimmender Charakteristiken ausgerüstet war. Die mit der „peak-and-through“-Methode berechneten Phasengeschwindigkeiten der Grundmode der Rayleigh-Wellen umfaßten den Periodenbereich von etwa 15–45 s und lieferten einen ersten Hinweis auf die Existenz einer Zone erniedrigter *S*-Geschwindigkeit im oberen Mantel unter Südwestdeutschland.

Die ersten systematischen Phasengeschwindigkeitsmessungen an Rayleigh-Wellen mit langperiodischen Seismographen wurden in den Alpen und im Alpenvorland von Knopoff et al. (1966) im Stationsnetz Stuttgart/Neuhausen – Besançon – Chur – Oropa (s. Abb. 10) durchgeführt. Durch Anwendung neu entwickelter Verfahren der numerischen Dispersionsanalyse konnten die Phasengeschwindigkeiten für die Grundmode der Rayleigh-Wellen für Perioden von etwa 15–80 s entlang verschiedener Stationslinien abgeleitet werden. Die Inversion beweist die Existenz eines ausgeprägten Asthenosphären-Kanals im gesamten Untersuchungsgebiet mit einer mittleren *S*-Geschwindigkeit um 4,2 km/s. Die Mächtigkeit der Lithosphäre beträgt etwa 80 km. Im kurzperiodischen Spektralbereich stehen die Dispersionsdaten in Einklang mit den aus refraktionsseismischen Messungen abgeleiteten Modellen der Erdkruste. Erste Vermutungen über regionale Schwankungen im Aufbau des Asthenosphären-Kanals konnten durch Dispersionsmessungen im Stationsnetz Stuttgart – Strasbourg – Pirmasens – Karlsruhe – Heidelberg (s. Abb. 10) bekräftigt werden (Seidl et al., 1966). Abbildung 11 zeigt, daß die experimentellen Phasengeschwindigkeiten beim Drehen der von Stuttgart ausgehenden Stationslinien im Gegenurzeigersinn systematisch abnehmen. Dies deutet auf eine Abnahme der *S*-Geschwindigkeit im Asthenosphären-Kanal bei Annäherung an den Alpenkörper hin. Die Dispersionsdaten für das Alpenvorland lassen sich befriedigend durch das Krusten-Mantel-Modell STU-3 (Reichenbach und Müller, 1974) erklären.

Die Oberflächenwellen von Fernbeben sind im kurzperiodischen Bereich

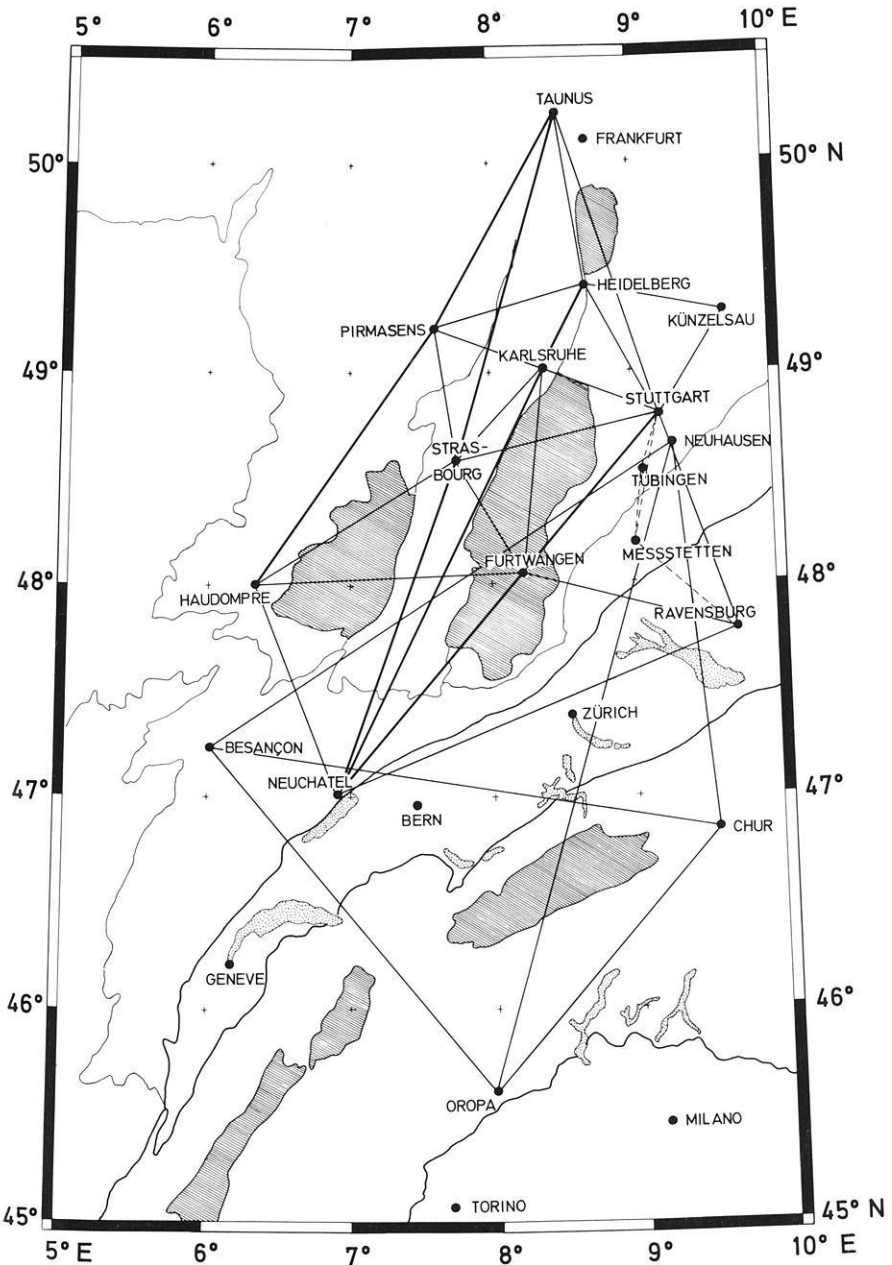


Abb. 10. Karte der regionalen Netzwerke langperiodischer Seismographenstationen im Alpenvorland, in den Alpen und im Riftsystem um den Rheingraben

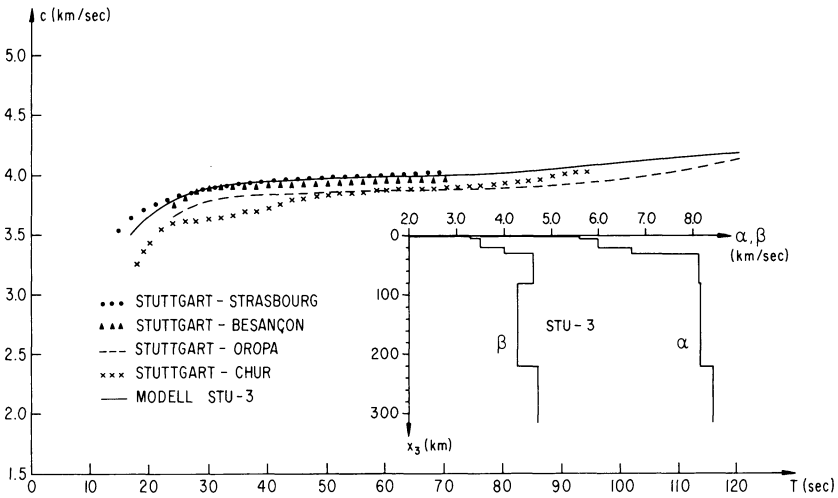


Abb. 11. Experimentelle Phasengeschwindigkeiten für die Grundmode der Rayleigh-Wellen entlang einiger Stationslinien in Abbildung 10. Die theoretische Dispersionskurve (ausgezogen) gehört zu einem einfachen Krusten-Mantel-Modell mit der Bezeichnung STU-3

($T < 15$ s) in der Regel durch Interferenzeffekte so stark gestört, daß eine Messung der Phasengeschwindigkeiten mit den in Abschnitt 4 beschriebenen Methoden nicht mehr möglich ist. Eine wertvolle Ergänzung bilden hier Gruppengeschwindigkeitsmessungen an Oberflächenwellen von Nahbeben nach der Ein-Stationenmethode, wie sie u.a. von Schneider et al. (1962) sowie von Zürn (1970) in mehreren geologischen Einheiten Mitteleuropas durchgeführt wurden. Kurzperiodische Dispersionsdaten dieser Art enthalten Informationen über den Aufbau der oberen Erdkruste und liefern wertvolle Nebenbedingungen bei der Inversion von Laufzeitdaten.

Phasengeschwindigkeitsmessungen im westlichen Mittelmeer (Berry und Knopoff, 1967) zeigen ebenfalls einen ausgeprägten Asthenosphären-Kanal mit deutlichen regionalen Strukturänderungen (s. Abb. 15). Im zentralen Teil des westlichen Mittelmeers (Stationslinien Algier – Cuglieri/Sardinien und Algier – Monaco) werden Lithosphärenmächtigkeiten von etwa 50 km und extrem niedrige S-Geschwindigkeiten im Asthenosphären-Kanal um 4.1 km/s beobachtet. Beide Werte erhöhen sich deutlich zu den Randzonen hin (Stationslinien Monaco – Tortosa und Monaco – Cuglieri) auf etwa 100 km bzw. 4.45 km/s. Ähnlich niedrige S-Geschwindigkeiten im Asthenosphären-Kanal (um 4.1 km/s) wie im westlichen Mittelmeerbecken wurden entlang der Linie Besançon – Monaco gefunden. Aus den bisherigen Messungen auf der Iberischen Halbinsel (Payo, 1970) ergibt sich eine Lithosphärenmächtigkeit von 80 km und eine mittlere S-Geschwindigkeit im Asthenosphären-Kanal von 4.2 km/s ähnlich wie im nördlichen Alpenvorland.

In Abbildung 12 sind die Ergebnisse von Phasengeschwindigkeitsmessungen an Rayleigh-Wellen im Riftsystem um den Rheingraben wiedergegeben. Eine Abschätzung der Beobachtungsfehler (Reichenbach und Müller, 1974) zeigt keine signifikanten Unterschiede für die vier Stationslinien Taunus (TNS)–

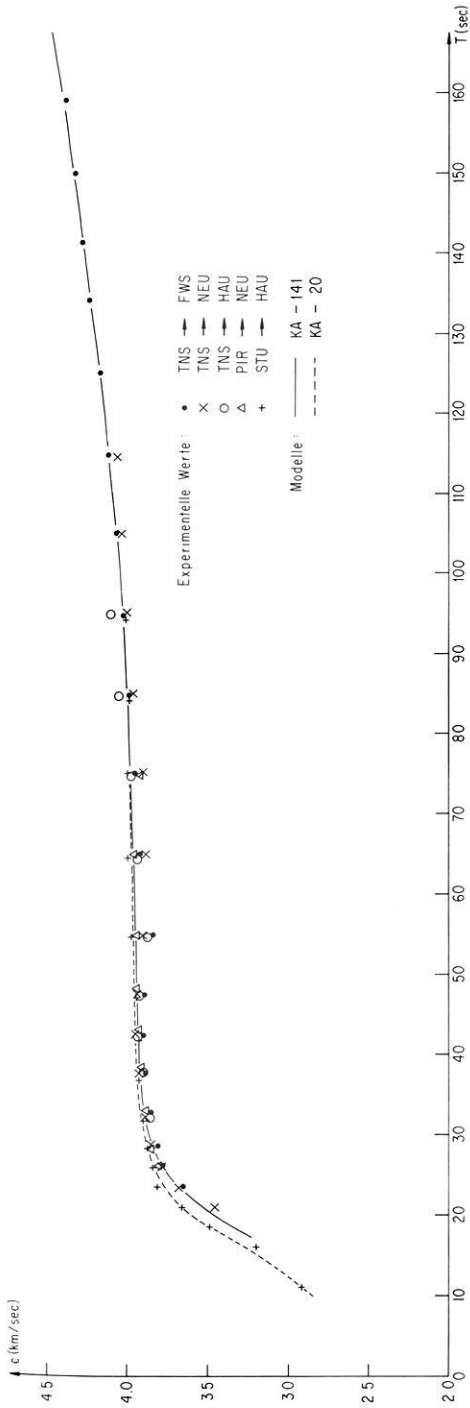


Abb. 12. Experimentelle Phasengeschwindigkeiten für die Grundmode der Rayleigh-Wellen im Riftsystem um den Rheingraben. Die theoretischen Dispersionskurven beziehen sich auf die Krusten-Mantel-Modelle KA-20 und KA-141 (s. Abb. 13)

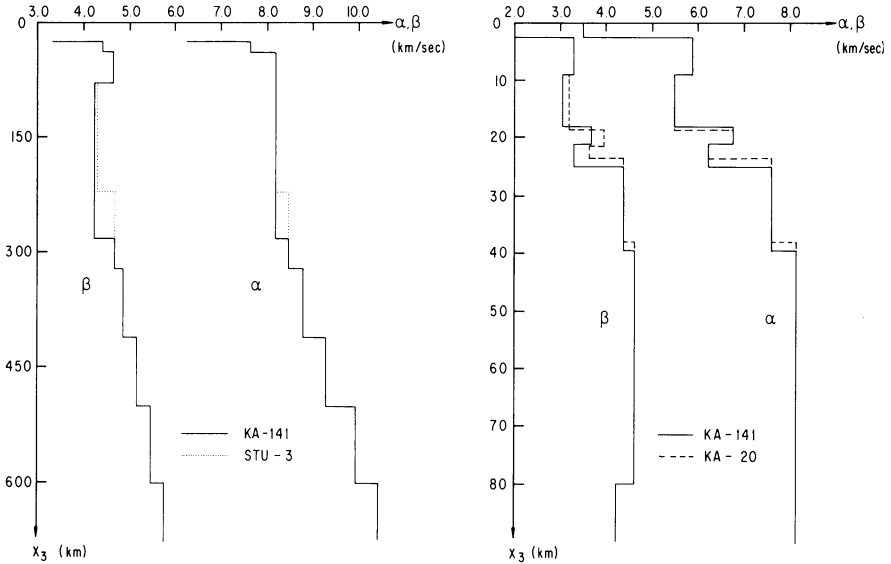


Abb. 13. Tiefenfunktionen der P - und S -Geschwindigkeiten für die Modelle KA-141, KA-20 und STU-3

Furtwangen (FWS), Taunus (TNS)–Neuchâtel (NEU), Taunus (TNS)–Haudompré (HAU) und Pirmasens (PIR)–Neuchâtel (NEU) (s. Abb. 10). Aus den Mittelwerten dieser vier Profile wurde das Krusten-Mantel-Modell KA-141 (Abb. 13) für die Grabenachse abgeleitet. Verglichen mit dem Modell STU-3 für das Alpenvorland, wo die untere Begrenzung der Mantel-Inversionszone nicht festgelegt werden konnte, ergibt sich hier eine Mächtigkeit des Asthenosphären-Kanals von ungefähr 200 km bei einer leicht erniedrigten S -Geschwindigkeit von etwa 4.25 km/s (s. Abb. 15). Für die quer zum Graben verlaufende Stationslinie Stuttgart (STU)–Haudompré (HAU) wurde das Krustenmodell KA-20 (Abb. 13) gefunden, das nur geringfügig von dem Modell KA-30 (Seidl et al., 1970) abweicht. Aus Abbildung 13 (rechts) sieht man, daß die S -Geschwindigkeiten des Modells KA-20 in der Kruste durchweg höher sind als für das Modell KA-141. Dies scheint darauf hinzudeuten, daß die S -Geschwindigkeiten gegen den Rand des Rift-systems hin zunehmen.

Um Aussagen über den tieferen Bereich des Asthenosphären-Kanals in Europa zu gewinnen, hat Seidl (1971) die Phasen- und Gruppengeschwindigkeiten langperiodischer Rayleigh-Wellen entlang der transeuropäischen Stationslinie Malaga (MAL)–Kopenhagen (COP) gemessen (s. Abb. 15). Es wurden die Aufzeichnungen eines Bebens bei den südlichen Sandwich-Inseln von 10 Stationen (9 europäische WWSS-Stationen sowie die Station Pirmasens im Rheingraben) analysiert. Die Ausbreitungsrichtung der Rayleigh-Wellen lag annähernd parallel zur Linie Malaga–Kopenhagen. Durch Inversion der experimentellen Dispersionsdaten (Abb. 14, oben) der Phasengeschwindigkeit c (für das Stationsnetz Malaga–Valentia/Irland–Stuttgart–Kopenhagen) bzw. der Gruppengeschwindigkeit U (für das Stationsdreieck Malaga–Stuttgart–Kopenhagen) mit der „Hedgehog“-Methode (s. Abschnitt 5) konnte das Modell KA-100 abgeleitet werden, dessen

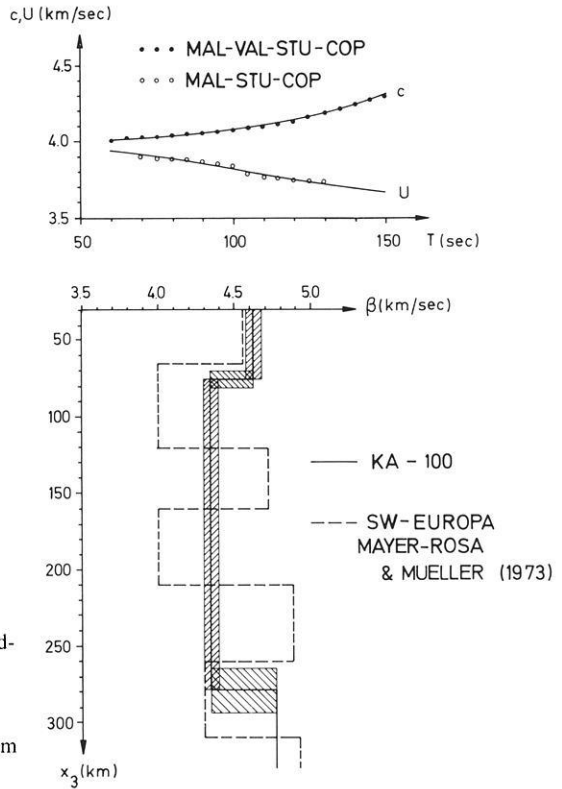


Abb. 14. Experimentelle Phasen- und Gruppengeschwindigkeiten für die Grundmode der Rayleigh-Wellen entlang der transeuropäischen Stationslinie Malaga-Kopenhagen. Die theoretischen Dispersionskurven (ausgezogen) entsprechen dem Modell KA-100

S-Geschwindigkeiten im Tiefenbereich 30 km (Krusten-Mantel-Grenze) bis 300 km in Abbildung 14 (unten) wiedergegeben sind. Die ausgezogenen Kurven in Abbildung 14 (oben) sind die theoretischen Dispersionskurven der Phasen- bzw. Gruppengeschwindigkeit des Modells KA-100. Die schraffierte Variationsbreite entspricht einem mittleren Fehler der experimentellen Phasengeschwindigkeiten von ± 0.03 km/s. Die Mächtigkeit der Lithosphäre beträgt demnach etwa (75 ± 5) km, die S-Geschwindigkeit in der Deckschicht (4.63 ± 0.05) km/s, die mittlere S-Geschwindigkeit im Asthenosphären-Kanal (4.34 ± 0.05) km/s. Die Untergrenze des Kanals liegt in einer Tiefe von etwa 280 km. Eine Untersuchung der lateralen Konsistenz des Modells KA-100 durch Variation des Stationsnetzes zeigt, daß dieses Modell als ein repräsentativer Mittelwert für einen regionalen Streifen quer durch Europa parallel zur Linie Malaga – Kopenhagen angesehen werden kann (s. Abb. 15). Abbildung 14 zeigt weiter einige Ergebnisse von Laufzeituntersuchungen an Raumwellen. Besonders bemerkenswert ist die Übereinstimmung der Kanal-Geschwindigkeit des Modells KA-100 (4.34 km/s) mit der über den Tiefenbereich von 65–310 km gemittelten S-Geschwindigkeit (4.33 km/s) des von Mayer-Rosa und Müller (1973) abgeleiteten Modells SW-Europa. Wie die numerischen Experimente aus Abbildung 9 zeigen, sind beide Modelle hinsichtlich der Signalverformung der Rayleigh-Grundmode für Stationsabstände um 2000 km (der Abstand Malaga – Kopenhagen beträgt etwa

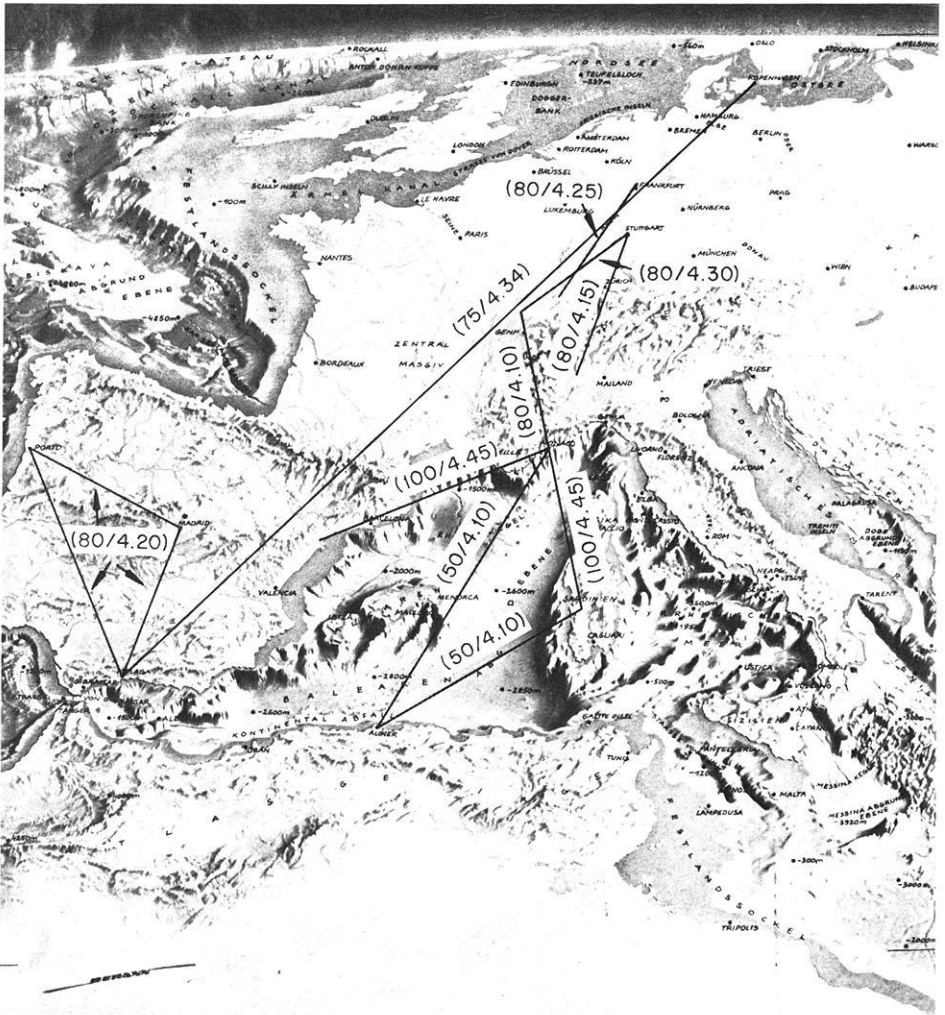


Abb. 15. Zusammenstellung publizierter Ergebnisse von Phasengeschwindigkeitsmessungen nach der Zwei-Stationen-Methode für die Grundmode der Rayleigh-Wellen in Europa (Karte aus der Illustrierten Stern). Die Zahlenpaare bedeuten die Mittelwerte der Lithosphärenmächtigkeit bzw. der mittleren S-Geschwindigkeit im Asthenosphären-Kanal für jede Stationslinie

2500 km) äquivalent. Einen Überblick über die bis jetzt bekannten Mittelwerte der Lithosphärenmächtigkeit und der S-Geschwindigkeit im Asthenosphärenkanal in Europa gibt Abbildung 15. Man kann daraus entnehmen, daß die Struktur des oberen Mantels in Europa deutliche regionale Änderungen aufweist.

Absorptionsmessungen

Obwohl die Kenngrößen seismischer Oberflächenwellen günstige Voraussetzungen für Absorptionsmessungen gewährleisten sollten (Anderson et al., 1965), ist es

erst in jüngster Zeit gelungen, einigermaßen konsistente Beobachtungsdaten für den spezifischen Gütefaktor Q_x abzuleiten (Burton, 1974). Die von Anderson et al., (1965), Ben-Menahem (1965), Marshall und Carpenter (1966), Kanamori (1970) sowie Smith (1972) und anderen Autoren publizierten Q_x -Daten zeigen sehr starke Streuungen, die sich nicht allein durch Beobachtungsfehler erklären lassen. Nach Überlegungen von Reiter (1973) könnten Energieverluste durch Reflexion, Refraktion und Modenkonversion an lateralen Inhomogenitäten in der Kruste und im Mantel einen entscheidenden Einfluß auf die Streuung der Absorptionsdaten von Oberflächenwellen und Eigenschwingungen ausüben. Trotz der noch sehr unvollständigen Beobachtungswerte lassen sich einige pauschale Aussagen über die anelastischen Eigenschaften des oberen Mantels machen. Die von Anderson, Ben-Menahem und Archambeau (1965) bzw. Smith (1972) abgeleiteten Modelle MM-8 bzw. LSM zeigen, daß der Asthenosphären-Kanal eine Zone erhöhter Absorption (erniedrigter Q -Werte) ist. Der Übergang zu den hohen Q -Werten im Tiefenbereich bis etwa 800 km dürfte durch eine relativ starke Gradientenzone an der Untergrenze des Kanals charakterisiert sein. Einen entscheidenden Fortschritt konnte Burton (1974) durch eine kritische statistische Analyse der an Rayleigh-Wellen von starken Kernexplosionen gemessenen Q_x -Daten erzielen. Seine Ergebnisse enthalten einen ersten Hinweis auf signifikante regionale Variationen der Absorption seismischer Oberflächenwellen.

Zusammenfassende Darstellungen über Absorptionsmessungen an Oberflächenwellen enthalten die Übersichtsartikel von Knopoff (1964), Yamakawa und Satô (1964), Satô (1967) und Smith (1972).

Literatur

Die Literaturzusammenstellung enthält nur die im Text zitierten Publikationen. Bei einer Übersicht über ein so weitgefaßtes Thema ist es unmöglich, alle Veröffentlichungen zu berücksichtigen. Die Verfasser bitten um Verständnis für die teilweise subjektive Literatúrauswahl.

- Alexander, S.S.: Surface wave propagation in the Western United States. Ph. D. Thesis, Calif. Inst. of Tech., 242 p., 1963
- Alterman, Z., Jarosch, H., Pekeris, C.L.: Oscillations of the earth. Proc. Roy. Soc. (London) A, **252**, 80–95, 1959
- Alterman, Z., Jarosch, H., Pekeris, C.L.: Propagation of Rayleigh waves in the earth. Geophys. J. **4**, 219–241, 1961
- Anderson, D.L., Archambeau, C.B.: The anelasticity of the earth. J. Geophys. Res. **69**, 2071–2084, 1964
- Anderson, D.L., Ben-Menahem, A., Archambeau, C.B.: Attenuation of seismic energy in the upper mantle. J. Geophys. Res. **70**, 1441–1448, 1965
- Anderson, D.L., Toksöz, M.N.: Surface waves on a spherical earth, I. J. Geophys. Res. **68**, 3483–3500, 1963
- Andrianova, Z.A., Keilis-Borok, V.I., Levshin, A.L., Neiganz, M.G.: Seismic Love waves. Consultants Bureau, New York, 1965
- Backus, G., Gilbert, F.: Numerical applications of a formalism for geophysical inverse problems. Geophys. J. **13**, 247–276, 1967
- Backus, G., Gilbert, F.: The resolving power of gross earth data. Geophys. J. **16**, 169–205, 1968
- Backus, G., Gilbert, F.: Uniqueness in the inversion of gross earth data. Phil. Trans. Roy. Soc. London **266**, 123–192, 1970
- Ben-Menahem, A.: Radiation of seismic surface waves from finite moving sources. Bull. Seism. Soc. Am. **51**, 401–435, 1961

- Ben-Menahem, A.: Observed attenuation and Q values of seismic surface waves in the upper mantle. *J. Geophys. Res.* **70**, 4641 – 4651, 1965
- Ben-Menahem, A., Harkrider, D.G.: Radiation pattern of seismic surface waves from buried dipolar point sources in a flat stratified earth. *J. Geophys. Res.* **69**, 2605 – 2620, 1964
- Berckhemer, H., Müller, St., Sellevoll, M.: Die Krustenstruktur in Südwestdeutschland aus Phasengeschwindigkeitsmessungen an Rayleigh-Wellen. *Z. Geophys.* **27**, 151 – 163, 1961
- Berry, M.J., Knopoff, L.: Structure of the upper mantle under the western Mediterranean basin. *J. Geophys. Res.* **72**, 3613 – 3626, 1967
- Biot, M.A.: General theorems on the equivalence of group velocity and energy transport. *Phys. Rev.* **105**, 1129 – 1137, 1957
- Biswas, N.N.: Earth-flattening procedure for the propagation of Rayleigh waves. *Pure and Appl. Geophys.* **96**, 61 – 74, 1972
- Biswas, N.N., Knopoff, L.: Exact earth-flattening calculation for Love waves. *Bull. Seism. Soc. Am.* **60**, 1123 – 1137, 1970
- Bloch, S., Hales, A.L.: New techniques for the determination of surface wave phase velocities. *Bull. Seism. Soc. Am.* **58**, 1021 – 1036, 1968
- Bolt, B.A.: Recent information on the earth's interior from studies of mantle waves and eigenvibrations. In: *Physics and chemistry of the earth*, Vol. 5, pp. 57 – 118, 1964
- Bolt, B., Dorman, J.: Phase and group velocities of Rayleigh waves in a spherical gravitating earth. *J. Geophys. Res.* **66**, 2965 – 2981, 1961
- Boore, D.M.: Love waves in nonuniform wave guides: Finite difference calculations. *J. Geophys. Res.* **75**, 1512 – 1528, 1970
- Boore, D.M.: Finite difference methods for seismic wave propagation in heterogeneous materials. In: *Methods in computational physics*, Vol. 11, *Seismology: Surface waves and earth oscillations*, pp. 1 – 37. London-New York: Academic Press 1972
- Brune, J.: Attenuation of dispersed wave trains. *Bull. Seism. Soc. Am.* **52**, 109 – 112, 1962
- Brune, J.N.: Surface waves and crustal structure. In: *The earth's crust and upper mantle*. *Geophys. Monograph* **13**, 230 – 242, 1969
- Brune, J., Dorman, J.: Seismic waves and earth structure in the Canadian Shield. *Bull. Seism. Soc. Am.* **53**, 167 – 209, 1963
- Brune, J.N., Nafe, J.E., Oliver, J.E.: A simplified method for the analysis and synthesis of dispersed wave trains. *J. Geophys. Res.* **65**, 287 – 304, 1960
- Burton, P.W.: Estimation of Q_7^{-1} from seismic Rayleigh waves. *Geophys. J.* **36**, 167 – 189, 1974
- Capon, J.: High resolution frequency-wavenumber spectrum analysis. *IEEE* **57**, 1408 – 1418, 1969
- Capon, J.: Analysis of Rayleigh wave multipath propagation at LASA. *Bull. Seism. Soc. Am.* **60**, 1701 – 1731, 1970
- Capon, J.: Comparison of Love and Rayleigh wave multipath propagation at LASA. *Bull. Seism. Soc. Am.* **61**, 1327 – 1344, 1971
- Capon, J., Evernden, J.F.: Detection of interfering Rayleigh waves at LASA. *Bull. Seism. Soc. Am.* **61**, 807 – 849, 1971
- Capon, J., Greenfield, R.J., Kolker, R.J.: Multidimensional maximum likelihood processing of a large aperture seismic array. *IEEE* **55**, 192 – 211, 1967
- Cooley, J.W., Tukey, J.W.: An algorithm for the machine calculation of complex Fourier series. *Math. of Comp.* **19**, 297 – 301, 1965
- Der, Z.A., Landisman, M.: Theory of errors, resolution and separation of unknown variables in inverse problems, with applications to the mantle and the crust in southern Africa and Scandinavia. *Geophys. J.* **27**, 137 – 178, 1972
- Der, Z., Massé, R., Landisman, M.: Effects of observational errors on the resolution of surface waves at intermediate distances. *J. Geophys. Res.* **75**, 3399 – 3409, 1970
- Dorman, J.: Seismic surface wave data on the upper mantle. In: *The Earth's crust and upper mantle*. *Geophys. Monograph* **13**, 257 – 265, 1969
- Dorman, J., Ewing, M.: Numerical inversion of seismic surface wave dispersion data and crust-mantle structure in the New York-Pennsylvania area. *J. Geophys. Res.* **67**, 5227 – 5242, 1962
- Dorman, J., Ewing, M., Oliver, J.: Study of shear-velocity distribution in the upper mantle by mantle Rayleigh waves. *Bull. Seism. Soc. Am.* **50**, 87 – 115, 1960
- Drake, L.A.: Love and Rayleigh waves in nonhorizontally layered media. *Bull. Seism. Soc. Am.* **62**, 1241 – 1258, 1972

- Drake, L.A.: Rayleigh waves at a continental boundary by the finite element method. *Bull. Seism. Soc. Am.* **62**, 1259–1268, 1972
- Drake, L.A., Mal, A.K.: Love and Rayleigh waves in the San Fernando Valley. *Bull. Seism. Soc. Am.* **62**, 1673–1690, 1972
- Dunkin, J.W.: Computation of modal solutions in layered, elastic media at high frequencies. *Bull. Seism. Soc. Am.* **55**, 335–358, 1965
- Dziewonski, A.: On regional differences in dispersion of mantle Rayleigh waves. *Geophys. J.* **22**, 289–325, 1970
- Dziewonski, A.: Upper mantle models from “pure-path” dispersion data. *J. Geophys. Res.* **76**, 2587–2601, 1971
- Dziewonski, A., Bloch, S., Landisman, M.: A technique for analysis of transient seismic signals. *Bull. Seism. Soc. Am.* **59**, 427–444, 1969
- Dziewonski, A., Hales, A.L.: Numerical analysis of dispersed seismic waves. In: *Methods in computational physics, Vol. 11, Seismology: Surface waves and earth oscillations*, pp. 39–85. London-New York: Academic Press 1972
- Dziewonski, A., Landisman, M.: Great circle Rayleigh and Love dispersion from 100 to 900 seconds. *Geophys. J.* **19**, 37–91, 1970
- Dziewonski, A., Landisman, M., Bloch, S., Satô, Y., Asano, S.: Progress report on recent improvements in the analysis of surface wave observations. *J. Phys. Earth* **16**, Special Issue, 1–26, 1968
- Dziewonski, A., Mills, J., Bloch, S.: Residual dispersion measurement—a new technique of surface wave analysis. *Bull. Seism. Soc. Am.* **62**, 129–139, 1972
- Ewing, W.M., Jardetzky, W.S., Press, F.: *Elastic waves in layered media*, 380 p. New York: McGraw-Hill 1957
- Ewing, M., Müller, St., Landisman, M., Satô, Y.: Transient analysis of earthquake and explosion arrivals. *Pure and Appl. Geophys.* **44**, 83–118, 1959
- Fischer, F.A.: *Einführung in die statistische Übertragungstheorie*. BI-Hochschultaschenbuch, Bibliographisches Institut Mannheim 1969
- Futterman, W.: Dispersive body waves. *J. Geophys. Res.* **67**, 5279–5291, 1962
- Gerver, M.: The inverse problem of seismology. *Tectonophysics* **13**, 483–496, 1972
- Gerver, M.L., Kazhdan, D.A.: Finding a velocity profile from a Love wave dispersion curve: Problems of uniqueness. In: *Computational seismology*, V.I. Keilis-Borok, ed., pp. 179–186. New York-London: Consultants Bureau 1972
- Gilbert, F., Backus, G.E.: Propagator matrices in elastic wave and vibration problems. *Geophysics* **31**, 326–332, 1966
- Gilbert, F., Backus, G.: Approximate solutions to the inverse normal mode problem. *Bull. Seism. Soc. Am.* **58**, 103–131, 1968
- Gilbert, F., MacDonald, G.J.F.: Free oscillations of the earth, I: Toroidal oscillations. *J. Geophys. Res.* **65**, 675–693, 1960
- Goodman, N.R.: Measuring amplitude and phase. *J. Franklin Inst.* **260**, 437–450, 1960
- Harkrider, D.G.: Surface waves in multilayered elastic media. Part I: Rayleigh and Love waves from buried sources in a multilayered elastic halfspace. *Bull. Seism. Soc. Am.* **54**, 627–679, 1964
- Harkrider, D.G.: Surface waves in multilayered elastic media. Part II: Higher mode spectra and spectral ratios from point sources in plane layered earth models. *Bull. Seism. Soc. Am.* **60**, 1937–1987, 1970
- Harkrider, D.G., Anderson, D.L.: Surface wave energy from point sources in plane layered earth models. *J. Geophys. Res.* **71**, 2967–2980, 1966
- Haskell, N.A.: The dispersion of surface waves in multilayered media. *Bull. Seism. Soc. Am.* **43**, 17–34, 1953
- Haskell, N.A.: Radiation pattern of surface waves from point sources in a multilayered medium. *Bull. Seism. Soc. Am.* **54**, 377–393, 1964
- Haskell, N.A.: Total energy and energy spectral density of elastic waves radiation from propagating faults. *Bull. Seism. Soc. Am.* **54**, 1811–1841, 1964
- Haskell, N.A.: Total energy and energy spectral density of elastic waves radiation from propagating faults. Part II: A statistical source model. *Bull. Seism. Soc. Am.* **56**, 125–140, 1966
- Hudson, J.A., Knopoff, L.: Transmission and reflection of surface waves at a corner—1. Love waves. *J. Geophys. Res.* **69**, 275–280, 1964
2. Rayleigh waves (theoretical). *J. Geophys. Res.* **69**, 281–289, 1964

- Iyer, H.M.: A frequency-velocity-energy diagram for the study of dispersive surface waves. *Bull. Seism. Soc. Am.* **54**, 183–190, 1964
- Jackson, D.D.: Marginal solutions to quasi-linear inverse problems in geophysics: The edgehog method. *Geophys. J.* **35**, 121–136, 1973
- Jeans, J.H.: The propagation of earthquake waves. *Proc. Roy. Soc. (London) A*, **102**, 554–574, 1923
- Julian, B.R.: The effect of lateral heterogeneity upon surface wave propagation. *Semiannual Technical Report*, Lincoln Laboratory, 1 Jan.–30. June, 23–24, 1972
- Kanamori, H.: Velocity and Q of mantle waves. *Phys. Earth Planet. Interiors* **2**, 259–275, 1970
- Kausel, E., Schwab, F.: Contributions to Love wave transformation theory: Earth-flattening transformation for Love waves from a point source in a sphere. *Bull. Seism. Soc. Am.* **63**, 983–993, 1973
- Keilis-Borok, V.I., Yanovskaja, T.B.: Inverse problems of seismology (structural review). *Geophys. J.* **13**, 223–234, 1967
- Knopoff, L.: Green's function for eigenvalue problems and the inversion of Love wave dispersion data. *Geophys. J.* **4**, 161–173, 1961
- Knopoff, L.: Higher-order Born approximations for the inversion of Love wave dispersion. *Geophys. J.* **7**, 149–157, 1962
- Knopoff, L.: A matrix method for elastic wave problems. *Bull. Seism. Soc. Am.* **54**, 431–438, 1964
- Knopoff, L.: *Q. Rev. Geophys.* **2**, 625–660, 1964
- Knopoff, L.: Phase and group slowness in inhomogeneous media. *J. Geophys. Res.* **74**, 1701, 1969
- Knopoff, L.: Observation and inversion of surface wave dispersion. *Tectonophysics* **13**, 497–519, 1972
- Knopoff, L., Aki, K., Archambeau, C.B., Ben-Menahem, A., Hudson, J.A.: Attenuation of dispersed waves. *J. Geophys. Res.* **69**, 1655–1657, 1964
- Knopoff, L., Berry, M.J., Schwab, F.A.: Tripartite phase velocity observations in laterally heterogeneous regions. *J. Geophys. Res.* **72**, 2595–2601, 1967
- Knopoff, L., Hudson, J.A.: Transmission of Love waves past a continental margin. *J. Geophys. Res.* **69**, 1649–1653, 1964
- Knopoff, L., Mal, A.K.: Phase velocity of surface waves in the transition zone of continental margins. 1. Love waves. *J. Geophys. Res.* **72**, 1769–1776, 1967
- Knopoff, L., Mal, A.K., Alsop, L.E., Phinney, R.A.: A property of long-period Love waves. *J. Geophys. Res.* **75**, 4084–4086, 1970
- Knopoff, L., Müller, St., Pilant, W.L.: Structure of the crust and upper mantle in the Alps from the phase velocity of Rayleigh waves. *Bull. Seism. Soc. Am.* **56**, 1009–1044, 1966
- Knopoff, L., Schlue, J.W.: Rayleigh wave phase velocities for the path Addis Ababa-Nairobi. *Tectonophysics* **15**, 157–163, 1972
- Knopoff, L., Schlue, J.W., Schwab, F.A.: Phase velocities of Rayleigh waves across the East Pacific Rise. *Tectonophysics* **10**, 321–324, 1970
- Knopoff, L., Schwab, F.A.: Apparent initial phase of a source of Rayleigh waves. *J. Geophys. Res.* **73**, 755–760, 1968
- Knopoff, L., Schwab, F.A., Kausel, E.: Interpretation of Lg. *Geophys. J.* **33**, 389–404, 1973
- Knopoff, L., Schwab, F.A., Schlue, J.W.: The dispersion of Rayleigh waves south of the Gulf of California. *Geophys. Int.* **9**, 39–52, 1969
- Kovach, R.L.: Seismic surface waves: Some observations and recent developments. In: *Physics and chemistry of the earth*, Vol. 6, pp. 251–314, 1965
- Kovach, R.L., Anderson, D.L.: Long-period Love waves in a heterogeneous spherical earth. *J. Geophys. Res.* **67**, 5243–5256, 1962
- Lamb, G.L.: The attenuation of waves in a dispersive medium. *J. Geophys. Res.* **67**, 5273–5277, 1962
- Lamb, H.: On the propagation of tremors over the surface of an elastic solid. *Phil. Trans. Roy. Soc. London A* **203**, 1–42, 1904
- Landisman, M., Dziewonski, A., Satô, Y.: Recent improvements in the analysis of surface wave observations. *Geophys. J.* **17**, 369–403, 1969
- Love, A.E.H.: *Some problems of geodynamics*. Cambridge University Press 1911
- Lysmer, J.: Lumped mass method for Rayleigh waves. *Bull. Seism. Soc. Am.* **60**, 89–104, 1970
- Lysmer, J., Drake, L.A.: The propagation of Love waves across nonhorizontally layered structures. *Bull. Seism. Soc. Am.* **61**, 1233–1251, 1971
- Lysmer, J., Drake, L.A.: A finite element method for seismology. In: *Methods in Computational*

- Physics, Vol. 11, Seismology: Surface waves and earth oscillations, pp. 181–216. London-New York: Academic Press 1972
- Macke, W.: Wellen. Ein Lehrbuch der Theoretischen Physik. Leipzig: Akadem. Verlagsges. 1962
- Mal, A. K., Knopoff, L.: Transmission of Rayleigh waves past a step change in elevation. *Bull. Seism. Soc. Am.* **55**, 319–334, 1965
- Mal, A. K., Knopoff, L.: Transmission of Rayleigh waves at a corner. *Bull. Seism. Soc. Am.* **56**, 455–466, 1966
- Marshall, P. D., Carpenter, E. W.: Estimations of Q for Rayleigh waves. *Geophys. J.* **10**, 549–550, 1966
- Mayer-Rosa, D., Müller, St.: The gross velocity-depth distribution of P - and S -waves in the upper mantle of Europe from earthquake observations. *Z. Geophys.* **39**, 395–410, 1973
- Müller, St., Ewing, M.: Synthesis of normally dispersed wave trains by means of linear system theory. *Lamont Geological Observatory, Contribution 559*, 230 p., 1962
- Oliver, J.: A summary of observed seismic surface wave dispersion. *Bull. Seism. Soc. Am.* **52**, 81–86, 1962
- Panza, G. F., Schwab, F. A., Knopoff, L.: Channel and crustal Rayleigh waves. *Geophys. J.* **30**, 273–280, 1972
- Panza, G. F., Schwab, F. A., Knopoff, L.: Multimode surface waves for selected focal mechanisms I. Dip-slip sources on a vertical fault plane. *Geophys. J.* **34**, 265–278, 1973
- Payo, G.: Structure of the crust and upper mantle in the Iberian shield by means of a long-period triangular array. *Geophys. J.* **20**, 493–508, 1970
- Pekeris, C. L.: Propagation of sound in the ocean. *Geol. Soc. Amer., Memoir 27*, 1–117, 1948
- Pestel, E. C., Leckie, F. A.: Matrix methods in elastomechanics. New York: McGraw-Hill 1963
- Pilant, W., Knopoff, L.: Observations of multiple seismic events. *Bull. Seism. Soc. Am.* **54**, 19–39, 1964
- Pilant, W. L., Knopoff, L.: Inversion of phase and group slowness dispersion. *J. Geophys. Res.* **75**, 2135–2136, 1970
- Press, F.: Determination of crustal structure from phase velocity of Rayleigh waves I: Southern California. *Bull. Geol. Soc. Am.* **67**, 1647–1658, 1956
- Press, F.: Earth models obtained by Monte Carlo inversion. *J. Geophys. Res.* **73**, 5223–5234, 1968
- Press, F.: Earth models consistent with geophysical data. *Phys. Earth Planet. Interiors* **3**, 3–22, 1970
- Press, F.: The earth's interior as inferred from a family of models. In: *The Nature of the Solid Earth*, E. C. Robertson, ed., pp. 147–171. New York: McGraw-Hill 1972
- Press, F., Harkrider, D. G., Seefeldt, C. A.: A fast convenient program for computation of surface wave dispersion curves in multilayered media. *Bull. Seism. Soc. Am.* **51**, 495–502, 1961
- Randall, M. J.: Fast programs for layered half-space problems. *Bull. Seism. Soc. Am.* **57**, 1299–1315, 1967
- Rayleigh, Lord: On waves propagated along the plane surface of an elastic solid. *Proc. Math. Soc., London* **17**, 4–11, 1885
- Reichenbach, H., Müller, St.: Ein Krusten-Mantel-Modell für das Riftsystem um den Rheingraben, abgeleitet aus der Dispersion von Rayleigh-Wellen. In: *Approaches to Taphrogenesis*, H. J. Illies & K. Fuchs, eds., pp. 348–354. Stuttgart: Schweizerbart 1974
- Reiter, L.: Reflection, refraction and mode conversion of long-period surface waves and the measurement of Q^{-1} for free oscillations. *Bull. Seism. Soc. Am.* **63**, 1709–1722, 1973
- Saito, M.: Excitation of free oscillations and surface waves by a point source in a vertically heterogeneous earth. *J. Geophys. Res.* **72**, 3689–3699, 1967
- Satō, R.: Attenuation of seismic waves. *J. Phys. Earth* **15**, 32–61, 1967
- Satō, Y.: Analysis of dispersed surface waves by means of Fourier Transform: Part 1. *Bull. Earthquake Res., Tokyo Univ.* **33**, 33–47, 1955
- Savarenski, E. F.: On the determination of group and phase velocities from observations. *Izvest. Akad. Nauk., Geophys. Ser.* **11**, 1550–1559, 1959
- Schneider, G., Müller, St., Knopoff, L.: Gruppengeschwindigkeitsmessungen an kurzperiodischen Oberflächenwellen in Mitteleuropa. *Z. Geophys.* **32**, 33–58, 1966
- Schwab, F.: Surface-wave dispersion computations: Knopoff's method. *Bull. Seism. Soc. Am.* **60**, 1491–1520, 1970
- Schwab, F., Knopoff, L.: Surface-wave dispersion computations. *Bull. Seism. Soc. Am.* **60**, 321–344, 1970

- Schwab, F., Knopoff, L.: Surface waves on multilayered anelastic media. *Bull. Seism. Soc. Am.* **61**, 893–912, 1971
- Schwab, F., Knopoff, L.: Fast surface wave and free mode computations. In: *Methods in Computational Physics*, Vol. 11, *Seismology: Surface waves and earth oscillations*, pp. 87–180. London-New York: Academic Press 1972
- Schwab, B. F., Knopoff, L.: Love waves and the torsional free modes of a multilayered anelastic sphere. *Bull. Seism. Soc. Am.* **63**, 1107–1117, 1973
- Seidl, D.: Spezielle Probleme der Theorie seismischer Oberflächenwellen mit Beobachtungsbeispielen aus Europa. Dissertation, Universität Karlsruhe, 105 p., 1971
- Seidl, D., Müller, St., Knopoff, L.: Dispersion von Rayleigh-Wellen in Südwestdeutschland und in den Alpen. *Z. Geophys.* **32**, 427–481, 1966
- Seidl, D., Reichenbach, H., Müller, St.: Dispersion investigations of Rayleigh waves in the Rhinegraben Rift System. In: *Graben Problems*, H. Illies and St. Müller, eds., pp. 203–206. Stuttgart: Schweizerbart 1970
- Smith, S. W.: The anelasticity of the mantle. *Tectonophysics* **13**, 601–622, 1972
- Takeuchi, H., Saito, M.: Seismic surface waves. In: *Methods in Computational Physics*, Vol. 11, *Seismology: Surface waves and earth oscillations*, pp. 217–295. Academic Press 1972
- Thomson, W. T.: Transmission of elastic waves through a stratified solid medium. *J. Appl. Phys.* **21**, 89–93, 1950
- Thrower, E. N.: The computation of the dispersion of elastic waves in layered media. *J. Sound Vib.* **2**, 210–226, 1965
- Toksöz, M. N., Anderson, D. L.: Phase velocities of long-period surface waves and structure of the upper mantle. 1. Great circle Love and Rayleigh wave data. *J. Geophys. Res.* **71**, 1649–1658, 1966
- Toksöz, M. N., Ben-Menahem, A.: Velocities of mantle Love and Rayleigh waves over multiple paths. *Bull. Seism. Soc. Am.* **53**, 741–764, 1963
- Tolstoy, I.: *Wave propagation*, 466 p. New York: McGraw-Hill 1973
- Tolstoy, I., Clay, C. S.: *Ocean acoustics*. New York: McGraw-Hill, 293 p., 1966
- Tolstoy, I., Usdin, E.: Dispersive properties of stratified elastic and liquid media: A ray theory. *Geophysics* **18**, 844–870, 1953
- Watson, T. H.: A note on fast computation of Rayleigh wave dispersion in the multilayered elastic half-space. *Bull. Seism. Soc. Am.* **60**, 161–166, 1970
- Weidner, D. H.: Rayleigh wave phase velocities in the Atlantic Ocean. *Geophys. J.* **36**, 105–139, 1974
- Wiggins, R.: The general linear inverse problem: Implications of surface waves and free oscillations for earth structure. *Rev. Geophysics* **10**, 251–285, 1972
- Yamakawa, N., Satô, Y.: *Q* of surface waves. *J. Phys. Earth* **12**, 5–18, 1964
- Zürn, W.: Analyse der Dispersion kurzperiodischer Oberflächenwellen im nördlichen Alpenvorland aus Magnetbandregistrierungen von Nahbeben. Dissertation, Universität Stuttgart, 110 p., 1970

Eingegangen am 27. April 1976

Original Investigations

**Crustal Structure of the Central Aegean Sea
and the Islands of Evia and Crete, Greece,
Obtained by Refractional Seismic Experiments**

J. Makris¹ and R. Veis²

¹ Institut für Geophysik, Universität Hamburg,
Bundesstraße 55, D-2000 Hamburg 13, Federal Republic of Germany

² Institut für Geophysik, T.U. Clausthal,
Arnold-Sommerfeld-Str. 1, D-3329 Clausthal-Zellerfeld, Federal Republic of Germany

Abstract. In 1973 and 1974 deep seismic sounding experiments were performed in the Aegean area by German and Greek geophysicists, from which two crustal sections were established. The one strikes along the islands of Amorgos-Mikonos-Andros and Evia and the other along Crete, in the E-W direction. The main results obtained are:

Along the Amorgos-Mikonos-Evia section the crust is updipping from 32 km below Evia to 26 km below Amorgos in the southern Aegean Sea.

The crust is of the continental type with $V_{pg} = 6.0$ km/s for the crystalline basement and 7.7 km/s for the upper mantle.

The average velocity of the crust computed from P_mP -reflections has a value of 6.21 km/s.

The sedimentary cover is very unevenly distributed with maximum thickness at North Evia. The crystalline basement outcrops at the southern part of the island and the Cyclades.

Along Crete the crust is somewhat thicker, than that below South-Evia with 34 km at the western part and about 30 km at the eastern part of the island.

At the western part of the island the nappes have their greatest thickness, the Messara Basin in the east containing the largest neogene sequences on Crete.

The crustal structure of Crete is also of the average continental type.

Key words: Seismic experiments – Crustal structure of Aegean Area, Greece.

1. Introduction

In March and April 1973, 28 MARS-66 seismic recording stations (Berckhemer, 1970) provided by various German universities¹ were used to record 8 shots fired east and west of Crete, south of Mikonos and at North Evia (see Fig. 1). The shots with charges ranging between 0.4 and 3 tons, were fired at sea and at a quarry of the "Skalistiris Mining Co." at Mandouthi, North Evia. Thus, by reversing both profiles we intended to obtain true *P*-wave velocities along the seismic sections and the crustal structure and thickness. Extrapolations from the Ionian Sea-Peloponnese seismic section (Makris, 1975, 1976) indicated that the crust below Evia had an approximate thickness of the order of 28–32 km. This result, however, was liable to errors, since no true velocities for the Peloponnese crust had been obtained by the Ionian Sea-Peloponnese seismic experiment of 1971 (Makris, 1972).

The measurements reported below were supported by the National Institute of Geological and Mining Researches (NIGMR) Athens, which provided the explosives and was responsible for permits and for contacting the various Greek authorities.

2. Location of the Profiles and Some Technical Details

The Evia-Mikonos profile has a length of 270 km and was observed at 46 locations with an average separation of 5.5 km. Two shots of 3 t. were fired at Mandouthi (SP2), North Evia, and gave excellent recordings over the whole length of the section. The reversed observations were obtained by firing two shots of 0.4 and 0.8 tons at sea south of Mikonos. The first shot (0.4 tons) also gave very good recordings for the first part of the seismic section and partly reversed the observations of the "Mandouthi" shots. The second shot (0.8 ton) could not be recorded due to very bad weather conditions. We repeated our observations on Evia in 1974 by firing a 0.8-ton shot south of Amorgos (see Fig. 1) and completed this section to a fully reversed profile (see Fig. 6).

¹ The following institutes and persons participated in the seismological program:

(1) Bundesanstalt für Geowissenschaften und Rohstoffe, Hannover: Sudhir Garde, Heinz Schröder, Hermann Schubart.

(2) Institut für Geophysik, Technische Universität, Clausthal-Zellerfeld: Tilmann Rothfuchs, Günter Wagenbreth, Michael Leppin, Dietrich Schöneck, Klaus Kaiser, Roland Vees, Friedrich Schildknecht, Bernd Kölln, Hermann Hemschmeier.

(3) Institut für Geophysik, Freie Universität, Berlin: Franz Renger, Peter Röwer, Detlev Damaske, Karl Georg Schütte, Christian Reichert.

(4) Institut für Geophysik, Technische Universität, Karlsruhe: Klaus Schulz, Peter Thorner, Sonja Faber.

(5) Institut für Meteorologie und Geophysik, Universität Frankfurt: Wolfgang Lorig, Timann Spohn.

(6) Institut für Geophysik, Universität Hamburg: Walter Grevsmühl, Hermann Richter, Walter Homann, Helmut Gertig, Jürgen Klufmann, Jürgen Rohde, Klaus Müller, Jannis Makris, Dorothee Ruhle von Berg, Monika Hamann.

(7) National Institute of Geological and Mining Researches, Athen: Agellos Stavrou, Nikos Tsambourakis, Spiros Prionas, Georg Laios

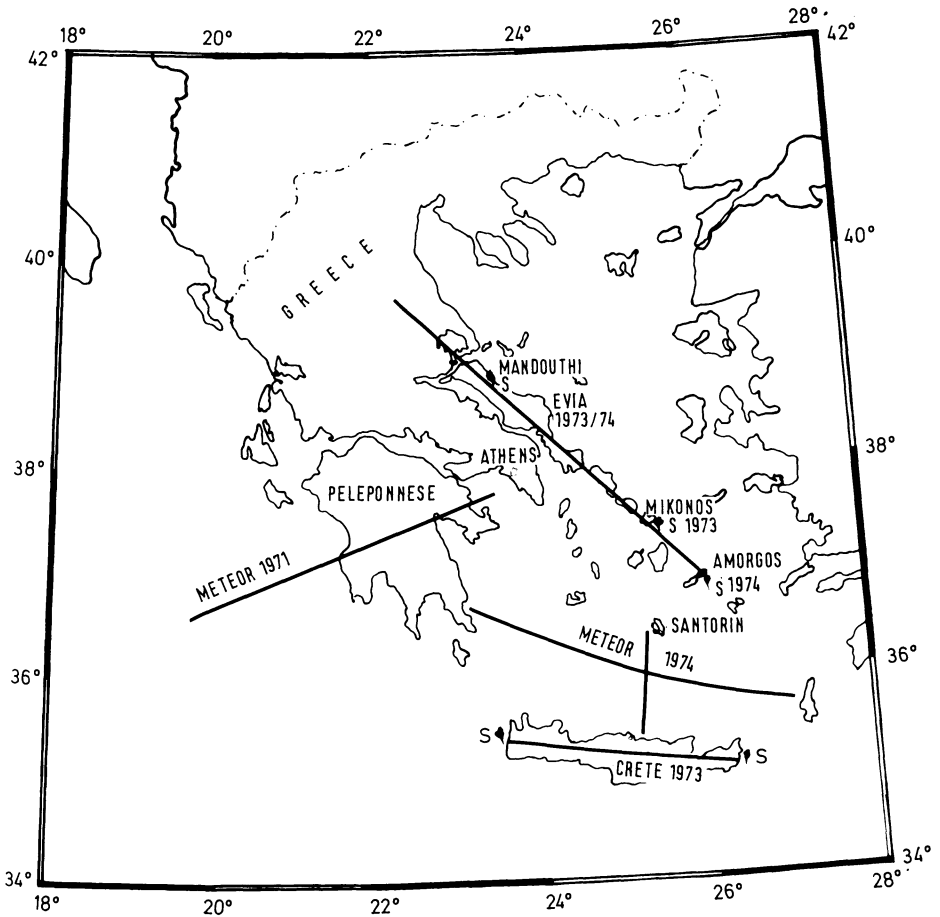


Fig. 1. Locations of profiles and distribution of recording stations and shots

The Cretan section has a length of 260 km. The mean separation of the seismic stations is app. 5.0 km. The section was also observed in two parts by firing four shots at sea; two at the eastern and two at the western coast of Crete. The explosions at the eastern coast gave good recordings all along the seismic section. The reversed profile, however, was not completed (see Fig. 8), since very bad weather conditions did not permit us to adjust the shot depth properly. A great part of the explosion energy was lost in the explosion fountain and no observations could be made at the distant stations.

Time signals and information to seismic stations were transmitted through "Radio Pallini" by Athens at 3.15 MHz. This Radio station had been put at our disposal by OTE (Organization of Telecommunications of Greece) and could be modulated through any telephone of the Greek telephone system. The OTE-organization supported our program very efficiently and contributed considerably to the success of this experiment.

3. Processing and Evaluation of Seismic Data

Most analogue tape recordings of both seismic sections were digitized at the CDC-1700 analogue-digital computer of the Institute of Geophysics, University of Hamburg. The data were band-pass filtered between 0.2 and 20 Hz and were plotted in time-distance curves. The time scale of the plots was reduced by 6 km/s, so that signals travelling with this velocity correlate to curves parallel to the distance axis. No elevation corrections were applied, since the locations of the stations do not differ significantly in altitude. The seismic arrivals that were used for the interpretation are the P_g , P_n and P_mP -phases. The velocity of the sediments was assumed to be 4 km/s. This was necessary, since the sedimentary cover was too thin and the 5 km spacing of the stations too large to permit first-arrivals through the sediments to be recorded. The P_g -phase gave true velocities of 6 km/s for all sections. The P_n -velocity appears with various apparent values from section to section according to the dip of the Moho-discontinuity. The true value of the P_n -phase was computed from the Evia sections and the Amorgos-shot of 1974 to 7.7 km/s. Below Crete the apparent velocity of the P_n -phase is 7.54 km/s. Since no reversed observations for this signal group were obtained, it is not possible to give a true P -wave velocity of the upper mantle below Crete. The fact, however, that the seismic section was positioned parallel to the strike of the morphological units and the very small gravity gradient along the section (Makris, 1976), indicate that the Moho-morphology in the east-west direction does not change significantly. Therefore, the P_n -velocity obtained must be very near to the true one. In any case, both profiles, that of Evia as well as that of Crete show P -wave velocities which are smaller than 8 km/s.

Strong PmP-phases were recorded at the Mikonos, Evia and Amorgos sections and permit a more reliable interpretation along the Amorgos-Mandouthi line than at Crete. The evaluation of the PmP-reflections according to the t^2 - Δ^2 -method gave a mean crustal thickness of 29 km and a mean P -wave velocity of 6.21 km/s for Evia.

The seismic data were evaluated in the following way: First, the directly correlated apparent velocities and intercept-times were used to construct a model of dipping first order seismic discontinuities. The model was then checked by means of gravity data and its parameters varied until the best fit between computed and observed Bouguer gravity anomalies was achieved. Finally, theoretical travel-times were computed and compared with the observed data. The method used for the computation of the travel-time curves is a modified version of the "trapezoid-method" (Stein, 1968). According to this method the model is divided into equidistant sections along the x-axis which are limited by first order discontinuities at depth. These discontinuities also limit intervals in which a prescribed velocity-depth function is valid. In all computations linear velocity-depth functions, $v^i(z) = v^i_0 + a^iz$, are used. The a^i velocity gradients are either automatically computed below the shot-point by defining velocities at the upper and lower limit of each interval, or, in the case of strong lateral variations, are given as constants for each section of the model involved. The travel-times are computed by summing up the time intervals, δt_k^j needed by the j -seismic

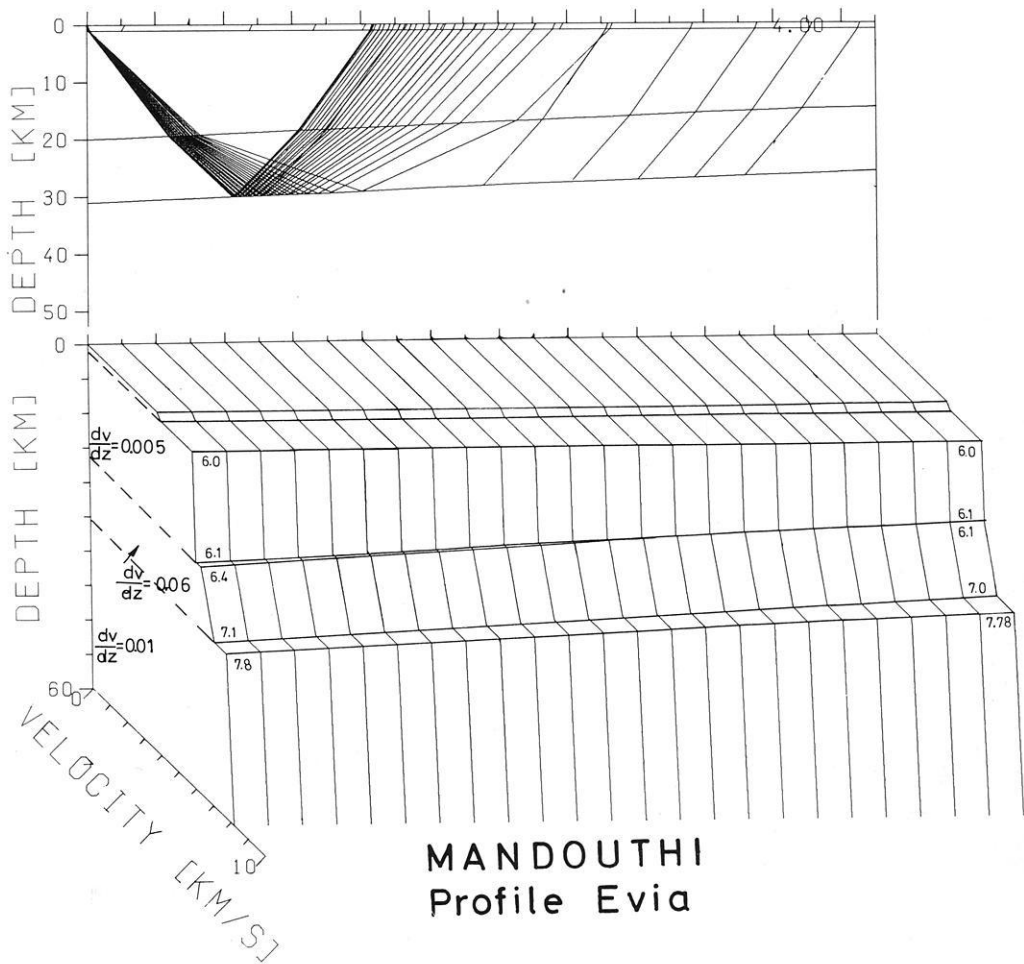
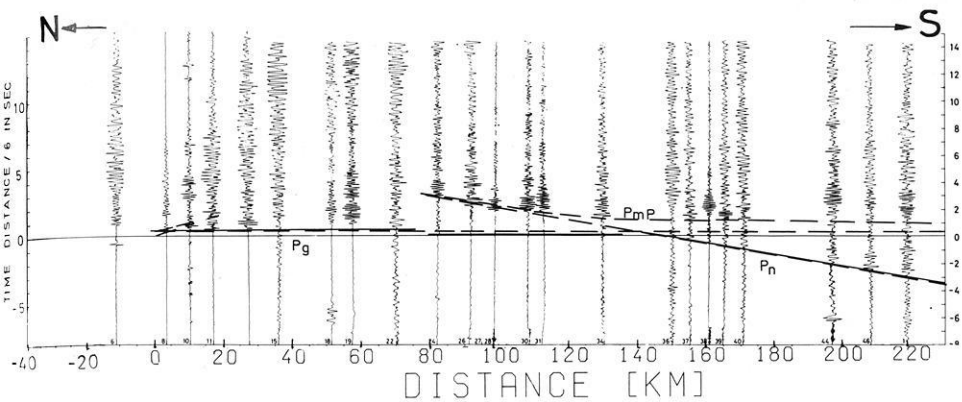
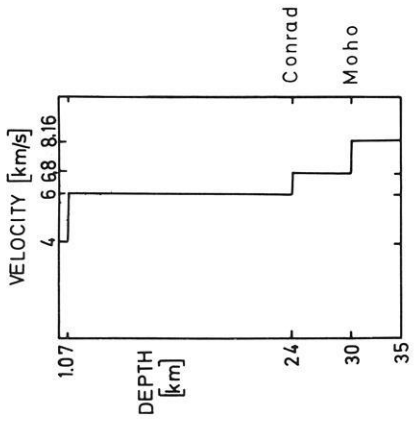


Fig. 2. Evia-section observed in N-S direction (Mandouthi-shot). In the upperpart of the drawing the travel-time diagram is given. The time-axis is reduced with 6 km/s. This is valid for all travel-time diagrams presented in this paper. — lines give the direct correlations. ---- lines give the theoretically computed travel-times according to the model presented at the middle part of the drawing. At the lower part, the $v(z)$ -curves along the model and the P -wave velocities and gradients dv/dz are given. By introducing a velocity gradient at the lower part of the crust, the best fit between computed and observed travel-times of the P_g - P_n - and P_mP -phases was obtained

Fig. 3. Evia-section observed in N-S direction (Mandouthi-shot) — First order discontinuity model. The velocity — depth function below the shotpoint is given at the upper left part of the drawing. The theoretically computed travel-time curves satisfy the observed P_g , P_mP and P_n travel-times. This model has to be rejected however, since no reflections from a 1.-order Conrad-Discontinuity have been observed. — Directly correlated ---- theoretically computed travel-times theoretically computed Conrad Reflections



PROFILE EVIA
SHOTPOINT MANDOUTH

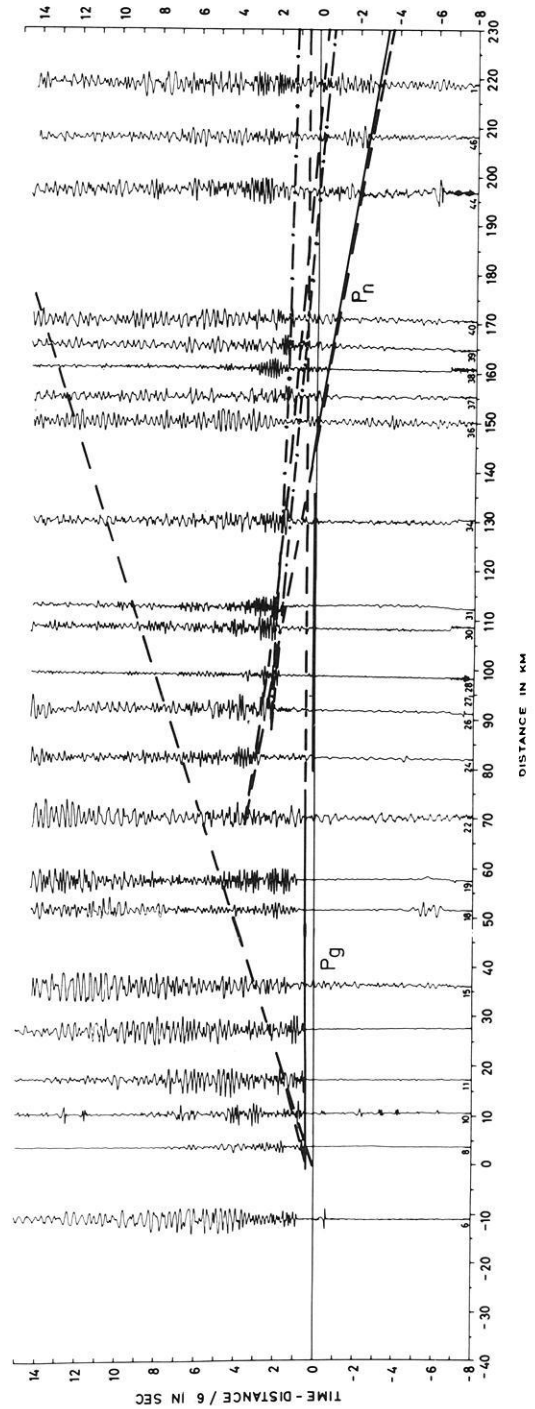
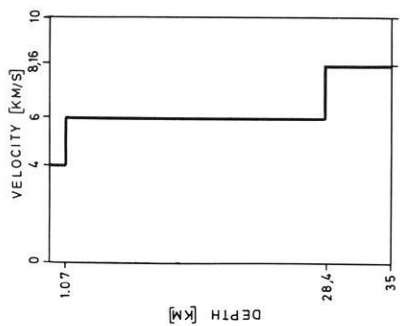
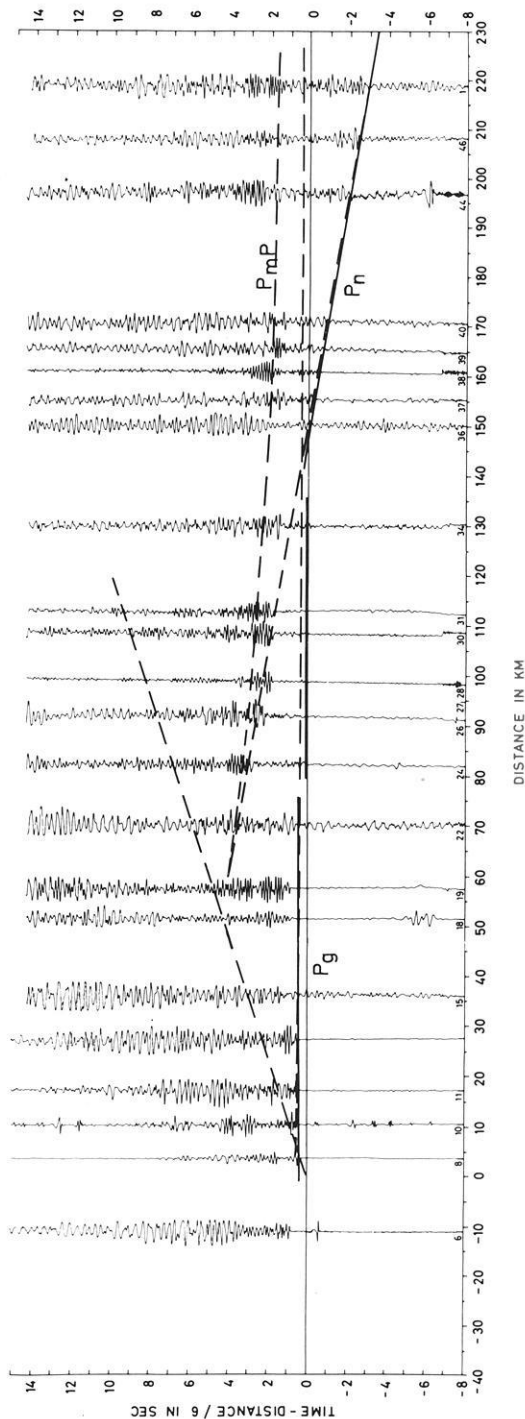


Fig. 4. Evia-section observed in N-S direction. This single-layer crust model limited by a 1.-order Moho discontinuity satisfies the P_g - and P_n -phases but not the P_m - P -wide angle reflections. For this reason it is rejected. --- Directly correlated --- theoretically computed travel-times



PROFILE EVIA
SHOTPOINT MANDOUTH1



PROFILE EVIA
SHOTPOINT MIKONOS

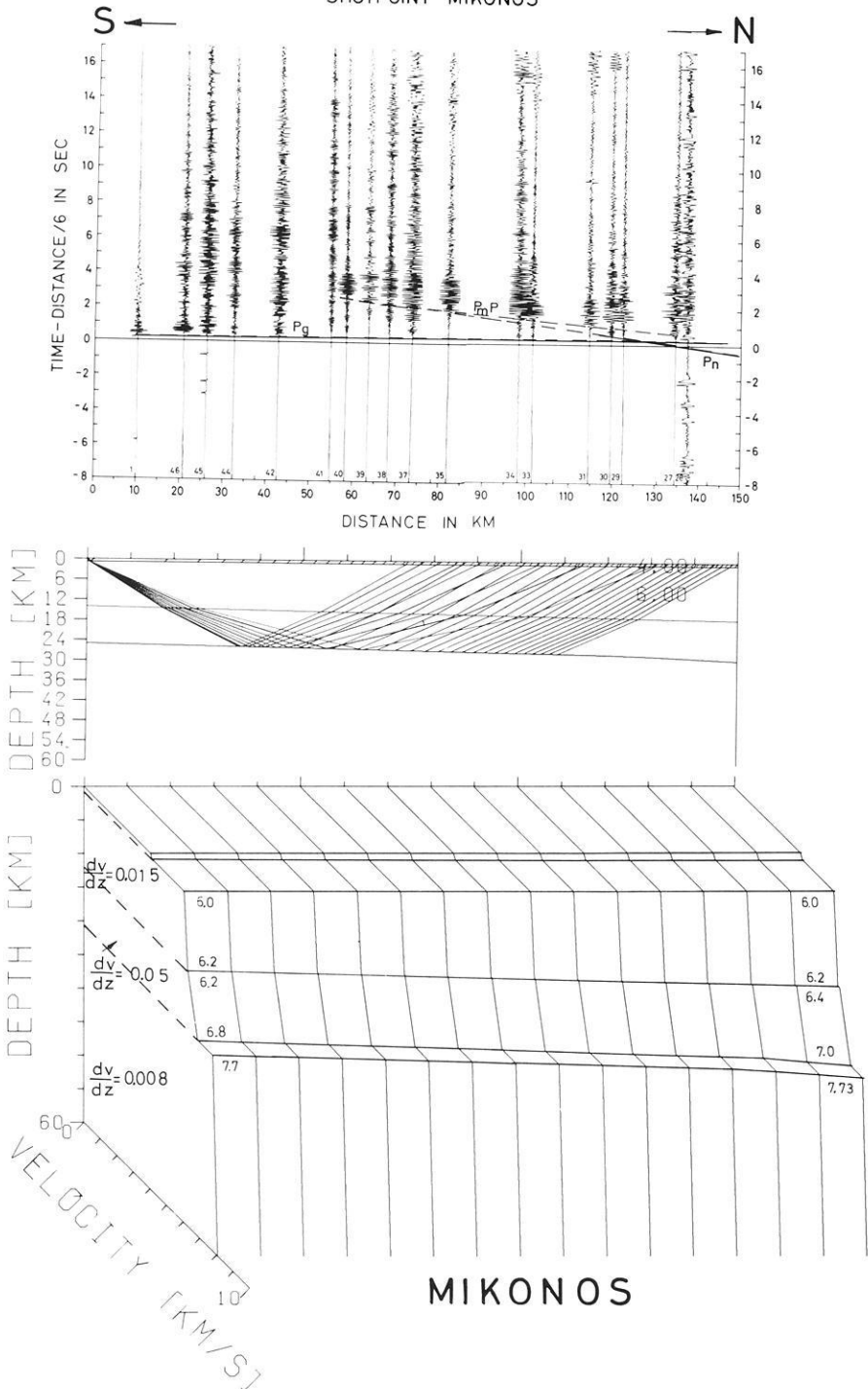


Fig. 5. Evia-section observed in S-N direction (Mikonos-shot). Symbols and their meaning as in Figure 2. Due to the shortness of this profile the P_n -phase does not exist as first arrival

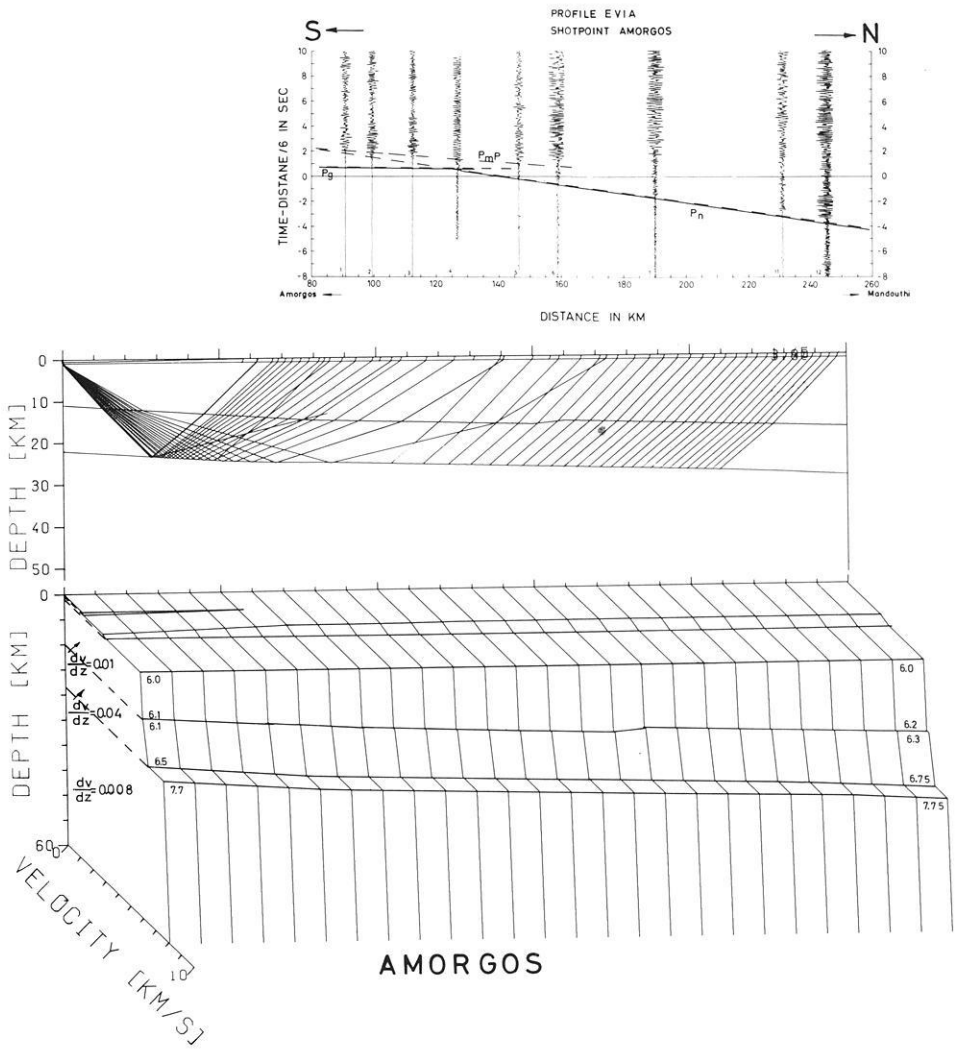


Fig. 6. Amorgos-Evia profile with stations located at Evia. Symbols and their meaning as used in Figure 2

ray to cross the k -trapezoid element of the model and emerge at the surface. The angle intervals, $\delta\varphi_k$, that the seismic ray forms with the horizontal are defined as variables of the computations. In this way the travel times are computed for different ray paths and compared with the observed travel times. The model parameters are iterated until the best fit between observed and computed travel times is achieved. The program is adjusted to a screen display so that a very fast parameter readjustment is possible. The results are then plotted automatically. This computational method is fairly fast, since it is only based on the refraction law and therefore only simple trigonometric functions with a short computation time are used. The accuracy and reliability of the

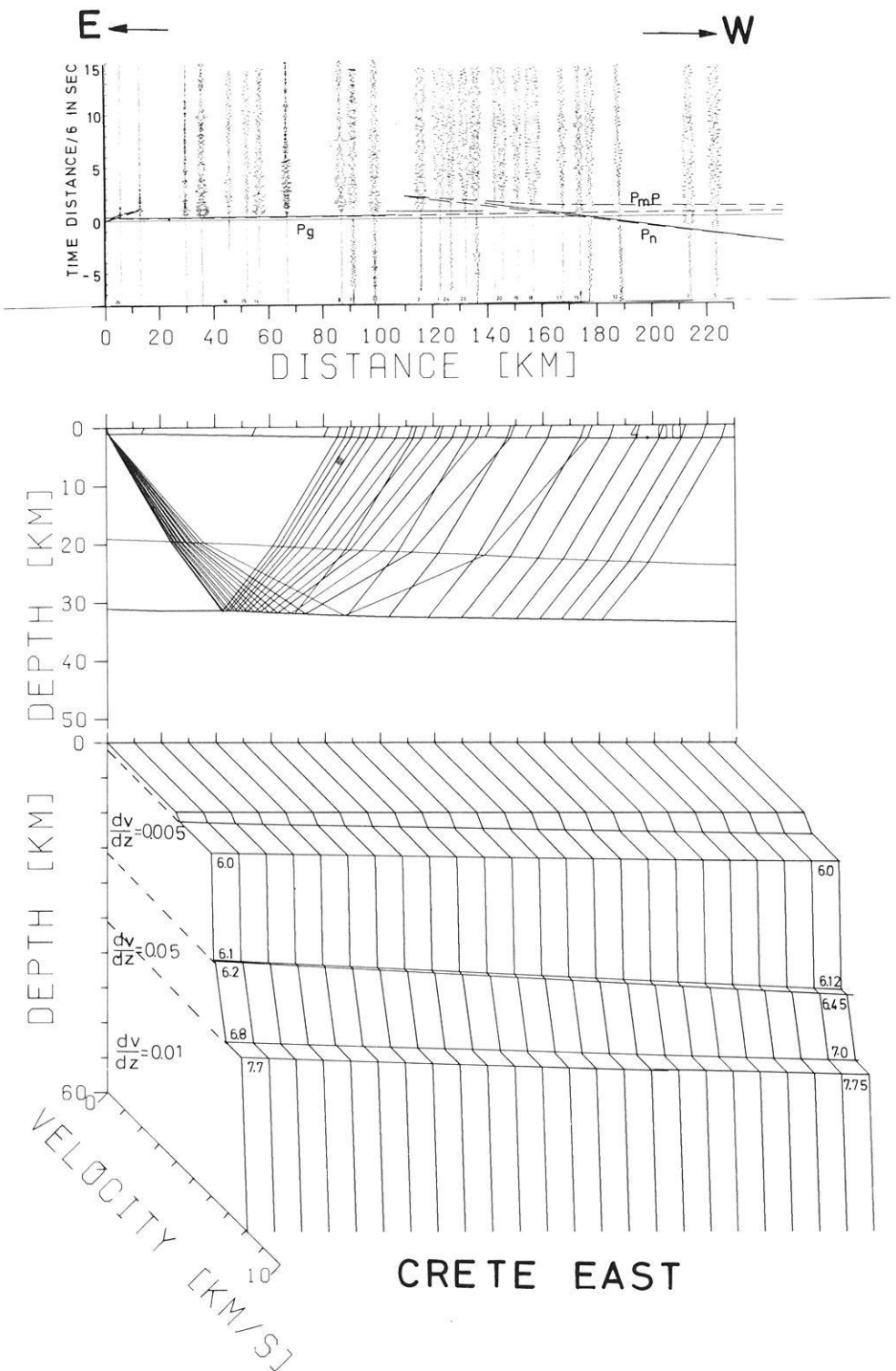


Fig. 7. Crete-section, observed E-W. The P_c - P_n and P_mP -phases are satisfied by a gradient model as demonstrated at Figure 2 for the Evia-section. The gradient of the P -wave velocity at the lower crust is $dv/dz=0.05$. The meaning of the symbols used is the same as in Figure 2

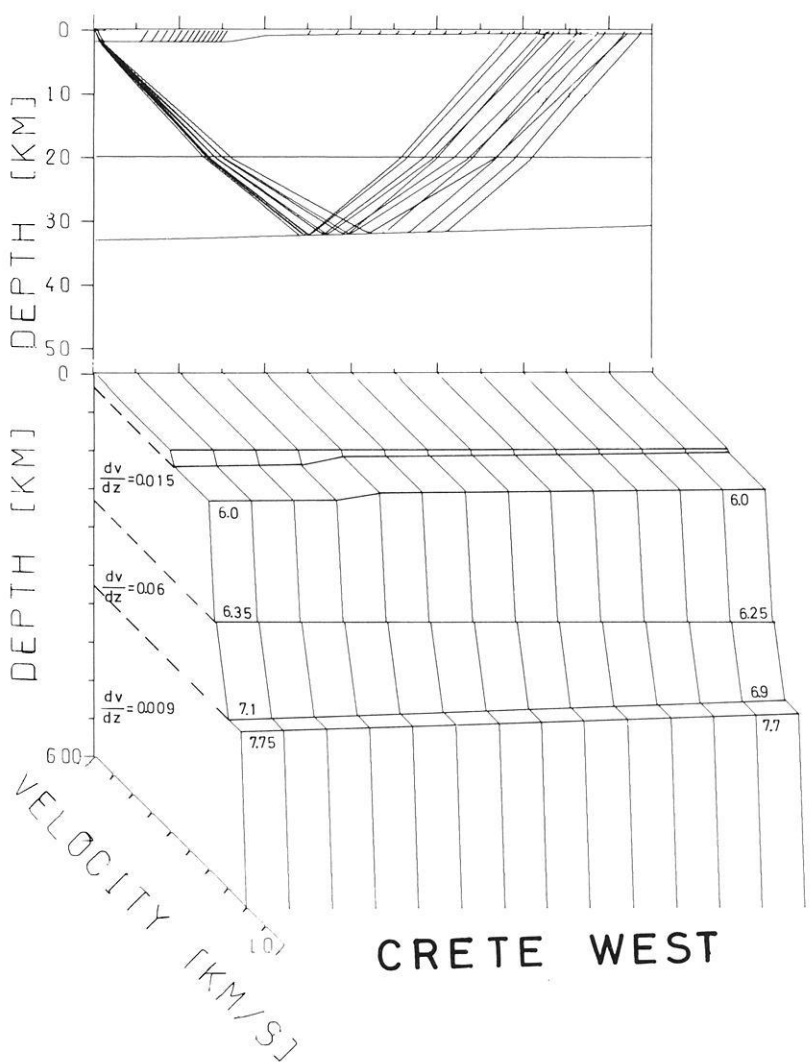
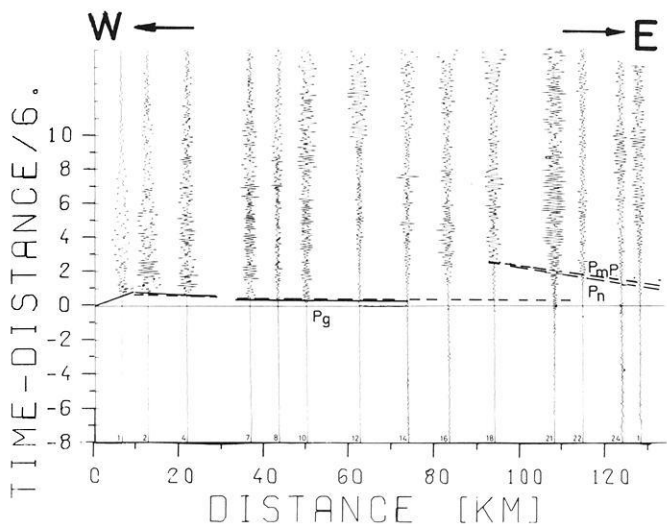


Fig. 8. The reversed profile to the section "Crete-East" was for technical reasons observed up to 120 km only. The significance of this section is therefore very limited

method were tested on a simple analogue model by classical evaluation methods and gave very good results.

The inversion of the simple Evia profile (Fig. 4) satisfied the P_g and P_n seismic arrivals. The computed P_mP reflections have delayed arrivals, however, which indicates that the mean crustal velocity used for the computations is too slow. Since no reflections or refractions from within the crust were recorded, we have introduced an arbitrary velocity increase with depth so that the P_mP reflected arrivals were satisfied. The limiting constraints on the $v(z)$ introduced are that the velocity at the crust-mantle boundary does not exceed 7.7 km/s and that its mean value for the crust is 6.21 km/s. Furthermore no 1st order discontinuities are permitted within the crust. In order to demonstrate the ambiguity involved in the computational process, we have given a model in Figure 4 that satisfies the observed P_g , P_n and P_mP by introducing a 1st order discontinuity at the lower part of the crust. In our opinion, the model that best satisfies the observations is that in Figure 2, which shows a velocity gradient of 6.4–6.8 km/s from 20 km depth to the Moho-discontinuity. Similar considerations have led to the model given for the Amorgos-Evia section and that at Crete. The Amorgos-Evia observations clearly demonstrate that the Moho in the Aegean area is up-dipping from north to south. The crust becomes attenuated from North Evia towards Amorgos from 32 km to approximately 28 km. The crustal velocities and thickness can be only attributed to a continental type of crust.

The Cretan crustal type is also continental, with a thickness of 30 km at the eastern part of the island increasing to approximately 34 km at the western part, see Figures 7 and 8.

The sediments are very thin and irregularly distributed, the Messara neogene basin causing a 0.2 s delay of the seismic arrivals (Fig. 7). The western limit of this basin is most probably fixed by a tectonically weak zone. In Figure 8 the traveltimes irregularities observed are due to the uneven distribution of the nappes which have a maximum thickness at the western part of the island.

In both profiles the P_g true velocity is 6 km/s and the crossover distance of the P_g - P_n seismic phases is approximately 170 km.

The true velocity of the upper mantle is not higher than 7.7 km/s. It could not be obtained from the shot fired at the western part of the island, since this profile was only 120 km long. For technical reasons it was not possible to extend it any further.

Summary and Conclusions

Deep seismic soundings along two sections in the Aegean area, Greece, have shown that the crust is of the continental type. Along the Amorgos-Mikonos-Evia line, the crust shows an up-dipping from 32 km at Mandouthi, North Evia, to 26 km at Amorgos, in the South Aegean Sea. The true velocities computed from the observations are: $V_{Pg}=6.0$ km/s for the crystalline basement and $V_{Pn}=7.7$ km/s for the upper mantle. The crust has a mean velocity of 6.21 km/s, which was computed from P_mP wide-angle reflections. The sedimen-

tary cover above the crystalline basement, which outcrops at South Evia and the Cycladic Islands, could not be determined, since it is too thin to be detected (perhaps 1–1.5 km) by the separation distance of our seismic stations. The best model computed requires a gradual velocity increase at the lower part of the crust, from 6.4–6.8 km/s.

The E-W observations at Crete showed results similar to those at the Evia-Amorgos section. The crust is also continental, increasing in thickness in the E-W direction from 30–34 km. The western part of the island, beginning at the western border of the Messara basin, is down-dipping to the west, where the nappes have their maximum thickness. The true velocity of the basement was obtained by the observations of both profiles and gave a true velocity of 6.0 km/s.

In order to explain the observed travel times of the P_mP reflections a similar gradual velocity increase at the lower part of the crust to that of the Evia-Amorgos section was introduced.

Acknowledgements. This study was sponsored by the Deutsche Forschungsgemeinschaft (German Research Society) as a contribution to the Geodynamics Program of the Eastern Mediterranean, and supported by the Hellenic Union of Geodesy and Geophysics. The field operations were performed by members of German universities and Greek scientists of the National Institute of Geological and Mining Researches, Athens. The authors are greatly indebted to the above-mentioned organizations and to the OTE (Organization of Telecommunications of Greece) and the "Skalitis"-Mining Company, Athens. We wish to thank Dr. Stein, Hannover, for his program for computing theoretical travel-times, and Mr. K. Müller and Miss B. Stöfen for programming and computational support. The theoretical travel-time curves were computed at the Rechenzentrum of the University of Hamburg.

References

- Berckhemer, H.: MARS 66—a magnetic tape recording equipment for deep seismic sounding, *Z. Geophys.* **36**, 501–518, 1970
- Makris, J.: Seismic refractational measurements along the line Ägina, Nafplion, Pirgos. Paper presented at the 1972 C.I.E.S.M. — Meeting in Athens, 1973
- Makris, J.: Geophysical investigations of the Hellenides. *Hamburger Geophysikalische Einzelschriften*, Heft Nr. 26, 92 pp., 1976

Received February 18, 1976; Revised Version August 23, 1976

Fault-Plane Solution of the Earthquake in Northern Italy, 6 May 1976, and Implications for the Tectonics of the Eastern Alps*

G. Müller

Geophysical Institute, University of Karlsruhe,
Hertzstr. 16, D-7500 Karlsruhe, Federal Republic of Germany

Abstract. The fault-plane solution of the North Italian earthquake of May 6, 1976, has been constructed from long-period records of 37 stations (mainly WWNSS stations), assuming a focus in the crust. It is essentially a thrust type solution, the compressional axis having an azimuth of about 160° , perpendicular to the strike direction of the Eastern Alps. One nodal plane is very well defined from first *P*-wave motions: it is steeply dipping approximately SSE with a dip angle of 77° . The second nodal plane has been determined from *S*-wave polarisations at stations in the United States and Japan: it dips roughly NW with a dip angle of about 16° . The dip direction of this nodal plane is less well defined. From the two possible interpretations of the fault-plane solution, either a shallow thrust of Italy under the Alps or a steep thrust of the Alps under Italy, only the first one is geologically plausible. The slip direction of the underthrusting block (or plate?) has an azimuth of 348° and a dip angle of 13° .

Key words: Fault-plane solutions – Alpine tectonics.

Introduction

The earthquake of May 6, 1976, in Northern Italy was the first strong event in the Alps (magnitude 6.5 according to USGS) that occurred during the time of operation of the Worldwide Network of Standardized Seismographs (WWNSS) and was recorded with sufficient amplitudes all over the world by the long-period instruments of this network. Therefore, it is possible to construct a fault-plane solution for this earthquake from long-period WWNSS records. It is well-known from investigations of various other regions of the globe that because of their quality fault-plane solutions based on WWNSS data are essential pieces of evidence for the present tectonic activity of the earth, and that they have greatly contributed to the construction of the main features of the theory

* Contribution No. 141, Geophysical Institute, University of Karlsruhe

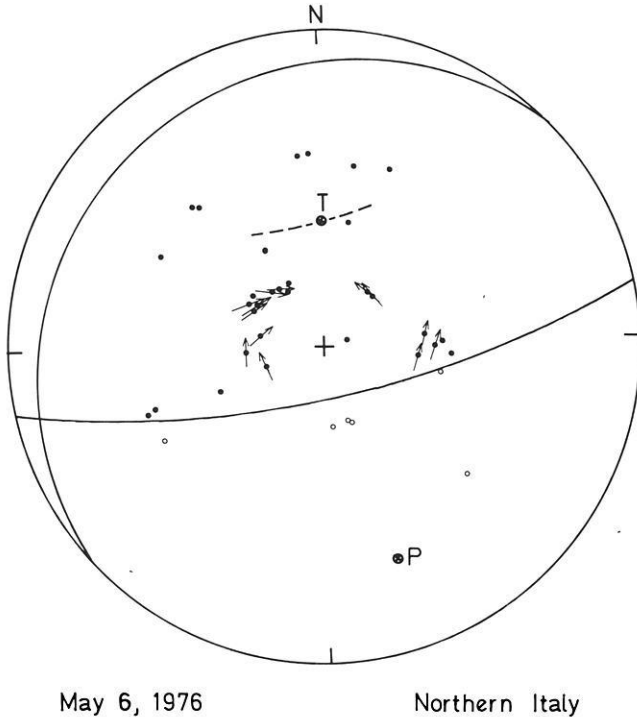


Fig. 1. Fault-plane solution of the North Italian earthquake of May 6, 1976 (equal area projection of the lower focal hemisphere). Dots (circles) indicate first *P*-wave motion away from (towards) the focus. Arrows indicate initial *S*-wave polarisation. The dashed line is the locus of the tensional axis, as following from the well-determined almost vertical nodal plane alone. The tensional axis chosen (symbol *T*) is in optimum agreement with the *S* polarisation directions. This determines the second nodal plane and the compressional axis (symbol *P*)

of plate tectonics. A fault-plane solution of the North Italian earthquake can therefore be expected to be of some importance for discussions of the tectonics of the Alpine-Mediterranean region and the complicated transition from the African to the Eurasian lithospheric plate (McKenzie, 1972; Ahorner et al., 1972; Gutdeutsch and Aric, 1976).

Fault-Plane Solution

For the construction of the fault-plane solution the epicentral coordinates 46.31° N and 13.31° E and a hypocenter in the crust have been assumed, in agreement with the determinations of the Centre Sismologique Européo-Méditerranéen at Strasbourg. *P*-wave radiation angles at the focus were calculated for a *P* velocity of 6.5 km/s, and *S* waves were assumed to have travelled along the same path as *P* waves. The fault-plane solution in Figure 1 was constructed from records of the following 35 WWNSS stations and 2 additional stations (Faro, Portugal, and Funchal, Madeira, operated by the Institute of Geophysics ETH, Zürich, Switzerland):

Station			AAM	ATL	ATU	BHP	BKS	BLA	BUL	COP
Distance (deg)			65	71	11	86	87	66	68	9
Azimuth (deg)			306	299	134	278	326	300	164	357
COR	DUG	ESK	GDH	GOL	KEV	KON	LPB	MAL	MAT	MSH
82	81	14	39	78	24	13	96	16	84	36
330	321	316	329	316	12	352	252	240	42	90
NDI	NUR	OXF	POO	PRE	QUE	RIV	SHI	SHK	STU	TAB
52	16	74	57	73	44	146	37	83	4	26
86	21	303	98	166	92	84	105	47	311	97
TOL	TRN	UME	VAL	WIN	Faro	Funchal				
14	72	18	16	69	18	37				
249	266	10	298	176	252	250				

One of the two nodal planes of the fault-plane solution is very well determined from the first *P*-wave motions alone. Figure 2 gives a few examples of vertical-component seismograms from stations relatively close to this nodal plane. The *P*-wave data at hand, however, do not restrict strongly the orientation of the second nodal plane, and, considering the WWNSS station distribution, it is unlikely that further *P*-wave data will do so.

Therefore, the *S*-wave polarisation at stations with epicentral distances between 44° and 96° was investigated in order to determine the tensional (*T*) axis and from this the second nodal plane. Figure 3 shows several horizontal-component seismograms, including examples from stations important for the purpose of fixing the *T* axis, namely stations in Japan (SHK, MAT) and the United States (BLA, OXF, DUG). The epicentral distances are large enough such that (1) linear polarisation of *S* can be expected (Nuttli and Whitmore, 1962) and (2) *S*-coupled PL where it exists is sufficiently separated from *S*, as for instance at BLA in Figure 3. At SHK, MAT and DUG interference of *S* and SKS is possible and therefore, depending on the amplitudes of SKS, a certain deviation of the true polarisation angle of *S* from the polarisation angle, following from the amplitudes indicated in Figure 3. At LPB which is situated close to the first nodal plane there is practically no SV energy which is demonstrated by the absence of SKS (theoretical arrival time 20:24:24 according to the Jeffreys-Bullen Tables). *S* and ScS which arrive almost simultaneously are of SH type alone, and the *S*-wave polarisation can be determined from their superposition.

In Figure 1 the possible locations of the *T* axis, as following from the first nodal plane, are indicated by the dashed line. This line is part of the intersection of the lower focal hemisphere and a cone of half apex angle 45° around the direction to the pole of the first nodal plane. In the neighborhood of the *T* axis the *S* polarisations should be directed towards the *T* axis. From this condition the most probable point on the dashed line is selected which fixes, finally, the corresponding compressional (*P*) axis and the second nodal plane. Because of the uncertainties in the *S* polarisations and hence in the *T* axis this nodal plane is not determined with the same precision as the first one. In particular,

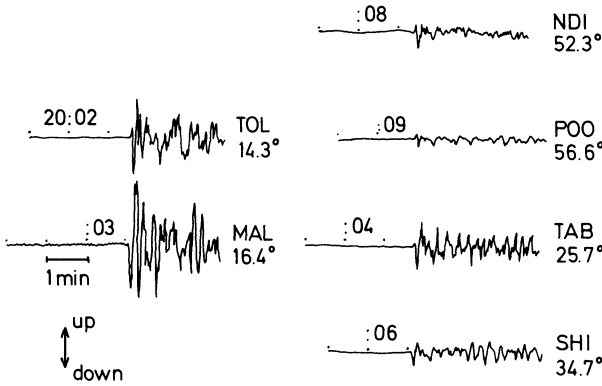


Fig. 2. Long-period vertical-component seismograms of the *P* wave at the WWNSS stations TOL, MAL, NDI, POO, TAB and SHI, showing the reversal in sign across the first nodal plane. The amplitude scale is the same for all traces. The numbers below the station codes are the epicentral distances

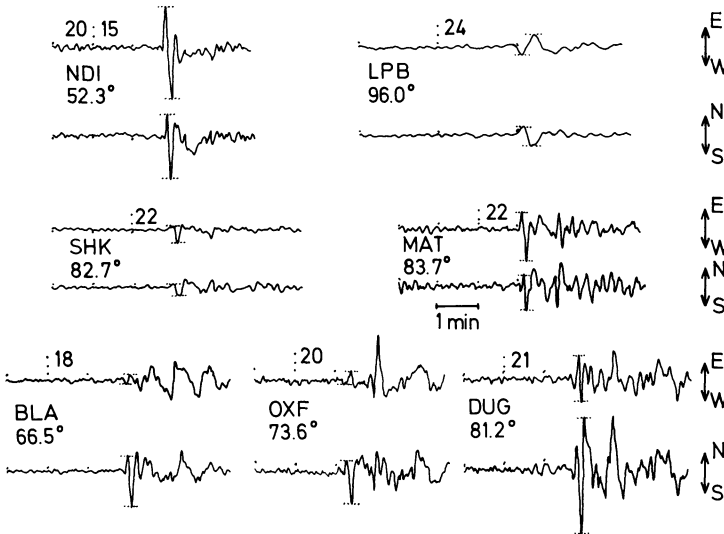


Fig. 3. Long-period horizontal-component seismograms (E-W and N-S) of the *S* wave at the WWNSS stations NDI, LPB, SHK, MAT, BLA, OXF and DUG. The peak-to-peak amplitudes that have been used for determining the *S*-wave polarisation are between the dotted horizontal lines. The amplitude scale is not the same for all stations. The time scale of LPB is extended by a factor of 2, compared with the other stations. The sign of the N-S component of NDI has been reversed, since only then the first *P*-wave motion is directed southwards, as it should be

its dip direction which in Figure 1 is about NW could probably have any direction between WNW and N. The parameters of the fault-plane solution in Figure 1 are:

	Azimuth (deg)	Dip angle (deg)
Pole of first nodal plane	348	13
Pole of second nodal plane	137	74
<i>P</i> axis	163	29
<i>T</i> axis	0	58

Discussion

The fault-plane solution represents essentially a thrust mechanism, unlike most of the solutions of earlier (and weaker) earthquakes in the Alps which are predominantly of strike-slip type (Ahorner et al., 1972). The mechanism is either a shallow underthrust of Italy under the Alps along the second nodal plane or a steep underthrust of the Alps under Italy along the first nodal plane. The nonuniqueness can be resolved, in the present case, by geological arguments: it seems that only the first kind of relative displacement is in agreement with the fact that the Alps exist and are uplifted at present, at least in parts, by rates of about 1 mm per year (Senftl and Exner, 1973; Jeanrichard, 1975; Schaer et al., 1975; Gutdeutsch and Aric, 1976). The slip direction of the underthrusting block which agrees with the direction to the pole of the first nodal plane has an azimuth of 348° and a dip angle of only 13° ; it is not influenced by the uncertainties in the orientation of the second nodal plane. It could be difficult to find clear geological evidence at the surface for motions on this shallow thrust fault, directly related to the earthquake, even if the rupture has reached the surface. However, it is known, partly from borehole investigations, that in the focal region quite often Eocene-Paleocene sediments are found below the older main dolomite of the Calcareous Southern Alps, the layers dipping shallow to the north on the average (Martinis, 1975). This situation is most plausibly explained by underthrusting from the south, in excellent agreement with the fault-plane solution of the North Italian earthquake.

The older explanation of the reversed layering, overthrusting from the north due to gravitational sliding during a phase of rapid uplift of the Alps, is physically much less plausible. Moreover, it requires a complicated history of the Eastern Alps with considerable changes in the tectonic stress field in order to explain rapid and slow (or vanishing) uplift, tilting of the overthrust layers and their substratum to the north, and the earthquake.

The interpretation of the *P* axis of the fault-plane solution faces the usual problem that in general the direction of the *P* axis agrees only approximately with the direction of maximum principal tectonic stress. Nevertheless, in the present case its azimuth is almost perpendicular to the strike direction of the Eastern Alps, and it is certainly safe to conclude that the maximum principal stress is also directed more or less perpendicular to this strike direction. Hence,

the forces that caused the North Italian earthquake are the forces that folded and still fold the Eastern Alps. Furthermore, the agreement between the azimuths of the P axes of many well-investigated earthquakes in Southwest Germany (Schneider et al., 1966; Bonjer, 1976) and the North Italian earthquake indicates a rather homogeneous compressional stress field at least through the Eastern Alps and Southwest Germany, the compressional direction having an azimuth of about 160° .

Finally, it is worth noting that the underthrusting mechanism of the North Italian earthquake fits well into the speculative picture which McKenzie (1972, Fig. 13) has given of the plate-tectonics situation around the Adriatic. He tentatively assumed that the Adriatic is a tongue-like continuation of the African plate whose boundary runs NW through Italy, bends in the Eastern Alps and continues towards SE through Yugoslavia and along the west coast of Greece. The Adriatic is assumed to move NW, relative to the Eurasian plate, which would produce converging motions of the two plates in the focal region of the North Italian earthquake, in agreement with its fault-plane solution. However, McKenzie's hypothesis is certainly not the only one in the framework of plate tectonics which is compatible with the fault-plane solution derived here. It may also be questionable to apply the idea of relatively sharp plate boundaries to the Alps. Rather the extensive underthrusting in the focal region of the North Italian earthquake and a similar situation at the northern boundary of the Alps, which may be interpreted as underthrust of the Molasse under the Calcareous Northern Alps, could indicate a *broad* collision zone of two plates. The plate motions could be predominantly horizontal and convergent at the southern and northern boundaries of the Eastern Alps. In the central parts of the Eastern Alps and below a certain depth motions could be directed more or less vertically downwards. Above this depth uplift and folding would take place. Should these speculations be correct, then they would imply that a considerable amount of the relative displacement occurs by creep, since the seismic activity of the Alps is restricted to depths less than about 40 km (Ahorner et al., 1972; Gutdeutsch and Aric, 1976). This, in turn, would probably require rather high temperatures already in the crust.

Acknowledgments. I am grateful to the directors and staff of about 50 WNWSS stations who responded to my request for seismogram copies, to W. Mironovas for records of the stations Faro and Funchal, to many colleagues, especially K.-P. Bonjer, H. Illies, D. Mayer-Rosa, H. Miller and R. Schick, for discussions on various aspects of the North Italian earthquake, and to K.-P. Bonjer and K. Fuchs for reading the manuscript.

References

- Ahorner, L., Murawski, H., Schneider, G.: Seismotektonische Traverse von der Nordsee bis zum Appennin. *Geol. Rundschau* **61**, 915–942, 1972
- Bonjer, K.-P.: Evidence for the rotation of the azimuth of the principal stress axis with depth in the crust of the Rhinegraben area. To be submitted to *J. Geophys.* 1976
- Gutdeutsch, R., Aric, K.: Erdbeben im ostalpinen Raum – Beobachtungsmethoden und tektonische Deutungsversuche. Publikation Nr. 210, Zentralanstalt für Meteorologie und Geodynamik in Wien, 1976

- Jeanrichard, F.: Summary of geodetic studies of recent crustal movements in Switzerland. *Tectonophysics* **29**, 289–292, 1975
- Martinis, B.: The Friulian and Julian Alps and Pre-Alps. In: *Structural model of Italy*, L. Ogniben, M. Parotto, A. Praturlon (eds.). Consiglio Nazionale delle Ricerche, Roma 1975
- McKenzie, D.P.: Active tectonics of the Mediterranean region. *Geophys. J.* **30**, 109–185, 1972
- Nuttli, O., Whitmore, J.D.: On the determination of the polarisation angle of the S wave. *Bull. Seism. Soc. Am.* **52**, 95–107, 1962
- Schaer, J.P., Reimer, G.M., Wagner, G.A.: Actual and ancient uplift rate in the Gotthard region, Swiss Alps: a comparison between precise levelling and fission track apatite age. *Tectonophysics* **29**, 293–300, 1975
- Schneider, G., Schick, R., Berckhemer, H.: Fault-plane solutions of earthquakes in Baden-Württemberg. *Z. Geophys.* **32**, 383–393, 1966
- Senftl, E., Exner, C.: Rezente Hebung der Hohen Tauern und geologische Interpretation. *Verh. Geol. Bundesanstalt Jg. 1973*, **2**, 209–234, 1973

Received August 31, 1976

Pseudo-Single-Domain Effects and Single-Domain Multidomain Transition in Natural Pyrrhotite Deduced from Domain Structure Observations

H. Soffel

Institut für Allgemeine und Angewandte Geophysik der Universität München,
D-8000 München 2, Theresienstraße 41, Federal Republic of Germany

Abstract. The domain configuration of primary pyrrhotite in a Devonian diabase was studied using the Bitter pattern technique. Due to the uniaxial symmetry the multidomain grains have a rather simple domain structure. The single-domain – multidomain transition occurs at an average particle diameter of 1.6 μm . In the multidomain grains clusters of inclusions seem to produce pseudo-single-domain effects with complicated domain configurations. Such pseudo-single-domain effects are necessary for the interpretation of the magnetically hard component of remanence which cannot be explained by the observed abundance of true single-domain particles alone.

Key words: Rock magnetism – Domain structure – Pyrrhotite – Diabase – Palaeomagnetism.

1. Introduction

The remanent magnetization of rocks can in general be interpreted by a mixture of multidomain and single-domain behaviour. The multidomain behaviour is restricted to the remanence components with coercive forces smaller than say 16 kA/m (= 200 Oe) depending on the material and grain size of the ferrimagnetic ore phase. Single-domain particles are believed to be responsible for the remanence components with large coercive forces, say larger than 24 kA/m (= 300 Oe), depending on the shape and nature of the ore fraction. In many cases it is not possible to explain the actually observed intensity of remanence of rocks with coercive forces larger than several hundred Oe with the observed abundance of true single-domain grains, although such attempts have been successful in some cases (Soffel, 1968; 1969). Stacey (1962; 1963) introduced the idea of pseudo-single-domain effects by assuming zones within or at the edges of large multidomain grains with single-domain properties. Clusters of lattice imperfections and small inclusions, exsolution features, cracks and very irregular shapes of the ore grains can lead to such pseudo-single-domain effects.

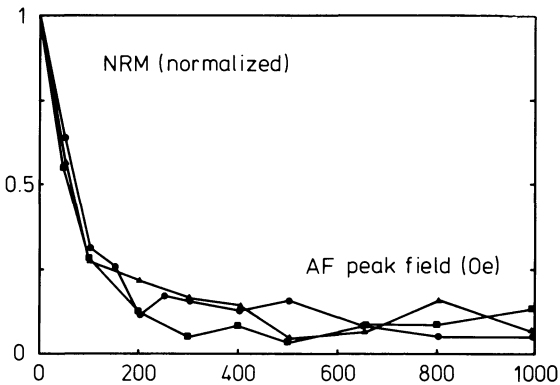


Fig. 1. AF-demagnetization of 3 pilot samples

Experimental proof for the existence of pseudo-single-domain grains has been established for instance from the study of alternating field demagnetization curves, and dependence of thermoremanent magnetization (TRM) upon grain size and external field strength. The experimental and theoretical results have recently be summarized by Stacey and Banerjee (1974).

This paper adds further experimental proof of the presence of pseudo-single-domain effects from the study of domain configurations and other rock magnetic parameters of primary pyrrhotite in a Devonian diabase from Northern Bavaria/Germany.

2. Palaeomagnetic and Rock Magnetic Properties of the Devonian Diabase

The Devonian diabase of Bad Berneck (Northern Bavaria, $\lambda = 11.7^\circ \text{E}$, $\varphi = 50.1^\circ \text{N}$) has an average natural remanent magnetization of about 0.5 A/m ($= 500 \mu\text{G}$) which is typical of a basic rock of that age. The mean direction of NRM is: $D = 286^\circ$, $I = +72^\circ$. AF-demagnetization of 3 pilot samples (Fig. 1) reveals the presence of components of remanence with different stabilities. Firstly a component carrying most of the NRM with low stability which can be removed by AF-fields up to about 8 kA/m (100 Oe). Secondly, a magnetically hard component which maintains more or less its intensity in AF-fields up to 80 kA/m (1000 Oe). The average intensity of this stable component (after AF-treatment in a peak field of 16 kA/m) is 0.082 A/m ($= 82 \mu\text{G}$), that is 16% of NRM. The mean direction is only slightly changed ($D = 260^\circ$, $I = 46^\circ$). Thirdly a transition zone between 8 kA/m (100 Oe) and 24 kA/m (300 Oe) with intermediate stability. Within this transition zone the intensity of remanence drops only by a factor of about two. The entire change of remanence direction occurs at demagnetizing fields smaller than 8 kA/m (100 Oe).

Thermal cleaning at 290°C also produced only a slight change of remanence direction ($D = 280^\circ$, $I = 36^\circ$). Bedding correction was not possible due to very uncertain tectonic conditions. However other diabase bodies nearby with reliable tectonic data yielded typical paleozoic pole positions.

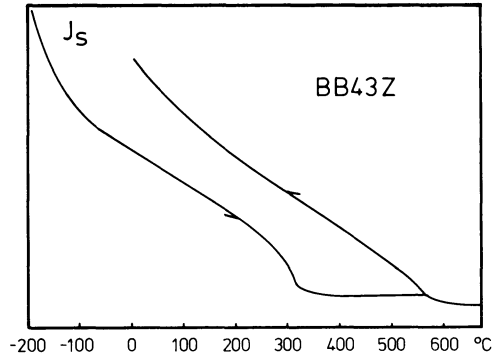


Fig. 2. Saturation magnetization J_s versus temperature of a natural diabase sample. Heating and cooling cycle are indicated by arrows

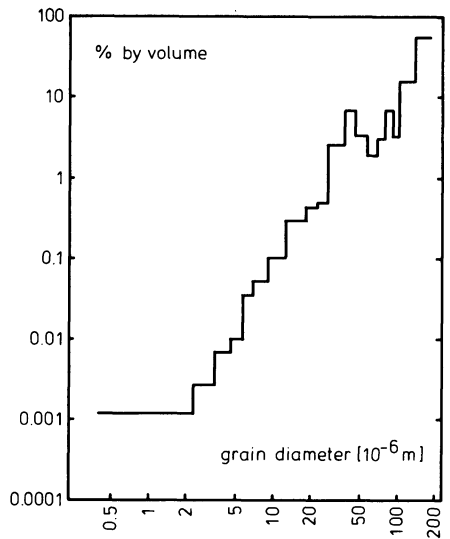


Fig. 3. Histogram of grain size versus their contribution in percent by volume to the total ore content

The saturation magnetization J_s (in a field of 800 kA/m) versus temperature from $-200\text{ }^\circ\text{C}$ up to $700\text{ }^\circ\text{C}$ is shown in Figure 2. A Curie temperature T_c of $320\text{ }^\circ\text{C}$ is observed in the heating curve. This phase is destroyed by heating up to $700\text{ }^\circ\text{C}$ and completely replaced by magnetite ($T_c=580\text{ }^\circ\text{C}$) with increased saturation magnetization as can be seen from the cooling curve of Figure 2. J_s/T -curves of basic rocks showing similar features are usually interpreted in terms of a nonstoichiometric titanomagnetite phase with a T_c of $320\text{ }^\circ\text{C}$ being exsolved into a phase close to magnetite plus a phase rich in Titanium close to Ilmenite upon further heating. Polished section studies revealed the presence of idiomorphic primary pyrrhotite which has a T_c of $320\text{ }^\circ\text{C}$ and for which an oxidation to magnetite takes place after heating to $700\text{ }^\circ\text{C}$. No indications of other primary ore phases like Titanomagnetite, Hematite, Magnetite or Chromites could be found by the polished section studies. Only primary pyrite occurs occasionally as separate grains or as intergrowths with pyrrhotite. The average total ore content of the diabase is about 0.5% by volume.

The grain sizes vary between 300 μm and about 1 μm . Most of the grains have a diameter of around 50 μm . Figure 3 shows a histogram of the grain sizes versus their abundance in percent by volume. It has been obtained from the study of several representative polished sections. Almost the entire ore content (99.7%) is contained in the grains with diameters larger than 20 μm with true multi-domain behaviour. A little less than 0.3% are in the range between 2 and 20 μm , that is in the transition stage between the multidomain and single-domain state. Only about 0.001% of the ore content is concentrated in grains smaller than 2 μm which are believed to be in the single-domain state as will be shown in the next section.

3. Domain Structure Studies of Pyrrhotite

The domain structure was studied with the Bitter pattern technique. Technical details can be taken from Bitter (1931) and Elmore (1938). Instead of the magnetite colloid proposed by Elmore (1938), a suspension called "Ferrofluid" was used. The advantages of the Ferrofluid are better resolution of the domain structures and the possibility for experiments at various temperatures.

In contrast to magnetite and titanomagnetites, where special techniques for the preparation of strainfree surfaces are necessary (Soffel, 1963; Hanss, 1964; Soffel, 1968; Soffel and Petersen, 1971; Soffel, 1971) this is not the case for the pyrrhotite which has been studied here. Careful polishing with very fine grained diamond paste was sufficient. Ionic etching (Soffel, 1968) showed no effect of further improvement of the domain configuration.

Pyrrhotite has an orthohexagonal structure which is slightly monoclinic. At room temperature the plane (001) is one of easy magnetization, the direction [001] is that of very difficult magnetization. According to Bin and Pauthenet (1963), crystal anisotropy is very large. The values for room temperature are: $K_1 = 0.35 \times 10^6 \text{ erg/cm}^3$; $K_2 = \text{nearly zero}$; $K_3 = 1.18 \times 10^6 \text{ erg/cm}^3$; $K_4 = 32.2 \times 10^6 \text{ erg/cm}^3$; saturation magnetization J_s at room temperature is about 96 kA/m (96 Gauss). J_s is therefore of about the same amount as for Ti-rich Titanomagnetites with T_c at about 150 $^\circ\text{C}$, while the crystal anisotropy at room temperature is by about two orders of magnitude larger (Syono, 1965). The value for the magnetostrictive constant is estimated in Section 5.

Due to the uniaxial crystal symmetry, low saturation magnetization and large crystal anisotropy a quite simple domain configuration with parallel lamellae without closure domains at the margins of the crystals can be expected. This is indeed the case as shown in Figure 4. Smaller grains have increasingly simpler domain configurations. Figure 5 shows a four domain grain. The larger grain in Figure 6 with a more complicated domain configuration is accompanied by a two domain and a single-domain particle.

Figure 7 shows a plot of number of lamellae shaped domains versus grain diameter. From this an extrapolation can be made for the determination of the single-domain-multidomain transition which seems to take place at a critical diameter $d = 1.6 \mu\text{m}$ for this material. From this value the specific wall energy

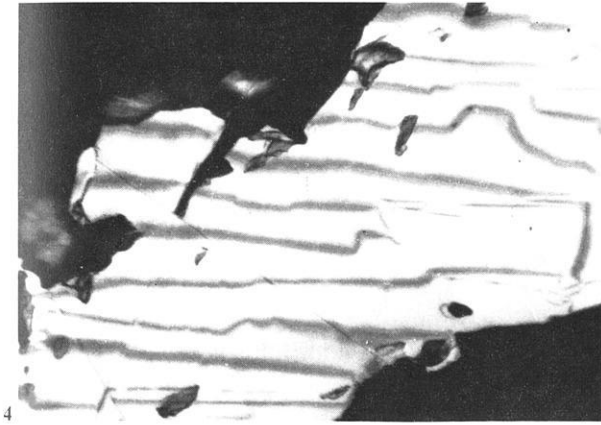


Fig. 4. Lamellae-shaped domains of a large ore grain. Diameter of the figure is 120 μm

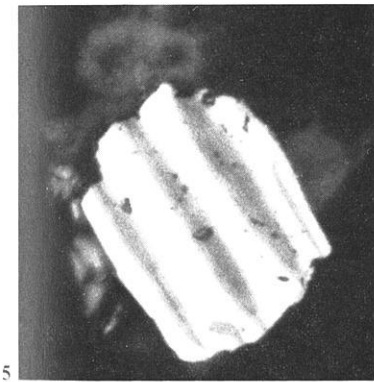
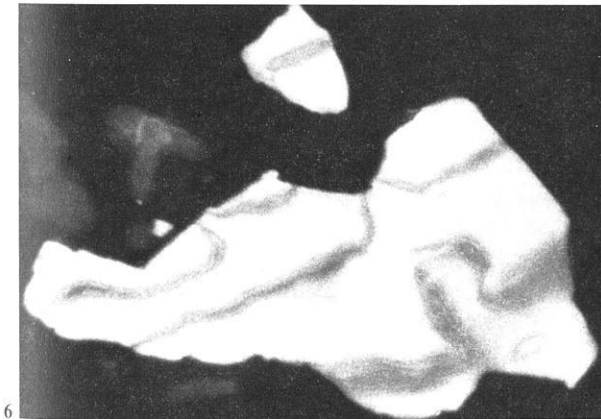


Fig. 5. Four domain grain with a diameter of 20 μm

Fig. 6. Large ore grain (length: 50 μm) with a more complicated domain configuration accompanied by a two domain and a single-domain grain



can be estimated according to Kittel (1949) and Soffel (1971) to be:

$$\begin{aligned} \gamma_w &= 2\pi dI_s^2/9 \\ &= 1 \text{ erg/cm}^2 \end{aligned} \tag{1}$$

using $d = 1.6 \cdot 10^{-6} \text{ m}$ and $J_s = 96 \text{ kA/m} = 96 \text{ Gauss}$. γ_w is therefore of about the same value as for other ferromagnetic and ferrimagnetic materials (Kneller,

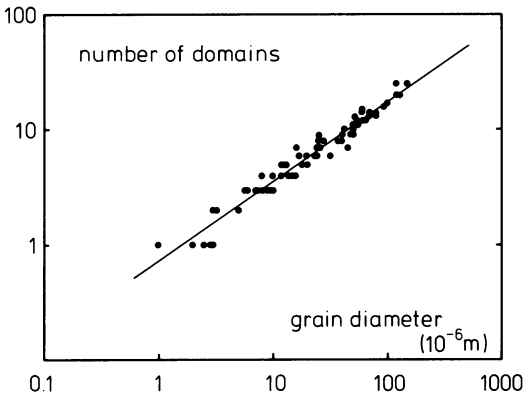


Fig. 7. Number of lamellae-shaped domains versus grain diameter

1962; Stacey and Banerjee, 1974). Due to the low saturation magnetization of pyrrhotite most of the still easily visible ore grains between 1 and 2 μm are already in the single domain state.

4. Intensity of Stable Remanence and Experimental Evidence for Pseudo-Single-Domain Effects

The observed abundance of true single-domain particles in the investigated rock samples is very low. They cannot explain the intensity of the stable component of NRM which was shown to be 0.082 A/m ($= 82 \mu\text{G}$) in the average (see Sect. 2). According to Néel (1949) and Soffel (1969) the TRM of a rock specimen containing $p\%$ of uniformly dispersed and randomly oriented single domain particles is given by:

$$J_{\text{TRM}, H_0, T_0} = \frac{1}{3} p J_s(T_0) \operatorname{tgh} \frac{v J_s(T_B) H_a(T_B)}{k T_B}$$

where $H_a(T_B) \approx 0.5 \text{ Oe}$ is the intensity of the external field when the blocking temperature T_B ($\approx 590 \text{ K}$) is passed. $J_s(T_B)$ is the saturation magnetization for this condition and is believed to be about 1/3 of the saturation magnetization $J_s(T_0)$ at room temperature (Stacey, 1963); v is the mean volume of a single-domain grain ($\approx 10^{-12} \text{ cm}^3$) and k is Boltzmann's constant. With $J_s(T_0) = 105 \text{ cgs}$ units and $p = 0.5\% \times 0.001\% = 5 \cdot 10^{-8}$ we have:

$$\begin{aligned} J_{\text{TRM}, H_0, T_0} &= \frac{1}{3} \times 5 \cdot 10^{-8} \times 105 \operatorname{tgh} \frac{10^{-12} \times 35 \times 0.5}{1.38 \times 10^{-16} \times 590} \\ &= 1.75 \times 10^{-6} \text{ G.} \end{aligned}$$

This is only about 2% of the observed stable component of NRM ($82 \mu\text{G}$). It is unlikely that only such a small fraction of the actually present single domain particles has been detected by the polished section studies. The more reasonable explanation of the discrepancy is that substantial parts of the stable component of NRM must be located in zones of the larger multidomain particles with pseudo-single-domain behaviour.

The domain configuration of the large multidomain particles was therefore investigated under this special point of view.

5. Evidence for Pseudo-Single-Domain Effects in the Multidomain Grains and Conclusions

The primary pyrrhotite crystals are idiomorphic and rather coarse grained (see Fig. 3). Typical for the material is the occasional occurrence of nonmagnetic inclusions with a diameter of up to several μm in the large ore grains.

According to Stacey (1962) and Stacey and Banerjee (1974) these zones are believed to be the location of pseudo-single-domain effects. Figure 8 shows a large multidomain grain with a cluster of nonmagnetic inclusions in its center. The other areas of the ore grain are more or less free from inclusions. The domain walls appear in the picture as dark lines. They reveal lamellae shaped domains in the zones of the ore grain outside the cluster of inclusions. Single inclusions obviously have no serious effect on the domain configuration. Due to the high concentration of inclusions in the center of Figure 8 the lamellae shaped large domains are obviously replaced by a large number of much smaller domains with irregular boundaries. The application of external fields up to several hundred Oe produced large changes of the domain configuration only in the areas of the ore grain outside the cluster of inclusions. Within the cluster the configuration changed only slightly or not at all. The domain structure of an ore grain with more or less equally distributed inclusions is shown in Figure 9. In this case the domains have still more or less the shape of lamellae. However the domain walls are more irregular and seem to be attached to larger inclusions or smaller clusters of inclusions. In the case of Figure 9 the inclusions have only the effect of increasing the wall friction of the multidomain grains. According to Soffel (1970) only moderate coercive forces ($\approx 100\text{--}200$ Oe) can be expected from the interaction between domain walls and inclusions. Obviously a critical concentration of inclusions exceeding a critical diameter is necessary for the replacement of the lamellae shaped domains by much smaller domains with irregular boundaries as shown in Figure 8. More detailed investigations of this subject are planned.

Regarding the AF-demagnetization curve (Fig. 1), the initial drop of the intensity of remanence with coercive forces smaller than 100 Oe seems to indicate the destruction of remanence of the large multidomain grains with little or no inclusions. The remanence components with coercive forces between 100 and 300 Oe seem to be located in the large multidomain grains with dispersed inclusions and the very small multidomain grains just above the critical diameter of $1.6\ \mu\text{m}$ for the single-domain – multidomain transition. The areas in the multidomain grains with clusters of inclusions are believed to be zones with pseudo-single-domain behaviour being responsible for the observed magnetically hard component together with the contribution from the true single-domain particles.

From the fact that no stress patterns can be observed on the investigated pyrrhotite after mechanical polishing, the upper limit for the magnetostrictive



Fig. 8. Large multidomain grain with lamellae-shaped domains. The cluster of nonmagnetic inclusions within the ore grain produces extremely small domains with presumably pseudo-single-domain behaviour. The diameter of the figure is 120 μm

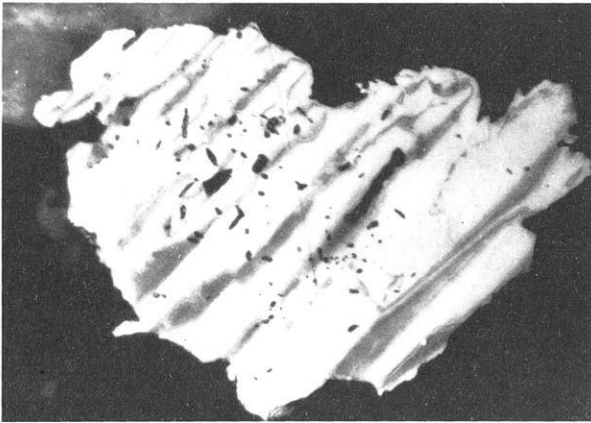


Fig. 9. Domain structure of a large ore grain (diameter: 100 μm) with a more or less equal distribution of nonmagnetic inclusions

constant of pyrrhotite can be estimated. According to Soffel (1966), the stress along a scratch is in the order of $2.5 \cdot 10^9$ dyne/cm². Using the model of Chikazumi and Suzuki (1955), the magnetostrictive constant of pyrrhotite must be smaller than 7×10^{-6} which is one order of magnitude smaller than for magnetite, according to Kneller (1962).

Acknowledgement. The investigations were made in the Institut für Allgemeine und Angewandte Geophysik, Universität München. The author is indebted to Dipl.-Geophys. H. Zinsser for doing part of the rock magnetic measurements. Thanks are also due to Prof. Dr. G. Angenheister, Dr. E. Schmidbauer, Dr. N. Petersen, Dr. A. Schult and Dr. J. Pohl for many helpful discussions. The financial support of the Deutsche Forschungsgemeinschaft is gratefully acknowledged.

References

- Bin, M., Pauthenet, R.: Magnetic anisotropy in pyrrhotite. *J. Appl. Phys.* **34**, 1161–1162, 1963
- Bitter, F.: On inhomogeneities in the magnetization of ferromagnetic materials. *Phys. Rev.* **38**, 1903–1905, 1931
- Chikazumi, S., Suzuki, K.: On the maze domain of silicon-iron crystal. *J. Phys. Soc. Japan* **10**, 523–534, 1955
- Elmore, W.C.: Ferromagnetic colloid for studying magnetic structures. *Phys. Rev.* **54**, 309–310, 1938
- Hanss, R.E.: Thermochemical etching reveals domain structure in magnetite. *Science* **146**, 398–399, 1964
- Kittel, C.: Physical theory of ferromagnetic domains. *Rev. Mod. Phys.* **21**, 541–583, 1949
- Kneller, E.: *Ferromagnetismus*. Berlin, Göttingen, Heidelberg: Springer 1962
- Néel, L.: Theorie du trainage magnétique des ferromagnétiques en grains fins avec leur applications aux terres cuites. *Ann. Géophys.* **5**, 99–136, 1949
- Soffel, H.: Untersuchungen an einigen ferrimagnetischen Oxyd- und Sulfidmineralien mit der Methode der Bitterschen Streifen. *Z. Geophys.* **29**, 21–34, 1963
- Soffel, H.: Stress Dependence of the Domain Structure of Natural Magnetite. *Z. Geophys.* **32**, 63–77, 1966
- Soffel, H.: Die Bereichsstrukturen der Titanomagnetite in zwei Basalten und die Beziehung zu makroskopisch gemessenen magnetischen Eigenschaften dieser Gesteine. Habilitation thesis, Nat. Fak. Univers. München 1968
- Soffel, H.: The origin of thermoremanent magnetization of two basalts containing homogeneous single phase titanomagnetite. *Earth Planet. Sci. Lett.* **7**, 201–208, 1969
- Soffel, H.: The Influence of the Dislocation Density and Inclusions on the Coercive Force of Multidomain Titanomagnetites of the Composition $0.65 \text{Fe}_2\text{TiO}_4 - 0.35 \text{Fe}_3\text{O}_4$ in Basalts as Deduced from Domain Structure Observations. *Z. Geophys.* **36**, 113–124, 1970
- Soffel, H.: The single-domain – multidomain transition in natural intermediate titanomagnetites. *Z. Geophys.* **37**, 451–470, 1971
- Soffel, H., Petersen, N.: Ionic etching of titanomagnetite grains in basalts. *Earth Planet. Sci. Letters* **11**, 312–316, 1971
- Stacey, F.D.: A generalized theory of thermoremanence, covering the transition from single-domain to multidomain magnetic grains. *Phil. Mag.* **7**, 1887–1899, 1962
- Stacey, F.D.: The physical theory of rock magnetism. *Adv. Phys.* **12**, 45–133, 1963
- Stacey, F.D., Banerjee, S.K.: *The physical principles of rock magnetism*. Amsterdam, London, New York: Elsevier Scientific Publishing Company, p. 110–114, 1974
- Syono, Y.: Magnetocrystalline anisotropy and magnetostriction of $\text{Fe}_3\text{O}_4 - \text{Fe}_2\text{TiO}_4$ -series with special application to rock magnetism. *Jap. J. Geophys.* **4**, 71–143, 1965

Received June 25, 1976

The Diurnal Variation of the Electron Density of the Mid-Latitude Ionospheric D-Region Deduced from VLF-Measurements

J. Schäfer

Astronomical Institutes, University of Bonn, Auf dem Hügel 71, D-5300 Bonn,
Federal Republic of Germany

Abstract. Amplitude and phase of the components of the electric and magnetic field of the VLF-transmitter GBR (16 kHz, near Rugby/England) observed at the 3 receiving stations Stockert (near Bonn), Braunschweig and Berlin have been related to the electron density profile of the ionospheric D-layer via an appropriate propagation theory. The calculated wave parameters have been plotted as contour lines in a map containing as coordinates a characteristic height and the number of the electron density at this height. From that the diurnal variations of the electron density profile during summer and winter as well as the behaviour of the D-region during solar flare events have been deduced.

Key words: VLF-propagation – Electron density profile of the ionospheric D-layer – Diurnal variations of VLF field quantities.

1. Introduction

VLF-waves (3–30 kHz) can propagate within the atmospheric wave guide between the surface and the ionospheric D-layer. While the earth's surface behaves like a sharp boundary for these waves, the ionospheric D-layer is an inhomogeneous and anisotropic reflector for VLF-waves. Any variation of the electron density profile changes the reflection coefficient of the VLF-waves in amplitude and phase. Therefore the measurement of the electric and the magnetic field vectors of a commercial VLF-transmitter enables one to deduce this variation of the ionospheric electrons density via an appropriate theory.

For propagation paths up to about 1500 km, ray optics is a reasonable approximation for VLF-propagation (Volland, 1968). In this case the theoretical interpretation of the observed field parameters must be done in 2 steps. Firstly, one has to calculate the reflection matrix of an anisotropic, homogeneously layered ionosphere with respect to plane waves, and a virtual reflection height has to be defined. Secondly the elements of the reflection matrix and the virtual

height as function of the angle of incidence, of the geomagnetic field and of the electron density and collision frequency profile are used to determine the vectors of the electric and the magnetic field strength from ray optics theory. Summaries of the theoretical foundation of the reflection matrix and of the VLF-propagation theory have been given by Budden (1961), Wait (1962), Volland (1968) and Galejs (1972).

Using Budden's formulation, a Runge-Kutta-integration procedure for numerical calculation of the ionospheric reflection matrix has been described by Pitteway (1965). More convenient and appropriate for computer calculation is the matricant algorithm developed by Volland (1968). This simple procedure has been used in the following calculations.

Measurements of the field of VLF-transmitters have been analysed e.g. by Bracewell et al. (1951), Volland (1968), Frisius (1970) and Stratmann (1970), for only one field component. Model fitting with discrete D-layer models for VLF propagation over great distances has been carried out by Rinnert (1972) using mode theory. In the present paper model calculations via ray optics have been adjusted to measurements of the complete electromagnetic field of the transmitter GBR recorded at 3 receiving stations. The use of a fast computer and an appropriate calculation algorithm made it possible to determine amplitude and phase of all components of the electromagnetic field for a large number of ionospheric models. The results are presented as contour mappings for each component. This method allows one to determine directly the variation of field quantities as a function of the parameters of the ionospheric D-layer model.

2. The Calculation of the Reflection Matrix

The reflection coefficient of the plane earth with respect to plane waves of frequency ω , incident at angle θ , is given by the Fresnel formulas:

$$R_{\text{TM}} = \frac{n_E^2 \cos \Theta - (n_E^2 - \sin^2 \Theta)^{0.5}}{n_E^2 \cos \Theta + (n_E^2 - \sin^2 \Theta)^{0.5}}, \text{ for TM-waves} \quad (1)$$

$$R_{\text{TE}} = \frac{\cos \Theta - (n_E^2 - \sin^2 \Theta)^{0.5}}{\cos \Theta + (n_E^2 - \sin^2 \Theta)^{0.5}}, \text{ for TE-waves} \quad (2)$$

with the refraction-index of the earth:

$$n_E = \left(\varepsilon_E - \frac{i \sigma_E}{\omega \varepsilon_0} \right)^{0.5}. \quad (3)$$

The electric conductivity σ_E varies between $4 \Omega^{-1} \text{ m}^{-1}$ for seawater and $10^{-4} \Omega^{-1} \text{ m}^{-1}$ for dry ground, and the dielectric constant ε_E is between 80 and 1 for these 2 cases. ε_0 is the dielectric constant of vacuum.

To determine the reflection properties of the ionosphere, the D-region is divided into horizontal homogeneous slabs of appropriate thickness. If the propagation plane of a homogeneous plane wave is in the $x-z$ -plane of a cartesian system with z vertically upward, Maxwell's equations can be written in the form:

$$\mathbf{c}' = -i k_0 \mathbf{K} \mathbf{c} \quad (4)$$

with the field strength vector:

$$\mathbf{c} = \frac{1}{\sqrt{Z_0}} \begin{pmatrix} E_x \\ Z_0 H_x \\ Z_0 H_y \\ -E_y \end{pmatrix}, \quad \mathbf{c}' = \frac{\partial \mathbf{c}}{\partial z} \quad (5)$$

and \mathbf{K} , a complex 4×4 coefficient matrix (Volland, 1968). Z_0 is the characteristic impedance of free space and k_0 is the wave number in vacuum. The matrix \mathbf{K} is a function of the electron-neutral collision number, the geomagnetic field and of the electron density profile. Integration between the upper and lower boundary of a slab, z_2 and z_1 , yields:

$$\mathbf{c}(z_1) = \mathbf{T} \mathbf{c}(z_2), \quad (6)$$

with T a transmission matrix, which is called "matrizant":

$$\mathbf{T} = \exp(i k_0 \mathbf{K} \cdot (z_2 - z_1)). \quad (7)$$

If an appropriate linear-combination of field quantities is used,

$$\mathbf{a} = \mathbf{Q}^{-1} \mathbf{c}, \quad \mathbf{a} = \begin{pmatrix} A_1 \\ A_2 \\ B_1 \\ B_2 \end{pmatrix}, \quad (8)$$

the coefficient matrix becomes diagonal:

$$\mathbf{a}' = -i k_0 \mathbf{N} \mathbf{a}. \quad (9)$$

The components of the vector \mathbf{a} are two upgoing characteristic waves A_1 and A_2 and 2 downgoing characteristic waves B_1 and B_2 . In vacuum A_1 and B_1 are pure TM-waves and A_2 and B_2 are pure TE-waves. The transmission behaviour of a slab with respect to characteristic waves is given by a matrix \mathbf{M} :

$$\mathbf{a}(z_1) = \mathbf{M} \mathbf{a}(z_2), \quad \mathbf{M} = \mathbf{Q}^{-1} \mathbf{T} \mathbf{Q}. \quad (10)$$

Defining the reflection-matrix of a homogeneous layered ionosphere by:

$$\mathbf{R} \begin{pmatrix} A_1 \\ A_2 \end{pmatrix} = \begin{pmatrix} R_{\text{TM TM}} & R_{\text{TM TE}} \\ R_{\text{TE TM}} & R_{\text{TE TE}} \end{pmatrix} \cdot \begin{pmatrix} A_1 \\ A_2 \end{pmatrix} = \begin{pmatrix} B_1 \\ B_2 \end{pmatrix}, \quad (11)$$

one obtains from Equation 9 and after elimination of A_1 and A_2 :

$$\mathbf{R}(z_1) = (\mathbf{M}_3 + \mathbf{M}_4 \mathbf{R}(z_2)) (\mathbf{M}_1 + \mathbf{M}_2 \mathbf{R}(z_2))^{-1}, \quad (12)$$

where \mathbf{M}_i are the submatrices (2×2) of \mathbf{M} . Thus one can determine the reflection-matrix of the whole ionosphere by repeatedly adding homogeneous slabs for any ionospheric model, angle of incidence or geomagnetic field (Frisius and Schäfer, 1976).

3. The Ray Optics Theory

The EM-field at the receiver represents the superposition of waves propagating along various ray paths. The waves, which are reflected at least once at the iono-

sphere, depend on the radiation characteristics of the transmitter as well as on the reflection properties of the earth and ionosphere. Sommerfeld's (1947) theory is applicable for the ground-wave. A superposition of all ionospheric waves and the ground wave yields the field of a vertical dipole (in cylindrical coordinates):

$$\begin{aligned} \begin{pmatrix} E_\rho \\ Z_0 H_\rho \end{pmatrix} &= C \cdot \left(2 \mathbf{W}(\rho)/n_E + \sum_{n=1}^{\infty} \{(\mathbf{R}_i \mathbf{R}_e)^n (\mathbf{I} + \mathbf{R}_e^{-1}) - (\mathbf{R}_e \mathbf{R}_i)^n (\mathbf{I} + \mathbf{R}_e)\} \sin^2 \theta_n \right. \\ &\quad \left. \cos \theta_n \exp(i k_0 (\rho - r_n)) \right) \cdot \begin{pmatrix} p_e \\ p_m \end{pmatrix} \\ \begin{pmatrix} E_z \\ Z_0 H_z \end{pmatrix} &= C \cdot \left(2 \mathbf{W}(\rho) + \sum_{n=1}^{\infty} \{(\mathbf{R}_i \mathbf{R}_e)^n (\mathbf{I} + \mathbf{R}_e^{-1}) + (\mathbf{R}_e \mathbf{R}_i)^n (\mathbf{I} + \mathbf{R}_e)\} \sin^3 \theta_n \right. \\ &\quad \left. \exp(i k_0 (\rho - r_n)) \right) \cdot \begin{pmatrix} p_e \\ p_m \end{pmatrix} \\ \begin{pmatrix} Z_0 H_\phi \\ -E_\phi \end{pmatrix} &= -C \cdot \left(2 \mathbf{W}(\rho) + \sum_{n=1}^{\infty} \{(\mathbf{R}_i \mathbf{R}_e)^n (\mathbf{I} + \mathbf{R}_e^{-1}) + (\mathbf{R}_e \mathbf{R}_i)^n (\mathbf{I} + \mathbf{R}_e)\} \sin^2 \theta_n \right. \\ &\quad \left. \exp(i k_0 (\rho - r_n)) \right) \cdot \begin{pmatrix} p_e \\ p_m \end{pmatrix} \end{aligned} \quad (13)$$

where \mathbf{R}_e and \mathbf{R}_i are the reflection matrices of earth and ionosphere, p_e and p_m are the electric and magnetic dipole moments of the transmitter, \mathbf{I} is the unit matrix, $\mathbf{W}(\rho)$ is the ground wave and

$$C = \frac{\omega Z_0 k_0 \exp(-i k_0 \rho)}{4 \pi \rho},$$

is the field of a vertical dipole in free space. ρ is the distance transmitter-receiver and r_n the length of the ray path of a reflection order n .

A VLF-transmitter can be modelled sufficiently well by a vertical electric dipole ($p_m=0$), for which in free space only the components E_z , E_ρ , H_ϕ exist. The conversion factors (non-diagonal members in \mathbf{R}_i) will, however, cause the appearance of additional field components H_ρ , H_z , E_ϕ for VLF-propagation in the terrestrial wave guide.

The values of the angles of incidence θ_n and of the ray paths r_n must be determined by taking into account the earth's curvature and the reflection heights for each reflection order. Neglecting or approximating these quantities would cause a considerable displacement of the interference pattern of ionospheric and ground waves. In addition, a convergence factor has to be introduced into the field strength calculation, which accounts for the focussing or defocussing of the wave energy density because of the curved reflectors (Bremmer, 1949).

4. The Data

Measurements for this analysis were available from Stockert near Bonn (distance GBR-Stockert: 580 km), Braunschweig (790 km) and Berlin (980 km). Amplitude and phase of the component H_ϕ of the transmitter GBR have been recorded since 1967 at the Stockert station. The phase measurements are stabilized by a

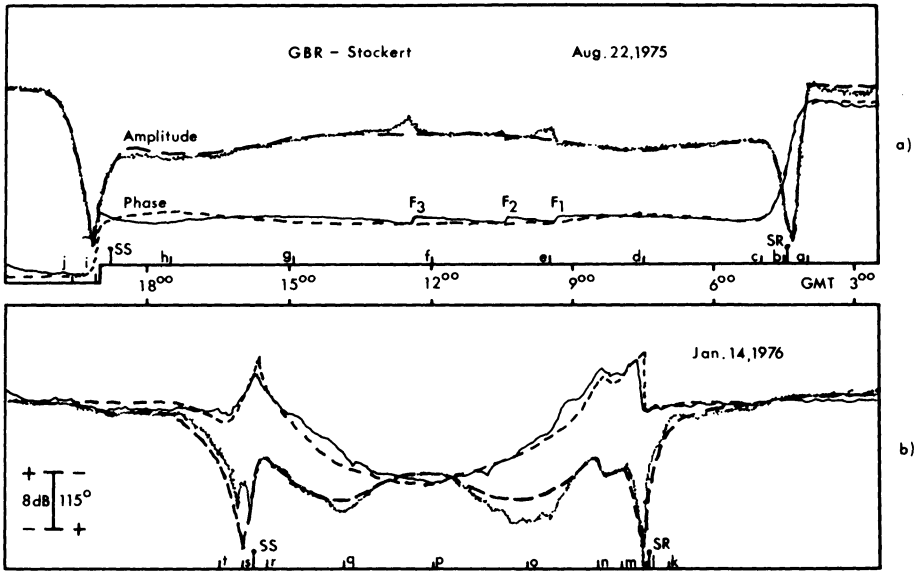


Fig. 1. Typical examples of the diurnal variations of amplitude and phase of the component H_ϕ at summer- and wintertime for the propagation path GBR-Stockert. The broken curves result from the fitting process. The time marks correspond to those in Figure 3. Solar flare events are indicated by "F"

rubidium frequency standard. Differences of 0.2 dB in amplitude and 4 deg in phase can be distinguished on the recordings. Examples of registrations are shown in Figure 1.

Another receiver, developed at the Heinrich-Hertz-Institute (HHI) in Berlin, measures the amplitudes of E_z and H_ϕ , the phase of E_z , the direction of arrival Φ , and the ratio of the smaller to the larger axis of the horizontal magnetic vector (HPR = H-polarisation-ratio) (Frisius et al., 1971). Similar detectors are operating at Braunschweig and Berlin. A monthly review of the results of all 3 stations has been published for the year 1971 by the HHI, Berlin. An example is shown in Figure 4.

5. The Graphical Presentation of the Field Quantities in a Contour Map

VFL-waves are reflected at heights where the electron density reaches a few hundreds of electrons cm^{-3} . Therefore the ionospheric D-layer is responsible for reflection of VFL-waves at daytime, while at night they are reflected at the E-layer.

Since the primary effects upon VLF-propagation arise from variations in the ionospheric electron density distribution (Rinnert, 1972), and since only relatively small variations of the collision frequency occur in the course of the day, it is reasonable to assume a collision frequency independent of time. The chosen dependence of collision frequency ν on the height z is (Frisius, 1974):

$$\nu(z) = 5 \times 10^6 \exp\left(\frac{70-z}{6.7}\right) (\text{s}^{-1}), \tag{14}$$

which is valid at altitudes between about 60 and 110 km (Galejs, 1972).

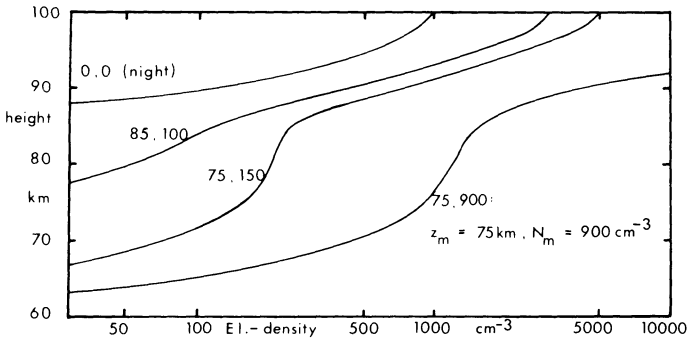


Fig. 2. Electron density profiles of the lower ionosphere with different parameters N_m and z_m of the D-layer

Within the ionospheric D-layer, where the effective recombination coefficient is proportional to

$$\exp\left(\frac{z_m - z}{H_s}\right),$$

Chapman theory leads to an electron density profile of the form:

$$N_e(z) = N_m \exp\left(0.5 \left(1 - \exp\left(\frac{z_m - z}{H_s}\right)\right)\right), \quad (15)$$

where N_m is the density at a reference height z_m , and H_s is the scale height. Whereas VLF-waves are reflected at this layer during the day, the D-layer vanishes nearly completely at nighttime, and the VLF-waves are then reflected at the E-layer. For convenience, the same profile (Eq. (15)) has been used for this layer, with a constant reference height of $z_m = 100$ km and a density N_m , which is 30 times larger than the value of N_m of the D-layer, at least 1000 cm^{-3} , however. The exact profile of the electron density at heights where N_e exceeds 1000 cm^{-3} is not relevant for VLF-propagation, because the reflection occurs below these heights. A first comparison between theory and observations revealed, that the data could be best reproduced with a constant scale height value of $H_s = 6$ km within the D- and E-layers.

The remaining parameters are the variables N_m and z_m of the D-layer. Using fixed conditions for the propagation path, the magnetic field, the properties of the ground and the collision frequency, the amplitudes and phases of the EM-field components depend now only on these two parameters. By varying N_m and z_m over a wide range, a large number of D-layer models used in the literature and many of the observed electron density profiles can be well approximated. Some of these profiles with different values of N_m and z_m are plotted in Figure 2.

To obtain a graphical presentation, the field values of each propagation path have been calculated at more than 300 control points, i.e. for N_m in a range between 0 and 1200 cm^{-3} at intervals of 50 cm^{-3} and for z_m between 60 and 90 km at intervals of 2.5 km. By using a plotter contouring program, diagrams for the different components have been obtained (Figs. 3, 5 and 6). Amplitudes are given in dB relative to free space field strength, phases in degrees. This representation

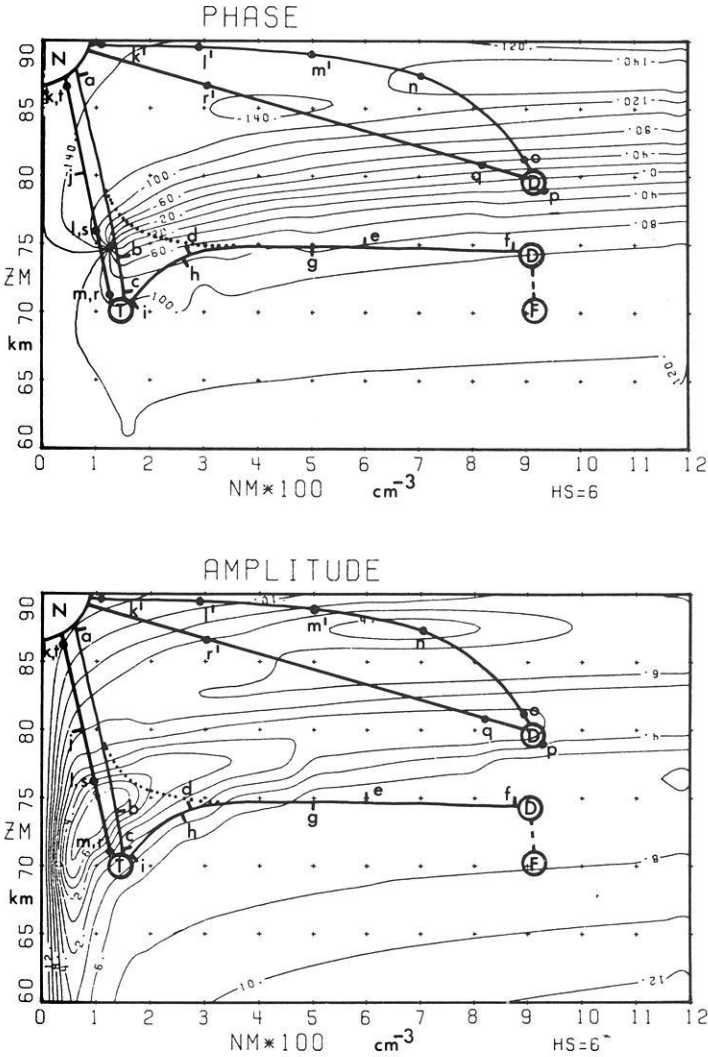


Fig. 3. Contour maps of phase and amplitude of H_ϕ for the propagation path GBR-Stockert. Amplitudes are given in dB relative to free space field strength, phases in degrees

allows, e.g., the simulation of a D-layer, in which the electron density parameter varies from $N_m=0$ to $N_m=1000 \text{ cm}^{-3}$ at a constant height of $z_m=60$ km. On the other hand a layer can be formed, which decreases its height parameter z_m from 90 km to 60 km at a constant electron content of $N_m=1000 \text{ cm}^{-3}$. One of these possibilities, or a mixture of them is taken at sunrise. A very special feature can be seen on the plot of H_ϕ for the propagation path GBR-Stockert (Fig. 3). Near the control point $N_m=100 \text{ cm}^{-3}$, $z_m=75$ km the field strength vanishes completely, and all phase contour lines converge. For this model and for this propagation path the ionospheric waves and the ground wave are equal in magnitude but phase shifted by 180 deg. The destructive interference leads to zero field strength.

6. Fitting an Ionospheric Model

The fitting process shall be demonstrated here for the propagation example GBR-Stockert. An analysis of the Stockert registrations of several years yields 2 main types of phase and amplitude curves for H_ϕ . The first ones are applicable mainly at summertime, the second are appropriate only for winter. Two typical examples are shown in Figure 1.

The summer propagation type can be interpreted in the following manner: Before sunrise a nighttime E-layer exists together with a depleted D-layer beneath with parameters $N_m < 100 \text{ cm}^{-3}$ and $z_m = 85\text{--}90 \text{ km}$. In the $N_m - z_m$ -diagrams this nighttime region is marked by an "N". From the records (Fig. 1a) one finds, that the daytime amplitudes are about 7 dB lower than at night, and the phases are nearly 250° larger. The noontime region is thus characterized by a point close to $N_m = 900 \text{ cm}^{-3}$, $z_m = 74 \text{ km}$, and is marked by a "D". The deep field strength minimum at and shortly before sunrise is caused by a thin layer with electron density $N_m = 150 \text{ cm}^{-3}$ descending down to $z_m = 70 \text{ km}$ (marked by "T"). This transient layer can be explained by the influence of solar radiation at solar zenith angles of more than 90° prior to ground sunrise (Thomas and Harrison, 1970). The further development of the D-layer is essentially due to the increase of N_m at an approximately constant height of $z_m = 75 \text{ km}$ on a path marked by the heavy line in the contour plots. Time marks are placed in Figures 1a and 3 to facilitate comparison between the measurements and computed values. The broken lines in Figure 1a are the curves resulting from the path in the contour map of Figure 3. They are in good agreement with the original recordings. When N_m has attained a value of about 300 cm^{-3} near 75 km height, the contour lines pass nearly parallel to the N_m -axis. Therefore a further increase in N_m at the same height z_m has only minimal effect on D-layer reflection properties and VLF-propagation. The phase curve sometimes decreases at sunrise to the value of 100° . This effect evidently occurs when the pole near $N_m = 100 \text{ cm}^{-3}$, $z_m = 75 \text{ km}$ is not passed in a clockwise manner, but in a mathematically positive sense. The return to night conditions at sunset is generally somewhat above the morning path, as indicated by the dotted line in Figure 3. Occasionally, however, the pole is passed clockwise, as can be concluded from the record of 8 Aug. 1975. A very thin layer, slowly disappearing after ground sunset, may be responsible for this occurrence.

Calculations for the other two stations also show satisfying agreement with measurements. For example, the records of Braunschweig of 30 Aug. 1971 are shown in Figure 4 and compared with the calculations in Figures 5 and 6. The field strength minimum occurs here about 1 h earlier than at Bonn, because the valley is approximately 10 km higher than at Bonn (Figs. 1 and 3) and the build up of the thin layer takes about this time. The daytime value of the amplitude is only little below night conditions, while the phase difference is 180° (Fig. 3). This can be simulated quite well by the calculations.

Figure 6, as well as similar plots for the other stations, shows that no substantial further information can be obtained by measuring the additional quantities HPR (the H-voltage-power-ratio) and Φ (the direction of arrival), because

only very small changes of the contour lines occur within a large vicinity centered on the point "D" (noontime value near $N_m = 900 \text{ cm}^{-3}$, $z_m = 75 \text{ km}$). On the other hand many small variations are possible in the twilight regions (Fig. 6). In addition, inhomogenities in the ionospheric layers at sunrise and sunset may be important, especially for HPR and Φ . These effects cannot be simulated well by our model. Nevertheless, the increase of the quantity HPR and the decrease of the angle Φ during twilight (Fig. 4) agrees with the corresponding model calculations (Fig. 6).

The diurnal variation of the field parameters during winter is quite different. On the Stockert records, at least 2 relative minima of the magnetic field strength can be seen shortly before and about 2 hours after sunrise in Figure 1 b of 10 Jan. 1976. The first minimum is the deepest and sharpest. The sunset records are similar, except that the two minima are generally not so sharp. The phase decreases by about 100° relative to the night value near sunrise and sunset. At noon the phase is only about 150° greater than during night. These registrations suggest, that at least two separate layers influence the VLF-propagation during winter. The first is a pre ground sunrise layer, similar to the summer transient layer, but with smaller thickness. The pole is therefore passed closely on the left side (marked by the symbols $k-l-m$ in Fig. 2), from which the deep minimum in amplitude and the phase jump of 100° arises. During the same time a second layer develops out of the nighttime E -layer (the path $k'-l'-m'$ in Fig. 2). When this layer has reached the height $z_m = 79 \text{ km}$ (path $n-o-p$), the reflection characteristics of the VLF-waves are dominated by that layer, which has now swallowed the thin transient layer. Therefore the phase gradually increases again by about 250° . The amplitude has to go through the deep and broad valley near $z_m = 80 \text{ km}$ during the build-up of the daytime layer. At noon it reaches a point near $N_m = 900 \text{ cm}^{-3}$, $z_m = 79 \text{ km}$. The way back to night conditions is indicated by the time marks $p-q-r-s-t$ in Figures 1 and 3. When the daytime layer has been depleted down to a point "r" near sunset, the remaining transient layer again plays a decisive role (marks $r-s-t$). Here again the calculation (dashed line in Fig. 1 b) fits the observations quite well. This consistency between observations and theory also exists for the other two stations.

A special application of this method is the simulation of solar flare effects on the lower ionosphere. Solar flare events are accompanied by phase jumps in the H_ϕ -component of up to 30° and an amplitude increase up to 5 dB, as can be seen on the record of 8 Aug. 1975 (marked by "F" in Fig. 1 a). From the contour map in Figure 3 one notices, that a daytime phase increase always indicates a downward movement of the D-layer height. However, the magnitude of the variations in field strength and phase depends strongly on the undisturbed conditions. The VLF-signal variation during solar flares generally becomes smaller for larger N_m and smaller z_m of the undisturbed daytime model. In particular, the quantities HPR and Φ are completely unsuitable for the detection of solar flares because they are not significantly influenced. The mean downward displacement of the height parameter z_m during 30 solar flares observed at Stockert during 1975 was 3–4 km. The maximum observed decrease in z_m over this data set was 8 km. The downward movement of the summer D-layer during an average solar flare is indicated by the mark "F" in Figure 3.

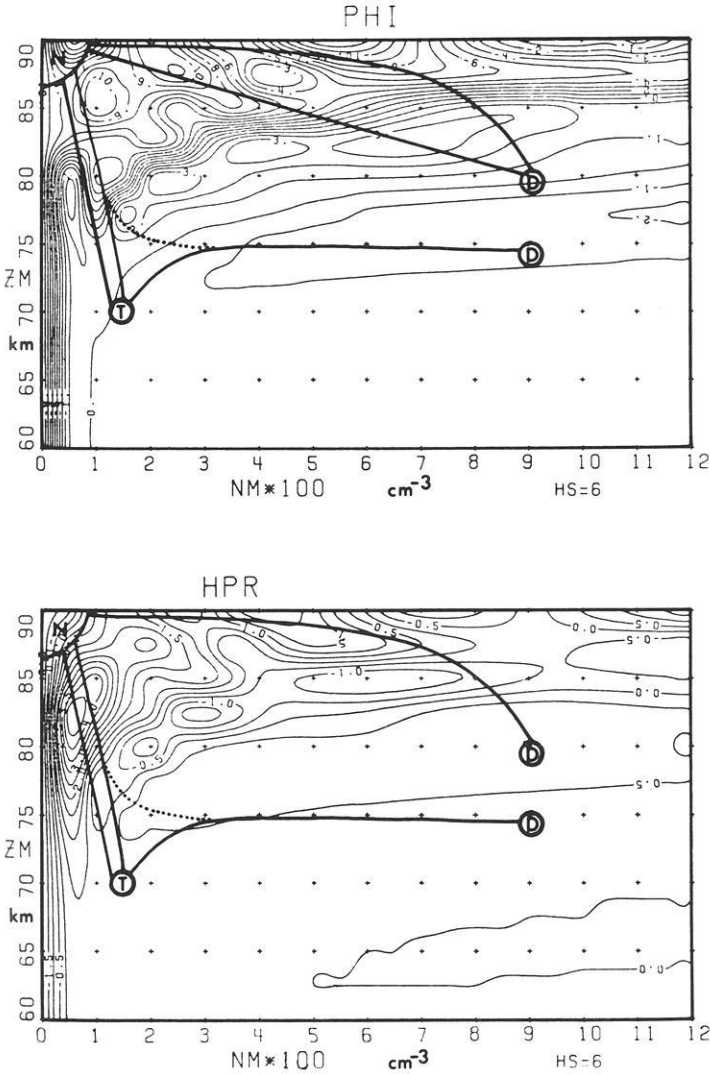


Fig. 6. Contour maps of HPR (in dB) and of the angle of incidence ϕ (in degrees) for the propagation path GBR-Braunschweig

7. Conclusion

Contour maps for the components of the electromagnetic field of the VLF-transmitter GBR have been plotted using a full wave ray optics theory. The coordinates are the two parameters N_m and z_m , which characterize the electron density profile of the ionospheric D-layer: N_m is the electron content of the D-layer at a reference height z_m . From a comparison between theory and measurements the diurnal variations of the D-layer electron density as well as variations due to solar flares can be determined. The measurements of the transmitter GBR, made

at the receiving stations Stockert, Braunschweig and Berlin, indicate, that 2 general types of the diurnal D-layer variations occur. The first one, seen during summer months, can be simulated by the variation of the two parameters of a single layer. The second type occurs only during winter, when the lower boundary of the ionosphere is about 5 km higher than at summertime. The parameters of two independent layers have to be varied for a simulation of the diurnal behaviour of this model.

The occurrence of a solar flare event causes a positive phase and amplitude shift in the H_{ϕ} -component of the Stockert records. One may deduce from the contour maps, that this behaviour is associated with a downward movement of the ionospheric D-layer over some kilometers.

Acknowledgement. I gratefully thank Prof. H. Volland for his encouragement and Dr. M. Bird for his critical reading and commenting on the first manuscript.

References

- Bracewell, R. N., Budden, K. G., Radcliffe, S. A., Straker, T. W., Bremmer, H.: *Terrestrial radio waves*. Amsterdam: Elsevier
- Budden, K. G.: *Radio waves in the ionosphere*. Cambridge: University Press 1961
- Frisius, J.: Observations of diurnal amplitude and phase variations on 16 kHz transmission path and interpretation by a simple propagation model. AGARD Conference Proceedings, No. 33, K. Davies, ed. Slough, Engl.: Technivision Services 1970
- Frisius, J.: Bemerkungen zur aeronomischen Interpretation von VLF-Registrierungen. Kleinheubacher Berichte **17**, 403, 1974
- Frisius, J., Heydt, G., Raupach, R.: Measurement of the complete electromagnetic field of VLF transmitters. Techn. Bericht Nr. 145, HHI, Berlin 1971
- Frisius, J., Schäfer, J.: Berechnung numerischer Näherungsfunktionen für die Reflexions- und Konversionsfaktoren der unteren Ionosphäre im Längstwellenbereich. Kleinheubacher Berichte, **19**, 517, 1976
- Galejs, J.: *Terrestrial propagation of long electromagnetic waves*. Oxford: Pergamon Press 1972
- HHI: Monthly reviews on VLF-CW-field strength measurements. Arbeitsgruppe VLF-Ausbreitung Heinrich-Hertz-Institut f. Schwingungsforschung, Berlin-Charlottenburg, 1971
- Pitteway, M. L. V.: The numerical calculations of wave fields, reflection coefficient and polarisation for long radio waves in the lower ionosphere. Phil. Trans. Roy. Soc. London, Ser. A **257**, 219, 1965
- Rinnert, K.: Untersuchungen der unteren Ionosphäre mit Hilfe der Längst-Wellenausbreitung über großen Entfernungen. Z. Geophys. **38**, 719, 1972
- Sommerfeld, A.: 1947 Partielle Differentialgleichungen der Physik, 6. Aufl. Leipzig: Akad. Verlagsges. Geest u. Portig 1966
- Stratmann, D.: Berechnung des Wellenfeldes eines Längstwellensenders im Entfernungsbereich bis 1000 km zur kontinuierlichen Sondierung der tiefen Ionosphäre durch Feldstärkenmessungen vom Sender. Mitteilungen aus dem MPI für Aeronomie, Berlin-Heidelberg-New York: Springer 1970
- Thomas, L., Harrison, M. D.: The electron density distribution in the D-region during the night and pre sunrise period. J. Atmospheric, Terrest. Phys. **32**, 1, 1970
- Volland, H.: *Die Ausbreitung langer Wellen*. Braunschweig: Vieweg 1968
- Wait, J. R.: *Electromagnetic waves in stratified media*. London: Pergamon Press 1962
- Weekes, K.: The ionospheric propagation of long and very long radio waves over distances less than 1000 km. Proc. IEE **98**, 221, 1951

A Detailed Investigation of the Canadian Cordillera Geomagnetic Transition Anomaly

H. Dragert^{1*} and G.K.C. Clarke²

¹ Earth Physics Branch, Gravity and Geodynamics, 1 Observatory Cres., Ottawa, K1A 0Y3 Canada

² Department of Geophysics and Astronomy, University of British Columbia, Vancouver, B.C. V6T 1W5, Canada

Abstract. Employing recently developed broad-band instrumentation, a geomagnetic depth-sounding study has been carried out investigating the detailed structure of the lateral conductivity discontinuity in the Cordillera geomagnetic transition zone along a profile between Clearwater, B.C., and Suffield, Alta. Analysis of data has revealed the presence of 3 conductive structures: 1) a near-surface conductor, which can be associated with the sediments of the Rocky Mountain Trench; 2) a parallel-striking lower-crust/upper mantle conductivity heterogeneity 40–50 km beneath the trench area, which can be associated with possible hydration or partial melting; 3) a second deep conductivity structure orthogonal to the previous structures, which is possibly associated with a buried Precambrian rift. The measured anomalous effect of the latter 2 conductors indicates that the induced current flow is not caused by local induction, but by local deflection of current patterns induced over a larger region.

Key words: Geomagnetic induction anomaly – Broad-band geomagnetic depth-sounding – Transfer function analysis – Canadian Cordillera crustal structure

Introduction

Over the past 10 years, various geomagnetic depth-sounding (GDS) and magnetotelluric (MT) studies (Hyndman, 1963; Caner and Cannon, 1965; Caner, et al., 1967; Caner, et al., 1971) have investigated the conductivity structure of the lower crust and upper mantle in western Canada. This work has established that a dominant geomagnetic feature for the Canadian Cordillera is the presence of a “low- I ” zone ($I = |\Delta Z| / \{\Delta H^2 + \Delta D^2\}^{1/2}$), a region in which vertical field variations having periods less than 30 min are greatly attenuated compared to variations observed further east (see Fig. 1). The transition zone,

* Previously Dept. of Geophysics and Astronomy, U.B.C., Vancouver

where I not only increases sharply but also shows strong azimuthal dependence, has been found to follow roughly a line along the western front of the Rocky Mountains from 49°N to at least 54°N latitude (Caner, et al., 1971). Hence, this geomagnetic transition zone constitutes a large scale variational anomaly, marking a relatively abrupt lateral conductivity change in the lower crust or the upper mantle.

The primary purpose of this study was to investigate in greater detail the nature of the lateral conductivity changes encountered in this transition region.

Data Collection and Reduction

The instruments used in the field were of 2 types: 1) the Askania geomagnetic variograph Gv3; and 2) an electronic broad-band system recently developed by Caner and Dragert (1972). The instrumental characteristics pertinent to data analysis can be summarized as follows. The Askania film registrations allowed a time resolution of 30s and an amplitude resolution between 1 and 2 γ within a dynamic range of about 55 db. The electronic system, using two overlapping frequency bands, produced magnetic tape records with a time resolution capability of 0.1s, an amplitude resolution of 0.1 γ , and a total dynamic range of 78 db (Dragert, 1974).

A geomagnetic depth-sounding profile of seven stations was operated for a period of two months during the fall of 1971. The location of the profile is shown in Figure 2 and the station identification detail is summarized in Table 1. Two obvious shortcomings of the chosen site locations could be mentioned at this point: 1) the average station spacing for the 4 broad-band sites (~60 km) is too large for accurate spatial resolution of possible short-period anomalies; and 2) the nature of the anomaly in this area is suspected to be three-dimensional (Caner, et al., 1971); thus, the quantitative interpretation of the data in terms of a best-fitting, two-dimensional, numerical model may be misleading. However, practical considerations such as the suitable protection of instruments, the accessibility of sites, the limited number of broad-band systems, the minimization of geomagnetic latitude effects, and the complete bracketing of the transition-zone anomaly, favoured the chosen profile location.

After preliminary editing of all data, simultaneous record sections with suitable continuous magnetic activity were chosen for analysis. For Band A, a digitizing interval of 1.00 min and record sections of 36 h were used, giving an effective period range of 5 to 180 min. Seven record sections or "magnetic events" recorded at all 7 stations were used for Band A analysis. Band B data were digitized using an interval of 2.50s and record sections of 100 min, resulting in an effective period range of 10–500s. Eleven events were used for Band B analysis, and these were naturally limited to the 4 broad-band systems.

Fig. 1. Location of GDS stations in western Canada up to 1970. Profile A are stations of Hyndman (1963) and Lambert and Caner (1965); Profile B and C are stations described by Caner et al. (1967); Profiles D and E are stations of Dragert (1970). The dashed rectangle identifies the area containing the 20-station network of Lajoie and Caner (1970). (After Caner et al., 1971)

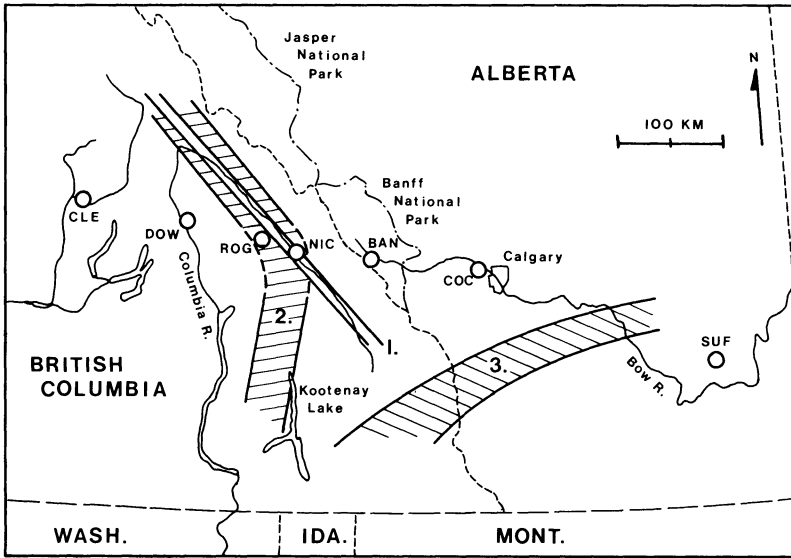


Fig. 2. Station locations for the field investigation of the geomagnetic transition-zone anomaly. The three indicated conductive structures deduced from this study are discussed in the conclusions.

Table 1. Summary of station identification and location for the geomagnetic transition anomaly profile

Station	Geographic Long. (°W)	Location Lat. (°N)	Geomagnetic Lat. (°N)	Type of Instrument	Time of Operation
CLE (Clearwater)	120.0	51.6	57.9	Askania	Aug. 23–Nov. 16
DOW (Downie Creek)	118.2	51.3	58.0	Broad-band	Sept. 17–Nov. 11
ROG (Rogers Pass)	117.6	51.2	58.1	Broad-band	Sept. 17–Nov. 12
NIC (Nicholson)	117.0	51.3	58.3	Broad-band	Sept. 18–Nov. 12
BAN (Banff)	115.6	51.2	58.6	Broad-band	Sept. 19–Nov. 13
COC (Cochrane)	114.2	51.1	58.8	Askania	Sept. 20–Nov. 15
SUF (Suffield)	111.1	50.2	58.6	Askania	Sept. 20–Nov. 14

The type of magnetic activity and the quality of the data chosen for analysis of Bands A and B are illustrated in Figures 3 and 4 respectively, which display computer-drawn traces of digitized registrations. A closer examination of these figures reveals good spatial coherence of magnetic variations in both bands as well as anomalous behaviour of especially the Z component at stations such as BAN and COC.

Analysis Techniques

To handle the large quantities of data efficiently, the periodogram spectral approach (c.f. Jones, 1965) employing the Fast Fourier Transform (Cooley and Tukey, 1965) was used for spectral analysis. A variable-width Parzen window

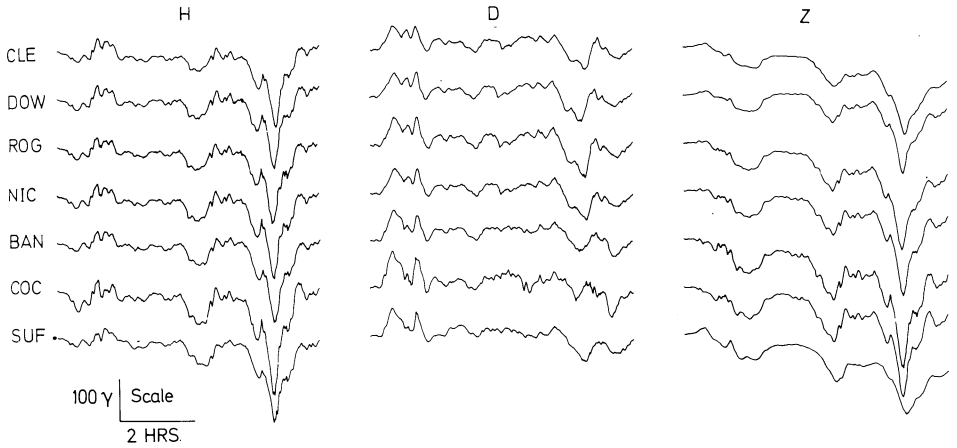


Fig. 3. Sample of digitized Band A data recorded simultaneously at all profile stations

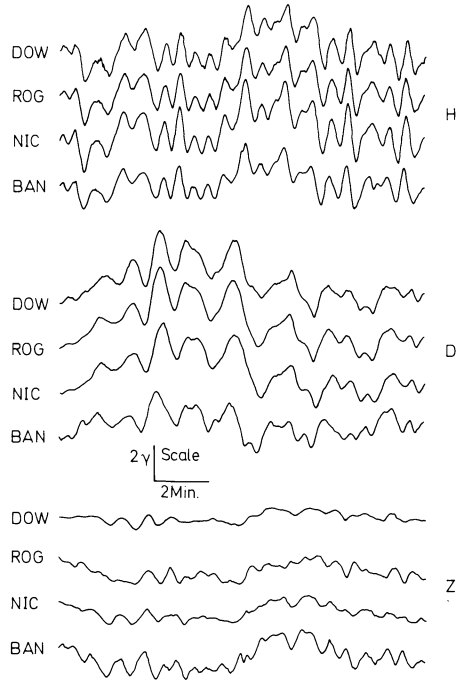


Fig. 4. Sample of digitized Band B data recorded simultaneously at the four broad-band stations

was used to convolve the raw power periodograms, yielding, as a function of frequency, smoothed spectral estimates of decreasing variance at a limited number of frequency bands having decreasing resolution. Figure 5 illustrates a normalized raw power spectral estimate and its smoothed form obtained by convolution with the Parzen window of varying width. Shown also are the extent of overlap between adjacent windows, and the change of window shape from low to higher frequencies. Such smoothed spectral estimates were

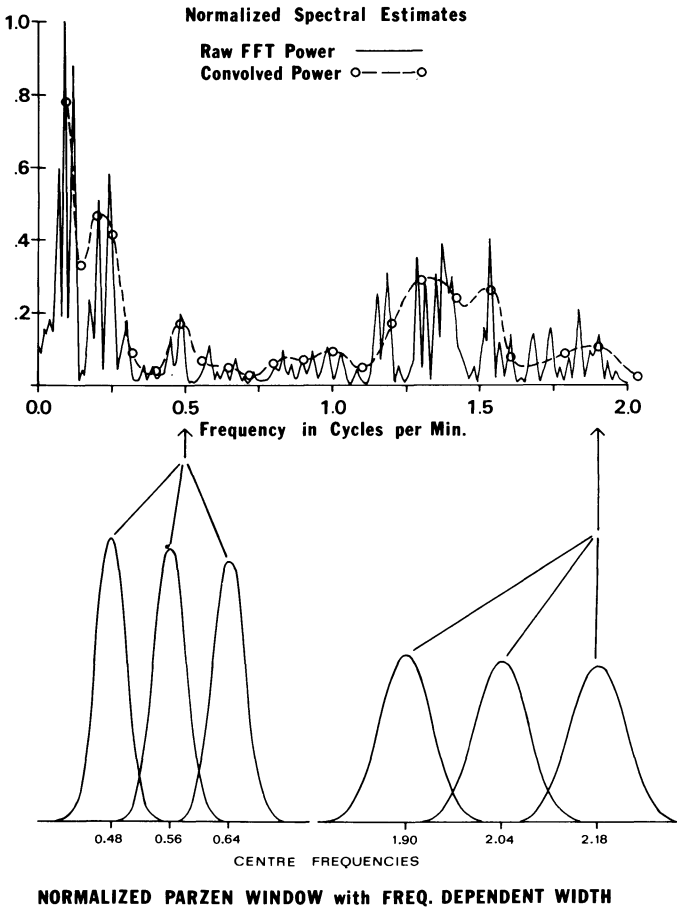


Fig. 5. An example of a periodogram spectral estimate calculated from the raw Fast Fourier Transform power, and its smoothed version obtained by convolution with a Parzen window of varying width

evaluated for each component and each storm event at all stations. To increase the stability of the spectral estimates even more, and to minimize possible time dependencies of these estimates, the component power and cross-power estimates were averaged over all analyzed events within each band at each station.

To determine the magnitude and phase of the anomalous field contributions at each station, 2 types of transfer functions were evaluated from the smoothed power and cross-power spectral estimates:

A. The Paired-Station Transfer Function Matrix, T

Under the assumption of a uniform source with infinite spatial wavelengths, the observed field variations, comprised of normal and anomalous field varia-

tions, can be statistically fitted to the frequency-domain relation (Schmucker, 1970)

$$\begin{pmatrix} H_A \\ D_A \\ Z_A \end{pmatrix} = \begin{pmatrix} h_H & h_D & h_Z \\ d_H & d_D & d_Z \\ z_H & z_D & z_Z \end{pmatrix} \begin{pmatrix} H_N \\ D_N \\ Z_N \end{pmatrix} + \begin{pmatrix} \delta_H \\ \delta_D \\ \delta_Z \end{pmatrix} \quad \text{i.e. } \bar{F}_A = T \cdot \bar{F}_N + \bar{\Delta} \quad (1)$$

where

T = the transfer function matrix of 9 complex elements.

\bar{F}_A = (H_A, D_A, Z_A) , the Fourier transform of the anomalous field; i.e., the field associated with lateral conductivity inhomogeneities.

\bar{F}_N = (H_N, D_N, Z_N) , the Fourier transform of the estimated normal field; i.e., the total field observed over a region of laterally homogeneous conductive structure.

$\bar{\Delta}$ = $(\delta_H, \delta_D, \delta_Z)$, the Fourier transform of a residual field containing uncorrelated parts of the anomalous components.

For this analysis, the field observed at a station well removed from the anomaly was taken to be representative of the normal field; hence the name "paired-station" transfer function matrix.

B. The Single-Station Vertical Transfer Function, T_Z

In the formulation of this simpler transfer function, only the vertical anomalous field is considered and 2 simplifying assumptions are made: 1) the anomalous field is produced by perturbations of only the *horizontal* normal field; and 2) there are no long term $H_N Z_N$ or $D_N Z_N$ correlations. Under these assumptions, the data observed at a single station are fitted to the relation (Cochrane and Hyndman, 1970).

$$Z_0 = z'_H H_0 + z'_D D_0 + \delta'_Z \quad (2)$$

where

T_Z = (z'_H, z'_D) , the vertical transfer function of two complex elements.

(H_0, D_0, Z_0) = the Fourier transform of the *observed* field.

δ'_Z = the Fourier transform of the vertical residual field.

It should be emphasized that Equation (2) uses the three field components observed at the same site; hence the name "single-station" vertical transfer function.

Both types of transfer functions express coherences or partial coherences between given field components. The formulation of T is more general, revealing anomalous perturbations of any normal field component as well as allowing for normal field component coherences; however, the complexity of its possible contributing factors (non-uniform source, change in normal field, and multiple

anomalies) make a quantitative interpretation difficult. T_z , on the other hand, is more easily computed and can be interpreted quantitatively by means of numerical modelling techniques; however, for the quantitative results to be meaningful, the simplifying assumptions for T_z must be satisfied (Dragert, 1973a).

In the transfer function analysis of the data, a measure of confidence was established empirically by evaluating T_z 's and T 's for each individual event and computing their standard deviations from the mean values.

Results of Analysis

A. Spectral Estimates

The smoothed spectral estimates for Bands A and B indicate that the "I-transition zone" is located in the vicinity of the Rocky Mountain Trench, as previously found by Caner et al. (1971). It must be added, however, that the power in Z at periods between 10 and 30 min is unexpectedly attenuated at the easternmost station SUF, which lies in an area previously thought to be a high-I region.

B. Single-Station Vertical Transfer Functions

Figure 6 illustrates the frequency dependence of the mean in-phase and quadrature components of T_z for the short-period band at each station. The general tendency for increased deviations for periods less than 40s is indicative of possible source non-uniformities. The features important to subsequent interpretation are:

- (1) For sites recording the short-period band, DOW shows the least anomalous perturbations and hence is a logical reference site for normal field estimation.
- (2) A reversal in anomalous Z occurs between ROG and BAN, with a corresponding reduction in anomalous Z at NIC.
- (3) Generally, with increasing period, the quadrature components become more significant and a rotation towards the south is apparent for in-phase components.

Figure 7a and 7b illustrate the mean amplitudes and directions of the in-phase and quadrature components of T_z for Band A, along with their computed standard deviations. The curves appear well-defined, and the increased deviations for periods greater than 45 min possibly reflect the greater variance (10–30%) of the spectral estimates at these frequencies. The real parts of the T_z 's appear to peak between 20 and 30 min periods at all anomalous sites except BAN where the maximum value occurs between 15 and 20 min periods. The following features are worth noting:

- (1) Minimum anomalous vertical field contributions are observed at CLE and SUF, indicating either as possible candidates for a reference site. It should also be pointed out that the similarity of T_z at CLE and SUF is quite striking

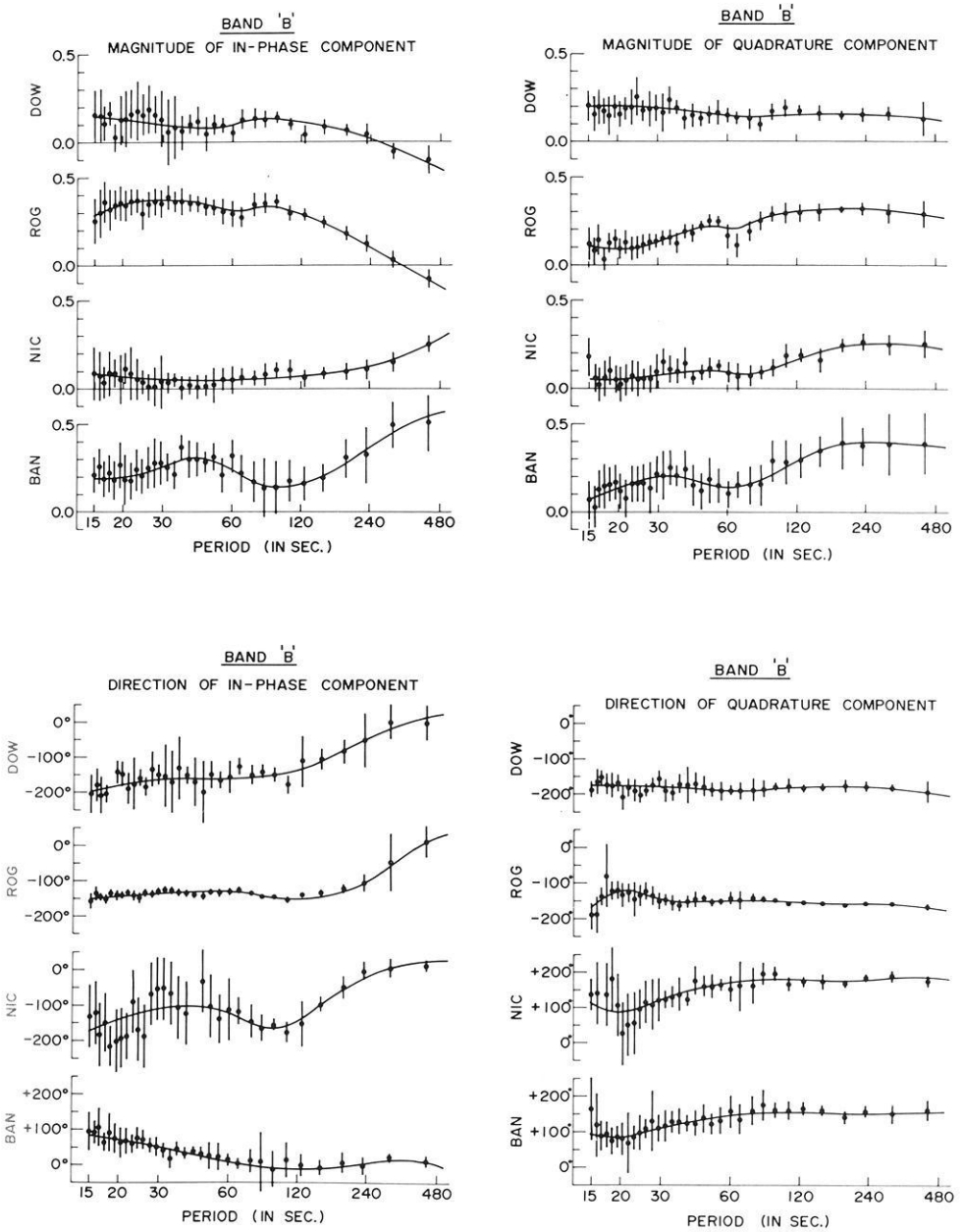


Fig. 6. Single-station transfer function amplitudes and directions for Band B. Directions are measured positive east of true north

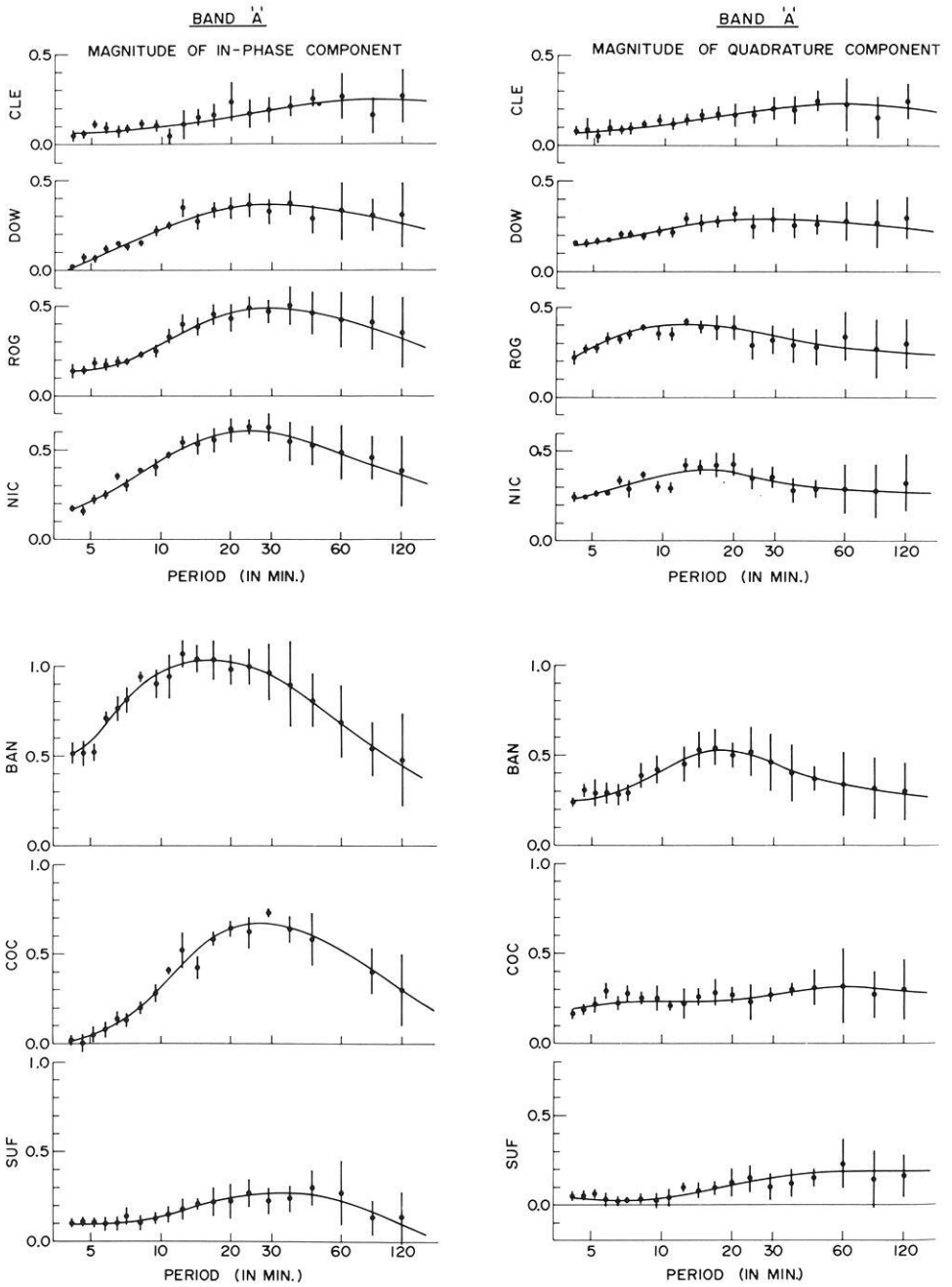


Fig. 7. a Single-station transfer function amplitudes for Band A

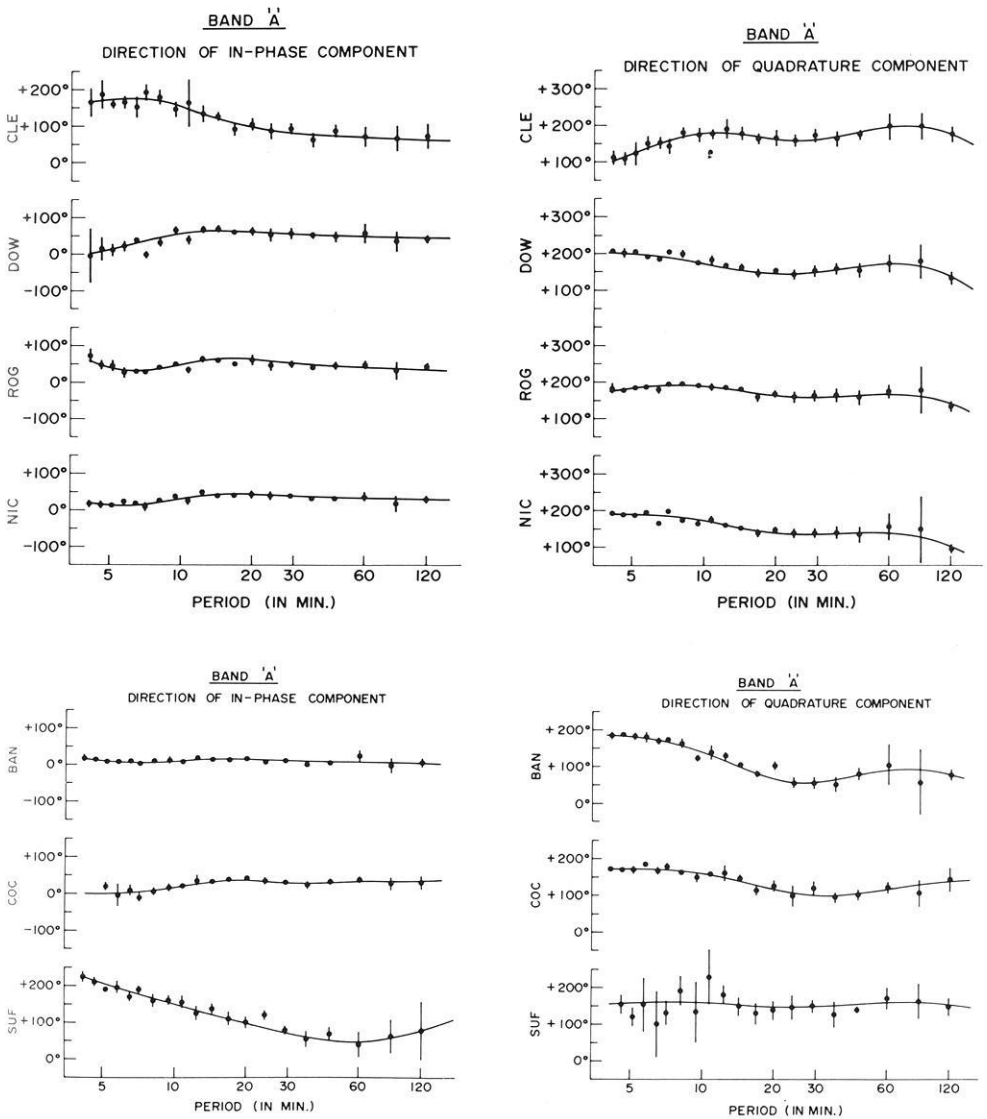


Fig. 7b. Single-station transfer function directions for Band A. Directions are measured positive east of true north

for two sites more than 600 km apart and supposedly located in quite distinct conductivity regions.

(2) No anomalous Z reversal is apparent across the transition zone for Band A.

(3) The in-phase and quadrature components are comparable in magnitude, and their directions tend to diverge with increasing period, indicating the presence of a three-dimensional conductivity structure.

(4) The directions of the in-phase components are dominantly southwest to south for all periods of this band.

C. Numerical Modelling for T_z

Since the validity of the restrictive assumption for T_z can be considered questionable, and a three-dimensional structure appears to be present, it follows that the observed anomaly cannot be interpreted in terms of an unambiguous, independent, two-dimensional conductivity model. Two-dimensional modelling techniques (Swift, 1971) were nonetheless applied using two previously proposed regional conductivity models (Caner, 1971; Camfield and Gough, 1975) in order to assess the validity of the principal features of each model for the area investigated. It was found that both models could account for barely one-half of the magnitude of T_z , and both failed to account for the quadrature terms of T_z . On the more positive side, a comparison of model transfer function curves with observed data indicated the following:

(1) A near-surface conductor with a depth extent of about 2 km must be present to account for the short-period T_z response. Such a conductor has not been included in previous models.

(2) The frequency responses of the in-phase components of the T_z 's suggest a conductivity model intermediate to the Caner and Camfield-Gough models; that is, the 20 km thick conductive layer underlying the western Cordillera region is more likely to be at a depth of 40–50 km in the Trench area.

(3) The double-anomaly structure as observed by Camfield and Gough for the Idaho Panhandle is not resolved by the long-period data of this profile.

D. Paired-Station Transfer Function Matrices

No meaningful transfer matrices could be evaluated for Band B data. The scatter associated with the elements of T was often 70% of the estimated mean values or higher, and both vertical and horizontal transfer terms were erratic and ill-defined functions of frequency. Spatial non-uniformity of the source fields within this frequency band, and the instabilities encountered in complex-matrix inversion were perhaps major sources of this scatter.

However, for Band A, stable mean transfer matrices could be derived using the westernmost station CLE as arbitrary reference, although a scatter ranging between 20% and 60% of the average values was still present. Such a high error level in itself precluded a meaningful quantitative interpretation of the individual matrix elements. Furthermore, since the transfer matrices at all sites are evaluated with respect to an arbitrary reference field, it follows that the T 's at each site will be affected by anomalous conditions at the reference site, by changes in the regional normal field, and naturally, by source nonuniformities. Data from a single profile of stations do not allow a separation of these effects, adding more uncertainty to a quantitative interpretation.

Nonetheless, the following qualitative observations were deemed significant:

(1) For periods greater than 15 min, the diagonal elements of T , shown in Figure 8, generally reflect a behaviour expected for the case of a reference site located over a horizontally-layered medium with higher conductivities at shallower depths (Dragert, 1973a); that is, these elements agree with the regional

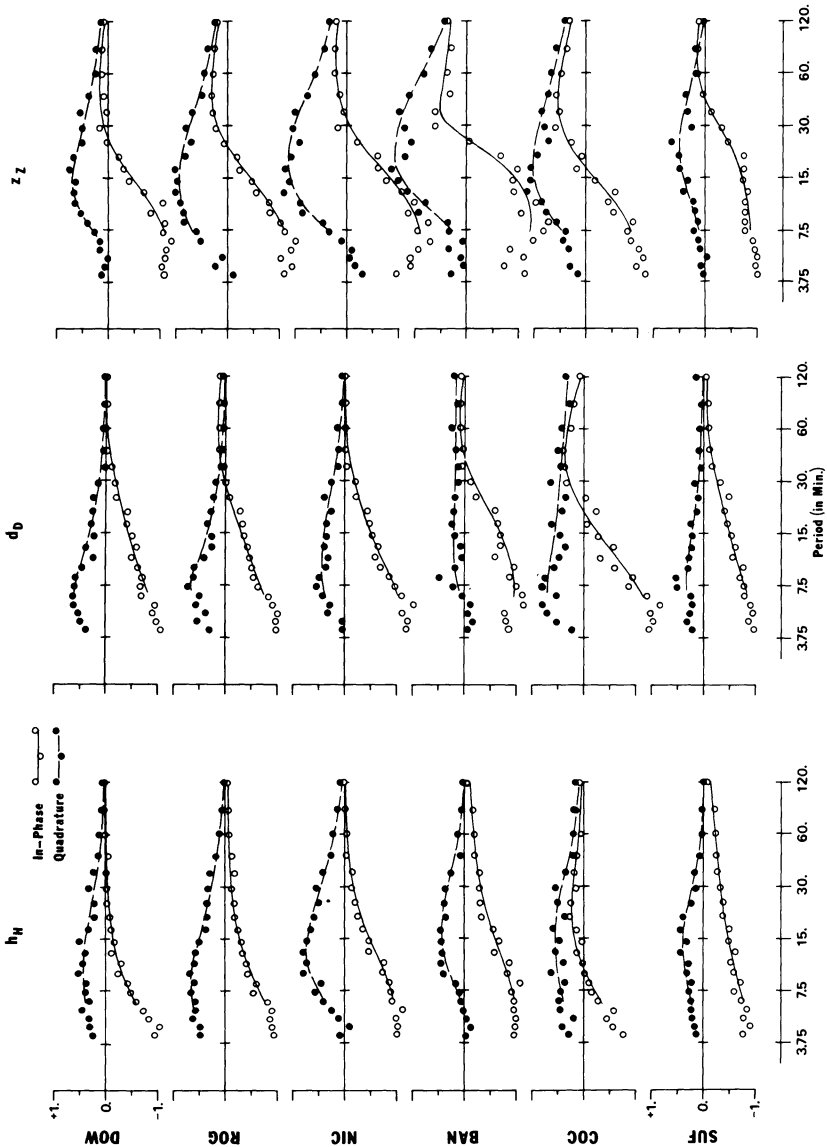


Fig. 8. Diagonal elements of the paired-station transfer matrix as functions of period (Band A) at each site

conductivity models proposed for this area. Only at BAN and COC does it appear necessary to invoke anomalous contributions to account for the changed pattern of the curves. It should be noted that due to the formulation, a lack of coherence between the analysis site and the reference site (CLE) will result in diagonal elements with in-phase and out-of-phase values of -1.0 and 0.0 respectively. This is illustrated by the trends at periods less than 7.5 min. The consistently large values of the quadrature parts of h_H , d_D , and z_Z in the period range of about $7-15$ min as shown in Figure 8, possibly reflect changes in the phases of the normal field components.

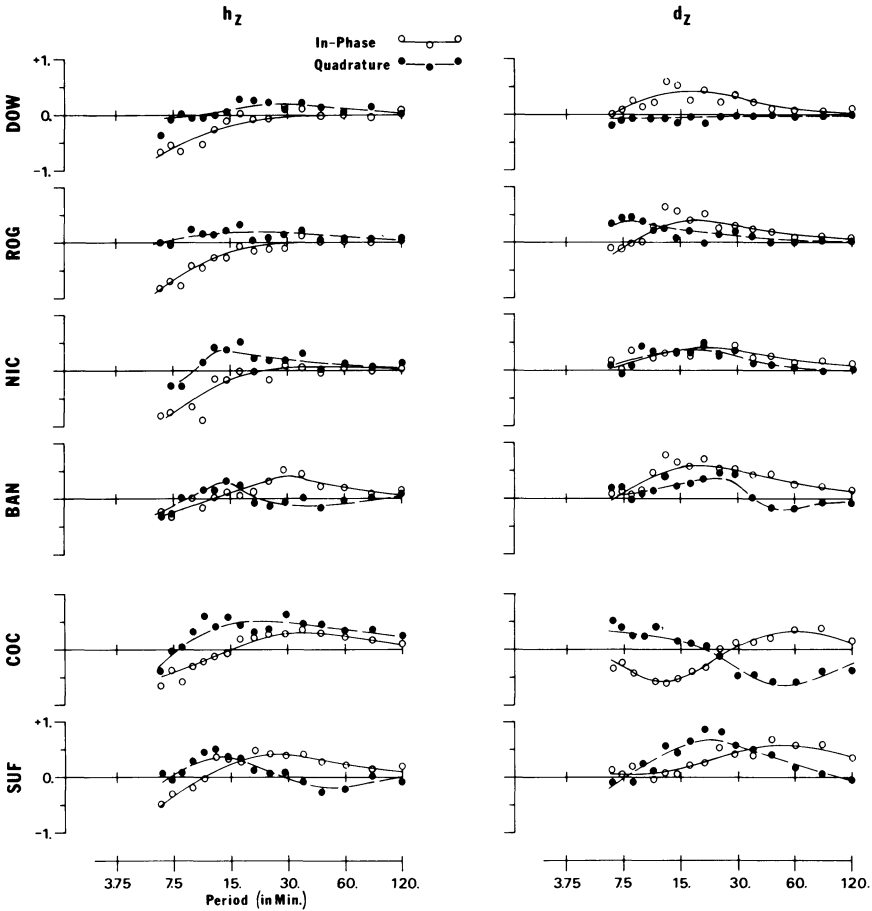


Fig. 9. Elements h_z and d_z of the paired-station transfer matrix as functions of period (Band A) at each site

(2) The transfer function elements h_z and d_z , shown in Figure 9, are characterized by ill-defined trends and an error scatter of over 50% from the mean values, reflecting the difficulty in obtained horizontal transfer function terms at anomalous sites referred to a "normal" site with little power in Z . It must be remembered that these elements exhibit the correlation of the horizontal field at a given site to the observed vertical field at the reference site. For the case of a uniform source field over a horizontally-layered medium, Z_N must be zero (Price, 1950); consequently, the reference field in this case is associated with a separate anomaly, source non-uniformity, or a channeled current system. The more clearly observable trends at COC and SUF are definite enough to call into question the simplifying assumptions for T_Z ; that is, normal component coherences brought about through current channeling or systematic source configurations are probably biasing the single-station vertical transfer function.

Fig. 10. Elements h_D and d_H of the paired-station transfer matrix as functions of period (Band A) at COC

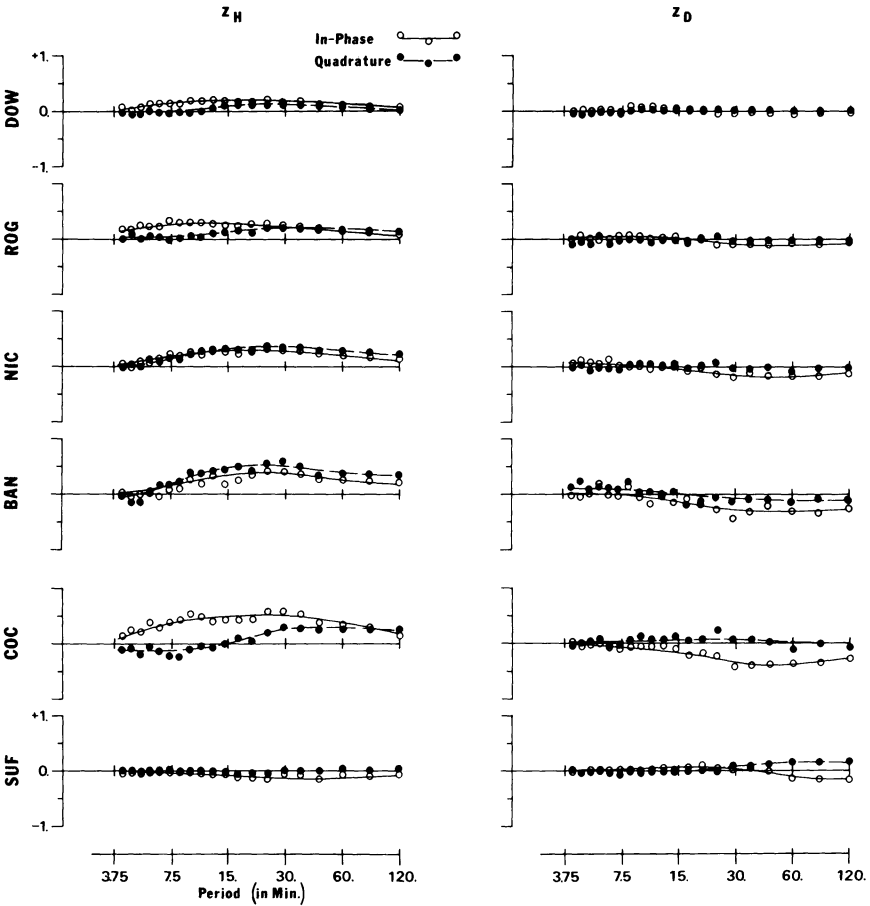
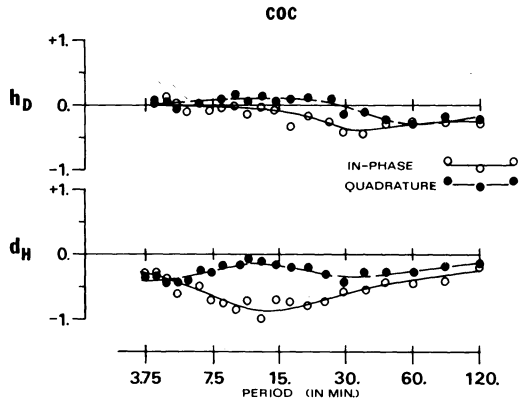


Fig. 11. The vertical transfer function elements z_H and z_D contained in the paired-station transfer matrix as functions of period (Band A) at each site

(3) Furthermore, at COC there are significant contributions to the observed horizontal field arising from the cross-terms h_D and especially d_H (see Fig. 10). These terms are well-defined functions of frequency, having an average scatter of 20 to 30% about the mean. This unique anomalous condition at COC indicates the presence of a three-dimensional conductivity structure, one which appears to deflect H -induced currents almost 90 degrees.

(4) The vertical transfer function elements, z_H and z_D (see Fig. 11), contained in the matrix T show a behaviour in agreement with the single-station transfer function elements z'_H and z'_D (refer to Fig. 7). That is, maximum anomalous contributions are apparent at BAN and COC at periods of about 20 min. However, the anomalous peaks exhibited by z'_H and z'_D appear significantly larger and broader. Again, this could be indicative of systematic normal-field component coherences, which are regarded as anomalous contributions by the single-station vertical transfer function.

Interpretation and Conclusions

A probable but by no means unique interpretation of the observed data can be summarized as follows. (For a point by point interpretation of the individual spectral features, transfer function characteristics, and modelling results, see Dragert, 1973 b.) In general terms, the geomagnetic I -transition zone between Revelstoke and Calgary marks the site of a three-dimensional conductivity structure which appears to be channeling or deflecting internal currents induced on a larger regional scale. In particular, three separate features are resolved (see Fig. 2):

- 1) The trench itself, most likely due to conductive sediments, acts as a near surface, two-dimensional conductor causing a spatial reversal of anomalous Z variations. The depth extent is of the order of 1–2 km and the conductivity roughly 0.1 ohm-m^{-1} . These values are not well defined due to the lack of spatial resolution of the limited number of broad-band stations.

- 2) *Within the limits of applicability of a two-dimensional model*, the conductive layer suggested by Caner and by Camfield and Gough to underlie the western Cordillera is probably at *or dips to* a depth of the order of 40–50 km beneath the trench. A thickness of about 15–20 km and a conductivity of 0.2 ohm-m^{-1} , adopted from the reference models, appear to agree with the observed data. Hydration or partial melting (Caner, 1970) along a thrust zone parallel to the crust/mantle interface appears as a likely cause of the enhanced conductivity of this layer which terminates beneath the transition zone. The Rocky Mountain Trench may therefore mark the eastern limit of the under-thrust.

- 3) A third conductive structure can be identified with a possible buried Precambrian rift in south-west Alberta (Kanasewich, 1968), which strikes almost perpendicular to the I -transition zone. The observed anomalous field directions in this study and from Cochrane and Hyndman's (1970) study indicate that this anomaly connects with the Kootenay anomaly along a line following this rift from Alberta into B.C. This implies that the Kootenay anomaly is not strike-slip caused as suggested by Lajoie and Caner (1970), but more likely

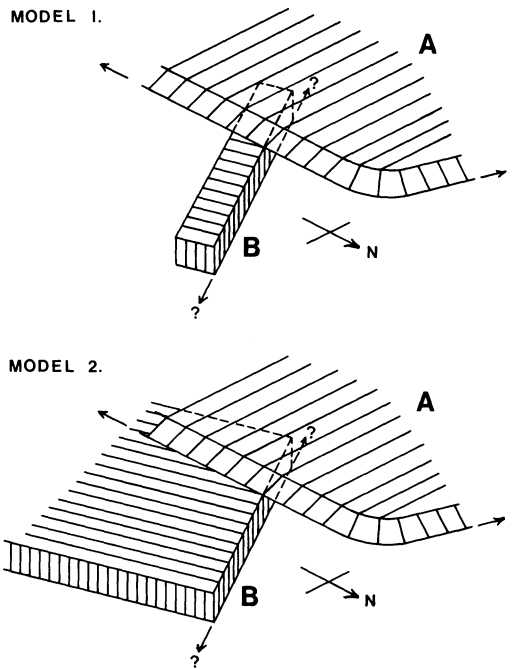


Fig. 12. Schematic diagrams of 2 simple three-dimensional conductivity structures which could account for the observed long-period transfer functions. Conductors A and B would correspond to conductive structures 2 and 3 respectively in Figure 2

associated with enhanced conductivities of evaporites suggested by Kanasewich to have been generated within the rift by syngenetic or hydrothermal deposition. Furthermore, it is possible that this rift marks the northern extent of a moderately conductive layer suggested by Camfield and Gough to underlie the Front Ranges and the Great Plains in the northwestern United States. The exact interrelation of the two deeper conductivity structures is not resolved, but a conductive connection appears likely.

From this summary it can be seen that the type of model required to represent the I-transition zone must be at least a simple three-dimensional model as suggested by the schematics of Figure 12, which are very similar to the speculative structural models suggested by Caner et al. (1971). These diagrams depict only possible deeper structures, and the actual transition anomaly in this region is further complicated by the presence of the surface conductor, the Rocky Mountain Trench, which has not been included in the model schematics. Either model could account for many of the observed features of the transfer matrices, and resolve some of the differences in the T and T_z estimates.

In conclusion, the following general inferences from this small-scale study are emphasized:

(1) The extended frequency coverage of the broad-band system proved invaluable in the separation of the shallow trench conductor from the deeper inhomogeneities.

(2) The more general transfer function matrix is useful in obtaining a more comprehensive picture of all field component coherences and allowing an evaluation of the validity of the simpler transfer function assumptions.

(3) The results of this study indicate that not local induction but local deflection of regionally induced fields should often be considered in model interpretation.

Acknowledgements. This work was supported in part by Grant No. 66-9521 (G.K.C. Clarke) from the Defence Research Board of Canada. Personal financial support from the National Research Council of Canada for one of us (H.D.) is also gratefully acknowledged.

References

- Camfield, P.A., Gough, D.I.: Anomalies in daily variation magnetic fields and structure under northwestern United States and southwestern Canada. *Geophys. J.* **41**, 193–218, 1975
- Caner, B.: Electrical conductivity structure in Western Canada and petrological interpretation. *J. Geomagn. Geoelectr.* **22**, 113–129, 1970
- Caner, B.: Quantitative interpretation of geomagnetic depth-sounding data in Western Canada. *J. Geophys. Res.* **76**, 7202–7216, 1971
- Caner, B., Auld, D.R., Dragert, H., Camfield, P.A.: Geomagnetic depth-sounding and crustal structure in Western Canada. *J. Geophys. Res.* **76**, 7181–7201, 1971
- Caner, B., Cannon, W.H.: Geomagnetic depth-sounding and correlation with other geophysical data in western North America. *Nature* **207**, 927–928, 1965
- Caner, B., Cannon, W.H., Livingstone, C.E.: Geomagnetic depth-sounding and upper mantle structure in the Cordillera region of western North America. *J. Geophys. Res.* **72**, 6335–6351, 1967
- Caner, B., Dragert, H.: Instrumentation for wide-frequency-band (0.01–100 millihertz) geomagnetic induction work. *Z. Geophys.* **38**, 121–132, 1972
- Cochrane, N.A., Hyndman, R.D.: A new analysis of geomagnetic depth-sounding data from Western Canada. *Can. J. Earth Sci.* **7**, 1208–1218, 1970
- Cooley, J., Tukey, J.W.: An algorithm for the machine calculation of complex Fourier series. *Math. Computation* **19**, 297–301, 1965
- Dragert, H.: A geomagnetic depth-sounding profile across central British Columbia, unpublished M.Sc. thesis, University of British Columbia, Vancouver, 1970
- Dragert, H.: A transfer function analysis of a geomagnetic depth-sounding profile across central B.C. *Can. J. Earth Sci.* **10**, 1089–1098, 1973a
- Dragert, H.: Broad-band geomagnetic depth-sounding along an anomalous profile in the Canadian Cordillera, unpublished Ph. D. thesis University of British Columbia, Vancouver, 1973b
- Dragert, H.: A field evaluation of Caner's broad-band geomagnetic induction instrumentation. *J. Geophys.* **40**, 121–129, 1974
- Hyndman, R.D.: Electrical conductivity inhomogeneities in the earth's upper mantle, unpublished M.Sc. thesis, University of British Columbia, Vancouver, 1963
- Jones, R.H.: A reappraisal of the periodogram in spectral analysis. *Technometrics* **7**, 531–542, 1965
- Kanasewich, E.R.: Precambrian rift: genesis of strata-bound ore deposits. *Science* **161**, 1002–1005, 1968
- Lajoie, J.J., Caner, B.: Geomagnetic induction anomaly near Kootenay Lake—a strike-slip feature in the lower crust? *Can. J. Earth Sci.* **7**, 1568–1579, 1970
- Lambert, A., Caner, B.: Geomagnetic depth-sounding and the coast effect in Western Canada. *Can. J. Earth Sci.*, **2**, 485–509, 1965
- Price, A.T.: Electromagnetic induction in a semi-infinite conductor with a plane boundary. *Quart. J. Mech. Appl. Math.* **3**, 385–410, 1950
- Schmucker, U.: Anomalies of geomagnetic variations in the southwestern United States. *Bull. Scripps Inst. Oceanog.*, **13**, University of California, 1970
- Swift, C.M.: Theoretical magnetotelluric and turam response from two-dimensional inhomogeneities. *Geophysics* **36**, 38–52, 1971

Magnetotelluric Investigation of a Nearly Circular Saltdome in North Germany

U. Breymann*

Institut für Geophysik und Meteorologie, Techn. Universität Braunschweig,
Mendelssohnstr. 1 A, D-3300 Braunschweig, Federal Republic of Germany

Abstract. In the years 1973 and 1974 magnetotelluric measurements were carried out over the salt dome of Höfer in North Germany, which has a nearly cylindrical structure. By statistical frequency analysis of the recorded signals a resistivity distribution was obtained, which allowed to localize the boundary of the salt dome. The results were in good agreement with data from seismic and gravimetric investigations. Exact statements about relations between depth and resistivity distribution, however, could not be made.

Key words. Magnetotellurics – Salt domes.

In the years 1973 and 1974 magnetotelluric measurements were carried out over the salt dome of Höfer in North Germany, which has a nearly cylindrical structure. Figure 1 shows the measuring site and the measuring profile lying in N76°E direction. The closed line represents the formerly assumed contour of the salt dome as suggested by Jaritz (1972), which together with the position of Mine Mariagluck (near point 7) was used to fix the profile. The measurements consisted in recording the time-dependent variations of the electromagnetic horizontal components $H_x(t)$, $H_y(t)$, $E_x(t)$, $E_y(t)$ for periods T between 2 s and about 1000 s (H = magnetic, E = electric fields at the surface). The x -axis was right-angled to the y -axis, which lay parallel to the measuring profile.

A complex impedance tensor Z as a function of T was determined from these variations for each of the eleven measuring points. This impedance tensor was used to calculate the apparent resistivities $\rho_{\parallel}(T)$ and the phases $\phi_{\parallel}(T)$ for E parallel to the x -axis (“ E -polarization”) as well as $\rho_{\perp}(T)$ and $\phi_{\perp}(T)$ for E perpendicular to the x -axis (“ H -polarization”), which was about parallel to the rim of the diapir. (The expressions “ H -” or “ E -polarization” are used by analogy to two-dimensional cases, because there are some similarities, for example the abrupt change in ρ_{\perp} along the profile.)

* Present address: Institut für Physikalische Chemie, Hans-Sommer-Straße 10, D-3300 Braunschweig

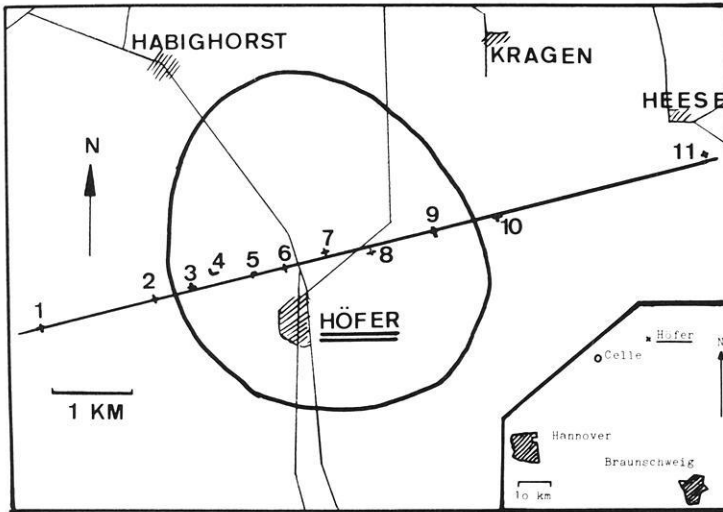


Fig. 1. Measuring sites and measuring profile. The closed line represents the contour of the salt dome after Jaritz (1972)

The impedance tensor Z introduced by Cantwell (1960) is defined by the equations

$$E_x = Z_{11} H_x + Z_{12} H_y$$

and

$$E_y = Z_{21} H_x + Z_{22} H_y.$$

The tensor elements were computed from the power- and cross-spectra of the digitized and fast Fourier transformed time series $H_x(t)$, $H_y(t)$, $E_x(t)$ and $E_y(t)$. An exact representation of this spectral analysis can be found in the works of Scheelke (1972) and Breymann (1975). To minimize $(Z_{11} + Z_{22})$ the tensor Z was rotated by a matrix D ,

$$D = \begin{pmatrix} \cos \varphi & \sin \varphi \\ -\sin \varphi & \cos \varphi \end{pmatrix}$$

according to

$$Z' = D Z D^{-1}.$$

The rotation angle φ gives the deviation of the main direction of the conductivity change from the measuring profile. The mean of φ for each station amounted to values between -10° and -20° . The apparent resistivities and phases were computed as follows:

$$\rho_{\parallel}(T) = 0,2 T |Z'_{12}|^2$$

$$\rho_{\perp}(T) = 0,2 T |Z'_{21}|^2$$

$$\phi_{\parallel}(T) = \arctan \left(\frac{\text{im}(Z'_{12})}{\text{re}(Z'_{12})} \right)$$

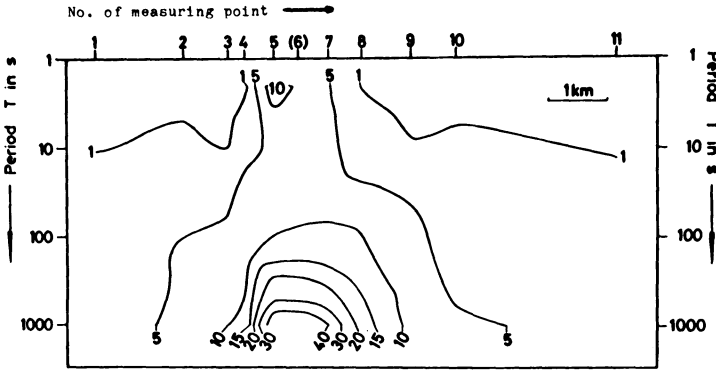


Fig. 2. Magnetotelluric pseudo cross section of the diapir (*E*-polarization), isolines of ρ_{\parallel} (in $\text{ohm} \cdot \text{m}$)

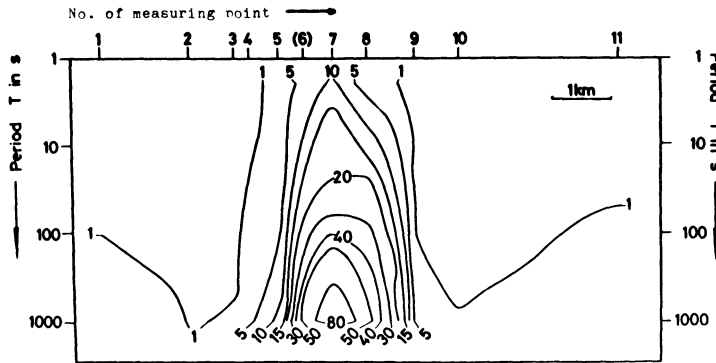


Fig. 3. Magnetotelluric pseudo cross section of the diapir (*H*-polarization), isolines of ρ_{\perp} (in $\text{ohm} \cdot \text{m}$)

$$\phi_{\perp}(T) = \arctan \left(\frac{\text{im}(Z'_{21})}{\text{re}(Z'_{21})} \right)$$

with

$$\text{im}(Z'_{ij}) = \text{imaginary part of } Z'_{ij}$$

$$\text{re}(Z'_{ij}) = \text{real part of } Z'_{ij}.$$

These equations are valid for ρ in $\text{ohm} \cdot \text{m}$, T in s, E in mV/km and H in γ .

All calculations were carried out with a computer program developed by Scheelke (1972). The values of $\log \rho_{\parallel}$ and $\log \rho_{\perp}$ were plotted vs. $\log T$. The strong fluctuations in the phases did not allow a reasonable interpretation, and so they are not regarded in this paper. For a graphic display pseudosections showing lines of same apparent resistivity were constructed for ρ_{\parallel} and ρ_{\perp} (Figs. 2 and 3). This method as applied to salt domes has been described by Losecke (1972). The values of measuring point 6, however, had to be omitted because of bad quality of data.

Figures 2 and 3 give an idea of the resistivity distribution. The numbers at the lines indicate the apparent resistivities. They should not be confused with the real

specific resistivities, which only approximate the apparent resistivities if the extensions of the structure are large compared with the skindepths of the observed periods.

In horizontal direction one can well localize the rim of the salt dome, which is between point 4 and 5 and 8 and 9 with the centre being between 6 and 7. As expected, a clear boundary effect is to be seen. ρ_{\parallel} varies smoothly for currents perpendicular to the profile, but ρ_{\perp} varies discontinuously (with an overshoot) for currents along the profile because the abrupt resistivity change causes an abrupt change in E_{\perp} , and hence in ρ_{\perp} (Breymann, 1975). Corresponding to this the conductivity contrast between sediment and salt becomes apparent much clearer in Figure 3 than in Figure 2. Looking at Figures 2 and 3 one finds that the lines of constant apparent resistivity are more dense at the west side, leading to the conclusion that the western flank is steeper than the eastern one.

These results were compared to a simple theoretical model, consisting of a vertical cylinder surrounded by a horizontal layer of high conductivity, bounded by an insulating half space above and below. The computer program used was developed by Rodemann (Personal Communication). It is based on an analytical approximation. Part of the calculation has already been described (Rodemann, 1974).

The best fit obtained was a model with a resistivity contrast of 1 ohm · m (layer) to 1000 ohm · m (cylinder). The cylinder's diameter was 2 km and the height of layer and cylinder 3 km.¹ The model differs from that one described earlier (Breymann, 1975), as the computations referring to the cylinder-model had to be carried out again because the approximation method was improved in the meantime. Although this model is very simple compared with the real diapir, the agreement between measured and calculated apparent resistivities was quite good (Figs. 4 and 5)² with the exception of measuring point 5, whose ρ -values were too low for H -polarization. A possible explanation, but not confirmed by model calculations, is the existence of a step or an overhang at the western rim. This asymmetry is also to be seen in Figures 2 and 3. In the case of E -polarization discontinuities appear strongly smoothed, and the resistivity distributions of point 5 and 7 look rather similar, in contrast to Figure 3 (H -polarization). In this case ρ_{\perp} responds to lateral changes in conductivity very sensitively. However, this is only a hint at a step or an overhang, for it is not automatically clear that a structure in the isolines represents a similar structure in reality, as Losecke and Müller (1975) have shown.

With regard to this circumstances the cross section shown in Figure 6 approaches the reality in a satisfactory way. The plotted depth of the Zechstein salt base (more than 3 km) and the thickness of the uppermost layer covering the salt (about 120 m) are based on Schachl (1968), just as the salt dome boundaries from seismic and gravimetric measurements. The bounds of the calculated cylinder-

¹ One can obtain fairly good models, too, by varying the diameter from 1.8 to 2.2 km, or by decreasing simultaneously the resistivity of the layer and the height of layer and cylinder. As resistivities less than 1 ohm · m in sediments are not realistic and the depth of the salt should be more than 3 km (after Schachl (1968)) the model used seems to be justifiable

² The values in Figures 2 and 4 and Figures 3 and 5 may differ slightly, as Figures 2 and 3 were derived from curves drawn by hand to smooth the course of ρ vs. the period T (Breymann, 1975)

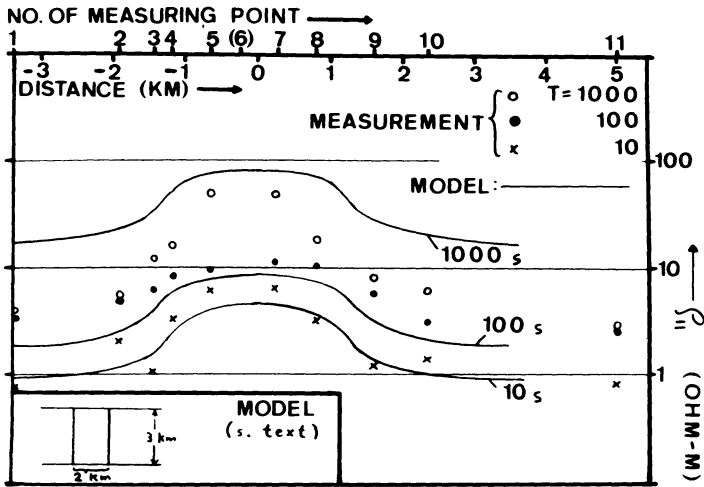


Fig. 4. ρ_{\parallel} -values along the measuring profile for different periods T (in s), compared with the apparent resistivities derived from the cylinder model (E -polarization)

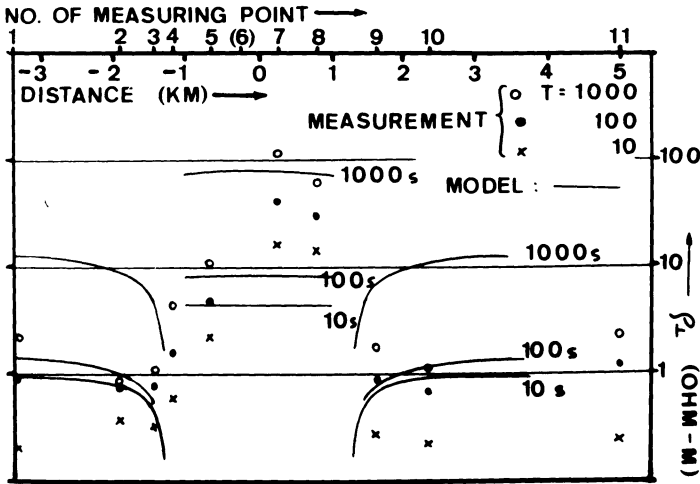


Fig. 5. ρ_{\perp} -values along the measuring profile for different periods T (in s), compared with the apparent resistivities derived from the cylinder model (H -polarization)

model coincide nearly with the flanks of the diapir derived from seismic investigation, and hence they are not drawn.

For the region undisturbed by the salt (point 11) a horizontally layered model of the sediment's resistivity distribution was developed. The best fit was a three-layer model with a 1 km thick first layer of 1 $\Omega \cdot m$ resistivity, a 7 km thick intermediate layer of 4 $\Omega \cdot m$, and an underlying substratum of 37 $\Omega \cdot m$ (Breyman, 1975). The method used was a least squares estimation of nonlinear parameters (= depths and resistivities), described by Müller (1974).

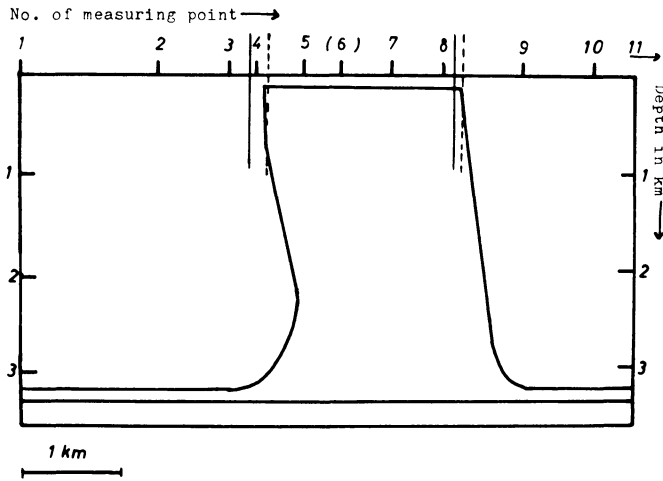


Fig. 6. Cross section of the diapir with boundaries derived from seismic (-----) and gravimetric (——) investigations

Summarizing the following can be stated: The magnetotelluric method allows to localize quite well the rim of salt domes, even if (like in this case) the dimensions of the salt dome are smaller than the skin depths of the considered periods (except for the “high” frequency domain with periods less than 10 s), and even if it is not possible to apply a two-dimensional model. Exact statements about the relation between resistivity and depth, however, cannot be made until detailed three-dimensional model calculations are made.

Acknowledgements. The author thanks Prof. Dr. W. Kertz for giving him the possibility of carrying out this work at the Institut für Geophysik und Meteorologie, Technische Universität Braunschweig, as well as Mr. H. Rodemann for letting him use the program for the cylinder-model and Dr. I. Scheelke for supporting the measurements and the evaluation.

References

- Breymann, U.: Magnetotellurische Untersuchung eines annähernd zylindrischen Salzdoms. Diplomarbeit, Inst. f. Geophysik und Meteorologie, Techn. Universität Braunschweig, 1975
- Cantwell, T.: Detection and analysis of low frequency magneto-telluric signals. Ph. D. Thesis, Dept. of Geology and Geophysics, M.I.T., Cambridge, Mass., 1960
- Jaritz, W.: Eine Übersichtskarte der Tiefenlage der Salzstöcke in Nordwestdeutschland. *Geol. Jahrb.* **90**, 241, 1972
- Losecke, W.: Über die Bestimmung von Salzstockgrenzflächen mit Hilfe der Magnetotellurik. *Z. Geophys.* **38**, 959–962, 1972
- Losecke, W., Müller, W.: Two-dimensional magnetotelluric model calculations for overhanging, high-resistivity structures. *Z. Geophys.* **41**, 311–319, 1975

- Müller, W.: Horizontalschichtinterpretationen mit Hilfe des "Umkehrverfahrens" von D. W. Marquardt. In: Protokoll über das Kolloquium "Erdmagnetische Tiefensondierung" in Grafrath/Bayern vom 11.-13. März 1974, A. Berktold (Ed.), pp. 462-467. Inst. f. Angew. Geophysik der Ludwig-Maximilians-Universität, München 1974
- Rodemann, H.: Modellrechnungen zur Magnetotellurik an kreissymmetrischen Strukturen. In: Protokoll über das Kolloquium "Erdmagnetische Tiefensondierung" in Grafrath/Bayern vom 11.-13. März 1974, A. Berktold (Ed.), pp. 391-399. Inst. f. Angew. Geophysik der Ludwig-Maximilians-Universität, München 1974
- Schachl, E.: Mine Mariagluck, Höfer. Int. Symposium on Geology of Saline Deposits, Exkursionsführer, 3 S., Hannover 1968
- Scheelke, I.: Magnetotellurische Messungen im Rheingraben und ihre Deutung mit zweidimensionalen Modellen. GAMMA 20, Inst. f. Geophysik und Meteorologie, Techn. Universität Braunschweig, 1972

Received April 29, 1976; Revised Version September 10, 1976

Letters to the Editor

Comments on:

**Postulated Rotation of Corsica not Confirmed
by New Palaeomagnetic Data**

by K.M. Storetvedt and N. Petersen

J. Geophys. 42, 59–71, 1976

M. Westphal

Institut de Physique du Globe, 5 rue Descartes, F-67084 Strasbourg cedex, France

Key words: Paleomagnetism – Corsica, rotation of.

Storetvedt and Petersen (1976) hold that the primary magnetization of Permian lavas and intrusives from Corsica was destroyed and that a complex chemical magnetization took place in the Tertiary. We would like the reader to be aware of a few facts and make some remarks.

1. The Geology of the Region

We know much better now the structure of Monte Cinto volcanics (Vellutini, 1973). Two different volcanic stages can be seen. The first one, calc-alkaline, (late Carboniferous, Early Permian) gave andesites (Osani) and ignimbrites (Fango valley). The second one, peralkaline (Upper Permian) gave ignimbrites, lavas, rhyolitic domes, dikes, organized in ring complexes (Cinto, Scandola, Porto and more south: Tolla-Cauro). The dikes seen on the road and studied by the authors took place at the end of this second stage. To the contrary of what they say, the Mesozoic and Cainozoic cover of Western Corsica is rather thin. For example, the Trias has a thickness of about 20 m (quartzites, dolomites and calcareous rocks) (Durand Delga, 1972). As Sardinia and Provence, Western Corsica *does not belong to the Tethyan geosyncline*. It is only its foreland. The Permian volcanics were subjected to surface conditions during Permian and post-Permian times. The volcanism was not continuous, lahars interbedded with ignimbrites are known and show that there was time enough for tectonic movements to take place between eruptions.

A geochronological study by $^{39}\text{Ar}/^{40}\text{Ar}$ and step heating does not show any evidence of post Permian reheating (Maluski and Lancelot, 1976). Moreover we do not know any Tertiary metamorphism in this region.

2. Magnetic Mineralogy

It is true that the dykes contain Fe and Ti hydroxides. They are dehydrated during heating and other reactions may take place after. Curie curves are then difficult to interpret. The maghaemite/haematite transformation would lower J_s but not the Curie point (p. 62, line 5). The authors seem to forget that this form of volcanism (mainly ignimbrites and pyroclasts) is due to the occurrence of a lot of gases which may be the reason for the observed transformations. Most dikes show also successive injections which may bring the necessary fluids. Nevertheless we would like to know the reactions and conditions that can give perovskite and sphene from titanomagnetites.

3. Rock Magnetism

A large number of samples and mostly those from the dikes show an important viscous remanent magnetization (V.R.M.). This V.R.M. can reappear during A.C. or thermal demagnetization process as spurious components. Storetvedt and Petersen rejected samples where intensities behave irregularly, but it is not enough. Spurious components may be added during high temperature demagnetization and be seen only in direction. The authors interpret such results without checking the relative importance of an artificial T.R.M. (It may be much larger than the N.R.M.). In other palaeomagnetic laboratories, demagnetization curves showing a change in direction at high temperature would be suspected as spurious components.

We do not see much evidence of the "strong normal demagnetization" or do they consider the direction of CO 50 ($D=350^\circ$, $I=-60^\circ$) as a normal one?

Storetvedt and Petersen say that composite magnetization may exhibit high directional stability (p. 66, line 8). It may also be the case for the few samples they kept.

The measurements published in 1968 by Nairn and Westphal show that the dikes have a large scatter of their magnetization directions, the declination varying from SSW to SE. No tectonic corrections could be made on these rocks, thus the results have to be taken with care. Storetvedt and Petersen retain only a small part of these directions.

Other formations (rhyolitic flows from Senino) and new measurements on Fango ignimbrites (Westphal et al., 1976) show stable magnetizations with stable end points and a low within site scatter. These directions span from S to SE. Tectonic corrections could be applied on these formations.

We are afraid Storetvedt and Petersen chose the worst rocks with the highest viscous magnetization for their interpretation.

4. Interpretation

Storetvedt and Petersen compare their results with those obtained by a similar manner on Lisbon volcanics. Against all geological and geophysical evidence

Storetvedt stated that the rotation of Iberia was post Oligocene. We must recall that Storetvedt's interpretation has been strongly criticized (Watkins and Richardson, 1971).

5. At last, both in Portugal and in Corsica, Storetvedt rejected more than 90% of his measurements and kept the few ones that allowed him to contradict systematically previous authors.

To conclude, we feel that we have no evidence that the modification of magnetic minerals took place more in the Tertiary than just after the eruptions.

(a) the rocks were subjected to surface conditions and were not buried deep.

(b) the so called "strong normal magnetization" may be only spurious magnetizations.

(c) Iberia having turned before Oligocene, this comparison made is not valid.

References

- Durand Delga, M.: La Corse. In: Géologie de la France, J. Debelmas, ed., pp. 465-478. Doin 1972
- Maluski, H., Lancelot, J.R.: Age permien des granites alcalins de Corse par les méthodes $^{39}\text{A}/^{40}\text{A}$ et U/Pb. 4^e réunion Ann. Sciences Terre, **278**, Paris 1976
- Nairn, A.E.M., Westphal, M.: Possible implications of the palaeomagnetic study of late Palaeozoic igneous rocks of Northwestern Corsica. *Palaeogeograph., Palaeoclimatol., Palaeoecol.* **5**, 179-204, 1968
- Storetvedt, K.M., Petersen, N.: Postulated rotation of Corsica not confirmed by new Palaeomagnetic data. *J. Geophys.* **42**, 59-71, 1976
- Vellutini, P.: Mise en évidence de deux cycles magmatiques dans le complexe volcanique du Cinto (Corse du North-Ouest). *C.R. Acad. Sc. Paris* **276** (série D), 913-916, 1973
- Watkins, N.D., Richardson, A.: Reply by the authors to "Palaeomagnetism of the Lisbon volcanics: A discussion of a recent paper by N.D. Watkins and A. Richardson" by K.M. Storetvedt. *Geophys. J.R. Astron. Soc.* **22**, 445-447, 1971
- Westphal, M., Orsini, J., Vellutini, P.: Le microcontinent Corso-Sarde, sa position initiale: données paléomagnétiques et raccords géologiques. *Tectonophysics* **30**, 141-157, 1976

Received May 26, 1976

Reply

K.M. Storetvedt¹ and N. Petersen²

¹ Department of Geophysics, University of Bergen,
Allégt. 70, N-5014 Bergen-Universitet, Norway

² Institut für Allgemeine und Angewandte Geophysik, Universität München,
Theresienstraße 41, D-8000 München, Federal Republic of Germany

We would like to comment on the points raised by Westphal as follows:

A. Magnetic Mineralogy

Westphal leans too strongly on the hypothesis that the severe mineral alteration concerned with is of late deuteric origin. This is a too narrow platform which eventually may lead to a biased and entirely unsound palaeomagnetic interpretation. In fact, the types of mineral “reconstitution” dealt with may have formed at any time after rock formation, including the late cooling stage (this has been clearly put forth at the end of our Chap. 2), though careful analysis of the remanence build-up may give us an idea of the time span (or time intervals) involved in the mineralogical alteration processes. The latter analysis is not in favour of a deuteric origin of present opaque mineralogy.

Naturally enough, there exist alternative explanations of most of the J_s - T curves but in some cases, like our sample Co 34, the results are in favour of a maghaemite/haematite transformation. Furthermore, the occurrence of perovskite and sphene are not unexpected in a complex mineral assemblage as here encountered—these phases may well have been formed at different times and need not be the product of a common chemical process.

B. Structure of Remanent Magnetization

To avoid that small uncompensated fields inside the furnace should give rise to systematic directional variation versus progressive demagnetization the specimens have been randomly placed and given new orientations before each succeeding demagnetization step. When specimens from different hand samples (after correction for a random field orientation) as well as from the same hand sample give preferred directional variations (as demagnetization progresses) the possibility of spurious components upsetting the natural remanence certainly

do not apply; i.e. the directional trends obtained in our study are likely to reflect inherent palaeomagnetic properties. A study of intensity decay patterns coupled with small demagnetization steps have on the whole proved to be an extremely good guideline for assessment of the relative importance of stray components. Polyphase magnetizations caused by prolonged chemical reactions (as encountered in the Corsican rocks) seem to be extremely common in nature. It is an elementary fact that in order to provide a relevant study of such complex magnetizations a careful study of the high stability region of the remanence is of prime importance; if one should follow Westphal's attitude to palaeomagnetic analysis the effect would basically be to "freeze" the initial bulk magnetization structure which palaeomagnetically may be completely irrelevant. The basic problem is not one of stability (as Westphal apparently believes) but the more difficult task of discriminating between various sub-components having largely overlapping stability spectra. Thus, the experimental work may only show up with directional trends and no stable end points (this is the reason for the few acceptable palaeomagnetic results). Westphal's oversimplified view in this respect explains why he has got problems in visualizing the normal magnetization component(s) which they nevertheless claim to have found in their original study (Nairn and Westphal, 1968); in the samples having bulk directions in the NE of NW quadrants, one or more normal magnetization vectors must predominate over existing reversed components producing fairly stable resultants which however are discordant with respect to known late/post Palaeozoic fields.

Finally, it is surprising that Westphal puts so much faith in his more recent palaeomagnetic results from Corsica (Westphal et al., 1976). In fact, the site mean directions exhibit an abnormal linear spread which certainly requires further laboratory tests before any sensible palaeomagnetic conclusion can be drawn.

C. Interpretation

Concerning the postulated rotation of Iberia Storetvedt (1973) has suggested this to be a late Eocene/early Oligocene phenomenon (and not post Oligocene as stated by Westphal). This timing is *not* in contradiction with relevant geological and geophysical information (Storetvedt, 1972). The reference to Watkins and Richardson (1971) is not concerned with the above aspect but with an earlier discussion of data by these authors (Watkins and Richardson, 1968). The movement of Iberia may well have had the effect as we suggest, though remagnetization in the Mesozoic (primarily Triassic) is another possibility to be explored in future work. In any case it is hard to understand how the Permo-Carboniferous andesites could obtain their complex remanence if they had been subjected to surface conditions throughout Kiaman time. A sediment cover and later erosion and weathering (probably in the Tertiary) appears to us to be the most reasonable explanation at present. However, we have *not* claimed that Western Corsica was necessarily covered by a *thick* sedimentary pile in Permian-Mesozoic times.

In summary we find no justification for the criticism raised by Westphal. We therefore uphold our conclusions. We would like to point out that we have not excluded the possibility that rotation may have taken place but would like to stress the complex palaeomagnetic record of Corsican formations which may easily give rise to false rotation estimates.

References

- Storetvedt, K.M.: Crustal evolution in the Bay of Biscay. *Earth Planet. Sci. Lett.* **21**, 22–28, 1972
- Storetvedt, K.A.: The rotation of Iberia: Caenozoic palaeomagnetism from Portugal. *Tectonophysics* **17**, 23–39, 1973
- Watkins, N.D., Richardson, A.: Palaeomagnetism of the Lisbon volcanics. *Geophys. J.* **15**, 287–304, 1968

Received Juli 29, 1976

Original Investigations

Structure of Lunar Impact Craters from Gravity Models

P. Janle

Institut für Geophysik der Universität, Bundesstr. 55/XIV, D-2000 Hamburg 13,
Federal Republic of Germany

Abstract. Bouguer anomalies for the lunar impact craters Copernicus, Theophilus, and Ptolemaeus have been computed. Copernicus and Theophilus have Bouguer gravity minima. Gravity models assume a zone of ruptured rocks below the craters.

Ptolemaeus has a strong Bouguer maximum. An isostatic upwelling of the mantle and intrusions of mantle material have been assumed in the gravity model. Ptolemaeus may be regarded as an intermediate structure between isostatically undercompensated craters and mascon-maria.

Key words: Lunar impact craters – Bouguer gravity – Gravity models.

1. Introduction

Many meteoric impact craters are known on the Earth. Their main structural properties are a basin, a ring wall, and a zone of breccia and ruptured rocks below the crater floors (Fig. 1a). This ruptured zone causes the negative Bouguer gravity of most of the terrestrial impact craters (Innes, 1961; Angenheister and Pohl, 1969; Jung et al., 1969). Low altitude Doppler gravity data with a resolution of 20–50 km, which permit model calculations, exist for only a few lunar impact craters. Sjogren et al. (1974c) modelled the negative gravity anomaly of the crater Copernicus. They replaced the topographic mass deficit and the rim by surface disks. However, they needed for their model a density of 3.57 g/cm^3 which is far too high in contrast to 2.6 g/cm^3 of the uppermost crust. In order to reduce the density value, the authors suggested a less dense debris layer below the crater.

Many of the maria represent another type of characteristic impact structures on the Moon (Fig. 1c). The formation of these structures can be described as follows: High-energetic large meteorites had excavated large, mostly circular basins. The resulting mass deficiency was partly compensated by an isostatic or dynamic upwelling of the mantle. Intrusions of mantle material penetrated

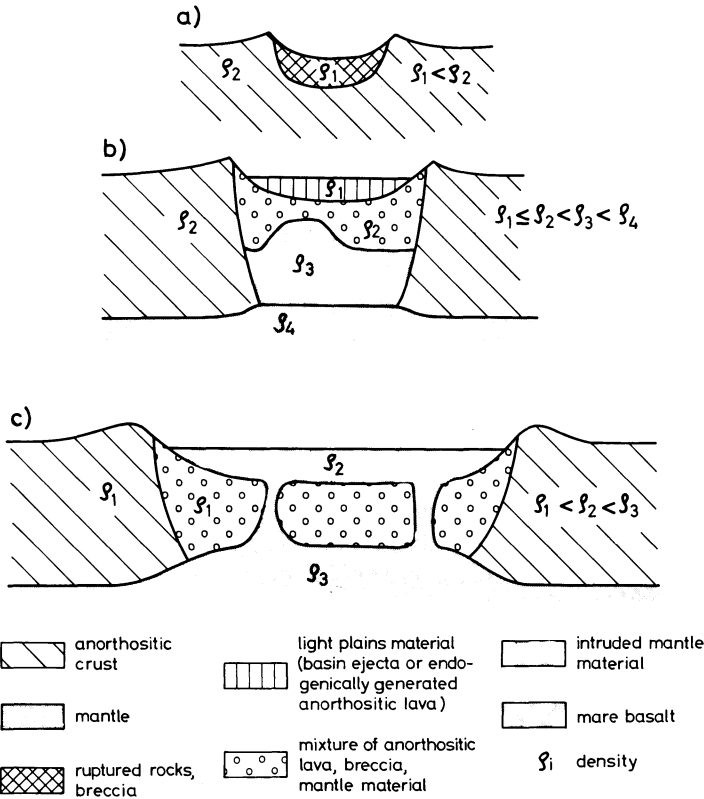


Fig. 1 a-c. Lunar impact structures. a isostatically undercompensated crater, b endogenically modified crater or basin, c mascon-mare (isostatically overcompensated model)

the thinned, fractured crust and filled the basins to overcompensation with basaltic lavas. The mass surpluses, which cause the enormous free air gravity anomalies of some 100 mgal, are called “mascons” (Wise and Yates, 1970; Phillips et al., 1974). Kunze (1974) suggested a model in which the mass surpluses are compensated isostatically by mass deficits at depth. The mascon possessing maria are also called “mascon-maria”.

So far only free air gravity models have been calculated without accurately considering the topographic effects. In this paper, Bouguer anomalies for the craters Copernicus, Theophilus, and Ptolemaeus will be presented and models of the depth structures will be computed (Fig. 2).

2. Calculation of the Bouguer Anomalies

The gravity data used in this paper are from Kunze (1975). Kunze converted the line-of-sight accelerations to vertical gravity values which were normalized

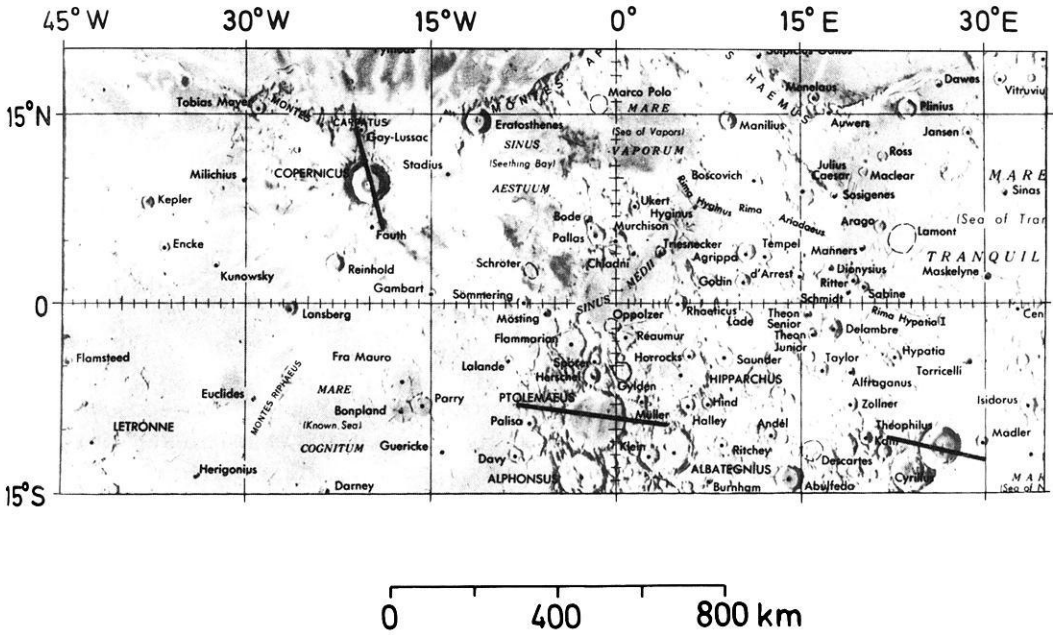


Fig. 2. Profile location

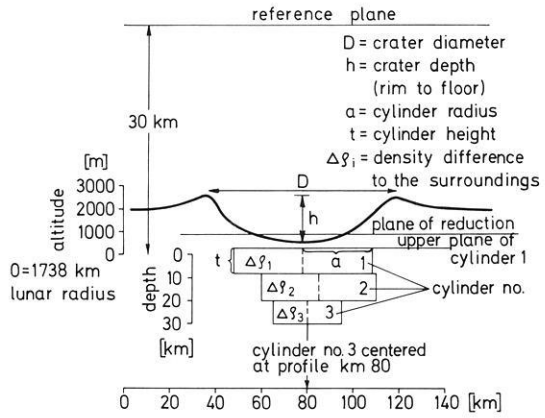


Fig. 3. Schematic crater model illustrating the elements for the calculation of the Bouguer anomalies and the gravity models

to 30 km altitude above mean lunar radius. Only the data of the southern part of Copernicus are unconverted; they correspond to a flight height of about 30 km according to Sjogren et al. (1974a). Nevertheless, the effects of amplitude decrease and angular shift for these data are small because Copernicus lies near the subearth point. The gravity values were enhanced by 30% in order to compensate for the effect of the least squares filter of the orbit determination program. This program derives the Doppler residuals from the tracking data (Gottlieb, 1970; Sjogren et al., 1972).

The Doppler gravity can be interpreted as free air gravity referred to a reference plane of 30 km altitude in this case.

Figure 3 shows the elements for the calculation of the Bouguer gravity and the gravity models. All altitude and depth values in the figures and in the text are referred to a normal datum of 1738 km mean lunar radius. The altitude data of the profiles and for the terrain correction are from Lunar Aeronautic Charts (LAC, 1962). The terrain correction removes the gravity effects of topographic masses above and below the plane of reduction which is the mean level of the crater floor. It was calculated up to a distance of 100 km using the formula for a cylindrical slice with a Bouguer density of 2.6 g/cm^3 .

Kunze (1975) does not discuss the accuracy of his gravity maps. But errors of 10 mgal seem to be reasonable. A density variation of 0.1 g/cm^3 causes a variation of 6 mgal for a terrain correction of 150 mgal. An accuracy of 100 m for relative heights is given on the LAC charts. A maximum error of 300 m is assumed for height determinations of the terrain correction causing an error of 10 mgal. The resulting mean error is $\pm 15 \text{ mgal}$ for the Bouguer gravity.

Figures 4–6 present the free air gravity, terrain correction, and Bouguer gravity for the three craters investigated.

3. Model Calculations

Copernicus (Fig. 4) and Theophilus (Fig. 5) have Bouguer gravity minima. Therefore the free air minima cannot be modelled simply by replacing the topographic mass deficit and the rim by surface disks as it was done in previous works (Sjogren et al., 1974c). As mentioned in the introduction the deficit density for these previous models is far too high. This suggests to compare the depth structures of lunar impact craters with their terrestrial analogues.

Many terrestrial impact craters have Bouguer minima which are caused by ruptured zones below the craters (Innes, 1961). Considering the stress tensor, the following formula can be derived for the depth parameter of the ruptured zone (Beals et al., 1963):

$$R = \sqrt[4]{S_{\text{shear}} / (8 S_{\text{comp}})} D$$

D = crater diameter,

R = depth of the ruptured zone relative to the undisturbed topography,

S_{shear} = tensile strength to cause rupture,

S_{comp} = compressive strength to cause rupture.

For granitic gneiss Beals et al. calculated $R = 1/3 D$ with $S_{\text{comp}} = 1.6 \times 10^3$ and $S_{\text{shear}} = 0.16 \times 10^3 \text{ kg/cm}^2$. Jaeger (1969) gives for gabbro $S_{\text{comp}} = 1.8 \times 10^3 \text{ kg/cm}^2$; Chung (1972) found that the elastic properties of lunar samples are about the same as those of similar terrestrial rocks. Considering that lunar anorthosite

Table 1. Crater and model parameters (compare with Fig. 3), all lengths in km, $\Delta\rho$ in g/cm^3

	Diameter D	Depth h	Altitude of the plane of reduction	Model peak anomalies (mgal)
Copernicus	93	3.3	-0.1	- 30
Theophilus	100	4.4	1.9	-116
Ptolemaeus	153	1.0-1.5	1.1	+ 92

	Altitude of upper plane	Radius a	Height t	Centered at prof. km	$\Delta\rho$	Radius a	Height t	Centered at prof. km	$\Delta\rho$	Radius a	Height t	Centered at prof. km	$\Delta\rho$	
	cylinder 1					cylinder 2					cylinder 3			
Copernicus	-0.1	36	10	138	-0.15	32	10	138	-0.1	25	9	138	-0.1	
Theophilus	1.9	30	25	150	-0.45	25	15	150	-0.4					
Ptolemaeus	30	75	15	200	0.05	70	16	200	0.1	80	4	195	0.3	
	cylinder 4					cylinder 5					cylinder 6			
Ptolemaeus	0	30	30	255	0.2	30	15	250	0.15	50	16	220	0.1	

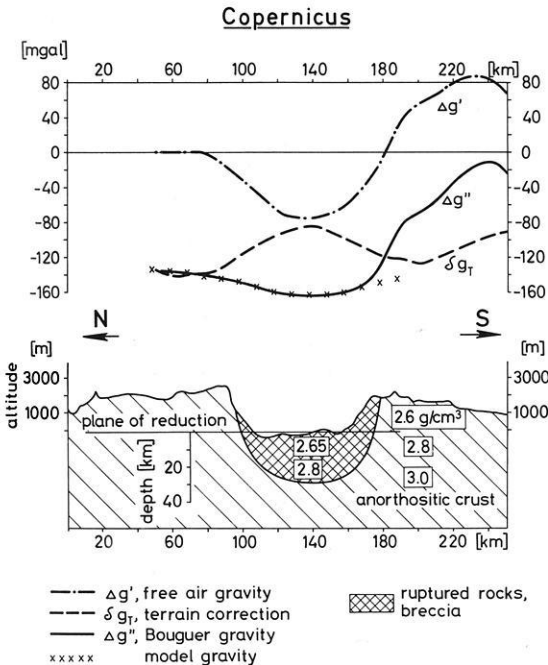


Fig. 4. Copernicus. Reference plane for the gravity anomalies at 30 km altitude; plane of reduction for the terrain correction at -0.1 km altitude

Theophilus

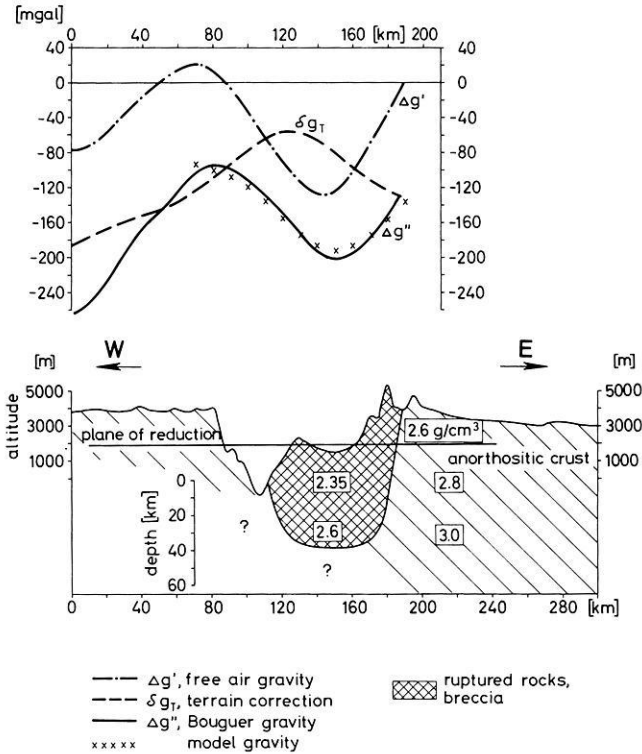


Fig. 5. Theophilus. Reference plane for the gravity anomalies at 30 km altitude; plane of reduction for the terrain correction at 1.9 km altitude

Ptolemaeus

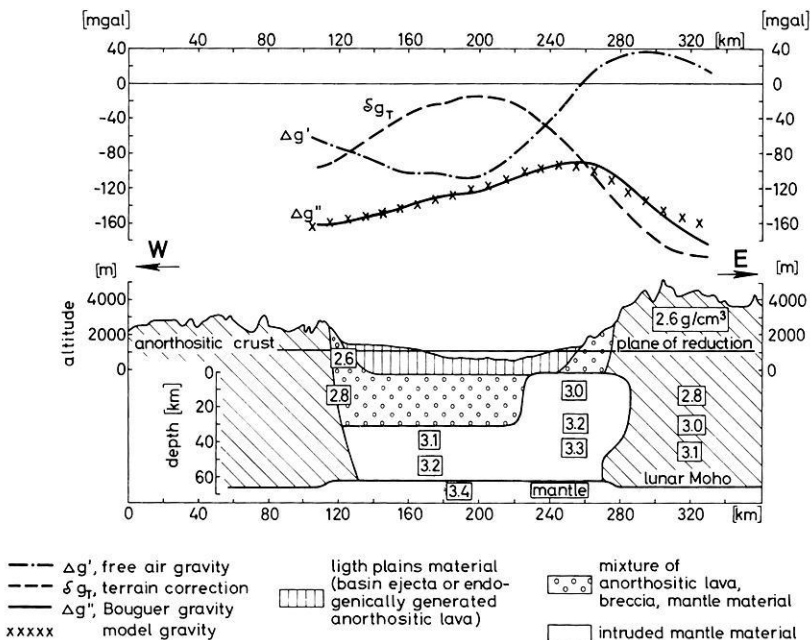


Fig. 6. Ptolemaeus. Reference plane for the gravity anomalies at 30 km altitude; plane of reduction for the terrain correction at 1.1 km altitude

comes petrologically close to gabbro and assuming a 50% variation of the ratio $S_{\text{shear}}/S_{\text{comp}}$ —that means a variation of the factor 0.33 from 0.28 to 0.37—the formula $R=1/3 D$ can be used as a first approximation also for lunar impact craters.

Another parameter for the model calculation is the density difference between the ruptured zone and the surrounding crust. For terrestrial craters it ranges between -0.1 g/cm^3 (e.g. Meteor Crater, Arizona (Regan and Hinze, 1975)) and -0.4 g/cm^3 (e.g. Deep Bay Crater, Canada (Innes, 1961)). For the lunar models the density difference was assumed to decrease slightly with increasing depth (see Copernicus and Theophilus, Table 1).

The form of the depth structure of the craters was modelled by several cylindrical disks (Fig. 3). Formulas for the gravity attraction of cylinders are from Telford et al. (1976). The crater and model parameters for the three craters investigated are summarized in Table 1.

The crater models of Figures 4–6 show absolute density values which are based upon publications of Solomon (1974) and Copper et al. (1974).

4. Description of the Craters

The three craters investigated are situated in transition zones between highlands and maria. The regional Bouguer anomalies are strongly negative. There is a general trend towards more negative values with increasing terrain elevations (Copernicus: $-40 \text{ mgal} \leftrightarrow 2000 \text{ m}$; Theophilus: $-200 \text{ mgal} \leftrightarrow 4000 \text{ m}$; Ptolemaeus: $-160 \text{ mgal} \leftrightarrow 2500 \text{ m}$ and $-180 \text{ mgal} \leftrightarrow 4000 \text{ m}$; the plane of reduction for these examples is at 1.1 km altitude which is also the plane of reduction of Ptolemaeus).

These values indicate in general an isostatic behaviour of the lunar crust outside the craters.

Copernicus (Fig. 4) has a Bouguer gravity minimum and a model gravity of -30 mgal . The ruptured zone of the model reaches a depth of 29 km which is in agreement with the 1/3 relation. A moderate density difference of -0.15 g/cm^3 is assumed for the first cylinder and -0.1 g/cm^3 for the next two cylinders. No attempt has been made to model the gravity high south of Copernicus because there is no correlation between this high and the topography.

Theophilus (Fig. 5) shows a strong Bouguer minimum shifted 20 km to the east of the crater center. The pronounced free air and Bouguer gravity low west of the crater cannot be correlated with topographic features. The map of Kunze (1975) shows a local extent of this free air low. In this case it is difficult to estimate the local anomaly for the model fit. The proposed model has a deficit density of -0.45 g/cm^3 for the first and -0.4 g/cm^3 for the second cylinder. These density differences are at the upper limit of corresponding terrestrial impact structures. The depth of the ruptured rocks should be 33 km according to the 1/3 relation; however, the model thickness of this zone is 43 km.

Local melting and intrusions of heavy mantle material in the western part of the crater could explain the shift of the gravity minimum. Possibly these

intrusions also cause the local relative high gravity values in the region of the western rim.

These considerations would reduce the high negative crater anomaly and the associated high deficit density and great depth of the ruptured zone for the model gravity data to the east and to the south of the crater.

Ptolemaeus (Fig. 6) shows a strong Bouguer maximum shifted to the east of the crater. The model gravity amounts to 92 mgal. This result is in contradiction to model computations of Sjogren et al. (1974b). They explained the free air gravity low of Ptolemaeus by means of a topographic mass deficit and in addition to this a low density crater filling material; but they did not compute the gravity effect of the irregular topography in this region. According to Sjogren et al. (1972), Sjogren and Wollenhaupt (1973), and Sjogren et al. (1974b) the Apollo laser altimetry yields the effective crater depth of Ptolemaeus to be 500 m less than LAC chart 77 (effective depth is measured from the undisturbed topography to the crater floor). Recalculations of the terrain corrections for this higher crater floor show no qualitative change of the relative Bouguer high.

Following considerations have been made for the model computations.

The 1/3 relation yields a depth of 51 km for the ruptured zone. Pike (1967) derived a depth (h)/diameter (D) relation for large highland craters (Fig. 3):

$$h = 0.880 D^{0.35}.$$

The resulting original depth of Ptolemaeus after the impact should be 5.1 km.

The topographic mass deficit and the ruptured crust caused an isostatic upwelling of the mantle which reduced the original crater depth. Considering an original crater depth of 5.1 km a density of 2.6 g/cm^3 for the uppermost crust, and a density difference of 0.3 g/cm^3 between the mantle and the lower crust, an upwelling of 4.5 km of the mantle is necessary for isostatic compensation. A 4 km upwelling has been assumed in the model calculations (cylinder 3 in Table 1) which, however, causes only about 1/8 of the Bouguer maximum. Intrusions of heavy mantle material have therefore been assumed to fit the rest of the maximum (cylinders 1, 2, 4, 5, 6 in Table 1). In the eastern part of the crater these intrusions come close to the surface. The rest of the original ruptured zone was less intruded by mantle material. This process equalized the density contrast to the surroundings. This model is consistent with the reduced present crater depth of about 1–1.5 km.

Other large craters like Humboldt and Posidonius have rilles on their crater floors which indicate an isostatic uplift and/or endogenic intrusional activity (Baldwin, 1971; Brennan, 1975). Such rilles are not visible on the crater floor of Ptolemaeus. They may either not exist or be covered by the crater filling classified as Cayley material. This material belongs to the light plains which can be found in more or less large patches over the entire surface of the Moon.

The discussion of the origin of the Cayley formation is controversial. Two possibilities have been proposed:

1. It is composed of basin ejecta from Imbrium or Orientale (Eggleton and Schaber, 1972; Chao et al., 1975).
2. It has been formed by other, perhaps endogenic, processes (Soderblom and Boyce, 1972; Neukum et al., 1975).

Chao et al. (1975) conclude a highly feldspathic composition of the Cayley material from investigations of samples. Geochemical remote sensing measurements (Adler et al., 1973) show no significant change in the chemical composition between the crater filling of Ptolemaeus and the neighbouring highland areas. These results exclude a high density crater filling by mantle or mare material. This statement favours the ejecta hypothesis.

Chao et al. (1975) assume a 2–3 km thick filling of Ptolemaeus with ejecta from the Orientale basin excavation. The density of this material may be equal or less than the surrounding density. A 2 km thick layer with a deficit density of -0.1 g/cm^3 contributes only -5 mgal to the gravity. Thus gravity calculations do not exclude a disk of basin ejecta.

According to relative age determinations of Soderblom and Boyce (1972), the Cayley formation cannot be part of basin ejecta blankets. Neukum et al. (1975) show that the cumulative crater frequency of the crater floor of Ptolemaeus lies between the Orientale and Imbrium frequency curves. These results favour an endogenic origin of some light plains.

Regarding the crater history of Ptolemaeus as proposed in this paper, one may assume that the intruded mantle material partly melted the original ruptured anorthositic zone. Some parts of the anorthositic lavas ascended to the crater floor forming a 2 km thick layer with no density contrast to the surrounding anorthositic crust. Therefore an endogenic origin of the crater filling is not in contradiction to the model proposed here.

The Vredefort Ring in South Africa may be a terrestrial analogue to Ptolemaeus. Its diameter of 100 km requires a ruptured zone of 33 km depth which is about crustal thickness. Dietz (1963) suggested an isostatic upwelling of the mantle for this structure which is in agreement with a positive residual gravity of 20–30 mgal (Uys and Enslin, 1970).

5. Conclusions

The Bouguer anomalies of the 3 investigated craters show that the neglect of the detailed topographic gravity effects leads to wrong interpretations of local free air gravity anomalies.

Copernicus and Theophilus have Bouguer gravity minima caused by a zone of ruptured rocks and breccia similar to terrestrial impact structures. No isostatic compensation of the mass deficit occurred. Both craters are of the type shown in Figure 1a.

Ptolemaeus has a strong Bouguer maximum. Isostatic uplift of the mantle associated with endogenic intrusional activity of mantle material has been assumed for model calculations and crater history. A near surface mascon as found in mascon-maria has not been considered because there are no indications for near surface mantle or mare materials. Neither an ejecta origin nor an endogenous origin of the crater filling Cayley material can be excluded.

The proposed model shows that this large crater is an intermediate structure between isostatically undercompensated craters and mascon-maria. This type

of craters may be termed “endogenically modified craters or basins”. Figure 1b shows the structural properties of this type.

Acknowledgement. I thank Dr. A. Behle for reading the manuscript and helpful discussions.

References

- Adler, I., Trombka, J.I., Lowman, P., Schmadebeck, R., Blodget, H., Eller, E., Yin, L., Lamothe, R., Osswald, G., Gerard, J., Gorenstein, P., Bjorkholm, P., Gursky, H., Harris, B., Arnold, J., Metzger, A., Reedy, R.: Apollo 15 and 16 Results of the integrated geochemical experiment. *The Moon* **7**, 487–504, 1973
- Angenheister, G., Pohl, J.: Die seismischen Messungen im Ries von 1948–1969. In: *Das Ries. Geologica Bavarica* Nr. 61, E. Preuss, H. Schmidt-Kaler, ed., pp. 304–326. München: Straub 1969
- Baldwin, R.G.: The question of isostasy on the Moon. *Phys. Earth Planet. Interiors* **4**, 167–179, 1971
- Beals, C.S., Innes, M.J.S., Rottenberg, I.A.: Fossil Meteorite Craters. In: *The moon, meteorites, and comets*. B.M. Middlehurst, G.P. Kuiper, ed., pp. 235–284. Chicago: The University of Chicago Press 1963
- Brennan, W.J.: Modification of preare impact craters by volcanism and tectonism. *The Moon* **12**, 449–461, 1975
- Chao, E.C.T., Hodges, C.A., Boyce, I.M., Soderblom, L.A.: Origin of lunar light plains. *J. Res. U.S. Geol. Survey* **3**, 4, 379–392, 1975
- Chung, D.H.: Laboratory studies on seismic and electrical properties of the moon. *The Moon* **4**, 356–372, 1972
- Cooper, M.R., Kovach, R.L., Watkins, J.S.: Lunar near-surface structure. *Rev. Geophys. and Space Phys.* **12**, 291–308, 1974
- Dietz, R.S.: Astroblemes: Ancient Meteorite-Impact Structures on the Earth. In: *The Moon, Meteorites and Comets*. B.M. Middlehurst, G.P. Kuiper, ed., pp. 285–300. Chicago: The University of Chicago Press 1963
- Eggleton, R.E., Schaber, G.G.: Cayley formation interpreted as basin ejecta. In: *Apollo 16, Prel. Sci. Rep. NASA SP-315*, 29-7–29-16, 1972
- Gottlieb, P.: Estimation of local lunar gravity features. *Radio Sci.* **5**, 301–312, 1970
- Innes, M.J.S.: The use of gravity methods to study the underground structure and impact energy of meteorite craters. *J. Geophys. Res.* **66**, 2225–2239, 1961
- Jaeger, J.C.: *Elasticity, fracture and flow with engineering and geological applications*, 3rd ed. London: Methuen 1969
- Jung, K., Schaaf, H., Kahle, H.G.: Ergebnisse gravimetrischer Messungen im Ries. In: *Das Ries. Geologica Bavarica* Nr. 61, E. Preuss, H. Schmidt-Kaler, ed., pp. 337–342. München: Straub 1969
- Kunze, A.W.G.: Lunar mascons: Another model and its implications. *The Moon* **11**, 9–17, 1974
- Kunze, A.W.G.: Lunar Crustal Density Profile from an analysis of doppler gravity data. *The Moon* **12**, 101–112, 1975
- LAC: Lunar Aeronautic charts LAC 1 through LAC 144, aeronautical chart and information center, 127 charts published, 1st ed. St. Louis, Mo.: 1962
- Neukum, G., König, B., Fechtig, H., Storzer, D.: Cratering in the earth-moon system: Consequences for age determination by crater counting. In: *Proc. Lunar Sci. Conf. 6th*, 2597–2620, 1975
- Phillips, R.I., Conel, J.E., Sjogren, W.L.: The nature of the circular maria based on gravity studies. *Space Res.* **14**, 635–645, 1974
- Pike, R.J.: Schroeter’s rule and the modification of lunar impact morphology. *J. Geophys. Res.* **72**, 2099–2106, 1976
- Regan, R.D., Hinze, W.J.: Gravity and magnetic investigations of meteor crater, Arizona. *J. Geophys. Res.* **80**, 776–788, 1975
- Sjogren, W.L., Gottlieb, P., Muller, P.M., Wollenhaupt, W.R.: Lunar gravity via Apollo 14 Doppler radio tracking. *Science* **175**, 165–168, 1972

- Sjogren, W.L., Wollenhaupt, W.R.: Lunar shape via the Apollo laser altimeter. *Science* **179**, 275–278 1973
- Sjogren, W.L., Wimberly, R.N., Wollenhaupt, W.R.: Lunar gravity via the Apollo 15 and 16 subsatellites. *The Moon* **9**, 115–128, 1974a
- Sjogren, W.L., Wimberly, R.N., Wollenhaupt, W.R.: Lunar gravity: Apollo 16. *The Moon* **11**, 35–40, 1974b
- Sjogren, W.L., Wimberly, R.N., Wollenhaupt, W.R.: Lunar gravity: Apollo 17. *The Moon* **11**, 41–52, 1974c
- Soderblom, L.A., Boyce, J.M.: Relative ages of some near-side and far-side terra plains based on Apollo 16 metric photography. In: Apollo 16, Prel. Sci. Report, NASA SP-315, 29-3–29-6, 1972
- Solomon, S.C.: Density within the moon and implications for lunar composition. *The Moon* **9**, 147–166, 1974
- Telford, W.M., Geldart, L.P., Sheriff, R.E., Keys, P.A.: *Applied geophysics*. Cambridge-London-New York-Melbourne: Cambridge University Press 1976
- Uys, N.J., Enslin, J.F.: *Geological Map of the Republic of South Africa and the Kingdoms of Lesotho and Swaziland, 1:1000000*. Gravity Edition. Department of Mines, Geological Survey 1970
- Wise, D.U., Yates, M.T.: Mascons as structural relief on a lunar 'Moho'. *J. Geophys. Res.* **75**, 261–268, 1970

Received July 28, 1976; Revised Version November 19, 1976

A Refined Crustal Model and the Isostatic State of the Scandinavian Blue Road Area

St. Goldflam, H.B. Hirschleber, and P. Janle

Institut für Geophysik der Universität Hamburg,
Bundesstr. 55, 2000 Hamburg 13, Federal Republic of Germany

Abstract. In this paper a detailed interpretation of the Blue Road data is presented. Combining the seismic and gravimetric data a refined crustal model is calculated. The Caledonian mountains show a weak mountain root with a Moho depth of 46 km. A further depression of the Moho is detected under the Gulf of Bothnia (44 km).

Isostatic calculations lead to a considerable lithospheric mass deficit in the area of the Gulf of Bothnia. Combining this result with the intensive recent uplift of this area, an ice-isostatic adjustment is proposed which is still active besides the general tectonic upwarping of Scandinavia. From the calculated mass deficits and isostatic Moho depths a thickness of 3.4 km for the original ice cover is estimated. This is in agreement with the recent ice cover of Greenland and the Antarctic.

Key words: Velocity-depth function – Seismic-gravimetric model – Isostasy – Land uplift.

Introduction

The Baltic Shield and the Caledonian mountain range – called Fennoscandia – form one of the oldest parts of the European continent and represent one of the most stable geotectonic units in the earth's history. The inner structure, the process and mechanism of the land uplift constitute one of the main problems of the geodynamic research in Fennoscandia. Maybe the recent land uplift originates from both the orogenic movement and the isostatic compensation after the last ice age.

In 1972 refraction seismic measurements were carried out along the Scandinavian Blue Road traverse crossing the Caledonides, the Svecofennides (Baltic Shield), and the zone of maximum land uplift in the Gulf of Bothnia (Fig. 1).

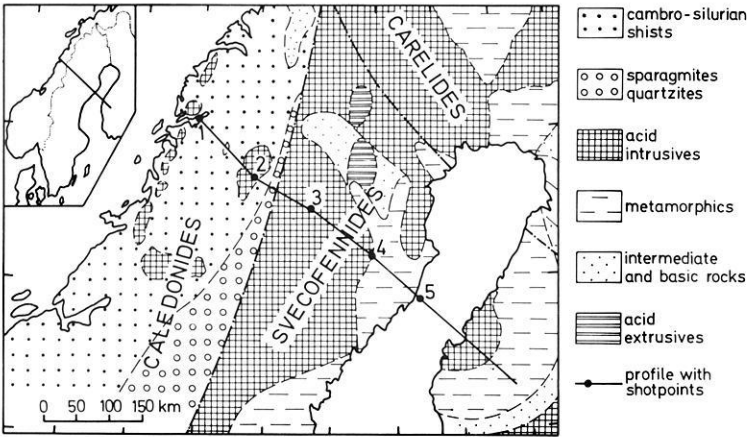


Fig. 1. Simplified geological map with Blue Road profile and locations of shotpoints (modified after Hirschleber et al., 1975)

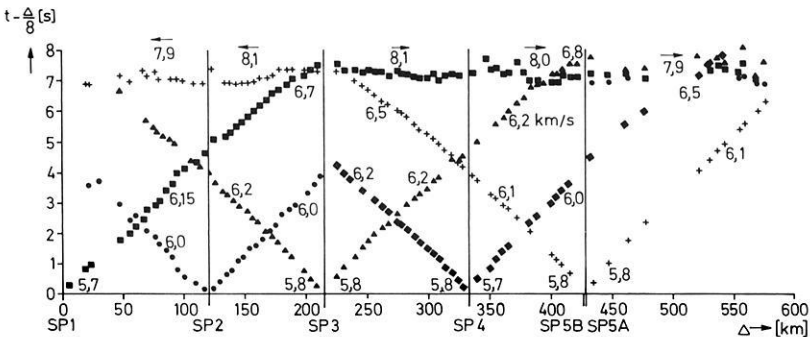


Fig. 2. Arrangement of shotpoints and recording stations with first arrivals and apparent velocities

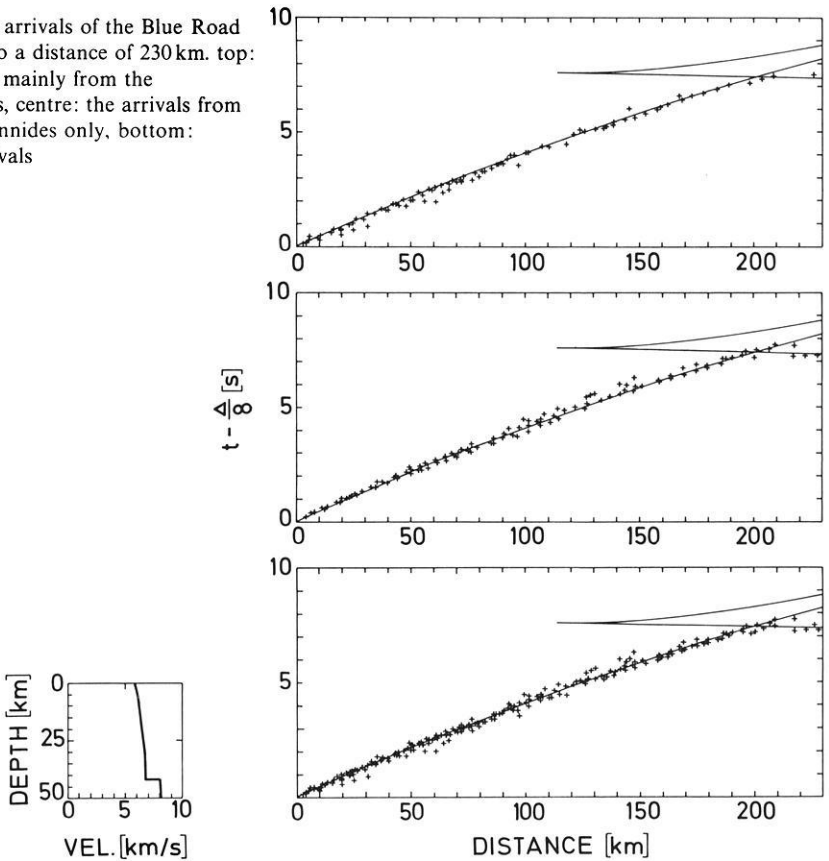
A description of the seismic field work, the record sections, and a first interpretation are given in a paper by Hirschleber et al. (1975). In Figure 2 all first arrivals and different apparent velocities are plotted.

Although excellent first arrivals were found along the whole profile, secondary arrivals were generally weak. No clear subcritical reflections have been detected.

Therefore, velocity-depth models without significant first order discontinuities are given preference. Apart from different structures near the surface the distribution of seismic velocities appears to be very similar within the Caledonides and the Svecofennides. The crust-mantle boundary shows only minor undulations between 37 and 42 km. No distinct roots below the Caledonian mountains were observed. The mantle velocity seems to be constant to depths of about 80 km, — at least it does not increase.

The purpose of this paper is to refine the seismic models with the aid of gravimetric data taken from a map of "Bureau Gravimétrique International"

Fig. 3. First arrivals of the Blue Road profile up to a distance of 230 km. top: the arrivals mainly from the Caledonides, centre: the arrivals from the Svecofennides only, bottom: all first arrivals



(Bouvet, 1971) and the results of a local research by Vogel and Tørne (1975). On the basis of a detailed model of the crust along the profile an isostatic investigation will follow. The reasons of the land uplift will be discussed.

A Refined Model of the Blue Road Traverse

Neglecting lateral velocity changes and dipping of the layers all shotpoints are equivalent. In place of five shotpoints only one is present. For this case all first arrivals up to a distance of 230 km are plotted in Figure 3 (bottom).

The traveltime curve represents a mean velocity depth function for the whole profile:

0.0 km	5.90 km/s
5.5 km	6.10 km/s
30.0 km	6.75 km/s
42.0 km	6.80 km/s
<hr/>	
42.0 km	8.1 km/s
50.0 km	8.2 km/s

In Figure 3 (centre) only the arrivals from the Svecofennides are plotted.

The scattering is less than in the general plot below. This may be due to the fact that the Svecofennides represent an ancient homogenous part of the earth's crust impressed by metamorphism at great depths. The first arrivals belonging mainly to the Caledonides are shown in Figure 3 (top). Apart from the larger scattering a lot of onsets are much earlier than the travel time curve up to a distance of 100 km. This indicates a body with a high velocity near the surface. The well known value of 6.6 km/s (gradient 0.005 (km/s)/km) for Scandinavia results from observations of the direct wave. In comparison with the geological map (Fig. 1) we can interpret the high velocity coming from plutonic rocks.

After detailed computations of the local travel time anomalies of the upper crust we have to decide on the course of the crust mantle discontinuity (Moho). In order to reduce the number of possible models gravimetric data were taken into consideration. The calculation of two-dimensional gravity models is justified because the profile transects the geological units nearly at a right angle. Then we have to look for fitting density values to seismic velocities. Using density-velocity diagrams (Nafe and Drake, 1957; Uspenskij, 1970) we get the following relations:

velocity (km/s)	density (g/cm ³)
5.90–6.10	2.78
6.00–6.75	2.80
6.75–6.80	3.01
8.10–8.20	3.37

In order to obtain the best-fitting model a kind of trial and error method is used. The starting depth of the Moho is taken from the seismic data, the course from the Bouguer data. When the computed gravimetric model fits the measured data, travel time curves for possible velocity-depth functions are calculated by the computer. The best model corresponding to the measured arrivals of the seismogram section is selected. Then the seismic model is tested again by the gravimetric data. Comparing continuously the computed models with both the seismic and gravimetric data, an optimal model is found. In this case Figure 4 shows the final model.

In the upper part of Figure 4 one sees the measured first arrivals for shotpoints 1 and 5 and the computed traveltimes curves. Here one sees again the larger scattering of the first arrivals in the Caledonian area (SP 1) as compared to the Svecofennian area (SP 5). In the centre one sees the observed and calculated Bouguer anomalies and on bottom the layering with the density values. This model is also consistent with the first arrivals from shotpoints 2–4. Starting on the left with a small root under the Caledonides (46 km), the Moho depth decreases in the eastern direction (38 km) and increases under the Gulf of Bothnia (44 km). The connection between the course of the Moho and the last ice-age including its influence on the land uplift of the Baltic shield will be discussed in the next chapter.

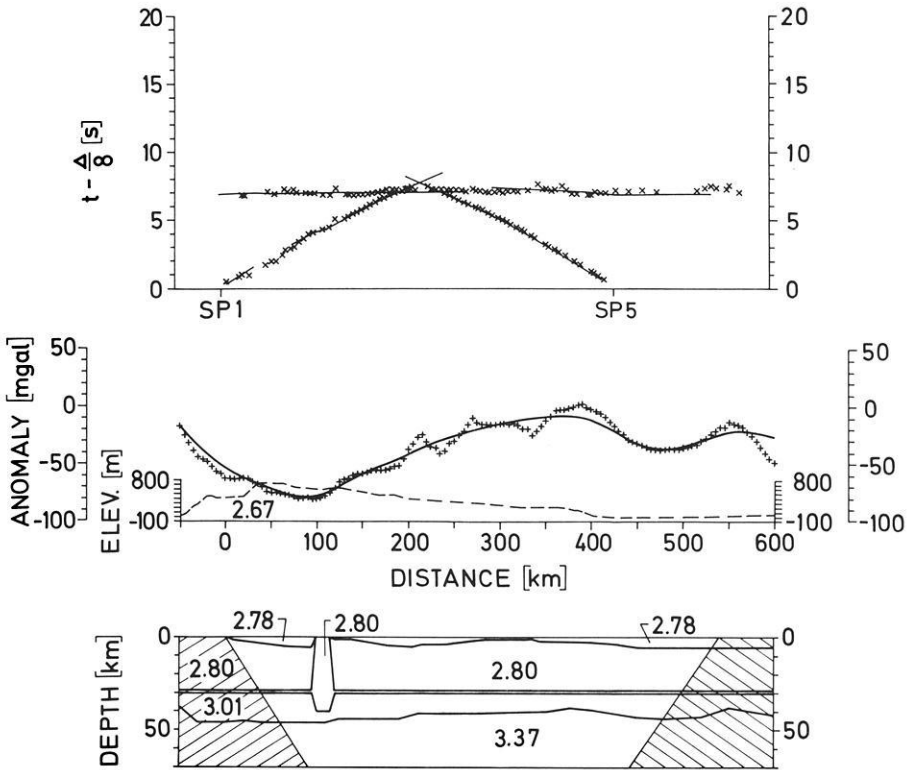


Fig. 4. The final model. top: the traveltime curves for shotpoints 1 and 5 (x = observed arrivals, — = calculated traveltime curve) centre: Bouguer anomaly (+ = observed, — = calculated) bottom: crustal model with density values in g/cm³ (shaded area: gravimetric data only)

The Isostatic State of the Investigated Area

A significant geophysical phenomenon of Scandinavia is the ancient and recent uplift and its consequences with respect to isostatic questions. Before the investigation of the isostatic state of the derived model some general remarks on isostasy will be made.

The hypotheses of isostasy are closely connected with the density distribution and with the rheologic behaviour of the earth (Jacoby, 1973). While former isostatic calculations only consider the general density distribution of the lithosphere, Janle (1973) and Goldflam (1976) show the advantage of using the local density distribution from crustal models. The density distribution of the investigated area was derived in the previous section of this paper and presented in the final model (Fig. 4). The rheologic behaviour of the earth's lithosphere depends on the length of time considered and on the strength.

Regarding the present hypothesis of plate tectonics, the 200 km thick plates of the lithosphere lie on the asthenosphere of secular fluidity. The lithospheric

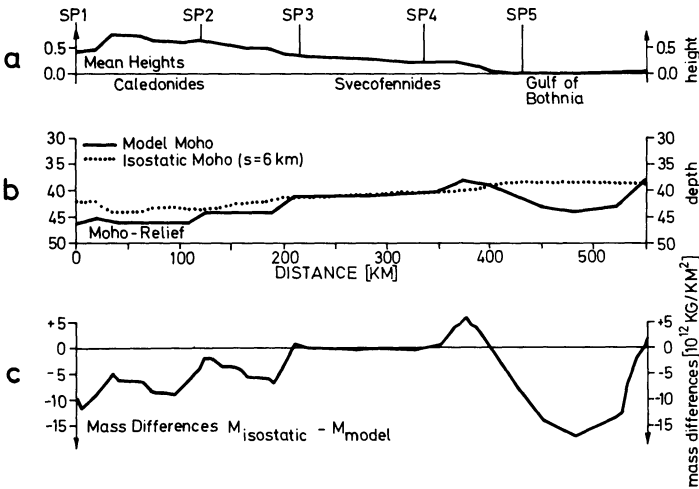


Fig. 5 a-c. Isostatic state of the Blue Road area. **a** mean heights; **b** Moho relief, $s=6$ km: surface of a free floating mantle; **c** mass differences

plates should react nearly ideal-elastically to stress for periods of time less than 10^6 years; for larger periods they may react more visco-elastically with a viscous component of about 10^{24} NS/m² (Walcott, 1970). The rheologic behaviour of a stratum is not simply described by viscosity. A minimal stress, called strength (Daly, 1940; Gutenberg, 1940), is needed to permit a flowing movement. Until now, there are only rough estimations of strengths. Barrell's (1915) estimation shows a decrease of strength below 30 km by a factor of 0.6×10^{-1} . Jeffreys (1962) calculated a strength decrease by a factor of 10^{-1} below 50 km.

Considering this decrease of strength at the zone of the Moho the following computations are based on Archimedean floating of solid crustal sections on a secular fluid mantle. Vertically free mobile crustal columns with a base surface of 5×5 km were considered for the investigation of the isostatic state of the derived model. The isostatic Moho depths were calculated for these columns according to Archimedes' principle. For the calculations a depth of 6 km was estimated for a free floating surface of mantle material. This is the Moho depth of deep sea areas with only a minimal cover of crustal material. The use of a free floating mantle is equivalent to the "normal crustal thickness" of the Airy hypothesis.

Outgoing from the model in Figure 4, the masses were summed up until the layer above the Moho was reached. Then the depth of the Moho was varied until hydrostatic equilibrium was obtained with regard to a column of free floating mantle material. The new Moho depth is called "isostatic Moho depth". The total masses down to the model Moho and the isostatic Moho are termed " M_{model} " and " $M_{isostatic}$ ". The difference between the depth of the model Moho and the depth of the isostatic Moho is due to the present topography. It does not mean that the model Moho has to rise by the amount of the difference to reach isostatic compensation.

Fig. 6. Illustration for calculations of the future uplift H_f and the thickness t of the original ice cover. *I* original stage with maximal ice cover (isostatically compensated); *II* present stage (not isostatically compensated, mass deficit); *III* future stage after isostatic adjustment; M_c = total mass of a crustal column of the model in Figure 4 (M_{model}); M_i = mass of maximal ice cover; ρ_c = crustal density; ρ_i = ice density; ρ_M = mantle density; s = surface of a free floating mantle (6 km depth); T_a = ancient Moho depth - s ; T_p = present (model) Moho depth - s ; T = thickness of a crustal column; H_a = ancient uplift; H_f = future uplift to isostatic adjustment; t = thickness of maximal ice cover

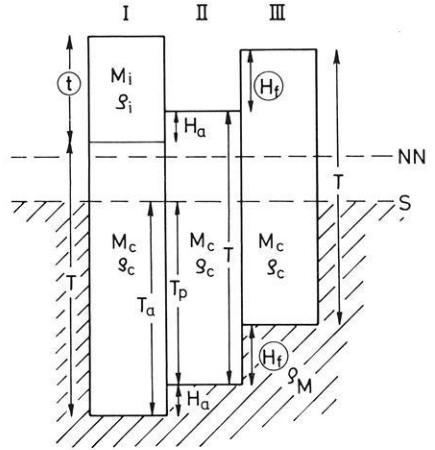


Figure 5b shows the model Moho of Figure 4 and the calculated isostatic Moho; Figure 5c shows the mass differences of crustal thickness between the isostatic compensated crust and the model crust ($M_{isostatic} - M_{model}$). A similar calculation of masses of crustal columns on profiles was carried out by Janle (1973) for southern Scandinavia.

The calculations of the isostatic Moho and of the mass differences (Fig. 5) permit an estimation: (1) of the uplift to be expected in the future and (2) of the thickness of the original ice cover. The calculations are based on two assumptions:

- the masses of crustal columns remain constant during uplift; erosion is neglected;
- there is Archimedean compensation, i.e. the elastic properties are not considered.

(1) Comparing columns II and III in Figure 6, the following equation is valid for isostatic adjustment:

$$(T_p - H_f) \rho_M = M_c$$

$$H_f = T_p - \left(\frac{M_c}{\rho_M} \right)$$

$$\rho_M = 3.37 \text{ g/cm}^3.$$

The following values result for the Gulf of Bothnia from the model in Figure 4 and the calculated mass differences:

$$T_p = 38 \text{ km}$$

$$M_c = 126 \times 10^{12} \text{ kg/km}^2.$$

The resulting uplift H_f for the future is 600 m.

(2) Comparing I and III in Figure 6, the following equations are valid for isostatic equilibrium:

$$T_a \rho_M = \rho_i t + T \rho_c$$

$$T_a \rho_M = (H_a + H_f) \rho_M + T \rho_c.$$

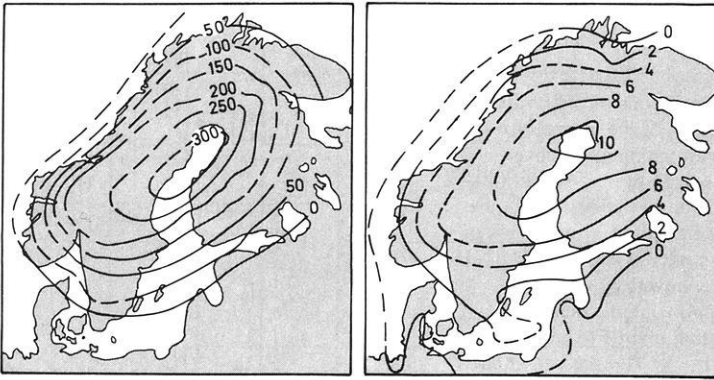


Fig. 7. Left: total ancient uplift in m for the last 7700 years. Right: contour lines of recent uplift in mm/year (Brinkmann, 1967)

These 2 equations lead to

$$t = \frac{\rho_M}{\rho_i} (H_a + H_f)$$

$$\rho_i = 0.9 \text{ g/cm}^3$$

$$H_a = 300 \text{ m (ancient uplift Fig. 7).}$$

The resulting original ice cover is 3.4 km.

It must be emphasized, however, that the calculated values are maximum values due to the neglect of the elastic properties.

The agreement of the isostatic Moho and the model Moho in Figure 5b indicates an isostatic equilibrium of the crust between SP 3 and SP 4. In the areas of the Caledonides and the Gulf of Bothnia the model Moho lies below the isostatic Moho. These areas must rise to achieve isostatic equilibrium. The mass differences show the same trend in Figure 5c. Negative values indicate mass deficits which can be compensated by an isostatic uplift of the crust. This resulting trend agrees with the ancient and recent crustal uplift (Fig. 7).

After presenting the computed mass deficits and crustal uplift possible causes for these phenomena shall be discussed now. Two components for the uplift have been proposed: a tectonic component has been continuously active since the Precambrian; superimposed on this component is an ice-isostatic component (Schwinner, 1928; Heiskanen, 1936; Sauramo, 1939; Daly, 1940; Artyushkov and Mescherikov, 1969). While the tectonic vertical movements amount maximally to 10–15 mm/year, the ice-isostatic uplift starts with more than 10 cm/year and declines rapidly in some 10^4 years to maximally 10 mm/year. Thus, it is difficult to decide whether the recent uplift is due to tectonic or ice-isostatic processes. Mörner (1973) concludes that the ice-isostatic component is nearly terminated.

Janle (1973) and this paper (Fig. 5) show that there is a considerable mass deficit within the lithosphere at least in the area of the Gulf of Bothnia. This

mass deficit is interpreted here as a relic of the ice age causing a part of the present uplift. Tectonic vertical movements have their origin in the mantle or, more specifically, in the asthenosphere, caused by convection currents or thermal and mass anomalies. However, there are no hints of recent local tectonic processes within the area of the Gulf of Bothnia such as earthquakes or geologic faults.

Conclusions

The seismic analysis yields a uniform $v-z$ function for the region of the Blue Road. However, there are some differences between the areas of the Caledonides and the Baltic Shield. Differing from the average for the Caledonian mountains a velocity of 6.6 km/s near the surface and a greater scatter of the first arrivals were observed. This effect is explained by: (1) numerous magmatic intrusions, (2) the lesser degree of metamorphism, and (3) the lesser age in comparison to the Svecofennides. The final model (Fig. 4) shows a weak mountain root in the Caledonides. The Moho depression of the Gulf of Bothnia coincides with the region of maximal uplift.

The fact of the considerable crustal mass deficit in the area of the Gulf of Bothnia combined with the maximum recent uplift of 10 mm/year is interpreted as an ice-isostatic adjustment which is still active in addition to the general tectonic upwarping of Scandinavia.

The calculated thickness of the original ice cover agrees quite well with the situation in areas with recent glaciations. The ice cover of Greenland has a thickness of about 3 km (Brinkmann, 1967) and in the Antarctic the ice cover amounts to a maximal thickness of 5 km (Thenius, 1974).

References

- Artyushkov, E. W., Mescherikov, Yu. A.: Recent movements of the earth's crust and isostatic compensation. In: *The earth's crust and upper mantle*, Monograph No. 13, P. J. Hart, ed., pp. 379–390. Washington, D.C.: American Geophysical Union 1969
- Barrell, J.: The strength of the earth's crust *J. Geol.* **1**, XXIII, 27–45, 1915
- Bouvet, J.: *Anomalies de Bouguer, Europe—Afrique*. Paris: Bureau Gravimétrique International 1971
- Brinkmann, R.: *Abriß der Geologie*, Bd. 1. Stuttgart: Enke 1967
- Daly, R. A.: *Strength and structure of the earth*. New York: Prentice-Hall 1940
- Goldflam, St.: Ein zweidimensionales Krustenmodell und die isostatischen Verhältnisse auf dem Profil Blaue Straße 1972 in Skandinavien. Diplomarbeit, Institut für Geophysik, Universität Hamburg 1976
- Gutenberg, B.: Geotektonische Hypothesen. In: *Handbuch der Geophysik*, Bd. 3, B. Gutenberg, ed., pp. 442–547. Berlin: Borntraeger 1940
- Heiskanen, W.: Das Problem der Isostasie. In: *Handbuch der Geophysik*, Bd. 1, B. Gutenberg, ed., pp. 878–951. Berlin: Borntraeger 1936
- Hirschleber, H. B., Lund, C. E. Meissner, R., Vogel, A., Weinrebe, W.: Seismic investigations along the Scandinavian “blue road” traverse. *J. Geophys.* **41** 135–148, 1975
- Jacoby, W. R.: Isostasie und Dichteverteilung in Kruste und oberem Mantel. *J. Geophys.* **39**, 79–96, 1973

- Janle, P.: Synoptische Bearbeitung des südlichen Teiles von Skandinavien aus seismischen und gravimetrischen Ergebnissen. Hamburger Geophysikalische Einzelschriften. Heft 19, 1973
- Jeffreys, H.: The earth. Cambridge: University Press 1962
- Mörner, N. A.: Eustatic changes during the last 300 years. Paleogeography, Paleoclimatology, Paleoecology **13**, 1–14, 1973
- Nafe, J. E., Drake, C. L.: Physical properties of crustal materials as related to compressional wave velocities. Annual Meeting of Soc. Explor. Geophys., Dallas, Texas, 1975
- Sauramo, M.: The mode of the land upheaval in Fennoscandia during late-quaternary time. Soc. Geol. de Finlande, C. R., No. 13, 1939
- Schwinner, R.: Geologische Bemerkungen zu den Norwegischen Schweremessungen. Gerlands Beitr. Geophys. **19**, 107–133, 1928
- Thenius, E.: Eiszeiten – einst und jetzt. Stuttgart: Franckh'sche 1974
- Uspenskij, D. G.: Study of the earth's crust under the oceans by the gravimetric method. Izvestia, Physics of the solid earth, 429–437, 1970
- Vogel, A., Törne, A.: Gravity map of the blue road profile. 2nd Discussion Meeting on the "Blue Road Project" in Uppsala, 1975
- Walcott, R. L.: Flexural rigidity, thickness, and viscosity of the lithosphere. J. Geophys. Res. **75**, 3941–3954, 1970

Received September 16, 1976; Revised Version November 12, 1976

Earth-Flattening Approximation for Body Waves Derived from Geometric Ray Theory – Improvements, Corrections and Range of Applicability[★]

G. Müller

Geophysical Institute, University of Karlsruhe,
Hertzstraße 16, D-7500 Karlsruhe, Federal Republic of Germany

Abstract. A new derivation of the earth-flattening approximation (EFA) for body waves from geometric ray theory is given which results in an improved version of the EFA. This version agrees with the EFA, derived by Chapman (1973) from wave theory. Moreover, it allows absolute, not only relative, body-wave amplitude calculations for given source time functions. The choice of the density transformation of the EFA is shown, by numerical calculations, to be uncritical for body-wave amplitudes in the period range up to 30 s. An error in an earlier derivation of the EFA (Müller, 1973a) is corrected. This error requires a new investigation of the range of applicability of the EFA, which is performed for the P-wave propagation through a homogeneous sphere. The results are similar to those of the earlier paper: long-period *P* waves with dominant periods up to about 20 s can be treated practically exactly, as long as they do not pass closer than about 800 km to the earth's center.

Key words: Earth-flattening approximations – Geometric ray theory – Wave theory

Introduction

Earth-flattening approximations (EFAs) for body waves have been derived from geometric ray theory (Müller, 1971, 1973a) and from wave theory (Chapman, 1973; see also Gilbert and Helmberger, 1972; Helmberger and Harkrider, 1972; Hill, 1972). Although the basic structure of both EFAs is the same, there is a notable difference: according to the EFA of Müller (1973a) (in the following called paper *I*) the velocity-density-depth distribution in the flat earth depends both on source and receiver radius whereas Chapman's EFA is independent of these radii. Because of the dependence on source and receiver radius the EFA of *I* requires frequency and time transformations, as long as these radii are different, which is not required with Chapman's EFA. The essential assumption in the derivation of the EFA of *I*, which entails its more complicated form, is that medium properties at the source should agree in the spherical and the flat

[★] Contribution No. 144 Geophysical Institute, University of Karlsruhe

earth, such that the radiation of P and S waves is the same. This condition can be relaxed, and it is shown in this paper that the resulting EFA, derived from geometric ray theory, agrees with Chapman's EFA in its essential features. Moreover, it allows the calculation of absolute (not only relative) body-wave amplitudes for a given source time function, e.g., the moment function in the case of a double-couple point source.

The density transformation of the EFA is not well determined in the case of P-SV waves, neither by geometric ray theory (which is not surprising) nor by wave theory. Therefore, numerical calculations of theoretical seismograms for different density transformations are desirable, and they should show whether or not the choice of the density transformation is critical for practical purposes. Results of calculations for the mantle P phase and the core reflection PcP are discussed in this paper.

Another purpose of this paper is to correct an error in I , related to the amplitude correction factor for diffracted waves. A correct application of geometric ray theory gives the same $(\Delta/\sin \Delta)^{1/2}$ factor as for other body waves (Δ = epicentral distance).

Finally, a new investigation of the range of applicability of the EFA is performed by calculating the P-wave propagation from an explosive point source through a homogeneous sphere. Exact results are available in this case, since it corresponds to propagation through a homogeneous unbounded medium. This test has already been used by Helmberger (1973) for P waves propagating as deep as 1150 km in a sphere of the size of the earth. These calculations are extended here to much greater depths in order to find out for which wavenumber times radius products the EFA still works with sufficient accuracy.

Theory

The following is a summary of the properties of rays in a sphere and a half-space, according to geometric ray theory. Most notations are explained in Figure 1, and subscripts s and f refer to the spherical and the flat earth, respectively. The formulas are given for the simple type of ray shown in Figure 1, but the results derived from them are also true for other types such as rays with a turning point or reflected rays.

Spherical earth:

$$\text{Epicentral distance: } x_s = P_s \int_{r_1}^{r_0} \frac{r_1}{r} \left(\frac{r^2}{V_s^2} - P_s^2 \right)^{-1/2} dr \quad (1)$$

$$\text{Travel time: } t_s = \int_{r_1}^{r_0} \frac{r}{V_s} \left(\frac{r^2}{V_s^2} - P_s^2 \right)^{-1/2} dr \quad (2)$$

$$\text{Ray parameter: } P_s = \frac{r_0 \sin \psi_0}{V_s(r_0)}$$

$$\text{Amplitude: } A_s = \left(\frac{\rho_s(r_0) V_s(r_0) a^2 \sin \psi_0}{\rho_s(r_1) V_s(r_1) r_1 \sin \Delta \left| \frac{\partial x_s}{\partial \psi_0} \right|_r \cos \psi_s} \right)^{1/2} A_{s,0} \quad (3)$$

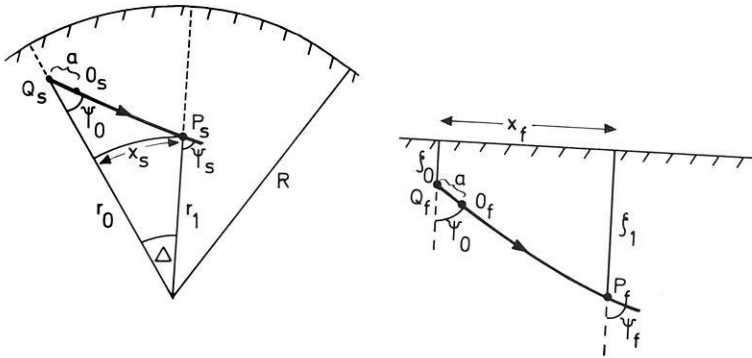


Fig. 1. The spherical earth (left), the flat earth (right) and two corresponding rays from the source $Q_{s,f}$ to the receiver $P_{s,f}$. The radiation angle is the same for both rays

$$\left. \begin{aligned} V_s(r) &= P \text{ or } S \text{ velocity} \\ \rho_s(r) &= \text{density} \end{aligned} \right\} \text{ at radius } r$$

A_{s_0} = amplitude at a reference point O_s on the ray with distance a from the source Q_s

Flat earth:

$$\text{Epicentral distance: } x_f = P_f \int_{\zeta_0}^{\zeta_1} \left(\frac{1}{V_f^2} - P_f^2 \right)^{-1/2} d\zeta \tag{4}$$

$$\text{Travel time: } t_f = \int_{\zeta_0}^{\zeta_1} \frac{1}{V_f} \left(\frac{1}{V_f^2} - P_f^2 \right)^{-1/2} d\zeta \tag{5}$$

$$\text{Ray parameter: } P_f = \frac{\sin \psi_0}{V_f(\zeta_0)}$$

$$\text{Amplitude: } A_f = \left(\frac{\rho_f(\zeta_0) V_f(\zeta_0) a^2 \sin \psi_0}{\rho_f(\zeta_1) V_f(\zeta_1) x_f \left| \frac{\partial x_f}{\partial \psi_0} \right|_{\zeta_1} \cos \psi_f} \right)^{1/2} A_{f_0} \tag{6}$$

$$\left. \begin{aligned} V_f(\zeta) &= P \text{ or } S \text{ velocity} \\ \rho_f(\zeta) &= \text{density} \end{aligned} \right\} \text{ at depth } \zeta$$

A_{f_0} = amplitude at a reference point O_f on the ray with distance a from the source Q_f .

The depth and velocity transformations of Gerver and Markushevich (1966),

$$\zeta = R \ln \frac{R}{r}, \quad V_f(\zeta) = \frac{R}{r} V_s(r), \tag{7}$$

which are independent of source and receiver radius yield, when inserted into (1) and (2),

$$x_s = \frac{r_1}{R} x_f \quad \text{or} \quad x_f = R \Delta \tag{8}$$

and

$$t_s = t_f.$$

Here, (4) and (5) have been used. It follows that the mapping of the sphere onto the half-space is independent of r_1 , and that the travel times between corresponding points in the sphere and the half-space agree for arbitrary values of r_0 and r_1 ; in both regards the EFA derived here differs from the EFA of *I*. The constancy of ray parameter along the ray in both media yields $\psi_s = \psi_f$. Inserting this and (7) and (8) into (3) one obtains, using (6):

$$A_s = \left(\frac{\Delta}{\sin \Delta} \right)^{1/2} \frac{R}{r_1} \left(\frac{r_0 \rho_s(r_0) \rho_f(\zeta_1)}{r_1 \rho_s(r_1) \rho_f(\zeta_0)} \right)^{1/2} \frac{A_{s0}}{A_{f0}} A_f.$$

A density transformation similar to the velocity transformation,

$$\rho_f(\zeta) = \left(\frac{R}{r} \right)^n \rho_s(r), \tag{9}$$

where according to wave theory n depends on the wave type investigated, yields finally the amplitudes in the sphere in terms of the amplitudes in the half-space:

$$A_s = \left(\frac{\Delta}{\sin \Delta} \right)^{1/2} \left(\frac{R}{r_1} \right)^{\frac{n+3}{2}} \left(\frac{r_0}{R} \right)^{\frac{n+1}{2}} \frac{A_{s0}}{A_{f0}} A_f. \tag{10}$$

The relation between the exponent of receiver radius r_1 and the exponent n in the density transformation (9) is the same as with Chapman's EFA. Thus, both EFAs agree in all essential points.

The amplitude correction formula (10) allows the calculation of absolute amplitudes in the sphere, provided the ratio A_{s0}/A_{f0} of the initial amplitudes is known. In the framework of geometric ray theory these amplitudes have to be considered as the amplitudes of the far-field term of displacement, taken close to the source. The simplest assumption is $A_{s0}/A_{f0} = 1$; this means that the source is described by its (far-field) displacement-time function. There may, however, be cases where one prefers to describe a double-couple source by its moment function $M(t)$ or an explosion by its excitation function (or reduced displacement potential) $F(t)$. From the far-field displacements of these sources in a homogeneous unbounded medium, one derives for a double-couple

$$\frac{A_{s0}}{A_{f0}} = \frac{\rho_f(\zeta_0) V_f^3(\zeta_0)}{\rho_s(r_0) V_s^3(r_0)} = \left(\frac{R}{r_0} \right)^{n+3}$$

and for an explosion

$$\frac{A_{s0}}{A_{f0}} = \frac{V_f(\zeta_0)}{V_s(r_0)} = \frac{R}{r_0}.$$

Discussion

As paper *I* and this paper show, geometric ray theory allows the construction of different EFAs. From a theoretical point of view preference should be given to

the EFA derived here, since it agrees with an EFA from wave theory, which has not yet been shown for the EFA of I . From a practical point of view, no essential differences exist, as follows from calculations of theoretical seismograms. For example, theoretical long-period P and PcP phases between 40° and 70° have been computed by Müller et al. (1977, Fig. 7) for the Jeffreys-Bullen earth model and a source at a depth of 600 km, using the EFA of I . Recalculation with the revised EFA shows agreement generally within 1% in absolute amplitudes and in the amplitude ratio PcP/P.

The density transformation of the EFA is not well defined from geometric ray theory. Chapman (1973) has shown from wave theory that in (9) $n=1$ is optimum, although not exact, for P waves in liquid media, i.e., for the acoustic case, and $n=-5$ for SH waves. For P-SV waves in solid media no optimum value could be found. Numerical calculations of theoretical seismograms, again for long-period P and PcP between 40° and 70° from a deep source, show changes in amplitudes from $n=1$ to $n=-5$ which do not exceed 2% in the case of P and 4% in the case of PcP. These numbers decrease for a closer approximation of the velocity-density-depth distribution by layers (which in the computational method used, the reflectivity method (Fuchs and Müller, 1971), are homogeneous in the flat earth and hence inhomogeneous with negative velocity gradients in the spherical earth). The conclusion from this is that for practical purposes the choice of n is not critical in body-wave studies. On this background, a theoretical argument can be made in all three cases (acoustic, SH and P-SV) in favor of $n=-1$. It is an experience from numerical calculations that the influence of density on body-wave amplitudes is strongest for vertically travelling waves. For these the controlling parameter is the impedance, i.e., the product of velocity and density. Therefore, it is reasonable to match the impedances of the spherical and the flat earth, which means $n=-1$. For waves travelling predominantly horizontal this value is as reasonable as any other from -5 to 1.

The amplitude correction formula (10) applies also in the case of diffracted rays, contrary to what was stated in I ; i.e., formulas (12) and (17) of I are wrong. The simplest argument is that a diffracted ray which runs parallel to the diffracting boundary can be approximated arbitrarily close by a ray of the type discussed so far, having a turning point. This is done by introducing in an arbitrarily thin layer above the diffracting boundary a velocity gradient $dV_s/dr = V_s(r_a)/r_a$ where r_a is the radius of the diffracting boundary and $V_s(r_a)$ the velocity directly above it. Then, (10) is applicable. For finite frequencies, i.e., non-zero wavelengths, the original and the new velocity distribution are equivalent, and thus (10) is also valid for diffracted rays. This qualitative argument is confirmed by strict geometric-ray-theory calculations of the changes in wave amplitude along the segments of a truly diffracted ray in the spherical earth and its image in the flat earth. The error in I is due to a wrong sequence in the treatment of the ray segments.

A consequence of the error is that in Müller (1973b) theoretical P_{diff} amplitudes are slightly incorrect (see Müller, 1976). As a more serious consequence, it seems no longer certain that the EFA can be applied in those body-wave propagation problems for which the product wavenumber times radius, kr ,

is greater than about 16. This lower limit had been inferred in I from a comparison of exact P_{diff} amplitudes with those following from calculations via the EFA, including the wrong amplitude correction factor for diffracted rays (I , Fig. 3). If the correct factor is used the agreement is less good, and hence one would derive a greater minimum value of kr and consequently a more restricted range of applicability of the EFA. This question requires further investigation which is reported in the next section.

Range of Applicability of the EFA

The range of applicability of the EFA can be tested by comparing theoretical seismograms for a model, for which they can be calculated analytically, with those calculated numerically via the EFA and the reflectivity method for a layered half-space. The simplest test model is a homogeneous sphere with an explosive point source and receivers at the surface. The radius of the sphere is assumed to be 6370 km, the P velocity 10.00 km/s, the S velocity 5.77 km/s and the density 5.50 g/cm³. In the corresponding flat medium the wave velocities increase exponentially with depth; the density decreases exponentially with depth, according to the exponent $n = -1$ in the density transformation (9). For application of the reflectivity method, this half-space is approximated by homogeneous layers which corresponds to saw-tooth-like velocity and density-depth distributions in the sphere. The thickness of the inhomogeneous layers in the sphere is 50 km in a first calculation; it is reduced in a second calculation to 25 km at depths greater than 4000 km and to 12.5 km below 5000 km, in order to test whether or not the approximation of the homogeneous sphere is sufficient. Both calculations give essentially the same results, the differences in the maximum peak-to-peak amplitudes being 2% or less.

The far-field term of the displacement of the spherical P-wave at a reference distance close to the source is assumed to be

$$s(t) = \sin 2\pi \frac{t}{T} - \frac{1}{2} \sin 4\pi \frac{t}{T}, \quad 0 \leq t \leq T = 20 \text{ s}. \quad (11)$$

The dominant wavelength is about 180 km in the sphere. The epicentral distance of the receivers increases from 120°–170°, such that the rays from the source to the receivers pass closer and closer to the center of the sphere where the EFA definitely breaks down. The influence of the free surface is disregarded, both at the source and at the receivers; in reality the test is one for an unbounded medium for which theoretical seismograms can be calculated analytically in a well-known manner from (11).

Figure 2 shows a comparison of exact theoretical seismograms for the displacement component along the ray from the source to the receiver with calculations using the EFA. The component perpendicular to the ray, which in theory vanishes, has maximum amplitudes less than 1% of those of the component along the ray. The agreement between analytical and numerical calculations is very good up to 150°. Then discrepancies gradually develop, and at 170° both amplitudes and pulse forms are significantly different. The most

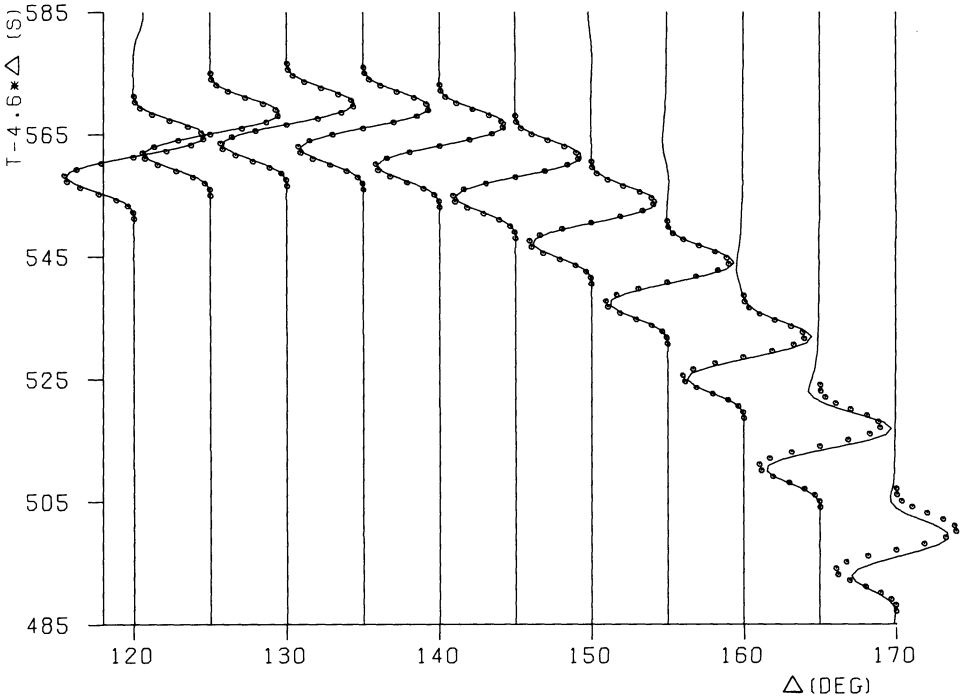


Fig. 2. P-wave propagation from an explosive point source through a homogeneous sphere: comparison of exact theoretical seismograms (circles) and numerical calculations, based on the earth-flattening approximation and the reflectivity method for a half-space (solid lines). For more details see text

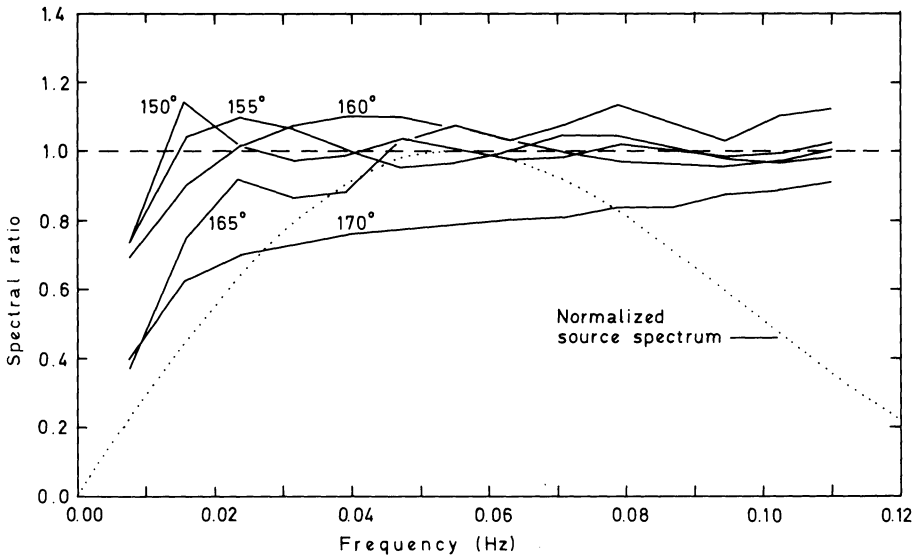


Fig. 3. Ratio of the amplitude spectra of the numerically calculated and the exact seismograms of Figure 2, for epicentral distances from 150°–170°. The length of the time interval considered is 127 s, and the time step 1 s. The normalized source spectrum follows from (11)

important conclusion can already be drawn by inspection from the seismograms at 165° where, in spite of certain differences in pulse form, the maximum peak-to-peak amplitudes are practically identical. The distance of the turning point of the ray from the center of the sphere is 831 km, which in the real earth corresponds to a depth of about 400 km below the boundary of the inner core. Since the velocity-depth distribution in the inner core is quite similar to the one in the homogeneous sphere under investigation, it is safe to conclude that the EFA can be applied without essential errors in amplitude studies of long-period core phases with dominant periods up to at least 20 s, provided that the waves do not propagate deeper than about 400 km below the inner-core boundary. Moreover, spectral analysis of the seismograms of Figure 2 shows (Fig. 3) that at low frequencies the EFA leads to systematically reduced spectral ratios of the numerically calculated to the analytical seismograms. At 165° the spectral ratio is in error by more than 10% at periods greater than about 30 s, taking a smoothed version of the spectral-ratio curve. Considering 10% as an acceptable error in the computational method, compared with the normally much larger observational error in amplitude studies of long-period waves, one derives $kr \geq 17$ as the admissible range of the product kr in studies of long-period body-wave amplitudes with the EFA. To be on the safe side, the waves should not pass closer than about 800 km to the earth's center. In essence, these are the same conclusions that had been reached in I.

Acknowledgements. The investigations of this paper were stimulated by discussions with C.H. Chapman and P.G. Richards during the 11th Symposium on Mathematical Geophysics at Seeheim/Odenwald. V. Červený, K. Fuchs and R. Kind read the manuscript and offered helpful and stimulating discussions. I. Hörnchen typed the manuscript. The computations were performed at the computing center of the University of Karlsruhe.

References

- Chapman, C.H.: The earth-flattening transformation in body wave theory. *Geophys. J.R.A.S.* **35**, 55–70, 1973
- Fuchs, K., Müller, G.: Computation of synthetic seismograms with the reflectivity method and comparison with observations. *Geophys. J.R.A.S.* **23**, 417–433, 1971
- Gerver, M., Markushevich, V.: Determination of a seismic wave velocity from the travel-time curve. *Geophys. J.R.A.S.* **11**, 165–173, 1966
- Gilbert, F., Helmberger, D.V.: Generalized ray theory for a layered sphere. *Geophys. J.R.A.S.* **27**, 57–80, 1972
- Helmberger, D.V.: Numerical seismograms of long period body waves from seventeen to forty degrees. *Bull. Seism. Soc. Am.* **63**, 633–646, 1973
- Helmberger, D.V., Harkrider, D.G.: Seismic source descriptions of underground explosions and a depth discriminate. *Geophys. J.R.A.S.* **31**, 45–66, 1972
- Hill, D.P.: An earth-flattening transformation for waves from a point-source. *Bull. Seism. Soc. Am.* **62**, 1195–1210, 1972
- Müller, G.: Approximate treatment of elastic body waves in media with spherical symmetry. *Geophys. J.R.A.S.* **23**, 435–449, 1971
- Müller, G.: Theoretical body wave seismograms for media with spherical symmetry – discussion and comparison of approximate methods. *Z. Geophys.* **39**, 229–246, 1973a
- Müller, G.: Amplitude studies of core phases. *J. Geophys. Res.* **78**, 3469–3490, 1973b
- Müller, G.: Correction. Submitted to *J. Geophys. Res.*, 1976
- Müller, G., Mula, A.H., Gregersen, S.: Amplitudes of long-period PcP and the core-mantle boundary. *Phys. Earth Planet. Int.* (in press), 1977

On the Variation of Kp at Sector Boundaries

H. Schreiber

Institut für Geophysik der Universität Göttingen
Herzberger Landstraße 180, D-3400 Göttingen, Federal Republic of Germany

Abstract. A superposed epoch analysis of Kp at well established sector boundaries of the interplanetary magnetic field (IMF) has been carried out for 4 classes of sector boundaries with the following results: The Kp increase at (+/–) sector boundaries near vernal equinoxes and at (–/+) boundaries near autumnal equinoxes is significantly greater than at sector boundaries with the opposite polarity change. For a smaller number of sector boundaries observed in the years 1966–1968, showing the same polarity- and season-dependent Kp variation, the influence of different components of the interplanetary magnetic field B and the solar wind velocity v on Kp is examined. From the results it is suggested that the observed Kp variations are controlled by the variation of the IMF southward component B_{SM} , which however, is not the only interplanetary parameter being responsible for the observed variations. A linear relation between Kp, B_{SM} and the solar wind velocity v gives a reasonable presentation of the Kp variations at sector boundaries.

Key words: Geomagnetic activity – Interplanetary magnetic field IMF – Sector structure – Solar wind velocity – Southward component of IMF.

Introduction

Since the discovery of the sector structure of the interplanetary magnetic field (IMF) many studies analysed the variation of interplanetary parameters and various geomagnetic indices within the sectors and at the boundaries (e.g. Wilcox, 1968, for a first review). On the average the solar wind velocity v as well as the IMF magnitude B vary systematically within the sectors with a relatively sharp increase near the boundaries, a maximum one or two days after the boundary, and a slow decrease to a pronounced minimum one day before the next boundary passage. The average slope is the same for (+) sectors when the IMF vector is pointing away from the sun and (–) sectors when the IMF vector is pointing towards the sun.

Geomagnetic indices as a measure of the interaction of the interplanetary medium with the magnetosphere show a similar variation during the passage of sectors and particularly in the vicinity of the boundaries (e.g. Wilcox and Ness, 1965; Ness and Wilcox, 1967; Wilcox and Colburn, 1972; Hirshberg and Colburn, 1973; Wilcox et al., 1975). The minimum of geomagnetic activity before sector boundaries seems to be more significant than the post boundary maximum which possibly is dependent on the sector polarity (Shapiro, 1974).

Correlations of geomagnetic indices have been found both with solar wind velocity v (Neugebauer and Snyder, 1966; 1967) and with B (Wilcox et al., 1967). Further studies gave evidence for a better correlation between geomagnetic activity and the fluctuations of the IMF (Ballif et al., 1969; Garrett, 1974), and with the IMF southward magnetospheric component B_{SM} (Hirshberg and Colburn, 1969; Arnoldy, 1971). It was also indicated that magnetic variations especially in the polar caps are related to the east-west component of the IMF perpendicular to the sun-earth line (Friis-Christensen et al., 1972; Berthelier et al., 1974). Since the parameters of the interplanetary medium are intercorrelated to a certain degree (e.g. an increased B implies increased values of the components of B and frequently enhanced fluctuations) it is often difficult to separate the influence of individual parameters on geomagnetic activity. This investigation analyses the average K_p variation at sector boundaries for the different geometrical configurations between the IMF and the magnetosphere in vernal and autumnal months. Comparing the variations of some interplanetary parameters with the observed polarity-dependent K_p variations the effect of the southward component of the IMF will be pointed out.

Analysis and Results

In a series of papers, lists of "well established" IMF sector boundaries have been published, giving the polarity, the dates and (generally) 3 h intervals of boundary observations at the earth (Wilcox and Colburn, 1969, 1970, 1972; Wilcox et al., 1975; Fairfield and Ness, 1974). "Well established" sector boundaries are defined in the way that at least for 4 days the IMF has one polarity followed by at least 4 days with the opposite polarity. From the above mentioned lists covering the years 1962–1972 four classes of sector boundaries have been selected: 50 boundaries near vernal equinoxes (26 (+/–) and 24 (–/+) polarity-changes) and 48 sector boundaries near autumnal equinoxes (22 (+/–) and 26 (–/+) polarity changes). The dates of the boundary observations are Feb 4–May 17 for the vernal and Aug 13–Nov 23 for the autumnal classes. To have nearly equal numbers in the 4 classes 3 sector boundaries of the last class tabulated in the list for 1964 have been omitted. A superposed epoch analysis was applied to calculate the average K_p indices from 3 days before until 3 days after the sector boundary passage. The K_p variation for the 4 classes are shown in Figures 1 and 2. It is seen from the figures that K_p has a minimum before the boundaries and increases near the boundaries, but the increase is strong for the (+/–) polarity change near vernal equinoxes and for (–/+) changes near autumnal equinoxes and weak for the respective opposite polarity changes.

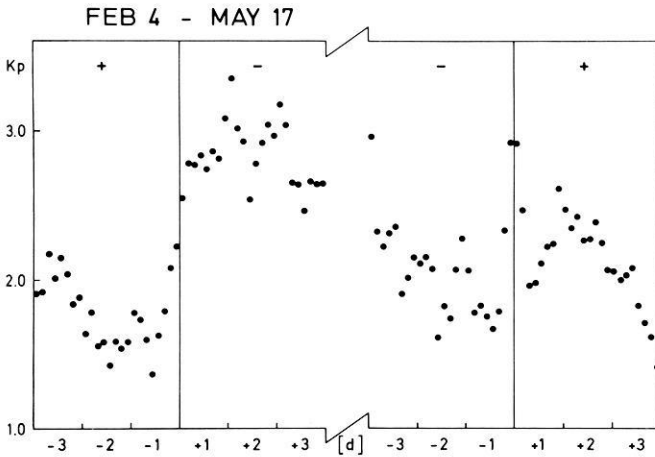


Fig. 1. The average Kp variation at (+/-) and (-/+) sector boundaries near vernal months from 3 days before until 3 days after the boundaries

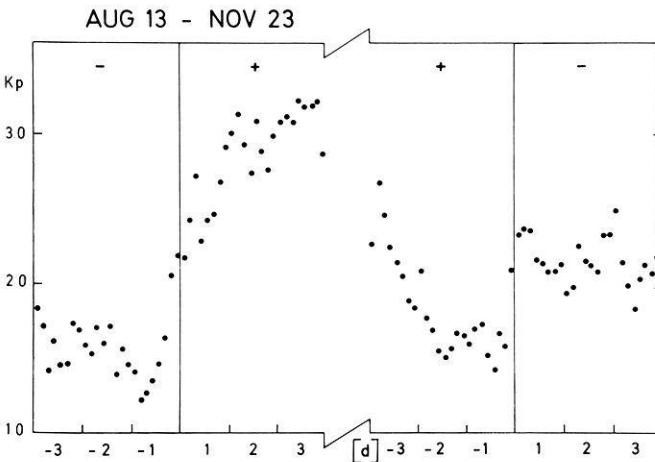


Fig. 2. The average Kp variation at (-/+) and (+/-) sector boundaries near autumnal months from 3 days before until 3 days after the boundaries

Daily averages of Kp for the intervals 36–12 h before and 12–36 h after the IMF polarity change have been calculated. From these values the average Kp increases were found to be:

1.38, vernal (+/-) change; 0.41, vernal (-/+) change;

1.36, autumnal (-/+) change; 0.48, autumnal (+/-) change.

Applying the *t*-test the significance of the polarity-dependent Kp increases can be proven: For the vernal as well as for the autumnal sector boundaries, the probability *P* for the null hypothesis (i.e. that the Kp increase is the same at the 2 sector boundaries) was found to be $P < 10^{-2}$.

Table 1. Dates and 3 h intervals of observed sector boundaries for which IMF measurements are available; (*v*) indicates that also measurements of the solar wind velocity are available

Vernal months		Autumnal months	
+/-	-/+	+/-	-/+
Feb 7, 67, 3-4 (<i>v</i>)	Mch 22, 67, 7-8	Sep 6, 67, 6-7	Oct 30, 66, 5-6
Feb 26, 68, 6-7 (<i>v</i>)	Feb 11, 68, 3-4 (<i>v</i>)	Oct 3, 67, 1-2	Aug 30, 67, 6-7
Mch 23, 68, 5-6 (<i>v</i>)	Mch 10, 68, 4-5 (<i>v</i>)	Aug 21, 68, 2-3	Sep 27, 67, 3-4
Apr 21, 68, 3-4	Apr 5, 68, 6-7 (<i>v</i>)	Sep 19, 68, 2-3	Oct 24, 67, 2-3
May 17, 68, 5-6	May 2, 68, 1-2	Oct 16, 68, 5-6	Aug 13, 68, 7-8

To compare the Kp variations with parameters of the interplanetary medium 5 sector boundaries for every class have been selected for which IMF measurements are available as "Multispacecraft hourly averaged interplanetary magnetic field vectors" on a tape prepared by the National Space Science Data Center (NSSDC), Greenbelt, Maryland, USA. For six of these sector boundaries listed in Table 1 also measurements of the solar wind velocity *v* are available on a NSSDC tape "Hourly averaged interplanetary plasma data".

The Kp variations at these sector boundaries indicate the same features as shown in Figures 1 and 2; therefore we averaged the Kp values of vernal (+/-) boundaries and autumnal (-/+) boundaries and also those of the respective opposite polarity changes. The result is shown in Figure 3 (closed circles) together with averaged threehourly values of IMF magnitude B (open circles). The variation of B is similar at both sector boundaries whereas Kp shows the different variation as it was seen in Figures 1 and 2.

A corresponding comparison of the average variation of Kp and *v* at sector boundaries was not possible because only 6 vernal sector boundaries with measurements of *v* (one of them with some gaps) have been available. Three hourly averages of *v* (omitting the gaps in the averaging procedure) at these sector boundaries are shown in Figure 4 together with the daily averaged Kp values of the day before and after the IMF polarity changes. The Kp increases at the boundaries resemble the increases shown in Figures 1-3 whereas the variation of *v* is quite different with less *v* increase at the (+/-) boundary where the Kp increase is greater. Though Figure 4 does not represent the average behaviour of *v* at vernal sector boundaries it is an example to show that the observed Kp variations are not caused by variations of *v* alone.

Rosenberg and Coleman (1969) found a heliographic latitude dependence of the dominant polarity of the IMF with more days of negative polarity at northern and more days of positive polarity at southern heliographic latitudes in the years 1964-1967. This dominant polarity effect changes sign after sunspot maximum (e.g. Rosenberg, 1975). Supposing that the solar wind velocity *v* is connected with the dominant polarity of the IMF in a way to cause the observed Kp variation of Figures 1-3, the Kp variations also should change after 1970. However, an analysis of Kp at sector boundaries of the years 1970-1972 gave the same results as they are shown in Figures 1-3.

Therefore we suggest that on the average the IMF magnitude B and the

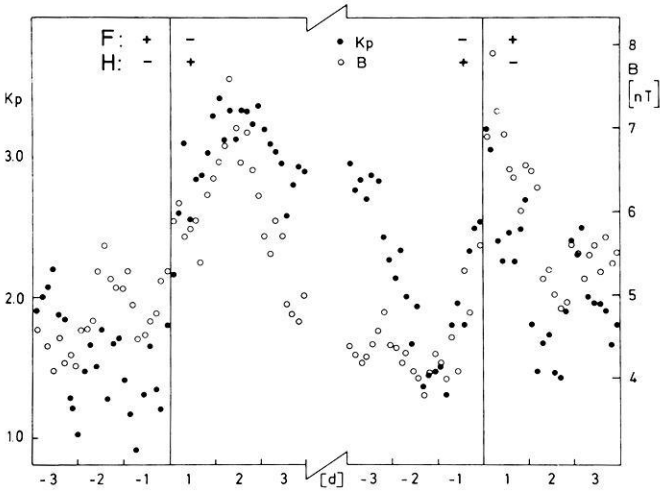


Fig. 3. Average Kp variation (full circles) for vernal $F(+/- \dots -/+)$ and autumnal $H(-/+ \dots +/-)$ boundaries and the respective 3 hourly values of IMF magnitude B (open circles)

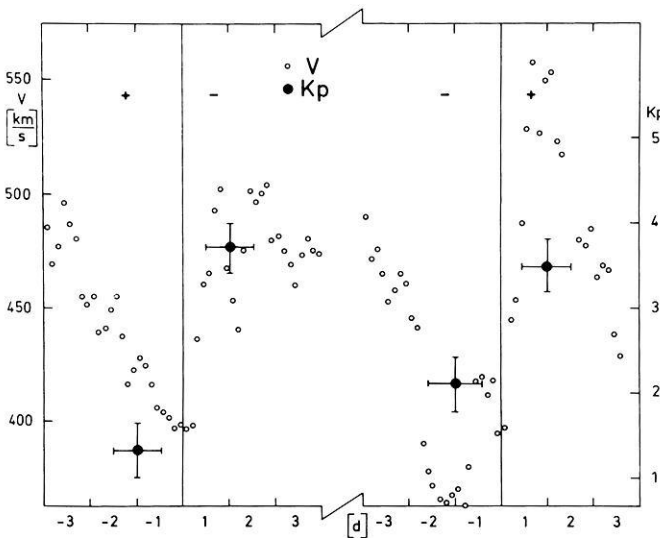


Fig. 4. Variation of 3 hourly values of the solar wind velocity v averaged for 6 vernal sector boundaries with available v data and daily averages of Kp 36–12h before and 12–36h after the boundaries

solar wind velocity v vary similarly at the four classes of sector boundaries and that the variations of these parameters alone do not cause the observed Kp variations.

In the following the influence of individual IMF vector components will be analysed in a somewhat more quantitative manner. The hourly IMF vector components three days before to three days after the 20 sector boundaries listed

Table 2. Changes Δ of 24 h average IMF magnetospheric components, Kp and solar wind velocity v at different sector boundaries (see text)

Season	Vernal months		Autumnal months	
	+/- (I)	-/+ (II)	-/+ (I)	+/- (II)
ΔKp	1.92	0.63	1.53	0.37
ΔB [nT]	1.64	0.60	1.24	3.38
ΔB_{XM} [nT]	3.53	-3.67	-6.67	6.15
$\Delta B_{XM} $ [nT]	0.67	1.91	1.79	1.83
ΔB_{YM} [nT]	-5.07	4.20	5.64	-4.72
$\Delta B_{YM} $ [nT]	0.11	-1.18	0.58	2.60
$-\Delta B_{ZM}$ [nT]	1.59	-1.90	1.71	-1.92
ΔB_{SM} [nT]	1.44	-1.04	1.03	-0.14
Δv [km/s]	$1.10 \cdot 10^2$	$1.10 \cdot 10^2$	$1.10 \cdot 10^2$	$1.10 \cdot 10^2$

in Table 1 have been transformed from the given ecliptic into magnetospheric coordinates (e.g. Russel, 1971). This coordinate system should be used for interaction between the IMF components and the magnetosphere (Hirshberg and Colburn, 1969; Arnoldy, 1971), because here the Z -axis Z_M is connected with the actual direction of the earth's magnetic dipole axis.

From the hourly values daily averages were calculated taking into account 36–12 h before and 12–36 h after the sector boundaries. The differences Δ between these 2 daily means before and after the IMF polarity changes are listed in Table 2 together with the respective average ΔKp -values. The Δv value of 110 km/s listed in Table 2 was assumed to be equal at the four classes of sector boundaries. It was calculated from the averages of the 6 boundaries listed in Table 1 and agrees with the average v increase reported in previous studies (e.g. Wilcox, 1968). In Table 2 B_{XM} and B_{YM} are the average magnetospheric X and Y components of B and B_{ZM} is the average IMF magnetospheric Z component including northward directed hourly values, whereas the southward component B_{SM} is defined as $B_{SM} = -B_{ZM}$ for $B_{ZM} < 0$ and $B_{SM} = 0$ for $B_{ZM} > 0$. This definition implies, when B_{SM} is compared with Kp, that northward directed IMF fields are unimportant for generating geomagnetic activity as Arnoldy's (1971) results indicate.

From the individual lines of Table 2 it can be seen that at the four classes of sector boundaries no parameter shows similar variations as Kp. If for example the Kp variations were influenced only by the B_{ZM} (or B_{SM}) component of the interplanetary magnetic field the ΔKp values at sector boundaries (II) should be negative. Thus at least two parameters must be taken to account for the ΔKp values.

We assume as a first simplified approximation a linear relation between Kp, v and one component B_{KM} (K indicating either one of X , Y , Z or S) of the interplanetary field to describe the variation of Kp at the sector boundaries:

$$\begin{aligned} Kp &= a + bv + cB_{KM} \\ \Delta Kp &= b\Delta v + c\Delta B_{KM}. \end{aligned} \quad (1)$$

At the boundaries (I) and (II) (in Table 2) we have two equations to calculate b and c from ΔKp , Δv and ΔB_{KM} . The coefficients b and c for sector boundaries near vernal months should approximately equal those for autumnal months. The calculations show that this condition is only satisfied, if we choose the Z -component $\Delta B_{KM} \equiv -\Delta B_{ZM}$ or $\Delta B_{KM} \equiv \Delta B_{SM}$.

In the first case we get $b_F=1.2$ (vernal), $b_H=0.90$ (autumnal), $b_M=1.1$ (average) and $c_F=0.37$, $c_H=0.32$, $c_M=0.34$ respectively. Assuming $\Delta B_{KM} \equiv \Delta B_{SM}$ we get $b_F=1.1$, $b_H=0.60$, $b_M=0.82$ and $c_F=0.52$, $c_H=0.85$, $c_M=0.67$, where in Equation(1) v is measured in units of 10^2 km/s and the IMF component in Nanotesla, $1 nT=1\gamma$. Though the vernal and autumnal coefficients seem to agree better for $\Delta B_{KM} \equiv -\Delta B_{ZM}$ this simple analysis cannot decide whether the average magnetospheric Z component B_{ZM} or the average southward directed component B_{SM} (ignoring northward directed fields) is the appropriate IMF parameter.

Using the absolute daily averages of Kp , v and B_{SM} and after the sector boundaries the coefficient a of Equation(1) may be calculated and we get with the data of 20 sectors listed in Table 1 an average relation

$$Kp = -2.38 + 0.82v + 0.67B_{SM}; \quad v[10^2 \text{ km/s}], \quad B_{SM}[nT]. \quad (2)$$

Independently a linear regression was calculated with daily averages of 120 days for which hourly IMF and solar wind velocity data have been available. The result

$$Kp = -1.89 + 0.81v + 0.50B_{SM} \quad (3)$$

is similar to relation (2) indicating that at least the coefficients for v and B_{SM} of the relation between Kp , v and B_{SM} are similar on days near sector boundaries and on all days.

Discussion

The polarity- and season-dependent Kp increase at sector boundaries shown in Figures 1 and 2 is explained by the influence of the southward IMF component in magnetospheric coordinates and it is shown that some other IMF parameters as the magnetospheric X - and Y -components are less important to account for the observed Kp variations. The variation of the average three hourly B_{SM} component near sector boundaries is illustrated in Figure 5: At the left boundaries we see a sharp increase of B_{SM} and this in addition to an increasing v results in the great Kp -increase at the corresponding boundaries. At the right boundaries B_{SM} is slightly decreasing, and this in addition to an increasing v (assumed to equal the v increase at the left boundaries) results in a slight Kp increase. The simple linear relation (2) describing our interpretation should not be overestimated because it only includes the influence of v and one IMF component. Equation(2) is regarded only as an average relation of Kp , v and B_{SM} for daily means; errors of the constants may be estimated by a comparison of the coefficients in (2) and (3). Calculating in an analogous manner the coefficients b and c in Equation(1) for the 6 vernal (+/-) and (-/+) boundaries with available IMF and v data we obtained coefficients differing to a

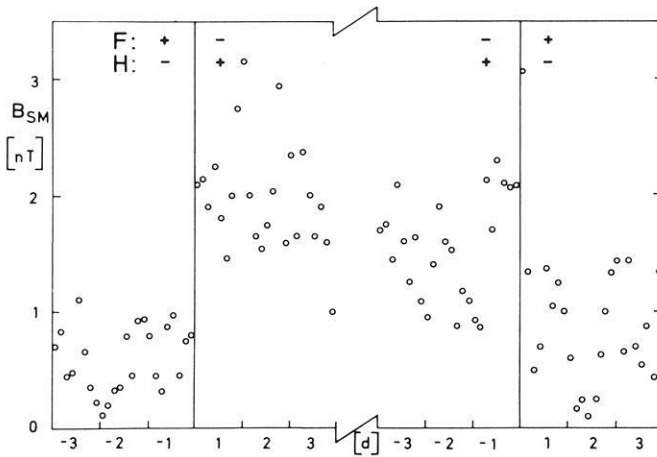


Fig. 5. Three hourly values of the southward magnetospheric IMF component B_{SM} ; averages of vernal $F(+/- \dots -/+)$ and autumnal $H(-/+ \dots +/-)$ boundaries

certain degree from those in (2). Assuming $B_{KM} \equiv B_{SM}$, we obtained $b_F = 1.4$ and $c_F = 0.82$, indicating that the assumed linear relation is not valid for all activity ranges, or that other parameters have to be included for a better description. However, these calculations also showed that the southward component should be included in the explanation of Kp. An exact error calculation for the coefficients in (2) is not possible with the few v data of only 6 sector boundaries.

The variation of IMF fluctuations and their possibly additional effects on geomagnetic activity as it was shown by Garrett (1974) is not examined and discussed here, and it is not excluded that IMF fluctuations may also be important for an explanation of the observed Kp variation. In the vicinity of the right sector boundaries of Figure 5 for example we find very high B_{SM} values which might be related to enhanced fluctuations at the boundaries, and corresponding high Kp values are seen in Figures 2 and 3 at the right boundaries.

The observed Kp variations at sector boundaries are in agreement with the hypothesis of Russel and McPherron (1973) to explain the different annual variation of geomagnetic activity for the two IMF polarities: Figures 1 and 2 show the predicted enhanced activity during vernal (-) sectors and autumnal (+) sectors. This should lead to an annual variation with vernal maximum for (-) and autumnal maximum for (+) sectors.

In a recent study Burton et al. (1975) relate the D_{st} index as a measure of the magnetospheric ring current to v and the product $v \cdot B_{SM}$. A corresponding relation of Kp being a linear function of v and $v \cdot B_{SM}$ also may explain the Kp variation of Figures 1 and 2 as it was examined by similar calculations as in the previous section. Thus we conclude that a relation of geomagnetic activity and parameters of the interplanetary medium should include the influence of the IMF southward component; however, it is also seen that the southward component is not the only parameter controlling geomagnetic activity. Theoretically the influence of the IMF southward component is described with merging models of interplanetary and geomagnetic field lines (e.g. Vasyliunas, 1975, for a review).

Acknowledgements. I would like to thank Prof. M. Siebert for helpful discussions. The IMF data and the interplanetary plasma data have been provided by the World Data Center, Greenbelt, Maryland, USA. The numerical calculations were carried out on the computer of the Gesellschaft für wissenschaftliche Datenverarbeitung, GWD, Goettingen.

References

- Arnoldy, R.L.: Signature in the interplanetary medium for substorms. *J. Geophys. Res.* **76**, 5189–5201, 1971
- Ballif, J.R., Jones, D.E., Coleman, P.J.: Further evidence on the correlation between transverse fluctuations in the interplanetary magnetic field and Kp. *J. Geophys. Res.* **74**, 2289–2301, 1969
- Berthelier, A., Berthelier, J.J., Guérin, C.: The effect of the east-west component of the interplanetary magnetic field on magnetospheric convection as deduced from magnetic perturbations at high latitudes. *J. Geophys. Res.* **79**, 3187–3192, 1974
- Burton, R.K., McPherron, R.L., Russel, C.T.: An empirical relationship between interplanetary conditions and D_{st} . *J. Geophys. Res.* **80**, 4204–4213, 1975
- Fairfield, D.H., Ness, N.F.: Interplanetary sector structure 1970–1972. *J. Geophys. Res.* **79**, 5089–5094, 1974
- Friis-Christensen, E., Lassen, K., Wilhelm, J., Wilcox, J.M., Conzalez, W., Colburn, D.: Critical component of the interplanetary magnetic field responsible for large geomagnetic effects in the polar cap. *J. Geophys. Res.* **77**, 3371–3376, 1972
- Garrett, H.B.: The role of fluctuations in the interplanetary magnetic field in determining the magnitude of substorm activity. *Planet. Space Sci.* **22**, 111–119, 1974
- Hirshberg, J., Colburn, D.S.: The interplanetary field and geomagnetic variations—A unified view. *Planet. Space Sci.* **17**, 1183–1206, 1969
- Hirshberg, J., Colburn, D.S.: Geomagnetic activity at sector boundaries. *J. Geophys. Res.* **78**, 3952–3957, 1973
- Ness, N.F., Wilcox, J.M.: Interplanetary sector structure 1962–1966. *Solar Phys.* **2**, 351–359, 1967
- Neugebauer, M.N., Snyder, C.W.: Mariner 2 observations of the solar wind. 1. Average properties. *J. Geophys. Res.* **71**, 4469–4494, 1966
- Neugebauer, M.N., Snyder, C.W.: Mariner 2 observations of the solar wind 2. Relation of Plasma properties to the magnetic field. *J. Geophys. Res.* **72**, 1823–1828, 1967
- Rosenberg, R.L., Coleman, P.J. Jr.: Heliographic latitude dependence of the dominant polarity of the interplanetary magnetic field. *J. Geophys. Res.* **74**, 5611, 1969
- Rosenberg, R.L.: Heliographic latitude dependence of the IMF dominant polarity in 1972–1973 using Pioneer 10 data. *J. Geophys. Res.* **80**, 1339–1340, 1975
- Russel, C.T.: Geophysical coordinate transformations. *Cosmic Electrodynamics* **2** (2), 184–196, 1971
- Russel, C.T., McPherron, R.L.: Semiannual variation of geomagnetic activity. *J. Geophys. Res.* **78**, 92–108, 1973
- Shapiro, R.: Geomagnetic activity in the vicinity of sector boundaries. *J. Geophys. Res.* **79**, 289–291, 1974
- Vasyliunas, V.M.: Theoretical model of magnetic field line merging, 1. *Rev. Geophys. Space Phys.* **13**, 303–336, 1975
- Wilcox, J.M., Ness, N.F.: Quasi-stationary corotating structure in the interplanetary medium. *J. Geophys. Res.* **70**, 5793–5805, 1965
- Wilcox, J.M., Schatten, K.H., Ness, N.F.: Influence of interplanetary magnetic field and plasma on geomagnetic activity during quiet-sun conditions. *J. Geophys. Res.* **72**, 19–26, 1967
- Wilcox, J.M.: The interplanetary magnetic field. Solar origin and terrestrial effects. *Space Sci. Rev.* **8**, 258–328, 1968
- Wilcox, J.M., Colburn, D.S.: Interplanetary sector structure in the rising portion of the sunspot cycle. *J. Geophys. Res.* **74**, 2388–2392, 1969
- Wilcox, J.M., Colburn, D.S.: Interplanetary sector structure near the maximum of the sunspot cycle. *J. Geophys. Res.* **75**, 6366–6370, 1970
- Wilcox, J.M., Colburn, D.S.: Interplanetary sector structure at solar maximum. *J. Geophys. Res.* **77**, 751–756, 1972
- Wilcox, J.M., Svalgaard, L., Hedgecock, P.C.: Comparison of inferred and observed interplanetary magnetic field polarities, 1970–1972. *J. Geophys. Res.* **80**, 3685–3688, 1975

Probleme bei der Untersuchung von räumlich und zeitlich veränderlichen Medien, dargestellt am Beispiel der Ionosphäre

W. Dieminger und G.K.Hartmann

Max-Planck-Institut für Aeronomie,
Postfach 80, D-3411 Katlenburg-Lindau 3, Bundesrepublik Deutschland

Problems in the Investigation of Space and Time Dependent Media Exemplified by the Ionosphere

Zusammenfassung. Die meisten in der Geophysik gewonnenen Daten sind vom Beobachtungsort und von der Beobachtungszeit abhängig. Anders als viele in der Laborphysik gewonnenen Daten, die ebenfalls räumlich und zeitlich veränderlich sein können, sind die meisten dieser geophysikalischen Daten zusätzlich *nicht reproduzierbar*, d.h. die gleichen Bedingungen, die zur Zeit t am Ort x bei der Messung herrschten, sind bei keiner folgenden Messung wiederherstellbar. Das zwingt die Geophysiker oft zur Messung langer Zeitreihen, deren Auswertung zu den unterschiedlichsten und zum Teil sehr komplexen Problemen führt. Einige Beispiele aus der Geschichte der Ionosphärenforschung, chronologisch geordnet und ergänzt durch einige ganz aktuelle Fragestellungen, verdeutlichen dies.

Abstract. Most data obtained in geophysics is dependent upon the time t and the location x where the measurement was carried out. In addition to the majority of data obtained in laboratory physics which may also be dependent upon space and time, most of the geophysical data is *non reproducible*. This means that the conditions at the time t and location x of the first measurement cannot be reproduced at any subsequent measurement. This implies very often that in geophysics long time series have to be measured which leads to different and partly very complex problems. This is illustrated by some examples from the history of ionospheric research supplemented by some very recent open questions in this field.

Key words: Time and space dependent data — Long-time series — Ionosphere.

Anmerkung des Herausgebers. Nicht reproduzierbare geophysikalische Daten werden seit geraumer Zeit hauptsächlich von den World Data Centers (WDC's) gesammelt. Neuerdings beschäftigt sich auch das Committee on Data for Science and Technology (CODATA) damit. Die vorliegende Arbeit ist ein Beitrag zu der aktuellen Diskussion über die Gestaltung der neu gegründeten bzw. geplanten Fachinformationssysteme (FIS) der Bundesrepublik Deutschland

Es gibt in der Geophysik Daten, die lediglich vom Beobachtungsort oder von der Beobachtungszeit abhängig sind. Ein Beispiel für reine Ortsabhängigkeit ist die geographische Position, die — jedenfalls in geschichtlichen Zeiträumen — gänzlich unabhängig von der Beobachtungszeit ist. Daneben gibt es viele Erscheinungen, die sowohl zeit- als auch ortsabhängig sind.

In der Geophysik sind diese Daten — im Gegensatz zu der Laborphysik — meistens zusätzlich auch nicht reproduzierbar.

Bemerkung: Daten sind reproduzierbar, wenn die gleichen Bedingungen, die zur Zeit t_1 am Ort x_1 bei der Messung herrschten, auch bei jeder folgenden Messung wiederherstellbar sind. Gilt dies nicht, sind die Daten nicht reproduzierbar [1]. In der Laborphysik gibt es viele Daten, z.B. die von den verschiedensten Wellenvorgängen, die orts- und/oder zeitabhängig sind, die jedoch reproduzierbar sind, da sie im Labor unter wohl definierten Bedingungen ablaufen. Im Gegensatz zur Geophysik benötigt man hier zur Erklärung der physikalischen Phänomene keine Zeitreihen, bei denen jede Beobachtung sowohl aus einer quantitativen Maßangabe bestehen muß als auch aus einer Angabe über die Zeit, zu welcher diese Maßzahl bestimmt wurde. Bei geophysikalischen Zeitreihen mit ihren spezifischen statistischen Eigenschaften ist außerdem zu beachten, daß sich viele der Standardverfahren der mathematischen Statistik nur mit Vorbehalt oder gar nicht anwenden lassen. Die Entwicklung adäquater statistischer Modelle und Methoden ist also von größter Wichtigkeit, kann aber wiederum nicht ohne Rückgriff auf die konkreten Beobachtungsreihen erfolgen. Die folgende Tabelle 1 zeigt einen Teil der Informationen auf, die man benötigt, wenn man nicht reproduzierbare, räumlich und zeitlich veränderliche Daten optimal miteinander vergleichen und im weitesten Sinn bewerten will.

Im einfachsten Fall ist die räumliche und zeitliche Abhängigkeit einer Größe durch ein einfaches Gesetz beschreibbar, z.B. der Elevationswinkel der Sonne durch die Geometrie, die durch Tageszeit und geographische Breite bedingt ist. Es gibt jedoch auch Fälle, in denen solche einfachen Gesetzmäßigkeiten nicht mehr feststellbar sind, in denen sich z.B. der Zeitablauf in schwer überschaubarer Weise mit dem Beobachtungsort ändert. Solche Daten stellen naturgemäß an die Beobachtungstechnik und an die analytische Darstellung besondere Anforderungen.

Zu diesen Erscheinungen gehört zweifellos der Zustand der Ionosphäre, ausgedrückt durch Parameter wie Elektronendichteverteilung und Gesamtelektroneninhalt. Dieser Tatbestand war zu Beginn der Ionosphärenforschung nicht bekannt. Ließ sich doch theoretisch eine einfache Beziehung zwischen der Elektronenproduktion durch das ultraviolette Sonnenlicht und dem Erhebungswinkel der Sonne ableiten. Dieser Konzeption entsprach es, daß man zunächst versuchte, mit 3 Beobachtungsstationen auszukommen: Washington D.C. auf der Nordhalbkugel; Huancayo, Peru, in der äquatorialen Zone und Watheroo/Australien auf der Südhalbkugel. Immerhin trug man mit der Einsetzung von 3 Stationen bereits dem Gesichtspunkt Rechnung, daß neben der Abhängigkeit vom Sonnenstand, der seinerseits ortsabhängig ist, eine weitere direkte Ortsabhängigkeit vorhanden sein könnte. Außerdem zeigte die Theorie, daß der Polari-

Tabelle 1. Benötigte Informationen für optimale Vergleiche von verschiedenen orts- und zeitabhängigen, nicht reproduzierbaren Daten

-
- I. Unmittelbare(r) Fach- und/oder Sachbereich(e) der Meßdaten
 - II. Gemessene Effekte
 - a. Bezeichnung der Effekte
 - b. Punktmessung: Meßdaten stammen von einer punktförmigen „Quelle“
 - c. Linienmessung: Daten werden längs einer Linie, z.B. Satellitenbahn, gemessen
 - d. Flächenmessung: Daten stammen von einer Fläche im Raum
 - e. Volumenmessung: Daten stammen aus einem Volumen
 - f. Integraler Meßwert: Der Meßwert entsteht durch Integration über Linien-, Flächen- oder Volumenelemente
 - g. In situ Messung: Meßgeräte befinden sich jeweils am Ort der Meßgröße
 - h. Remote Sensing: Meßgeräte befinden sich entfernt vom Ort der Meßgröße
 - III. Aus II abgeleitete Parameter
 - a. direkt
 - b. indirekt
 - c. durch Korrelation mit anderen Daten
 - d. Auswertegenauigkeit
 - e. Gesamtfehler: Meßfehler + Auswertefehler
 - IV. Zeiträume, für die auswertbare und/oder ausgewertete Daten zur Verfügung stehen
 - V. Art der Datenaufzeichnung
 - a. Analog mit dafür charakteristischem Auflösungsvermögen
 - b. Digital mit dafür charakteristischem Auflösungsvermögen
 - c. Datenfernübertragung
 - d. Zahl der betriebenen Meßstationen
 - VI. Zugriff zu den Daten
 - a. Beim Institut, das die Messung durchgeführt hat (ja, nein)
 - b. Bei nationalen Datenzentren (ja, nein)
 - c. Bei internationalen Datenzentren (WDCs usw.) (ja, nein)
 - d. Falls b. nein: Frage: „Ist es für die Zukunft geplant?“
 - e. Falls c. nein: Frage: „Ist es für die Zukunft geplant?“
 - f. Art der Zugriffsmöglichkeit
 - VII. Meßgerätecharakteristiken
 - a. Meßbereiche
 - b. Auflösungsvermögen des Meßgerätes, Empfindlichkeiten
 - c. Meßfehler
 - d. Raumauflösung
 - VIII. Ökonomische Fragen
 - a. Industriell in größerer Stückzahl gefertigte Geräte (Serienfertigung)
 - b. Industriell gefertigtes Gerät (Einzelfertigung)
 - c. Forschungsmuster in der Erprobung
 - d. Labormuster
 - e. Kombination aus a – d
 - f. Entwicklungskosten, Entwicklungszeit
 - g. Betriebskosten einer Einzelstation
 - h. Betriebskosten eines Meßnetzes
 - IX. Welche schriftlichen Unterlagen existieren über die Meßgeräte sowie die Datenverarbeitung (Aufbereitung und Auswertung)?
 - X. Welche wissenschaftlichen Publikationen existieren?
-

sationszustand reflektierter Wellen von der Orientierung des erdmagnetischen Feldes abhängt.

Tatsächlich zeigte der Vergleich der Beobachtungen, daß für die E-Schicht der Ionosphäre (100–140 km) die einfache Theorie in guter Näherung anwendbar ist. Dagegen wurden für die F-Schicht (200–400 km) große Abweichungen beobachtet. Es fehlte in den 20er und 30er Jahren nicht an Versuchen, aus den Beobachtungsdaten der drei genannten Stationen die Gesetzmäßigkeiten dieser Ortsabhängigkeit wenigstens empirisch zu ermitteln. Das gelang einigermaßen für den sog. mittleren Tages- und Jahresgang – später kam noch die Abhängigkeit von der Sonnenaktivität hinzu. Versuchte man aber diese zeitlichen Gänge auf andere geographische Positionen zu übertragen, so ergaben sich gravierende Differenzen zwischen erwarteten und beobachteten Werten. Es blieb schließlich nichts anderes übrig, als auf Grund eines relativ dichten Netzes von etwa 200 Beobachtungsstellen eine weltweite Darstellung der mittleren Beobachtungswerte zu zeichnen und „weiße Flecken“ durch Interpolation auszufüllen. Auch dabei ergaben sich noch beträchtliche Abweichungen von der Realität. Bot schon die Darstellung der mittleren Werte beträchtliche Schwierigkeiten, so verstärkten diese sich bei den Tag zu Tag-Schwankungen, die man – soweit sie mit bestimmten solarerrestrischen Ereignissen verknüpft sind – als Störungen der Ionosphäre bezeichnet. Einigermaßen übersehbar sind nur die Veränderungen, die durch chromosphärische Eruptionen von UV- und Röntgenstrahlung bedingt sind. Hier ist der Effekt proportional dem Elevationswinkel der Sonne und der Stärke der Eruption auf der Sonne. Beim Eindringen von Korpuskeln in die Polarlichtzonen sind die Veränderungen nicht nur von der Intensität des Ereignisses und von der magnetischen Breite, sondern auch von der Ortszeit oder mit anderen Worten der magnetischen Länge abhängig. Wohl erkennt man gewisse Grundzüge im Ablauf solcher Störungen, aber es gibt wohl kaum zwei, die im einzelnen völlig identisch ablaufen würden.

Daß korpuskulare Störungen erheblich vom Ort abhängen, ist verständlich, da hier die erzeugende Ursache bereits starke lokale Variationen aufweist. Da die gestörten Zeiten in die Mittelwertbildung eingehen, sind auch bei diesen schon aus diesem Grunde ortsabhängige Variationen, die nicht durch den Sonnenstand bedingt sind, zu erwarten. Aber auch die Mittelwerte der „ungestörten“ Zeiten gehorchten nicht dem Sonnenstandgesetz. So gelang es z.B. nicht, die Tagesgänge der Nordhalbkugel mit einer Zeitverschiebung von 6 Monaten auf die Südhalbkugel zu übertragen. Ebenso wenig steigt die maximale Elektronenkonzentration der F-Schicht mit abnehmender Breite bis zum Äquator an. Tatsächlich fand man zwei Maxima in etwa 20° nördlicher und südlicher Breite und einen Trog längs des Äquators. Dabei ist die Symmetrielinie nicht der geographische, sondern der magnetische Äquator. Das war ein deutlicher Hinweis, daß das Erdmagnetfeld nicht nur hinsichtlich der Polarisierung, sondern auch in der Bilanz der Elektronenproduktion eine wichtige Rolle spielt.

Der Schlüssel zum Verständnis der Zusammenhänge lag in der Idee, daß neben der Produktion durch unsichtbare Sonnenstrahlung und dem Verlust durch Wiedervereinigung und Ablagerung der Elektronen Transportvorgänge eine wichtige Rolle im F-Gebiet der Ionosphäre spielen. Mathematisch drückt sich das durch die Einführung eines Divergenz-Terms in die Kontinuitätsglei-

chung aus. Horizontale Strömungen des Plasmagases in der hohen Atmosphäre unter der Wirkung von Gezeitenkräften sind vorstellbar, ihre Wirkung reicht aber keinesfalls aus, um die beobachteten kräftigen Effekte zu erklären. Man mußte vielmehr eine vertikale Drift der Elektronen annehmen, die dafür sorgt, daß diese in ein Höhengebiet mit höheren oder niedrigeren Verlusten gebracht werden. Hierbei genügten relativ geringe Verschiebungen, um die beobachteten Effekte zu erklären. Nun zeigt die Theorie, daß in einem dünnen Plasma, wie es im F-Gebiet der Ionosphäre vorhanden ist, das Magnetfeld eine Vorzugsrichtung für die geladenen Teilchen bestimmt: die Elektronen können sich nur längs des Magnetfeldes verschieben. Quer zum Magnetfeld werden sie zum Kreisen um die Feldlinien gezwungen. Hat die horizontale Bewegung des Ionosphären-gases eine Nordsüdkomponente, so führt dies wegen der Neigung der Magnetfeldlinien (Inklination) zu einer vertikalen Drift der Elektronen. Diese Hypothese erwies sich als außerordentlich fruchtbar, vor allem als man entdeckte, daß neben den Gezeitenwinden weitere Bewegungsvorgänge in der Ionosphäre vorhanden sind, die durch die ungleichmäßige Erwärmung der hohen Atmosphäre im Tagesablauf entstehen. Unter ihrer Wirkung strömt Ionosphären-gas, wobei es gleichzeitig von der Coriolis-Kraft abgelenkt wird, von einem warmen Hochdruckgebiet auf der belichteten Halbkugel zu einem kalten Tief auf der Nachtseite. Darnach könnte man erwarten, daß zwei Orte mit gleicher geographischer Breite und gleicher Inklination den gleichen ungestörten Tagesverlauf aufweisen. Daß dies nicht der Fall ist, konnte durch eine Verfeinerung der Theorie erklärt werden: Neben der Inklination hat auch die Deklination, also die Abweichung der Magnetfeldlinien von der Meridianrichtung, einen Einfluß. Da es kaum zwei Orte gibt, bei denen geographische Breite, Inklination und Deklination identisch oder komplementär sind, hat praktisch jeder Punkt auf der Erde seine individuelle Ionosphäre.

Unter diesen Umständen verzichtet man darauf, eine theoretisch gestützte Darstellung des weltweiten mittleren Zustandes der Ionosphäre anzustreben. Man begnügt sich vielmehr damit, praktisch wichtige Parameter der Ionosphäre, wie die Elektronendichte als Funktion der Höhe, auf Grund von Beobachtungen zu kartieren. Dabei sind Extrapolationen nur auf relativ kurze Entfernungen (≤ 1000 km) praktikabel. Diese Mittelwerte zeigen nun langfristig ($T \geq 100$ Tage) einen recht deutlichen Zusammenhang mit der Sonnenaktivität, wobei der „Hub“ allerdings auch wieder von Ort zu Ort erheblich verschieden ist und empirisch bestimmt werden muß. Hierauf beruht im wesentlichen die heute praktizierte Vorhersage von Ionosphärenparametern und daraus abgeleiteten Ausbreitungsbedingungen der Kurzwellen. Im „Störungsfall“ ist natürlich mit erheblicher Abweichung zu rechnen. Nun besteht zwar bei den Störungen, die durch solare Korpuskeln verursacht werden, ein Zusammenhang mit der Stärke der solaren Strahlung und eine Abhängigkeit von der geomagnetischen Breite. Ersteres ist wegen einer gewissen Voreilung der erdmagnetischen Störung bedingt ausnutzbar. Letzteres hat Bedeutung für die Planung, wenn die Möglichkeit besteht, stark gestörte Gebiete, nämlich die Polarlichtzonen, zu umgehen. Beobachtungen, die erst die Raumfahrt ermöglichte, haben aber gezeigt, daß neben den Veränderungen, die korpuskularen Effekte zugeordnet werden können, auch solche bestehen, deren Ursache in vermutlich meteorologisch bedingten Variatio-

nen der Zusammensetzung des Gases in der hohen Atmosphäre gesucht wird. So zeigt die Elektronendichte in der unteren Ionosphäre (60–90 km) Tag zu Tag-Schwankungen, die offenbar durch die mesosphärische Zirkulation gesteuert werden. Auch der totale Elektroneninhalt und seine örtlich-zeitliche Variation zeigt unerwartete Tag zu Tag-Schwankungen, deren Ursprung noch unklar ist.

Insgesamt kann die Ionosphäre als Paradebeispiel für ein örtlich-zeitlich veränderliches Medium gelten. Dabei ist die Anzahl der Wirkungsmechanismen so groß, daß eine rein theoretische Beschreibung zumindest z.Z. noch nicht möglich ist. Genau wie in der Meteorologie kann man auf eine laufende Beobachtung im Hinblick auf die praktische Anwendung und die weitere Erforschung nicht verzichten.

Dabei sehen wir uns folgender Problematik gegenüber. Wir finden zwar mit wachsender Länge der Zeitreihen, ergänzt durch neuartige Messungen, Antworten auf einige Teilfragen, können jedoch dabei nicht unbedingt damit rechnen, daß wir damit schon ein großes Stück vorangekommen sind in unserem Bemühen, ein widerspruchsfreies Gesamtbild des so komplexen Mediums Ionosphäre zu zeichnen. Im Gegenteil, wir scheinen mit der Beantwortung jeder dieser Teilfragen gleich mehrere neue Fragen aufzuwerfen. Aus ökonomischen Gründen und wegen der beschränkten Datenverarbeitungskapazitäten führt dies zu einigen großen Problemen, deren Natur wir gerade erst zu erkennen beginnen.

Welche Konsequenzen ergeben sich für die weitere Beobachtung und Erforschung der Ionosphäre? Zunächst die Anwendung auf die Vorhersage der Kurzwellenausbreitung. Die langfristige und mittelfristige Prognose, die nur auf Mittelwerte ausgerichtet ist, besteht in einer Extrapolation ausreichend langer Zeitreihen auf die Zukunft. Hier sind die Zusammenhänge mit der Sonnenaktivität genügend gesichert. Das Problem ist hier eine sichere Voraussage der Sonnenaktivität. Die Fortsetzung der ionosphärischen Beobachtungen hat hier in erster Linie die Funktion einer laufenden Kontrolle.

Bei den Störungen greift man auf die ebenfalls gesicherten Zusammenhänge zwischen erdmagnetischen und ionosphärischen Störungen zurück, die beide auf die gleiche Ursache, nämlich Eindringen solarer Korpuskeln in die hohe Atmosphäre, zurückgehen. Hier sind noch Verbesserungen durch die Erforschung der Prozesse zu erwarten, die sich auf der Sonne, im interplanetaren Raum und in der hohen Atmosphäre abspielen. Hier sind kontinuierliche koordinierte Beobachtungen unabdingbar, da sonst die Gefahr besteht, daß gerade die interessantesten Ereignisse verfehlt werden. Der behauptete Zusammenhang mit Planeten-Konstellationen wäre ebenfalls durch weitere Beobachtungen zu prüfen. Noch am Anfang steht die Forschung hinsichtlich der aeronomisch-meteorologischen Zusammenhänge, wobei hier nicht nur die Meteorologie der Tropo- und Stratosphäre, sondern der Zustand der Neutralgashülle bis in die untere Magnetosphäre einzuschließen ist. Die Rolle der Ionosphäre im GHz-Bereich bedarf vordringlich einer gründlichen Klärung wegen der Auswirkung speziell in der Funknavigation mit Hilfe von Satelliten. Hier ist wohl der Einfluß erkannt, das Ausmaß der zu erwarteten Fehler als Funktion von Tageszeit und geographischer Position noch festzulegen.

In der Grundlagenforschung ist ein Hauptanliegen die Erfassung der Vorgänge in der gesamten Atmosphäre von der Troposphäre bis zur Magnetopause.

Hier verspricht eine Koordinierung der verschiedenen Methoden, bodengebundene und trägergebundene Ergebnisse, die merklich über den bisherigen Stand der Erkenntnisse hinausgehen. Methoden zur künstlichen Beeinflussung der Ionosphäre können durch dosierbare Veränderung *eines* Parameters das komplexe Geschehen, das die Natur in den verschiedensten Variationen durchspielt, durchsichtiger machen. Es ist auch zu erwarten, daß die Erforschung der Planeten-Ionosphären gerade wegen der abweichenden Bedingungen neue Anregungen für die Deutung der Vorgänge in der irdischen Ionosphäre gibt.

Literatur

1. Hartmann, G.K.: Why do we need data, what are data, what principal data evaluation problems have to be considered? Wird veröffentlicht als ZAED-Report (Zentralstelle für Atomkernenergie Dokumentation, 7514 Eggenstein-Leopoldshafen), 1977

Eingegangen am 1. November 1976

Heat Flow Map of the Bohemian Massif

Vladimír Čermák

Geophysical Institute, Czechoslovak Academy of Sciences,
141 31 Praha, Boční II/1a, Czechoslovakia

Abstract. The heat flow pattern of the Bohemian Massif is presented by the compilation of 47 heat flow values. The isolines of the geothermal activity were constructed using also data in the neighbouring countries. A clear relationship between heat flow and the tectonic structure can be observed, higher geothermal activity corresponds to the zones of the weakened earth's crust coinciding with two major deep faulted zones bordering the most rigid central part of the whole massif.

Key words: Geothermics – Heat flow – Bohemian Massif.

The Bohemian (Czech) Massif is an approx. lozenge-shape consolidated segment of the Variscides (part of Meso-Europe) situated in Central Europe. Tectonically the Bohemian Massif represents a platform-type block, genetically and structurally complicated, emerging in a form of a horst from the surrounding area. In the south and south-east the massif submerges below the Neogene foredeep of the Alpine-Carpathian Neogenic belt, in the west it is limited by a number of faults separating it from the Mesozoic of the Bavarian plate and in the north and north-east it is bordered by Permian and Triassic sediments of the Palaeozoic platform (North-German – Polish Lowland).

Already the first geothermal measurements in the Bohemian Massif revealed the characteristic heat flow pattern (Čermák, 1968). At present there are 47 heat flow determinations in the Czechoslovak part of the massif (Čermák, 1976); additional information was obtained from geothermal measurements in or close to the marginal parts on the territories of the Federal Republic of Germany (Haenel, 1971), Austria (Haenel and Zoth, 1973), German Democratic Republic (Hurtig and Schlosser, 1975) and Poland (Majorowicz, 1973). Extensive heat flow investigation revealed the heat flow field along the Carpathian Frontal Foredeep (Čermák, 1975 b), the contact zone between the Bohemian Massif and the Western Carpathians.

The mean heat flow in the Bohemian Massif is 67.9 mWm^{-2} (i.e. $1.62 \mu\text{cal}$

Table 1. Heat flow in the Bohemian Massif

Region	Number of data	Mean heat flow		Standard deviation mWm^{-2}	Standard error mWm^{-2}
		$\mu\text{cal/cm}^2\text{s}$	mWm^{-2}		
Intramontane stable block	14	1.40	58.6	6.5	1.7
Cretaceous Table	20	1.70	71.4	12.8	2.9
Area of intensive Variscan tectogenesis	10	1.76	73.8	11.5	3.6
Total	44	1.62	67.9	12.4	1.9

cm^2s), when 3 anomalous values from the hydrothermally disturbed area of Teplice (Čermák, 1967) were excluded. More statistics of the mean heat flow values within the Bohemian Massif can be found in Table 1.

Figure 1 shows the heat flow map of the Bohemian Massif. The lowest heat flow was observed in southern and central parts, i.e. in areas where the crustal thickness reaches its maximum value of about 40 km (Beránek and Dudek, 1972). The characteristic heat flow value in the so-called stable intramontane block, which forms the nucleus and the most rigid part of the whole massif (Zoubek and Malkovský, 1974), is 50–60 mWm^{-2} . Generally the heat flow is increasing in all directions as the crustal thickness is decreasing. To the north-west and to the north-east the central part is bounded by two zones of the relatively weakened crust (32–34 km), which separate the stable intramontane block from the area of intensive Variscan tectogenesis. Both these zones, called rift structures by Kopecký (1972), are typical with increased geothermal activity.

In the Labe rift zone or in the Bohemian Cretaceous Table in the north-eastern Bohemia the highest heat flow values group into a belt which roughly coincides with the axis of the whole sedimentation basin (Čermák et al., 1968). This zone is believed to represent an old tectonic suture in the frontal area of the Caledonian range and it has been steadily subsiding relatively to the adjacent regions since the Late Palaeozoic.

The geothermal activity in the north-western part of the Bohemian Massif is also higher and is probably connected with higher content of radioactive matter in the basement rocks of the Krušné Hory Mts. The igneous rocks forming the roots of the mountains and some Late Variscan granitic plutons belong to the most radioactive rocks of the Bohemian Massif (Matolín, 1970). There are no direct data on the heat flow inside the Krušné Hory graben (Ohře rift zone), however, in view of the deep structure the situation here is similar to, that beneath the Cretaceous Table and the increased geothermal activity may be expected here. The increased supply of heat from below this zone can be further related to intensive Tertiary volcanism, thermal springs and discharges of CO_2 along both these zones (Kodým, 1960; Kačura et al., 1969).

While the characteristic temperatures at the Mohorovičić discontinuity beneath the most stable parts of the Bohemian Massif are 500–550 °C at the

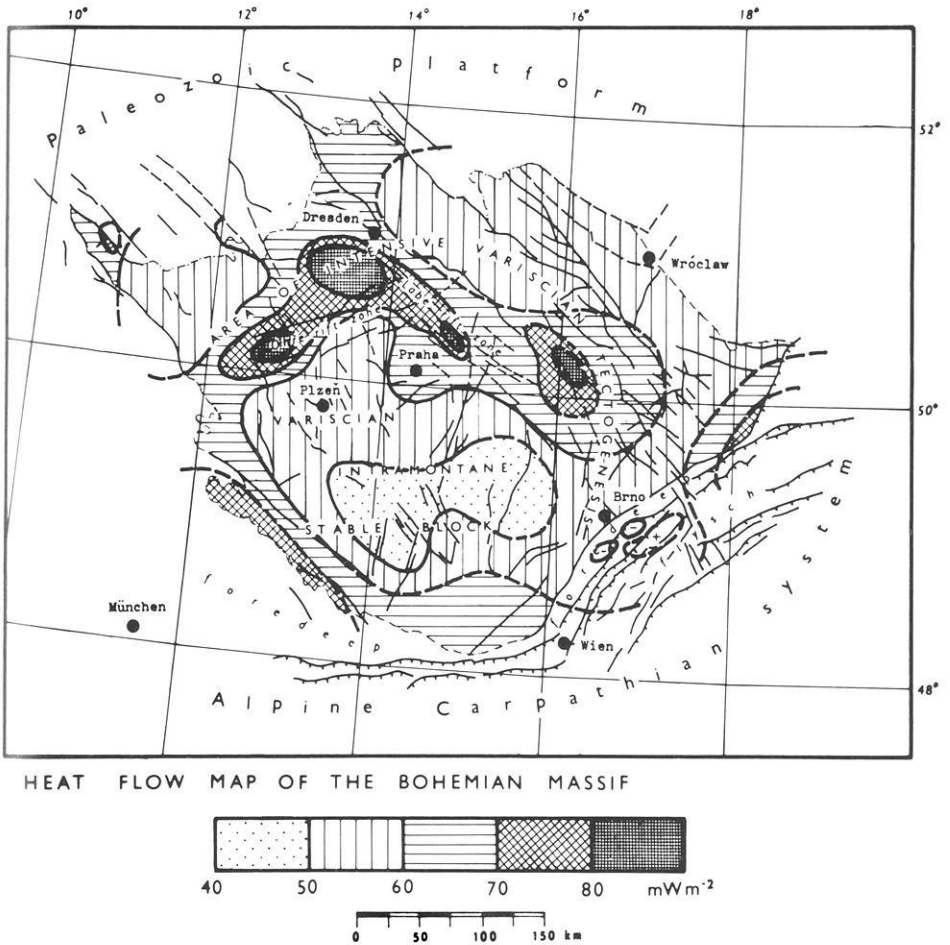


Fig. 1. Heat flow map of the Bohemian Massif

depth of about 40 km, and the Moho-temperature slightly increases towards the north up to 550–600 °C beneath the Assyntian region; the Moho-temperatures can reach 600 °C and more at the depth of 32 km below the Krušné Hory Mts. and the Cretaceous Table (Čermák, 1975a). The upper mantle heat flow contribution may also rise from 20–25 mWm^{-2} in the centre of the stable intramontane block to 25–30 mWm^{-2} beneath the Cretaceous Table. The degree of tectonic rejuvenation of the Bohemian Massif since the Palaeozoic (especially during the Alpine-Carpathian orogeny) may thus be accompanied by the thinning of the earth's crust together with the increase of energy influx from the depth, and the increase of crustal and subcrustal temperatures.

The proposed heat flow pattern may help in preliminary recognition of probable areas of geothermal resources. It is quite clear that the most of the territory of the Bohemian Massif will never be of any practical meaning in

the utilization of geothermal energy, however, there are some prospects to find exploitable sources along both disturbed contact zones between the stable block and the crooked arc of the area of intensive Variscan tectogenesis. At the present level of exploration, the most promising is the thermal spring area near Děčín (Jetel, 1975), i.e. approx. at the cross point of both rift zones. Near to this area the highest heat flow values by Teplice (Čermák, 1967) were recorded, as well. Other potentially prospective locations can be found close to high heat flow anomalies (over 80 mWm^{-2}) (see Fig. 1) between Karlovy Vary and Doubovské Hory Mts. to the south-west along the Ohře rift zone, and/or close to Mělník to the south-east in the Labe rift zone, resp. The most eastern high heat flow anomaly (at approx. 50°N , 16°E) is not quite clear yet.

References

- Beránek, B., Dudek, A.: The results of deep seismic sounding in Czechoslovakia. *Z. Geophys.* **38**, 415–422, 1972
- Čermák, V.: Heat flow near Teplice in North Bohemia. *Geophys. J.* **13**, 547–549, 1967
- Čermák, V.: Terrestrial heat flow in Czechoslovakia and its relation to some geological features. 23. Inter. Geol. Congr., Prague **5**, 75–85, 1968
- Čermák, V.: Temperature-depth profiles in Czechoslovakia and some adjacent areas derived from heat-flow measurements, deep seismic sounding and other geophysical data. *Tectophysics* **26**, 103–119, 1975a
- Čermák, V.: Terrestrial heat flow in the Neogene foredeep and the flysch zone of the Czechoslovak Carpathians. *Geothermics* **4**, 8–13, 1975b
- Čermák, V.: First heat flow map of Czechoslovakia. *Trav. Inst. Géophys. Tchecosl. Acad. Sci. Geofysikální sborník 1976*, Academia, Praha (in press)
- Čermák, V., Jetel, J., Krčmář, B.: Terrestrial heat flow in the Bohemian Massif and its relation to the deep structure. *Sborník geol. věd, UG 7*, 25–38, 1968
- Haenel, R.: Heat flow measurements and a first heat flow map of Germany. *Z. Geophys.* **37**, 975–992, 1971
- Haenel, R., Zoth, G.: Heat flow measurements in Austria and heat flow maps of Central Europe. *Z. Geophys.* **39**, 425–439, 1973
- Hurtig, E., Schlosser, P.: Untersuchungen des terrestrischen Wärmeflusses in der DDR. *Gerl. Beitr. Geoph.* **84**, 235–246, 1975
- Jetel, J.: Perspektivy využití zdrojů geotermální energie v ČSR. *Geol. průzkum*, **17**, 4–7, 1975
- Kačura, G., Franko, O., Gazda, S., Šilar, J.: Thermal and mineral waters of Czechoslovakia. 23. Inter. Geol. Congr. Prague, Proc. Symp. II, A, 17–29, 1969
- Kodým, O.: Upper Palaeozoic of the Bohemian Massif. In: *Tectonic Development of Czechoslovakia*, V. Zoubek, ed. Nakl. ČSAV, Praha, 122–138, 1960
- Kopecký, L.: Riftové struktury, fenity a mladý alkalický magmatismus jako nositelé rudní mineralizace v Českém masívu. *Geol. průzkum* **14**, 195–198, 1972
- Majrowicz, J.: Heat flow in Poland and its relation to the geological structure. *Geothermics* **2**, 24–28, 1973
- Matolin, M.: Radioaktivita hornin Českého masívu. Nakl. ČSAV, Praha, 1970
- Zoubek, V., Malkovský, M.: The Czechoslovakian part of the Bohemian Massif. In: *Tectonics of the Carpathian-Balkan Region*, M. Mahel, ed. GÜDŠ, Bratislava, 407–414, 1974

Received June 21, 1976

Palaeomagnetic and Rock Magnetic Investigations of Tertiary Volcanics in Northern Bavaria

J. Pohl and H. Soffel

Institut für Allgemeine und Angewandte Geophysik
Theresienstr. 41, D-8000 München 2, Federal Republic of Germany

Abstract. Palaeomagnetic measurements were carried out on 26 Tertiary basalt occurrences for sites in the Oberpfalz (OPF), the Heldburg dyke swarm and several isolated occurrences between these 2 groups (HEB). The mean coordinates for all OPF sites are: long=12.2° E, lat=50.0° N, for all OPF+HEB sites: long=11.4° E, lat=50.1° N. After af-cleaning in fields of 8 to 16 kA/m (100–200 Oe) the mean directions of characteristic remanent magnetization (CARM) of OPF sites are: N=16, dec=12.7°, inc=59.5°, $\alpha_{95}=7.6^\circ$, of OPF+HEB sites: N=22, dec=12.4°, inc=59.0°, $\alpha_{95}=5.8^\circ$. Two thirds of the investigated sites have a reverse polarity. Sites with reverse CARM have shallower inclinations (OPF+HEB: -55.9°) than sites with normal polarity (OPF+HEB: $+65.5^\circ$). This is explained by the presence of viscous components which cannot be erased completely by af-demagnetization. The pole position (northern hemisphere) for OPF sites is: long=135° E, lat=78° N, $\alpha_{95}=9.4^\circ$, for OPF+HEB sites: long=140° E, lat=78° N, $\alpha_{95}=7.2^\circ$. The OPF sites have radiometric ages between 19 and 24 My and the HEB sites between 16 and 41 My. Rock magnetic and ore microscopic investigations indicate that with the exception of a few sites, which have not been included in the averaging for the data given above, the direction of the CARM can be considered to be a good approximation to the direction of the primary magnetization.

Key words: Palaeomagnetism – Rock magnetism – Tertiary volcanics – Bavaria

Introduction

The Tertiary volcanic rocks in northern and northeastern Bavaria belong to the Central European volcanic provinces and are the result of cratonic igneous activity on the European plate. Palaeomagnetic data of a great number of these volcanic provinces have been reviewed by Duncan, Petersen and Hargraves

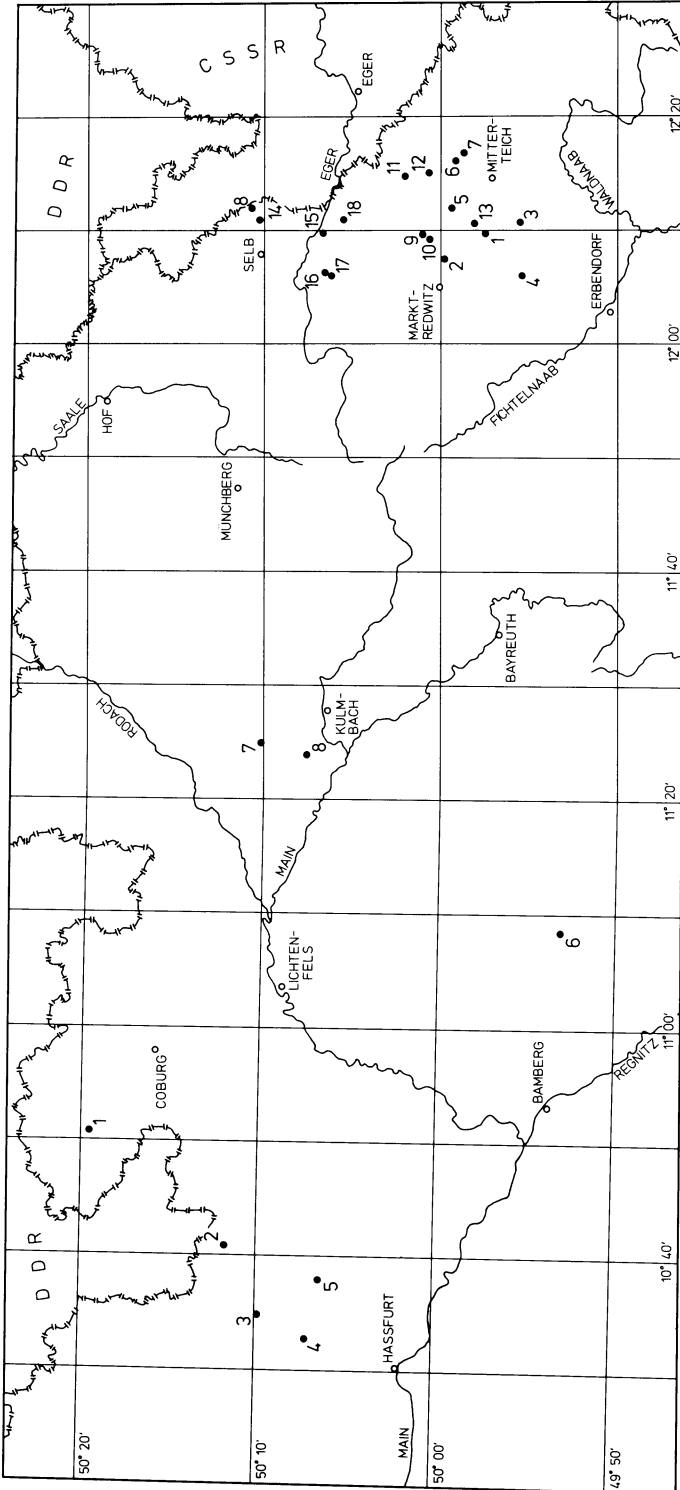


Fig. 1. Sampling sites. Sites east of Bayreuth are named OPF in text, tables and figures. Sites west of Bayreuth are named HEB

(1972). For the southern part of the volcanics in northeastern Bavaria some palaeomagnetic measurements have been made by Refai (1962) and by Soffel and Supalak (1968). In the present paper palaeomagnetic results of previously not investigated localities in northeastern Bavaria (Oberfranken and Oberpfalz), of part the Heldburg dyke swarm in northern Bavaria and of several small basalt occurrences between these 2 groups are presented. For part of these volcanic rocks radiometric age determinations have been made or are under work (Todt and Lippolt 1975; Lippolt, personal communication). They have confirmed the upper Tertiary age which was generally assumed on the basis of geological investigations (Schröder, 1962, 1965). The available radiometric ages have been included in Table 2.

In order to identify the carriers of magnetism in the investigated volcanics and to obtain a general idea of the reliability of the palaeomagnetic results, rock magnetic and ore microscopic studies were carried out. They are summarized in Section 4.

2. Sampling Areas, Petrology and Ages of the Volcanic Units

2.1. Oberpfalz Basalts (OPF 1-18)

The northeastern group of volcanics are called Oberpfalz basalts in the present paper (OPF 1-18, Fig. 1). They represent the western limit of the volcanic province of northern Bohemia which is associated with the Eger Graben. The Oberpfalz volcanic rocks are exclusively basalts, generally olivine-nephelinites and in part nepheline basanites (Richarz, 1920; Wurm, 1961; Noussinanos, 1973; Todt and Lippolt, 1975). They occur as isolated dykes striking approximately NE-SW, parallel to the Eger Graben, as effusive sheets and as lava filled vents which have resisted later erosion. Radiometric age determinations (Todt and Lippolt, 1975) on 19 basalts from the Oberpfalz indicate that the main eruptive phase was between 24 and 19 My, with a possible onset in upper Oligocene (28.8 ± 1.8 My for one site). However, an upper Pliocene or even Pleistocene age (≈ 3 My) was determined for Kammerbühl near the town of Eger (Fig. 1) indicating a younger volcanic phase in the same area.

For the present study 18 localities which had not been previously investigated palaeomagnetically were sampled in the northern part of the Oberpfalz basalts. Between 6 and 37 samples (drill cores) were collected at the different sites depending on the size of the volcanic unit. The samples were taken mostly in quarries, where fresh material could generally be found. Details for the localities are given in Table 1.

2.2. Heldburg Dike Swarm (HEB 1-5)

The Heldburg dyke swarm covers an area about 60 km in length and 20 km in width. The main part of the area is situated in E-Germany. On the Bavarian side only five suitable sites (HEB 1-5, Fig. 1) were found for sampling. In

Table 1. Sampling site coordinates and natural remanent magnetization (NRM, $1 \text{ A/m} \approx 10^{-3} \text{ G}$). N = number of samples, n = number of specimens, k = precision parameter, R = resultant vector, susceptibility: $10^{-3} \text{ SI units} \approx 80 \cdot 10^{-6} \text{ G/Oe}$, Q = Koenigsberger ratio for an inducing field of 47,000 nT (47,000 gamma)

Site No.	Locality	r	h	Topographic Map	N/n	NRM (A/m)	Dec ($^{\circ}$)	Inc ($^{\circ}$)	α_{95} ($^{\circ}$)	k	R	Susceptibility Q (10^{-3} SI)
				1:25000, No.								
OPF 1	Teichelberg	⁴⁵ 11900	⁵⁵ 35900	Waldershof, 6038	30/90	2.23	202.8	-49.7	5.7	21.7	28.7	66.4
OPF 2	Rehberg	⁴⁵ 09040	⁵⁵ 40040	Waldershof, 6038	20/63	0.91	44.6	+24.2	10.5	10.5	18.2	40.0
OPF 3	Triebendorf	⁴⁵ 12900	⁵⁵ 32160	Mitterteich, 6039	37/100	1.44	197.9	-55.4	10.1	6.4	31.4	48.7
OPF 4	Plössberg	⁴⁵ 07380	⁵⁵ 31940	Waldershof, 6038	7/18	1.38	356.8	+62.0	10.2	35.8	6.8	49.3
OPF 5	Hirschentanz	⁴⁵ 14400	⁵⁵ 39360	Mitterteich, 6039	12/38	1.36	200.6	-61.6	10.6	17.5	11.4	49.0
OPF 6	Gommelberg	⁴⁵ 19260	⁵⁵ 38900	Mitterteich, 6039	12/33	3.84	204.8	-61.7	4.0	117.6	11.9	31.9
OPF 7	Steinmühle	⁴⁵ 20000	⁵⁵ 38000	Mitterteich, 6039	14/42	2.25	191.5	-53.6	5.0	61.8	13.8	52.6
OPF 8	Längenau-E	⁴⁵ 13860	⁵⁵ 60300	Schönberg, 5939	10/28	1.36	196.9	-36.5	12.8	15.1	9.4	29.8
OPF 9	Brand-E	⁴⁵ 11540	⁵⁵ 42120	Marktedwitz, 5938	10/25	1.35	221.5	-55.7	5.9	66.7	9.9	21.7
OPF 10	Brand-SE	⁴⁵ 11160	⁵⁵ 41200	Marktedwitz, 5938	10/22	0.71	(195.1)	(-74.6)	46.2	2.0	5.7	45.9
OPF 11	Grün	⁴⁵ 17600	⁵⁵ 44180	Waldsassen, 5939	10/24	1.64	37.0	+72.5	8.2	35.5	9.8	39.3
OPF 12	Wolfsbühl	⁴⁵ 18020	⁵⁵ 41800	Waldsassen, 5939	9/22	1.00	193.7	+5.7	20.2	7.3	7.9	19.6
OPF 13	Steinhübel	⁴⁵ 12800	⁵⁵ 37000	Mitterteich, 6039	6/13	4.45	7.5	+66.4	4.3	242.2	6.0	9.5
OPF 14	Längenau-S	⁴⁵ 12980	⁵⁵ 59500	Schönberg, 5939	12/31	1.82	227.9	-28.2	7.7	31.9	11.7	32.5
OPF 15	Ruine Neuhaus	⁴⁵ 11680	⁵⁵ 52700	Selb, 5838	8/15	2.67	189.6	-41.8	7.4	56.4	7.9	20.8
OPF 16	Ruine Thierstein	⁴⁵ 07460	⁵⁵ 52420	Selb, 5838	7/15	4.29	134.4	+68.4	24.3	7.1	61.6	24.9
OPF 17	Thierstein (Stbr.)	⁴⁵ 07280	⁵⁵ 51940	Selb, 5838	11/31	3.23	42.6	+70.5	10.2	20.7	10.5	38.2
OPF 18	Steinberg	⁴⁵ 13125	⁵⁵ 50650	Waldsassen, 5939	10/18	1.12	(96.4)	(+14.1)	43.4	2.1	5.9	56.7
HEB 1	Grosswalbur	⁴⁴ 18120	⁵⁵ 77180	Meeder, 5631	3/6	2.02	-	-	-	-	-	40.2
HEB 2a	Zeilberg	⁴⁴ 06140	⁵⁵ 63140	Heldburg, 5730 und Pfarrweisach, 5830	17/43 18/49	1.22 1.30	217.2 (215.0)	-37.0 (-25.8)	13.7 24.8	7.6 2.9	14.9 21.2	24.6 27.5
HEB 3	Manau	⁴³ 93960	⁵⁵ 59520	Hofheim in UFr., 5829	7/13	1.17	185.3	-59.8	18.5	11.5	6.5	26.0
HEB 4	Hügel	⁴³ 96200	⁵⁵ 54700	Hofheim in UFr., 5829	11/23	1.99	23.4	+71.9	11.1	17.6	10.4	49.0
HEB 5a	Bramberg	⁴⁴ 02460	⁵⁵ 53330	Hofheim in UFr., 5829	7/15	1.25	218.0	+54.0	21.0	9.1	6.3	31.8
					7/20	0.57	(166.2)	(+5.5)	90	1.3	-	35.7
HEB 6	Oberleinleiter	⁴⁴ 38550	⁵⁵ 27875	Buttenheim, 6132	7/14	1.33	60.7	+28.9	14.3	18.5	6.7	43.8
HEB 7	Lössau	⁴⁴ 57675	⁵⁵ 59350	Kulmbach, 5834	6/11	4.43	8.1	+61.0	12.7	28.7	5.8	42.9
HEB 8	Veitlahm	⁴⁴ 56750	⁵⁵ 54925	Kulmbach, 5834	11/20	2.80	355.3	+65.2	5.0	82.0	10.9	22.3

Table 2. Characteristic remanent magnetization (CARM, $1 \text{ A/m} \approx 10^{-3} \text{ G}$). $H \sim$ = alternating field used for af-demagnetization ($8 \text{ kA/m} \approx 100 \text{ Oe}$), k = precision parameter, R = resultant vector

Site No.	N	$H \sim$ (kA/m)	CARM (A/m)	Dec ($^{\circ}$)	Inc ($^{\circ}$)	α_{95} ($^{\circ}$)	k	R	Polar- ity	Radiometric Age (My)
OPF 1	31	8	1.97	199.8	-52.2	2.7	89.8	30.7	-	21.4 ± 1.1
OPF 2	20	16	0.49	87.3	-69.9	3.4	93.0	19.8	-	
OPF 3	37	8	1.87	189.5	-63.1	2.3	103.0	36.6	-	
OPF 4	9	8	0.99	356.6	+55.0	7.2	50.8	8.8	+	
OPF 5	12	8	1.33	188.9	-64.9	4.4	97.5	11.9	-	
OPF 6	12	8	3.78	200.1	-65.6	3.6	142.8	11.9	-	
OPF 7	14	8	2.07	190.6	-59.0	4.6	75.1	13.8	-	
OPF 8	11	8	1.48	191.6	-51.0	5.5	68.8	10.8	-	
OPF 9	10	16	0.80	218.7	-62.6	6.4	57.5	9.8	-	22.8 ± 1.8
OPF 10	10	16	0.43	176.7	-78.5	12.6	15.4	9.4	-	22.9 ± 1.0
OPF 11	10	8	0.78	53.6	+59.2	4.3	123.1	9.9	+	
OPF 12	9	8	0.60	179.9	-22.6	12.6	17.5	8.5	-	
OPF 13	6	8	3.81	3.9	+65.3	2.2	891.5	6.0	+	
OPF 14	12	16	0.90	210.8	-49.5	6.1	51.1	11.8	-	
OPF 15	8	8	2.99	187.5	-52.5	3.1	314.3	7.9	-	
OPF 16	7	8	1.31	33.9	+80.3	7.4	67.3	6.9	+	
OPF 17	11	16	1.06	18.4	+68.7	4.6	99.3	10.9	+	
OPF 18	10	16	0.33	156.1	-48.1	6.2	61.5	9.8	-	23.0 ± 1.3
HEB 1	3	no stable remance		-	-	-	-	-	-	(24.0)
HEB 2	34	16	1.25	204.0	-46.8	3.4	50.7	33.3	-	(16.0)
HEB 3	7	8	1.21	199.8	-63.4	10.1	36.4	6.8	-	(41.6)
HEB 4	11	16	1.36	27.3	+58.9	4.8	78.9	10.9	+	(34.0)
HEB 5	14	12	0.09	180.8	-44.1	12.2	11.5	12.9	-	(16.0)
HEB 6	6	16	0.30	68.8	+20.6	6.8	70.1	5.9	+	(30.8)
HEB 7	6	6	1.60	2.6	+61.3	11.0	37.4	5.9	+	
HEB 8	11	10	1.37	352.9	+65.2	4.6	98.8	10.9	+	(26.9)

the sampled area the swarm consists mainly of dykes several dm to several m in thickness. The strike direction is parallel to the dominant NNE trend of the Rhine graben. Site HEB 2 (Zeilberg) is a large eruptive center. The petrological composition is basaltic for all sites. The age is estimated to be upper Miocene to upper Pliocene (Schröder, 1965). Preliminary radiometric ages are given in Table 2. The sampling of site HEB 1 was made in a weathered dyke about 60 cm thick. Site HEB 2 is a large quarry and sites HEB 3-5 are small abandoned quarries in broad dikes.

2.3. Oberleinleiter Basalt (HEB 6)

An isolated occurrence of nepheline basanite is found E of Bamberg. It is a small dyke striking in the same direction as the Heldburg dykes. A preliminary radiometric age is given in Table 2. Sampling was made in an abandoned quarry.

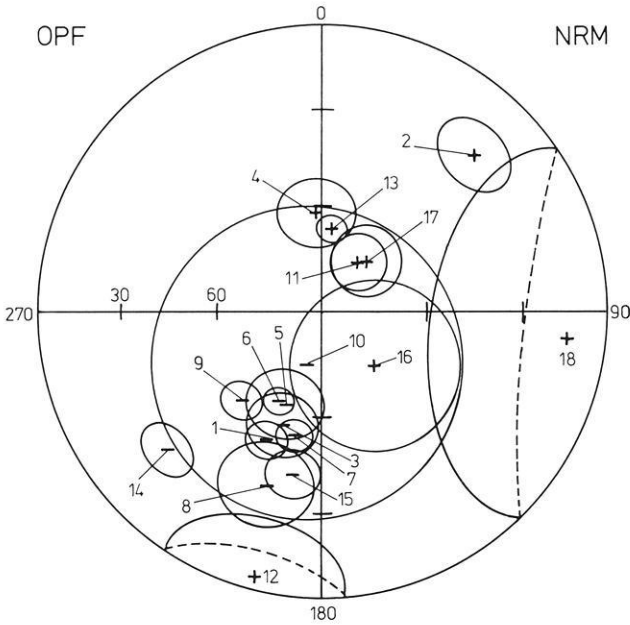
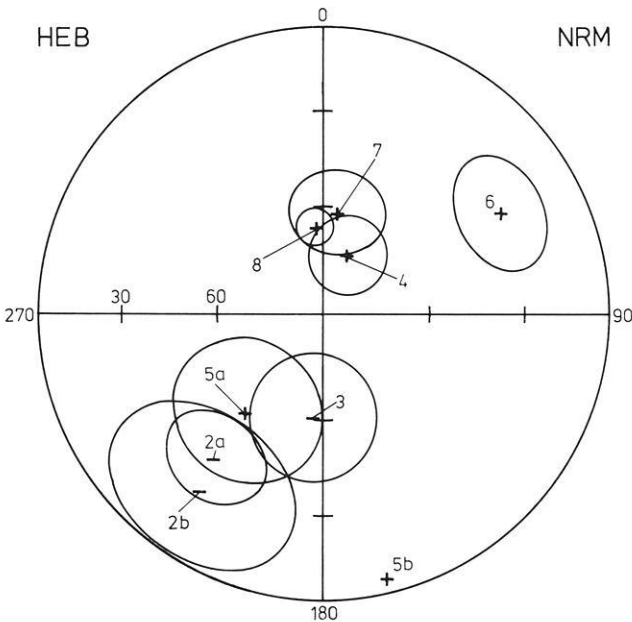


Fig. 2. Directions of the natural remanent magnetization (NRM) of OPF and HEB sites. Site mean values with the α_{95} angle of confidence ovals. Schmidt equal area projection



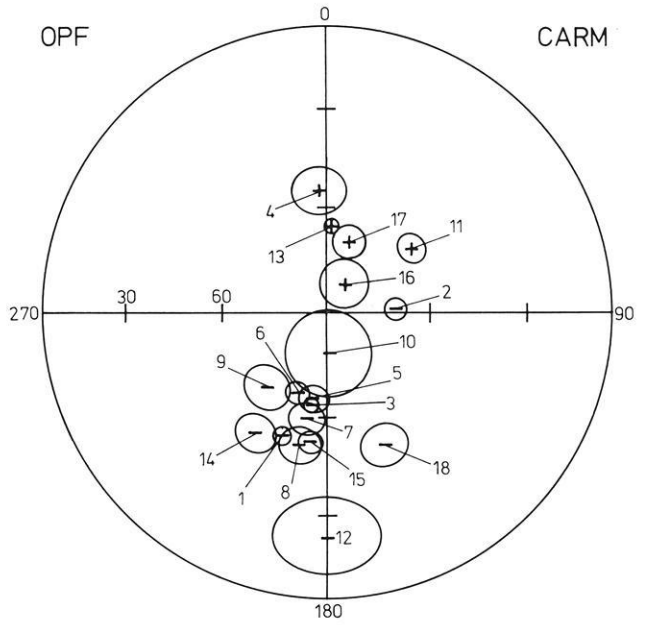
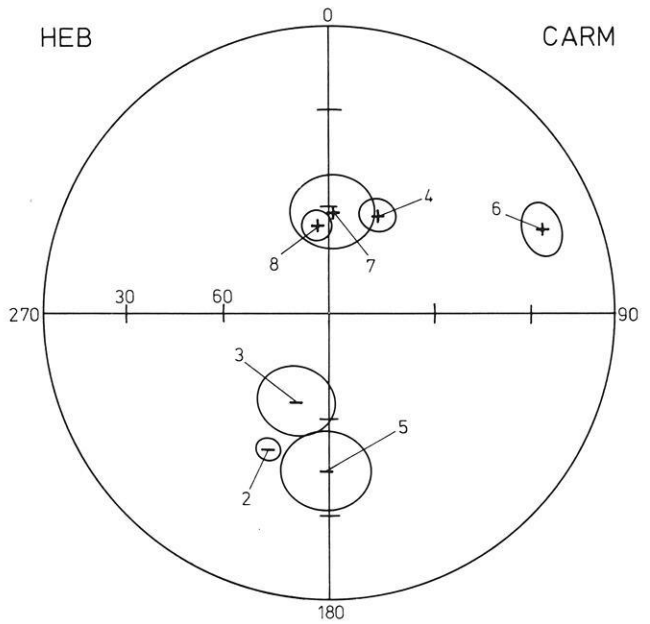


Fig. 3. Directions of the characteristic remanent magnetization (CARM) obtained after af-demagnetization. Site mean values with the α_{95} angle of confidence ovals. Schmidt equal area projection



2.4. *Veitlahm—Grafendobrach Dykes (HEB 7–8)*

Several small basalt occurrences are found N and NW of Kulmbach (Gudden, 1955). They occur as dykes several dm to several m large. The strike direction is 50–60° and is parallel to the Eger Graben. The age is estimated as Miocene (Dorn, 1930). Preliminary radiometric ages are also given in Table 2. Site HEB 7 is a dyke about 80 cm in width and site HEB 8 is an abandoned quarry in a dyke.

3. Palaeomagnetic Results

3.1. *Natural Remanent Magnetization (NRM)*

Measurements of remanent magnetization were made with a fluxgate spinner magnetometer. The data of the NRM are listed in Table 1. The site mean values were calculated from the mean values of the samples. Figure 2 shows the mean NRM directions of all sites together with the α_{95} cones of confidence for the OPF and HEB basalts respectively. The data are shown in equal area projection. The considerable scatter of the sample means of some sites (OPF 8, 10, 12, 16 and 18) in Figure 2 and in some cases the indication of a great circle distribution of the NRM directions reveals the presence of secondary magnetization components. With the exception of sites OPF 2, 12, 16 and 18 and site HEB 5 in Figure 2 the NRM already indicates the polarity of the characteristic remanent magnetization.

3.2. *Alternating Field Demagnetization*

A test of the stability of the NRM was done by demagnetizing two pilot samples from each locality in af-fields with peak values up to 80 kA/m (1000 Oe). The curves showing the variation of intensity of remanence during af-demagnetization were classified according to the schematic curves shown in Figure 4. In this classification scheme the letters A–D indicate increasing stability against af-demagnetization. One asterisk indicates the presence of a maximum and two asterisks indicate the presence of a relative maximum and a relative minimum as shown in Figure 4. The last 2 cases generally occur when the primary remanence is reversed and a viscous component in the direction of the present field is superposed on the primary remanence (assuming only 2 components of remanent magnetization). This is rather frequent among the basalts investigated here, the majority of which show a reversed primary remanence. The results of the classification are included in Table 4, together with the results of rock magnetic investigations described in Section 4.

From the af-demagnetization curves and the corresponding changes in direction of the pilot samples, the appropriate demagnetizing field for the remaining samples of a locality was determined. The demagnetization was then carried out in several steps and the characteristic remanent magnetization (CARM)

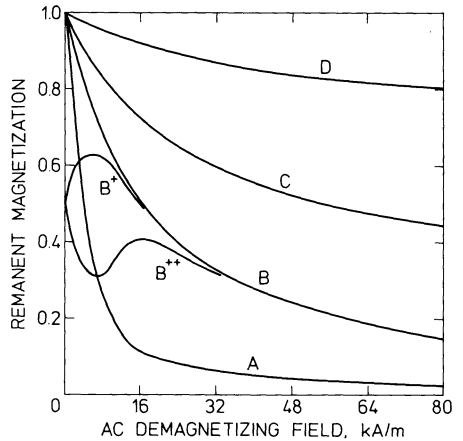


Fig. 4. Classification scheme used in Table 4 for the classification of af-demagnetization curves. Further explanations in the text (Sect. 3.2)

was taken from the demagnetization step giving the lowest amount of scatter, i.e. the minimum α_{95} angle of confidence. In all cases alternating fields between 8 and 16 kA/m (100 and 200 Oe) gave the best results. The scatter of the directions of remanence could be considerably reduced for the individual sites (Figs. 2 and 3) and the grouping of the different sites around a mean normal and a mean reversed value was ameliorated. For site HEB 1 a CARM could not be determined because of unstable remanent magnetization.

The specific af-values used for the determination of CARM are listed in Table 2.

3.3. Characteristic remanent magnetization (CARM)

The site mean data of CARM are listed in Table 2. The mean directions together with their α_{95} cones of confidence are plotted in equal area projections in Figure 3. The majority of the sites have CARM directions which are in general agreement with palaeomagnetic directions obtained from other upper Tertiary rocks in Central Europe. A few sites have directions which deviate considerably from upper Tertiary directions (OPF 2 and 12 and HEB 6). As tectonic movements must be discarded, the deviating directions may be attributed to excursions of the magnetic field.

3.4. Mean Directions and Pole Positions

According to the geological descriptions (Schröder, 1962, 1965) and the radiometric age determinations (Todt and Lippolt, 1975) the main volcanic activity in the Oberpfalz and Oberfranken (OPF 1–18) occurred between 24 and 19 My. This corresponds to upper Oligocene and lower Miocene in the stratigraphic

Table 3. Mean directions, mean coordinates of sampling sites and pole positions. For the calculation of mean values of all sites the sites with reverse polarity were inverted to the other hemisphere.

Pole positions were calculated from the individual pole positions of the different sampling sites. Sites OPF 2 and HEB 6 were omitted because of too great departure from a Fisherian distribution, site OPF 13 was omitted because of a too low Curie temperature and site HEB 1 was omitted because of unstable remanence. k = precision parameter

Mean directions

Sites	N	Dec ($^{\circ}$)	Inc ($^{\circ}$)	α_{95} ($^{\circ}$)	k
OPF	16	12.7	59.7	7.6	24.0
OPF + HEB	22	12.4	59.0	5.8	28.7
OPF normal	4	23.3	67.5	17.9	27.0
OPF + HEB normal	7	16.2	65.5	9.7	39.6
OPF reverse	12	190.2	-56.9	8.8	24.7
OPF + HEB reverse	15	191.1	-55.9	7.4	27.5

Mean coordinates of sampling sites

Sites	Long ($^{\circ}$)	Lat ($^{\circ}$)
OPF	12.2 E	50.0 N
OPF + HEB	11.4 E	50.1 N

Pole positions (North poles)

Sites	N	Long ($^{\circ}$)	Lat ($^{\circ}$)	α_{95} ($^{\circ}$)	k
OPF	16	135	78	9.4	16.3
OPF + HEB	22	140	78	7.2	19.4
OPF normal	4	86	75	27.0	12.5
OPF + HEB normal	7	103	79	14.7	17.7
OPF reverse	12	152	77	10.1	19.0
OPF + HEB reverse	15	152	75	8.4	21.2

scale (Odin et al., 1975; Van Eysinga, 1975). Assuming that all the investigated basalts (OPF 1–18) erupted more or less within the same time interval, it is reasonable to calculate a mean direction and the corresponding pole position for the Oberpfalz basalts. Site OPF 2 is excluded because of too great departure from a Fisherian distribution and site OPF 13 because of the low Curie-point discussed in Section 4. The mean direction and the pole position for the northern hemisphere are given in Table 3 and Figure 6. The mean pole position was calculated from the pole positions determined individually for each site. As there is a characteristic difference between directions of normal and reversed sites, the mean directions of normal and reversed sites and the corresponding pole positions are also given in Table 3 and Figure 6. – For sites HEB 1–8 no pole position was calculated because of the small number of sites and the large time interval of the eruptions. Preliminary age determinations give ages

between 16 and 41 My (Table 2). Some of these ages may be too high because of excess argon (Lippolt, personal communication 1976). — A mean direction and a mean pole position were calculated for all OPF and HEB sites, except OPF 2, 13 and HEB 6. The results have been included in Table 3 and Figure 6, which contain also the mean pole positions for all OPF+HEB normal and reversed sites respectively.

4. Rock Magnetic and Ore Microscopic Investigations

The results of rock magnetic measurements are presented in Table 4, which contains the following parameters:

- af-demagnetization curve type of NRM according to the classification described in Section 3.2
- coercive force H_c determined from a hysteresis curve with maximum magnetizing field of 96 kA/m (1200 Oe)
- magnetization M_{96} in the field of 96 kA/m (1200 Oe)
- ratio M_{rem}/M_{96} of the remanent magnetization obtained after magnetizing the samples in the field of 96 kA/m to the magnetization in this field. In a field of 96 kA/m the investigated samples were almost saturated, as could be seen from the measured hysteresis curves
- magnetization M versus temperature T curve type according to the partial classification scheme for basaltic rocks shown in Figure 5. The M - T curves were measured with a translation balance of the Weiss-Forrer type. Heating of the powdered samples up to 600° C and cooling was made in air within about 60 min. The applied magnetic field was 240 kA/m (3000 Oe).
- Curie-temperatures determined from the heating ($T_c \uparrow$) and from the cooling cycle ($T_c \downarrow$)
- ratio M/M_0 of the magnetization M in the field of 240 kA/m after the heating and cooling procedure to the magnetization M_0 before this procedure.

The ore microscopic data obtained with a magnification $\times 600$ and oil immersion are also summarized in Table 4 with the following abbreviations:

- TMT indicates members of the titanomagnetite group
- LTO is the abbreviation for low temperature oxidation, characterized by the presence of titanomaghemite. A relative degree of LTO is indicated by 1 and 2 crosses, 2 crosses indicating that a substantial part of the titanomagnetite has been replaced by titanomaghemite (Ade-Hall et al., 1971)
- HTO is the corresponding abbreviation for high temperature oxidation. The roman numerals indicate the oxidation class according to Wilson and Haggerty (1966).
- Il_p indicates the presence of primary ilmenite
- Sf indicates the presence of sulphides, generally pyrite
- Crt means that part of the titanomagnetites have dark grey cores, which are considered to be remnants of a previous chromiferous spinel (Babkine et al., 1965; Wright, 1967)
- Diam indicates an estimated mean diameter of the magnetic ores in μm .

Table 4. Rock magnetic and ore microscopic characteristics. For explanation of the symbols see text (Sect. 4)

Site No.	a.f. type	H_c (kA/m)	M_{96} (A/m)	M_{rem}/M_{96}	M-T curve type	$T_c \uparrow$ (°C)	$T_c \downarrow$ (°C)	M/M_0	TMt	LTO	HTO	Il_p	Sf	Crt	Diam (μm)
OPF 1	B ⁺	6.4	4980	0.19	1a-2a	160-350	480	1.1-1.6	++	/-++	I-III	+	+		
OPF 2	C	4.0	4230	0.14	1a	240	520	1.59	++	+	I				30
OPF 3	B ⁺	3.2	5340	0.07	1a	260	510	1.43	++		I				15
OPF 4	B-C	4.8	4990	0.12	2a-3c	300-510	510	1.5-1.0	++	++	II	+			15
OPF 5	B ⁺	5.6	3000	0.17	2a	ca. 300	520	1.54	++	+	I				10
OPF 6	A ⁺	5.6	4570	0.15	1a	ca. 300	520	2.78	++	+	I				10
OPF 7	B ⁺	6.4	4170	0.15	3e	500	510	1.09	++	+	II	+			30
OPF 8	B ⁺	9.6	3360	0.33	2a	ca. 350	520	2.50	++	+	I				5
OPF 9	B ⁺	5.6	2780	0.18	1a	250	490	2.04	++	+	I				15
OPF 10	A ⁺ -B ⁺	5.6	4450	0.16	2a	ca. 330	500	1.61	++	++	II	+			10
OPF 11	A	3.2	3170	0.10	2a	ca. 280	480	1.33	++	++	II				40
OPF 12	A	5.6	2440	0.22	2a	ca. 250	480	1.83	++	+	II	+			15
OPF 13	B	(8.0)	-	(0.22)	1a	ca. 50	480	-	++	+	I				40
OPF 14	A ⁺ -B ⁺	5.6	3590	0.18	1a	190	530	1.67	++		I				5
OPF 15	C ⁺	9.6	2120	0.30	1a	180	470	1.72	++	+	I				5
OPF 16	A	5.6	2530	0.22	1a	190	500	2.08	++	+	I				20
OPF 17	A-B	8.0	2910	0.30	1a	200	500	1.96	++	+	I				20
OPF 18	A-A ⁺	4.8	5030	0.12	1a	220	480	1.34	++		I		+		40
HEB 1	A-A ⁺	5.6	5500	0.15	2a	ca. 350	550	1.15	++		I		+	+	15
HEB 2	B ⁺ -B ⁺⁺	7.2	3120	0.17	7a	ca. 500	480	1.19	++	+	II	++	+		60
HEB 3	A ⁺	12.0	3720	0.35	2a	ca. 380	500	1.35	++	+	I		+	+	30
HEB 4	A	6.4	5700	0.08	3b	550	530	0.80	++	+	II	+	+		10
HEB 5	A	2.4	3170	0.08	1a	260	500	1.37	++		I	+			60
HEB 6	A ⁺	(5.6)	7690	0.13	3b	450	480	0.83	++		I			+	30+1
HEB 7	A	4.8	5070	0.12	4a	ca. 300	510	1.52	++		I		+	+	30
HEB 8	A	9.6	3120	0.21	4a	ca. 300	520	1.25	++		I		+	+	30+5

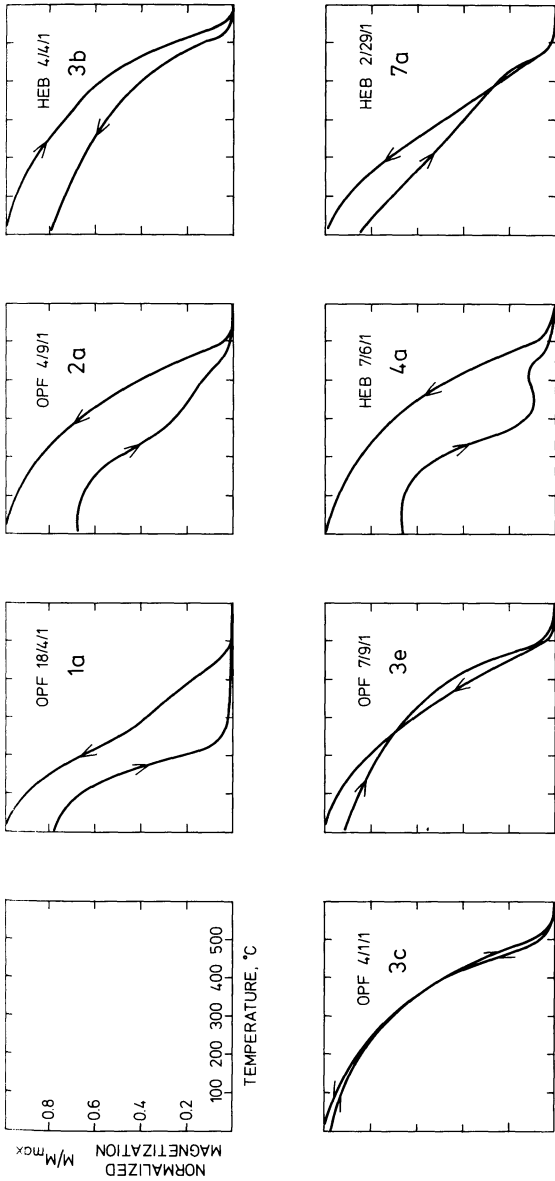


Fig. 5. Magnetization versus temperature curve (*M-T* curves) types found in the investigated basalts. Measurements were made in air and in an applied magnetic field of 240 kA/m (3000 Oe)

The ore microscopic and rock magnetic investigations show that titanomagnetites are the main magnetic phase. Most of the titanomagnetites exhibit a low temperature oxidation, but some appear to be very homogeneous as indicated by the *M-T* curves and the microscopic data. High-temperature oxidation is not frequent. We assume that high-temperature oxidation occurred during the original cooling of the lava in the generally isolated eruptions characteristic of the volcanism in the investigated areas. The time and the temperatures for

the low-temperature oxidation are not so easily estimated. The Curie-temperatures measured in the apparently unoxidized or only slightly oxidized basalts are however around 200° C and it is therefore probable that low-temperature oxidation occurred below the Curie-point of the phase carrying the primary remanence. Thus changes of the intensity of the remanent magnetization but not of the direction can be expected (Marshall and Cox, 1971).

As a conclusion we can assume that the measured CARM generally represents a primary direction of magnetization. An exception is site OPF 13, which has a Curie-temperature of about 50° C. The remanent magnetization of this site is very close to the direction of the present geomagnetic field in the sampling area and is probably a recent thermoremanent magnetization acquired during heating by the sun.

5. Discussion

The palaeomagnetic measurements and testing procedures described above, as well as the additional rock magnetic and ore microscopic investigations summarized in the previous section show that, according to usual standards the palaeomagnetic results (CARM and Pole positions) can be considered as reliable.

The mean pole position for all sites, as well as for the OPF sites alone agrees well with the upper Tertiary pole position of McElhinny (1973) for continental Europe. The longitude $< 180^\circ$ given by McElhinny is confirmed and is in contrast to previous pole position determinations with longitudes $> 180^\circ$ (Fig. 6).

About two thirds of the investigated sites have a reversed polarity. For sites where the radiometric age is known, a comparison with a Tertiary polarity scale has been made by Todt and Lippolt (1975).

A remarkable feature is the difference in inclination between normal and reversed magnetizations (reversed magnetizations have shallower inclinations) and the corresponding difference of the pole positions (Fig. 6 and Table 3). This is apparently in agreement with similar differences between normal and reversed pole positions discussed by Wilson (1972) and by Wilson and McElhinny (1974).

We think that in the present case at least part of this difference can be explained by incomplete demagnetization of viscous components of the remanence. During af-demagnetization the directions of the remanence of many sites with reversed CARM move along a great circle which is defined by the present field direction, the NRM direction and the mean direction of the reverse CARM. This is particularly obvious for sites where the NRM direction strongly differs from the CARM direction. In these cases (Figs. 2 and 3) the CARM determined by the criterium of minimal scatter during af-demagnetization still lies rather far away from the mean CARM direction. Further af-demagnetization with higher fields yields no significant changes of the CARM direction. This suggests the existence of a viscous component in the direction of the present geomagnetic field, which could not be erased completely af-demagnetization. Thermal demagnetization might help in such cases. Incompletely erased secondary magnetiza-

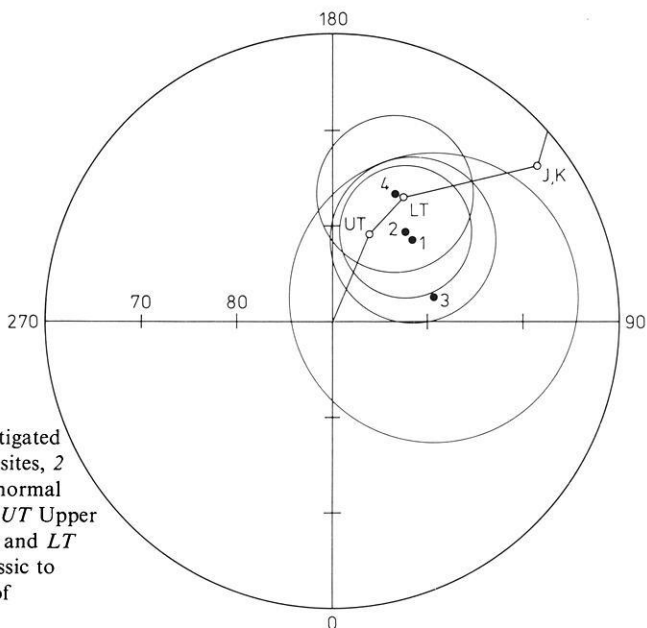


Fig. 6. Pole positions of the investigated basalts (see also Table 3). 1 OPF sites, 2 OPF + HEB sites, 3 OPF + HEB normal sites, 4 OPF + HEB reverse sites. *UT* Upper Tertiary, *LT* Lower Tertiary (*UT* and *LT* after McElhinny 1973), *J, K* Jurassic to Cretaceous (from a compilation of Schweitzer 1975)

tions in the direction of the present geomagnetic field produce shallower inclinations when the reversed primary magnetization has a shallower inclination than the present geomagnetic field at the sampling site and when the remaining secondary component is only a fraction of the primary magnetization.

The steeper inclinations of the normally magnetized sites cannot be explained by this mechanism. The number of sites may be too small in the present case to give a good Fisherian distribution and a satisfactory mean value of the inclination.

Acknowledgement. We thank Prof. G. Angenheister for his support and F. Führer, H. Gudden, A. Hussain, K. Peters, N. Petersen, G. Stettner and H. Zinßer for useful discussions and help during the collection of samples. The financial support of the Deutsche Forschungsgemeinschaft is gratefully acknowledged.

References

- Ade-Hall, J.M., Palmer, H.C., Hubbard, T.P.: The magnetic and opaque petrological response of basalts to regional hydrothermal alteration. *Geophys. J.* **24**, 137–174, 1971
- Babkine, J., Conquéré, F., Vilminot, J.C., Phan, K.D.: Les spinelles des basaltes de Monistrol d'Allier (Chaîne du Dèves, Haute-Loire). *Bull. Soc. Franc. Minér. Crist.* **88**, 447–455, 1965
- Bayerisches Geologisches Landesamt: Erläuterungen zur Geologischen Karte von Bayern 1: 500 000. München: Bayer. Geol. Landesamt 1964
- Duncan, R.A., Petersen, N., Hargraves, R.B.: Mantle plumes, movement of the European plate, and polar wandering. *Nature* **239**, 82–86, 1972
- Gudden, H.: Erläuterungen zur Geologischen Karte von Bayern 1: 25000. Blatt Nr. 5834 Kulmbach. München: Bayer. Geol. Landesamt 1955

- Marshall, M., Cox, A.: Effect of oxidation on the natural remanent magnetization of titanomagnetite in suboceanic basalt. *Nature* **230**, 28–31, 1971
- McElhinny, M.W.: *Palaeomagnetism and plate tectonics*, 358 p. Cambridge: University Press 1973
- Noussinanos, T.: *Geochemie und Petrologie Oberpfälzer Olivinnephelinite, Nephelinbasanite und ihrer Ultramafiteinschlüsse*. Dissertation, Fakultät für Geowissenschaften, Universität München. 94 S., München 1973
- Odin, G.S., Hunziker, J.C., Lorenz, C.R.: L'âge radiométrique du Miocène inférieur en Europe Occidentale et Centrale. *Geol. Rundschau* **64**, 570–592, 1975
- Refai, E.: Magnetic anomalies and magnetization of basalts in the area around Kemnath (Opf.). *Z. Geophys.* **27**, 175–187, 1961
- Richarz, S.: Die Basalte der Oberpfalz. *Z. Deut. Geol. Ges.* **72**, 1–100, 1920
- Schröder, B.: Zur Altersstellung der oberpfälzer Vorlandsbasalte. *Geol. Bl. NO-Bayerns* **12**, 1–15, 1962
- Schröder, B.: Tektonik und Vulkanismus im oberpfälzer Bruchschollenland und fränkischen Grabfeld. *Erlanger Geol. Abhandl.* **60**, 90 S., 1965
- Schweitzer, C.: Vergleich mehrerer Methoden zur Bestimmung der Intensität des Erdmagnetfeldes an rezenten Laven und ihre Anwendung auf mesozoische und paläozoische magmatische Gesteine. Dissertation, Fachbereich Geowissenschaften, Universität München, 157 S., München 1975
- Soffel, H., Supalak, P.: Paläomagnetische Messungen am Basalt des Parkstein bei Weiden (Bayern). *Z. Geophys.* **34**, 287–296, 1968
- Söllner, K.: Der Olivinnephelinit vom Teichelberg bei Groschlattengrün (Fichtelgebirge). *Neues Jahrb. Mineral., Abhandl.* **93**, 324–388, 1960
- Todt, W., Lippolt, H.J.: K-Ar-Altersbestimmungen an Vulkaniten bekannter paläomagnetischer Feldrichtung. I. Oberpfalz und Oberfranken. *J. Geophys.* **41**, 43–61, 1975
- Van Eysinga, F.W.B.: *Geological time table*, 3rd ed. Amsterdam: Elsevier 1975
- Wilson, R.L.: Palaeomagnetic differences between normal and reversed field sources, and the problem of far-sided and right-handed pole positions. *Geophys. J.* **28**, 295–304, 1972
- Wilson, R.L., Haggerty, S.E.: Reversals of the earth's magnetic field. *Endeavour* **25**, 104–109, 1966
- Wilson, R.L., McElhinny, M.W.: Investigation of the large scale palaeomagnetic field over the past 25 million years. Eastward shift of the Icelandic spreading ridge. *Geophys. J.* **39**, 570–586, 1974
- Wright, J.B.: The iron-titanium oxides of some Dunedin (New-Zealand) lavas, in relation to their paleomagnetic character (with an appendix on associated chromiferous spinel). *Mineral. Mag.* **36**, 425–435, 1967
- Wurm, A.: *Geologie von Bayern*. Berlin: Borntraeger 1961

Received May 14, 1976; Revised Version November 3, 1976

Palaeomagnetism of Upper Jurassic Limestones from Southern Germany*

F. Heller

Institut für Geophysik, ETH Zürich, CH-8093 Zürich, Switzerland

Abstract. Flat-bedded, shallow water, marine limestones interlayered with marls are well exposed in Franconia and Swabia, Southern Germany. The Upper Jurassic sediments sampled have been dated in detail palaeontologically, and cover the interval from middle Lower Oxfordian to middle Lower Kimmeridgian. Bed by bed sampling of sections at 11 localities throughout a thickness of more than 130 m yielded about 400 samples (1100 specimens) for palaeomagnetic analysis. The NRM intensities appear to correlate with the clay content and averaged 2×10^{-7} Gauss. Progressive alternating field demagnetization of each specimen was used to isolate the direction of the characteristic remanence, whose mean intensity averaged 5×10^{-8} Gauss. Only normally magnetized rocks are found in the lower part of the section, but distinct zones of normal and reversed polarity are found in the upper part (middle Lower Kimmeridgian) in both regions of investigation. The polarity sequence is tentatively correlated with the ocean floor Mesozoic magnetic anomaly sequence. The data yield a reliable estimate of a Late Jurassic palaeomagnetic pole position for stable Europe.

Key words: Palaeomagnetism – Marine magnetic anomaly sequence – Mesozoic limestones – Southern Germany.

1. Introduction

At present the palaeomagnetic record of the Mesozoic and especially of the Jurassic in stable Europe is still very poorly established. Four years ago, when Hicken et al. (1972) published their catalogue of palaeomagnetic directions and poles, not a single reliable palaeomagnetic pole position of Jurassic age could be cited for Europe. This lack of data results in a large degree of uncertainty in establishing the Mesozoic apparent polar wander curve. Reconstructions such as that of Van der Voo and French (1974) suffer from this paucity of

* Contribution No. 174, Institut für Geophysik, ETH Zürich

palaeomagnetic information in certain geological periods, especially in the Jurassic.

Interpretation of the Mesozoic magnetic polarity reversal sequence inferred from the oceanic magnetic surveys has recently undergone revision. The original Mesozoic reversal time scale of Larson and Pitman (1972) was criticized and refined in some respects. Larson and Hilde (1975) derived an improved scheme which comprised 18 new intervals of reversed polarity during the time span associated with anomalies M25–M17 covering part of the Late Jurassic. Since the marine magnetic anomaly sequence in itself provides only an undated record of relative polarity inversions, it is of great importance to calibrate the sequence by establishing its radiometric or biostratigraphic age by means of well-dated land-based sections. Lowrie and Alvarez (1977) succeeded in correlating in detail the Late Cretaceous marine anomalies (anomalies 34–29) with a contemporaneous land section in Italy. For the Late Jurassic, Steiner and Helsley (1975) tried to correlate the sedimentary record of two sections in Colorado with the oldest sea floor anomalies (M25–M23). Their correlation seems to be less positive than that of Lowrie and Alvarez.

The purpose of this paper is firstly to establish a reliable Late Jurassic palaeopole position for Europe and, secondly, to find out if a reversal stratigraphy on land can be correlated with the corresponding marine magnetic lineation pattern. The main reason for the lack of palaeomagnetic information for the Jurassic (and the rest of the Mesozoic) is that to a great extent only very weakly magnetized rocks were formed in Europe during this period. The development of extremely sensitive magnetometers (e.g. cryogenic magnetometers) permits the investigation of the natural remanent magnetization (NRM) of those rocks which are preferentially of sedimentary origin. The Upper Jurassic limestones exposed throughout Southern Germany are a suitable rock type to answer the two above problems, because they are unaltered, tectonically undisturbed and distributed over large geographical areas.

2. Geology

Rocks of Jurassic age are very well exposed in Southern Germany along a broad girdle which extends from Franconia (Northern Bavaria) in the north to the Danube river in the south and then continues southwestwards to Swabia (Württemberg) as shown in Figure 1. The uppermost part (Malm) contains the stages Oxfordian to Portlandian and is developed in carbonate facies, whereas the middle and lower Jurassic sections (Dogger, Lias) consist mainly of sandstones and shales.

Three facies types of carbonates can be distinguished in the Upper Jurassic sequence: well bedded, mainly chemical limestones and layered (biostromes) and unlayered moundlike (bioherms) biogenetic limestones. During the present study we have concentrated on the layered limestones. We have sampled sections from the beginning of Middle Oxfordian up to the end of middle Lower Kimmeridgian (Malm α – δ , Table 1). Thus according to the London Geological Society time scale (Howarth, 1964) the sampled profile covers the time interval from 156 my–147 my approximately.

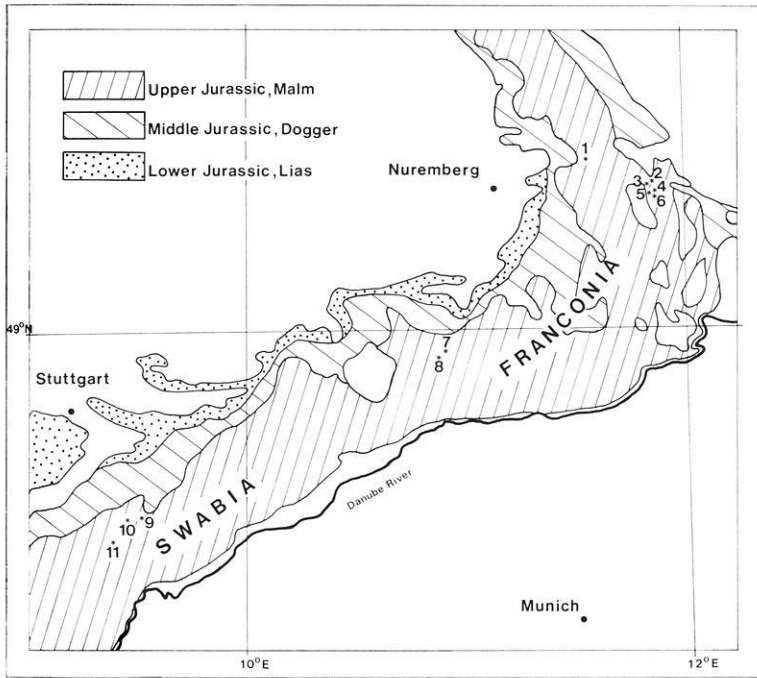


Fig. 1. Geological sketch map of the Jurassic in Southern Germany. Numbers indicate sampling localities 1-11

Table 1. Stratigraphic zonation of the Upper Jurassic section sampled

Stratigraphic stages	Zonation fossils (ammonites)	Regional sub-divisions	Absolute age (10 ⁶ yrs)
Malm	Kimmeridgian		
	Upper		
			146?
	Virgataxioceras setatum Sutneria subeumela	Malm ε (25 m)	
	Lower		
	Aulacostephanus eudoxus Aulacostephanus eulepidus	Malm δ (60 m)	
	Crussoliceras divisum Ataxioceras hypselocyclum	Malm γ (30 m)	
			151
	Oxfordian		
	Upper		
	Sutneria galar Idoceras planula	Malm β (16 m)	
	Middle		
	Epipeltoceras bimammatum Epipeltoceras berrense Divisosphinctes bifurcatus Arisphinctes plicatilis	Malm α (32 m)	
	Lower		
	Cardioceras cordatum Quenstedtoceras mariae		

The limestone sequence is flat-bedded throughout the whole region of investigation without any signs of major tectonic deformation. The limestones have been formed under marine shallow water conditions. In the lower part of the profile (Malm α - γ), fine-grained, fairly pure micrites with varying clay content (up to 10% by volume) are interlayered with marls, whereas in the upper part (Malm δ) biostrome facies predominate (especially in Franconia) which in the highest parts of the sections sampled show signs of beginning dolomitization. For most of the profile continuous sedimentation has been established. Minor sedimentation breaks are mooted for the Oxfordian/Kimmeridgian boundary (A. Zeiss, personal communication). The mean sedimentation rate is of the order of 1–2 cm/1000 y, and seems to increase as the age decreases.

The stratigraphy of the limestones has been studied in great detail (Schmidt-Kaler, 1962; v. Freyberg, 1966; Ziegler, 1959) and due to palaeontological bed by bed sampling well defined biostratigraphic zones have been delineated using ammonites as zone markers (Table 1). Thus even if facies changes took place between different regions, accurate correlation is still possible over lateral distances of several hundred kilometres (Zeiss, 1964).

For the present palaeomagnetic study about 400 cores which gave more than 1100 single specimens, were drilled bed by bed at 11 localities. They are spaced with a mean stratigraphic separation of 0.5 m throughout the entire profile of about 130 m thickness. Most sites are situated in Franconia (nrs. 1–8, Fig. 1) covering the lower three quarters (Malm α - γ) of the profile and generally overlap stratigraphically with one another. Three other localities (nrs. 9–11, Fig. 1) were chosen in Swabia to compare with the Malm δ data of Franconia and to extend the section up to the Malm δ/ϵ boundary.

3. Laboratory Procedures

The analysis of extremely weakly magnetic samples presents special problems not normally encountered in a palaeomagnetic study. To ensure as objectively as possible that the data obtained were reliable a set of laboratory procedures was used that enabled rejection criteria to be uniformly applied to all specimen measurements.

3.1. *The Measurement and Reliability of Weak Remanences*

The measurements of natural remanent magnetization (NRM) were carried out using a three-axis cryogenic magnetometer in which the components of magnetization along three orthogonal directions were simultaneously, and almost instantaneously, determined. The magnetometer was interfaced with an output terminal, and from there the data was transferred by cassette tape and telephone directly to the university's central computer.

Replicate observations were obtained by measuring each specimen twice, in an upright and in an inverted position. Initially, and between each pair of sample measurements, the signal of the empty sample holder was recorded.

Each of the 6 magnetization component readings was treated as an independent observation and was combined with two appropriate orthogonal components, thus giving eight estimates of the remanent magnetization vector. The internal dispersion of the directions about their mean, and the standard deviation of the intensity estimates, were used as control parameters for judging the reliability of each remanence measurement.

3.2. Selection of the Optimally Cleaned Direction

Each specimen was progressively demagnetized in alternating magnetic fields at 50 Oe increments to a peak field of 200 Oe. Some selected specimens were demagnetized to 3000 Oe. The directional stability of each specimen was judged objectively using a numerical index as follows. The direction cosines (l, m, n) were calculated at each demagnetization step. The change of direction (on a great circle) from the previous demagnetization step with direction cosines (l', m', n') is given by

$$\vartheta = \cos^{-1} (ll' + mm' + nn').$$

On dividing by the increment in field, a parameter ($\Delta\vartheta/\Delta H$) was described which has minimum value in the most stable region of the demagnetization and whose average value over the entire demagnetization curve allows an objective estimate of the quality of the remanence stability.

3.3. Rejection Criteria

Individual remanence measurements were discarded if the sample signal was weaker than the signal of the quartz-made sample holder, equivalent to a magnetization of around 5×10^{-9} Gauss. Large values of the internal dispersion parameter (angular standard deviation $> 50^\circ$) or of the scatter of magnetization components (standard deviation $> 50\%$ of mean) were used as indicators of unreliable measurements. Such large scatter could indicate the presence of very unstable components that remagnetize between each measurement in the weak fields in the laboratory, or it could indicate extreme inhomogeneity of the magnetization, or it could result merely from a faulty procedure (e.g. wrongly oriented sample in either measurement position). If the angular variation $\Delta\vartheta/\Delta H$ during stepwise AF demagnetization of a specimen always exceeded $0.5^\circ/\text{Oe}$, the specimen was rejected. Between 2 and 3 specimens were obtained from each bed by bed cored sample. As a final check on the data reliability the individual specimen directions were combined to give a sample mean. Again, if this mean were poorly defined, all data for the sample were rejected.

As a result of the cumulative application of these objective tests, about 15% of the collection of limestone samples was rejected. The remainder are considered to possess the characteristics for a reliable palaeomagnetic study.

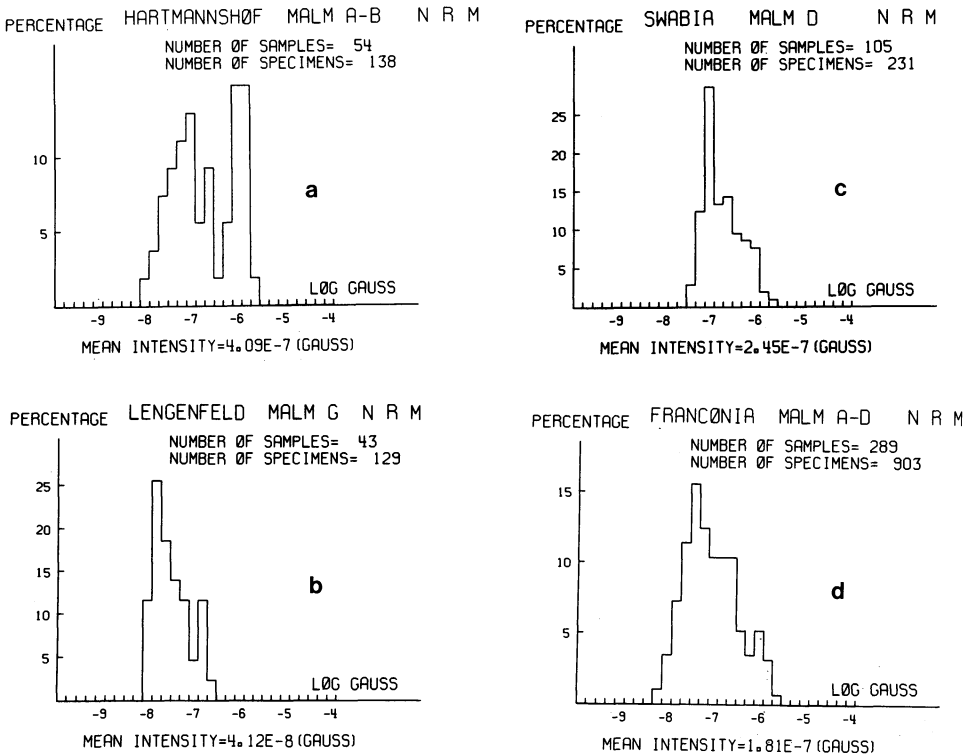


Fig. 2a-d. Histograms of NRM intensities before AF-cleaning. **a** Malm $\alpha + \beta$, site Hartmannshof (site no. 1, Fig. 1). **b** Malm γ , site Lengenfeld (site no. 2, Fig. 1). **c** Malm δ , all Swabian limestones (site nos. 9-11, Fig. 1). **d** Malm $\alpha - \delta$, all Franconian limestones (site nos. 1-8)

4. Palaeomagnetic Results

The initial NRM intensities average around 2×10^{-7} Gauss for all of the Franconian limestones (Fig. 2d), and appear to depend mainly on the clay content of the limestones. A higher intensity (peaking around 1×10^{-6} Gauss) was measured in 40% of the samples from the Hartmannshof site (Fig. 2a). These correspond to the marl-rich Malm α limestones, whereas the lower intensities belong to the very pure Malm β limestones.

AC demagnetization fields of 100-120 Oe lowered the remanent intensity drastically in many cases (for example, the Hartmannshof site, Fig. 3a), and on average to less than 50% of the initial value. Median destructive fields vary between 40 and 80 Oe. On the other hand not all samples were so unstable. Mainly samples in the biostrome limestones of Malm δ displayed extremely stable directions and intensities during AF demagnetization up to 3000 Oe peak field. The effect on these stable samples is seen by comparing the intensity histograms of the Swabian Malm δ rocks in Figures 2c and 3c, where almost all samples with higher initial NRM intensity retain the initial value after demagnetization.

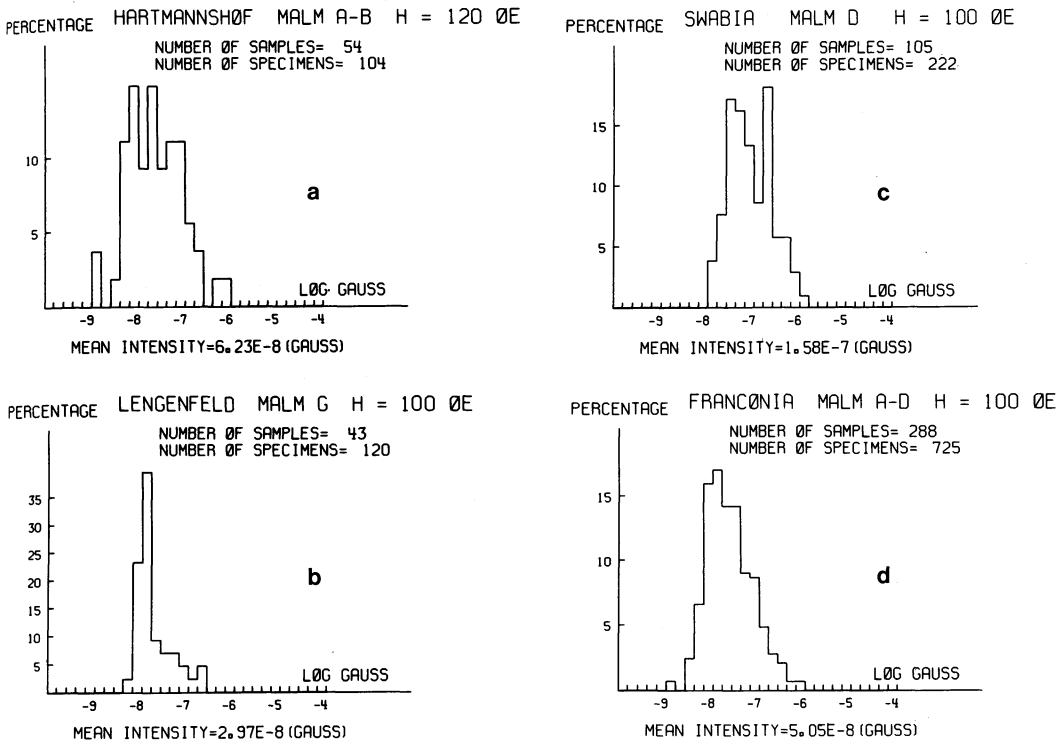


Fig. 3. Histograms of NRM intensities after AF-cleaning with peak fields of 100 Oe, respectively 120 Oe. Figures 3a-d refer to the same localities as shown in Figures 2a-d

Detailed studies of the rockmagnetic properties of the limestones have been initiated and will be published at a later date when complete. Preliminary indications are that in most cases magnetite is the remanent magnetization carrier. A second, high-coercivity mineral, not yet positively identified, is present in some samples. In most cases, the magnetite dominates, except in the Malm δ biostrome limestones where the roles often are reversed. Where both minerals are present the NRM direction associated with the high-coercivity mineral are close to those associated with the magnetite. The majority of samples probably carry a primary magnetization, but as no fold test were possible in these tectonically undisturbed flat lying beds, the effect of secondary magnetization can not be well estimated. All interpretation is made on the assumption that the age of the NRM is the same as the palaeontological age of the sediment.

Before AF cleaning the NRM directions are widely scattered (Fig. 4) with normal directions dominant. After using optimum cleaning fields ranging between 100 Oe and 200 Oe the scatter is reduced, but still appreciable. Areas with high density both of normal and reversed directions can be recognized. The reversed directions occur only in the higher part of the composite profile (cf. Swabian Malm δ data, Fig. 4). Mean directions for each geological subdivision and for the combined data from Franconia, and the resulting virtual palaeomagnetic pole position are listed in Table 2.

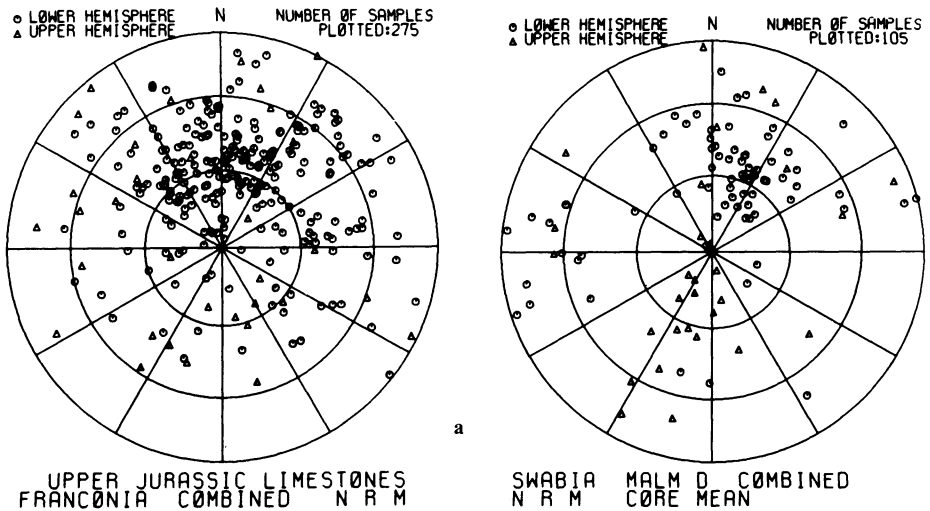


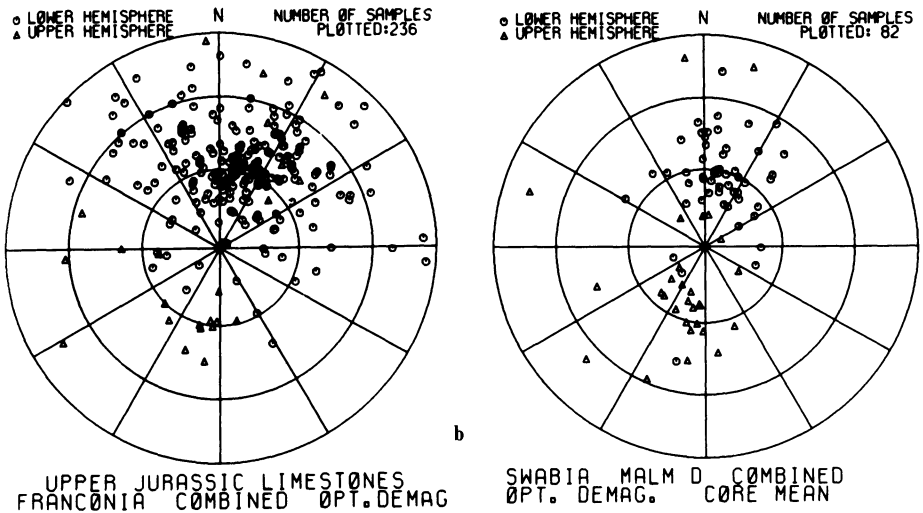
Fig. 4a and b. Equal area stereogram of Franconian and Swabian NRM directions a before AF-cleaning and b after optimum demagnetization

The declination and inclination data (Fig. 5) plotted against stratigraphic position after optimum AF cleaning do not show evidence for polarity reversals until the Malm γ/δ boundary. Although there is a lot of directional scatter, it is apparent that the whole Oxfordian and the lower part of the Lower Kimmeridgian are normally magnetized. Above the Malm γ/δ boundary several reversed intervals are observed in Franconia as well as in the partly overlapping section of Swabia. Correlation between Franconia and Swabia is fairly good, although the stratigraphic duration of normal and reversed zones seems to differ slightly, e.g. the normal interval between reversed intervals b and c (cf. the corresponding letters in Fig. 5). We think that these differences are due to varying sedimentation rates and sedimentation conditions between the two regions. (The clay content of the limestones in Swabia is generally higher than in the regions sampled in Franconia.)

The consistency of the occurrence of normal and reversed rocks within the same limestone beds was checked by comparing the results from two quarries

Table 2. Mean directions of AF-cleaned NRM and virtual geomagnetic pole positions (VGP)

Malm sub-division	Region	Number of samples	Site nos. (cf. Fig. 1)	Direction of magnetization			VGP position	
				D	I	α_{95}	Lat. N	Long. E
$\alpha-\delta$	Franconia	172	1-8	22	55	4	69	128
δ	Swabia	80	9, 10, 11	16	64	5	79	107
δ	Franconia	45	3, 7, 8	11	59	5	79	142
γ	Franconia	48	2, 3, 5	31	51	8	62	122
$\alpha + \beta$	Franconia	79	1, 4, 6	23	53	5	68	130



(localities 7 and 8 in Fig. 1) situated close together and representing the lowermost Malm δ . Their limestone layering is equally developed and both sections have nearly the same thickness (Fig. 6). The distribution of truly reversed and normal samples is very similar and the thickness of polarity zones varies from less than a metre to several metres, the corresponding time intervals ranging between 10,000 and about 100,000 years. In at least some cases documented, transitions occur within a few centimetres which would imply within a few thousand years. The polarity zones frequently contain samples with intermediate direction which sometimes even have the “wrong” polarity. The polarity profile (Fig. 6) shows an increase of the reversal frequency towards the bottom of the section.

5. Discussion

The Larson and Hilde (1975) model of the Mesozoic reversal sequence is bounded at both ends by prolonged periods of constant normal polarity (the so-called “magnetic quiet zones”). In particular a normal interval has been proposed for the Middle and Late Jurassic which corresponds to the quiet zone found for example in the North-Atlantic ocean between the Keathley lineations and the continental margin.

On the basis of our data (Fig. 7) we can confirm this period of normal magnetic polarity during the Oxfordian and the beginning of the Lower Kimmeridgian, thus spanning a time interval with minimum duration of about 6 my. The lower end of this normal period was not found in our profile. The upper end of the normal period is assigned a younger age than that suggested by Larson and Hilde. This discrepancy is rather negligible compared with the

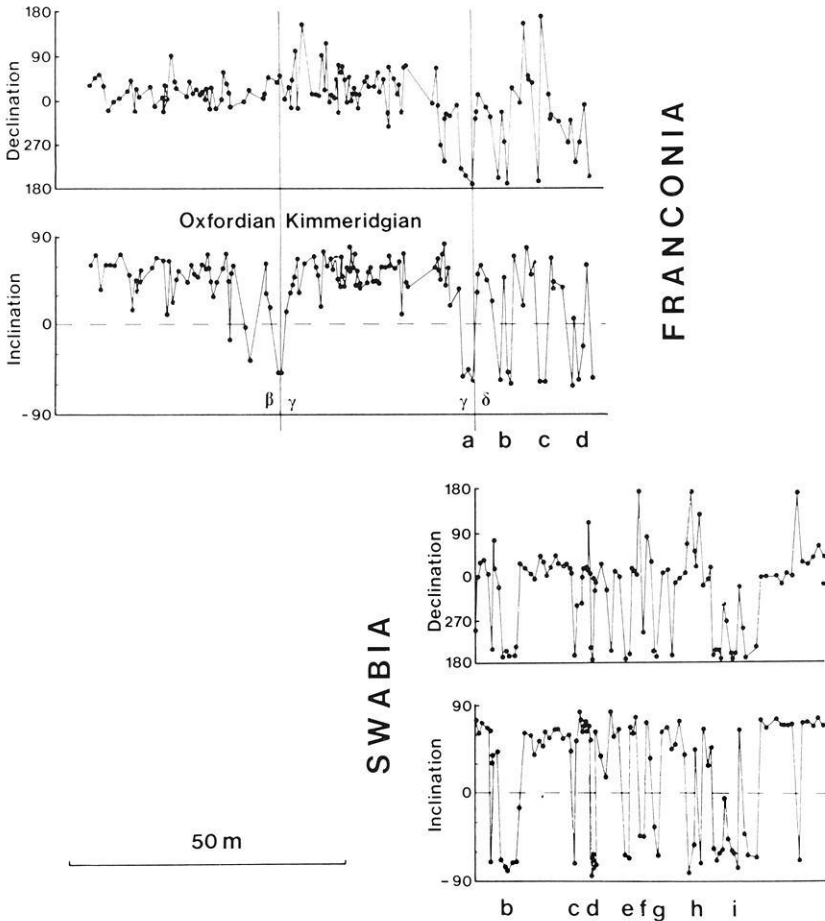


Fig. 5. Variation of declination and inclination of optimally AF-cleaned NRM across a composite profile of the Franconian limestones (above) and a composite profile from Swabia which extends the Franconian profile towards the Malm δ/ϵ boundary. Geological stage boundaries as well as boundaries of the regional Malm subdivisions (Malm β/γ , Malm γ/δ) are indicated. The sections constituting both profiles are taken from localities 1, 2, 7, 9, 10, 11 of Figure 1

probable errors arising from differences between micro- and macropalaeontological zonation and uncertainties in radiometric dating. However, if the ages of magnetic polarity zones are to be referred to stages of the geological time scale, then the onset of reversals is more safely dated from our profile than from the oceanic anomalies, as the ammonites which define the original Jurassic stage divisions control the stratigraphy of our profile.

5.1 Frequency of Reversals

If we compare the beginning of the Mesozoic sea-floor magnetic anomaly sequence (Fig. 7) with our land-based reversal pattern, a higher frequency of

Fig. 6. Comparison of polarity distribution between two sites (nos. 7 and 8, Fig. 1) situated close together. The 2 sections cover the same stratigraphic horizons and the thickness of the layers is nearly equally developed. Small numbers along both sections according to the layer numbers introduced by Streim (1960). Full squares and full triangles indicate the position of samples with reversed, respectively normal NRM directions which are close to the overall mean of Malm δ rocks. The corresponding open symbols refer to intermediate directions with flat negative, respectively positive inclination. The symbols have been plotted exactly at the stratigraphic position where the cores had been drilled mostly \pm parallel to the bedding plane. The combined polarity profile which results from the polarity distribution of the samples of both profiles has been drawn in between the 2 limestone sections

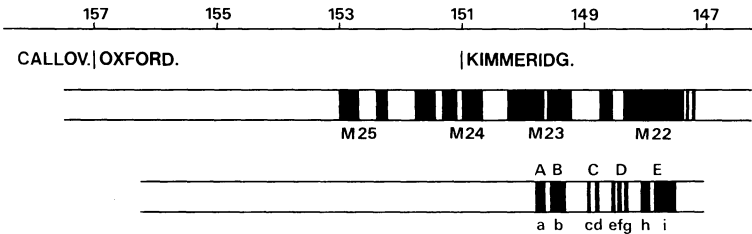
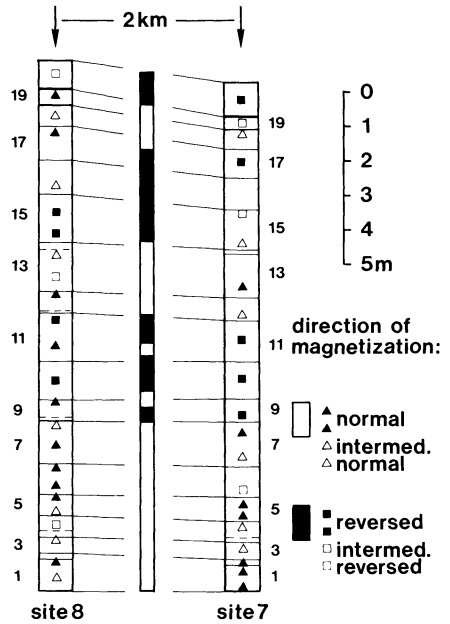


Fig. 7. Early Mesozoic sea-floor anomaly pattern (above) according to Larson and Hilde (1975) compared to the polarity profile (below) which has been observed in the land-based limestone sequence of Southern Germany. White zones within the profiles indicate record of normal polarity, black zones correspond to reversed polarity

reversals is recognized in the limestone section. Part of the higher frequency may be attributable to samples with intermediate directions possibly representing short magnetic field excursions; part may also be due to single samples with inverted directions possibly indicating a polarity event. Neither of these contributions has been filtered out of our reversal pattern in Figure 5 and both possibilities must therefore be taken into consideration. We think that two possible explanations for the correlation of the land-based profile with the marine anomaly sequence are at hand.

There is a tendency in the Mesozoic marine anomaly model for the reversal frequency to increase appreciably towards the lower end (M25) of the anomalies. Also the amplitude of the anomalies appears to decrease uniformly from about M21 to M25. Larson and Hilde (1975) suggested that this decrease was due to a corresponding variation of the geomagnetic field intensity at, and since,

the end of the Jurassic quiet period. The remanence intensities of the limestones are too scattered and their magnetic properties too variable to be able to sustain or disprove this idea. The palaeointensity variation of the geomagnetic field can only be estimated in sediments when the remanence intensity can be normalized for variation in lithology. Extensive rockmagnetic studies on these limestones will be needed before a description of variation of the geomagnetic field intensity can be attempted.

The high reversal frequency in our data (Figs. 5, 6, 7) was also observed by Steiner and Helsley (1975, Fig. 1), but is not present in the reversal sequence inferred from analysis of oceanic magnetic anomalies. The apparent decrease of the oceanic anomaly amplitudes towards the Jurassic quiet zone may indicate the presence of a high frequency of reversals that cannot be resolved at the oceanic surface. This interpretation would be compatible with our data. The reversed zones of the Southern German land-based composite section (identified by A to E in Fig. 7) may correspond to the pattern of reversals between anomalies M25 and M24.

It is conceivable that the reversal sequence we have identified does not correspond to any of the Mesozoic zones of mixed polarity derived from oceanic anomalies. Low amplitude fluctuations do exist within the Jurassic quiet zone and it may be that these represent earlier reversals. Larson and Hilde (1975) terminate the Jurassic quiet zone earlier than our dating suggests, thus if our reversal sequence is associated with quiet zone fluctuations, the discrepancy in dating the onset of the Mesozoic mixed polarity sequence is increased.

Such a large error in dating of oceanic anomalies is unlikely, and our best estimate at present is to associate our reversed zones A–E with the M25–M24 reversal pattern.

5.2. Comparison with Apparent Polar Wander Path

The polar wander path for Europe is very poorly defined in the Cretaceous and Jurassic. The need to fill this gap was one of our prime motivations in undertaking the present investigation. Van der Voo and French (1974) attempted to reconstruct the polar wander path for each of the Atlantic-bordering continents by combining plate motion reconstructions with the best acceptable palaeomagnetic data for all the continents. The Jurassic-Cretaceous part of their European polar wander path is determined by data that is largely non-European and especially the Jurassic pole positions are poorly defined.

The virtual geomagnetic pole positions (VGP) for each of the Malm subdivisions have been plotted in Figure 8 and the European polar wander path of Van der Voo and French has been added excluding their very poorly defined Jurassic pole positions. The Malm $\alpha+\beta$ and γ VGP's are very near to the Late Triassic pole position. This implies that only minor apparent polar wander or, neglecting true polar wander, continental movement took place. On the other hand the Malm δ positions of the Franconian and Swabian locations are slightly different from one another and are situated closer to the rotation axis than the VGP's of the older limestones. The discrepancy between Van der Voo and French's (1974) Early Cretaceous pole and our Late Jurassic

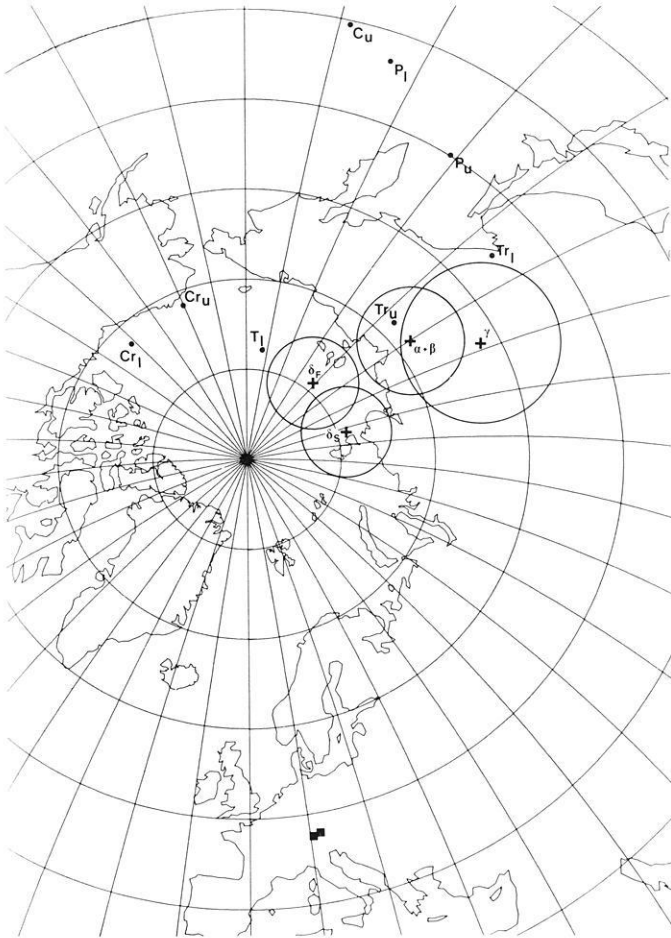


Fig. 8. Late Jurassic VGP positions from Southern German Malm subdivisions $\alpha + \beta$, γ and δ (δ_F = Franconian data, δ_S = Swabian data) and Van der Voo and French's (1974) reconstructed polar wander path for Europe (C_u : Late Carboniferous, P_1 and P_u : Early and Late Permian, Tr_1 and Tr_u : Early and Late Triassic, Cr_1 and Cr_u : Early and Late Cretaceous, T_1 : Early Tertiary)

pole position requires a fairly rapid motion of the pole at a rate of 10 cm/yr between the Oxfordian and the Early Cretaceous, assuming the simplest path of movement. This sudden movement is in close agreement with the data of Steiner and Helsley (1972) who found very similar palaeomagnetic evidence in the Jurassic of North America. The steeper inclinations and westerly declinations of the Malm δ rocks (Table 2) suggest northward movement and anticlockwise rotation of the whole continental mass, beginning in the middle Lower Kimmeridgian.

6. Conclusions

Although the Upper Jurassic limestones of Southern Germany are extremely weakly magnetized, they seem to be reliable recorders of palaeomagnetic infor-

mation. They yield a consistent estimate of a Late Jurassic pole position: Lat.N:=69°, Long.E:=128°, A_{95} :=4°. As this pole position is very close to the Late Triassic VGP of Van der Voo and French (1974), major movement of Europe with respect to the pole did not occur between Late Triassic and Late Jurassic. Probably commencing in the Lower Kimmeridgian major apparent polar wander or continental movement of about 30° of arc took place to reach the Lower Cretaceous pole position of Van der Voo and French. Although the rockmagnetic properties of the limestones are not yet completely worked out, we believe that the relatively close correlation of polarity distribution between our land profile and the marine magnetic anomaly pattern suggests a primary magnetization in the rocks investigated. The existence of a Jurassic normal quiet zone can be confirmed during at least the Oxfordian and the lower part of Early Kimmeridgian. The onset of the Mesozoic reversal sequence takes place during the middle Early Kimmeridgian.

Acknowledgements. I am very indebted to Prof. Dr. W. Lowrie and Dr. J. Channell who made a lot of extremely useful suggestions and valuable improvements on the manuscript. Thanks are also due to Mr. M. Grieder and Mr. W. Gruber for field assistance and help with the measurements.

References

- Freyberg, B.v.: Der Faziesverband im Unteren Malm Frankens. Erlanger geol. Abh. **62**, 1966
 Hicken, A., Irving, E., Law, L.K., Hastie, J.: Catalogue of palaeomagnetic directions and poles. first issue, Publ. Earth Phys. Branch **45**(1), 1972
 Howarth, M.K.: The Jurassic period. In: The Phanerozoic time scale. Quart. J. Geol. Soc. London (Suppl.) **120**, 260–262, 1964
 Larson, R.L., Pitman, W.C.: World-wide correlation of Mesozoic magnetic anomalies, and its implications. Geol. Soc. Am. Bull. **83**, 3645–3662, 1972
 Larson, R.L., Hilde, T.W.C.: A revised time scale of magnetic reversals for the Early Cretaceous and Late Jurassic. J. Geophys. Res. **80**, 2586–2594, 1975
 Lowrie, W., Alvarez, W.: The Gubbio section: Upper Cretaceous magnetic stratigraphy. Geol. Soc. Am. Bull., in press, 1977
 Schmidt-Kaler, H.: Stratigraphische und tektonische Untersuchungen im Malm des nordöstlichen Ries-Rahmens. Erlanger geol. Abh. **44**, 1962
 Steiner M.B., Helsley, C.E.: Jurassic polar movement relative to North America. J. Geophys. Res. **77**, 4981–4993, 1972
 Streim, W.: Geologie der Umgebung von Beilngries (Südliche Frankenalb). Erlanger geol. Abh. **36**, 1960
 Van der Voo, R., French, R.B.: Apparent polar wandering for the Atlantic-bordering continents: Late Carboniferous to Eocene. Earth Sci. Rev. **10**, 99–119, 1974
 Zeiss, A.: Zur Malm Gamma/Delta-Grenze in Franken. Geol. Bl. NO-Bayern **14**, 104–115, 1964
 Ziegler, B.: Profile aus dem Weissjura δ der Schwäbischen Alb. Arb. Geol. Paläont. Inst. TH Stuttgart, NF **21**, 1959

Received December 3, 1976

The Maximum Entropy Approach to Inverse Problems

Spectral Analysis of Short Data Records and Density Structure of the Earth*

E. Rietsch

Deutsche Texaco Aktiengesellschaft, Hauptlaboratorium für Erdölgewinnung,
D-3101 Wietze/Celle, Federal Republic of Germany

Abstract. The maximum entropy principle as described in the first, introductory part of the paper is applied to 2 problems: the estimation of the power spectrum from a finite number of values of the autocovariance function, and the determination of the density within the Earth from its mass, radius, and moment of inertia. In both cases the available information is given in terms of known values of linear functionals and the maximum entropy principle is used to derive a probability distribution for the values of the unknown function. The expectation value of the probability distribution for the spectral power is shown to be equal to the well-known maximum entropy power spectrum. The expectation value for the density within the Earth is in – with respect to the few data used – good agreement with that of accepted Earth models.

Key words: Maximum entropy – Probability distribution – Inverse problem – Power spectrum – Density – Earth.

Introduction

The problem of estimation of a large number of unknowns or an unknown function from only few measured values of functionals of these unknowns constitutes a typical task in geophysics. A deterministic approach to its solution is, for example, achieved by the well-known Backus-Gilbert inversion technique (Backus and Gilbert, 1967, 1968, 1970).

In this paper it is proposed to handle such problems by means of probabilistic methods based on the maximum entropy principle as put forward by Jaynes in 1968.

The paper starts with a review of the ideas which lead to the formulation of this principle. This introductory part is of a more tutorial character and intends

* Edited version of a paper presented at the Institute for Geophysics, Technical University Clausthal, on June 10, 1976

to explain the reasons for maximizing the entropy of a probability distribution. The equations established in this part are then applied to two examples. In the first a probability distribution for the spectral power of a band-limited time series is derived from the first few values of its autocovariance function. The expectation value of this probability distribution is shown to be the well known maximum entropy spectrum. In the second example a probability distribution is derived for the density as a function of depth of a spherically symmetric Earth assuming radius, mass, and moment of inertia to be known. The expectation value of the density obtained from of this probability distribution agrees amazingly well with the, according to Bullen (1975), most likely density distribution.

The Concept of Entropy

The Entropy of Discrete Probability Distributions

In probability theory a finite, complete system of events is understood to mean a set of events

$$A_1, A_2, \dots, A_n$$

such that, as a result of a certain experiment, one and only one of these events must occur. To each of these events A_k there is associated a probability of occurrence $p_k \geq 0$. The system of events and the associated probabilities may be arranged in the scheme

$$A = \begin{pmatrix} A_1 & A_2 & \dots & A_n \\ p_1 & p_2 & \dots & p_n \end{pmatrix},$$

and the completeness of the scheme A is expressed by

$$\sum_{j=1}^n p_j = 1. \quad (1)$$

The tossing of a coin, for example, may be described by the scheme

$$A = \begin{pmatrix} A_1 & A_2 \\ 1/2 & 1/2 \end{pmatrix},$$

which consists of the two events A_1 and A_2 representing the two possible outcomes heads and tails.

Any such scheme describes a situation of uncertainty. One knows that an experiment will lead to one of n possible events but is unable to predict with certainty which of these events will eventually occur.

Obviously, the amount of uncertainty concerning the outcome of an experiment is different in different schemes. Consider the scheme

$$B = \begin{pmatrix} B_1 & B_2 \\ 1 & 1023 \\ \frac{1}{1024} & \frac{1}{1024} \end{pmatrix}$$

which describes the simultaneous tossing of ten coins. The event B_1 occurs when all ten coins show heads, and the event B_2 comprises all other possible combinations of heads and tails for these ten coins. Clearly, in this scheme there is much less uncertainty than in scheme A . An experimenter will be almost sure to have the event B_2 as outcome of his experiment whereas he would refrain from any prediction in the situation described by scheme A .

Realization of a given scheme, i.e. performing of the experiment the possible outcomes (events) of which are described by this scheme, completely removes the uncertainty. Hence the average information obtained by carrying out the experiment (namely the information which of the possible events actually occurred) may be regarded as proportional to the uncertainty that existed before the experiment. Sometimes the notion "average information" is used synonymously with "uncertainty".

In this situation it seems desirable to have a measure for the amount of uncertainty inherent in a particular scheme or, equivalently, a measure of the average information obtained from a realization of this scheme.

Such a measure – which will be a function of the probabilities of the different events – must satisfy a number of reasonable consistency requirements (Aczél and Daróczy, 1975). From among these conditions the following three are sufficient to define a function $H(\mathbf{p}) = H(p_1, \dots, p_n)$ which serves this purpose and is unique – apart from a positive constant factor (Khinchin, 1957).

a) *The uncertainty associated with a finite complete scheme A takes its largest value if all events are equally likely.*

Because of Equation (1) this means

$$H(p_1, \dots, p_n) \leq H(1/n, \dots, 1/n). \tag{2}$$

b) *Addition of an impossible event to a scheme does not change the amount of uncertainty.*

The amount of uncertainty is therefore equal in the two schemes

$$\begin{pmatrix} A_1 & A_2 & \dots & A_n \\ p_1 & p_2 & \dots & p_n \end{pmatrix} \quad \text{and} \quad \begin{pmatrix} A_1 & A_2 & \dots & A_n & A_{n+1} \\ p_1 & p_2 & \dots & p_n & 0 \end{pmatrix}.$$

In terms of the function $H(\mathbf{p})$ this condition reads

$$H(p_1, \dots, p_n) = H(p_1, \dots, p_n, 0). \tag{3}$$

c) *The uncertainty in the product AB of the two schemes A and B is equal to the uncertainty in scheme A increased by the uncertainty remaining in scheme B after a realization of scheme A .*

Alternatively, by means of the previously introduced notion of the "average information", this third condition may be expressed as follows: The average information obtained from a realization of scheme AB is equal to the average information obtained from a realization of scheme A increased by the additional average information expected from a realization of scheme B after realization of scheme A .

The meaning of this condition is explained in the following. Let A and B denote 2 finite schemes with n and m possible events, respectively. The product scheme AB consists of the nm combinations $A_j B_k$ of events. Let p_j denote the probability

of event A_j in scheme A and let q_{jk} stand for the (conditional) probability that the event B_k of scheme B occurs provided that the event A_j in scheme A occurred. Then the product scheme AB has the form

$$AB = \begin{pmatrix} A_1 B_1 & A_1 B_2 & \dots & A_1 B_m & A_2 B_1 & \dots & A_n B_m \\ p_1 q_{11} & p_1 q_{12} & \dots & p_1 q_{1m} & p_2 q_{21} & \dots & p_n q_{nm} \end{pmatrix}$$

and condition c) demands that

$$H(AB) = H(A) + H(B|A). \tag{4}$$

The abbreviations

$$H(AB) = H(p_1 q_{11}, \dots, p_n q_{nm}), \quad H(A) = H(p_1, \dots, p_n)$$

denote the uncertainty in schemes AB and A , respectively, and

$$H(B|A) = \sum_j p_j H(q_{j1}, \dots, q_{jm})$$

describes the uncertainty in scheme B after a realization of scheme A . $H(q_{j1}, \dots, q_{jm})$ denotes the uncertainty in scheme B after occurrence of event A_j in scheme A . This function is multiplied with the probability p_j of event A_j and summed over all possible events of scheme A to obtain $H(B|A)$.

If the two schemes A and B are independent a realization of scheme A does not convey any information concerning the outcome of a realization of scheme B : the q_{jk} do not depend on j . In this case $H(B|A) = H(B)$.

On the other hand, $H(B|A) = 0$ if the outcome of scheme A completely determines the outcome of scheme B .

The above three conditions lead to a function (Khinchin, 1957)

$$H(p_1, \dots, p_n) = -\lambda \sum_{j=1}^n p_j \log p_j \tag{5}$$

which is called "entropy" in view of an analogy with the entropy in thermodynamics. It is unique apart from the positive factor λ which frequently is set to $1/\log 2$. Hence it can be omitted if the logarithm is to the base 2 as done in the following.

It is easy to show that the function H defined in (5) satisfies the above stated three basic conditions.

Another obviously necessary property of the uncertainty in a finite scheme can also be easily established from (5): the entropy is zero if and only if one of the numbers p_j is unity and all others are zero. This is just the case when the outcome of an experiment can be predicted with certainty.

Incorporation of Information

The first of the three conditions which lead to the mathematical expression for the entropy specified that the entropy must have a maximum when all possible outcomes of an experiment are equally likely. Such a situation exists if there is no

reason to consider one possible outcome of an experiment to be more likely than any other. This condition is related to Bernoulli's principle of insufficient reason or Keynes' principle of indifference (Rowlinson, 1970). It is a subjective principle and does not necessarily mean that all events are really equally probable but only that one's state of knowledge is not sufficient to assign to some of the outcomes a higher probability than to others. However, if one is given information concerning the outcome of the experiment it should be exploited to obtain better estimates of the probabilities. The foregoing analysis gives a clue how this can be accomplished. The distribution of probabilities among the possible events should maximize the uncertainty of the scheme without contradicting the given information. Any other choice of probabilities would either lead to a probability distribution with lower entropy—thus implying that further information has been assumed—or contradict the available information or both.

Let this information be given in the form of mean values $\bar{f}_1, \dots, \bar{f}_m$ of m functions $f_1(A_j), \dots, f_m(A_j)$ of the n possible outcomes A_j , where $m < n$. The distribution of probabilities complying with this information and free from all other assumptions is the one which maximizes the entropy

$$H = - \sum_j p_j \log p_j \tag{6}$$

subject to the constraints

$$\sum_j p_j = 1 \tag{7}$$

$$\sum_j p_j f_k(A_j) = \bar{f}_k \quad k = 1, 2, \dots, m. \tag{8}$$

Here and in the following the summations over j and k are understood to extend from 1 to n and 1 to m , respectively. Condition (7) means that the system of events is complete while the m equations (8) specify the known mean values \bar{f}_k of the functions $f_k(A_j)$. The solution to this problem by means of Lagrange multipliers is straightforward and leads to

$$p_j = \frac{1}{Z(\lambda)} \exp \left[\sum_k \lambda_k f_k(A_j) \right]. \tag{9}$$

The form of the partition function

$$Z(\lambda) = Z(\lambda_1, \dots, \lambda_m) = \sum_j \exp \left[\sum_k \lambda_k f_k(A_j) \right] \tag{10}$$

makes immediately clear that the normalization condition (7) is satisfied. The m Lagrange multipliers λ_k are to be determined from the m conditions (8) which can be brought into the form

$$\frac{\partial}{\partial \lambda_k} \ln Z(\lambda) = \bar{f}_k. \tag{11}$$

The entropy reads

$$H = (\ln Z(\lambda) - \sum_k \lambda_k \bar{f}_k) / \ln 2. \tag{12}$$

Entropy of Continuous Probability Distributions

The derivation of the entropy (5) as a measure of the uncertainty is only valid for discrete probability distributions. This represents a limitation and, in view of the success of the maximum entropy principle in discrete cases, makes it desirable to extend the concept of entropy to random variables for which a continuum of values is permitted.

Let X denote a random variable which may have values x in some interval $[a, b]$ and let $p(x)dx$ denote the probability that a value of X be in the interval¹ $[x, x+dx]$. A selfsuggesting approach to the definition of the entropy of this continuous probability distribution is to subdivide the interval $[a, b]$ into sub-intervals $[x_{j-1}, x_j]$ where

$$a = x_0 < x_1 < \dots < x_n = b$$

and to denote by $p_j \Delta x_j$ the probability that x is in the interval $[x_{j-1}, x_j]$ of length $\Delta x_j = x_j - x_{j-1}$. The entropy of this discretized probability distribution reads

$$\begin{aligned} H &= - \sum_j p_j \Delta x_j \log(p_j \Delta x_j) \\ &= - \sum_j p_j \Delta x_j \log p_j - \sum_j p_j \Delta x_j \log \Delta x_j. \end{aligned} \quad (13)$$

For $n \rightarrow \infty$ and $\max(\Delta x_j) \rightarrow 0$ the first term to the right of the last equality sign in (13) passes to

$$\int p(x) \log p(x) dx$$

where the integral is understood to extend over the interval $[a, b]$. The second term requires special analysis. By means of weights w_j defined as

$$\Delta x_j = \delta / w_j \quad \sum_j w_j \Delta x_j = n \delta = 1 \quad (14)$$

and the discretized normalization condition

$$\sum_j p_j \Delta x_j = 1$$

it can be rewritten as

$$- \sum_j p_j \Delta x_j \log \Delta x_j = \sum_j p_j \Delta x_j \log w_j + \log n.$$

By means of this procedure the last term in (13) has been separated into a finite term which approaches the Riemann integral

$$\int p(x) \log w(x) dx$$

for $n \rightarrow \infty$ and $\max(\Delta x_j) \rightarrow 0$ and a divergent term which, however, does not depend on the particular subdivision of the interval $[a, b]$. Neglecting of this divergent term leads to the following equation for the entropy of a continuous probability distribution

$$H = - \int p(x) \log [p(x)/w(x)] dx \quad (15)$$

¹ In order to avoid unnecessary complications open and closed ends of intervals are not distinguished

which depends not only on $p(x)$ but also on $w(x)$, an “invariant measure” function (Jaynes, 1968) proportional to the varying density of the x_j in the limiting case.

Incorporation of Information

Let the information about the probability distribution $p(x)$ again be given in form of known mean values \bar{f}_k of m different functions $f_k(x)$.

$$\int p(x) f_k(x) dx = \bar{f}_k \quad k = 1, \dots, m. \tag{16}$$

Maximization of H subject to these conditions leads to

$$p(x) = [w(x)/Z(\lambda)] \exp \left[\sum_k \lambda_k f_k(x) \right]$$

$$Z(\lambda) = \int w(x) \exp \left[\sum_k \lambda_k f_k(x) \right] dx \tag{17}$$

and the Lagrange multipliers λ_k are determined by means of Equation (11).

At this stage there appears a practical difficulty not present in the discrete case discussed before. The measure $w(x)$ defining the distribution of the x_j in the limiting case is as yet undetermined unless there exists an obvious limiting process. The meaning of $w(x)$ becomes clear if a situation is considered in which no prior information is available. In this case there are no Lagrange multipliers and from Equations (17) follows

$$p(x) = w(x) \tag{18}$$

by virtue of

$$\int w(x) dx = 1 \tag{19}$$

obtained from (14) by passing to the limit $n \rightarrow \infty$, $\max(\Delta x_j) \rightarrow 0$. Hence $w(x)$ represents the prior probability distribution existing in the case of complete ignorance. Since the Lagrange multipliers may only be determined if $w(x)$ is known the question arises how to find this prior probability distribution.

A uniform prior probability distribution can not generally be appropriate since it is not invariant under coordinate transformations *and* since there exists apparently no general criterion for finding a “distinguished” coordinate system.

Jaynes (1968) proposed to use group theoretical reasoning, in particular to search for transformations under which there is no change in the level of ignorance and to require that $w(x)$ be invariant with respect to these transformations. This approach has been used to determine the prior probability distribution in the first of the following 2 examples.

Another possibility has already been mentioned. As often is the case with physical quantities, the variable X may be continuous as a result of an abstraction process; i.e., in principle, only a discrete set of values x_j is permissible for X with the difference $\Delta x_j = x_j - x_{j-1}$, however, so small that, for practical applications, X may be assumed to be continuous. Then there exists an obvious discretization and $w(x)$ can be determined. This possibility is employed in the second example.

Multivariate Probability Distributions

Generalization to multivariate probability distributions of Equations (15) to (17) is straightforward. Let \mathbf{X} denote a vector of random variables (X_1, \dots, X_n) and let $p(\mathbf{x})$ denote the multivariate (or joint) probability distribution $p(x_1, \dots, x_n)$. With $w(\mathbf{x})$ representing the multivariate prior probability distribution the entropy reads

$$H = - \int p(\mathbf{x}) \log [p(\mathbf{x})/w(\mathbf{x})] dv. \tag{20}$$

Here and in the following dv denotes the n -dimensional volume element, and the integration is extended over all possible values of the random variables X_j .

If the information about \mathbf{X} is given in the form

$$\int p(\mathbf{x}) f_k(\mathbf{x}) dv = \bar{f}_k \tag{21}$$

multivariate probability distribution and partition function are given by

$$p(\mathbf{x}) = [w(\mathbf{x})/Z(\lambda)] \exp \left[\sum_k \lambda_k f_k(\mathbf{x}) \right] \tag{22}$$

$$Z(\lambda) = \int w(\mathbf{x}) \exp \left[\sum_k \lambda_k f_k(\mathbf{x}) \right] dv.$$

Spectral Analysis of Time Series by Means of the Autocovariance Function

Statement of the Problem

Let

$$A_n = \int P(f) \exp(2\pi i f n \Delta t) df \tag{23}$$

denote the autocovariance function of a time series sampled at equidistant time values $n \Delta t$. The upper frequency limit be equal to the Nyquist frequency $f_v = 1/(2\Delta t)$ and the integral in (23) is understood to extend from $-f_v$ to f_v . For a real-valued time series the A_n are real and symmetric and $P(f)$ is real, symmetric, and nonnegative.

It is required to estimate $P(f)$ from a limited number of values of the autocovariance function.

Usually this is accomplished by invoking the Fourier inversion theorem. Owing to the finite number of available values of the autocovariance function only a smoothed version

$$\tilde{P}(f) = \Delta t \sum_n A_n W_n \exp(-2\pi i f n \Delta t)$$

of the true power spectrum $P(f)$ may be obtained (Kanasewich, 1975)

$$\tilde{P}(f) = \int K(f - f') P(f') df'.$$

The amount of smoothing can be influenced by proper selection of the coefficients W_n of the Fourier kernel

$$K(f) = \Delta t \sum_n W_n \exp(-2\pi i f n \Delta t).$$

A formally identical result is obtained if the problem is attacked by the Backus-Gilbert inversion technique which leads to a particular kernel (Backus and Gilbert, 1968, appendix B). Kernels of this type have been investigated by Papoulis (1973).

It is the objective of this example to show how this problem can be handled by means of the above derived maximum entropy equations. For this purpose Equation (23) is considered as the limiting case of the periodic autocovariance function A_n^T with period T .

$$A_n = \lim_{T \rightarrow \infty} A_n^T = \lim_{M \rightarrow \infty} \left[\Delta f \sum_m P_m \exp(2\pi i n m/M) \right]. \tag{24}$$

Here

$$\Delta f = 1/T, \quad P_m = P(m/T), \quad M = 2f_v T \gg 2N.$$

The summation over m in Equation (24) extends from $[-(M-1)/2]$ to $[(M-1)/2]$ or from 0 to $M-1$ (here brackets denote the greatest integer less or equal to the enclosed expression). This reduces the problem to the determination of the spectral power at discrete frequencies $f_m = m/T$.

Since the number of unknowns grossly exceeds the number of known values of the autocovariance function no attempt is made to determine a fixed value of the spectral power at each of the discrete frequencies. Instead, a probability distribution of the spectral power is derived. In the spirit of the foregoing analysis it is requested that this probability distribution maximizes the entropy while accounting for the information available in form of the known values of the autocovariance function. Hence the maximum entropy principle may be formulated as follows.

Maximize the entropy

$$H = - \int p(\mathbf{P}) \log [p(\mathbf{P})/w(\mathbf{P})] dv \tag{25}$$

of the multivariate probability distribution $p(\mathbf{P}) = p(P_{[-(M-1)/2]}, \dots, P_{[(M-1)/2]})$ subject to the normalization condition

$$\int p(\mathbf{P}) dv = 1 \tag{26}$$

and

$$\Delta f \int p(\mathbf{P}) \left[\sum_m P_m \exp(2\pi i n m/M) \right] dv = \bar{A}_n \quad n = -N, \dots, N. \tag{27}$$

The last condition implies that the expectation value of the Fourier transform of the power spectrum should agree with the known values \bar{A}_n of the autocovariance function. The integrations in Equations (25), (26) and (27) are performed over all positive values of $P_{[-(M-1)/2]}, \dots, P_{[(M-1)/2]}$, and dv denotes the M -dimensional volume element.

The resulting multivariate probability distribution has the form (Eq.(22))

$$p(\mathbf{P}) = [w(\mathbf{P})/Z(\lambda)] \exp\left(-\sum_m L_m P_m\right) \tag{28}$$

$$Z(\lambda) = \int w(\mathbf{P}) \exp\left(-\sum_m L_m P_m\right) dv \tag{29}$$

where

$$L_m = \sum_n \lambda_n \exp(2\pi i n m/M) \quad (30)$$

and λ_n denote the $2N+1$ Lagrange multipliers.

Here and in the following summation over n is understood to extend from $-N$ to N while summation over m goes from $[-(M-1)/2]$ to $[(M-1)/2]$.

Prior Probability Distribution of the Power Spectrum

Determination of the Lagrange multipliers requires knowledge of $w(\mathbf{P})$. This prior probability distribution of the spectral power can be determined on the basis of the following 3 conditions.

1. *The spectral power $P(f)$ can be represented as the sum of the squares of the Fourier cosine component $C(f)$ and the Fourier sine component $S(f)$.*

$$P(f) = C^2(f) + S^2(f).$$

2. *$C(f)$ and $S(f)$ are independent from each other, i.e. knowledge of one of the Fourier components conveys no information concerning the value of the other Fourier component.*

3. *The probability distribution of $C(f)$ and $S(f)$ does not depend on the origin of the time axis.*

This last condition means that the new Fourier coefficients

$$C'(f) = \cos \varphi C(f) - \sin \varphi S(f)$$

$$S'(f) = \sin \varphi C(f) + \cos \varphi S(f)$$

which are obtained in place of $C(f)$ and $S(f)$ if the origin of the time axis is shifted by τ should have the same probability distribution—for any $\varphi = 2\pi f\tau$.

The joint probability distribution for C and S (for the sake of simplicity the argument f is omitted) is, because of condition 2, equal to the product $p_c(C) p_s(S)$ of the probability distribution of the individual Fourier components. Condition 3 requires that

$$p_c(C) p_s(S) = p_c(\cos \varphi C - \sin \varphi S) p_s(\sin \varphi C + \cos \varphi S). \quad (31)$$

Putting $\varphi = \pi/2$ one finds

$$p_c(C)/p_s(C) = p_c(-S)/p_s(S)$$

for any C and S . Hence the two Fourier components must have the same probability distribution.

Let $y = \cos \varphi C$, $z = \sin \varphi C$, $S = 0$. Then Equation (31) reduces to the well known functional equation

$$p_c(\sqrt{y^2 + z^2}) p_c(0) = p_c(y) p_c(z)$$

which has the normalized solution (Rao, 1965)

$$p_c(C) = \sqrt{\lambda/\pi} \exp(-\lambda C^2) \tag{32}$$

with the arbitrary positive constant λ . Because of condition 1 the probability distribution for the spectral power derived from Equation (32) reads

$$w(P) = \lambda \exp(-\lambda P). \tag{33}$$

If knowledge of the power at one frequency does not convey information concerning the power at any other frequency the multivariate prior probability distribution is the product of the prior probability distributions of the spectral power at the frequencies f_m . Furthermore the parameter λ should be equal for all frequencies.

Hence

$$w(\mathbf{P}) = \lambda^M \exp(-\lambda \sum_m P_m). \tag{34}$$

Probability Distribution and Expectation Value of the Spectral Power

The parameter λ in Equation (34) plays the role of a scaling factor and may be included into the Lagrange multiplier λ_0 in L_m (Eqs.(28) and (30)). The multivariate probability distribution $p(\mathbf{P})$ factors into the product of the probability distributions for the individual frequencies

$$p(\mathbf{P}) = \prod_m p_m(P_m)$$

with

$$p_m(P_m) = L_m \exp(-L_m P_m). \tag{35}$$

The expectation value of the spectral power at frequency f_m reads

$$\bar{P}_m = \int P_m p_m(P_m) dP_m = 1/L_m. \tag{36}$$

At this stage it is convenient to pass to the limit $T \rightarrow \infty$. Then

$$L_m \rightarrow L(f) = \sum_n \lambda_n \exp(2\pi i f n \Delta t) \tag{37}$$

$$\bar{P}_m \rightarrow \bar{P}(f) = 1/L(f). \tag{38}$$

In order to determine the Lagrange multipliers λ_n we note that the power spectrum must be positive and integrable. Hence $L(f)$ must be nonnegative and, by the Fejér-Riesz Theorem (Akhiezer, 1956), allows factoring

$$L(f) = \lambda G(f) G^*(f) = \lambda |G(f)|^2$$

where

$$G(f) = \sum_{v=0}^N g_v \exp(2\pi i f v \Delta t),$$

and λ denotes a factor chosen to make $g_0 = 1$.

Multiplication of both sides of (38) by $G^*(f) \exp(2\pi i f n \Delta t)$ and integration from $-f_v$ to f_v leads to (Edward and Fitelson, 1973)

$$\sum_{v=0}^N \bar{A}_{n-v} g_v = \frac{1}{\lambda \Delta t} \delta_{n0} \tag{39}$$

where \bar{A}_n denote the given values of the autocovariance function and δ_{n0} the Kronecker symbol. From this linear system of equations the g_v can be identified as the coefficients of the $(N + 1)$ -length prediction error filter with $P_{N+1} = 1/(\lambda \Delta t)$ being the power of the unpredictable noise. Thus the expectation value $\bar{P}(f)$ of the probability distribution for the spectral power is equal to the well known maximum entropy power spectrum

$$\bar{P}(f) = 1/[\lambda |G(f)|^2] = P_{N+1} \Delta t / |\sum_v g_v \exp(2\pi i f v \Delta t)|^2 \tag{40}$$

which has found application in many different branches of geophysics (e.g. Ulrych, 1972; Smylie, Clarke and Ulrych, 1973; Jensen and Ulrych, 1973; Phillips and Cox, 1976).

Density Distribution within a Spherically Symmetric Earth

Statement of the Problem

This second example to be discussed refers to the following question: What can be said about the density distribution $\rho(r)$ within a (spherically symmetric) planet if its mass M , radius R , and moment of inertia J are known (in order to have specific data this planet is assumed to be the Earth).

This problem which constitutes part of an investigation by Cook (1971) could, in principle, be attacked by the Backus-Gilbert inversion method which would result in a smoothed version of the true density distribution. Here, however, the data are so inadequate with respect to the desired solution that the "resolution length" which characterizes the amount of smoothing is of the order of R and thus renders the results rather useless.

Parker (1972) has adopted another approach to this problem. He proposed to look for inequalities resulting from these data such that all Earth models complying with the given data satisfy the inequalities. In this way he concluded, for example, that the maximum density in the Earth must not be less than ρ_0 where

$$\rho_0 = \bar{\rho}/y^{3/2} = 1.299 \bar{\rho} = 7.166 \text{ g/cm}^3 \tag{41}$$

and

$$\bar{\rho} = 5.517 \text{ g/cm}^3, \quad y = 5J/(2MR^2) = 0.84 \tag{42}$$

denote mean density (Bullen, 1975) and a dimension less factor proportional to the ratio of the actual moment of inertia of the Earth and the moment of inertia of a homogeneous sphere with the same mass and radius, respectively.

This bound has much in common with error bounds e.g. in numerical integration, summation, or inversion of matrices. These bounds are safe but usually overly pessimistic; in general, the error is much lower than indicated by the bounds.

This example is to demonstrate the maximum entropy approach to this problem. To this aim the Earth is subdivided into N equivoluminous shells and to each shell there is assigned a constant density ρ_n . By means of this discretization

$$M = 4\pi \int_0^R \rho(r) r^2 dr \rightarrow \frac{4\pi}{3} \sum_n \rho_n (r_n^3 - r_{n-1}^3) \tag{43}$$

$$J = \frac{8\pi}{3} \int_0^R \rho(r) r^4 dr \rightarrow \frac{8\pi}{15} \sum_n \rho_n (r_n^5 - r_{n-1}^5) \tag{44}$$

with

$$r_n = R(n/N)^{1/3} \tag{45}$$

denoting the outer radius of the n -th shell. Here and in the following the summation over n is understood to extend from 1 to N .

For $N > 2$ it is impossible to uniquely determine the ρ_n and hence a probability distribution $p(\rho)$ is established for the densities of the N shells. This multivariate probability distribution should maximize the entropy

$$H = - \int p(\rho) \log [p(\rho)/w(\rho)] dv \tag{46}$$

subject to condition

$$\int p(\rho) dv = 1. \tag{47}$$

Furthermore, the expectation values

$$\bar{\rho}_n = \int \rho_n p(\rho) dv \tag{48}$$

should satisfy

$$\sum_n \bar{\rho}_n = \bar{\rho} N \tag{49}$$

$$\sum_n \bar{\rho}_n [n^{5/3} - (n-1)^{5/3}] = y \bar{\rho} N^{5/3}. \tag{50}$$

Prior Probability Distribution

Before proceeding further we shall determine the appropriate prior probability distribution for the densities ρ_n . In this case it is easiest to look for a physically reasonable discretization.

In view of the atomistic nature of matter the density of a pure material is proportional to the number of molecules per volume element. Therefore the density can have values from a discrete set only. Adding or removing one molecule from the volume element changes the density by a fixed constant amount. Thus the range of possible values for the density is to be subdivided into intervals of equal width and the concentration of subdivision points is a constant. Hence a constant prior probability distribution is appropriate.

This line of argument is not invalidated if different types of molecules are permitted. In this case the density can change in different steps, and as long as the change in density is independent from the number of molecules already present the limiting distribution of subdivision points is still a constant. Since the Earth has been subdivided into shells of equal volume the prior probability distribution is the same for all shells.

Probability Distribution and Expectation Value for the Density

Maximization of the entropy (46) subject to Equations (47), (49) and (50) leads to

$$p(\rho) = \exp\left[-\sum_n \rho_n h_n(\lambda)\right]/Z(\lambda) \quad (51)$$

where

$$h_n(\lambda) = \lambda_1 + \lambda_2 [n^{5/3} - (n-1)^{5/3}]/N^{2/3} \quad (52)$$

$$Z(\lambda) = \int \exp\left[-\sum_n \rho_n h_n(\lambda)\right] dv. \quad (53)$$

From (51) follows that the multivariate probability distribution $p(\rho)$ is the product of the probability distributions

$$p_n(\rho_n) = \exp[-\rho_n h_n(\lambda)]/Z_n(\lambda) \quad (54)$$

of the densities of the N shells.

Let $\rho_l \geq 0$ and $\rho_u \leq N\bar{\rho}$ denote the lowest and highest possible density, respectively. Then by (53) and (54)

$$Z_n(\lambda) = \exp[-\rho_l h_n(\lambda)] [1 - 1/E_n(\lambda)]/h_n(\lambda) \quad (55)$$

with

$$E_n(\lambda) = \exp[(\rho_u - \rho_l) h_n(\lambda)], \quad (56)$$

and the expectation value $\bar{\rho}_n$ has the form

$$\bar{\rho}_n = \int \rho_n p_n(\rho_n) d\rho_n = \rho_l + 1/h_n(\lambda) - (\rho_u - \rho_l)/[E_n(\lambda) - 1]. \quad (57)$$

The unknown Lagrange multipliers λ_1 , λ_2 can be obtained from Equations (49) and (50) with $\bar{\rho}_n$ substituted from Equation (57).

For the upper density limit ρ_u sufficiently large (say $\rho_u \geq 300$ g/cm³) the third term in Equation (57) may be neglected. In this case Equations (49) and (50) take the form

$$\sum_n 1/h_n(\lambda) = (\bar{\rho} - \rho_l) N \quad (58)$$

$$\sum_n [n^{5/3} - (n-1)^{5/3}]/h_n(\lambda) = (y\bar{\rho} - \rho_l) N^{5/3}. \quad (59)$$

Combination of (58) and (59) leads to

$$(\bar{\rho} - \rho_l) \lambda_1 + (y\bar{\rho} - \rho_l) \lambda_2 = 1 \quad (60)$$

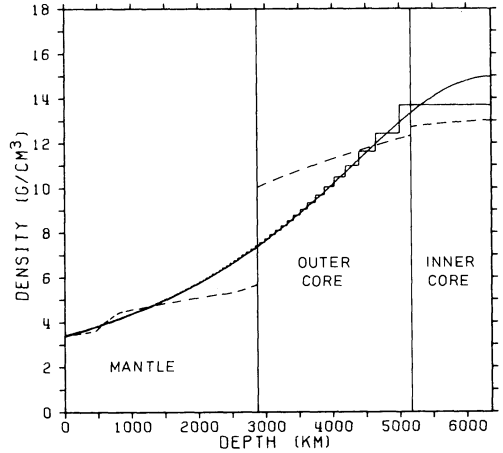


Fig. 1. Discrete ($N = 100$, step function) and continuous ($N \rightarrow \infty$) density distribution for lower density limit $\rho_l = 0$. Bullen's (1975) density distribution is represented by the dashed curve

which can be used to eliminate one of the unknowns from either Equation (58) or (59). The resulting nonlinear equation for the other unknown can be easily solved with standard methods.

For $N = 100$, $\rho_l = 0$ and $\rho_u = N \bar{\rho}$, for example,

$$\lambda_1 = 0.06667, \quad \lambda_2 = 0.13640 \quad [\text{cm}^3/\text{g}]. \tag{61}$$

The density $\bar{\rho}_n$ obtained from (57) by means of these parameters is shown in Figure 1 (step function).

With $\rho_u = N \bar{\rho}$ and $N \rightarrow \infty$, Equation (57) becomes

$$\bar{\rho}(r) = \rho_l + 1/h(r, \lambda) \tag{62}$$

with

$$h(r, \lambda) = \lambda_1 + \frac{5}{3} \lambda_2 (r/R)^2 \tag{63}$$

where λ_1 and λ_2 are solution of

$$\int_0^1 x^2 dx/h(xR, \lambda) = (\bar{\rho} - \rho_l)/3 \tag{64}$$

$$\int_0^1 x^4 dx/h(xR, \lambda) = (y \bar{\rho} - \rho_l)/5, \tag{65}$$

the continuous equivalent to Equations (58) and (59). The integrals can be evaluated in closed form and determination of the Lagrange multipliers proceeds in much the same way as in the discrete case discussed before. For $\rho_l = 0$ the following values are obtained.

$$\lambda_1 = 0.06674, \quad \lambda_2 = 0.13633 \quad [\text{cm}^3/\text{g}]. \tag{66}$$

The continuous density distribution computed with these Lagrange multipliers is shown in Figure 1 superimposed on the discrete density distribution. Both

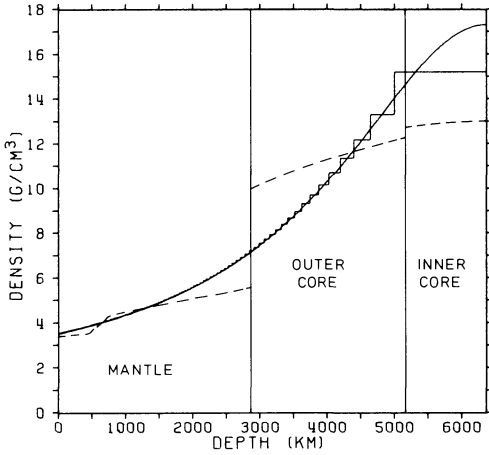


Fig. 2. Discrete ($N = 100$, step function) and continuous ($N \rightarrow \infty$) density distribution for lower density limit $\rho_l = 1 \text{ g/cm}^3$. Bullen's (1975) density distribution is represented by the dashed curve

agree surprisingly well with the – according to Bullen (1975) – most likely density distribution indicated by dashed lines.

The density distribution changes when $\rho_l > 0$ as shown in Figure 2 where $\rho_l = 1 \text{ g/cm}^3$ has been assumed. The Lagrange multipliers read

$$\lambda_1 = 0.06107, \quad \lambda_2 = 0.19924 \quad [\text{cm}^3/\text{g}] \tag{67}$$

$$\lambda_1 = 0.06120, \quad \lambda_2 = 0.19910 \quad [\text{cm}^3/\text{g}] \tag{68}$$

in the discrete ($N = 100$) and continuous case, respectively. For depths greater than 4500 km the agreement between this curve and the “most likely” density distribution is poorer than in the previous case. This seems to be in disagreement with the fact that more information (i.e. that the density of the Earth is not less than 1 g/cm^3) has been supplied. In order to show that the uncertainty concerning the density has actually been reduced it is necessary to interpret the expectation values of the density in a different way.

Equations (54) and (55) give the probability distribution for the density in the n -th interval. The cumulative distribution function

$$\text{cdf}_n(\rho) = \{1 - \exp[(\rho_l - \rho) h_n(\lambda)]\} / \{1 - \exp[(\rho_l - \rho_u) h_n(\lambda)]\} \tag{69}$$

gives the probability that $\rho_l \leq \rho_n \leq \rho$. For large $\rho_u \gg \rho_l$

$$\text{cdf}_n(\rho) = 1 - \exp[-(\rho - \rho_l)/(\bar{\rho}_n - \rho_l)]. \tag{70}$$

Hence the probability that ρ_n be in the interval $[\rho_l, \bar{\rho}_n]$ is $1 - 1/e = 0.632$ for any n : i.e. with a probability of 63.2% we expect the true density to be between the lower density limit and the expectation value of the density. This 63.2% interval is smaller in Figure 2 for depths less than ca. 4900 km.

From the form of the probability distribution (Eq. (54)) follows an important property of the average density

$$\rho = \frac{1}{N} \sum_n \rho_n. \tag{71}$$

The expectation value of this average density has been requested to be equal to the known mean value $\bar{\rho}$ of the Earth's density (Eq. (49)).

$$\frac{1}{N} \int p(\rho) \left(\sum_n \rho_n \right) dv = \frac{1}{N} \sum \bar{\rho}_n = \bar{\rho}.$$

It can be shown that the variance of the average density disappears for $N \rightarrow \infty$.

$$\begin{aligned} \text{var}(\rho) &= \int p(\rho) \left(\frac{1}{N} \sum_n \rho_n - \bar{\rho} \right)^2 dv = \int p(\rho) \left(\frac{1}{N} \sum_n \rho_n \right)^2 dv - \bar{\rho}^2 \\ &= \left[\sum_{\substack{n,m \\ n \neq m}} \bar{\rho}_n \bar{\rho}_m + 2 \sum_n \bar{\rho}_n^2 \right] / N^2 - \bar{\rho}^2 = \sum_n \bar{\rho}_n^2 / N^2. \end{aligned} \quad (72)$$

Since the $\bar{\rho}_n$ are bounded for $N \rightarrow \infty$ the last term in (72) vanishes for $N \rightarrow \infty$. Hence for the continuous density distribution the variance of the average density is equal to zero (weak law of large numbers).

An analogous result holds for

$$\sum_n \rho_n \{ [n/N]^{5/3} - [(n-1)/N]^{5/3} \}.$$

The expectation value of this expression is $y \bar{\rho}$ (see Eq. (50)) and its variance approaches zero for $N \rightarrow \infty$.

Concluding Remarks

This last example has not been presented to propose a new model for the density within the Earth. Rather it was to demonstrate that, based on the maximum entropy principle, a powerful method exists for extracting useful information from a very limited number of measured data.

For the density distribution within the Earth it leads to a quantification of qualitative statements (e.g. that the density increases with depth). Furthermore a probability (based on the given data and the prior probability distribution) can be established that the density in a certain depth is within a certain density interval.

The maximum entropy concept is, of course, far from being exhaustively treated in this text. In fact many lines of thought have only been sketched, many problems have only been touched and require more detailed analysis. It is hoped that this paper provokes further investigation of the maximum entropy concept for handling of inverse problems. In any case it should be clear that this method must not be used indiscriminately and in no case substitute but only complement observations, measurements, and physical reasoning.

References

- Aczél, J., Daróczy, Z.: On measures of information and their characterizations. New York: Academic Press 1975
- Akhiezer, N.I.: Theory of approximation. New York: Ungar 1956
- Backus, G., Gilbert, F.: Numerical applications of a formalism for geophysical inverse problems. *Geophys. J.* **13**, 247-276, 1967
- Backus, G., Gilbert, F.: The resolving power of gross Earth data. *Geophys. J.* **16**, 169-205, 1968
- Backus, G., Gilbert, F.: Uniqueness in the inversion of inaccurate gross Earth data. *Phil. Trans. Roy. Soc. London, Ser. A* **266**, 123-192, 1970
- Bullen, K.E.: The Earth's density. London: Chapman and Hall 1975
- Cook, A.H.: The dynamical properties and internal constitutions of the Earth, the Moon, and the Planets. *Quarterly J. Roy. astron. Soc.* **12**, 154-168, 1971
- Edward, J.A., Fitelson, M.M.: Notes on maximum entropy processing. *IEEE Trans. Inf. Theory (Corresp.)* **IT-19**, 232-234, 1973
- Jaynes, E.T.: Prior probabilities. *IEEE Trans. Systems Sci. Cybern.* **SSC-4**, 227-241, 1968
- Jensen, O. G., Ulrych, T.J.: An analysis of the perturbations on Barnard's star. *Astron. J.* **78**, 1104-1114, 1973
- Kanasewich, E.R.: Time sequence analysis in geophysics. 2nd ed. Edmonton, Alberta: The University of Alberta Press 1975
- Khinchin, R.T.: Mathematical foundations of information theory. New York: Dover Publications 1957
- Papoulis, A.: A new class of Fourier series kernels. *IEEE Trans. Circuit Theory* **CT-20**, 101-107, 1973
- Parker, R.L.: Inverse theory with grossly inadequate data. *Geophys. J.* **29**, 123-138, 1972
- Phillips, J.D., Cox, A.: Spectral analysis of geomagnetic reversal time scales. *Geophys. J.* **45**, 19-33, 1976
- Rao, C.R.: Linear statistical inference and its applications. New York: Wiley 1965
- Rowlinson, I.S.: Probability, information and entropy. *Nature* **225**, 1196-1198, 1970
- Smylie, D.E., Clarke, G.K.C., Ulrych, T.J.: Analysis of irregularities in the Earth's rotation. *Methods in Computational Physics* **13**, 391-430, 1973
- Ulrych, T.J.: Maximum entropy power spectrum of long period geomagnetic reversals. *Nature* **235**, 218-219, 1972

Received September 15, 1976

Electromagnetic Scale Model Experiments for the Coastline Effect of Geomagnetic Variations

P. Spitta

Institut für Geophysik der Universität Göttingen,
Herzberger Landstr. 180, D-3400 Göttingen, Federal Republic of Germany

Abstract. Geomagnetic induction problems at coastlines and edges are studied on a reduced scale. Aluminium conductors are used to represent the oceans and conducting matter at greater depth within the earth. In the two-dimensional case the direction of the edges is either perpendicular or parallel relative to the inducing magnetic field (*E*- or *H*-polarization). In the three-dimensional case two edges are intersecting at right angles, forming a superposition of both polarizations. Measurements of the total magnetic field in three components are carried out over the whole area of each of the three scale models, showing the different behaviour of the models when exposed to the inducing field. In order to show the pattern and strength of the induced currents, an equivalent current system in the plane of observation is introduced. Measurements across the coast of California are interpreted by an appropriate scale model.

Key words: Scale model experiments – Geomagnetic induction – Equivalent current system

1. Introduction

The interpretation of induced magnetic fields, observed at the earth's surface above an internal conductivity distribution, is generally done by assuming an electrical conductivity model with several free parameters, which in turn are adjusted to the data either by model calculations or by scale model experiments. Both methods have to simplify the geometry of the inducing field as well as the structure of the conducting matter within the earth, in which the induced currents are flowing. Model calculations are confined more or less to two-dimensional structures [Schmucker, 1973] although progress is made in treating three-dimensional conductivity distributions [Jones, 1973; Weidelt, 1975].

These limitations are not to be found in scale model experiments, they can be readily used to study rather complex three-dimensional induction prob-

lems, if only the conductivity contrast in nature is large enough to be modelled with the existing materials. It is more difficult to produce small differences in conductivity than great ones because of the lack of appropriate materials. Dosso [1973] uses the contrast between graphite as a good and an electrolytic solution as a poor conductor, the conductivity ratio is in the order of $10^4:1$ or greater. Hermance [1968], Launay [1970], and Spitta [1973] are studying the coast effect by using the conductivity contrast between metal and air, which is much greater, and the effect tends to be overestimated [Hermance, 1968]. But at a conductivity contrast of $10^4:1$ it is anyhow unlikely for the induced currents in the metal to penetrate into the poor conductor to close the current-loops. Bearing this in mind, the deviation from reality will be small, when the poorly conducting layers on land are replaced by air in model experiments.

Maxwell's field equations are invariant against changes of scale in time and space, if for a quasi-stationary electromagnetic skin-effect problem the condition for physical similarity under change of scale

$$\frac{\omega_m}{\rho_m} d_m^2 = \frac{\omega_n}{\rho_n} d_n^2 \quad (1)$$

is satisfied. Here ω , ρ , and d denote the frequency, the resistivity, and a characteristic linear dimension, the subscript m refers to the model, the subscript n to nature. For any corresponding pair of points in model and nature Equation (1) must be valid. An example of the transformation between nature and scale model is given in Table 1 in Section 4.

2. The Experimental Arrangement

The experimental set-up has been reported elsewhere [Spitta, 1973]. Hence, only recent improvements are mentioned here. They are described in detail by Spitta [1975]. Now, the phase meter admits phase determinations in the full range from 0° to 360° instead of the former range from 0° to 180° . This allows the recording of all phase angles in respect to the reference voltage. The reference voltage is produced by the inducing current as a voltage drop on a small resistance, which replaces the transformer used before. The phase shifter is no longer necessary and therefore omitted.

The arrangement of the field generating coil, the pick-up coils for field measurements, and the scale model are shown in Figure 1. A system of right-handed rectangular coordinates x , y , and z is adopted. Its origin is the centre of the lower side of the coil, z points downwards, x is directed parallel to the axis of the coil, and y is the direction of the currents of the inducing field. H_x , H_y , and H_z are the amplitudes of the components of the magnetic field in the appropriate directions, or, with an additional subscript R or I , the in-phase or out-of-phase parts of the magnetic field, respectively.

The pick-up coils for the magnetic field components are driven 66 cm below the rectangular field-generating coil on a rigid beam by a pulley-and-belt system, allowing a continuous recording of amplitudes and phases for traverses across the model. These profiles can be shifted parallel to each other to measure

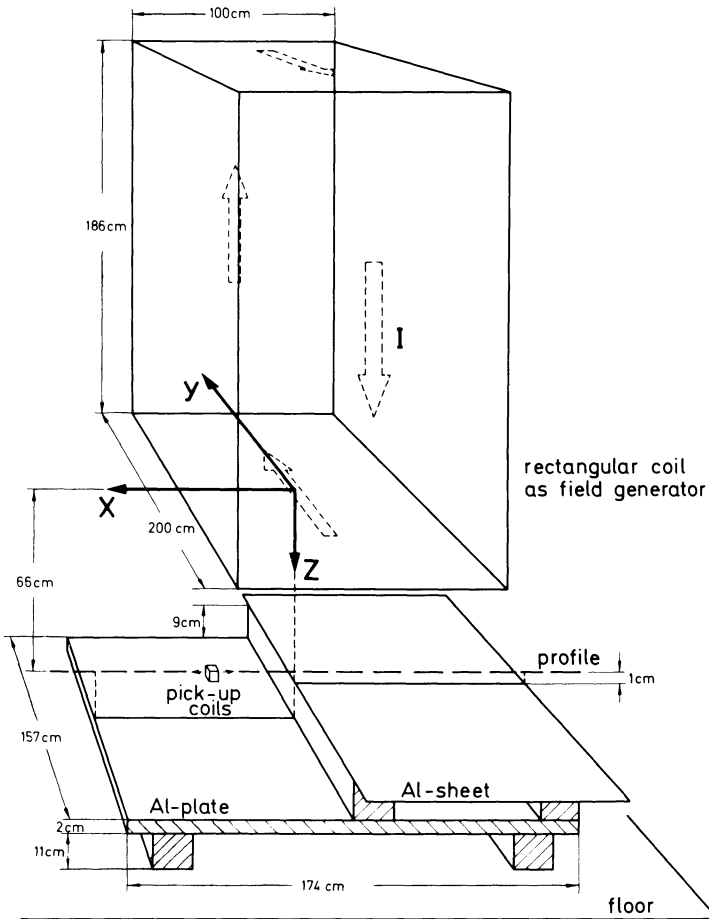


Fig. 1. Diagram of the model measurement system. The rectangular coil with 100 turns per meter of copper wire and with the axis directed in the x -direction produces the magnetic field that induces currents in the scale model below. The total magnetic field is scanned by a small pick-up coil tripl between the rectangular coil and the model. The profile in x -direction can be shifted both in y - and z -direction. For an inducing current of 1 A the magnetic field intensity in the level of the Al-sheet is of the order of 10 A/m. The model shown is that of the half-sheet anomaly in E -polarization (cf. Fig. 4)

the magnetic field at each point of the model. The aluminium plate, which represents the conducting mantle within the earth, is situated 76 cm below the field generating coil. Anomalies near the surface of the earth, e.g. the coast effect, are being modelled by thin aluminium sheets 9 cm above the aluminium plate, as shown in Figure 1.

The comparison of the measured magnetic field on the central profile ($y=0$, $z=66$ cm), measured without conductor at a frequency of 215 Hz, with the computed values of the magnetic field of the coil for free space shows a good agreement (Fig. 2). The small difference between the two curves is due to induction in the steel reinforced concrete floor. The phases of the measured

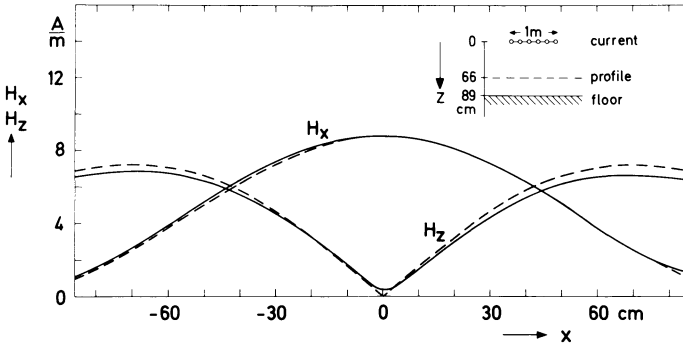


Fig. 2. Magnetic field amplitudes H_x and H_z of a 100 cm sheet current for the frequency 215 Hz, measured across a profile placed 66 cm below the current system at $y=0$ (solid lines), compared with the calculated magnetic field for free space along the same profile (dashed line). The deviation of the two curves is due to the induction in the steel-reinforced concrete of the floor

magnetic field deviate very little from 0° or 180° and therefore they are not shown.

The measured amplitudes and phases are converted in in-phase and out-of-phase parts, which are equivalent to amplitude and phases, but allow further mathematical treatment such as subtracting the inducing field to get the magnetic field of the induced currents alone. The conversion formulas are given by the following equations:

$$H_R = H \cdot \cos \phi \quad (2)$$

$$H_I = H \cdot \sin \phi, \quad (3)$$

H_R denotes the in-phase part (R =real part), H_I the out-of-phase part (I =imaginary). H is the amplitude, ϕ the phase lead of the observed field component relative to the inducing field, generated by the coil above the model.

In nature induction takes place everywhere according to the conductivity of the earth. The conductivity is not only determined by the chemical and mineralogical composition of the rocks, the porosity and the contents of salt solution, but also by the temperature. At increasing temperature the semiconducting nature of the rocks becomes evident [Keller, 1971; Schult, 1974]. It can be stated that sufficiently low resistivities around $1 \Omega\text{m}$ exist within the earth's mantle at several hundred kilometers depth. They are covered by relatively poor conductors of at least $100 \Omega\text{m}$ resistivity [Rikitake, 1966].

For an inducing magnetic field of external origin the measurements on the earth's surface yield an enhancement of the horizontal components and a decrease of the vertical component of the total field due to the induced currents within the earth. According to the transformation formula (1) of Section 1 this is valid also for scale models, as it is demonstrated in Figure 3. Here the x - and z -components of the magnetic field across the aluminium plate (solid line) are compared with the measured field without Al-plate (dash-dotted line). The thickness of the Al-plate (2 cm) is more than 3 times the penetration depth (0.58 cm) for 215 Hz, therefore the plate can be regarded as infinitely thick for 215 Hz or higher frequencies.

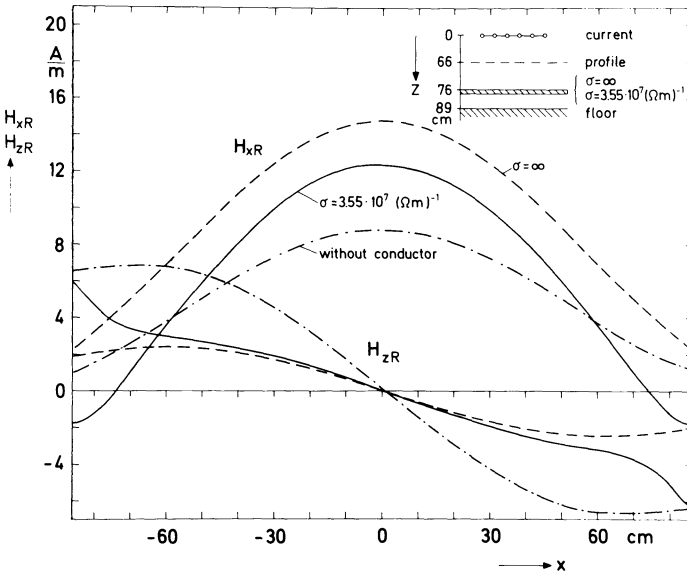


Fig. 3. In-phase parts H_{xR} and H_{zR} of the total magnetic field, measured across a profile in the x -direction 66 cm below the coil. The field is composed of the fields of the inducing sheet current and the induced currents in an Al-plate 76 cm below the current system. The plate has a conductivity of $3.55 \cdot 10^7 (\Omega\text{m})^{-1}$ and a thickness of 2 cm, the frequency is 215 Hz (solid line). These curves are compared with the magnetic field across a half-space of infinite conductivity, calculated for the same profile (dashed line), and with the measured magnetic field (real parts) for the same profile without conductor below (dash-dotted line)

On the other hand comparing the measurements across the Al-plate (solid line) with the computed field above a half-space of infinite conductivity (dashed line), there is a discrepancy between the 2 curves. The magnetic field above a half-space can be computed as a superposition of the inducing field and the induced field, which is a reflection of the inducing field at the surface of the half-space. It can be shown by an approximation formula by Pollaczek [1926] that the difference in the surface fields due to infinite and finite conductivity ($\sigma = 3.55 \cdot 10^7 (\Omega\text{m})^{-1}$) is less than 1%. Therefore the dashed curves in Fig. 3 represent the theoretical field for an infinitely conductive half-space as well as for an half-space with $\sigma = 3.55 \cdot 10^7 (\Omega\text{m})^{-1}$. It is obvious, that the induced currents in the aluminium plate are weaker than the currents to be expected in the half-space. The current loops in the half-space are closing at infinity, whereas the currents in the plate have to form closed loops within the dimensions of the plate. The horizontal magnetic field of the return currents at the edge of the plate overcompensates the inducing field, leading there to a reversal of the horizontal magnetic field. Therefore the in-phase horizontal x -component of the magnetic field is decreased around the centre of the plate, whereas the in-phase vertical z -component is slightly increased near the edge. This effect arising from the limited dimensions of any scale model has to be kept in mind when planning a scale model experiment.

3. Experimental Results

Edge effects such as the coast effect have been treated by various authors both as scale models and model calculations. A summary and a comparison of these works is given by Dosso [1973]. The present paper investigates the response of a coast line to inducing magnetic fields perpendicular and parallel to the edge (E - and H -polarization) [Schmucker and Jankowski, 1972]. Measurements for both polarizations are plotted separately in Figures 4 and 6. The model consists of an aluminium plate of the size of $174 \text{ cm} \times 157 \text{ cm} \times 2 \text{ cm}$, which represents the highly conducting mantle at a depth of 360 km, and an aluminium sheet, $180 \times 100 \text{ cm}^2$ in area and 0.1 cm thick, placed 9 cm above the plate. It simulates an ocean with the depth of 4 km with a sea water resistivity of $0.25 \Omega\text{m}$. It can be regarded as a thin sheet in the sense that its thickness is small in comparison to the skin depth at the experimental frequency. With this change of length scale and resistivity the frequency of 215 Hz corresponds in nature to a period of 3.7 h, according to the transformation formula (1). No electrical contact exists between sheet and plate.

In Figure 4 the sheet has been placed at the right hand side, extending from $x=0$ to $x=-100 \text{ cm}$ and from $y=-80 \text{ cm}$ to $y=+80 \text{ cm}$, forming a half-sheet anomaly in E -polarization. It can be seen both in the in-phase and out-of-phase parts, that the x -component suddenly increases across the coast from "land" to "ocean" and remains enhanced above the sheet due to the induced currents in the sheet. The same currents produce a decrease of amplitude in the in-phase z -component above the sheet, whereas the out-of-phase z -component is enhanced. A strong coast effect in the z -component is to be seen immediately at the edge. Since in the y -direction no conductivity contrast is encountered, almost no anomalous behaviour in the y -component is found. A comparison of measurements across the coast of California and an appropriate scale model is given in Section 4.

In order to show the pattern and strength of the induced currents, flowing in the sheet above the aluminium plate, an equivalent sheet current distribution in the level of observation 1 cm above the thin sheet is introduced. The magnetic field of the induced currents can be found by subtracting the measured magnetic field without sheet (but including the Al-plate), as shown by solid lines in Figure 3, from the magnetic field across the whole model including the Al-sheet (Fig. 4), in in-phase and out-of-phase parts. Since the distance between the plane of observation and the sheet is small compared with the horizontal dimensions of the sheet, it is assumed that the current system derived from the magnetic field in the plane of observation is similar to the true current system on the sheet. Let \hat{z} be the unit vector in z -direction. Then the equivalent sheet-current density \mathbf{j} connected with the magnetic field \mathbf{H} at point \mathbf{r} is given by

$$\mathbf{j}(\mathbf{r}) = -2 \hat{z} \times \mathbf{H}(\mathbf{r}). \quad (4)$$

In the equivalent current density plots of Figures 5, 7, and 9 direction and strength of \mathbf{j} are represented at equally spaced points in a rectangular grid by direction and length of arrows.

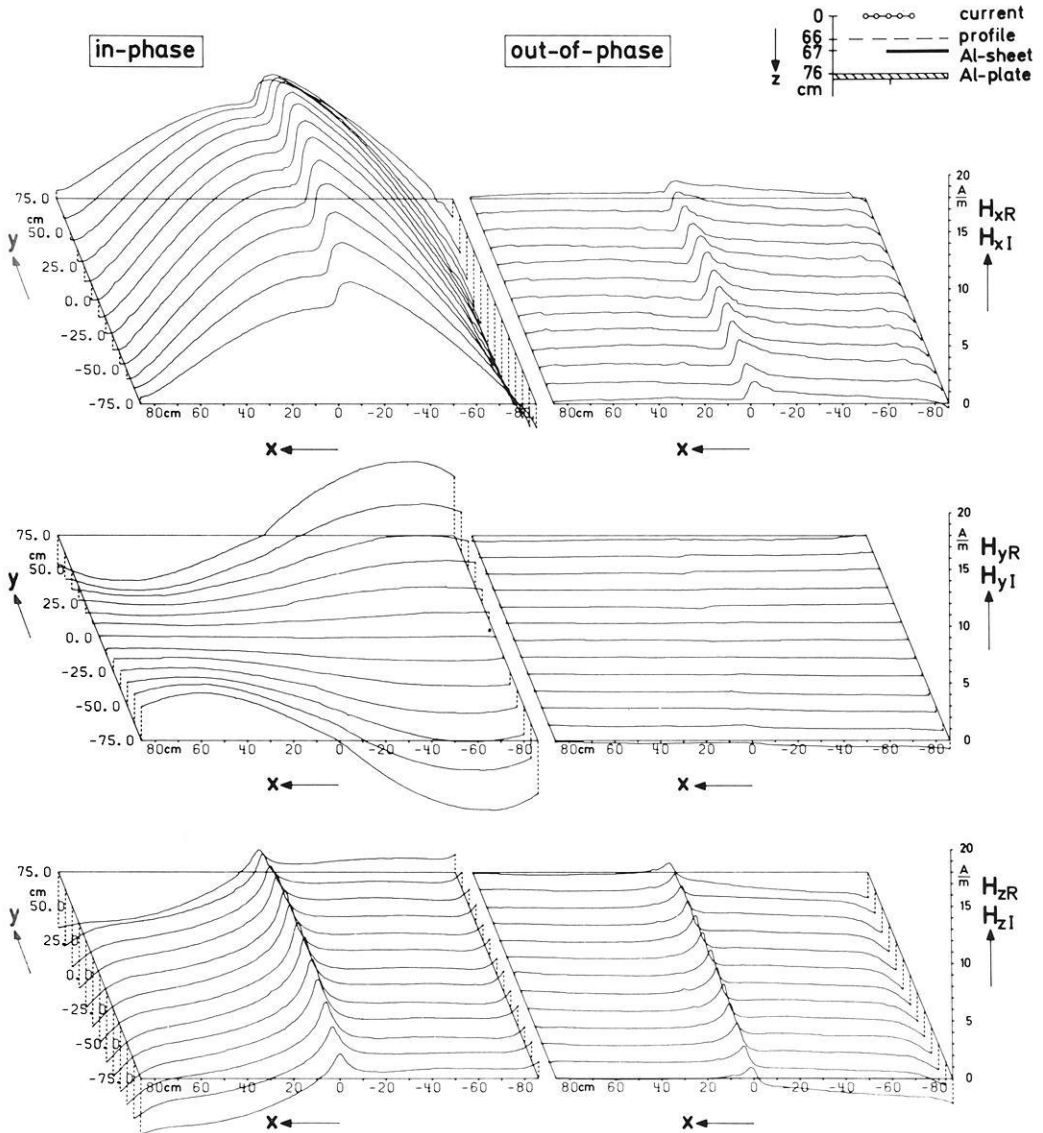


Fig. 4. Edge-effect in *E*-polarization: In-phase parts (left) and out-of-phase (right) of the magnetic field components H_x , H_y , and H_z , measured 66 cm below the coil over the whole area of the scale model, which consists of a thin Al-sheet, partly covering an Al-plate 9 cm below. The half-sheet extends from $x=0$ to $x=-100$ cm, the frequency used is 215 Hz

The equivalent currents density arrows for the aluminium sheet are shown in Figure 5. Only the in-phase parts of the induced currents are considered here. As expected, the currents in the sheet are forming an elongated eddy. The fairly small currents outside the sheet can be attributed to two effects. First, the distribution and strength of the magnetic field of the equivalent currents depends on the distance of the plane of observation from the sheet. The

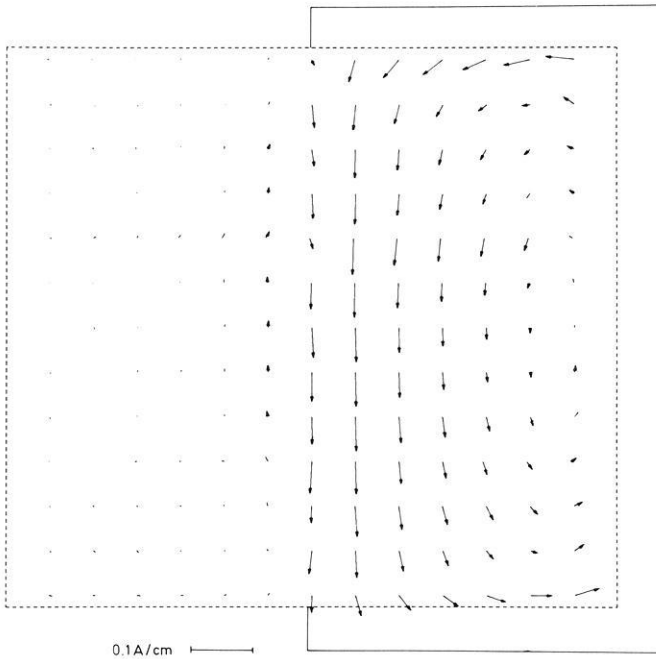


Fig. 5. Equivalent current density arrows in the half-sheet in E -polarization (Fig. 4), as seen from the plane of observation. The arrows which are starting at equally spaced grid points represent in direction and strength the in-phase parts of the induced surface current density vectors

lines of force of the induced currents in the sheet tend to spread into space and show in the plane of observation "equivalent currents" just in the neighbourhood of conductors. That can be seen in Figure 5 left of the edge of the sheet. Secondly, the currents in the two conducting layers of sheet and plate are influencing each other. The induced currents in the plate section beneath the Al-plate will be somewhat smaller than in the absence of the sheet. Therefore the induced field from the plate alone, which is subtracted, is too large. Consequently, small equivalent currents outside the sheet remain [Spitta, 1975].

With regard to the coast in H -polarization the response of the sheet is quite different. For that purpose the sheet is turned by 90° and placed at the rear side of the scale model of Figure 1. The sheet extends from $y=0$ to $y=+100$ cm and from $x=-80$ cm to $x=+80$ cm. The edge of the sheet is parallel to the most intense x -component of the inducing field. Since the changes of the magnetic field along a profile are more prominent perpendicularly to the edge, the direction of the profiles has been changed too, as it can be seen in Figure 6. Here y is directed from right to left, parallel to the profiles, the x -direction is from the rear side to the front. The ordinate is the intensity of the magnetic field in in-phase and out-of-phase parts. The sheet is lying on the left hand side, as indicated by the model sketch in the upper right corner. Since no change in conductivity is encountered, the amplitude in the

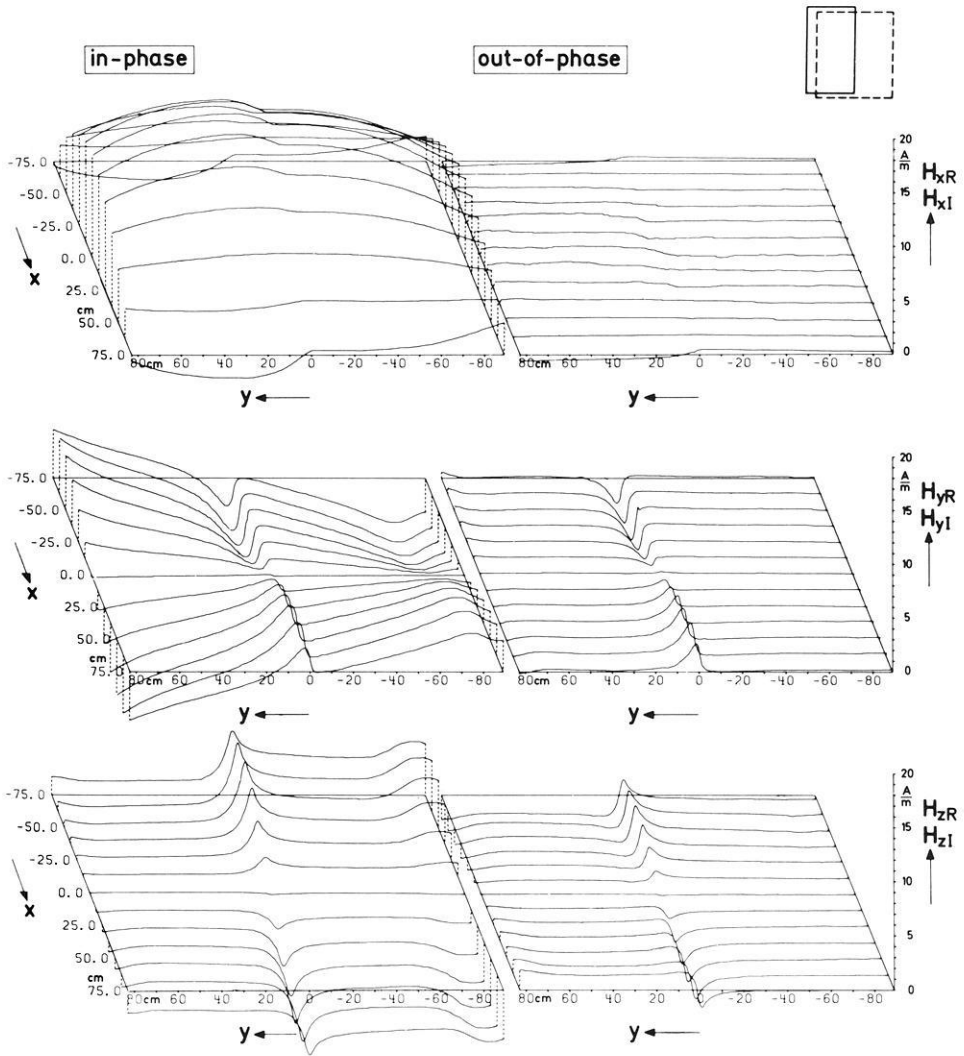


Fig. 6. In-phase parts (left) and out-of-phase parts (right) of the magnetic field components H_x , H_y , and H_z for the edge effect in H -polarization. The Al-sheet, which is partly covering the Al-plate, extends from $y=0$ to $y=+100$ cm

x -component is not affected by the edge (disregarding the extreme profiles at $y = \pm 75$ cm). But the currents, induced by the x -component, are flowing in the y -direction and are forced by the edge to change their direction: they have to flow in the positive or negative x -direction. Their magnetic fields contribute to the magnetic field in y -direction, but opposite in sign to the inducing field. So the coast effect is shown by the y -component here, similar in strength as the x -component in E -polarization. In the z -component only the different geometry of the inducing field is to be seen as a new effect. The equivalent current density arrows (real parts) for the half-sheet in H -polarization are shown in Figure 7.

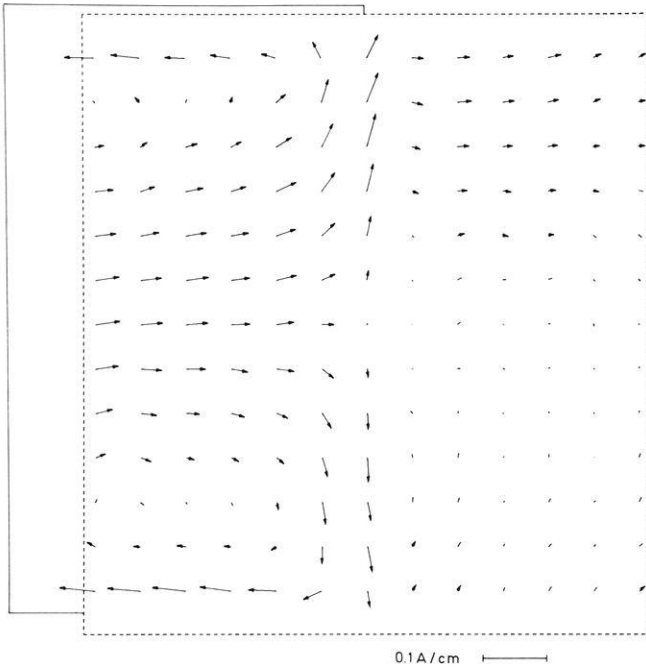


Fig. 7. Equivalent current system in the half-sheet in H -polarization (Fig. 6), representing the density of the in-phase parts of the induced currents in the sheet

The half-sheet anomalies in E - or H -polarization can be treated as 2-dimensional structures, they are still tractable by model calculations [Schmucker, 1971]. In spite of the progress in three-dimensional model calculations more complicated coast lines, as the coastline of southwestern Australia [Everett and Hyndman, 1967], require scale model experiments for the interpretation of the observation in nature. Wide oceans with a depth of 3–4 km exist along the southern and western coast of Australia, which are intersecting approximately at right angles. This configuration of land and sea can be modelled by 2 aluminium sheets, representing the oceans, placed one upon another, forming an angle of 90° , and covering three quadrants of the aluminium plate. They are not in electrical contact with each other, the aluminium plate being placed 9 cm below the sheet. Now the effect of two edges is expected, one along $x=0$ for the sheet in “ E -polarization”, and the other along $y=0$ for the sheet in “ H -polarization”. The edge effects will be less pronounced at points where the sheets cover each other.

This is evident when comparing single profiles of the half-sheet anomaly in E -polarization and the just mentioned corner anomaly. Figure 8 shows three profiles across the half-sheet as solid lines and three profiles across the corner anomaly as dashed lines. Hardly any difference is to be seen in the x -component at the profiles at $y=0$ and $y=-50$ cm, in the y -component at $y=-50$ cm and $y=+50$ cm, and in the z -component at $y=-50$ cm due to the almost same geometry. The effect of the induced currents in the second sheet which

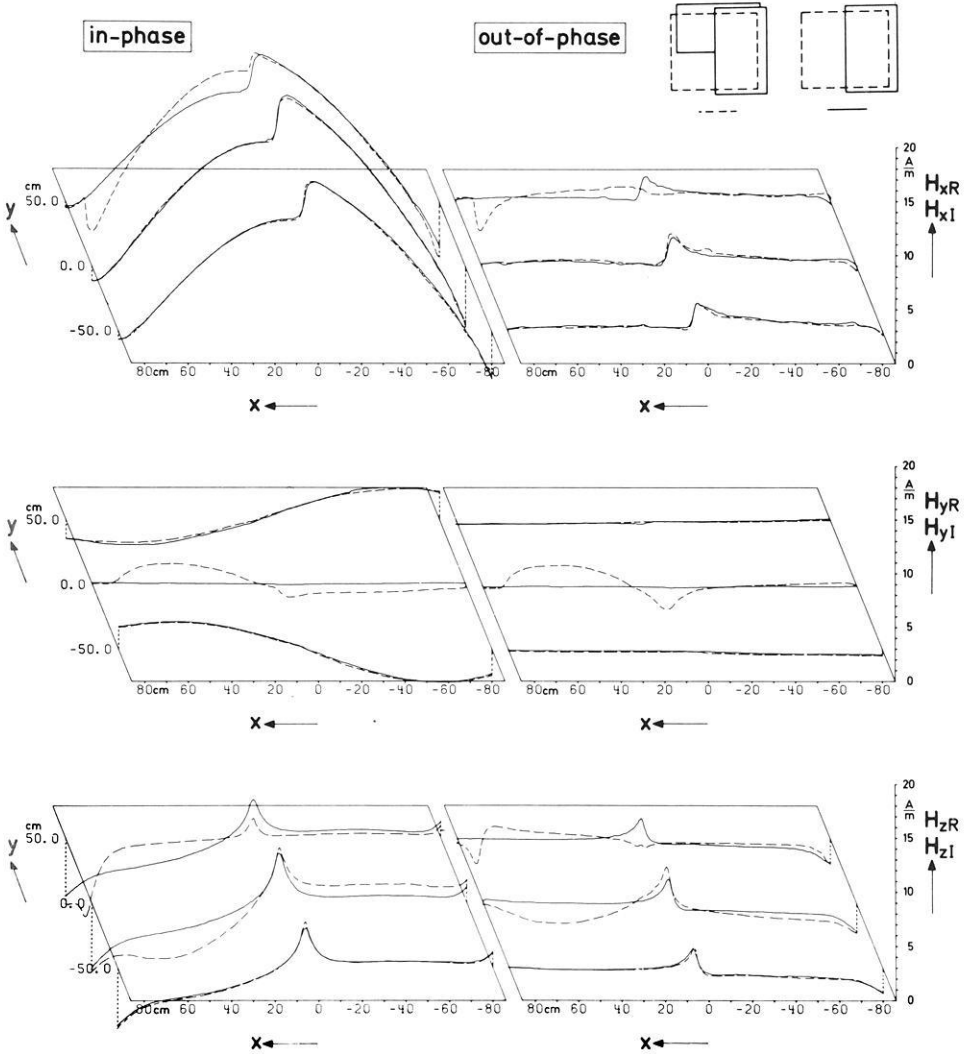


Fig. 8. Comparison of single profiles of the half-sheet anomaly in E -polarization (solid lines) and the corner anomaly (dashed lines). The corner anomaly consists of two Al-sheets forming a right angle, covering three-quarters of the Al-plate 9 cm below. Drawn are on the left the in-phase parts, on the right the out-of-phase parts of the magnetic field components H_x , H_y , and H_z .

is in “ H -polarization” is seen in the difference between the two curves in the x - and z -component at $y = +50$ cm. At $y = 0$ the edge effect is clearly demonstrated in the y - and z -component. Here H_{yR} and H_{yI} increase in amplitude from almost zero for a single half-sheet (solid line) to a substantial edge anomaly on the left hand side of the profile (dashed line). The z -component has a pronounced peak at the corner point ($x = 0, y = 0$) and preserves a remarkable amplitude along the edge of the second half-sheet parallel to x .

The equivalent current density arrows (real parts) for this scale model are shown in Figure 9. It makes a difference whether the half-sheet with the edge

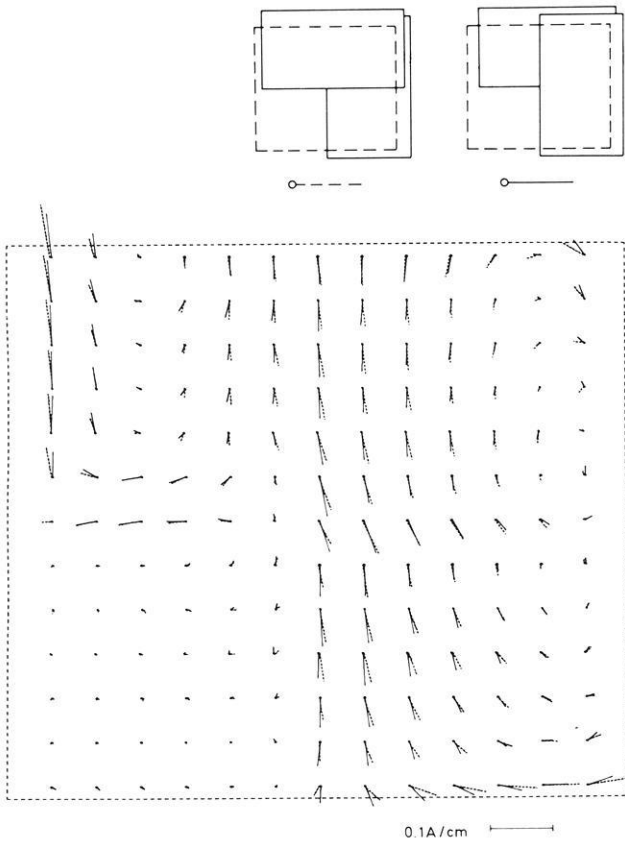


Fig. 9. Equivalent current system in the half-sheets of the corner anomaly, presented by two different arrangements of the sheets. The arrows are representing the density of the in-phase parts of the induced currents in the sheet

in y -direction is placed on top or below the second half-sheet with the edge in x -direction. The currents of both arrangements are plotted in the same picture “ y -sheet on top” with solid lines, “ y -sheet below” with dashed lines. The currents are forming two eddies, separated by the edge at $x=0$ in the case the y -sheet is on top, whereas the line of separation is shifted more to the left in the case the y -sheet is below. The difference between the two arrangements turns out to be mostly a deviation in direction of the currents with only slight differences in amplitude.

4. Application of Scale Models

In this last section an application of scale models is given by interpreting actual measurements across a coast. Since the depth of the sea water on the continental shelf is small (about 100 m) compared with the deep ocean (about 3 km), the shelf can be regarded as belonging to the land. Referring to Table 1 where modelling data are compared with data from nature, the depth of water on the shelf would be represented in the model by a very thin foil (0.03 mm),

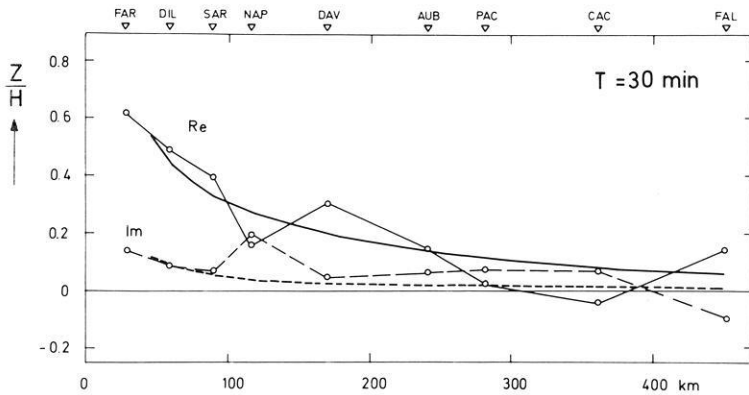


Fig. 10. Comparison between measurements (small circles) and transformed scale model results for the ratio of the anomalous Z to the normal H across the coast of California. The scale model results refer to the plane of the sheet, in-phase and out-of-phase parts are drawn by solid and dashed lines, respectively. The simulated depth of the ocean is 3 km, the simulated depth of the high mantle conductivity is 270 km

Table 1. Transformation between scale model and nature by using the transformation formula (1)

Variables	Scale model	Nature
Thickness of the surface layer d	1 mm aluminium sheet	3 km ocean
Depth of the deep conductor	9 cm (aluminium plate)	270 km (conductosphere)
Resistivity ρ of the surface layer	$4.5 \cdot 10^{-8} \Omega m$	$0.25 \Omega m$ seawater
Frequency $\omega/2\pi$	1 kHz	$6.17 \cdot 10^{-4} Hz \cong 27$ min bay disturbance

that is unlikely to be seen magnetically. Therefore the “coastline” has to be placed on the continental margin, all of the measurements in nature are performed on the “land” side, the origin of the distance scale of Figure 10 is at this edge.

Figure 10 shows the ratio Z/H along a profile at the coast of California, beginning 30 km east of the edge of the continent on Farallon Island and ending near Fallon in Nevada [Schmucker, 1970]. Here H denotes the normal horizontal component perpendicular to the edge, Z the anomalous vertical component. Shown are in-phase (Re) and out-of-phase (Im) parts for a period of 30 min. The measured values are marked with small circles. For the scale model the ocean is replaced by an aluminium sheet, the conductivity of the mantle is represented by the aluminium plate, the continent by air. The geometry is quite similar to the half-sheet anomaly in E -polarization. The increase of conductivity ρ and reduction of the size d , following the transformation formula (1), is listed in Table 1. The measured values of the in-phase parts (solid line) and the out-of-phase parts (dashed line) of the scale model agree fairly well with the curves of Schmucker.

The magnetic field of the scale model has been obtained in the same level of the surface of the ocean. Hence, a small horizontal distance from the edge

had to be kept due to the size of the pick-up coils. Otherwise, by guiding the pick-up coils across the sheet at a small height of 1 cm—this corresponds to a height of 30 km above the earth's surface in nature—the curves at this altitude would be smoothed and reduced in amplitude in relation to the surface fields. Therefore it is difficult to compare them with measurements taken at the earth's surface.

Acknowledgements. I am grateful to Prof. Dr. M. Siebert for providing the basis to carry out the experiments within the scope of my thesis. I am also indebted to Prof. Dr. U. Schmucker and Dr. P. Weidelt for their helpful comments and interest in this work. Moreover, I wish to acknowledge the financial support by the Deutsche Forschungsgemeinschaft, Bad Godesberg. The numerical calculations and part of the drawings have been performed at the UNIVAC 1108 of the Gesellschaft für wissenschaftliche Datenverarbeitung in Göttingen.

References

- Dosso, H.W.: A review of analogue model studies of the coast effect. *Phys. Earth Planet. Interiors* **7**, 294–302, 1973
- Everett, J.E., Hyndman, R.D.: Geomagnetic variations and electrical conductivity structure in south-western Australia. *Phys. Earth Planet. Interiors* **1**, 24–34, 1967
- Hermance, J.F.: Model studies of the coast effect on geomagnetic variations. *Can. J. Earth Sci.* **5**, 515–522, 1968
- Jones, F.W.: Induction in laterally non-uniform conductors: Theory and numerical models. *Phys. Earth Planet. Interiors*, **7**, 282–293, 1973
- Keller, G.V.: Electrical studies of the crust and upper mantle. In: *The structure and physical properties of the earth's crust*, J.G. Heacock, ed. *Geophysical Monograph Ser. No. 14*, 107–125. American Geophysical Union, Washington D.C., 1971
- Launay, L.: Modèle réduits magnéto-telluriques: principe et premiers résultats. *Ann. Géophys.* **26**, 805–810, 1970
- Pollaczek, F.: Über das Feld einer unendlich langen wechselstromdurchflossenen Einfachleitung. *Elektr. Nachrichtentechn.* **3**, 339–359, 1926
- Rikitake, T.: *Electromagnetism and the earth's interior*. Amsterdam: Elsevier 1966
- Schmucker, U.: Anomalies of geomagnetic variations in the southwestern United States. *Bull. Scripps Inst. Ocean. Univ. Calif.* **13**, 1970
- Schmucker, U.: Neue Rechenmethoden zur Tiefensondierung. In: *Protokoll „Erdmagnetische Tiefensondierung“* Rothenberge/Westf., 14.–16.9.1971, P. Weidelt, ed., pp. 1–39. Institut für Geophysik, Göttingen, 1971
- Schmucker, U.: Regional induction studies: A review of methods and results. *Phys. Earth Planet. Interiors*, **7**, 365–378, 1973
- Schmucker, U., Jankowski, J.: Geomagnetic induction studies and the electrical state of the upper mantle. In: *The upper mantle*, A.R. Ritsema, ed. *Tectonophysics*, **13**, (1–4), 233–256, 1972
- Schult, A.: The electrical conductivity of minerals and the temperature distribution in the upper mantle. In: *Approaches to Taphrogenesis*, J.H. Illies and K. Fuchs, eds., pp. 376–378. Stuttgart: Schweizerbarth 1974
- Spitta, P.: Scale model experiments with solid conductors. *Phys. Earth Planet. Interiors* **7**, 445–449, 1973
- Spitta, P.: *Modellversuche zur elektromagnetischen Induktion in räumlichen metallischen Leitern mit Anwendungen auf die erdmagnetische Tiefensondierung*. Diss. Math.-Nat. Fak. Göttingen, 1975
- Weidelt, P.: Electromagnetic induction in three-dimensional structures. *J. Geophys.*, **41**, 85–109, 1975

Model Studies on Redox Logging for Minerals

K.K. Roy¹* and S.S. Baksi²

¹ Department of Geology and Geophysics, Indian Institute of Technology, Kharagpur-2, West Bengal, India

² Well logging division, Oil and Natural Gas Commission, Ahmedabad, Gujrat, India

Abstract. Physical models are prepared in the laboratory to study the variations of oxidation-reduction potentials in the simulated boreholes through the ore bodies and the surrounding media. The study reveals the following facts: (i) Redox logs will be useful for approximate delineation of depth and thickness of the mineralized bed (ii) Variations, rather than the absolute values of the redox potentials, will be of interest in redox logging (iii) Acidic borehole fluids are found to be better to sharpen the redox anomalies (iv) The redox potential is found to be almost independent of ore concentrations (from 10% to 80% by weight in plaster of paris model) with tap water (pH=6.0) and other alkaline solutions as borehole fluid (pH=7.0–12.0). Some trends of variations are observed for acidic borehole fluid (v) The changes in potentials per unit change in pH are found to differ widely for different minerals (vi) The redox potential value takes a significant time to remain stable over a time span of half an hour to one hour. The potential value changes significantly over a long time span. The values are not reproducible within 5% in most of the cases (vii) The potential changes considerably for every cleaning operation of the platinum electrodes.

Key words: Model experiment – Simulated borehole measurement of redox potential

1. Introduction

Oxidation-reduction potentials and the redox reactions are well known phenomena in electrochemistry. Even the existence of spontaneous flow of stationary currents (not telluric currents which are quasi-stationary) within the earth's sedimentary covers and the ohmic potential drop therefrom are known to the

* To whom offprint requests should be sent

geophysicists for more than one hundred years. The surface measurements extend back to the work of Fox (1830). But the systematic use of the method started from about 1930. Since then an immense amount of field, theoretical and experimental works have been done to understand the variations of the self potentials (S.P.), which are primarily of oxidation reduction origin, near the ore bodies. Developments are done both on the theories of origin of S.P. and on the field data interpretation sides. Mention may be made of the following authors: Schlumberger et al. (1934), Poldini (1938), Heiland (1940), de Witte (1948), Yüngül (1950, 1954), Roy and Chawdhuray (1959), and Sato and Mooney (1960).

It has been realized since then that the electrochemical mechanism of self potentials, associated with the ore bodies, results from ohmic potential drops within the country rock. The current is produced by separable but simultaneous reduction of oxidizing agents near the surface and oxidation of reducing agents at depths. The ore body does not participate directly in either reactions but serves as a conductor to transfer electrons from the oxidizing agents to the reducing agents. Thus the surface self potential method of geophysical prospecting has become a fairly established method for the last 40 years and is used for shallow base metal sulphides, graphite, coal, etc. The convenience and ease in measurement and interpretation kept the method still alive. Here the geophysicists are primarily interested in the relative changes of the potentials rather than their absolute values of the redox e.m.f. near the ore bodies.

Simultaneously several authors (Latimer, 1938; Zobell, 1946; Krumbein and Garrels, 1952; Garrels, 1954; Baas Becking et al., 1960; Sato, 1960) have contributed significantly on the redox phenomena in the earth's natural environment and improved the techniques of redox potential measurements. They have outlined the practical difficulties in measurements of redox potentials in natural environments and indicated that the absolute values of the redox potentials are not reproducible even with precision measurements. As a result quite a few workers have given up the idea of redox measurements since the absolute values of the non-reproducible potentials did not make any sense to them.

Concurrently the existence of borehole S.P., which can be of use in delineating porous and permeable beds and are of diffusion and diffusion-adsorption origin, was first detected by Schlumberger et al. (1934). Since then many authors (e.g. Doll, 1948; Gondouin et al., 1957) have established the S.P. logging as a regular tool for borehole geophysics. On the contrary, the borehole S.P. of redox origin in the sedimentary, igneous and metamorphic mineralized zones remained fairly unattended till 1958 when G.B. Salimbeni carried out his first redox logging in pyrite, lignite and oil wells of central Italy. Since then a large number of workers have contributed significantly in the understanding of the behaviour of redox logs in mineral and oil wells (e.g. Colombo et al., 1959; Pirson, 1968, 1970; Karaoguz et al., 1970). The theories of redox potentials are discussed in detail by Zobell (1946), Glasstone (1962, 1969), Garrels (1970), and Pirson (1968, 1970). The different techniques of redox logging are reported by Colombo et al. (1959), Pirson (1970), Karaoguz (1970).

The present authors started model experiments keeping in view firstly the possibilities of enhancing the redox anomalies by changing the pH of the drilling

fluids instead of adding any oxidizing or reducing agents and secondly to study the effect of concentration of mineral grains on redox anomaly. The results of our experience are enumerated in the following sections.

2. Experimental Set-up, Measurements and Discussion of the Results

A. Standardization of the Measuring Probes

Before trying to measure the potentials of unknown systems, we tried to standardize our electrodes (Platinum-Calomel) by inserting them in a Zobell solution and measuring the potentials in an accurate (± 10 micro volts) potentiometer. The standard techniques of potentiometric measurements are well known and therefore are omitted here. We could measure 0.35209 gms of $K_4Fe(CN)_6 \cdot 3H_2O$ and 0.311130 gms of $K_3Fe(CN)_6 \cdot 3H_2O$ whereas the theoretically required weights to prepare solutions of strength M/300 in 250 cc of distilled water are 0.35200 gms and 0.311100 gms respectively.

25 cc of each of M/300 $K_4Fe(CN)_6 \cdot 3H_2O$, M/300 $K_3Fe(CN)_6 \cdot 3H_2O$ and M/10 KCL are taken in a beaker and the potentials are measured (Fig. 1) with platinum-calomel electrodes. The value is found to be 175 mV at $86^\circ F$ or $30^\circ C$. Hence $E_h = 175 + 245 = 420$ mV at $30^\circ C$ or 423 mV at $25^\circ C$. The correct value should be 428 mV as reported by Zobell (1946).

In the same solution the Pt-Pb electrode is immersed and the stable potential observed was 512 mV. In other words the level of Pt-Pb potential is found to be at 347 mV above that of (Pt-Cal) potential.

B. Effect of Concentration of Mineral Grains on Redox Potential

Samples of various ores were collected from different field sites¹ of India. The ore samples are crushed to make powders and are mixed with plaster of paris in different percentage by weight. Cylindrical casts of plaster of paris are then prepared with holes in the centres (Fig. 2). 10 gms of hematite ore in 100 gms of plaster of paris makes a sample of 10% hematite.

The central hole of the model is plugged by rubber stopper at the bottom (Fig. 2) and solutions of certain pH value are poured in steps till the pore spaces in the cast are saturated with the solutions and the solution remains in the hole without any infiltration loss. The cast is left as such for about half an hour in this form and then the potential is measured in the hole with Pt-Cal and Pt-Pb electrodes (Fig. 2). When the measurements are made with the Pt-Cal electrodes, the Calomel electrode is placed in the 10% KCL bath

¹ 1. Hematite (Kiruburu, Singhbhum, Bihar, 98% hematite); 2. Pyrite (Amjhor, Sasaram, Bihar, 50% Pyrite); 3. Chalcopyrite (Mosabani, Singhbhum, Bihar, 10% Chalcopyrite, It was present in the disseminated form); 4. Galena (Zawar, Rajasthan, 20% Galena; It was also present in the disseminated form); 5. Bauxite (Lohardaga, Singhbhum, Bihar, 60% Bauxite); 6. Graphite (Athmallik, Dhenkanol, Orissa, 90% Graphite); 7. Bituminous Coal (Ranigang, West Bengal); 8. Lateritic surface clays (Kharagpur, West Bengal)

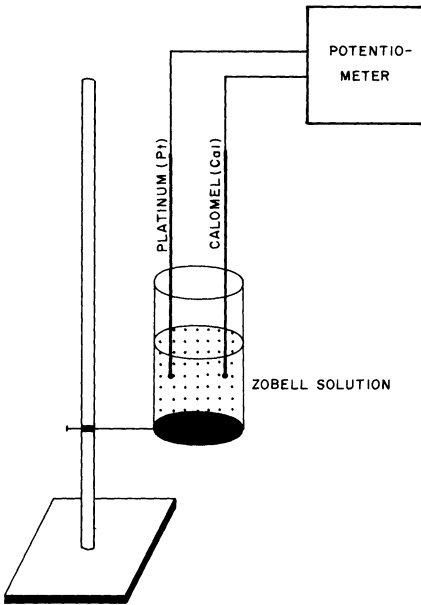


Fig. 1. Standardization of electrodes in Zobell solution

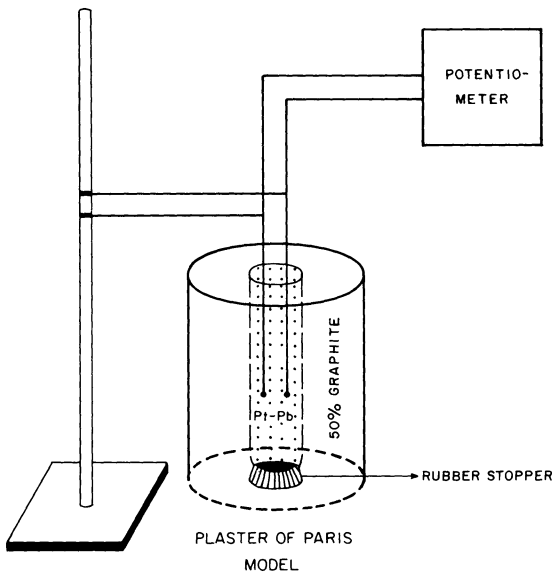


Fig. 2. Redox potential measurement in the plaster of paris model

and the connection with the plaster of paris cast is made by an agar-agar bridge. A similar type of set up is shown in Figure 3.

We have taken about 700 observations in hematite and 400 observations each in graphite, chalcopyrite, and bauxite. The results of our investigations are summarized as follows:

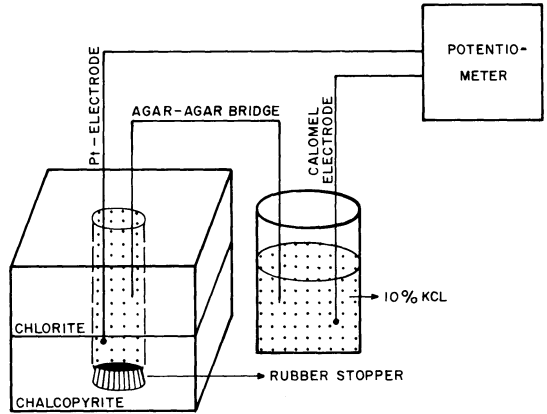


Fig. 3. Redox potential measurement with Pt-Cal electrodes using agar-agar bridge across chlorite-chalcopyrite block

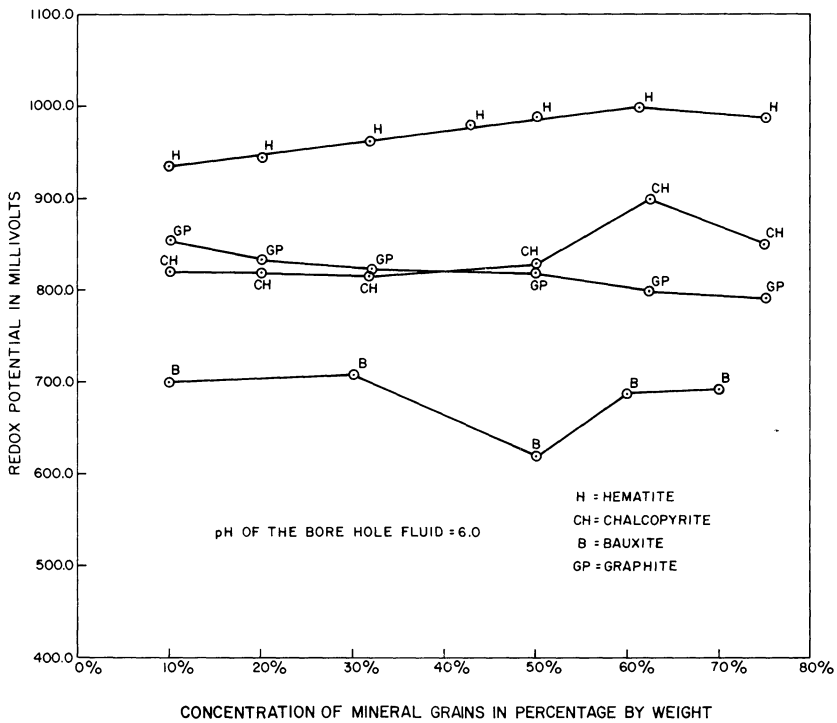


Fig. 4. Effect of mineral concentrations in the plaster of paris models on redox potential (pH=6.0)

- (a) The potential takes about 10 min–2 h before it gets stable within a limited time span of 30 min–60 min.
- (b) When the measurements are repeated after a long time gap of 16–20 h, a significant change in the potential, of the order of 200 mV, is observed.
- (c) For every cleaning operation of the platinum electrode a sudden jump in the potential is observed. Therefore we decided to clean the platinum electrode

at the beginning of each observation and chose the value as our reading when it remained more or less stable within a time span of half an hour.

(d) The potential is found to be almost independent of concentration of the minerals in percentage by weight when the observations are taken with tap water (pH=6.0) and also with alkaline electrolytes (pH=7.0 to 12.0) (Fig. 4). However, some distinct trends of variations of potentials are observed when acidic electrolytes are used for measurements. Observations with pH=0.5 are presented in Figure 5. Almost similar type of trends are observed when solutions of pH=1.0 and 2.0 are used. It appears that the sensitivity of the redox anomaly may increase with gradual decrease in the pH of the borehole fluid.

(e) Although the level difference between Pt-Pb and Pt-Cal electrode in the Zobell solution was found to be 347 mV, the level differences in the plaster of paris model for hematite are found to be slightly on the higher side, i.e., about 430 mV on an average. Similar results are obtained with other models also.

C. Potential Difference across Natural Field Samples

Chalcopyrite and chlorite samples were collected from the Mosabani field. The samples are trimmed to make rectangular blocks and they are attached to one another by araldite (fixer) to make a leak proof block. The field geologic successions are maintained in the model (Fig. 3). A hole (diameter 2 cm) was drilled through the middle of this block. Tap water was poured through the hole and the water was allowed to stay for 3 days before the redox logs were taken with Pt-Pt and Pt-Cal electrodes using the agar-agar bridge.

Remarkable difference in the redox potentials across the chlorite chalcopyrite blocks are observed when the observations are repeated in 4 consecutive days (Figs. 6 and 7). Although the absolute values could not be reproduced, the trends of variations remained more or less the same. This experiment has given us the idea of investigating the variations of the redox potentials, rather than their absolute values, in the laboratory models.

D. Model Tank Experiment

A semi-cylindrical model tank, height 51.5 cm and radius 30 cm with a front transparent face of 61 cm × 51.5 cm, was prepared in the laboratory. Alternate layers of lateritic surface clays and ores are simulated in the tank as shown in Figure 8. A borehole in the model tank was simulated by holding a wooden rod vertically during the packing of the tanks with clays and ores. Afterwards the rod is taken out from the tank and a borehole is made through the entire cross section of the clay/ore/clay. The model tank is constructed over a bakelite base. A small hole is drilled below the borehole such that the borehole fluid can be changed from time to time. Platinum-lead electrodes are used for measurement of potentials keeping the Pt-electrode at the top of the borehole

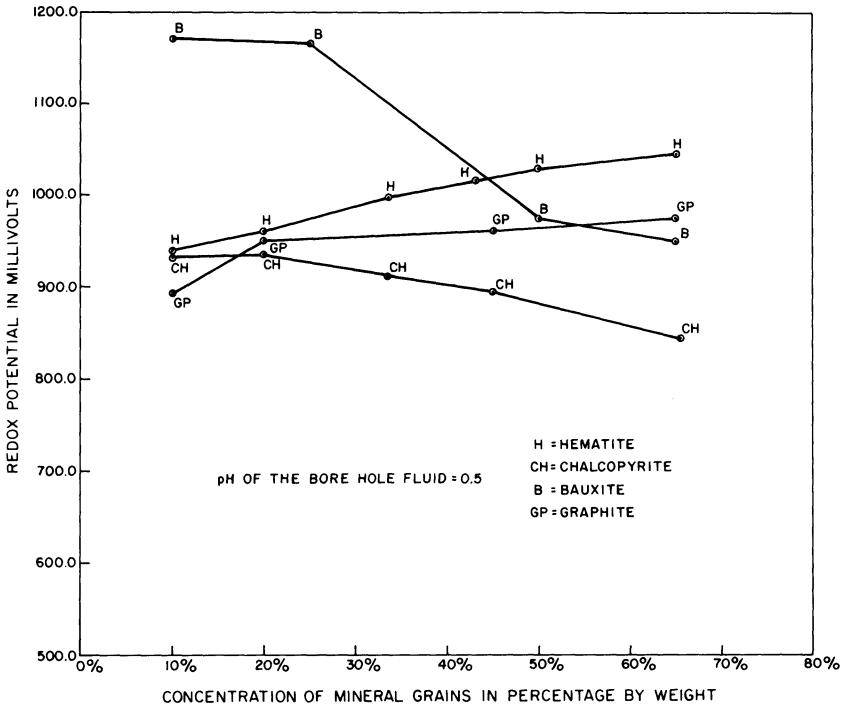


Fig. 5. Effect of mineral concentration in the plaster of paris models on redox potential (pH=0.5)

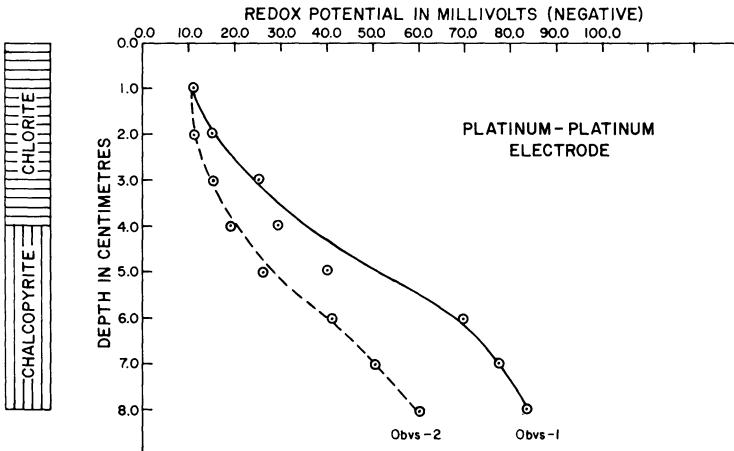


Fig. 6. Redox log across chlorite-chalcopyrite block with Pt-Pt electrodes (borehole fluid – tap water)

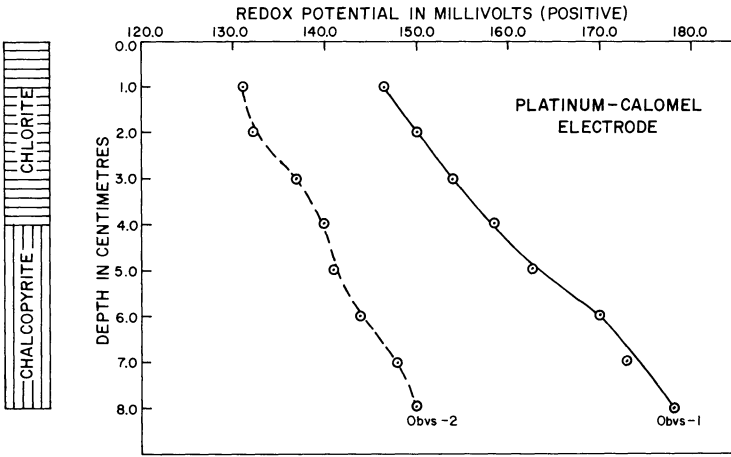


Fig. 7. Redox log across chlorite-chalcopyrite block with Pt-Cal electrodes (borehole fluid – tap water)

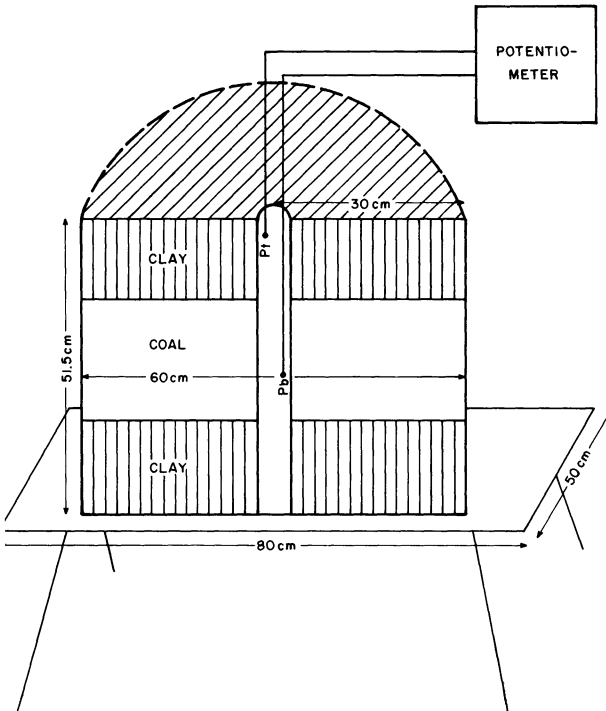


Fig. 8. Model tank for redox potential measurements inside a simulated borehole

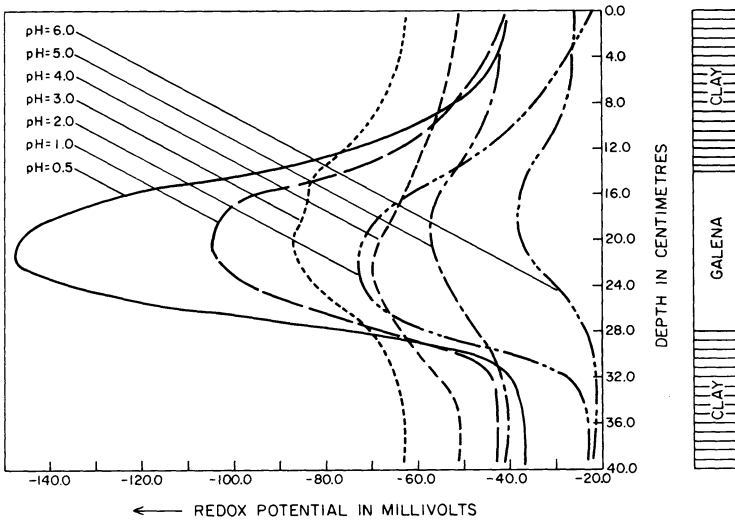


Fig. 9. Redox log across clay/galena/clay with Pt-Pb electrodes

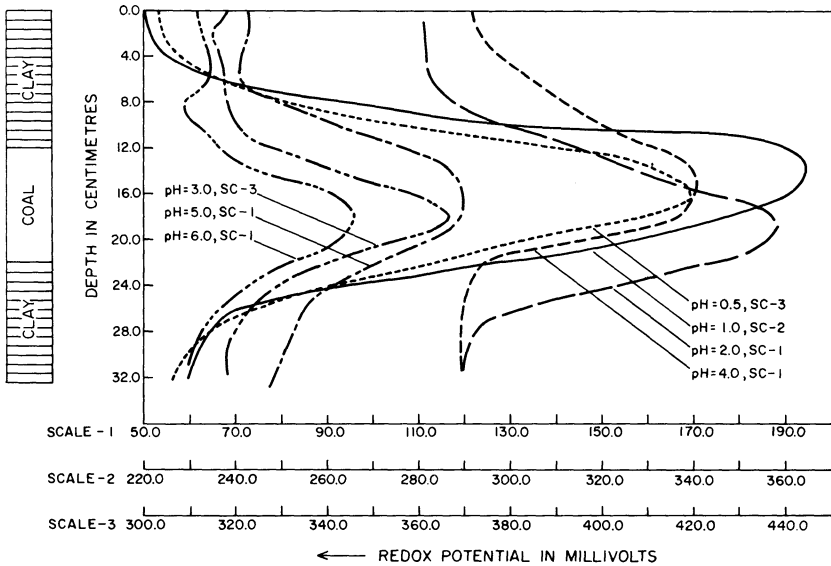


Fig. 10. Redox log across clay/coal/clay with Pt-Pb electrodes

and allowing the Pb electrode to move through the entire cross section. The fluids of different pH are inserted in the borehole and the observations are repeated. The results are presented in Figures 9, 10, 11 and 12. In order to economize space only a few curves are presented. However, the results are summarized in Figure 12. They reveal the following facts:

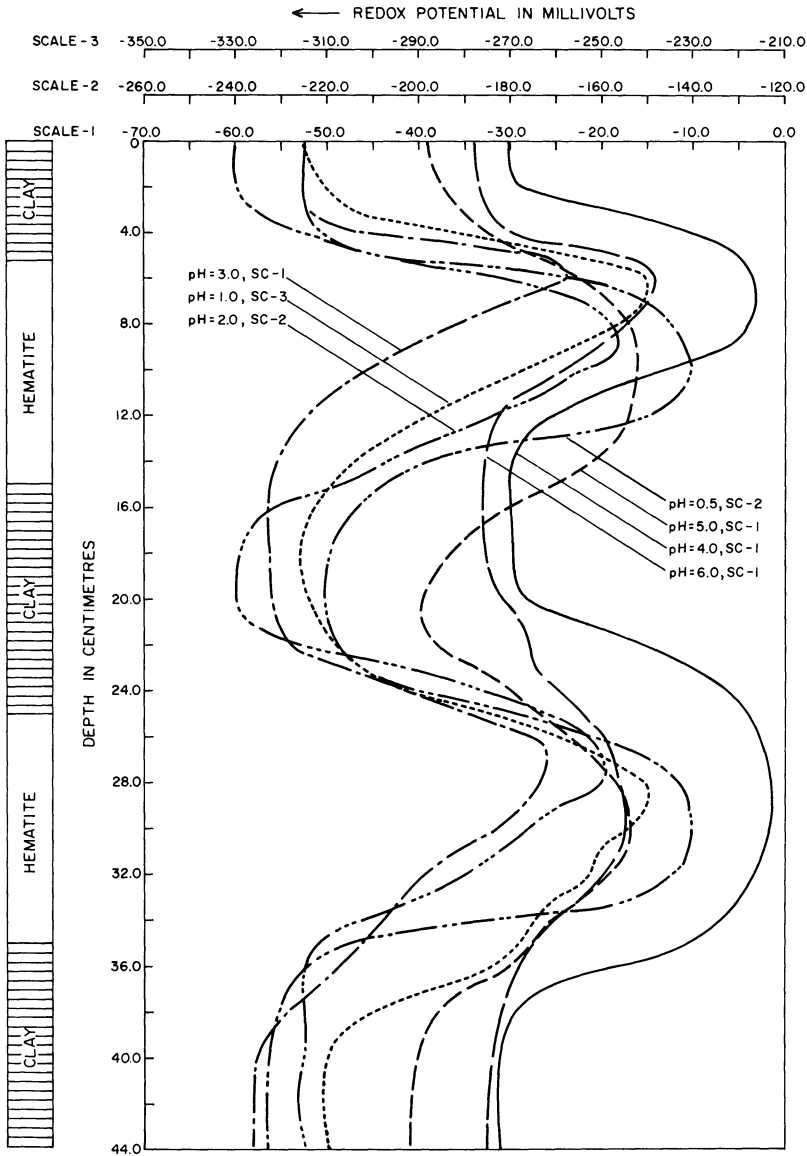


Fig. 11. Redox log across clay/hematite/clay/hematite/clay with Pt-Pb electrodes

1. The redox logging is good enough to detect the depths and approximate thicknesses of the ore bodies.

2. The absolute values of the potentials are not reproducible and therefore these values cannot be used for any quantitative interpretation.

3. The redox anomaly is found to become sharper and sharper with the increasing acidity of the borehole fluids.

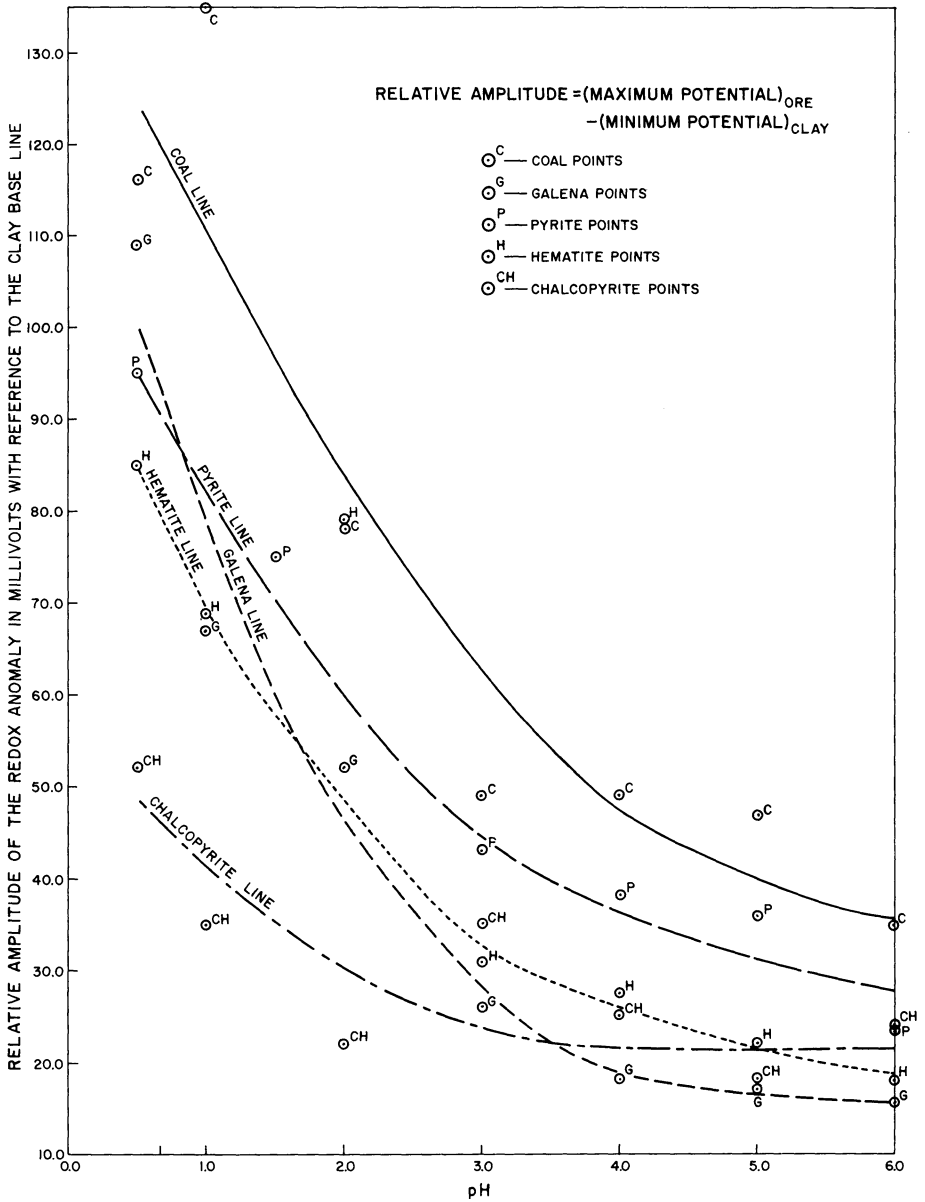


Fig. 12. Variations of redox anomalies with pH

4. Like other geophysical methods viz. gravity and magnetic methods, the relative change of the redox potential rather than their absolute values will be of more interest to the geophysicists.

5. The change in potential per unit change in pH is found to differ widely for different minerals.

The present set of data shows how the signals become prominent surpassing

the high noise levels in redox measurement. These data are presented largely as a qualitative measure and no attempt is made to go for any quantitative analysis, since the data could not be made reproducible within 5% in all cases. Sometimes the variations are significant. The instrumental complications in redox measurements are minimum. All we need are (i) a pair of Pt-Pb or Pt-Ag AgCl electrodes (ii) one reel of two core cable and (iii) a potentiometer.

Acknowledgement. Authors are grateful to Prof. D.K. Ganguli, Head of the Department of Geology and Geophysics, I.I.T., Kharagpur for providing facilities for research. Thanks are due to Dr. S.C. Sarkar of the Department of Metallurgy, I.I.T. Kharagpur, for some helpful suggestions. Thanks are due to Sri B.S. Chakraborty and Sri C.K. Bhattacharyya for their help during the fabrication of the models. We are indebted to various mining companies for allowing us to collect samples of ores and associated rocks from their mining areas. We are grateful to the Chemistry and Metallurgy Department of I.I.T. Kharagpur for their interest in our work. We express our deep sense of gratitude to Miss Lucie Lalonde for typing the manuscript and G.W. McKinnon for drawing the diagrams so nicely. Lastly the authors are grateful to the Council of Scientific and Industrial Research, Rafi Marg, New Delhi, India for financing the project.

References

- Baas Becking, L.G.M., Kaplan, I.R., Moore, D.: Limits of the natural environment in terms of pH and oxidation-reduction potentials. *J. Geol.* **68**, 243–284, 1960
- Colombo, U., Salimbeni, G., Sironi, G., Veneziani, I.: Differential electric log. *Geophys. Prosp.* **7**, 91–118, 1959
- Doll, H.G.: The S.P. log: Theoretical analysis and principles of interpretation. *Bull. Am. Inst. Mining Metall. Eng.* **29**, 1–40, 1948
- De Witte, L.: A new method of interpretation of self potential field data. *Geophysics* **13**, 600–609, 1948
- Fox, R.W.: On the electromagnetic properties of metalliferous veins in the mines of Cornwall. *Phil. Trans. Roy. Soc. London*, **120**, A, 399–414, 1830
- Garrels, R.M.: Mineral species as function of pH and oxidation-reduction potential, with special reference to the zones of oxidation and secondary enrichment of sulphide ore bodies. *Geochim. Cosmochim. Acta.* **5**, 153–168, 1954
- Garrels, R.M., Christ, Ch.L.: *Solutions, minerals and equilibria*, 2nd. ed. New York: Harper and Row 1965
- Garrels, R.M.: *Mineral equilibria at low temperature and pressure*, pp. 61–75. New York: Harper 1970
- Glasstone, S.: *An introduction to electrochemistry*, 10th printing. Princeton, N.J.: D. Van Nostrand 1962
- Glasstone, S.: *Thermodynamics for chemists*, 11th printing. New York: Van Nostrand 1969
- Gondouin, M., Tixier, M.P., Simard, G.L.: An experimental study on the influence of the chemical composition of electrolytes on the S.P. curve. *J. Petrol. Technol.* **9**, 58–70, 1957
- Heiland, C.: *Geophysical exploration*. Englewood Cliffs, N.J.: Prentice Hall 1940
- Karaoguz, D., Helander, D.P., Kemp, M.K.: An experimental study of redox logging. *The Log Analyst* **11**, 8–16, 1970
- Krumbein, W.C., Garrels, R.M.: Origin and classification of chemical sediments in terms of pH and oxidation-reduction potentials. *J. Geol.* **60**, 1–33, 1952
- Latimer, W.M.: *The oxidation states of elements and their potentials in aqueous solutions*. New York: Prentice-Hall 1938
- Pirson, S.J.: Redox log interprets reservoir potentials. *Oil and Gas J.* **66**, 69–75, 1968
- Pirson, S.J.: Environmental logging and mapping the search for minerals. *The Log Analyst* **11**, 23–44, 1970

- Poldini, E.: Geophysical exploration by spontaneous potential methods. *Mining Mag.* **59**, 278–282, 1938
- Roy, A., Chawdhury, D.K.: Interpretation of self potential data for tabular bodies. *J. Sci. Eng. Res.* **3**, 33–55, 1959
- Sato, M.: Oxidation of sulphide ore bodies (I): Geochemical environment in terms of Eh and pH. *Econ. Geol.* **55**, 928–961, 1960
- Sato, M., Mooney, H.M.: The electrochemical mechanism of sulphide self potentials. *Geophysics* **25**, 226–249, 1960
- Schlumberger, C., Schlumberger, M., Leonardon, E.G.: Electrical coring: A method of determining bottom hole data by electrical measurements. *Trans. AIME.* **110**, 273–289, 1934
- Yungul, S.H.: Interpretation of spontaneous polarisation anomalies caused by spherical ore bodies. *Geophysics* **15**, 237–246, 1950
- Yungul, S.H.: Spontaneous potential survey of copper deposits at Sariyer, Turkey. *Geophysics* **19**, 455–458, 1954
- Zobell, C.E.: Studies on redox potential of marine sediments. *Bull. Am. Assoc. Petrol. Geol.* **30**, 477–513, 1946

Received December 15, 1975; Revised Version October 18, November 19, 1976

Short Communications

**Modelling of the Ionosphere and Comparison
of the Calculated and Observed Cosmic Radio
Noise Absorption over Delhi**

M.C. Sharma and S.B.S.S. Sarma*

Radio Science Division, National Physical Laboratory, New Delhi 110012, India

Abstract. Making use of the latest available information, the collision frequency and the electron density profiles, appropriate for the latitude of Delhi, for sunspot maximum and minimum conditions are constructed and the absorption coefficients at the riometer operating frequencies are evaluated. From these the expected absorption is evaluated and compared with the observed absorption over Delhi. The observed and calculated absorptions are in agreement within the limits of the observational errors.

Key words: Ionospheric modelling electron density – Collision frequency – Absorption coefficient – Riometer absorption – Cosmic radio noise

1. Introduction

In recent years theoretical modelling of the ionosphere has become important for the studies of prediction of radio wave propagation like absorption. Development of these models to match the observed cosmic radio noise absorption in the VHF range over Delhi has been described in this investigation. These models will be useful in the propagation calculations in the VHF range for any system designer. Shortcomings of these models are judged directly to the extent to which the absorption calculated from these models match with the observed absorption from riometers.

2. Methods of Computation

2.1. Collision Frequency Model

The neutral atmospheric model of Groves (1970) combined with collision frequency calculations of Itikawa (1971) are employed in deriving the collision

* To whom offprint requests should be sent

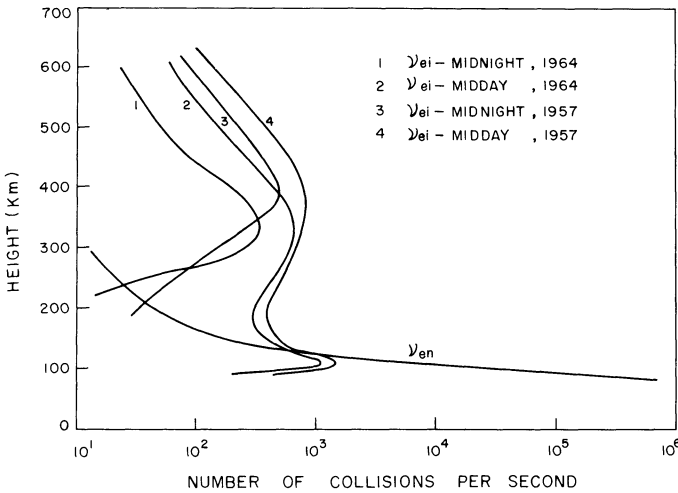


Fig. 1. Collision frequency model profiles

frequency profile below 100 km. We also made use of the equations given by Jacchia (1971) for deducing the number densities of major neutrals in calculating the collision frequency (Itikawa, 1971). The effect of electron ion collisions was neglected in this region and the electron and ion temperatures were assumed equal to the neutral temperature. It was observed that the derived collision frequency is in agreement with that obtained by Thrane and Piggot (1966). Further, the electron-ion collision frequency is calculated using the equation suggested by Anderson and Goldstein (1955). The electron collision frequency with neutrals is assumed to be the same for both the minimum and maximum solar epochs (Beynon and Rangaswami, 1969). Figure 1 shows the derived profiles for daytime and nighttime for both epochs of the solar cycle.

2.2. Electron Density Models

In developing the electron density profiles a major effort is put in to obtain profiles which are internally consistent and match with the observational data, at this latitude, in various regions of the ionosphere. In this process we made use of the International Reference Ionosphere (Rawer et al., 1975), ionosonde and satellite observations over Delhi and the semi-empirical D-region profiles. The electron density up to 100 km is taken from Chakrabarty and Mitra (1974). From h_mE to h_mF_2 , the true height electron density profiles are derived from ionosonde data over Delhi. From h_mF_2 to 600 km (riometer absorption from heights above about 600 km is within the experimental accuracies of the system), maintaining the shape of the IRI profile, normalization with IRI profile is carried out with the observed foF_2 values. Thus we have developed N_e profiles for Delhi at intervals of every 2 h which are shown in Figures 2 and 3.

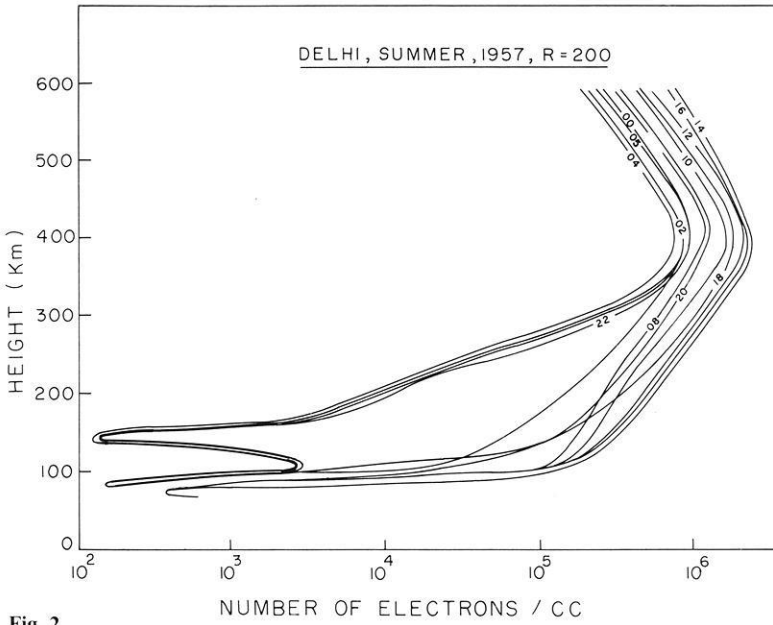


Fig. 2

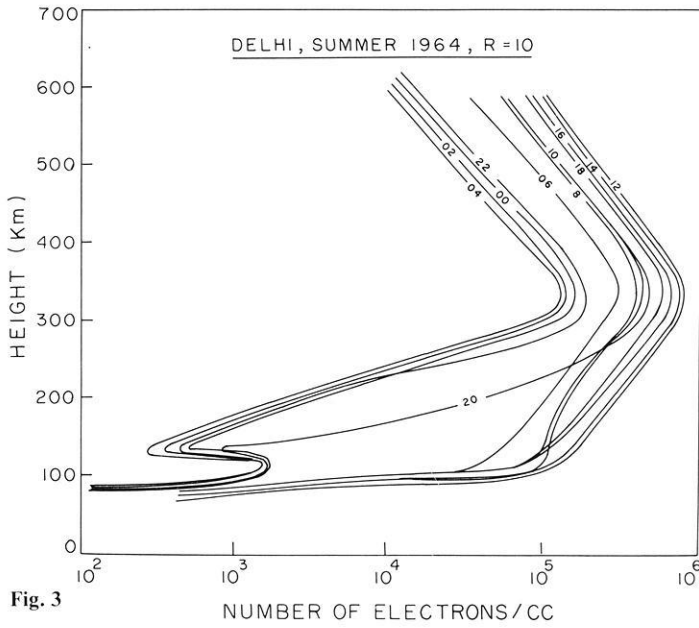


Fig. 3

Figs. 2-3. Electron density model profiles

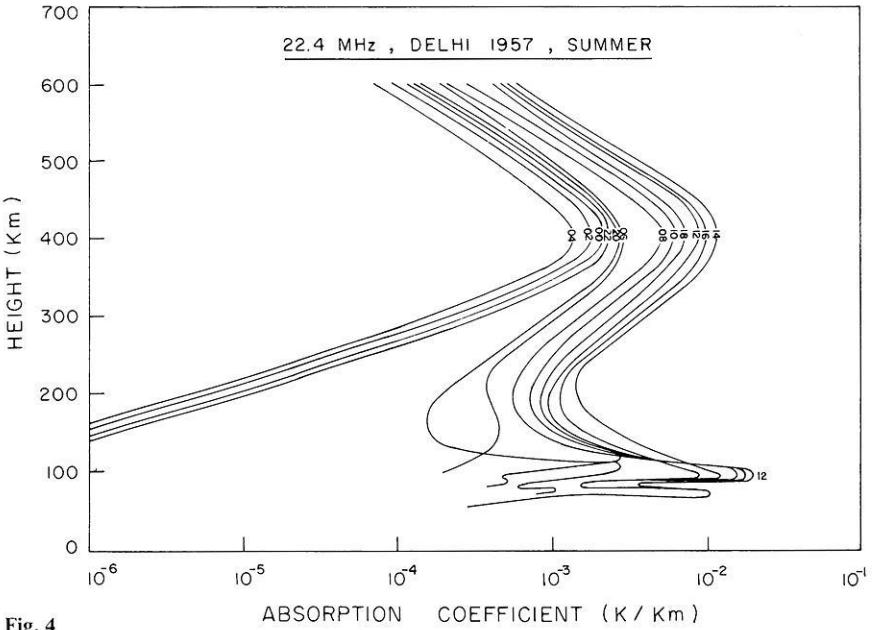


Fig. 4

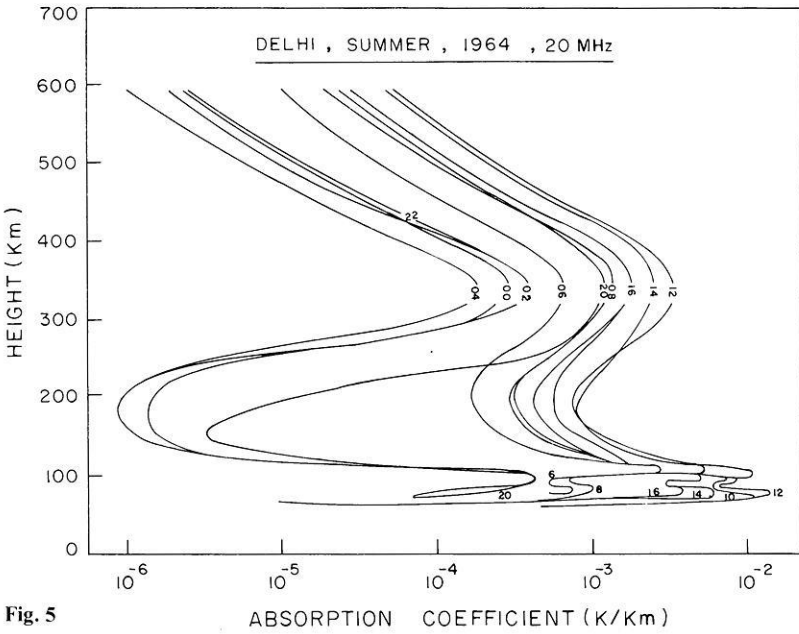


Fig. 5

Figs 4-5. Absorption coefficient versus height

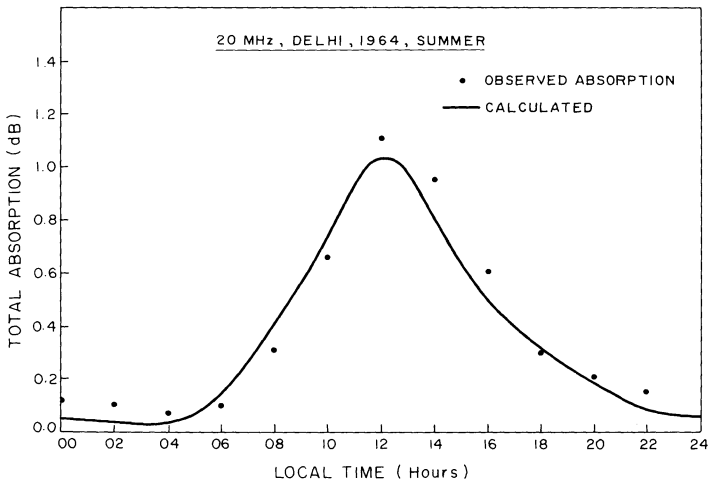


Fig. 6. Comparison of calculated and observed absorption

2.3. Absorption Coefficient Evaluation

From the above models the absorption coefficient at various height intervals is calculated for different hours of the day both for solar minimum and maximum conditions and are shown in Figures 4 and 5. The absorption coefficients are summed up using the Simpson rule to get total absorption. Absorption from 60–100 km is termed as lower region contribution and from 100–600 km is named as F region contribution.

3. Comparison of Riometer Absorption with Model Calculations

The calculated absorptior (at 20 MHz) discussed above is compared with that of the measured riometer absorption for low solar activity. Figure 6 indicates the diurnal variation. It can be seen that the calculated absorption is generally in good agreement with the observed absorption within the limits of the experimental errors (in case of riometer absorption accuracy is limited to ± 0.1 db). A similar result is observed for high solar activity (Sharma, 1976).

4. Conclusions

During the low solar activity the observed and calculated absorptions are in agreement within the limits of observational errors indicating that the models of collision frequency and electron density profiles developed for this latitude can be considered to be consistent with the observations. The internal consistency in the observations and the general agreement with model absorption calcula-

tions suggests that the riometer method of determination of normal absorption at low and temperate latitudes is dependable.

Acknowledgements. The authors are grateful to Dr. A.P. Mitra for his helpful comments and interest in this subject.

5. References

- Anderson, J.M., Goldstein, L.: Interaction of electromagnetic waves of radio frequency in isothermal plasma: Collision cross-section of Helium atoms and ions for electrons. *Phys. Rev.* **100**, 1037–1046, 1955
- Beynon, W.J.G., Rangaswami, S.: Model electron density profiles for the lower ionosphere. *J. Atmos. Terr. Phys.* **31**, 891–903, 1969
- Chakrabarty, D.K., Mitra, A.P.: Theoretical models of D-region electron density profiles under different conditions. *Ind. J. Radio and Space Phys.* **3**, 76–86, 1974
- Groves, G.V.: Cospar 14th planary meeting June 18–July 12. Seattle, Washington, 1970
- Itikawa, Y.: Effective collision frequency of electrons in atmospheric gases. *Planet. Space Sci.* **19**, 993–1007, 1971
- Jacchia, L.G.: Revised static models of the thermosphere and exosphere with empirical temperature profiles. Smithsonian Astrophysical Observatory, Special Report. 332, 1971
- Rawer, K., Ramakrishnan, S., Bilitza, D.: Preliminary reference profiles for International Reference ionosphere. Scientific Report No. W-B2 IPW D 78 (FRG) 1975
- Sharma, M.C.: Ph.D. Thesis. Submitted to Delhi University, 1976
- Thrane, E.V., Piggott, W.R.: The collision frequency in the E- and D-regions of the ionosphere. *J. Atmos. Terr. Phys.* **28**, 721–737, 1966

Received December 10, 1976

Winter Anomaly in VHF Absorption Studies over Delhi

S.B.S.S. Sarma* and M.C. Sharma

Radio Science Division, National Physical Laboratory,
Hillside Road, New Delhi-110012, India

Abstract. In an effort to understand the seasonal anomaly in absorption over this latitude the riometer and pulse absorption data over a period of 2 solar cycles is examined. The analysis indicates that during the high solar activity periods the riometer absorption and foF2 values are always larger in winter than in summer months, whereas during the low solar activity period an exactly opposite feature is observed both for foF2 and absorption. It is concluded that during the high sunspot period the seasonal anomaly is mainly due to F region parameters alone.

Key words: Ionosphere – Absorption – Solar activity – F-region – D-region.

Riometer is a device for measuring the ionospheric absorption using cosmic radio noise. In the present case 22.4 MHz equipment has a directional antenna system of a half power bandwidth (HPBW) of $17^\circ \times 24^\circ$ followed by an ultrastable low noise receiving system. The 20 and 30 MHz equipments are, Mark II-A Model ARI-100B, loaned from AFCRL, U.S.A. In these the receiver assumes the role of a sensitive null indicator. The antennas are three element Yagi with HPBW of 60° in E-plane and 110° in H-plane. Every care is taken to maintain the equipments in a stable condition over long periods of operation. The equipments are located at a relatively interference free site and the bandwidth of the receiving systems are kept at 3 KHz so as to keep interference to a minimum. The errors in unattenuated cosmic noise intensity over a sidereal day are eliminated using the sky brightness distribution to get reliable absorption data. The blocking effect of the ionosphere, for zenith angles greater than a critical value, (window effect) is thoroughly examined, in the present case for all the three systems during the period of data collection by evaluating the window angles. The window angle is given by

$$\cos \phi = \frac{foF2}{f}$$

* To whom offprint requests should be sent

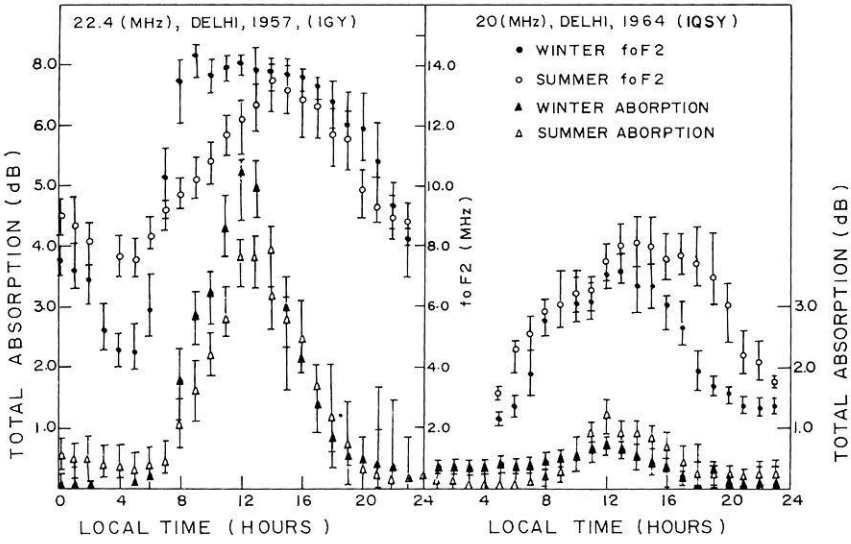


Fig. 1. Seasonal variation of absorption and foF2. (a) Sunspot maximum day foF2 (Summer) < foF2 (winter) also day absorption (summer) < absorption (winter). (b) Sunspot minimum day foF2 (summer) > foF2 (winter) also day absorption (summer) > absorption (winter)

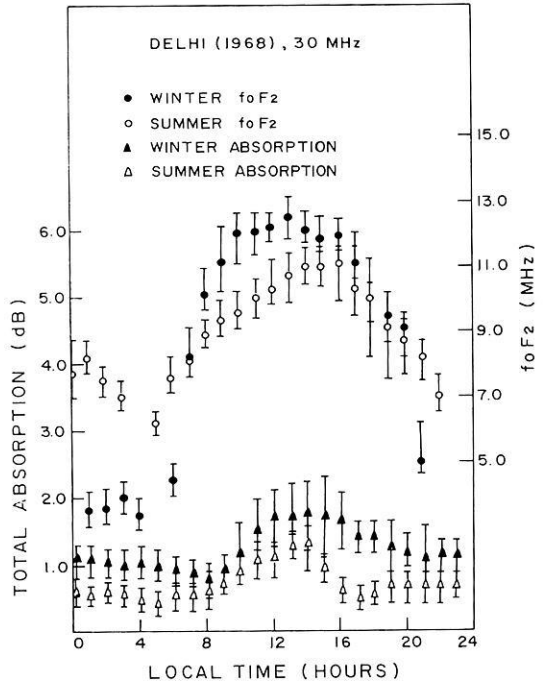


Fig. 2. Seasonal variation of absorption and foF2. Sunspot maximum day foF2 (summer) < foF2 (winter) also day absorption (summer) < absorption (winter)

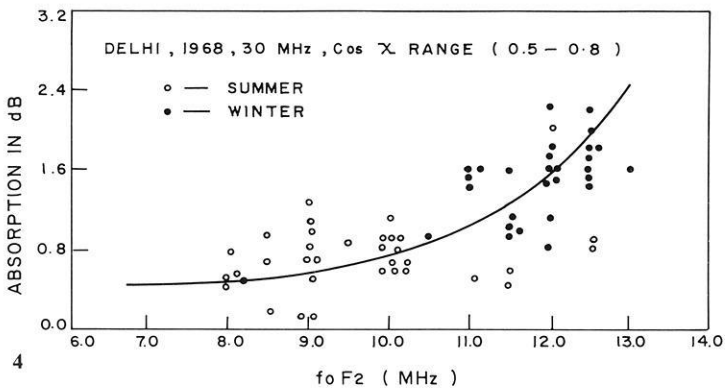
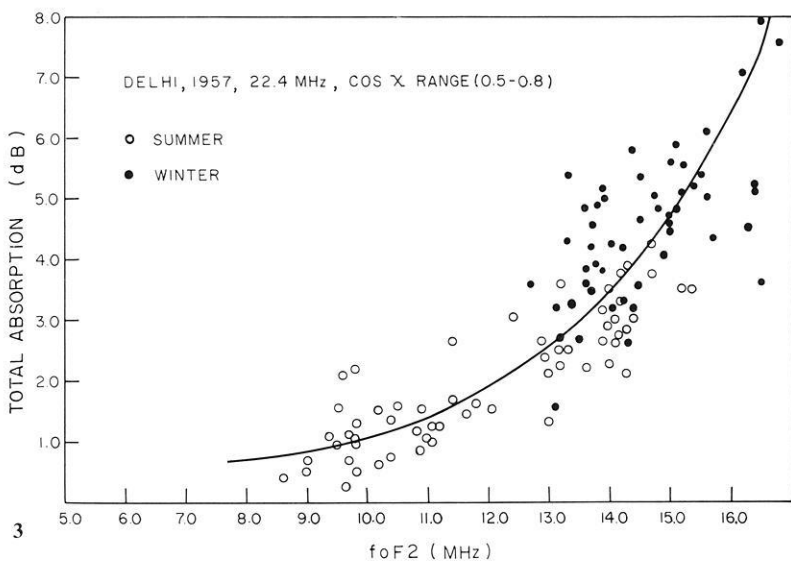
where ϕ is the window angle, foF2 is the critical frequency of the F2 layer and f is the operating frequency. It is observed that the window effect is outside the edge of the effective antenna beams during the periods of measurements for all the three equipments (Sharma, 1976). Hence, the contribution to absorption through the window effect is non-existing. It is also seen that factors like refraction, ionospheric noise etc. have negligible affect on absorption evaluation. The reliability of the data at Delhi has been discussed (Sharma, 1976) by comparing the calculated absorption (using model electron density and collision frequency profiles appropriate for this station) with the observed values. As there is a remarkable agreement between the two (Sharma, 1976) it is concluded that observed values can safely be used for the study of winter anomaly over this latitude.

Riometers are under operation at Delhi since 1957. Intensive studies on cosmic radio noise absorption at this latitude covering the periods IGY, IQSY and IASY have revealed certain anomalous behaviour when plotted against seasons (Sharma, 1976). For high solar activity period (IGY) Sarada and Mitra (1961) reported, for this latitude, an absorption maximum during winter and minimum during summer. Sarma et al. (1970) reported, for this latitude, for low solar activity conditions (IQSY) exactly the reverse of the above results i.e., the absorption was maximum during summer and minimum in winter. The same type of behaviour as reported by Sarada and Mitra (1961) was repeated, for the years 1968–69 (IASY), again a high solar activity period. This type of behaviour has raised the curiosity to investigate further into this aspect in greater detail. The present investigation is mainly dealt with to have a thorough understanding regarding the above seasonal anomaly in absorption over this latitude. For this purpose we also made use of the data on pulse absorption and foF2 for the corresponding periods at this latitude.

We have plotted the values of total riometer absorption against local time for summer and winter months separately for the high and low solar activity periods along with the corresponding foF2 values and are shown in Figures 1a, b and 2. An examination of these figures indicate:

1. The daytime absorption in winter is larger than in summer during the high sunspot period. The winter anomaly is nonexistent in low sunspot years.
2. foF2 values show a corresponding trend. However, it is also to be noted that during IGY and IQSY foF2 values behave exactly in opposite manner.

After establishing that there exists seasonal anomaly in absorption and that it is at least partly due to the F region, we tried to see if there is any contribution from the D region. To examine the F region contribution quantitatively we have plotted absorption against foF2 for a fixed range of values of $\text{Cos } \gamma$ where γ is the zenith distance (so that the D region absorption is maintained constant) as shown in Figures 3 and 4. It is seen from the figures that for a given foF2 the absorption is larger in winter than in summer (in both high solar activity periods) even when $\text{Cos } \gamma$ values are essentially kept invariant. This feature is brought out more clearly in Figure 5, where $\text{Cos } \gamma$ is kept at 0.5 a fixed value (instead of a range), a more restrictive plot. Further, the pulse absorption values do not show this type of behaviour instead they are always



Figs. 3-4. Absorption versus foF2 for a fixed range of solar zenith angles. (χ is the zenith distance)

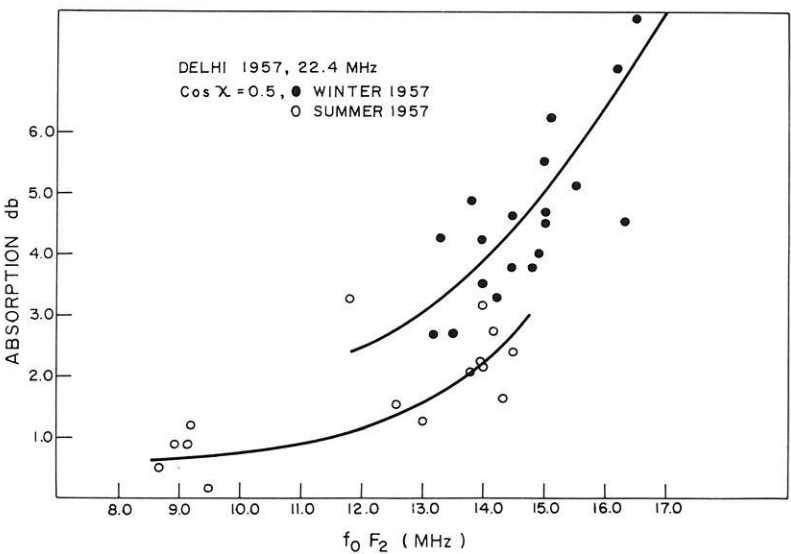
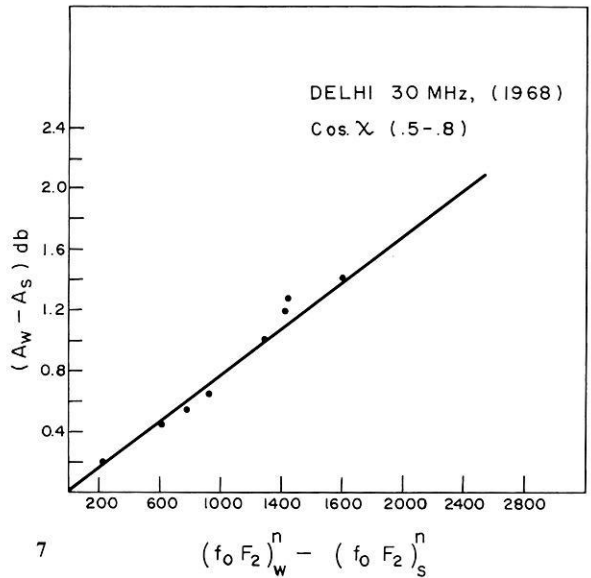
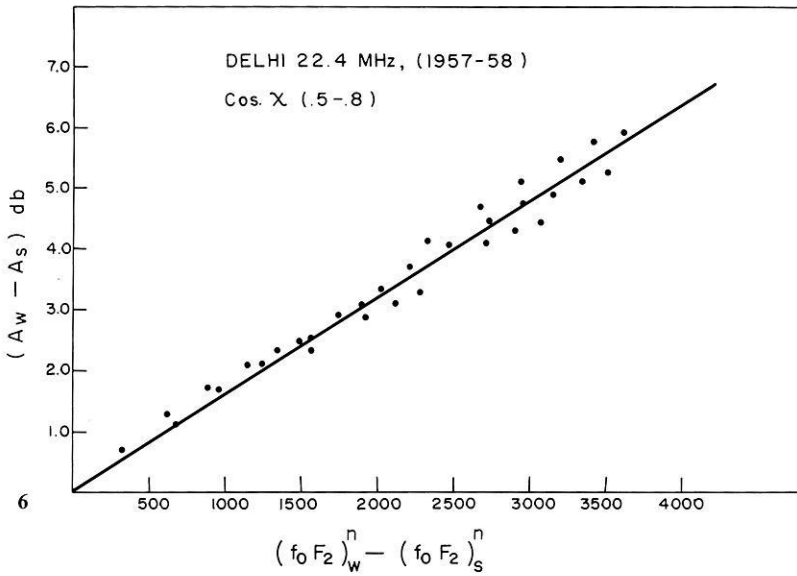


Fig. 5. Absorption versus foF2 for a fixed value of solar zenith angle (χ is the zenith distance)



Figs. 6-7. Excess absorption during winter versus $(f_o F_2)_w^n - (f_o F_2)_s^n$

more in summer than in winter months irrespective of the solar activity (Sharma, 1976). The result is somewhat intriguing. One may infer that not only is the winter absorption anomaly during high solar activity period a result of the F region, but that it is not foF2 alone that controls the anomaly. Otherwise, when plotted against foF2 (and with fixed Cos γ) the winter and summer values should be indistinguishable. This additional factor might be due to F region electron temperature.

This predominant control of the winter anomaly by the F region parameters give us an additional method of separating the D and F region absorption contributions. One can write:

$$A_t = A_D + b(\text{foF2})^n$$

where

A_t = Total cosmic noise absorption.

A_D = D region contribution.

$b(\text{foF2})^n$ = F region contribution with b and n are constants appropriate for this latitude.

Then $(A_t)_w = (A_D)_w + b(\text{foF2})_w^n$

and

$$(A_t)_s = (A_D)_s + b(\text{foF2})_s^n$$

where the suffixes w and s refer to winter and summer values respectively.

Further, if $\text{Cos } \gamma$ values are kept reasonably constant, then

$$(A_D)_w \approx (A_D)_s$$

Hence

$$(A_t)_w - (A_t)_s = b[(\text{foF2})_w^n - (\text{foF2})_s^n].$$

When $(A_t)_w - (A_t)_s$ is plotted against $(\text{foF2})_w^n - (\text{foF2})_s^n$ for this latitude the result was a straight line as shown in Figures 6 and 7. This confirms our conclusion that the seasonal anomaly is entirely due to the F region alone.

References

- Sarda, K.A., Mitra, A.P.: Results of cosmic noise observations at Delhi on 22.4 MHz. Proc. IGY Symposium, **1**, 98-116, 1961
- Sarma, S.B.S.S., Sharma, M.C., Juneja, S.L.: Cosmic noise absorption measurements in Delhi. Ind. J. Pure & App. Phys. **8**, 529-532, 1970
- Sharma, M.C.: Ph.D. Thesis submitted to Delhi University 1976

Received December 8, 1976; Revised Version January 7, 1977



In Memoriam Hermann Reich

Im Mai dieses Jahres verstarb Dr. phil. nat. Hermann Reich, em.o.ö. Professor für Angewandte Geophysik an der Universität München. Damit verlosch ein Leben, das in seltener Weise im Dienst unserer Wissenschaft gestanden hatte. Wenn sich heute immer mehr die Erkenntnis durchsetzt, daß für den Fortschritt in den Geowissenschaften neben der Pflege des Spezialistentums das Überbrücken der Trennlinien zwischen den einzelnen Fächern von größter Wichtigkeit ist, so können wir H. Reich als ein Vorbild würdigen.

Schon als Schüler eines humanistischen Gymnasiums begann er mit geologischen Studien, wandte sich unter der Anleitung von Salomon und Deecke der Geologie zu und studierte außerdem Mineralogie, Chemie, Zoologie und Botanik. Er promovierte mit Auszeichnung nach 9-semesterigem Studium im Jahre 1914 mit einer Arbeit über das Uracher Vulkangebiet. Während des ersten Weltkrieges war er Soldat im Felde und war dabei fast ein Jahr mit der Lösung hydrogeologischer Fragen beauftragt. Nach seiner Rückkehr setzte er sein Studium in Göttingen fort, z.T. bei Stille (Geologie), z.T. bei Wiechert (Seismologie). Als Assistent in Königsberg arbeitete er am dortigen seismischen Observatorium

mit, legte die Staatsprüfung für das höhere Lehramt mit Auszeichnung ab und trat als Probegeologe 1921 in die Preußische Geologische Landesanstalt ein. 1925 habilitierte er sich für das Fach Angewandte Geophysik an der TH Berlin und nahm dort ohne Unterbrechung, ab 1938 als a.pl. Professor, einen Lehrauftrag wahr bis 1945. Nach dem Kriege arbeitete er von seinem neuen Wohnsitz Göttingen aus am Neuaufbau eines geologischen Dienstes in Niedersachsen mit und setzte gleichzeitig seine Lehrtätigkeit in Göttingen fort. 1948 wird er nach München als Ordinarius mit dem Auftrag berufen, ein Institut für Angewandte Geophysik an der Ludwig-Maximilians-Universität aufzubauen. Er gliedert ihm ein Geophysikalisches Observatorium in Fürstfeldbruck an (erdmagnetisches Observatorium, geophysikalische und Erdbebenwarte). Der Geologe, dessen erste Publikation wenige Semester nach Studienbeginn Neufunde von Fossilien in den Südalpen behandelt hatte, der 1920 einmal schrieb, er sei „davon überzeugt, daß nur die engste und ständige Berührung mit der Natur“ als praktischer Geologe besser wäre als „noch so fleißige, einseitige Bücherweisheit“, der im Selbststudium neben seinem Geologenberuf Mathematik und Physik, soweit dies überhaupt möglich ist, erlernt hatte, konnte nun uneingeschränkt seine wissenschaftliche Lebenserfahrung an jüngere Generationen weitergeben und zur Erforschung seiner engeren Heimat Wichtiges beitragen. 60 Diplomarbeiten, ca. 40 Dissertationen, weit mehr als 100 Publikationen seiner Mitarbeiter aus der Berliner und Münchner Zeit legen beredtes Zeugnis für seine Leistung als akademischer Lehrer ab. Das Münchner Institut, das inzwischen in die Reihe der führenden Institute in der Bundesrepublik eingerückt ist, trägt noch heute den Stempel seines Gründers.

Als Geologe hatte Reich einen Schwerpunkt in der Kartierung des Paläozoikums im Rheinischen Schiefergebirge (Laasphe, Eibelshausen, Berleburg, Battenberg, Wetter). Bis 1939 liefen diese Arbeiten neben der geophysikalischen Betätigung. Ein anderer Schwerpunkt lag in einem Kartiergebiet des Emslandes (Bentheim, Schüttorf). In der Geophysik forschte Reich auf zwei Hauptgebieten: Seismik und Magnetik.

Erste tastende Versuche mit magnetischen Messungen begannen Anfang der 20er Jahre im Karbon Oberschlesiens. 1925 schon vertritt H. Reich aufgrund von gezielten Messungen im Gelände entschieden den Standpunkt, daß die „Diluvial-Theorie“ falsch sei, wonach für alle wesentlichen Anomalien Norddeutschlands die magnetische Wirkung der kristallinen Komponenten in der diluvialen Deckschicht verantwortlich sein sollte. Auch einer anderen Theorie, die als Ursache unterschiedliche Erdströme im Grundwasser annahm, widersetzte er sich. Er befürwortet immer wieder die Förderung dieses Zweiges der Angewandten Geophysik. Er ist unermüdlich in der Erarbeitung von Daten. Bis zu 80 km werden täglich mit Fahrrad von Meßpunkt zu Meßpunkt zurückgelegt. 1926 wird die magnetische Anomalie von Erkelenz entdeckt, und im Grundsatz, wie wir heute wissen, richtig gedeutet. Die Anomalien von Leba (Pommern) und Johannisberg (Ostpreußen) werden untersucht. Allerdings hatten spätere Tiefbohrungen, die ersten in Deutschland auf magnetischen Anomalien, nicht den erhofften Erfolg, Magnetitlagerstätten zu erbohren. Ein Intrusivkörper wurde in Johannisburg in der vorhergesagten Tiefe aufgefunden. Meßgebiet reihte sich an Meßgebiet (Eifel, Mecklenburg, Schleswig-Holstein). Reich wirkte

2 Jahre lang an der „Neuen Magnetischen Vermessung I. Ordnung“ von Deutschland mit. Während der Geophysikalischen Reichsaufnahme wurde das bisher Geleistete vervollkommenet. So konnte Reich 1948 eine geschlossene Aufnahme der magnetischen Anomalien in Z für Norddeutschland vorlegen, die bis vor kurzem das Beste auf diesem Gebiet war. Natürlich erkannte Reich, daß die geologische Deutung von der Kenntnis des Gesteinsmagnetismus abhängt. Er hat eine Feldmethode zur Bestimmung der Magnetisierung von Bohrproben erdacht und benutzte seine Erkenntnisse, die er an hunderten von Bohrkerne gewonnen hatte, für eine in der Tendenz richtige Abschätzung der Tiefen der großen Anomalien Norddeutschlands (Größenordnung nach Reich 5–6 km) – eine wichtige neue Erkenntnis. Reich beschränkte seine Arbeit nicht nur auf Norddeutschland. Er erlebte noch als Emeritus die Erfolge der Paläomagnetik und schreibt darüber einen seiner letzten Artikel.

In der Seismik begann der Geologe mit einem Versuch über Oberflächenwellen von Erdbeben. In einer Veröffentlichung ist schon von der Verbindung geologischer und physikalischer Methoden die Rede, von der Untersuchung des Meeresuntergrundes und Teilen der Erdkruste, die von jungen Bildungen verschüttet sind, wie z.B. die Norddeutsche Tiefebene. Damit ist schon ein Lebensprogramm umrissen. Wohl als erster erkennt er, daß der Elastizitätsmodul von Gesteinen von der tektonischen Beanspruchung, der sie ausgesetzt waren, sehr stark abhängt (1927). Im gleichen Jahr finden Schweydar und Reich zu feldseismischen Versuchen zusammen. 1930 wird über refraktionsseismische Ergebnisse aus verschiedenen Teilen Norddeutschlands berichtet (Lausitz, Mecklenburg, Schleswig-Holstein). Bei Organisationen des Bergbaues tritt er als Mahner auf und weist auf die großen Anstrengungen auf dem Gebiet der Angewandten Geophysik in den USA und Rußland hin.

Aufgrund seiner umfassenden Kenntnis der Angewandten Geophysik hat er an einer nutzbringenden Ausgestaltung des Lagerstättengesetzes, das in seinen Grundzügen auch heute noch Gültigkeit hat, mitgewirkt. Mit der bald danach einsetzenden „Geophysikalischen Reichsaufnahme“ (1935) war der Zeitpunkt gekommen, in welchem H. Reich sein ganzes in jahrelanger Kleinarbeit erarbeitetes Wissen in grandioser und schöpferischer Weise einsetzen konnte. Zusammen mit Barsch und Bentz werden die Pläne entwickelt, die das geologische Bild Norddeutschlands und des bayerischen Alpenvorlandes in kurzer Zeit entscheidend verändern. Zusammen mit Mitarbeitern der Seismos wird die Konstruktion von flächenhaften Laufzeitplänen basierend auf Fächerschießen ausgearbeitet. Für die Auswertung wird die Abhängigkeit der seismischen Geschwindigkeit vom Hangenddruck berücksichtigt. 1937 werden schon die ersten Karten des Untergrundes von Schleswig-Holstein veröffentlicht, die alles bisher Bekannte und Vermutete als unvollkommenes Stückwerk erscheinen lassen. Es folgen ähnliche Ergebnisberichte z.B. für Ostpommern und das Alpenvorland. Die Bedeutung dieser neuen geologischen Erkenntnisse für die gleichzeitig laufende Erdölbohrfähigkeit kann nicht genug betont werden. 1949 erscheint eine Karte von Nordwestdeutschland, die alle Ergebnisse zusammenfaßt.

Wiederum als erster entdeckt Reich, daß Tangentialspannungen, die von den Alpen her ausgelöst sind, sich im Geschwindigkeitsverhalten der ungefalteten Molasse deutlich bemerkbar machen.

Nun wird ein neuer Forschungsbereich in der Seismik erschlossen: die Krustenforschung. Anlaß dazu waren die Großsprengungen Helgoland und Haslach, an deren Zustandekommen und Auswertung H. Reich intensiv mitwirkte (1947/48). Dadurch angeregt, veranlaßte H. Reich die Aufnahme von zwei Großsprengungen bei Blaubeuren durch damals moderne Reflexionsapparaturen, und es gelang zum erstenmal in Europa, eindeutige Reflexionen bis zur Mohodiskontinuität zu registrieren. Es folgte die Auswertung von Sprengungen von Tiefbohrungen am Alpennordrand (Kirchbichl, Lenggries). Das wichtigste und überraschendste Ergebnis war, daß die Oberfläche des kristallinen Grundgebirges möglicherweise bis zu 40 km vom nördlichen Alpenrand in \pm horizontaler Lagerung in den Alpenkörper nach Süden zu verfolgen ist. So wurde Reich der „Vater“ der modernen Krustenforschung in Deutschland.

Von 1929 an hat das Riesphänomen seine Aufmerksamkeit gefunden. Noch als 75jähriger äußert er sich zum Ergebnis der von ihm veranlaßten ersten wissenschaftlichen Riesbohrung.

Wie sehr Reich als Fachmann anerkannt war, zeigt, daß er zur Mitarbeit an zwei Handbüchern (Handbuch für Experimentalphysik, Handbuch der Geophysik) zugezogen worden ist. Er hat ein Buch über Angewandte Geophysik verfaßt, das beste in deutscher Sprache zu damaliger Zeit (1933/34). Er war Herausgeber eines Taschenbuches der Angewandten Geophysik (1943). Über Jahrzehnte hinweg war er Mitherausgeber der Ergänzungshefte von „Gerlands Beiträge zur Geophysik“ und gehörte dem Herausbergremium der Zeitschrift für Geophysik an.

Reich wurde 1947 von der Deutschen Geologischen Gesellschaft, der er von 1921 bis zu seinem Tode, also mehr als 50 Jahre, angehörte, mit der Stille-Medaille geehrt. Er wurde zum korrespondierenden Mitglied der Bayerischen Akademie der Wissenschaften 1958 ernannt, und 1973 verlieh ihm die Deutsche Geophysikalische Gesellschaft die Ehrenmitgliedschaft.

H. Reich war ein Pionier der Angewandten Geophysik in Deutschland, weil er frühzeitig als Geologe erkannt hatte, daß sich in der Kombination mit der Physik eine neue Dimension in der Erkenntnis über unsere Erde erschließen läßt. In eiserner Selbstdisziplin und manchmal auch schweren inneren Kämpfen ist er konsequent einen nicht alltäglichen Weg gegangen, der ihn zu Erfolg und Ehre führte. Sein bester, verstehender und so oft verzichtender Begleiter war seine Ehefrau Gertrud, die den am Ende 4 Jahre ans Bett Gefesselten in denkbar großer Aufopferung gepflegt hat, so daß er, der 85-Jährige, umgeben von seinen „geliebten Büchern“ ruhig sterben konnte. Man sagt: Reich hatte viele Freunde und Verehrer, er hatte keine Feinde.

Hannover, November 1976

H. Closs

Journal of Geophysics Zeitschrift für Geophysik

Volume 42 · Number 6 · 1977 Last issue of this volume

**First Scientific Results
of the Helios Mission**

Edited by H. Porsche



Springer International

Original Investigations

- 551 **H. Porsche:** General Aspects of the Mission Helios 1 and 2. Introduction to a Special Issue on Initial Scientific Results of the Helios Mission
- 561 **H. Rosenbauer, R. Schwenn, E. Marsch, B. Meyer, H. Miggenrieder, M.D. Montgomery, K.H. Mühlhäuser, W. Pilipp, W. Voges, S.M. Zink:** A Survey on Initial Results of the Helios Plasma Experiment
- 581 **U. Isensee:** Plasma Disturbances Caused by the Helios Spacecraft in the Solar Wind
- 591 **G. Musmann, F.M. Neubauer, E. Lammers:** Radial Variation of the Interplanetary Magnetic Field between 0.3 AU and 1.0 AU. Observations by the Helios-1 Spacecraft
- 599 **F.M. Neubauer, H.J. Beinroth, H. Barnstorf, G. Dehmel:** Initial Results from the Helios-1 Search-Coil Magnetometer Experiment
- 615 **H. Kunow, M. Witte, G. Wibberenz, H. Hempe, R. Mueller-Mellin, G. Green, B. Iwers, J. Fuckner:** Cosmic Ray Measurements on Board Helios 1 from December 1974 to September 1975: Quiet Time Spectra, Radial Gradients, and Solar Events
- 633 **E. Keppler, A.K. Richter, K. Richter, G. Umlauf, B. Wilken, D.J. Williams:** A Survey on Measurements of Medium Energy Protons and Electrons Obtained with the Particle Spectrometer E8 on Board of Helios
- 645 **A.K. Richter, E. Keppler:** Interaction of Low-Energy (> 80 keV) Protons with the January 6 and 8, 1975, Shock Waves: Helios-1 Observations
- 659 **H. Volland, M.K. Bird, G.S. Levy, C.T. Stelzried, B.L. Seidel:** Helios-1 Faraday Rotation Experiment: Results and Interpretations of the Solar Occultations in 1975
- 673 **P. Edenhofer, P.B. Esposito, R.T. Hansen, S.F. Hansen, E. Lüneburg, W.L. Martin, A.I. Zygielbaum:** Time Delay Occultation Data of the Helios Spacecrafts and Preliminary Analysis for Probing the Solar Corona
- 699 **C. Leinert, E. Pitz, M. Hanner, H. Link:** Observations of Zodiacal Light from Helios 1 and 2
- 705 **R.H. Giese:** Interpretation of the Optical Properties of Interplanetary Dust
- 717 **E. Grün, H. Fechtig, J. Kissel, P. Gammelín:** Micrometeoroid Data from the First Two Orbits of Helios 1
- 727 **G. Schwehm, M. Rohde:** Dynamical Effects on Circumsolar Dust Grains
- 737 **K.D. Schmidt:** Micrometeoroid Orbits Observable by the Helios Micrometeoroid Detector (E10)

Indexed in Current Contents

Diese Seite fehlt in der Vorlage

This page is missing in the book

Diese Seite fehlt in der Vorlage

This page is missing in the book

Diese Seite fehlt in der Vorlage

This page is missing in the book

Diese Seite fehlt in der Vorlage

This page is missing in the book

Diese Seite fehlt in der Vorlage

This page is missing in the book

Diese Seite fehlt in der Vorlage

This page is missing in the book

Diese Seite fehlt in der Vorlage

This page is missing in the book

Diese Seite fehlt in der Vorlage

This page is missing in the book

Diese Seite fehlt in der Vorlage

This page is missing in the book

Diese Seite fehlt in der Vorlage

This page is missing in the book

Diese Seite fehlt in der Vorlage

This page is missing in the book

Diese Seite fehlt in der Vorlage

This page is missing in the book

Diese Seite fehlt in der Vorlage

This page is missing in the book

Diese Seite fehlt in der Vorlage

This page is missing in the book

Diese Seite fehlt in der Vorlage

This page is missing in the book

Diese Seite fehlt in der Vorlage

This page is missing in the book

Diese Seite fehlt in der Vorlage

This page is missing in the book

Diese Seite fehlt in der Vorlage

This page is missing in the book

Diese Seite fehlt in der Vorlage

This page is missing in the book

Diese Seite fehlt in der Vorlage

This page is missing in the book

Diese Seite fehlt in der Vorlage

This page is missing in the book

Diese Seite fehlt in der Vorlage

This page is missing in the book

Diese Seite fehlt in der Vorlage

This page is missing in the book

Diese Seite fehlt in der Vorlage

This page is missing in the book

Diese Seite fehlt in der Vorlage

This page is missing in the book

Diese Seite fehlt in der Vorlage

This page is missing in the book

Diese Seite fehlt in der Vorlage

This page is missing in the book

Diese Seite fehlt in der Vorlage

This page is missing in the book

Diese Seite fehlt in der Vorlage

This page is missing in the book

Diese Seite fehlt in der Vorlage

This page is missing in the book

Diese Seite fehlt in der Vorlage

This page is missing in the book

2. Calculation of the Potential $\phi(\mathbf{x})$

The density of the ions is not affected by the potential. Therefore, the structure of the ion density is given by simple cones which describe the thermal diffusion of the ions into the wake. The densities of the plasma- and photo-electrons, however, are strongly influenced by interaction with the potential $\phi(\mathbf{x})$.

2.1. A Two-Dimensional Model for Numerical Plasma Simulation

The motion of the solar wind around the probe and the development of the potential $\phi(\mathbf{x})$ is calculated by means of a two-dimensional model with simplified probe geometry. This is not able to describe the real three-dimensional situation correctly, but it may be used as a tool to understand the essential interaction between plasma and spacecraft. Moreover, the two-dimensional model is chosen in order to save computer time and storage requirements.

The floating potential of the probe is calculated from the balance of currents arriving at the probe or leaving it. With increasing simulation time, the floating potential reaches a stationary value with only small statistical fluctuations.

The plasma electrons are simulated as discrete (super-) particles by the particle-in-cell method (Morse, 1970; Birdsall et al., 1970). They are created at the outer boundaries of the simulation region according to the undisturbed distribution function. A Maxwellian distribution, shifted according to the solar wind bulk velocity, is assumed for that purpose. Several thousand particles are moved together in the potential like real electrons and the potential is updated from the resulting charge density at every time step. The path of any particle is followed until it leaves the simulation region or until it reaches the surface of the probe and contributes to the current balance. Photoelectrons with a mean energy of only 1 eV are emitted from the sunlit side of the probe. They are regarded as a third constituent of the plasma. For their number density an approximation is used (Schröder, 1974) which describes the strong interaction with the potential $\phi(\mathbf{x})$. Another approximation gives the amount of negative charge transported from the surface into the undisturbed plasma region (Könemann, Schröder, 1974) as dependent on the surface potential.

For further details concerned with this model, the reader may be referred to Isensee (1975).

2.2. Results

In order to obtain the potential $\phi(\mathbf{x})$, the simulation program was executed with a simulation area of $9 \text{ m} \times 19.75 \text{ m}$, divided into $0.25 \text{ m} \times 0.25 \text{ m}$ cells. Up to 10^4 particles have been used, each representing $1.5 \cdot 10^6$ electrons. With a time step of $7.5 \cdot 10^{-8} \text{ s}$, the potential reached a stationary value yielding the self-consistent potential in the Vlasov-Poisson system after approx. 200 steps. The simulation process has been continued for about 300 additional steps to average out the statistical fluctuations which are due to the mathematical method. Then the

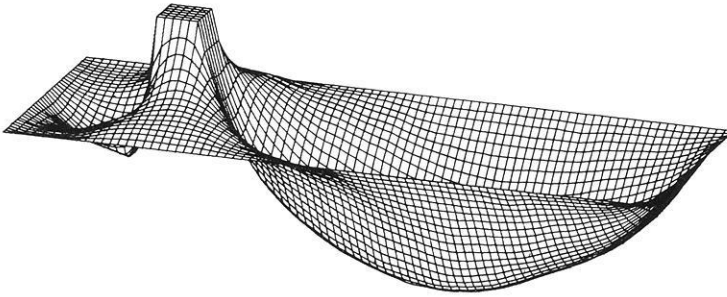


Fig. 1. The potential $\phi(\mathbf{x})$ for solar wind conditions at 0.2 AU distance from the sun. The solar wind flows from the left to the right. The spacecraft is represented by the square with a surface potential of 2.9 V. The minimum in front of the probe (-1.4 V) is due to the photo electron cloud. The minimum in the wake has a depth of -4.5 V

potential $\phi(\mathbf{x})$ is used as input data for subsequent calculations. This model for the potential is shown in Figure 1. The floating potential of the probe surface has the value of 2.9 V. The potential is characterized by the negative minima. Behind the probe is a region of very low ion density. This results in an expanded region of negative potential with a minimum of -4.5 V. A very dense cloud of photoelectrons develops immediately in front of the sunlit side of the probe. This is the reason for the second negative minimum with -1.4 V.

At greater distances from the sun, the negative minima are less distinctive. At 1.0 AU distance, the very rarefied plasma modifies the vacuum potential ($\Delta\phi = 0$) only slightly. With increasing distance from the sun, all particle densities decrease in the same way (inverse square law). This effect would keep the floating potential constant. However, the floating potential depends on the current densities; therefore it also depends on the temperatures. The temperature of the photoelectrons is constant. The plasma electron temperature, on the other hand, decreases, resulting in a smaller plasma electron current. The result is that the floating potential assumes a higher value with increasing distance from the sun.

3. Distortion of Distribution Function

In this chapter, let us assume that a measuring instrument is located at the surface of the spacecraft. It is considered as a device that counts electrons coming from a discrete direction but with different energies to give a velocity distribution function $f_s(\mathbf{v})$ at the location \mathbf{x}_s on the surface of the probe.

The instrument detects the electrons that have penetrated the potential in the vicinity of the probe, but cannot detect those undisturbed electrons far away from the probe directly. Therefore the velocity distribution measured by the instrument differs from the undistorted distribution present in the solar wind.

Because of the positive surface potential, all electrons have been accelerated. That means that no plasma electrons can be counted below an energy that corresponds to the surface potential. This energy range is filled by photoelectrons emitted from the surface.

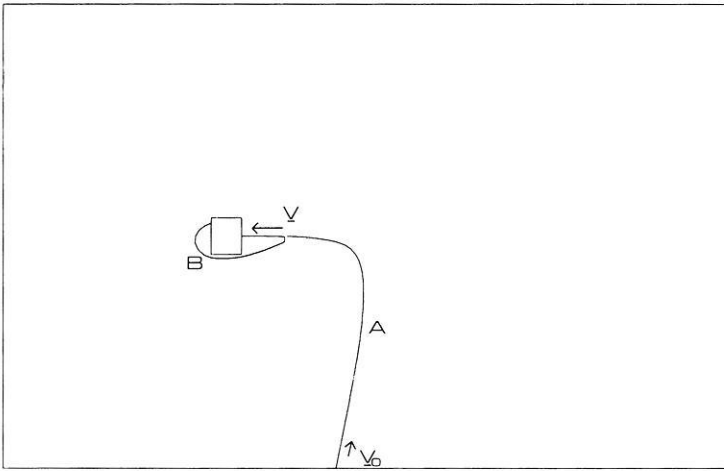


Fig. 2. The method of retracing electron trajectories. Electrons with the initial velocity v_0 in the undisturbed solar wind are deflected by the potential and arrive at the probe with the velocity v (case a). Photoelectrons are deleted from the distribution f_s (case b)

3.1. The Method: Characteristics of the Vlasov Equation

The velocity distribution function $f(\mathbf{x}, \mathbf{v})$ for the plasma electrons is the solution of the Vlasov equation

$$\mathbf{v} \cdot \nabla_{\mathbf{x}} f(\mathbf{x}, \mathbf{v}) + e/m \nabla_{\mathbf{x}} \phi(\mathbf{x}) \cdot \nabla_{\mathbf{v}} f(\mathbf{x}, \mathbf{v}) = 0 \tag{1}$$

with the potential $\phi(\mathbf{x})$ from chapter 2.

The equation is solved for $f(\mathbf{x}, \mathbf{v})$ by means of the fact, that the distribution function f is a constant along a path in phase space, i.e. the trajectories in phase space are the characteristics of the partial differential equation (1) (Courant, Hilbert, 1968). If the points $(\mathbf{x}_1, \mathbf{v}_1)$ and $(\mathbf{x}_2, \mathbf{v}_2)$ in phase space are connected by a trajectory, then

$$f(\mathbf{x}_1, \mathbf{v}_1) = f(\mathbf{x}_2, \mathbf{v}_2). \tag{2}$$

In order to calculate the distorted value $f_s(\mathbf{v}) = f(\mathbf{x}_s, \mathbf{v})$ at a certain point \mathbf{x}_s on the surface of the probe, the path of an electron arriving at that point with the velocity \mathbf{v} is followed back through the potential (Fig. 2). Two cases are possible:

(a) If the electron has come from the undisturbed solar wind region with the initial velocity $\mathbf{v}_0(\mathbf{x}_s, \mathbf{v})$, then

$$f(\mathbf{x}_s, \mathbf{v}) = f(\mathbf{x}_0(\mathbf{x}_s, \mathbf{v}), \mathbf{v}_0(\mathbf{x}_s, \mathbf{v})) \tag{3}$$

or

$$f_s(\mathbf{v}) = f_M(\mathbf{v}_0(\mathbf{x}_s, \mathbf{v})) = \exp(-m/2kT(\mathbf{v}_0 - \mathbf{w}_0)^2). \tag{4}$$

f_M is the undisturbed Maxwellian distribution in the solar wind with the bulk velocity \mathbf{w}_0 . It is independent of the position \mathbf{x}_0 .

(b) If the electron has come from the probe surface, then

$$f_s(\mathbf{v}) = 0. \tag{5}$$

That means that photoelectrons emitted from the surface are not taken into account in calculating the distribution.

It is important that the electric fields modify the absolute values of the velocities as well as the direction of the incoming electrons. The difference between the absolute values of \mathbf{v} and \mathbf{v}_0 is easily derived from the energy conservation.

$$\mathbf{v}_0^2 = \mathbf{v}^2 - 2e/m\phi_s \quad (6)$$

with the surface potential ϕ_s .

The result of these changes of the absolute values of the velocities alone would be a simple shift to higher energies. The following figures show this kind of curves as reference spectra $f_r(\mathbf{v})$.

$$f_r(\mathbf{v}) = \begin{cases} f_M(|\mathbf{v}_0| \mathbf{v}/|\mathbf{v}|) & \text{if } \mathbf{v}^2 - 2e/m\phi_s \geq 0 \\ 0 & \text{if } \mathbf{v}^2 - 2e/m\phi_s < 0 \end{cases} \quad (7)$$

The differences between f_s and f_r are the result of the deviation in the direction of the initial velocity \mathbf{v}_0 together with the anisotropy of the streaming solar wind plasma. The trajectories become more probable with an initial velocity more parallel with the bulk velocity \mathbf{w}_0 . That gives a greater value of f_s . To emphasize the effects of the curvature of the electron trajectories, the curves are calculated with a high solar wind velocity ($w_0 = 800 \text{ km/s}$).

3.2. Results

The negative charge densities by volume result in regions of negative potential. This leads to the following disturbances of the electron velocity distribution at the surface of the probe:

(a) Plasma electrons with very low energy may be reflected by the potential minima. This results in an energy range above the surface potential in which no plasma electron can be counted by the instrument.

(b) The trajectories of electrons with a little more energy are curved considerably. This results in modifications of the distribution together with the anisotropy of the solar wind plasma (which is due to the bulk velocity \mathbf{w}_0). Generally speaking, in this energy range the number of electrons decreases at the front of the probe and increases at the rear.

Electrons with energies above 20 eV are hardly influenced by the potential.

These main effects of the negative potential minima are shown in the following two examples.

The spectra in Figure 3 simulate a measurement in antisolar direction. At energies above 20 eV there is no difference between the distribution function and the reference curve. With decreasing energy, the number of electrons arriving from antisolar direction becomes greater than indicated by the reference curve. The reason is the deflection by the negative wake as shown in Figure 4. The initial value of the velocity in the undisturbed solar wind becomes more and

Fig. 3. Disturbed distribution function f_s and reference curve f_r for a measurement in antisolar direction (cf. Fig. 4)

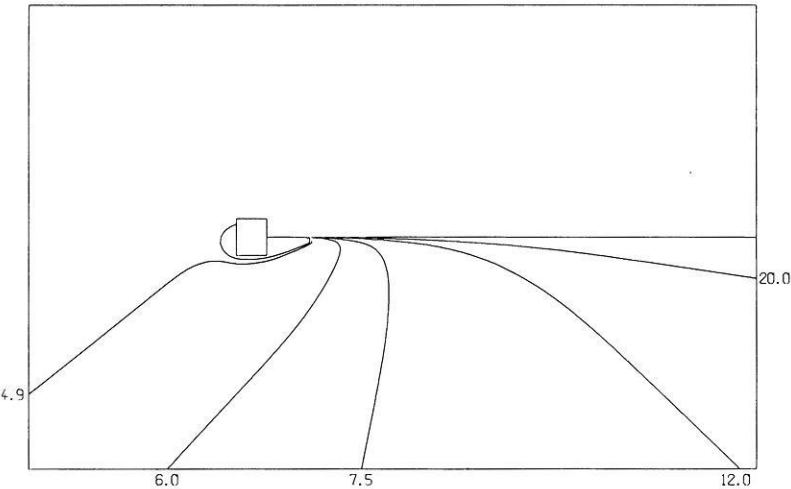
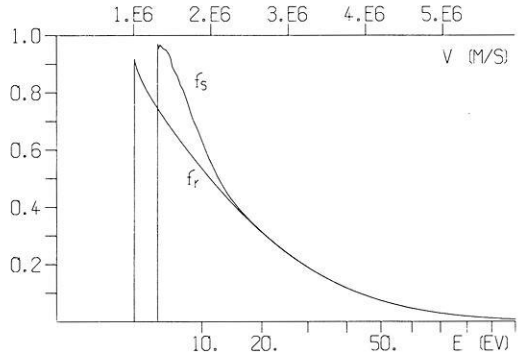


Fig. 4. Examples of trajectories of electrons arriving at the probe from antisolar direction. The numbers denote the energy in eV belonging to the trajectory. The deflection of the electrons by the wake is demonstrated

more parallel with the bulk velocity—the number of electrons increases (see Eqs.(4) and (7)). Below 4.9 eV, no electrons can be detected from antisolar direction: they are screened by the wake. In addition, Figure 4 shows a possible path for photo electrons reaching the measuring instrument at the back side of the spacecraft, in spite of an energy (4.8 eV) above the surface potential (2.9 eV). Figures 5 and 6 show the influence of the photo electron cloud. The instrument is situated at the front of the probe. The angle of incidence of the electrons is 30 degrees. Electrons counted between 5 eV and 10 eV are reflected at the potential minimum in front of the probe, their initial velocities have been nearly perpendicular to the bulk velocity. In the range between 4 eV and 5 eV the direction of the initial velocity is again more parallel to the bulk velocity, since the electrons are reflected at the wake before they come under the influence of the photo-electron minimum. This results in the peak within the distribution function.

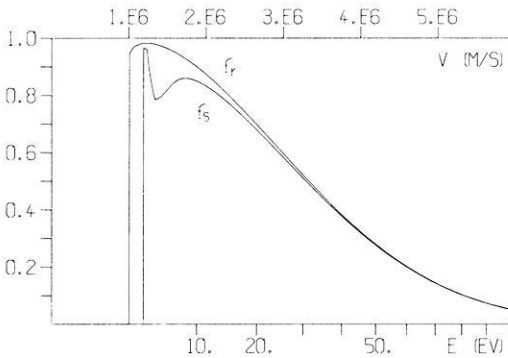


Fig. 5. Distribution for a measurement at the front side with an angle of incidence of 30 degrees (cf. Fig. 6)

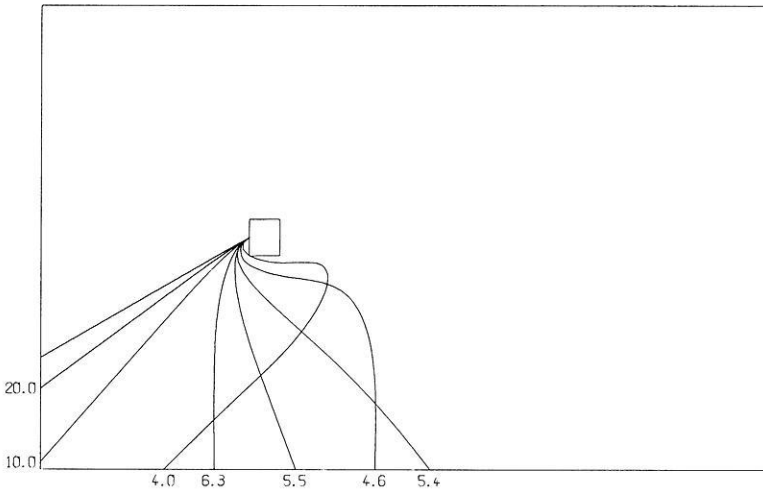


Fig. 6. Examples of electron trajectories concerning Figure 5. In the energy range between 4 eV and 5 eV the electrons are first deflected at the wake before being directed into the instrument by the photoelectron minimum

4. Conclusions

The two-dimensional model enables us to calculate modifications of the electron velocity distribution which are caused by the charge densities in the wake and by the photo electron cloud. These disturbances must be taken into account for a correct interpretation of the electron distribution measurements in the low energy range. However, it must be emphasized that the effects of non-conductive probe surface elements (solar cells) are of the same order of importance as the disturbances described in this paper. The effects of non-conductive probe surfaces are not included in the present model as yet but must be considered in future work.

Acknowledgement. This work was partially supported by a grant of DFVLR-BPT Nr. 01QCO26A-Z24WRSO108 (project HELIOS). I am indebted to Dr. G.H. Voigt and H. Massberg (TH Darmstadt, Angewandte Geophysik) for many fruitful discussions.

Major parts of this paper were completed at the Technische Universität Braunschweig, Lehrstuhl B für Theoretische Physik under the direction of Prof. Richter. I am greatly indebted for his kind support.

References

- Birdsall, Ch.K., Langdon, A.B., Okuda, H.: Finite-Size Particle Physics Applied to Plasma Simulation: in Methods of Computational Physics, **9**, New York and London: Academic Press 1970
- Courant, R., Hilbert, D.: Methoden der mathematischen Physik, 2nd ed. Berlin-Heidelberg-New York: Springer 1968
- Isensee, U.: Anwendung numerischer Plasmasimulation bei der Berechnung von Plasmastörungen durch ein Raumfahrzeug im solaren Wind. BMFT-Forschungsbericht FBW 75-20, 1975
- Könemann, B., Schröder, H.: Planet. Space Sci. **22**, 321–331, 1974
- Morse, R.L.: Multidimensional Plasma Simulation by the Particle-in-Cell Method: in Methods of Computational Physics, **9**, New York and London: Academic Press 1970
- Schröder, H.: Thesis, Lehrstuhl B für Theoretische Physik, TU Braunschweig, 1974

Received November 29, 1976; Revised Version May 20, 1977

Radial Variation of the Interplanetary Magnetic Field between 0.3 AU and 1.0 AU

Observations by the Helios-1 Spacecraft

G. Musmann, F.M. Neubauer and E. Lammers

Institut für Geophysik and Meteorologie, Technische Universität Braunschweig,
Mendelssohnstr. 1A, D-3300 Braunschweig, Federal Republic of Germany

Abstract. We have investigated the radial dependence of the radial and azimuthal components and the magnitude of the interplanetary magnetic field obtained by the Technical University of Braunschweig magnetometer experiment on-board of Helios-1 from December 10, 1974 to first perihelion on March 15, 1975. Absolute values of daily averages of each quantity have been employed. The regression analysis based on power laws leads to $2.55 \gamma \times r^{-2.0}$, $2.26 \gamma \times r^{-1.0}$ and $F = 5.53 \gamma \times r^{-1.6}$ with standard deviations of 2.5γ , 2.0γ and 3.2γ for the radial and azimuthal components and magnitude, respectively.

Here r is the radial distance from the sun in astronomical units. The results are compared with results obtained for Mariners 4, 5 and 10 and Pioneers 6 and 10. The differences are probably due to different epochs in the solar cycle and the different statistical techniques used.

Key words: Interplanetary magnetic field – Helios-1 results.

Introduction

The study of the variation of the components and magnitude of the interplanetary magnetic field with heliocentric distance is very interesting at the present time.

The mission of Mariner 10 to the inner solar system to a heliocentric distance of 0.46 AU and the missions of Pioneer 10 and Pioneer 11 to the outer solar system to heliocentric distances beyond 5 AU have provided new data over a wide range of heliocentric distance. For a recent review see Behannon (1975).

In the mean-time the two Helios-1 and -2 missions are under way with perihelion distances of 0.31 AU and 0.29 AU, respectively, closer to the sun than any spacecraft in the past and in the foreseeable future.

The first perihelion of Helios-1 was reached on March 15, 1975 with a heliocentric distance of 0.31 AU while Helios-2 first reached the closest distance to the sun of 0.29 AU on April 17, 1976.

Due to the high degree of magnetic cleanliness of the two Helios spacecrafts and the proper operation of the spacecrafts and the magnetometer experiments the two Helios-1 and -2 missions will expand our information on the radial variation of the interplanetary magnetic field appreciably. It is the purpose of this paper to present first results on gradients of components and magnitude of the interplanetary magnetic field.

Instrumentation

The Institute for Geophysics and Meteorology of the Technical University of Braunschweig magnetometer is a three component flux-gate magnetometer (Förstersonde) with 4 automatically switchable measurement ranges of $\pm 100 \gamma$ and $\pm 400 \gamma$. The highest resolution is $\pm 0.2 \gamma$ with a maximum sampling rate of 8 vectors/s. The experiment sensors are located at a distance of approximately 2.75 m from the center of the spacecraft. Included in the experiment is a mechanical flipper device which makes it possible to flip by command the sensor parallel to the spin axis into the spinning plane of the spacecraft to help determine the zero-offset of the Z-component parallel to the spin axis. The overall offsets of the components in the spin plane composed of sensor offsets and spacecraft field are removed by properly averaging over the spin variation. The experiment also includes a so called Shock Identification Computer (SIC) for triggering a memory-mode to observe discontinuities and shocks characterised by positive increases of field magnitude. Results using this capability will be presented in the future.

A detailed description of the experiment is given by Musmann et al. (1975).

Radial Variation of the Interplanetary Magnetic Field with Heliocentric Distance

The interplanetary magnetic field is due to solar magnetic fields dragged out from the sun by the solar wind. By the solar rotation this field is twisted into an Archimedean spiral structure. Assuming axial symmetry Parker (1963) has derived the field variation with distance from the sun in the solar equatorial plane. According to this simple model the magnetic field components B_r , B_ϕ , B_θ in a polar coordinate system based on the rotational axis of the sun are given by

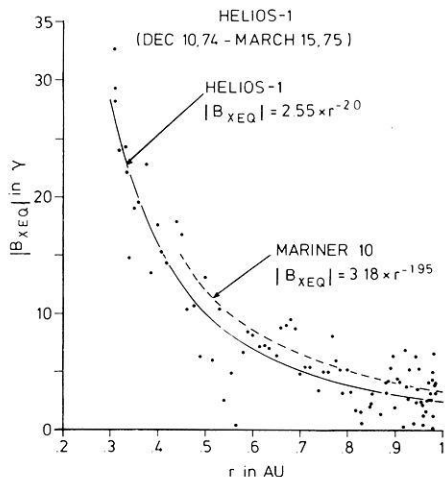
$$B_r = B_0 \left(\frac{r_0}{r} \right)^2$$

$$B_\phi = B_0 \frac{r_0}{r} \frac{r_0 \Omega}{V_s}$$

$$B_\theta = 0,$$

where Ω is the angular speed of the sun – more precisely of the source regions of the interplanetary magnetoplasma – and V_s is the solar wind speed assumed to be constant. B_0 is the radial component at distance r_0 . Because of the inclination

Fig. 1. Magnitude of daily average radial magnetic field component $|B_{XEQ}|$ versus heliocentric distance according to measurements by the Helios-1 TU Braunschweig magnetometer during the time interval from launch on December 10, 1974 to first perihelion on March 15, 1975. Least-mean-squares best fit curves for Mariner 10 (dashed) and Helios-1 (solid) are also shown



of the solar equator of only $7^{\circ} 15'$ a spacecraft like Helios moving in the ecliptic plane does not deviate more than $7^{\circ} 15'$ from the equatorial plane.

During the primary mission of Helios-1 defined as the time interval between launch and the first black-out by sun occultation the first perihelion was reached on March 15, 1975. The following analysis is based on this interval from launch to first perihelion. We shall use the daily average solar equatorial components $B_{XEQ} = -B_r$, $B_{YEQ} = -B_{\phi}$ and $B_{ZEQ} = -B_{\theta}$ and the magnitude $|B| = F$. With a few exceptions the data available for the days used was more than 75%.

In Figure 1 absolute values of the daily averages radial component B_{XEQ} are shown. A best fit curve was calculated from the data in a least mean squares regression-analysis. The result is shown in Figure 1 as a solid curve. An inverse power law dependence with an exponent of -2.0 was found (standard dev. $= 2.5\gamma$). This exponent is in excellent agreement with the theoretical model. As can be seen from Figure 1 there is a large variability of even the daily averages around the best fit curve. This large variability of the daily average components $|B_{XEQ}|$ is probably mostly due to variations in heliographic longitude and to a lesser extent to variations in latitude and time. The figure also includes the best fit curve calculated for the 24-h averages of the magnitude of the radial component observed by Mariner 10 (Behannon, 1976) as a dashed curve. Note that we are always using absolute values of daily averages and not daily averages of absolute values.

So far the distance range between 0.29 AU and more than 5.0 AU has been covered by different spacecrafts. Mariner 5 covered the region between earth and the orbit of Venus at 0.71 AU (Rosenberg and Coleman, 1973). Solar rotation averages of $|B_{XEQ}|$ from Mariner 4 and 5 and Pioneer 6 are shown in Figure 2.

A dependence on heliocentric distance with an exponent -1.78 for the power law was found from Mariner 5 data. For Mariner 4 Coleman et al. (1969) calculated an exponent of -1.46 . Villante and Mariani (1975) have confirmed the r^{-2} dependence of the radial field component using Pioneer 6 data.

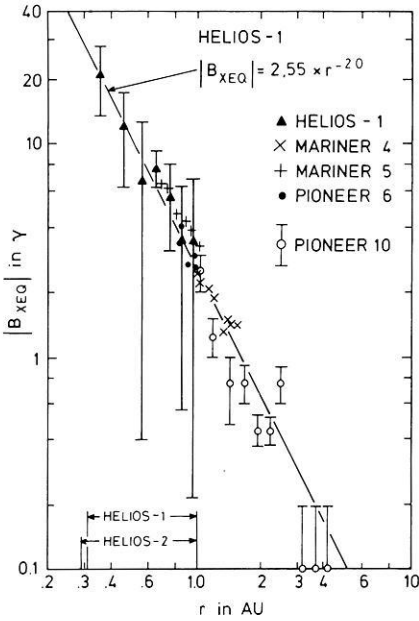


Fig. 2. Range and central value (black triangle) of $|B_{XEQ}|$ for heliocentric distance bins of 0.1 AU versus distance from the sun. The regression curve for Helios-1 is shown together with the results from the spacecrafts (see text for further explanation)

Pioneer 10 has observed the magnetic yield out to beyond the orbit of Jupiter. For observations out to 4.3 AU Smith (1974) calculated the most probable value for each solar rotation while the vertical lines in Figure 2 represent the maximum and minimum values of the distribution from which the most probable value was selected. Helios-1 covered essentially three solar rotations during the time interval considered. For the Helios data Figure 2 shows the maximum and minimum values for distance bins of 0.1 AU by vertical bars with the central values represented by black triangles. The straight solid line through all the measured values is the inverse power law calculated for Helios-1 according to Figure 1 with an exponent of -2.0 .

From Figure 2 one may then conclude, that for the magnitude of the radial component $|B_{XEQ}|$ the observed radial dependence between 0.3 and 4.3 AU is in excellent agreement with the inverse square power law predicted by the Parker model. The differences between the various results are probably due to the different times during the solar cycle and of Pioneer 10 due to the different definitions of the displayed value of $|B_{XEQ}|$.

The radial dependence of the daily average azimuthal component $|B_{YEQ}|$ for the same time interval of Helios-1 is shown in Figure 3.

The best fit curve calculated from the 24-h averages shows a dependence of $r^{-1.0}$ very close to the Parker model. It is shown as the solid curve. The Mariner 10 data evaluation of the transverse component $B_t = \sqrt{B_{XEQ}^2 + B_{YEQ}^2}$ gives an exponent for the inverse power law of -1.4 . It is presented by the dashed curve in the figure.

The observations of the radial dependence of the azimuthal component for the total range between 0.3 AU and 4.3 AU covered by Helios-1, Mariner 4, Mariner 5, Pioneer 6 and Pioneer 10 are shown in Figure 4. The Helios-1 data

Fig. 3. Magnitude of daily average solar equatorial azimuthal component $|B_{YEQ}|$ versus heliocentric distance. The least-mean-squares best fit curve for $|B_{YEQ}|$ from Helios-1 (solid) is compared with the least-mean-squares best fit curve for $\sqrt{B_{XEQ}^2 + B_{YEQ}^2}$ from Mariner 10

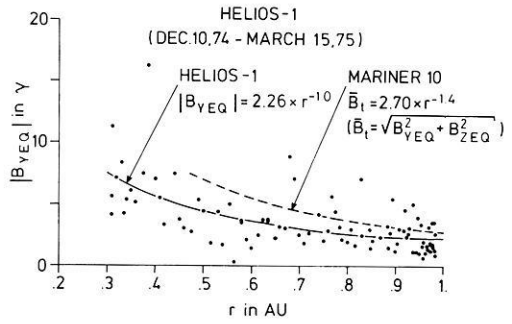
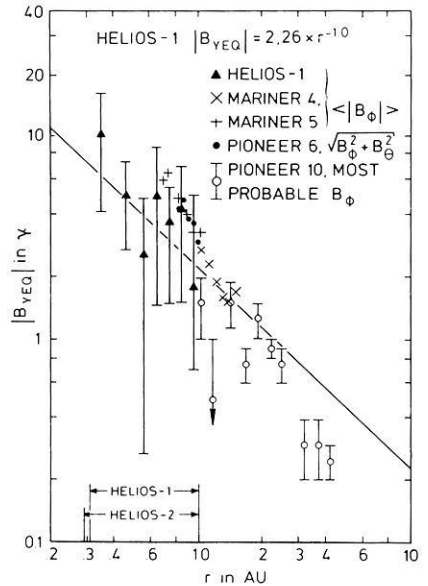


Fig. 4. Range and central value (black triangle) of $|B_{YEQ}|$ for distance bins of 0.1 AU versus heliocentric distance. Also shown are data from other spacecrafts in comparison with the least-mean-squares best fit power law for Helios-1. (For further explanation see text)



in this figure give again the minimum and maximum values for distance bins of 0.1 AU by a vertical bar and the central value by a black triangle. The Helios-1 power law shows the best agreement with the prediction of the simple Parker model i.e. a r^{-1} dependence whereas all other spacecrafts yield a much steeper dependence e.g. Mariner 4 shows an average power law of $r^{-1.29}$ and for Mariner 5 a best fit curve of $r^{-1.85}$ was computed. Villante and Mariani (1975) deduced a $r^{-2.5}$ dependence from the Pioneer 6 data.

Apart from the small distance variation of Pioneer 6 and to a decreasing extent of Mariner 5 and Mariner 4 leading to appreciable uncertainties the differences in the results for a power law dependence can firstly be due to the different statistical techniques and magnetic field components used. Note that in the case of Helios-1, Mariner 4 and Mariner 5 the azimuthal components B_{YEQ} were used, in the case of Pioneer 6 and Mariner 10 $\sqrt{B_{XEQ}^2 + B_{YEQ}^2}$ and in the case of Pioneer 10 the most probable value of $|B_{YEQ}|$ during a solar rotation. In addition latitude variations and time variations have to be considered. Also

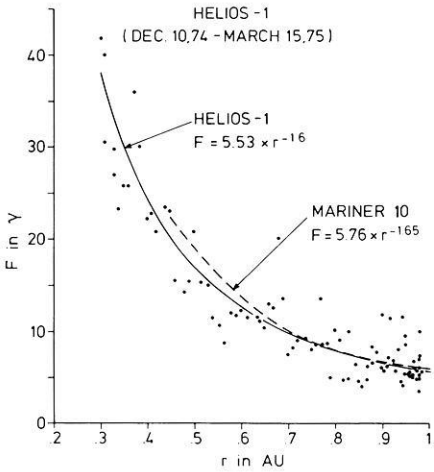


Fig. 5. Daily averages of magnetic field magnitudes versus distance from the sun. The least-mean-squares best fit power law curve from Helios-1 (solid) is compared with the corresponding curve for Mariner 10

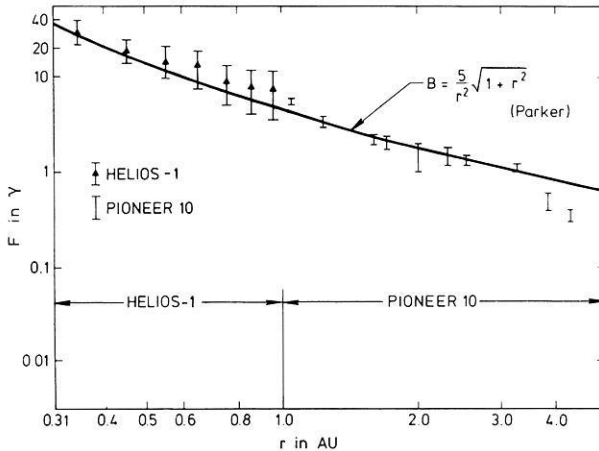


Fig. 6. Range and central value (black triangle) of F for distance bins of 0.1 AU versus distance from the sun. Also shown are Pioneer 10 results beyond 1 AU and a simple interpolation curve based on theory

Jokipii (1975) studied the role of fluctuations on the radial variation of the azimuthal component. Parker and Jokipii (1976) explain the Pioneer 10 results on the radial variation of the transverse component in terms of the systematic increase in velocity during the corresponding part of the missions.

For the same time period as for the components (Dec. 10, 1974–March 15, 1975) the 24-h averages of the field magnitude F calculated from the components are shown in Figure 5.

The solid best fit curve gives an inverse power law dependence of $r^{-1.6}$ (standard dev. = 3.7γ). The dashed line in Figure 5 represents the Mariner 10 best fit curve with an exponent of -1.65 calculated by Behannon (1975).

The relation $F = 5\gamma \cdot \sqrt{1+r^2}/r^2$ with r in AU is shown in Figure 6 together with the Helios-1 data and the Pioneer 10 data. For Pioneer 10 the vertical lines are again the most probable values of the field magnitude for each solar rotation.

It can be seen from Figure 6 that the Parker model is in good agreement with Pioneer 10 data except for heliocentric distances beyond 3 AU. The Helios data shown in Figure 6 are presented in the same way as in Figures 2 and 4. The agreement with the theoretical formula is good again.

Conclusions

As a first step to understand the macrostructure of the interplanetary magnetic field between 0.3 AU and 1 AU we have used the data from the TU Braunschweig fluxgate magnetometer experiment on-board Helios-1 from launch on December 10, 1974 to first perihelion on March 15, 1975 to investigate the radial variation of the solar variation of the solar equatorial radial component, azimuthal component and the magnitude of the magnetic field. Daily averages covering more than three solar rotations have led to the following results:

1. The radial component $|B_{XEQ}|$ varies as $2.55\gamma \cdot r^{-2.0}$ with a standard dev. of 2.5γ , where r is the distance from the sun in AU.
2. The azimuthal component $|B_{YEQ}|$ varies like $2.26\gamma \cdot r^{-1.0}$ with a standard dev. of 2.0γ .

These results are in very good agreement with the simple Parker theory of the interplanetary magnetic field. They differ somewhat from results of previous spacecrafts covering fractions of the distance range of Helios i.e. Mariner 5, Mariner 10 and Pioneer 6. The distance range covered by Mariner 5 and Pioneer 6 is too small to make strong statements on the radial variation. In addition the regression analysis in each case implies a different weighting due to the differing orbital characteristics. The difference between Helios-1 and Mariner 10 may be due to the different latitude profile, the time difference of about one year between both missions and to the different way of computing $|B_{XEQ}|$ and $|B_{YEQ}|$.

Extrapolation of the Helios regression results to distance beyond 1 AU are in reasonable agreement with Mariner 4 data out to Mars (1.5 AU) and with Pioneer 10 data out to about 3 AU where appreciable deviations start to occur.

The magnetitude F can be described by $5.5\gamma \cdot r^{-1.6}$ with a rms deviation of 3.2γ between 0.3 and 1.0 AU. In the range from 0.3 AU to 3 AU the law $5\gamma\sqrt{1+r^2}/r^2$ based on simple Parker theory provides a good representation.

Acknowledgements. We appreciate the contributions to the Helios TU-Braunschweig flux-gate magnetometer experiment by Prof. Kertz, Drs. Maier, Gliem, Kugel, Krupstedt and Messrs. Lange, Barnstorf and Biethahn at the TU Braunschweig. This work was supported financially by the Bundesministerium für Forschung und Technologie under the Helios program.

References

- Behannon, K.: Observations of the interplanetary magnetic field between 0.46 and 1 AU by the Mariner 10 spacecraft, NASA-X-692-76-2, January 1976
- Behannon, K.W.: Variation of the interplanetary magnetic field with heliocentric distance, GSFC Rep. X-692-75-143, June 1975

- Coleman, P.J., Smith, E., Jr., Davis, L., Jones, E.D.: The radial dependence of the interplanetary magnetic field: 1.0–1.5 AU. *J. Geophys. Res.* **74**, 2826–2850, 1969
- Jokipii, J.R.: Fluctuations and the radial variation of the interplanetary magnetic field. *Geophys. Res. Lett.* **2**, 473–475, 1975
- Musmann, G., Neubauer, F.M., Maier, A., Lammers, E.: Das Förstensoniden-Magnetfeldexperiment (E2). *Raumfahrtforschung* **19**, 232–237, 1975
- Neugebauer, M.: Large scale and solar-cycle variations of the solar wind. *Space Sci. Rev.* **17**, 221–254, 1975
- Parker, E.N.: *Interplanetary dynamical processes*. New York: Interscience 1963
- Parker, G.D., Jokipii, J.R.: The spiral structure of the interplanetary magnetic field. *Geophys. Res. Lett.* **3**, 561–564, 1976
- Rosenberg, R.L., Coleman, P.J., Jr.: The radial dependence of the interplanetary magnetic field: 1.0–0.7 AU, Institute of Geophysical and Planetary Physics No. 1196–26, Univ. of California, Los Angeles, 1973
- Smith, E.J.: Radial gradients in the interplanetary magnetic field between 1.0 and 4.3 AU: Pioneer 10, Jet Propulsion Lab., California, Institute of Techn., Pasadena, California 91103, 1974
- Villante, U., Mariani, F.: On the radial variation of the interplanetary magnetic field: Pioneer 6, *Geophys. Res. Lett.* **2**, 73–74, 1975

Received January 31, 1977; Revised Version April 19, 1977

Initial Results from the Helios-1 Search-Coil Magnetometer Experiment

F.M. Neubauer¹, H.J. Beinroth¹, H. Barnstorf¹, and G. Dehmel²

¹ Institut für Geophysik und Meteorologie, TU Braunschweig,
Mendelssohnstr. 1A, D-3300 Braunschweig, Federal Republic of Germany

² Institut für Nachrichtentechnik, TU Braunschweig,
Mühlenpfordtstr. 23, D-3300 Braunschweig, Federal Republic of Germany

Abstract. The Helios search-coil magnetometer experiments provide a unique potential for studies of electromagnetic plasma wave modes in the solar wind between 0.3–1 A.U. because of excellent background noise levels, high time-resolution and high accuracy. Daily average spectral densities ($\gamma/\sqrt{\text{Hz}}$) in the frequency range from 4.7 Hz–220 Hz show a pronounced increase as the sun is approached with complex superposed variations. Their values have a range of more than an order of magnitude. The shock of January 6, 1975 provides an interesting example for the use of high time-resolution spectral data. The fine structure and the long term variations in wave fields after the perpendicular shock are discussed. Also two interesting examples of “magnetic holes” are presented.

Key words: Magnetic fluctuations in the solar wind – Helios search-coil magnetometer.

1. Introduction

The Helios search-coil magnetometer experiment has been designed to observe the high-frequency component of magnetic fluctuations in the interplanetary medium in the frequency-range from about 4 Hz–2.2 kHz. This frequency-range has been chosen such as to allow observations up to the maximum expected electron gyro frequency on the orbit of Helios. To fix ideas note that at 50γ the electron gyro frequency $f_{ce} = 1.4$ kHz. From a plasma physics point of view the observed fluctuations may be due to Doppler shifted Whistler waves or convected non-propagating structures. A more detailed discussion of this point is contained in Neubauer et al. (1977).

The experiment has the following scientific objectives:

1. Observation of the background interplanetary magnetic fluctuation levels in relation to macroscopic features like high-speed streams, shock-flow systems (as opposed to shock fine structure).

2. Study of the plasma physics of shocks, rotational and tangential discontinuities and other short time-scale phenomena.
3. Search for wave phenomena at high frequencies not connected with local plasma-and-magnetic field features particularly close to the sun.

Interesting examples of the wave phenomena connected with directional discontinuities, shocks and small "magnetic holes" (e.g. Turner et al., 1976) have been reported in a more specialized publication (Neubauer et al., 1977).

In this paper we shall present an overview of the average fluctuation levels observed during a time period from mid-January 1975 through March 1975 as a first contribution to objective one. In addition we shall discuss the magnetic wave phenomena observed in connection with the shock of January 6, 1975 and its flow system.

2. Instrumentation

Helios-1 has been launched on December 10, 1974 into an orbit with a perihelion of 0.31 AU. Helios-2 has been launched on January 15, 1976 with a perihelion of 0.29 AU. The pay-load of the two spacecraft includes almost identical search-coil magnetometer experiments which are still operating and providing excellent data at the time of this writing.

A detailed technical description of the search-coil magnetometer experiment has been given in the paper by Dehmel et al. (1976). We shall here summarize a few essential features with the aid of Figure 1. Each instrument consists of three orthogonal search-coil sensors with the Z -axis parallel to the spin-axis and the X - and Y -axis in the equatorial plane. The output voltage of each sensor-preamplifier unit is proportional to the time derivative of the component under consideration i.e. \dot{B}_x , \dot{B}_y , \dot{B}_z . The essential part of the on-board data processing system is the spectrum analyzer. It consists of two sets of eight bandpass filters spaced logarithmically in frequency with the center frequencies f_{cn} given in the figure. One of the filter sets is used for the Z -sensor output, the other one for the X or Y -component. The filter outputs are squared and averaged by a digital mean-value-computer over successive time intervals of length T_A . For most of the primary mission of Helios-1 $T_A = 1.125$ s. For the same time interval T_A the peak reading from each filter output is also obtained and transmitted to the earth in addition to the mean square values M_n . All the filters are processed in parallel. Use of the digital mean-value-computer guarantees an accuracy for the power spectral density estimates not achieved by interplanetary wave experiments in the past. The mean square values M_n are related to the power spectral density $P(f)$ of a given component of the magnetic field by

$$M_n = \int_0^{\infty} |T_n(f)|^2 f^2 P(f) df, \quad (1)$$

where $T_n(f)$ is the complex transfer function of filter n which quickly tends to 0 beyond the 3dB-points for each filter as shown in the inset of Figure 1. The power spectral densities \bar{P}_n or square-roots thereof assigned to the center

SEARCH-COIL ON-BOARD DATA PROCESSING

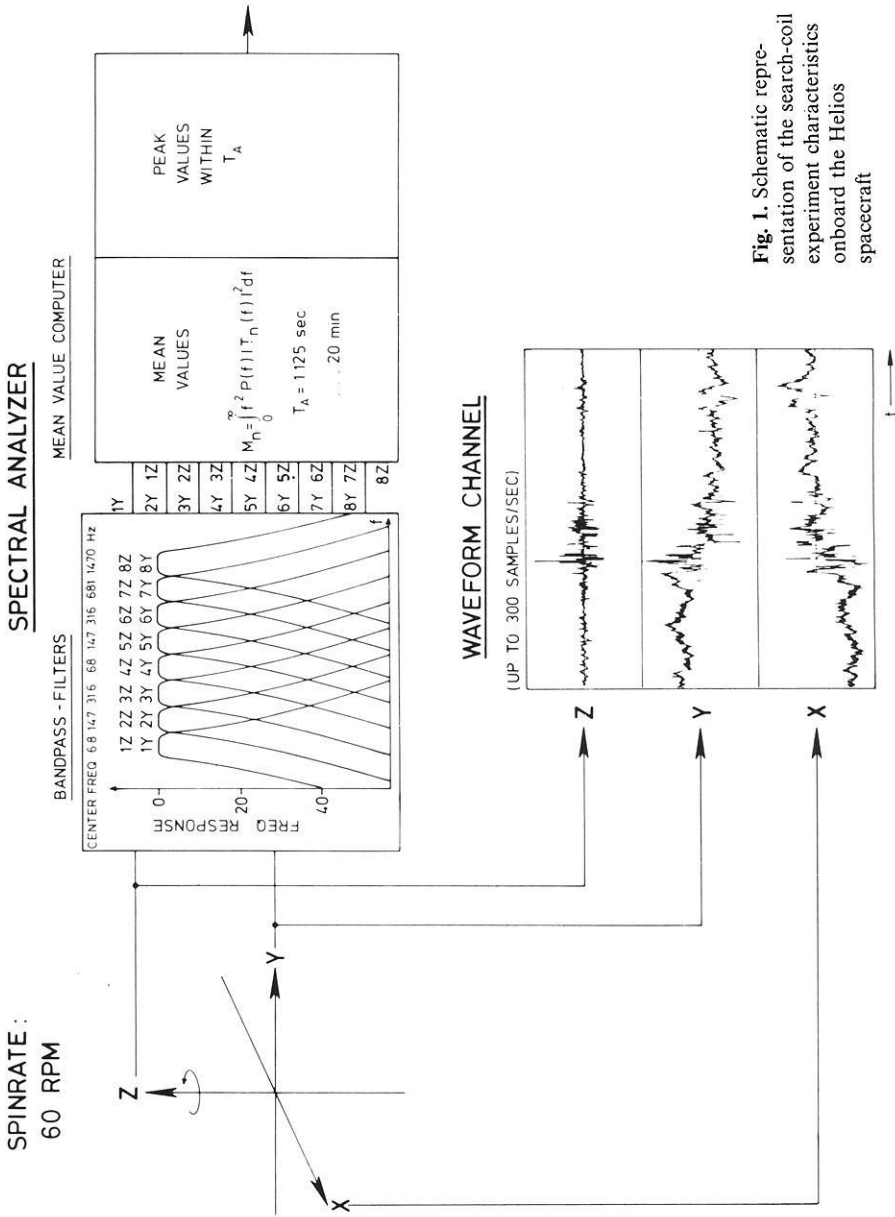


Fig. 1. Schematic representation of the search-coil experiment characteristics onboard the Helios spacecraft

frequencies f_{cn} in this paper are given by

$$\bar{P}_n = \frac{M_n}{\Delta f_n f_{cn}^2} = \int_0^{\infty} |T_n(f)|^2 (f/f_{cn})^2 P(f) \frac{df}{\Delta f_n}$$

or

$$\bar{P}_n(f_{cn}) \approx \int_{f_{in}}^{f_{un}} P(f) (f/f_{cn})^2 \frac{df}{\Delta f_n}$$

(2)

because of the high quality of the filters. Here f_{in} and f_{un} are the lower and upper frequency limits (3 dB-points) of filter n , respectively, and $\Delta f_n = f_{un} - f_{in}$ is the bandwidth. The square-root of $\overline{P}_n(f_{cn})$ will be displayed in all plots in this paper.

In our studies of short time-scale phenomena later in this paper we shall sometimes need the mean squared time derivative of a magnetic field component e.g. B_z in a given frequency band. Using Equations (1) and (2) we obtain

$$\frac{1}{T_A} \int_0^{T_A} (\dot{B}_z)^2 dt = \dot{B}_z^2(N, M) = 30.77 \times \left\{ \sum_{n=N}^M f_{cn}^3 \overline{P}_n(f_{cn}) \right\} \quad (3)$$

where $\overline{B}_z^2(N, M)$ is the contribution to the overall \overline{B}_z^2 by filters N through M .

In case of the availability of high data transmission rates wave form data can be transmitted to the ground at rates of up to 57 vectors/s. More precisely, in the waveform channels the outputs from the three orthogonal sensors are transmitted after appropriate filtering etc. In the case of Helios-1 the waveform vector data represent the magnetic field vector \mathbf{B} in the frequency band from 4 Hz to approximately half the sampling frequency. In the case of Helios-2 the waveform vector data represent the time derivative $\dot{\mathbf{B}}$ of the magnetic field vector in the same frequency ranges as on Helios-1 i.e. analog integration circuits used on Helios-1 have been omitted on Helios-2.

In a special memory mode initiated by an on-board event detector wave form data at rates up to 300 vectors/s can be obtained for short time intervals.

An outstanding feature of this experiment is the low background noise level (see Neubauer et al., 1977) which allows the continuous observation of interplanetary magnetic fluctuations in the lower frequency channels 1Z–5Z and 1Y–5Y even at 1 AU. This is due to the magnetic cleanliness of the spacecraft and the low sensor-preamp noise levels.

Daily Averages of Spectral Densities

To obtain an overview of the spectral densities observed we have computed daily averages of the spectral densities in the frequency channels centered at 7 Hz, 15 Hz, 32 Hz, 68 Hz and 147 Hz for the Z-component and the Y-component which give essentially identical results. By spectral density (measured in $\gamma/\sqrt{\text{Hz}}$) we always mean the square-root of the power spectral density $P(f)$ which is measured in γ^2/Hz . Averages are always square-roots of averaged power spectral densities or equivalently Pythagorean spectral density averages.

The results for the time interval from January 19, 1975 to April 5, 1975 are plotted in Figure 2 on a logarithmic scale for several solar rotations. Relative heliographic longitude is based on the Carrington rotation period. The origin has been chosen to make best use of the space in the figure. The radial distance variation is also indicated in the figure. On the right hand side the background noise levels of the various channels are indicated. The background noise values have not been subtracted from the averaged power spectral densities. Except for a few days it is only channel five which is affected by the background noise levels in the upper panel of Figure 2.

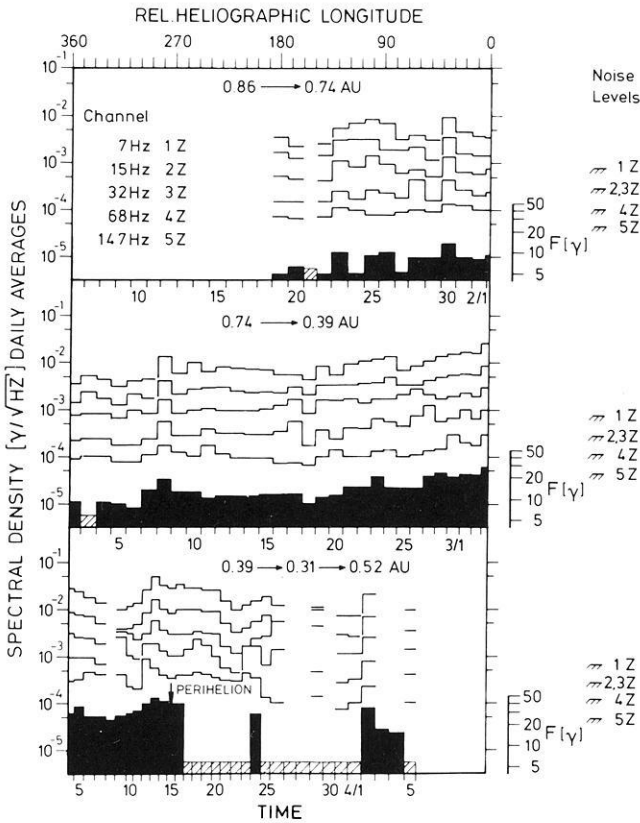


Fig. 2. Daily average spectral densities for channels 1Z, 2Z, 3Z, 4Z and 5Z as a function of time or relative heliographic longitude from January 19 to April 6, 1975. Magnitudes of daily magnetic field averages are also shown for most days. Days with insufficient data for the computation of averages are shown cross-hatched

We have used heliographic longitude as an independent variable and we have plotted daily average magnitudes of the magnetic field to aid in finding relationships between the corotating macrostructure of the magnetic field measured by the flux-gate and the high-frequency wave fields observed by the search-coil wave experiment. Inspection of the magnetic field averages since launch clearly reveals corotating structures the properties of which vary as a function of distance from the sun. In this comparison it has to be taken into account that the corotating features in $|\mathbf{B}|$ are aligned along spirals details of which will be presented in a future publication. A simultaneous variation in heliographic latitude makes the situation even more complicated. The wave fields do not show a clear behavior of this type although a few corotating features may be present. However, it is interesting to note that the outstanding maxima in spectral density on January 30, February 8, March 4, March 13 and April 2 are always connected with maxima in magnetic field magnitude. The reverse is not true.

As expected there is a clear increase in spectral densities as the sun is approached. For example, in channel 1Z the spectral density varies between 2×10^{-3} to $8 \times 10^{-3} \gamma/\sqrt{\text{Hz}}$ in the upper panel of Figure 2 corresponding to 0.86–0.74 AU. Near the sun from 0.39 AU–0.31 AU the spectral density varies between 10^{-2} and $5 \times 10^{-2} \gamma/\sqrt{\text{Hz}}$.

Concerning the frequency dependence of the spectral densities we note that positive slopes do not occur in the daily average spectra. Sometimes regions with small negative slope or zero slope are found as on days February 26 between about 15 and 32 Hz, March 9 between about 15 and 68 Hz and March 23 between about 32 and 68 Hz. Apart from this clustering of spectra with small negative slope close to the sun the spectral characteristics of the daily averages only change in a minor way as a function of distance. If we relate the spectral densities for channels 1Z and 4Z by a power law $\sqrt{P}(f) \sim f^{-\alpha}$ the spectral index α varies from 0.9–1.6 in the upper panel of Figure 2 corresponding to 0.86–0.74 AU. In the lower panel it varies from 0.6–1.5 between 0.39 and 0.31 AU.

We have noted in the previous paper on Helios results (Neubauer et al., 1976) that in one-hour-plots a slowly varying component with a time scale of several minutes and longer can generally be distinguished from so-called events” with time scales of a minute and loss due to discontinuities, “magnetic holes” etc. The overall daily averages considered here are sometimes determined by large events and sometimes by the slowly varying component only. For example, the maximum on March 13 is essentially determined by half a day of large slowly varying component. March 11, 1975 with only a minor daily average contains the most dramatic “events” of the primary mission of Helios-1 except for the shocks of January 6 and 8, 1975.

We conclude this section with a brief discussion of the physical explanation of these results. For the source location there are 2 general possibilities: The source may be a local one or at some distance from the location of observation. Since visual inspection of 24h-plots and 1h-plots reveals no evidence for frequency dispersion we favor the former alternative i.e. a local origin of these fluctuations. There are several interesting candidates for a local wave source. First, thermal magnetic fluctuations which would be extremely small for an equilibrium plasma are enhanced appreciably for distribution functions near marginal instability or even in the instability regime. Such distribution functions are encountered in the solar wind (see e.g. Hollweg, 1975). Also these fluctuations may be produced by nonlinear cascading of high amplitude and long period waves. Third, the possibility cannot be excluded that we are dealing with convected electron structures (Lemaire and Burlaga, 1976). Firm conclusions on the applicability of these ideas can only be reached after further detailed observational analysis including plasma data.

The Shock of January 6, 1975

The fine structure of collisionless shocks is still one of the most interesting problems of plasma physics. For a recent review see Galeev (1976). Briefly the physical problem can be described as follows. An ideal nonlinear compression

wave in a magnetoplasma is known to steepen as time progresses. In collision dominated magnetogasdynamics the steepness is finally limited by internal friction and other dissipative processes. Since the steepening can be visualized as the generation of short wavelength wave energy in the overall spatial spectrum describing the nonlinear wave we can say that finally these newly generated short wavelength components are dissipated at the same rate as they are generated. The dissipation is determined by collisions in this case.

In the collisionless case where the collision frequencies are negligible compared with all other characteristic frequencies of the magnetoplasma the steepening may finally be limited by the propagation of short wavelength waves away from the steepening region due to dispersion effects. Depending on the precise initial conditions this basic mechanism may be modified or even replaced by the onset of microinstabilities during the steepening. Also macroinstabilities may play an important role as for example the nonlinear decay instability. Obviously waves play an important role in the physics of collisionless shocks. Therefore they are an important diagnostic tool for the study of collisionless shocks. Apart from the waves in the "wake" region downstream of the shock waves may propagate in the upstream direction or they may be excited by fast particles moving in the upstream direction. The latter waves are generally referred to as "precursors".

A large number of possibilities exists for the shock structure which finally arises. It depends on a number of important dimensionless parameters: β the ratio of total plasma pressure over magnetic field pressure, the angle θ between the shock normal and the magnetic field vector ahead of the shock, the Alfvén Mach number M_A (say), the ratio of electron and ion temperature T_e/T_i , the mass ratio m_e/m_i , collision frequency divided by plasma frequency $\nu_{ei}/\omega_{pe} \ll 1$, plasma frequency over electron gyro frequency (say) etc.

A considerable fraction of the parameter space β , θ , M_A , T_e/T_p etc. can be investigated experimentally in the laboratory. Laboratory studies and shock investigations in space plasmas like the plasma of the solar wind can complement each other in an important way (Schindler, 1969). Generally the value of β defined above is in the vicinity of one in the solar wind. The theory of collisionless shocks in $\beta \approx 1$ plasmas is still in its infancy, however. This fact further enhances the value of observational studies of the plasma physics of shocks in the solar wind.

Most studies of the plasma physics of shocks in the solar wind have dealt with the earth's bow shock. A difficulty with these bow shock studies has always been the question of the observational determination of the location of the observing satellite with respect to the shock due to the largely unknown fluctuations in shock positions. This difficulty does not exist for outward propagating interplanetary shocks in most cases. The advantages and disadvantages of bow shock studies as compared with the studies of shocks of solar origin have briefly been discussed in the more special paper by Neubauer et al. (1977) in connection with the shock of January 8, 1975.

We shall here discuss observations of the fine structure of the shock of January 6, 1975, using spectral analyzer data of the search-coil experiment and fluxgate vector data. In addition to the structure of the shock transition we

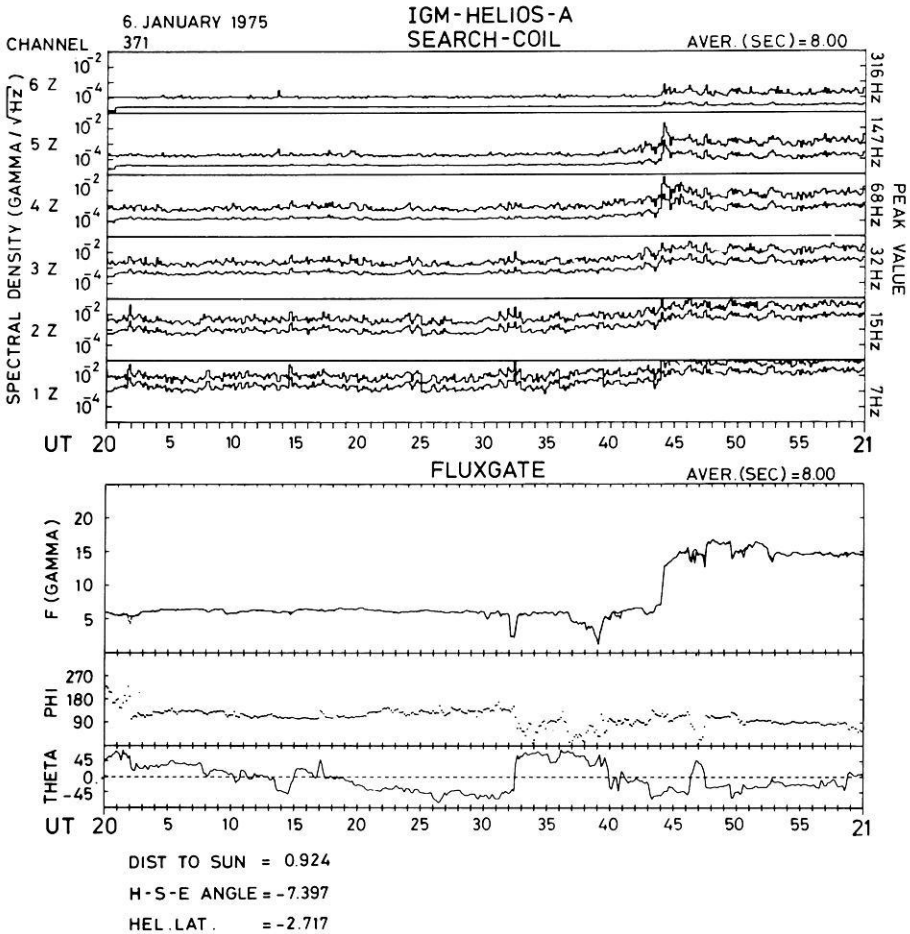


Fig. 3. Search-coil (upper panels) and flux-gate (lower panels) data for January 6, 1975, 20h-21h including the shock event

discuss the high frequency fluctuations following the shock transition and preceding it. The macroscopic properties of the overall flow system are left to a later study.

First we shall give an overview of our data in the two-hour interval containing the shock. Figures 3 and 4 show vector magnetic field data from the fluxgate experiment in the usual solar ecliptic representation with F the magnitude of the magnetic field and ϕ and θ the azimuth of the projection into the ecliptic plane and the elevation with respect to the ecliptic plane, respectively. Note also that two types of magnitude have been plotted, the magnitude of the average vector and the average of the individual magnitudes as a measure of activity within the averaging interval. The degree of agreement between both types of magnitudes is a useful measure for the amount of time variations during the averaging interval of 8 s. Figures 3 and 4 display appreciable time variations

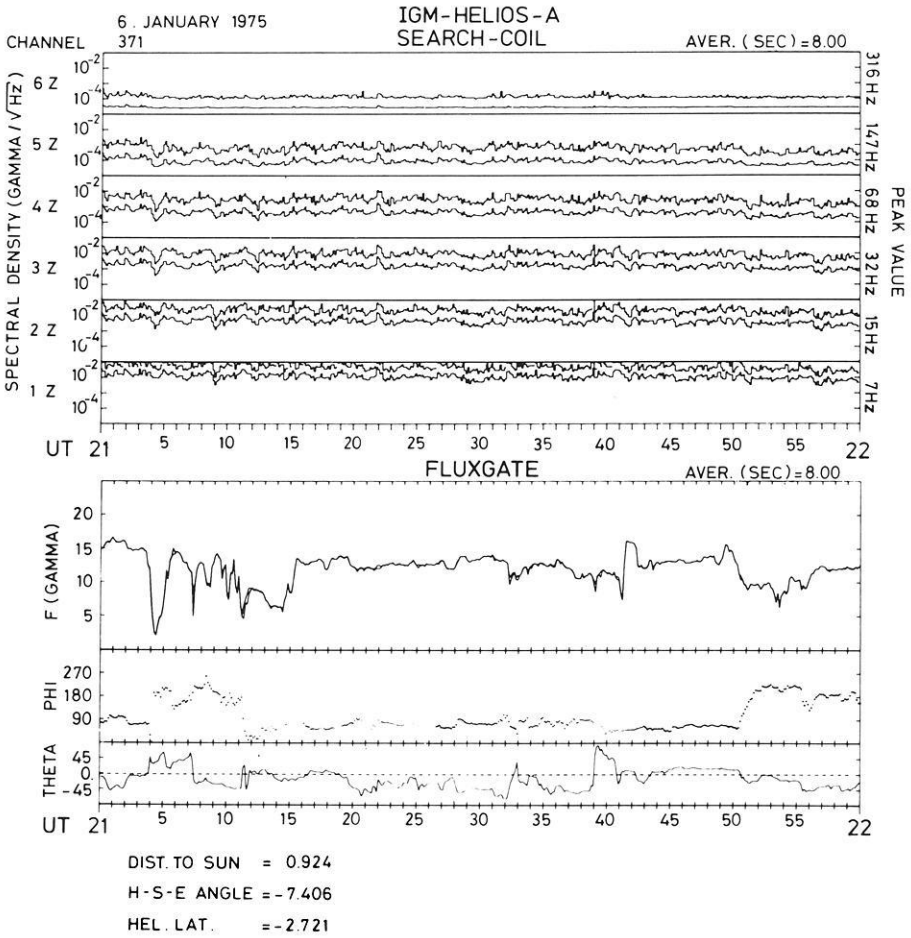


Fig. 4. Search-coil and flux-gate data for January 6, 1975, 21 h–22 h, i.e. the time interval following the shock

in the averaging interval only on a few occasions. The upper eight panels of the figures show spectral densities and peak values from the search-coil experiment for successive intervals of eight seconds which is also the averaging interval for the flux-gate data. The peak values are scaled such that for a monochromatic signal they would be above the spectral density by a factor of $\sqrt{2}$.

The shock occurs at 20 h 44 m 6 s. It is moving through a system of “magnetic holes”. This name has been coined by Turner et al. (1976) for structures in the interplanetary magnetic field characterized by a strong minimum in magnetic field magnitude generally covering time intervals of several seconds. The first big one occurs at 20 h 32 m the second one at 20 h 39 m before the shock. Other magnetic holes have already been run over by the shock the most dramatic one occurring around 21 h 4 m. The magnetic holes are connected with strong variations in direction.

Let us now consider the shock transition itself. This is shown in some more detail in Figure 5. Here 4 vectors/s are plotted together with one spectrum each $T_A = 1.125$ s for the spectrum analyzer. With 20 vectors before and behind the shock we obtain

$$\bar{\mathbf{B}}_1 = (-2.59, 3.77, -5.64)\gamma \quad \text{and} \quad \bar{\mathbf{B}}_2 = (-4.18, 7.11, -10.00)\gamma$$

for the magnetic field vectors before and behind the shock, respectively. Here the coordinate system used is defined by the X -direction pointing towards the sun and the Z -direction towards the north ecliptic pole. This also defines the Y -direction. Due to an as yet unknown zero-offset the Z -component is uncertain by $\pm 2\gamma$. The difference vector $\Delta\bar{\mathbf{B}} = \bar{\mathbf{B}}_2 - \bar{\mathbf{B}}_1 = (-1.58, 3.34, -4.36)\gamma$ must lie in the shock plane i.e. $\Delta\bar{\mathbf{B}} \cdot \mathbf{n} = 0$, where \mathbf{n} is the shock normal. The angle between $\bar{\mathbf{B}}_1$ and $\bar{\mathbf{B}}_2$ is always less than 7° if we vary the unknown offset of the Z -component. Making use of the conservation of the normal magnetic field component in a shock it is easy to show that the shock must be close to a perpendicular one. Because of the small angle between $\bar{\mathbf{B}}_1$ and $\bar{\mathbf{B}}_2$ the coplanarity theorem cannot be used to determine the normal direction.

Using plasma data (H. Grünwaldt and R. Schwenn, personal communication) and assuming a perpendicular shock a normal direction $\mathbf{n} = (-0.785, 0.363, 0.502)$ is found corresponding to the solar ecliptic angles $\phi_n = 155 \pm 15^\circ$ and $\theta_n = 30 \pm 15^\circ$. The shock velocity in the direction of \mathbf{n} turns out to be 625 km/s.

The shock transition as observed by the flux-gate occurs between two successive vectors i.e. in less than 0.25 s. The jump is $\Delta\mathbf{B} = (-1.5, 2.3, -4.0)\gamma$ which is not much different from the jump in averaged vectors $\Delta\bar{\mathbf{B}}$. The jump in the magnetic vector field is followed by enhanced magnitude and particularly directional variations. Approximately 4 s after the shock transition a double spike in direction extending over 2 s occurs. During 20 more s magnetic fluctuations occur which have relatively high amplitudes and are relatively well ordered. This region is limited by a directional discontinuity with a dip in magnitude. In order to investigate the nature of the magnetic wave fields following the shock we make use of a minimum variance analysis of the Sonnerup type (Sonnerup and Cahill, 1967). Briefly, the method consists of the subtraction of the average magnetic field vector from the individual vectors during a given time interval and the subsequent determination of the eigenvectors and eigenvalues of the covariance matrix of these perturbation vectors. It has extensively been used to analyze discontinuities (e.g. Smith, 1973) and waves (e.g. Russell et al., 1971). The variance analysis applied to the time interval from 20 h 44 m 6 s–20 h 44 m 30 s yields a minimum eigenvalue of $6 \times 10^{-2} \gamma^2$ with an eigenvector close to the average \mathbf{B} -direction and a Pythagorean sum of $2.19 \gamma^2$ for the components perpendicular to it. In other words, the variations in magnitude are only 16% of the variations perpendicular to the average vector. At least for these variations with relatively low frequency the wave modes are therefore essentially directional.

The accompanying behavior of the spectrum analyzer data is very interesting as Figure 5 shows. Ahead of the shock the magnetic fluctuations are well above

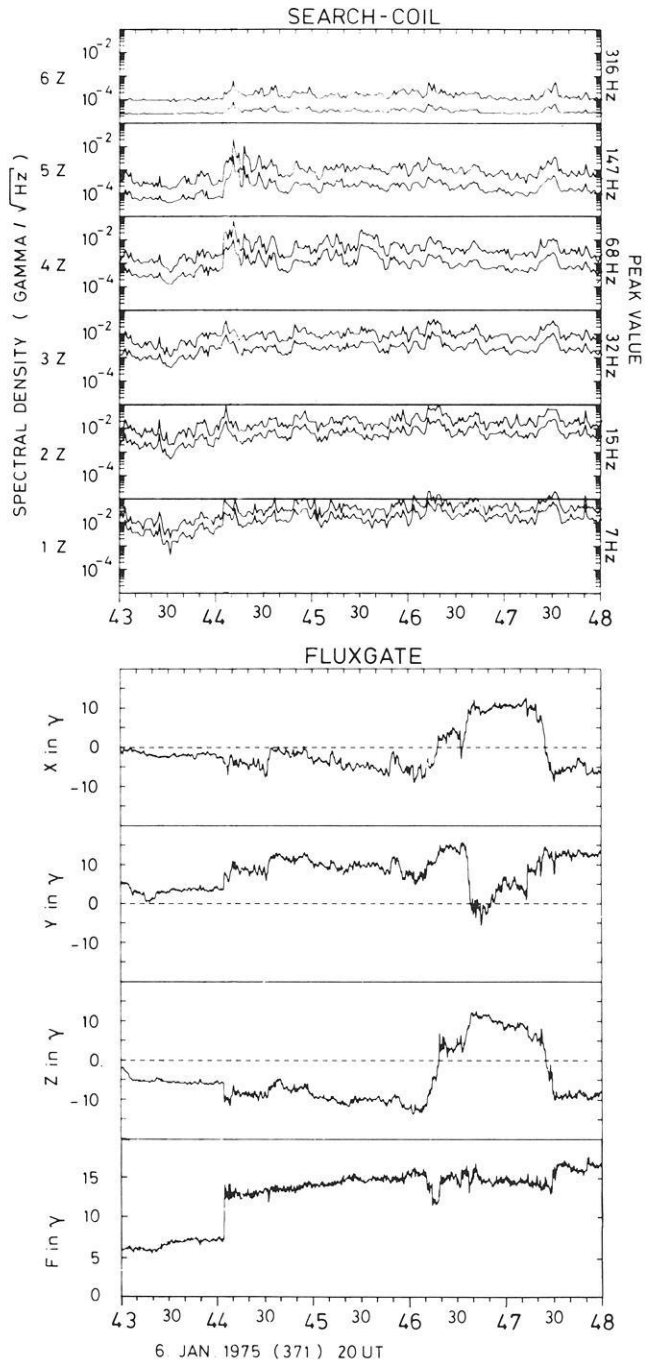


Fig. 5. High-time-resolution search-coil and flux-gate data around the shock of January 6, 1975

the background noise level except for channel 6Z around 316 Hz. At the shock transition spectral densities jump to reach a relative maximum simultaneously in all channels. The jumps are most conspicuous in the channels centered around 68 Hz and 147 Hz. In the channel around 316 Hz the noise level is just exceeded.

In order to estimate the shock thickness let us try to model it by a linear ramp of height ΔB_z and length Δt connecting 2 constant states of the magnetic field in the Z -direction. The squared time derivative of the simple ramp averaged over the basic measuring time interval T_A is given by

$$\frac{1}{T_A} \int_0^{T_A} \dot{B}_z^2 dt = \frac{(\Delta B_z)^2}{T_A \Delta t}. \quad (4)$$

The measured contribution from 4.7 Hz–220 Hz for the Z -component according to Equation 3 is

$$\overline{B_z^2}(1,5) = 410(\gamma/s)^2.$$

Together with the $\Delta B_z = -4\gamma$ jump from the flux-gate within 0.25 s and Equation 4 this indicates a transit time Δt of >30 ms for this shock. However, the ratio of peak value over spectral density can be taken as a crude indication of the nature of the signal. It is found not to be different from the ratios usually encountered for 1.125 s intervals. It seems therefore reasonable to conclude that the shock consisted of a ramp of “thickness” much greater than 30 ms but below 250 ms which is dominated by turbulent magnetic wave fields. Using the shock velocity of 625 km/s the thickness must be between 19 km and 160 km. In units of the proton gyro radius at the Alfvén speed ahead of the shock the thickness should be between 0.2 and 1.7, respectively.

Four seconds after the first jump in wave activity the maxima occur in the channels centered around 7 Hz, 68 Hz, 147 Hz and 316 Hz apparently in connection with the double spike mentioned above. Relative maxima occur in all channels except channels 7 and 8 which exhibit no activity at all. After these maxima the wave activity decreases within a few minutes to a level which remains above the preshock values for several hours. Note that for a magnetic field of $F_2 = |\mathbf{B}_2| = 13\gamma$ the electron gyro frequency $f_{ce} = 360$ Hz. Even without the use of plasma data it is clear that for propagation perpendicular to the magnetic field these frequencies can only be reached by strongly Doppler shifted waves near the lower hybrid frequency. If waves propagating parallel to \mathbf{B}_2 are involved their Doppler shifts are generally small since \mathbf{B}_2 is almost perpendicular to the solar wind flow direction. Such waves would then extend up to an appreciable fraction of the electron gyro frequency f_{ce} . A third possibility is the occurrence of very thin convected structures like the electron sheaths treated by Lemaire and Burlaga (1976). The wave peak region near the double spike contributes the 1.125 s averages $\overline{B_z^2} = 2800 (\gamma/s)^2$ in the frequency range from 47–470 Hz. For an unresolved jump in B_z by $\Delta B_z = 2\gamma$ this would correspond to $\Delta t \approx 1.3$ ms. Again the ratio peak value over spectral density suggests high levels

of broad band fluctuations as the cause of the peaks with a broad spectral maximum around 68 Hz.

It is interesting to speculate that the structure just described is a part of the shock fine structure. However, because of the somewhat disturbed conditions before the shock it can also be due to some interplanetary structure like a directional discontinuity which is overtaken by the shock. Peaks in spectral density are clearly visible in Figure 5 ahead of the shock. Small but clear signatures can also be distinguished in the magnetic field data. Since the "magnetic holes" are convected structures (Turner et al., 1976) it is reasonable to assume that some of these small fluctuations are also convected.

It is then very interesting to investigate the change of stability characteristics during the shock transition. Since the shock is perpendicular, we can easily make the following simple estimate. If the thickness of a convected structure with a normal in the direction of the shock normal is d_1 ahead of the perpendicular shock it will be

$$d_2 = \frac{F_1}{F_2} d_1 \quad (5a)$$

behind the shock. A magnetic disturbance \mathbf{B}' in the direction of $\bar{\mathbf{B}}_1 \times \mathbf{n}$ changes according to

$$\mathbf{B}'_2 = \mathbf{B}'_1 \frac{F_2}{F_1}. \quad (5b)$$

The current density j then changes according to

$$j_2 = j_1 \left(\frac{F_2}{F_1} \right)^2.$$

Considering instabilities for which the relative velocity between electrons and ions in relation to the Alfvén speed is important (e.g. Gary et al., 1976) we obtain

$$M_{j,2} = M_{j,1} \left(\frac{F_2}{F_1} \right)^{1/2}$$

where $M_j = \frac{|\mathbf{v}_1 - \mathbf{v}_e|}{F/\sqrt{4\pi\rho}}$ with the density ρ . We have used $\rho_2/\rho_1 = F_2/F_1$ in a

perpendicular shock. This result shows that current instabilities in convected structures may be strengthened during the shock transition. A complete discussion would require inclusion of plasma densities as well as electron and proton temperatures. In our case $(F_2/F_1)^{1/2} = 1.33$ which may be sufficient to enhance some instabilities in a noticeable way.

The fluctuation levels following the shock transition decrease to levels which are well above the preshock values and continue for several hours with only a small decrease as Figures 3 and 4 indicate. An interesting question is how much of this enhanced fluctuation level is due to the transmitted fluctuations before

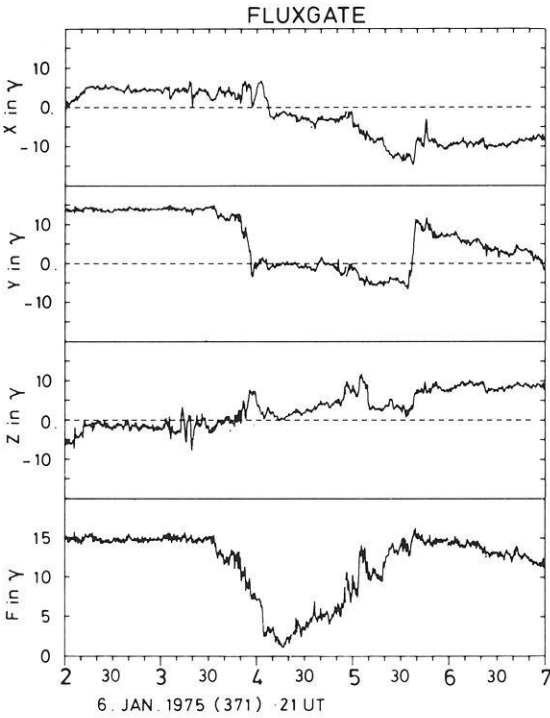
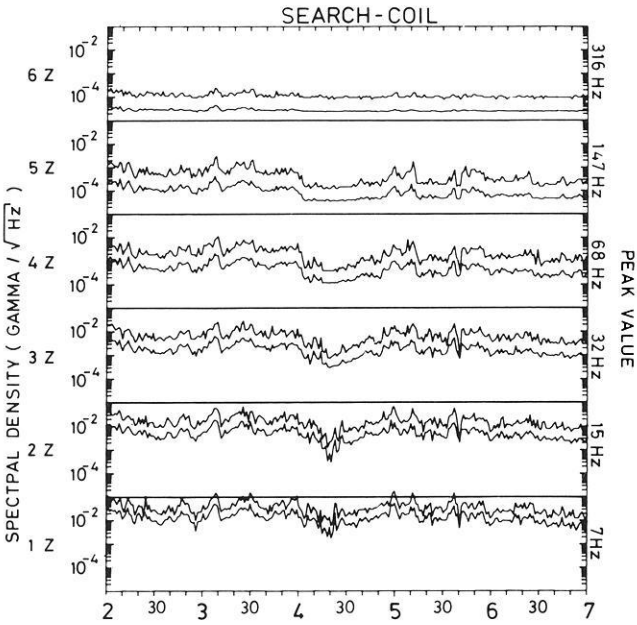


Fig. 6. "Magnetic hole" with pronounced dip in magnetic wave activity

the shock. Since the physical nature of the fluctuations has not been identified yet the question cannot be answered rigorously.

Magnetic Holes in the Vicinity of the Shock of January 6, 1975

Several magnetic holes (Turner et al., 1976) can be identified near the January 6, 1975 shock. Depending on the width and depth of the hole one might expect different kinds of observational features. In a very deep hole i.e. with a very small minimum in F , the frequency range of propagation in the plasma rest frame is very restricted because of the low electron gyro frequency. The frequency range in the satellite frame depends in addition strongly on the Doppler effect. Figure 6 shows as an interesting example the magnetic hole of 21 h 4 m in some more detail.

The narrowing of the propagation band leads to a pronounced drop in wave activity even below the background noise levels in the upper channels. At $F_{\min} \approx 1\gamma$ $f_{ce} = 28$ Hz.

If the hole is very narrow strong current densities are implied which may lead to instabilities with an electromagnetic signature. It has been suggested that in some magnetic holes merging is taking place (Turner et al., 1976). Anomalous resistivity in the merging region may be due to electromagnetic wave instabilities. This may be the reason for the very short noise spike occurring in the center of the magnetic hole starting at 20 h 32 m. The spike could also just be a consequence of the very narrow current sheet producing the directional discontinuity inside the hole without merging.

Conclusions

Initial results from the Helios-1 search-coil magnetic wave experiment have been presented. We stress the following points:

1. The low background noise levels, accurate spectral density determinations and high frequency-time resolution combined with the orbit covering 0.3–1.AU in distance allow unique studies of electromagnetic wave phenomena in the magnetoplasma of the solar wind.

2. Daily averages of the spectral densities between 0.86 AU and 0.31 AU obtained during the interval January 19, 1975 to April 5, 1975 exhibit spectra with negative slope the spectral characteristics of which do not change significantly as the sun is approached. Superposed on the increase in spectral density during the approach to the sun we find variations not clearly associated with macroscopic solar wind properties like magnetic field magnitude. In each channel spectral density variations by more than an order of magnitude (in $\gamma/\sqrt{\text{Hz}}$) have been observed.

3. As a dramatic example of the wave fields on short time scales we have investigated the shock of January 6, 20 h 44 m 6 s. Using Helios-1 flux-gate and

search-coil data the following properties have been found. The shock is close to a perpendicular one with a thickness between 19 km and 160 km but probably closer to the upper limit. In proton gyro radii at the Alfvén speed based on the plasma density before the shock the respective numbers are 0.2 and 1.7. It is followed within 4 s by a structure with a strong peak in the frequency spectrum around 68 Hz. This may either be part of the shock structure or produced by a feature in the disturbed medium into which the shock propagates.

The overall enhancement of fluctuation levels following the shock for hours may partly be due to transmitted preshock fluctuations.

4. The shock is moving into an ensemble of “magnetic holes” (Turner et al., 1976). A pronounced example of a magnetic hole with $F_{\min} = 1 \gamma$ is characterized by a significant dip in wave activity.

Another hole with a longer F_{\min} but a very narrow directional discontinuity produces a pronounced wave spike.

During the discussion we have pointed to a number of interesting subjects which are presently being studied or will be studied in the future.

Acknowledgements. We appreciate the contributions of Prof. Kertz, Drs. Lammers, Musmann, Maier, Glim and Messrs. Wawretzko, Lukoschus to the experiments of the TU Braunschweig onboard of Helios-1 and Helios-2. Also we are grateful to Drs. Rosenbauer and Schwenn of the MPI für extraterrestrische Physik in Garching for providing the plasma data for the shock event. The work was supported by the Bundesministerium für Forschung und Technologie under the Helios program.

References

- Dehmel, G., Neubauer, F.M., Lukoschus, D., Wawretzko, J., Lammers, E.: Das Induktionsspulen-Magnetometer-Experiment (E4). Raumfahrtforschung. **19**, 241–244, 1975
- Galeev, A.A.: Collisionless shocks. In: Proc. Symp. on Solar Planet. Relationships, D.J. Williams, Ed., Boulder, 1976
- Gary, S.P., Gerwin, R.A., Forslund, D.W.: Electromagnetic current instabilities. Phys. Fluids, **19**, 579–586, 1976
- Hollweg, J.V.: Waves and instabilities in the solar wind. Rev. Geophys. Space Phys. **13**, 263–289 1975
- Lemaire, J.F., Burlaga, L.F.: Diamagnetic boundary layers in the solar wind: kinetic theory. Submitted to Astrophys. Space Sci., 1976
- Neubauer, F.M., Musmann, G., Dehmel, G.: Fast magnetic fluctuations in the solar wind: Helios 1. Accepted by J. Geophys. Res., 1977
- Russell, C.T., Childers, D.D., Coleman, P.J.: Ogo 5 observations of upstream waves in the interplanetary medium: discrete wave packets. J. Geophys. Res. **76**, 845–861, 1971
- Schindler, K.: Laboratory experiments related to the solar wind and the magnetosphere. Rev. Geophys. **7**, 51–75, 1969
- Smith, E.J.: Identification of interplanetary tangential and rotational discontinuities. J. Geophys. Res., **78**, 2054–2063, 1973
- Sonnerup, B.U.Ö., Cahill, Jr., L.J.: Magnetopause structure and attitude from Explorer 12 observations, J. Geophys. Res. **72**, 171–183, 1967
- Turner, J.M., Burlaga, L.F., Ness, N.F., Lemaire, J.F.: Magnetic holes in the solar wind, EOS. Trans. Am. Geophys. Union **57**, 320, 1976

Cosmic Ray Measurements on Board Helios 1 from December 1974 to September 1975: Quiet Time Spectra, Radial Gradients, and Solar Events*

H. Kunow, M. Witte, G. Wibberenz, H. Hempe, R. Mueller-Mellin,
G. Green, B. Iwers, and J. Fuckner

Institut für Reine und Angewandte Kernphysik, Universität Kiel,
Olshausenstr. 40–60, D-2300 Kiel, Federal Republic of Germany

Abstract. The University of Kiel cosmic ray experiment on board Helios 1 measures nucleons above 1.7 MeV/nucleon and electrons above 0.3 MeV in the inner solar system between 1.0 and 0.3 AU from the sun. A first survey is given on quiet time proton and Helium spectra which are compared near earth and close to perihelion. The anomalous Helium component is also present at radial distances within 0.4 AU. Quiet time Helium spectra from 3.8 to 48 MeV/nucleon gradually increase between December 1974 and June 1975. For the integral radial gradient (protons above 51 MeV) we estimate a value of $(11 \pm 2.5)\%/AU$ during a period of slowly increasing cosmic ray intensity.

We discuss solar particle events on January 5 (at 0.93 AU), March 7 (at 0.41 AU), and March 19, 1975 (at 0.32 AU). The March 19 event was measured closer to the sun than any other event before. It exhibits sharp temporal structures, differences in the time profiles of various particle species, and a large abundance of Helium 3, with a ${}^3\text{He}/{}^4\text{He}$ ratio of 2 to 3 in the range 5 to 7 MeV/nucleon. This event occurred close to the peak of a high speed solar wind stream.

Key words: Cosmic rays — Quiet time energy spectra — Radial gradients — Solar events — ${}^3\text{He}$ -rich events.

1. Introduction

The solar probe Helios 1 was launched successfully into a heliocentric orbit on December 10, 1974. It reached its first perihelion at a distance of 0.31 AU from the sun on March 15, 1975. For the first time a fully equipped “particles and fields” instrumentation probed a region that close to the sun. Figure 1

* Dedicated to Professor Dr. Erich Bagge with best wishes for his 65th anniversary

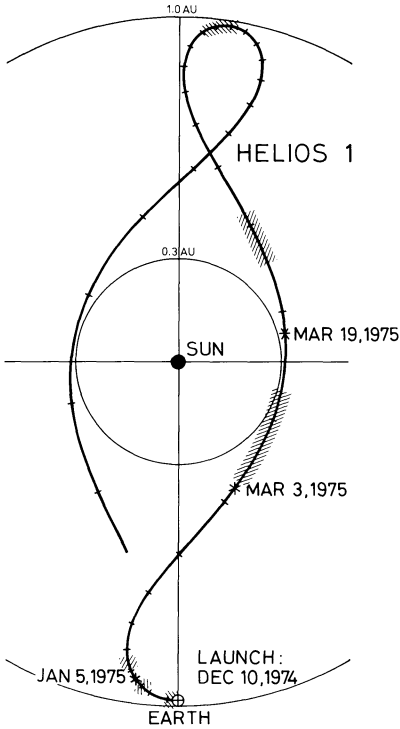


Fig. 1. Helios 1 orbit in a coordinate system with a fixed earth-sun line from December 10, 1974 through September 1975. The perihelion distance is 0.31 AU. Time tags indicate every 10th day of the year. Shaded parts of the orbit represent quiet times outside 0.87 AU or inside 0.47 AU. The positions of the space probe during the solar particle events under discussion are marked too

shows the Helios 1 orbit for the first 10 months of operation in a coordinate system with the earth-sun line fixed.

The University of Kiel experiment on board Helios is capable to measure protons and heavier nuclei above 1.7 MeV/nucleon and electrons above 0.3 MeV. It is designed to study the low intensity galactic cosmic radiation with good energy and charge resolution; for intense solar events we obtain in addition good temporal resolution and measurement of the angular distribution using eight sectors. Isotopes of hydrogen and Helium can be separated.

It is the purpose of this paper to give a first overview of results obtained during the first part of the Helios 1 mission (December 1974–September 1975). This time period is characterized by a general decrease of solar activity towards solar minimum which occurred in July 1976. These relatively quiet conditions facilitate the separation of the gradually varying galactic cosmic radiation from superimposed events of different nature. After a brief description of the instrumentation in section 2 we present in section 3 the temporal variation of selected instrument channels during the above time period.

Long term variations in the integral proton channel (protons above 51 MeV) are partly due to a generally increasing cosmic ray density throughout the whole inner solar system. Nevertheless it is possible to obtain a preliminary estimate for a finite positive radial gradient during this period of decreasing solar activity.

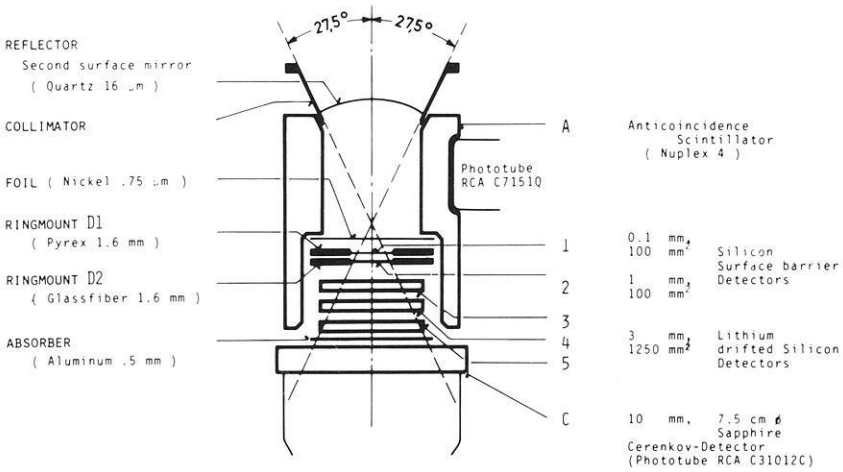


Fig. 2. Cross section of the detector telescope

Quiet time spectra for low energy protons and Helium nuclei as observed near the earth and inside 0.4 AU are compared in section 4. In section 5 we discuss three solar events during the “prime mission” until April 1975. Two of these events occurred when Helios 1 was at 0.41 and 0.32 AU, respectively. The latter event is of particular interest because of its high Helium 3 content and its temporal fine structure. Here we take advantage of the close approach to the sun: it allows a better resolution of small solar events from the galactic background and, in addition, we can study details of the solar injection process which are smeared out for observations at 1 AU due to interplanetary propagation effects.

2. Instrumentation

The detector telescope of the cosmic ray experiment is shown in a cross section in Figure 2. It consists of five semiconductor detectors “1” through “5”, one sapphire Cerenkov detector “C”, and an anticoincidence scintillator “A” surrounding the detector stack. This configuration has a full opening angle of 55° and geometric factors of 0.48 cm²sr for nuclei below 51 MeV/N and 2.23 cm²sr for nuclei above 51 MeV/N. The lower energy thresholds of the instrument are 1.3 MeV for protons, 1.7 MeV/N for heavier nuclei, and ~0.3 MeV for electrons.

Coarse energy ranges are defined by the thickness of detectors and absorbers. Protons are distinguished from heavier nuclei by their different energy loss in the penetrated detectors. Electrons are identified by the fact that contrary to nuclei they pass the first thin detector without triggering it.

Each particle is counted in one of 87 different counters with respect to its energy range, species (electron, proton or $Z \geq 2$ -nucleus) and direction of incidence.

A statistical sample of these particles is further analysed. The pulse heights of the last three penetrated detectors are digitized by logarithmic analog-to-digital converters with a resolution of 8 bits. This allows

- better energy resolution
- separation of isotopes
- measurement of the relative abundances of particles with $Z \geq 2$
- background reduction

Further details of the instrument are given by Kunow et al. (1975) and by Green et al. (1970).

3. Intensity Time Profiles and Preliminary Radial Gradients

Let us start with a survey over the first part of the mission by presenting daily intensity averages of selected experiment channels. This allows the selection of quiet times for construction of energy spectra (section 4) and gives a first insight into possible radial and temporal variations. In Figure 3 we show the time variations in some energy ranges for electrons (E), protons (P), and $Z \geq 2$ nuclei (A), which consist mainly of alpha particles. Each curve is denoted by the corresponding particle species and energy window (e.g. A 2–4 stands for alpha particles between 2 and 4 MeV/N). Daily intensity averages are plotted for the first ten months of the mission corresponding to 1.5 orbits of Helios 1. There are time tags for perihelion and aphelion.

Channel P 13–27 indicates the very low level of solar activity during this time. Only a few solar events concentrated in December/January and July/August generated particles with energies above 13 MeV/N.

In the energy range below 13 MeV/N several additional intensity increases occurred due to corotating streams (e.g. in February) or minor solar activity (e.g. in March). The small event shortly after perihelion is of special interest because of its unusually high abundance of ^3He . This event together with the events on January 5 and March 3 will be discussed in section 5.

The time profiles of the alpha particles show a behaviour similar to those of the protons. Note, however, that channels A 2–4 and A 4–13 display much less fluctuations than the corresponding proton channels P 1–4 and P 4–13. This can be explained by a higher non solar background, in particular the slowly varying “anomalous Helium component” which might mask fluctuations of the solar Helium component.

In Figure 3 we have also plotted on an expanded linear scale the integral intensity of protons above 51 MeV ($P > 51$). The limitations of using counting rate information only (instead of individual particle identification) are well-known, but we wish to draw some preliminary conclusions from the behaviour of this channel, representing a mean energy of about 1 GeV. Its striking feature is the relatively constant level between December and March, when Helios 1 travelled from 1 AU to 0.3 AU, followed by an increase between March and June, when the space probe returned to 1 AU, and a subsequent slow decrease between June and September during the second approach to the sun.

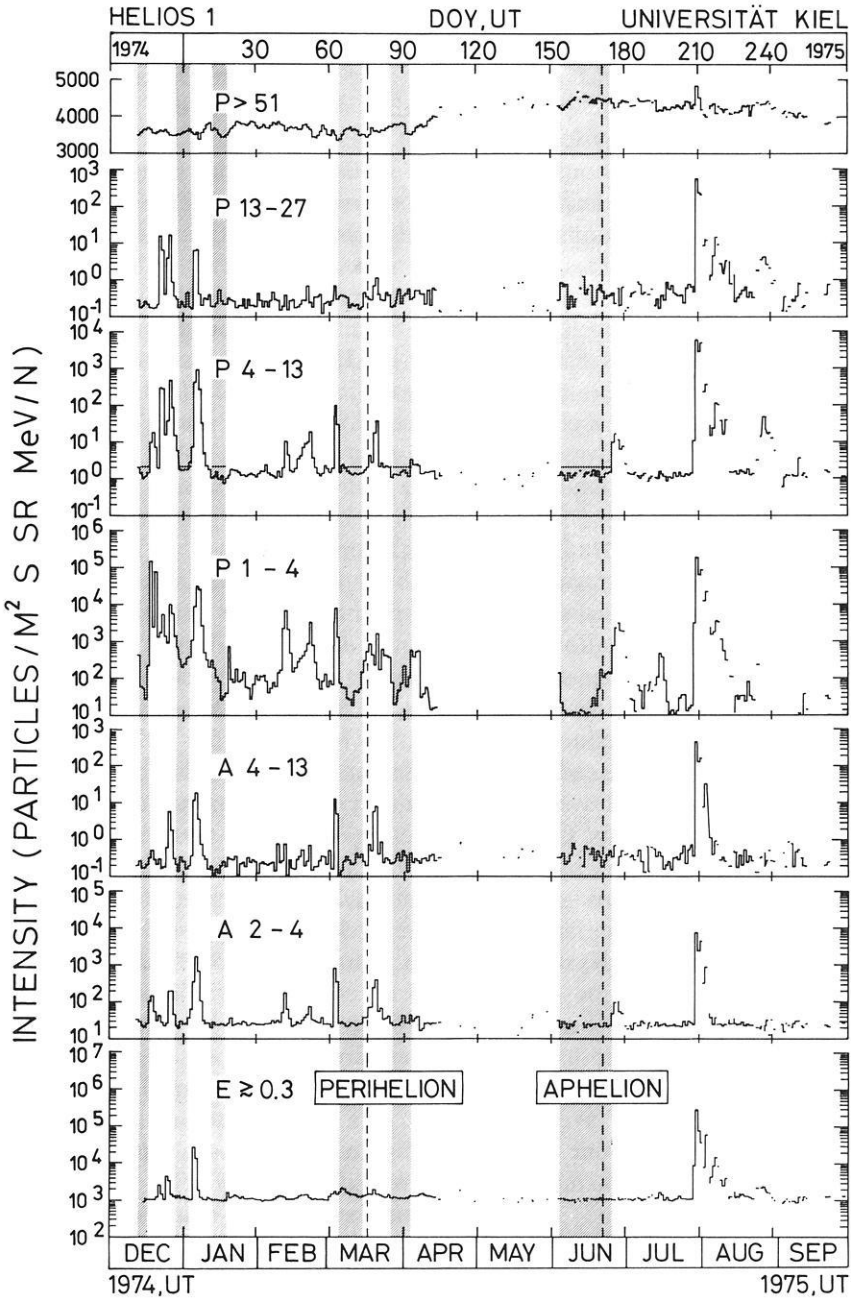


Fig. 3. Daily intensity averages as measured with Helios 1 between December 10, 1974 and September 30, 1975. The different panels show protons (*P*) between 1 and 4, 4 and 13, 13 and 27, and above 51 MeV, $Z \geq 2$ nuclei (*A*) between 2 and 4, and 4 and 13 MeV/N, and electrons (*E*) above ~0.3 MeV respectively. Shaded areas indicate those quiet times for which energy spectra have been derived

The interpretation of this behaviour requires a careful separation of temporal and spatial variations.

In the following we restrict ourselves to the period from December 1974 to June 1975. Inspection of neutron monitor data at Kiel (courtesy O. Binder) and Deep River (Solar-geophysical Data, 1975) shows a gradual increase during this period with a relatively constant slope of $0.50 \pm 0.04\%$ per month for the Deep River data, corresponding to a total increase of $2.7 \pm 0.4\%$ for the full period. There are no indications of severe disturbances of the interplanetary medium.

We performed a regression analysis of the intensity in channel $P > 51$ versus the counting rate of the Deep River neutron monitor for December, January, May and June, when Helios 1 was close to 1 AU. This yields a correlation coefficient of about 0.9 and a ratio of 6.1 ± 0.4 of the fractional change in channel $P > 51$ to the fractional change of the neutron monitor rate. The neutron monitor increase quoted above is then consistent with the $\sim 17\%$ change in channel $P > 51$ between launch to the next aphelion, when Helios was close to 1 AU.

Let us now discuss the radial variation. From launch to perihelion the intensity in channel $P > 51$ varies only by about 1% whereas we see almost the full excursion during the subsequent outward motion. This variation implies that temporal and radial variations roughly cancel each other during the inward motion and add to one another on the outbound pass. This leads to a numerical value for the integral radial gradient of $11 \pm 2.5\%/AU$ in the radial interval 0.3–1.0 AU. Previously, a value of $5\%/AU$ has been reported from Pioneer 10/11 for the integral radial gradient (Teegarden et al., 1973; McKibben, 1975). The larger value obtained above from Helios may have a number of different reasons: (1) Latitudinal effects. Close to perihelion one has to take into account possible variations with heliographic latitude. Helios changes its position with respect to solar latitude from -6° to $+6^\circ$ within 20 days, and the solar wind measurements show a large latitudinal effect related to coronal structures (Schwenn et al., 1976). (2) Hysteresis effects. Our conclusion that we see a radial gradient effect superimposed on long-term temporal variations was based on a regression analysis in comparison with neutron monitor data, for time periods when Helios was close to 1 AU. Here we ignore possible hysteresis effects between various energies ($\simeq 1$ GeV for the Helios integral channel as compared to the several GeV average response of a high latitude neutron monitor). A sudden jump from one regression line to another in a time span of several weeks (Stoker, and Carmichael, 1971) would lead to different time variations at different energies. (3) Transient modulation. For a given phase in the solar cycle, the experimentally determined gradients are not constant, but vary with time and distance (see McKibben, 1975). Our value of $11\%/AU$ has been obtained by averaging over a limited time period and over a radial distance of ~ 0.7 AU. It may therefore differ from long-term averages over a larger radial distance. It has been noted in particular that larger-than-average gradients are observed during periods of increasing galactic cosmic ray intensity (McKibben et al., 1975). This behaviour is expected qualitatively, if non-stationary solutions of the diffusion-convection model are considered (O’Gallagher, private communication).

Further studies (see section 6) will show which of the explanations are appropriate.

4. Quiet Time Energy Spectra

In this part the energy spectra of protons and Helium nuclei during quiet times at different solar distances will be discussed. Quiet times are defined as those times when the intensity in the 4 to 13 MeV—proton channel does not exceed 2 counts $(\text{m}^2 \text{s sr MeV})^{-1}$. This level is indicated in curve P 4–13 of Figure 3. In order to see radial gradient effects data were taken only, when Helios was outside 0.87 AU from the sun (datasets aphelion 0 and aphelion 1) or inside 0.47 AU (perihelion). The resulting time periods are indicated by shaded areas in Figures 1 and 3, and are given together with the amount of data included in these datasets in Table 1.

During quiet times a very high percentage (about 95%) of the counted particles can be pulse height analysed. Thus the background in each count rate channel, partly due to particles traversing the telescope from the backward direction, can be accurately identified by a 2- or 3-dimensional pulse height analysis. A normalization to absolute intensities can be easily performed with the respective count rate.

The proton spectra for these three time periods are shown in Figure 4a. The intensities above 30 MeV increase with time by roughly 25%. For the lowest energy channel, however, the trend is reversed. Thus for the time periods which were defined (somewhat arbitrarily) as “quiet”, the lowest energy protons apparently decrease with decreasing solar activity; this might indicate a residual effect of protons of solar origin.

The energy spectra of Helium nuclei (Figure 4b) show a more regular pattern. In all cases the spectrum is relatively flat in the energy range 3.7 to 48 MeV/N with no low energy turn up, showing the features of the “anomalous” Helium component (Garcia-Munoz et al., 1973, see also Hovestadt et al., 1973, McDonald et al., 1974).

A superposition of the proton and Helium spectra at perihelion is shown in Figure 4c. In the energy range from 10 to 40 MeV/N the Helium intensities are well above the proton intensities by a factor of about 2 at 20 MeV/N.

Table 1. Periods of quiet times, used for evaluation of the energy spectra

Dataset	Radial distance of Helios (AU)	Period	Quiet time data (h)
aphelion 0	0.98 to 0.87	74 Dec 13, 2–74 Dec 17,2 74 Dec 28, 2–75 Jan 2,23 75 Jan 11,12–75 Jan 17,23	296
perihelion	0.31 to 0.47	75 Mar 4,12–75 Mar 14,23 75 Mar 26, 0–75 Apr 2,0	348
aphelion 1	0.98 to 0.96	75 Jun 2, 0–75 Jun 24, 0	262

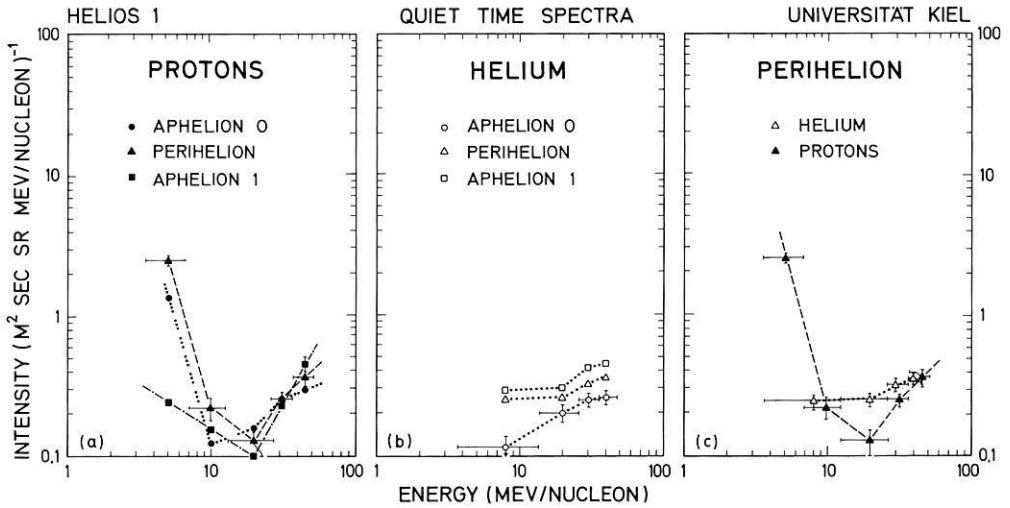


Fig. 4a-c. Quiet time spectra of protons and Helium nuclei during different time periods close to aphelion 0 (>0.87 AU), perihelion (<0.47 AU), and aphelion 1 (>0.96 AU) (see Table 1 and Fig. 1 and 3). **a** Proton spectra near aphelion 0 (December 1974/January 1975), perihelion (March/April 1975), and aphelion 1 (June 1975). **b** Helium spectra near aphelion 0, perihelion and aphelion 1. **c** Proton and Helium spectrum at perihelion. Error bars and energy intervals indicated at one spectrum only are typical also for the other spectra

This confirms the presence of the anomalous Helium component also in the vicinity of the sun between 0.4 and 0.3 AU.

Let us draw some preliminary conclusions from the data presented in Figure 4b. In the integrated Helium intensity in the energy range 13 to 47 MeV/nucleon we find a relative increase of $24 \pm 18\%$ from Dec 74/Jan 75 to March 1975, and a relative increase of $26 \pm 8\%$ from March to June 1975. This means that in contrast to the behaviour of the high energy protons discussed in the preceding section there is no significant difference between the inward and outward motion of Helios. Therefore, the influence of a possible radial gradient is small. This is in agreement with the small gradients reported beyond 1 AU from the Pioneer 10/11 missions (10%/AU between 10 and 19 MeV/nucleon according to McKibben et al. (1975); 12%/AU between 8.8 and 23.5 MeV/nucleon according to Webber et al. (1975)). Converting these values to a radial separation of 0.7 AU, we would expect an effect of the order 7–8% variation between 1.0 and 0.3 AU, which would indeed be unresolvable from the above temporal variation within the statistical uncertainties. According to Garcia-Munoz et al. (1975) the first “flat” Helium spectrum was observed to occur first in 1972, and the Helium intensity below about 80 MeV/nucleon was significantly higher than 1971. Time variations in this anomalous component between 1972 and 1974 are less pronounced. Comparison of published measurements (Garcia-Munoz et al., 1973, 1975; Christon et al., 1975; Mewaldt et al., 1975a, 1975b; Zamov, 1975) shows that there exist discrepancies between results from different instruments on different spacecraft. Part of these discrepancies may

be due to different criteria in the selection of “quiet times”. However, combination of the available measurements reveals a trend of a general intensity increase between 1972 and 1974. This trend is clearly continued in the 13 to 47 MeV/nucleon Helium data from Helios between December 1974 and June 1975.

Fisk et al. (1974) have proposed that the anomalous composition of low energy cosmic rays be caused by interstellar neutral particles which enter the solar cavity and are ionized here. In a model developed by Fisk (1976a) these ions with energies in the keV/nucleon range are accelerated by the solar wind to tens of MeV/nucleon. Fisk (1976b) compares the consequences of this model with a direct galactic origin of the anomalous component. His conclusion is that for an origin by interplanetary acceleration the modulation of these particles can be understood in the context of present modulation theory, whereas the galactic origin would require a considerable modification of the present cosmic ray diffusion scheme in the interplanetary medium.

Klecker (1977) has summarized the arguments in favor of an interplanetary origin for the anomalous component. His model calculations reproduce the 1973 quiet time data for Helium nuclei above 10 MeV/nucleon reported by Garcia-Munoz et al. (1975). It will be further studied whether the temporal variations seen on Helios can be related simply to a change of the modulation parameter, or whether changes in the acceleration rate (Fisk, 1976a) are also involved. In principle, the modulation *and* the acceleration rate should be variable with the solar cycle. Both parameters are contained in present models for the anomalous component (Fisk, 1976a, 1976b; Klecker, 1977).

5. Solar Particle Events

In the previous section we discussed measurements during solar quiet times of the Helios 1 prime mission. These times are marked by shaded columns in Figure 3. Several solar events occurred during the remaining intervals. The three events on January 5, March 3, and March 19, 1975, will be discussed in more detail because they represent examples of solar events with very different characteristics. At the time of the three events Helios was at radial distances of about 0.93, 0.41, and 0.32 AU, respectively.

Figure 5 shows in the upper panel the constellation of Helios with respect to sun and earth in the ecliptic plane for the three events. Black dots on the solar surface mark the position of active regions. The spiral lines indicate the ideal interplanetary magnetic field. The lower panel of Figure 5 sketches the intensity time profiles of the events for 4–13 MeV protons. Note that all three profiles are presented on the same time scale.

January 5, 1976, Event

On January 5, 1975, Helios was at a solar distance of 0.93 AU and 7° east of the earth. Two active centers were located nearly 180° apart in solar longitude, roughly symmetric to the Helios connection longitude (see Fig. 5). Both active centers had the capability to accelerate particles.

Green et al. (1975) have performed a preliminary analysis of this event by

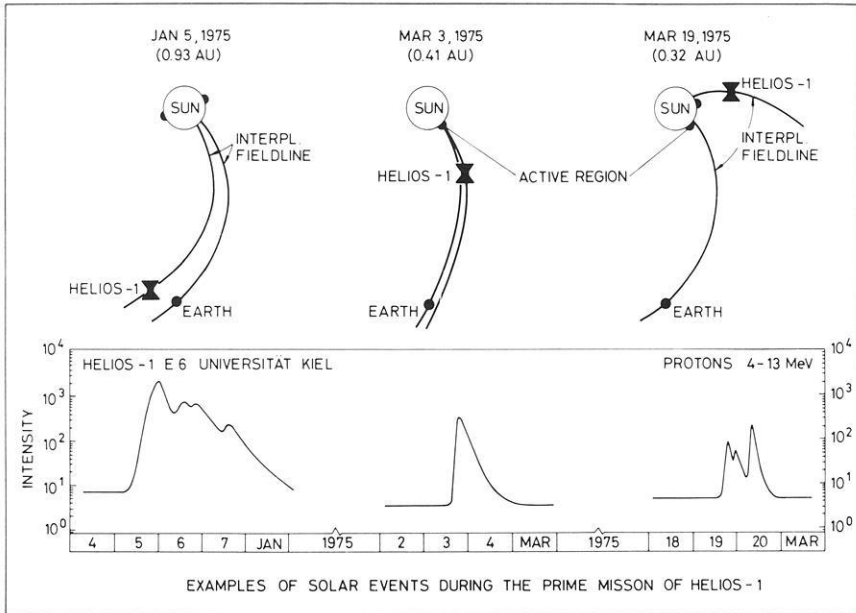


Fig. 5. Smoothed time profiles of 4 to 13 MeV protons during selected solar events, observed from different radial and azimuthal distances

studying the velocity dispersion between electrons and protons of different energies, using the method of Reinhard and Wibberenz (1974) and Ma Sung et al. (1975) to separate solar and interplanetary propagation processes. They found that the probable acceleration time of the particles is close to 0800 UT on January 5. It is interesting that an importance 1n flare was reported at 0730 UT on the same day from McMath region 13411 which was at 58° E at this time. On the other hand, the second active region 13404 had produced X-rays and pronounced radio activity during its passage over the visible disk.

As discussed by Green et al. (1975) it is very probable that an interplanetary shock observed at Helios on January 6, 2040 UT, originated from a flare close to the *west* limb on January 5. Thus, both active regions are indeed candidates for the particle acceleration but they are roughly at the same longitudinal distance from the Helios connection longitude. Green et al. (1975) estimated the coronal parameters for this event: a solar drift time of 8 h for the bulk of particles, and of 2 h for the first particles. These parameters are in agreement with the average behaviour for solar events where the originating flare is 80° to 90° away from the observer (Reinhard and Wibberenz, 1974; Ma Sung et al., 1975).

The main interest in this event may come from the study of the shock related increases superimposed on a long decay phase lasting more than three days (see Fig. 5). It should be possible to infer the large-scale structure of the interplanetary magnetic field related with two shocks on January 6 and January 8 from simultaneous measurements on Helios and near earth. This large-scale structure is one of the prerequisites to distinguish between various

models of ESP-events. Analysis of the angular distribution of low energy alpha particles and protons shows a preferred streaming of particles *away* from the shock associated structures both before and after the shock passages.

March 3, 1975, Event

The relative location of the two interplanetary field line bundles connecting Helios and the earth to the sun is very similar to the situation in January (see Fig. 5), but at this time Helios is located at 0.41 AU from the sun. The flare occurred probably within the fast propagation region with respect to both Helios and earth. The time profile of this event is very smooth. The onset for the 4–13 MeV protons occurs at 1635 UT on March 3. The maximum intensity is reached 3 h later, followed by a rapid decrease with an e-folding time of ~ 4.5 h. An attempt to fit this profile with a simple diffusion model and a delta-function injection at the sun leads to a relatively small cosmic ray scattering mean free path of the order of 0.04 AU. In addition, the anisotropy we observed is very large, of the order of 80% and 60% between 5 and 10 h after the onset. These large values are in clear contradiction with a prompt injection at the sun (see e.g. Schulze et al., 1975).

If we take the extreme position that the propagation during this event is totally scatter-free we obtain a decay time constant of 4.5 h. It is interesting to note that this value for protons of this energy range is in good agreement with the conclusion drawn by Reinhard (1975) on the decay times of the solar injection process.

March 19/20, 1975, Event

The days of March 7 through 14, 1975, had been very quiet in the various cosmic ray channels. After March 16, however, when Helios was close to its first perihelion, the sun became rather active in X-rays as seen from Helios (Trainor, private communication). In addition, several small intensity increases occurred in the low energy cosmic ray data. The largest peaks occurred on March 19/20 and are shown in Figure 6 for four selected channels. The peaks are marked as “1”, “2”, and “3” in the insert to channel A 2–4. We note the following different features in the various channels: (a) Near-relativistic electrons are seen only in peak 1. (b) The onset of peak 1 is rather different for the various channels. The sharp first rise in channel A 2–4 is in coincidence with a sharp interplanetary magnetic field directional discontinuity (Neubauer and Musmann, private communication). After correction of this effect—which leads to a break in the P 4–13 onset phase—one sees the clear velocity dispersion between the electrons and protons. (c) Peak 2 is most clearly seen in the lowest energy Helium counting rates (A 2–4) and seems to coincide with an increase in channel A 4–13. It seems unlikely that the absence of this peak in the proton channel P 4–13 is due to insufficient statistics. (d) The nucleons show a new significant increase around 0800 UT on March 20 (peak 3). Inspection

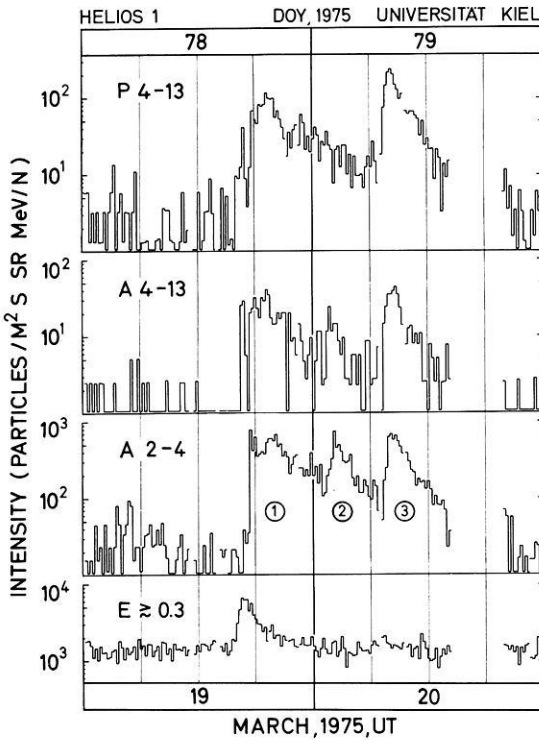


Fig. 6. Intensity variations in selected channels during the ${}^3\text{He}$ -rich events shortly after perihelion

of the anisotropies indicates a new injection of particles from the sun. (e) Rise and decay times are remarkably short for the nucleon channels (decay time of less than 2 h for peak 3). We suggest that this is related to the small distance r from the sun: in a model of diffusive propagation with the scattering mean free path independent of r , time constants vary proportional to r^2 . This means that for $r=0.32$ AU the diffusive widening of an intensity-time profile is reduced by a factor of the order of 10 as compared to near-earth observations.

The most interesting feature of this sequence of events is their large He^3 content. Pulse height information from individual nucleons can be used above 4 MeV/nucleon for charge, mass, and energy identification. Within the time interval 1530 UT, March 19, to 1200 UT, March 20, we have identified 225 protons and 80 Helium nuclei in the energy range 5–7 MeV/N.

Figure 7 shows the mass histogram in the range of 3 to 4 nucleon masses for Helium nuclei in the energy/nucleon range from 5 to 7 MeV/nucleon.

Table 2 summarizes the results. For peaks 1 and 2, the ${}^3\text{He}/{}^4\text{He}$ -ratio is larger than 2 and does not change from one peak to the other within the statistical limits. For peak 3, the ratio is smaller than one; the difference in the ratio would be consistent with a fresh injection of particles as concluded above under (d) from anisotropies. If we assume power law differential spectra $j(E)=j_0E^\gamma$, we obtain $\gamma \simeq -4.5$. Within statistical errors this value does not change between the three peaks and, in addition, does not depend on the particle type.

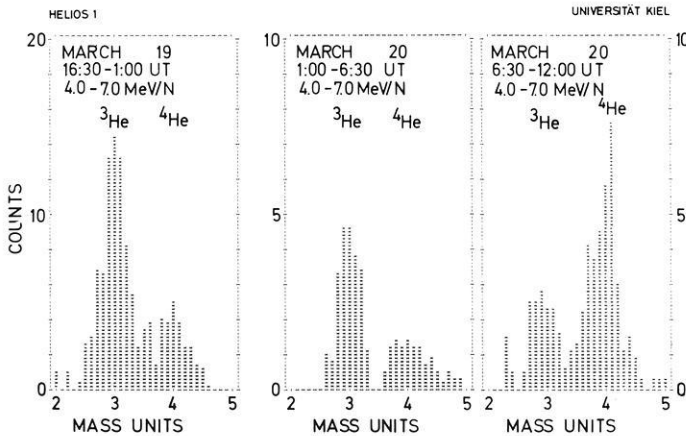


Fig. 7. Mass histograms at different time intervals during the solar particle event of March 19, and 20, 1975 in the Helium range. The histograms clearly demonstrate the separation of ^3He and ^4He and the high ^3He contribution

Table 2. Number of identified Hydrogen and Helium nuclei in the range 5–7 MeV/N and related ratios of $^4\text{He}/P$ and $^3\text{He}/^4\text{He}$

Date Time	March 19 15:30–1.00	March 20 1:00–6:30	March 20 6:30–12:00
P	95	26	104
^4He	12	4	12
^3He	34	8	10
$^4\text{He}/P$	0.13 ± 0.04	0.15 ± 0.08	0.12 ± 0.04
$^3\text{He}/^4\text{He}$	2.83 ± 0.95	2.00 ± 1.22	0.83 ± 0.36

^3He -rich events were first reported by Garrard et al. (1973) and Anglin et al. (1974). There is no or only a weak flare correlation, and large He^3 contents are restricted to small events. No measurable amount of Deuterium or Tritium has been found in these events so far. Hovestadt et al. (1975) pointed out that the sun and the interplanetary conditions during the Helium 3–rich events are very quiet in general and that sometimes the solar wind density is exceptionally high.

Three He^3 -rich events are reported by Serlemitsos and Balasubrahmanyam (1975). They find $^3\text{He}/^4\text{He} \approx 1.5$ for the 1969 May 28 event, and also a relatively small amount of protons, $P/(^3\text{He} + ^4\text{He}) \approx 1$.

We can confirm most of the earlier findings for ^3He -rich events for the March 19/20, 1975, case:

- On March 19, Helios is at the peak of a high speed solar wind stream, connected with the north polar coronal hole (Schwenn et al., 1976).

- The events are small; the ratio of alpha particles to protons is larger than on the average in “normal” solar events. No deuterons or tritons are detected.

- There seems to be no (easy) identification with a solar flare. In principle, two active centers on the sun could be the source region. McMath region

13532 was rather active during its passage over the solar disk; it was close to the Helios connection longitude at the time of the events, but about 40° beyond the west limb as seen from the earth. This means that this region could not be observed in H_x after March 16. However, the X-ray data from the Goddard Space Flight Center experiment on board Helios (Trainor, private communication) does not show any X-ray activity from region 13532 prior to peak 1. The time of a subflare in the other active region, McMath 13540, near the magnetic fieldline connection point of the earth (c.f. Fig. 5) corresponds to the observed onset time of peak 1. However, this region showed no significant activity before and after this event. As there is no information related to peaks 2 and 3, the origin of the sequence of events on March 19 and 20, 1975, remains open at this time.

6. Discussion and Summary

We present cosmic-ray results from the first part of the Helios 1 mission for the period December 1974 to June 1975. The level of solar activity is very low, and still decreasing. The inspection of neutron monitor data shows that this period is characterized by a slow increase of the high energy galactic cosmic radiation with a relatively constant rate.

In our discussion of radial gradients and quiet time spectra (section 3 and 4) we have assumed that longitudinal and latitudinal effects can be neglected. The observed variation in the integral > 51 MeV proton channel was interpreted by the superposition of a radial on a temporal variation. The resulting integral radial gradient of $(11 \pm 2.5)\%/AU$ is larger than obtained previously from the Pioneer 10/11 missions. We discussed several physical reasons for this difference. Possible systematic errors (influence of a variable background and threshold drifts) will be reduced in the future; a detailed study is in progress which makes use of the three detector outputs for energy and particle determination.

During March 1975, the anomalous Helium component is also present close to 0.3 AU. The radial gradient is small. In the energy interval 13 to 47 MeV/nucleon, this component shows an intensity change of about 50% between December 1974 and June 1975; for both of these periods Helios was close to 1 AU. It should be noted that this change of about +50% is accompanied by a 2.7% steady increase of the Deep River neutron monitor counting rate.

In future studies we shall improve the separation of spatial and temporal variations. Neutron monitor data as a reference will be replaced by near-earth satellite observations of particles with energies comparable with those on Helios. In addition, for further investigations of radial gradients and quiet time spectra we will make use of the long lifetime of the Helios mission (as of May 15, 1977, Helios 1 is still in operation, and Helios 2 has delivered additional data since January 1976) and of its orbit: the orbital period of half a year allows to scan the same interval of radial distances from the sun in subsequent phases of the solar cycle; the alternate inward and outward motion will cause radial gradients to be superimposed on existing temporal variations with alternating sign.

Three selected solar particle events were discussed in section 5. With their low particle fluxes they belong to the class of micro events. They represent examples of the very different properties which solar events can exhibit. The January 5, 1975, event shows a long-lasting decay phase. Interplanetary disturbances are partly the reason for considerable modulation during the decay. The March 3, 1975, event has a very regular time structure with smooth and short rise and decay phases. There is some indication that the observed profile is very directly related to the solar injection process and only moderately modified by interplanetary propagation. The relative position between Helios 1 and the earth—on closely neighbouring interplanetary magnetic field lines, but about 0.6 AU apart from each other—will be ideal to separate interplanetary and solar transport processes by comparative studies.

The March 19/20 event consists of three different peaks with at least two separate injections. It is of special interest because of its unusual high ${}^3\text{He}/{}^4\text{He}$ -ratio of the order of two to three. If observed from earth this event would probably be masked by the background level; furthermore, it seems improbable that the relatively fast time structures would remain undisturbed by interplanetary propagation for an observer located at 1 AU. The presentation of the events observed close to the sun reveals some of the advantages of the Helios orbit for the study of solar events as compared to measurements at 1 AU. Discrimination between repetitive events occurring with small temporal separation is improved. Smaller events can be resolved from background, which is important because small solar events may exhibit some unusual features with respect to chemical and isotopic composition (cf. Gloeckler, 1975). The reduced influence of interplanetary scattering processes allows to draw hitherto unknown conclusions on the particle injection close to the sun. Full advantage of this situation will be taken during the double mission of Helios 1 and Helios 2, in particular in the period March to May 1976, when both spacecraft were relatively close to the sun during a period of minor solar activity.

Acknowledgements. The German-American cooperative space project Helios was initiated and sponsored by the Bundesminister für Forschung und Technologie (BMFT) and by the National Aeronautics and Space Administration (NASA). The University of Kiel experiment was supported by the BMFT through the DFVLR-Bereich Projektträgerschaften. We express our gratitude to the program manager K. Käsmeier and to the program scientist M. Otterbein.

The authors appreciate the good cooperation with all members of the German project office at the DFVLR-BPT under the project manager Mr. A. Kutzer, especially with the experiment managers W. Wodsack, H. Dodeck, W. Kempe, and R. Vogel as well as with H.-J. Galle and W. Schmolz. We appreciate also the extraordinary effort of the American project management group under the project manager G. Ousley (NASA-GSFC).

The Helios experimenters team was headed by the project scientists H. Porsche, L. Meredith, and J. Trainor. We thank them for their extraordinary efforts to coordinate the often diverging interests of the scientific groups and to advocate the scientific goals of the project.

This experiment was designed by a team at Kiel originally headed by H.-G. Hasler; part of the electronics design is due to F. Gliem (TU Braunschweig). The instrument was developed to flight standard and manufactured by Dornier System, Friedrichshafen, under the management of A. Popp, H.-G. Maschmann, K. Rembach, and F. Wurth took responsibilities for major working packages. Subcontractors were AEG-Telefunken, Ulm, and Matrix Corp., Acton, Mass.. We appreciate the excellent job all involved companies did cooperatively resulting in two perfectly working space instruments.

We are indebted to various accelerator groups for their very helpful support during experiment calibration at the University of Hamburg (G. Lindström and E. Fretwurst), University of Maryland (R. Berg), and Physikalisch-Technische Bundesanstalt Braunschweig (H. Feist).

The spacecraft was built by Messerschmitt-Bölkow-Blohm, Ottobrunn, as main contractor. We appreciate in particular the outstanding jobs of the experiments and integration groups headed by R. Grün, H.-J. Schuran, and A. Ziegler.

After launch the German Space Operation Center (DFVLR-GSOC) was responsible for mission operations and experiment data recording. Representative for the complete team we express our thanks to G. Hiendlmeier, J. Kehr, H.-J. Panitz, H.-P. Piotrowski, and K. Wiegand. The completeness of the data return was only possible with the outstanding support also from Deep Space Network and Jet Propulsion Laboratories, Pasadena, California, represented by K. Heftmann. The Max-Planck-Institut für Radioastronomie, Bonn, allowed use of the 100 m Radioteleskop Effelsberg for Helios data reception. The access of observation times at Effelsberg for the benefit of the Helios experiments is gratefully acknowledged.

The authors thankfully acknowledge the continuous support which the Helios project has found by Professor E. Bagge from the early phases on. Excellent administrative assistance was provided by R. Schlottau and A. Stender. The mechanical, drawing, and photographic shops, represented by K.F. Jesse, J. Drechsler, and R. Löwe, contributed by prompt and accurate returns.

The experiment would have been impossible without the engaged cooperation of all other members of the Kiel Helios team: V. Fleißner, L. Leu, U. Mende, R. Rehbein, E. Rode, and G. Salzmann. We highly appreciate their long-lasting efforts which guaranteed the excellent flight performance and data quality.

The authors express their gratitude for excellent cooperation with the other Helios experimenters and for permission to use their data for interpretation of the cosmic ray measurements. This applies especially to H. Rosenbauer and R. Schwenn (Experiment 1), G. Musmann and F.M. Neubauer (Experiment 2), and J.H. Trainor (Experiment 7).

During the lifetime of the Helios project we had to rely on the professional and responsible contribution of every single person which was involved in the project. Only some of them could be personally mentioned above. We appreciate highly their effort which resulted in a great success of the whole project.

References

- Anglin, J.D., Simpson, J.A., Zamow, R.: Solar Flare ^2H , ^3H and ^3He . (Abstract) *Bull. Am. Phys. Soc.* **19**, 457–457, 1974
- Christon, S., Daly, S., Eraker, J.H., Lampert, J.E., Lentz, G., Simpson, J.A.: Nucleon Radial Gradients between 0.45 and 1.0 AU from the Mariner-10 Mission to Mercury. *Proceedings, 14th Internat. Cosmic Ray Conference, München, 1848–1849, 1975*
- Fisk, L.A.: The Acceleration of Energetic Particles in the Interplanetary Medium by Transit Time Damping. *J. Geophys. Res.*, **81**, 4633–4640, 1976a
- Fisk, L.A.: Solar Modulation and a Galactic Origin for the Anomalous Component Observed in Low Energy Cosmic Rays. *Astrophys. J.*, **206**, 333–341, 1976b
- Fisk, L.A., Kozlovsky, B., Ramaty, R.: An Interpretation of the Observed Oxygen and Nitrogen Enhancement in Low Energy Cosmic Rays. *Astrophys. J.*, **190**, L35–L37, 1974
- Garcia-Munoz, M., Mason, M., Simpson, J.A.: A New Test for Solar Modulation Theory: The 1972 May–July Low Energy Galactic Cosmic Ray Proton and Helium Spectra. *Astrophys. J.*, **182**, L81–L84, 1973
- Garcia-Munoz, M., Mason, G.M., Simpson, J.A.: The Anomalous ^4He Component in the Cosmic Ray Spectrum at ≈ 50 MeV per Nucleon during 1972–1974. *Astrophys. J.*, **202**, 265–275, 1975
- Garrard, T.L., Stone, E.C., Vogt, R.E.: The Isotopes of H and He in Solar Cosmic Rays. In: *High Energy Phenomena on the Sun. Symposium Proceedings, R. Ramaty and E.C. Stone, eds., pp. 341–354. Goddard Space Flight Center, Greenbelt, Maryland, 1973*
- Gloeckler, G.: Low Energy Particle Composition. *Proceedings, 14th Internat. Cosmic Ray Conference, München, 3784–3804, 1975*
- Green, G., Hasler, H.G., Kunow, H.: An Adaptive Data Compression Method for a Cosmic Ray Experiment on Board a Space Probe. *Nucl. Instrum. Methods*, **86**, 213–216, 1970

- Green, G., Wibberenz, G., Müller-Mellin, R., Witte, M., Hempe, H., Kunow, H.: Two Solar Cosmic Ray Events Measured on Helios 1. Proceedings, 14th Internat. Cosmic Ray Conference, München, 4257–4263, 1975
- Hovestadt, D., Klecker, B., Vollmer, O., Gloeckler, G., Fan, C.Y.: Heavy Particle Emission of Unusual Composition from the Sun. Proceedings, 14th Internat. Cosmic Ray Conference, München, 1613–1618, 1975
- Hovestadt, D., Vollmer, O., Gloeckler, G., Fan, C.Y.: Differential Energy Spectra of Low Energy ($E < 8.5$ MeV per Nucleon) Heavy Cosmic Rays During Solar Quiet Times. Phys. Rev. Letters, **31**, 650–653, 1973
- Klecker, B.: The Anomalous Component of Low Energy Cosmic Rays – A Comparison of Observed Spectra with Model Calculations. To be published in J. Geophys. Res., 1977
- Kunow, H., Wibberenz, G., Green, G., Müller-Mellin, R., Witte, M., Hempe, H.: Das Kieler Experiment zur Messung der Kosmischen Strahlung zwischen 1.0 und 0.3 AE. Raumfahrtforschung, **19**, 253–257, 1975
- Ma Sung, L.S., Van Hollebeke, M.A.I., McDonald, F.B.: Propagation Characteristics of Solar Flare Particles. Proceedings, 14th Internat. Cosmic Ray Conference, München, 1767–1772, 1975
- McDonald, F.B., Teegarden, B.J., Trainor, J.H., Webber, W.R.: The Anomalous Abundance of Cosmic Ray Nitrogen and Oxygen Nuclei at Low Energies. Astrophys. J., **187**, L105–L108, 1974
- McKibben, R.B.: Cosmic Ray Intensity Gradients in the Solar System. Rev. Geophys. and Space Phys., **13**, 1088–1092, 1975
- McKibben, R.B., Pyle, K.R., Simpson, J.A., Tuzzolino, A.J., O’Gallagher, J.J.: Cosmic Ray Radial Intensity Gradients Measured by Pioneer 10 and Pioneer 11. Proceedings, 14th Internat. Cosmic Ray Conference, München, 1512–1517, 1975
- Mewaldt, R.A., Stone, E.C., Vogt, R.E.: The Isotopic Composition of Hydrogen and Helium in Low Energy Cosmic Rays. Proceedings, 14th Internat. Cosmic Ray Conference, München, 306–311, 1975a
- Mewaldt, R.A., Stone, E.C., Vogt, R.E.: The Quiet-Time Spectra of Low Energy Hydrogen and Helium Nuclei. Proceedings, 14th Internat. Cosmic Ray Conference, München, 774–779, 1975b
- Reinhard, R.: The Exponential Decay of Solar Flare Particles. II: Western Hemisphere Events. Proceedings, 14th Internat. Cosmic Ray Conference, München, 1687–1691, 1975
- Reinhard, R., Wibberenz, G.: Propagation of Flare Protons in the Solar Atmosphere. Solar Phys., **36**, 473–494, 1974
- Schulze, B.M., Richter, A.K., Wibberenz, G.: On the Influence of Injection Profiles and of Interplanetary Propagation on the Time-Intensity and Time-Anisotropy-Profiles of Solar Cosmic Rays at 1 AU. Proceedings, 14th Internat. Cosmic Ray Conference, München, 1749–1753, 1975
- Schwenn, R., Montgomery, M.D., Rosenbauer, H., Miggenrieder, H., Bame, S., Hansen, R.T.: The Latitudinal Extend of High Speed Streams in the Solar Wind: Correlations of Helios, Imp, and K-Corona Measurements. (Abstract). EOS, Transactions Am. Geophys. Union, **57**, 999, 1976
- Serlemitsos, A.I., Balasubrahmanyam, V.K.: Solar Particle Events With Anomalously Large Relative Abundance of ^3He . Astrophys. J., **198**, 195–204, 1975
- Solar-Geophysical Data, 1975: Solar-Geophysical Data, 366 through 375, Part I, U.S. Department of Commerce. February–November 1975
- Stoker, P.H., Carmichael, H.: Steplike Changes in the Long-term Modulation of Cosmic Rays. Astrophys. J., **169**, 357–368, 1971
- Teegarden, B.J., McDonald, F.B., Trainor, J.H., Roelof, E.C., Weber, W.R.: Pioneer 10 Measurements of the Differential and Integral Cosmic Ray Gradient between 1 and 3 AU. Astrophys. J., **185**, L155–L159, 1973
- Webber, W.R., McDonald, F.B., Trainor, J.H., Teegarden, B.J., Von Roseninge, T.T.: Further Studies of the New Component of Cosmic Rays at Low Energies. Proceedings, 14th Internat. Cosmic Ray Conference, München, 4233–4238, 1975
- Zamov, R.: The 1964–1972 quiet-time spectra of protons and helium at 2–20 MeV/N. Astrophys. J., **197**, 767–780, 1975

A Survey on Measurements of Medium Energy Protons and Electrons Obtained with the Particle Spectrometer E8 on Board of Helios

E. Keppler*, A.K. Richter, K. Richter, G. Umlauf, B. Wilken,
and D.J. Williams**

Max-Planck-Institut für Aeronomie, D-3411 Katlenburg-Lindau 3,
Federal Republic of Germany

Abstract. We briefly describe a magnetic particle spectrometer for measuring protons ($E > 80$ keV) and electrons ($E > 15$ keV), flown on Helios-1 and -2. Showing examples of measurements obtained in interplanetary space, we show the capability of the instrument to resolve structures in time with 13 s resolution, and demonstrate the importance of having this high time resolution. A second feature is its energy resolution, which for the first time allows for precise measurements in this energy domain. A third feature is the angular resolution in 16 sectors. Again we demonstrate, that having this resolution is indispensable for correct interpretation of data. By combining these features, we are able to apply the Compton-Getting transformation without a priori assumptions.

Key words: Helios spacecrafts – Solar wind protons – Solar wind electrons.

1. Introduction

Helios-1 (launched Dec. 10, 1974) and Helios-2 (launched Jan. 15, 1976) are in orbits around the sun with aphels of ~ 1 AU, and perihels of 0.31 and 0.29 AU, respectively. While Helios-1's antenna is pointing northward, Helios-2 operates upside down. Both spacecraft are spinning in the same sense at a rate of about 1 rotation per second, with the spin axis normal to the ecliptic plane, Helios-1 counter-clock-wise, when viewed from the north.

Both spacecraft are operating almost perfectly since launch, and have been tracked by the DSN-ground-network and by the German stations Effelsberg and Weilheim. This allowed for very good data coverage since launch. In addition, when the spacecraft are not viewed by antennas, they are put into a storage mode, where, dependent upon the time gap to the next receiving period, the data

* To whom offprint requests should be sent

** Permanent address: NOAA-ERL-SEL, Boulder, CO, USA

are stored in the 500 kbit memory of the S/C, utilizing low bitrate and eventually a certain data frame deletion rate. Due to this peculiarity, Helios data are obtained for 24 h/day, even if there is realtime coverage only for a fraction per day. For this reason, Helios became the spacecraft with the most complete data coverage since launch. As all instruments are working nominally and also the S/C is in good condition, it is hoped to have this continued for quite a while.

2. The Charged Particle Spectrometer E8

The instrument uses an inhomogeneous magnetic field to separate electrons and ions and detect them by using separate semiconductor surface barrier detectors. The instrument utilizes a geometrical factor, which is $1.5 \cdot 10^{-2} \text{ cm}^2 \text{ ster}$ for ions, and $\leq 5 \cdot 10^{-2} \text{ cm}^2 \text{ ster}$ for electrons. Due to the operational principle (Fig. 1), electrons are deflected according to their rigidity; thus each of the detectors covers a certain energy range. The design of the magnetic system realizes focussing of electrons in a certain energy range. As this feature disappears with increasing energy, efficiency degrades somewhat. As a result of this, efficiency is a function of energy as shown in Figure 2. Efficiency has been measured in an electron spectrometer. Curves in Figure 2 are least square fits to the measurements. Efficiency is in this context being defined by the ratio of the actual count rate of a particular detector at a given energy to the counting rate of a reference detector of sensitive area equal to the entrance aperture, moved to replace the aperture before and after the measurement. So efficiency, as defined here, does not take into account backscattering. However, this effect tends to be cancelled out by the applied technique, so we feel that our figures are uncertain by a few % only.

The signals from each detector are amplified and fed to a 16-channel-pulseheight-analyzer. The energy range covered is 20 keV to 2 MeV. Channel allocation is given in Table 1.

Protons and ions are almost unaffected by the magnetic field (800 Gauss maximum) and are detected in a telescope arrangement. Again the front detector signal is analyzed in 16 channels (see Table 1) in anticoincidence with the backdetector signal. The frontdetector is covered by a $120 \mu\text{g}/\text{cm}^2$ Al-layer. Correspondingly, protons are analyzed above 80 keV (utilizing $\Delta E \geq 20 \text{ keV}$ of energy loss in the frontdetector). Alpha particles contribute to the various energy channels if their energy is $E \geq 100 \text{ keV}$. Particle entrance is through the aluminium layer. All detectors are surface barrier detectors, fully depleted, operated at about 150 % overbias.

The energy ranges for the various channels are shown in Table 1. All channels, except where indicated, are differential of the form $D_i \overline{D_{i+1}}$. Channel width is quasilogarithmically increasing. In addition to the differential channels, integral channels are formed. The latter are used to obtain simultaneously the intensity from 16 directions, ions and electrons being obtained in alternating sequence.

The instrument is mounted on the spacecraft to include an angle of 7° with the normal to the spin axis, thus scanning approximately within the ecliptic

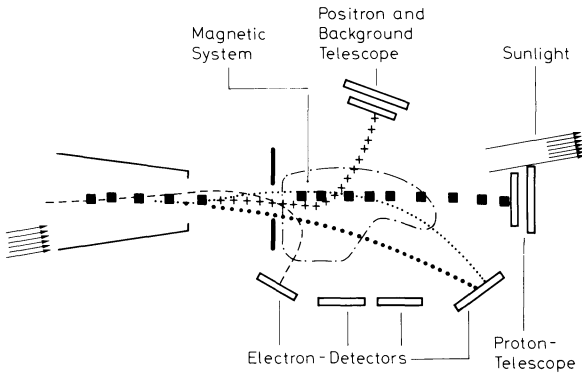


Fig. 1. Particle separation in the magnetic spectrometer E8, schematically. An inhomogeneous magnetic field is applied to improve efficiency by focussing

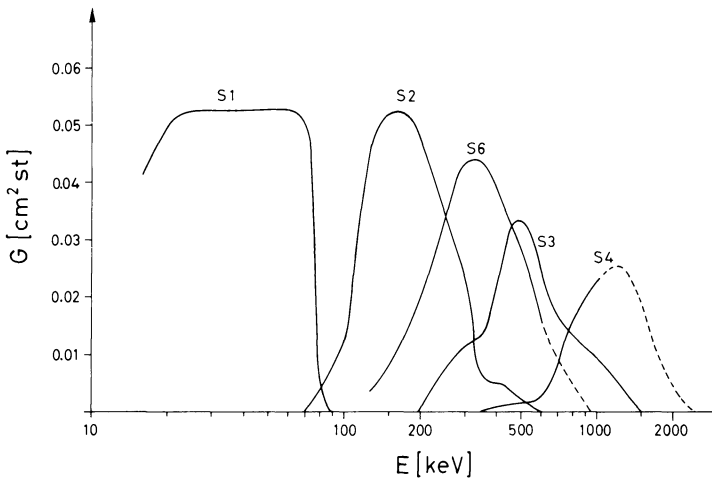


Fig. 2. Efficiency of electron detection as a function of particle energy. S1–S4 are electron detectors, covering different energy ranges: S1: 16–100 keV; S2: 90–350 keV; S3: 230–850 keV; S4: 600–2000 keV

plane (opening angle 20° full angle). While spinning, data collection is being sectorized in 16 sectors. A set of integral rates from all 16 sectors is obtained alternating between ions and electrons. Energy spectra from ions and electrons are obtained from all 16 directions subsequently, two at a time. The time resolution, which will be obtained, is bitrate dependent; the Helios bitrate may be varied from 8–4096 bps. The instrument is adjusted to bitrate changes by changing the accumulation time (maintaining the sectorization) correspondingly. At the highest bitrate the highest time resolution, which may be achieved for angular distributions, is 13.5 s, while a full set of energy spectra from 16 directions takes 108 s. At low bitrate a reduced format is used, which, at 8 bps, provides a full set of information from 8 sectors (instead of 16) in 19 min.

Table 1. Energy channels for protons and electrons (in keV)

	Channel No.																Integral	Coincidence
	1	2	3	4	5	6	7	8	9	10	11	12	13	14	15	16		
Protons																		
Helios-1	80	87	96	105	117	130	146	165	190	225	267	320	390	475	585	730	>20, >134	
Helios-2	87	95	102	110	121	135	153	176	200	235	280	340	415	500	620	750	>21, >137	
Electrons																		
Helios-1	17	22	28	35	46	58	74	92	120	155	202	250	325	412	525-2000	16		
Helios-2	20	25	32	41	52	62	80	102	125	158	201	254	324	411	519-2000	19		

Table 2. Sectorization

	Sector number																West East
	1	2	3	4	5	6	7	8	8	10	11	12	13	14	15	16	
Helios-1				Sun				East				Anti-sun				West	
Helios-2				Sun				West				Anti-sun				East	

Sector formation is done such, that the sector pattern remains fixed relative to the sun throughout the mission, sector 4 always facing the sun. Due to the opposite orientation of Helios-1 and -2, the direction of sectors relative to the S/C-sun-line ("west" being in the right side, when viewing towards the sun) is as given in Table 2.

3. Data Evaluation

While ion detection is performed through a two-element-telescope arrangement (coincidence signals are used to suppress analysis of frontdetector signals, coincidence resolution time is $0.8\mu\text{s}$), which provides for a reasonable background suppression, electron detectors are not protected by anticoincidence detectors, and therefore suffer from the 4π cosmic ray background. As this was anticipated, a backgrounddetector has been included into the instrument, which is completely protected from being reached by particles entering through the aperture. Both, electron detectors and backgrounddetector are shielded by the same amount of matter (2.5 g/cm^2 , average) equivalent to 4 MeV electron range or 46 MeV for protons. The backgrounddetector is monitored by a 80 keV electronic threshold, well below the energy loss of minimum ionizing particles in a $300\mu\text{m}$ detector, sufficient to provide for Landau spread. The counting rate of the backgrounddetector is being transmitted along with each data sample, thus allowing for determination of the penetrating particle flux.

For data presentation the following procedure is applied on a routine basis: During quiet times the ratio λ_i of the counting rate N_{iq} for each channel to the backgrounddetector counting rate N_{uq} is being determined throughout the mission. Thus for all data channels the true rate N_i^* is being calculated by $N_i^* = N_i - \lambda_i N_u$. Conversion to differential fluxes j_i is obtained by

$$j_i = \frac{N_i^*}{k_i G_i \Delta E_i} \quad (1)$$

where G_i is the effective geometric factor ($0.015\text{ cm}^2\text{ster}$ for protons, for electrons as given by Figure 2 (S1, S2, S3, S4)); ΔE_i is the differential energy interval $\Delta E_i = E_{i+1} - E_i$, summarized in Table 1; k_i is a filter correction factor, which is calculated from the actual channel noise figure σ keV (RMS) (determined during inflight calibration periods) by

$$k_i = \frac{\int_{U_i}^{U_{i+1}} j(E(U)) dU}{\int_0^\infty j(E(U)) F(U, \sigma) dU} \quad (2)$$

In Equation (2) U is the energy deposited in the detector, E is the kinetic energy of the particle. $E(U)$ takes into account that a particle loses energy in the deadlayer of the detector; it is determined experimentally for protons, while for

electrons $E \approx U$. $F(z)$ is the filter function defined by the properties of the pulseheight-analyzer

$$F(z) = \frac{1}{2}(\operatorname{erf} z - \operatorname{erf}(z - a_i)) \quad (3)$$

$\left(z = \frac{U - U_i}{\sqrt{2}\sigma}; a_i = \frac{\Delta E_i}{\sqrt{2}\sigma}\right)$. k_i therefore is the ratio of the channel rate which would be obtained for a noise-free channel, to the rate obtained in the real channel. For $j(E)$ a powerlaw $j(E) \sim E^{-\gamma}$ was adopted. The dependence of k_i on γ is very small for $\gamma \lesssim 5$, but rises beyond. It approaches unity when $\Delta U_i > 5\sigma$, as is to be expected (which is above channel 7 for protons, for electrons above channel 8).

This procedure of course is a first approximation, but of sufficient reliability for overview purposes. Whenever a detailed analysis is required, the energy spectrum will be calculated by solving the integral equation, which relates counting rate and differential flux. A similar procedure is being followed when angular distributions are evaluated, which significantly differ from isotropy, as has been shown by Richter (1972). Details are described by Keppler et al. (1976).

N_i^* , the true rate, is then, by definition zero (and of course may reach negative numbers for statistical reasons). The rates shown in Figure 9 are obtained through this procedure. This procedure is valid as long as background is due to galactic cosmic rays only (also during Forbush-type decreases), however breaks down if solar particles above some tens of MeV appear. Then to the CR-background rate a solar particle contribution is added which changes the ratio slightly. Then a more sophisticated procedure has to be applied. However, the difference is small as long as the energy spectrum is steep ($\gamma \geq 4$), and is relevant only during low intensity electron events, where counting rates are close to background, as electron detectors suffer from the full 4π contribution. The proton detector is protected by the coincidence shield, therefore in this case these effects may be ignored.

The proton detector is also sensitive to heavier particles, however, is not able to resolve their contribution (along with protons, $E > 80$ keV, α -particles with $E \gtrsim 100$ keV will be measured). So for brevity we refer for the rest of the paper to protons, as probably most of the contributions to the detectors counting rate is due to protons.

4. Instrument Performance

In the following section we shall show a few examples of measurements, obtained during the mission in order to demonstrate the instrument's capability. We do not intend to discuss the physical meaning of the observations here in any depth. It is, however, our intention to show the significance of high resolution measurements in deep space.

Figure 3 shows as an example a 16-channel-energy-spectrum, obtained for ions, presumably protons, in the energy range 80–700 keV during the passage of Helios-1 through the dusk magnetosheath on December 10, 1974, averaged over time and direction. At the time of magnetosheath crossing, a magnetospheric

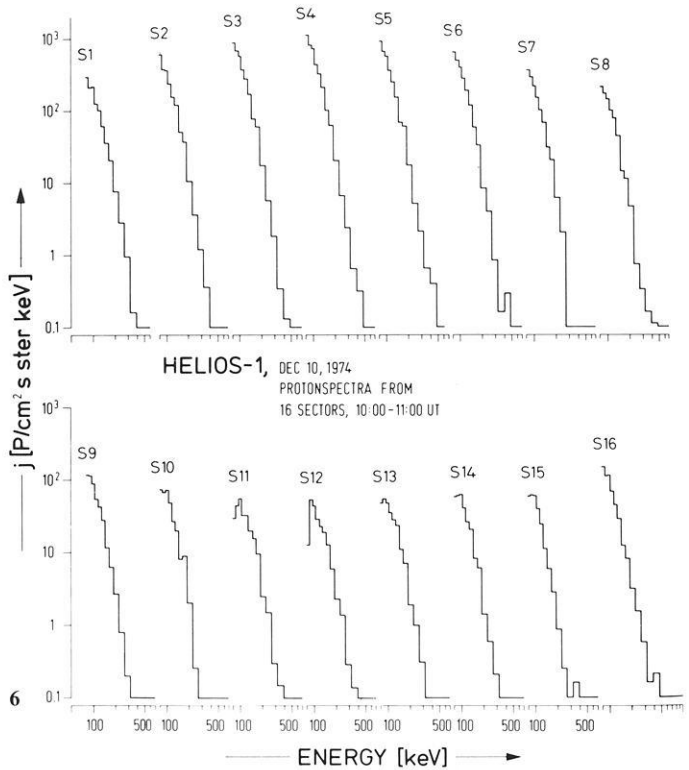
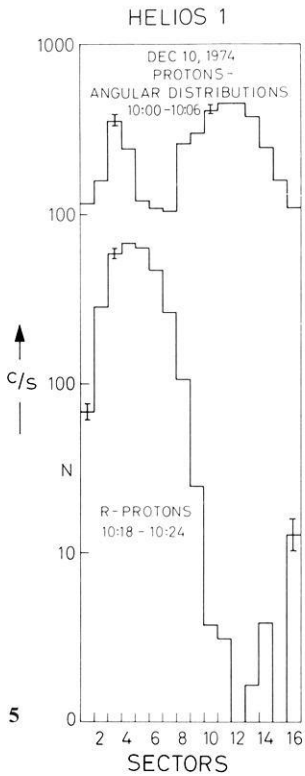
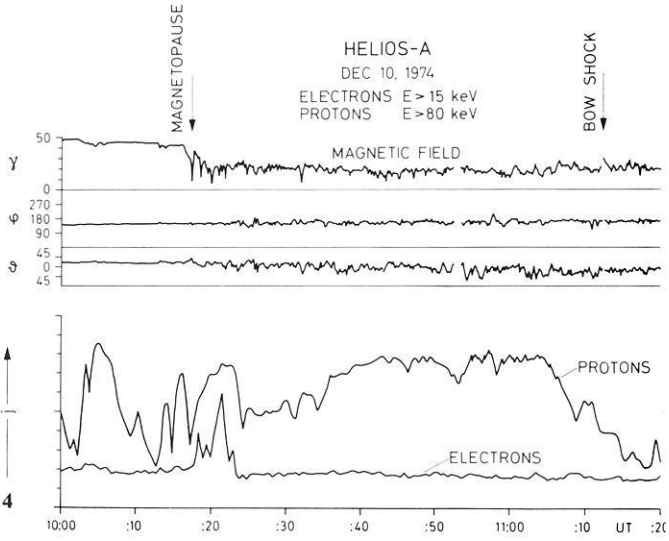
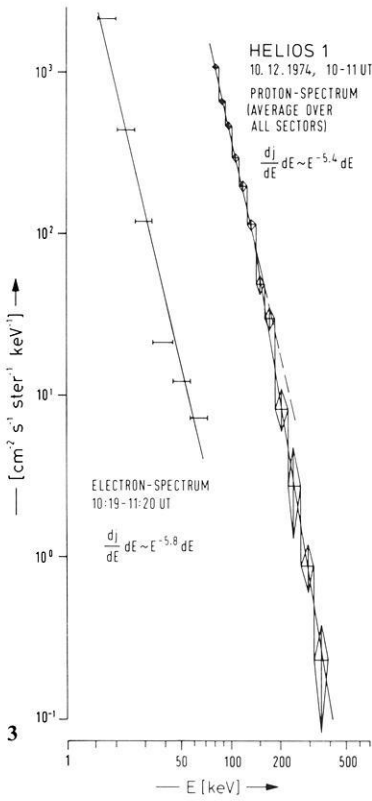
substorm was in progress ($K_p = 4^-$). It is likely, that these protons constitute a “proton burst”, i.e. particles released from the tail region. Those events have been described in the literature quite often (e.g. Sarris et al., 1977). At the same time the APL-instrument on IMP-7 (Sarris, personal communication) being in interplanetary space on the sunward side of the magnetosphere has detected a burst with peak flux at 10 UT. We therefore tentatively assume that both instruments observed the same event.

In Figure 3 we also show the electron spectrum obtained during the electron burst at 10:20 UT (Fig. 4) at the time of magnetopause crossing, again averaged over all directions. While the proton spectrum is time averaged over 1 h, the electron spectrum is only averaged over 1 min. Consequently, the proton spectrum could be obtained through 4 orders of magnitude in intensity with good statistical significance, while the electron spectrum in higher energy channels becomes statistically insignificant.

Figure 4 shows the intensity variations of electron- and proton-integral rate channels along with the magnetic field data throughout the magnetosheath. Magnetopause and bowshock crossing have been tentatively marked. Full time resolution is being utilized (13 s). It is seen, that there are statistically significant intensity variations within time scales of minutes. These fluctuations resemble fluctuations of the magnetic field, in particular those of theta, the angle out of the ecliptic plane. The bowshock crossing is assumed to have occurred at 10h11m30s UT as indicated by the magnetic field variation, accordingly the proton flux decayed gradually at this time and reached background levels afterwards. Figure 5 shows two examples of angular distributions of protons during magnetosheath crossing. It is seen, that there are remarkable changes in the anisotropy. Clearly the anisotropy is much more pronounced when utilizing 16 sectors. It would have been considerably underestimated, if e.g. only 8 sectors would have been used. Data shown are raw data, i.e. background has not been subtracted, nor was the distribution transformed to the frame of reference comoving with the plasma (see below). This would have changed the proton angular distribution quite certainly.

In Figure 6 we demonstrate the third important feature of this instrument, which is the determination of the energy spectrum from 16 directions. Only proton spectra are shown, electron fluxes were too low. It is these spectra, from which Figure 3 has been constructed by averaging over all directions. Most remarkable is the deviation of the spectra from monotony at low energies in sectors 10–15 (anti-sun-direction). Plasma flow in the magnetosheath is generally in the anti-sun-direction. Therefore in transforming these spectra to the comoving plasma frame of reference, they tend to become “lifted” at the low energy end. It is to be expected therefore, that in most of the magnetosheath measurements after transformation (see Ipavich, 1974) to the plasma frame the spectra from all directions become the same, and the directional distribution, showing its maxima in the solar direction, becomes isotropic. We have not done this here as plasma data have not been available to us.

On the other hand we note, that the measurements indeed show different spectra in different directions as is to be expected. However, this example (Fig. 6) demonstrates, that it is incorrect to assume e.g. power law spectra and then



apply the Compton-Getting transformation. This has often been done in the past, because spectral informations were sometimes derived from counting rates in 2 or 3 energy ranges only. In applying the Compton-Getting transformation intensity, angle and energy are being transformed. However, the concept as outlined by Ipavich (1974), which starts from power law approximations in the spacecraft frame, is not generally applicable. This is also shown by Figure 8 (from Keppler et al., 1974), where for a proton event on January 6, 1975, power law fits ($E^{-\gamma}$) have been applied to the measured data. γ is seen to vary considerably in the spacecraft frame (observed), but do not result, after transformation, in a unique spectral slope. This would have been expected, as the angular distribution (similar to Fig. 7, middle of panel, right side) in this event fits nicely to a cosine in angle.

Having this in mind, the Compton-Getting transformation should not be biased by unrealistic assumptions on the energy spectrum in the S/C-frame, but rather start from the measured flux in given differential energy channels and directions. Applying this procedure (Richter et al., 1977), one obtains the correct transformation of flux, energy and angle to the comoving frame of reference without a priori assumption.

In Figure 7 several examples of measured angular distributions are shown. These measurements have been made after the spacecraft has been tilted with its spin axis now normal to the ecliptic plane (2 days after launch). Bidirectional and unidirectional distributions for protons are shown (right panel) together with a distribution obtained during quiet times. The left panel (Fig. 7) shows two examples of electron angular distributions. Close to perihel, one of the four electron detectors (S2, Fig. 1) suffers from straylight. Despite its $120 \mu\text{g}/\text{cm}^2$ Al-contact, facing incoming particles, it was affected by light, if more than 6 solar constants were present. This was, however, restricted to the sun-viewing sector (No. 4) and did not affect the measurements as obvious from comparison of the two quiet time distributions (January 14, 1975 and March 5, 1975; perihel was on March 15, 1975).

In Figure 8 (left panel) we show as another example observations obtained during a proton event on March 18, 1975. Again (power law fits have been used here for simplicity) the spectral exponent is being determined in the 16 directions in the S/C frame. Using the solar wind velocity, this has been transformed to the solar wind frame to give the angular variation of the spectrum in the solar wind frame. It is seen, that in this case the differences in spectral slope are

Fig. 3. Proton and electron spectrum averaged in time and over all directions, for magnetosheath passage (December 10, 1974)

Fig. 4. Intensity variations of electrons ($E \geq 16 \text{ keV}$) and protons ($E \geq 80 \text{ keV}$) within the dusk magnetosheath shortly after Helios launch on December 10, 1974. Magnetic field data are shown along with the data (courtesy G. Musmann and F.M. Neubauer)

Fig. 5. Examples of angular distributions of electrons and protons (raw data) during magnetosheath crossing (December 10, 1974)

Fig. 6. Proton energy spectra from 16 different directions

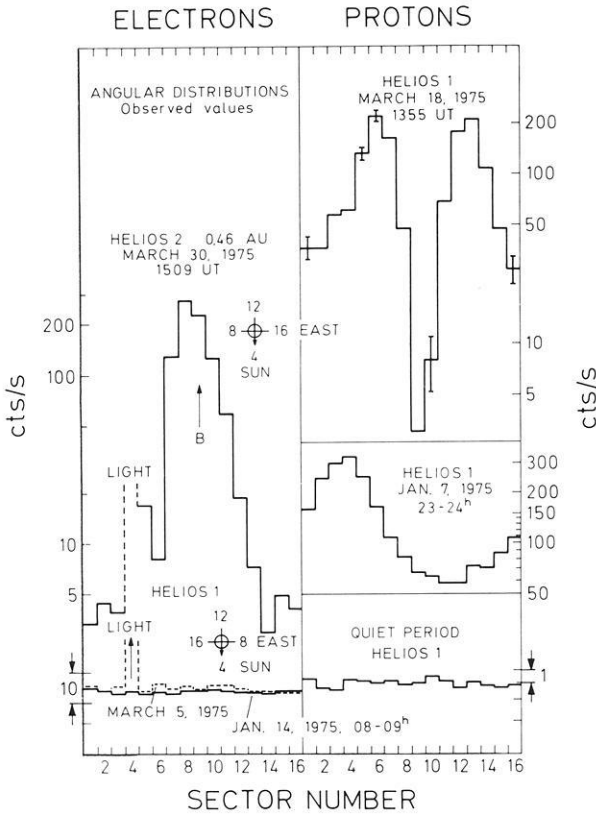


Fig. 7. Examples of angular distributions, measured with Helios-1 in interplanetary space (raw data)

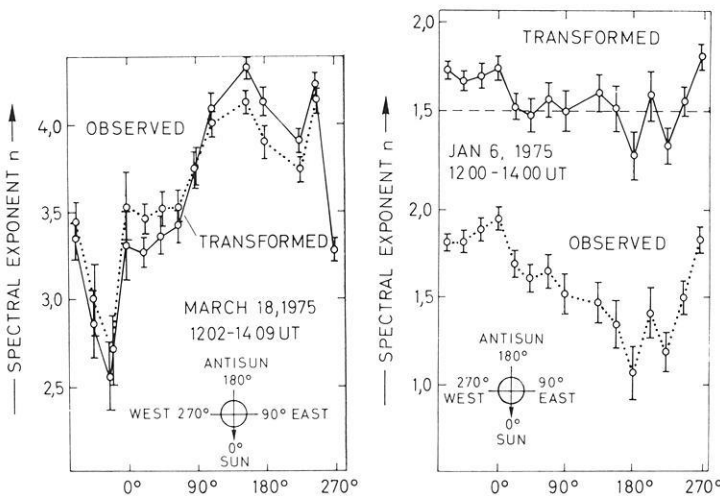


Fig. 8. Exponent of a power law fit to proton energy spectra from different directions, as observed and after being transformed to the frame of reference, comoving with the solar wind (Compton-Getting transformation)

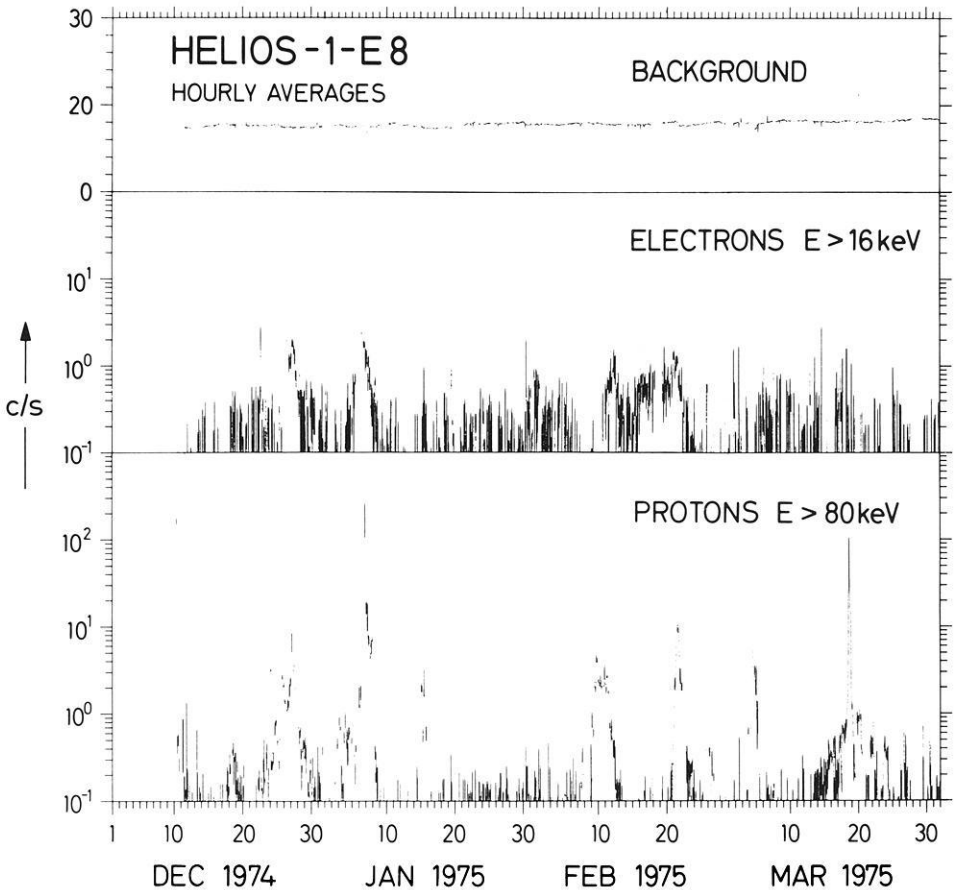


Fig. 9. Summary plot of 4 months of Helios-1 data, from launch to after perihelium. Proton- ($E \geq 80$ keV) and electron- ($E \geq 16$ keV) integral rates are shown along with the background detector rate. Background has been subtracted for both electron- and proton-rates

increased. This has to be interpreted as being indicative of different particle populations moving opposite to each other along the interplanetary field.

Figure 9 finally shows a summary of 4 months of Helios-1 data, displaying integral rates of protons (ions) ($E > 80$ keV), electrons ($E > 16$ keV) along with the background detector rate. Background has been subtracted by applying the procedure outlined in section 3. The scale has been cut off at 10^{-1} c/s, which is for this averaging time the limit below which no statistical meaningful conclusions may be drawn. Despite the fact that the sun was extraordinary quiet during this period, several events have been observed, some of which are corotating, some due to particles from active regions, some probably originating from interplanetary acceleration processes. One of these events (January 1975) will be discussed in a subsequent paper by Richter et al. (1975). The others will be dealt with in forthcoming work.

The importance of having high time resolution, high angular resolution and the capability of determination of energy spectra from different directions, is obvious from the examples shown above. It is this tool, which will enable more distinct conclusions on details of interplanetary low energy particle propagation and behaviour.

This work has been supported in part by the Bundesminister für Forschung und Technologie through grants RS-12, WRS-10/7 and WRS-10/8.

References

- Ipavich, F.M.: The Compton-Getting effect for low energy particles. *Geophys. Res. Lett.* **1**, 149–152, 1974
- Keppler, E., Nielsen, E., Richter, K., Umlauf, G., Wilken, B., Williams, D.J.: Directional variations of proton energy spectra. Presented at the 14th International Cosmic Ray Conference, München, August 18–28, 1975
- Keppler, E., Wilken, B., Richter, K., Umlauf, G., Fischer, K., Winterhoff, H.-P.: Ein Spektrometer für geladene Teilchen mittlerer Energie – Experiment E8 Helios –. Forschungsbericht des Bundesministers für Forschung und Technologie, BMFT-FB 76-14, 1976
- Richter, K.: A method of calculating the pitch angle distribution of particle fluxes based on rocket and satellite data. *IEEE Transact. Nucl. Science* **NS-19**, Nr. 4, 32–36, 1972
- Richter, A.K., Keppler, E., Richter, K., Wilken, B.: Observations of low-energy (>80 keV) protons ESP-shock spike-events in interplanetary space during January 6–8, 1975: *Helios 1. J. Geophys.*, this issue, 1977
- Sarris, E.T., Krimigis, S.M., Bostrom, C.O., Armstrong, T.P.: Simultaneous multispacecraft observations of energetic proton and electron bursts inside and outside the magnetosphere. *J. Geophys. Res.* to be published, 1977

Received January 31, 1977; Revised Version May 10, 1977

Interaction of Low-Energy (> 80 keV) Protons with the January 6 and 8, 1975, Shock Waves: Helios-1 Observations*

A.K. Richter and E. Keppler

Max-Planck-Institut für Aeronomie, D-3411 Katlenburg-Lindau 3, Federal Republic of Germany

Abstract. During January 6–8, 1975, both the fluxgate magnetometer (IGM, Braunschweig) and the plasma experiment (MPE, Garching) on board HELIOS 1 observed two shock-events separating certain regions in space, which exhibit different structures as far as the type and the magnitude of interplanetary fluctuations are concerned. At the same time the low-energy charged particle spectrometer (MPAE, Lindau) on board HELIOS 1 measured the energy- and directional-distribution of 80–6150 keV protons in 16 different energy- channels and in 16 different directions for each energy simultaneously. The influence of the observed interplanetary fluctuations on the energy-, the spectral- and the directional distributions of these low-energy protons are discussed in view of local acceleration mechanisms and interplanetary propagation effects.

Key words: HELIOS mission – Interplanetary shock waves – Proton observation in interplanetary space.

Introduction

On December 10, 1974, the solar probe HELIOS 1 was launched into a heliocentric orbit with an aphelion of ~ 0.98 AU and a perihelion of ~ 0.3 AU, respectively. The spaceprobe is spinning at a rate of about 1 rev./s with its spin axis normal to the ecliptic plane. The charged particle spectrometer (CPS) of the Max-Planck-Institut für Aeronomie, Lindau, Germany, on board HELIOS 1 measures electrons and protons in the energy range 20 keV – 1 MeV and 80–6150 keV, resolved in 16 quasilogarithmically scaled energy-intervals and in 16 angular directions. The separation of the electrons and protons is performed by an inhomogeneous magnetic field of ~ 800 Gauss. The instrument's aperture is pointing radially outwards of the spaceprobe in the ecliptic plane with an

* Dedicated to Prof. G. Pfozter on the occasion of his 68th birthday

opening angle of 10° half angle. At the highest bitrate energy-integral, angular distributions for electrons or protons are obtained every 13.5 s, while a full set of spectral measurements in all 16 directions takes 108 s (Keppler et al., 1976 and 1977). Thus, the CPS instrument is marked by its high time-, energy- and directional-resolutions and by the fact that it is the first instrument deep in interplanetary space to observe protons and electrons as low in energy as 80 and 20 keV, respectively. In combination with the plasma- and magnetic field experiments this CPS experiment is therefore favoured to study "wave-particle-interactions" in interplanetary space well away from the influence of the earth's bow shock.

In this article we want to report on the interaction of two shock-waves and associated magnetic field fluctuations, as observed both by the fluxgate magnetometer (Institut für Geophysik und Meteorologie, Universität Braunschweig) and by the plasma experiment (Max-Planck-Institut für Extraterrestrische Physik, Garching), with low-energy protons, as detected by our CPS experiment during January 6–8, 1975. We shall discuss the influence of these magnetic fluctuations on the energy, the spectral, and the directional distributions of these low-energy protons in view of local and global acceleration mechanisms and interplanetary propagation effects.

Observations of the Interplanetary Medium

During January 6–8, 1975, HELIOS 1 was located at a distance of about 0.92 AU away from the sun, and at a mean earth-sun-probe angle of about 8° east of the earth-sun line. At this time the spaceprobe was therefore well away from the influence of the earth bow shock. According to the observations of the CPS and the high-energy cosmic ray experiments during this period of time, HELIOS 1 was right at the trailing edge of a solar cosmic ray event which was, most probably, associated with a flare that took place on the sun at January 5, 08.00 UT. During the decreasing part of this event both the fluxgate magnetometer and the plasma experiment observed two well defined shock waves: The first one on January 6, at about 20.44 UT, and the second one on January 8, at about 00.22 UT. In Figure 1 we show the locations of HELIOS 1 during January 6–8, 1975, and of the planes of the two shocks in question projected into the ecliptic plane. The associated shock normals are perpendicular to these two planes. Following Neubauer (1977, private communication) the characteristic parameters of the first, the January 6 shock are:

$$\left. \begin{aligned} \Delta N_p &\approx 6.7 \text{ (cm}^{-3}\text{)} \\ \Delta V_p &\approx 82.1 \text{ (km}\cdot\text{s}^{-1}\text{)} \\ \Delta F &\approx 5.8 \text{ (}\gamma\text{)} \\ \varphi_s &\approx 335.2^\circ \\ \theta_s &\approx 30.1^\circ \\ V_s &\approx 625 \text{ (km}\cdot\text{s}^{-1}\text{)} \\ \mathbf{B}_1 \cdot \mathbf{n} &\approx 0 \end{aligned} \right\} \quad (1)$$

HELIOS 1: January 6-8, 1975

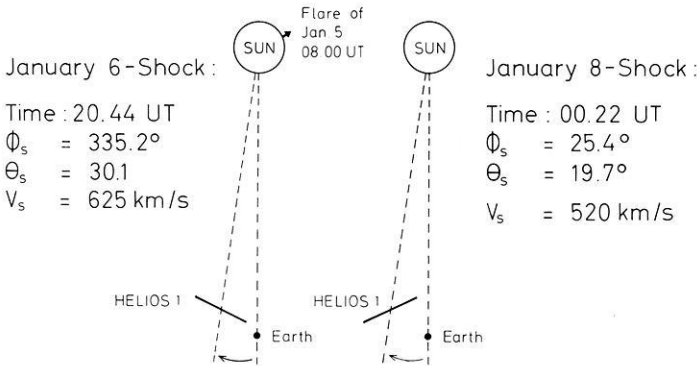


Fig. 1. Location of HELIOS 1, the earth and the two shock-planes during January 6-8, 1975

Thereby N_p and V_p denote the solar wind density and velocity as measured for its proton component, respectively, F the magnitude of the interplanetary magnetic field \mathbf{B} , \mathbf{n} the vector of the shock normal with its angles φ_s and θ_s , where φ (Phi) measures in the ecliptic plane with $\varphi=0^\circ$ pointing towards the sun, and θ (Theta) out of the ecliptic plane with $\theta=0^\circ$ in the ecliptic plane, and V_s the shock speed in the direction of its normal. Δ stands for the difference of the pre- (index 1) to the post-shock (index 2) values of the parameters in question. For the second, the January 8 shock Neubauer et al. (1977) quote the following values:

$$\left. \begin{aligned}
 \Delta N_p &\approx 3.12 \text{ (cm}^{-3}\text{)} \\
 \Delta V_p &\approx 50.0 \text{ (km}\cdot\text{s}^{-1}\text{)} \\
 \Delta F &\approx 5.9 \text{ (}\gamma\text{)} \\
 \varphi_s &\approx 25.4^\circ \\
 \theta_s &\approx 19.7^\circ \\
 V_s &\approx 520 \text{ (km}\cdot\text{s}^{-1}\text{)} \\
 \mathbf{B}_1 \cdot \mathbf{n} &\neq 0
 \end{aligned} \right\} \tag{2}$$

Though these two shocks seem to have some similarities (e.g. in their shock speeds and the changes in the proton densities, velocities and the magnitudes of the interplanetary magnetic field across the shocks) there is, however, one very important difference between these two shocks: The first shock-wave is more or less perpendicular while the second one is oblique to the averaged pre-shock field direction. This has, as we shall see, some important consequences for the interplanetary low-energy ions.

In the two lower panels of Figure 2, labelled E2-IGM and E1-MPE, we have plotted 40 s averages of the magnitude of the interplanetary magnetic field (F) in gamma and its angles phi (φ) and theta (θ), and the solar wind velocity (V_p) in km/s and its density (N_p) in cm^{-3} , as measured for the proton component. From these figures it readily follows that these two shock waves

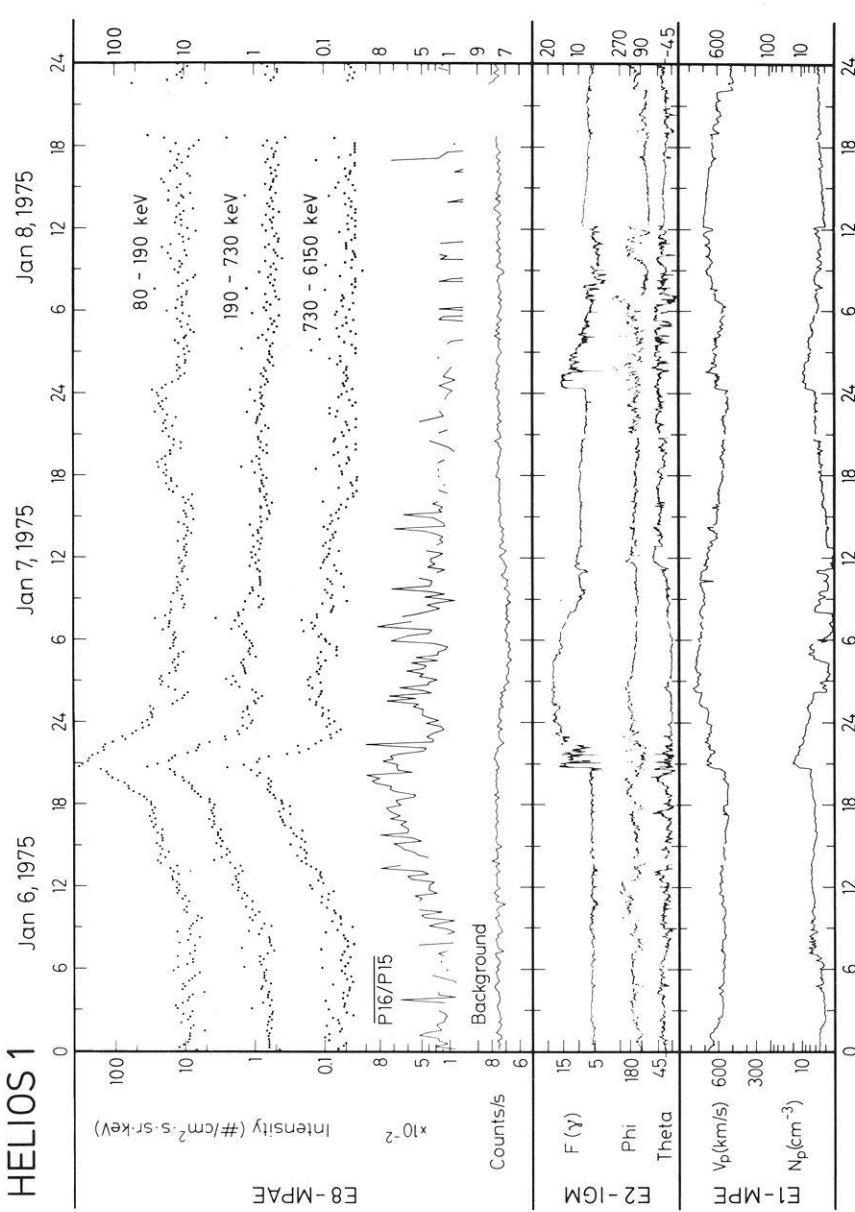


Fig. 2. Time profiles of the ion intensities at different kinetic energies, of the magnitude and the directional angles of the interplanetary magnetic field, and of the solar wind velocity and density during January 6-8, 1975

separate different regimes in interplanetary space with different intensities in the plasma and magnetic-field fluctuations: In the pre-shock regime of the first shock (hour 0-6 of January 6) we find only little fluctuations in the magnetic field magnitude, the solar wind velocity and the proton density. Only for the period from hour 5-9 of January 6 there are some larger (N_p is plotted logarithmically) irregularities in the density. However, taking the directions of the inter-

planetary magnetic field into account, we first find large directional fluctuations (especially of the angle ϕ) of increasing amplitudes for a decreasing distance from the first shock front after approximately hour 6. For the subsequent discussion we shall assume that these fluctuations are primarily of Alfvénic type. After we have passed the first shock front we enter into a second regime with enhanced density-fluctuations. These fluctuations could be due to “acoustic” waves most probably generated by the interaction of the shock wave with the pre-shock Alfvén-waves: If the shock normal and the directions of both the background field and the wave-vector of the Alfvén-waves are not co-planar, acoustic waves are generated. This second region extends right up to the tangential discontinuity occurring at 22.18 UT of January 6. After this discontinuity the fluctuations are smoothed out as far as the intensity and the direction of the interplanetary magnetic field are concerned. The interplanetary medium is now characterized by a large gradient in the magnetic field strength of about $12 \text{ gamma}/5.5 \text{ h}$. At about 11.00 UT of January 7, we enter into a fourth regime which exhibits a similar structure to the pre-shock region of the first shock wave: This regime is again dominated by transverse, directional fluctuations of increasing amplitude. After passing the second shock wave which occurs at 00.22 UT on January 8 there are again superimposed density fluctuations, which last until the tangential discontinuity at 12.13 UT of January 8 is reached. Behind this discontinuity the interplanetary fluctuations are smoothed out nearly instantaneously with a small magnetic field gradient being superimposed.

Observations of Low-Energy Protons

In the upper half of Figure 2 (labelled E8-MPAE) we have plotted 12 min averages of the omnidirectional intensities ($\text{particles} \cdot \text{cm}^{-2} \cdot \text{s}^{-1} \cdot \text{sr}^{-1} \cdot \text{keV}^{-1}$) of the 80–190 keV, 190–730 keV and the 730–6150 keV protons as observed by the CPS experiment on board HELIOS 1. The intensities of the medium- and the high-energy channel have been multiplied by a factor of 10 and 100, respectively. Below these three curves the averaged ratio of the ion-energy channels 16 (730–6150 keV) and 15 (585–730 keV) is shown. If the spectral dependence on energy of the protons is known, this ratio is a measure for the proton-to-alpha ratio for alphas with energies greater than about 350 keV/nucl. The fifth and final curve represents the counts/s-time profile of the 4π -omnidirectional cosmic-background radiation as observed by the background telescope of the CPS experiment.

From an overall inspection of Figure 2 it readily follows that there is a strong correlation between the different intensity profiles of the low-energy protons and the large-scale fluctuations of the plasma and magnetic field parameters: (1) The intensities of the $> 80 \text{ keV}$ protons peak directly at the first shock front. (2) Around the first shock front the intensities of the three energy intervals indicated are more or less symmetrically distributed. This distribution is narrowest for the $> 730 \text{ keV}$ protons, and relatively wide-spread and asymmetric with a much slower decrease toward the post-shock regime for the 80–190 keV protons. (3) In case of the first shock the intensities of, in particular, the $> 190 \text{ keV}$

protons start to increase already far ahead of the shock front. This increase starts at around 9 o'clock on January 6, and it takes place over exactly that region in space where the magnetic field fluctuations are predominantly Alfvénic. The intensities of the low- and medium-energy protons get flatter and gain local maximum values at around 17.00 h. (4) Combining (2) and (3) we find that the intensity increases in the pre-shock medium of the first shock-wave seem to take place in two separate steps: First, there is the rather slow, long-lasting increase starting well *ahead* of the shock. Secondly, there is the more rapid, steeper well defined increase to the overall maxima *at* the shock front itself. Especially from the low- and medium-energy particles' intensities it follows that this second increase seems to take place shortly after the first increase flattens off. For the 80–190 keV protons this first-step increase is smallest (a factor of about 3.7 in intensity) and largest for the higher energy ions (~ 11.3), whereas the second-step increase is largest for the low-energy protons (~ 8.5) and smallest for the 730–6150 keV protons (~ 3.1). (5) In case of the second shock wave the situation is more or less inverse: Now, the intensities of the low-energy protons increase ahead of the shock front, whereas there is nearly no effect of the shock wave on the overall tendency of the intensities of the > 190 keV protons. This first step increase of the intensity of the low-energy ions starts at about 16.00 h on January 7. Contrary to the first shock-wave there is no pronounced intensity increase associated with the second shock for the > 80 keV protons, i.e., there is no pronounced second-step increase. (6) For the 80–190 keV protons, however, the first-step increases ahead of the two shock-waves seem to have one common feature: In both cases the intensities increase by the same factor of about 3.7 over the same period of time of about 7.8 h. (7) Behind the first shock the intensities stay well above background for at least another 10 h. Especially for the > 190 keV ions there are, however, several sharp decreases of the corresponding intensities. The reason is that during that time the interplanetary magnetic field turns out of the plane of the ecliptic by 45° and more. Behind the second shock-wave the intensities are roughly equal to the background intensities observed at around 0–6 h on January 6. (8) Between the overall intensity decrease after the first shock and the following increase ahead of the second shock, all intensities gain locally their background values: For the 80–190 keV protons from about 12.00–16.30 h on January 7 and for the 190–730 keV ions from about 14.15–17.45 h. Thus, the two intensity-time histories associated with the two shock-waves are well separated in space and/or time. (9) The intensity-time profile of the P16/P15 ratio indicates that there is an increase of the alpha-to-proton ratio ahead of the first shock. This ratio exhibits roughly the same time history around the first shock-wave as the 730–6150 keV protons. (10) The overall background radiation shows a well defined, long lasting decrease after the first tangential discontinuity has passed the spaceprobe. This is known as a Forbush decrease.

As the background radiation is very smooth and steady and as no extraordinary solar activity has been observed over the time period in question, we may conclude that the strong correlation mentioned above is due to interactions of the ions with the shock waves and associated fluctuations. Thus, in order to study the spectral dependence of the protons on energy, the anisotropy

and the direction of anisotropy, we have to transform the corresponding intensities, energies and characteristic angular directions from the spacecraft into the solar wind frame. As there are observations available in 15 energy intervals in the 80–730 keV range, we are able to undertake the most general, non-linear Compton-Getting transformation between the two frames by making no assumptions about, for instance, the spectral shape, the dependence of the spectral index γ on the direction etc. After performing this transformation we calculated the value A of the anisotropy from the maximum (I_{\max}) and minimum (I_{\min}) intensities of the angular directions respectively, via the equation

$$A = (I_{\max} - I_{\min}) / (I_{\max} + I_{\min}). \quad (3)$$

As the CPS instrument is pointing in the ecliptic plane, the directional information (intensity *vs.* direction) can be transformed into the angular information (intensity *vs.* ecliptic angle φ (Phi)). Thus, we are able to plot intensity *vs.* φ and time. Determining then the overall omnidirectional intensities of the 15 energy-channels, we are able to calculate the spectral index γ by assuming a power-law dependence of the intensity on energy and by applying a least-squares fit procedure.

In Figures 3a and b we have plotted the 12 minutes averaged values of the intensities J (protons/cm²·s·sr·keV) of 100 keV protons *vs.* the ecliptic angle φ and time t in the upper halves, and of the values A of the anisotropy as defined by equation (3) *vs.* time t in the lower halves. For the directional plots of the intensities (upper halves) we have subjected the J -values to a grey-shading scale of 6 settings, ranging from black (lowest intensities) to white (highest intensities). On the right hand sides we have indicated the corresponding threshold values. As the intensities associated with the first shock are, on the average, much higher than for the second shock-wave, we had to make two separate plots in order to show the effects. Figure 4 shows the distributions of the magnitude and angles Phi and Theta associated with the interplanetary magnetic field \mathbf{B} (see Fig. 1) and of the exponent (spectral index) γ for those time-periods around the two shock-waves where the intensities are above their background values.

From these three Figures we find: (11) In case of the first shock (Fig. 3) the value of the anisotropy starts to increase and to gain overall higher values in front of the shock wave, and to decrease more or less abruptly across the shock front itself. In the pre- and post-shock regions the anisotropy is rather high. However, it exhibits some longer-lasting depression around 9–12 o'clock on January 6. This is about the time interval where the interplanetary magnetic field starts to fluctuate in its direction, especially in the angle φ . (12) In case of the second shock-wave (Fig. 3b) the anisotropy increase is not very much pronounced, nor its decrease across the shock front itself. In the pre-shock regime the anisotropy stays at about 0.8 and is therefore rather high. (13) Turning to the directional plots of the anisotropy, we find around the first shock-wave: There is well defined bi-directional anisotropy in the pre-shock region from hour 0 to about hour 17 on January 6. Note the enormous difference in the intensity values, ranging from below 5 up to over 200 protons/

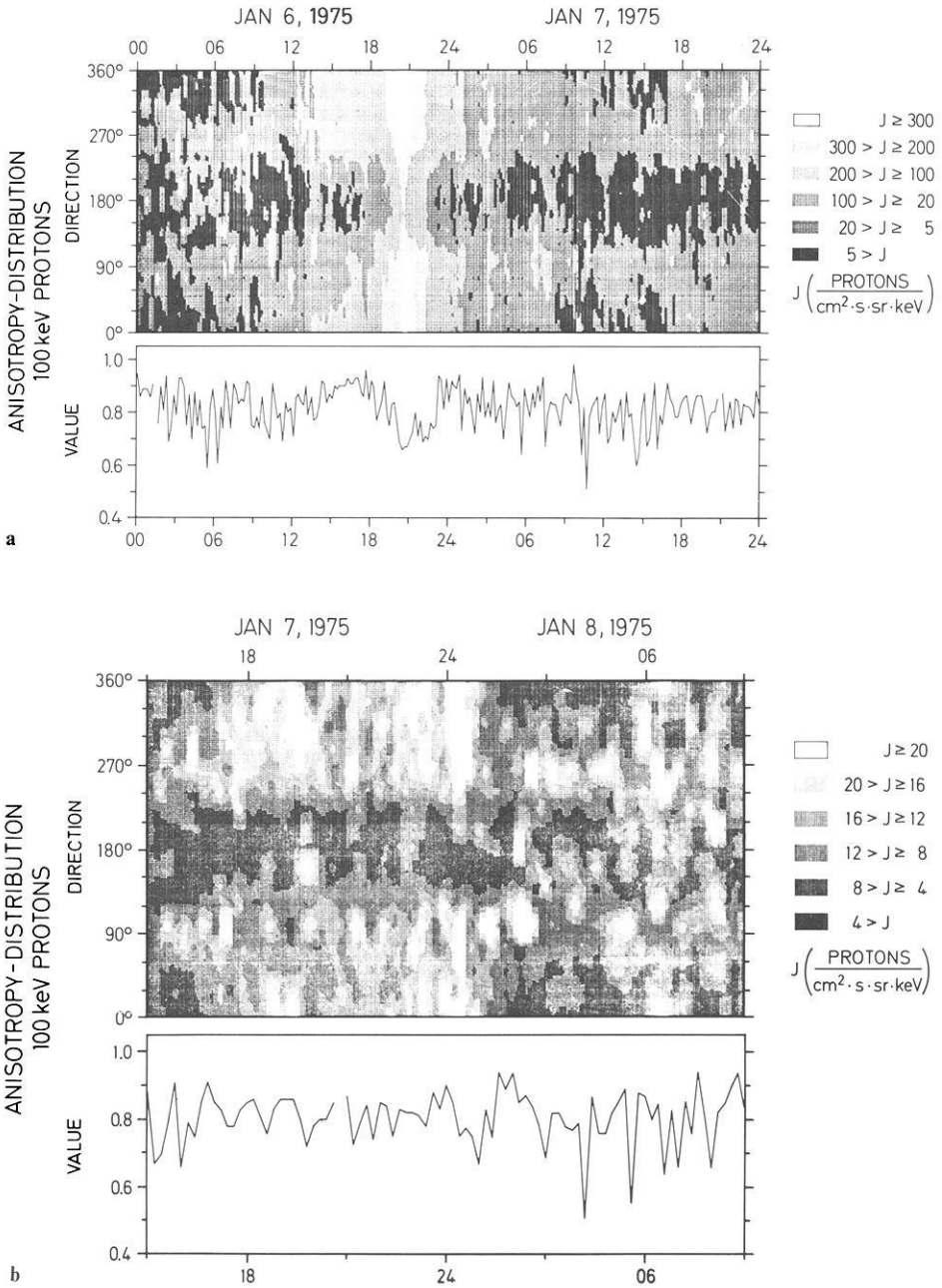


Fig. 3a and b. Distribution of the directional anisotropy (intensity vs. time and ecliptic angle ϕ) and the anisotropy value vs. time for 100 keV protons transformed into the solar wind frame around the two shock-waves observed on January 6 and 8, 1975

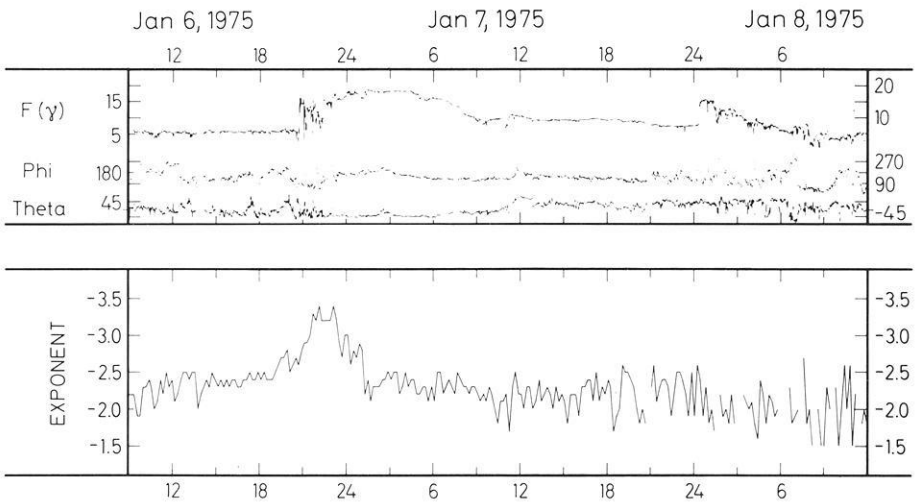


Fig. 4. Time profiles of the magnitude and the directional angles of the interplanetary magnetic field, and of the spectral exponent γ determined by a least-squares fit procedure of the transformed omnidirectional intensities of 16 energy-channels ranging from 80–6150 keV

$\text{cm}^2 \cdot \text{s} \cdot \text{sr} \cdot \text{keV}$. Over this period of time the maximum fluxes are separated by about 180° , indicating a flow of the 100 keV protons towards and away from the shock front at the same time. This type of a strong, bi-directional anisotropy is also found in the post-shock region from about hour 23 onwards. It should be noted that these two bi-directional regimes coincide with the pre- and post-shock intensity distributions of the 80–190 keV ions in Figure 2. Over that period of time, i.e., from hours 17–23, where in Figure 2 the low-energy protons exhibit their second-step increase to their overall maximum, their anisotropy distribution becomes more isotropic, and therefore the value of their anisotropy decreases. (14) In case of the second shock wave we again find a rather strong, bi-directional anisotropy distribution in front and behind the shock plane. The directions of the corresponding maximum particle fluxes are again separated by approximately 180° , i.e., the low-energy protons are streaming towards and away from the shock plane at the same time. Around the shock front itself the distribution of the 100 keV protons again gets more isotropic. (15) We want to mention that for 300 keV protons, i.e., for particles belonging to the second of our three energy intervals depicted in Figure 2, we find roughly the same overall distributions around the two shocks what the directional anisotropy as well as the anisotropy value is concerned. (16) Turning finally to Figure 4 we find for the spectral index γ that it gains overall higher values of around 2.4 in the pre-shock regime of the first shock at around 14.00 h on January 6, and of about 2.3 in the pre-shock region from around hours 1–9 of January 7. Across the shock front itself γ increases only slightly. Its absolute maximum value of 3.4, however, the spectral index reaches well *behind* the shock front at about hours 22.00–23.30. In case of the second shock-wave we can state that γ exhibits no systematic changes in front, at, or behind the

shock. However, it should be noted that the mean overall value of γ drops from about 2.2 to a value of 2.0 across the shock plane with a change in the maximum-to-minimum values of about 2.6 to 1.7.

Discussions

According to the theory of, e.g., Scholer and Morfill (1975) and Morfill and Scholer (1977a) (see also references cited in there), cosmic ray particles can be accelerated by interaction with oblique shock waves due to the induced electric field in the shock front (first order Fermi acceleration). If the particles' mean free path in the pre-shock region of the shock is small enough, then a repeated interaction with the shock front and thus a repeated acceleration can take place, while the shock is propagating from the sun out to 1 AU. The authors have shown that already 5–10 interactions per AU with a normal strong shock wave and relatively *high* diffusion coefficients of the order of $(2-5) \times 10^{20} \text{ cm}^2 \cdot \text{s}^{-1}$ for the pre-shock region can already accelerate protons from thermal energies to some hundreds of keV. It is stressed that this type of acceleration is by more than an order of magnitude more effective than any pile-up process ahead of shock fronts discussed by, e.g., Palmer (1972). Monte-Carlo model calculations have led to the following results: First, the repeated acceleration leads to a maximum intensity of the accelerated particles which occurs at some time τ (hour) *before* the shock arrives. Roughly it is $\tau \propto 1/V_s$ and energy-independent, where V_s is the shock velocity. Then the intensity decreases rather rapidly behind the shock by about an order of magnitude within one hour. Second, the actual maximum value of the intensity depends on the value of the diffusion coefficient in the pre-shock region. If this value is, e.g., too high the particles being accelerated once can easily 'disappear' into interplanetary space. Third, the anisotropy value A increases in front of the shock-wave and then decreases across the shock front itself. Fourth, due to the acceleration process itself the anisotropy distribution in the pre-shock regime should be bi-directional with a difference of 180° in the streaming directions of particles of maximum intensities, indicating that particles are propagating towards and away from the shock at the same time. Particle increases due to this type of acceleration process are sometimes called 'ESP (*Energetic Storm Particle*) Events'. From the discussion on the ESP-acceleration mechanism it directly follows that it has to operate for a rather long time (t_{ESP}) in order to produce significant increases in the particles' intensity to be observed above certain energy-thresholds (e.g., 80 keV for our CPS instrument) and well above the instrumental background.

Following Sarris and Van Allen (1974) a very intensive acceleration of charged particles can take place, if the shock wave is nearly perpendicular, i.e., if the pre-shock magnetic field is almost parallel to the shock surface itself. Schindler (1965) has shown that this acceleration is not of the type of first or second order Fermi acceleration. In this case low-energy protons, e.g., can be accelerated nearly instantaneously up to ε -times their initial energy,

where $\varepsilon = B_2/B_1$ is the ratio of the averaged magnetic strengths in the post- and pre-shock regions, respectively. If t_{\parallel} is the time that the pre-shock magnetic field stays parallel to the shock front, and if t is the time spent by an ion in the shock front, then the only restraint for this fast and strong acceleration mechanism is that t should be less than t_{\parallel} . Then for the peak-to-background (p/b) intensities one roughly finds $p/b = \varepsilon^{\gamma+1}$, where γ is the ion spectral index. As the time t is roughly proportional to the particles' initial rigidity, this mechanism is strongest for the low-energy ions. Due to fluctuations in the direction of the interplanetary magnetic field in the pre-shock regime, both the background field and the shock front will stay parallel only for a short time. Thus, this acceleration mechanism is only a local effect, and it will mostly operate only for a short time (t_{SSE}). Particle increases due to this kind of acceleration are called "Shock-Spike Events". From the discussions above it clearly follows that $t_{\text{SSE}} \ll t_{\text{ESP}}$.

Studying energetic charged particles in association with interplanetary oblique shocks one rather often finds increases in their intensities in the post-shock regimes. According to Morfill and Scholer (1977b) these 'Post-Shock Events' could be due to the following post-shock acceleration processes: First, after a shock wave there are out- and inwardly propagating waves present. Thus, there is a strong possibility of second order Fermi acceleration behind shock waves. Second, there are very often more acoustic waves present after a shock than in the quiet solar wind in front of the shock. This could lead to particle acceleration by nonlinear wave-particle interactions. Third, due to an enhanced gradient of the solar wind velocity after the shock front the adiabatic deceleration could be much smaller in the post-shock regime. Another, different theory on the formation of these post-shock events has been discussed by Sarris and Van Allen (1974): Whenever an oblique shock becomes a perpendicular one, particles are instantaneously accelerated in the way discussed above. Due to the directional fluctuations of the post-shock magnetic field these accelerated particles very easily are able to penetrate into the post-shock regime and to cause an increase in the overall particles' intensity. However, there should be at least two differences in the mechanisms mentioned: First, the time-scale of the first process to operate (t_{PSE1}) and of the second one (t_{PSE2}) should be such that $t_{\text{PSE2}} \ll t_{\text{PSE1}}$. Second, if the first process is primarily a Fermi process, then the directional anisotropy should be bi-directional for the first mechanism, but primarily uni-directional for the second one.

Combining the observational results for the intensity-, the anisotropy-, and the spectral index-time profiles of the >80 keV ions in Figures 2-4 together with the theoretical studies summarized above, we propose that the particles' intensity distributions during January 6-8, 1975, can be understood in terms of classical ESP-, Shock-Spike-, and Post-Shock-Events in the following sense: (A), the first-step intensity increases *in front* of the two shock waves are ESP-Events in the sense discussed above. (B), the second-step intensity increases *at* the first shock-wave a Shock-Spike-Event in the sense mentioned before. (C), the high, but overall decreasing intensities behind the first shock are due to post-shock acceleration mechanisms. In the following three sections we shall briefly list our arguments and draw some implications:

(A) The intensity of the >730 keV protons starts to increase already 10 h before the first shock arrives, or of the >80 keV ions at least 8 h in front of the second shock. In both cases there is a well defined *bi-directional* anisotropy with a separation by 180° . This indicates that protons are propagating towards the shocks and away from them into the pre-shock regions at the same time. We want to emphasize that this holds even for the 100 keV protons. Thus, even for these low energies some kind of “diffusive” process has to take place at least in the pre-shock regimes. In case of the first shock the anisotropy value does increase in front of the shock-wave, and does decrease drastically across the shock front. We find relatively high values of the spectral index of ~ 2.4 over the time-periods in question, which might also indicate that some kind of acceleration takes place. At least for the 80–730 keV protons we find some local intensity maxima $\tau \approx 4\text{--}5$ h in front of the first shock-wave. Using the relation of Morfill and Scholer, we find, because of equation (1), $\tau \approx 5.6$ h, and therefore some coincidence. However, in contrast to theory the τ -values are not energy-independent: The τ -value for the 730–6150 keV protons is much smaller than for the 80–730 keV ions. We believe that this is due to a strong energy-dependence of the diffusion coefficient in the pre-shock medium in the sense that this diffusion coefficient increases for decreasing energies. That this could be indeed the case can also be deduced from the different values for the p/b -ratios for the three energy-intervals depicted in Figure 2: In accordance to theory, we find higher values ($p/b \approx 11.3$) for the 730–6150 keV protons, however, only $p/b \approx 3.7$ for the 80–730 keV ions (for a second argument for our hypothesis see also (B)). In case of the second shock the situation is inverse: Now the ESP-type behaviour increases for decreasing energies. Thus, the magnetic fluctuations in front of the second shock should be such that the particles’ mean free paths should be smaller for the lower-energy protons. Another possibility could be that the second shock was formed somewhere between sun and earth, and therefore did not last long enough to accelerate thermal particles to energies much larger than 200 keV.

(B) The intensities of protons of all energies >80 keV peak directly at the shock. The anisotropy gets omni-directional. In accordance with the theory the shock-spike acceleration is rigidity dependent: We find larger intensity increases for the low-energy protons with $p/b \approx 8.5$ for the 80–190 keV particles than for the higher-energy ions, for which $p/b \approx 3.1$ in the 730–6150 keV range. Using Figures 2 and 4 we calculated a value for p/b predicted by theory of ~ 8.4 , which is in excellent agreement with the value for the low-energy protons. The more or less symmetric intensity distributions on the two sides of the shock could be due to the following effect: The accelerated particles can penetrate into the up- and down-stream medium whenever, due to the large-amplitude directional fluctuations of the magnetic field, both the field direction and the direction of the shock front are oblique and no longer parallel to each other. These particles would then only steam away from the shock, i.e., they would be characterized by an uni-directional anisotropy distribution. Following Figure 3 a the clear bi-directional anisotropy gets indeed mixed up around 18.00 h when, according to Figure 2, we find the onset of the second-step increase of the intensity of the 80–190 keV protons. As was stated in (2), the intensity

distributions directly at the first shock are much broader for the low- than for the high-energy protons. Again (see also (A)) we believe that this is due to an energy-dependence of the pre- and post-shock diffusion coefficients in the sense, that they are larger for the 80–190 keV than for the 730–6150 keV ions.

(C) If the first-step particles' increases in front of the first shock are due to an ESP event, then the intensities do not, as they should according to theory, decrease by an order of magnitude within one hour behind the shock-wave. Quite contrary, at least for the 80–190 keV protons the post-shock intensity remains as high as for the maximum value of the ESP event itself. Thus, some particle release into the post-shock regime and/or some type of post-shock acceleration has to take place. We believe that at least about the time of observation the acceleration hypothesis should be favoured: First, the increasing value of γ could be some index for such a mechanism. Second, the clear *bi-directionality* of the anisotropy over this region (Fig. 3a) is a strong argument for a Fermi-type acceleration mechanism in the post-shock region. As was stated before (7) the several sharp decreases of the intensities are due to the fact that during these time-intervals the interplanetary magnetic field turns out of the ecliptic plane by 45° and therefore out of the cone of acceptance of our instrument.

Acknowledgements. We are very grateful to Prof. F. Neubauer and Dr. G. Musmann (IGM, Braunschweig) and Drs. H. Rosenbauer and R. Schwenn (MPE, Garching) for submitting the magnetic field and plasma observations prior to publication. We also want to thank Drs. K. Richter and M. Schüßler for their assistance.

This work was supported in part by the Bundesministerium für Forschung und Technologie, grant WRS 10/8.

References

- Keppler, E., Richter, A.K., Richter, K., Umlauf, G., Wilken, B., Williams, D.: A Survey on Measurements of Medium Energy Protons and Electrons obtained with the Particle Spectrometer E8 on Board of HELIOS, *J. Geophys.*, this issue, 1977
- Keppler, E., Wilken, B., Richter, K., Umlauf, G., Fischer, K., Winterhoff, H.P.: Ein Spektrometer für geladene Teilchen mittlerer Energie: Experiment E8 HELIOS, BMFT-FB W 76-14, 1976
- Morfill, G.E., Scholer, M.: Influence of Interplanetary Shocks on Solar Particle Events, *Astrophys. Space Sci.* **46**, 73–86, 1977a
- Morfill, G.E., Scholer, M.: Der Diffusionskoeffizient hinter interplanetaren Stoßwellen, Frühjahrstagung der Arbeitsgemeinschaft Extraterrestrische Physik, Braunschweig, Vortrag C8-1, 1977b
- Neubauer, F.M., Musmann, G., Dehmel, G.: Fast Magnetic Fluctuations in the Solar Wind: HELIOS 1, *J. Geophys. Res.*, in press, 1977
- Palmer, I.P.: Shock Wave Effects in Solar Cosmic Ray Events, *Solar Phys.* **27**, 466–477, 1972
- Sarris, E.T., van Allen, J.A.: Effects of Interplanetary Shock Waves on Energetic Charged Particles, *J. Geophys. Res.* **79**, 4157–4173, 1974
- Schindler, K.: Adiabatic Orbits in Discontinuous Fields, *J. Math. Phys.* **6**, 313–321, 1965
- Scholer, M., Morfill, G.E.: Simulation of Solar Flare Particle Interaction with Interplanetary Shock Waves, *Solar Phys.* **45**, 227–240, 1975

Helios-1 Faraday Rotation Experiment: Results and Interpretations of the Solar Occultations in 1975

H. Volland and M.K. Bird

Radioastronomisches Institut, Universität Bonn,
Auf dem Hügel 71, D-5300 Bonn, Federal Republic of Germany

G.S. Levy, C.T. Stelzried, and B.L. Seidel

Jet Propulsion Lab., Pasadena CA 91103, U.S.A.

Abstract. The polarization angle of the HELIOS-1 downlink signal has been monitored during two solar occultations in 1975 at two widely separated ground stations. Significant Faraday rotation of the signal occurs whenever the signal ray path passes through the solar corona near superior conjunction. Large-scale variations in the data arise both from rotation of the solar corona and from the slowly changing solar offset (point of smallest heliocentric distance along ray path). A simplified model of the solar corona has been developed to simulate the results of the Faraday rotation measurements. In this model the known polarity of the large-scale interplanetary magnetic field is employed as an aid in determination of the product $N \cdot B$ (electron density \times magnetic field) as a function of heliographic longitude and heliocentric distance r within $2\text{--}10 R_{\odot}$. In this distance range $N \cdot B$ is proportional to $r^{-5.5}$. If the magnetic field can be assumed to follow an inverse square law over this range, the electron density is found to be decreasing as $r^{-3.5}$, in good agreement with previous results. The derived longitudinal structure for the corona during both occultations is consistent with synoptic coronal white light observations.

Key words: Faraday rotation — Corona — Solar Occultation.

1. Introduction

Two solar occultations of the satellite HELIOS-1 occurred in 1975. The first one was in the latter half of April when the satellite's ray path approached the west limb of the Sun to a minimum distance of 1.63 solar radii (Fig. 1) and the second one took place in late August/early September when HELIOS-1 was totally eclipsed by the photosphere (Fig. 2). Measurements of the polarization angle of the linearly polarized telemetry signal were performed with automatic tracking polarimeters at the 64 m Goldstone Tracking Station of the NASA Deep Space Network in California, and also at the 100 m radio telescope of the Max-Planck-

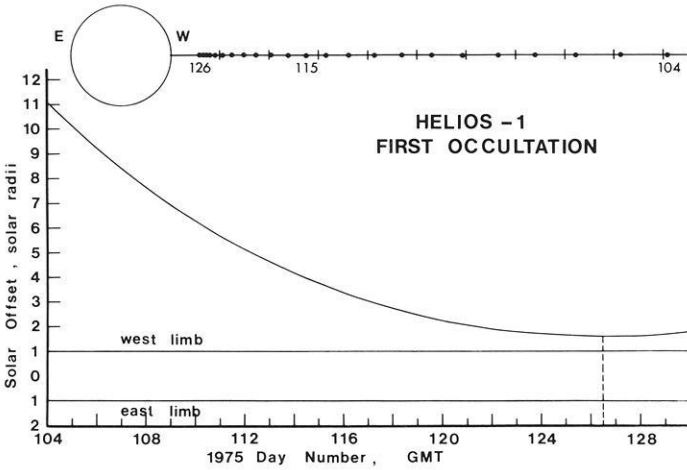


Fig. 1. Solar offset (ray path parameter) in solar radii during the first occultation of HELIOS-1 in 1975. The dashed vertical line denotes the epoch of minimum approach of the HELIOS-Earth line-of-sight to the Sun

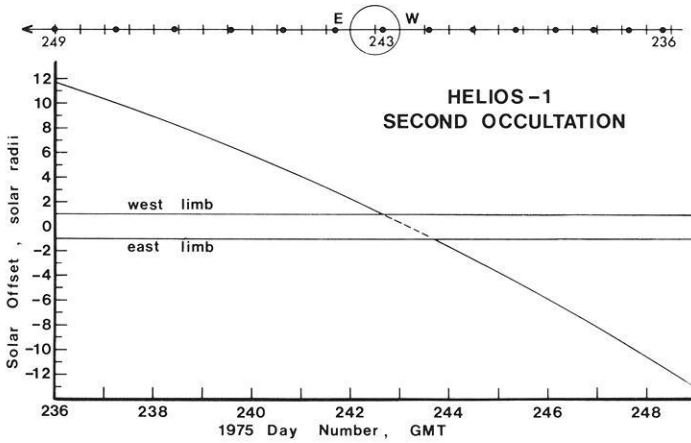


Fig. 2. Solar offset (ray path parameter) in solar radii during the second occultation of HELIOS-1 in 1975

Institut für Radioastronomie in Effelsberg near Bonn, Germany. The HELIOS-1 antenna transmits a linearly polarized carrier signal in the S-band (2.3 GHz), the electric vector being orthogonal to the ecliptic plane. The transformation of the orientation of the plane of polarization received on Earth to values referred to the ecliptic plane is straightforward (Stelzried et al., 1972).

2. Observations

Figures 3 and 4 show the polarization angle Ω (signal Faraday rotation) as a function of time (UT). The solar offset (minimum approach of signal ray path to

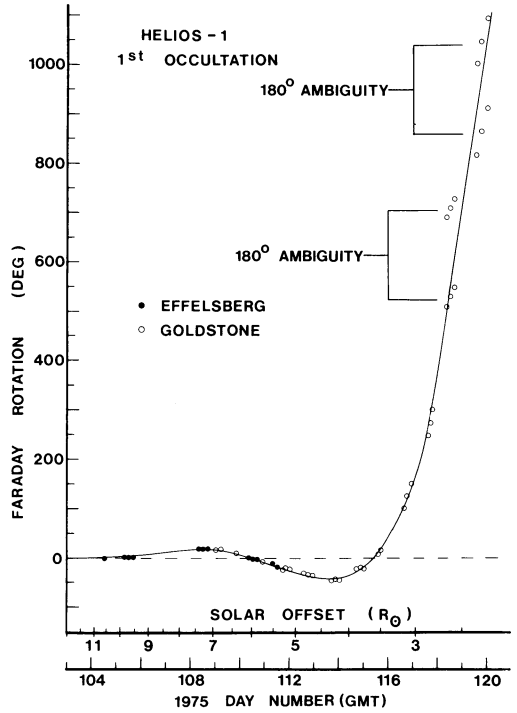


Fig. 3. Coronal Faraday rotation (uncorrected for ionosphere) versus solar offset during first occultation (circles: measurement; solid curve: theory). Note ambiguity on days 118-119

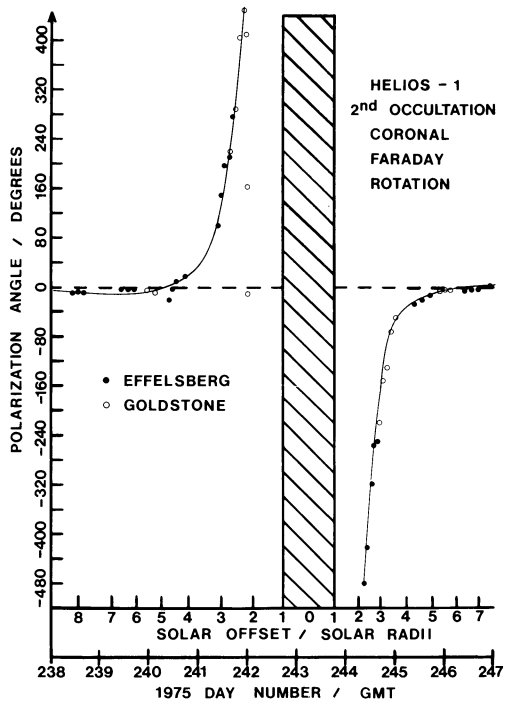


Fig. 4. Coronal Faraday rotation (uncorrected for ionosphere) versus solar offset during second occultation (circles: measurement; solid curve: theory)

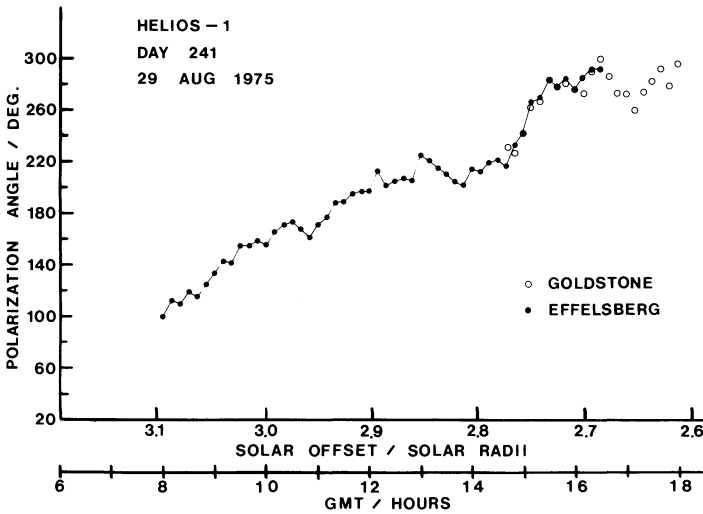


Fig. 5. Polarization angle (coronal Faraday rotation) measured on 1975 day no. 241 during the second occultation. Note overlapping of Goldstone and Effelsberg measurements

Sun) is also plotted along the abscissa. For both occultations the Goldstone measurements are denoted by open circles and Effelsberg by solid circles. The Faraday rotation of the signal is defined to be positive when the plane of polarization rotates counterclockwise as viewed from the receiver looking up at HELIOS. The maximum diurnal influence of the ionosphere is typically of the order of 4° at Goldstone and 2° at Effelsberg and is therefore neglected in this first order approximation. The ionospheric contribution to the observed Faraday rotation can be estimated from radio beacon experiment data from the geostationary satellites ATS-1 (at Goldstone) and ATS-6 (at Effelsberg). This correction will be incorporated into all subsequent analyses of HELIOS Faraday rotation data, but is not expected to significantly effect the results of this paper. Similarly, no correction has been attempted here for the deviation of the spacecraft spin (antenna) axis from the normal to the ecliptic. The nominal configuration is specified at less than 0.5° .

Figure 5 shows a detailed registration plot taken on 1975 day no. 241, demonstrating that the fine structure of the variation of Ω is observed at Goldstone as well as at Effelsberg during times of overlapping station coverage, and therefore is caused very probably by coronal effects. The design of the automatic tracking polarimeters (see Ohlson et al., 1974) theoretically allows for a measurement of Ω to an accuracy less than 0.5° for effective system time constants $\tau \approx 30\text{--}100$ s. Increase in system operating noise due to solar radiation in the antenna sidelobes can raise the error to typically 5° at solar offsets around $3 R_\odot$. The polarimeters are incapable of recording variations in Ω with characteristic periods smaller than τ . Moreover, Figure 5 clearly demonstrates the importance of employing at least two widely separated stations in order to resolve the 180° ambiguity at one station alone due to the missing nighttime data. A surprising result during both occultations was that one was able to

follow the telemetry signal to offsets as near to the Sun as 2 solar radii and to observe variations in Ω up to 800° . This is in contrast to earlier experiments (Stelzried et al., 1970) where only values $\Delta\Omega < 130^\circ$ at distances no nearer than 4 solar radii have been registered. There are two primary reasons for this: (a) HELIOS-1 had a better signal-to-noise ratio than the previous measurements due to higher antenna gain and transmitter power, and (b) the earlier occultations occurred in 1968 near solar maximum, while the HELIOS-1 occultations in 1975 took place during a solar cycle minimum. The closer approach of the HELIOS-1 ray path to the Sun and the two station coverage during the occultation phases of the mission render the present data much more amenable to a quantitative interpretation. In particular, because of the solar minimum conditions, we expect rather regular and long-lasting features on the Sun which may assist in the formulation of an unambiguous interpretation of the results.

3. Theory

The magnetic field and electron density structure within the outer corona (2–10 solar radii) may be rather complicated. Direct measurements in this region are limited mainly to disturbed (flare and burst) conditions (Hildner et al., 1975). The values of the electron density during quiet conditions are based primarily on photometric measurements of the integral white coronal light during solar eclipses (Newkirk, 1967). An experimentally determined form for the magnetic field in this region during quiet conditions virtually does not exist to our knowledge. The magnetic field can be inferred from the magnetic configuration observed on the photosphere (see, for example, Schatten et al., 1969, and Newkirk et al., 1972). On the other hand, it is well known that at least beyond 0.3 AU the solar wind shows a simple sector structure which can be very stable over many solar rotations (Svalgaard and Wilcox, 1975). A two-sector structure has prevailed in interplanetary space since about 1972 which can be observed either on or near the Earth (Hedgecock, 1975; Svalgaard et al., 1974) as well as on board HELIOS (Neubauer and Musmann, 1976). In each sector the interplanetary magnetic field is unipolar and changes its polarity from one sector to the next. The electron density as well as the radial component of the interplanetary magnetic field (IMF) decrease within each sector proportionally to r^{-2} . The general solar magnetic field as deduced if the Sun is seen as a star seems to be related to the structure and polarity of the IMF (Severny et al., 1970). Moreover enhanced intensities in the coronal white light (Hansen et al., 1974) seem to be related to the sector boundaries. The closed magnetic field lines within the streamers seldom reach beyond 2 solar radii (Newkirk et al., 1972).

Because of this limited knowledge about the outer corona we have attempted to try first a model which is as simple as possible, yet accounts for a basic sector structure in heliographic longitude. Although variations in heliographic latitude are certainly present (Rosenberg and Coleman, 1969; Rosenberg, 1975) over the $\pm 7^\circ$ covered by the HELIOS ray path, they are considered to be considerably weaker than the longitudinal variation and are therefore neglected. We further assume a single power law radial dependence of the electron density N and radial

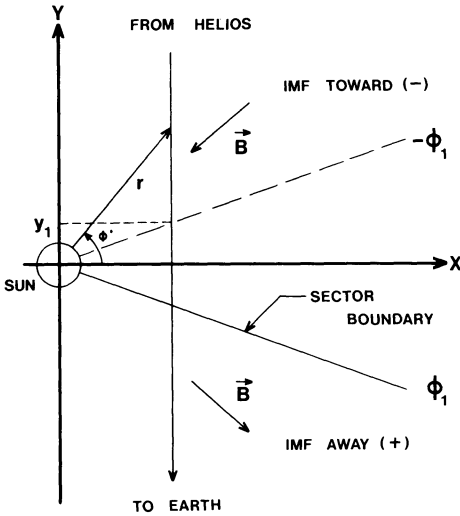


Fig. 6. Geometric configuration of system HELIOS-Sun-Earth for a single regional boundary on the west limb at $\phi = \phi_1$. The region from $-y_1$ to $+y_1$ makes no contribution to the net Faraday rotation of the signal

component of the magnetic field B_r in each sector, and neglect other components of \mathbf{B} in our region of interest ($2R_\odot < r < 10R_\odot$):

$$N = N_i r^{-\alpha}; \quad B_r = B_i r^{-\beta} \quad (1)$$

with N_i , B_i values extrapolated to the solar surface in the i^{th} sector and r the distance from the Sun in solar radii. α and β are exponents to be determined and are assumed to be the same in all sectors. B_i negative (positive) is associated with toward (away) sector polarity.

At S-band ($\lambda = 13$ cm) one may employ a simplified expression for the electron induced Faraday rotation along a given ray path (e.g. Stelzried et al., 1970). This "quasi-longitudinal approximation" is valid for the case when (a) the frequency f meets the criteria $f \gg f_c$, $f \gg f_g$, $f \gg f_p$, where f_c , f_g and f_p are the electron collision, electron Larmor, and plasma frequencies respectively, and (b) the wave does not travel transverse to the magnetic field. Under these conditions, which are easily satisfied by the HELIOS signal propagating through the solar corona and ionosphere, the Faraday rotation is given by

$$\Omega = \frac{K}{f^2} \int N \mathbf{B} \cdot d\mathbf{s} \quad \text{radians} \quad (2)$$

where

$$K = 2.36 \times 10^4 \quad \text{in mks units.}$$

$$f = 2.296 \text{ GHz}$$

Since refraction in our region of interest in the solar corona is negligible, the straight line ray path geometry shown in Figure 6 can be employed to reduce (2)

to the more practical form

$$\Omega = C \int_{-\infty}^{\infty} N B_r \sin \phi dy \quad \text{degrees} \tag{3}$$

with

$C = 1.786 \times 10^{-4}$ in mks units if

N is in electrons/m³

B_r is in Tesla

dy is in solar radii.

Assuming one sector boundary on the west limb at the angle ϕ_1 with the Earth in sector number 1 (Fig.6), one obtains from symmetry arguments and by combining (1) with (3):

$$\Omega = C(N_1 B_1 - N_2 B_2) \int_{y_1}^{\infty} \frac{y dy}{r^{\alpha+\beta+1}} = \frac{C D_1}{\gamma} \left(\frac{\cos \phi_1}{x} \right)^\gamma \tag{4}$$

with

x the solar offset of the ray path

$\gamma = \alpha + \beta - 1$; $D_1 = (N_1 B_1 - N_2 B_2)$

$\phi_1 = \Phi_1 + \omega(t - t_0)$; $-90^\circ \leq \phi_1 \leq 90^\circ$ (5)

$\omega = 2\pi/27$ days = 13.3 deg/day

= the angular frequency of the solar rotation

Φ_1 = the angle of the sector boundary from the x -axis at the time t_0 .

Calculations for the east limb ($x < 0$, $90^\circ < \phi_1 < 270^\circ$) require that $D_1 \rightarrow -D_1$ in the above.

If we assume m sectors with boundaries at the angular positions ϕ_{i-1} , ϕ_i , ϕ_{i+1} , etc., we obtain the series

$$\Omega = \frac{C}{\gamma} (-1)^\delta \sum_{i=1}^m D_i \left(\frac{\cos \phi_i}{x} \right)^\gamma \tag{6}$$

with

$-90^\circ \leq \phi_i \leq 90^\circ$; $\delta = 0$ west limb,

$90^\circ \leq \phi_i \leq 270^\circ$; $\delta = 1$ east limb,

and

$D_i = N_i B_i - N_{i+1} B_{i+1}$.

The sectors are numbered sequentially starting at sector 1 and proceeding around the sun in a counterclockwise direction as viewed from above the ecliptic.

The sum (6) over “sector boundaries” to compute the theoretical Faraday rotation includes only those terms for which the quantity $(\cos \phi_i/x)$ is positive, otherwise the term is set equal to zero. This insures that the sum is extended only over those “boundaries” on the appropriate solar limb. It should also be noted that the sign of $N_i B_i$ in “sector” i is not required to flip polarity across its boundaries. Therefore, Equation (6) may be viewed as a sum over regional subdivisions in heliographic longitude, each region characterized by its constant $N_i B_i$ and its width given by its boundaries ϕ_i and ϕ_{i-1} . Many such regions may in fact be contained within a classical large-scale solar sector of uniform polarity.

4. Comparison between Observations and Theory

The time derivative of the Faraday rotation (6) is given by

$$\dot{\Omega} = -\gamma \Omega \frac{\dot{x}}{x} - C \omega (-1)^\delta \sum_{i=1}^m D_i \left(\frac{\cos \phi_i}{x} \right)^\gamma \tan \phi_i. \quad (7)$$

The first term of (7) arises from the motion of the spacecraft’s solar offset in the corona, while the second term results from the rotation of the corona itself. At times of small solar offset and large spacecraft motion, achieved for example during the second occultation, one expects the first term of (7) to be dominant. Under these conditions one may estimate γ from the slope of a plot $\ln \Omega$ vs. $\ln x$. Such estimates yield $\gamma \simeq 4.1$ at $x = \pm 3 R_\odot$. Due to the uncertainty in the second term of (7), however, one must accept a rather large tolerance on the allowed values of γ , especially if this parameter is to be approximated as a constant in the range $2-10 R_\odot$. In practice, values of γ as low as 3.5 and as high as 5.0 were found to yield good fits to the Faraday data.

The terms of the sum (6) may be regrouped into a form more adaptable to model calculations by summing essentially over “regions” rather than “regional boundaries”:

$$\Omega = \frac{C}{\gamma} (-1)^\delta \sum_{i=1}^m N_i B_i \{ (\cos \phi_i/x)^\gamma - (\cos \phi_{i-1}/x)^\gamma \}. \quad (8)$$

There are then $2m+1$ parameters to be derived from a fit of (8) to the Faraday rotation observations: γ and the m pairs of regional weight factors $N_i B_i$ and boundaries Φ_i . A systematic determination of the optimum model parameters was accomplished using the following program: (1) γ was varied in steps of 0.5 over the range $3.0 < \gamma < 6.0$. (2) Two of the regional boundaries denoted by the Φ_i were fixed to conform with the location of sector boundaries inferred from polar cap observations during the occultation. This establishes two “large-scale” sectors for each model, within which one particular magnetic field polarity is dominant. (3) The remaining “free” regional boundaries are then varied over all

possible angular positions (except those occupied by the above mentioned two "fixed" boundaries) in steps of one day of solar rotation. A step size smaller than this is impractical, since localization of solar features in heliographic longitude from coronal white light or IMF measurements cannot be accomplished to an accuracy of better than one day anyway. The number of possible boundary configurations generated in this way is given by the binomial coefficient $\binom{j}{k}$, where j = number of possible positions for a regional boundary = 25; k = number of "free" regional boundaries. This results in 12,650 trial models for $m=6$. (4) For a given set of regional boundaries and a given γ , the coronal structure is assumed to remain constant (rigid rotation) on a time scale at least comparable with the duration of the occultation. Each measurement of Ω thus yields a linear equation from (8) in the unknowns $N_i B_i$, $i=1, m$. Selecting n spaced measurements ($n > m$), the system is then solved for the set $N_i B_i$, $i=1, m$ for which deviations between measured and computed values of Ω are minimized in the least-squares sense.

It should be noted that no demands are placed on the polarity of the various regions as controlled by the sign of the factor $N_i B_i$ when solving the normal equations for the best least-squares solution. Indeed, many models can be immediately rejected if the polarities of the regions disagree with those extrapolated from inferred polarities of the IMF made at Earth (Solar Geophys. Data, Nov. 1975). Similarly, some models yield magnitudes for the product $N_i B_i$ which are inconsistent with reasonable coronal values. Coronal models were rejected which contained $N_i B_i$ outside the range $10^7 < N_i B_i < 10^{10}$ Tesla m^{-3} .

It should be mentioned that polarity agreement within the large-scale sectors was considered to hold even if an occasionally isolated region within the sector was determined to have the wrong polarity as long as the width of that region was not greater than one day. This allows for the often observed smaller structures of opposite polarity that are apparent in interplanetary space. Requiring that each region conform in polarity to that in its respective large-scale sector results in a rejection of all trial models. It is thus apparent that some medium-scale structure is important for the generation of the observed Faraday rotation profile.

Although one goal of this analysis was to simulate the observed Faraday rotation time profile with the simplest possible coronal model, no satisfactory fit to the data could be accomplished with $m < 6$ using models with an acceptable set of γ and $N_i B_i$, $i=1, m$ under the above polarity and magnitude restrictions. Considerably better results are obtained for $m=6$, at which point the coronal models have enough longitudinal structure to adequately follow the zeros and extrema observed in the Faraday data, and yet one is able to make a unique determination of the one basic coronal configuration which satisfies both the Faraday data and the restrictions on the polarity/magnitude of the $N_i B_i$. Models with $m > 6$ were not tested since the integral nature of the Faraday data does not justify attempts to determine a finer spatial resolution of solar features.

The absolutely best models for both occultations, based on minimum root-mean-square deviation of theoretical Faraday rotation from the observed one, were obtained for $m=6$, $\gamma=4.5$. For the first occultation only a small fraction

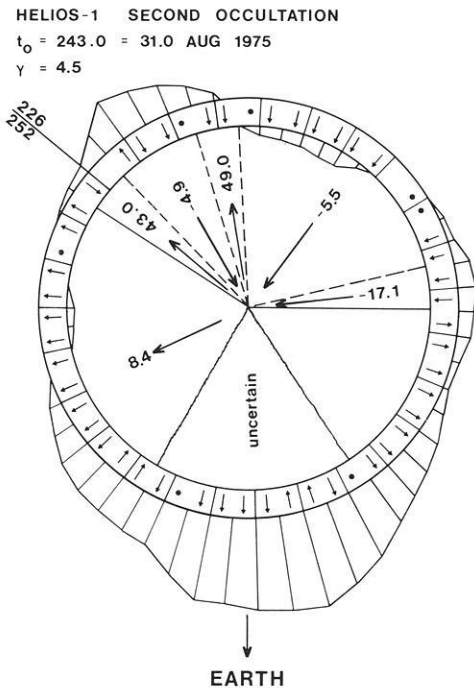
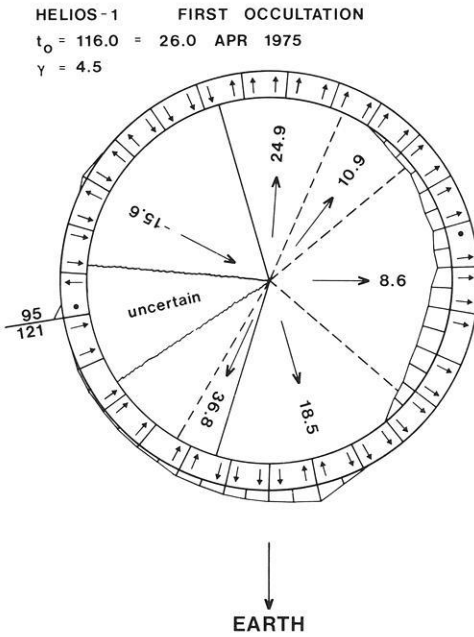


Fig. 7. Inferred coronal structure as seen from above the ecliptic plane during the first occultation. The epoch (UT) is $t_0 = 116.0$ days (26.0 APR 1975), and the power law exponent for the radial fall off of $N \cdot B$ is 5.5 ($\gamma = 4.5$). Two of the six regional boundaries are fixed from IMF sector observations (solid radial lines), and the remaining four are free parameters determined from a least-squares analysis (dashed lines). The polarity and magnitude of the factors $N_i B_i$ are indicated in each region (unit: $10^8 T m^{-3}$). The outer circle displays the inferred IMF polarity, shifted 4.5 days, for the solar rotation from 1975 days 95–121. A black dot signifies “mixed polarity” or “effect doubtful or not discernable”. No information about the region marked “uncertain” can be derived from the Faraday data, since the ray path did not probe these longitudes. Finally, the striped regions bounded by the radial plotted curves show the relative intensities of the west limb pB measurements at $1.5 R_\odot$ from R.T. Hansen et al., from which one infers a qualitative enhancement in electron density (curve outside outer circle) or a region of low density (curve inside inner circle)

Fig. 8. Inferred coronal structure during the second occultation (see Fig. 7 for explanation). The epoch (UT) is $t_0 = 243.0$ days (31.0 AUG 1975), and $\gamma = 4.5$. The interplanetary polarities are given for the solar rotation from 1975 days 226–252

(2.89%) of the 12,650 trial models were found to yield acceptable values of $N_i B_i$. The eight acceptable models with the best fits to the Faraday data all display strong qualitative similarities (i.e. one regional boundary moved one day with correspondingly small adjustment in the associated value of $N_i B_i$), so that only one unique general configuration could be acclaimed compatible with all measurements. The theoretical Faraday rotation from the best fitting model not qualitatively similar to those first eight exhibited a much higher deviation from the observed and can be excluded from consideration.

The acceptable models with the best fits to the Faraday data are shown in Figures 7 and 8 for the first and second occultations respectively. The diagrams are "snapshots" of the rigidly rotating corona from above the north solar pole at the UT times $t_0 = 116.0$ days (first occultation) and $t_0 = 243.0$ days (second occultation). The theoretical Faraday rotation computed from (8) for these models is drawn as a solid curve in Figures 3 and 4. The polarity and value of the weight factor $N_i B_i$ (in units of 10^8 Tesla m^{-3}) are indicated within each region. For comparison, the IMF direction inferred from polar cap magnetograms are shown in the outer circle (Solar Geophys. Data, Nov., 1975). The inferred polarities are given for the time period between the days on either side of the solar rotation "cut line" (extended radial line) and are shifted 4.5 days in time to account for the solar wind transit time to Earth. The region marked "uncertain" contains those heliographic longitudes not effectively probed by the HELIOS-Earth ray path during the occultation. Note that the second occultation (Fig. 8) occurred 4.7 solar rotations after the first one. Although coronal features are often observed to remain stable over such extended intervals, it is not really surprising that the detailed structure has undergone considerable redistribution. An indication that this is indeed the case for the interval between occultations is evident in the K-corona limb intensity measurements provided to us by R.T. Hansen and colleagues (private communication). The coronal pB (polarization \times brightness) intensities at $1.5R_\odot$ on the west limb can be interpreted as a qualitative measure of electron density. These measurements over one solar rotation yield the curves drawn in Figures 7 and 8 outside the outer circle (heliolongitudes with intensity above specified threshold) and inside the inner circle (below average intensity, or "coronal holes"). Qualitative agreement with the configurations derived from the Faraday data is evident for both occultations.

Figure 9 shows the electron density radial-profile obtained from the mean weighted values of $N_i B_i$ from the models in Figures 8 and 9, and also from models (not shown) with $\gamma = 4.0$. The magnetic field is assumed to be purely radial ($\approx r^{-2}$) with a mean strength at the coronal base of 1 gauss. Also shown are a modified Allen-Baumbach profile with an extra term in r^{-2} (Stelzried et al., 1970), and a model based on time-delay measurements during the occultations of Mariner-6 and Mariner-7 (Muhleman et al., 1977). The mean value of $N_i B_i$ increases with increasing γ , so that even the single-power approximation appears to be adequate over the range $2R_\odot < r < 10R_\odot$ for both models shown.

The data gaps on the last two days of the first occultation (Fig. 3) resulted in an unresolved $n\pi$ ambiguity in measured polarization angle. The best estimates of the probable values on these days were used in additional investigations to determine the influence of this effect on the derivation of a coronal model. Since

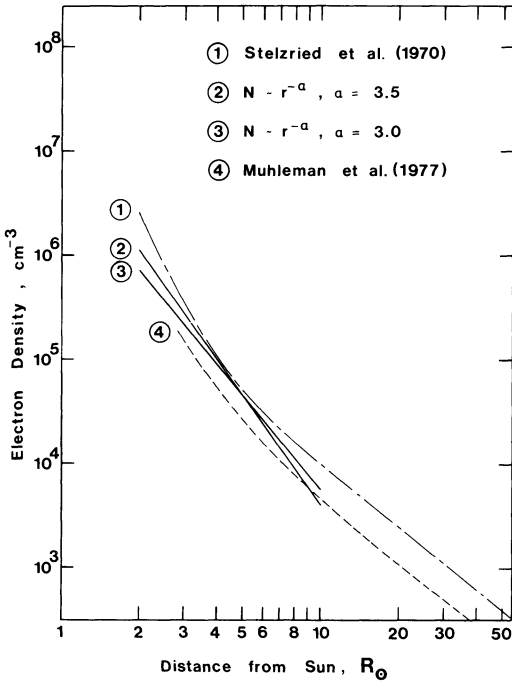


Fig. 9. Radial profile of the coronal electron density. The single power fall-off approximation to be used over the range $r=2-10R_{\odot}$ is a straight line in this representation. The mean value of $N_i B_i$ weighted over all regions has been computed for the models of Figures 7 and 8 ($\gamma=4.5$) and also for two unpictured models ($\gamma=4.0$). The electron density profile results if one assumes the magnetic field to be purely radial ($\approx r^{-2}$) and has a strength of 1 gauss at the solar surface. This yields electron density fall off rates $\alpha=3.0$ and 3.5 (Curves 3 and 2). The approximations are reasonably close to the semi-empirical models (Curves 1 and 4), at least over the radial range of interest for Faraday rotation data

a considerably poorer fit to the observations was realized upon fitting to the upper points of Figure 3, one is inclined to prefer the lower values.

The sharp drop in measured Faraday rotation toward the end of day 241 during the second occultation (Fig. 4) cannot be due to the slowly varying solar offset and rotation solar corona. The abrupt decline is similar to the initial phase of the "transient events" seen during the occultation of Pioneer 6 near solar maximum (Levy et al., 1969). Measurements during the event were ignored for the quiet corona simulation attempted in this work.

5. Summary and Conclusions

A simplified model of the solar corona has been developed to simulate the results of Faraday rotation measurements taken during the two 1975 solar occultations of the satellite HELIOS-1. The sun is divided into m "regions" of arbitrary width in heliographic longitude, within which the electron density N and the radial magnetic field B_r are assumed to decrease with radial distance according to a simple power law. The values of the product $N \cdot B_r$ at the solar surface, $N_i B_i$, $i=1, m$ within each region are determined from a least-squares solution to a set of normal equations of the form (8) for all possible locations of the "regional boundaries". Two of these boundaries are fixed from the observed positions of the large-scale sector boundaries in interplanetary space.

The radial dependence of the product $N_i B_i$ from $2-10R_\odot$ is found to fall off as $r^{-5.5}$. The longitudinal structure is sufficiently complex that the data cannot be adequately simulated for $m < 6$. With 6 regions one obtains only a small fraction of the original trial models for which the values of $N_i B_i$ are both compatible with the direction of the inferred interplanetary magnetic field and also lie within the range of observed coronal magnitudes. The quality of the fits of these compatible coronal models to the Faraday data ranges from very poor to excellent. In the two cases investigated, a smaller subgroup of coronal configurations with very similar parameter values provided a least-squares fit far superior to all remaining contending models. The hypothesis that this subset of trial models defines a basically "unique" coronal configuration is supported by their qualitative agreement with synoptic white light coronal observations.

Future studies will include a comparison of such derived models with solar radio observations and with electron densities inferred from the HELIOS ranging experiment (Edenhofer et al., 1977). The method introduced here will be refined and expanded upon in an effort to improve the convergence to a unique coronal configuration, while retaining an inherently simple model basis.

References

- Edenhofer, P., Esposito, P.B., Hansen, R.T., Hansen, S.F., Lüneburg, E., Martin, W.L., Zygielbaum, A.I.: Time delay occultation data of the Helios spacecrafts and preliminary analysis for probing the solar corona. *J. Geophys.* **42**, 673–698, 1977
- Hansen, S.F., Sawyer, C., Hansen, R.T.: K corona and magnetic sector boundaries. *Geophys. Res. Lett.* **1**, 13–15, 1974
- Hedgecock, P.C.: The heliographic latitude dependence and sector structure of the interplanetary magnetic field 1969–1974: Results from the HEOS satellites. *Solar Phys.* **44**, 205–224, 1975
- Hildner, E., Gosling, J.T., MacQueen, R.M., Munro, R.H., Poland, A.I., Ross, C.L.: The large coronal transient of 10 June 1973, I: Observational description. *Solar Phys.* **42**, 163–177, 1975
- Levy, G.S., Sato, T., Seidel, B.L., Stelzried, C.T., Ohlson, J.E., Rusch, W.V.T.: *Pioneer 6*: Measurement of transient Faraday rotation phenomena observed during solar occultation. *Science* **166**, 596–598, 1969
- Muhleman, D.O., Esposito, P.B., Anderson, J.D.: The electron density profile of the outer corona and the interplanetary medium from *Mariner-6* and *Mariner-7* time-delay measurements. *Astrophys. J.* **211**, 943–957, 1977
- Neubauer, F.M., Musmann, G.: Observation of magnetic sector structure and streams during the primary mission of HELIOS-1. Paper presented at Helios Project Seminar on Scientific Results, Bonn, 19–21 May 1976
- Newkirk, Jr., G.: Structure of the solar corona. *Ann. Rev. Astron. Astrophys.* **5**, 213–266, 1967
- Newkirk, Jr., G., Trotter, D.E., Altschuler, M.D., Howard, R.: Atlas of magnetic fields in the solar corona. *Solar Phys.* **24**, 370–372, 1972
- Ohlson, J.E., Levy, G.S., Stelzried, C.T.: A tracking polarimeter for measuring solar and ionospheric Faraday rotation of signals from deep space probes. *Trans. IEEE* **23**, 167–177, 1974
- Rosenberg, R.L.: Heliographic latitude dependence of the IMF dominant polarity in 1972–1973 using Pioneer 10 data. *J. Geophys. Res.* **80**, 1339–1340, 1975
- Rosenberg, R.L., Coleman, Jr., P.J.: Heliographic latitude dependence of the dominant polarity of the interplanetary magnetic field. *J. Geophys. Res.* **74**, 5611–5622, 1969
- Schatten, K.H., Wilcox, J.M., Ness, N.F.: A model of interplanetary and coronal magnetic fields. *Solar Phys.* **6**, 442–455, 1969
- Severny, A., Wilcox, J.M., Scherrer, P.M., Colburn, D.S.: Comparison of the mean photospheric magnetic field and the interplanetary magnetic field. *Solar Phys.* **15**, 3–14, 1970

Solar Geophysical Data, **375**, Nov. 1975

Stelzried, C.T., Levy, G.S., Sato, T., Rusch, W.V.T., Ohlson, J.E., Schatten, K.H., Wilcox, J.M.: The quasi-stationary coronal magnetic field and electron density as determined from a Faraday rotation experiment. *Solar Phys.* **14**, 440–456, 1970

Stelzried, C.T., Sato, T., Abreu, A.: Transformation of received signal polarization angle to the plane of the ecliptic. *J. Spacecraft* **9**, 69–70, 1972

Svalgaard, L., Wilcox, J.M.: Long term evolution of solar sector structure. *Solar Phys.* **41**, 461–475, 1975

Svalgaard, L., Wilcox, J.M., Duvall, T.L.: A model combining the polar and the sector structured solar magnetic fields. *Solar Phys.* **37**, 157–172, 1974

Received November 29, 1976; Revised Version May 10, 1977

Time Delay Occultation Data of the Helios Spacecrafts and Preliminary Analysis for Probing the Solar Corona

P. Edenhofer^{1*}, P.B. Esposito², R.T. Hansen³, S.F. Hansen³, E. Lüneburg¹, W.L. Martin², and A.I. Zygielbaum²

¹ DFVLR-Institut für Flugfunk und Mikrowellen, D-8031 Oberpfaffenhofen; Federal Republic of Germany

² Jet Propulsion Laboratory, California Institute of Technology, Pasadena, CA 91103, USA

³ High Altitude Observatory, National Center for Atmospheric Research, Boulder, CO 80303, USA

Abstract. S-band time delay measurements were collected from the spacecrafts Helios A and B during three solar occultations in 1975/76 within heliocentric distances of about 3 and 215 R_{\odot} in terms of range, Doppler frequency shift, and electron content. A description is given concerning some characteristic features of the methods of measurement and data processing. Typical data sets are discussed to probe the electron density distribution near the sun (west and east limb as well) including the outer and extended corona. Steady-state and dynamical aspects of the solar corona are presented and compared with earth-bound K-coronagraph measurements. Using a weighted least squares estimation 3 parameters of an average coronal electron density profile ($30/r^6 + 1/r^{2.2}$) $\times 10^{12} \text{ m}^{-3}$ are derived in a preliminary analysis to yield electron densities of about 1.3×10^{11} ; 1×10^8 ; $7 \times 10^6 \text{ m}^{-3}$ at $r=3$; 65; 215 R_{\odot} . Transient phenomena are discussed and a velocity of propagation $v \approx 900 \text{ km/s}$ for plasma ejecta from a solar flare is determined from an extraordinary set of Helios B electron content measurements on April 30/May 1, 1976.

Key words: Helios occultations – Time delay measurements – Remote probing – Solar corona electrons.

1. Introduction

This paper deals with Helios experiment no. 12 which is essentially a radio science occultation experiment for probing the solar corona by analysing propagation effects of the spacecrafts' radio signal after passage through the coronal plasma (S-band: carrier frequency 2.115 GHz uplink/2.295 GHz downlink; wave length $\approx 14 \text{ cm}$). Likewise spacecraft Pioneer 6 (Stelzried et al., 1970) the first part of this experiment (Volland et al., 1976; also this issue) exploits the Faraday rotation effect yielding significant measurements within heliocentric distances of about 2 and

* To whom offprint requests should be sent

now: University of Bochum, Institut für Hoch- und Höchstfrequenztechnik, D-4630 Bochum

$10 R_{\odot}$. The second part, reported here (also Edenhofer et al., 1977), makes use of what is summarized as two-way time delay measurements in terms of range, Doppler frequency shift, and electron content (Martin, 1969) in order to derive the electron density distribution between about 3 and, principally, up to $215 R_{\odot}$ at the earth's orbit. The lower limit is due to the increasing turbulence of the solar plasma destroying wave coherence. For Helios it turned out that the upper limit is essentially given by the orbital geometry but not by the intrinsic system noise level of the signal. From Helios B, for example, significant variations of the columnar electron content were measured as far away from the sun as approximately 190 (before) and $80 R_{\odot}$ (after first inferior conjunction). Whereas Faraday rotation measurements involve the electron density and the magnetic field, time delay measurements are related only to electron densities but require precise orbital information to be analysed (at least for range and Doppler data). Both parts of this radio science experiment cover complementary aspects in probing the solar corona as far as data collection and analysis is concerned. So it is one of the final scientific objectives to model the magnetic field by a combined data analysis of both parts of the occultation experiment. Thus in situ-measurements along the Helios trajectory and earth-bound observations of the inner corona up to about $3 R_{\odot}$ (Hansen et al., 1969) are supplemented by indirect measurements from propagation effects of electromagnetic waves, remote sensing the intermediate coronal and interplanetary medium.

2. Data Collection

Similar radio science (and celestial mechanics) experiments of an occultation type have been performed to explore planetary atmospheres and the outer corona as well: Kliore et al. (1971); Rasool and Stewart (1971); Muhleman et al. (1971, 1977); MacDoran et al. (1971); Callahan (1975); Anderson et al. (1975). It is also possible to make use of solar occultations of natural, discrete radio sources: Newkirk (1967); Counselman and Rankin (1972).

2.1. Orbital Geometry. There were 2 superior conjunctions for spacecraft Helios A in 1975: First occultation (probing the sun's west limb only: May 6, day of year (DOY) 126) and second occultation (west to east limb passage: August 31, DOY 243). For the first occultation (elongation or sun-earth-probe angle $SEP_{\min} \approx 0.6^{\circ}$) the impact parameter p (distance between earth-Helios sight line and center of sun; $p_{\min} \approx 2.2 R_{\odot}$) is slowly varying ($0.6 \times 10^{-3} R_{\odot}/h$; value averaged over two days around occultation) as compared with the second occultation after aphelion (140 times faster). The earth-Helios distances and the corresponding roundtrip travel times of the radio signal for the occultations are $1.8/30$ and $1.5 \text{ AU}/25 \text{ min}$, respectively. For the first occultation, Figure 1 shows the earth's orbit as related to the orbit of Helios A within the ecliptic plane (orbital motion is indicated by arrows, time is shown by intervals of 10 days). The occultation position is illustrated by a broad line (alignment earth-sun-Helios), the positions for entering and leaving the 5° -cone by lines (less broad) about $18 R_{\odot}$ off the sun's west limb. Also there are marks for those time intervals corresponding to the 27 day rotational period of the sun (Carrington rotation no. 1626/dashed lines – no. 1629; also sect. 3.3).

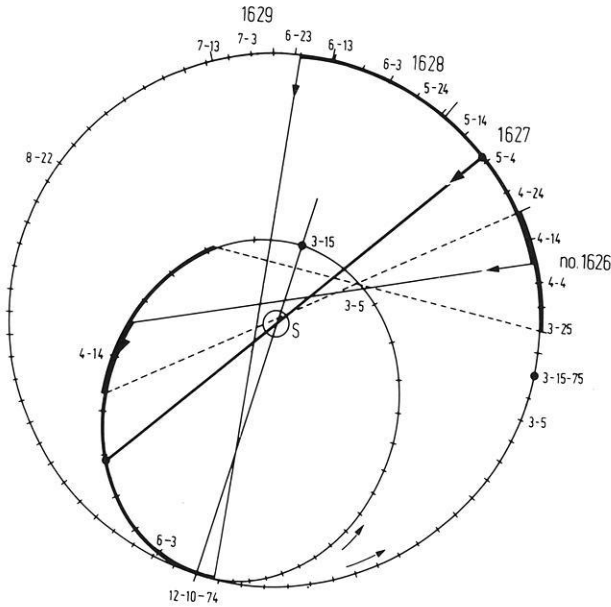


Fig. 1. Orbital geometry for first occultation of Helios A

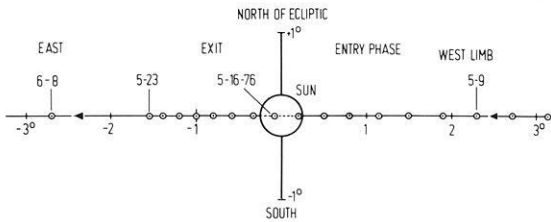


Fig. 2. Helios B trajectory behind solar disk as seen from earth (first occultation)

The orbital geometry for Helios B during 1976 includes, after first perihelion (April 15), 3 successive occultations on May 16, July 10, and September 25. The first occultation of Helios B as seen from earth along the ecliptic plane is shown in Figure 2 (time indicated by intervals of 1 day); the spacecraft was behind the sun's disk for about 40 h.

2.2. *Data Acquisition.* Considered with comparable interplanetary missions the Helios mission was especially suitable for solar occultation experiments due to a variety of reasons. The orbital geometry of both Helios A and B included distinct occultations ($SEP \ll 1^\circ$). There were several, successive occultations separated by weeks only (1975/76). The solar plasma could therefore be probed and compared for several rotational periods of the sun involving west and east limb observations as well. Slow and fast occultations separated time scales of plasma activity, when the Helios raypath intercepted the corona for long or short periods of time. In early

May 1976 there was a special orbital configuration where a joint analysis of Helios A and B time delay data seems to be promising (the raypath of Helios A was overtaking that of Helios B). The scientific analysis of wave propagation effects is facilitated by the Helios raypath bound to the ecliptic plane. The only latitudinal variation of solar plasma effects comes from the 7° inclination of the sun's rotational axis to the ecliptic. In addition, the prime time of the Helios mission was during the descending and minimum phase of a solar cycle (no. 20 started in 1965), so conditions were quiet and stable for coronal remote sensing. Those parts of the trajectory where the earth-Helios sight line was nearly tangential facilitate separation of radial and angular (longitudinal) coronal probing, because the raypath was nearly constant with respect to radial variations of coronal electron densities. Since the Helios spacecrafts approached the sun closer than any other spacecraft before, one can make a correlative analysis of occultation data (both time delay and Faraday rotation) with in situ-measurements. Finally, there is a very characteristic feature: on the average the Helios ranging signal was about 30 or 40 dB stronger than for missions like Mariner 6, 7, and 9. This is mainly due to a low noise, double conversion phase locked loop receiver with variable bandpass limiter and a high power mode of operation for the transponder together with a 23 dB-high gain antenna. Thus substantially less noisy time delay data could be collected closer to the sun. Moreover for Helios B (also partly Helios A) an improved ranging machine (MU 2) especially suitable for solar occultation experiments was available. On the other hand, a disadvantage was the lack of dual frequency capability aboard the Helios spacecrafts (such as S/X-band for Mariner 10 and Vikings 1, 2).

The time delay measurements have been taken by NASA's Deep Space Network (DSN), operated by the Jet Propulsion Laboratory (JPL), California Institute of Technology, Pasadena, USA. During occultation preferably the 64-m parabolic antennas of this network were used with 100 kW of transmitted power. The notation time delay measurements means data acquisition in terms of three different data types also called radiometric data: range (roundtrip time delay), Doppler frequency shift (coherent two-way range rate), and electron content (differential phase). It is evident that the measurement technique and procedure are crucial to perform such an occultation experiment (Martin, 1969; Martin and Zygielbaum, 1977; Edenhofer et al., 1977a). The time delay data are determined by precisely measuring the elapsed time between the transmission of an encoded signal from the tracking station and its return, retransmitted from the spacecraft, back to the ground. A highly accurate and stable rubidium vapor oscillator, a frequency synthesizer, and a binary counter are used to generate and modulate the range signal. Together with the roundtrip travel time of the signal it took up to an hour or so to obtain the value of a single range measurement (non-automatic mode of operation). Usually the strategy of the Helios radio science experimenters was to collect one or two range points at the beginning and end of a tracking pass, respectively. For a typical 8h-tracking pass sometimes up to 10 or 15 range measurements were collected. Range rate or Doppler data, respectively, were measured by using a sampling time of generally 60 s.

Comparing the magnitude of the time delay measured due to the solar corona (from 0.1–30 μ s; via differential phase even some 10 ns) to typical roundtrip signal travel times of 30 min makes evident the principal requirement of utmost internal

stability within the ranging system. Extensive calibration tests of the total ranging system have shown the capability to meet such a precision requirement (Martin, 1970; Böttger et al., 1975). Test data results indicate that the maximum drift in the ranging system's time delay experienced over a full 8 h-Helios tracking pass was less than 10 ns (0.3% with respect to the average value of the system delay).

Electron content measurements were collected by using a special technique developed at JPL (MacDoran and Martin, 1970; MacDoran, 1970) and first applied to the Mariner 6 and 7 missions (MacDoran et al., 1971). This measurement technique is based upon the group delay and phase advance accumulated along the raypath according to wave propagation in a dispersive medium like the solar corona. Group and phase velocity $v_{g,p} \approx c(1 \mp \beta N/f^2)$ differ by the same, small amount (magnetic field and collisions neglected; c -velocity of light, β -constant, N -electron density, f -carrier frequency). Specifically, taking the resulting, opposite signed phase displacement (differential phase) in terms of the difference between the range data and the integrated Doppler data collected yields a quantity $D(t)$ proportional to variations ΔI of the columnar electron content $I(t)$:

$$\begin{aligned} \Delta I(t) &= I(t) - I(t_0) = \alpha D(t), \\ I(t) &= \int N(s, t) ds \quad [\text{m}^{-2}]. \end{aligned} \quad (1)$$

The physical meaning of the quantity D is the difference between the signal's group and phase path. Since Helios did not have dual frequency capability, the quantity $\Delta I(t)$ is an average value of the up- and downlink columnar electron content variation where the reference value $I(t_0)$ is unknown (the factor $\alpha \approx 6 \times 10^{16} [\text{m}^{-3}]$ depends upon the up- and downlink carrier frequency). Thus what is actually measured are variations of the electron content with respect to some reference or background level. A set of electron content measurements $\Delta I(t)$ starts at time t_0 with an integration interval Δt generally equal to 2 min. By comparing the phase measured during succeeding intervals with the initial determination the variations of the phase displacement are analogous to changes in the number of charged particles along the raypath. For this data type the notation DRVID has been introduced (*Differenced Range Versus Integrated Doppler*).

It is obvious from the concept of this technique of measurement that all effects contributing to D in a non-dispersive way (independent of frequency) are cancelled. These effects include purely geometrical effects (e.g. orbital motions, antenna nutation), tropospheric propagation effects and relativistic delay, or any equipment delays common to both the range and Doppler measurement subsystem. As a consequence the data evaluation is widely decoupled from the problem of orbit determination. Contrary to the range and Doppler data, the information sensitive to the solar corona is directly accessible to a scientific analysis (i.e. comparable with a Faraday rotation type of measurement).

Only the range data, however, provide information about absolute values for geometric range and the coronal effects. A reasonable compromise had to be found in order to have long, uninterrupted sets of electron content data (e.g. 6 h from a standard 8 h-tracking pass) and still obtain a sufficient number of range data. In terms of coronal probing this means to prefer watching for short- or long-term variations of the electron density, respectively (time scale: hours/days or weeks).

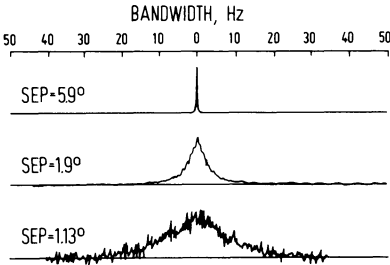


Fig. 3. Spectral distribution of the amplitude of received S-band radio signal ($1.13^\circ \cong 4.2 R_\odot$)

Figure 3 gives an idea of the difficulties in establishing a coherent link and obtaining valid range acquisitions close to the sun (data taken from a previous Mariner mission). Spectral broadening of the radio signal (about 10–20 Hz for $p \approx 4 R_\odot$) complicates the operation of both spacecraft and ground phase locked loop receivers. By monitoring the actually measured signal spectrum it was possible, in real time, to adjust the ground receiver's bandwidth. Around occultation the spacecraft's receiver bandwidth (Böttger et al., 1975) could be set to a minimum value of about 5 Hz for adverse signal-to-noise ratios (SNR) and a bit rate of 8 bit/s (variable by steps of 8, 16, etc. up to 2048 bit/s). Real time DRVID-plots provided information on trends in plasma activity facilitating decisions to give up an electron content data set in favor of additional range data or, alternatively, to change parameters of the ranging system (e.g. integration times, number of range components) to meet sudden enhancements of the noise level. During the Helios B mission an improved ranging machine was available with a variety of features particularly favorable for solar occultation type experiments (Edenhofer et al., 1977a).

As a result of all efforts the quality and quantity of the time delay measurements from spacecraft Helios B are excellent. A total number of 141 range acquisitions was attempted within 3 weeks of May 1976 (at the main tracking station), about 80% of these were found to be successful (43 pre-, 69 post-occultation range measurements). Because 16 range measurements turned out to be marginal (quality based on orbit fit), they were processed by a maximum likelihood estimator. High flexibility made it possible in real time to respond to adverse conditions. For example, day-to-day variations of the input signal level of as much as 30 dB were observed with a 50 dB decrease over 2 weeks towards occultation. Maximum use could be made of the tracking time allocated to Helios and to be shared with other space projects like Viking and Pioneer in an extremely competitive situation. The acquisition of validated range data during an occultation as close to the sun as $SEP = 0.84^\circ/p = 3.1 R_\odot$ (estimated SNR for the ranging channel ≈ -15 dB) was never achieved before.

3. Observations-Preliminary Analysis

The Helios A time delay measurements to be reported here cover the time interval March till September 1975. The DSN provided a total number of approximately 340 range measurements. Contrary to Helios B the primary mission of Helios A did

not include the first occultation, so most of the range measurements were collected just around the first and second perihelion (March plus April: 120; September: 105), i.e. the tracking coverage was supporting the entry phase of the first (May 6) and the (late) exit phase of the second (August 31) occultation. First efforts to run a precision orbit determination program in order to fit the Helios A radiometric data yielded poor results, e.g. probably more than 50% of the range acquisitions are expected to be invalid or at least questionable. Information from station calibration data seems to be insufficient, 4 spacecraft maneuvers had to be taken into account. Due to difficulties in data handling and processing, about 55 MU 2-range measurements (around May/June) are not yet included in the orbit fit. So the concept was first to start the scientific orbital analysis for the Helios B spacecraft, where the overall status of this experiment looks much more promising.

3.1. Typical Data Sets. Doppler data from Helios A were analysed by Berman and Wackley (1976) to estimate parameters of an heuristic Doppler noise model for solar occultations. Figure 4 represents the Doppler noise versus time as derived by using a data processing scheme with moving average. Usually the noise level is as low as 3 or 5 mHz increasing to values between 0.1 and 1 Hz during occultation (numbers become questionable close to occultation). This figure gives an idea of the distinct influence of the solar corona during the slow first and the fast second occultation. Significant structures of minor peaks can be distinguished, for instance around DOY 83 (March 24) in coincidence with unusual variations of electron content measurements (sect. 3.5).

Figure 5 shows representative time delay (roundtrip) or range (one-way) residuals from a preliminary analysis of a $2\frac{1}{2}$ month pre-occultation arc of Helios B radiometric data (March 1 till May 16, 1976) assuming a 3-parameter, steady-state coronal electron density model to be discussed in sect. 3.4 (a significant quantity of range data from other tracking stations is not yet included). As is evident, some systematic trends are still present in the residuals (there is no sense to show raw data), and expected to be removed with a more detailed analysis. The solid curve gives the average coronal time delay signature. Away from occultation ($SEP = 37^\circ$) a normal value is about $0.1 \mu\text{s}$, during April and May there is a steep increase; the last eight, validated range measurements were taken on May 13 as close to the sun as $3.1 R_\odot$ (coronal time delay $\approx 28 \mu\text{s}$: roundtrip signal travel time 27.3 min corresponding to $245.4 \times 10^6 \text{ km}$ in range). The first valid range data acquired after occultation occurred on May 20 ($3.8 R_\odot/1^\circ$).

As far as electron content data are concerned there are approximately 45 sets of high quality measurements from Helios A varying between a duration of 0.5 until 6 h. Only about 1/3 of these sets lasts longer than 3 h. The set closest to the sun ($6.2 R_\odot/1.7^\circ$) and still unquestionable was taken on April 21, 1975 during the entry phase of the first occultation and is as short as 1.7 h. Figures 6a and b represent 2 typical data sets. Elongation and impact parameter are indicated and the noise level is shown with error bars. The time scale is given in UT and local mean time. On March 7, for example, the electron content ΔI (right scale) was measured for about 4 h, showing an increase (rate of change approximately $4.5 \times 10^{13} \text{ m}^{-2} \text{ s}^{-1}$) as usually expected during pre-occultation. The number of electrons along the raypath is steadily increasing towards the sun (Helios' distance to sun still $76 R_\odot$).

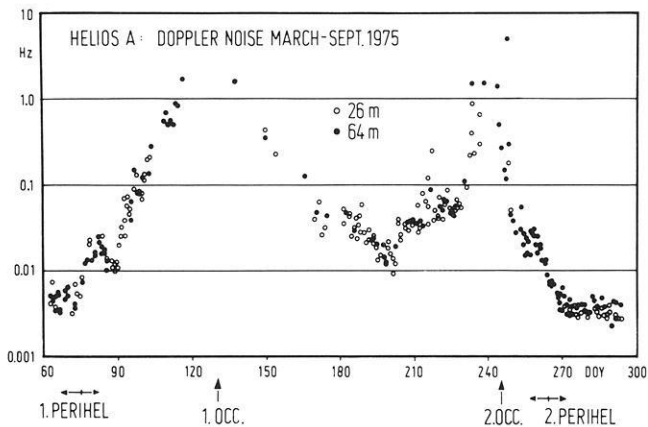


Fig. 4. Helios A Doppler noise for first and second occultation

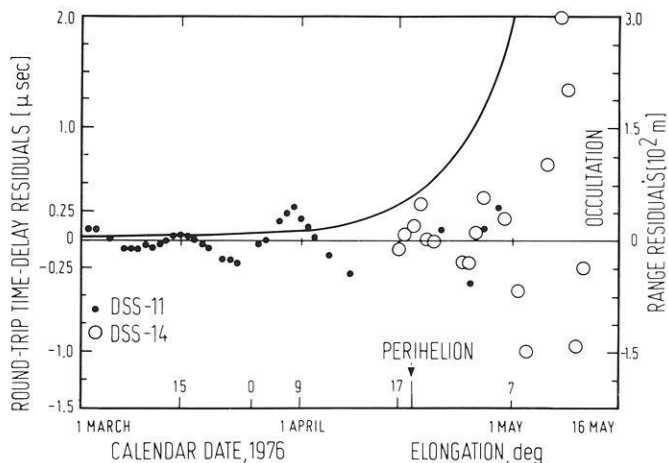


Fig. 5. Helios B range residuals and coronal time delay (entry phase of first occultation)

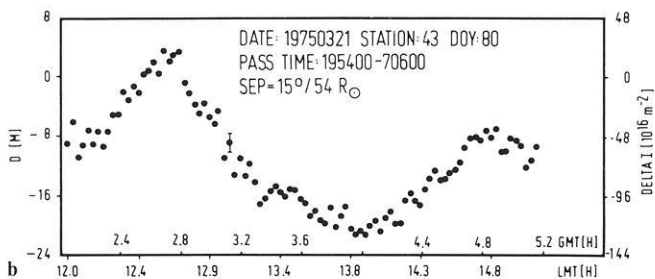
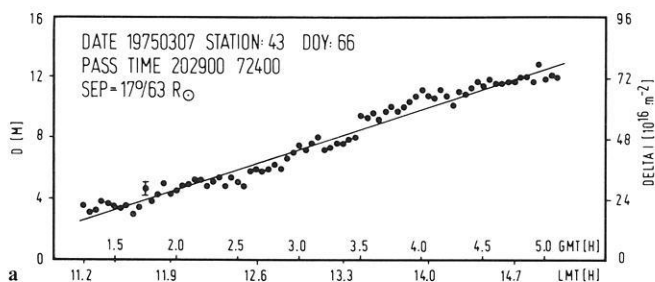


Fig. 6. Helios A electron content data:

a March 7, 1975 (SEP=17.4°); **b** March 21, 1975 (SEP=14.8°)

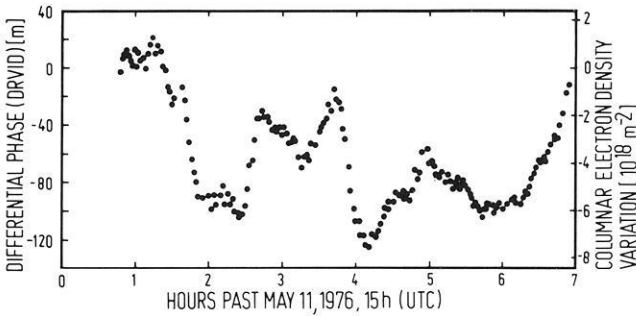


Fig. 7. Helios B electron content data closest to sun (west limb): May 11, 1976 ($\text{SEP} = 1.55^\circ/p = 5.8 R_\odot$)

Typical rates of change taken from averages on at least 2 or 3 h of observation vary like $(0.7\text{--}50) \times 10^{13} \text{ m}^{-2} \text{ s}^{-1}$. The noise level is as low as $\sigma \approx \pm 2 \times 10^{16} \text{ m}^{-2}$. An example of unusual temporal variations for a relatively large impact parameter $p = 54 R_\odot$ is shown by a data set from March 21 (only a few days after perihelion on March 15). The noise level is enhanced (up to $15 \times 10^{16} \text{ m}^{-2}$), typical time constants run as long as 1.5 or 2 h. Figure 7 shows Helios B electron content data taken on May 11, 1976 extending as long as 6 h; the raypath's offset from the sun's west limb was only $4.8 R_\odot$. To our knowledge there are no spacecraft supported coronal electron content measurements closer to the sun. The total variation of the electron content turns out to be approximately $0.9 \times 10^{19} \text{ m}^{-2}$, the maximum rate of change is as high as $6 \times 10^{15} \text{ m}^{-2} \text{ s}^{-1}$ (averaged over some 20 min). The excellent data quality is obvious from the noise level being as low as $0.8 \times 10^{17} \text{ m}^{-2}$.

3.2. Data Processing. For indirect measurements especially from an occultation type experiment data calibration is one fundamental part of the analysis. It is understandable from sect. 2.2 that for the electron content measurements calibration is not a serious problem, at least when compared with calibrating the range data. The electron content measured via DRVID-technique has to be corrected for dispersive propagation effects contributed by that part of the signal's raypath traversing the terrestrial ionosphere. So far approximately half of the Helios A data are corrected by using a standard calibration procedure developed by Yip (1974) using actual VHF-Faraday rotation measurements. On March 21 (Fig. 6b), for instance, the ionospheric contribution to the variation in electron content (time resolution approximately $\frac{1}{2}$ h) was as small as about $3 \times 10^{16} \text{ m}^{-2}$ within 4 h of observation (for elevation angles of the tracking antenna down to 30°), whereas the total variation measured by Helios is $1.5 \times 10^{18} \text{ m}^{-2}$ (2% error contribution). During the occultations of Helios A the maximum influence of the ionosphere turned out to be typically of the order of $(3\text{--}9) \times 10^{16} \text{ m}^{-2}$ at low elevation angles. As the raypath approaches the sun, ionospheric effects become negligible in comparison to solar plasma effects.

The station calibration of the time delay data as outlined in sect. 2.2 introduced no critical restriction. For a full tracking pass time delay drift and standard deviation were certainly less than 10 and 5 ns, respectively. Until now the transponder calibration is accounted for only by a constant.

An essential part of the analysis of the range and Doppler data deals with the problem of orbit determination. Evidently the determination of coronal electron densities is critically dependent on a precise knowledge of the spacecraft's orbital motion, because both these types of radiometric data are taken to solve for the orbit and corona as well. A highly sophisticated double precision orbit determination program developed at JPL was used to integrate the equations of motion numerically (e.g. Moyer, 1971). The current best knowledge of the planetary and lunar ephemerides and the locations of the DSN tracking stations have been utilized in this work. From an extensive orbital analysis of space missions Anderson et al. (1975) found that for purposes of high precision orbit determination generally there is some 6 month-optimal length of data arc to be covered. Though this length may be somewhat different for the Helios B mission, it is positively due to the quantity and excellent quantity of Helios B radiometric data that even a $2\frac{1}{2}$ month data arc yields acceptable range residuals (Fig. 5) and preliminary, surprisingly good estimates of steady-state coronal parameters (sect. 3.4). So far strong evidence has been found that for Helios B the ranging accuracy seems to be limited just by plasma effects from the coronal and interplanetary medium. However, additional analysis concerning the Helios solar radiation pressure model, station and transponder calibration, and calibration due to the turbulent corona have yet to be fully determined.

It should be noted that for relativistic perturbations affecting the spacecraft motion or the radio signal an Einstein model was used. The relativistic time delay effect (to be investigated by Helios exp. no. 11) is similar to that of the corona but much larger (e.g. Helios B prediction for May 13: corona $20\ \mu\text{s}$ /measured $28\ \mu\text{s}$; relativity $170\ \mu\text{s}$) and also different in time scale (half-decrease: 1 or 2 days; 14 days). There is abundant evidence in the literature strongly to support Einstein's theory (e.g. Anderson et al., 1975) and this implicit assumption has been made in the analysis thus far. So far no error analysis has been conducted to see how a 1% error in the relativistic effect maps into the estimated coronal parameters (sect. 3.4).

For this experiment the weighting scheme for the radiometric data as an input to the orbit determination process is especially important. The total a priori standard deviation σ_t on the roundtrip time delay measurements is assumed to follow $\sigma_t = (\sigma_s^2 + \sigma_p^2)^{\frac{1}{2}}$, where $\sigma_s = 0.2\ \mu\text{s}$ ($\cong 30\ \text{m}$ in range) stands for a constant value of system noise and $\sigma_p = \sigma/p^{1.5}\ \mu\text{s}$ ($\sigma = \text{const} = 33$) denotes the coronal plasma noise following the "frozen turbulence" hypothesis as given by Muhleman et al. (1977). The dependence on the impact parameter p essentially corresponds to an inverse quadratic law of a steady-state coronal model (sect. 3.4); at present the value σ is given by a least squares fit to range residuals from Mariners 6, 7 data. In terms of meters (one-way) the plasma noise for the Helios observations is assumed to vary between $\sigma_p \approx 950$ and $10\ \text{m}$ ($p = 3$ and $65\ R_\odot$). However, there is evidence that this weighting scheme is too conservative for the analysis of Helios data: Firstly, there were some substantial technical (on ground and aboard as well) and operational improvements in favor of ranging measurements for Helios B; secondly, the Mariner data were collected at a different time (solar maximum). Moreover this scheme assumes that the spacecraft is always far behind the solar corona (as was indeed the case for Mariner 6 and 7).

In order to derive a more realistic, refined weighting scheme for the range data in case of the Helios missions information on the actually measured variations of the

electron content during an individual tracking pass is most valuable. A direct measure of these variations is given by the DRVID data (differential phase) but this data type has the disadvantage that it can be measured only after the acquisition of a range point. It has been demonstrated by Esposito and Lüneburg (1976/77) that the same information can be extracted directly from the Doppler residuals of a preliminary orbit determination. A constant or even linear bias in these residuals resulting from an imperfect knowledge of the orbit can be determined by fitting integrated Doppler residuals (phase residuals) with the DRVID measurements in a least squares sense. The advantage of using phase residuals is to have a better time resolution (sampling time for Doppler data often 10s, but generally 2 min for DRVID), usually a higher accuracy (less or no noise from ranging modulation) and longer data stretches of electron content variation information. As an example, Figure 14 shows the agreement between the electron content variations either measured via differential phase (solid line) during a 7 h data set or via construction from phase or integrated Doppler residuals (dotted; data set extended by about 1 h); a 20 m-offset makes the comparison more readily evident.

After subtracting the differential increase of the electron content variation as predicted (and iteratively improved) by the average steady-state electron density model due to the relative motion of earth and spacecraft with respect to this steady-state model (a purely geometrical effect) the remaining variation of the electron content measurements are assumed to reflect the turbulence characteristics of the medium. A detailed investigation of these phase fluctuations is presently carried out. The difference between the actually measured phase variation and the time average of the electron content variations over the whole pass at those times when ranging data have been measured form “turbulence range calibrations” and will be subtracted from the measured range value in the same way as for instance station calibrations. The variance between the calculated time average over the finite pass length and the ensemble average will provide new weights for the weighting scheme. They depend critically upon the pass length and the correlation function of the phase fluctuation.

3.3. Comparison with Ground-Based Observations of the Inner Solar Corona. An essential part of the data analysis of any solar occultation experiment is to compare the results with other information about the global structure of the corona at that time. So the scientific analysis of the experiment was prepared and started in cooperation with the High Altitude Observatory (HAO)/National Center for Atmospheric Research, Boulder, USA. Since 1964 HAO has been carrying out a program of synoptic measurements of the intensity distribution of the sun’s white light (“K”) corona over the height range 1.1–2.7 R_{\odot} (solar radii from sun center) with sun-eclipsing K-coronameters (Wlérick and Axtell, 1957) from Mauna Loa, Hawaii. Azimuthal scans (steps of 5°) are made around the solar limb at discrete heights (as many as 10) with a polarimeter, providing a two-dimensional intensity distribution in the plane of the sky of the product “pB” (polarization times brightness) which is due to Thomson scattering from electrons in the solar atmosphere. Because of the earth’s orbital motion, the sun appears to rotate for the ground-based observer with a period of approximately 27 days, so that successive daily measurements can be combined to generate three-dimensional maps of the overall large-scale intensity distribution at these various heights in the corona. In

principle, pB-measurements can be deconvolved into coronal electron density models (such as discussed by Altschuler and Perry, 1972) but an entirely satisfactory, inexpensive computational program has not yet been developed. Though it is still some kind of an unsolved problem to invert pB-values via an integral relationship into electron densities, a height-dependent conversion factor can be introduced by an averaging process. Nonetheless, the raw pB-data are being used successfully for studies of short-term, transient changes (Hansen et al., 1974) as well as for studies of the longer-term evolution of magnetically-controlled structures of the inner corona (Hansen et al., 1972). These measurements can provide a basis for extrapolating optical determinations of electron density of the innermost corona (below $3 R_{\odot}$) to the much greater heights above the sun's west or east limb in the ecliptic plane where the electron content was actually measured along the raypath to Helios spacecrafts. Unfortunately, during the Helios occultations, there were no satellite-borne coronagraphs in operation; such instruments can provide information about coronal structures to distance of $6-10 R_{\odot}$ (reviewed by Tousey, 1973).

The interpretation of the Helios time delay data as an indicator of coronal plasma conditions is greatly simplified by the fact that with the general decline of solar activity near the end of the solar cycle, the overall shape of the corona became quite stable from rotation to rotation with a nearly axially symmetric distribution as typical near solar minimum (Hansen et al., 1969, 1976; Saito, 1970; Hundhausen et al., 1976; Jager, 1959; Scheffler and Elsässer, 1974). This is illustrated in Figure 8 with a pair of isophotal maps of the coronal intensity distribution at $1.5 R_{\odot}$ during November 1974 (shortly before launch of Helios A) and July 1976 (after first occultation of Helios B), as typical of the descending phase and minimum phase of the present solar cycle, respectively. An enormous simplification in the global shape is seen between those two times with the corona becoming limited to a nearly uniform, moderately bright band around the solar equator.

Figure 9 presents the Mauna Loa K-coronal measurements in a different form. Here only the equatorial intensities are plotted (schematically), at successive limb passages around the first occultation of Helios A (starting at Carrington rotation no. 1625: east/west limb data DOY 42.5/56.1 or February 11/February 25, 1975). The horizontal line represents the average coronal intensity around that time so that below-average values are indicative of coronal "holes". Dashed lines indicate times when east and west limb observations had to be combined to fill data gaps. Maximum occultation was during no. 1627 on May 6 (DOY 126) at the west limb. The stability of coronal structures is obvious as far as quiet conditions and extreme intensities are concerned, e.g. the particularly stable and intensive coronal hole around 270° solar longitude extending from the northern hemisphere of the sun for these eight solar rotations, with a longitudinal variation of ± 10 to 20° . A second, less intensive coronal hole extending from the southern hemisphere around $90-120^{\circ}$ longitude existed from before rotation no. 1625 and was developing again over about six rotational periods until no. 1634, including the second Helios A occultation.

The consequences for the analysis of the Helios time delay data are evident: Conditions were most favorable to probe stationary and quasi-stationary features of the solar corona (sect. 3.4, Fig. 10; Fig. 6a, sect. 3.5); conditions were also

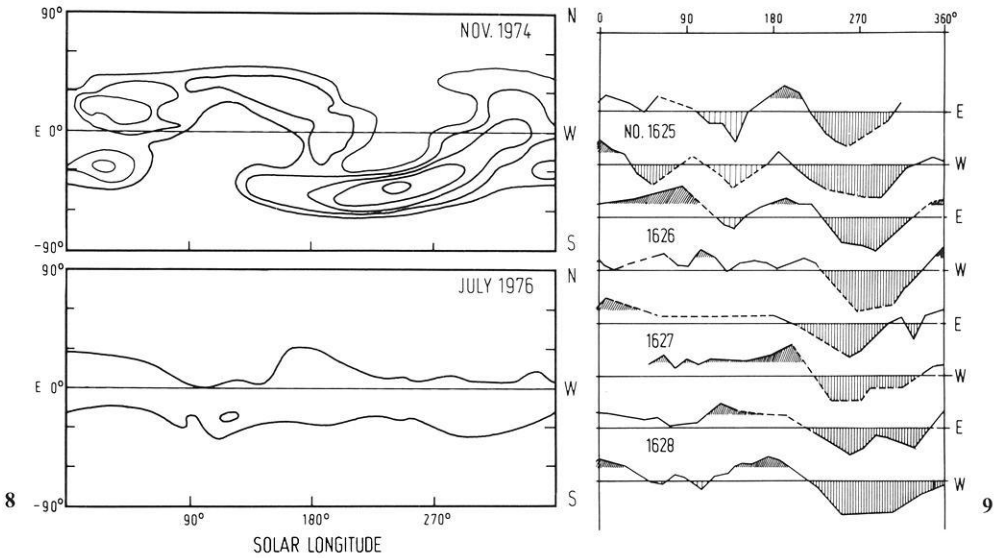
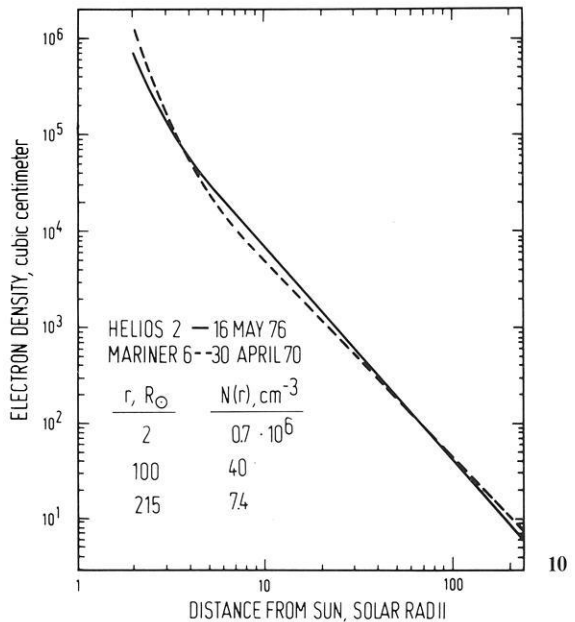


Fig. 8. Isophotal maps showing simplification of coronal structures (contours of constant pB-values at 1.5R_⊙) during descending versus minimum phase of solar cycle (1974/76)

Fig. 9. K-coronal intensity at sun's equator for successive limb passages around first occultation of Helios A (4 rotational periods, east and west limb)

Fig. 10. Stationary coronal electron density profile (Helios B)



favorable to relate transient features of the electron content measurements (e.g. Fig. 6b, sect. 3.6) to phenomena within the innermost corona generally associated with structures corotating for several solar rotational periods as actually visible from HAO's K-coronagraph data. There is evidence that a correlation of plasma phenomena from different regions of the solar corona or interplanetary medium is useful and promising (e.g. Hundhausen, 1972; Stewart et al., 1974; Gosling et al.,

1975; Hansen et al., 1976). This is also true with respect to a potential extrapolation into those regions where Helios in situ-measurements have been taken (such as data from plasma experiment no. 1).

3.4. Stationary Corona. A major part of the scientific objectives of this experiment covers the derivation of the spatial and temporal distribution of coronal electron densities.

Sophisticated filter algorithms properly combined with all the relevant a priori information are necessary to derive the density distribution with a sufficient resolution from remote sensing measurements via integral relationships involving propagation effects of electromagnetic waves in inhomogeneous media like planetary and solar atmospheres (e.g. Fjeldbo and Eshleman, 1968; Kliore et al., 1971; Colin et al., 1972; Edenhofer, 1974). There are, for instance, problems of numerical instability to invert the integral equations of time delay measurements for electron densities. This is particularly true when analysing range data not only for a radial electron density profile but also for longitudinal (and much less latitudinal) coronal effects, and when analysing electron content data for effects of coronal plasma dynamics by a sequential filtering concept to probe also time variations (Pirraglia and Gross, 1970; Saito, 1970). Generally a compromise has to be balanced between numerical stability and power of resolution in space and time. Simulated Helios time delay data were analysed in a simplified computer experiment to study issues like data redundancy necessary and noise levels to be expected (Lüneburg, 1974).

As a first attempt to solve for coronal electron densities a parameterization of the problem seems to be reasonable. Following, for example, Muhleman et al. (1971, 1977) and Anderson et al. (1975) the coronal electron density is modeled as a steady-state (time scale: months), spherically (at least axially) symmetric distribution given by a 3-parameter Baumbach-interpolation formula (also Scheffler and Elsässer, 1974)

$$N(r) = \frac{A}{r^6} + \frac{B}{r^{2+\varepsilon}}, \quad (2)$$

where the quantity N denotes the electron density [m^{-3}], r the dimensionless heliocentric distance in solar radii ($r > 3 R_{\odot}$), and A , B , ε are coronal parameters to be determined from the experimental data as average spatial and temporal values. No time delay measurements were collected closer than $3.1 R_{\odot}$ (Helios B), where powers like r^{-16} arise dominating for $r < 1.1 R_{\odot}$. The first term in (2) is expected to contribute significantly only for distances $r < 4 R_{\odot}$, so the parameter A might merely be determinable from Helios B data.

The parameters B and ε are highly correlated (Table 2). The coronal electron density may vary by a factor of 2 or 3 depending on heliographic latitude (equatorial versus polar) and phase of solar cycle (Jager, 1959; Hansen et al., 1969; Scheffler and Elsässer, 1974). Density models like (2) are also used to describe an average brightness function of the white light corona. Table 1 summarizes a priori values of the coronal parameters A , B , ε as well as results from Mariners 6 and 7 as an example of previous occultation type experiments.

Table 1. Solar corona parameters

$A/10^{14} \text{ m}^{-3}$	$B/10^{12} \text{ m}^{-3}$	ε	
1.3 ± 0.9	1.14 ± 0.7	0.3 ± 0.3	a priori
0.69 ± 0.85	0.54 ± 0.56	0.047 ± 0.24	Mariner 6
–	0.66 ± 0.53	0.08 ± 0.24	Mariner 7

Whereas the first term of (2) – including the term r^{-16} all the more – is known also from earth-bound solar eclipse observations (e.g. coronagraph measurements), the second term with the parameters B and ε is considered to be known only with insufficient reliability (“diffuse corona”) and to vary less with solar activity (mainly observations along the earth’s orbit).

Due to the solar corona there is a time delay τ accumulated along the earth-Helios raypath

$$\tau = \frac{1}{c} \int \frac{1}{n} ds - \frac{1}{c} \int ds, \quad (3)$$

or equivalently, expressible in terms of the difference between the radio signal’s group path and the purely geometrical distance ($n = v_g/c < 1$ is the radio refractive index of the coronal medium). Likewise for (1) it is a good approximation for S-band signal frequencies and media like the solar corona to neglect the effects of magnetic field and collisions in the dispersion relation for n . Assuming $\varepsilon = 0$ in order to get a closed, approximate expression the coronal time delay is given by

$$\tau \approx \frac{k}{f^2} \text{PSE} \left(\frac{A}{p^5} + \frac{B}{p} \right), \quad (4)$$

where k is a constant and PSE denotes the probe-sun-earth angle (close to π around occultation). Thus, the time delay τ is inversely proportional to the frequency squared and to the fifth and first power of the ray’s impact parameter.

With the density model (2) fully incorporated into JPL’s double precision orbit determination program the problem of determining the solar corona electron density distribution is reduced to the problem of estimation of the three steady-state coronal parameters A, B, ε . In a preliminary analysis Helios B radiometric data have been analysed that were acquired within March 1–May 16, 1976 ($2\frac{1}{2}$ months data arc with $3 < p < 65 R_\odot$). The residuals (observed minus computed values) for the range and Doppler data (see also Fig. 5) were formed and analysed using the classical weighted least squares algorithm (batch filter) to minimize the sum of the squares of the weighted data residuals Δz as well as weighted corrections $\Delta \tilde{x}$ to a priori estimates of the parameters. The equations for the corrections Δx to the estimated parameters and for the estimated parameter covariance matrix A are given by

$$\begin{aligned} \Delta x &= (A'WA + \tilde{A}^{-1})^{-1} [A'W\Delta z + \tilde{A}^{-1}\Delta \tilde{x}], \\ A &= (A'WA + \tilde{A}^{-1})^{-1}, \end{aligned} \quad (5)$$

where W is the weighting matrix, \hat{A} the a priori parameter covariance matrix, and the matrix A contains the partial derivatives of the data with respect to the unknown parameters (superscripts t and -1 mean matrix transposition and inversion, respectively). For this preliminary analysis a basic set of 12 parameters was estimated, including: the 6 orbital elements of the Helios B trajectory (or equivalently the spacecraft's velocity components and coordinates), 3 parameters of a solar radiation pressure model (directly coupled to the equations of orbital motion), and the 3 coronal parameters of the density model (2).

A typical and preliminary solution for the coronal parameters A , B , and ε estimated from Helios B range and Doppler data as outlined above is summarized in Table 2. The electron density modeled by this parameter set is shown by Figure 10 as a function of the heliocentric distance in comparison with the Mariner results (Muhleman et al., 1977).

Table 2. Preliminary estimate of coronal parameters (Helios B)

		correlation coefficients		
$A/10^{14} \text{ m}^{-3}$	0.3	–	–0.371	–0.369
$B/10^{12} \text{ m}^{-3}$	1.0	–0.371	–	0.998
ε	0.2	–0.369	0.998	–

So far it is impossible to present standard deviations of the coronal parameters which can be regarded as realistic values. However, the values already obtained show clearly that the Helios B time delay occultation data are potentially very powerful for a determination of a steady-state electron density model.

On the other hand, the information on the time averaged electron density profile obtained so far will be improved by containing the weighted least squares solutions for the coronal parameters (which are principally non-unique) in such a way that reasonable mean values and standard deviations for the electron densities are attained in regions where it was impossible to collect time delay data. Close to the sun ($p < 3 R_{\odot}$) HAO's coronagraph measurements can be introduced for a data fitting mainly affecting the parameter A ; farther away from the sun ($p \geq 65 R_{\odot}$) the Helios in situ-plasma measurements supplemented by measurements of the earth-bound IMP 7, 8 satellites (at $215 R_{\odot}$) provide excellent a priori constraints to be imposed on the possible values for B and ε as supported by the estimation algorithm. Thus for the Helios occultations there is a unique opportunity for a combined analysis of indirect and direct measurements from various sources to obtain information about the electron density distribution at heliocentric distances extending from 1.1 – $215 R_{\odot}$. It is expected that such a data extrapolation is one way to reduce the averaging time intervals (i.e. subdivided lengths of data arcs or batches determining time resolution) for sets of estimated coronal parameters or resulting electron density profiles associated with the corresponding radial sectors in the ecliptic plane (longitudinal coronal probing).

At the present some comparative remarks may be added. According to coronagraph measurements of Hansen et al. (1969) in 1964 near solar minimum an average equatorial electron density was found to be $1.4 \times 10^{13} \text{ m}^{-3}$ for $r = 1.5 R_{\odot}$.

Extrapolating this value to $4 R_{\odot}$ with the aid of the Helios B coronal model yields $2.5 \times 10^{11} \text{ m}^{-3}$. For both distances Newkirk (1967) gives representative coronal electron densities (likewise equatorial values at sunspot minimum) of 1.7×10^{13} and $1.2 \times 10^{11} \text{ m}^{-3}$, respectively, where the latter value is in good agreement with the extrapolated density. For a distance of $r = 30 R_{\odot}$ the value $5.6 \times 10^8 \text{ m}^{-3}$ from the Helios B coronal model nicely agrees with Newkirk's corresponding density $4.6 \times 10^8 \text{ m}^{-3}$. Near Helios perihelion and near the earth's orbit the coronal model yields electron densities of about 10^8 and $7 \times 10^6 \text{ m}^{-3}$, respectively. A comparison with the Mariner 6 coronal model needs some care. There are 2 basic differences: the Mariner 6 occultation ($p > 3.6 R_{\odot}$) on April 30, 1970 was during solar maximum and the orbital geometry caused the raypath to move through the full range of solar latitudes, passing over the sun's north pole for about 8 days around occultation. The determination of coronal parameters actually depends on the assumption of a spherically symmetric model for the electron density distribution (different from Helios mission). Generally during sunspot maximum electron densities at high (low) solar latitudes are greater (smaller) than those values existing for sunspot minimum conditions (e.g. Hansen et al., 1969). To some extent the general expectation seems to be confirmed for the Mariner model to have greater (smaller) electron density values close to (farer away from) the sun ($p < 4$; $4 < p < 70 R_{\odot}$). On the other hand, it may be questionable whether or not a latitudinal dependence of the electron density can be resolved from Helios data.

3.5. Quasi-Stationary Corona. The set of Helios A electron content measurements on March 7, 1975 (Fig. 6a; sect. 3.1) is taken to discuss some quasi-stationary features of the solar corona (time scale: h or days). Figure 11 shows the isophotal map (height $1.5 R_{\odot}$) for the corresponding Carrington rotation no. 1625 and also 1626 covering most of the entry phase of the first occultation (time runs from right to left). The global structure of the corona is illustrated by 3 intensity levels of contours equivalent to constant electron densities of $(5.5; 7.2; 8.9) \times 10^{12} \text{ m}^{-3}$. None of the two brightness centers (oblique lines) approximately located at solar longitudes 250° (35°S) and 100° (30°N) was intercepted by the Helios raypath indicated by a solid line from the ecliptic plane at 7°S (\approx constant during both rotational periods). However, the Helios raypath did pass through a pronounced, significant coronal hole (vertical lines) near the equator at about 70° longitude.

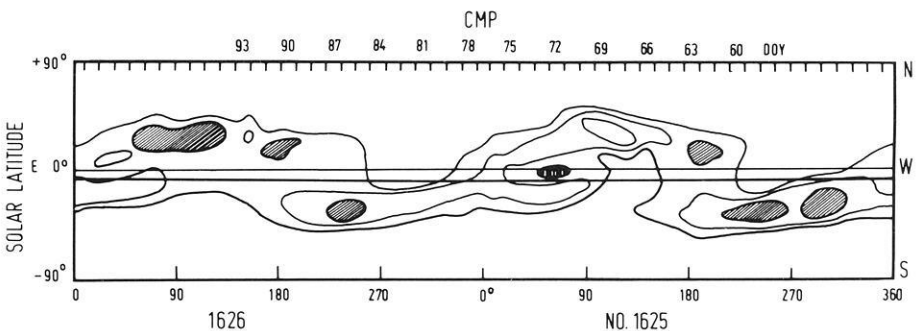


Fig. 11. Isophotal maps (CMP date) to correlate with Helios A radiometric data from March, 1975

Quite different are large-scale, long-lived coronal hole structures extending from northern and southern latitudes across the ecliptic plane around longitudes 250 and 130°, respectively (sect. 3.3). In a rough approximation now the following relationships can be established: On March 7 (DOY 66) the elongation is about $\text{SEP} = 17^\circ$ and the distance earth-Helios is 0.75 AU (i.e. the signal's roundtrip travel time equals 13 min) resulting in a PSE-angle of 38° . This date of observation corresponds to a central meridian passage (CMP) date of $38^\circ: 13.2^\circ/\text{d} \approx 3$ d earlier (DOY 63, solar longitude some 180°). As can be seen from Figure 11 this observational geometry relates to a coronal structure which looks just like a saddle point configuration, amidst a broad band of low-leveled brightness (equivalent to electron densities of about $6 \times 10^{12} \text{ m}^{-3}$) crossing the sun's equator between some 220 and 150° longitude. Though in some respects it is hypothetical to extrapolate even quiet coronal conditions from $1.5 R_\odot$ to distances of $76 R_\odot$, this data set seems to be related to a time interval prevailing approximately ($220^\circ\text{--}150^\circ$): $13.2^\circ/\text{d} \approx 5$ d with a nearly uniform longitudinal distribution of coronal plasma within the ecliptic plane; there is even a good deal of latitudinal homogeneity around the Helios raypath. Thus, the linear increase of the electron content measured ($6.3 \times 10^{17} \text{ m}^{-2}$) should mainly be due to the radial dependence of such a quasi-stationary electron density distribution. The physical concept of such an interpretation is experimentally supported by another set of electron content data measured only two days earlier (DOY 64); this data set looks quite similar to that discussed above.

From Helios A there is a total number of 13 sets of electron content measurements ($\approx 30\%$ of all data sets) which also vary linearly with respect to time. The correlation coefficients from a regression analysis are as high as 0.6 to 0.9 and even more (Fig. 6a: 0.98). Most of these sets belong to the early entry and the late exit phase of occultation. Since Helios B electron content measurements could be collected closer to the sun the percentage of such "linear" data sets is smaller.

In a first order approximation a linearized approach was developed to derive a coronal parameter B from the slope of such data sets according to a density model like (2). For a physical model as simple as possible (to be described by using just one parameter) the parameter B alone describes a purely inverse quadratic law for a spherically symmetric electron density distribution. This "quadratic" coronal model is expected to hold for heliocentric distances $r > 4 R_\odot$ setting $A = 0$ (no Helios electron content data sets were obtained closer than $p = 5.8 R_\odot$). The parameter $\varepsilon \neq 0$ means considerable complications (analytical and numerical as well), if such an exponential parameter is to be derived only from electron content data (which is even true for long arcs of range and Doppler data). Since physically the coronal parameter $\varepsilon = \varepsilon(r)$ accounts for the conservation of mass (time derivatives neglected, i.e. stationary flux density and flux) associated with a radially dependent velocity profile (e.g. Hundhausen, 1972), an approximation $\varepsilon = \text{const} \approx 0$ may be justified specifically for the electron content measurements: linear slopes were observed preferably at the beginning of the entry phase of occultation ($p > 20$ or $30 R_\odot$), where the velocity is still nearly constant with respect to r (e.g. 400 km/s, slowly decreasing towards occultation in those plasma regions around the raypath closest to the sun); the time interval to measure a data set is too short (less than 8 h) to yield significant radial velocity variations from the geometry of a Helios-like

orbital configuration. Even from an analysis of months of data arcs the ε -values actually derived turned out to be small ($\varepsilon=0.05$ /Mariner 6; 0.2/Helios B, preliminary). Taking a quadratic model corona and neglecting refractive effects (fully consistent with the assumption $A=0$) yields an analytical expression for the total, one-way electron content I according to (1)

$$I = \bar{I} \times \frac{1}{p} \left(\text{arc cos } \frac{p}{r_E} \pm \text{arc cos } \frac{p}{r_p} \right), \quad (6)$$

$$\approx \pi \bar{I} \frac{1}{p}; \quad p \ll r_E, r_p.$$

Heliocentric distances to earth and Helios are denoted by r_E, r_p in solar radii, an a priori value $B = 1.15 \times 10^{12} \text{ m}^{-3}$ (Table 1) gives the order of magnitude for $\bar{I} = B R_\odot = 8 \times 10^{20} \text{ m}^{-2}$. The plus-sign (after perihelion) combines the contributions to the electron content along the raypath from the earth to the point of closest approach to the sun (heliocentric distance p) and from this point to the spacecraft. For small values of the impact parameter p as typical for a solar occultation the electron content I essentially depends on p only, i.e. variations of the electron content (\sim integrated density) can be probed farer away from the sun than the associated density variations. Assuming a quasi-stationary corona as outlined ($B = \text{constant}$ with respect to time) and referring to some reference time t_0 , the time variations of the electron content $\Delta I(t) = I(t) - I(t_0)$ turn out mainly to be due to the time variations of geometrical quantities like $p = p(t)$ and $r_p = r_p(t)$ which can be approximated for occultation as linear functions of time with sufficient accuracy for observation intervals no longer than some hours ($\dot{r}_E \ll \dot{r}_p, \dot{p}$). Truncation of a Taylor series expansion in terms of powers of $t - t_0$ yields

$$\Delta I(t) \approx B R_\odot \left[-\pi \frac{\dot{p}_0}{p_0^2} + \frac{\dot{r}_{p0}}{r_{p0}^2} \right] (t - t_0), \quad (7)$$

where dotted quantities mean differentiation with respect to time and index 0 refers to quantities for $t = t_0$ (entry/exit phase: $\Delta I \geq 0$). So only known geometrical quantities are involved to derive the coronal parameter B from a linear rate of change of electron content data. On the other hand, if sets of electron content measurements show a time variation which is essentially linear (where the correlation coefficient is an appropriate criterion), then the expectation is that something like a quadratic spatial decay may be a useful approximate model for an electron density distribution to start with.

Figure 12 shows a typical example for the diurnal variation of the electron content as computed by using the exact relationship (6) for the Helios A orbit on March 6, 1975. Even on a full 24 h-time scale the orbital geometry gives no significant deviation from a linear slope. One day earlier and later actual 3 h- and 4 h-data sets of electron content measurements could be obtained (indicated by solid lines) with correlation coefficients for a linear functional dependence as high as 0.98. The slopes of these data sets were determined by a least squares fit to yield about 62×10^{12} and $45 \times 10^{12} \text{ m}^{-2} \text{ s}^{-1}$ (straight line in Fig. 6a); a priori values of B yield some $6 \times 10^{12} \text{ m}^{-2} \text{ s}^{-1}$. Owing to the high Helios SNR the uncertainty

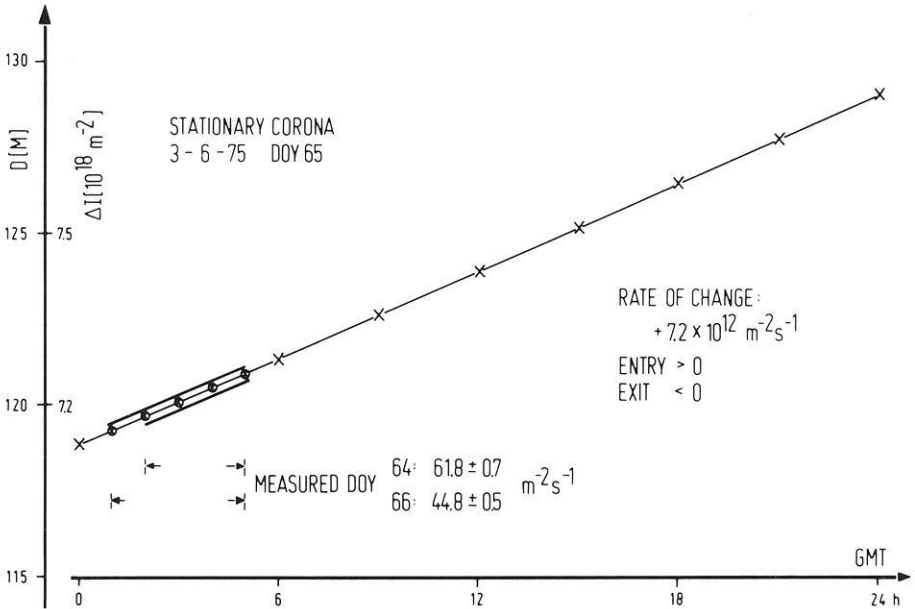


Fig. 12. Diurnal variation of electron content (quasi-stationary corona)

associated with these slopes is as low as $\pm 10^{12} \text{ m}^{-2} \text{ s}^{-1}$; the ionospheric influence is already corrected for. For instance, according to (6) a preliminary value of $6.3 \times 10^{12} \text{ m}^{-3}$ was derived (March 7) for a coronal parameter B in terms of a quasi-stationary electron density distribution. In order to get an idea of the corresponding electron density at $76 R_{\odot}$ according to (2) this value can be used to give: $1.1 \times 10^9 \text{ m}^{-3}$ ($\varepsilon=0$); 3×10^8 (0.3; a priori); 1.3×10^8 (0.5; Scheffler and Elsässer, 1974). The preliminary results for the coronal parameters from Helios B data (Table 2) yield $7.3 \times 10^7 \text{ m}^{-3}$ for the same distance.

It should be pointed out that so far these values are merely formal. The electron content measurements from spacecrafts Helios A and B indicate a distinct day-to-day variation of the slope of those data sets linearly depending on time. Thus, B-parameters derived by such a concept actually describe an overall, but local coronal electron density distribution which is thought to be quasi-stationary on a time scale of some hours. Certainly these quasi-stationary B-parameters are different from the B-parameters as usually derived from an analysis of all the radiometric data covering the entire period of occultation. Generally it turns out from Helios data sets similar to Figure 6a that the quasi-stationary B- and N-values associated only with local coronal regions (p typically varies by about $0.3 R_{\odot}$) are too high. Analysing radiometric data from a long orbital arc results in parameters of a stationary corona averaged on a time scale of months. Obviously it is necessary, e.g. to include non-vanishing ε -values (also supported by the high correlation with the coronal parameter B) to obtain realistic values for the electron density. However, this means to extend the time scale of the data span and to include temporal variations of the electron content deviating from linear slopes. It is expected that the parameter ε cannot be determined on a quasi-stationary time scale, i.e. the ε -

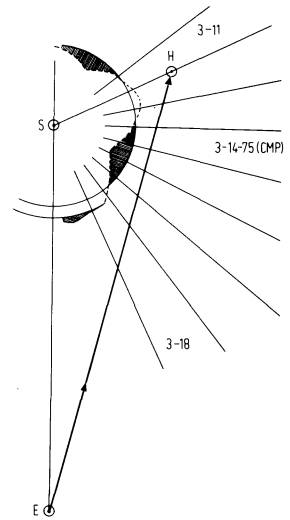


Fig. 13. Orbital geometry (sun-earth-Helios) and equatorial K-coronal intensities (west limb) around March 21, 1975 (Helios A)

values should be taken as fixed. The question is being investigated whether or not the discrepancies are fully due to the shorter averaging time intervals of the quasi-stationary values.

3.6. Special Events – Transient Phenomena. This preliminary analysis is completed by a brief discussion on 2 examples of unusual data sets from the Helios electron content measurements.

The extraordinary feature of the Helios A electron content data set on March 21, 1975 \cong DOY 80 (Fig. 6b; sect. 3.1) may roughly be related to the concurrent global structure of the white light corona (Fig. 11) as follows: Assuming the strongest interference with the coronal plasma around the raypath's point of closest approach (impact parameter $p = 54 R_{\odot}$, elongation angle $SEP = 15^{\circ}$) according to $\Delta I \sim 1/p$ one should look for an unusual coronal structure approximately belonging to a CMP date of DOY 74 during Carrington rotation no. 1625, i.e. ($90^{\circ} - 15^{\circ}$): $13.2^{\circ}/d \approx 6d$ earlier. This is pretty close to the pronounced coronal hole extending at some 70° longitude along the sun's equator and intercepted by the Helios raypath as already illustrated. A more detailed description is shown by Figure 13. On March 21 the Helios A spacecraft was situated about 25° beyond the west limb of the sun (in reference to the sun-earth line). Around this date the longitudinal distribution of the equatorial K-coronal intensities is indicated and divided into sectors of uniform angular width corresponding to the solar rotation on a day-to-day basis (13° longitude; CMP date relative to an earth-based observer) simplifying the actual sectors of Archimedian type. As can be seen the 70° -coronal hole (also Fig. 9) is really closest to the Helios ray-path as compared with adjacent structures of the inner corona. The total variation of the electron content measured on a time scale of 2.7 h is $\Delta I = 1.4 \times 10^{18} \text{ m}^{-2}$, i.e. some 5% with reference to the order of magnitude of $2.6 \times 10^{19} \text{ m}^{-2}$ for the corresponding background electron content approximated by using the Helios B model corona. In addition to that a preliminary discussion with experimenters from plasma exp. no.

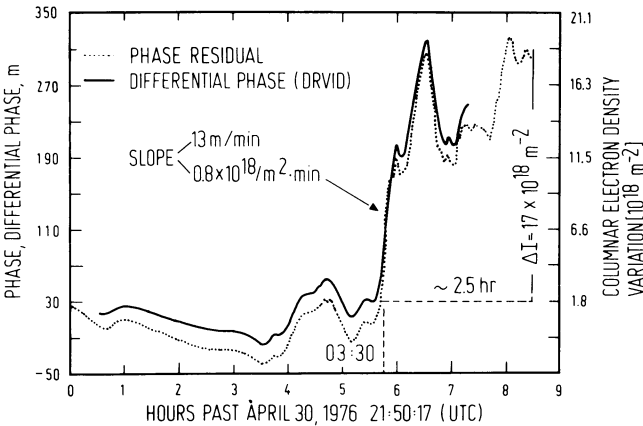


Fig. 14. Electron content variation from Helios B on April 30/May 1, 1976 (flare event)

¹ has shown that for electron content data sets of such kind there might have been an interaction between the Helios raypath and the spiral of a stream of high speed plasma originating from a coronal hole. A detailed investigation is being carried out proving whether or not the effects measured are in fact due to regions of compressed plasma formed at the leading edge of a high speed stream (e.g. Hundhausen, 1972).

Figure 14 refers to the phenomenon of plasma ejecta from a solar flare intercepting the ray path of Helios B on April 30/May 1, 1976 and recorded via differential phase (DRVID) and phase residual (fully equivalent to each other) as an enormous variation in electron content $\Delta I = 1.7 \times 10^{19} \text{ m}^{-2}$ with a maximum rate of change of about $2.2 \times 10^{14} \text{ m}^{-2} \text{ s}^{-1}$. The values of elongation and impact parameter are 6.92° and $26.1 R_\odot$, respectively, the latter decreasing by $0.8 R_\odot$ within the interval of observation. Taking the Helios B model corona an approximate value of the background electron content may be $2.7 \times 10^{18} \text{ m}^{-2}$ at maximum, i.e. only about 1/6 of the variation measured. During the first 4 h of this electron content data set the noise is small and characteristic of reasonably quiet solar conditions. The return of the data back to a background level is not evident since the pass ended while the ejecta was still within the raypath; the flare ejecta duration intercepting the raypath is in excess of 2.5 h. So far the observed duration of enhanced columnar electron density in the Helios-earth raypath at impact parameter of $26.1 R_\odot$ may be interpreted in either of two ways: 1. The flare-induced disturbance led to the continuous outward streaming (as a fire hose) of a dense plasma for at least 2.5 h, or alternatively 2. The flare ejection process itself was short-lived but produced a plasma cloud having a wide range of speeds (at $26.1 R_\odot$) varying from a maximum of about 900 km/s (corresponding to the delay time of 402 min for the leading edge) to a minimum of less than 660 km/s (corresponding to the last Helios measurement at 652 min after flare onset).

A correlation with the optical emergence of the flare on the solar surface gives

¹ Private communication from R. Schwenn and M. Montgomery

an estimation of the flare ejecta propagation speed (roughly assuming radial direction). Table 3 gives an informative survey on earth-based observations referring to this solar flare and was provided by the Space Environment Services Center, Boulder.²

Table 3. Solar disturbance on April, 30, 1976

Optical flare, importance 2 bright start 2048 UT, maximum 2114 UT position S9°, W 47° from CMP
Type III radio emission, large group, importance 3+ (8–80 mHz) 2103 to ≈2113 UT
Type II radio emission, ≈2116 to 2125 UT
Type IV continuum, 2103 to >2400 UT

Combined with the approximate location of the onset of the flare in the electron content data at 03:30 UTC (Fig. 14), May 1, 1976 (i.e. implying a travel time of 6 h 42 min), and a distance estimate of $31.3 R_{\odot}$ from the flare position on the solar surface to the radial intersection with the Helios B raypath, a preliminary value of the flare propagation speed may be inferred to be $v \approx 31.3 R_{\odot}/6 \text{ h } 42 \text{ min} \approx 900 \text{ km/s}$. At present it is hypothesized that the sharp rise in the electron content data at 03:30 UTC coincides with the leading edge of flare ejecta. Also the minor variation immediately preceding the rapid rise may be an evidence for a shock front preceding the main body of the flare ejecta (Hundhausen, 1972).

Some final remarks may be added as to the time variation of the Helios electron content data. Because of the high ranging power of the Helios spacecrafts the noise level of the electron content measurements is nearly two orders of magnitude below that from Mariners 6, 7, 9 (Callahan, 1975). So even minor time variations of the electron content data become distinguishable. Owing to the variable bandwidth of the Helios transponder (5 Hz up to about 1.3 kHz) there are also no on-board limitations as to the high frequency time resolution for the electron content data sets with a Nyquist frequency of generally 4.2 mHz as given by the sampling theorem. Obviously there are periodical structures in the data superimposed on the linear increase (or decrease) and the transient behavior as well. So the temporal variations of nearly half of the Helios A electron content measurements consistently reveal significant periodicities within a frequency range of about 0.2 (and even less) up to 3 mHz, for instance distinct frequency peaks around, e.g. 0.35; 0.9; 2 mHz preferably on successive days. Work is in progress to extend a maximum entropy spectral and correlation analysis (e.g. Chen and Stegen, 1974; Ulrych and Bishop, 1975) already initiated for the Helios electron content data. The question is being investigated whether or not wavelike plasma structures due to preferred individual modes can be identified (Hollweg, 1975). On the other hand, the Helios electron content data are being analysed to describe the statistical fluctuations in terms of power spectra especially as far as the slope is concerned as a function of the impact parameter. An analysis towards high frequency scintillations (e.g. Jokipii,

² Also private communication from G. Dulk, UC Boulder

1973) is particularly supported by using the phase residual data type (sect. 3.2) with a higher Nyquist frequency (up to 50 mHz). Improving the weighting scheme of the range and Doppler data by proper noise models is one aspect of application for such a statistical approach.

Finally, the information on the coronal electron density distribution obtainable from a scientific analysis of this occultation experiment may be useful to other Helios experiments such as measuring the zodiacal light (exp. no. 9). It may be possible to analyse observations of the zodiacal light closer to the sun ($p < 20 R_{\odot}$) with a higher reliability, if the scattering effect due to the electrons can be corrected for, e.g. by using coronal models like (2) with parameters actually representative for the in situ-measurements during the Helios mission.

4. Conclusions

Time delay occultation data of high quality were collected in 1975/76 from the Helios spacecrafts as close to the sun as $3.1 R_{\odot}$ (range) and $5.8 R_{\odot}$ (electron content), respectively; plasma effects could be measured directly as far away as about $190 R_{\odot}$ (before first inferior conjunction of Helios B). The Helios orbital geometry and the global structure of the corona during solar minimum conditions are especially in favor of remote probing the coronal electron density distribution (west and east limb as well) including the outer and extended corona. From a preliminary data analysis steady-state and dynamical features of the electron density distribution became obvious (time scale of months/h). Three coronal parameters for an average electron density model (i.e. spatial decay in terms of inverse powers of the heliocentric distance) are determined by a weighted least squares estimation to yield electron densities of e.g.: 1.3×10^{11} ; 6.3×10^9 ; 1.4×10^9 ; 1×10^8 ; 4×10^7 ; $7 \times 10^6 \text{ m}^{-3}$ at distances 3; 10; 20; 65; 100; $215 R_{\odot}$. Electron content variations mainly linear with respect to time are related to an inverse quadratic power law for electron densities of a quasi-stationary corona. For typical electron content data sets there are indications that correlations may be established with earth-bound K-coronagraph measurements revealing long-lived, corotating coronal structures. Two examples of transient plasma phenomena are discussed for Helios electron content measurements on March 21, 1975 and April 30/May 1, 1976 as probably related with an equatorial coronal hole and the special event of a solar flare. The latter is associated with an electron content enhancement of about five times typical background values (at about $30 R_{\odot}$ distance from sun), the velocity of propagation for flare ejecta turns out to be some 900 km/s. More detailed coronal structures are expected to result from a correlative analysis of time delay data together with Faraday rotation data and Helios in situ-measurements.

Acknowledgements. This work was supported by the Bundesministerium für Forschung und Technologie (BMFT) and the National Aeronautics and Space Administration (NASA). Gratitude is expressed to a great number of people involved with the data acquisition, processing, and analysis: G.L. Spradlin and G. Hiendlmeier representing all team efforts from the Deep Space Network (DSN) and the DFVLR-Hauptabteilung Raumflugbetrieb (GSOC); D.L. Cain, Dr. R.M. Georgevic, H.N. Royden, Dr. K.W. Yip from the Tracking and Orbit Determination Sec. at JPL together with A.I. Beers, A.C. Bouck; K. Heftman, Drs. W.G. Melbourne, W. Foggy for their continuous support likewise the Helios project

scientist Dr. H. Porsche and project management G. Ousley, A. Kutzer. We would also like to thank Dr. F.H. Hibbered, H. Haumer, P. Schanz, Dr. M. Eckstein, Jacob, M. Malchow for their efforts. Gratitude is expressed to Drs. J.V. Hollweg, H.T. Howard, D.O. Muhleman for valuable discussions. The numerical calculations were performed with the aid of the DFVLR and JPL Computing Centers.

References

- Altschuler, M.D., Perry, R.M.: On determining the electron density distribution of the solar corona from K-coronameter data. *Solar Phys.* **23**, 410–428, 1972
- Anderson, J.D., Esposito, P.B., Martin, W., Thornton, C.L., Muhleman, D.O.: Experimental test of general relativity using time delay data from Mariner 6 and Mariner 7. *Astrophys. J.* **200**, 221–233, 1975
- Berman, A.L., Wackley, J.A.: Doppler noise considered as a function of the signal path integration of electron density during solar conjunctions. Inter. Mem. 412G-76-075, Jet Propulsion Lab., California Institute of Technology, Pasadena, 1976
- Böttger, H., Benöhr, H., Mann, D., Prem, H., Adamek, P.: Helios mission critical assessment of spacecraft system design goals versus actual orbit performance. Proc. IAF XXVth Congr., Lisbon, 1975
- Callahan, P.S.: Columnar content measurements of the solar-wind turbulence near the sun. *Astrophys. J.* **199**, 227–236, 1975
- Chen, W.Y., Stegen, G.R.: Experiments with maximum entropy power spectra of sinusoids. *J. Geophys. Res.* **79**, 3019–3022, 1974
- Colin, L., ed.: Mathematics of profile inversion. NASA Techn. Mem. X-62,150, 1972
- Counselman, C.C., III, Rankin, J.M.: Density of the solar corona from occultations of NP 0532. *Astrophys. J.* **175**, 843–856, 1972
- Edenhofer, P.: Inversionsmethoden bei Remote Sensing mit elektromagnetischen Wellen. *Kleinheubacher Ber.* **17**, 343–358, 1974
- Edenhofer, P., Esposito, P.B., Hansen, R.T., Hansen, S.F., Lüneburg, E., Martin, W.L., Zygielbaum, A.I.: Preliminary analysis of coronal electron content measurement from spacecraft Helios A around first solar occultation. *Kleinheubacher Ber.* **20**, 67–80, 1977
- Edenhofer, P., Esposito, P.B., Hansen, R.T., Hansen, S.F., Lüneburg, E., Martin, W.L., Zygielbaum, A.I.: Time delay occultation data of the Helios spacecrafts for probing the electron density distribution in the solar corona. Research Rept. BMFT-FB W 77 (to be published), 1977a
- Esposito, P.B., Lüneburg, E.: Correspondence between DRVID (differential phase) and integrated Doppler (phase) residuals – extension of domain of direct solar corona data. JPL Engrg. Mem. 315-4/315-10, 1-20/1-36, 1976/77
- Fjeldbo, G., Eshleman, V.R.: The atmosphere of Mars analysed by integral inversion of the Mariner IV occultation data. *Planetary Space Sci.* **16**, 1035–1059, 1968
- Gosling, J.T., Hildner, E., MacQueen, R.M., Munro, R.H., Poland, A.I., Ross, C.L.: Direct observations of a flare related coronal and solar wind disturbance. *Solar Phys.* **40**, 439–448, 1975
- Hansen, R.T., Garcia, C.J., Hansen, S.F., Loomis, H.G.: Brightness variations of the white light corona during the years 1964–67. *Solar Phys.* **7**, 417–433, 1969
- Hansen, R.T., Garcia, C.J., Hansen, S.F., Yasukawa, E.: Abrupt depletions of the inner corona. *Publications of the Astron. Soc. of the Pacific* **86**, 500–515, 1974
- Hansen, R.T., Hansen, S.F., Sawyer, C.: Long-lived coronal structures and recurrent geomagnetic patterns in 1974. *Planetary Space Sci.* **24**, 381–388, 1976
- Hansen, S.F., Hansen, R.T., Garcia, C.J.: Evolution of coronal helmets during the ascending phase of solar cycle 20. *Solar Phys.* **26**, 202–224, 1972
- Hollweg, J.V.: Waves and instabilities in the solar wind. *Rev. Geophys. Space Phys.* **13**, 263–289, 1975
- Hundhausen, A.J.: *Coronal expansion and solar wind*, 1st ed. Berlin-Heidelberg-New York: Springer 1972
- Hundhausen, A.J., Hansen, R.T., Hansen, S.F., Feldman, W.C., Asbridge, J.R., Bame, S.J.: The evolution of coronal and solar wind structure in 1973 and 1974. Proc. AGU Int. Symp. on Solar-Terr. Phys., Boulder, 1976
- Jager, C.: Structure and dynamics of the solar atmosphere. In: *Encyclopedia of physics*, Vol. LII/III, S. Flügge, ed., pp. 80–362. Berlin-Heidelberg-New York: Springer 1959

- Jokipii, J.R.: Turbulence and scintillations in the interplanetary plasma. *Ann. Rev. Astr. Astrophys.* **11**, 1–28, 1973
- Kliore, A.J., Fjeldbo, G., Seidel, B.L.: Summary of Mariner 6 and 7 radio occultation results on the atmosphere of Mars. *Space Res.* **XI**, 1, 165–175, 1971
- Lüneburg, E.: Determination of the electron density profile of the solar corona from simulated time delay effects of Helios occultation data. *Kleinheubacher Ber.* **17**, 359–367, 1974
- MacDoran, P.F.: A first-principles derivation of the Differenced Range Versus Integrated Doppler (DRVID) charged-particle calibration method. *JPL Space Progr. Sum.* 37–62, **II**, 28–34, 1970
- MacDoran, P.F., Callahan, P.S., Zygielbaum, A.I.: Probing the solar plasma with Mariner radio tracking data. In: *Proc. conf. on experimental tests of gravitation theories*, R.W. Davies, ed., pp. 105–110. JPL Techn. Mem. 33–499. Pasadena, 1971
- MacDoran, P.F., Martin, W.L.: DRVID charged-particle measurement with a binary-coded sequential acquisition ranging system. *JPL Space Progr. Sum.* 37–62, **II**, 34–41, 1970
- Martin, W.L.: A binary-coded sequential acquisition ranging system. *JPL Space Progr. Sum.* 37–57, **II**, 72–81, 1969
- Martin, W.L.: Performance of the binary-coded sequential acquisition ranging system of DSS 14. *JPL Space Progr. Sum.* 37–62, **II**, 55–61, 1970
- Martin, W.L., Zygielbaum, A.I.: Mu-2 Ranging. *JPL Techn. Mem.* 33–768 (in press)
- Moyer, T.D.: Mathematical formulation of the double precision orbit determination program. *JPL Techn. Rept.* 32–1527, 1971
- Muhleman, D.O., Anderson, J.D., Esposito, P.B., Martin, W.L.: Radio propagation measurements of the solar corona and gravitational field: Applications to Mariner 6 and 7. *JPL Techn. Mem.* 33–499, 92–104, 1971
- Muhleman, D.O., Esposito, P.B., Anderson, J.D.: The electron density profile of the outer corona and the interplanetary medium from Mariner 6 and 7 time delay measurements. *Astrophys. J.* **211**, 943–957, 1977
- Newkirk, G., Jr.: Structure of the solar corona. *Ann. Rev. Astr. Astrophys.* **5**, 213–266, 1967
- Pirraglia, J., Gross, S.H.: Latitudinal and longitudinal variation of a planetary atmosphere and the occultation experiment. *Planetary Space Sci.* **18**, 1769–1784, 1970
- Porsche H.: Die Helios-Sonde als Experimenten-Träger. *Raumfahrtforschung* **19**, 223–225, 1975
- Rasool, S.J., Stewart, R.W.: Results and interpretation of the S-band occultation experiments on Mars and Venus. *J. Atmospheric Sci.* **28**, 869–878, 1971
- Saito, K.: A non-spherical axisymmetric model of the solar K-corona of the minimum type. *Annals of the Tokyo Astron. Observatory* **12**, 53–120, 1970
- Scheffler, H., Elsässer, H.: *Physik der Sterne und der Sonne*, 1st ed. Zürich: Bibliographisches Institut 1974
- Stelzried, C.T., Levy, G.S., Sato, T., Rusch, W.V.T., Ohlson, J.E., Schatten, K.H., Wilcox, J.M.: The quasi-stationary coronal magnetic field and electron density as determined from a Faraday rotation experiment. *Solar Phys.* **14**, 440–456, 1970
- Stewart, R.T., McCabe, M.K., Koomen, M.J., Hansen, R.T., Dulk, G.A.: Observations of coronal disturbances from 1 to $9 R_{\odot}$. *Solar Phys.* **36**, 203–217 (I), 219–231 (II), 1974
- Tousey, R.: The solar corona. *Space Res.* **XIII**, 713–730, 1973
- Ulrych, T.J., Bishop, T.N.: Maximum entropy spectral analysis and autoregressive decomposition. *Rev. Geophys. Space Phys.* **13**, 183–200, 1975
- Volland, H., Bird, M.K., Levy, G.S., Stelzried, C.T., Seidel, B.L.: Helios-1 Faraday rotation experiment: Results and interpretation of the solar occultation in 1975. *Rept. Radioastronomisches Institut, Universität Bonn*, 1–19, 1976
- Wlérick, G., Axtell, J.: A new instrument for observing the electron corona. *Astrophys. J.* **126**, 253–258, 1957
- Yip, K.W.: The ionospheric calibration technique for the VO 75 celestial mechanics and radio science experiments. *JPL Engng. Mem.* 391–606, 1–17, 1974

Received March 14, 1977; Revised Version May 16, 1977

Observations of Zodiacal Light from Helios 1 and 2

C. Leinert, E. Pitz, M. Hanner, and H. Link

Max-Planck-Institut für Astronomie, D-6900 Heidelberg-Königstuhl,
Federal Republic of Germany

Abstract. A short description of the instrument is given. The inflight performance during the first one and a half years was stable. The observations are compatible with a radial dust distribution $n(r) \sim r^{-\nu}$ with $\nu \approx 1.3$. The symmetry plane of interplanetary dust is observed to be inclined to the ecliptic. No effect of a zone of reduced dust density near the sun was found.

Key words: Zodiacal light photometry — Spatial distribution of interplanetary dust — Dust free zone.

1. Introduction

Zodiacal light, which is sunlight scattered from the interplanetary dust grains, is well suited to probe the average spatial distribution of the dust, since the observed zodiacal light intensity is composed of the scattering from dust particles distributed over a large volume in interplanetary space (see Fig. 1). The relationship between zodiacal light intensity $I(\varepsilon)$, solar flux at 1 A.U. F_0 , number density $n(r)$ and average scattering function $\sigma(\theta)$ of the dust,

$$I(\varepsilon) = \text{const.} \cdot \int_0^{\infty} \frac{F_0}{r^2} \cdot n(r) \cdot \sigma(\theta) d\Delta, \quad (1)$$

shows that earth-based observations do not allow a unique separation of the spatial distribution from the angular dependence of scattering by the dust particles. This separation can be achieved only by varying the heliocentric distance of the observing instrument. In this case, with the additional assumption that the average scattering function is independent of heliocentric distance, radial dependence of zodiacal light intensity and spatial distribution of dust are related by

$$I(\varepsilon, R) \cdot R = \text{const.} (\varepsilon) \cdot n(R), \quad (2)$$

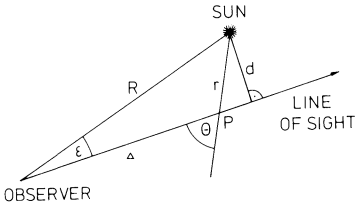


Fig. 1. Geometry of scattering for a dust particle at point P

which follows from Equation(1) and the geometry of Figure 1. Therefore one important goal of the zodiacal light experiment on Helios is deriving the spatial distribution of dust within 1 A.U. from the sun and of detecting any changes in the average properties of dust with heliocentric distance. A second important goal is the study of temporal changes in zodiacal light, from locations well removed from earth-related disturbances.

The information on large-scale distribution of dust given by this experiment and the data of the micrometeoroid detector on Helios which measures mass, velocity and chemical composition of individual dust particles encountered during flight, mutually complement each other.

2. Instrument

The zodiacal light photometer consists of three separate $f/5.5$ lens telescopes with apertures of 30 to 36 mm and EMR 541 N photomultipliers as pulse counting detectors. In each sensor intensity and polarization of zodiacal light are measured in visual, blue and ultraviolet ($\lambda_{\text{eff}} = 540 \text{ nm}, 420 \text{ nm}, 360 \text{ nm}$). The polarization foils (Polacoat 105 UV) and the Schott filters defining the band pass (GG 10, BG 3 + GG 385, UG 2) are exchanged by stepping motors.

The sensors are mounted on Helios with viewing directions of approximately 15° , 30° and 90° below the spacecraft equatorial plane xy (see Fig. 2). As the spacecraft spins (1 rps) with the spinaxis perpendicular to the ecliptic plane, two of them scan on circles of constant ecliptic latitude, $\beta \approx 15^\circ$ and $\beta \approx 30^\circ$, while the third one remains oriented toward the ecliptic pole. The scans are divided into 32 sectors 5.6° to 22.5° long to provide adequate angular resolution in longitude. The width of the strips is 1° and 2° , respectively. The signal is accumulated simultaneously for the 32 sectors of one scan over 513 s. For the 90° sensor the field of view is 3° diameter and the accumulation period 126 s. The 8 sectors of this sensor are used to measure polarization by the method of rotating polaroid, the rotation being provided by the spacecraft.

Because of the reversed orientation of the two Helios spacecraft, the viewing directions are south of the ecliptic for Helios 1, north for Helios 2. This situation is advantageous for determining the plane of symmetry of the dust distribution.

Calibration has been done on the ground with a diffusely attenuated tungsten filament lamp calibrated – in several steps – against the black body of Landessternwarte Heidelberg (Klüppelberg, 1975) and in flight by bright stars ($\alpha \text{ CMi}$, $\beta \text{ Ori}$, $\gamma \text{ Ori}$) crossing the field of view. Both methods agree within 10%.

Fig. 2. Schematic view of the lower spacecraft cone with the mounting positions of the experiment sensors

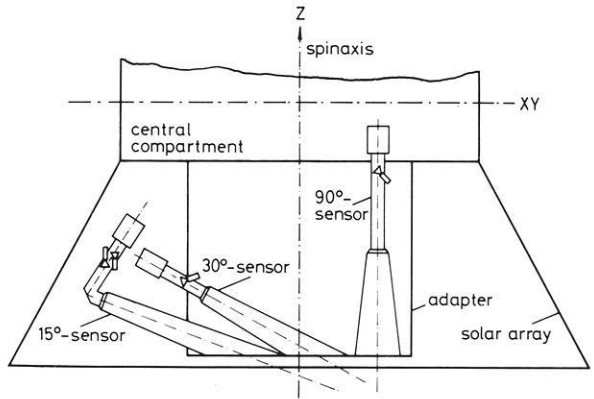
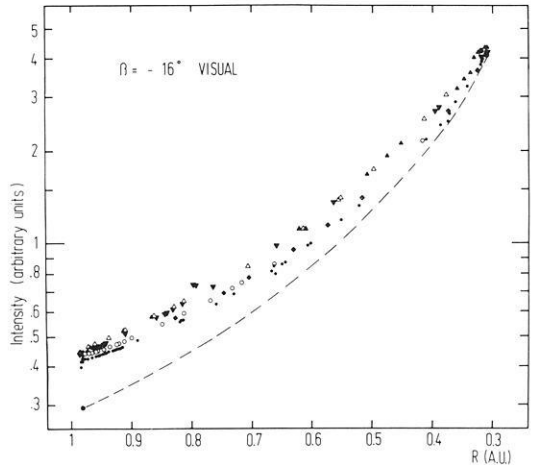


Fig. 3. Integrated total brightness observed with the 15°-sensor of Helios 1, visual band. Different symbols refer to the first (●, ○, ◆) and second half (▲, △, ▼) of the first three orbits, respectively. Brightness after star background correction is given by *broken line*



The method to account for the changes of calibrating source and instrument sensitivity over the broad bandpasses (50 nm–100 nm) is described by Leinert et al. (1974).

Protection from stray light is provided by the coronagraph-like optical design, by large baffle systems and by mounting the sensors completely in the shadow of the solar array. The darkness of this shadow and hence the amount of residual stray light is a function of the angle between spinaxis and spacecraft–sun line. From the constancy of the observed signal during attitude maneuvers, when this angle changed up to 1°, it follows that any remaining stray light contribution to the measurements of Helios 1 and Helios 2 must be smaller than a few percent.

3. Results

In this paper we limit ourselves to discuss data of the 15°-sensors which yield the observations closest to the sun. Figure 3 shows the increase in total bright-

ness observed with the 15° -sensor on Helios 1, which amounts to a factor of 10 between 1 A.U. and Perihelion at 0.31 A.U. Each data point gives the total observed brightness integrated over the circle of constant ecliptic latitude scanned by this photometer. This quantity was chosen because then the contribution of star background to the observed signal is essentially constant, independent of the position of Helios in its orbit, thus reducing the influence of uncertainties in the value of background starlight. After subtraction of the star background, as determined from the tables of Roach and Megill (1961) and the Catalogue of Bright Stars (Hoffleit, 1964), the resulting zodiacal light brightness (broken line) can be fitted by a power law $R^{-2.3}$. Provided the average scattering properties of interplanetary dust do not change over the involved range of heliocentric distances, the spatial distribution according to Equation (2) is given by a power law, $n(r) \sim r^{-\nu}$, where the uncertainty in the exponent $\nu = 1.3$ probably does not exceed ± 0.2 . This is similar to the Pioneer 10 zodiacal light results (Hanner et al., 1976), where the best fit to the data between 1 A.U. and 2 A.U. was with a power law $n(r) \sim r^{-1}$ to $n(r) \sim r^{-1.5}$. It is practically equal to the value $\nu = 1.2$ which Dumont and Sanchez (1975) deduced from a discussion of brightness gradients in the zodiacal light and the F corona as given by ground-based observations in comparison with the results of Pioneer 10. Since the other Helios sensors gave the same power law increase of zodiacal light intensity, the above assumption of constant scattering properties seems justified. This is further supported by the fact that the same increase of zodiacal light intensity is found in U, B and V.

Figure 3 illustrates the good reproducibility of the data from one orbit to the next, indicating that over one and a half years both the experiment and the zodiacal light were quite stable. The short-term stability of the measurements is illustrated in Figure 4 for the viewing direction $\beta \approx -16^\circ$, $\varepsilon \approx 16^\circ$. The experiment stability is probably even better than depicted in Figure 4, since some fluctuation in the total brightness is caused by the varying stellar background as the orbital position of Helios changes. Therefore the experiment is well suited to search for short period brightness fluctuations in the zodiacal light which are reported by Levasseur and Blamont (1975) to last a few days. It will also be important to look for any changes related to solar activity during the current rising branch of the solar cycle.

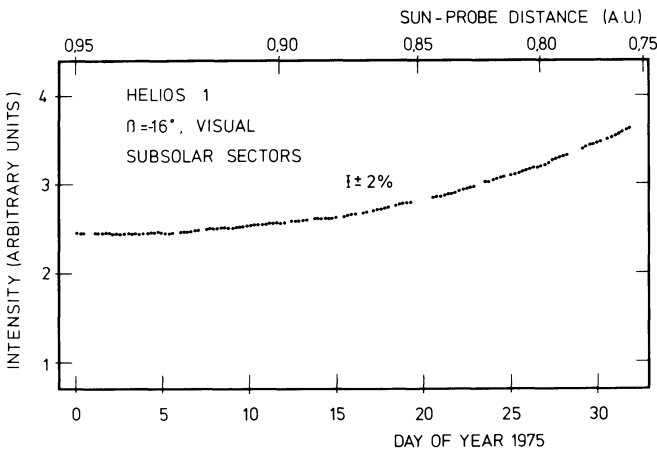


Fig. 4. Variation of the observed total brightness for January 1975. The data points represent the average signal of the two sectors closest to the sun, $\varepsilon = 16^\circ$

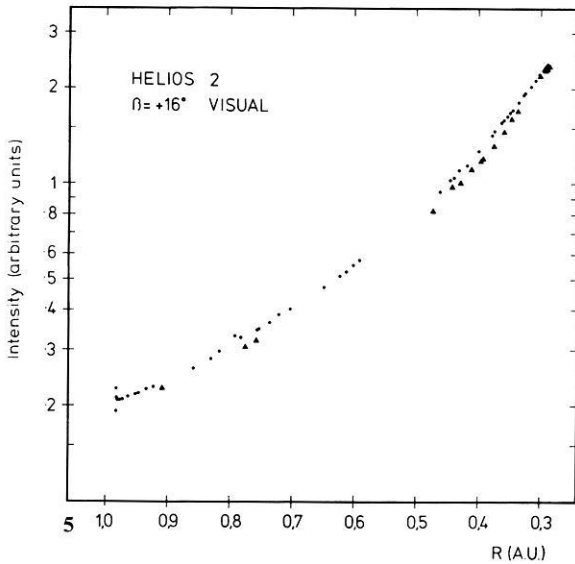


Fig. 5. Integrated total brightness observed with the 15°-sensor of Helios 2. Points refer to the inbound, triangles to the outbound half of the first orbit

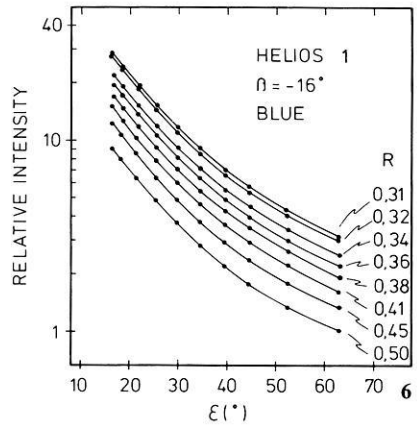


Fig. 6. Observed intensity profiles of the zodiacal light for heliocentric distances 0.50 A.U. to 0.31 A.U.

It is evident from Figure 3 that the zodiacal light brightness was systematically lower during the first half of the Helios 1 orbits. We interpret this as an effect of the tilt between ecliptic and plane of symmetry of interplanetary dust, with the ascending node near the perihelion of Helios 1 ($\lambda = 78^\circ$). Then Helios 1 would be south of the plane of symmetry for the first half of its orbit and the photometers would miss the region of highest dust concentration, while Helios 2 should show the opposite effect, because the sensors are pointing northward. This is indeed apparent in the Helios 2 data shown in Figure 5. Model calculations have shown that the inclination of the invariable plane of the solar system ($i = 1.6^\circ$) is too small to account for the size of the observed effect. Further model calculations are in process.

Infrared observations by MacQueen (1968) and Peterson (1967) have detected emission peaks near $3.5 R_\odot$ and $4.0 R_\odot$. These peaks have been interpreted as thermal emission from silicate grains just outside a zone of decreased dust density. The zodiacal light experiment on Helios does not reach those “dust-free” zones. However, for spacecraft positions near 0.3 A.U. it is possible to search the region of heliocentric distances $R \geq 19 R_\odot$ for a zone of dust depletion. Heliocentric distance $R \approx 24 R_\odot$ is predicted by Lamy (1974) to be the extent of a “dust-free” zone for iron particles. The presence of a dust free zone would lead to a reduction in brightness when the line of sight intersects the zone, i.e. for small heliocentric distances of Helios and small elongations. Quantitative predictions have been given by Hanner and Leinert (1972). In Figure 6 brightness profiles taken with Helios 1 at different heliocentric distances are shown, corrected for dark current, temperature effects, background starlight

and scattering by the electrons of the solar wind. To get rid of the influence of the inclination of the plane of symmetry and of slight changes in the spin axis of Helios, profiles before and after perihelion taken at the same heliocentric distance, were averaged. To the estimated accuracy of $\pm 3\%$ there is no change in the brightness profiles.

In conclusion the Helios observations discussed in this paper are compatible with a steady dust distribution, increasing as a power law $n(r) \sim r^{-\nu}$, $\nu \approx 1.3$, from 1 A.U. to 0.09 A.U. the smallest distance observable from Helios 1. Strictly speaking this result applies to the scattering cross section per unit volume which, however, is proportional to the spatial density of dust if the scattering properties of dust particles do not change considerably with heliocentric distance.

Acknowledgements. In mentioning a few individuals we want to thank the many involved in the project who helped to make this experiment a success. Prof. H. Elsässer initiated the experiment and gave important support and guidance, especially through the rough first phases of the project. Our first steps into space were greatly relieved by DFVLR, Institut für Satellitenelektronik, where K. Mertens, B. Kunz and coworkers developed the electronics and the test equipment. Dornier System with project managers E. Achtermann and R. Hartig was responsible for the technical realization of the instrument. The friendly cooperation and professional workmanship is gratefully acknowledged. We thank H. Schuran and the MBB Helios team for efficient support during system test. The project management at BPT with experiment manager K.O. Pfeiffer was very helpful in technical and financial questions. Our scientific needs and sometimes strong requirements received valuable support by Project Scientist H. Porsche throughout the project. We thank J. Kehr and the other mission operations staff at GSOC for their patient and effective cooperation. The important task of data processing was done by I. Mistrik and M. Al-Makadsi. This research was supported by Bundesministerium für Forschung und Technologie with grants WRS01071 and WRS0108. One of us (M.H.) thanks the Humboldt-Stiftung for fellowship.

References

- Dumont, R., Sanchez, F.: Zodiacal light photopolarimetry. II. Gradients along the ecliptic and the phase functions of interplanetary matter. *Astron. Astrophys.* **38**, 405, 1975
- Hanner, M.S., Leinert, C.: The zodiacal light as seen from the Pioneer F/G and Helios probes. *Space Res.* **XII**, 445–455, 1972
- Hanner, M.S., Sparrow, J.G., Weinberg, J.L., Beeson, D.E.: Pioneer 10 observations of zodiacal light brightness near the ecliptic: changes with heliocentric distance. In: *Interplanetary dust and zodiacal light. Proceedings of IAU-Colloquium, No. 31* (H. Elsässer, H. Fechtig, eds.), Lecture notes in physics, Vol. 48, pp. 29–35. Berlin-Heidelberg-New York: Springer 1976
- Hoffleit, D.: *Catalogue of bright stars*, 3rd rev. ed. New Haven: Yale University Observatory 1964
- Klüppelberg, D.: *Eichung der Helios-Zodiakallicht-Photometer*. Diplomarbeit, Max-Planck-Institut für Astronomie und Landessternwarte, Heidelberg, 1975
- Lamy, P.L.: The dynamics of circum-solar dust grains. *Astron. & Astrophys.* **33**, 191–194, 1974
- Leinert, C., Link, H., Pitz, E.: Rocket photometry of the inner zodiacal light. *Astron. & Astrophys.* **30**, 411–422, 1974
- Levasseur, A.C., Blamont, J.E.: The distribution of dust along the earth's orbit deduced from satellite measurements of zodiacal light. *Space Res.* **XV**, 573–578, 1975
- MacQueen, R.M.: Infrared observations of the outer solar corona. *Astrophys. J.* **154**, 1059–1076, 1968
- Peterson, A.W.: Experimental detection of thermal radiation from interplanetary dust. *Astrophys. J.* **148**, L 37–L 39, 1967
- Roach, F.E., Megill, L.R.: Integrated starlight over the sky. *Astrophys. J.* **133**, 128–242, 1961

Interpretation of the Optical Properties of Interplanetary Dust

R. H. Giese

Bereich Extraterrestrische Physik, Ruhr-Universität Bochum,
Geb. NA 01/130, D-4630 Bochum, Federal Republic of Germany

Abstract. Recent micrometeorite flux curves and optical results about the radial distribution of interplanetary dust particles obtained by the Helios space probes provide valuable criteria for interpretation of zodiacal light measurements. It is shown, that models based on Mie-theory and small ($\lesssim 1 \mu\text{m}$) particles are no longer consistent with observational results. The main contribution to zodiacal light seems to be based on larger ($> 10 \mu\text{m}$) particles. If polarization is taken into account, absorbing particles of fluffy structure must be adopted as an important component of the interplanetary dust cloud.

Key words: Zodiacal light – Interplanetary dust – Light scattering by small particles.

1. Introduction

The sun is surrounded by a thin dust cloud of particle number density $n(\vec{r})$ decreasing with increasing solar distance r . It is flattened and has its plane of symmetry (see Leinert et al., 1977) close but not exactly at the plane of the earth's orbit (ecliptic plane). Figure 1 illustrates roughly the shape (surfaces of equal n) of the cloud and the regions accessible by Helios (H) and by a possible out-of-ecliptic mission (E).

Solar light, scattered by interplanetary dust particles is observable as a component of the diffuse brightness of the night sky. It is also concentrated towards the ecliptic plane (zodiacal light), and decreases in intensity with increasing angle between the solar direction and the line of sight (elongation ε), except close to the antisolar direction ($160^\circ \lesssim \varepsilon \lesssim 180^\circ$), where a slight (ca. 30%) increase of intensity is observed (Gegenschein). For small elongation the zodiacal light continuously merges into the dust component of the corona (F -corona).

Ground based observations and photometry from rockets and space vehicles have covered large regions of the sky including the ecliptic pole and small

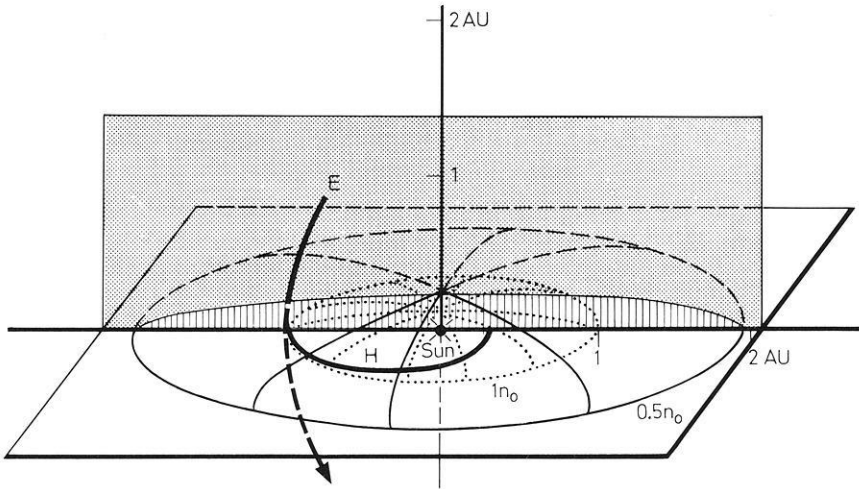


Fig. 1. Schematic view of the interplanetary dust cloud in the case of an ellipsoid model. The shape of the cloud (fan-like, ellipsoidal etc.) is still controversial (Fechtig et al., 1976; Dumont, 1976; Leinert et al., 1976). Distances in astronomical units, $1n_0$ and $0.5n_0$ surfaces of equal particle number density, H Helios orbit, E ecliptic mission

elongations ($\epsilon < 30^\circ$). Latest results are reviewed by Leinert (1975), Dumont (1976), and Weinberg (1976).

Direct access to the interplanetary dust cloud has been possible by micrometeorite impact detectors on space vehicles (rockets, HEOS, Pioneer, Helios) and by analysis of microcraters on lunar samples. From these in situ records a rather reliable cumulative curve of interplanetary micrometeorite fluxes near 1 AU (astronomical unit) solar distance could be derived. Methods and results are reviewed by Fechtig (1976).

Interpretations of observational data, which were performed in connection with the Helios program proved the compatibility between the results of optical and of impact measurements. They suggest that the main contribution to the zodiacal light should be due to larger ($> 10 \mu\text{m}$) particles of fluffy material. The arguments, which lead to this conclusion and the role Helios played in this field will be outlined in the following sections.

2. Problem and Definitions

For comparison with flux data obtained by impact detectors, the observations of zodiacal light need appropriate interpretation to convert brightness into number density and into properties of dust particles. The basic problem and its geometry is shown in Figure 2. If an observer O_b at solar distance a in the ecliptic plane looks in a given direction into a cone of the solid angle $d\Omega$, he receives scattered radiation from all dust particles in his viewing cone. The contribution of a volume element dV on the line of sight to the surface brightness I of the zodiacal

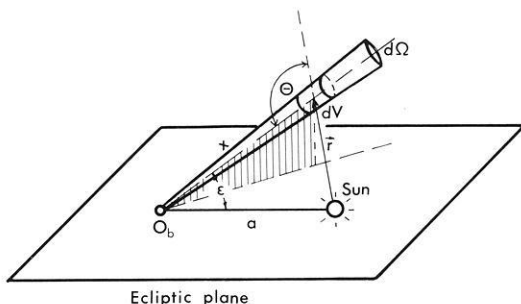


Fig. 2. Basic geometry for interpretation of the zodiacal light

light observed from O_b , is dependent on the illumination of dV , i.e. on the solar distance r , and on the local properties of the interplanetary dust cloud. These are

- the spatial distribution of the particle number density $n(\vec{r})$,
- the distribution function of particle sizes in the volume element $F(s) ds$,
- the properties of the individual particles (sizes, shape, material), represented by the light scattering function $\sigma(\theta, s, \lambda, m)$.

Here $m = m_1 - im_2$ is the complex refractive index (which depends on wavelength and material), θ the scattering angle (Fig. 2), λ the wavelength, and s the size (e.g. the radius) of the scattering particle. The absolute size can be substituted by a dimensionless size parameter α , which is in the case of a spherical particle defined $\alpha = 2\pi s/\lambda$. For visible light ($\lambda = 0.5 \mu\text{m}$) a particle of $\alpha = 10$ is $0.8 \mu\text{m}$ in radius. The scattering function $\sigma(\alpha, m, \theta)$ is defined in this work as usual according to van de Hulst (1957). It has no dimension and is related to the differential scattering cross section (e.g. $[\text{cm}^2 \text{sr}^{-1}]$) by the factor $\lambda^2/8\pi^2$. If the number density of particles contained in a volume is $n[\text{cm}^{-3}]$ a scattering function per unit of volume (volume scattering function, e.g. $[\text{cm}^2 \text{cm}^{-3} \text{sr}^{-1}]$) can be defined as $\Sigma = (\lambda^2/8\pi^2) n\bar{\sigma}$.

For the surface brightness one obtains (Fig. 2)

$$I \sim \int_0^\infty \frac{n(\vec{r}) \bar{\sigma}(\theta) dx}{r^2} \tag{1}$$

where

$$\bar{\sigma}(\theta) = \frac{\int_0^\infty \sigma(\theta, s, \lambda, m) F(s) ds}{\int_0^\infty F(s) ds} \tag{2}$$

is the average scattering function per one particle of the dust mixture within dV . For the purpose of this paper $\bar{\sigma}$ will be adopted as independent of location.

The problem can be treated separately for the component of the scattered light I_\perp and I_\parallel having the electric vector perpendicular and parallel to the plane

of vision (sun-particle-observer), respectively. Therefore it is also possible to derive the degree of linear polarization

$$P = \frac{I_{\perp} - I_{\parallel}}{I} \quad (3)$$

where $I = I_{\perp} + I_{\parallel}$. In a similar way linear polarization can be defined for scattering functions by $P = (\sigma_{\perp} - \sigma_{\parallel})/\sigma$, where $\sigma = \sigma_{\perp} + \sigma_{\parallel}$.

Observations can provide

- the surface brightness I
- the degree of polarization P
- the wavelength dependence of I and P

as a function of the observer's position in the solar system and of the viewing direction. From these $n(\hat{r})$, $F(s)$ and σ are to be derived.

Furthermore $\sigma(\theta, s, \lambda, m)$ has to be explained in terms of physical properties, such as material (absorbing, dielectric), shape (spherical, convex, lengthy, irregular), and structure (rough, fluffy, compact) of the dust particles.

Explicit formulae for (1) corresponding to different models of the three dimensional dust distribution (ellipsoidal, fan-like etc.) have been applied recently by Dumont (1975), Giese and Dziembowski (1969), Giese (1975), Fechtig et al. (1976), and Leinert et al. (1976). The following discussion, however, will be restricted to the dust distribution in the ecliptic plane. Further the well known approximation by a power law $n = n_0 r^{-\nu}$ will be used for the particle number distribution, where n_0 is number density of dust particles near the earth's orbit (r in AU). In this case (1) yields after some geometric conversions

$$I(\varepsilon) \sim n_0 (a \sin \varepsilon)^{-(\nu+1)} \int_{\varepsilon}^{\pi} \bar{\sigma}(\theta) (\sin \theta)^{\nu} d\theta. \quad (4)$$

3. Observational Material

Interpretations of the zodiacal light were suffering for a long time from large spread of observational data in both, photometric measurements and micrometeorite fluxes. Recent investigations have removed ambiguities and provided significant facts to be considered in any interpretation:

- The decrease of particle number densities with solar distance r derived from zodiacal light measurements by space probes (Helios, Pioneer 10) can be approximated by $n(r) \sim r^{-\nu}$ with values of $\nu \approx 1$ (Hanner et al., 1976) or $\nu \approx 1.3$ (Link et al., 1976), which is in excellent agreement with the value of $\nu \approx 1.2$ derived from ground based observations by Dumont and Sánchez (1975).

- Rather reliable volume scattering functions of the interplanetary dust were empirically derived from optical measurements (Dumont and Sánchez, 1975; Leinert et al., 1976).

- The spectrum of the zodiacal light is close to the solar spectrum not only in the visible range but up to infrared wavelength of some $2 \mu\text{m}$ (Nishimura, 1973; Frey et al., 1974).

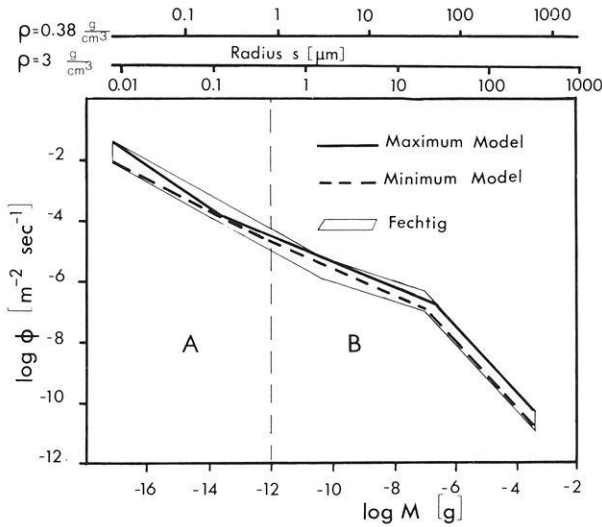


Fig. 3. Cumulative dust flux ϕ at 1 AU (Fechtig, 1976). *A* relative velocity ca. 50 km/s from solar direction, *B* relative velocity ca. 10 km/s from earth apex, *M* particle mass, ρ density of particle material. Minimum and maximum model: Approximations for calculation of the brightness of the zodiacal light on the basis of the flux curve (Giese and Grün, 1976; Leinert et al., 1976)

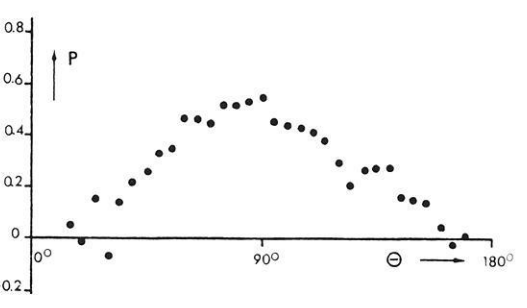
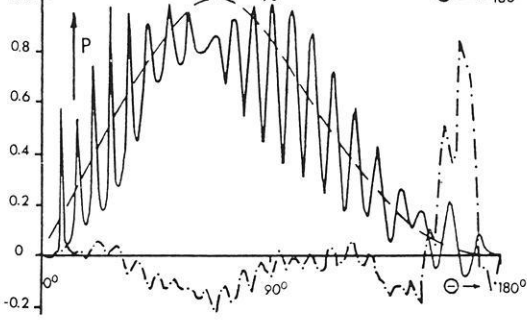
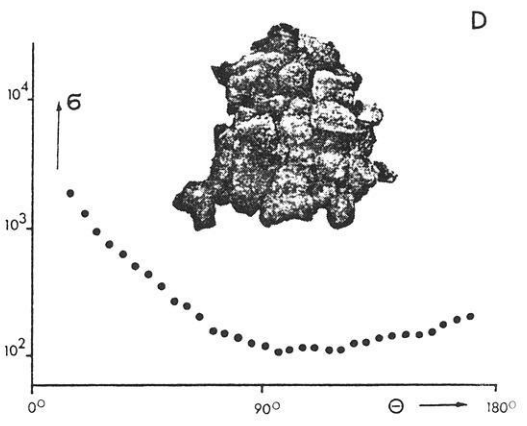
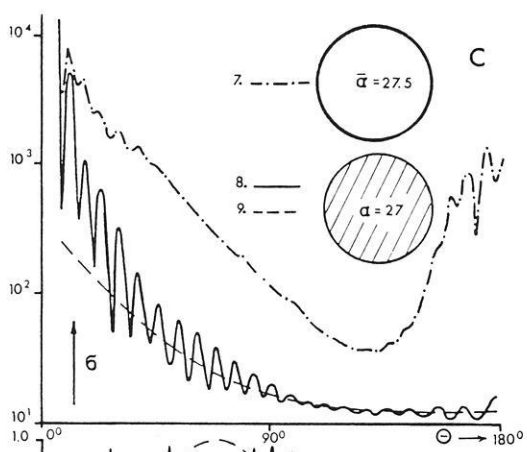
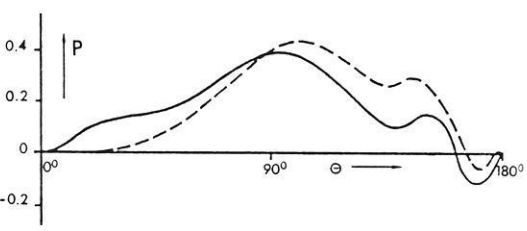
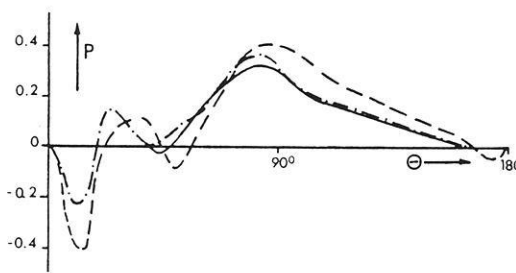
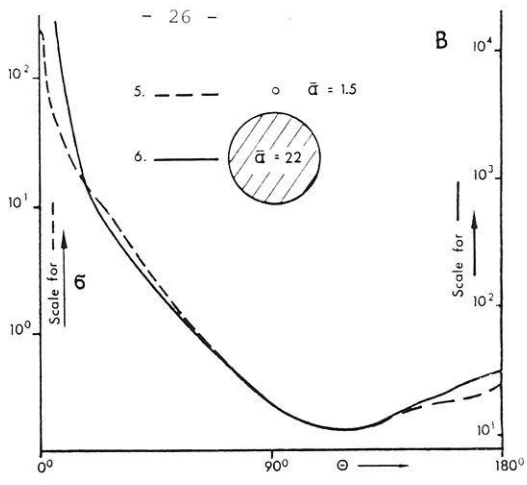
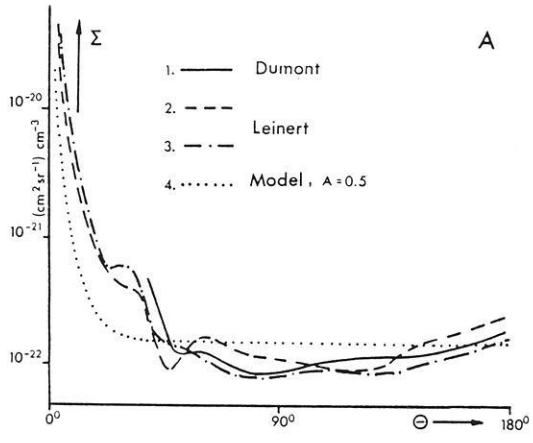
– There is now a consistent curve (Fig. 3) for cumulative dust fluxes in interplanetary space near 1 AU (ref. Fechtig, 1976).

4. Interpretation

4.1. Empirical Scattering Functions

Earlier interpretations of the zodiacal light were based on models fitted to the observed brightness $I(\epsilon)$ by use of Equation (1). Since the integral implies both, number density and scattering properties, n and σ could not be derived independently.

It is a most important result of the Helios and Pioneer missions to show on a direct way, that the spatial density of interplanetary dust between 0.1 AU and 1.5 AU can be characterized by a value of ν between $\nu=1$ and $\nu=1.5$ if no spatial changes of the optical particle properties have to be taken into account. These results are based on the zodiacal light $I(\epsilon_0, a)$ observed in a fixed looking direction ($\epsilon_0 = \text{const}$) while the space probe was changing its solar distance a . According to Equation (4) in this case the relative variation of brightness $I(\epsilon_0) \sim a^{-(\nu+1)}$ is independent of $\bar{\sigma}(\theta)$. After ν is derived in this way it can be used independently to determine volume scattering functions $\Sigma(\theta)$ from observations of the run of $I(\epsilon)$ with elongation. Empirical volume scattering functions as derived with $\nu=1$ by Leinert et al. (1976) and for $\nu=1.2$ by Dumont and Sánchez (1975) from terrestrial zodiacal light observations are combined in Figure 4A. Every dust mixture promising for interpretation of the zodiacal light



has to reproduce the essential properties of such empirical scattering functions: One feature is the rather isotropic behaviour of Σ and therefore also of $\sigma(\theta)$ between $60^\circ \lesssim \theta \lesssim 140^\circ$. Outside this region $\sigma(\theta)$ rises by approximately a factor of 10 for forward scattering at $\theta \simeq 20^\circ$ and in backward scattering region by about a factor of 2 towards $\theta = 180^\circ$. Linear polarization $P(\theta)$ is positive in the region $60^\circ \lesssim \theta \lesssim 170^\circ$ with its maximum $P \simeq 0.3$ to 0.4 between $\theta = 80^\circ$ to 90° . The region of negative polarization at $\theta \lesssim 50^\circ$ will be excluded from discussion, since this region is considered as poorly reliable by Dumont and Sánchez (1975).

4.2. Models Based on Mie-Theory

Interpretations of the zodiacal light were often based on the Mie-theory (see van de Hulst, 1957; Born and Wolff, 1965). They are restricted to the model of spherical particles but can take into account polarization and colour. The components necessary to approximate the observed polarization for $\varepsilon > 30^\circ$ according to Mie-theory were either dielectric ($m = 1.33$) "submicron particles" of some tenth of a micrometer (Giese, 1962; Weinberg, 1964; Little et al., 1965) or absorbing particles of about half a micron in size (Giese and Dziembowski, 1969) or slightly absorbing particles in the micrometer range. Other possibilities were excluded by extensive survey calculations varying sizes and refractive indices (Giese, 1973). Leinert et al. (1976) with some reservations also used Mie-theory. They preferred larger ($> 1 \mu\text{m}$) and slightly absorbing particles to explain the polarization at low elongations ($\varepsilon \simeq 15^\circ$) and the colour of the zodiacal light. But even these models, which are rather neutral in the colour dependence of scattered radiation (Giese et al., 1973) are based on a considerable percentage of particles in the size range below $10 \mu\text{m}$.

In principle Mie-models are also appropriate to explain features like the Gegenschein (Walter, 1958) and the negative polarization observed in the region $170^\circ \lesssim \varepsilon \lesssim 180^\circ$ (Weinberg, 1964; Wolstencroft and Rose, 1967; Frey et al., 1974). This, however, could be attributed exclusively to a component of dielectric ($m_2 = 0$) or at most only slightly absorbing ($m_2 \lesssim 0.05$) particles since larger absorbing particles show positive polarization and a rather isotropic run of $\sigma(\theta)$ in the region of backward scattering (see 4.3).

Fig. 4. A Empirical volume scattering function $\Sigma(\theta)$ and polarization $P(\theta)$ of interplanetary dust. θ scattering angle (see Fig. 2), No. 1. Σ after Dumont and Sánchez (1975), No. 2 and No. 3. Σ after Leinert et al. (1976), No. 4. Model calculation (diffraction plus isotropic reflection, albedo $A = 0.5$). B Scattering functions σ and polarization P of typical Mie-models, m refractive index, α size parameter (= circumference/wavelength), size distribution $\sim \alpha^{-\kappa} d\alpha$, average size parameter $\bar{\alpha} = \int \alpha \cdot \alpha^{-\kappa} d\alpha / \int \alpha^{-\kappa} d\alpha$. No. 5. mixture of dielectric submicron particles ($m = 1.33$, $\kappa = 4$, $1 \leq \alpha \leq 120$), No. 6. mixture of slightly absorbing particles of micron size ($m = 1.33 - 0.01i$ and $m = 1.33 - 0.05i$; mixing ratio 1:2; $\kappa = 2.5$; $10 \leq \alpha \leq 120$). C Scattering functions σ and polarization P for larger spheres. No. 7. mixture of dielectric spheres after Mie-theory ($m = 1.5$; $\kappa = 0$; $25 \leq \alpha \leq 30$), No. 8. single absorbing sphere after Mie-theory ($m = 1.45 - 0.05i$; $\alpha = 27$). No. 9. Same as No. 8, but Fresnel-reflection. D Scattering function σ and Polarization P of a fluffy particle (insert). Average over many spatial orientations according to microwave measurements by Weiß (1977). $m = 1.45 - 0.05i$; $\alpha = 27$ (α for a sphere of same volume)

Figure 4B shows the average scattering functions ($\bar{\sigma}(\theta)$ and $P(\theta)$) of two typical Mie-models. The curves No. 5 correspond to a model of dielectric submicron particles ($\bar{\alpha}=1.5$ or $\bar{s}\approx 0.12\ \mu\text{m}$) having a steep size distribution ($\kappa=4$). If the run of $\bar{\sigma}(\theta)$ is adjusted to the volume scattering functions Figure 4A in the region $90^\circ\lesssim\theta<180^\circ$ the number density of such particles at 1 AU is found to be of the order $n_0\approx 1\cdot 10^{-11}\ \text{cm}^{-3}$.

The other model (curve No. 6) presents the case of slightly absorbing particles with a flat size distribution ($\kappa=2.5$), mainly containing particles in the micrometer size range ($\bar{\alpha}=22$, $\bar{s}\approx 1.75\ \mu\text{m}$). The particle number density obtained for this type of models (curve No. 6) by comparing with Figure 4A is $n_0\approx 2\cdot 10^{-13}\ \text{cm}^{-3}$.

If these number densities are converted into cumulative dust fluxes ϕ at 1 AU by assuming a relative velocity of 20 km/s, one arrives at $\phi\approx 0.25$ for the model of curve No. 5 or $3.8\cdot 10^{-3}$ particles $\text{m}^{-2}\ \text{s}^{-1}$ for the model of curve No. 6, respectively. The corresponding masses of the smallest particles contained in the models are $M\approx 6\cdot 10^{-15}$ or $6\cdot 10^{-12}$ g, if a density of $3\ \text{g/cm}^3$ is adopted for the material.

Before about 1970 there was no reason to reject such Mie-models, since there was a large divergence in cumulative flux values published on the basis of in situ measurements. For example, the cumulative flux at $M=6\cdot 10^{-12}$ g predicted by models like that presented in curve No. 6 was by a factor of 10^4 too low compared to the compilation of particle fluxes presented in McCracken and Alexander (1965), but by more than a factor of 40 too high compared to the interplanetary flux model presented by McDonnell (1971).

For the spatial variation of $n(r)$ the Mie-models referred to above required values of $\nu\approx 0$ to 0.5. This was due to the increase of the scattering functions to forward scattering, starting at scattering angles $\theta\lesssim 100^\circ$. Therefore, to fit the observed increase of $I(\varepsilon)$ for decreasing elongation by use of Mie-scattering functions in Equation (4) it was not necessary to adopt any considerable increase of $n(r)$ towards the sun.

4.3. Consequences of Recent Results

Further analysis of Helios data (Leinert et al., 1977) confirmed definitively the spatial dependence $n\sim r^{-\nu}$ with $\nu\approx 1.3$. Furthermore the interplanetary flux curve seems now to be well represented by the rather narrow band given by Fechtig (1976) in Figure 3. Mie-models like in Figure 4B are not compatible with these results: They require $\nu\lesssim 0.5$; their scattering functions are not isotropic for $60^\circ\lesssim\theta\lesssim 140^\circ$; and the cumulative dust fluxes necessary to reproduce the zodiacal light are too high compared to Figure 3 (see 4.2).

To investigate in a more general way the compatibility between fluxes and zodiacal light data, Giese and Grün (1976) used the whole flux curve of Figure 3. They approximated $\phi(M)$ in different regions by appropriate power laws and converted them into differential size distributions by adopting $\rho=3\ \text{g/cm}^3$ for the particle density. The "Maximum Model" (Fig. 3) approximates the upper and the "Minimum Model" the lower limit of the fluxes. From this, $I(\varepsilon)$ was

computed according to Equation (4) with $v=1$ and scattering functions which were constructed by diffraction plus isotropic reflection, allowing for an albedo A (see Leinert, 1975). It turns out, that $I(\varepsilon)$ can be easily reproduced, except the rise towards the Gegenschein. With $A=1$ the calculated intensity for example at $\varepsilon=90^\circ$ elongation is about twice the observed brightness for the Maximum Model or half the observed brightness for the Minimum Model, respectively. If instead of $\rho=3 \text{ g/cm}^3$ some fluffy material with $\rho=0.38 \text{ g/cm}^3$ were adopted, the particle diameters would be twice as large, which would result in an increase of the scattered intensity by a factor of 4. Therefore the particle number densities corresponding to $\phi(m)$ are completely sufficient to reproduce the observational brightness. One even can allow also for $A<1$. Including the region of low elongations ($\varepsilon \lesssim 15^\circ$) the Maximum Model with $A \simeq 0.5$ approximates the observations of $I(\varepsilon)$ and the volume scattering functions fairly well (see Fig. 4A; Leinert et al., 1976). When one separates the total brightness into contributions from different size intervals one sees that submicron particles and particles of only a few micrometers in size do not considerably contribute to the zodiacal light. For $\rho=3 \text{ g/cm}^3$ the contribution of particles with $s \lesssim 6 \mu\text{m}$ is only about 10%. The main contribution (70%) is due to particles in the size range between $s=10$ to $80 \mu\text{m}$.

4.4. Interpretation by Large and Fluffy Particles

Approximations by diffraction and isotropic reflection have also been used for earlier interpretations of light scattering by interplanetary dust. Elsässer (1955), for example, derived from the brightness of the F -corona a flat run to the size distribution function ($\kappa \simeq 2$) and particle sizes in the region between 1 and $1000 \mu\text{m}$. In so far, his early results are in excellent agreement with the present view. On the other hand this and preceding models failed to explain polarization. They adopted as cause of polarization in the zodiacal light Thomson scattering by an extremely high number of electrons ($n_0=600 \text{ electrons/cm}^{-3}$; Behr and Siedentopf, 1953), which later on turned out to be not realistic. Therefore it became necessary to base polarization on scattering properties of the dust particles. A first approach was to substitute Thomson scattering by scattering of small ($s \simeq 0.1 \mu\text{m}$) dielectric particles, which can produce polarization similar to Rayleigh scattering. Later models, such as No. 6 of Figure 4B, were proposed to avoid submicron particles and to obtain a flat ($\kappa=2.5$) size distribution. All these models, which in principle were appropriate to reproduce polarization, at least for $\varepsilon > 30^\circ$, must now be abandoned according to the arguments of Section 4.3. Therefore—as 20 years ago—there is again the problem of explaining polarization solely by scattering of larger ($\gtrsim 5 \mu\text{m}$) dust particles.

Dielectric spheres are not promising for this purpose. They produce, by no means, the isotropic scattering at medium scattering angles required by the empirical functions (Fig. 4A), but rather, show an increase with decreasing θ in the whole region of $\theta \lesssim 90^\circ$ and an enhancement by more than one order of magnitude towards backward scattering. Polarization shows drastic positive peaks in the region of $130^\circ \lesssim \theta \lesssim 180^\circ$, completely inconsistent with Figure 4A.

These properties, demonstrated for spheres of $\bar{\alpha} \simeq 27.5$ ($\bar{s} \simeq 2.2 \mu\text{m}$) in Figure 4C (No. 7), have also been found for larger ($\alpha = 600$, $s = 48 \mu\text{m}$) dielectric spheres (Hansen and Travis, 1974).

Effects like the strong peaks in the backward scattering region—for water droplets known as hazebow—are due to spherical geometry. They should not be present for mixtures of nonspherical, dielectric particles in random orientation. Indeed microwave analog measurements simulating mixtures of practically dielectric ($m = 1.57 - 0.006i$) cubes and octahedrons corresponding to particles in the micrometer size range showed rather neutral polarization and approximately isotropic scattering—in contrast to spherical particles (Zerull, 1976). Dielectric particles of nonspherical shape in random orientation may therefore be a component of interplanetary dust, which helps to lower strong polarization produced by other scattering processes, but they are not appropriate to explain the positive polarization of the empirical volume scattering functions.

Large absorbing spheres show mainly Fresnel-reflection outside the diffraction region, since most of the refracted radiation is absorbed inside the particle. In this case polarization is positive (Fig. 4C, No. 8), but with the maximum much stronger and at lower scattering angles than in the empirical curves. Only for rather unusual indices of refraction (like $m = 0.3 - 0.6i$) the position of the maximum (Brewster angle) can be shifted towards $\theta \simeq 90^\circ$ (Matsumoto, 1973). Furthermore $\sigma(\theta)$ does not show an enhancement towards backward scattering like the scattering functions of Figure 4A.

Large absorbing nonspherical particles in random orientation having smooth and convex surfaces should show the same properties outside the diffraction region if only reflection at the surface has to be considered (van de Hulst, 1957). Zerull (1976) and Weiß (1977) proved by microwave analog measurements even in the size range $10 \lesssim \alpha \lesssim 30$ with $m = 1.45 - 0.05i$ and $1.65 - 0.25i$ that for absorbing compact bodies of irregular shape polarization is positive and close to Fresnel-reflection, i.e. the maximum is too strong and at a lower scattering angle than in Figure 4A. There still remains the problem to explain the correct run of polarization.

The solution may be found in the existence of fluffy particles (conglomerates of smaller particles) as shown by the insert of Figure 4D. If such particles are absorbing, they can produce at the same time a rather isotropic run of $\sigma(\theta)$ for medium scattering angles, slightly enhanced backward scattering approximately in agreement with Figure 4A, and positive polarization close towards the position of the maximum polarization in the empirical volume scattering function derived from the zodiacal light. Figure 4D shows an example obtained by microwave measurements (Weiß, 1977). Generally such measurements suggest that the maximum of positive polarization decreases in magnitude and is shifted towards $\theta = 90^\circ$ the more the particle structure is fluffy, i.e. the more it deviates from a compact and smooth surface (Zerull, 1976). The same tendency was found for the dependence of polarization on the surface of lunar samples (Dollfus et al., 1971).

A theoretical model is presented by Wolff (1975). He explains by superposition of single and double Fresnel reflection and by shadowing effects features like the shift in the position of the maximum of positive polarization

and the enhanced backward scattering. Even the negative polarization observed in the photometric curves of the moon and minor planets at large scattering angles is explained. This could also be interesting for interpretation of the negative polarization of the zodiacal light without dielectric particles.

However Wolff's model is based on Fresnel reflection on facets, i.e. on geometric optics. On the other hand the microwave measurements were done with scattering objects of only some wavelengths in size ($\alpha \lesssim 30$). The fact, that in both cases similar effects were found suggests, that the scattering properties referred to above are rather independent of size and typical for particles having a fluffy surface microstructure.

These aspects are very fortunate for interpretations of the zodiacal light. They suggest that the scattering properties of interplanetary dust grains causing the zodiacal light can be explained rather unconstrained by very rough or fluffy, absorbing particles in the size range of some microns to even some hundred of microns, i.e. by a type of particle which is also suggested by meteors and by samples of interplanetary particles captured in experiments with high flying aeroplanes and rockets. A similar model for zodiacal light particles is also proposed by Hayakawa et al. (1975) on the basis of results concerning light scattering by cometary dust. It is quite possible that detailed models based on components of absorbing and fluffy particles are quite appropriate to explain the complete run of $I(\varepsilon)$ from the corona to the Gegenschein, polarization including negative polarization at high elongations, and colour of the zodiacal light. This statement, however, has to be still corroborated by further laboratory experiments on rough and fluffy particles including sizes from 10 to some 100 μm and by model calculations which cover a much larger range of parameters than the few special examples referred to in this work.

Acknowledgements. I wish to thank Drs. R. Dumont, E. Grün, M. Hanner, C. Leinert, R. Zerull, and Dipl.-Phys. G. Schwehm for useful discussions. This work was in part supported by the Bundesministerium für Forschung und Technologie via DFVLR-BPT contract WRS 0108.

References

- Behr, A., Siedentopf, H.: Untersuchungen über Zodiacallicht und Gegenschein nach Lichtelektrischen Messungen auf dem Jungfrauoch. *Z. Astrophys.* **32**, 19–50, 1953
- Born, M., Wolf, E.: Principles of optics, 3rd ed. Oxford: Pergamon Press 1965
- McCracken, C. W., Alexander, W. M.: Interplanetary dust particles. In: Introduction to space science (M. N. Hess ed.), pp. 423–472. New York-London-Paris: Gordon and Breach 1965
- Dollfus, A., Geake, J. E., Titulaer, C.: Polarimetric and photometric properties of Apollo lunar samples. Summary of the report presented at the Lunar Science Conference Houston (Texas), Observatoire de Paris-Meudon, 1971
- Dumont, R., Sánchez, F.: Zodiacal light photopolarimetry. II. Gradients along the ecliptic and phase functions of interplanetary matter. *Astron. & Astrophys.* **38**, 405–412, 1975
- Dumont, R.: Ground-based observations of the zodiacal light. In: Lecture notes in physics, Vol. 48 (Interplanetary dust and zodiacal light) (H. Elsässer, H. Fechtig, eds.), pp. 85–100. Berlin-Heidelberg-New York: Springer 1976
- Elsässer, H.: Fraunhofer-Korona und Zodiacallicht. *Z. Astrophys.* **37**, 114–124, 1955
- Fechtig, H.: In-situ records of interplanetary dust particles – Methods and results. In: Lecture notes in physics, Vol. 48 (H. Elsässer, H. Fechtig, eds.), pp. 143–158. Berlin-Heidelberg-New York: Springer 1976
- Fechtig, H., Giese, R. H., Hanner, M. S., Zook, H. A.: Investigation of interplanetary Dust from Out-

- of-Ecliptic Space Probes. In: GSFC-X-660-76-53 Proc. of the Symposium on the Study of the Sun and Interplanetary Medium in Three Dimensions (L. A. Fisk, W. I. Axford, eds.), pp. 298–320. Greenbelt, Md.: Goddard Space Flight Center Technical Information Division 1976
- Frey, A., Hofmann, W., Lemke, D., Thum, C.: Photometry of the zodiacal light with the balloon-borne telescope THISBE. *Astron. & Astrophys.* **36**, 447–454, 1974
- Giese, R. H.: Light scattering by small particles and models of interplanetary matter derived from the zodiacal light. *Space Sci. Rev.* **1**, 589–611, 1962
- Giese, R. H.: Optical properties of single-component zodiacal light models. *Planet. Space Sci.* **21**, 513–521, 1973
- Giese, R. H.: Out-of-ecliptic dust. *Eldo-Cecles/Esro-Cers Scient. and Tech. Rev.* **7**, 43–51, 1975
- Giese, R. H., Dziembowski, v., C.: Suggested zodiacal light measurements from space probes. *Planet. Space Sci.* **17**, 949–956, 1969
- Giese, R. H., Grün, E.: The compatibility of recent micrometeoroid flux curves with observations and models of the zodiacal light. In: *Lecture notes in physics*, Vol. 48 (H. Elsässer, H. Fechtig, eds.), pp. 135–139. Berlin-Heidelberg-New York: Springer 1976
- Giese, R. H., Hanner, M. S., Leinert, C.: Color-dependence of zodiacal light models. *Planet. Space Sci.* **21**, 2061–2072, 1973
- Hanner, M. S., Sparrow, I. G., Weinberg, J. L., Beeson, D. E.: Pioneer 10 observations of the zodiacal light brightness near the ecliptic: Changes with heliocentric distance. In: *Lecture notes in physics*, Vol. 48 (H. Elsässer, H. Fechtig, eds.), pp. 29–35. Berlin-Heidelberg-New York: Springer 1976
- Hayakawa, S., Matsumoto, T., Ono, T.: Optical properties of cometary dust. In: *Lecture notes in physics*, Vol. 48 (H. Elsässer, H. Fechtig, eds.), pp. 323–327. Berlin-Heidelberg-New York: Springer 1976
- Hansen, J. E., Travis, L. D.: Light scattering in planetary atmospheres. *Space Sci. Rev.* **16**, 527–610, 1974
- van de Hulst, H. C.: *Light scattering by small particles*. New York: Wiley 1957
- Leinert, C.: Zodiacal light – A measure of the interplanetary environment. *Space Sci. Rev.* **18**, 281–339, 1975
- Leinert, C., Link, H., Pitz, E., Giese, R. H.: Interpretation of a rocket photometry of the inner zodiacal light. *Astron. & Astrophys.* **47**, 221–230, 1976
- Leinert, C., Pitz, E., Hanner, M., Link, H.: Observations of the zodiacal light from Helios 1 and 2. *J. Geophys.* **42**, 699–704, 1977
- Link, H., Leinert, C., Pitz, E., Salm, N.: Preliminary results of the Helios A zodiacal light experiment. In: *Lecture notes in physics*, Vol. 48 (H. Elsässer, H. Fechtig, eds.), pp. 24–28. Berlin-Heidelberg-New York: Springer 1976
- Little, S. J., O'Mara, B. J., Aller, L. H.: Light scattering by small particles in the zodiacal cloud. *Astronomical J.* **70**, 346–352, 1965
- Matsumoto, T.: On the origin of the zodiacal light. *Publ. Astron. Soc. Japan* **25**, 469–480, 1973
- McDonnell, J. A. M.: Review of in situ measurements of cosmic dust particles. *Space Research XI*, pp. 415–435. Berlin: Akademie-Verlag 1971
- Nishimura, T.: Infrared spectrum of zodiacal light. *Publ. Astron. Soc. Japan* **25**, 375–384, 1973
- Walter, H.: Theoretische Deutung des Gegenseins durch Lichtstreuung an sphärischen Partikeln. *Z. Astrophys.* **46**, 9–16, 1958
- Weinberg, J. L.: The zodiacal light at 5300 Å. *Ann. Astrophys.* **27**, 718–738, 1964
- Weinberg, J. L.: Space observations of the zodiacal light. In: *Lecture notes in physics*, Vol. 48 (H. Elsässer, H. Fechtig, eds.), pp. 3–18. Berlin-Heidelberg-New York: Springer 1976
- Weiß, K.: *Untersuchung des Streuverhaltens von unregelmäßig geformten, absorbierenden Partikeln mit Mikrowellen*. Diplomarbeit, Bereich Extraterrestrische Physik, Ruhr-Universität Bochum 1977
- Wolff, M.: Polarization of light reflected from rough planetary surface. *Applied Optics* **14**, 1395–1405, 1975
- Wolstencroft, R. D., Rose, L. J.: Observation of the zodiacal light from a sounding rocket. *Astronomical J.* **147**, 221–292, 1967
- Zerull, R. H.: Scattering measurements of dielectric and absorbing nonspherical particles. *Beitr. Phys. Atmosph.* **49**, 168–188, 1976

Micrometeoroid Data from the First Two Orbits of Helios 1

E. Grün^{1*}, H. Fechtig¹, J. Kissel¹, and P. Gammel²

¹ Max-Planck-Institut für Kernphysik, Saupfercheckweg, Postfach 1248, D-6900 Heidelberg, Federal Republic of Germany

² Electronic Projectierung, D-6948 Wald-Michelbach, Federal Republic of Germany

Abstract. For the first time interplanetary dust has been detected directly by the micrometeoroid experiment on board of Helios 1 as close as 0.3 AU from the Sun. The experiment contains two sensors with a total effective area of 120 cm². One sensor (south sensor) is facing the southern ecliptic hemisphere while the other sensor (ecliptic sensor) detects particles about the ecliptic plane. Particle impacts are reliably identified by the presence of three independent signals, measured upon impact, including time-of-flight spectra of the ions released.

A total of 58 distinct micrometeoroid impacts was detected during 352 days of experiments operation during the first two orbits. The rate of large impacts (impact charge greater than 10⁻¹³ Coulombs) increases steeply (a factor of approximately 20) between 1 AU and perihelion. Also the average impact speed is found to increase by a factor 2 to 3 in the same distance interval. Most impacts were detected by the ecliptic sensor when it was pointing in the direction of motion of Helios 1 (probe apex). In contrast to that the south sensor detected also many impacts when facing the probe antapex. About twice the number of small impacts were detected when the south sensor was facing the Sun compared with the antisolar direction. This result supports qualitatively the finding of the Pioneer 8 and 9 dust experiments that small particles are leaving the solar system on hyperbolic orbits.

Key words: Interplanetary dust — Micrometeoroids — Helios mission.

The Helios mission represents the first opportunity to measure micrometeoroids at closer than 0.75 AU heliocentric distance. This region of interplanetary space is of special interest since it was predicted that the spatial density of dust particles should increase close to the Sun due to the Poynting Robertson effect (Briggs, 1962) a force which causes the particles to spiral

* To whom offprint requests should be sent

towards the Sun and is one of the major loss mechanisms of particles in the zodiacal complex. Due to this higher spatial density the micrometeoroids collide more frequently with each other (Dohnanyi, 1976). Additionally comets, which are considered to be a major source for micrometeoroids, release most of their dust in the vicinity of the Sun (Whipple, 1955). All three effects can be more easily studied at 0.3 AU from the Sun than at the Earth's orbit.

1. Instrument Description

The micrometeoroid experiment on board Helios 1 measures the impact of individual dust particles. The experiment consists of 2 individual sensor units and a common electronic data processor. Figure 1 shows a schematic cross-section of the spaceprobe with the mounting positions of the two sensors. The spin axis of Helios is perpendicular to its orbital plane which is identical with the ecliptic plane. While the spacecraft spins around its axis with a period of 1 s the two sensors scan a full circle in azimuth. Two sensors are installed in order to allow a rough determination (two channels) of the ecliptic elevation of the particle's orbits. The field of view of each sensor is a cone with approximately 60° half angle centered on the sensor axis. In elevation the field of view is limited by the spacecraft rim and by an external blind. One sensor (south sensor) is facing the southern ecliptic hemisphere and detects particles which have trajectory elevations from -90° to -10° . The other sensor (ecliptic sensor) detects particles with elevations from -45° to $+55^\circ$ with respect to the ecliptic plane.

The cross-section of the south sensor is shown in Figure 2. The sensor consists of the solar wind protection system, the impact ionisation detector and the time-of-flight spectrometer. Two small electronic boxes containing preamplifiers and high voltage power supplies are directly attached to the sensor. A detailed description has been given by Dietzel et al. (1973). Five quantities are generally measured if a micrometeoroid hits the venetian blind type target: (1) the total negative charge (electrons) (2) the total positive charge (ions) released upon the impact, (3) the rise-time of the negative charge pulse, (4) the rise time of the positive charge pulse and (5) the time-of-flight spectrum of the ions. The instrument is triggered when a signal exceeds the threshold of either the positive or negative charge channel. With the south sensor additionally the electrostatic charge (6) of the dust particles is measured by the charge induced on a grid in front of the target. The ecliptic-sensor is covered by a thin film (3,000 Å parylene coated with 750 Å aluminium) as protection against solar radiation. Here the time (7) is measured between the penetration of the film and the impact on the target.

Besides these parameters measured directly from the impact, additional information is gathered and transmitted to earth: (8) various coincidences between the measured signals, enabling one to discriminate between noise and "probable" impacts, (9) the time at which the event has occurred, and (10) the pointing direction (azimuth) of the sensor. If a "probable" impact is indicated by the proper coincidences, the count on one out of four registers is increased by one, this register is selected according to the amplitude of the positive charge signal

Fig. 1. Schematic view of the Helios spacecraft with mounting positions of the dual sensor micrometeoroid experiment

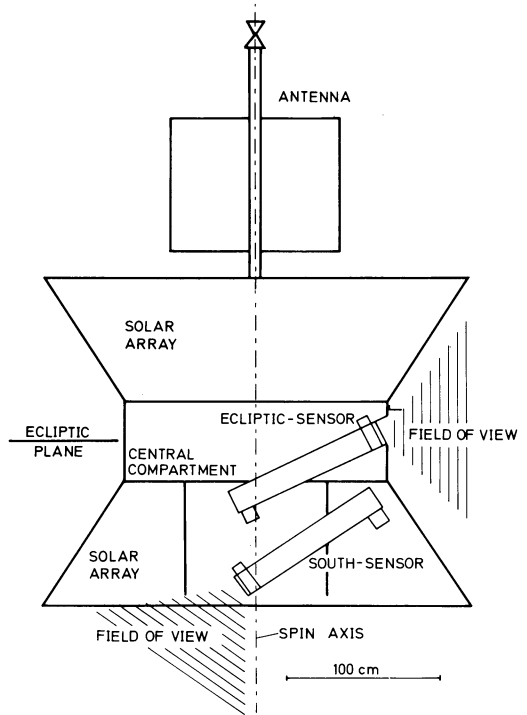
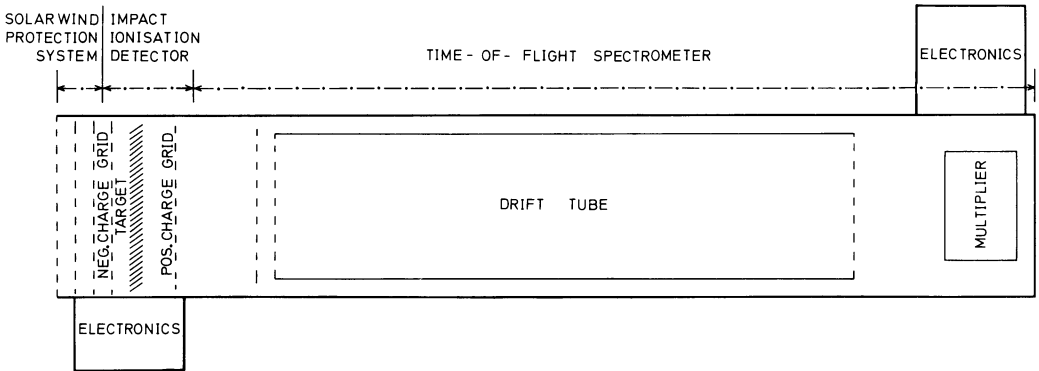


Fig. 2. The Helios micrometeoroid experiment, south sensor



(IA). By this method one obtains from the four counters the number of “probable” impacts within 4 positive charge intervals roughly corresponding to 4 different mass intervals of micrometeoroids. All the information on one event is contained in an experiment-data-frame of 256 bits which is transmitted to earth once every 20 s–20 min (depending on the Helios-Earth distance). The experiment worked satisfactorily, except for a total of 26 days during the first 3 months of the mission when the experiment was blocked in a non-measuring mode.

The experiment has a sensitivity threshold for micrometeoroids with masses of 3×10^{-13} g at an impact speed of 10 km/s. The measured parameters allow the determination of the particle mass, speed, electrostatic charge and composition of the plasma produced by the impact onto the sensor.

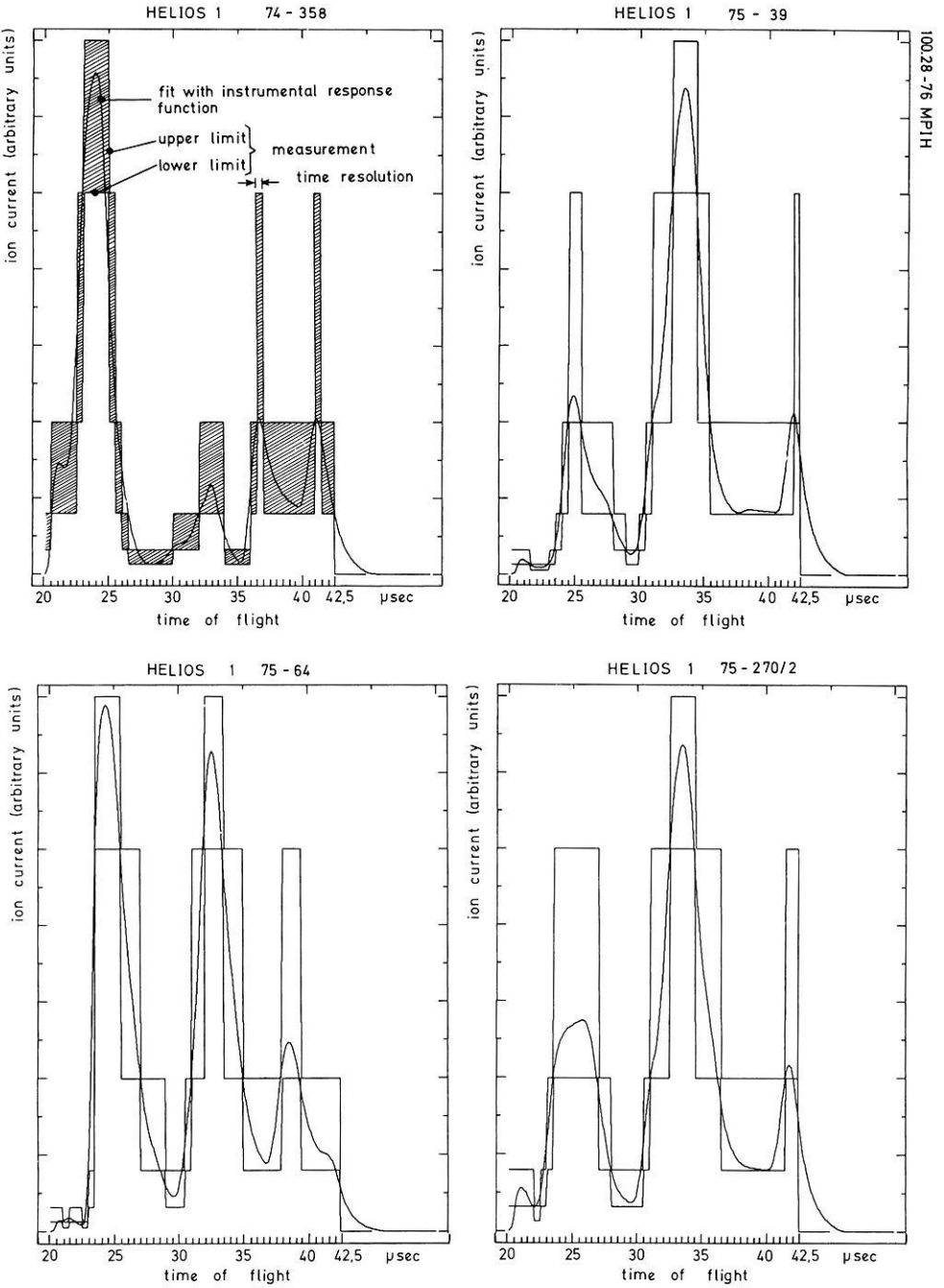


Fig. 3. Time-of-Flight spectra of ions released upon micrometeoroid impact onto the Helios sensors

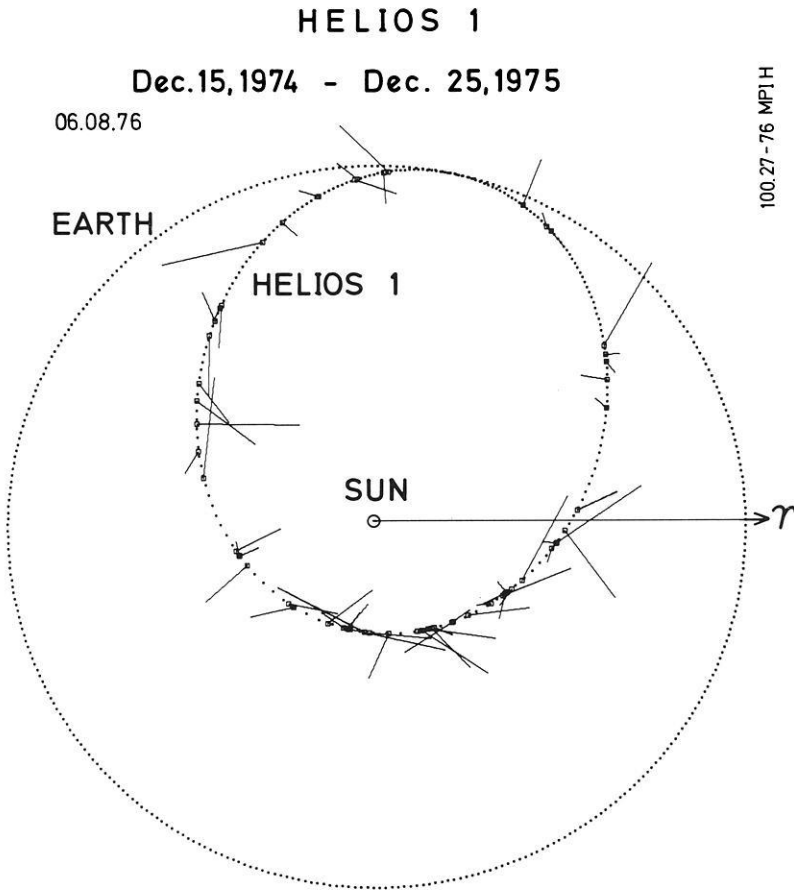


Fig. 4. Impacts detected during the first two orbits of Helios around the Sun (\square). Bars attached to the small squares indicate the pointing direction of the experiment at the time of impact. The length of the bars represent the magnitude of the ion charge released upon impact

2. Impact Identification

The identification of an impact of a dust particle onto a sensor requires narrow time-coincidences between several signals measured from this event. These requirements were established and verified during the calibration of the instrument with artificially accelerated dust particles. The most affirmative coincidences are the occurrence of both the positive and negative charge signals within a $12 \mu\text{s}$ time interval and the subsequent measurement of a time-of-flight spectrum of the ions released upon impact. By the first criterion, the simultaneous occurrence of both the electron and ion signal, some 80 "probable" impact events were found in the data. Fifty-eight of these events had measurable time-of-flight spectra and were identified as "true" impacts. Figure 3 gives four examples of time-of-flight spectra as measured by Helios 1. The digitized output current of the multiplier is shown for the period from $22.5 \mu\text{s}$ – $45 \mu\text{s}$ after the impact.

The upper and lower limit of the measurement refer to the uncertainties of the analog-to-digital conversion. A preliminary best fit of the data representing approximately the original time-of-flight spectrum is also shown. This fit takes into account the instrumental response function. At this stage of analysis the total ion charge contained in the spectrum is used only to identify true impact events. The evaluation of the spectra themselves is in progress. Laboratory studies of impact spectra were recently published by Dalman et al. (1977).

The fifty-eight impacts which were detected during the first two revolutions of Helios 1 around the Sun are shown in Figure 4. The dotted circle and ellipse give the orbits of the Earth and Helios 1, respectively. The distance between two adjacent dots represents the flight path during one day. Within this first year Helios 1 had completed two heliocentric orbits. The squares superimposed onto the Helios orbit mark the places where micrometeoroid impacts were observed and the direction of the bars attached to these squares represents the sensor pointing direction at the time of impact. Since the sensors have a field of view of approximately $\pm 60^\circ$ around their axis, the true impact direction may deviate from the direction shown by as far as 60° . The length of the bars indicate the measured amount of positive charge (IA) produced upon impact. This charge is a measure of the combined effect of the particle mass and impact speed. The charge represented by the longest bars (IA = 15) is 10^4 times larger than the charge represented by the shortest bars (IA = 0).

The true number of micrometeoroid impacts onto the experiment within the first mission year is greater than the number of impacts detected in the data because of the incomplete data coverage and instrumental dead-time. The most complete set of data (better than 90% coverage) exists for larger impact events (IA > 4) because these events are reliably identified by the experiment itself and counted in special impact counters. All the events which have been recorded by these counters were found in the data and 30 of them were identified as true impact events. Small events (IA \leq 4) which had triggered the appropriate counter were not completely found in the data received on ground. The data coverage for small impacts corresponds to approximately 70% of the available measurement time.

3. Results

One of the prime objectives of the Helios micrometeoroid experiment is the determination of the radial dependence of the impact rate. Figure 5 shows this result from the first two revolutions of Helios 1. The number of large impacts (IA > 4) per 0.1 AU interval normalized to the time spent in this distance interval is plotted versus the radial distance. The error bars represent the statistical $\pm\sigma$ -error limit of the number of impacts and the 0.1 AU interval, respectively. The impact rate increases steeply with decreasing distance. Approximately 20 times more impacts were recorded at the 0.3 AU as compared with 1 AU. This increase can be fitted by a power law with an exponent of -2.5 ± 0.8 . This impact rate on the experiment which has a total effective area of 120 cm^2 yields a micrometeoroid flux of 2.1×10^{-5} particles/m² s onto a sensor mounted

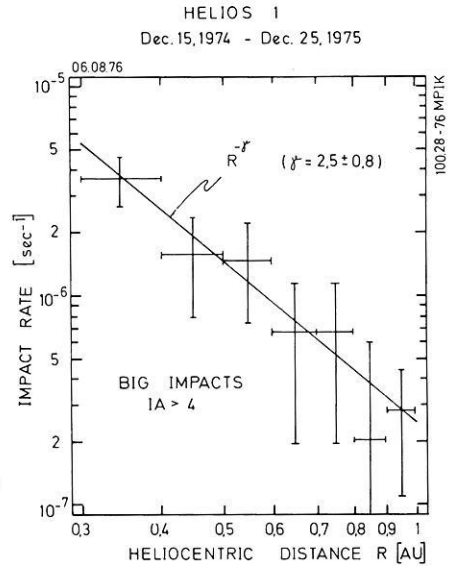


Fig. 5. Radial variation of the observed impact rate onto the Helios micrometeoroid experiment

on a spinning spacecraft at 1 AU distance from the Sun. This flux is within a factor of 2 of the flux as measured by the HEOS-2 satellite (Hoffmann et al., 1975) and comparable to the flux values derived from lunar crater statistics by Schneider et al., 1973). The latter fluxes correspond to micrometeoroids with masses greater than 10^{-12} g which is also the mass threshold for the impact charge $IA=4$ at an impact speed of 10 km/s to 15 km/s.

The increase of the impact rate measured by this experiment can also be compared with the measurement of the zodiacal light from Helios 1. From these measurements Link et al. (1976), derived a spatial density of interplanetary dust at 0.3 AU which is 4–5 times the density obtained at 1 AU. The impact rate on a sensor is proportional to the spatial density multiplied with the average relative velocity between the sensor and the micrometeoroids. A preliminary analysis of the impact speed determined by the micrometeoroid experiment yields an increase of the average impact speed of a factor 2–3 between 1 AU and 0.3 AU.

This increase of the average impact speed at 0.3 AU causes a corresponding decrease in the minimum mass of particles detected by the sensor. The increase of the impact rate for a constant mass threshold will therefore be lower than the measured increase for constant charge threshold. Taking into account all these effects the measurements of interplanetary dust by the zodiacal light photometers and by the micrometeoroid experiment on board Helios 1 are compatible.

The pulse height distribution of the positive impact charge (IA) is shown in Figure 6. Impacts onto the ecliptic sensor are displayed separately from impacts on the south sensor. The linear pulse-height scale corresponds to a logarithmic impact charge scale covering a dynamic range of 10^4 . Impacts with pulse-heights $IA \leq 4$ are not complete and have to be corrected by a factor of approximately 1.5 in order to be comparable with big impacts ($IA > 4$). The number of big impacts

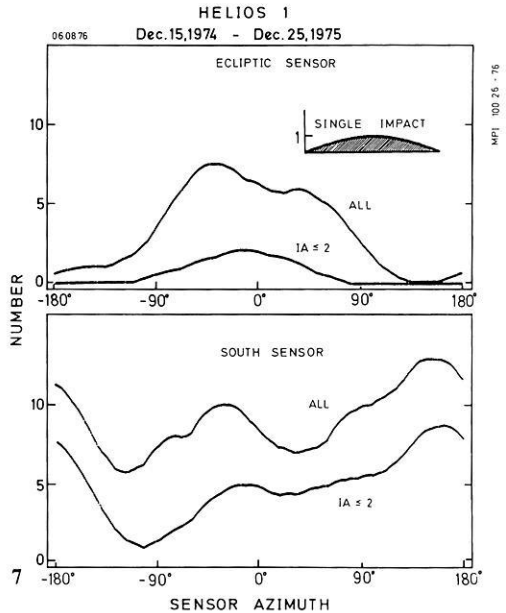
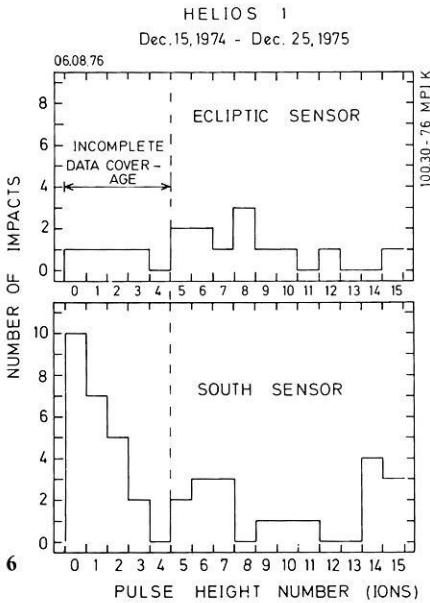


Fig. 6. Pulse height distribution of the ion charge (IA) released upon impact

Fig. 7. Azimuthal distribution of impacts detected by Helios 1. A single impact is represented by an angular probability distribution centered on the sensor pointing direction at detection. The area of this function is shown in the upper right hand corner

on both sensors is similar within the statistical uncertainty indicating a wide distribution of dust orbit inclinations. Small impacts ($IA \leq 4$) however, are counted 6 times more often by the south sensor than by the ecliptic sensor. This effect is attributed to the entrance film which covers the ecliptic sensor only and causes a cut-off in the detection limits of the smaller micrometeoroids. This film effect will be studied further in a laboratory program. As with the larger particles, the orbital inclination distribution of small micrometeoroids can not also be strongly concentrated to the ecliptic plane because impacts onto the south sensor require trajectory elevations greater than 10° with respect to the ecliptic plane.

Figure 7 shows the azimuthal distribution of dust impacts on both the ecliptic sensor and the south sensor. Each individual impact is represented by an area which corresponds to the angular sensitivity of the instrument as shown in the upper right hand corner of the graph. A sensor azimuth of 90° corresponds to a pointing of the sensor axis towards the Sun. 0° sensor azimuth points to the approximate apex direction of Helios. The impacts detected by the ecliptic sensor show a symmetric distribution peaking at the apex direction. In contrast to that a comparable number of impacts were detected by the south sensor from the antapex direction (180°).

The azimuthal distribution of small impacts $IA \leq 2$ is asymmetric with respect to the apex direction. 15 impacts were detected while the sensor was pointing to

the solar hemisphere (0° – 180°) compared with only 7 impacts from antisolar direction (-180° – 0°). This finding supports the measurements from Pioneer 8 and 9 spaceprobes reported by Berg and Grün (1973) and McDonnell et al. (1975), who observed a concentration of large impacts from apex direction whereas small impacts were concentrated towards solar direction. Due to the high eccentric orbit of Helios a quantitative comparison requires a detailed analysis. The concept of this analysis is presented by Schmidt (1977).

Acknowledgements. The successful development, implementation and operations of this experiment would not have been possible without the collaboration of a great number of individuals from various departments of the Max-Planck-Institut für Kernphysik, from outside institutions and companies.

The authors are especially indebted to D. Linkert, W. Schneider, G. Dräger and Mrs. O. Kress for their personal engagement during that campaign. The support given to the instrument development, testing, calibration and project administration by D. Dörflinger, H. Geldner, S. Hägele, P. Kaiser, G. Matt, G. Ochmann, G. Schäfer, H. Schmidt, V. Träumer, H. Unser, H. Voth, H. Weber, W. Weiß and A. Zahlten is gratefully acknowledged. We thank for the support which we received by the project scientist Dr. H. Porsche.

The experiment was electronically developed, manufactured and tested by rfe Raumfahrt elektronik GmbH und Co. with a subcontract to Walter Fischer Gerätebau. The unremitting efforts and competent workmanship of F. Eckl, F. Eder, M. Steinich and their colleagues is gratefully appreciated.

The authors wish to thank J. Triolo from NASA Goddard Space Flight Center and Dr. M. Spivack from Union Carbide Corporation for their ingenious development and preparation of the crucial entrance film.

Careful attention and effective support to the experiment operations and data processing was given by J. Kehr and P. Piotrowsky and their teams of the German Space Operations Center (GSOC). The experiment was effectively coordinated with the Helios project by Drs. H. Dodeck, H.D. Dohmann, W. Kempe, K.O. Pfeiffer and P. Stampfl of the Gesellschaft für Weltraumforschung. Their contributions are gratefully acknowledged.

This work was supported by the Bundesminister für Forschung und Technologie with grant RS 10-7.

References

- Berg, O.E., Grün, E.: Evidence of hyperbolic cosmic dust particles. Space Research XIII, M.J. Rycroft, S.K. Runcorn, eds., pp. 1047–1055. Berlin: Akademie-Verlag 1973
- Briggs, R.E.: Steady-State space distribution of meteoric particles under the operation of the Poynting-Robertson effect. *Astron. J.*, **67**, 710–723, 1962
- Dalmann, B.K., Grün, E., Kissel, J., Dietzel, H.: The ion composition of the plasma produced by impact of fast particles. *Planetary Space Sci.*, **25**, 135–147, 1977
- Dietzel, H., Eichhorn, G., Fechtig, H., Grün, E., Hoffmann, H.-J., Kissel, J.: The HEOS A-2 and Helios micrometeoroid experiments. *J. Phys. E: Sci. Instr.* **6**, 209–217, 1973
- Dohnanyi, J.S., Flux of hyperbolic micrometeoroids. In: *Interplanetary dust and zodiacal light*, H. Elsässer, H. Fechtig, eds. *Lecture Notes Phys.* **48**, pp. 170–180. Berlin-Heidelberg-New York: Springer 1976
- Hoffmann, H.-J., Fechtig, H., Grün, E., Kissel, J.: First results of the micrometeoroid experiment S 215 on the HEOS-2 satellite. *Planetary Space. Sci.* **23**, 215–224, 1975
- Link, H., Leinert, C., Pitz, E., Salm, N.: Preliminary results of the Helios A zodiacal light experiment. In: *Interplanetary dust and zodiacal light*, H. Elsässer, H. Fechtig, eds., *Lecture Notes Phys.* **48**, pp. 24–28. Berlin-Heidelberg-New York: Springer 1976

- McDonnell, J.A.M., Berg, O., Richardson, F.F.: Spatial and time variations of the interplanetary microparticle flux analysed from deep space probes pioneers 8 and 9. *Planetary Space. Sci.* **23**, 205–214, 1975
- Schneider, E., Storzer, D., Hartung, J.B., Fechtig, H., Gentner, W.: Microcraters on Apollo 15 and 16 samples and corresponding cosmic dust fluxes. *Proc. Lunar Sci. Conf. 4th.* **3**, 3277–3290, 1973
- Schmidt, K.D.: Micrometeoroid orbits observable by the Helios experiment E 10. *J. Geophys.* 1977
- Whipple, F.L.: A comet model, III. The zodiacal light. *Astrophys. J.* **121**, 750–770, 1955

Received January 31, 1977

Dynamical Effects on Circumsolar Dust Grains

G. Schwehm and M. Rohde

Bereich Extraterrestrische Physik, Ruhr-Universität Bochum,
Universitätsstr. 150, D-4630 Bochum, Federal Republic of Germany

Abstract. The motion of the interplanetary dust particles in the vicinity of the Sun is not only governed by the gravitational attraction of the Sun but much more effected by the interaction with the solar radiation field. For the interpretation of the data of the micrometeoroid experiment on board Helios 1 we want to establish theoretically a dynamical model of the interplanetary dust cloud.

This requires a thorough investigation of the various interactions of the interplanetary dust grains with the solar radiation field. In this paper we present our results for the radiation pressure force and the temperature distribution of cosmic dust grains in the grain size interval 0.01 to 100 μm .

Key words: Dynamics of interplanetary dust – Grain temperatures.

1. Introduction

Small dust particles in interplanetary space are caused by the Poynting-Robertson effect (Robertson, 1937; Wyatt and Whipple, 1950) to spiral in towards the Sun. With decreasing heliocentric distance evaporation from the surface of such particles increases due to increasing temperature and their size is being reduced accordingly. With decreasing particle size the solar radiation pressure gradually becomes more effective reducing the solar gravitational attraction. By this effect the particle evaporation tends to increase the orbit dimensions, thus acting against the Poynting-Robertson effect. Therefore the inward spiraling, far exceeding the dynamical effect from evaporation at large heliocentric distances, slows down as the particle approaches the sun and ceases when the critical distance is reached, where the two forces approximately balance each other. Then the perihelion distance stabilizes, while the eccentricity starts increasing very rapidly until the particle leaves the solar system. A schematic view of the dynamical effects acting on solid particles in the solar system is given in Figure 1. Not included in the picture are the electric charging of the particles, the interactions with the interplanetary plasma and magnetic field and the rotational bursting (c.f. Schmidt and Elsässer, 1967).

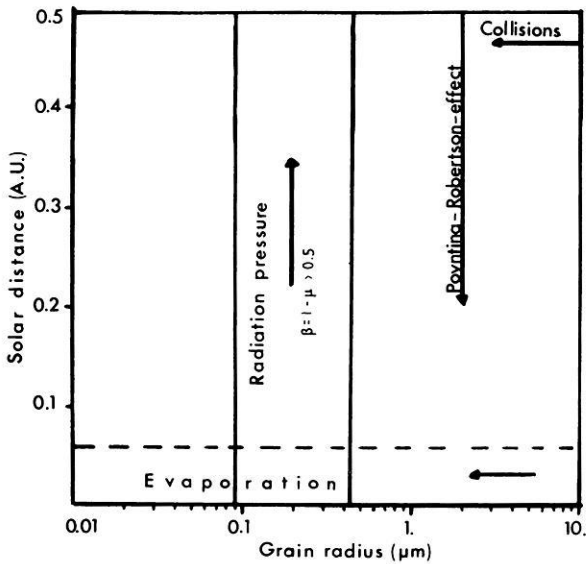


Fig. 1. Dynamical effects acting on solid particles in the solar system. The arrow indicates the direction where the effect changes mass or orbit (ref. Grün, 1974)

All dynamical effects influence the orbit and mass distribution of micrometeoroids: the distribution of cosmic dust reflects the distribution of sources and sinks altered by a variety of dynamical effects acting on the particles. To establish a dynamical model of the interplanetary dust cloud all these effects must be thoroughly investigated. In the following we want to discuss our results for the radiation pressure force acting on the grains and for the temperature distribution $T(R, r)$ of grains of given material as a function of the heliocentric distance R and grain radius r .

2. Radiation Pressure

The force acting on an interplanetary dust particle due to solar radiation pressure at a distance R from the Sun is given by

$$F_{\text{rad}} = \frac{\pi r^2 R_0^2}{c R^2} \int_0^{\infty} Q_{\text{pr}}[m(\lambda), x(\lambda)] s_{\lambda} d\lambda$$

with $R_0 = 1$ a.u., r the radius of the particle, $m(\lambda)$ its complex refractive index, c the velocity of light, λ the wavelength, s_{λ} the solar flux outside the earth's atmosphere per unit area and wavelength range. The function Q_{pr} is the efficiency factor for the radiation pressure as given by Mie-theory for spherical particles, which depends on the refractive index m and the size parameter x of the particle defined as the ratio of the circumference of the particle to the wavelength (Debye, 1909).

The radiation pressure acts against the gravitational attraction

$$F_{\text{grav}} = \frac{f \cdot M_{\odot} \cdot m}{R^2}$$

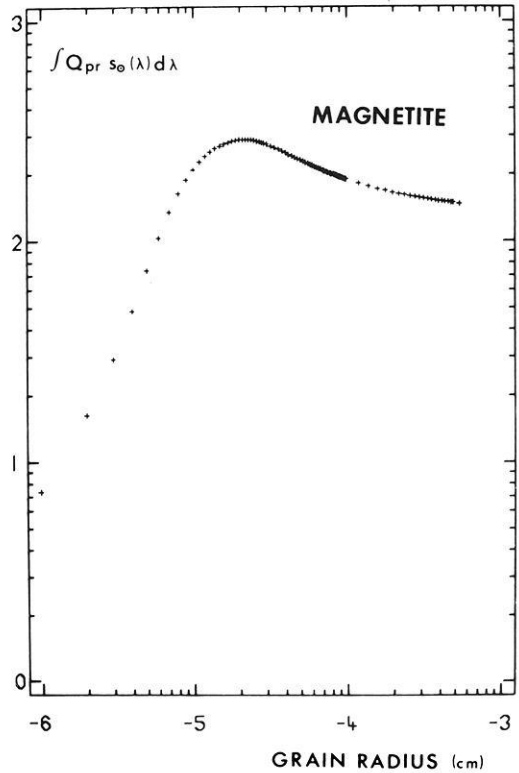


Fig. 2. Integral for radiation pressure for magnetite as a function of grain radius logarithmic scale)

by the Sun (M_{\odot}) on the dust grain (m). As both forces fall off with the square of the distance R from the Sun we can subtract the radiation pressure force from the gravitational force

$$F = -F_{\text{grad}} + F_{\text{rad}} = -F_{\text{grav}}(1 - \beta)$$

and can look at a particle as it moves in a gravitational potential, which is modified by a factor $(1 - \beta)$. The parameter β fully describing the particle properties with respect to this effective potential is given by

$$\beta = \frac{F_{\text{rad}}}{F_{\text{grav}}} = \frac{3 \cdot R_0^2}{4 c f M_{\odot}} \cdot \frac{1}{\rho \cdot r} \int_0^{\infty} Q_{\text{pr}} \cdot s_{\lambda} d\lambda$$

which is the ratio of the force due to gravitational attraction to the solar radiation pressure. It is independent of the distance of the particle from the sun and is essentially determined by the radius r and the density ρ of the particle.

The computer program which has been used to calculate the efficiency factors is described in detail in Giese et al. (1974). For the solar radiation flux, values given by Labs and Neckel (1970) have been used. In Figure 2 a typical curve for the efficiency factor for radiation pressure integrated over the solar radiation field is plotted for magnetite as a function of particle radius. β has been

Table 1

Material	References
Ice	Irvine and Pollack (1968)
Obsidian	Pollack et al. (1973)
Andesite	Pollack et al. (1973)
Quarz	Isobe (1975)
Olivine	Huffman (1976)
Magnetite	Steyer and Huffman (1976)

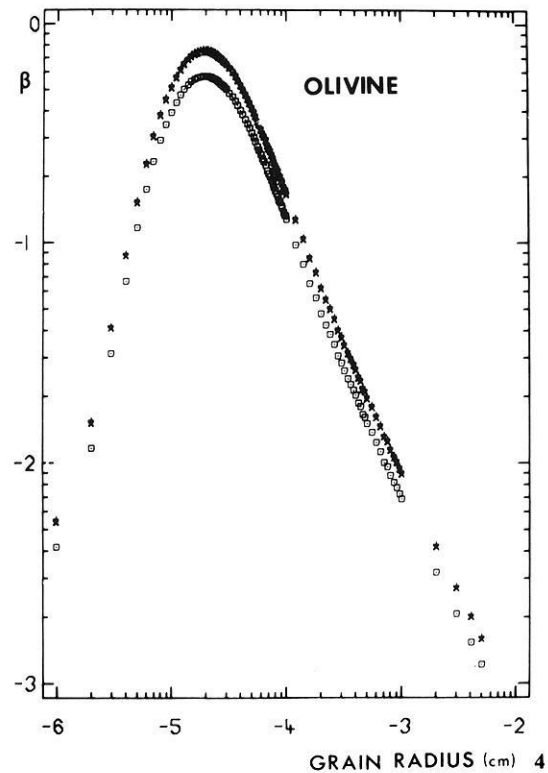
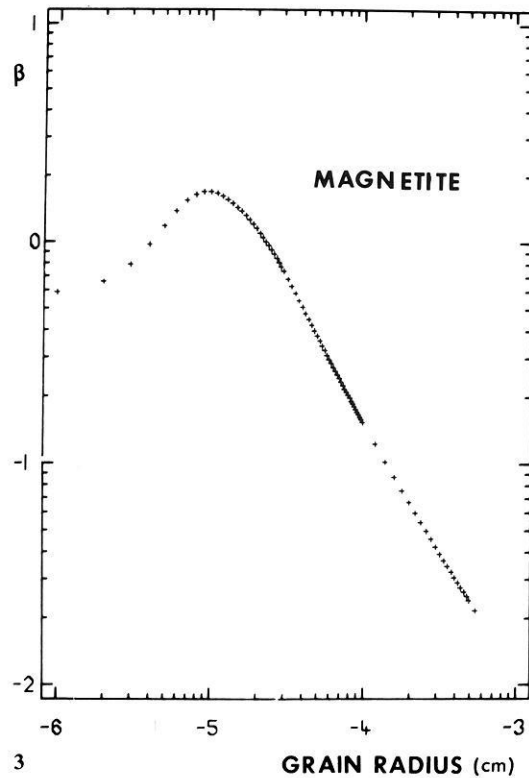


Fig. 3. The ratio β — in logarithmic scale — of the solar radiation pressure force to the solar gravitational force for magnetite spheres as a function of their radii ($\rho_{\text{magnetite}} = 5.2 \text{ g/cm}^3$)

Fig. 4. β values — in logarithmic scale — for olivine as a function of particle radius for different densities of the material ($\square = 4.39 \text{ g/cm}^3$, $\times = 3.4 \text{ g/cm}^3$, $- = 3.28 \text{ g/cm}^3$)

evaluated for different materials regarding the wavelength dependence of their complex indices of refraction. The integration was carried out for every value of the radius over the whole range of wavelengths from 0.1 to 100 μm .

The materials we used in our calculations and the references for their measured refractive indices are given in Table 1.

Figures 3 and 4 show two examples of the β -values for magnetite (Fig. 3) and olivine spheres (Fig. 4). The shape of both curves is very similar, with the maximum of β being at a grain radius of 0.2 microns. While in the case of olivine and the other materials the radiation pressure is not effective for very small particles ($<0.08\mu$), for submicron magnetite particles β is always greater 0.5, the critical limit for the particles to escape from the solar system (Dohnanyi, 1972). For larger particles ($>0.8\mu$) β drops off very sharply in all cases considered, so that the radiation pressure force is effective only for particles in a very narrow size interval and one should expect a cutoff size for small particles leaving the solar system on hyperbolic orbits (cf. Fig. 7 of the paper by Grün et al., this volume).

One should note, however, that these calculations have been based on the idealistic assumption of spherical particles and of refractive indices of pure materials using the density of the material as found on earth. In space we have to assume a rather "fluffy-type" material with much lower densities (ref. Giese, this volume), therefore the radiation pressure force on the particle can be much higher than the calculated β , as it is inversely proportional to the density of the particle. Further we have to consider radiation damage effects in the grains (Dratz and Michel, 1977), which yield higher absorption and lead to higher efficiency cross sections for radiation pressure.

3. Temperature Distribution

To determine the temperature distribution we look for the energy balance of a spherical particle in local thermodynamic equilibrium (LTE). This implies that the solar energy absorbed is balanced by the energy reemitted by the particle. To get a simple equation we assume that the particle will have the equilibrium temperature, which is acceptable since the sizes of the grains are so small that the heating is isotropic and heat flow by conduction inside the grain can be neglected. The energy absorbed by a spherical grain of radius r during one second is

$$r^2 \left(\frac{R_0}{R} \right)^2 \int_0^{2\pi} Q_{\text{abs}} [m(\lambda), x(\lambda)] s_\lambda d\lambda$$

where Q_{abs} is the efficiency factor for the absorption of radiation, s_λ again the solar radiation flux.

The energy reemitted by the grain is equal to

$$4 \pi r^2 \int_0^\infty Q_{\text{abs}} [m(\lambda), x(\lambda)] \pi B(\lambda, T_g) d\lambda$$

where $B(\lambda, T_g)$ is the Kirchhoff-Planck-function for a grain with temperature T_g .

We thus get for the equation to calculate T_g

$$\left(\frac{R_0}{R} \right)^2 \int_0^{2\pi} Q_{\text{abs}} s_\lambda d\lambda = 4 \int_0^\infty Q_{\text{abs}} \pi B(\lambda, T_g) d\lambda.$$

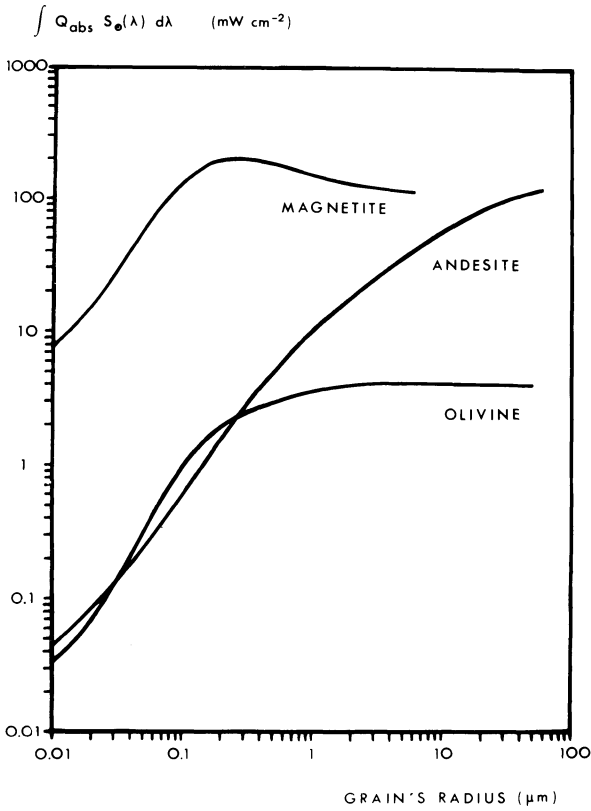


Fig. 5. Energy absorbed per unit area by interplanetary dust grains of different materials as function of grain size

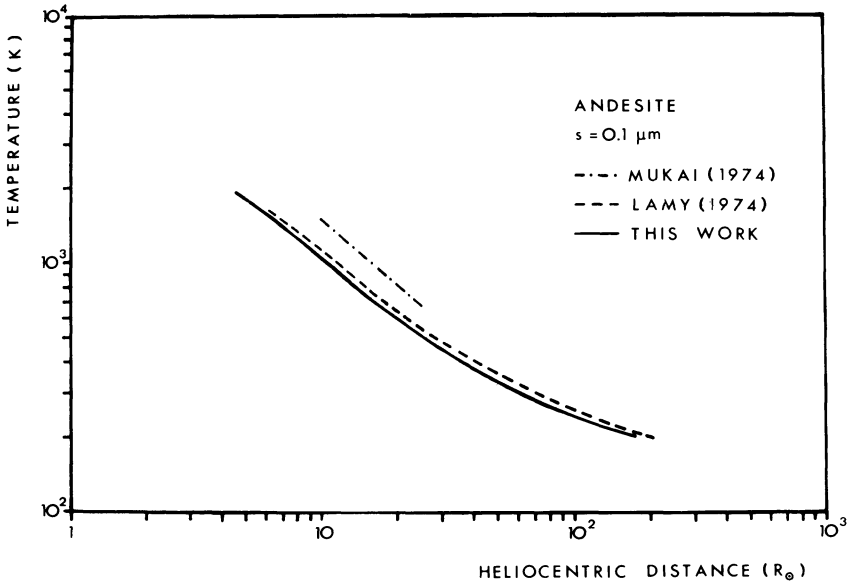


Fig. 6. Temperature of an andesite grain as a function of heliocentric distance. The dashed and dashed dotted lines give the results published by Lamy (1974) and Mukai (1974), respectively, for the same particle.

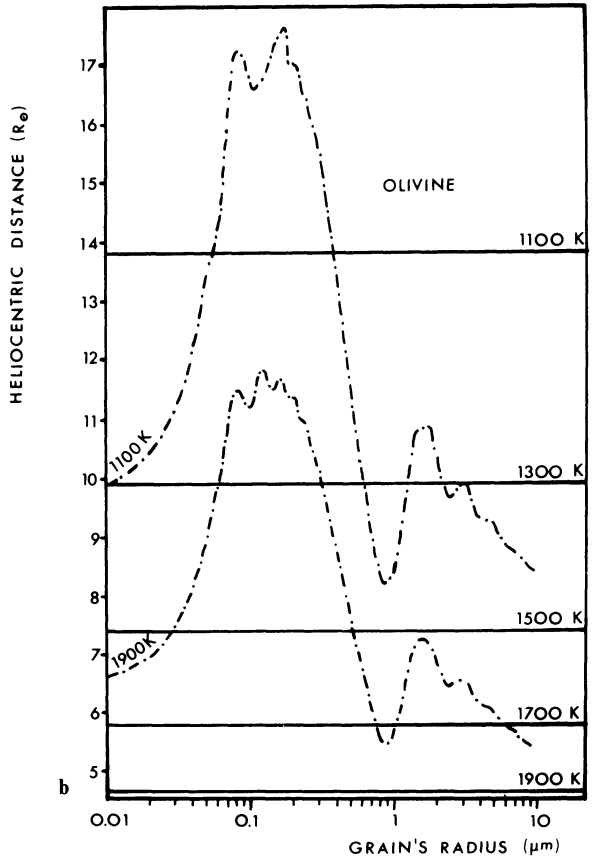
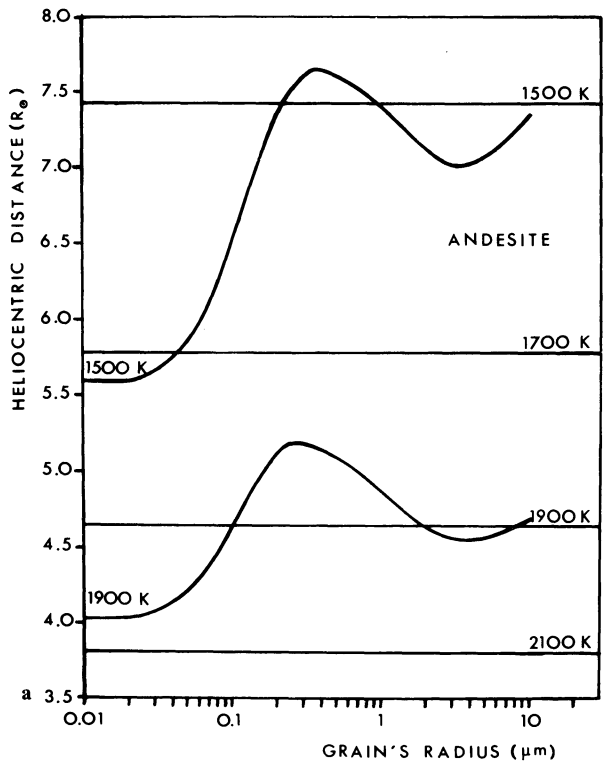


Fig. 7a and b. Temperatures of andesite and olivine grains in units of K are shown as functions of grain radius and heliocentric distance (in solar radii [R_{\odot}]). The straight parallel lines denote black body temperatures at each distance

This equation is very easy to solve for R ; we therefore take T_g as the parameter and evaluate the corresponding distance from the sun for a grain with the chosen temperature. The integral on the left-hand side of the equation gives the amount of energy per unit area absorbed by the particle. The dependence of this quantity on the size and the material of the particles is demonstrated in Figure 5.

The temperature of a $0.1 \mu\text{m}$ andesite particle as a function of its distance from the sun (in solar radii R_\odot) is plotted in Figure 6. For comparison values given by Mukai et al. (1974) and Lamy (1974) are also included in the diagram. The slight differences in the results are due to the higher accuracy in our computations and to the accurate values for the whole solar energy spectrum, whereas Mukai and Lamy take for certain intervals of the wavelengths a black body approximation for this spectrum (cf. Schwehm, 1976).

To give an idea what the temperature distribution looks like, we have plotted in Figure 7a and b the isothermals for andesite and olivine spheres as a function of grain radius. The distance from the sun, where the particle takes a distinct temperature is given in solar radii. The straight parallel lines give the distances, at which a black body would assume the temperatures indicated. If one takes into account the wavelength dependence of the refraction indices the temperature distribution becomes much more complicated than in the case of a black body approximation (temperature variations of the refraction indices were not considered). The two curves for 1500 K and 1900 K, respectively, give the distance from the sun at which a grain of a certain size will have this temperature, e.g. a $0.01 \mu\text{m}$ particle has a temperature of 1900 K at $4.0 R_\odot$ from the sun, a $0.3 \mu\text{m}$ particle already at $5.2 R_\odot$, but a $10 \mu\text{m}$ grain is again colder and reaches this temperature at $4.7 R_\odot$.

Much more striking is the temperature behaviour of olivine, where the deviation from a black body approximation is very significant (Fig. 7b). In this case the general statement given by Lamy (1974), that the heliocentric distance corresponding to a given temperature tends to increase with increasing grain radius, does not account for the important variation in the temperature distribution for the submicron grains. In the case of olivine heating is most effective for the same size range for which the force due to radiation pressure is highest. This fact plays an important role in the discussion of the orbits and lifetimes of submicron particles and for the existence of a dust free zone around the sun.

Acknowledgements. This work was supported by the Bundesminister für Forschung und Technologie by grant WRS 0108.

References

- Debye, P.: Der Lichtdruck auf Kugeln von beliebigem Material. *Ann. der Physik* **335**, 57–136, 1909
- Dohnanyi, J.C.: Interplanetary objects in review: Statistics of their masses and dynamics. *Icarus* **17**, 1–48, 1972
- Drapatz, S., Michel, K.W.: Optical and thermal properties of perturbed interstellar grains. Preprint, to be published in *Astron. and Astrophys.*
- Giese, R.H., Schwehm, G., Zerull, R.: Grundlagenuntersuchungen zur Interpretation extraterrestrischer Zodiakallichtstreuungen und Lichtstreuung von Staubpartikeln verschiedener Formen. BMFT-FB W 74–10, 1974

- Giese, R.H.: Interpretation of the optical properties of interplanetary dust. *J. Geophys.* **42**, 705–716 1977
- Grün, E., Fechtig, H., Kissel, J.: Cosmic dust measurements by space probe experiment. In: Project HELIOS (H. Porsche, ed.), pp. 175–194, BMFT, FB W 74–08, 1974
- Grün, E., Fechtig, H., Kissel, J., Gammel, P.: Micrometeoroid data from the first two Orbits of HELIOS I. *J. Geophys.* **42**, 717–726, 1977
- Huffman, D.R.: Private communication, 1976
- Irvine, W.M., Pollack, J.B.: Infrared optical properties of water and ice spheres. *Icarus* **8**, 324–360, 1968
- Isobe, S.: *Ann. Tokyo Astron. Obs., Second Series* **14**, 141, 1975
- Labs, D., Neckel, H.: Transformation of the Absolute Solar Radiation Data Into the “International Practical Temperature Scale of 1968”. *Solar Physics* **15**, 79–87, 1970
- Lamy, Ph. L.: Interaction of interplanetary dust grains with the solar radiation field. *Astron. and Astrophys.* **35**, 197–207, 1974
- Mukai, T., Mukai, S.: Temperature and motion of grains in interplanetary space. *Publ. Astron. Soc. Japan* **25**, 481–488, 1973
- Pollack, I.B., Toon, O.B., Khare, B.N.: Optical properties of some terrestrial rocks and glasses. *Icarus* **19**, 372–389, 1973
- Robertson, H.P.: Dynamical effects of radiation in the solar system. *Monthly Notices R.A.S.* **97**, 423–438, 1937
- Schmidt, Th., Elsässer, H.: Dynamics of submicron particles ($a < 10^{-5}$ cm) in interplanetary space. In: *The zodiacal light and the interplanetary medium* (J.L. Weinberg, ed.), NASA SP-150, Washington, pp. 287–289, 1967
- Schwem, G.: Radiation pressure on interplanetary dust particles. In: *Interplanetary dust and zodiacal light* (H. Elsässer, H. Fechtig, eds.), *Lecture notes in physics*, Vol. 48, pp. 459–463. Berlin-Heidelberg-New York: Springer 1976
- Steyer, T.R., Huffman, D.R.: Private communication, 1976
- Wyatt, S.P., Whipple, F.L.: The Poynting-Robertson effect on meteor orbits. *Astrophys. J.* **111**, 134–141, 1950

Received February 3, 1977; Revised Version March 30, 1977

Micrometeoroid Orbits Observable by the Helios Micrometeoroid Detector (E 10)

K.D. Schmidt

Bereich Extraterrestrische Physik, Ruhr-Universität Bochum,
Universitätsstraße 150, D-4630 Bochum, Federal Republic of Germany

Abstract. Sensor characteristics of the micrometeoroid detector (experiment 10) and Helios' spin and eccentric orbital motion give rise to selection effects. In this paper we discuss the influence of the spacecraft's motion on the computed osculating orbital elements (semimajor axis, eccentricity) of detectable dust particles. This constitutes a first step in the statistical treatment of dust orbits measured by Helios.

Key words: Interplanetary dust – Dust orbits.

The micrometeoroid detectors on board Helios detect dust particles in the interplanetary space along the spacecraft's orbit around the sun (Grün et al., 1976; Grün et al., 1977). The detectors are able to measure mass, speed, direction, chemical composition and charge of these particles. Therefore, in addition to information about spatial distribution, it is possible to compute orbital elements (here: semimajor axis and eccentricity) of the dust particles. But this is true only in a certain impact-velocity-range, where mass- and velocity-information can be separated. For this separation the upper impact velocity value is about $100 \text{ km} \cdot \text{s}^{-1}$, and it decreases when the mass of the impacting particle increases (Dietzel et al., 1973). For velocities exceeding $100 \text{ km} \cdot \text{s}^{-1}$ only direction and composition are measurable. Both the mass- and velocity-information are necessary for orbit calculations. The orbital parameters may be calculated from the heliocentric location of the impact and from magnitude and direction of the velocity. These parameters change when the particle interacts with the solar electromagnetic radiation (radiation pressure, Poynting-Robertson-effect). The magnitude of these interactions depends, amongst other things (refractive index etc.) on the particle's radius (Schwehm, 1976) which may be roughly calculated by the measured mass and an assumed density.

The sum of the measured impact velocity (\mathbf{v}_{imp}) and Helios' orbital velocity (\mathbf{v}_{Hel}) yields the heliocentric dust velocity (\mathbf{v}_d) (see Fig. 1). Velocities due to the space probe's spin can be neglected here because they are about 3 orders of magnitude below the other velocities.

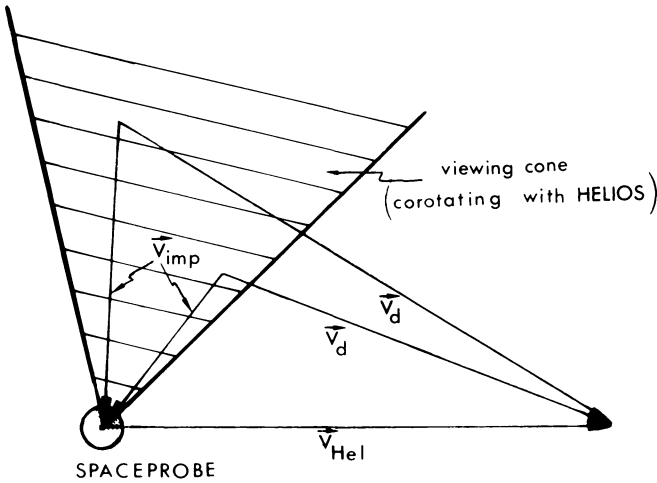


Fig. 1. Two examples of observable dust velocities (situation at impact)

All the dust velocities that can be observed during one spin period at one point on Helios' orbit and for which v_{imp} is less than or equal to $100 \text{ km} \cdot \text{s}^{-1}$ are transformed into osculating orbital elements, here: semimajor axis a and eccentricity e . This is done by means of the energy integral and Kepler's second law. The combinations of semimajor axis and eccentricity corresponding to the observable dust velocities make up areas in the $(1/a, e)$ -plane, where by definition the semimajor axis of hyperbolic orbits ($e > 1$) is counted negative. Elliptical orbits occur for $0 < e < 1$, whereas $e = 0$ gives circular and $e = 1$ parabolic and degenerated orbits.

v_d perpendicular to the Sun-Helios line yields the smallest eccentricity values for $e < 1$, whereas the opposite is true for eccentricities greater than one. v_d parallel to this line results in degenerated orbits.

Figure 2 shows regions in the $(1/a, e)$ -plane which are observable by the detector at different heliocentric distances r . These are calculated for $|v_{imp}| \leq 100 \text{ km} \cdot \text{s}^{-1}$, and one example for another impact velocity limit is given.

The shape and size of these regions are affected by various parameters such as inclination i and radiation pressure β . For simplicity the following calculations are done in the ecliptic plane, but calculations of inclined orbits (dashed line in Fig. 2) or for the north or south viewing sensor respectively are similar.

For impact velocities up to $100 \text{ km} \cdot \text{s}^{-1}$ and for $\beta = 0$ the regions in Figure 2 are surrounded by solid lines. These regions are the greatest ones, because in the ecliptic plane and for $|v_{imp}| = 100 \text{ km} \cdot \text{s}^{-1}$ the highest dust velocities are measurable. The dotted line shows the decrease in the size of the regions, when for the upper impact velocity limit $50 \text{ km} \cdot \text{s}^{-1}$ ($r = 0.6473 \text{ AU}$) is assumed.

Figure 3 gives an idea of radiation pressure effects. Here the parameter is β , which is the ratio of radiation pressure and gravitational force acting on a dust particle. The increase of the regions with increasing β is evident.

Due to the upper impact velocity limit and due to the spin and orbital motion of Helios, not all dust velocities can be observed. Examples are given in

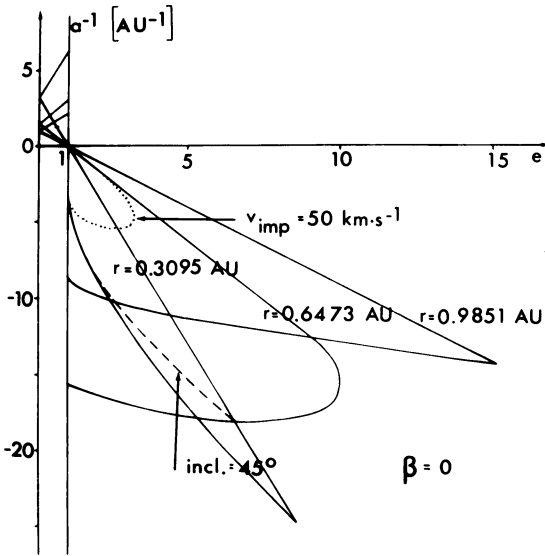


Fig. 2. Different observable regions in the $1/a, e$ -plane

Figure 4, where relative observing times are given for different velocities at various distances from the sun. Here a viewing cone of 60° was assumed. Therefore a weighting of all the points in the $\frac{1}{a}-e$ -plane has to be carried out, so that these points are weighted with respect to their observing times. The different observing times of dust velocities now correspond to a weighting along the $1/a$ -axis, whereas selections of the angle between the sun-Helios line and the dust velocity transform into a weighting along the e -axis. The weighting over all the regions in the $(1/a, e)$ -plane is achieved by taking into account the time Helios spends in the different distance intervals from the sun.

The above mentioned effects are global ones, whereas local effects, that is the angular sensibility of the sensors, play a role when starting backward calculations of dust orbits from measured impacts with a given position and a given viewing direction.

As pointed out earlier, heavier particles are detectable only at lower impact velocities. For example, the mass of an incoming particle has to be greater than $3 \cdot 10^{-13} \text{ g}$ for velocities less than $10 \text{ km} \cdot \text{s}^{-1}$. In this group we expect particles on bounded orbits spiralling towards the sun due to the Poynting-Robertson-effect. These particles will have orbital elements in the region for $e < 1$ of the $(1/a, e)$ -plane. For smaller particles mainly undergoing radiation pressure (β -meteoroids) we expect higher velocities, because they are on hyperbolic or highly eccentric orbits. Therefore, as far as we know, relevant regions in the $\frac{1}{a}-e$ -plane are covered by the micrometeoroid sensors on board the two Helios-probes.

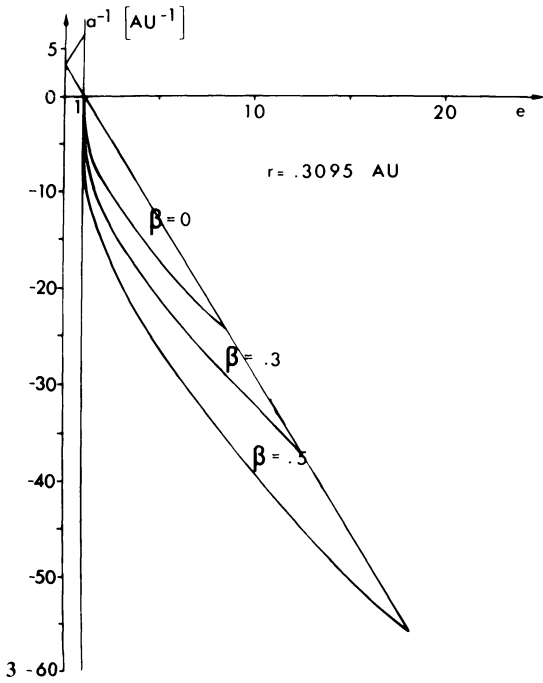
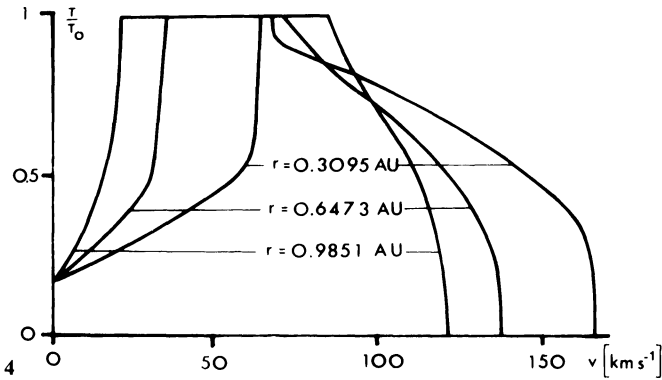


Fig. 3. Change of $1/a$, e -regions due to radiation pressure β

Fig. 4. Relative observing times of dust velocities at different heliocentric distances r (viewing cone of 60°)



All the above mentioned statistics are the first step when starting a dynamic model of the interplanetary dust cloud with the orbits of the dust particles detected by the micrometeoroid experiment. Further analysis will be a consideration of the actual data, taking into account the described weighting in order to produce a picture of the orbital elements in the dust cloud similar to studies of meteors done before (Southworth and Sekanina, 1973).

References

- Dietzel, H., Eichhorn, G., Fechtig, H., Grün, E., Hoffmann, H.-J., Kissel, J.: The HEOS 2 and HELIOS micrometeoroid experiments. *J. Phys. E.: Sc. Instr.* **6**, 209–217, 1973
- Grün, E., Fechtig, H., Kissel, J., Gammelín, P.: Micrometeoroid data from the first two orbits of Helios 1. *J. Geophys.*, **42**, 717–726, 1977
- Grün, E., Kissel, J., Fechtig, H., Gammelín, P., Hoffmann, H.J.: Preliminary results of the micrometeoroid experiment on board Helios A. In: *Interplanetary dust and zodiacal light*, H. Elsässer, H. Fechtig, eds., *Lecture Notes Phys.* **48**, pp. 159–163. Berlin-Heidelberg-New York: Springer 1976
- Schwehm, G.: Radiation pressure on interplanetary dust particle. In: *Interplanetary dust and zodiacal light*, H. Elsässer, H. Fechtig, eds., *Lecture Notes Phys.* **48**, pp. 459–463. Berlin-Heidelberg-New York: Springer 1976
- Southworth, R.B., Sekanina, Z.: Physical and dynamical studies of meteoroids. NASA Contractor Report CR-2316, 1973

Received February 3, 1977; Revised Version May 9, 1977